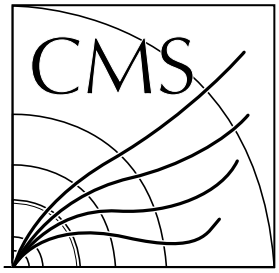

CERN/LHCC 98–6
CMS TDR 5
15 April 1998

CMS

Tracker Technical Design Report

CMS Tracker		
Project Manager	**Technical Coordinator**	**Resource Manager**
Rino Castaldi INFN Pisa Rino.Castaldi@pi.infn.it	Patrice Siegrist CERN Patrice.Siegrist@cern.ch	Jean-Eudes Augustin IPN Lyon Augustin@in2p3.fr
Chairperson Inst. Board: Günter Flügge, Aachen III B, Fluegge@physik.rwth-aachen.de		

CMS Spokesperson	CMS Technical Coordinator
Michel Della Negra CERN Michel.Della.Negra@cern.ch	Ernst Radermacher CERN Ernst.Radermacher@cern.ch

TDR Editorial Board

A. Cattai, V. Karimäki, M. Mannelli, P. Siegrist

Chapter Editors

H. Breuker, A. Caner, R. Castaldi, A. Cattai, K. Freudenreich, G. Hall,
R. Horisberger, M. Huhtinen, V. Karimäki, M. Mannelli, P. Siegrist

Acknowledgements

The CMS Tracker Community wishes to thank all the technical staff involved in the design, testing and prototyping work for their invaluable contributions.

We wish to express our thanks to our LHCC Referees who closely followed our work in the last several years with continuous support, advice and constructive criticism:
R. Cashmore, E. Iarocci, G. Wormser and J. Engelen, J. Carr, C. Damerell,
H. Kolanoski, S. Komamiya, A. Read and G. Zech.

Special thanks are due to our CMS internal Reviewers D. Imrie, Ph. Bloch and
H. Newman for substantial help and critical constructive contributions to this work.

We also thank K. Aspola, M. Azeglio, D. Labrousse, G. Martin, M.C. Pelloux and
A. Vignes of the CMS Secretariat for precious help given during all phases of this work.

We wish to thank M. Jouhet and all the staff from the DTP centre for their help in processing the text of this report. Special thanks to I. Canon and S. Leech O'Neale.

The continuous support and friendly cooperation of the CMS management and of our colleagues from the other CMS sub-detectors are warmly acknowledged.

Cover Page

LO INFERNO
Sergio Cittolin pinxit

CMS Collaboration

Yerevan Physics Institute, Yerevan, ARMENIA
G. Bayatian, N. Grigorian, V. Khachatrian, A. Margarian, A. Sirunyan, S. Stepanian

Institut für Hochenergiephysik der ÖAW, Wien, AUSTRIA
W. Adam, R. Frühwirth, J. Hrubec, M. Krammer, N. Neumeister, H. Pernegger, M. Pernicka, P. Porth, D. Rakoczy, H. Rohringer, L. Rurua[1], F. Szoncsó, A. Taurok, G. Walzel, C.-E. Wulz

Byelorussian State University, Minsk, BELARUS V. Petrov, V. Prosolovich

Research Institute for Nuclear Problems, Minsk, BELARUS
V. Baryshevsky, A. Fedorov, M. Korzhik, O. Missevitch

National Centre for Particle and High Energy Physics, Minsk, BELARUS
I. Akushevich, N. Chekhlova, V. Chekhovsky, O. Dvornikov, I. Emelianchik, A. Khomich, V. Kolpaschikov, A. Kurilin, V. Kuvshinov, A. Litomin, V. Mossolov, A. Panfilenko, A. Raspereza, S. Reutovich, N. Shumeiko, A. Solin, R. Stefanovich, V. Strazhev, S. Sushkov, S. Vetokhin, Yu. Yurenya, V. Zalessky, F. Zyazyulya

Research Institute for Applied Physical Problems, Minsk, BELARUS
F. Ermalitsky, P. Kuchinsky, V. Lomako

Université Catholique de Louvain, Louvain-la-Neuve, BELGIUM
K. Bernier, D. Favart, J. Govaerts, G. Grégoire

Université de Mons-Hainaut, Mons, BELGIUM
I. Boulogne, E. Daubie, Ph. Herquet, R. Windmolders

Université Libre de Bruxelles, Brussels, BELGIUM
O. Bouhali, J. Sacton, J. Stefanescu, C. Vander Velde, P. Vanlaer

Universiteit Antwerpen (UIA), Antwerpen, BELGIUM
W. Beaumont, T. Beckers, J. De Troy, Ch. Van Dyck, F. Verbeure

Vrije Universiteit Brussel, Brussels, BELGIUM
O. Devroede, J. Lemonne, S. Tavernier, F. Udo, W. Van Doninck, L. Van Lancker, V. Zhukov

Institute for Nuclear Research and Nuclear Energy, BAS, Sofia, BULGARIA
T. Anguelov, G. Antchev[2], I. Atanasov, D. Bourilkov, L. Dimitrov, V. Genchev, G. Georgiev, P. Hristov, P. Iaydjiev, I. Ivanov, L. Penchev, V. Penev, A. Shklovskaja, G. Sultanov, I. Vankov

University of Sofia, Sofia, BULGARIA
C. Cheshkov, A. Gritskov, A. Jordanov, L. Litov, M. Mateev, P. Petev, V. Spassov, R. Tsenov, G. Velev

CERN, European Laboratory for Particle Physics, Geneva, [CERN]
D. Abbaneo, V. Arbet-Engels, P. Aspell, E. Auffray, P. Baillon, D. Barney, W. Bell, G. Benefice, L. Bertolotto, D. Blechschmidt, Ph. Bloch, B. Borgia[3], M. Bosteels, J. Bourotte[4], M. Bozzo, S. Braibant, H. Breuker, A. Calvo[5], D. Campi, A. Caner, E. Cano, A. Cattai, G. Cervelli, J. Christiansen, S. Cittolin, B. Curé, C. D'Ambrosio, S. Da Mota Silva[6], D. Dattola, Th. de Visser, D. Delikaris, M. Della Negra, N. Demaria[7], A. Desirelli, G. Dissertori, A. Elliott-Peisert, L. Feld, H. Foeth, M. Freire[6], A. Fucci, A. Furtjes, F. Gagliardi, J.C. Gayde, H. Gerwig, K. Gill, W. Glessing, E. Gonzalez Romero[8], R. Goudard, J.P. Grillet, J. Gutleber, F. Hahn, R. Hammarstrom, M. Hansen, M. Hansroul, A. Hervé, M. Hoch, K. Holtman, M. Huhtinen, S. Ilie, V. Innocente, W. Jank, P. Jarron, F. Jensen, Th. Kachelhoffer, K. Kershaw, M. Kloimwieder[9], Z. Kovacs, A. Kruse, T. Ladzinski, Ch. Lasseur, J.M. Le Goff, M. Lebeau, P. Lecoq, V. Lefébure, F. Lemeilleur, M. Letheren, P. Liénard, Ch. Ljuslin, B. Lofstedt, R. Loos, R. Mackenzie, R. Malina, M. Mannelli, E. Manola-Poggioli, A. Marchioro, J.M. Maugain, R. McClatchey[10], F. Meijers, A. Merlino, Th. Meyer, C. Mommaert, P. Nappey, T. Nyman, A. Onnela, M. Oriunno, L. Orsini, S. Paoletti, G. Passardi, D. Peach, F. Perriollat, E. Pesen[11], P. Petagna, M. Pimiä, R. Pintus, B. Pirollet, A. Placci, J.P. Porte, H. Postema, J. Pothier, M.J. Price, A. Racz, E. Radermacher, S. Reynaud, R. Ribeiro, H. Rick, J. Roche, P. Rodrigues Simoes Moreira, L. Rolandi, E. Rosso, D. Samyn, J.C. Santiard, R. Schmidt,

B. Schmitt, M. Schröder, P. Siegrist, L. Silvestris[12], N. Sinanis, P. Sphicas[13], G. Stefanini, B.G. Taylor, T. Toifl, A. Tsirou, Ch. Tully[14], P. Van der Stok, J. Varela[15], F. Vasey, T.S. Virdee[16], P. Wertelaers, T. Wikberg, M. Wilhelmsson, I.M. Willers, G. Wrochna

Institute of High Energy Physics, Beijing, CHINA, PR
G.M. Chen, Y. Chen, B.S. Cheng, Y.F. Gu, Y.N. Guo, J.T. He, B.N. Jin, Z.J. Ke, J. Li, W.G. Li, X.N. Li, J. Liu, B.W. Shen, C.Q. Shen, P.R. Shen, X.Y. Shen, H.Y. Sheng, H.Z. Shi, X.F. Song, Y.Y. Wang, Y.R. Wu, R.S. Xu, B.Y. Zhang, S.Q. Zhang, W.R. Zhao, J.P. Zheng, G.Y. Zhu

University for Science and Technology of China, Hefei, Anhui, CHINA, PR
Q. An, Z. Bian, C. Li, Ch. Shi, L. Sun, X. Wang, Z. Wang, J. Wu, S. Ye, Z. Zhang

Peking University, Beijing, CHINA, PR
Y. Ban, J.E. Chen, H. Liu, S. Liu, B. Lou, S. Qian, Y. Ye

Technical University of Split, Split, CROATIA
N. Godinovic, M. Milin[17], I. Puljak, I. Soric, M. Stipcevic[17], J. Tudoric-Ghemo

University of Split, Split, CROATIA
Z. Antunovic, M. Dzelalija

University of Cyprus, Nicosia, CYPRUS
A. Hasan, P.A. Razis, A. Vorvolakos

Charles University, Praha, CZECH REPUBLIC
M. Finger, T. Kracikova, M. Slunecka, M. Sulc

Czech Technical University, Praha, CZECH REPUBLIC
M. Finger (Jr), M. Laub, R. Nova'k, M. Vognar, J. Zicha

Institute of Computing Machines, Praha, CZECH REPUBLIC
M. Tomasek

Institute of Scientific Instruments, CAS, Brno, CZECH REPUBLIC
J. Dupak, A. Srnka

Nuclear Research Institute, Rez, CZECH REPUBLIC
A. Janata

Institute of Chemical Physics and Biophysics, Tallinn, ESTONIA
R. Aguraiuja, A. Hall, E. Lippmaa, J. Subbi

Department of Physics, University of Helsinki, Helsinki, FINLAND
S. Lehti, T. Lindén

Helsinki Institute of Physics, Helsinki, FINLAND
N. Eiden, C. Eklund, A. Heikkinen, A. Honkanen, V. Karimäki[2], R. Kinnunen, J. Klem, M. Kotamäki, T. Mäenpää, E. Pietarinen, S. Ruotsalainen, H. Saarikoski, K. Skog, J. Tuominiemi

Department of Physics, University of Jyväskylä, Jyväskylä, FINLAND
J. Äystö, R. Julin, V. Ruuskanen

Digital and Computer Systems Laboratory, Tampere University of Technology, Tampere, FINLAND
J. Niittylahti, O. Vainio

Department of Physics & Microelectronics Instrumentation Laboratory, University of Oulu, Oulu, FINLAND
A. Keränen, L. Palmu, M. Piila, K. Remes, R. Skantsi, E. Suhonen, T. Tuuva

Laboratory of Advanced Energy Systems, Helsinki University of Technology, Helsinki, FINLAND
P. A. Aarnio

Laboratoire de Physique Nucléaire des Hautes Energies, Ecole Polytechnique, IN2P3-CNRS, Palaiseau, FRANCE
J. Badier, M. Bercher, L. Buiron, A. Busata, Ph. Busson, D. Chamont, C. Charlot, B. Chaurand, A. Debraine, L. Dobrzynski, O. Ferreira, K. Geun Beom, A. Heurtel, H. Hillemanns, A. Karar, L. Kluberg, D. Lecouturier, P. Matricon, G. Milleret, Ph. Miné, P. Paganini, P. Poilleux, A. Romana, R. Tanaka, J.-C. Vanel, C. Violet

Laboratoire d'Annecy-le-Vieux de Physique des Particules, IN2P3-CNRS, Annecy-le-Vieux, FRANCE
Y. Baek, G. Bassompierre, G. Bohner, J. Ditta, O. Drobychev, M. Forlen, J.P. Guillaud, J. Lecoq, T. Le Flour, S. Lieunard, M. Maire, J.-P. Mendiburu, S. Murray, P. Nedelec, L. Oriboni, J.P. Peigneux, M. Schneegans, D. Sillou, J.M. Thenard, J.P. Vialle

DSM/DAPNIA, CEA/Saclay, Gif-sur-Yvette, FRANCE
M. Anfreville, P. Besson, P. Bonamy, E. Bougamont, R. Chipaux, V. Da Ponte, M. De Beer, P. De Girolamo, M. Dejardin, D. Denegri, J.L. Faure, M. Geleoc, F.X. Gentit, A. Givernaud, Y. Lemoigne, E. Locci, J.P. Pansart, J. Rander, Ph. Rebourgeard, J.M. Reymond, F. Rondeaux, A. Rosowsky, P. Roth, P. Verrecchia, G. Villet

Institut de Recherches Subatomiques, IN2P3-CNRS-ULP Strasbourg, LEPSI Strasbourg, UHA Mulhouse, FRANCE
F. Anstotz, Y. Benhammou, G. Berges, J.D. Berst, J.M. Brom, F. Charles, J. Coffin, J. Croix, F. Drouhin, W. Dulinski, H. Eberlé, J.C. Fontaine, W. Geist[18], U. Goerlach, J.M. Helleboid, Y. Hu, D. Huss, F. Jeanneau, P. Juillot, A. Lounis, J. Michel, Ch. Racca, Y. Riahi, I. Ripp, Ph. Schmitt, J.P. Schunck, B. Schwaller, J.L. Sohler, T. Todorov, R. Turchetta, A. Zghiche

Institut de Physique Nucléaire de Lyon, IN2P3-CNRS, Univ. Lyon I, Villeurbanne, FRANCE
M. Ageron, P. Antilogus, J.E. Augustin, M. Bedjidian, D. Bertini, V. Chorowicz, P. Cluzel, D. Contardo, P. Depasse, N. Djaoshvili, O. Drapier, L. Ducroux, M. Dupanloup, H. El Mamouni, J.-P. Ernenwein, J. Fay, R. Genre, N. Giraud, M. Goyot, R. Haroutounian, B. Ille, G. Jacquet, S. Katsanevas, P. Lebrun, Ch. Lemoine, N. Madjar, F. Martin, J.-P. Martin, H. Mathez, L. Mirabito, S. Muanza, M. Rebouillat, P. Sahuc, G. Smadja, S. Tissot, J.-P. Walder, F. Zach

High Energy Physics Institute, Tbilisi State University, Tbilisi, GEORGIA
N. Amaglobeli, Yu. Bagaturia, L. Glonti, V. Kartvelishvili, R. Kvatadze, D. Mzavia, T. Sakhelashvili, R. Shanidze

Institute of Physics, Academy of Science, Tbilisi, GEORGIA
I. Iashvili[19], A. Kharchilava[20], N. Roinishvili, V. Roinishvili

Humboldt-Universität zu Berlin, Berlin, GERMANY
Th. Hebbeker, S. Piperov

Institut für Experimentelle Kernphysik, Karlsruhe, GERMANY
P. Blüm, S. Chowdhury, W. de Boer, V. Drollinger, M. Feindt, E. Gregoriev, S. Heising, S. Junghans, K. Kärcher, D. Knoblauch, M. Kräber, R. Metri, A. Menchikov, Th. Müller, D. Neuberger, A. Pallares, H.J. Simonis, A. Theel, W.H. Thümmel, H. Wenzel, S. Weseler

RWTH, I. Physikalisches Institut, Aachen, GERMANY
Ch. Berger, W. Braunschweig, J. Breibach, W. Gu, W. Karpinski, Th. Kirn, T. Kubicki, Ch. Kukulies, K. Lübelsmeyer, D. Pandoulas, G. Pierschel, F. Raupach, C. Rente, D. Schmitz, A. Schultz von Dratzig, J. Schwenke, R. Siedling, O. Syben, F. Tenbusch, M. Toporowsky, W. Wallraff, B. Wittmer, W.J. Xiao

RWTH, III. Physikalisches Institut A, Aachen, GERMANY
K. Banicz, S. Bethke, O. Biebel, H. Faissner, H. Fesefeldt, D. Rein, H. Reithler[2], H. Schwarthoff, V. Sondermann, V. Tano, H. Teykal, M. Tonutti, J. Tutas, M. Wegner

RWTH, III. Physikalisches Institut B, Aachen, GERMANY
S. Bachmann, F. Beissel, K. Boffin, C. Camps, V. Commichau, G. Flügge, K. Hangarter, R. Ischebeck, J. Kremp, D. Macke, A. Novack, G. Otter, M. Petertill, O. Pooth, P. Schmitz, R. Schulte

Institute of Nuclear Physics "Demokritos", Attiki, GREECE
M. Barone, N. Dimitriou, G. Fanourakis, D. Fassouliotis, S. Harissopulos, E. Karvelas, P. Kokkinias, A. Kyriakis, D. Loukas, A. Markou, Ch. Markou, E. Saragas, I. Siotis, M. Spyropoulou-Stassinaki, S. Tzamarias, A. Vayaki, E. Zevgolatakos

University of Athens, Athens, GREECE
L. Resvanis

University of Ioánnina, Ioánnina, GREECE
A. Assimidis, V. Christofilakis, I. Evangelou, K. Kloukinas, N. Manthos, A. Pagonis, F.A. Triantis

KFKI Research Institute for Particle and Nuclear Physics, Budapest, HUNGARY
G. Bencze[2], A. Csilling, J. Ero[2], C. Hajdu, D. Horvath[21], D. Kiss, I. Manno, G. Odor, G. Pa'sztor, F. Sikler, A. Ster, L. Urban, G. Vesztergombi, P. Zalan, M. Zsenei

Kossuth Lajos University, Debrecen, HUNGARY
L. Baksay, T. Bondar, L. Brunel[2], S. Juhasz, G. Marian, S. Nagy, P. Raics, J. Szabo, Z. Szabo, S. Szegedi, Z. Szillasi, T. Sztaricskai, G. Zilizi

Institute of Nuclear Research ATOMKI, Debrecen, HUNGARY
G. Dajko, A. Fenyvesi, J. Molnar, J. Palinkas, D. Sohler, Z. Trocsanyi, J. Vegh

Bhabha Atomic Research Centre, Mumbai, INDIA
R.K. Chaudhury, M.D. Ghodgaonkar, S.B. Jawale, B. John, S.K. Kataria, R.S. Koppikar, A.K. Mohanty, S.V. Sastry, R.V. Srikantiah

Institute of Physics, Bhubaneswar, INDIA
D.P. Mahapatra, J. Maharana

Panjab University, Chandigarh, INDIA
S. Beri, T.K. Chaterjee, M. Kaur, J.M. Kohli, J.B. Singh

Tata Institute of Fundamental Research - EHEP, Mumbai, INDIA
T. Aziz, Sn.Banerjee[2], S.N. Ganguli, S.K. Gupta, A. Gurtu, M. Maity, K. Mazumdar, K. Sudhakar, S.C. Tonwar

Tata Institute of Fundamental Research - HECR, Mumbai, INDIA
B.S. Acharya, Sd. Banerjee, S. Dugad, M.R. Krishnaswamy, N.K. Mondal, V. S. Narasimham

University of Delhi South Campus, New Delhi, INDIA
T. Chand, J. Cherian, R.K. Shivpuri, V.K. Verma

Università di Bari e Sezione dell' INFN, Bari, ITALY
M. Abbrescia, M. Angarano, A. Bader[21], A. Colaleo, D. Creanza, M. De Palma, D. Diacono, L. Fiore, G. Iaselli, F. Loddo, G. Maggi, M. Maggi, B. Marangelli, S. My, S. Natali, S. Nuzzo, G. Pugliese, A. Ranieri, G. Raso, F. Romano, F. Ruggieri, G. Selvaggi, P. Tempesta, G. Zito

Università di Bologna e Sezione dell' INFN, Bologna, ITALY
A. Benvenuti, P. Capiluppi, F. Cavallo, M. Cuffiani, I. D'Antone, G.M. Dallavalle, F. Fabbri, P.L. Frabetti, G. Giacomelli, P. Giacomelli[22], C. Grandi, M. Guerzoni, S. Marcellini, P. Mazzanti, A. Montanari, F.L. Navarria, F. Odorici, A. Perrotta, A.M. Rossi, T. Rovelli, G. Siroli, G. Valenti

Università di Catania e Sezione dell' INFN, Catania, ITALY
S. Albergo, V. Bellini, D. Boemi, Z. Caccia, P. Castorina, S. Costa, L. Lo Monaco, R. Potenza, A. Tricomi, C. Tuve

Università di Firenze e Sezione dell' INFN, Firenze, ITALY
F. Becattini, U. Biggeri, E. Borchi, M. Bruzzi, S. Busoni, M. Capaccioli, G. Castellini, E. Catacchini, C. Civinini, R. D'Alessandro, E. Focardi, G. Landi, M. Lenzi, M. Meschini, G. Parrini, G. Passaleva, M. Pieri, S. Pirollo, S. Sciortino

Università di Genova e Sezione dell' INFN, Genova, ITALY
A. Carraro[2], P. Fabbricatore, S. Farinon, R. Musenich, C. Priano

Università di Padova e Sezione dell' INFN, Padova, ITALY
P. Azzi, N. Bacchetta, M. Benettoni, L. Berti[23], A. Bettini, D. Bisello, G. Busetto, A. Candelori, R. Carlin, A. Castro, S. Centro, P. Checchia, E. Conti, M. Da Rold, M. De Giorgi, A. De Min, U. Dosselli, C. Fanin, F. Gasparini, U. Gasparini, A. Giraldo, P. Guaita, I. Lippi, M. Loreti, G. Maron[23], G. Martignon, R. Martinelli, A.T. Meneguzzo, A. Paccagnella, M. Pegoraro, L. Pescara, P. Ronchese, A. Sancho Daponte, P. Sartori, L. Stanco, I. Stavitski, N. Toniolo[23], E. Torassa, L. Ventura, S. Ventura, G. Vedovato[23], P. Zotto[24], G. Zumerle

Università di Pavia e Sezione dell' INFN, Pavia, ITALY
S. Altieri, V. Arena, G. Belli, G. Bonomi, G. Gianini, M. Merlo, S.P. Ratti, C. Riccardi, L. Viola, P. Vitulo

Università di Perugia e Sezione dell' INFN, Perugia, ITALY
G. Anzivino, E. Babucci, G.M. Bilei, P. Cenci, B. Checcucci, P. Ciampolini, P. Lariccia, Y. Li, P. Lubrano, G. Mantovani, A. Nappi, D. Passeri, P. Placidi, A. Santocchia, L. Servoli, M. Valdata, Y. Wang

Università di Pisa e Sezione dell' INFN, Pisa, ITALY
F. Angelini, G. Bagliesi[2], A. Bardi, A. Basti, F. Bedeschi, S. Belforte, R. Bellazzini[2], G. Bisogni, L. Borrello, F. Bosi, C. Bozzi, P.L. Braccini, A. Brez, R. Carosi, R. Castaldi, U. Cazzola, G. Chiarelli, M. Chiarelli, V. Ciulli, M. D'Alessandro Caprice, M. Dell'Orso, R. Dell'Orso, S. Donati, S. Dutta, A. Frediani, A. Gaggelli, S. Galeotti, P. Giannetti, A. Giassi, L. Latronico, F. Ligabue, D. Lucchetti, N. Lumb, G. Magazzu, M.M. Massai, E. Meschi, A. Messineo, O. Militaru, F. Morsani, F. Palla, A. Papanestis, G. Punzi, F. Raffaelli, R. Raffo, L. Ristori, F. Rizzo, G. Sanguinetti, G. Sguazzoni, G. Spandre, M. Spezziga, F. Spinella, A. Starodumov, A. Talamelli, R. Tenchini, G. Tonelli, A. Toropin, E. Troiani, C. Vannini, R. Ventola, A. Venturi, P.G. Verdini, Z. Xie

Università di Roma I e Sezione dell' INFN, Roma, ITALY
S. Baccaro[25], L. Barone, F. Cavallari, I. Dafinei, G. De Canio[25], F. De Notaristefani, M. Diemoz, A. Festinesi[25], E. Leonardi, A. Leone, E. Longo, M. Mattioli, M. Montecchi[25], G. Organtini, M. Puccini[25], E. Valente

Università di Torino e Sezione dell' INFN, Torino, ITALY
M. Arneodo, F. Bertolino, M. Bigi, R. Cirio, M. Costa, M.I. Ferrero, S. Maselli, E. Migliore, V. Monaco, C. Peroni, M.C. Petrucci, A. Romero, R. Sacchi, A. Solano, A. Staiano, A. Vitelli

Chonnam National University, Kwangju, KOREA
H.I. Jang, J.Y. Kim, T.I. Kim, I.T. Lim

Dongshin University, Naju, KOREA
M.Y. Pac

Seonam University, Namwon, KOREA
S.J. Lee

Wonkwang University, Iksan, KOREA
S.Y. Bahk

Gyeongsang National University, Jinju, KOREA
S.H. Chung, I.G. Park, C.S. Yoon

Korea University, Seoul, KOREA
B.S. Hong, S.J. Hong, Y.S. Kim, D.H. Lee, K.S. Lee, S.K. Park, K.S. Sim

Cheju National University, Cheju, KOREA
Y.J. Kim

Chungbuk National University, Chongju, KOREA
Y.U. Kim

Kangwon National University, Chunchon, KOREA
S.K. Nam

Kon-Kuk University, Seoul, KOREA
J.T. Rhee

Seoul National University of Education, Seoul, KOREA
D.G. Koo

Pohang University of Science and Technology, Pohang, KOREA
G.N. Kim

Kyungpook National University, Taegu, KOREA
H. Jeon, D. Kim, W.Y. Kim, I.H. Park, D. Son

Kangnung National University, Kangnung, KOREA
J.S. Chai, K.S. Kang, D.S. Kim, D.W. Kim, S.C. Lee

Quaid-I-Azam University, Islamabad, PAKISTAN
P. Hoodbhoy, A. Niaz, I.E. Qureshi, K.N. Qureshi

Ghulam Ishaq Khan Institute of Engineering Sciences and Technology, Topi, PAKISTAN*
J. Ahmad, I.U. Awan, N. Iftihkhar, A. Khan, C. Krey, A.J. Michel, M.U. Mirza, A. Muhammad

Institute of Experimental Physics, Warsaw, POLAND
M. Cwiok, W. Dominik, A. Fengler, M. Kazana, M. Konecki, J. Krolikowski, I. Kudla, P. Majewski, K. Pozniak

Soltan Institute for Nuclear Studies, Warsaw, POLAND
R. Gokieli, M. Gó' rski, P. Zalewski

Laboratório de Instrumentação e Física Experimental de Partículas, Lisboa, PORTUGAL
C. Almeida[26], J. Augusto[26], P. Bordalo, M. Calha[26], A. Chichkov[26], J. Da Silva, O. Dias[26], J. Gomes, J. Martins[26], J. Morgado, R. Nobrega, S. Ramos, H. Sarmento[26], S. Silva, I. Teixeira[26], J. Teixeira[26], G. Varner, I. Videira[26]

Budker Institute for Nuclear Physics, SB RAS, Novosibirsk, RUSSIA
V. Aulchenko, A. Bondar, A. Buzulutskov, S. Eidelman, V. Nagaslaev, L. Shekhtman, V. Sidorov, A. Tatarinov, V. Titov

Institute for High Energy Physics, Protvino, RUSSIA
V. Abramov, I. Azhgirey, S. Bitioukov, A. Dolgopolov, S. Donskov, A. Dyshkant, V. Evdokimov, P. Goncharov, A. Gorin, A. Inyakin, V. Katchanov, V. Khodyrev, A. Kondashov, A. Korablev, Y. Korneev, A. Kostritskii, A. Krinitsyn, V. Kryshkin, A. Kuznetsov, I. Manuilov, V. Medvedev, M. Oukhanov, D. Patalakha, V. Petrov, V.V. Rykalin, P. Semenov, P. Shagin, A. Singovsky[27], V. Solovianov, V. Sougonyaev, A. Surkov, A. Sytin, S. Tereschenko, S. Troshin, L. Turchanovich, N. Tyurin, A. Uzunian, A. Volkov, A. Zaitchenko

Institute for Nuclear Research, RAS, Moscow, RUSSIA
G. Atoyan, V. Bolotov, R. Djilkibaev, S. Gninenko, N. Goloubev, E. Gushin, M. Kirsanov, V. Kovselev, N. Krasnikov, S. Laptev, V. Matveev, V. Oustiojanine, A. Pashenkov, A. Polarush, S. Popov, V. Popov, V. Postoev, A. Proskouriakov, I. Semeniouk, B. Semenov, V. Shmatkov, A. Skassyrskaia

Institute for Theoretical and Experimental Physics, Moscow, RUSSIA
S. Abdullin, E. Doroshkevich, V. Gavrilov, Y. Gershtein, I. Gorelov, E. Grigoriev, V. Kaftanov, A. Khanov[2], I. Kisselevitch, V. Kolossov, S. Koulechov, D. Litvintsev, A. Nikitenko[2], O. Pogorelko, V. Semechkin, N. Stepanov[2], V. Stoline, Y. Trebukhovsky, A. Ulyanov, S. Uzunian, A. Yumashev

Moscow State University, Institute for Nuclear Physics, Moscow, RUSSIA
A. Belsky, V Bodyagin, A. Demianov, M. Dubinin, A. Gribushin, V. Ilyin, O. Kodolova, V. Korotkikh, N. Kruglov, A. Kryukov, I. Lokhtin, V. Mikhailin, L. Sarycheva, A. Snigirev, I. Vardanyan, A. Vasil'ev, A. Yershov

P.N. Lebedev Physical Institute, RAS, Moscow, RUSSIA
E. Devitsin, A. Fomenko, N. Konovalova, V. Kozlov, A. Lebedev, S. Potashov, S. Rusakov, A. Terkulov

Petersburg Nuclear Physics Institute, RAS, St Petersburg, RUSSIA
V. Astashine, Y. Blinnikov, N. Bondar, G. Gavrilov, A. Golyash, Y. Gusev, O. Kisselev, F. Moroz, E. Orichtchine, O. Prokofiev, V. Rasmislovich, V. Sedov, D. Seliverstov, V. Sknar, I. Smirnov, S. Sobolev, V. Soulimov, I. Tkach, G. Velitchko, A. Vorobyov

Joint Institute for Nuclear Research, Dubna, RUSSIA, [JINR]
S. Afanasiev, Y. Anisimov, A. Artiomov, D. Bandurin, S. Chatrchyan, A. Cheremukhin, A. Chvyrov, A. Dmitriev, V. Elsha, R. Eremeev, Y. Erchov, I. Golutvin, N. Gorbunov, I. Gramenitsky, I. Ivantchenko, V. Kalagin, V. Karjavin, S. Khabarov, V. Khabarov, Y. Kiryushin, V. Kolesnikov, V. Konoplyanikov, V. Korenkov, I. Kossarev, A. Koutov, V. Krasnov, A. Litvinenko, V. Lysiakov, A. Malakhov, G. Mechtcheriakov, I. Melnichenko, P. Moissenz, S. Movchan, V. Palichik, V. Perelygin, Y. Petukhov, M. Popov, D. Pose, R. Pose, A. Samoshkin, M. Savina, S. Selunin, S. Sergeev, S. Shmatov, N. Skachkov, D. Smolin, E. Tikhonenko, V. Uzhinskii, N. Vlasov, A. Volodko, A. Yukaev, N. Zamiatin, A. Zarubin, P. Zarubin, E. Zubarev, K. Zubov

Slovak University of Technology, Bratislava, SLOVAK REPUBLIC
P. Ballo, J. Lipka, M. Liska, M. Nagy, V. Necas, J. Safarik, M. Seberini, K. Vitazek

Centro de Investigaciones Energeticas Medioambientales y Tecnologicas, Madrid, SPAIN
M. Aguilar-Benitez, J. Alberdi, J.M. Barcala, J. Berdugo, C. Burgos, M. Cerrada, N. Colino, M. Daniel, M. Fernandez, A. Ferrando, M.C. Fouz, M.I. Josa, P. Ladrón de Guevara, B. Lopez Somalo, J. Marin, F. Martin Suarez, J. Mocholi, A. Molinero, J. Navarrete, J.C. Oller, J.L. Pablos, L. Romero, J. Salicio, C. Willmott

Universidad Autónoma de Madrid, Madrid, SPAIN
C. Albajar

Universidad de Oviedo, Oviedo, SPAIN
J. Cuevas

Instituto de Fisica de Cantabria (IFCA), CSIC-Universidad de Cantabria, Santander, SPAIN
P. Arce, E. Calvo, C.F. Figueroa, N. Garcia, I. Gonzalez, J.M. Lopez, J. Marco, F. Matorras, T. Rodrigo, A. Ruiz, I. Vila

Institut für Teilchenphysik, Eidgenössische Technische Hochschule (ETH), Zürich, SWITZERLAND
H. Anderhub, A. Barczyk, F. Behner, B. Betev, A. Biland, D. Bourilkov, V. Brigljevic, M. Campanelli, P. Cannarsa, G. Chevenier[2], R. Della Marina, F. Di Lodovico, M. Dittmar, R. Eichler, G. Faber, M. Felcini, K. Freudenreich, C. Grab, A. Hasan, H. Hofer, I. Horvath, P. Ingenito, K. Lassila-Perini, P. Le Coultre, P. Lecomte, W. Lustermann, P. Marchesini, F. Nessi-Tedaldi, F. Pauss, D. Pitzl, M. Pohl, G. Rahal-Callot, D. Ren, A. Robohm, U. Roeser, H. Rykaczewski, H. Suter, J. Ulbricht, G. Viertel, H. Von Gunten, S. Waldmeier-Wicki, F. Wittgenstein

Paul Scherrer Institut, Villigen, SWITZERLAND
O. Ayranov, R. Baur, W. Bertl, K. Deiters, P. Dick, A. Dijksmann, M. Fabre, K. Gabathuler, J. Gobrecht, G. Heidenreich, R. Horisberger, Q. Ingram, D. Kotlinski, R. Morf, D. Renker, R. Schnyder, H.Ch. Walter, D. Zürcher

Universität Basel, Basel, SWITZERLAND
B. Henrich, L. Tauscher, S. Vlachos, M. Wadhwa

Universität Zürich, Zürich, SWITZERLAND
C. Amsler, R. Kaufmann, F. Ould-Saada, Ch. Regenfus, P. Robmann, S. Spanier, S. Steiner, P. Truöl, T. Walter

Cukurova University, Adana, TURKEY
I. Dumanoglu, E. Eskut, A. Kayis, A. Kuzucu-Polatöz, G. Önengüt, N. Ozdes Koca, H. Ozturk

Middle East Technical University, Ankara, TURKEY
A.S. Ayan, M. Serin-Zeyrek, R. Sever, P. Tolun, M. Zeyrek

Institute of Single Crystals of National Academy of Science, Kharkov, UKRAINE
V. Koba, V. Trofimenko

National Scientific Center, Kharkov Institute of Physics and Technology, Kharkov, UKRAINE
L. Levchuk, A. Nemashkalo, V. Popov, A. Rubashkin, P. Sorokin, A. Zatzerklyany

Kharkov State University, Kharkov, UKRAINE
N. Kluban, V. Lebedev

Brunel University, Uxbridge, UNITED KINGDOM
B. Camanzi, P.R. Hobson, D. C. Imrie, C.K. MacKay, J. Matheson, A. McKemey, M. Osborne, M. Solanky, S.J. Watts

Imperial College, University of London, London, UNITED KINGDOM
G. Barber, J. Batten, R. Beuselinck, D. Britton, W. Cameron, D. Clark, I. Clarke, G. Davies, J. Fulcher, D. Gentry, D. Graham, G. Hall, J. Hays, A. Jamdagni, K.R. Long, B.C. MacEvoy, N. Marinelli, E.B. Martin, D.G. Miller, A. Potts, D.M. Raymond, J. Reilly, F. Sciacca[2], J. Sedgbeer, C. Seez, L. Toudup, J. Troska

Rutherford Appleton Laboratory, Didcot, UNITED KINGDOM
S.A. Baird, J.E. Bateman, K.W. Bell, R.M. Brown, P. Burch, D.J.A. Cockerill, J.F. Connolly, J.A. Coughlan, L.G. Denton, P.S. Flower, M. French, R. Halsall, J. Hartley, W.J. Haynes, F.R. Jacob, P.W. Jeffreys, L. Jones, B.W. Kennedy, A.L. Lintern, A.B. Lodge, G. Noyes, G.N. Patrick, B. Smith, M. Sproston, R. Stephenson, M. Torbet

University of Bristol, Bristol, UNITED KINGDOM
D.S. Bailey, O. Barret, R.D. Head, G.P. Heath, H.F. Heath, A. Mass, D.M. Newbold, A. Pressland, E.C. Reid, V.J. Smith, R.J. Tapper

University of Alabama, Tuscaloosa, Alabama, USA
L. Baksay, B. Fenyi, J. Huang, J. Rodin

Boston University, Boston, Massachusetts, USA
R. Carey, E. Hazen, U. Heintz, O.C. Johnson, E. Kearns, S.B Kim, E. Machado, J. Miller, D. Osborne, B.L. Roberts, J. Rohlf, J. Salen, L. Sulak, J. Sullivan, W. Worstell

University of California at Davis, Davis, California, USA
R. Breedon, Y. Fisyak, B. Holbrook, W. Ko, R. Lander, F. Lin, S. Mani, D. Pellett, J. Rowe, J. Smith

University of California at Los Angeles, Los Angeles, California, USA
K. Arisaka, Y. Bonushkin, F. Chase, D. Cline, S. Erhan, J. Hauser, M. Lindgren, C. Matthey, S. Otwinowski, J. Park, Y. Pischalnikov, P. Schlein, Y. Shi, B. Tannenbaum

University of California, Riverside, California, USA
D. Chrisman, I. Crotty[2], J.W. Gary, W. Gorn, J.G. Layter, B.C. Shen

University of California San Diego, La Jolla, California, USA
J.G. Branson, H. Kobrak, G. Masek, M. Mojaver, H. Paar, G. Raven, M. Sivertz, R. Swanson, A. White

California Institute of Technology, Pasadena, California, USA
J. Bunn[2], Q. Deng, G. Denis[2], A. Favara, Ph. Galvez, M. Gataullin, H. Newman, S. Shevchenko, A. Shvorob, R. Wilkinson, L. Zhang, R. Zhu

Carnegie Mellon University, Pittsburgh, Pennsylvania, USA
S. Blyth, A. Engler, Th. Ferguson, H. Hoorani, R. Kraemer, M. Procario, J. Russ, N. Terentyev, H. Vogel

Fairfield University, Fairfield, Connecticut, USA
C.P. Beetz, V. Podrasky, C. Sanzeni, T. Toohig, D. Winn

Fermi National Accelerator Laboratory, Batavia, Illinois, USA
M. Atac, E. Barsotti, A. Baumbaugh, U. Baur, A. Beretvas, M. Binkley, M. Bowden, J. Butler, N. Chester, I. Churin, M. Crisler, D. Denisov, M. Diesburg, D.P. Eartly, J.E. Elias, S. Feher, B. Flaugher, J. Freeman, I. Gaines, H. Glass, D. Green, J. Hanlon, R. Harris, U. Heintz, J. Incandela, U. Joshi, W. Knopf, S. Kwan, M. Lamm, S. Lammel, R. Lipton, P. Lukens, K. Maeshima, J. Marraffino, C.S. Mishra, N. Mokhov, V. O' Dell, J. Ozelis, J. Patrick, A. Pla-Dalmau, R. Raja, P. Rapidis, M. Reichanadter, A. Ronzhin, M. Shea, R.P. Smith, L. Spiegel, D. Stuart, L.E. Temple, S. Tkaczyk, R. Tschirhart, R. Vidal, D. Walsh, R. Wands, W.J. Womersley, W. Wu, A. Yagil, V. Yarba

University of Florida, Gainesville, Florida, USA
D. Acosta, P. Avery, R.D. Field, L. Gorn[2], S. Klimenko, J. Konigsberg, A. Korytov, G. Mitselmakher[28], A. Nomerotski, P. Ramond, J. Yelton

Florida State University - HEPG, Tallahassee, Florida, USA
H. Baer, M. Bertoldi, S. Hagopian, V. Hagopian, K. Johnson, H. Prosper, J. Thomaston

Florida State University - SCRI, Tallahassee, Florida, USA
M. Corden, Ch. Georgiopoulos, K. Hays, S. Youssef

University of Illinois at Chicago, (UIC), Chicago, Illinois, USA
M. Adams, M. Chung, J. Solomon

The University of Iowa, Iowa City, Iowa, USA
N. Akchurin, A. Cooper, M. Fountain, E. McCliment, J.P. Merlo, M. Miller, Y. Onel

Iowa State University, Ames, Iowa, USA
E.W. Anderson, J. Hauptman, J. Wightman

Johns Hopkins University, Baltimore, Maryland, USA
T. Anticic, B. Barnett, C.Y. Chien, M. A. Frautschi, D. Gerdes, D. Newman, J. Orndorff, A. Pevsner, X. Xie

Lawrence Livermore National Laboratory, Livermore, California, USA
L. Bertolini, J. Kerns, D. Klem, M. Kreisler, X. Shi, K. Van Bibber, T. Wenaus, D. Wright, C.R. Wuest

Los Alamos National Laboratory, Los Alamos, New Mexico, USA
R. Barber, Z. Chen, J. Hanlon, B. Michaud, G. Mills, A. Palounek, H.J. Ziock

University of Maryland, College Park, Maryland, USA
A. Baden, A. Ball, R. Bard, S.C. Eno, D. Fong, M. Garza, N.J. Hadley, R.G. Kellogg[2], Sh. Kunori, M. Murbach, A. Skuja

Massachusetts Institute of Technology, Cambridge, Massachusetts, USA
G. Bauer, J. Friedman, E. Hafen, S. Pavlon, L. Rosenson, K.S. Sumorok, S. Tether, J. Tseng

University of Minnesota, Minneapolis, Minnesota, USA
P. Border, P. Cushman, K. Heller, M. Marshak, R. Rusack, Ch. Timmermans

University of Mississippi, Oxford, Mississippi, USA
K. Bhatt, M. Booke, L. Cremaldi, R. Kroeger, J. Reidy, D. Sanders, D. Summers

University of Nebraska-Lincoln, Lincoln, Nebraska, USA
W. Campbell, D.R. Claes, M. Hu, C. Lundstedt, G.R. Snow

Northeastern University, Boston, Massachusetts, USA
G. Alverson, H. Fenker, J. Moromisato, Y. Musienko[29], Th. Paul, S. Reucroft, D. Ruuska, J. Swain, L. Taylor, E. Von Goeler, D. Wood, T. Yasuda

Northwestern University, Evanston, Illinois, USA
D. Buchholz, B. Gobbi, P. Rubinov, R. Tilden

University of Notre Dame, Notre Dame, Indiana, USA
B. Baumbaugh, J.M. Bishop, N. Biswas, N.M. Cason, R. Ruchti, J. Warchol, M. Wayne

The Ohio State University, Columbus, Ohio, USA
B. Bylsma, L.S. Durkin, J. Hoftiezer, R. Hughes, M. Johnson, D. Larsen, T.Y. Ling, C.J. Rush, V. Sehgal, B. Winer

Princeton University, Princeton, New Jersey, USA
P. Denes, V. Gupta, D. Marlow, P. Piroué, D. Stickland, H. Stone, R. Wixted

Purdue University - Task D, West Lafayette, Indiana, USA
A. Bujak, D. Carmony, L. Gutay, S. Medved

Purdue University - Task G, West Lafayette, Indiana, USA
V.E. Barnes, G. Bolla, D. Bortoletto, M. Fahling, A.F. Garfinkel, A.T. Laasanen

Rice University, Houston, Texas, USA
D.L. Adams, M. Corcoran, G. Eppley, H.E. Miettinen, B.P. Padley, E. Platner, J. Roberts, P. Yepes

University of Rochester, Rochester, New York, USA
S. Blusk, A. Bodek, H. Budd, P. De Barbaro, M. Kruse, D. Ruggiero, W. Sakumoto, E. Skup, P. Tipton

Rutgers, the State University of New Jersey, Piscataway, New Jersey, USA
E. Bartz, J. Conway, T. Devlin, P. Jacques, M. Kalelkar, S. Schnetzer, S. Sherman, S. Somalwar, R. Stone, G. Thomson, T. Watts

University of Texas at Dallas, Richardson, Texas, USA
R.C. Chaney, E.J. Fenyves, H.D. Hammack, M.R. O'Malley, D.J. Suson, A.V. Vassiliev

Texas Tech University, Lubbock, Texas, USA
D. Benjamin, O. Ganel, V. Papadimitriou, A. Sill, R. Wigmans

Virginia Polytechnic Institute and State University, Blacksburg, Virginia, USA
H. Meyer, L. Mo, Th.A. Nunamaker

University of Wisconsin, Madison, Wisconsin, USA
W. Badgett, D. Carlsmith, S. Dasu, F. Feyzi, C. Foudas, M. Jaworski, J. Lackey, R. Loveless, S. Lusin, D. Reeder, W. Smith

Institute of Nuclear Physics of the Uzbekistan Academy of Sciences, Ulugbek, Tashkent, UZBEKISTAN
A. Avezov, N. Bisenov, A. Gafarov, E. Gasanov, R. Gulamova, E. Ibragimova, G. Kim, Y. Koblik, D. Mirkarimov, A. Morozov, N. Rakhmatov, I. Rustamov, A. Urkinbaev, B. Yuldashev

---

[1] On leave of absence from Institute of Physics Academy of Science, Tbilisi, Georgia
[2] Also at CERN, Geneva, Switzerland
[3] Also at Università di Roma I e Sezione dell' INFN, Roma, Italy
[4] Also at Laboratoire de Physique Nucléaire des Hautes Energies, Ecole Polytechnique, IN2P3-CNRS, Palaiseau, France
[5] Also at Politecnico di Torino, Torino, Italy
[6] Programme between CERN and Portugal financed by AdI (Agência de Inovação), Portugal
[7] Also at Università di Torino e Sezione dell' INFN, Torino, Italy
[8] Also at Centro de Investigaciones Energeticas Medioambientales y Tecnologicas, Madrid, Spain
[9] Also at Institut für Hochenergiephysik der ÖAW, Wien, Austria
[10] Also at University of Bristol, Bristol, United Kingdom
[11] Also at Middle East Technical University, Physics Department, Ankara, Turkey
[12] Also at Università di Bari e Sezione dell' INFN, Bari, Italy
[13] Also at Massachusetts Institute of Technology, Cambridge, Massachusetts, USA
[14] Also at Princeton University, Princeton, New Jersey, USA
[15] Also at Laboratório de Instrumentação e Física Experimental de Partículas, Lisboa, Portugal
[16] On leave of absence from Imperial College, London, United Kingdom
[17] Also at Institute Rudjer Boskovic, Zagreb, Croatia
[18] Also at M.P.I. Münich, Germany
[19] Also at Humboldt-Universität, Berlin, Germany
[20] Also at DESY, Hamburg, Germany
[21] Also at Inst. of Nuclear Research ATOMKI, Debrecen, Hungary
[22] Also at University of California, Riverside, California, USA
[23] Also at Laboratori Nazionali di Legnaro, Legnaro, Italy
[24] Also at Dip. di Fisica del Politecnico di Milano, Milano, Italy
[25] Also at ENEA, S. Maria di Galeria, Italy
[26] Also at INESC, Lisbon, Portugal
[27] Also at Laboratoire d'Annecy-le-Vieux de Physique des Particules, IN2P3-CNRS, Annecy-le-Vieux, France
[28] Also at Fermi National Accelerator Laboratory, Batavia, Illinois, USA
[29] Also at Institute for Nuclear Research, RAS, Moscow
[*] Subject to approval by the CMS Collaboration Board

Contents

Chapter 1

Introduction

The CMS detector has been designed to detect cleanly the diverse signatures of new physics at the Large Hadron Collider. It will do so by identifying and precisely measuring muons, electrons, photons, and jets over a large energy range [1-1],[1-2],[1-3],[1-4]. Experience has shown that robust tracking and detailed vertex reconstruction within a strong magnetic field are powerful tools to reach these objectives.

The overall layout of the CMS detector is illustrated in Colour Figs. 1.i, 1.ii and 1.iii. In this chapter an overview of the tracking system is given, together with a discussion of the physics goals and the design considerations which motivate our basic approach and technological choices.

The subsequent chapters discuss in detail the three main sub-detector elements of the Tracker: the Pixel vertex detector system is described in Chapter 2, while the Silicon Strip (SST) and the Micro Strip Gas Chamber (MSGC) trackers are described in Chapters 3 and 4 respectively. Chapter 5 discusses the readout electronics of the Silicon Strip and MSGC detectors, the control and monitoring electronics and the low and high voltage power supplies. Chapter 6 describes the Tracker support structure, alignment, general engineering, services, beam pipe, installation and maintenance procedures. The safety aspects are also discussed in Chapter 6. In Chapters 7, 8 and 9 we discuss the detector simulation, the track and vertex reconstruction algorithms, and finally the performance of the Tracker in its important aspects. In Chapter 10 cost, funding, institutional responsibilities and management of the Tracker project are described. Chapter 10 ends with the construction schedule and planning. The radiation environment and the simulation methods to evaluate it are described in Appendix A.

1.1 Physics Objectives

Robust tracking and detailed vertex reconstruction are expected to play an essential role for an experiment designed to address the full range of physics which can plausibly be accessed at the LHC. The following considerations are illustrative of the performance requirements which the Tracker must satisfy.

The characterisation of events involving Gauge bosons, W and Z, will certainly be of primary importance at the LHC. In particular, their leptonic decays provide especially clean experimental signals. Indeed, possible heavier W' and Z' bosons in the TeV range are also best evidenced through leptonic decays. To fully exploit these signatures, the Tracker must be able to provide as good a momentum measurement for energetic leptons as can reasonably be achieved. Both the efficiency and resolution for isolated electrons are affected by the material in the Tracker, because of bremsstrahlung. This degradation in performance must be kept to a minimum. In CMS, Tracker measurements are combined with track segments reconstructed in the outer muon system to further extend the kinematic region over which a precise muon momentum

measurement can be performed. This latter requirement will place stringent constraints on the alignment of the Tracker relative to the muon chambers.

Efficient isolated lepton reconstruction is also both necessary and sufficient to fulfil another of the important tasks for the Tracker, namely electron and photon identification for isolated electromagnetic clusters. However, not only must the Tracker be able to reconstruct and identify isolated leptons and photons efficiently, it must also establish that they are in fact isolated. For example, lepton isolation is required to suppress $t\bar{t}$ and $Zb\bar{b}$ backgrounds to a level which allows observation of $H \rightarrow ZZ^* \rightarrow 4l^{\pm}$ and $H \rightarrow ZZ \rightarrow 4l^{\pm}$ for the full mass range $120 \leq m_H \leq 800$ GeV. Lepton isolation criteria also play an important role in SUSY particle searches, in particular for sleptons, charginos and neutralinos. The sensitivity to Higgs decay in the $\gamma\gamma$ channel is also greatly enhanced by Tracker isolation criteria applied to suppress the $\gamma - \pi^0$ (jet) and $\pi^0 - \pi^0$ (jet–jet) backgrounds to a level significantly below the irreducible $\gamma\gamma$ background. Effective isolation criteria rely on the efficient reconstruction of all hadronic tracks down to transverse momenta of approximately 2 GeV, and may be further improved by the reconstruction of tracks as low as 1 GeV in p_T.

The ability both to tag and to reconstruct in detail b jets, and B-hadrons within these jets, is also of fundamental importance. Indeed, not only are b jets particularly useful signatures for a broad spectrum of new physics, and essential tags for top quark physics, their detailed study may also yield fundamental insight into the question of CP violation. The latter requires the ability to identify unambiguously tracks coming from multiple vertices, the ability to reconstruct a variety of decay chains and the accurate determination of the b decay proper time, based on the characterisation of displaced vertices and the kinematics of the associated tracks.

As signals for new physics, b jets may result either from the decays of a new particle, or in associated production via gluon–gluon fusion mediated by b quark exchange. In the first case, sensitivity to heavy particles requires efficient b tagging for high momentum jets, resulting in severe constraints on two-track separation capability, while for the second case good b tagging efficiency is required over the full Tracker acceptance up to $\eta = 2.5$. In order to ensure satisfactory performance of b tagging algorithms based on displaced vertices, it is mandatory to control tails in the impact parameter measurement due to errors in pattern recognition, as well as hadronic interactions within the active volume of the Tracker.

In addition, a variety of plausible new physics channels including, for example, decay chains pertinent to a possible SUSY Higgs sector, result in τ leptons in the final state. Tau lepton identification requires the application of isolation criteria, and may also benefit substantially from displaced vertex information. Achieving the tracking performance required for b tagging and b physics studies will also ensure useful τ recognition capability.

Many of the most interesting physics questions require the highest luminosities achievable at LHC and therefore the stringent demands placed on the tracking system must continue to be satisfied for luminosities up to 10^{34} cm^{-2}s^{-1}. At the LHC, this implies the superposition of typically 20 to 30 unrelated minimum bias events within each bunch crossing, and puts a major additional burden on the task of correct pattern recognition.

Moreover, the ability of the Tracker to characterise in detail these multiple event vertices may also play a crucially important role in CMS for the Higgs to $\gamma\gamma$ search. Indeed, the spectrum of charged particles recoiling against the Higgs provides a useful signature with which to differentiate the Higgs production vertex from the multitude of minimum bias event vertices. This will allow the required $\gamma\gamma$ mass resolution to be preserved at high luminosity.

In order to avoid significant loss of sensitivity in the Higgs to $\gamma\gamma$ channel, the fraction of such decays where neither photon converts should be close to 50%. This requirement, together with the need to minimise the effects on tracking performance of electron bremsstrahlung and hadronic interactions, impose severe constraints on the material budget allowed and are an important criterion for for the Tracker design.

As well as proton–proton collisions, the LHC will provide a unique opportunity to explore the physics of heavy-ion collisions at very high energy. These collisions give rise to extremely large charged particle multiplicites: up to 25 000 in the case of a central lead–lead collision. Although the CMS Tracker was not explicitly designed with such physics in mind, in conjunction with the CMS muon system it actually provides a useful tool for the reconstruction of muon-pair invariant masses even in this environment. This, in turn, is a powerful probe for the study of quark–gluon plasma physics which may be evidenced in heavy-ion collisions at the LHC.

1.2 CMS Tracker Performance

The requirements described in the previous section have led to the design of a Tracker for CMS with the following performance:

- As shown in Fig. 1.1, high p_T isolated tracks are reconstructed with a transverse momentum resolution of better than $\delta p_T/p_T \approx (15 \cdot p_T \oplus 0.5)\,\%$, with p_T in TeV, in the central region of $|\eta| \leq 1.6$, gradually degrading to $\delta p_T/p_T \approx (60 \cdot p_T \oplus 0.5)\,\%$, with p_T in TeV, as η approaches 2.5. This resolution is well suited to the reconstruction of narrow states decaying into charged particles, and is sufficient to ensure reliable charge assignment for muons and electrons up to the highest kinematically accessible momenta.
- From Fig. 1.2 it can be seen that, in combination with the outer muon chamber system, the muon momentum resolution above approximately 100 GeV can be parametrised as $\delta p/p \approx (4.5 \cdot \sqrt{p})\%$, with p in TeV, for rapidities extending up to at least $\eta = 2$ [1-4]. This results in a momentum resolution better than 10% even at 4 TeV.

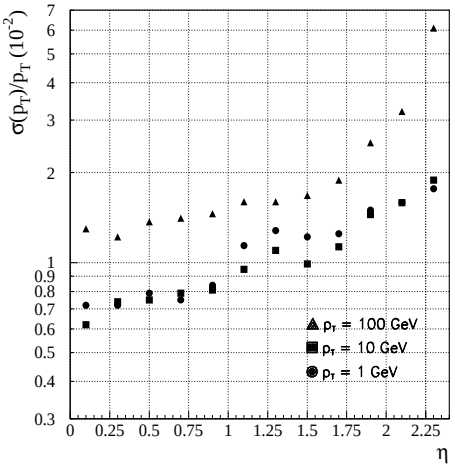

Fig. 1.1: CMS Tracker stand-alone transverse momentum resolution as a function η, for muons of p_T = 1, 10 and 100 GeV, without beam constraint.

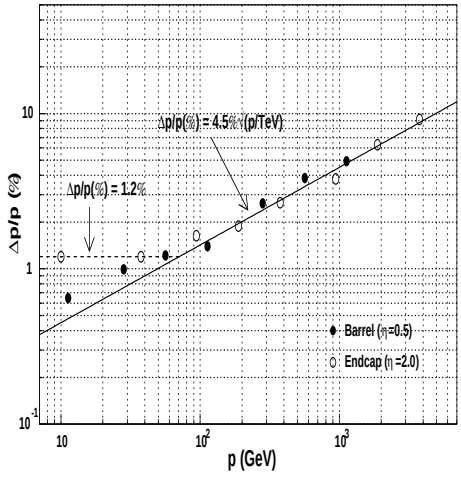

Fig. 1.2: Combined CMS Tracker and Muon Chamber momentum resolution as a function of momentum, in the central and forward rapidity regions.

- In dense jet environments, charged hadrons with p_T above 10 GeV are reconstructed with an efficiency approaching 95%, and even hadrons with p_T as low as 1 GeV are reconstructed with an efficiency better than 85%. The reconstruction efficiency for muons is better than 98% over the full η range, even for values of p_T as low as 1 GeV. High energy electrons are reconstructed with an efficiency above 90%.

- The impact parameter resolution in the plane perpendicular to the beams, shown in Fig. 1.3, is better than 35 μm over the full $|\eta| \leq 2.5$ range for particles with p_T above 10 GeV. The longitudinal impact parameter resolution, shown in Fig. 1.4, is significantly better than 75 μm over most of the rapidity range. At low luminosity it is possible to place the innermost Pixel layer closer to the beam line. This results in an appreciable improvement in impact parameter resolution, as can be seen from Figs. 1.5 and 1.6. These estimates do not take into account any degradation due to detector misalignement. Tails due to errors in track reconstruction are at a level well below the rate of displaced vertices due to long-lived particles.
- In the central rapidity region tagging efficiencies of 50% or better can be obtained for b jets ranging from 50 GeV to 200 GeV E_T, with a mistagging probability of around 1% to 2%. In the forward rapidity region, for equal mistagging probability, the tagging efficiency remains around 40%.

The pattern recognition performance and track reconstruction quality listed above are achieved at the highest luminosity foreseen for LHC operation.

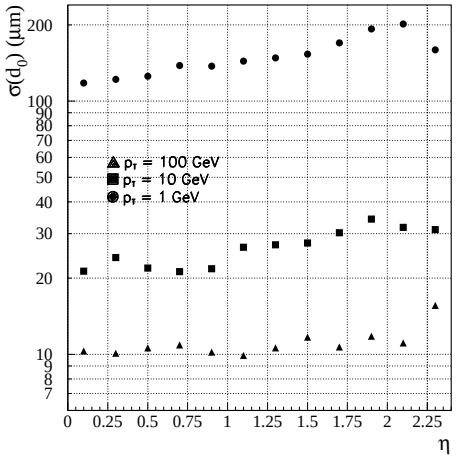

Fig. 1.3: Transverse impact parameter resolution as a function of η, for muons of p_T = 1, 10 and 100 GeV. High luminosity CMS Pixel configuration.

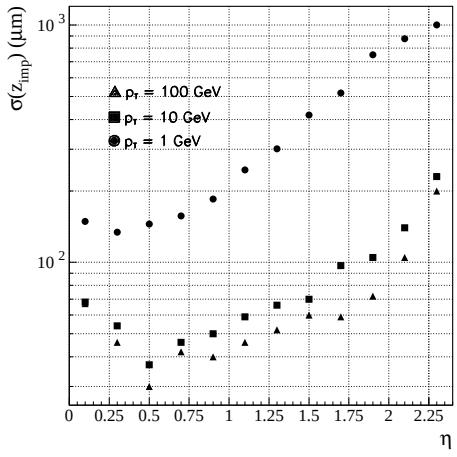

Fig. 1.4: Longitudinal impact parameter resolution as a function of η, for muons of p_T = 1, 10 and 100 GeV. High luminosity CMS Pixel configuration.

1.3 Overview and Layout of the CMS Tracking System

Momentum analysis in CMS makes use of a 4 T magnetic field, provided by a super-conducting solenoidal magnet around which the entire experiment is built [1-1]. The active envelope of the CMS Tracker extends to a radius of 115 cm, over a length of approximately 270 cm on each side of the interaction point. Momentum measurements of charged particles in the region $|\eta| \lesssim 1.6$ therefore benefit from the full momentum analysing power. In this region, a charged particle with p_T of 1000 GeV has a sagitta of 195 μm. The Tracker acceptance extends further to $|\eta|$ of 2.5, with a reduced radial lever arm of approximately 50 cm.

The very high magnetic field of CMS affects event topologies, by confining low p_T charged particles to small radius helical trajectories. Coupled with the steeply falling p_T spectrum

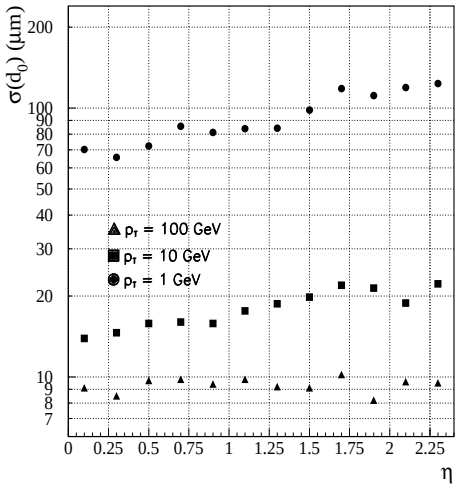

Fig. 1.5: Transverse impact parameter resolution as a function of η, for muons of p_T = 1, 10 and 100 GeV. Low luminosity CMS Pixel configuration.

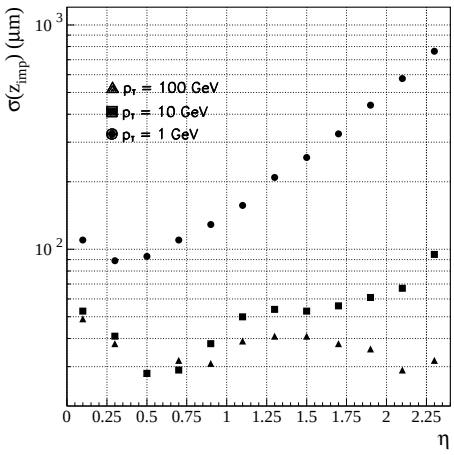

Fig. 1.6: Longitudinal impact parameter resolution as a function of η, for muons of p_T = 1, 10 and 100 GeV. Low luminosity CMS Pixel configuration.

characteristic of minimum bias events, this results in a track density which rapidly decreases with increasing radius.

This is illustrated in Fig. 1.7, where typical primary charged particle densities are shown for several different radii with 0 and 4 T solenoidal field, at $\eta = 0$. In the absence of a magnetic field, the charged track density simply falls off as $1/r^2$. Under the effect of the 4 T field, the decrease in charged track density with radius is initially more gradual, and then significantly more pronounced than $1/r^2$. It can be seen that, as a result, the charged particle rate at 20 cm is almost twice the value with no field, that at about 65 cm the rates are the same for both cases, and that the 4 T field reduces the charged particle rate at the outermost radius of the tracker by as much a factor of four. This has important implications for the architecture of the CMS Tracker.

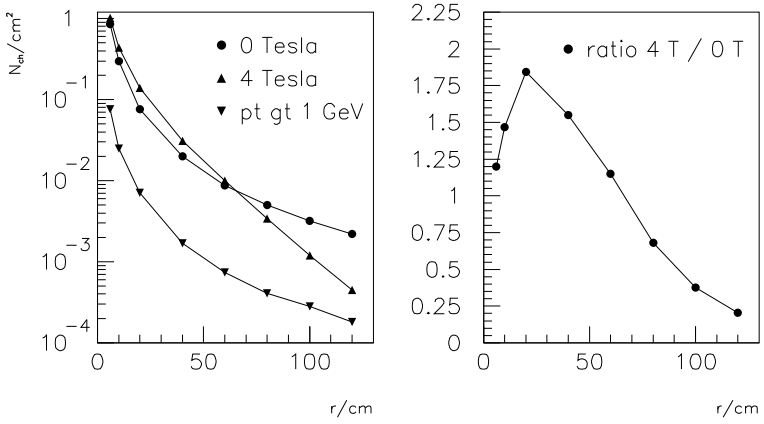

Fig. 1.7: Primary charged particle density per cm^2 at $\eta = 0$, for 20 minimum bias events superimposed (in units of %).

To satisfy the performance requirements and constraints outlined in the previous sections, we have adopted a strategy aimed at providing a set of coordinate measurements of sufficient precision and robustness so that track reconstruction can be reliably performed based on a relatively small number of measurements per track. To do this, we rely on sufficiently fine granularity such that typical single channel occupancy at high luminosity, for detectors with at least one hit in them, is kept between 1% and 3% everywhere in the Tracker. The required hit resolutions, at least in the transverse plane, are in the range of 15 μm to 40 μm at the inner and outer radii of the Tracker respectively.

We have chosen three detector technologies, each best matched to the task of satisfying our stringent resolution and granularity requirements in the high, medium and lower particle density regions. These are Pixels, Silicon Strip, and Micro Strip Gas Chambers (MSGCs) respectively. They are arranged in concentric cylindrical volumes, each corresponding to three occupancy regimes: the region below $\approx$ 20 cm, between $\approx$ 20 and $\approx$ 60 cm, and from $\approx$ 70 to 120 cm. The three detector types chosen are all fast on the scale of 25 ns, allowing event pile-up to be limited to a single bunch crossing for Pixels and Silicon and, for the MSGCs, to two bunch crossings.

The presence of a very large irreducible background due to minimum bias event pile-up at high luminosity challenges the pattern recognition capability of the Tracker. Therefore, strong emphasis is put on robust pattern recognition within each of the three sub-detectors. The unambiguous three-dimensional space points provided by the Pixels are essential for correct pattern recognition at these small radii. Each of the SST and MSGC volumes provides sufficient information to allow independent verification of the overall pattern recognition results, yielding a powerful measure of redundancy. This feature of the CMS Tracker is an essential tool to ensure tracking which is both efficient and ghost-free in the very high luminosity environment.

In the central rapidity region detectors are arranged in a barrel geometry, while at higher values of rapidity they are deployed as disks, organised into end-caps. In total there are 13 barrel layers, and the CMS Tracker geometry, shown in Fig. 1.8, has been defined so as to provide typically 13 distinct high resolution measurement planes for stiff tracks up to $|\eta|$ of about 2.0, gradually falling off to a minimum of 8 planes at $|\eta|$ of 2.5. This is shown in Fig. 1.9. The CMS tracker layout, as well as the overall mechanical structure, are also illustrated in Colour Figs. 1.iv and 1.v.

At the smallest radii (from 4 cm up to 7 cm at low luminosity and from 7 cm up to 11 cm at high luminosity) the interaction region is surrounded by two barrel layers of silicon Pixel detectors. Two end-cap disks cover radii from 6 cm to 15 cm. The cell size in the Pixel detectors is 150 μm by 150 μm. The CMS Pixel detectors are n-on-n devices so that, in the barrel, their response is strongly affected by the 32° Lorentz angle of the electrons. The barrel Pixel geometry is deliberately arranged such that this large Lorentz angle induces significant charge sharing across neighbouring cells and this results in expected hit resolutions of approximately 10 μm and 15 μm in the ϕ and z coordinates respectively. Similar resolutions, between 15 μm to 20 μm, are obtained in the end-cap Pixels, by rotating the sensors 20° around their central radial axis. In the high luminosity configuration, the Pixel detector will have an active surface of close to one square metre, instrumented with approximately 40×10^6 channels.

The intermediate region, from 22 cm up to 60 cm, is instrumented with a 5-layer Silicon Strip Barrel detector, complemented by 10 disks in each end-cap. Layers 3 to 5 of the Silicon Barrel are approximately 170 cm long. To avoid unfavourably shallow crossing angles, the length of the inner two layers is limited to 90 cm. The rest of the coverage is provided by incorporating 3 mini end-cap disks on each side. Barrel layers 1, 2 and 5 are double-sided layers, with stereo geometry for the longitudinal coordinate measurement. Correspondingly, the inner and outer radii of the end-cap disks are also instrumented with double-sided layers, where a stereo geometry is employed to measure the radial coordinate. The mini end-cap disks, closer to the interaction region, are fully double-sided.

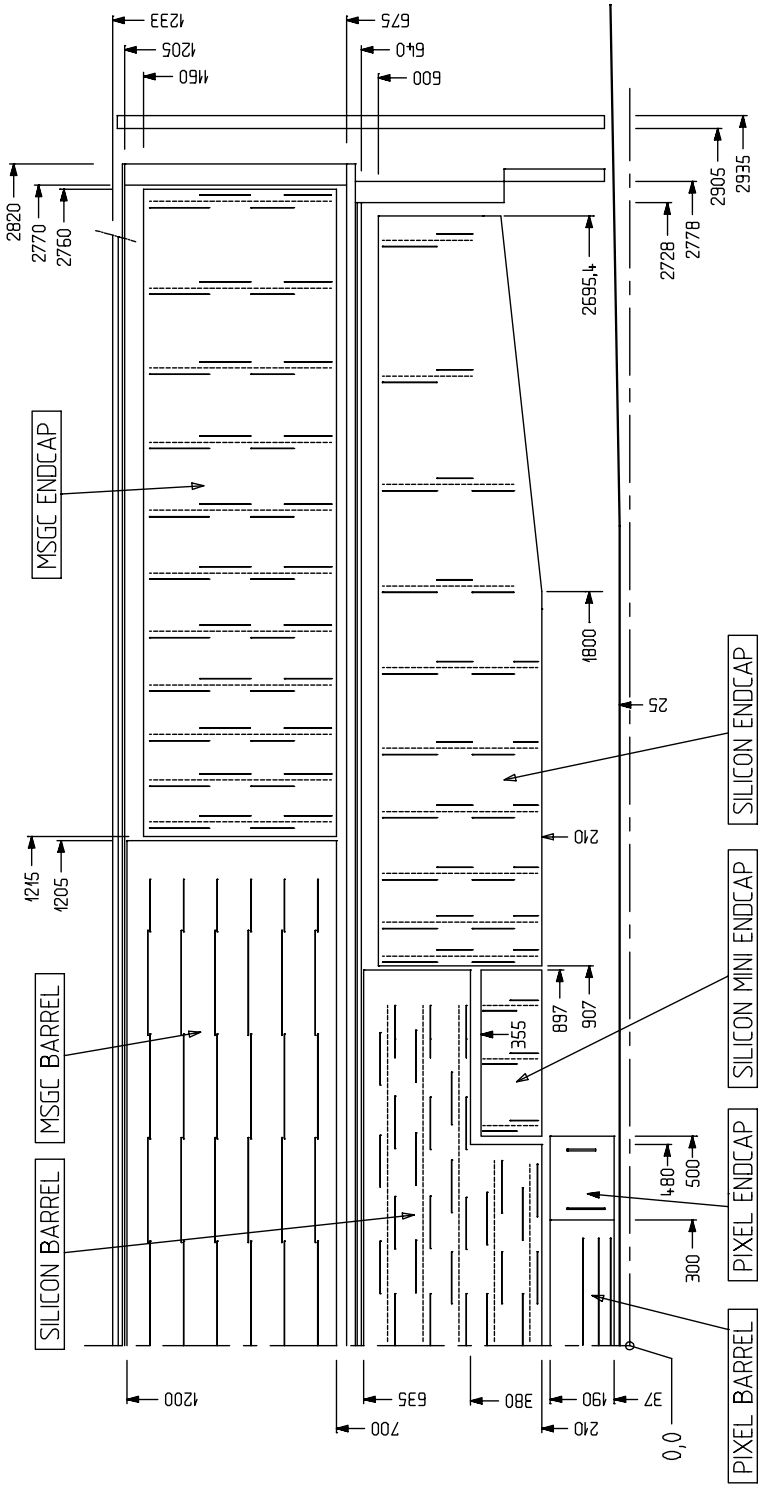

Fig. 1.8: A cut view of the CMS Tracker layout.

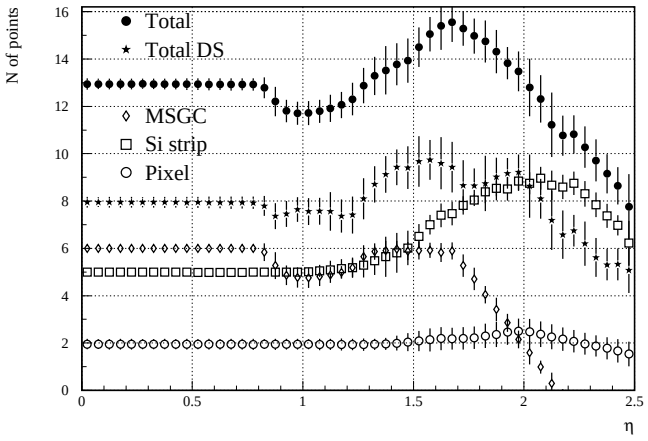

Fig. 1.9: Average number of measurement planes intersected by infinite momentum tracks, as a function of rapidity.

The outer volume of the Tracker, from 70 cm up to 120 cm, is instrumented with a 240 cm long barrel with 6 cylindrical layers of MSGCs, and by 11 discs of MSGCs for each end-cap. Layers 1, 4 and 6 of the barrel MSGC detector are double-sided, with a stereo geometry for the longitudinal coordinate measurement. Double-sided detectors with a stereo geometry are used at the inner and outer radii of the end-cap MSGC disks to provide measurements of the radial coordinate.

In addition to benefiting from an intrinsic response time shorter than the 25 ns bunch crossing interval, silicon sensors are especially well suited to the high and medium occupancy environment thanks to an active substrate thickness of only 300 μm and the very fine pitch which can thus be put to use. For the silicon detectors the typical strip length is 12.5 cm, and the pitch ranges from 61 μm to 122 μm and from 81 μm to 244 μm for the primary and stereo views, respectively. The hit resolution is around 15 μm for the 61 μm pitch, and approaches the digital limit (pitch/$\sqrt{12}$) for the larger pitches, where most of the charge is deposited on a single strip.

In the lower occupancy region of the Tracker, excellent resolution can be obtained with MSGCs with a significantly lower channel density. Here strip length ranges from 10 cm for the inner layers to 25 cm for the outer ones, and the pitches are around 200 μm and 400 μm for the primary and stereo views. The corresponding resolution is approximately 35 μm and 100 μm respectively. This lower channel density in the outer region of the Tracker is used to keep under control the overall cost of the Tracker, as well as to reduce the material in front of the electromagnetic calorimeter.

Overall, the CMS Silicon and MSGC trackers cover approximately 300 m^2 of active surface, consisting of more than ten thousand independent detector modules instrumented with 12 $\times$ 10^6 channels. The total active surface of the Silicon tracker is close to 75 m^2 and the total number of channels is 5.4×10^6, about equally distributed between barrel and end-caps. The total active area of the MSGC tracker is about 225 m^2 and the total number of channels 6.6×10^6, again approximately equally distributed between barrel and end-caps.

Silicon and MSGC detectors are not only natural complements in terms of their performance in the LHC environment, they also share basic technical characteristics. In particular, the same front-end electronics chain can be used for both, with only minor adaptations to best match the different pulse shapes of the two types of detector. This has proven to be a key advantage in

the development of the electronics chain and is also expected to be an important factor in the production phase.

The readout of all the Tracker sub-detectors is analog. Analog information allows a better optimisation of the coordinate reconstruction, resulting in an improved resolution and more Gaussian error distributions, with respect to a digital scheme. Furthermore, analog information can be used to verify the pattern recognition in instances where clusters from distinct tracks appear to have been merged. Finally, analog readout lends robustness to the overall system, in particular by providing the means for efficient online common mode noise subtraction.

1.4 Progress Since the Technical Proposal

On account of its high centre of mass energy and unprecedented luminosity, the LHC will create a very hostile radiation environment for the Tracker (Section 1.7). Radiation damage will set a limit to the operational lifetime of detectors and requires the use of radiation-hard electronics everywhere in the Tracker volume. A vigorous R&D programme has been carried out on both the detectors and the front-end electronics chain, to ensure full functionality of the Tracker after exposure to 10 years of LHC operation or more.

The readout architecture has changed conceptually very little since the Technical Proposal [1-5] but has progressed considerably in design and implementation. The detailed implementation of the key components of our front-end analog readout chain, in radiation-hard technologies, is well advanced. The control system, involving a small number of ASICs which distribute clock, triggers and commands internally in the tracker, has been fully specified. The analog optical link, a cornerstone of the system, is now based on edge-emitting semiconductor lasers of the type extensively used for TELECOM and DATACOM applications.

Radiation effects on silicon Pixel and strip detectors are now much better understood. For Pixel detectors, the viability of silicon for the sensor material has been demonstrated, so that this is chosen instead of other more exotic materials. In the very extreme environment in which they must operate, the n-on-n architecture works best. The expected lifetime of the Pixel detectors and electronics is compatible with reasonable maintenance and upgrade scenarios.

For silicon strip detectors, both the sophistication of the devices and the quality of the technologies used in producing them have significantly advanced with respect to the state of the art as of a few years ago. The behaviour under irradiation of a broad spectrum of devices has been characterised in detail. It has been confirmed that both double-sided detectors as well as simple p-on-n truly single-sided sensors are viable at the LHC, provided they are of good quality. The latter devices, in particular, make use of essentially standard micro-electronics technologies, and can therefore be produced in large quantities and at relatively low cost. We have chosen to use single-sided devices throughout the SST, with double sided modules obtained by coupling two such sensors back-to-back.

The advances made in silicon strip detector technology, and the cost reductions these have resulted in, have made possible a far more extensive use of these devices than previously envisaged. At the time of the Technical Proposal, the SST provided only three detector layers, and was limited in radius to below 40 cm and in length to only ± 150 cm. In the present configuration the full region up to 60 cm in radius, where typical primary track densities are above 1 cm^{-2}, is covered by the SST.

An important milestone for the CMS Tracker has been the successful development of MSGC detectors with the demonstrated capability of stable and efficient operation in the LHC environment. To this end a new technique of 'advanced passivation' has been developed within CMS, which extends the safe operating regime of the MSGC to a range of gains well above the minimum required for efficient track finding. The effectiveness of this technique has been thoroughly

studied in laboratory measurements and demonstrated in extremely high-intensity low-energy hadron beams (PSI) this past summer.

In addition, a great deal of progress has been made in both the mechanical engineering and system aspects of the Tracker. In the past year a series of large scale 'milestone' prototypes have been completed for each of the barrel and end-cap SST and MSGC sub-detectors, which have allowed detailed tests of the important aspects of their designs. The overall mechanical support structure, as well as the integration of services, has also been studied extensively. Comparisons between several alternative schemes resulted in the choice of a central cylindrical structure, which supports both the SST and MSGC trackers, on which our design is based.

1.5 Tracker Material Budget

Great care has been taken throughout the design of the Tracker to ensure that it meets stringent material budget constraints. Indeed this consideration limits the total number of active layers which can be usefully deployed and motivates the choice of materials used.

In some respects, however, we have been forced to accept inevitable compromises. In particular, for stable long term operation in the LHC environment, the Silicon tracker and Pixel vertex detectors must be operated at -10 °C, whereas the MSGC Tracker will be operated at 18 °C. This requirement for a thermal separation and screening of the SST and MSGC volumes has important consequences on the mechanics of the Tracker, and especially on the organisation and routing of services within it. Indeed, all services for the Silicon tracker must be removed axially to the Tracker end-flanges at a radius of 60 cm, not an optimum configuration in terms of the effect on material budget. Similarly, the constraints imposed on the installation of the Pixel detector require their services to be removed axially to the end-flanges at a radius below 20 cm.

This situation clearly results in an undesirable local peak in the material density, in particular between the SST and MSGC volumes. The ability of each of the Pixel + Silicon and MSGC Trackers to verify independently the pattern recognition results provides a powerful means with which to address this problem.

We have performed a thorough analysis of the material budget of the CMS Tracker design. A detailed accounting has been made of all the Tracker components and implemented within a GEANT simulation. This tool allows us both a general overview of the situation, as well as a detailed breakdown of the effect of individual components on the material budget. Figure 1.10 summarises the situation.

In Chapter 9 it is shown that pattern recognition even for low p_T hadrons remains very good, and the effects of bremsstrahlung on electrons can be controlled at a satisfactory level. A Monte Carlo study of Higgs to $\gamma\gamma$ decays propagated through the detailed detector geometry shows that in 46% of such decays both photons leave the Tracker volume without converting. Most of the events where photon conversions do take place are still well reconstructed. It has been shown that, with this rate of conversions, the loss of efficiency in CMS for the Higgs to $\gamma\gamma$ search does not exceed other irreducible inefficiencies [1-2].

We consider that, as our detailed understanding of the critical engineering issues continues to improve, we will be able to further reduce the overall material budget without compromising the integrity of the detector.

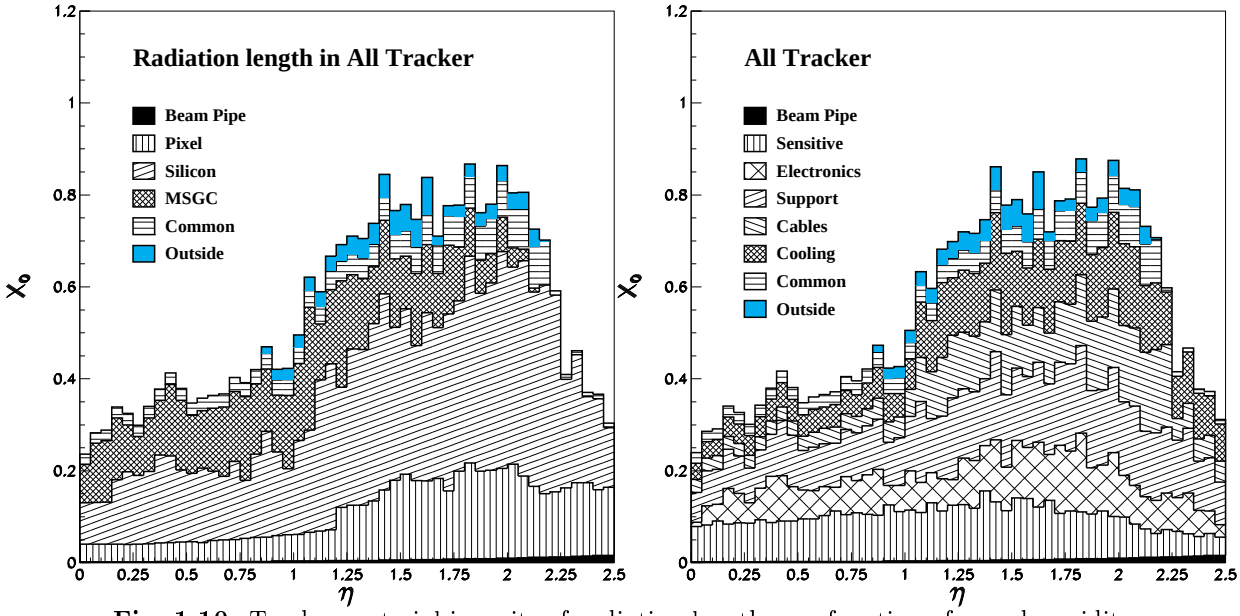

Fig. 1.10: Tracker material in units of radiation length as a function of pseudorapidity.

1.6 Staged Deployment of the CMS Tracker

The extremely high rate of interactions (up to 10^9 Hz) and the 25 ns bunch crossing frequency characteristic of the LHC environment greatly complicate the task of achieving the required level of performance. As discussed above, this mandates a certain level of redundancy in the detector design and sets the scale for the number of precision measurements required to define tracks, as well as their organisation in Pixel, Silicon and MSGC volumes. Together with considerations of two track resolution required to reconstruct tracks in high energy jets, this also basically defines the total number of readout channels.

At low luminosity, the performance requirements in terms of two-track resolving power, momentum and impact parameter resolution remain as stringent as in the high luminosity environment. The absence of minimum bias event pile-up, however, allows to relax significantly the redundancy which is an essential feature of the high luminosity layout. Because the highest luminosities will be attained only after several years of LHC running, and due to a shortage of currently available financial resources, we propose to install the detector in two stages.

We have identified an initial 'Phase I' configuration, consisting of a subset of the fully instrumented detector, which is well matched to the much cleaner environment expected for the low luminosity operation of the LHC. For the Phase I Silicon tracker we omit the fourth, single-sided, Silicon Barrel layer as well as two complete disks in each end-cap. For the MSGC tracker we omit the fourth, double-sided, barrel layer and, once again, two complete disks in each end-cap. The position of the end-cap disks is modified so that, on average, 11 distinct measurement points are ensured for $|\eta|$ less than about 2.0, falling off to 6 points at $|\eta|$ of 2.5. This reduced configuration still preserves the required performance of the Tracker at low luminosity and is matched to the currently available funding for the Tracker project.

Full deployment of the Tracker will follow as 'Phase II', to be completed in time for the high luminosity LHC running. The support mechanics are designed so as to allow the later installation of the missing barrel layers and end-cap disks. Furthermore, we plan to include all services for these detectors in the initial installation phase, from the counting rooms to the Tracker patch panel inside the magnet coil. The transition from the Phase I to the Phase II configuration, which ensures full functionality of the Tracker to the high luminosity LHC conditions, should thus be possible within a regular LHC shutdown period.

1.7 The LHC Radiation Environment

The radiation field within the Tracker is characterised by two distinct sources. Secondaries from the pp interaction, the products of their interactions in the Tracker structures and some decay products, give the dominating contribution to the fluences at the inner layers of the Tracker. This component of the fluence is almost independent of the z-coordinate and behaves roughly as $1/r^2$, where r is the distance from the beam-line. Almost all of the charged hadron fluence originates from the vertex. On the other hand, most of the neutrons observed in the Tracker region are due to albedo from the surrounding electromagnetic calorimeter. The most intense source of albedo neutrons is the end-cap ECAL. While the fluence originating from the vertex is irreducible, a neutron moderator lining of the ECAL is shown to efficiently reduce the neutron albedo, which is particularly intense for the heavy $PbWO_4$ crystals.

Figure 1.11 shows approximate values for the absorbed dose, which is to some extent material dependent, as well as the fast neutron and charged hadron (and neutral kaon) fluences at different radii in the Tracker region. A more detailed analysis, as well as a thorough discussion of the methods used for estimating the radiation levels, can be found in Appendix A.

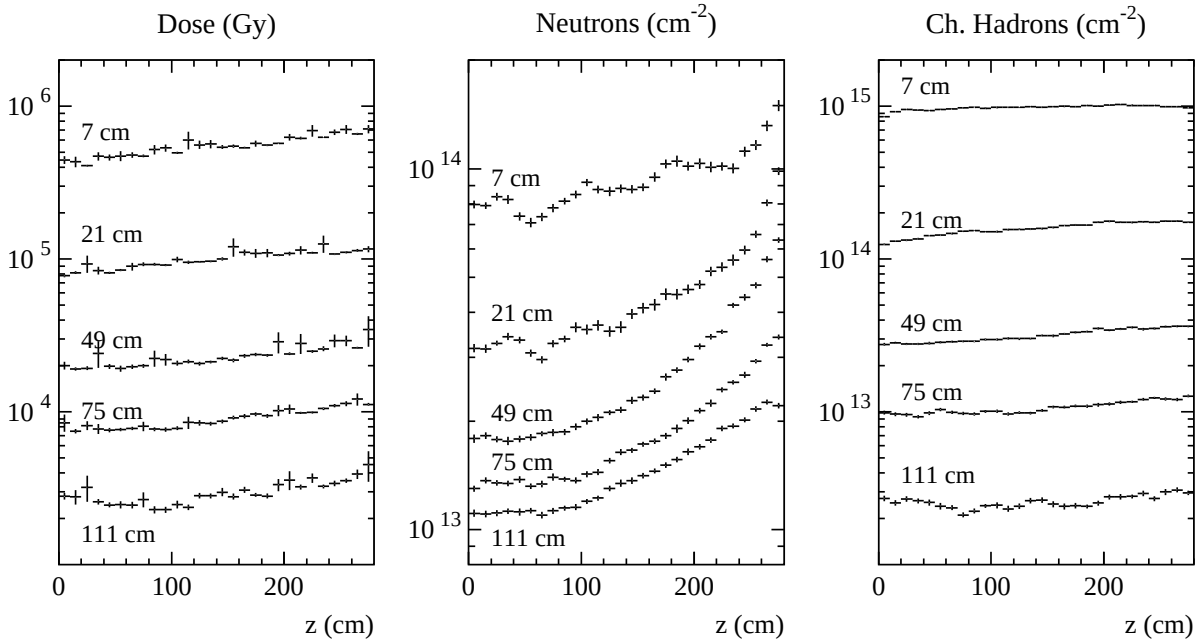

Fig. 1.11: Radiation levels at selected radii in the CMS Tracker region. All values correspond to an integrated luminosity of 5×10^5 pb^{-1}. The error bars indicate only the statistics of the simulations. The neutron fluences include only the part of the spectrum above 100 keV.

Chapter 2

The Pixel Detector System

2.1 Overview and Requirements

The most interesting events at the LHC are likely to contain several b-jets originating from the decay of heavy particles. In order to allow an efficient tagging of these jets as well as of other objects (c, τ) the tracking must extend as closely as possible towards the reaction vertex. Owing the extremely high particle fluxes at these small distances pattern recognition arguments require the innermost tracking layers to be composed of pixel devices delivering true space point information with high resolution. Over the full acceptance of the CMS detector the pixel system should provide two or more hits per track, which allow secondary vertices to be found for tagging long-lived objects, like b or c quarks and τ-leptons, and to distinguish them against a large background of light quark- and gluon jets. For detecting Higgs or SUSY particles b-tagging in particular will play an important role. Conventional B-hadron physics, including CP-violation, B_S- oscillations and rare B-decays, and top quark physics will begin immediately after LHC startup, making it imperative that the pixel system be ready on the first day of LHC operation. With increasing luminosities the pixels will help greatly in pattern recognition of the many tracks present in one bunch crossing. The pixel detectors will confirm or reject track segments proposed by the outer Tracker layers. Once a track has been successfully followed to the pixel layers, the two pixel hits will be crucial to extrapolate this track to the vertex with high precision. For heavy-ion operation the pixels will have small enough occupancy values to single out particular tracks in the very high multiplicity environment.

The CMS pixel system will have two barrel layers and two end layers (end disks) on each side of the barrel. The layers are composed of modular detector units. These modules consist of a thin, segmented sensor plate with highly integrated readout chips connected to them using the bump bonding technique (see Fig. 2.1). The chips are connected through bond wires to hybrid circuits, which distribute the readout control and clock signals and where the data signals are collected. Kapton cables connected to the hybrids transmit the signals to and from a periphery situated at the outer region of the pixel system frame where detector control chips and electro-optical converters for optical signal transmission are located. The modules are attached to cooling frames, with the cooling tubes being an integral part of the mechanical structure.

The minimal pixel size is dictated by the readout circuit area needed to accommodate each pixel. In finding and localising secondary decay vertices, both $r\varphi$ and $z(r)$ hit coordinates will be important in the barrel (end disks), respectively. Therefore a square pixel shape is preferred, combined with analog signal readout to profit from position interpolation, where effects of charge sharing among pixels are present. In the barrel charge sharing in the $r\varphi$-direction will be large due to the very high magnetic field in CMS (Lorentz drift angle = 32° for e^- in silicon at 4 T). With a sensitive detector thickness of between 200 and 250 μm and by deliberately not tilting the detectors in the barrel, the natural pixel size will be around (150 μm)^2 giving favourable

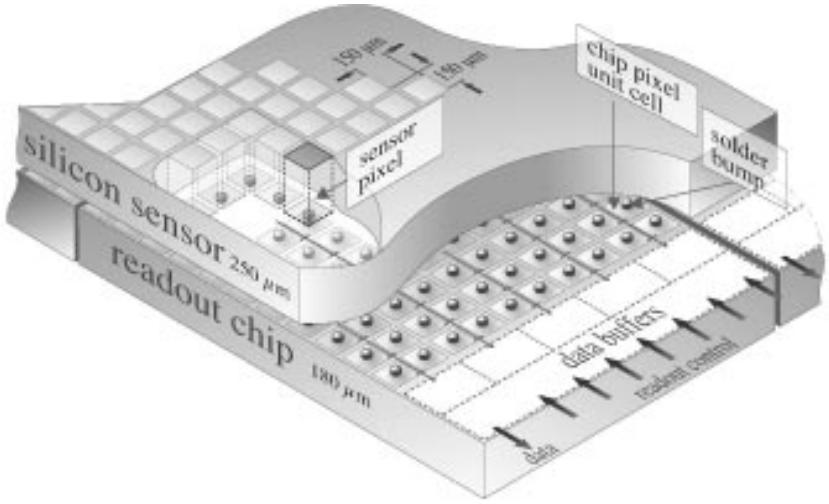

Fig. 2.1: Schematic view of a pixel detector element. Each sensor pixel is connected via a solder bump to a pixel unit cell on the readout chip, where the signal is amplified. The hit data are stored on the edge of the chip where they wait for trigger confirmation.

resolution and cluster size conditions. Charge sharing along the z-direction is also present in the barrel for inclined tracks. The end disks have been completely redesigned since the CMS Technical Proposal, in which the rectangular end cap pixels had good resolution in the $r\varphi$ direction only. The detectors will be rotated by 20° about a radial axis such that the tilt angle and induced $E \times B$ effects increase the charge sharing among neighbouring pixels in both r and $r\varphi$ directions. The square pixels will have 50% greater area, whilst retaining good resolution in $r\varphi$ and achieving comparable resolution in r, a factor of 5 improvement over the Technical Proposal design.

At radii smaller than 10 cm the hostile radiation environment will reduce the lifetime of both sensors and readout chips below the expected lifetime of the experiment. Therefore the pixel detectors placed closest to the beam must be replaced at least once during the experiment.

To profit from the improved secondary vertex resolution at very small radii, it is proposed to build the pixel barrel system in two stages. For the initial low luminosity period of the LHC, radial positions down to 4 cm will be covered. When the luminosity reaches the design value the innermost sensors will be removed and modules added at larger radii.

The greatest challenges in the design of the pixel system are the radiation hardness of all components and the extremely large number of pixels to be handled in a high rate environment. Both sensor material and readout chips must be robust enough to survive the first six years of LHC running (goal for a radius of 7 cm from the beam axes), without an unacceptable degradation of their performance. The large number of pixel channels requires autonomous hit detection at the detector level and storing of hits during the first level trigger latency time. This must be accomplished in the very limited chip area available, with rather coarse feature electronics structures of a radiation-hard process.

In the last three years the CMS pixel community has performed feasibility studies on three important topics, which have been defined as milestones to be met before proceeding further in the design phase:

1. **Specification of detector material**
   The detector material must survive the fluences of up to 6×10^{14} hadrons per cm^2 anticipated in the first six years of LHC running at a radius of 7 cm, and provide sufficient signal charge throughout this period.

2. **Specification of analog readout block suitable for LHC**
   The analog block must be able to deal with increased leakage currents, reduced charge collection and other changes in the detector that are induced by radiation damage, as well as with damage to the circuit itself. With a low power budget, good signal to noise performance and small time walk to ensure safe bunch crossing identification are required.
3. **Specification of front-end readout architecture**
   The front-end readout architecture must operate with good efficiency in spite of high hit and trigger rates. Adequate buffering must minimise the loss of data corresponding to triggered bunch crossings. The chosen design must be robust against device changes due to radiation damage.

This chapter describes mainly the results obtained for these three milestones, and the conceptual design derived for a pixel system which performs adequately under the difficult conditions at the LHC. Some technical design choices still remain to be made in the coming years. Since the pixel system is small compared to the rest of the Tracker, mass production and assembly of the pixel system need not start before mid 2002. Where appropriate, alternative solutions are mentioned, which must be selected at suitable times to match the prototyping and construction schedule.

2.2 Experimental Constraints and Layout

2.2.1 Design constraints

The impact parameter resolution depends crucially on three design parameters of the pixel vertex detector:

- The distances of the layers from the interaction region
- The hit resolution
- The material budget

When optimising these parameters important design constraints must be taken into account:

- The pixel size is influenced by the area needed on the readout chip for the pixel analog front-end and readout circuitry.
- The extremely high power density, requiring efficient cooling, and the necessary mechanical stability of the sensor frames will dictate the material budget.
- The radiation environment close to the interaction region limits the lifetime of sensor and readout chip.

Other design constraints are imposed by the chosen insertion scheme of the pixel system. The novelty and complexity of the pixel detectors suggest that yearly access to the detectors will be required, at least in the first years of LHC operation. Removal and insertion of the pixel system must be possible without strongly affecting other subdetectors and without taking too much time. Hence it is envisaged to insert the pixel system together with all its services along the z-axes, with the beam pipe installed and baked-out prior to the pixel system installation. The vertical beam pipe suspensions and the increasing beam pipe diameter with increasing $|z|$ require building the pixel system separable into a left and a right half with respect to the beam axis. During insertion the two halves, initially separated, move on converging rails bringing them together to form a hermetic structure in the final position.

2.2.2 Pixel size and shape

The choice of pixel size and shape is influenced by a number of partially conflicting arguments. Besides obvious parameters like resolution, hit cluster size, occupancy, pixel rate etc., other arguments must be taken into consideration:

- The choice between analog or digital readout
- The area needed to accommodate the individual pixel electronics
- The dependence of the pixel capacitance on the pixel shapes considered
- The power density of the pixel array
- The expected sensitive detector thickness
- The total available signal charge
- The Lorentz drift angle of the charge
- The mean track incident angle

Conventionally the coordinate perpendicular to the magnetic field is favoured in tracking detectors and efforts to measure the parallel coordinate well are relaxed. While this is justified for optimal momentum resolution, it is not obvious for the pixel system whose main task is to measure track impact parameters. Here either coordinate can be important, depending on the topology of the vertex. Our approach is therefore to optimise the resolutions in both coordinates simultaneously, which suggests a square pixel shape. This also gives the smallest pixel capacitance.

The minimum pixel area needed for the readout circuitry is believed to be around 0.015 mm^2, resulting in a side length of around 120 μm. Without charge sharing a resolution of 35 μm would result. This can be much improved by the consistent use of charge sharing effects together with analog readout for interpolation between pixels sharing the hit signal. Consequently charge sharing effects will be deliberately favoured in the layout of the CMS pixel detector. In this respect a large Lorentz drift angle is of great interest. As outlined in Section 2.3.1 the baseline sensor material is silicon, where the electron drift angle (32° in a 4 T magnetic field) is three times larger than for holes. Therefore n-pixels which collect the electrons will be used. When the electrons arrive at the pixel surface, they are spread in the barrel over an $r\varphi$ distance of sensitive detector thickness $\times$ tan(32°), see Fig. 2.2. So that this distance extends over no more than two pixels, a natural pixel dimension in $r\varphi$ for the barrel can be deduced from the sensitive detector depth. With a sensor thickness chosen to be 250 μm a pixel dimension of about 160 μm is suggested. However, in order also to accommodate running with partial depletion, the pixel dimension is chosen to be 150 μm where, due to threshold effects in the readout, three-pixel clusters will still be negligible.

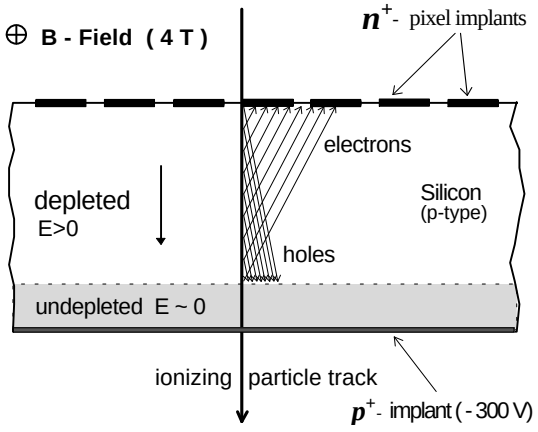

Fig. 2.2: Charge sharing induced by Lorentz drift. After type inversion the detector depletes from the n-pixel side. With increasing radiation dose the detector cannot be fully depleted and the charge sharing effect is reduced.

The fraction of single pixel hits will increase with decreasing depletion depth. As outlined in Section 2.3.2 the depletion depth in silicon can be expected to be greater than 200 μm until the specified radiation fluence of 6×10^{14} hadrons/cm^2 is reached. Consequently up to 20% of hits

will be single pixels, occuring in a small, a priori known sub-area of the pixel. Therefore, in spite of using a pixel dimension of 150 μm in the $r\varphi$-direction for the barrel, intrinsic hit resolutions at the 10–15 μm level can be obtained for the entire range of depletion depths expected during the required lifetime of the sensors.

In the z-direction, with an identical pixel width of 150 μm, similar resolutions can be obtained for inclined tracks. The hit cluster length will be indicative for the polar angle of the track, which can be used e.g. to distinguish hits of steep looper tracks from direct tracks [2-1].

The choice of pixel size and shape outlined above is driven by the barrel design. In the end disks, there would be little charge sharing, since the electric and magnetic fields are parallel, and most tracks are close to normal incidence. Therefore geometric and $E \times B$ charge sharing effects are induced by rotating the detector blades by 20° around their central radial axes. Although the amount of charge sharing is still less than in the barrel, good resolutions at the level of 15 μm are expected for both r and $r\varphi$ coordinates at the start of LHC, degrading to around 20 μm as the depletion depth falls towards 200 μm.

In summary, a square pixel of (150 μm)^2 is now proposed, in contrast to (125 μm)^2 in the Technical Proposal. This change is mainly motivated by the larger achievable depletion depth in silicon, even after considerable radiation fluences, than expected earlier. The increase in pixel area will allow a more complex readout electronics if required, or a more conservative design with a higher chip yield reducing the costs. The increased occupancy is readily acceptable. The hit resolution can essentially be maintained and cluster multiplicities are reduced. The power budget per unit area will decrease by 30%. The leakage current per pixel and the pixel capacitance will, however, increase.

2.2.3 Pixel system layout

LHC vacuum conditions require a minimal beam pipe radius of 25–30 mm at the vertex. Including the necessary clearance the first pixel layer can be positioned at a radius of roughly 40 mm. With a postulated radiation hardness of up to 6×10^{14} hadrons per cm^2, sensors and readout chips would survive here during the first four years of LHC operation (assuming that the first three years of LHC operation will represent roughly one year of full luminosity, and full luminosity operation starts in year 4). During the low-luminosity phase the barrel will have two layers at approximately 4 cm and 7 cm (low-luminosity barrel configuration). When reasonable operation of the innermost layer is no longer provided, it will be removed and a new layer will be installed at 11.5 cm. Together with the layer at 7 cm it forms the high-luminosity barrel configuration. While the layer at 11.5 cm will remain operational at least until year 10 after LHC startup, the layer at 7 cm must be replaced in year 6 or 7. By this means it is possible to take advantage of an improved impact parameter resolution during the first years.

Two end disks will be placed on each end of the barrel in order to complement the η-coverage for two pixel hits. Rapidities up to $\eta = 2.4$ (2.2) are covered for tracks originating from the centre (1 σ from the centre) of the interaction region. It is also anticipated to replace the innermost modules of the end disks once during the experiment. Figure 2.3 shows a perspective view of the CMS pixel system in the high-luminosity configuration. The pixel system envelope extends from $3.7 \leq r \leq 21$ cm and for $-50 \leq z \leq 50$ cm.

2.2.3.1 Pixel barrel layout

Table 2.1 summarises the main parameters of the barrel.

Layer 1 and 2 form the low luminosity configuration, layer 2 and 3 will be used at high luminosity. Each layer consists of two half-cylinders with half-faces at the azimuthal edges (see Fig. 2.4).

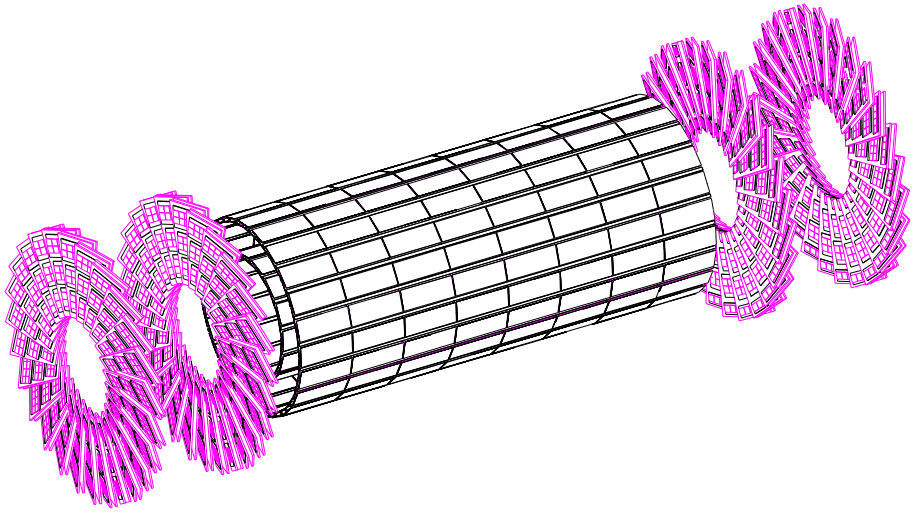

Fig. 2.3: Perspective view of the CMS pixel system in the high-luminosity configuration.

Table 2.1: Parameters of CMS pixel barrel

	Configuration	Radius [mm]	Faces (∗)	full/half Modules	Chips	Pixels	Area [m^2]
Layer 1	low luminos.	41–45	18	128/32	2304	6.35×10^6	0.15
Layer 2	low & high luminos.	70–74	30	224/32	3840	10.6×10^6	0.25
Layer 3	high lumi	107–112	46	352/32	5888	16.2×10^6	0.38

(∗) Two half-faces are counted as one face

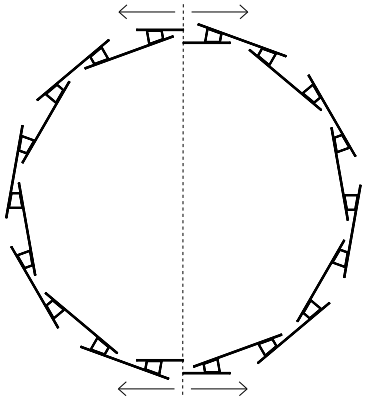

Fig. 2.4: Radial cut of the mechanical frame of barrel layer 1. Trapezoidal cooling tubes are connected through thin cross pieces. Left and right halves are separable.

The number of faces is arranged such that a smooth joining of the two halves is guaranteed when inserting the barrel (note that the two halves are *not* mirrored). The regular shape of each half-cylinder is given by trapezoidal cooling tubes held in place by two end-flanges and cross-connected through thin carbon fibre blades glued to the tubes. The shape of the cooling tubes is different for each layer. All cooling tubes have the same thermal load. The three layers are identical in length, each face consisting of 8 sensors of 65.9 mm length and 17.45 mm width. The modules, mounted onto the carbon-fibre blades, are not tilted. No overlap in z is foreseen in the present design, while the overlap in φ is 6%. The distance between the sensitive regions of two adjacent sensors in the z-direction will be 1.5 mm, representing a loss of 2.3% per layer. However, at a cost of increasing the material budget the sensors could be tilted to provide overlap in z. Full modules have 2 rows of 8 readout chips with 53 ($r\varphi$) $\times$ 52 (z) square pixel unit cells, half-modules have one row.

2.2.3.2 End disk layout

Table 2.2 summarises the main parameters of the pixel end disks. Each of the four disks includes 24 wedge-shaped blades. Figure 2.5 displays the configuration of the blades arranged in a 'turbine' geometry. The blades are each rotated by 20° around their radial symmetry axis. The disks located at $+z$ and -z share charge along the same directions only if they have point symmetry relative to the interaction region. This requirement is incorporated in the support of the blades.

Table 2.2: Parameters of CMS pixel end disks

z cm	Radius mm	Blades	Sensor Modules	Chips	Pixels	Area m^2
$\pm$ 32.5	60–150	24	7	1080	3.0×10^6	0.07
$\pm$ 46.5	60–150	24	7	1080	3.0×10^6	0.07

Fig. 2.5: The turbine blade geometry to one disk of forward pixels.

The insert in Fig. 2.5 shows the concept of a blade. It is a low-mass trapezoidal structure made with two panels of carbon-fibre. Between the two panels runs a U-shaped cooling tube. Sensors on different sides of the blades overlap radially by 5% to allow for the alignment of the detectors on the blade. Detectors on adjacent blades have an additional overlap of 4% to ensure the alignment with particles of all the blades on a disk. The outside dimensions of the sensors can only have discrete values dictated by the size of the readout chip (see Section 2.3.4.2). To ensure maximal coverage of the solid angle and also to keep the material budget to a minimum the dimensions of the sensors have been chosen such that the loss in coverage is at the 2% level. Each blade has 7 sensor arrays with sizes that accommodate between 2 and 10 readout chips. The two detectors at the innermost and at the outermost radius on a blade are read out by a single row of chips, while the other sensors have two. For installation purposes the 24 blades of one disk are configured in two half-disks. The disks on each side of the interaction region will then be installed on a cylindrical space frame split along a vertical axis. Insertion will take place using the same approach as for the barrel.

2.3 Pixel Sensors

2.3.1 Choice of detector material

The radiation environment close to the interaction region will cause damage to the pixel sensors and hence limit their lifetime. At the time of the CMS Technical Proposal three candidates for the sensor material were singled out to be evaluated for sufficient radiation hardness: Silicon, gallium arsenide and diamond. While silicon was known at that time to suffer significant performance changes induced by non-ionising energy loss, GaAs and diamond, though performing worse than silicon before irradiation, were believed to keep their performance after intense neutron irradiation. They were therefore claimed to be radiation-hard.

Meanwhile many detailed irradiation studies have been performed, in particular with low-energy pions which at LHC will represent the bulk of hadronic radiation. In summary, these studies have delivered the following results: In spite of the radiation hardness of GaAs to moderate fluences of neutrons the material is quite susceptible to charged hadrons, resulting in a significant and unacceptable signal loss (see Ref. [2-2] and Section 2.9.1). Diamond was shown to be resistant to at least 10^{15} pions/cm^2 (see Section 2.9.2). Up to 250 μm charge collection depth has been reached [2-3] and further improvements can be expected. Therefore diamond might become a candidate again at a later time, provided it can be mass produced at an affordable price. However, the radiation sensitivity of the readout chips will likely be a more limiting factor. In this case it would be necessary to find a procedure to replace the damaged readout chips on the diamond detectors in order to really profit from the radiation hardness of diamond. A possible solution could be to reprocess the diamond detectors and bump bond new chips.

As outlined in the next section, silicon is a viable detector material and has been chosen as the baseline material.

2.3.2 Performance of irradiated silicon pixel detectors

The consequences of non-ionising energy loss in silicon are well known:

- Increase of the bulk leakage current leading to increased noise and power dissipation.
- Build-up of an effective p-doping, which requires ever increasing depletion voltages.
- Charge trapping in the depleted region.
- After initial annealing a reverse annealing occurs where initially electrically inactive defects become active during several months after irradiation, thereby increasing the effective

doping still more. This effect is temperature dependent and can be controlled by keeping the detectors at appropriate temperatures below 0 °C all the time once operation of the LHC has started. This also helps in reducing the leakage currents.

In order to increase the useful operational lifetime of the silicon detectors, running with partial depletion must be anticipated. This is more suitable for n-pixel readout, because after type inversion the depleted region will be on the pixel side. The choice of n-pixels is also motivated by the large Lorentz angle of 32° for electrons in the 4 T field, which leads to appreciable charge sharing among pixels and thus improves the spatial resolution.

To obtain a detailed picture of the signal loss effects after irradiation, silicon pixel detectors were irradiated with pions of 300 MeV/c. The pixel arrays consisted of 8×32 squared n-pixels of 125 μm side length. All 256 pixels were routed to the edge of the 5×8 mm^2 test structure and connected to readout chips. In order to sense the response of the irradiated detector at various depths of the pixels, pions penetrating the test structure at an extremely small angle were used (grazing angle method [2-4], see Fig. 2.6). With this method charge-trapping effects can be separated from charge lost due to a reduced depletion depth.

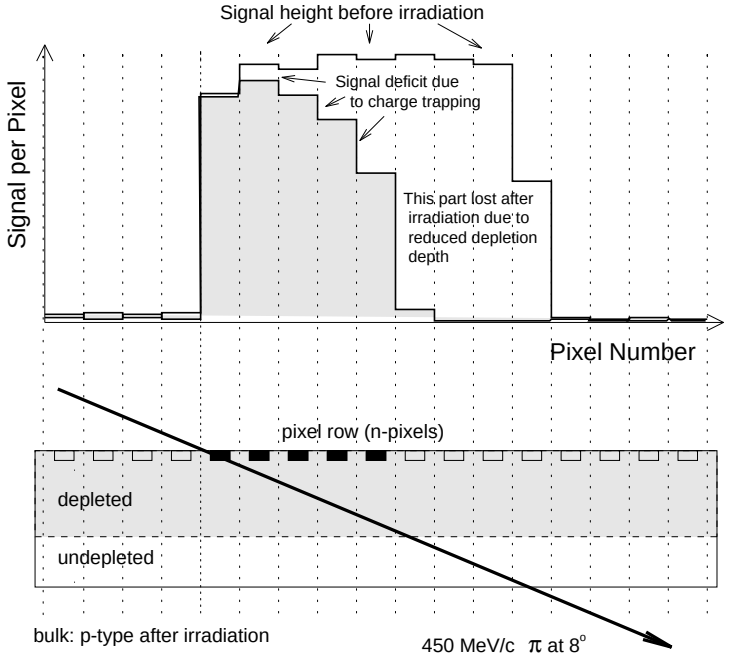

Fig. 2.6: Minimum ionising pions of 450 MeV/c graze the pixel array at an angle of 8° (bottom). The signals from the hit pixel row exhibit the response of pixels at various depths (top). Each pixel senses a depth layer of 17.5 μm.

After a pre-irradiation measurement with grazing angle pions three pixel arrays were irradiated with 3, 6 and 9×10^{14} pions/cm^2, respectively. During and after the irradiation, the detectors were kept at temperatures below 3 °C. Twenty days after irradiation the measurement was repeated. In Fig. 2.7 the depth profile of the signals obtained for various bias voltages for one detector is compared with the pre-irradiation result. A rather sharp separation between depleted and undepleted region is visible. However some charge also emerges from the undepleted region which could be shown to be collected over longer times than charge from the depleted region. A decreasing signal at increasing depth is seen due to charge trapping in the depleted region, but at high bias voltage the charge trapping can be kept below the 10% level.

Figure 2.8 shows the depletion depths as a function of the bias voltage as deduced from the profile of hit pixels. For the maximum specified fluence of 6×10^{14} pions/cm^2 a depletion depth of 150 μm is obtained for -300 V.

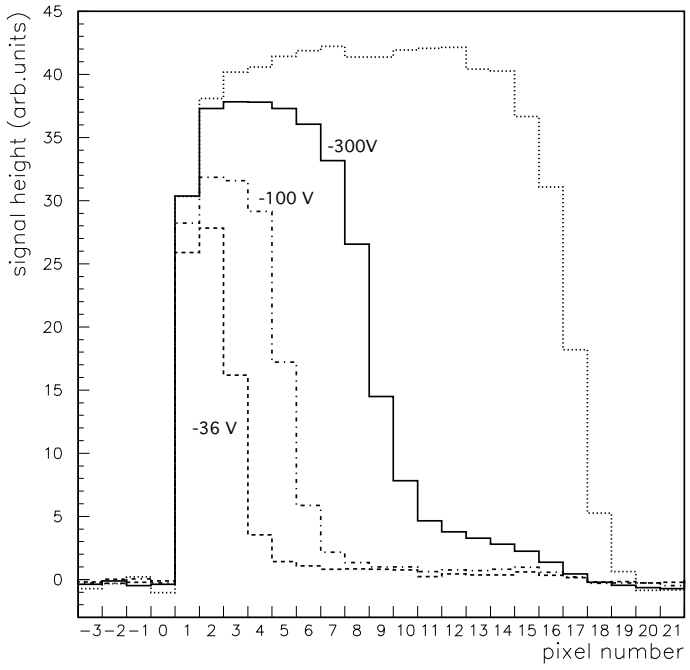

Fig. 2.7: Depth profiles of charge collected from a pixel array irradiated with 6×10^{14} pions/cm^2. The dotted histogram is for the unirradiated array.

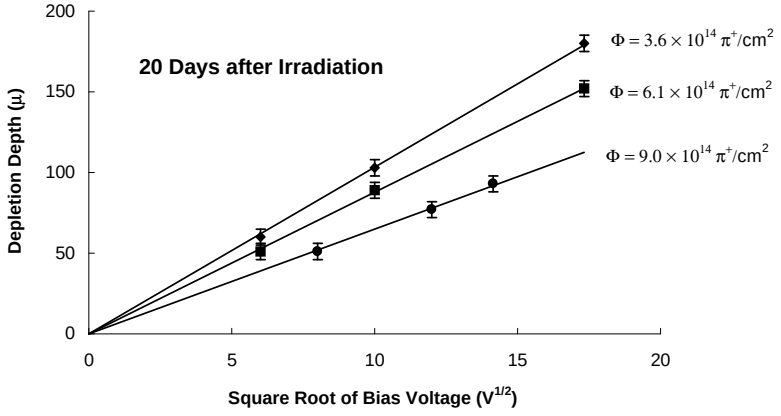

Fig. 2.8: Depletion depth vs. bias voltage. The linear behaviour with $V^{1/2}$ suggests a homogeneous distribution of the radiation-induced p-doping.

The irradiated detectors were measured again 6 and 12 months after irradiation and storage at 3 °C. Figure 2.9 demonstrates beneficial annealing for the pixel array irradiated to 6×10^{14} pions/cm^2. The depletion depth at -300 V has increased to almost 200 μm. The signal charge for perpendicular tracks, as obtained from a comparison with pre-irradiation data, increased from 10 000 electrons (20 days after irradiation) to 14 000 electrons (one year after irradiation).

The average leakage current per (125 μm)^2 pixel was measured at a temperature of -5 °C by integrating the preamplifier output over a fixed time and comparing the output level to that obtained from minimum ionising pions prior to irradiation. For a fluence of 6×10^{14} pions/cm^2 and -300 V bias it decreased from initially 11 nA (20 days after irradiation) to 7 nA (one year after irradiation), in spite of the increased depletion depth. For (150 μm)^2 pixels the leakage current is expected to be 44% higher.

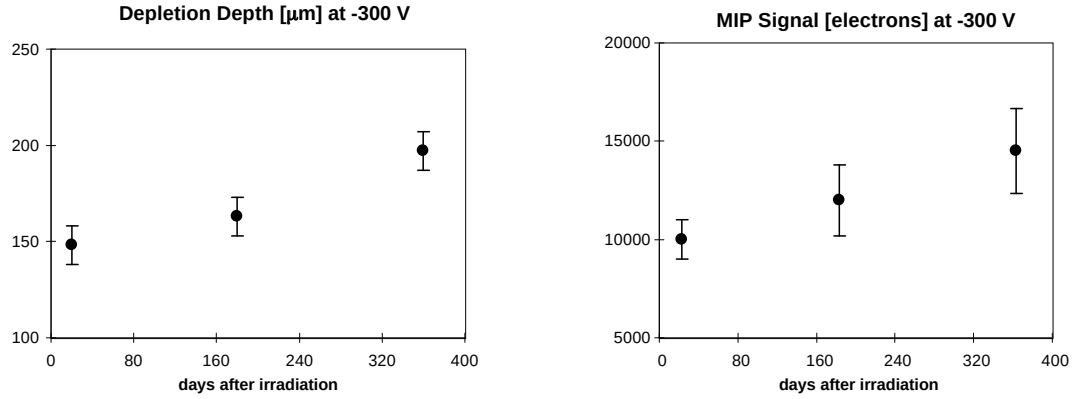

Fig. 2.9: Depletion depth and minimum ionising pion signal for perpendicular tracks for the pixel array irradiated with 6×10^{14} pions/cm^2.

In summary, a larger depletion depth than anticipated at the time of the Technical Proposal was found at acceptable bias voltages. This has allowed the pixel size to be increased from (125 μm)^2 to (150 μm)^2 as described in Section 2.2.2. At high bias voltages the charge trapping in the depleted region is below the 10% level. The signal charge from minimum ionising particles is expected to exceed 12 000 electrons during the specified lifetime of the detectors. To profit from analog interpolation, the readout should have a hit threshold not larger than 2000–3000 electrons. With the threshold at 5 σ noise, the equivalent noise charge should remain below about 400–600 electrons. Leakage currents of up to 100 nA must be absorbed by the preamplifiers. In order to limit the noise induced by this leakage current, the sensor temperature during running should be below -5 °C.

2.3.3 Specification of sensors

Silicon sensors having n-pixels on an n-type substrate have been chosen. This leads to double-sided processing, which for very thin wafers reduces the yield considerably. In the material budget the sensor material amounts to less than 20% of a pixel layer (see Tables 2.9 and 2.10). Hence reducing the thickness at the cost of a reduced yield is not worthwhile. The sensor thickness will be 250 μm and wafers are thinned to this thickness before processing.

On the n-side of the wafer, the charge collecting pixels are defined by n-implants surrounded by isolating p-stop rings. Figure 2.10 shows the detailed mask layout. The width of the n-implants is foreseen to be 78 μm, resulting in a pixel-to-pixel gap similar to the test pixels used in the pion irradiation study (Section 2.3.2). The n-implants are covered by a standard metallisation, followed by a passivation layer with bump pad windows of $\approx$ 13 μm diameter.

In each pair of pixel columns the bump pads are shifted by 25 μm to the outside, in order to fit the double column layout on the readout chip. This gives an alternating 100 μm/200 μm bump pad pattern. In the other direction the bump pad windows are shifted down in order to allow butting of the readout chips (see 2.3.4.1). Around the n-implant of each pixel, two concentric p-stop rings are foreseen. Spacing and width of the floating rings is on the order of 8 μm and will be subject to further optimisation. The use of two p-stop rings is a change to the current prototype pixel structures where only one floating p-stop ring was used. With multiple p-rings we expect a reduction of the nearest-neighbour capacitance that dominates the total pixel capacitance. The p-stop rings both have a small opening opposite each other (see Fig. 2.10). This creates a high-resistive surface path between neighbouring pixels of several hundred kΩ [2-5]. This resistive inter-pixel network has little effect on the fast signals, but keeps the n-implants for those pixels, where a bump bond connection to the readout amplifier has failed to form, at appropriate potential. With this measure we expect to solve problems of stochastic discharges in non-connected pixels, which have been observed in the pion irradiated prototype sensors and which are visible in the readout of neighbouring pixels.

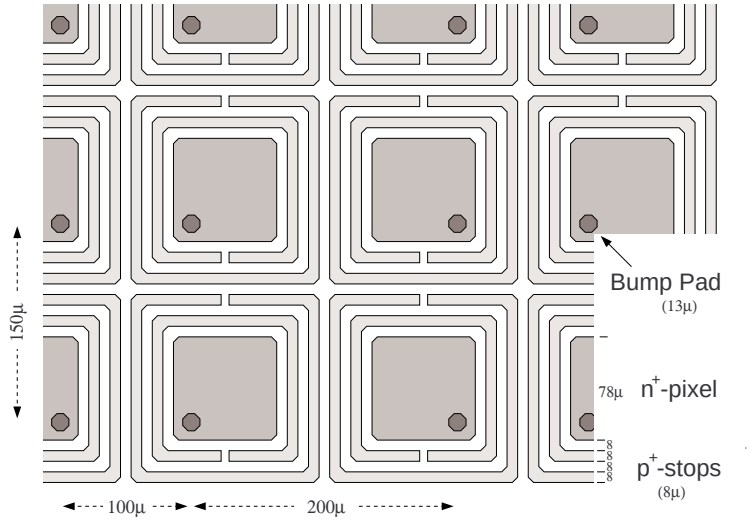

Fig. 2.10: Layout of 150 μm $\times$ 150 μm pixel sensor. The double p-stop rings around each n-pixel are floating and allow a high resistive path to neighbours.

On the p-side of the wafer, a diode is implanted with appropriate metallisation, followed by a thick passivation (several microns). Special precautions will be taken for the guard rings on the p-side, where the whole potential drop between the bias voltage and the readout chips will occur. This is required since the cutting edge of silicon must be at the potential of the n-side and especially of the readout chips. Without this measure, a potential difference between sensor edge and overlapping readout chip (typically 15–20 μm above the sensor surface) could result in discharges across the gap. The use of p-doped wafers as a starting material has been dropped because of this problem although it would allow single-sided processing [2-6].

The need to operate the detectors at bias voltages up to 300 V influences the sensor design. The breakdown voltage must be in excess of 500 V for detectors irradiated finally with up to 6×10^{14} hadrons/cm^2 in order to avoid micro-discharges. Although our 256 pixels prototype sensors [2-7] have demonstrated safe operation at 300 V and more, even after irradiation, we will continue our development of improving high voltage operation, especially to achieve the best possible yield for larger sensors. A comprehensive study on guard ring structures has been initiated [2-8] to optimise the geometry of the guard rings. Several wafers were produced with a variety of test structures and a selection of pixel arrays with 1 to 15 guard rings. They have been

characterised before and after irradiation with fast neutrons of a fluence up to 6×10^{14} n/cm^2. Designs with seven or more guard rings were shown to be appropriate for operating the test structures at bias voltages of 500 V even after irradiation. The guard rings take a total of 500 μm width. This is important since the inactive sensor area should be kept at a minimum.

For the final depletion depth after several years of operation, the initial resistivity of the starting n-material is not important, since type inversion will occur very early in the experiment. Based on the good charge collection results from the pion irradiated prototype sensors, the use of high resistivity n-material is foreseen. However, we will continue to follow the ongoing research activities on radiation hardness of silicon [2-9]. The initial leakage current requirement is not a critical item, since after a few days of LHC operation it will be dominated by the irradiation-induced contribution. The leakage current for new devices at full bias voltage (500 V) will be required to be less than 100 nA/cm^2. The high resistive network between the pixels will allow testing of the overall leakage current of a complete pixel module before bump bonding.

2.3.4 Layout of sensors

2.3.4.1 Barrel sensors

The active area of the full barrel sensors will be 6.450 cm (z) $\times$ 1.605 cm ($r\varphi$), that of the half-sensors 6.450 cm (z) $\times$ 0.795 cm ($r\varphi$). Full sensors will accommodate two mirrored rows of eight readout chips each; half-sensors are covered by one row of eight chips. Each readout chip will house 53 ($r\varphi$) $\times$ 52 (z) pixel unit cells of (150 μm)^2 area.

Table 2.3: Number of pixels on a barrel module

Pixel size [μm]	Full module	Half-module
150 ($r\varphi$) $\times$ 150 (z)	41808	21306
225 ($r\varphi$) $\times$ 150 (z)	804	–
150 ($r\varphi$) $\times$ 300 (z)	1456	742
225 ($r\varphi$) $\times$ 300 (z)	28	–

Between the chips some part of the sensor cannot be covered by active chip area. From the edge of a pixel unit cell, located at the rim of one chip, to the edge of the neighbouring unit cell, situated on the rim of the adjacent chip, a distance of about 300 μm must be left for the chip borders and the gap between the chips (see Fig. 2.11). This requires pixel rows and columns situated between chips that are larger in size than the majority of ordinary pixels. In order to maintain a square grid of 150 μm $\times$ 150 μm on the entire sensor, two pixel rows of 225 μm height ($r\varphi$) are introduced along the symmetry line between the two rows of eight chips (Fig. 2.11). Between two neighbouring chips within a chip row two pixel columns will be twice as wide as the ordinary pixels. Table 2.3 gives the list of pixels on a full and on a half-module.

Around the pixel array a border of 700 μm is foreseen for guard rings on the p-side. The overall dimensions of the full barrel sensors will be 6.590 cm (z) $\times$ 1.745 cm ($r\varphi$), and 6.590 cm (z) $\times$ 0.935 cm ($r\varphi$) for a half-sensor.

2.3.4.2 The end disk sensors

The pixel detectors covering the forward region are read out by the same chip used for the barrel. To optimise the coverage, while keeping material to a minimum, the disk geometry requires sensors with five different sizes.

Figure 2.12 shows the layout of the sensors on the two panels that form a blade. Table 2.4 lists the outside dimensions of the five different types of sensors required and how many of each are needed to assemble one blade. The detectors are 250 μm thick. The clearance space between

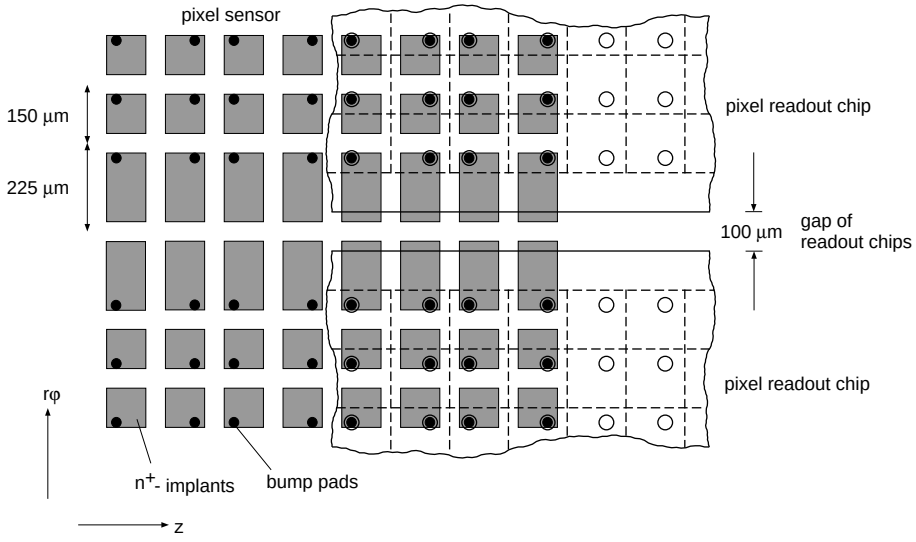

Fig. 2.11: Layout of sensor in the neighbourhood of the two adjacent readout chip rows, where special pixels are inserted.

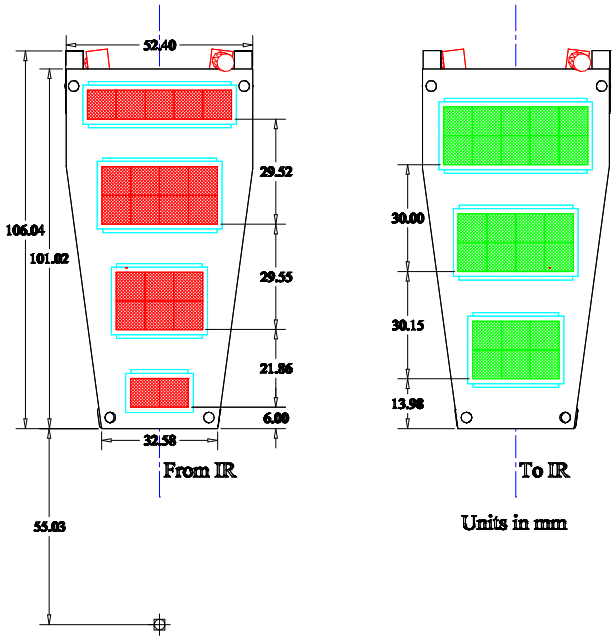

Fig. 2.12: The dimensions of the blades and the sensor arrays.

neighbouring chips (100 μm) and the space for guard rings (700 μm) is the same as for the barrel detectors. The number of chips per sensors is shown in Table 2.5.

Table 2.4: Outside dimensions of sensors

Columns × rows	Sensors/ blade	$(r\varphi)$ [cm]	r [cm]
2 × 1	1	1.730	0.935
3 × 2	2	2.540	1.745
4 × 2	2	3.350	1.745
5 × 2	1	4.160	1.745
5 × 1	1	4.160	0.935

Table 2.5: Number and sizes of pixel cells on a blade

Pixel size [μm]	Chips/sensor unit (Units needed for one blade)					Pixels/ blade
	2 chips (1)	5 chips (1)	6 chips (2)	8 chips (2)	10 chips (1)	
150 (r) × 150 $(r\varphi)$	5406	13356	15808	21008	26208	118602
225 (r) × 150 $(r\varphi)$	–	–	304	404	504	1920
150 (r) × 300 $(r\varphi)$	106	424	416	624	832	3442
225 (r) × 300 $(r\varphi)$	–	–	8	12	16	56

Table 2.5 summarises the number of pixels of each size located on one blade (see Fig. 2.12). An advantage of choosing sensors with segmentation along r is the ability to separately bias sensors that have suffered different radiation doses. There is an order of magnitude difference between the amount of radiation received by the pixels at the innermost radius as compared to the outermost ones. Detectors at the inner radius will have a faster reduction of their depletion depth compared to the outer sensors and consequently will have smaller signals. By biasing sensors separately the drop in signal can be avoided by increasing the bias voltage only where needed.

2.4 Pixel Readout Electronics

2.4.1 Overview

As outlined in Section 2.2.2 an analog readout scheme is implied by the choice of a pixel size of 150 μm × 150 μm. Analog information is extremely valuable in the off-line reconstruction, in order to distinguish small noise pulses from real single pixel hits, or to separate low-momentum looper hits from high-momentum tracks due to their difference in the observed $\mathrm{d}E/\mathrm{d}x$ pattern. The implementation of an analog readout scheme does not lead to a significant increase in complexity of the readout chip.

A schematic view of the pixel readout is shown in Fig. 2.13. Each sensor pixel is connected via a bump bond to its own readout circuit on the readout chip (Pixel Unit Cell, PUC). Two PUC columns form a double column, which represents an independent readout unit controlled by a circuit sitting in the column periphery (see Fig. 2.13). Local bus lines connect all PUCs of a double column with the column periphery, one of them being the Column OR which combines all PUCs in the double column into a global OR.

The circuit of each PUC can naturally be separated into two functional blocks. The analog block amplifies the tiny signal charge from the sensor. If the signal is above a tunable threshold,

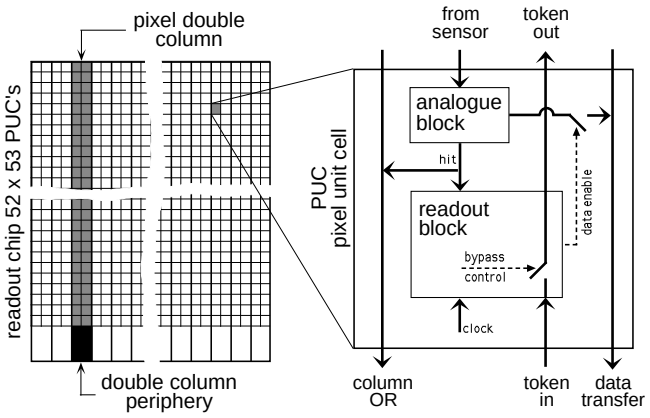

Fig. 2.13: A schematic view of the pixel readout system.

the periphery is notified via the Column OR. The column periphery registers the associated bunch-crossing number (time stamping) and sends a token signal up and down the double column, bypassing empty pixels. In the readout block of the hit pixels the token signal initiates the transfer of pixel address and analog signal, which are stored in a data buffer located in the periphery, waiting for the first level trigger (1LT). The confirmed time-stamps with their associated signals and addresses are transmitted directly from the periphery through analog optical links to the front-end driver in the counting room, where digitization is performed.

The design of the readout electronics has been guided by a detailed simulation of the behaviour of the sensor and the readout chain at the expected particle rates. Typical hit rates and pixel multiplicities, and the performance of the pixel detector as a function of the hit threshold and the quality of the analog readout are detailed in Section 2.4.2. Section 2.4.3 describes some selection criteria for the radiation-hard processes used for prototype chips.

Two early milestones have been set for developing the pixel readout scheme suitable for LHC. The first concerns the analog front-end that must cope with very high bunch-crossing rates and deal with increased radiation damage of both sensor and chip. The work on this milestone is described in Section 2.4.4. The second milestone is the choice of the readout architecture (Section 2.4.5). Here extensive time domain simulation studies have been performed quantifying data losses for different column-based architecture variants (Section 2.4.5.2).

A complete precursor chip in radiation-hard technology with 22 by 30 pixels having a stripped-down readout architecture, but incorporating many of the required functions, has been constructed and operated. Some important building blocks for the full readout architecture have also been designed and tested (Section 2.4.5.5).

2.4.2 Simulation of experimental conditions

In order to understand the performance and the various rates under which a pixel readout system has to operate, a detailed simulation of the pixel detector was carried out. This Monte Carlo simulation has been the basis for estimating data rates and readout inefficiencies of various sensor and readout scenarios. The simulation includes not only the generation of track hits in the sensor, but also the data flow inside the readout chip. Signal and pile-up events were generated with PYTHIA and traced through a precise model of the pixel detector using the CMSIM program. Low-momentum tracks (down to 40 MeV/c) were included in order to account for all looping tracks. In the GEANT simulation all reaction mechanisms were enabled including generation of delta rays. Detector hits were digitised to produce a list of pixel hits together with the charge from each pixel. The procedure for generating pixel hits from GEANT tracks is described in detail in Section 7.8. As signal events we used $t\bar{t}$ jets with a transverse momentum

p_T of typically 100 GeV/c. For high luminosity conditions a Poisson distributed sample of pile-up events was also generated in the same bunch crossing. The average number of pile-up events (minimum bias) per bunch crossing is set to 25. After a Gaussian noise contribution of 300 electrons added to each pixel, the pixel pulse heights are digitised and stored. For hit discrimination a pixel threshold of 4 σ is normally used, unless stated otherwise. In this section more general simulation results concerning rates, multiplicities and the effects of analog readout are presented, whereas results dealing with the specific problems of data flow, data buffering and the overall readout architecture are treated in Section 2.4.5.2.

2.4.2.1 Expected hit rates

The average data rates for a (150 μm)^2 pixel size are summarised for the different barrel layers in Table 2.6.

Table 2.6: Average data rates for the barrel

Radius [cm]	4	7	11
Luminosity [10^{34}]	0.1	1.0	1.0
Pixel hit rate [kHz]	7.6	13.0	6.9
Double column hit rate (2 × 53 pixels) [MHz]	0.47	0.77	0.44
Average number of hit pixels in a hit column	1.9	1.9	1.7
Readout chip hit rate (26 double columns) [MHz]	6.5	11	7.6
Average number of hit pixels in a hit chip	3.3	3.5	2.6
Barrel module hit rate (16 chips) [MHz]	36	40	38
Average number of hit pixels in a hit module	9.3	15	8.1
Pixel occupancy [10^{-4}]	1.9	3.3	1.7

These rates, simulated with an assumed threshold of 1000 electrons, have different contributions coming from noise tail hits, $t\bar{t}$ events and minimum bias events. The average pixel hit rate of 13 kHz at a radius of 7 cm translates into an occupancy of 0.00033 per bunch crossing. Here noise hits and hits from $t\bar{t}$ events each contribute 10%, and the rest comes from minimum bias events. There will be occupancy fluctuations due to jets. For 100 GeV b-jets the local occupancy in a chip hit by the jet is 0.0017. This is 5 times the average occupancy. The pixel rates in the barrel are almost constant with rapidity. The pixel rates in the end disks are lower than for the 7 cm barrel layer. Therefore most of the following simulation studies have been performed for the 7 cm barrel layer which represents the most critical case.

The $r\varphi$ position resolution in the barrel is based on charge sharing between pixels induced by the Lorentz effect. The ratio of pixel pitch to depletion depth is one of the parameters that defines over how many pixels the charge is distributed. The average number of pixels per track in the $r\varphi$ direction is shown in the left part of Fig. 2.14 as a function of rapidity. With a pixel size of (150 μm)^2 the signal charge is distributed on average over about two pixels for the irradiated detector with reduced depletion depth. As expected, there is no significant η dependence of the $r\varphi$ charge sharing for the barrel. For the cluster size in the z-direction on the other hand (right part of Fig. 2.14) the expected geometrical dependence is observed. This can be used to extract information on the polar angle of the track.

A crucial parameter for the conceptual design of the readout scheme is the pixel column data rate. By this we refer to the rate in a double column of pixels, which will be dealt with by a single column periphery. We split this rate into a column hit rate (average rate at which a double column gets hits) and an average number of pixels above threshold in this column (see Table 2.6). The column hit rate is relevant for the number of time-stamp registers required in the column periphery, while the number of hit pixels in a column affects the size of the column

data buffer. More detailed results and their implications for the readout architecture are given in Section 2.4.5.2.

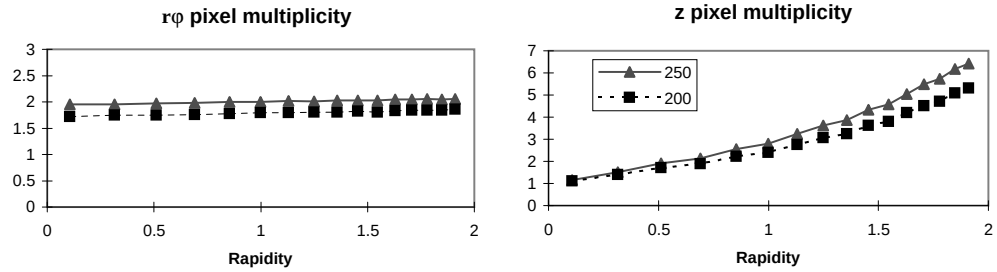

Fig. 2.14: Average number of pixels hit in the barrel layer at 7 cm (pixel size (150 μm)^2) versus rapidity for a single 100 GeV muon track. The solid line (triangles) is for a fully depleted detector (250 μm) and the dashed line (squares) is for a detector with partial depletion of 200 μm. The pixel threshold has been raised by 50% from the default value to 1600 electrons. All tracks are assumed to come from the detector centre (no primary vertex smearing).

2.4.2.2 Analog readout and threshold effects

The question of how accurately the analog pulse height needs to be read out is presented in Fig. 2.15. The position resolution has been calculated as a function of analog pulse height granularity (number of ADC-bits) with a detailed Monte Carlo simulation (see Section 7.8). The results of this study indicate that a four bit digitisation of the analog signal is sufficient to obtain most of the resolution that is possible. A moderate pulse-height accuracy of 4 bits will certainly also be sufficient for various off-line studies of noise hits and track hit patterns used in the track reconstruction.

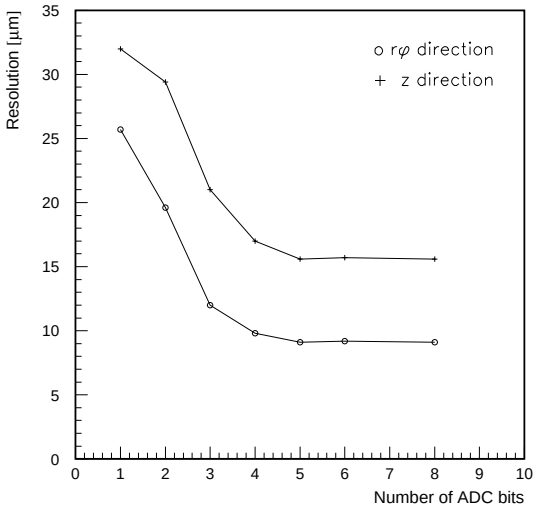

Fig. 2.15: Pixel barrel position resolution as a function of the number of ADC bits used in the conversion of the analog signals. The simulation was done for (150 μm)^2 pixels, 250 μm thick, in the 7 cm barrel layer. Single muon tracks of 100 GeV were used.

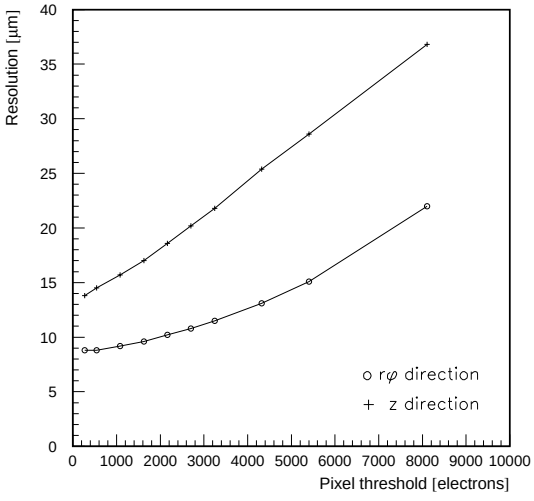

Fig. 2.16: The position resolution versus threshold in the $r\varphi$ (circles) and z (crosses) directions in the 7 cm barrel layer. For all data points the amount of noise was scaled to 1/4 of the threshold value. The simulation was done for 100 GeV single muon tracks.

The possibility of precisely setting each pixel threshold, giving uniform response, is indispensable for controlling the pixel readout system. We are planning to set a threshold that is 5 σ above the amplifier noise. The random count rate due to noise is a very steep function of the discriminator threshold of each pixel. The non-uniformity and the threshold variation of the discriminators, due to variations in the CMOS integrated circuit (especially after irradiation), is potentially a problem. Since the number of pixels in the system is large, it would be almost fatal if the discriminator thresholds would be below 4 times the r.m.s. noise. In this case the readout system would be flooded with a high rate of noise pulses and as a consequence would cause significant dead time and data losses. With this consideration in mind one would like to keep the pixel threshold as high as possible. However, this would counteract a precise position interpolation by charge sharing since it will suppress pixels with low pulse height. We have studied the degradation of the position resolution in the barrel for different pixel thresholds. The results have been obtained from a detailed Monte Carlo simulation where the energy deposition in the silicon detector is calculated every 10 μm along the ionising particle track (see Section 7.8 and Ref. [2-10]). As can be seen in Fig. 2.16, there is a rather weak dependence of the position resolution with increasing pixel threshold. A pixel threshold of 2500 electrons would still allow an overall tracking precision of 15 μm in the $r\varphi$ direction if an overall alignment error of 10 μm is assumed. After several years of operation the detector signal charge will degrade but the pixel thresholds must stay or will even have to be raised due to increasing noise. For the position resolution this acts like an effective threshold increase, but with a rather gentle slope.

Although precision measurements from the pixel detector are crucial for good impact parameter resolution, the most basic task of the Tracker is to find all the hits in each layer and correctly reconstruct the tracks. The cluster identification must stay intact even under severe threshold changes. Figure 2.17 shows the efficiency to find a cluster per track as a function of the threshold. It can be seen that for thresholds above 9000 electrons the detector becomes inefficient. The curve (diamonds) is calculated for a fully depleted 250 μm thick silicon sensor. As the depleted zone is expected to degrade to 200 μm after several years of running we expect that the maximal threshold for full efficiency is scaled proportional to the reduction of the signal charge. We estimate according to our present knowledge on sensor degradation a maximum threshold of about 7000 electrons.

In summary we can expect a rather robust readout scheme with slowly degrading performance that can be tolerated. The basic functionality of providing unambiguous 3-D hits for track reconstruction will remain intact even after several years of running.

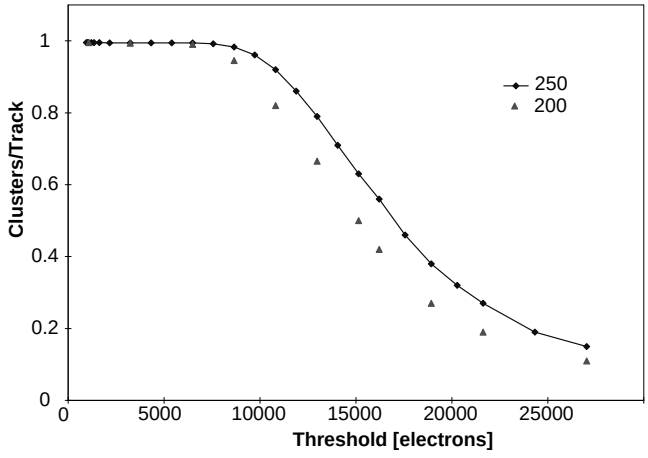

Fig. 2.17: Fraction of found tracks as a function of pixel threshold for the barrel layer at 7 cm. The pixels are of size (150 μm)^2 and 250 μm thick. The solid line (diamonds) is for a fully depleted detector (250 μm) and the triangles are for a detector with partial depletion of 200 μm.

2.4.3 Radiation-hard processes

Most of our prototype chips are designed in radiation-hard CMOS processes. This ensures that the development of the final readout chip uses realistic assumptions on the design area and the performance before, as well as after, irradiation. So far the DMILL (Temic) process was used exclusively. However, recently we have also translated some designs into the RICMOS IV (Honeywell) process. Both processes are based on SOI technology (Silicon On Insulator) which is known to have good crosstalk properties. This is crucial for our mixed digital/analog readout chip. The SOI processes have an intrinsic device isolation and are immune to charge collection on high impedance nodes through carrier diffusion in the CMOS bulk substrate. This is not only of concern for charge injected into the substrate by nearby active digital nodes but also for charge carriers generated in the substrate by ionising energy depositions from particle tracks (e.g. stopping or shallow tracks).

The SOI processes tend to have an excessive noise performance compared to bulk CMOS technologies. Although the transistor noise requirement for a pixel readout chip is not so severe as for a microstrip detector readout, we demand from the process that the observed excess noise factors be not too large. Another rather important issue for a pixel chip, however, is the question of transistor matching after irradiation, since it is a crucial factor for reliable and uniform hit discrimination.

At the innermost part of the tracking system of CMS the pixel detector is exposed to the highest particle rates. The question of certified radiation hardness of a specific CMOS process is therefore of high importance to our application. The DMILL process is certified to 100 kGy and the RICMOS IV to 10 kGy. However, chips from both processes have been successfully tested to much higher radiation levels. More details about other specific properties of these CMOS processes are given elsewhere [2-11].

2.4.4 Analog front-end

2.4.4.1 Design considerations

The design of the analog front-end block depends very much on the choice of the sensor material as the signal charge generated by the sensor is one of the most important parameters. After several years of running under LHC conditions the low noise performance of the front-end will be degraded, as well as the signal charge from the sensor. With our choice of silicon as a detector material we base our design on an initial signal charge of 3 fC for an undamaged detector reduced to about 2.3 fC after the equivalent of four years of full luminosity LHC running at 7 cm radius. The choice of silicon implies typical leakage currents of 10 nA per pixel. For the analog design this has two consequences: It leads to additional noise contributions that increase with shaping time, and the sensor leakage current must be absorbed by the preamplifier circuit, since we use a DC connected readout scheme. For 10 nA leakage current and shaping times comparable to the LHC bunch crossing time, only a small noise contribution is expected ($<$50 e). However, after irradiation the distribution of pixel leakage currents may have tails extending to much higher values [2-1]. We therefore require that leakage currents of up to 100 nA can be absorbed.

A low noise performance is extremely important since the signal-to-noise ratio is the basis for a robust hit discrimination. Since the pixel capacitance can be kept small and the equivalent noise charge (ENC) is directly proportional to this capacitance connected to the input node, a good low noise performance can be expected. Given the pixel area, one expects the capacitance to be minimal for square pixels, estimated in the range of 80 fF [2-12]. The equivalent noise charge of the analog front-end block with all capacitances included (pixel sensor, bump pad etc.) should not exceed 500 electrons, even after several years of LHC running.

As the rate of noise hits is a very steep function of the pixel threshold, it is vital to have a precise control of the applied thresholds. Pixel-to-pixel variations are expected that could become even more severe with increasing irradiation levels. Therefore, in addition to a common pixel threshold for each chip a trim mechanism for individual pixels should be implemented. An individual trim mechanism can be used to set an infinite threshold for noisy pixels, which effectively will blank them out if needed.

Pixel hits must be correctly associated to the LHC bunch crossing. However, precise determination of the hit time is often limited by pulse-height-dependent delay effects (time-walk). One strategy to minimise the time-walk is to keep the peaking time of the amplifier smaller than the LHC bunch crossing time of 25 nsec. This implies a high bandwidth circuit at the limits of CMOS technology and therefore becomes excessively power consuming, with an impact on the material budget from enlarged cooling and power lines. We intend to keep the total dissipated power for the analog block below 40 μW per pixel. An alternative strategy, which we shall rely on, is the use of a pulse-height-independent timing circuit based on a 'zero'-level threshold for timing, which is activated when a hit discrimination threshold is crossed. Since we have adopted analog readout we have an additional possibility to perform a pulse-height-dependent time-walk correction at the VME level or even offline. However, this requires also the readout of the bunch crossing following the one which generated the level-1 trigger and therefore doubles the data flow for the optical links. Since the CMS data acquisition system will not generate a first-level trigger at subsequent bunch crossings this would not result in additional data losses. Although we are not relying on this scheme, it could serve as a fall-back solution if the robustness of the time-walk performance is degraded due to severe irradiation.

The pixel readout system must have simultaneous readout and data taking capability that is almost dead-time-free (below the 1% level). The potential interference of digital readout circuits with the sensitive analog block is the main worry. Unlike in a strip detector readout chip where a geographical separation of analog inputs to digital control and readout circuits can be achieved, the pixel readout chip is much more congested favouring a CMOS process that provides maximal device isolation properties like the Silicon On Insulator (SOI) technology. The most sensitive node of the analog block is the preamplifier input with the bump-pad attached. The bump-pad has a rather big parasitic capacitance and is therefore vulnerable to pick-up from the nearby digital readout block. We try to minimise the bump-pad capacitance in order to reduce any undesired pick-up, which improves the equivalent noise charge performance of the analog block since it represents a significant part ($\approx$ 15 fF) of the total input node capacitance ($\approx$ 100 fF). Compared to this, the estimated capacitance ($\approx$ 3–4 fF) of the bump itself appears to be negligible.

The power distribution within the chip, especially along a double column, requires special attention. A voltage surge on the analog power rail can inject a fake signal charge that is proportional to the input node capacitance. We have considered amplifier concepts that suppress such power/ground surges. For different functional blocks (analog, digital etc.) in the pixel unit cell separate power rails are used.

The analog block of the pixel unit cell has to provide a signal tap that allows analog pulse information to be extracted and stored, e.g. by a switched capacitor, together with the necessary circuitry for readout to the column periphery.

2.4.4.2 Conceptual design of the pixel analog block

Figure 2.18 shows a pixel unit cell (PUC) with separate analog block and digital readout block. As a general strategy we try to keep the number of transistors in the PUC as small as possible. This can be achieved in transferring many tasks of the readout to the column periphery.

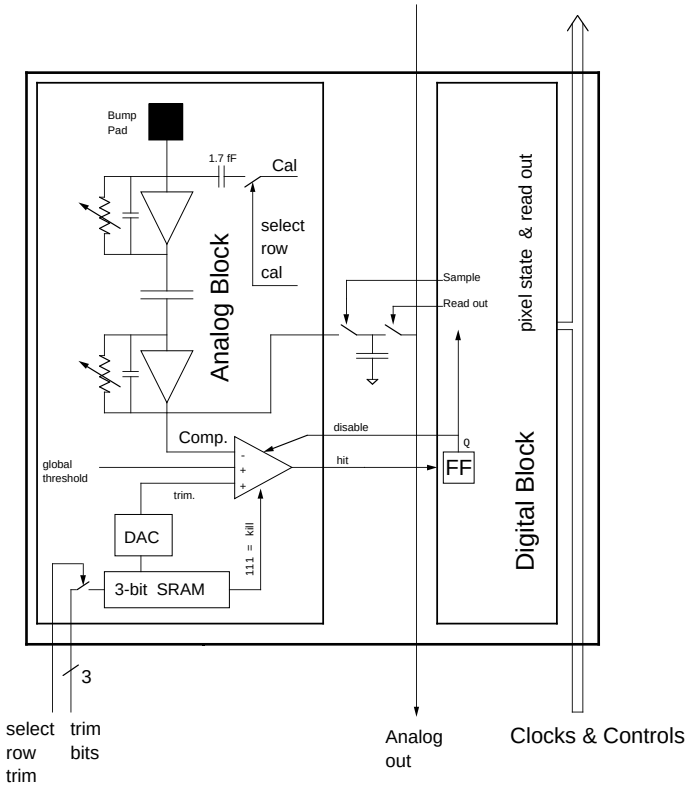

Fig. 2.18: Schematic block diagram of the pixel unit cell on the readout chip.

For signal amplification we use a charge sensitive preamplifier and shaper configuration. The feedback capacitor of the preamplifier stage has a value of about 30 fF. The leakage current from the DC coupled silicon pixel is automatically absorbed through an additional resistor in the feedback path of the preamplifier. Results on the current sink capability in a DMILL prototype chip are shown in Section 2.4.4.3.

Since the shaper is capacitively coupled to the preamplifier its working point will not be affected by slow leakage current variations. This coupling capacitance also defines the gain of the shaper by the ratio to the shaper feedback capacitance. At the shaper output we have a total gain of about 20–30 e/mV. If this gain would have to be obtained in a single stage, a very small feedback capacitance of 3–5 fF would be required. Although such an approach is not excluded, such tiny feedback capacitances present a set of problems (leakage current compensation, cross-coupling to neighbours, stability under irradiation etc.) which would have to be solved with additional transistor circuits.

The shaper output signal is brought to the hit discriminating comparator. A common threshold for all pixels can be set for each chip. For pixel-to-pixel variations a threshold trim mechanism is foreseen using a static memory cell (SRAM) on each pixel for storing the trim data. This has the advantage that, once a trim pattern has been programmed and down-loaded into the pixels, it remains stable as long as power stays on the chips. This keeps the system aspects during data taking rather simple. A trim system based on dynamic memory cells (capacitors) was also considered. This would need less transistors, but would cause considerable system complications due to the required refresh mechanism and radiation-dependent droop rates. We foresee a 3-bit trim circuit which allows to set eight trim states. In order to allow pixel masking, one of the eight trim states is reserved to set an infinite threshold. In Fig. 2.18 this is indicated as binary 111 and effectively kills a pixel. The need for such a pixel masking capability already requires a 1-bit memory cell per pixel with the corresponding programming mechanism.

The basic principle of the programming and calibration mechanism is also shown in Fig. 2.18. In order to keep the transistor count per pixel to a minimum a column and row addressing scheme is used. Only complete rows can be programmed at a time. When changing the settings of an individual pixel the memories in all the other pixels in the same row are simply overwritten with their previous settings. This system keeps the pixel circuits very simple, but requires a row selection circuitry which is placed on one side of the chip. Although this takes about 40 μm of space, it does not have significant impact on the butting capability of the chips in a module assembly. Reading back the written trim data for verification will be possible without any additional transistors in the PUC.

In data taking mode the same column–row addressing mechanism can be used to inject a calibration test charge into selected pixels. This scheme allows to choose any pixel pattern that can be addressed by a projective column–row selection (single pixels, fraction of rows or columns, multiple column–row areas of any size).

The output signal of the comparator sets a hit flip-flop, which in Fig. 2.18 is drawn as part of the digital readout block. The output node (Q) of the flip-flop acts on the comparator and disables any further operations. Through this digital hysteresis mechanism we ensure that a pixel stays quiet after having been hit.

The hit flip-flop also activates the sample command to store the analog pulse height on a switched capacitor. Based on the sampled voltage a current is then modulated onto the analog readout bus upon a token signal from the digital readout block. Figure 2.18 shows the analog readout bus only in schematic form; the circuit is not very complicated and requires only one transistor to perform the current modulation.

2.4.4.3 Radiation-hard prototype analog chips

We have designed a number of prototype chips that explore the performance limits and design constraints for realistic pixel layouts. The results from these chips have been crucial for the concept of the readout system. In an early phase (1994) of the project several prototype pixel chips were designed in a non-radhard CMOS process (SACMOS 1.2 μm). The first chip (SAC1_PSI24) contained a 3 by 3 pixel matrix exploring many of the functions described in the previous section. Further chips followed for column periphery circuits like content addressable memory cells and complete time-stamp circuits. However, we soon realized that the translation of a pixel unit cell into a radiation-hard technology (DMILL 0.8 μm) was not guaranteed. Comparative layouts showed that specific features of a radiation-hard process like DMILL allow certain tasks to be realised efficiently whereas one-to-one layout translations from the SACMOS process sometimes required up to 60% more area.

In order to ensure that the radiation-hard readout chip would maintain a realistic integration density and have sufficient performance even after irradiation, prototype work was continued using a radiation-hard technology. Most designs were done in the DMILL process but some designs were also translated into the RICMOS IV process. More details about the two processes are given in Section 2.4.3. In the following subsections some of our analog block developments and results are described.

DM_PSI26 (DMILL) This early prototype chip in DMILL contains a mini column of nine pixels and has been used to study the performance of a preamplifier/shaper system as described in Section 2.4.4.2.

The analog block included a comparator circuit for hit discrimination but no pixel trim mechanism. The minimal readout block consisted of a simple shiftregister for multiplexed readout of the analog pulse height and the comparator status. The chips were irradiated with pion fluences of 1,3,6,9 $\times$ 10^{14} pions/cm^2. Although the circuits seemed to stay operational even up

to the highest fluences we concluded that our final readout chip should be designed to withstand a maximal integrated fluence of 6×10^{14} pions/cm^2. For the barrel layer at 7 cm this fluence is expected after the first six years of LHC operation. At this level the leakage currents of silicon pixel sensors will have increased by several orders of magnitude. The current sink capability of the analog block was therefore tested by bleeding a well-defined DC current onto the bump-pad and at the same time injecting a signal test charge into the amplifier input. Figure 2.19 shows the signal pulse height at the shaper output as a function of the imposed leakage current. The curve shows that the analog block can absorb at least 10 times the expected pixel leakage current of 10 nA. The injection of the test signal charge is done through the tiny (1–2 fF) calibration capacitor at the amplifier input (see Fig. 2.18).

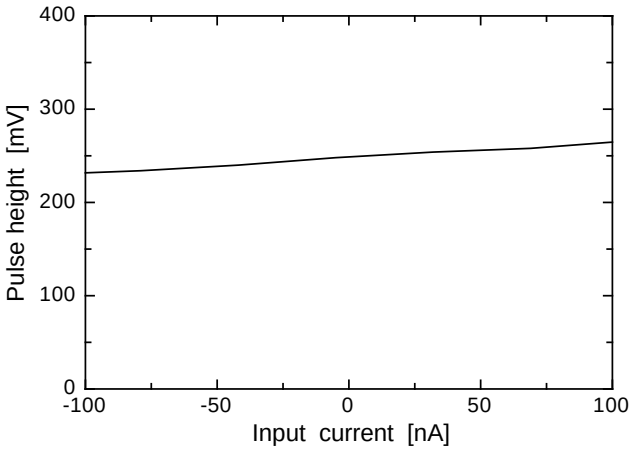

Fig. 2.19: Pulse-height variation with absorbed leakage current.

In order to calibrate this capacitor the pulse-height spectrum from an americium source has been used. The capacitance of the pixel sensor that was attached for these measurements was about 400 fF.

We have also measured [2-13] the input referred noise spectrum of the complete preamplifier before and after irradiation with 6×10^{14} pions/cm^2. The increase in the noise spectrum can be seen as a function of the frequency in Fig. 2.20. The spectrum has a strong $1/f$ component and in the relevant frequency region of 6–10 MHz a noise increase by a factor of 3 is observed. With the total input node capacitance amounting to 160 fF (without input FET gate capacitance), this results in an equivalent noise charge of 650 electrons after irradiation. At present there is unfortunately no measurement of the pixel capacitance for 150 μm $\times$ 150 μm pixels after irradiation. We estimate the total pixel capacitance (including bump-pad) to be of order of 100 fF which would result in about 400 electrons of noise after irradiation. Further studies of new preamplifier designs, which are expected to show improved noise performance after irradiation, were implemented in a new prototype chip DM_PSI32 and first results are shown below.

DM_PSI30 (DMILL) Figure 2.21 shows a SEM-picture of pixel unit cells from a 22 by 30 pixel chip (DM_PSI30) that was realised in the DMILL technology. A more detailed description of the readout architecture of this chip is given below in Section 2.4.5.5. Here we concentrate on the pixel unit cell and the analog block. The main purpose of this chip is to implement and test a complete analog block with all the realistic complications of a system like power surges, crosstalk and device variations in a larger pixel array. The analog block has all functions implemented that are shown in Fig. 2.18. It uses 47 transistors out of a total of 75 in the complete pixel cell (125 μm $\times$ 125 μm). The remaining 28 are used for the readout block, including the hit flip-flop and the analog pulse-height readout. This readout block has a reduced

circuit architecture and needs to be changed for full luminosity operation at the LHC. For this purpose an empty region of about 15% of the pixel area has been kept open in our design. More details about the realisation and first results from pixels with a full luminosity readout block are given in Section 2.4.5.5.

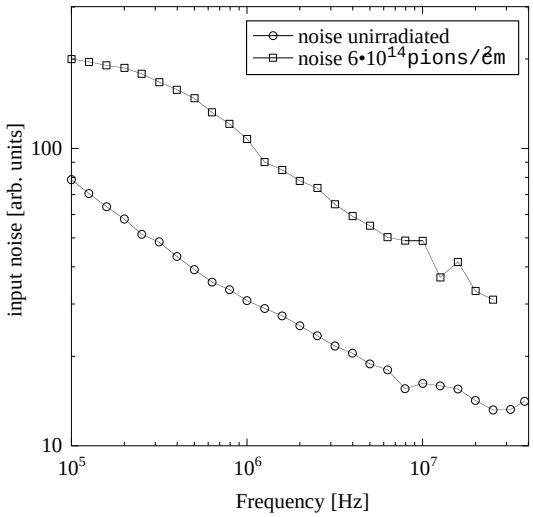

Fig. 2.20: Input referred noise spectrum of DMILL pixel amplifier before and after irradiation with 6×10^{14} pions/cm^2.

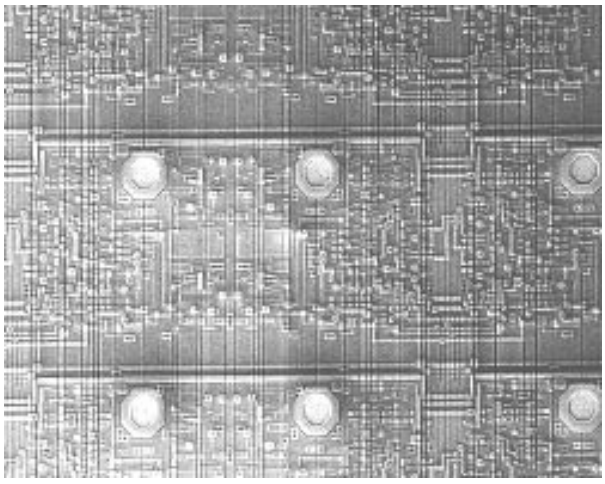

Fig. 2.21: SEM scan of pixel unit cells on the DM_PSI30 chip (DMILL).

Compared to the simplified schematics in Fig. 2.18 a few points have to be added. For the threshold trim mechanism a range has to be specified over which the three trim bits can be used for adjustment. This trim range can be set by a voltage which at the moment is adjusted externally. In the final pixel chip this will be done by an on-chip DAC and a control register that is programmed through the slow control bus (I^2C). The complete trim and mask circuit uses 28 transistors out of the 47 in the analog block. The programming mechanism for the pixel trims allows complete rows to be programmed at a time and works exactly as described in Section 2.4.4.2. The down-load into the chip is done through the transfer of a 104 bit long serial bit-stream. To completely program the whole 22 by 30 pixel matrix a series of 60 transfers is needed.

We have measured the variations of the pixel threshold before and after trimming. The distribution of the untrimmed pixel thresholds in a complete double column is shown in Fig. 2.22(a) while the same distribution after a trimming procedure is shown in Fig. 2.22(b). For this measurement the chip was running in its regular mode, using the time-stamp mechanism. The threshold distribution was obtained by measuring the minimal calibration test pulse that is required to trigger a pixel. Figure 2.22 shows that after individual pixel trimming the width of the threshold distribution has significantly decreased. The global pixel threshold was set to 1900 electrons. This measurement was done on a non-irradiated readout chip where the distribution even before trimming was quite good, but it should be kept in mind that after irradiation the pixel variations could become considerably worse and a trimming capability becomes indispensable.

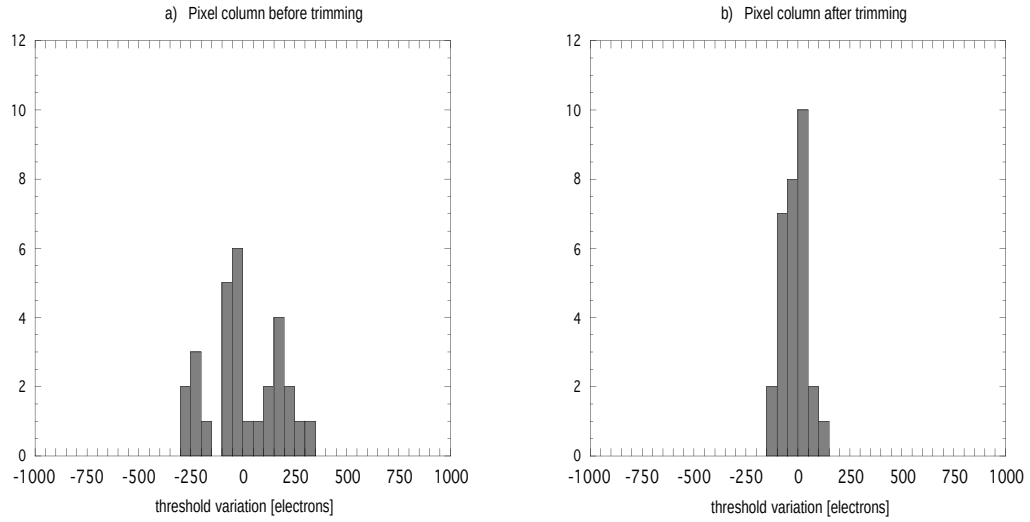

Fig. 2.22: Pixel threshold distributions before and after trimming.

Our present experience indicates that a certain trim pattern is rather stable in time, unless the transistor parameters are changed due to irradiation. During LHC operation we are planning to use a simple feedback algorithm in order to control the trimming of the 4×10^7 pixels in the complete system. The procedure is based on a pixel hit map (e.g. at the VME-level) that allows of identification of single high rate or low rate pixels. For these pixels the trim levels are then increased or decreased respectively by one step at a time and, after a new pixel hit map has been accumulated, the procedure is iterated. This leads to uniform pixel rates within a chip. The average chip rates can be adjusted by setting the overall chip thresholds.

The pulse-height sampling and analog readout mechanism uses five transistors and one small capacitor and thus represents only a small fraction of the overall pixel circuit.

The layout of the pixel unit cell is done by placing two pixels back to back with a common signal bus in the middle (see Fig. 2.21). The clocking bus lines are placed in metal 1 and occupy about 8.3% of the total pixel area. They are screened from the very sensitive pixel electrodes of the bump-bonded silicon detector by the metal 2 lines which are used for ground and power. We have studied internal crosstalk from the bus lines to the amplifier input. A surprisingly small effect was found which is attributed to the excellent properties of the SOI chip technology and to precautions taken in the layout. Crosstalk problems due to voltage surges on the supply rails (power/ground) have to be considered by using tolerant circuit concepts (e.g. symmetric amplifier design) and by having strictly separated supplies for different functional blocks.

The signal pulse at the shaper output is shown in Fig. 2.23. The peaking time is about 32 ns for a power dissipation of 35 μW. The picture is taken with a picoprobe attached to the shaper output which represents an additional capacitive load of $\approx$ 100 fF.

The noise of the bare chip has been measured to be 130 electrons before irradiation, again calibrated with an ^{241}Am spectrum. More details are given in Section 2.4.5.5 where the overall architecture of this chip is described.

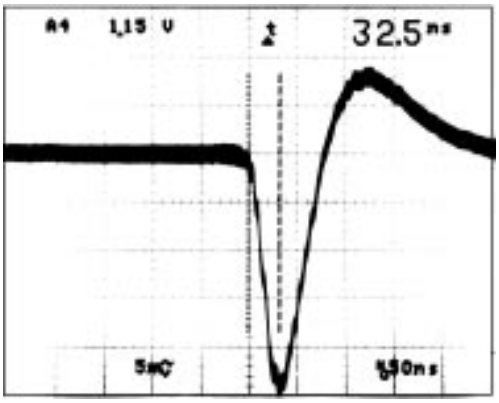

Fig. 2.23: Signal pulse at shaper output of DM_PSI30 (DMILL). The horizontal scale is in units of 50 ns.

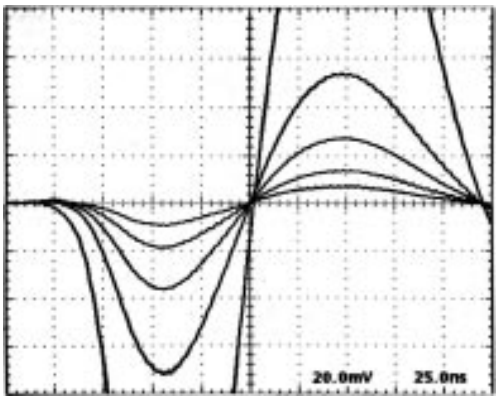

Fig. 2.24: Bipolar shaped amplifier pulses for different injected pixel signal charges in the DMILL chip (DM_PSI26) after being irradiated with 10^{14} pions/cm^2. The horizontal scale is in units of 25 ns.

DM_PSI31 (DMILL) The problem of the pulse-height-dependent time-walk of the comparator hit signal has already been explained in Section 2.4.4.1. For small pulses the main problem is that small amplifier signals reach the comparator threshold later and thus may fall into the next bunch crossing. With the prototype chip DM_PSI31 we extract a pulse-height-independent timing signal, allowing amplifier rise times slower than the bunch crossing time.

The basic idea can be seen in Fig. 2.24, which was measured with pixels from the chip DM_PSI26 after irradiation with 10^{14} pions/cm^2. The picture shows superimposed amplifier pulses at the level of the comparator input for different injected signal charges (1200, 2400, 4800, 9600 and 30 000 electrons). The bipolar pulse shape exhibits a common 'zero-crossing' point that is remarkably stable in time. This can be exploited for a pulse-height-independent timing signal, as is shown in Fig. 2.25. After the normal hit comparator has triggered, a second 'zero-crossing' comparator is activated, giving the required timing information. The schematic diagram of the analog block with 'zero-crossing' circuit is shown in Fig. 2.26. Compared to the standard analog block it requires a second comparator with a disable/enable function. We have tested pixels equipped with this additional circuit block.

The time-walk behaviour of the normal hit discriminator and the 'zero-crossing' discriminator is shown in Fig. 2.27 for different injected signal charges. Although the results look rather promising, there could be pixel to pixel variations (threshold variations of 'zero-crossing' discriminator, 'zero-crossing' spread of bipolar pulse), that, especially after irradiation, need to be studied further before final conclusions can be drawn.

DM_PSI32 (DMILL) The most recent DMILL prototype chip (received Dec. 1997) explores a number of functional blocks that are crucial for the final pixel readout chip. The DM_PSI32 chip contains unit cells with the complete readout blocks for high-luminosity LHC operation as well as a number of new circuits (preamplifiers, comparators) that are especially designed for robustness and better performance after irradiation. Figure 2.28 shows the layout of a double pixel cell with the complete readout block for high-luminosity operation. The analog block is basically the same as in the 22×30 pixel chip described before but the readout block contains the fast skipping mechanism that is the basis of the column drain architecture described in Section 2.4.5.1. The double pixel in Fig. 2.28 is still based on the old pixel size of $(125\ \mu\text{m})^2$. For the new pixel size of $(150\ \mu\text{m})^2$ an additional 44% area allows us to relax the layout density which could result in considerable yield benefits. This area could, however, also be invested into additional transistors for circuits like the zero-crossing comparator or more complicated amplifier designs.

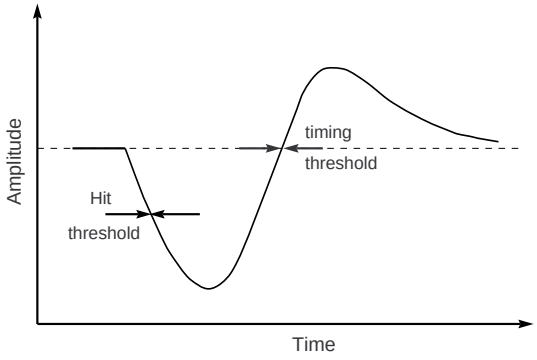

Fig. 2.25: Principle of 'zero-crossing' detection for minimal time-walk

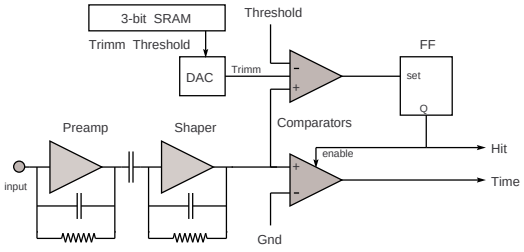

Fig. 2.26: Basic schematics of zero-crossing circuit implemented in pixels of DM_PSI31 (DMILL) chip.

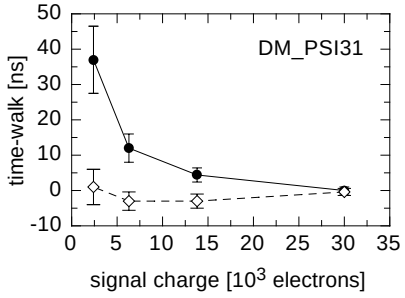

Fig. 2.27: Measured time-walk behaviour of hit comparator (dots) and zero-crossing comparator (diamonds).

A number of different preamplifier circuits have been implemented in order to study their speed and noise performance before and after irradiation. The designs explore a variety of circuit options, including the bipolar transistor capability of DMILL or different low capacitance layouts in order to reduce amplifier peaking times. Figure 2.29 shows the pulse shape at the comparator input with a cascode circuit used for the preamplifier. A systematic evaluation of the different circuits is under way.

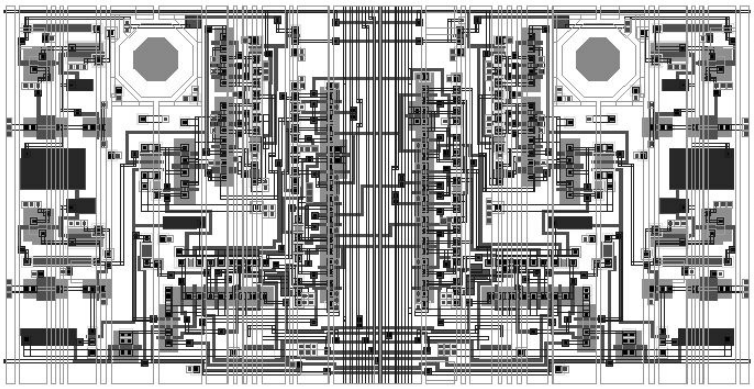

Fig. 2.28: Double pixel unit cell implemented in the prototype chip DM_PSI32. Back-to-back layout of two pixels (125 μm $\times$ 125 μm) with common signal bus in middle.

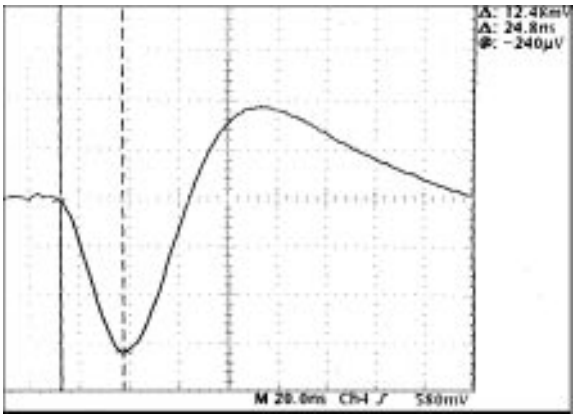

Fig. 2.29: Pulse shape of pixel analog block with cascode preamplifier in DMILL technology (DM_PSI32). The horizontal scale is in units of 20 ns. The peaking time is 25 ns.

One of the most critical elements in the pixel analog block is the comparator stage which must be as robust as possible against irradiation effects. Figure 2.30 shows the simplified schematics of such a comparator stage. The basic idea is to stabilise its working point through a forward diode characteristics expected to be rather invariant under irradiation. Since the comparator is AC-coupled a constant output offset is fixed by the forward voltage drop of the diode used as a feedback element. This voltage drop is generated by bleeding a small bias current into the input node. On account of the very steep diode characteristics, one expects only small changes in the comparator output offset even for rather large irradiation induced variations of the bias current. A small set of nine diode stabilised comparators has been implemented in the DM_PSI32 chip and irradiated to 100 kGy. Operating at a threshold of $\approx$ 1950 electrons we observed a r.m.s. spread of about 200 electrons after irradiation. Further studies with a larger number of irradiated chips will be done soon. A time-walk curve of this comparator with the preamplifier and shaper chain explained above is shown in Fig. 2.31.

Honeywell (RICMOS IV) The suitability of the Honeywell SOI CMOS technology for front-end electronics in LHC experiments is under investigation. The process has an 0.8 μm minimal feature size, offers a third metal layer and is certified for a maximal dose of 10 kGy. In order to explore its potential for the analog block at anticipated irradiation levels a number of measurements of the DC, AC and noise parameters of different transistors before and after ^{60}Co irradiation have been carried out [2-14]. All devices remained fully functional after irradiation,

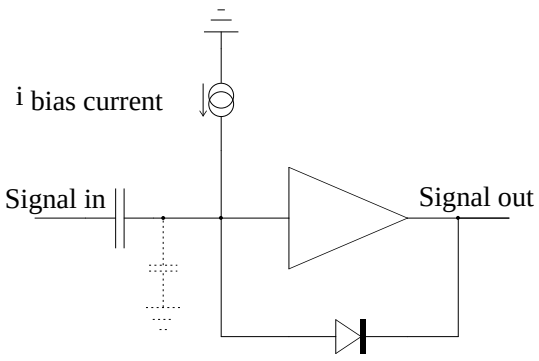

Fig. 2.30: Basic schematics of a diode stabilised comparator circuit.

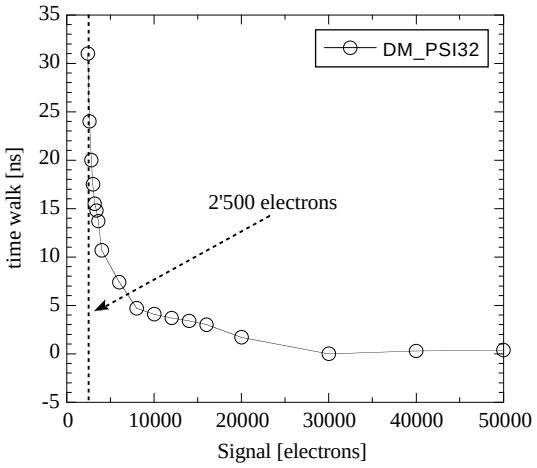

Fig. 2.31: Time-walk curve of the complete analog block with diode.

with no anomalous behaviour. Recent process developments have led to improved stability of the analog transistor parameters even well beyond the certified irradiation levels. For a new submission (Jan. 1998) a number of prototype pixel circuits [2-15] have been designed. The test chip contains the central analog and digital functional blocks of the pixel readout architecture. In addition, several devices were included to evaluate precisely the noise behaviour of the improved process technology. The submission also contains a translation of the 22×30 pixel chip. A number of pixel unit cells with the zero-crossing mechanism have been implemented as well.

For the 40 MHz analog data transmission of the chip output signals through Kapton cables to the optical transmitters, a transmission line driver circuit has been developed and included. First result are expected in mid 1998.

2.4.4.4 Conclusions

The results obtained from the radiation-hard prototype chips indicate that we are well within reach of the performance required at the LHC. In particular the studies of crosstalk from the digital block to the analog block show that this problem is less severe than previously feared. This is attributed to the excellent properties of the SOI CMOS process and to special precautions taken in the layout and circuit concept.

A pixel threshold of 2500 electrons will be used which is far above the crosstalk level. With a minimal 5 σ requirement this implies a maximal allowed noise level of 500 electrons after irradiation. Although a considerable increase of the noise level is observed after irradiation ($\approx$ 200 kGy of hadronic particles) it is possible to stay within the required limits unless there are unexpected high pixel capacitances way beyond 100 fF.

The time-walk should stay below 25 ns for the same pixel threshold in order to have a correct bunch-crossing identification. At this time the question of whether a zero crossing scheme in the comparator stage will be appropriate is not settled. In any case the analog pixel readout offers a backup solution in case an unexpected system degradation (e.g. by heavy irradiation) would shift the small pixel hits into the next bunch crossing. They could be recovered by an offline time-walk correction, provided the next bunch crossing is read out as well. With the foreseen number of fibre links this extra data transfer rate could be handled.

The adjustment of the pixel thresholds or the masking of very noisy pixels is indispensable for a large pixel system. If the variation after irradiation of the analog block can be kept small (e.g. by the diode stabilised comparator) a reduction from 3 trim-bits to 2 bits (3 trim steps and pixel mask) could be envisaged.

All prototype results shown in the previous section have been obtained with a power dissipation that is within the analog power budget of 40 μW per pixel.

2.4.5 Readout architecture

2.4.5.1 Column drain architecture

The level-1 trigger latency time in CMS will be 3.2 μs (128 bunch crossings). When discussing different readout schemes, a key question is whether the information of a hit pixel, including the associated bunch crossing number information and the analog pixel signal, should be kept on the pixel itself during this time. With the hit frequencies summarised in Table 2.6 the probability of a pixel being hit again at another bunch crossing within 3.2 μs will be 2–4%. This is not readily acceptable and therefore an additional data buffer would be desirable on each pixel. The association of a hit stored in the pixel with the bunch-crossing information located in the column periphery would be quite complicated. Although this architecture variant has been dropped it is still mentioned in the next section for comparison.

In the architecture chosen for the CMS pixel readout, the basic idea is to copy all pixel hits occuring in a pixel double column into the column periphery as soon and as fast as possible in order to free the pixels for the next hit (Column Drain Architecture). If this can be accomplished within typically 7–8 bunch crossings following the hit, then the probability of having a second hit in the pixel reduces to 0.14% (see the simulation results in Section 2.4.5.2). The bunch-crossing number association to the pixel hits (time-stamping) can be done much more simply in the column periphery through a hard-wired link.

Each double column is equiped with a Column OR which informs the column periphery immediately of any hits that occur in the double column. This OR must be fast enough to associate the hits uniquely to the correct bunch-crossing. The column periphery hosts a circular buffer for time-stamping the hits with an 8-bit bunch-crossing number from a local bunch-crossing counter running at 40 MHz (Write Counter). Monte Carlo simulations show that a buffer depth of 8 is sufficient for storing most events from a double column occuring during the first-level trigger latency.

Upon a hit registered by the Column OR, a token-bit runs up and down the double column and initiates the transfer of the hit information from the hit pixels to the periphery. The hit pixels route the token-bit such that it stops and initiates the readout, while empty pixels are bypassed. The hit information is stored in the column periphery until the trigger decision time has passed.

Without any extra measures the double column will suffer a dead time of about 10% during the draining of the hits down to the periphery. With relatively little increase in complexity the column drain mechanism can be made doubly buffered, i.e. during a token-bit scan, which on average will take several bunch-crossing cycles, an additional time-stamp can be recorded. Its associated pixel hits are read out immediately after the readout of the previous hit is finished. This reduces the dead time to the 0.5% level (for details see Section 2.4.5.2).

The pixel drain concept is economical in pixel area; however, the required column periphery area is enlarged by the data buffer necessary to store all information of hit pixels (address and analog signal) for 3.2 μs. For each double column a common set of data buffer cells is planned. More details about the time-stamp and data buffer management are given in the section on the column periphery design (see Section 2.4.5.4). Pixel hits belonging to different time-stamps share this common data buffer with the use of pointers. Monte Carlo calculations suggest that

the data buffer in the double column must be able to accept 24 pixel hits in order to limit the data loss to an acceptable minimum (jets in particular can lead to large hit multiplicities in a double column).

The verification of all active time-stamps in each column is based on a second bunch-crossing counter (Search Counter) at the chip periphery. This counter is running concurrently with the actual time-stamp counter (Write Counter) but delayed by the trigger latency time of 128 bunch crossings (3.2 μs). For each bunch crossing the search counter value is compared with the stored time-stamps in each column. If a coincidence is detected, this time-stamp is eliminated from the list. However, if in addition a first-level trigger is present for this bunch crossing this time-stamp and the corresponding data buffer content is transferred to the CMS data acquisition system. Any trigger latency time can be adopted by the programmable delay between Write Counter and Search Counter.

2.4.5.2 Simulations of architecture performance

Introduction The simulations concerning average data rates in the barrel was described in Section 2.4.2. For each simulated event the information of the hit pixels was stored in a file. These files were used as input to a stand-alone program which performed the readout simulations. Results of such simulations depend on the average data rates but are also influenced by the data size fluctuations (e.g. local track density) and the fluctuations in the trigger rate.

In the readout simulation for each clock pulse (at 40 MHz) a number of operations are done autonomously in each double column (all double columns within a detector module are considered):

- new pixels are populated from the input file,
- the time-stamping mechanism is initiated, the time-stamp is stored in the column buffer,
- the pixel readout is started if the readout mechanism is not busy,
- the readout of the previous events, if any, is continued,
- the read out pixel information is stored in the column data buffer,
- the data buffer and the time-stamp buffer is monitored, overflows are flagged,
- time-stamps and pixels corresponding to bunch crossings older than the trigger delay, which were not confirmed by the first level trigger, are erased,
- time-stamps and pixels confirmed by the trigger are not allowed to be overwritten until they are read out by the data link.

As a result of this simulation various classes of data losses can be identified. All results presented here are for the barrel layer at 7 cm which, at high luminosity, will have the largest occupancies in the pixel system.

Required buffer sizes Each double column periphery has two buffers. One is used for storing the time-stamps associated with the bunch crossing which produced hits in the column. The second stores amplitudes and coordinates of the hit pixels. Because of the small area available on the readout chip these two buffers cannot be very large, but should prevent significant data losses.

Figure 2.32 shows the distribution of the number of time-stamps stored in the column buffer for a few event types. A buffer size of about 4 is required when storing noise events only. For pure $t\bar{t}$ events the required buffer size is about the same. Full luminosity events need a buffer of size 8. It does not seem to matter whether the event includes the $t\bar{t}$ tracks or contains only the minimum-bias pile-up. There is almost no difference between the required buffer size for (125 μm)^2 and (150 μm)^2 pixels. The distributions are normalised to one event; therefore the integral under each distribution is equal to the number of double-columns in the barrel layer at

7 cm (99 840). In this way the average number of columns (vertical axis) having a given number of time-stamps (horizontal axes) can be extracted.

If, at any given time, the time-stamp buffer happens to be full, the next time-stamp will be lost, resulting in the loss of all data in the column for this particular bunch crossing. This is shown in the right part of Fig. 2.32 as a function of the time-stamp buffer size. The size of the time-stamp buffer needs to be at least 8 in order to avoid losses greater than 10^{-3}. This result does not depend on the readout architecture and is valid for any column-oriented readout which uses the time-stamp method.

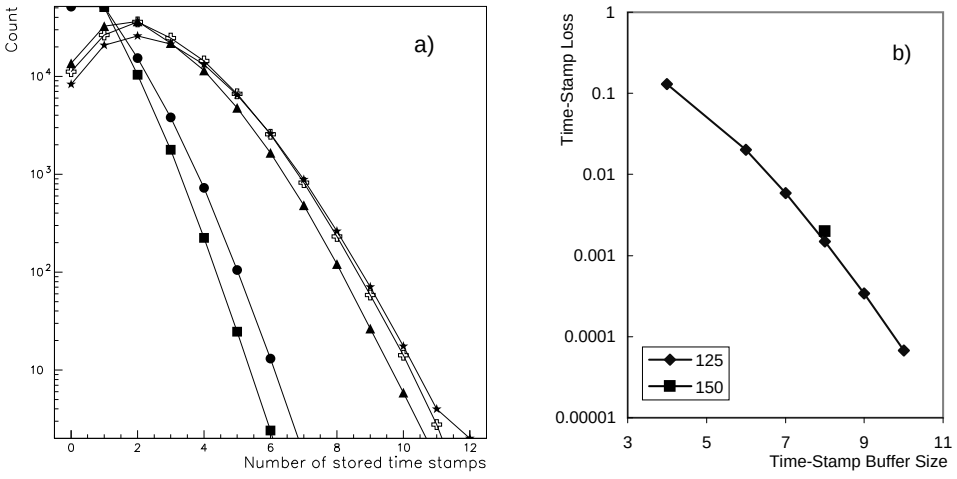

Fig. 2.32: a) Distribution of the number of time-stamps stored in the column buffer. Several types of events are plotted: full luminosity $t\bar{t}$ event with (150 μm)^2 pixels (stars), same with (125 μm)^2 pixels (crosses), and without the $t\bar{t}$ event (triangles), pure $t\bar{t}$ events (circles), noise at 4 σ (squares). b) Data loss by time-stamp buffer overflow as a function of the buffer size for two different pixel sizes.

Figure 2.33 shows the distribution of the number of pixel hits stored in the column data buffer. The same classes of events as in Fig. 2.32 are shown, using the same normalisation. With the buffer set to 24 locations one covers most data. Whenever the data buffer is full, the next pixel will be lost. The data loss is shown in Fig. 2.33. Any buffer size equal or larger than 24 gives data losses below 10^{-3}. This is independent of the readout architecture and almost independent of the pixel size.

Evaluation of readout architectures The main difference between the readout architectures considered is the amount of time the pixel information stays on the pixel before it is read out. The longer this time, the higher is the chance that the next hit on the same pixel will be lost. Another source of loss is related to the column readout busy time. During the time a set of hit pixels in a column is being read out, more hits will occur in the same column. In our readout scheme using the Column Drain Architecture one subsequent time-stamp can be stored and associated hits will not be lost; however, a second time-stamp occurring during the column readout busy time cannot be handled and will be lost. To minimise the probability that the same column will be hit more than once within a column readout time, the column readout speed should be maximised.

We have considered various column readout configurations:

- **1LT-8TS**. Time-stamps are stored in a column buffer 8 deep, but the pixel information stays on the pixel until the first level trigger (1LT) arrives. With the trigger delay of 3.2 μs and the expected hit rate the loss amounts to 2–4%.
- **110**. Time-stamp is stored and pixel readout is started immediately without waiting for a 1LT signal. One clock pulse (at 40 MHz) is used to set up the readout, one clock pulse

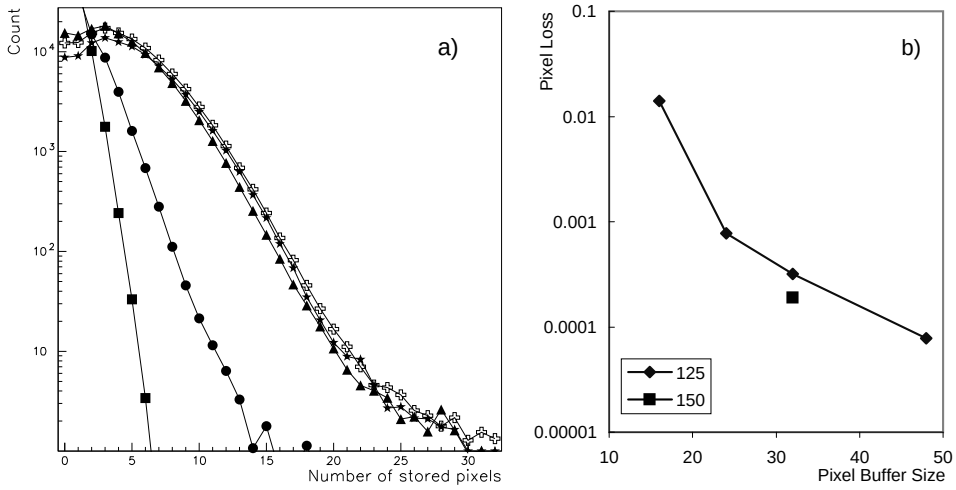

Fig. 2.33: a) Distribution of the number of pixel hits stored in the data buffer. The same labels as in Fig. 2.32 are used. b) Data loss caused by the column data buffer overflows as a function of the buffer size for two different pixel sizes.

is needed per hit pixel and no time is needed for skipping empty pixels. This gives the highest possible readout speed using a column drain architecture.
- **211–32**. As 110, but with two clock pulses for readout setup, one clock pulse for each hit pixel and one clock pulse for each group of 32 empty pixels.
- **211–16**. As previous, but one clock pulse is used for skipping a group of 16 empty pixels.
- **211–16W**. As previous, but if the column is hit while the previous hits have not yet been drained out, the data of the second time-stamp are lost.

Except for the first configuration 1LT-8TS all readout methods considered here are variations of the Column Drain Architecture with different drain speed assumptions.

The loss of columns due to the readout being busy is shown in Fig. 2.34A. It shows that a readout scheme where a column cannot accept a second hit, while it is busy reading an earlier hit (211–16W), is unacceptable. The best result is given by the fastest readout (110). In general, this 'dead-time' related data loss is very sensitive to the column readout speed. The 1LT-8TS produces no loss of this kind since pixels are read only after 1LT confirmation, which results in a much lower data traffic and therefore negligible dead time.

Figure 2.34B shows the data loss due to the pixel information being overwritten before the pixel signal is moved to the column periphery. Except for the 1LT-8TS readout all other architectures give losses equal to or less than 2×10^{-3}.

In Fig. 2.35 the four readout-related data losses discussed in the text are added together and plotted as a function of luminosity. Four readout schemes are shown. The data losses for the architecture (211–32), which is the chosen design variant, remain below 1% for an average of 25 minimum bias events per bunch crossing, which corresponds to the design luminosity of the LHC.

For this case Table 2.7 summarises the data losses for the barrel layer at 7 cm. Other data losses not related to the readout, but due to the finite size of the pixels, are also listed in Table 2.7. They concern tracks overlapping in one single pixel, and merging clusters.

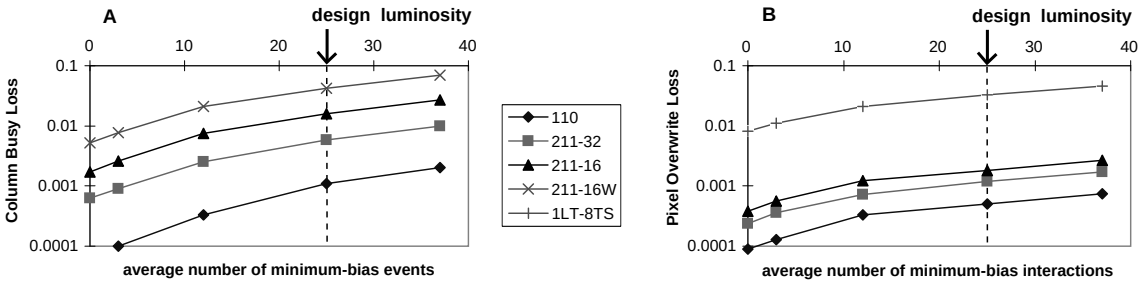

Fig. 2.34: (A) Fraction of data lost by the column readout being busy (column dead-time). The loss is shown for several readout architectures as a function of luminosity (average number of minimum-bias interactions per bunch-crossing). The abbreviated notation for the readout architectures is described in the text. (B) Fraction of data lost by pixels being overwritten before they are read out and stored in the column periphery.

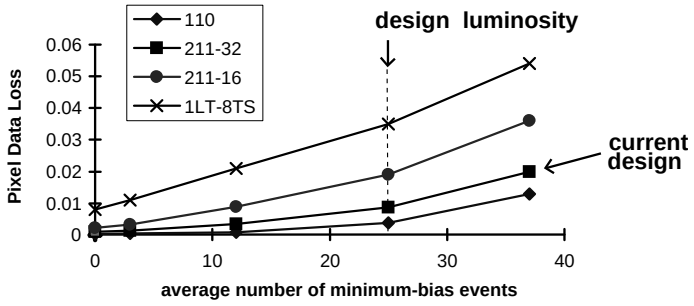

Fig. 2.35: Total fraction of data lost due to the readout mechanism versus luminosity (measured by the average number of minimum-bias events per bunch-crossing), for the barrel layer at 7 cm. The abbreviated notation for the readout architectures is described in the text. The design architecture chosen is the variant **211–32**.

Table 2.7: Summary of fractional data losses for the design readout architecture **211–32**

Time-stamp buffer overflow (8-deep)	0.0020
Data buffer overflow (24-deep)	0.0010
Column readout busy (dead time)	0.0053
Pixel overwrite	0.0014
Total	0.0097
Overlapping tracks	0.00035
Merging clusters	0.0013

2.4.5.3 Pixel unit cell design

The design of the pixel unit cell for the column drain architecture [2-16] is based on the idea to transmit a pixel hit as soon as possible to the column periphery and to perform on the pixel unit cell only the tasks of signal amplification, hit detection and temporary single-hit storage. The tasks of time-stamp identification, multiple hit storage and readout buffering are shifted to the column periphery. There they can be performed more efficiently, minimising the number of transistors in each pixel unit cell.

The mechanism to drain a double column containing a few hit pixels is based on a token-bit running up and down the double column, stopping at hit pixels and bypassing the pixels without a hit. The block diagram of such a bypassing mechanism is shown in Fig. 2.36. The output signal of the comparator C, indicating a pixel hit above threshold, pulls the *Column OR* line from its original high state to the low state by a switch connecting the *Column OR* to ground. This transition is detected at the column periphery, where the current status of the local time-stamp counter is copied into the time-stamp buffer. The *Column OR* line is kept low by the periphery, beyond the duration of the comparator pulse, and is only lifted by the periphery to its high state just before a token-bit is sent on its way through the double column.

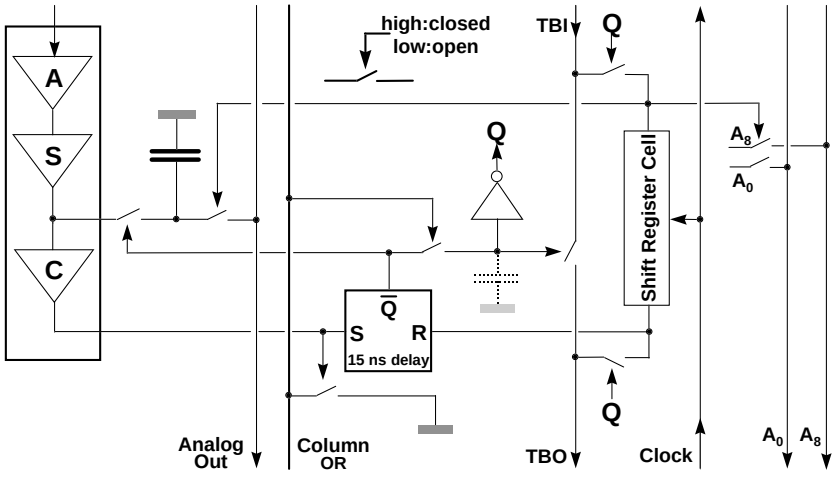

Fig. 2.36: Pixel unit cell for column drain architecture

The output $\overline{Q}$ of the hit flip-flop is slightly delayed with respect to the comparator output signal. It is used on the one hand to disconnect the sampling capacitor from the amplifier/shaper output, thereby freezing the analog amplitude on this capacitor. On the other hand, the states $\overline{Q}$ and Q control the bypass mechanism for the token-bit through a line that can be blocked by the *Column OR* being in its low state (open switch, see Fig. 2.36). The shift register cell of the pixel is normally bypassed (no hit, *Column OR* and $\overline{Q}$ high). Once the hit flip-flop is set by a comparator pulse and the switch controlled by the *Column OR* is opened, the parasitic capacitance on the inverter input ensures that the bypass condition remains unchanged ($\overline{Q}$ changes its state only after the internal delay of the flip-flop). Only when the column periphery starts a readout cycle it lifts up the *Column OR* line and thereby imposes the hit flip-flop status $\overline{Q}$ of each pixel in the column on the bypass mechanism, thus defining the path of the token-bit through the double column. The token-bit is passed from hit pixel to hit pixel, where it is routed through the shift register cell, while it skips empty pixels, until it returns to the periphery indicating the end of the readout cycle.

When the token-bit enters the shift register cell of a hit pixel (TBI in Fig. 2.36), it connects the switched capacitor, where the analog pulse height is stored, to a readout line and routes the octal coded address currents onto the two address lines *A0* and *A8* (see Fig. 2.36). The token-bit

clears the hit flip-flop as it leaves the shift register cell (TBO), putting it into sensitive mode ready for a new hit.

During a column drain only a few pixels are normally involved, whereas most of them (typically 98%) are in standby mode and waiting for a hit. If they are hit during an ongoing drain cycle the *Column OR* line goes from high to low again, allowing the periphery to record the next time-stamp. Since the *Column OR* line stays low, the current pattern of bypasses is not modified and the readout cycle continues as normal. However, after the periphery has registered the returning token-bit, it immediately starts a new readout cycle for the latest time-stamp. By setting the *Column OR* to the high state before the token-bit is sent again to the column, the switch in the output line $\overline{Q}$ of each pixel flip-flop in the column is closed, and the new bypass pattern belonging to the new time-stamp is imposed. The capability to pre-record a new time-stamp during an ongoing column drain effectively gives a double buffering at the column level and reduces the dead time to a range of 0.5%, as shown in the simulation Section 2.4.5.2.

Without any refresh mechanism the delay time of the token-bit on its way through the double column has a parabolic dependence on the number of pixels skipped. For long skips this leads to unacceptably long delays. In the design of the prototype pixel cell (see Fig. 2.28) we have therefore implemented an active bypass mechanism, ensuring a very high speed of the token-bit when skipping empty pixels. Results on this active bypass mechanism are given in Section 2.4.5.5. Furthermore, the clocked shift register cell has been replaced with a token-bit mechanism based on a handshake protocol. However, the basic concept outlined in Fig. 2.36 remains the same.

With the hit rates expected for high luminosity at a radius of 7 cm, the column drain mechanism is typically running 10% of the time. This is favourable for the digital power dissipation of the readout chip, since apart from the pixel analog block, the column drain circuit is the highest contributor to the overall power budget of the chip.

2.4.5.4 Column periphery design

The concept of the column drain architecture is based on immediate data transfer from the pixel unit cells to the column periphery. The pixel unit cells and the column periphery interactively control the data transfer along the columns. The column periphery performs the following basic tasks of:

- recording the time-stamps,
- organising the readout of the hit pixel cells,
- receiving pixel hits and their addresses and storing them in the data buffer,
- managing the time-stamp buffer and the associated hits in the data buffer,
- marking confirmed time-stamps and clearing unconfirmed ones,
- preparing and buffering confirmed hit data for chip readout.

In addition, the periphery allows pre-recording of one new time-stamp during a column drain cycle.

A design of the column periphery exists at the gate level. It has been tested by logical simulation [2-17]. In contrast to a fixed association of data buffer cells with each time-stamp, we have adopted a scheme using a pool buffer for all pixel hits. This allows a variable number of pixel hits to be stored for each time-stamp and ensures that large variations in the pixel multiplicity can be accepted. This is very important for events where the pixel chips are hit by a high-p_T jet or in the case of heavy-ion collisions.

Figure 2.37 shows schematically the column periphery design (generalised version of the column periphery implemented in the 22×30 pixels prototype chip DM_PSI30; see Section 2.4.5.5). For each clock cycle (at 40 MHz) the value of a bunch crossing counter ($Write\ BC$ in Fig. 2.37,

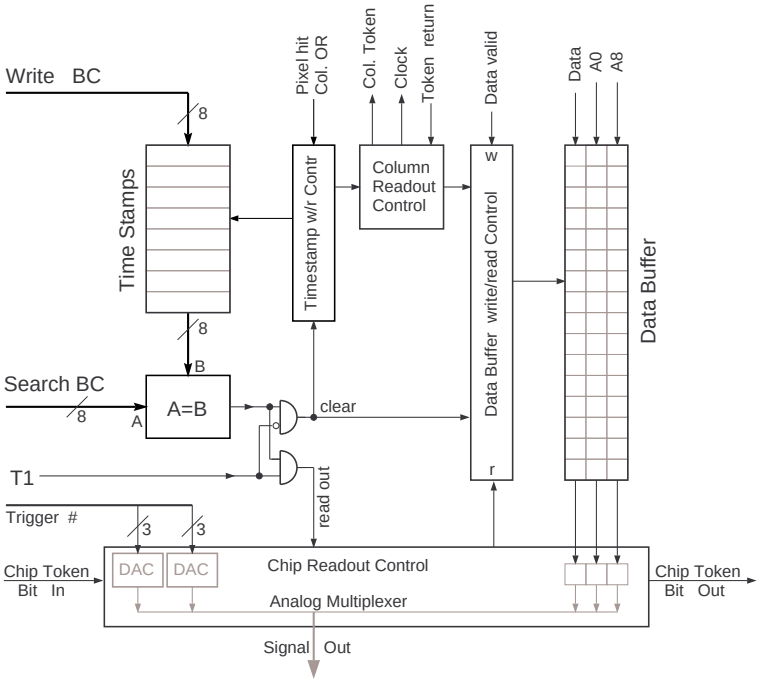

Fig. 2.37: Schematics of the column periphery mechanism with multiple time-stamp and data buffer management.

8 bit) is presented to all double columns across the whole chip. In case a *Column Or* signal indicates pixel hits in a column the *Write BC* value is stored in the next free time-stamp register. The time-stamp registers are 8 bit wide with one extra bit to keep track of the free registers. The write/read control is performed by an extra circuit organising the time-stamp buffer in a FIFO structure of variable length. From the simulation studies described in Section 2.4.5.2 we conclude that 8 time-stamp registers are needed in order to keep the probability of data losses below 10^{-3}.

After the *Write BC* number has been latched the readout control block starts a column drain cycle which is terminated by registering the return of the token-bit. For each clock pulse during the readout cycle the analog pixel data (pulse-height and octal coded addresses) are received and stored in a cell of three switched capacitors in the data buffer. The octal coded addresses are treated identically to the analog pixel pulse height, a distinction is only done after digitisation in the Front-End Driver (FED), where the signals are interpreted according to their position in the data stream. The method of using octal coded addresses has been implemented and tested in the 22×30 pixel prototype chip DM_PSI30 (see Section 2.4.5.5 and Fig. 2.40). The number of data buffer cells has been set to 24, based on the simulation results in Section 2.4.5.2. The partitioning of the data buffer and the association to the different time-stamp registers is managed by the two w/r control blocks shown in Fig. 2.37.

The content of the time-stamp register is now waiting for comparison with the value of the *Search BC* counter running behind the *Write BC* counter by the (programmable) trigger latency time. When the value of the *Search BC* counter has reached the time-stamp register value, identity is detected and a coincidence with the 1LT signal is checked. If the 1LT signal is absent the time-stamp register and its associated data buffer cells are cleared and given free. However, if a coincidence occurred, the chip readout control is activated. The chip readout control block latches the confirming trigger number (6 bit) into two DAC registers (3 bit). The octal coded values of the trigger number, the chip number and the column address are enabled to leave the chip as a sequential analog signal stream, followed by the octal coded pixel address

and pulse height. More details of how the chips are daisy chained and read out are given in Section 2.4.5.6.

Based on the design of the column periphery at the gate level we conclude that the layout should fit into the foreseen area of 300 μm by 1500 μm. Some functional blocks, e.g. the data overflow handling, are not shown in Fig. 2.37. In the current design a column reset is generated when a time-stamp or data buffer overflow is detected. However, this can be changed to a different procedure without too many complications.

The column periphery described in Fig. 2.37 should also be compatible with running conditions in heavy-ion collisions. In such events the system will be confronted with very high pixel multiplicities (8000 tracks/unit of rapidity) but at a rather low rate (typically 60 Hz). A typical occupancy of 2% is expected at the layer of 4 cm radius. Since the low rate will need only one time-stamp buffer all pool buffers (24) are available for pixel hits corresponding to 23% of all pixels.

2.4.5.5 Radiation-hard prototype readout chips

DM_PSI30 This readout chip contains a 22 by 30 pixel array realised in the radiation-hard DMILL process. The size of the pixel unit cell is 125 μm $\times$ 125 μm. Details of the design and the observed performance of the pixel analog block have been given in Section 2.4.4.3. The layout of the pixels is a back-to-back configuration with a common signal bus for the 250 μm wide double column. This results in a readout organisation of 11 double columns with 60 pixels each. The chip has been designed as a complete system with all necessary periphery circuits like pixel trim programming, time-stamp counter and trigger mechanism, as required in a real experiment. The lower right corner of the chip is shown in Fig. 2.38.

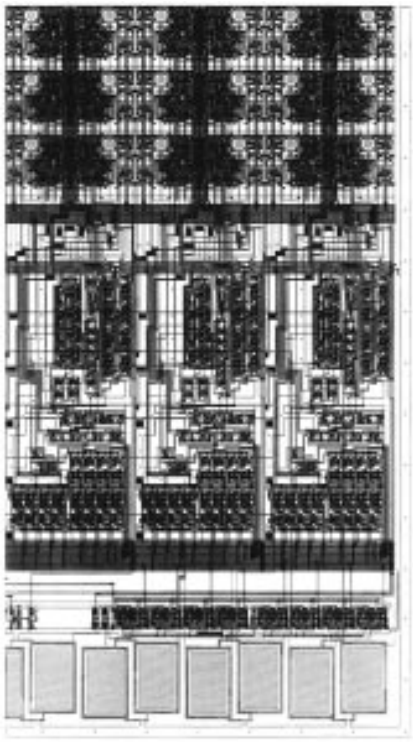

Fig. 2.38: Lower right corner of 22 $\times$ 30 pixel chip (DM_PSI30) with column periphery and first pixel rows visible. The column periphery contains the time-stamp mechanism with trigger coincidence, octal coded header generation of time-stamp and column number, programming circuits for pixel threshold trims, mask and calibration signals.

The first three pixel rows are visible at the top of the picture with the column periphery underneath. One of the goals for this design was to confront in a realistic way all the problems encountered in a complete chip, for instance the power and clock distribution to the outermost double columns while still ensuring chip butting. On the right side of the chip the distance between the bump pad centre and the cutting edge is 120 μm and on the top side 100 μm, whereas on the left side an extra space of 40 μm is required for the pixel programming and test pulse mechanism.

The time-stamp and trigger verification mechanism in the column periphery is based on the principle described in Section 2.4.5.4. The basic schematic of the time-stamp verification for each column is shown in Fig. 2.39. In comparison to Fig. 2.37 there is only one time-stamp register available compared to eight registers in the generalised column periphery. This means that a time-stamp from a pixel hit in a double column will block further hits until the trigger arrives. The value of the bunch-crossing counter (12 bit wide) is distributed to the time-stamp registers in all columns by an 8 + 4 bit wide bus ($WriteBC$). In case of a hit the bus value will be latched into the time-stamp register (8 bit). The other 4 bits (not shown in Fig. 2.39) serve as an extended time identification in case of a readout. The time-stamp verification counter (8 bit) that follows the bunch-crossing counter by a fixed delay (trigger latency) is distributed over an 8 bit wide bus ($SearchBC$) to all columns. The trigger latency is programmable up to 255 bunch crossings. Both counter mechanisms have been tested up to 50 MHz. Although we have not observed any real problems with our currently used binary code, we may eventually switch to a Gray Code counter in the future. If a trigger pulse validates the coincidence between the time-stamp register and the $SearchBC$ bus, a readout flag is set which prepares the whole column for readout. The different columns operate completely independently and therefore allow simultaneous data taking and readout activity in the same chip. We have tested this feature and found very little crosstalk in nearby columns with pixels waiting to be hit (< 690 electrons, no detector attached).

The chip has one output for the analog pixel signals with an address header attached and a second output for a digital hit signal including an octal coded pixel addressing scheme for study purposes. This feature allows the testing of the uniformity and reproducibility of such a discrete coded current addressing scheme planned for future chips. Figure 2.40a shows the measured output signals from the octal coded pixel addresses of a complete double column (60 pixels). The histogram in Fig. 2.40b represents the same data but sorted according to the observed pixel address value. Although the spacing is not completely uniform the different address values are clearly separated ($\approx 20\ \sigma$) and allow a safe address recognition in the FED. For a final answer, however, the same measurements are in preparation for irradiated chips (100 kGy).

For the readout of a complete column an additional time-stamp and column address header is added which appears like four special pixels, resulting in a transfer 64 clock-pulses long. The first three pulses contain the DAC (4 bit) modulated time-stamp (12 bit) and the fourth pulse the column address level. A readout speed of 20 MHz seems feasible, but for a future 40 MHz readout a number of improvements on the readout amplifier chain and the off-chip driver are needed. In our planning for the number of optical links we assume the more pessimistic scenario of 20 MHz. The DM_PSI30 chip contains the complete serial programming mechanism to download the different trim values for the pixel thresholds. The results on threshold variations before and after trimming, shown in Fig. 2.22, were measured with the complete time-stamp verification mechanism in operation and a pixel threshold of about 1900 electrons. More details about the implemented pixel trim/masking mechanism and the programming circuit for test pulse injection into selected pixels can be found in Section 2.4.4.3.

The calibration of the test pulse capacitance has been done with 60 keV X-rays from an ^{241}Am source. The pulse-height spectrum shown in Fig. 2.41 has been obtained with the chip running in regular time-stamp verification mode and from the normal analog chip output signal brought

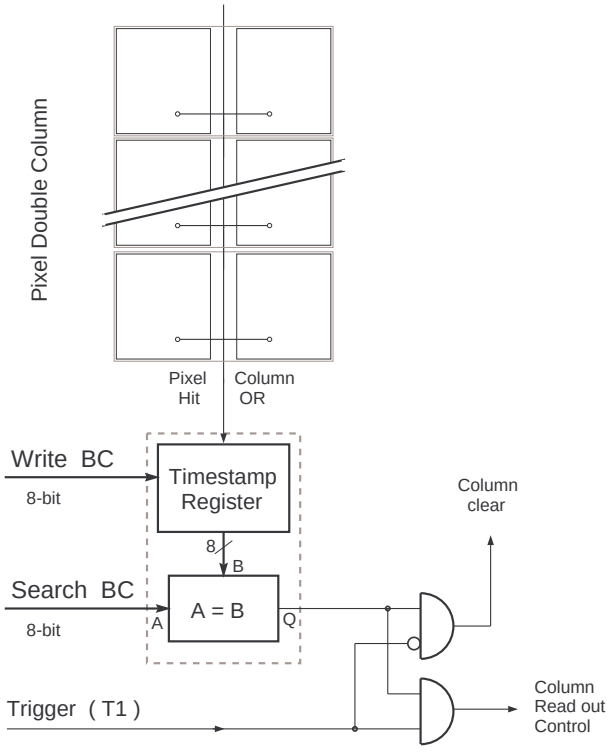

Fig. 2.39: Simplified schematics of the column periphery with time-stamp mechanism in DMILL prototype pixel chip (22 × 30 pixels).

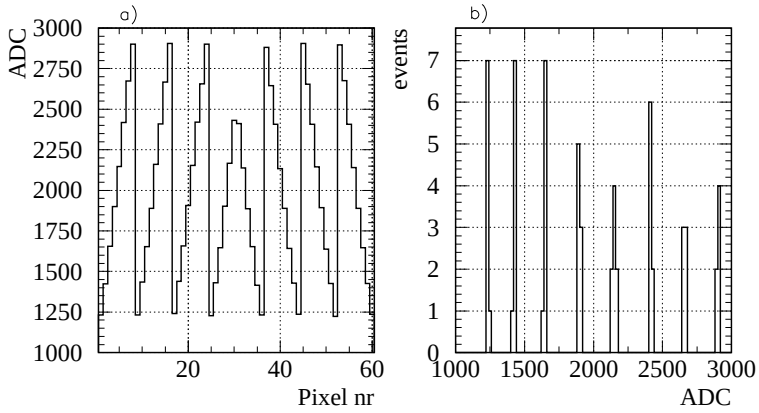

Fig. 2.40: Octal coded pixel addresses from the 22 × 30 pixel chip (DM_PSI30). (a) Measured pulse form of the octal coded address output from a complete double column (2 × 30 pixels). (b) Histogram of the octal coded address values of a double column.

to a VME-based ADC board. As a sensor we have used a silicon pixel diode of approximately 400 fF capacitance.

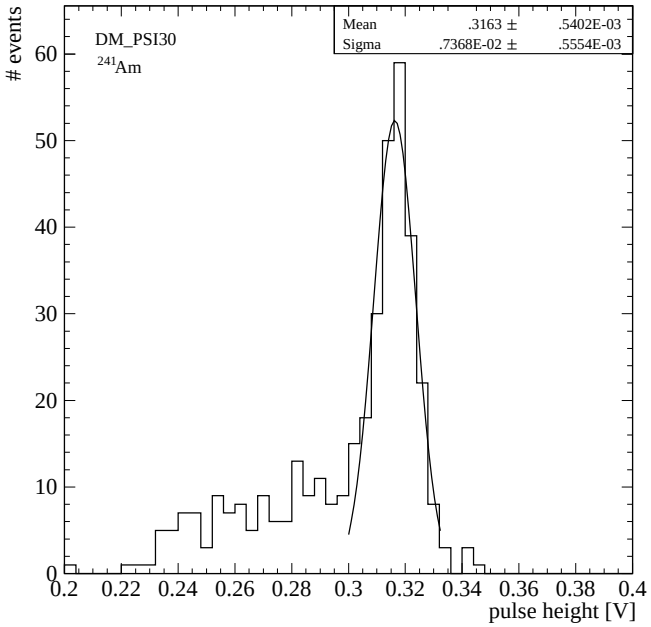

Fig. 2.41: Pulse-height spectrum with 60 keV peak from ^{241}Am source measured with the 22 × 30 pixel chip (DM_PSI30).

DM_PSI32 The test of a high-speed bypass mechanism is crucial for the Column Drain Architecture operation. In the DM_PSI32 chip we realised a pixel unit cell with the full architecture that was used in various column configurations for tests of speed and crosstalk behaviour to the analog block. The crucial part in the pixel readout block is an active bypass circuit that allows a

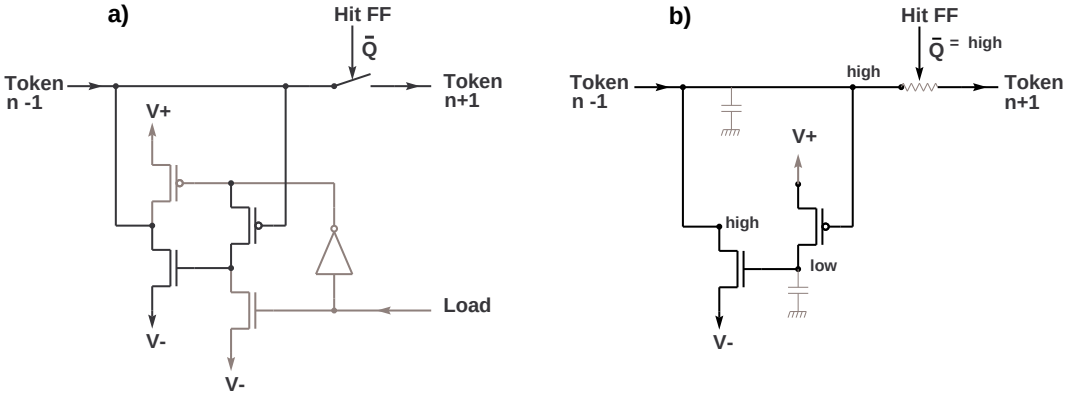

Fig. 2.42: (a) Basic transistor schematics of the active pixel bypass circuit for skipping column drain readout. Transistors used for load operation in grey. (b) Reduced circuit drawing in load condition, ready for column drain readout.

fast token bit transfer skipping empty pixels. Figure 2.42a shows the transistor schematic of the basic circuit idea. For empty pixels the hit flip-flop leaves the bypass switch of the token bit line closed. The circuit is based on a precharge logic with positive feedback for speed acceleration. The transistors used for load operation are shown in grey. In the stand-by mode, the token bit line and the load line are high, waiting for the skipping readout procedure to start. Just before the column drain readout begins, the load line goes low. In Fig. 2.42b a reduced circuit drawing

shows the crucial elements taking part in the token bit propagation. The bypass transistor is closed, representing a serial resistance that for long skips quickly becomes the speed limiting factor in a purely passive token bit bypass mechanism. As the token line (n-1) from the previous pixel goes low, the two transistors become conducting, discharge their node capacitances and therefore further accelerate the high to low transition for the next pixel. The discharge current of the token line capacitance during this very fast wave transition flows locally to the capacitance ground. The wave will propagate through all empty pixels at maximum speed until it reaches a hit pixel where the bypass switch has been opened. The running up wave is sensed and used to put the pixel data onto the column readout bus. After acknowledgement by the column periphery the bypass switch is closed, allowing the token wave to continue to the next pixel hit. We have measured the token wave delay time for different long pixel skips. The result is shown in Fig. 2.43a. A pixel delay time of 620 ps has been measured for a digital supply voltage of 4.5 V. The dependence of the skip frequency on different supply voltages is shown in Fig. 2.43b. The precise propagation speed is not critical, since the whole column drain system is based on a handshake mechanism. With the measured 1.6 GHz skipping speed a full column skip takes 65 ns, which is better than the 75 ns assumed in the simulation of the architecture variant 211–32 (see Section 2.4.5.2).

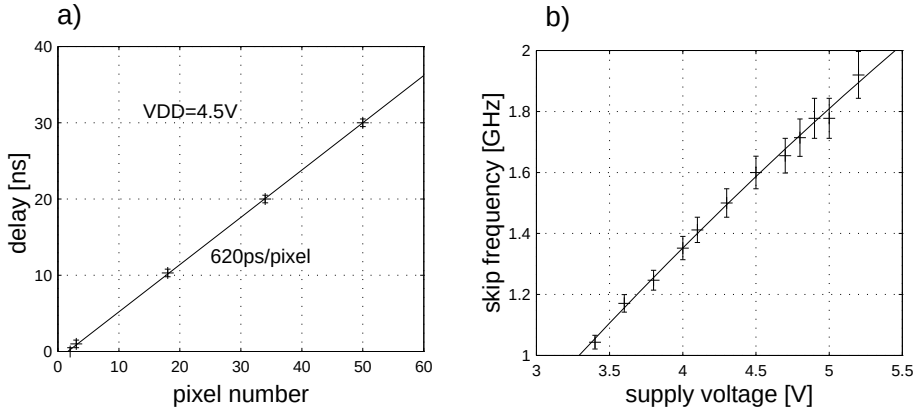

Fig. 2.43: (a) Measured delay time versus number of pixels skipped for the DM_PSI32 chip at $VDD = 4.5$ V. (b) Skipping frequency for empty pixels in the column drain readout for different digital supply voltages. (DM_PSI32 (DMILL))

Great care has been taken to measure the crosstalk of the token wave mechanism onto the analog pixel block. By lowering the comparator threshold of pixels while a token wave was propagated through these pixels a column internal crosstalk of 700–750 electrons was measured. Between columns an upper limit of < 450 electrons could be measured [2-18]. With a foreseen pixel threshold of 2500 electrons there should be enough margin to tolerate this crosstalk. These results were obtained with a pixel size of 125 μm $\times$ 125 μm. For the future pixel size of 150 μm by 150 μm the distances to the column bus lines will be larger and thanks to the additional pixel area, more elaborate trench separations can be implemented, reducing the crosstalk even further.

2.4.5.6 Data transmission

Introduction Data from bunch crossings accepted by the first level trigger (1LT) must be transmitted from the column buffers on the readout chips to the Front-End Driver (FED) modules located in the counting room. Figure 2.44 shows schematically the pixel readout scheme. Several readout chips are connected sequentially to a readout bus (analog out) which proceeds as an analog optical link to a FED. No intermediate data buffering is foreseen; the data are

held in the column buffers until they can be transmitted. A group of readout chips connected to the bus looks just like a continuous series of independent columns. All pixel addresses and time-stamps will be sent in an octal coded analog form.

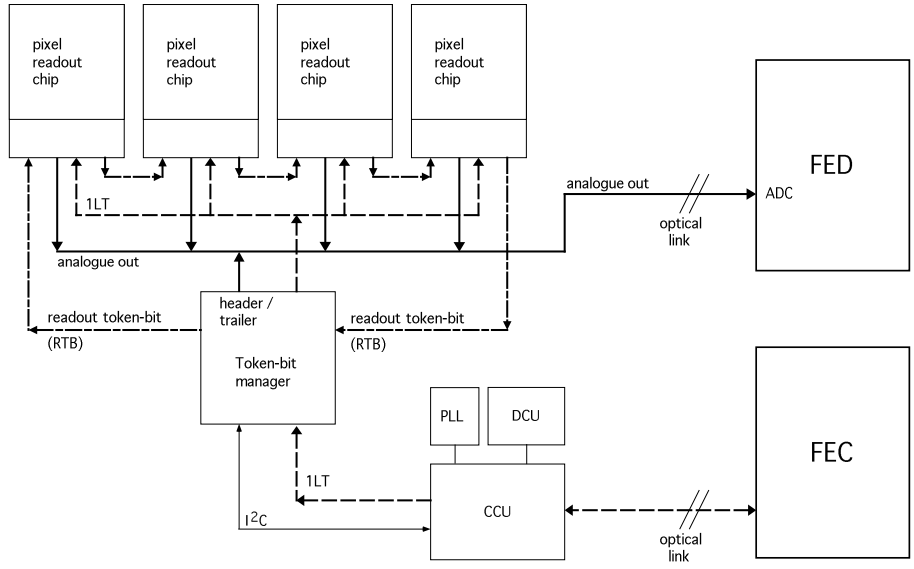

Fig. 2.44: A schematic diagram of the pixel readout front-end system. The FED and FEC modules are located in the counting room. A single set of CCU&DCU chips (see Section 2.4.5.7) services a number of readout links. The token-bit manger chip is placed on the module hybrids for the barrel and on the port cards for the end disks.

Token-bit manager chip The token-bit manager chip, sitting close to the front-end readout chips, plays a central role in the readout scheme. It has several functions:

1. It distributes the clock to a group of readout chips;
2. After receiving the 1LT signal from the PLL module it passes it to the readout chips, sends the readout header on the data link (Analog Out), increments the event counter, increments the 'queue' stack and sends the readout token-bit signal to the first chip;
3. After the readout token-bit comes back from the last chip it sends the readout trailer label and decrements the 'queue' stack;
4. If a 'queue' stack overflow occurs, the token-bit manager inhibits the 1LT signals from being transmitted to the readout chips and just sends an empty readout frame. The stack overflow value will be set between 4 and 8.
5. It provides the event number to the readout chips;
6. It sends the reset signal or any other control function to the readout chips whenever this is requested by the front-end control unit (FEC).

When a 1LT signal is present, the token-bit manager puts a readout header signal on the Analog-Out bus, and sends the readout token bit (RTB) on its way. Upon entry of the RTB into the first chip, a 'black' (very high) level is sent onto the Analog-Out bus. Then the RTB arrives in the first column periphery which either transmits its data or if it is empty passes the RTB on to the next column. This is repeated until the RTB has passed the last column of the chip, when a 'white' (very low) level is sent, indicating the end of the chip. The 'black' and 'white' levels are useful as distinctive marks for the data stream pattern recognition and are already incorporated in the DM_PSI30 chip (see Section 2.4.5.5). They are chosen such that they are outside the range of the octal coded address levels. When the RTB has passed through all chips and returns to the token-bit manager chip, a readout trailer signal is sent.

An important feature of the pixel readout system is that data from different time-stamps can be mixed in one readout frame. As the RTB traverses the columns, any 1LT confirmed data will be sent, including all pixels from triggers coming after the one which initiated the readout sequence. The token-bit manager does not know if all hit data from a trigger have been swept together with the previous trigger. Therefore it will always issue another RTB cycle, even if this results in an empty readout frame.

The functionality of the 'queue' stack mentioned above is to control the data traffic on the link. If for any reason there is a large backlog of triggers (4–8) to be sent to the FED the token-bit manager will stop sending 1LT signals to readout chips.

Data format In addition to the analog pixel signal a number of digital address and time-stamp data have to be sent to the FED. In order to save bandwidth a compressed data format for the digital signals will be used. Each group of three digital bits will be transmitted as an octal coded analog signal. For each hit pixel the following signals are transmitted:

- time-stamp (event number), 6 bits coded in 2 analog signals.
- chip number, 3 bits coded in 1 analog signal;
- pixel column index, 5 bits coded in 2 analog signals;
- pixel row index, 7 bits coded in 2 analog signals (7th bit combined with the pixel column index);
- pixel amplitude, 1 analog signal;

A data packet for a single pixel is therefore eight signals long. For one readout frame the data packets are arranged sequentially with a header at the beginning and a trailer at the end. For events containing no data in a set of pixel readout chips a frame with only the header, 'black' and 'white' levels marking the chips, and the readout trailer is sent. Error flags are encoded into the header.

Data rates At high luminosity a single readout chip in the barrel layer 2 (at 7 cm) will have on average one hit pixel per bunch crossing. Note that the distribution is very correlated; some chips will have 4–8 hit pixels while others will be empty.

Figure 2.45 shows for the three barrel layers the simulated readout data rate from one readout chip as a function of the luminosity. This data rate was calculated assuming that 10 signals per pixel are transmitted and that the 1LT rate is 100 kHz.

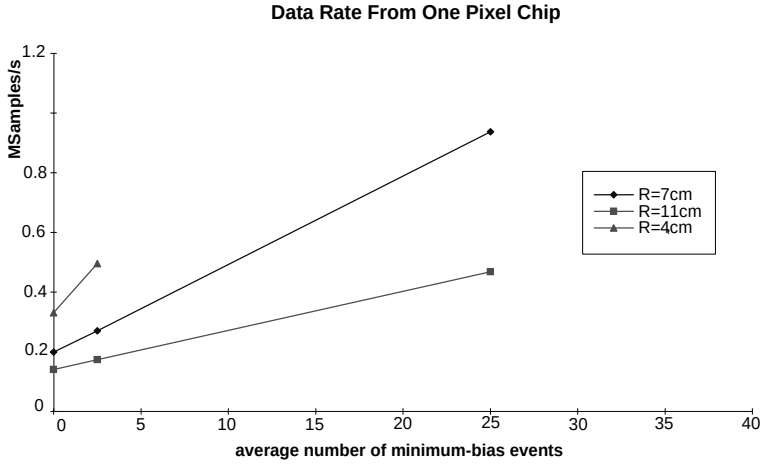

Fig. 2.45: Data rate sent by one readout chip as a function of luminosity measured by the average number of minimum-bias events per bunch crossing. Rates at three detector radii are compared. The data rate is calculated assuming a 100 kHz 1LT rate and 10 signals per pixel.

The number of pixel chips read by one link has to be chosen in such a way that the link does not saturate even for data bursts exceeding the average rates. A chip hit by a jet can have a data rate which is 3–4 times higher than the average. A safety factor of 5 seems therefore appropriate. A realistic assumption is made that the analog links will run at least at 20 MHz.

Table 2.8: Pixel data rates

	Layer 1 (4 cm)	Layer 2 (7 cm)	Layer 3 (11 cm)	4 Disks
Number of readout chips	2304	3840	5888	4320
Luminosity $\mathcal{L} = 10^{34}$ cm^{-2}s^{-1}	0.1	1.0	1.0	1.0
Average number of hit pixels per chip	0.52	0.94	0.47	0.52
Number of transmitted signals per hit pixel	10	10	10	10
Average number of signals per chip per event	5.2	9.4	4.7	5.2
Chips per link	4	4	8	3–9
Average data rate per link [MHz]	2.0	3.8	3.8	2.1
Number of links	576	960	736	768
Number of FEDs	9	15	12	12

Based on these arguments four readout chips per link were chosen for pixel layer 2 (at 7 cm), eight chips per link for layer 3 (at 11 cm) and four chips per link for layer 1 (4 cm at low luminosity). For the end disks, each blade has eight links (only seven are used), with an average of seven chips per link. Table 2.8 summarises the numbers of links required and the expected average data rate transmitted per link, assuming a 100 kHz 1LT rate. The data rates for layers 2 and 3 and for the end-cap disks are calculated for high luminosity, the numbers for layer 1 are for low luminosity.

Performance From Table 2.8 the average time delay needed to transmit one event can be estimated. For example a layer 2 link has to transmit an average of 40 signals per event which, for a 20 MHz link, gives 2 μs in addition to the 3.2 μs 1LT delay. This is well below the average time gap between two subsequent triggers (10 μs). However, because of data length fluctuations and of the non-uniformity of the 1LT distribution the event transmission delay can vary. The simulated delay time distribution for 40, 20 and 10 MHz is shown in the left part of Fig. 2.46.

If, due to these delays, a confirmed time-stamp must wait to be read out, and since such registers are not allowed to be overwritten, further time-stamps cannot be recorded in the buffer until the confirmed time-stamp register is read out and released. This leads to an additional data loss on top of the losses discussed in Section 2.4.5.2. Simulation results for the total data loss as a function of the 1LT rate are shown in the right part of Fig. 2.46 for 40, 20 and 10 MHz links. For very low trigger rates the loss is identical to the one given in Table 2.7. The additional loss due to increasing trigger rates is very small for link frequencies $\geq$ 20 MHz.

FED functionality for the pixel detector The standard CMS design will be adopted for the pixel FED [2-19]. This design will include standard components like the timing chip (TTC), data gathering and data monitoring units and the bus interfaces. The pixel detector dependent unit (DDU) will follow closely the silicon-strip and MSGC design made by the Tracker Electronics group (see Chapter 5).

The main functionality of the Tracker DDU is to perform the analog-to-digital conversion, process hits, build event fragments and present them to DAQ buffers.

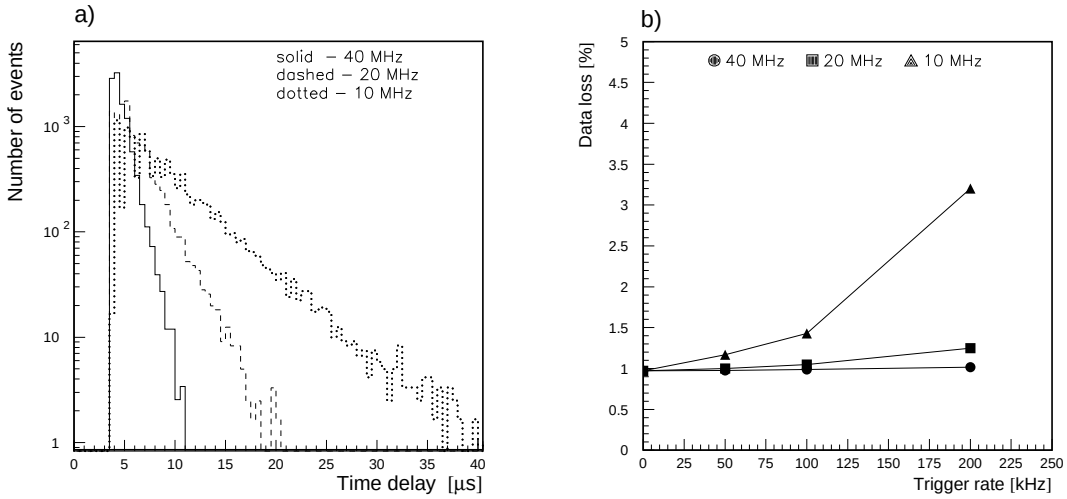

Fig. 2.46: a) Distribution of simulated delay times between the bunch crossing which generated the 1LT confirmed events and the time, when the complete event has been received in the FED. The simulation is at high luminosity for the barrel layer at 7 cm and with a 100 kHz 1LT rate. The data shown are for different link frequencies. b) Total data loss in the readout as a function of the 1LT rate.

The pixel specific hit processing includes the following steps:

1. Decode the octal packed digital signals;
2. Subtract the pixel pedestals;
3. Sort the pixel hits according to the event number;
4. Build event fragments from pixels with the same event number;
5. Monitor the synchronisation of the incoming events.

The hit processing algorithm will be implemented either in FPGA technology or, if speed is a problem, as an ASIC. Prototyping and simulation work related to the pixel hit processing has been started using ALTERA FPGAs.

Pixel data sent from the FED to the DAQ (DPM) will have the following format:

1. One header per FED with event number (4 bytes) and the number of modules with hits (1 byte);
2. For each module a header will include the detector ID (2 bytes), number of hit pixels (1 byte);
3. Each hit pixel will have 3 bytes of data:
   - digitised amplitude 4/6 bits,
   - chip number 4 bits,
   - column number 5 bits,
   - row number 7 bits.

It is possible that the FED data buffers will become full. In such a case the FED has to signal this condition to the DAQ and to the corresponding FEC module, which will inhibit the 1LT signal sent to part of the front-end system. Any error conditions signaled from the front-end system (typically included in the data packet header) will be transmitted further to the control system. The FED will monitor the event synchronisation by comparing the event number counted by the TTC system with the event number received from the front-end system (counted by the token-bit manager chip). The number of arriving data packets will also be counted and has to agree with the TTC event number. The FED has to signal any disagreement to the corresponding FEC in order to initiate a front-end system reset procedure.

2.4.5.7 Front-end system set-up, control and monitoring

Overview: This section briefly describes the initialisation of the front-end chips and column peripheries in order to process events or to test/debug procedures. The embedded electronics used for this purpose are, in addition, able to perform the controlling and monitoring of environmental parameters. It can also initiate recovery from readout errors. However, the detection of readout errors (e.g. bad event data format) is the responsibility of the Front-End Driver (FED), because the sparsified pixel data are directly transmitted without intermediate buffering.

Requirements: The front-end chips and column peripheries require only LHC clock and first-level trigger signals to store and transmit pixel amplitudes and addresses. Initialisation of the front-end logics is performed by activating registers embedded in the front-end chips and their peripheries, respectively. This requires a bus connection to a supervisor and an appropriate communication protocol. In contrast to the clock and trigger signals no synchronous operation of these registers is needed, therefore allowing an asynchronous communication architecture. Environmental parameters at the front-end must be continuously monitored and checked. If they exceed preset limits an alarm must be issued and, in few specific cases (e.g. cooling interruption), actions have to follow immediately (e.g. switching off the power).

Conceptual design: The requirements given above are met by the control system developed for the CMS Tracker (see Chapter 5) and will be adopted for use with the pixel detector too. It consists of three functional blocks:

1. An external Front-End Controller (FEC) located in a VME crate to provide the connection with the CMS slow control system DCS (Detector Control System) and to deliver clock and trigger signal to the front-end.
2. A radiation-hard local slow control master embedded in the pixel detector system. This master is made up of three different ASICs: a Communication Control Unit CCU, a Detector Control Unit DCU and a Phase Locked Loop delay chip PLL (see Section 5.6.6).
   The PLL receives the combined clock and level-1 trigger signal from the FEC and regenerates individual clock and trigger signals which are transmitted to the front-ends with programmable phase delays.
   The DCU receives various environmental signals (e.g. temperature, supply voltages etc.) which after digitisation are compared with preset limits and transmitted to the CCU. This enables the monitoring of slow control signals and interruptions in case of alarm conditions.
   The CCU serves as an interface between the communication network and various busses, the I^2C-bus being of particular importance. The I^2C-bus will be used to set the front-end chips into the required state by addressing their control registers. The parallel port of the CCU can be used to connect with the DCU. Another I^2C-port is utilised to adjust the phase delay of the PLL ASIC.
   It is foreseen to mount all three ASICs together with the necessary line drivers and receivers on one multi-chip module named CCUM.
3. An optical link between 1) and 2) maintaining a simple token-ring protocol at 40 Mbits/s. The link consists of four lines. Two of them are used to send data signals and the combined clock and level-1 trigger signal, the other two lines are required for the corresponding return signals.

Arrangement: The CCU modules (CCUM) will be mounted at the largest possible radii within the pixel system volume on the barrel end-flanges and the port cards of the end disks. From there, electrical links to the front-end are made by flat Kapton cables to exchange signals

and monitoring voltages respectively. Signals from the pixel modules are passed directly to the electro-optical converters placed on the service tube (see Fig. 2.53 for the barrel). In addition, at least four lines between each CCUM and the corresponding optical links must be maintained (twice as many, if redundancy on the links is requested). Soldered twisted-pair cables will provide the connection with the service tube.

In the following a tentative list of signals assigned to the front-end Kapton cable (HDI for the end-disks) is given:

- Pixel hit data (amplitude, analog coded pixel address, time-stamp and control data-bits) transmitted with at least 20 MHz from the front-end chips to the optical links (differential signals). A driver chip on the hybrids will be necessary to transmit these signals over a distance of up to 50 cm.
- LHC clock and Level-1 trigger (both are differential signals occupying in total four lines) provided by the PLL-delay chip with correctly adjusted phase. Note that because of the small dimensions of the pixel detector no PLL chip needs to be embedded into the front-end.
- An I^2C bus connection with only two electrical lines for the digital communication with the front-end modules. The various registers needed on the front-end are not yet specified in detail, but there are several tasks which can be already identified:
  - The selection of any specific pixel element.
  - The setting of the comparator threshold of each pixel element (3 bits), used also to completely switch off noisy pixels.
  - The enabling/disabling of a calibration signal on individual pixel elements used to inject a well-determined amount of charge into the preamplifier.
  - The setting of the level-1 trigger delay to assure correct association of pixel hits with bunch crossings.
  - The setting of various DACs and executable registers to assist test and debug procedures.

  For the addressing of these registers we shall adopt an extended addressing mode. The destination is an individual readout chip of one detector module and the subaddress is pointing towards an individual register.
- The detector bias voltage and its ground return path (two lines).
- The remaining lines are available to transfer steady-state signals to a DCU for digitisation.

Given the current design of the CCU supporting up to 16 I^2C ports and a single parallel bus (PBUS), one CCUM can for example supervise eight detector modules. On each end of the barrel a total amount of 40 CCUMs must be implemented to serve 320 modules of the high luminosity barrel. For the end-disks one CCUM per blade is foreseen. The DCU (which is not yet designed) must then be capable of monitoring up to about 50-steady state signals.

2.4.6 Conceptual design of full pixel readout chip

A schematic view of the readout chip is shown in Fig. 2.47. The chip has an array of 52×53 pixels of 150 μm by 150 μm size organised in 26 double columns.

One chip allows to be read out a sensor area of 8.025 mm along the columns and 8.100 mm in the other direction. This requires on the sensor special pixel sizes along the edge of the chip. The total chip height, including column periphery and the Control & Interface Block, is planned as 10.450 mm. The width of the readout chip is 8.000 mm, leaving 100 μm space for butting the chips. On the chip this includes an extra area of 40 μm on the left side required to host the pixel programming and calibration mechanism (see Section 2.4.5.5, DM_PSI30).

Two columns of 53 **Pixel Unit Cells** each are laid out in a mirrored configuration, forming a 300 μm wide double column, which has a common signal bus running along its middle. When

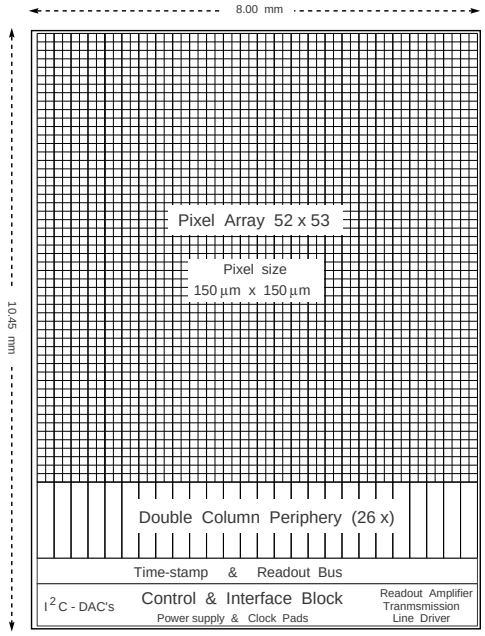

Fig. 2.47: Conceptual layout of the pixel readout chip.

making a scan for hit pixels, the token signal must traverse all 106 pixels on its way up and down the double column.

The pixel unit cells are subdivided geometrically into an analog block and a digital readout block. The *analog block* and its performance requirements has been described in Section 2.4.4.2. The anticipated power dissipation is around 40 μW per pixel and is likely to increase somewhat after irradiation. In order to guarantee a clear and uniform pixel hit discrimination, a common pixel threshold on the chip can be set by a DAC register in the Control & Interface Block, and a 3 bit trim for individual threshold adjustment will be available on each pixel, which also allows the masking of unstable pixels. The trim values are stored in SRAM bit cells in the pixels and can be programmed and re-read for verification by the I^2C serial bus interface. Calibration signals sent to selected pixels can be programmed as well. The chip will be run with a pixel threshold of 2500 electrons which implies a noise requirement of 500 electrons or less after irradiation. Details about the rather low observed crosstalk coming from the digital readout block in the PUC are given in Section 2.4.5.5. For the complete analog block (see Section 2.4.4.2) a total of $\approx$ 50 transistors is foreseen.

The *digital readout block* performs the skipping readout of the hit pixels in a double column as described in Section 2.4.5.3. The measured skipping speed of 1.6 GHz for empty pixels and the crosstalk of $\approx$ 750 electrons observed for skipped pixels (see 2.4.5.5) form the basis for a successful realisation of the complete readout chip. For this functional block a total of $\approx$ 50 transistors are used. The readout of the analog pixel signals requires about 6% of the total number of transistors in the PUC. Given the PUC area, a transistor can occupy an average area of up to 160 μm^2.

The **Column Periphery** organises the skipping pixel hit readout and takes care of time-stamp and trigger verification (see Fig. 2.37). This circuit should manage up to 8 time-stamps and store up to 24 pixel hits which have been copied down into the periphery data buffer.

The **Time-stamp & Readout Bus** block (see Fig. 2.47) contains two bunch-crossing counters ($WriteBC$ and $SearchBC$), and the necessary buses for the distribution of their codes to the time-stamp buffers in all columns. It also contains the readout logic for collecting all hits

in a chip readout cycle, i.e. the octal coded pixel address data (trigger, chip, column and row number), and the analog pulse height from the pixel hits. Upon entering and leaving the chip, the readout token bit passes two synchronising shift register cells, which modulate a 'black' and 'white' mark, respectively, on the analog output bus.

In the **Control & Interface Block** (see Fig. 2.47) all control voltages and currents required for proper chip operation are generated by digital-to-analog converters (DAC). The digital registers for the DACs are programmable through the serial communication block (I^2C). This interface is also used for programming the individual pixel thresholds and the calibration signals of selected pixels. The trigger latency time can be set in a register as well. A read-back option for verification purposes will be implemented. All input and output circuits and the wire bond pads for power and clocking lines are placed at the rim of this block. Special care will be taken for the realisation of the high bandwidth readout amplifier with a differential transmission line driver needed to send the high speed analog data off-chip. The number of supply and control pads is expected to be in the order of 30. These include also the chip identity pads (3 bit) used to set a certain chip number by wire bonding. All clocking signals will be differential for inputs as well as outputs. With a chip width of 8 mm there will be sufficient space per supply pad to allow reserve pads for testing and repair.

The total number of transistors in the final readout chip is estimated to amount to 380 000. The realisation of the readout chip will proceed in steps, where blocks are designed and tested for performance before and after irradiation. In a first iteration the column periphery with time-stamp and data buffer management will be realized and then merged with a double column of pixels. In a next step this will be integrated with the Time-stamp & Readout Bus block and finally the Control & Interface block will be added. Some of these blocks can be developed in parallel, e.g. the Control & Interface block. The definition of signals and controls between different blocks will be done at the appropriate time.

2.4.7 Low voltage power and bias voltage distribution

The front-end readout chips must be supplied with an analog voltage V_a (-2.0 to -2.5 V) and a digital voltage V_d (-4.5 to -5.0 V), with separate return lines. The detector bias voltage supply should have a range of at least 500 V. Its ground will be referenced on the module to the analog ground.

Modular voltage supply channels delivering both V_a and V_d will provide power to a group of pixel modules. The same group of modules will be served by one bias voltage channel. In the barrel a natural group of modules to be supplied by one channel would be a half-ladder (4 modules). The radiation dose within such a group is expected to be quite uniform, allowing the use of one common bias voltage. This results in 96 (152) channels of each low voltage power and bias voltage for the low (high) luminosity barrel. For the end disks the grouping should be done in radial rings, since the radiation dose will have a strong radial dependence. Therefore all members of one detector variant within a half-disk will form one group. For the largest detector variant with 10 readout chips two groups will be formed. The total number of channels for the end disks will thus be 64 of each low voltage power and bias voltage. With this grouping each analog (digital) power channel must deliver a current of up to 5 A (1 A).

2.5 Modules

The modules for the barrel and the blades for the end disks are the basic building blocks of the pixel detector system. They consist of one or more sensor tiles each, equipped with several front-end readout chips and a hybrid circuit or port card for the distribution of power and signals.

2.5.1 Barrel module

The barrel module, as shown in Fig. 2.48, consists of one sensor substrate with the front-end readout chips bump-bonded to it, and a hybrid circuit mounted on top of the sensor. A thin carbon fibre plate glued to the readout chips serves as the module base which can be attached to the cooling frame. The readout chips are wire-bonded to the hybrid circuit. On the hybrid, clock and control signals arriving via a copper-on-Kapton cable are distributed to the readout chips, involving the Token-bit manager chip, and the hit signals from triggered events are sent by a driver chip through the same Kapton cable to the barrel periphery mounted at the ends of the barrel. This Kapton cable also carries the bias voltage. Power is brought from the barrel periphery to the hybrid via a Kapton-aluminium sandwich. Both Kapton cables are glued and wire bonded to the hybrid.

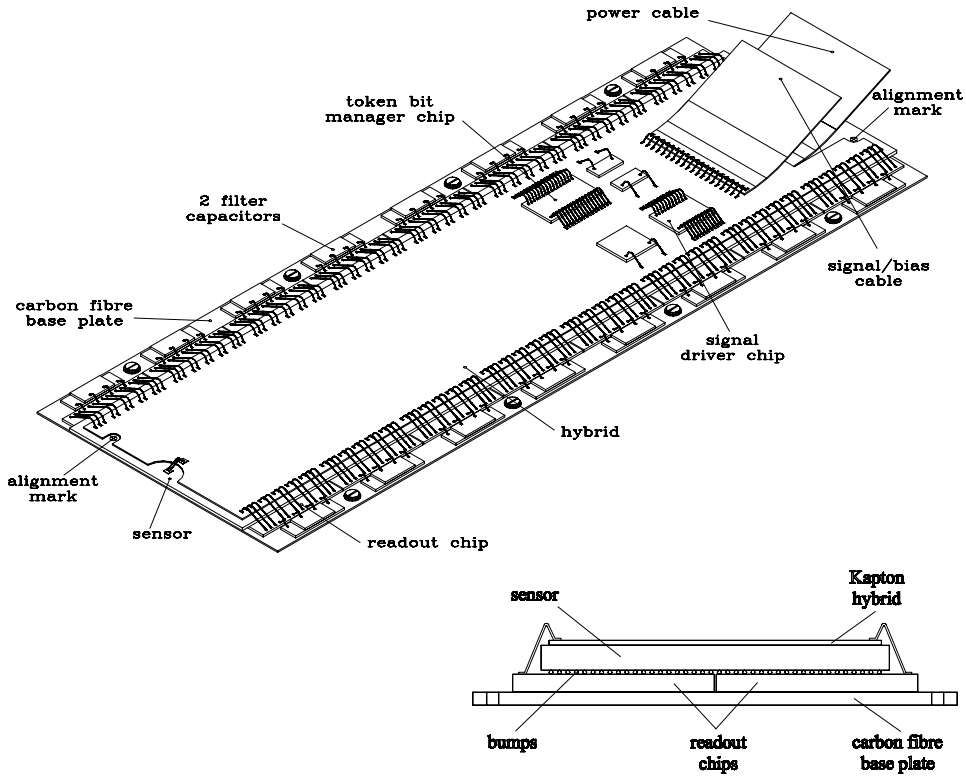

Fig. 2.48: View of a pixel barrel module. In the insert the vertical scale is raised by a factor of 5.

Two rows of eight front-end readout chips with 53 ($r\varphi$) $\times$ 52 (z) pixel unit cells of (150 μm)^2 area are bump-bonded to the sensor of 250 μm thickness. The chip thickness will be 180 μm. The overall chip dimension in the z-direction is 0.800 cm, leaving a gap of 100 μm between two adjacent chips, therefore very precise cutting of the chips will be required. In the $r\varphi$-direction the chips are extended to incorporate the column peripheries of 0.23 cm width at the end of the pixel columns, where also the connection pads of the chips are situated. The overall chip dimension in the $r\varphi$-direction is 1.045 cm. Between the two chip rows a gap of 100 μm is left.

The hybrid will be a three-layer, high-density polymer flex-print glued onto the p-side of the sensor. It is 6.4 cm long, 1.6 cm wide and its thickness will be about 50 μm. Connection pads for wire-bonding at the long rims face the ones on the front-end readout chips. A control chip (Token-bit manager) and a driver chip for the analog pixel signals are among a few active elements wire bonded onto the hybrid. Slow control sensors (temperature, guard ring current) will also be placed on the hybrid. These active elements must be radiation hard to the required

level. Two indentations in the hybrid allow the marks on the p-side of the sensor to be used for alignment purposes.

The signal/bias Kapton cable will be 1.1 cm wide accommodating 22 copper traces of 250 μm width and 4 μm thickness. The Kapton substrate will be 50 μm thick. The power cable will have a 40 μm thick Al foil glued on a 50 μm thick Kapton film with gaps between the conductors.

A carbon fibre base plate of 270 μm thickness, 24.3 mm width and 65.9 mm length will be glued onto the readout chip array. On the long sides, exceeding the chips, precision holes will be drilled for screwing the module onto the mechanical/cooling frame. Glass substrate capacitances of a few mm^2 area placed between the screws, are used to filter the low voltage power for the readout chips.

2.5.2 The end disk blades

Twenty four blades make up one of the disks, and the blade is the basic component of the end disk system. Modules are glued to a thin carbon panel after bump-bonding of the front-end chips. The panel facing the interaction region has four sensors and the downstream panel has three. The chips are glued onto the panels while the bias plate of the sensors face away from the blade. Pairs of panels, with a cooling tube in between, form a blade. The chips are configured to exhibit the wire bonding pads along lines running in the $r\varphi$-direction. The signals from the chips are collected by a four layer hybrid (HDI). On the panel with four sensors, the HDI are glued to the panel in the space between neighbouring sensors. On the panel with three sensors (all read out by a double row of chips), the HDI are also mounted on the outside of the sensors at the inner and outer radius. Dimensions of the HDI are tailored to the $r\varphi$-size of the sensors and the space between them along r. Each layer of the HDI is a single-sided printed circuit flex of 50 μm Kapton with copper lines. The chips' outputs are wire bonded to the HDI. These wires are protected by encapsulating them in a low mass radiation hard wax. Each HDI is connected to an interface board, the port card, with a 2 cm wide single-sided flex cable (pigtail) made of 50 μm Kapton. Pigtail cables vary in length from 6 to 15 cm. These cables are glued to the top of the sensors, for strain release, and connected to the HDI through wire bonding. (One design option considers the pigtail as being an integral part of the HDI.) The HDI will distribute the power to the chips, and one of its layers is a ground plane collecting also the current of the guard rings. Other components located on the HDI include filtering capacitors for the power, temperature monitors and Radiation Sensing Field Effect Transistors (RADFET) to keep track of the level of radiation. The bias voltage to the sensors and the monitoring signals are carried by one additional pigtail on each side of the blade.

The Port Card is a low-mass PC board. It houses the electronics needed to interface the front-end chips with the power supplies and the VME electronics located in counting room. Two port cards (one for each panel) are required for a blade. They are physically installed on the space-frame supporting the disks and are located at the largest possible radius to reduce the damage from radiation. The pigtails are connected to the port card using sub-miniature connectors. The port card transmits the clock signal, the L1 trigger and the slow control signals to the front-end electronics. It distributes low voltages to the chip and the bias voltage to the sensors. It also monitors currents and voltages on the sensors, as well as the temperature and the level of radiation on each panel of the blade. These functions are carried out by ASICs that are common to the CMS tracking electronics (see Section 5.6.6). Such units are the Detector Control Unit (DCU) for monitoring functions, the Phase Locked Loop (PLL) for timing and the Communication Control Unit (CCU). An additional chip, the token-bit manager, is required to organise the readout.

2.5.3 Bump bonding

2.5.3.1 Introduction

The construction of a hybrid pixel detector is fraught with a large number of complex processing tasks. No task is without its technical challenges. Selecting and implementing an appropriate process to connect the pixel readout electronics chips to the PIN diode sensor arrays is no exception.

The mating of two pieces of silicon with a bond that allows for electrical connections between the substrates, along with the requisite mechanical strength, is relatively straightforward. Commercial vendors have been studying this problem for over 30 years and there are a number of acceptable solutions that have been developed for industrial markets. For 'bump' technologies, the basic process flow that has evolved includes a substrate preparation step, a 'bumping' or electrode fabrication step, and finally a 'bonding' or flip chip attachment step. These steps are fairly universal, but may be combined, hidden, or dropped depending on the technology chosen.

Given the pervasiveness of Al in CMOS processing foundries, a substrate preparation step is invariably performed to obviate the insulating properties of aluminium oxide which develops on bare Al. Typically this under-bump metallisation (UBM) step includes removal of the aluminium oxide layer followed by deposition of conductive material which does not oxidise. This step is critical for ensuring good performance of the final interconnect. The electrode growth step typically involves plating or evaporation of metal onto one or both of the substrates to be mated. For industrial markets, the trend is toward electroless plating processes which do not require masking of the substrate to define the electrode regions. Such maskless processes are typically not compatible with the small electrode requirements of pixel detectors used in particle physics. Once the electrodes have been fabricated, the two substrates may be mated. This usually requires special machines which provide the necessary alignment accuracy to place the substrates in their proper relative locations, and then to apply the necessary heat and pressure to form the mechanical bond. Such equipment is fairly specialised, costly, and requires some level of expertise and maintenance to ensure reliable processing.

2.5.3.2 Technology considerations

For the CMS pixel detector, the constraints placed on a bump bond technology are fairly significant. From a practical standpoint, the cost and availability of a given technology is a driving consideration. Since there is currently no readily available commercial technology that is ideally suited, the technology chosen must be adapted.

Since the signal path between the PIN diode array and the readout electronics passes through the interconnect, a primary consideration will be the stray capacitance added to the input of the electronics by the interconnect. This should be minimised by employing a technology with a minimum interconnect area. Also important to the electrical performance is the minimisation of the interconnect resistance. Typically, this is not constrained by the actual conductors used in the interconnect, but by the preparation of the Al pad below. The mechanical strength of the bond is also a very important consideration. Once attachment of the diode and electronics chips has been made, the multi-chip module will need to be robust enough to survive the subsequent handling during the many remaining stages of assembly, testing, transportation, and insertion. Along with this, the bond should also perform reliably after it is cooled. Since the detector will operate at near zero degrees Celsius, the bond should not present a significant thermal mismatch between itself and the substrates. Also of importance is the reliability of the bond as it ages during operation for 5 to 10 years in the collider hall. Finally, the interconnect yield during the attachment process is very important since the interconnect density for the CMS pixel detector is close to $4500/\mathrm{cm}^2$.

2.5.3.3 Current research

Indium solders A number of different technologies have been investigated at PSI, Aachen and UC Davis. The UC Davis effort has focused on materials useful in cold pressure welding, such as indium and indium alloys. Indium is attractive for several reasons. It is widely employed as the technology of choice by manufacturers of infrared focal plane arrays and emerging medical X-ray devices, so expertise exists in the implementation of this technology in systems very similar to our pixel detector. It is also well suited for use in fine pitch or 'small' feature size applications and where thermal mismatch between the interconnect and the substrate may be of concern as in the CMS pixel detector.

Indium is deposited on both substrates using photolithography and evaporative techniques. Some form of UBM processing is required, and this is often accomplished by performing an in situ sputter etch of the Al interconnect pads, followed by sputtering of a layer of Ti/W or Ti/Ni. The interconnection is usually made at room temperature utilising pressure to force the cold weld. Since no reflow is performed, there is no increase of the thermal budget during the detector production. The two substrates being attached must be aligned with a degree of accuracy which is a fraction of the interconnect size. This implies a need for $\approx 2-3$ μm or better placement accuracy, which necessitates the specialised bonding equipment. Once the cold weld has been made, the electrical/mechanical bond may be used as is, or the mechanical bond may be augmented by wicking an epoxy between the substrates. In the case of CMS, it would be necessary to identify an appropriate radiation-hard epoxy with the correct fluid characteristics to wick.

To date, studies involving approximately 100 flip-chip attachments of dummy electronics and sensor die, and measurements of over 10 000 indium bump interconnects have provided the following preliminary data on pure indium:

Bond pressure	1.5–3.0 mg/μm^2
Bond temperature	25–40 °C
Bond time:	$\approx$ 60 s
Die attach cycle	$\approx$ 5 min.
Interconnect yield	$(99.78 \pm 0.06)\% > 99.7\%$ @ 95 % CL
Tensile strength	$>$ 144 μg/μm^2.

As an alternative to pure indium, an In/Sn/Ag alloy has also been investigated. This alloy is applied to the substrates in the same manner as pure indium, with the same UBM processing required. This material is also amenable to cold pressure weld. Approximately 10 die attachments have been made with this alloy, and over 5400 interconnects have been measured, providing the following data:

Bond pressure	15–20 mg/μm^2
Bond temperature	25–40 °C
Bond time	$\approx$ 60 s
Die attach cycle	$\approx$ 5 min.
Interconnect yield	$>$ 99.9%
Failure rate @ -20 °C & 100 g's @ 2 kHz	$<$ 0.2%

Preliminary tensile strength measurements have shown the In/Sn/Ag alloy to have superior strength to the pure indium alloy, but the bond pressures require machinery with significant bonding capability as the typical CMS readout attachment would need in excess of $\approx$ 50 kg of bonding force.

There are several commercial sources of indium and indium alloys available at the time of this writing. Indium bumps from Boeing North America and Advanced Interconnect Technology

have been studied to date. To ensure quality control and a cost-effective means for prototype development, UC Davis and PSI have developed indium deposition facilities.

Pb/Sn solders Pb/Sn solders are also of interest for use in assembling the CMS pixel detector. As with the other processes, the solder process requires an UBM processing step, which is either accomplished through chemical plating using a zinc-ate solution or through techniques similar to those used for In. After the UBM step is complete, Pb/Sn solder bumps are usually electroplated onto the substrates. Attachment is made by performing a tack of the solder onto the mating bond pad, and then temperature cycling the die to the melting point of the solder, to reflow the solder bump and to cause it to wet the bond pad it was tacked to. Once cooled, a single interconnect is formed. Pb/Sn solder has already been successfully used by the DELPHI and the Omega Spectrometer pixel detectors. Given its use in particle physics detectors already, the main area of research that remains is the qualification of vendors who can provide an appropriate service. Effort at UC Davis is underway to characterise such vendors.

2.5.3.4 Conclusion and future direction

From the work accomplished to date, we conclude that two candidate technologies are suitable for assembling the CMS pixel detector hybrid arrays. Pure In and Pb/Sn solder both appear to meet all the requirements for providing adequate electrical and mechanical bonds. While this does not prevent continued investigation of emerging technologies which may provide simpler or more cost-effective techniques, it is clearly necessary to start qualifying vendors of either of these materials in preparation for the final assembly. This involves identifying vendors with facilities to provide the appropriate services and demonstrating these services by providing bumps and bonding of dummy pixel detectors. To date, several vendors of Pb/Sn solder and In have been identified, and initial negotiations are in progress.

2.5.4 Assembly and tests

Prior to the assembly of the modules all major components (sensors, readout chips) must undergo tests and fulfil a number of specifications set by the pixel collaboration. While the vendors will be requested to perform a minimum set of global tests using various special structures or circuits implemented on the wafers, the pixel collaboration will have to carry out extensive electrical and visual tests of the actual components at their home institutions.

After delivery of the sensor and readout chip wafers, and some preliminary tests, the aluminium bump pads will be provided with a metal layer which does not oxidize (under-bump metallization), and bumps must be grown on the bump pads ('bumping'). These steps are preferably performed at industrial firms. For this, a suitable procedure for mass production must be developed together with potential vendors. After the wafers have been 'bumped', they are distributed to the home institutes of the pixel collaboration for extensive on-wafer tests.

The number of sensor wafers needed is limited, and the tests can be performed at a manual probe station. Contacting the backside will be required. Due to the large number of pixels, it is impractical to test them individually. Therefore the tests will concentrate on special baby-detectors of typically 1 cm^2 area implemented at two or three locations on the wafer. These baby-detectors consist of typically ten various size groups of $(150\ \mu m)^2$ pixels connected together on the metal layer, each group having a pad for placing a probe needle. From the behaviour of these pixel groups a fairly reliable extrapolation of the quality of the wafer can be obtained. Visual scans of the metal pattern will also be performed. After dicing of the wafers the leakage current and breakdown voltage of the sensors must be measured.

For the complete pixel system, about 50 000 readout chips must be tested, assuming a yield of 30%. Rather sophisticated test routines must be performed, and the chips sorted in three or

four classes of quality. Depending on the yield, one or more classes will be accepted for use in the pixel system. We anticipate to perform the tests of the chips on the 400 6″ wafers with the help of an automatic probe station. After dicing, the selected chips will be tested again just before bump bonding them to the sensors. This second test may be dropped if experience shows that the cutting of the chips very close to the outermost pixels does not cause any damage.

The bump bonding of the readout chips onto the sensors is likely done within the pixel collaboration. Bump bonding facilities exist at UCD and PSI. The quality of the bump bonding can be tested by pulsing the backplane of the sensor.

As outlined above, the readout chips will be tested during the assembly of the modules at various stages using probe cards, which could damage the wire bond pads. Therefore the chips will be equipped with a duplicate set of connection pads which will be used exclusively for wire bonding.

2.6 Mechanics

2.6.1 Requirements

In the design of the mechanical frame which hosts the pixel modules the following criteria are important:

- Its material budget must be kept to a minimum.
- Its structural stiffness must guarantee positional stability within 10 μm during time periods of a few days.
- It must provide sufficient cooling to keep the sensor temperature at -10 °C during operation.
- Its distortion due to operation temperature variations must be kept below 10 μm for periods lasting a few days.
- It must be built in two halves separated along a vertical line in order to accommodate the pixel insertion scheme.

Less emphasis is given to the a priori knowledge of pixel positions within the basic CMS coordinate system. This information will be regularly extracted using tracking data on a time scale of a few days. Distortions induced by cooling the detector from room temperature down to operation temperature are thus dealt with automatically, as are imprecisions in absolute position after pixel installation.

The choice of material must mainly be driven by minimising the radiation length. Aluminium for the cooling tubes and carbon fibre composites as structural material are among a rather narrow choice of realistic material candidates. These materials exhibit quite different thermal expansion coefficients. Epoxy cured at room temperature is therefore used to limit stresses induced in the glue layers when cooling from room temperature down to operation temperature ($\Delta T \approx 30$ °C).

2.6.2 Barrel mechanical frame

The barrel mechanical frame is shown in Fig. 2.49. Parallel trapezoidal Al cooling tubes arranged in a half-cylinder are cross-connected by carbon fibre blades (cross pieces) glued alternately onto two inner or outer faces of two adjacent tubes (see Fig. 2.4). The distance between the tubes is 11 mm at the face of the cross pieces. The cooling tubes are 56 cm long, have a wall thickness of 0.2 mm, and the faces glued to the cross pieces are 4 mm wide. The inner cross section of the tubes is 9 mm^2. Prototypes with acceptable straightness and twist have been obtained [2-20]. The cross pieces will be made from unidirectional high modulus carbon fibre composite arranged in four layers ($0°/90°/90°/0°$) of 270 μm total thickness. They will be 52.65 cm long and 24.3 cm

wide to accommodate eight modules in a row. Threads for screwing the modules onto the cross pieces will be glued into prepared holes. Rectangular holes are cut into the cross pieces in order to reduce material. All four half-cylinders of the 2-layer barrel must be manufactured in separate pieces, because modules must be mounted inside and outside of the half-cylinders, and the layer configuration will be changed after the low luminosity period. Half-ring-shaped end pieces of carbon fibre/honeycomb material are glued onto short round cooling pipe extensions on both sides, which combine into manifolds on the outside of the end-flanges (4 or 5 cooling tubes into one manifold, see Fig. 2.49).

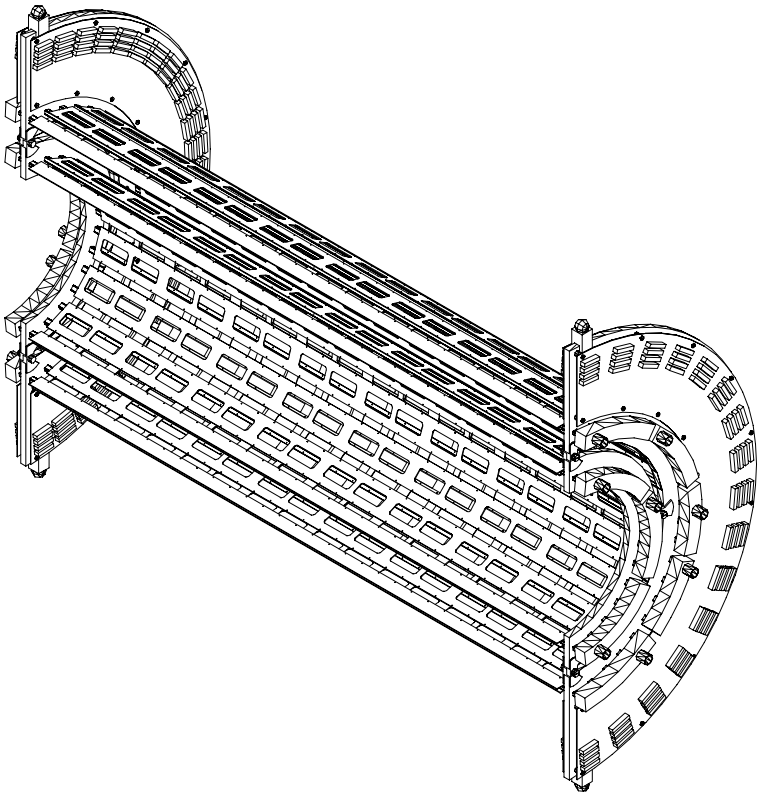

Fig. 2.49: Perspective view of a pixel half-barrel mechanical/cooling frame (high-luminosity configuration). The structure is compatible with leaving the low-luminosity layer in place ($r = 4$ cm).

Onto the end-flanges of the outer barrel layer an extension from the same material and thickness will be fixed which reaches out to a radius of 18 cm. PCBs attached on both sides of the end-flanges will house Kapton cable connectors and detector control chips (CCU modules, see Section 2.4.5.7). At the outer rim of the PCBs, short twisted-pair cables with miniature connectors at their ends are soldered which will establish the connection to the service tube (see Section 2.7). Ball bearings are fixed to the end-flanges for inserting the barrel on a rail system. Table 2.9 lists the material used in a pixel barrel layer. All contributions are smeared over $r\varphi$ and overlaps are included.

2.6.3 The mechanical concept of the end disks

2.6.3.1 The blade

Figure 2.50 is an expanded view of a blade. It is assembled with three components: a cooling pipe, two A-frames, and two panels made of carbon fibre on which the detectors are mounted. The cooling pipe forms with the two A-frames the mechanical structure of the blade: the panel support structure (PSS). This unit must supply mechanical rigidity, transfer the heat generated

Table 2.9: Material budget of a pixel barrel layer

Module component	X/X_0 smeared (overlap included)
Base of module, carbon fibre, 270 μm	0.00166
Glue, 50 μm, base to chips, $X_0 = 25$ cm	0.00025
Readout chips, 180 μm	0.00252
Solder bumps, indium	0.00007
Sensors, 250 μm	0.00280
Glue, 50 μm, hybrid to sensor, $X_0 = 25$ cm	0.00020
Hybrid, 50 μm Kapton, Cu equivalent to 6 μm with 100% coverage	0.00063
Components on hybrid, Si/Si-oxide, 0.07 cm^3 per module	0.00065
Wire bonds, 400 per module	0.00005
Mean of 2 signal Kapton cables, 50 μm Kapton, Cu equivalent to 2 μm with 100% coverage	0.00044
Mean of 2 power Kapton cables, 50 μm Kapton, 40 μm Al with 100% coverage	0.00078
Total module	0.0101
Cooling frame	
Cooling tubes, aluminium, 200 μm wall thickness	0.00198
Coolant, Hydrofluoroether, $X_0 = 23$ cm	0.00268
Glue, 50 μm, tubes to cross pieces, $X_0 = 25$ cm	0.00010
Cross pieces, carbon fibre, 270 μm	0.00075
Conductive grease, 50 μm, cross pieces to modules, $X_0 = 25$ cm	0.00030
Fixation of modules onto cross pieces (8 screws/nuts)	0.00059
Total cooling frame	0.0064
Total radiation length per pixel barrel layer	0.0165

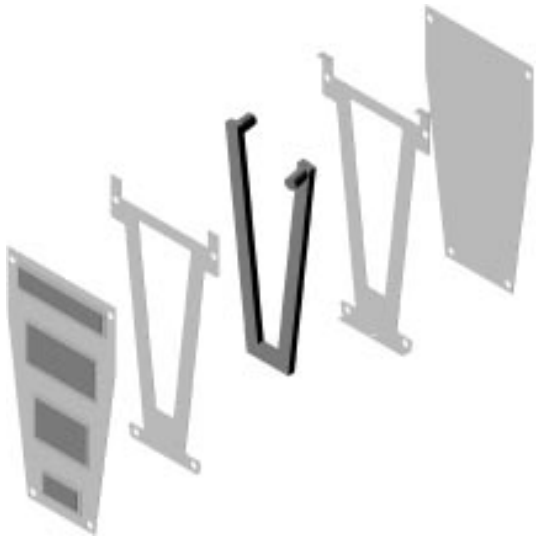

Fig. 2.50: An exploded view of the blade showing the parts and assembly.

by the electronics to the coolant, and at the same time have a mass as small as possible. In addition the detectors are operated at $-10\,^{\circ}$C and in the presence of a very large flux of particles. The design of the PSS presents the largest challenge to the mechanical part of the end disks.

The cooling pipe will be a U-shaped aluminium tube with a 4 mm outer diameter and a wall thickness of 0.2 mm. After the bending and before the A-frames are mounted to the tube, the section covered by the two panels is flattened to a 2.5 mm thickness. Short, thin tubes are used for connections between the blades or to the lines from the refrigerator. The amount of material in a blade is listed in Table 2.10.

The base material considered for the A-frame is a thin (400 μm) sheet of carbon-fibre or an aluminium plate. The two A-frames are shaped in order to form a rigid trapezoidal box with the pipe. One of the frames is flat and the other is cut from a U-shaped channel. At the locations where the sheets are mounted to the PSS and where the PSS are fastened to rings to form the disk, nuts (positioned with alignment jigs) are glued on the inside walls. They are accessible from the outside through holes in the A-frames. The positioning of the cooling pipe within the PSS structure is not critical, but the precise positions of the nuts and of the two alignment pins for each panel are important. The carbon sheets are formed in molds using thermoplastic prepregs and cyanite resins and then cut to size using a water jet saw. These panels are then glued to the flattened aluminium pipe. The design with the A-frames made of aluminium sheets uses the aluminium tube in its cylindrical shape. Both the tube and the frames are first gold plated and then connected by dip brazing. It is expected that for this design the PSS will be more rigid, and the thermal coupling between frame and tube is superior to the one with carbon-fibre sheets. The increase in mass is negligible.

The third component of a blade is a set of two panels. They are plates of carbon-fibre, 250 μm thick, on which the sensors with chips, the HDIs, and the monitoring devices are glued, using a by-stage epoxy.

The panels carry the sensors and the associated front-end electronics. They are assembled and tested individually and then anchored to the PSS after configuring them into half-disks. It is very important to be able to propagate the alignment of the sensors relative to the panels to their final position within the CMS Tracker. To achieve this goal, three reference marks (the monuments) are mounted on each panel (see Section 2.8).

2.6.3.2 The disk

Twelve panel support structures (PSS) are mounted between two half-rings (with small rims to add rigidity) made of PEEK (Fig. 2.51).

The 20° rotation along the radial symmetry axis of the blade is introduced in this assembly. The direction of this rotation is opposite for disks on different sides of the interaction region. Two disks of each kind will be assembled. Each PSS is anchored to the inner ring at one point, and to the outer ring at two points. The connections between cooling pipes are made with short (1.5 cm) union tubes of 4.5 mm inner diameter aluminium. The ends of the two lines to be connected are glued into the union tube. Depending on the choice of the coolant, it is expected that groups of either 3 or 4 blades will be supplied in series. The supply and return lines are tubes of 5 mm outer diameter with 0.2 mm walls. These lines are an integral part of the space frame supporting the disks and the service cylinder.

After the mechanical structure for each half-disk is assembled, the cooling lines are tested for leaks and the full loaded and tested panels are mounted on the PSS. Two pins for each panel ensure the alignment between the panels and the PSS. The thermal contact between the panels and the PSS is made with thermal grease.

Fig. 2.51: The end-cap pixel disk structure, including service connections.

Table 2.10 compiles the material used in the pixel end disk wheels. All contributions are smeared over the area of a blade, with the overlaps included. With a water based coolant the material budget could be decreased by 0.13%.

Table 2.10: Material budget of end disk blade

Blade components	X/X_0 (overlap included)
Sensors, 250 μm silicon (7 per blade)	0.00316
Readout chips, 180 μm silicon (45 per blade)	0.00199
Bump bonds, indium	0.00003
HDI/pigtails, multi layer cables, Cu on Kapton	0.00411
Components on HDI, silicon-oxide, 105 mm^3 per blade	0.00064
Wire bonds, aluminium, 20 per readout chip	0.00004
Panels, 250 μm carbon fibre (2 per blade)	0.00352
Glue, 50 μm thick, readout chips to panels	0.00033
Total panel	0.01382
Support structure and cooling	
A-frames, 400 μm thick aluminium	0.00316
Conductive grease, 50 μm thick between panels and A-frame	0.00014
Screws to secure panels to A-frame	0.00001
Cooling pipes, 200 μm thick Al walls	0.00258
Coolant (HFE–7100), $X_0 = 23$ cm	0.00373
Total support structure and cooling	0.00962
Total radiation length per wheel	0.02344

2.6.3.3 The space frame

The half-disks are mounted on space frames (see Fig. 2.52). This structure is a light shell made with two skins of carbon sheets (0.3 mm thick) spaced by ribs of annular shape and 0.5 mm thick. The sheets are connected with light, high strength composite material bars along the height of the cylinder. The ribs have holes distributed around the half-circle to allow the passage of the cooling lines, the power cables, and the optical fibres. Structural reinforcements are inserted in the shell where the disks are attached to the space frame and where the space frame is connected

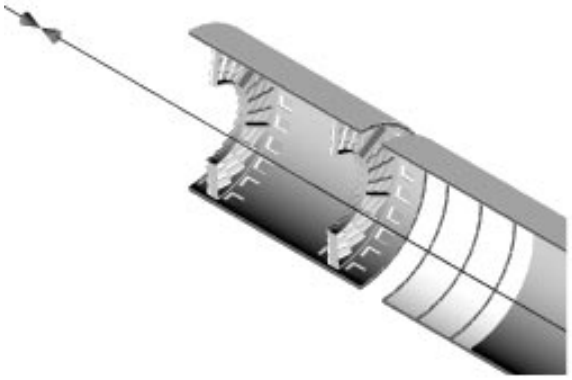

Fig. 2.52: Half-disks mounted in space frame. The service tube is also shown.

to the rails for installation. The skin on the inside has apertures to permit access to the shell's volume, facilitating the insertion of the different lines. A thin sheet of aluminium is glued on the outside of the space frame shell, serving as an electrostatic shield. In addition to the half-disks, the space frame holds the port cards along with the electronics interfacing the front-end chips to the counting room.

2.6.4 Cooling

Present estimates indicate a power consumption per pixel of around 60 μW, including about 3 μW from the sensor leakage current and an equivalent 3 μW per pixel from various signal driver chips sitting on the modules (barrel). For the total of ≈ 39 million pixels this adds up to 2.3 kW (high luminosity version). The power load on the cooling tubes is therefore expected to be about 40 W/m. Additional power will be consumed at other places, e.g. on the pixel system peripheries by control chips and in the service tubes due to the optical drivers and the minimised cross sections of the voltage supply lines. The total power to be removed by the cooling system is estimated to be about 3 kW.

The sensor temperature must be maintained at -10 °C. To cope with expected temperature differences due to thermal resistances and limited heat transfer a coolant inlet temperature of -15 to -20 °C is required. Since the coolant must be supplied through long tubes with the smallest possible radii, a liquid having a low viscosity at this temperature must be found. For safety reasons it is desirable that the coolant be electrically isolating, non-flammable and non-toxic.

The heat transfer liquid HFE-7100 from 3M is a possible candidate having the required properties. However, it has a relatively short radiation length of 23 cm. Because of its poor thermal conductivity, turbulent flow must be used with relatively high flow velocities, producing appreciable pressure drops. To limit this effect the tube diameters and modularities of the various supply tube sections must be carefully chosen, with space limitations and the material budget in mind. For the barrel, the coolant enters at $+z$ and exits at $-z$. Four or five cooling tubes of the barrel cooling frame are combined into one 6 mm inner diameter aluminium tube following an axial path out to $|z| = 3$ m / $r = 0.2$ m. Here two tubes merge into one supply tube of 10 mm inner diameter, leaving (entering) the CMS magnet on a 15 m long path. Eight supply tubes and eight return tubes are needed for the barrel (high-luminosity version). The flow in one barrel cooling circuit will be around 70 cm^3/s.

The following pressure drop Δp and coolant temperature rise ΔT is estimated:

- Barrel supply tube length = 2×15 m, inner diameter = 10 mm, $\Delta p = 550$ mbar.
- Barrel supply tube length = 2×3 m, inner diameter = 6 mm, $\Delta p = 367$ mbar.

– Barrel cooling tube length = 0.55 m, inner cross section = 9 mm^2, Δp = 33 mbar, ΔT = 1.8 °C.

The total pressure drop is below 1 bar. A temperature difference of about 3 °C between coolant and cooling tube due to the limited heat transfer is estimated. Between cooling tube and barrel sensor a temperature drop of about 3 °C is expected.

The coolant for the two disks on each side of the interaction region is supplied and reclaimed from the same z side. A cooling loop similar to the one for the barrel supplies coolant to each set of disks at $+z$ and $-z$. The supply tube feeds at $z = 3$ m into a manifold that distributes the liquid for the two disks through 8 aluminium tubes of 5 mm diameter and 0.2 mm thick wall. A similar system of 8 tubes collect the return flow. Based on measurements of the pressure drop on a single blade we estimate the pressure drop in a loop to be only slightly above 1 bar. The layout of the cooling system on the disk, as well as the routing of the supply lines, strongly influences the amount of material encountered by the particles. A compromise must be found between the minimum tube cross-section and a safe operating pressure.

2.7 Pixel Services and Installation

The insertion scheme for the pixel detectors is strongly affected by maintenance of the beam pipe. In-situ bake-out will be necessary which is not possible with the pixel detectors already installed. The insertion will therefore take place on a rail system installed parallel to the beam pipe after bake-out. On account of the beam pipe suspensions and the increasing diameter of the beam pipe at large distances from the centre of the experiment, the pixel system must be constructed in two halves, separated along a vertical line. In case the pixel system needs maintenance it can be extracted without disconnecting the beam pipe and with the rest of the Tracker untouched. The access time is mainly determined by the time required to open the CMS endcaps.

The closest point of access to the beam pipe region with the endcaps retracted is at $z = \pm 3$ m. Therefore all pixel services (service tubes, see below) attached to barrel and end disks and extending out to $z = \pm 3$ m must be inserted or retracted together with the detectors. This complicates the installation of the pixel barrel since it will have services leaving in both directions, while the end disk systems are confined to a single side. Hence it is planned to first insert the barrel from the $+z$ side, with the service tube for the $-z$ side put at the head of the train, followed by the barrel, with the service tube for the $+z$ side at the end. Afterwards the end disk systems with their service tubes will be installed from both sides.

All services including cooling tubes, power lines, optical fibres etc. will be integrated into light carbon-fibre space frames (service tubes) forming half-cylinders. The barrel service tubes extend from $|z| = 0.3$ m to $|z| = 3$ m and cover a radial width between 18.1 cm and 18.9 cm in order to leave space for the end disk insertion. The end disk service tubes start at $|z| = 0.55$ m with their radial extension limited to 17.9 cm. Cooling tubes and power lines will be grouped in the service tubes in order to remove ohmic heat from the relatively thin aluminium conductors. The first ≈ 30 cm of the service tube close to the pixel detector will be covered with cylindrical PCBs. These will have miniature electrical connectors which receive short thin twisted-pair cables from the pixel system peripheries facing the service tube (see Fig. 2.53). The PCB routes the pixel signals to electro-optical converters with the fibres attached to them. The fibres run along the service tube and leave it, combined into groups of fibres, having at their end multi-fibre optical connectors which are plugged to patch panels located at $|z| = 3$ m / $r = 25$ cm. With this arrangement only electrical connections have to be established between pixel detectors and service tubes, when inserting the pixel system. The fibres are safely integrated into the service tube, leaving it as robust bundles.

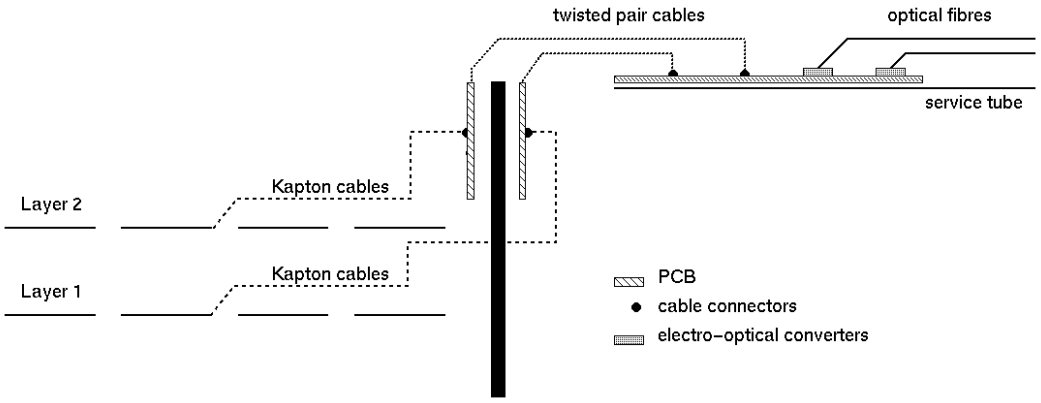

Fig. 2.53: Connection scheme of the pixel barrel. Kapton cables from the modules are plugged into PCBs sitting on the barrel end-flanges. Twisted-pair cables establish the connection to the service tube, where the electro-optical converters are placed

There will be a large number of short connecting services between pixel detectors and service tubes which, although individually flexible, will as an ensemble provide considerable stiffness. Relative radial movements between both attachment ends of these connections must be avoided, and bending angles between pixel system and service tube during insertion must be restricted to a minimum. Figure 2.54 shows the proposed layout of the insertion rails. The outer rails provide a radial movement (in a horizontal plane) of 5 cm between $z = 3.7$ m (where the elements of the train will be sequentially put onto the rails and interconnected) and the end position. This is necessary in order to remain clear from the beam pipe for the most critical case of the low luminosity barrel. At $z = \pm 88$ cm vertical beam pipe suspensions must be passed. Other vertical and horizontal beam pipe suspensions are located around $z = \pm 2.3$ m. The latter suspensions can be reached from outside. During insertion the horizontal parts of this suspension must be temporarily removed. Openings in the service tubes will allow the horizontal suspensions to re-established at the end of the installation.

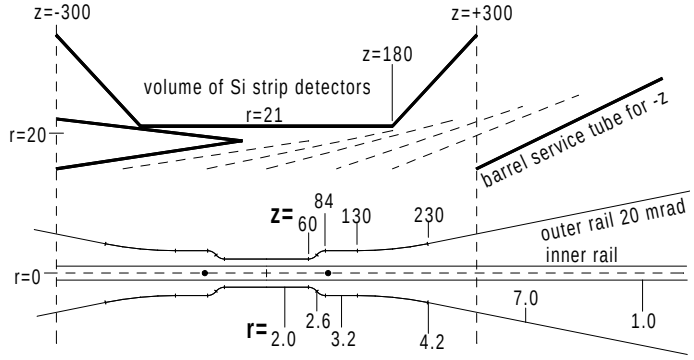

Fig. 2.54: Layout of the proposed rail system for the pixel insertion (top view). The course of the rails is given at various positions in centimetres. The outermost contour of the barrel service tube ($-z$) is shown at different positions. The positions of the innermost vertical beam pipe suspensions are indicated.

In Fig. 2.54 two pairs of rails are shown. The inner straight rails will be used by the very ends of the barrel train, which after insertion will be at $z = \pm 3$ m. This is necessary in order to pass the long stiff barrel service tubes through the available insertion opening. Various positions of the service tube for the $-z$ side during insertion are shown in Fig. 2.54 (horizontal cut). Once in the final position, the barrel service tubes must be rotated outwards by 1.5 degrees in order to give room for the subsequent insertion of the end disks.

Because of this pixel insertion scheme there must be a separating skin between the volume of the pixel system, extending out to $|z| = 3$ m, and the volume housing the silicon strip Tracker. During operation, both volumes must be kept at $-10\,^{\circ}$C. During insertion/retraction of the pixel system, with the silicon strip detector in place and cooled, the power to the silicon strip detector must be switched off, with the cooling system remaining in operation in order to absorb heat entering the silicon strip volume from the open pixel volume. During this time the temperature of the silicon strip detector should be raised to a few degrees centigrade and its volume should be flushed with dry, cold nitrogen in order to avoid condensation humidity.

2.8 Alignment

The pixel system consists of three components (the barrel and two end-disk systems) loosely connected by the same system of insertion rails which also serves as a fixture of the three components. The relative alignment between the subsystems will be achieved by a relatively simple analysis of isolated tracks going through more than one subsystem. Similarly the pixel system will be related to the overall CMS coordinate frame.

The final internal alignment of the pixel subsystems will also be achieved by using tracking data; however, these systems will be measured individually prior to installation using a 3-dimensional survey machine. These survey data serve as starting points to the alignment algorithm which will use isolated tracks. The alignment process must be repeated periodically or after a change in position has been detected. For this the internal alignment system of the Tracker will be used to detect any movements of the detectors.

In the barrel each module will have two cross marks on the visible p-side of the sensor which is very accurately related to the pixel array, due to the double-sided processing of the sensors. With a 3-dimensional survey machine, these marks allow determination of the relative positions of the modules within a half-layer of the barrel. After assembling of two half-layers in a half-barrel, these two layers can be related to each other and to common reference marks on the end-flanges, which will be visible to an external survey system. After the insertion of the pixel barrel, but prior to the insertion of the end disks, the positions of the two half-barrels can be surveyed through a line of sight along the beam pipe, using the reference marks on the end-flanges.

The relative alignment of the two half-barrels can also proceed with the help of event vertices having tracks in both halves. Using an algorithm which optimises the quality of individual vertices in a large number of events simultaneously, the six parameters relating one half-barrel to the other can be determined (vertex constraint method). This method has been successfully used for the internal alignment of the H1 vertex detector.

For the end disks, reference marks, called monuments, are first glued to the panels using a precision gluing jig. A monument is a thin, small piece of silicon with a cross mark engraved on one surface. This fiducial mark can be referenced optically by a microscope as well as mechanically by a touch probe (to a few microns). The next step in the assembly of the panels is the gluing of the sensors with readout chips followed by gluing the HDIs and the Kapton pigtails. All these steps are carried out using Zeiss500 UMM units, which have an accuracy of ≈ 1 μm. During the assembly of the sensors on the panel, the position of the pixels relative to the monuments will be optically measured with high precision by using alignment marks on the p-side of the sensors, which can be related very accurately to the pixels due to the double-sided processing of the sensors. After the panels have been mounted on the panel support structure and the half-wheels have been installed into the space frame, the position of the monuments will be surveyed with a touch probe. These measurements will interconnect three components, the two half-disks relative to each other and each one relative to the space frame. Reference marks on the space frame and on the side of the half-disk visible from large z are located such

that they can be surveyed optically after the units are installed. These fiducial marks have been referenced to the monuments on the blades. After installation these marks allow the forward disks to be related to the rest of the tracking system. In addition, after both space cylinders are installed, the same marks will allow the two visible half-disks to be related to each other. Additional alignment will be done using tracks.

In summary, the final alignment with an accuracy of around 10 μm in all three dimensions will be achieved using alignment algorithms based on tracking data. The survey data will serve as starting points in these algorithms.

2.9 Appendix

2.9.1 Radiation hardness of gallium arsenide

Detectors made of semi-insulating gallium arsenide (GaAs) have been developed and investigated for use as pixel sensors in the CMS experiment. The detectors have been processed with Schottky contacts (Ti/Pt/Au or Ni/Cr/Au). The typical thickness of the GaAs detectors is 250 μm.

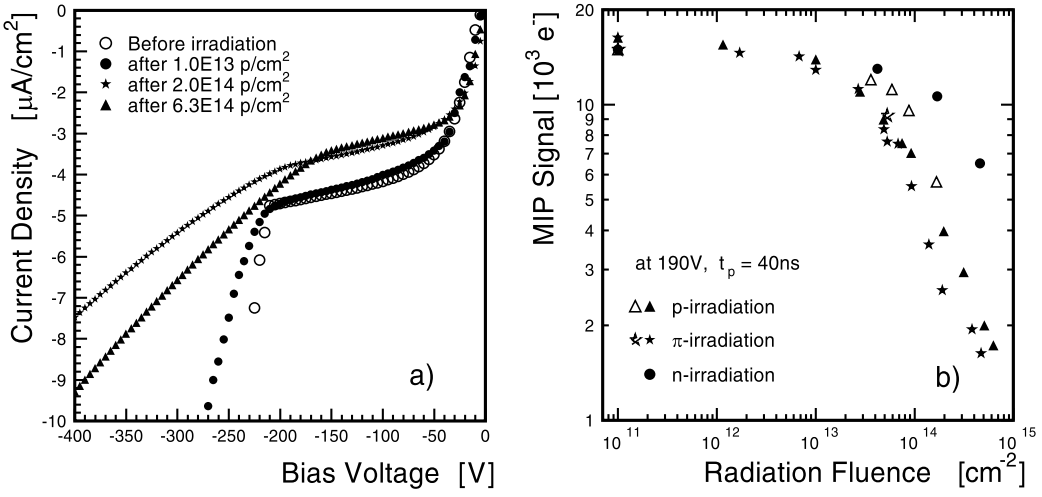

Fig. 2.55: (a) $I-V$ characteristics of GaAs detectors before and after proton irradiation; (b) The most probable signal for MIPs as a function of fluence of different particle species.

To study their radiation hardness, GaAs detectors have been systematically irradiated [2-2] by neutrons (peak energy 1 MeV), protons (23 GeV), pions (191 MeV) and photons (^{60}Co source). Figure 2.55a shows the $I-V$ characteristic curves of GaAs detectors at 20 °C before and after exposure to protons. Before irradiation the detectors show an initial sharp turn-on of the current density followed by a slow increase with increasing voltage up to an eventual breakdown. After irradiation the general form of the $I-V$ curves is similar for all irradiation levels: The current density rises continuously with the voltage, showing a clear increase of the slope at the full activation voltage.

The most probable signal for MIPs, measured at room temperature with a bias voltage of 190 V and a peaking time of 40 ns, is shown in Fig. 2.55b as a function of neutron, proton and pion fluence for detectors made of two different GaAs ingots. For all particle species, the MIP signals show a reduction with increasing fluence. The signal loss is most pronounced for low-energy pions, which will represent the bulk of radiation at the LHC.

2.9.2 Radiation hardness of diamond

The use of diamond as detector material for tracking at low radii has been studied by RD42 since 1994. The material is produced by the diamond manufacturers St. Gobain/Norton and De Beers by chemical vapour deposition (CVD). More details can be found in Ref. [2-3].

Irradiation studies with CVD diamond samples have been carried out at the ISIS spallation source (mainly 10 keV/c and 1 MeV/c neutrons) and at the Paul Scherrer Institute (300 MeV/c positive pions). Up to a fluence of about 5×10^{14} neutrons/cm^2 no degradation of the charge collection distance is observed and only at a fluence of 8×10^{14} neutrons/cm^2 a decrease of about 15% is detected. For the irradiation with pions the samples with a charge collection distance of about 50 μm showed no reduction of the charge collection distance up to a fluence of 1.8×10^{15} pions/cm^2. These results prove the expected radiation hardness for the material tested so far.

Irradiation studies with protons, photons, electrons and alpha particles were also performed. CVD diamond samples with the best charge collection properties have been irradiated up to a fluence of about 1.9×10^{15} pions/cm^2. The measurements are under scrutiny and the preliminary analysis gives further evidence that diamond detectors would survive ten years of operation at the smallest envisaged radii.

Chapter 3

The Silicon Strip Tracker

3.1 Introduction

The Silicon Strip Tracker (SST) is a sub-detector, based on micro-strip silicon devices, instrumenting the intermediate radial region of the Central Tracker of CMS. In combination with the Pixel Detector in the inner part and with an outer Tracker based on Micro-Strip Gas Chambers (MSGCs) the SST aims at performing pattern recognition, track reconstruction and momentum measurement for all tracks above 2 GeV/c transverse momentum originating from high-luminosity interactions at $\sqrt{s} = 14$ TeV. The advantages and the physics potential of the precise tracking performance provided by micro-strip silicon detectors have been extensively demonstrated both by LEP experiments [3-1] and by CDF [3-2]. In CMS we aim at a similarly sophisticated performance on a larger scale of apparatus and in a much more difficult environment. This chapter of the TDR is intended to describe the design, the construction procedure of the SST and its various components. The document is subdivided into nine sections organized as described below.

General overview and requirements are described in Sections 3.2 and 3.3. The technical design of the different elements (silicon sensors, read-out system, DAQ, detector modules and support structures) are covered in Sections 3.4 to 3.7. The alignment system is described in Section 3.8. Section 3.9 summarizes the system prototyping work performed so far.

3.2 Overview and Requirements

3.2.1 Overview

The SST consists of approximately 70 m^2 of instrumented silicon micro-strip detectors. It is composed of a barrel region and two end-cap regions (see Fig. 3.1). The barrel region consists of five cylindrical layers and of six mini-disks. The end-cap regions are each composed of ten disks.

The barrel part instruments the radial region between 22 and 60 cm. All cylindrical layers are equipped with rectangular detectors and provide $r - \phi$ information; in addition layers 1-2 and 5 deliver also small-angle stereo measurements for reconstruction of the z-co-ordinate. The mini-disks are equipped with wedge-shaped detectors and provide a $z - \phi$ and a radial measurement.

In the end-cap tracks are reconstructed in the radial region between 22 and 60 cm. Each of the twenty disks is made out of concentric rings of wedge-shaped detectors. On each side, disks 1 to 6 are fully instrumented with four rings. Disks 7-8 are equipped with three outer rings and disks 9-10 with two outer rings only. Rings 1 and 4 provide double-sided information while rings 2 and 3 are single-sided.

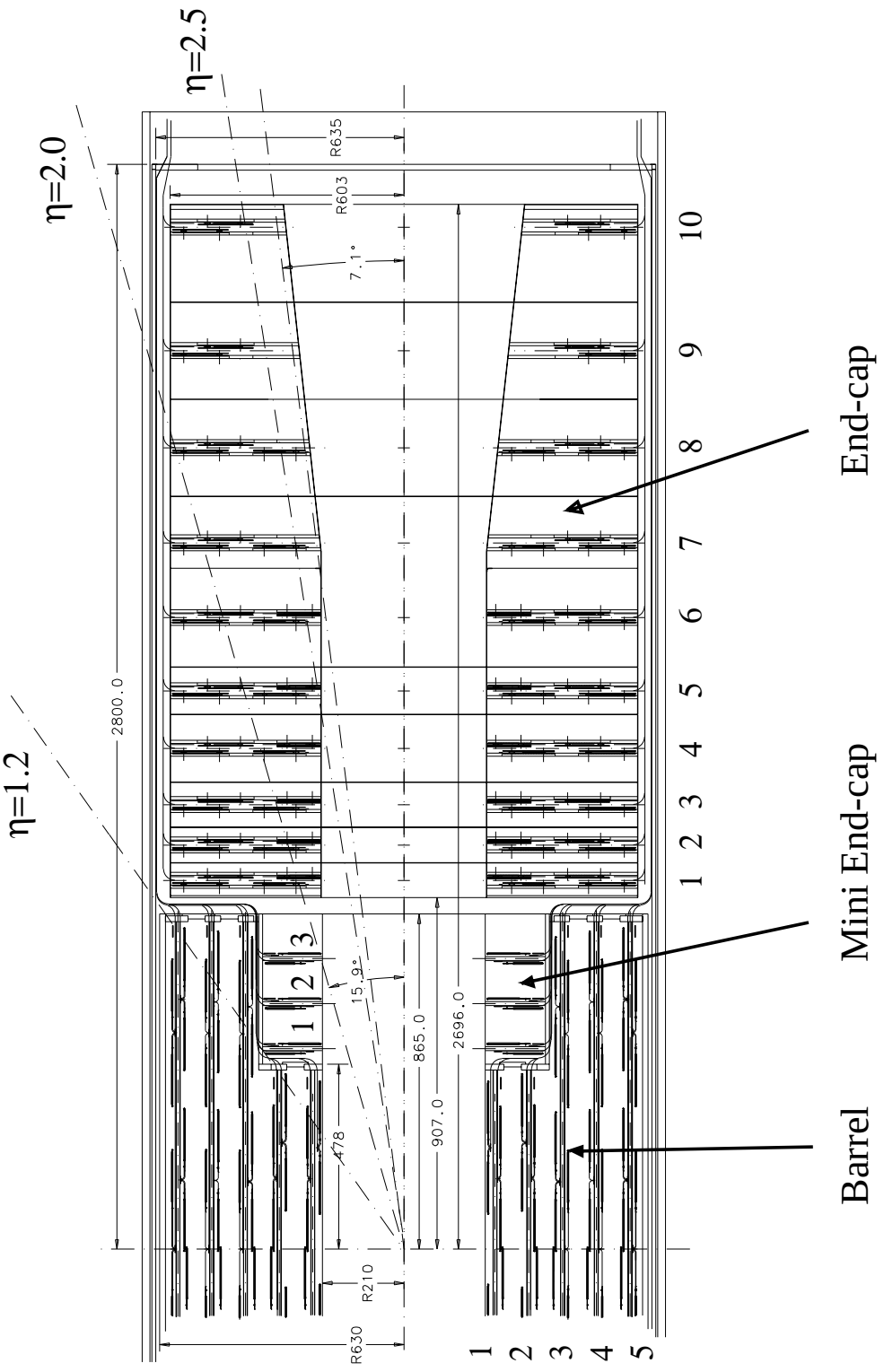

Fig. 3.1: Longitudinal view of the SST.

The SST extends longitudinally for about 5.6 m and covers the pseudo-rapidity region to $|\eta| = 2.5$. Each silicon detector is 300 μm thick and is read out by front-end electronics on a pitch, varying for different layers and disks, between 60 and 270 μm. The silicon sensors are organized in detector modules formed by one or two detectors for an overall strip length between 7 and 12.5 cm. Detectors and on-board electronics are assembled on low mass supporting elements. The detector modules are mounted on very light and stiff supporting structures incorporating cables, cooling system and all other services.

With respect to the Technical Proposal [3-3], the most relevant changes are:

- An extended radial and longitudinal coverage.
- The use of single-sided detectors for the whole system.

These changes, made possible by the excellent results of our R&D programme, yielded a substantial cost reduction by using p^+ on n devices, improved the robustness of pattern recognition and allowed the reconstruction of tracks to be extended down to transverse momenta as low as 1 GeV/c.

We are confident that the proposed layout will provide excellent tracking performance for the CMS detector.

3.2.2 Requirements

The CMS Central Tracker is designed to ensure high quality momentum resolution, precise e/γ separation and excellent isolation of calorimeter showers. In particular, isolated high p_T muons and electrons should be reconstructed with efficiencies greater than 98%, the fake track rate should be lower than 1% and the momentum resolution should be better than $\Delta p_T/p_T = 0.15\ p_T$ (in TeV/c) over the full rapidity range of $|\eta| \leq 2.5$. Once the tracks have been correctly identified, the measurement of the momentum becomes a relatively easy task within the 4 T magnetic field and the large lever arm of the tracking system.

In the case of non-isolated tracks inside jets of transverse energy up to a few hundred GeV, the Central Tracker is required to reach a track finding efficiency of better than 90% for tracks of $p_T \geq 2$ GeV/c and ghosts at the level of 1%. The SST will extend the p_T limit down to values of around 1 GeV/c.

These requirements for the full tracking system translate in the case of the SST as described in the following sections.

3.2.2.1 Pattern recognition and momentum measurement

The SST, in combination with the Pixel Detector and with the outer MSGC Tracker, is a key element for pattern recognition within the tracking system. The approach is based on very high granularity, adequate segmentation in z, high hit efficiency and single-cell occupancy at the level of a per cent.

For the SST these requirements become really stringent since the radial region occupied by the silicon layers is the most congested one due to the combined effect of the very strong magnetic field of CMS and the average p_T of the tracks produced in minimum bias events.

The fast charge collection time of silicon allows single bunch-crossing identification, while in a standard thickness of about 300 μm of silicon the average cluster size, even for tracks at low incidence angle, is small. All this contributes to limit the number of fired channels to a manageable level.

Previous running experience of silicon vertex detectors [3-4] and a lot of test beam data show that with a signal-to-noise ratio around 10:1 it is possible to obtain a single hit efficiency close to 100% (see Section 3.4.6.2).

Extensive simulation work (see Chapter 7) shows that 13 precise hits in the bending plane, typical of each high p_T track in the full tracking system, allows us to perform good pattern recognition. The five precise points provided by the SST in the intermediate radial region allow good efficiency in linking the hits produced by the Pixel Detector in the vertex region and the hits reconstructed by the MSGC Tracker outside.

A single hit resolution of better than 20 μm and a two-track resolution in the inner layers of better than 200 μm are required from the SST to allow an efficient overall pattern recognition. These requirements determine the read-out pitch while a maximum strip length of about 12 cm is necessary to maintain the cell occupancy at the per cent level. The combined effect of the requirements on resolution and segmentation leads to many thousands of detector modules and several million electronic channels.

The need to reconstruct helices in space requires at least eight tracking layers providing space points in the full Tracker. Three double-sided layers will be needed in the SST to link in space the two pixel points with the three space points provided by the MSGC Tracker.

With five layers of silicon we foresee also the possibility of performing track segment reconstruction and momentum measurement within the SST alone. An independent measurement of the momentum, eventually extended to the pixel points, may be used to match the track segment reconstructed in the less congested region of the outer MSGC Tracker. This handle can be used as an additional powerful tool to reduce further ambiguities and resolve ghosts in congested events.

In addition, this option will allow internal alignment and facilitate the alignment among the different sub-detectors of the Central Tracker.

3.2.2.2 Tracking efficiency and vertex capability

The ability to reconstruct the vertex of a hard collision and to distinguish it from the additional vertices produced by multiple interactions in the same bunch crossing is a key element for the physics programme of CMS. The major role in this exercise is played by the combined use of the Pixel Detector and of the SST.

The presence of b-hadrons can be tagged with reasonable efficiency by displaced vertices produced in their weak decays. Impact parameter measurements play an essential role in B-physics and in tagging b-jets in high p_T events. The system of pixel and micro-strip silicon detectors may provide vertexing capability in both co-ordinates not only to distinguish among different interaction vertices at full luminosity but also to provide a precise measurement of the impact parameter of tracks in both co-ordinates and over a large range of momenta. We aim at 3D vertex reconstruction, at a tagging efficiency for b-jets above 20% with a mistag probability below 1%. Further constraints come from the requirement of K^0 reconstruction at low luminosity with good mass resolution. For tracks with $p_T > 10$ GeV/c we require an impact parameter resolution in the transverse plane better than 40 μm over the full η-region while the corresponding impact parameter resolution in the r–z plane is required to be better than 100 μm in the central region.

These requirements on vertexing demand the accuracy for the z measurements provided by the silicon layers to be better than 500 μm.

3.2.2.3 Lifetime

The lifetime of the Silicon Strip Tracker is required to be 10 years of LHC running. Given standard LHC operating conditions and taking into account a low luminosity start-up phase [see Appendix A], an integrated luminosity of 5×10^5 pb^{-1} is expected over ten years of operation corresponding to 5×10^7 seconds of running at the LHC peak luminosity of 10^{34} cm^{-2}s^{-1}.

3.3 Experimental Constraints and Layout

3.3.1 Experimental constraints

Several experimental constraints must be taken into account in the definition of the design. The most relevant ones are the radiation environment, the limits on the material budget, and the size and complexity of the system.

3.3.1.1 The radiation environment

The most critical issue of the SST is the long-term survival after heavy irradiation. The system must be designed to guarantee stable operating conditions for several years of running at the highest luminosity.

The levels of radiation due to primary interactions will be very high around the collision region. In addition, a high flux of neutrons will be present in the tracking volume due to backscattering of neutrons evaporated from nuclear interactions in the material of the electromagnetic calorimeter.

In 10 years of LHC running the most irradiated detector of the SST will be subject to an average fluence of 1.6×10^{14} 1-MeV-equivalent neutrons per cm^2.

This value is considered as design value for the radiation resistance of the full system. In addition we consider a safety factor of 1.5 to take into account unexpected higher fluxes or uncertainties in the damage constants (see Section 3.4).

The design of the micro-strip devices for the SST will be based on the use of single-sided p^+ segmented implants in an initially n-type bulk silicon [3-5]. This option implies the coupling of two single-sided detectors back-to-back to equip the double-sided layers. Since p^+ on n detectors are the simplest devices that can be manufactured, they offer a great advantage in terms of both cost and industrial production capacity. This choice does, however, present a significant challenge in that, after the type-inversion of the bulk induced by radiation, the detectors must be substantially over-depleted in order to maintain satisfactory performance. Since the expected depletion voltage after type-inversion increases rapidly as a function of the fluence, the single detector elements and the system as a whole must be designed to allow for high voltage operation of the silicon devices.

To survive the high radiation environment of the LHC, the silicon wafers will need to be kept cold. The silicon operating temperature becomes increasingly important as the effect of the radiation becomes more pronounced. The entire volume of the SST will be permanently kept at -10 °C during running and only for limited periods of time will it be allowed to reach temperatures above 0 °C for maintenance purposes.

3.3.1.2 Low mass and high mechanical stability

The amount of material within the Tracker volume will affect the Tracker performance in various ways, i.e. multiple scattering, delta rays, photon conversions and strong interactions. Even more critical is the effect of the Tracker material on the ECAL performance. Strong emphasis has been put in the CMS design to allow efficient reconstruction of the $H \to \gamma\gamma$ decay mode. This places stringent requirements on the performance of ECAL, which in turn seriously constrains the material of the Tracker. It leads to a design goal of 40% of a radiation length for the SST over the full η range.

On the other hand, in order to maintain the tracking performance achievable with micro-strip devices, the modules and their supporting structures must be sufficiently stiff to ensure manageable and well-controlled distortions under the various conditions foreseen.

3.3.1.3 Size and complexity

The size and complexity of the system are such that an easy assembly and disassembly procedure of the detector as a whole and of the individual modules should be envisaged. High modularity is foreseen to guarantee a manageable construction procedure with the entire system made out of several independent subsystems which may be independently assembled, surveyed and tested. A realistic disassembly procedure is needed to allow maintenance of the system in between running periods in case of need. Simple operations should allow the metrology of the detector elements and of the system as a whole. Furthermore the layout should be such as to accommodate naturally all required services, allowing sufficient latitude for the uncertainties still surrounding them.

3.3.2 Design choices

3.3.2.1 Detectors

The choice of AC coupled, poly-biased, single-sided p^+ on n-bulk devices as baseline sensors allows very high voltage operation, achievable in simplified technologies [3-6]. The radiation resistance of these devices has been proven to be above the expected fluence in CMS. They are relatively simple and low cost devices since their production is compatible with standard micro-electronics technology. For the same reason they can be produced in large quantities with high yield by several manufacturers.

For the double-sided layers we plan to use two single-sided back-to-back sensors, one of which will have small angle stereo strips. To avoid dead regions the use of double metal connections is envisaged. This choice simplifies high voltage operation since the electronics can be operated without an offset ground which is necessary when truly double-sided devices are used. Radiation resistant double-sided devices have also been produced and tested within our R&D activities but they are intrinsically more expensive because of the special handling they require during production and because of yield problems. Furthermore, the need to use a floating ground for the electronics introduces severe problems at the system level. The n^+ on n-bulk devices, although interesting, do not seem to offer definite advantages in our system. They are more expensive than truly single-sided devices since their technology is not compatible with the standard production lines because of the pattern needed on the front side. Finally, optimization of the performance of these devices in the 4 T field of CMS would be highly problematic due to the higher Lorentz angle of the electrons.

3.3.2.2 Read-out electronics

We have chosen a fully analog architecture based on a fast amplifier followed by an analog pipeline and a deconvolution circuit. The analog read-out allows efficient common mode noise subtraction. In addition, it allows better control of the behaviour of the detectors, giving us a powerful tool for understanding and following the change of the system performance induced by irradiation. Diagnostics of faults will be easier and fine tuning of the on-line and off-line thresholds will be possible to obtain the best performance for different running conditions in different layers. Multi-layer aluminized Kapton hybrids will be used to reduce the overall material budget.

High speed optical links, based on laser technology, will feature radiation hardness, small size, low power dissipation and high analog transmission quality. The use of a system very much in line with the current and emerging telecommunication standards will allow us to benefit from technology improvements, multiple source availability and cost reductions expected in the coming years.

A fully parallel power supply scheme is chosen. Aluminum conductors on thin Kapton ribbons will be used as cables within the tracking volume to minimize the impact of the power cables on the material budget. High voltage lines will independently supply the bias voltage of each module.

3.3.2.3 Modules

Simple module design allows mass production in several independent centers with an efficient use of equipment and manpower distributed in various institutions. With 12.5 cm as maximum strip length both for the barrel and end-cap modules we expect to have a signal-to-noise ratio of 12:1 on average at the end of the detector lifetime (10 years of LHC running).

By assembling a few hundred modules into independent sub-units (disks or half-cylinders), one can organize parallel assembly and test lines of the different parts of the final system with advantages in terms of time and reliability.

3.3.2.4 Mechanical structure

Low mass supporting structures are foreseen. The mechanics will incorporate the cooling system, cables and optical links and all other services (alignment, monitoring and survey systems). High performance carbon fiber composites are foreseen as the basic material of the mechanical structure. Since a temperature variation of about 40 °C is expected between the assembly and running temperature of the most critical parts the structure will be fabricated with the constraint of having a thermal expansion coefficient (CTE) close to zero. Symmetric structures will be used for all mechanical elements incorporating materials with CTE different from zero (i.e. the detector modules) to avoid bi-metallic effects. The adhesives will be selected in such a way that mechanical stress is released in them.

Low cost fabrication procedures have been selected. Easy assembly and disassembly procedures for the different sub-units will be possible.

3.3.2.5 Cooling

The operating temperature of the SST will be −10 °C. The cooling system will be based on fluids used to cool by direct conduction all elements producing power (electronics, optical links and service cards; cables and silicon detectors) and on cold dry nitrogen circulated through the system. A thermal shield will isolate the volume occupied by SST and pixel detectors from the volume of the MSGC running at +18 °C. Small, thin walled metal pipes will be used for the cooling system.

3.3.2.6 Alignment and mechanical stability

The final position of each detector strip in space will be determined by using tracks. Survey data will be used to constrain the initial information on position to speed up the iterative procedure. A monitoring system will be used to control the stability of the detector with time.

The individual detector modules will be fabricated with an internal precision of 5 μm in the detector plane and of about 30 μm in the co-ordinate perpendicular to the plane. The mechanical structure will allow a survey procedure during the assembly of the modules to know the absolute initial position of each strip in space with an accuracy better than 10 μm. Maximum displacements from the nominal positions due to the combined effects of machining precisions, gravity and thermal deformations will be kept below 100 μm. Stability with time under stable operating conditions will be at the level of 10 μm.

3.3.3 Layout

3.3.3.1 The barrel detector

The barrel system contains five equally spaced cylindrical layers instrumenting the radial region between $r_{min} = 210$ mm and $r_{max} = 635$ mm (see Fig. 3.2). The length of the entire system is 1730 mm. The last active element of layers 3, 4 and 5 is positioned at $|z| = 822$ mm while the first two cylindrical layers end at $|z| = 446$ mm. All cylindrical layers contain modules based on rectangular detectors. The average radius of the first active element is 235 mm while 583 mm is the average radius of the outermost active layer. Layers 1, 2 and 5 are double-sided; layers 3 and 4 are single-sided.

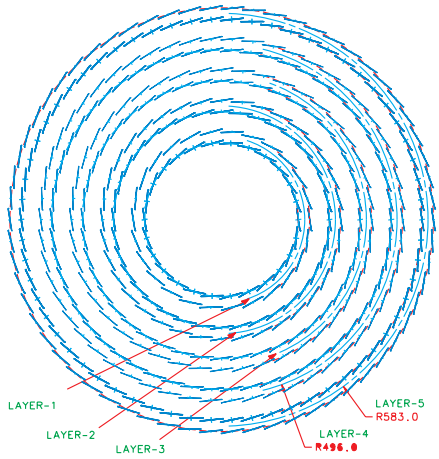

Fig. 3.2: Transverse view of the silicon barrel detector.

A mini end-cap is included in the barrel system: three small disks on each side complement the first two barrel layers with wedge shaped detectors. The use of this geometry reduces the number of detector modules while optimizing the detector performance for very inclined tracks.

Tracks at $|\eta| < 1.2$ are fully contained in the barrel detector and cross only cylindrical layers. For $|\eta| > 1.2$ tracks cross both the cylindrical layers and the mini end-cap disks. The pseudo-rapidity coverage of the last disk of the mini end-cap extends to $|\eta| = 2$.

Two (four) detectors per module are used in all cylindrical single-sided (double-sided) layers. The dimensions of the silicon detectors are 64×64 mm^2, the active area being 62.5×62.5 mm^2. Table 3.1 lists the pitch-size and the number of channels per module in each layer. The strips in the stereo view are tilted by 100 mrad with respect to the beam line, thus allowing a measurement of the z-co-ordinate.

The detectors are tilted by 9° to compensate for the Lorentz angle and are arranged to allow ϕ and z overlap to avoid dead regions. The 0.6 mm overlap in z also takes into account the spread of the primary vertex. No dead region is allowed in each layer apart from the 1.7 mm wide z region in the middle of each detector module. The acceptance of each detector layer is listed in Table 3.2 (due to the overlap, acceptance numbers $> 100\%$ are listed).

To allow for an easy assembly and disassembly procedure the detector modules are positioned on both sides of each supporting cylindrical element. This option frees space for handling and connections while keeping the full coverage. Positioning pins are incorporated in the structure which also houses cables, optical links, optical fibers and control and service cards. Optical links are located in the empty space between two detector modules for optimal matching of the modularity of the read-out channels and the optical system. Control cards are positioned for each layer close to the end flanges. All these elements, and in particular all of them dissipating

power, are in good thermal contact with the cooling pipes incorporated in the structure itself. Cooling ledges made out of very high conductivity carbon fiber are inserted to house and cool down the most critical elements (electronics, detectors, optical links).

Table 3.1: Read-out pitch and number of channels per module in the barrel detector

layer #	r-ϕ read-out pitch [μm]	# of channels per module	stereo read-out pitch [μm]	# of channels per module
1	61	1024	122	512
2	81	768	122	512
3	81	768	–	–
4	122	512	–	–
5	122	512	244	256

Table 3.2: Radial positions and relevant numbers of the barrel detectors

	layer 1	layer 2	layer 3	layer 4	layer 5	total
r_{in} [mm]	217	304.5	391.5	479	566	
r_{out} [mm]	249	336.5	423.5	511	598	
$N_{mod}(\phi)$	26 + 26	36 + 36	44 + 44	54 + 54	62 + 62	
$N_{mod}(z)$	4 + 4	4 + 4	8 + 6	8 + 6	8 + 6	
N_{mod}	208 (d.s.)	288 (d.s.)	616 (s.s.)	756 (s.s.)	868 (d.s.)	1364 (d.s.) 1372 (s.s.)
N_{waf}/mod	4	4	2	2	4	
N_{waf}	416 (ax.) 416 (ster.)	576 (ax.) 576 (ster.)	1232 (ax.) –	1512 (ax.) –	1736 (ax.) 1736 (ster.)	5472 (ax.) 2728 (ster.)
$N_{chip}(\phi)$/mod	8	6	6	4	4	
$N_{chip}(\phi)$/tot	1664	1728	3696	3024	3472	13584
$N_{chip}(z)$/mod	4	4	–	–	2	
$N_{chip}(z)$	832	1152	–	–	1736	3720
$N_{chann}(\phi)$	212608	221184	473088	387072	444416	1738368
$N_{chann}(z)$	106496	147456	–	–	222208	476160
acc.(in-r)(ϕ)[%]	116	115	110	110	107	
acc.(out-r)(ϕ)[%]	101	104	101	103	101	
z-overl. [mm]	0.6	0.6	0.6	0.6	0.6	

Cables, optical fibers and cooling pipes run parallel to the supporting cylinders until they reach the end-flanges where they are brought to the outermost radius. From there they run parallel to the beam line along the external supporting cylinder to the outer flange of the SST around $|z| = 2.8$ m.

To maintain a high level of modularity each cylindrical layer is made as two independent parts (half-cylinders) which may be independently assembled, surveyed and tested before being rigidly connected together for the final survey and for the test operation of each layer. The system as a whole is built by assembling together first the two inner layers with the mini end-cap and then the three external layers.

The number of modules, detectors and electronic channels of each layer is listed in Tables 3.2 and 3.3 together with the most relevant information on the geometry of the system.

A total of 1372 single-sided and 1364 double-sided modules will be used to equip the cylindrical layers of the barrel detector. Eight thousand two hundred silicon detectors will be needed (5472 with axial strips and 2728 with stereo strips and double-metal connections). In total, an area of 33.59 m^2 of silicon sensors and 2 214 528 analog channels have to be produced.

Table 3.3: Longitudinal positions of the detector edges in the barrel detector

Layer number	z-position 1 [mm]	z-position 2 [mm]	z-position 3 [mm]	z-position 4 [mm]	z-position 5 [mm]	z-position 6 [mm]	z-position 7 [mm]
1	−2.00	94.17	232.45	301.97			
2	−2.00	101.90	241.00	321.12			
3	−2.00	123.79	222.43	369.05	448.62	613.94	678.46
4	−2.00	125.59	228.79	371.31	458.66	616.06	689.79
5	−2.00	125.34	231.86	372.00	464.93	617.84	697.22

Mini end-cap

The layout of one disk of the mini end-cap detector is shown in Fig. 3.3. Each disk is an independent unit containing two rings of detectors housing 36 modules each. Ring 1 covers the radial region between $r = 218$ mm and $r = 285$ mm, ring 2 between $r = 285$ mm and $r = 354$ mm. The sensitive area of adjacent detectors overlaps, with criteria similar to the ones used in the cylindrical layers.

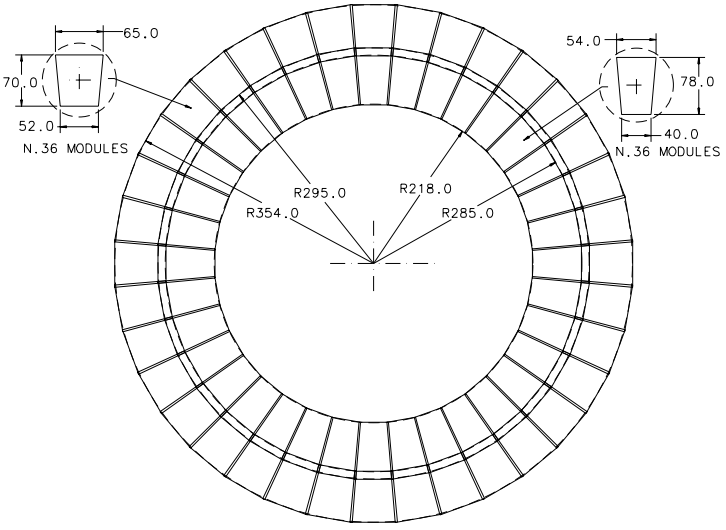

Fig. 3.3: Radial coverage of the mini end-caps.

In each disk the two rings of detectors are positioned on the two sides of the supporting structure. This allows free space for the optical links, services and connections. The supporting structures are held in place by a cylindrical element connected to the two inner layers. Cables, optical fibers and services run radially along the disks up to the cylindrical structure where they join the services of the two inner layers to reach the barrel end flanges.

The basic detector element of the mini-disks is a pair of wedge-shaped detectors, coupled back-to-back. In the front device, radial strips point to the beam line (ϕ-view). In the device on the back, the strips are tilted by 100 mrad (stereo-view), thus pointing to a point on a concentric ring around the beam line (see Fig. 3.4). This point moves on the concentric ring when moving from module to module.

The most important parameters of the mini end-cap detectors are listed in Tables 3.4 and 3.5.

The 6 disks of the mini end-cap contain 864 silicon detectors (432 with radial strips and the other half with stereo strips and double-metal connections) resulting in a total area of 1.7 m^2 and 552 960 analog channels.

The grand total for the barrel detector amounts to 9928 silicon sensors (36 m^2) and 2 767 488 electronic channels.

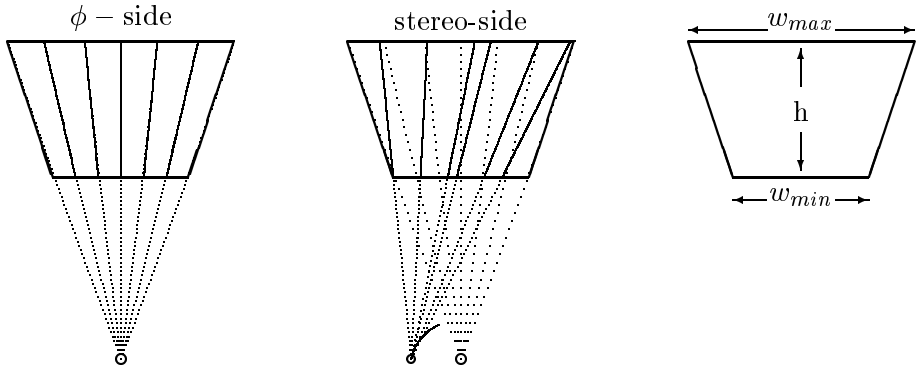

Fig. 3.4: The layout of the strips on the wedge-shaped detector, ϕ-side and stereo-side. Definition of the dimensions of the wedge-shaped detectors.

Table 3.4: Dimensions and channel numbers of the detectors in the barrel mini end-caps

ring #	w_{min} [mm]	w_{max} [mm]	h [mm]	ϕ average pitch [μm]	# of channels per module radial view	stereo average pitch [μm]	# of channels per module stereo view
1	40.4	54.3	78.2	60	768	89	512
2	52.4	64.9	70.2	74	768	111	512

Table 3.5: Radial positions and relevant numbers of the barrel mini end-cap detectors

	disk ± 1	disk ± 2	disk ± 3	total
r_{in} [mm]	218	218	218	
r_{out} [mm]	354	354	354	
z-position [mm]	± 518	± 634	± 750	
N_{mod}	72	72	72	432
N_{waf}/mod	2	2	2	
N_{waf}/tot	144	144	144	864 (432 ϕ), (432 stereo)
$N_{chip}(\phi)$/mod	6	6	6	
$N_{chip}(\phi)$/tot	432	432	432	2592
N_{chip}(stereo)/mod	4	4	4	
N_{chip}(stereo)/tot	288	288	288	1728
$N_{chann}(\phi)$	55296	55296	55296	331776
N_{chann}(stereo)	36864	36864	36864	221184

3.3.3.2 The end-cap detector

The end-cap detector complements the barrel detector at both ends with detector planes perpendicular to the beam. Each end-cap consists of 10 disks occupying the radial region 210 mm $< r <$ 635 mm (see Fig. 3.5). The z positions of the disks have been adjusted to obtain full coverage and to optimize the track reconstruction performance over the pseudo-rapidity region $1.2 \leq |\eta| \leq 2.5$. Beyond $|\eta| \approx 2.5$ the radiation level and the track density become too high to operate silicon micro-strip detectors reliably. This implies that the inner radius of the active detector area on the disks has to increase with increasing z-position of the disk. Therefore three different types of disks will be installed on which the active area will start at $r = 218$ mm, $r = 285$ mm and $r = 390$ mm respectively (see Table 3.6 and Fig. 3.6). On all disks the active area extends up to $r = 608$ mm. This leaves enough space for cables and services of both the barrel and the end-cap detector to be routed along the outer radius of the end-cap detector to the end-flange of the SST at $|z| = 2.7$ m.

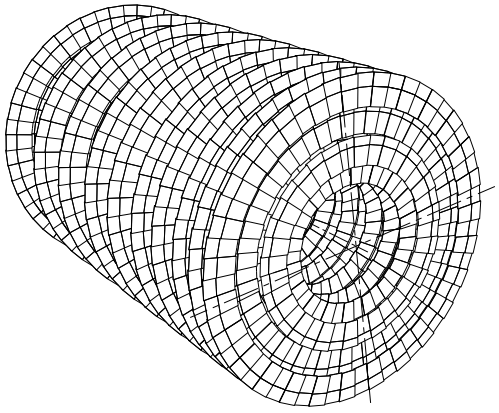

Fig. 3.5: Perspective view of one side of the end-cap detector.

Table 3.6: Description of the three types of disks in the end-cap Tracker

disk type	number of disks	z-position [mm]	radial acceptance [mm]	ring types
A	2×6	$\pm 952, \pm 1042 \pm 1147,$ $\pm 1293, \pm 1441, \pm 1630$	218–608	1–4
B	2×2	$\pm 1823, \pm 2068$	285–608	2–4
C	2×2	$\pm 2319, \pm 2638$	390–608	3–4

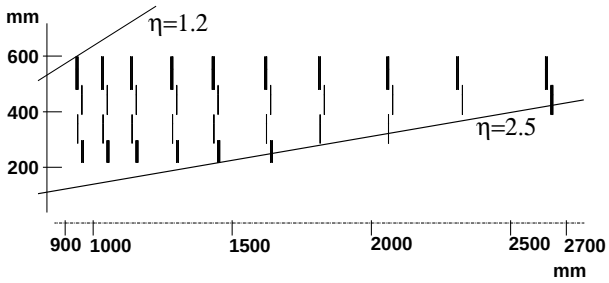

Fig. 3.6: Side view of one quarter of the end-cap detector.

Each disk carries up to four rings of wedge-shaped detector modules. They are mounted alternately on the two sub-disks, of which each disk is composed. In this way they overlap in r. Within each ring the detector modules are mounted alternately on both sides of a pair of support rings, which allows overlap in ϕ. Each of these support rings houses two cooling pipes which will be operated with a liquid in counter flow. This ensures effective and uniform cooling of both the electronics and the detectors.

The detector modules are made of wedge-shaped silicon detectors which are glued on a U-shaped carbon fiber frame that also carries the front-end hybrid. Each module contains two (one for the innermost ring) silicon detectors with radial strips to measure the ϕ position of a hit. The modules of rings 1 and 4 are complemented with a second set of silicon detectors in stereo geometry which is attached on the back side of the module and allows a measurement of both r and ϕ with these modules. Table 3.7 summarizes the layout of the silicon detectors used in each ring. On the outermost disk, ring 3 is also equipped with $r\phi$-modules (the mean stereo-side pitch being 206 μm), which increases the number of chips in this ring to 324.

Table 3.7: Description of the rings of detector modules on the end-cap Tracker disks

ring	type	radial acceptance [mm]	number of modules	mean pitch ϕ-side [μm]	mean pitch stereo-side [μm]	number of chips
1	$r\phi$	218–295	36	60	89	360
2	ϕ	285–386	36	78		216
3	ϕ	390–499	54	103		216
4	$r\phi$	484–608	54	127	254	324

The structure of each sub-disk incorporates cables, electronics, optical links and cooling pipes necessary to operate the detectors it carries. Therefore, the sub-disks can be assembled and tested independently. This provides a high degree of modularity and easy (dis)mounting of the detector modules which can all be accessed directly without any modification of the services.

In summary, the silicon end-cap Tracker consists of 3168 detector modules (1548 ϕ-type and 1620 stereo-type) carrying 8712 silicon detectors with a total surface of 32.03 m^2. The total number of read-out channels is 2 405 376.

3.4 The Silicon Detectors

3.4.1 Radiation resistance

The survival of silicon detectors in the LHC radiation environment depends strongly on careful detector design and wise choice of the material. The design value for the radiation resistance of the system is set by the flux of neutral and charged particles received by the innermost barrel layer. Already mentioned in Section 3.3 a total fluence of 1.6×10^{14} cm^{-2} 1-MeV neutrons is the prediction at this radius. Broadly speaking, the radiation damage suffered by the detectors can be divided into two classes: effects which are due to surface damage and those which are due to bulk damage. As will be shown in the following sections, the effects of bulk damage are considered to be the greatest source of concern and it is here that every effort must be made to guarantee reliable performance for the lifetime of the experiment.

3.4.1.1 Surface damage

Surface damage occurs when the holes produced by ionizing radiation in the surface oxide layer either become trapped in the oxide or interact with atoms at the silicon-oxide interface to form

interface states. Fixed positive charge in the oxide layer modifies the oxide field, while interface states give rise to new energy levels in the forbidden gap which can modify device behavior. These changes can lead to a decrease in inter-strip isolation, causing unwanted signal charge sharing, and an increase in inter-strip capacitance, which is a major factor in determining the electronic noise of the system.

However, it has been demonstrated that a careful choice of fabrication technology and geometry can minimize the changes in device behavior to an acceptable level. The capacitive coupling between each strip and its neighbors is dominated by the quality of the oxide at the interface (which is process-dependent) and by the ratio of strip width to strip pitch. After irradiation, the value of the coupling can be increased by as much as a factor of ~ 3, when the trapped charge in the oxide saturates. It is possible to reduce the damage-induced coupling by substantially over-depleting the device. This produces high fields on the strip side and confines the oxide charge in the region between the strips, thus reducing the capacitance. Hence a technology which allows high voltage operation of irradiated devices will keep the impact of these changes on system performance under control.

The use of AC coupling is not believed to present any particular problems with regard to radiation damage. Poly-silicon bias resistors have been shown to be relatively insensitive to ionizing radiation [3-6], while the use of high quality dielectric layers for the coupling capacitors should guarantee stable operation for the duration of the experiment.

3.4.1.2 Bulk damage

Leakage current

The bulk leakage current in detectors is described in terms of the quantity J_v, which is the leakage current per unit volume. It is well established [3-7] that the increase in J_v during irradiation is directly proportional to received fluence:

$$\Delta J_v \;=\; \alpha\ \Phi \tag{3.1}$$

where the proportionality constant, α, is known as the 'damage constant'.

The bulk current exhibits temperature-dependent annealing effects which must be taken into account. The usual quantity for measuring the leakage current increase is α_∞, the value of α after all annealing has ceased. At room temperature, α_∞ is achieved ~ 20 days after the end of the irradiation. At the projected operating temperature (-10 °C), the current will fall to α_∞ within three years. The annealing effect will be considered in the following.

The current itself is strongly dependent on temperature. The data are found to fit the form:

$$I \propto T^2\ \exp\left(\frac{-E_a}{k\ T}\right) \tag{3.2}$$

The average value of E_a from the various measurements taken [3-8, 3-9, 3-10] is (0.62 ± 0.03) eV. The value of α_∞ for irradiation with 1 MeV neutrons at 20 °C is (2.9 ± 0.2) $\times$ 10^{-17} $A\mathrm{cm}^{-1}$ [3-11]. At -10 °C, α_∞ falls to $(1.4 \pm 0.2) \times 10^{-18}$ A cm^{-1}. Hence, for the innermost micro-strip layer in the barrel region, a current density of $\sim 6\mu A/\mathrm{cm}^2$ is expected after 10 years of operation (see Fig. 3.8).

We have chosen AC coupling between strips and amplifiers which avoids baseline shifts in the amplifier. The fast shaping time of the front-end amplifiers (50 ns or less, with deconvolution) minimizes the noise contribution of the leakage current.

It should be noted that, with heavily irradiated silicon detectors, one must take into account the possibility of thermal runaway. This is reflected in the requirements imposed on the mechanical structure and cooling system discussed in Section 3.7.

Charge collection efficiency

The signal-to-noise ratio is also affected by decrease in charge collection efficiency, which are caused by the trapping of charge carriers at radiation-induced defects in the silicon bulk. It has been shown by several groups that the resulting signal loss is moderate and has a value of $< 10\%$ after a fluence of 1×10^{14} n cm^{-2} (see, for example, Ref. [3-12]). Recent results [3-13] demonstrate that $\sim 40\%$ of the signal remains after 1×10^{15} n cm^{-2}. On the basis of the references quoted there, it is estimated that the ballistic deficit suffered by the innermost microstrip layers — for an effective shaping time of 25 ns — will not exceed 15%, which is considered tolerable.

Effective doping concentration

The depletion voltage of a silicon detector depends upon the effective doping concentration of the substrate material:

$$V_{depl} = \frac{e\ d^2}{2\ \varepsilon_{Si}}\ N_{eff} \tag{3.3}$$

where d is the depth of the diode. The value of N_{eff} is determined by the concentration of space charge in the depletion region. In an un-irradiated device, the space charge arises predominantly from the phosphorus dopant.

Irradiation results in an accumulation of negative space charge in the depletion region due to the introduction of acceptor defects which have energy levels deep within the forbidden gap. n-type detectors therefore become progressively less n- type with increasing hadron fluence until they invert to effectively p-type and then continue to become more p-type beyond this point, apparently without limit [3-7, 3-14, 3-8]. The inversion fluence, Φ_{inv}, depends strongly on the initial resistivity of the substrate material and has been parametrized for 24 GeV protons as [3-15],[3-16]:

$$\Phi_{inv} \approx (18.0\ \pm\ 0.6)\ N_{eff0} \tag{3.4}$$

Detectors still work beyond the inversion fluence as the junction moves from the p^+ strips to the n^+ back-plane contact. At high fluences, however, N_{eff} can be such that the depletion voltage exceeds the breakdown voltage of the device and efficient operation is no longer possible.

In the period after irradiation, the annealing behavior of N_{eff} displays two distinct phases. There is an initial reduction in negative space charge (beneficial annealing), which is later dominated by a slower, but much larger, increase in acceptor concentration [3-7, 3-14, 3-17]. This second phase is known as 'reverse annealing'. The rate at which reverse annealing proceeds is highly temperature dependent; the changes, up to saturation, can take many years at -10 °C but are accelerated to a matter of weeks at room temperature. Consequently, reverse annealing imposes strict limits on the operation temperature of the SST and requires that maintenance and warm-up periods be kept to a minimum.

It follows that the changes in N_{eff} can be written as the sum of three components:

$$\Delta\ N_{eff}\ =\ N_{eff0}\ - N_{eff}\ =\ N_a + N_c + N_Y \tag{3.5}$$

where

$$N_a = g_a\ \Phi\ \exp\left(-k_a\ t\right) \tag{3.6}$$

corresponds to the beneficial annealing,

$$N_c = N_{c0}\ (1\ -\ \exp\left(-c\ \Phi\right))\ +\ g_c\ \Phi \tag{3.7}$$

to the stable damage and

$$N_Y = g_Y \ \Phi \ (1 - (1 + k_{Y1} t)^{-1}) \tag{3.8}$$

to the reverse annealing. The most recent and accurate parametrization of these three terms has been carried out by Feick et al. [3-18]. The parameter values are shown in Table 3.8.

The predicted evolution of V_{depl} with time is shown in Fig. 3.7.

Table 3.8: Measured values of the relevant parameters for bulk damage

Parameter	Value or expression
N_{c0}	$(0.3 \times \ N_{eff0}) + 10^{11}$ cm^{-3}
N_{eff0}	1×10^{12} cm^{-3}($\rho = 4$ $k\Omega$cm); 4×10^{12} cm^{-3}($\rho = 1$ $k\Omega$cm)
c	2×10^{-13} cm^2
g_c	1.77×10^{-2} cm^{-1}
g_Y	4.6×10^{-2} cm^{-1}
g_a	1.54×10^{-2} cm^{-1}
k_a	$k_{a0}\ exp(-E_{aa}/k\ T)$
k_{a0}	2.3×10^{13} s^{-1}
E_{aa}	1.08 eV
k_{Y1}	$k_{Y10}\ exp(-E_{aY}/k\ T)$
k_{Y10}	8.74×10^{14} s^{-1}
E_{aY}	1.31 eV

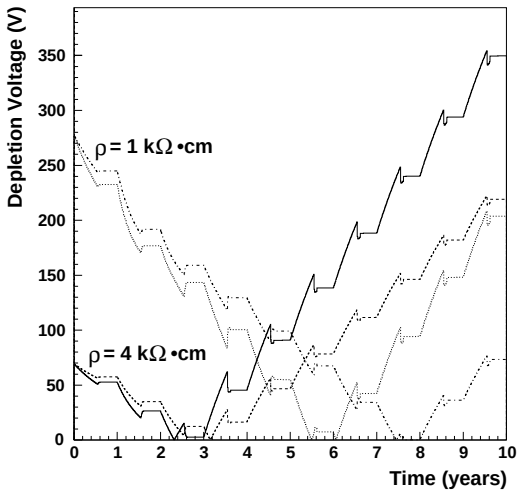

Fig. 3.7: Predicted evolution of V_{dep} with time for barrel layer 1 for two different initial resistivities. The worst-case scenario of a total fluence of 2.4×10^{14} n/cm^2 is also shown for each initial resistivity.

A conservative scenario comprising running operation at -10 °C and stand-by at -15 °C apart for periods of 21 days at 10 °C and 7 days at 20 °C per annum for repairs and maintenance has been assumed. Results have been calculated for two different values of initial resistivity (4 kΩcm and 1 kΩcm). A worst-case scenario using our safety factor of 1.5 is also shown. It is clear that efficient operation can be guaranteed for the duration of the experiment if the breakdown voltage is high enough. From these calculations and from signal-to-noise considerations which are discussed in Section 3.4.6, we require that the detector be safely operated up to 500 V.

Figures 3.8 and 3.9 show the leakage current and the corresponding dissipated power. The worst-case scenario including the safety factor of 1.5 is shown as well. The same maintenance scenario as for Fig. 3.7 has been assumed. The power dissipation has been calculated with

an operating voltage which is $1.5 \times V_{depl}$. From these figures we conclude that safe operation conditions can be obtained.

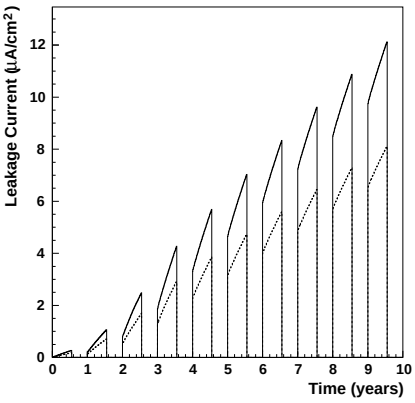

Fig. 3.8: I_{leak} versus time for the most irradiated detectors (dotted line). The simulation was done for a 4 kΩcm substrate. The solid line shows I_{leak} for a maximal fluence of 2.4×10^{14} n/cm^2.

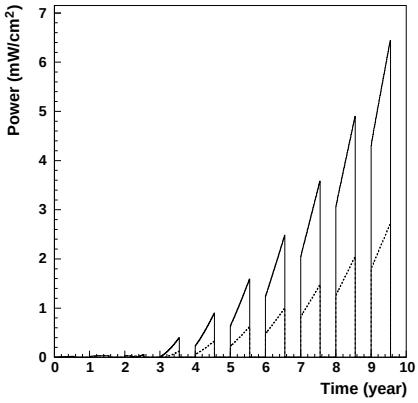

Fig. 3.9: Power density dissipated on a silicon module (dotted line). The simulation was done for a 4 kΩcm substrate. The solid line shows the power dissipated for a maximal fluence of 2.4×10^{14} n/cm^2.

3.4.2 Detector design considerations

As discussed above, the central issue for reliable performance of the detectors during the lifetime of the experiment is the need for high voltage operation. We consider here the critical technological steps to produce high breakdown devices:

- Selection of substrates of good quality is needed to avoid excessive radial resistivity variations and local mechanical defects. Double-sided polishing will assure higher process yield and will keep surface effects under control.
- Carefully controlled dose and doping profile will limit the occurrence of critical fields at the junction edge.
- Good ohmic contact is needed to avoid charge injection from the back contact.
- Edge stabilization will avoid high fields in the area damaged by the cutting procedure. We foresee the use of an n-well on top of the cutting area on the junction side.
- Multi-guard structures between the detector active area and the n^+ edge implant are important to distribute the voltage drop on the junction side over a larger region, enhancing the breakdown performances of the device.

With regard to AC coupling, the following considerations apply. Concerning the signal-to-noise ratio and tracking performance the design is guided by the following considerations:

- Thin multiple dielectric layers for the coupling capacitors will minimize the fraction of pinholes, allowing high enough specific capacitance to guarantee efficient charge collection.
- Quality control of the oxides and nitrides is needed to minimize both the interface states and the inter-strip coupling, assuring stability of electrical performances in time.
- The read-out pitch being defined by the requirements on spatial accuracy and two-track resolution, the strip width will be determined by a compromise between wider implants

and safety in terms of field gradients close to the implants. It will also help to increase the coupling to the metal electrodes. Narrower implants which minimize the coupling to the adjacent implants will reduce the system noise too.
- The value of the poly-silicon resistor needed to bias the implants is a compromise guaranteeing good uniformity and a negligible voltage drop, minimizing the contribution to the thermal noise.
- The thickness of all metal electrodes is chosen as high as possible to reduce the total series resistance of the read-out strips.

Lastly detectors which imply a minimal number of masks must be adopted to reduce the technological steps and consequently the costs. Design and process are compatible with the most common $4''$, $5''$ and $6''$ technologies and compatible with large production volumes in the limited time available for sensor production. The most efficient use of the wafer surface as active area of the devices is envisaged to reduce the detector cost per unit area.

3.4.3 General detector specifications

The starting material will be 300 μm thick, high resistivity, n-type phosphorus doped silicon. A standard thickness of 300 ± 20 μm is chosen as compromise between signal-to-noise and depletion voltage after irradiation. This thickness assures also very good mechanical properties and thus very good production yield. The precision required in thickness and bending allows little spread in depletion voltage throughout the wafer and easiness of testing and assembly.

A resistivity of ~ 2 kΩcm is envisaged. The high voltage necessary to deplete the silicon bulk in the first and last LHC operation periods has implications both in the design and technology of the detectors.

The high purity, as well as the excellent uniformity in doping concentration, suggest the use of silicon grown following the Float-Zone technique. A $< 111 >$ crystal orientation allows excellent quality thermal oxides and lowers the probability of aluminum pitting into the silicon (thus causing pinholes in the decoupling oxides and weakening the junction on the p-side) while keeping the fabrication process simpler. The technology is a derivation of the standard planar process usually employed in the IC industry. A p^+ implantation is performed on the front side in order to define the strip-shaped diodes. On the back side an n^+ implantation is necessary in order to allow excellent ohmic contact between the bulk and the metal contact. Moreover, the presence of this highly doped n^+ layer acts as a barrier for minority carriers coming from the depleted bulk and for majority carriers injected from the metal contacts, keeping the overall leakage current, and thus the shot noise, very low. The implantations and the following thermal diffusion are tuned in order to:

- allow junctions to be deep and smooth, enhancing breakdown and noise features;
- keep lateral dimensions under control;
- activate as much dopant as possible;
- keep the overall thermal budget of the fabrication process as low as possible, the latter being an important cause of dark current.

An n^+ implantation is required on the front side along the edges of the devices in order to prevent the space charge region from reaching the cutting edge, thus protecting the active area from injection of charge originated in this heavily damaged region.

Arrays of integrated capacitors are produced on the detector by using a multi-layer of thin dielectrics. An arrangement of grown and deposited oxides and nitrides is chosen in order to:

- exploit the excellent properties of thermally grown oxide by means of its high density, low trapped charge, homogeneous coverage and low intrinsic pinhole distribution;

- decouple layer-intrinsic defects by means of a dielectric multi-layer structure, strongly reducing the overall number of metal-implantation short circuits (pinholes);
- allow good precision and stability of decoupling capacitances. The high dielectric constant of silicon nitride allows an easier control of the thickness;
- enhance the breakdown performance of the decoupling capacitor.

This choice allows integrated capacitors of (20 $\pm$ 3)pF/cm and rated to more than 100 V of applied bias. The overall percentage of defective capacitors for each detector should be strictly lower than 1%. The effective coupling of each strip to the neighboring ones (measured at 100 kHz and at full depletion) should not exceed 1.3 pF/cm before irradiation.

A structure of multiple p^+ guard rings is used in all detectors around the active area in order to prevent breakdowns caused by high voltage drops between the detector and the guard ring. The innermost ring is used to bias the implants through arrays of poly-silicon resistors distributed one every second strip on each side of the detector.

The choice of poly-silicon from among other biasing techniques such as punch-through or FOXFET is mainly due to its higher radiation resistance, and relies on the very much enhanced ability of producers in defining the resistance value by means of controlled dopant implantation or diffusion. The choice of a value of (2.0 $\pm$ 0.6) MΩ for the resistors is driven by the need of keeping the Johnson parallel noise as low as possible, as well as the voltage drop between the strips and the bias guard ring. Moreover the lower the poly-silicon specific resistance, the higher the precision and the stability in the nominal values.

The detectors are required to operate in a stable way at above 500 V bias, both before and after radiation-induced type-inversion on the bulk (I_{leak}(500 V) < 0.5 μA at 21 °C before irradiation). The leakage current in itself is not a crucial parameter for our application but it is nevertheless considered an important indicator of the quality and operational stability of the detectors. Before irradiation we require that the leakage current does not significantly exceed 50 nA/cm^2 at full depletion at 21 °C.

Given an aluminum resistivity of 27 m$\Omega \cdot \mu$m, and to cope with the foreseen strip metal width, we require the metal thickness of all metal lines to be (1.5 $\pm$ 0.3) μm) in order to keep as low as possible the series resistance contribution to the detector noise.

The strip pitch varies from the inner to the outer layers. The pitch is tuned in order to match the electronic modularity of 256 channels and to allow the maximum detector width compatible with a given technology. Both width and pitch geometrical dimensions are defined by means of the photolithographic precision attainable with these technologies, which is of the order of 1 μm.

The detectors used to provide the second co-ordinate read-out in the double-sided layers will have strips arranged in a stereo geometry. They will therefore require additional inter-strip connections to achieve full read-out coverage. We envisage the use of a double metal layer separated from the electrode plane by at least 4 μm of SiO_2 in order to keep the stray capacitance lower than 0.2 $\div$ 0.3 pF/cm. The same comments made on the first metal layer resistance apply to the second metal layer. The inter-metallic contacts will feature a large area (at least 16 μm^2) which means safe contact holes. The thickness of the second metal layer will be at least 1.5 μm in order to reduce series resistance, and its width will be kept close to the layout rules dimension in order to reduce the capacitive coupling to the metal layer underneath.

A low-temperature silicon-dioxide passivation layer will protect both sides from accidental scratches and will considerably weaken the influence of ambient conditions (like humidity) or other pollutants (like alkaline metals) on the detector performances. Moreover the passivation both simplifies the handling and enhances the stability in time of the electrical performance.

3.4.4 Sensor design

Eighteen different sensor designs are needed for the SST. All designs share several characteristics: the minimal distance of the active area from the cutting edge has been fixed as 750 μm (see Fig. 3.10). The n-well at the edges extends for 150 μm; the multi-guard structure starts with the first p^+ guard-ring at 350 μm from the edge and extends for 200 μm to 550 μm from the detector edge. The main guard and bias rings are positioned in the remaining 200 μm wide region. Two double rows of pads are used at the edges of the strips on each side of the detectors to allow for micro-bonding on a pitch which is a factor 2 wider than the read-out pitch. Bonding pads are 70 μm wide and 250 μm long to allow repair in case of failures during micro-bonding. A row of test pads is used to contact each implant for testing purposes (see Fig. 3.11).

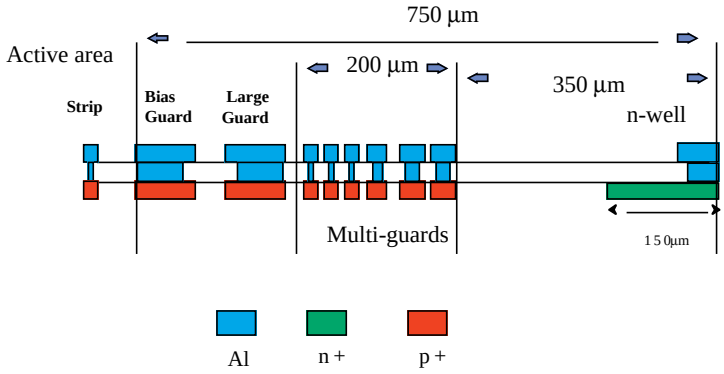

Fig. 3.10: Layout of the multi-guard structure for the microstrip detector. The scribe line is on the right while the active area (strips) is on the left side. Distances are in microns.

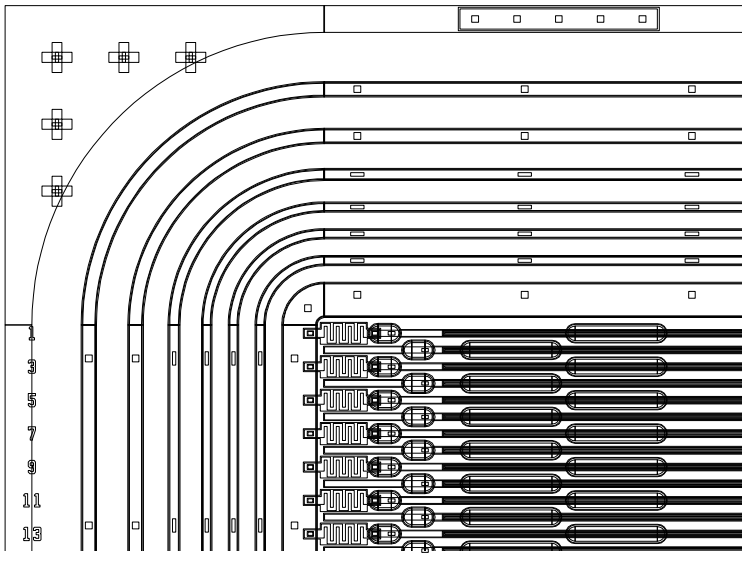

Fig. 3.11: Sensor design: corner view of a full size detector.

Series of poly-silicon resistors are foreseen in the empty area between the multi-guard structure and the n-well for testing purposes. In the same area, close to the corners, a series of reference marks is foreseen for positioning and mechanical survey purposes. All strips are numbered and all devices are passivated with at least 1 μm of silicon dioxide.

For each sensor we require also that the wafer surface not used by the main detector will be used for several test structures developed to measure and control the stability of the technology and the main critical characteristics of the device.

Single-sided barrel sensors

Because a different read-out pitch is used in the inner and outer cylindrical layers, three different designs are needed for the single-sided detectors of the barrel. All devices have rectangular geometry and r-ϕ strips. The physical area of the devices is 64×64 mm^2, the active area is 62.5×62.5 mm^2. Table 3.9 displays the dimensions of the three different designs.

For the single-sided detectors of the mini-disks two other designs are required. Trapezoidal detectors are used for both cases. Table 3.10 lists the implant and metal width of the detectors in each ring.

Table 3.9: Details of the regular sensors in the barrel

layer #	r-ϕ pitch [μm]	implant width [μm]	electrode width [μm]	read-out pitch [μm]	total # of detectors
1	61	14	11	61	416
2,3	81	20	17	81	1808
4,5	122	20	17	244	3248

Table 3.10: Details of the wedge-shaped detectors in the barrel

ring number	width min [mm]	width max [mm]	height [mm]	mean pitch [μm]	implant width [μm]	metal width [μm]	total number of detectors
1	40.4	54.3	78.2	60	14	11	216
2	52.4	64.9	70.2	74	20	17	216

Double-sided stereo sensors for the barrel

Two detector designs are used for the rectangular stereo detectors which have the same physical and active dimensions as the r-ϕ devices (respectively 64×64 mm^2 and 62.5×62.5 mm^2). The implementation of the double-metal read-out is illustrated in Fig. 3.12. Table 3.11 summarizes the details of the stereo detectors in the barrel.

In Table 3.12 the main features of each ring of the barrel mini-disks are displayed.

Table 3.11: Details of the rectangular stereo detectors in the barrel. The strips are tilted by 100 mrad

layer #	r-ϕ pitch [μm]	implant width [μm]	electrode width [μm]	read-out pitch [μm]	# of detectors
1,2	122	25	22	122	992
5	122	25	22	244	1736

End-cap sensors

The silicon detectors of the end-cap Tracker are wedge-shaped. Their dimensions (see Table 3.13) have been chosen in order to make best use of the surface available on a 4-inch wafer.

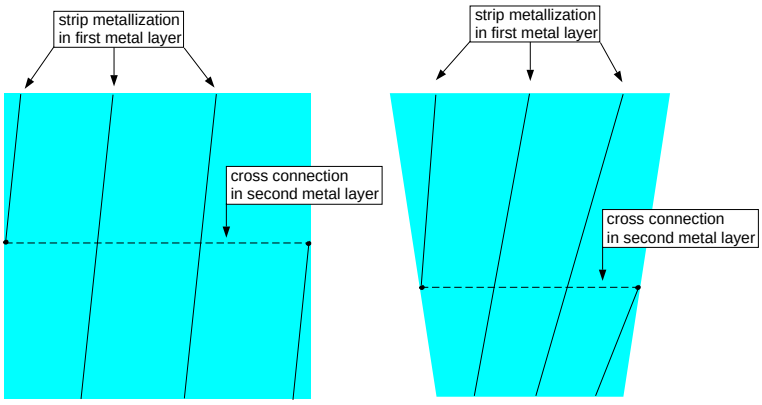

Fig. 3.12: Schematic layout of the stereo detectors in the barrel (left) and end-cap (right) region. They are made in the double-metal technique (not to scale). Only three strips are shown in each case.

Table 3.12: Details of the detectors in the barrel mini-disks

ring number	width min [mm]	width max [mm]	height [mm]	mean pitch [μm]	implant width [μm]	metal width [μm]	total number of detectors
1	40.4	54.3	78.2	89	20	17	216
2	52.4	64.9	70.2	111	20	17	216

A pair of the detectors used in rings $2b$ and $3b$ fits on a single wafer, while each of the other detectors occupies its own wafer.

The single-sided modules contain two (one for the innermost ring) detectors with radial strips to measure the ϕ-co-ordinate of a particle track. The double-sided modules contain in addition a set of detectors with stereo geometry which allows to measure both the r- and ϕ-co-ordinate. The stereo geometry is implemented by moving the location to which all strips on a detector point slightly away from the center of the ring (see Fig. 3.4). Strips which, due to this inclination, do not fit on the wedge over their full length are connected using lines in a second metal layer in order to avoid dead regions on the detector (see Fig. 3.12). The implant width on the end-cap detectors will vary with r, being typically 20% of the pitch.

Table 3.13: Description of the wedge-shaped silicon detectors used in the end-cap Tracker. Rings of modules carrying two daisy-chained detectors are split into a and b. The modules in rings 1 and 4 are double-sided and the mean pitch on the detectors on both sides is given. On the outermost disk, ring 3 is also equipped with double-sided modules

ring	width min [mm]	width max [mm]	height [mm]	mean pitch ϕ-side [μm]	mean pitch stereo-side [μm]
1	40.4	54.3	78.2	60	89
$2a$	52.4	64.9	70.2	74	
$2b$	65.0	70.7	32.2	86	
$3a$	47.8	56.8	75.3	99	(199)
$3b$	56.8	61.0	35.9	112	(224)
$4a$	59.1	67.0	66.6	120	240
$4b$	67.0	74.0	58.7	135	270

3.4.5 Results on prototypes

In this paragraph we report on the results of measurements on test structures or detector prototypes. These results were used to validate the design choices and processing technologies for our detectors.

Poly-silicon bias resistors

We have tested several series of prototypes to check the reproducibility of the poly-silicon bias resistors and their radiation resistance.

In general the resistivity of the poly-silicon layer depends mainly on the implant dose which is used to tune the conduction properties of the layer. Because of this strong dependence, a careful tuning of this phase of the process is required. Figure 3.13 displays the poly-silicon resistance as a function of doping dose.

Within a given technology several parameters may seriously affect the final results: the type of poly-silicon (i.e. the grain size), the thermal cycle of the process, the thickness and uniformity of the deposition. We have checked results obtained from different technologies. Figure 3.13 also shows the effect of different thermal budgets within a given technology and for a fixed implant dose. Figure 3.14 shows how the obtainable uniformity is higher for lower resistivities.

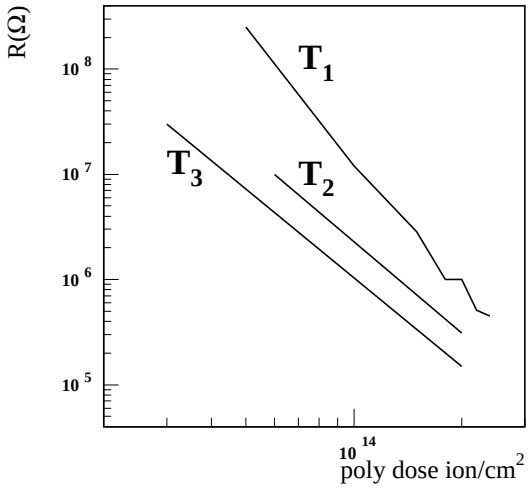

Fig. 3.13: Poly-silicon resistor values (Ω) as a function of poly-silicon doping dose. Different curves are displayed for thermal budgets (T_1 = 900 °C, T_2 = 1000 °C and T_3 = 1050 °C)

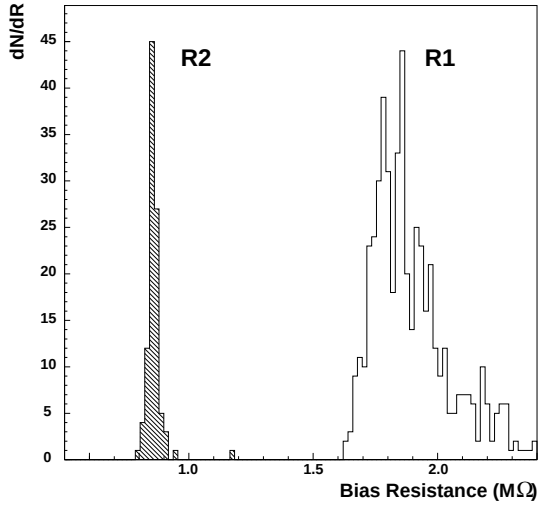

Fig. 3.14: A distribution of resistance values for different doping values. The mean value of R2 is (860 ± 20) $k\Omega$. R1 has a mean value of (1800 ± 150) $k\Omega$.

Differences at the level of 5% related to radial non-uniformities or up-down asymmetries in the deposition phase or in the lithographic steps have also been measured within the same wafer.

By using a large number of squares (50–60) and a standard poly-silicon thickness of 300 nm it is possible to obtain a uniformity better than 10% for resistivities in the range of 30–40 kΩ/□. The requirement of an average value of resistance of (2.0 ± 0.6) MΩ can be fulfilled in several technologies from different manufacturers.

The stability with radiation of the poly-silicon resistors has been directly tested in CMS prototypes up to fluences of 3.6×10^{14} neutrons/cm^2 and we observed variations within 10%.

Coupling capacitors

Several options for the multi-layer of dielectrics used for the coupling capacitors have been investigated: two thin layers of SiO_2, different combinations of SiO_2 and Si_3N_4 (oxide+nitride -ON-, oxide+nitride+oxide -ONO-), different processes (thermal growth or low temperature deposition), different thicknesses. When nitride was used we have also tested the effect of patterning the nitride layer by removing it from the inter-strip region compared to the simple case where the dielectric layer is left all over the surface.

We consider the use of nitride as a second dielectric to be important since the higher dielectric constant increases the coupling of the signal to the read-out electrodes for a given overall thickness.

The specific capacitance obtained for a given design depends on the control of the thickness and on the uniformity of the insulating layers. On test structures and full size devices we have tested the reproducibility of the coupling capacitors for different technologies. We measured the coupling capacity of the various strips within the same wafer and observed uniformity within a few percent.

In general the deposition of the oxide layers is better controlled (thickness variations $\leq 5\%$) with respect to the nitride layers ($\leq 10\%$). Good control of the process is needed since variations in thickness may appear from batch to batch within the same process, from wafer to wafer within the same batch and also from strip to strip within the same wafer.

A good yield in coupling capacitors is one of the most challenging production goals. The quality of the dielectric layers and the many technological steps used to deposit and pattern oxide and nitride may greatly affect this yield. We have measured the fraction of broken capacitors in many series of prototypes fabricated with several technological variants. As a conclusion of this R&D work, we have reached a control of the process with a few manufacturers which guarantees a yield higher than 99%. Figure 3.15 shows how in a pilot production of several tens of full-sized detectors featuring the CMS design an average yield better than 99.5% was obtained.

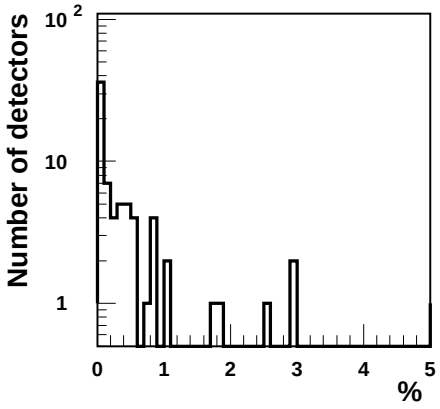

Fig. 3.15: Fraction of defective capacitors. The average is 0.34%.

Although in the final detector modules, for normal running conditions, the potential difference across the coupling capacitors will be negligible, we require good breakdown characteristics. The reason for this is the possible risk of irreversible damage to the detectors in case of a severe radiation accident. If a fraction of the beam is lost in one detector the accumulated charge may discharge the detector with a time constant depending on the total capacitance of the bias circuit. Under these extreme conditions we estimate that a potential difference as high as

100 V may appear across the coupling capacitors. For this reason we require a good breakdown performance of the coupling capacitors. We have tested several series of prototypes in different conditions: Figure 3.16 shows the results obtained for the multi-layer of oxide and nitride that we plan to use. Breakdown performance exceeding 150 V has been obtained after testing several hundreds capacitors under different conditions of electrical stress.

The stability of the coupling capacitance with time and irradiation has been verified both in terms of possible changes in the effective coupling due to charge trapped at the interface and in terms of degradation of the breakdown performance after irradiation.

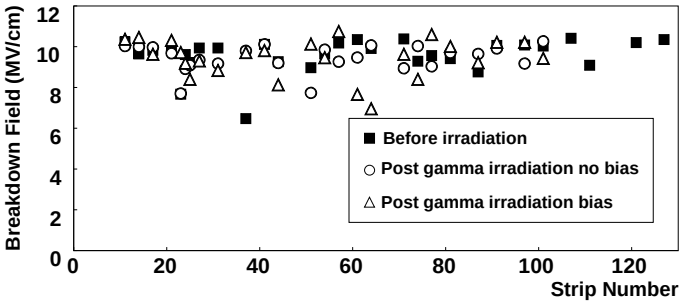

Fig. 3.16: Breakdown field for coupling capacitors before and after irradiation with Co^{60}, 10 Mrad with and without bias during irradiation. The minimum breakdown value of 6 MV/cm is equal to 120 V across the coupling capacitor section.

Strip resistance and capacitance

All strips, being fabricated as p^+ on n devices, are highly isolated before irradiation. After type inversion we have measured lower values for the inter-strip resistance but they are still high enough to guarantee acceptable noise figures.

The strip series resistance depends on the geometry and the resistivity of the metal line. Using standard aluminum-silicon we have measured resistivities around 27 $m\Omega \cdot \mu$m, which results in a series resistance of the order of 90 Ω for metal electrodes 12 μm wide, 1.5 μm thick and 62.5 mm long.

Since it is the dominant source of electronic noise, the inter-strip capacitance has been carefully measured on test structures and prototype devices. The coupling of each strip to the adjacent ones is dominated by the field lines connecting the p^+ implants through the silicon and by the charge at the Si-SiO_2 interface. Figure 3.17 a) shows the behavior of the inter-strip capacitance (one neighbor) as a function of the bias voltage for four different devices. The limiting values (after full depletion) for different wafers depends on the amount of trapped oxide charges.

Figure 3.17 b) shows the behavior of the inter-strip capacitance as a function of the frequency at full depletion. At high frequency the limiting value shows a plateau at a typical value of 0.4 pF/cm.

The role of various designs and technologies has been investigated before and after irradiation with measurements performed at 100 V bias voltage and 1 MHz frequency. Figure 3.18 shows for a given technology the value of the total capacity coupling

$$C_{tot} = C_b + 2(C_{1n} + C_{2n}) \tag{3.9}$$

as a function of the ratio of the width over pitch of the electrodes. C_b is the capacitance to the back while C_{1n} describes the coupling to the first and C_{2n} the coupling to the second neighboring strip. To a good approximation the total capacitive coupling is a linear function of the strip over pitch ratio and a width/pitch ratio of about 0.2 is chosen for an optimized detector design. By

plotting the total interstrip capacitance per unit length as a function of the width/pitch ratio divided by the gap, a good parametrization can be obtained for different designs and technologies (see Fig. 3.19).

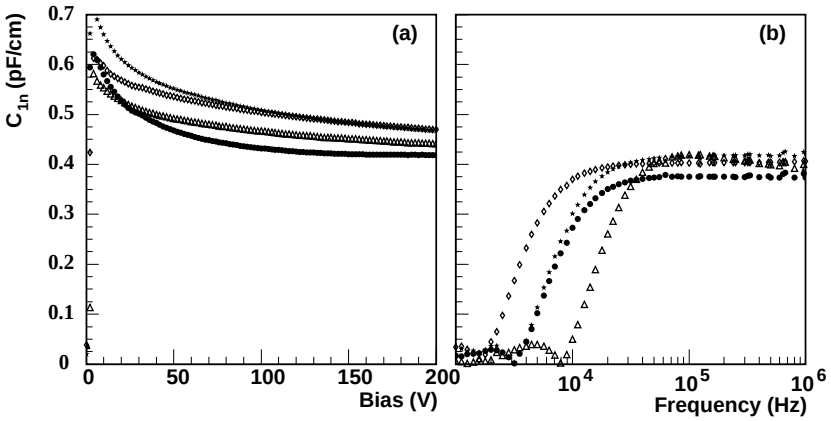

Fig. 3.17: Inter-strip capacitance (pF/cm) before irradiation: a) vs backplane bias voltage (V) for four different wafers. b) vs frequency at full depletion bias voltage.

With irradiation the concentration of the positive fixed charge in the oxide will increase to the saturation value. The higher concentration of negative charge at the interface will result in a stronger inter-strip coupling. A reduction of inter-strip capacitance can be obtained in all devices by increasing the bias voltage, since a higher field on the p^+ side confines the electrons at the interface to the middle of the gap between the two implants. Figure 3.20 shows the inter-strip capacitance versus the bias voltage after different irradiations.

Inter-strip capacitances measured after irradiation show a very strong bias dependence (Fig. 3.20). At full depletion the coupling is still high but it sharply decreases by increasing the bias voltage. Asymptotic values at most 25% higher with respect to the pre-irradiation values can be reached for a bias voltage 1.5 higher than V_{depl}.

Breakdown performance

The breakdown characteristics of several series of devices from different manufacturers have been measured before and after irradiation. Variations within the same technology are probably due to the quality of the substrate and the back surface. In this paragraph we describe the breakdown performance obtained with a single edge treatment: n-well on the cutting area and two guard-rings only. In the following paragraph the improvements achievable with an optimized edge design will be described. Figure 3.21 shows the I–V curve obtained for a series of devices (Hamamatsu). Figure 3.22 shows the distribution of the breakdown voltage for a series of devices produced by another manufacturer (CSEM).

Most detectors fulfill the requirement of breakdown voltage $V_{bkdn} \geq 500$ V. Some exhibit excellent performance ($V_{bkdn} \geq 800$ V) and for a few it was not possible to measure any breakdown up to the limit of our measuring system (1000 V). It is worth noticing that these measurements were performed on full-sized devices (54×64 mm^2) with 1024 implants on a 50 μm pitch, and the results were stable after cutting.

The stability of the breakdown performance under irradiation and different operating conditions has been carefully tested. Figure 3.23 shows the breakdown performance before and after neutron irradiation at a fluence of 10^{14} n cm^{-2} (CSEM devices) and for different temperatures. Figure 3.24 shows the breakdown performance after local irradiation with a proton beam focussed onto a device area of 2×1 cm^2. The breakdown performance seems not to be seriously

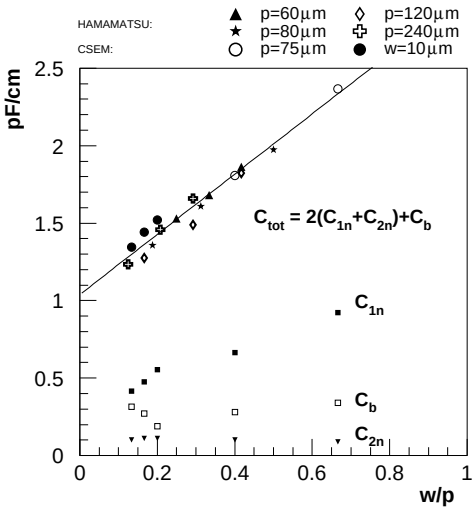

Fig. 3.18: Total capacitance per unit length as a function of strip width/strip pitch ratio (w/p) for detectors from Hamamatsu and CSEM.

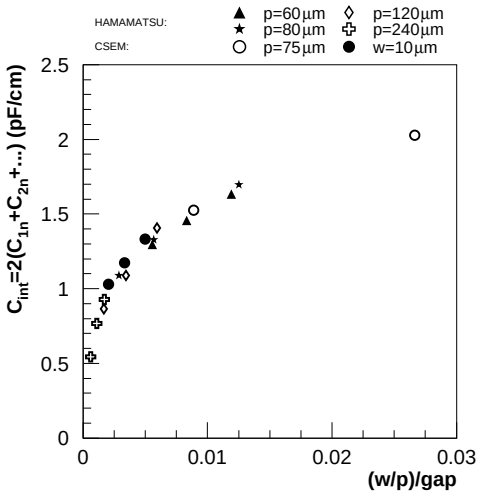

Fig. 3.19: Total interstrip capacitance $C_{int} = 2\sum_i C_{in}$ per unit length, as a function of the w/p over gap ratio. The gap is the difference between strip pitch and width. Same detectors as Fig. 3.18.

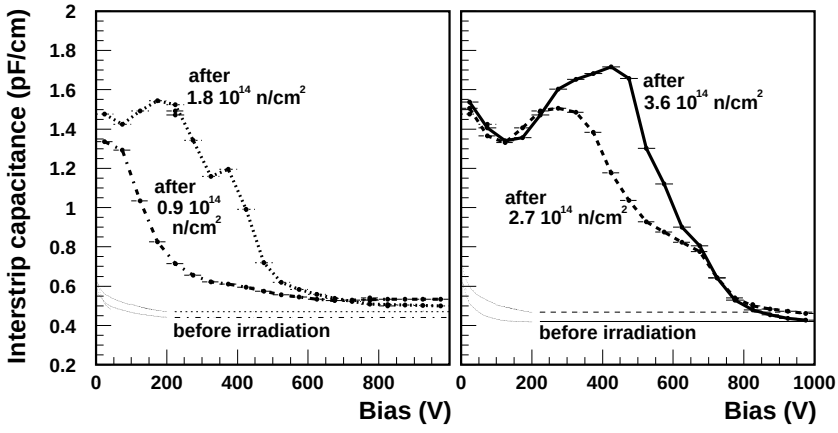

Fig. 3.20: Capacitance between first neighboring strips before and after different neutron irradiations as a function of the bias voltage. Detectors manufactured by CSEM.

affected by the non-uniformity of the irradiation. Figures 3.25 and 3.26 show the breakdown behavior characteristics after neutron irradiation.

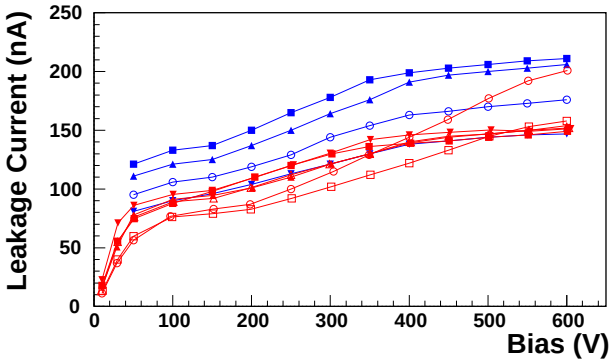

Fig. 3.21: I–V plots for different detectors before irradiation. The detectors (3×6 cm^2) are produced by Hamamatsu. The breakdown value is higher than 600 V and for some detectors it is up to 900 V.

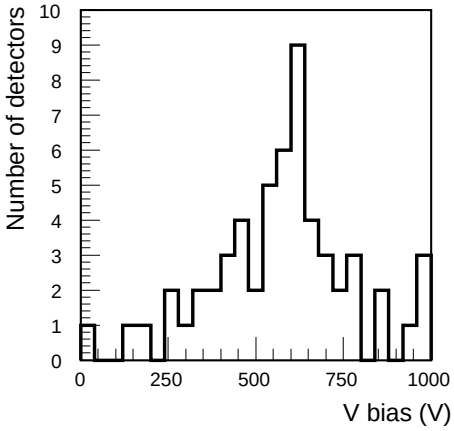

Fig. 3.22: Breakdown voltage values for full size detectors produced by CSEM. The average value is at 580 V with a r.m.s. spread of 200 V.

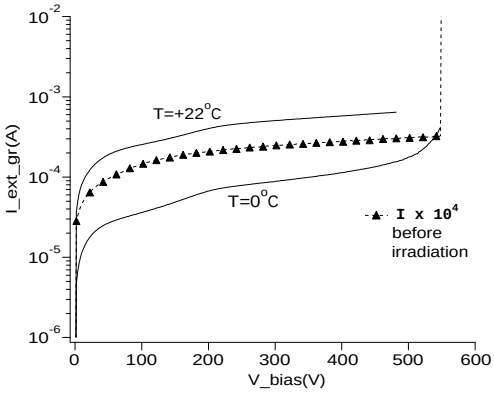

Fig. 3.23: I–V curves showing the breakdown for full-sized devices at different temperatures after irradiation at 0.9×10^{14} n/cm^2 (CSEM).

3.4.5.1 Breakdown protection

Breakdown phenomena usually occur in the proximity of the silicon surface close to the junction termination. Besides breakdown, other sources of current increase can be surface generated leakage or current injection from the edge, where generation-recombination centers are induced by cutting. This current can be an unwanted source of noise. The biased guard-ring around the active area collects the surface current, while the n-well along the scribe line creates a barrier for hole injection.

When a high reverse bias is applied to the detector active area and to the guard-ring, intense electric fields may lead to avalanche breakdown on the external side of the guard-ring enhancing detector noise and eventually causing physical breakdown of the device [3-19]. The electric field

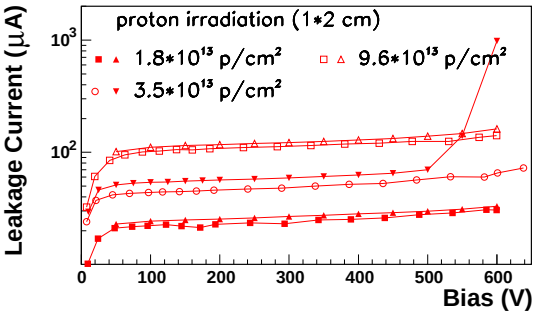

Fig. 3.24: I–V curves for full-sized devices after proton irradiation (Hamamatsu).

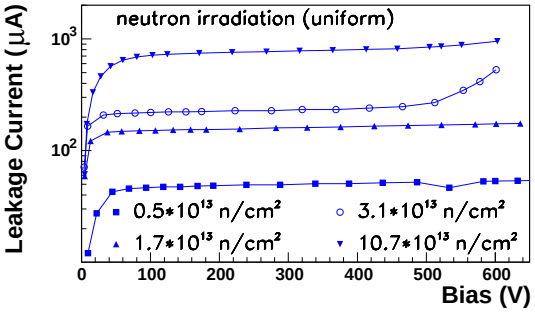

Fig. 3.25: I–V curves for full-sized devices after neutron irradiation (Hamamatsu).

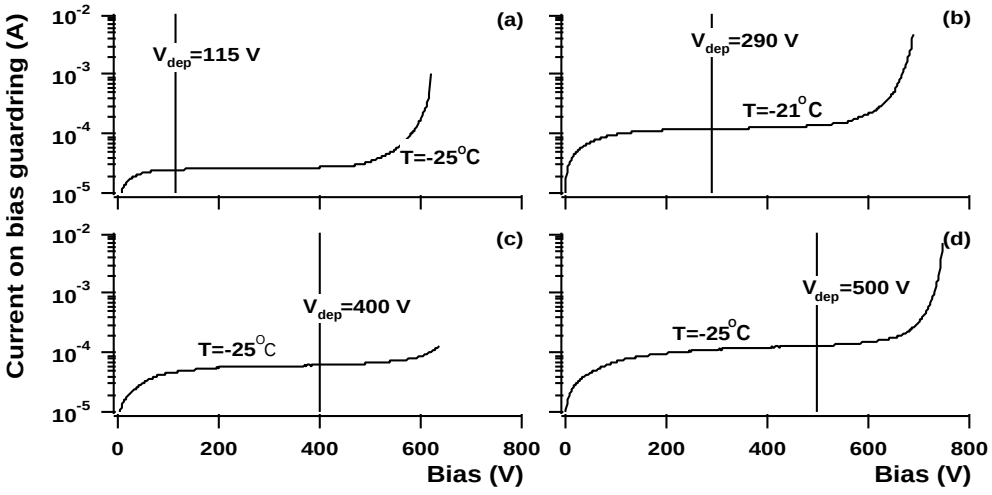

Fig. 3.26: I–V curves for neutron irradiated detectors. a) at 0.9×10^{14} n/cm^2, b) at 1.8×10^{14} n/cm^2, c) at 2.7×10^{14} n/cm^2 and d) at 3.6×10^{14} n/cm^2.

can be influenced by the position of the external n^+ well and can be controlled by a series of multiple floating p^+ rings around the guard-ring: the multi-guard structure [3-20].

The position of the n-well with respect to the most external p^+ implant has been thoroughly studied on test structures in which the distance was varied from 25 μm to 250 μm. The study was also supported by computer simulations and compared to analytical model predictions. The conclusion of both is that the minimal safe distance is 150 μm [3-21].

Multi-guard optimization studies have been performed by means of device characterization, irradiation tests and simulations [3-22]. A typical layout with several p^+ rings and a narrow spacing between them is shown in Fig. 3.27. For this device, I–V characteristics before and after irradiation are shown in Fig. 3.28. The breakdown, above 1000 V before irradiation, is reduced to 650 V just after irradiation and recovers almost completely 21 days later due to annealing of the surface damage, which is responsible for the breakdown voltage reduction. Further tests with 1 Mrad photons under bias show that no breakdown appears up to 1000 V in these devices.

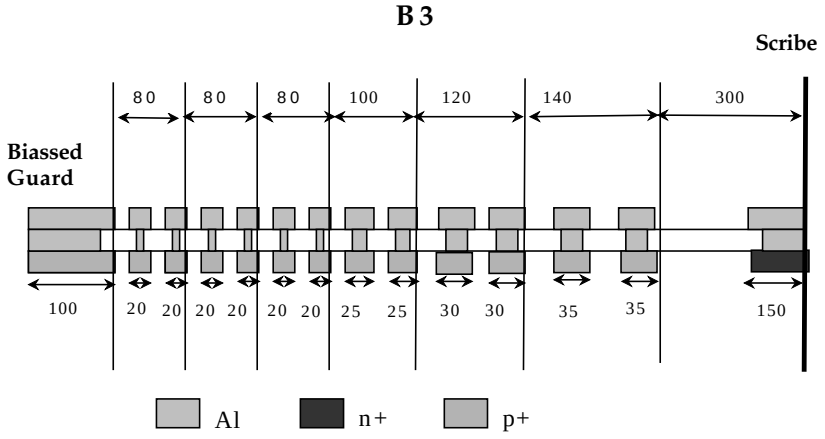

Fig. 3.27: Multi-guard structure layout B3, the biased guard is on the left, while the scribe line is on the right. Distances are expressed in microns.

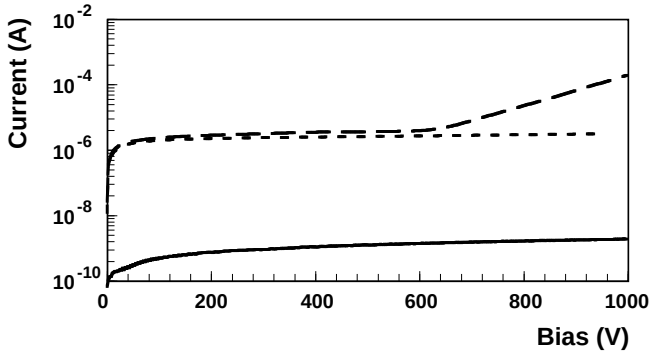

Fig. 3.28: I–V characteristics before irradiation (solid) after 1.8×10^{13} cm^{-2} protons (dashed), and 21 days after irradiation (dotted).

Double-metal read-out

The use of a double-metal layer to read out the stereo strips without introducing dead areas has been validated by several series of prototypes. The quality of contacts between the two metal layers may affect the number of dead channels in the system. A series of test chain structures

was implemented to find the best solution to this problem. With a contact area of about 16 μm^2 and a 4 μm thick insulator in between the two electrodes a failure rate lower than 10^{-4} was measured. The additional coupling capacitance introduced by the second metal layer has been estimated to add a 10% contribution to the total input capacitance. Measurements performed in test devices confirm this assumption.

3.4.6 Test beam results

We carried out several beam tests in order to check carefully the performances of barrel and end-cap devices in terms of signal-to-noise ratio, detection efficiency and space resolution under different conditions of bias voltage, temperature, radiation damage and incident angle. Fast analog amplifiers (PREMUX) with peak mode readout and 50 ns shaping time, based on a similar input stage that is used in the final front-end chip, were used as readout electronics. Data were analyzed with a set of algorithms, described in Ref. [3-23].

3.4.6.1 Signal to noise ratio

Signal-to-noise (S/N) is defined as the ratio of the most probable value of the Landau fit to the signal distribution with the average single strip noise.

Signal-to-noise ratios as high as 25:1 were obtained for non-irradiated full-sized detectors (Fig. 3.29).

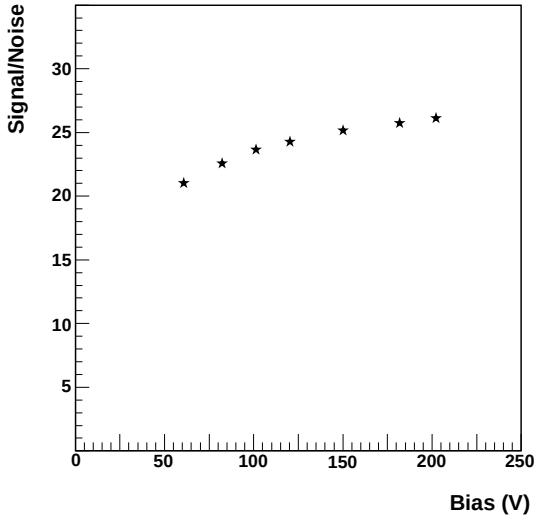

Fig. 3.29: S/N ratio vs. bias voltage for a detector, manufactured by CSEM, with 50 μm strip pitch and 12.5 cm length, at 21 °C temperature.

The effect on the S/N ratio due to the geometrical parameters of the sensor design has been studied widely in non-irradiated devices for both barrel and end-cap type detectors.

For the barrel detectors the relevant geometrical parameters are the strip pitch, the implant width and the strip length. Figures 3.30 and 3.31 show, as a function of V_{bias}, a similar behavior in cluster charge and S/N for readout pitch values ranging from 60 to 240 μm and comparable width/pitch ratios (0.21–0.33).

Owing to the trapezoidal shape of the end-cap detectors, we could choose different design options to lay out the strips on the sensor. Therefore we have carried out a preliminary comparative study on a wedge device whose strips on the p-side were subdivided into three groups: one based on a constant strip width of 14 μm, the second based on a constant width over pitch ratio

of 0.37, and the last featuring a variable strip width from 14 to 26 μm maintaining a constant inter-strip gap of 24 μm along the detector. We tested one of these devices at a bias voltage of 100 V and in good conditions of signal-to-noise ratio. The three options imply, in principle, only small differences in the inter-strip and coupling capacitance. To check this, we subdivided the tracks hitting the device according to the incident region and for each we compared the relevant distributions, finding no significant differences except for a slight worsening of the noise in the constant-gap region (Fig. 3.32). Based on this result, the wedge detectors are designed with a constant width over pitch ratio.

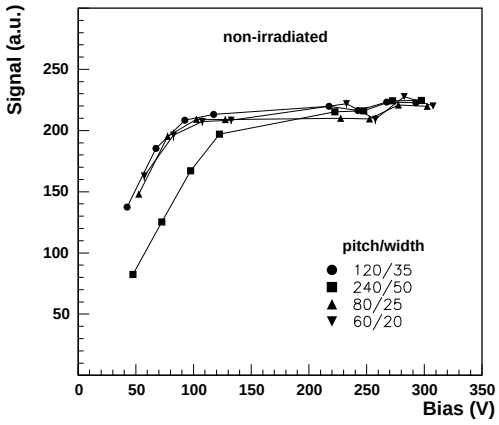

Fig. 3.30: Cluster charge as a function of the bias voltage. Hamamatsu detectors with strip pitches varying from 60 μm to 240 μm and a 6.25 cm strip length.

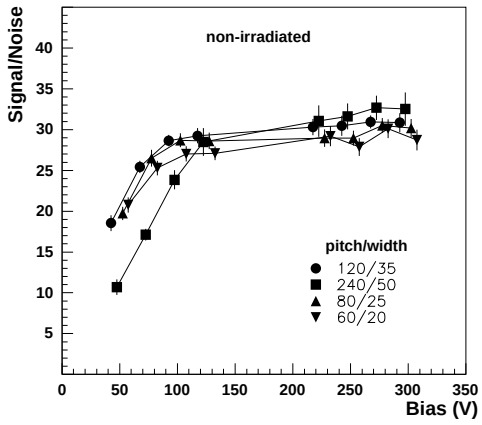

Fig. 3.31: Signal-to-noise ratio vs. bias voltage for the same detectors as Fig. 3.30.

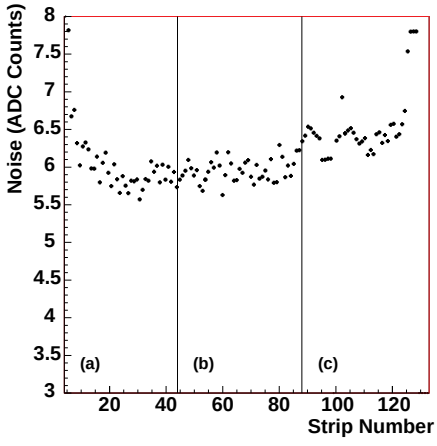

Fig. 3.32: Data for a wedge detector: strip noise for the three different regions: constant strip width (a), constant w/p (b), constant inter-strip gap (c).

Since a significant fraction of particles will cross the detectors at non-orthogonal incident angles, the effect of inclined tracks has been studied in detail. The amount of charge released in the silicon and the number of fired strips is expected to increase while the average single strip

noise should remain unaffected. Figure 3.33 shows that the detector behaves as expected: there is a clear widening of the clusters and an increase of the signal-to-noise ratio. This is compatible with the predicted $1/\cos\theta$ dependence of the cluster charge and a constant strip noise.

Another important parameter which determines the behavior of the detectors is the temperature at which the silicon is operated. This can in fact influence sizeably both the amount of charge collected and the noise. We have studied the dependence of noise and charge collection efficiency as a function of temperature, [3-24] obtaining an increase in the signal-to-noise ratio up to 20% going from room temperatures to $-10\,^{\circ}$C, which is our choice as operating temperature (Fig. 3.34).

The last important parameter that influences the signal-to-noise performance is radiation damage. The irradiation produces both an increase of the noise, as a consequence mainly of the increased inter-strip capacitance (Fig. 3.20), and a decrease of the charge collection efficiency due to bulk damage [3-25].

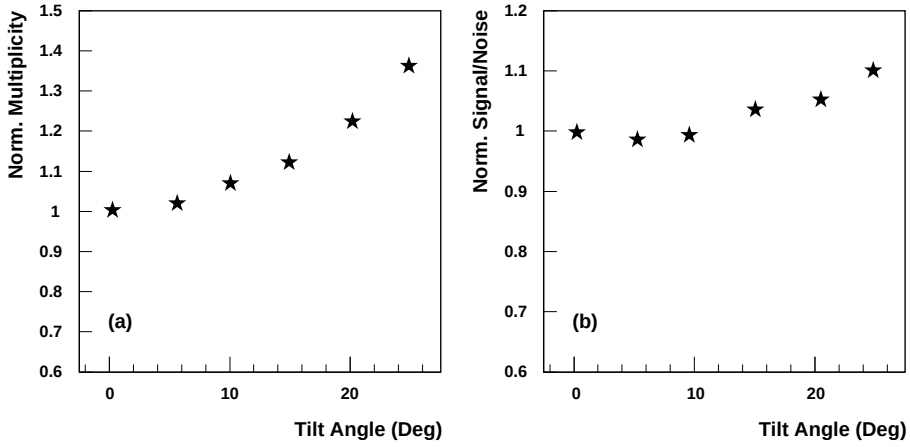

Fig. 3.33: Cluster multiplicity (a) and S/N ratio (b) as a function of the tilt angle. All points are normalized to the orthogonal incidence values. The readout pitch is 50 μm.

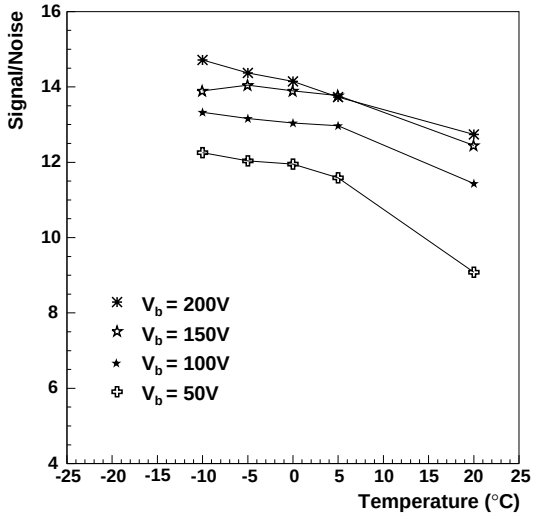

Fig. 3.34: Signal-to-noise ratio as a function of temperature at various bias voltages for a detector from CSEM irradiated at 1×10^{13} n/cm^2. The readout pitch is 50 μm.

These two effects can both be partly reduced by increasing the bias voltage above the full depletion point, as shown in Figs. 3.35 and 3.36 for two detectors which have been irradiated with 1.0×10^{13} and 3.6×10^{13} n/cm^2 and then heated to produce an anti-annealing simulating an effective fluence of 1×10^{14} n/cm^2. We observe also (Fig. 3.36) that the collected signal grows with V_{bias}, reaching an asymptotic value for bias voltages significantly higher than the depletion voltage. Figure 3.37 shows the collected signal for proton irradiated devices. For the highest dose of 1.6×10^{14} p/cm^2 the loss in charge collection efficiency is not more than 10%.

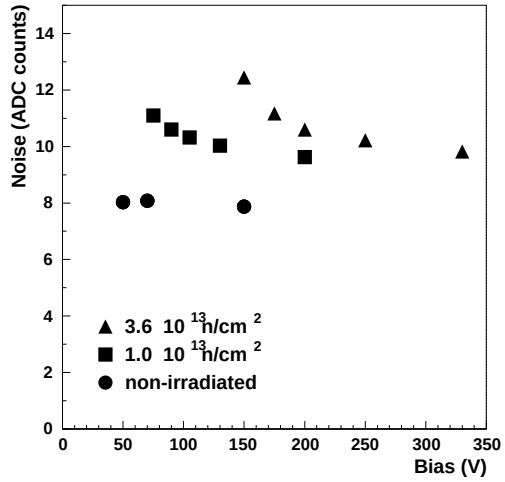

Fig. 3.35: Noise in ADC counts vs. bias voltage for SINTEF detectors of 50 μm pitch, 12.5 cm length.

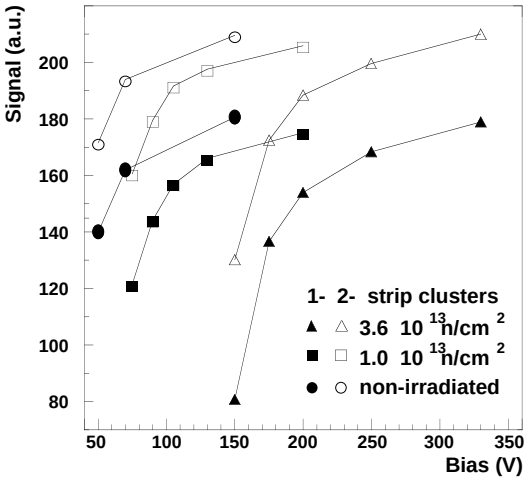

Fig. 3.36: Signal in ADC counts vs. bias voltage for the same detectors of Fig. 3.35, for 1- and 2-strip clusters.

As a consequence, the signal-to-noise ratio for the irradiated devices approaches a plateau value at higher bias voltage (Fig. 3.38). There is still a 20% loss of signal-to-noise that is not recovered even going to the highest bias voltage. The effect of proton irradiation on shorter detectors with 80 μm pitch is shown in Fig. 3.39. We have also investigated the performance of detectors irradiated up to 3.6×10^{14} n/cm^2 [3-26]. The corresponding signal-to-noise ratio as a function of bias voltage is shown in Fig. 3.40. We see that for all fluences a similar dependence on V_{bias}/V_{dep} is observed. An extrapolation to the expected LHC conditions is given in Section 3.5.5.

A special case arises with the radiation damage suffered by the end-cap detectors because the fluence depends strongly on the radial co-ordinate, causing a non-homogeneous irradiation over the active area. In order to study the influence of this effect we have used a narrow proton beam to illuminate only a 1 cm^2 area near the shorter edge of a wedge detector. This defines a non-irradiated, an intermediate and an irradiated zone, where the last is type-inverted. To check and define the different zones we measured the strip bias resistance on the n-side strips. The result is shown in Fig. 3.41.

The signal-to-noise as a function of temperature and bias voltage is reported in Figs. 3.42 and 3.43. Differences between the inverted, intermediate and non-inverted regions of this detector are minor.

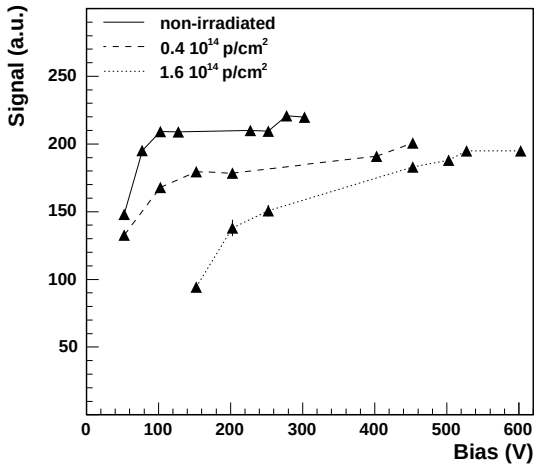

Fig. 3.37: Collected signal as a function of the bias voltage for proton irradiated devices, produced by Hamamatsu, 6.25 cm strip length, 80 μ strip pitch.

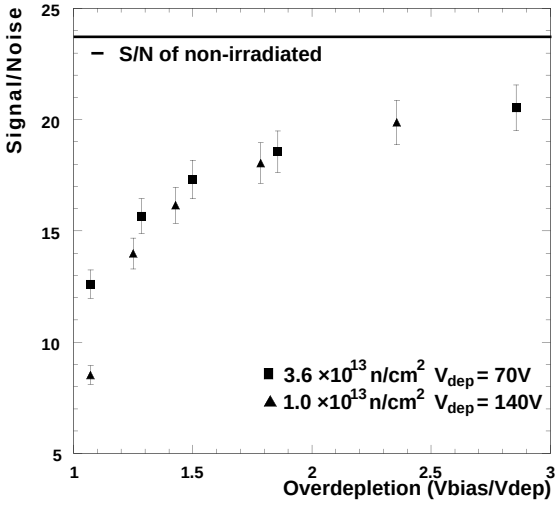

Fig. 3.38: Signal-to-noise ratio vs. bias voltage in over-depletion units for the same detectors of Fig. 3.35.

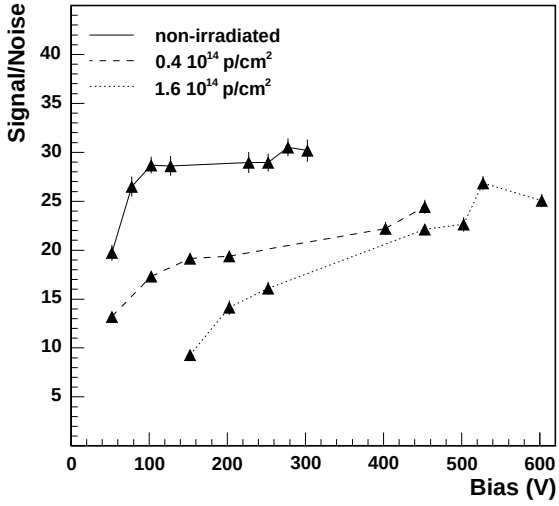

Fig. 3.39: Comparison of the signal-to-noise ratio vs. bias voltage before and after irradiation for Hamamatsu detectors with 80 μm pitch and 6.25 cm strip length.

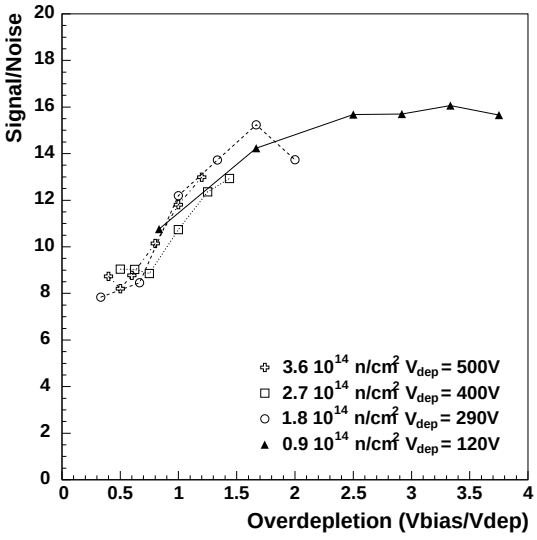

Fig. 3.40: Signal-to-noise ratio for heavily irradiated CSEM detectors of 50 μm pitch, 12.5 cm length. Lower values with respect to Fig. 3.38 are due to a different, noisier experimental setup.

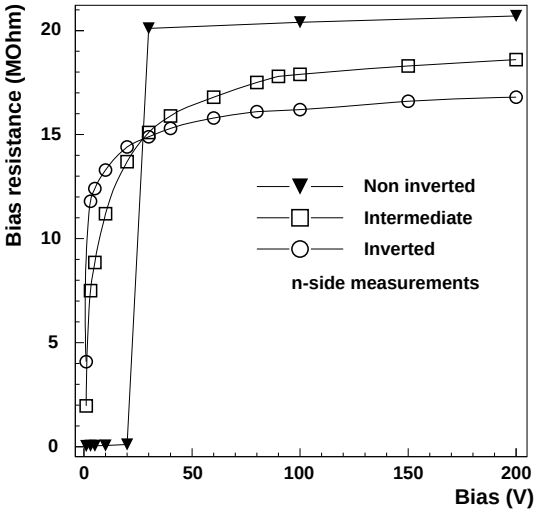

Fig. 3.41: Bias resistance on n-side for a wedge detector irradiated with 0.8×10^{14} p/cm^2.

3.4.6.2 Detector efficiency

The global hit efficiency is defined as the ratio between the number of reconstructed hits and the number of tracks predicted to cross the detector under test within its geometrical acceptance and away from dead or noisy strips. Figures 3.44 and 3.45 show the dependence of the efficiency on bias voltage and signal-to-noise ratio, respectively.

At full depletion both irradiated and non-irradiated detectors reach an efficiency compatible with 100%. It is worthwhile to note that in Fig. 3.45 even when S/N is 7.5 we have an efficiency greater than 95%.

The efficiency for an end-cap detector has also been checked before and after irradiation. Full efficiency is obtained also for non-uniformly irradiated devices at full depletion.

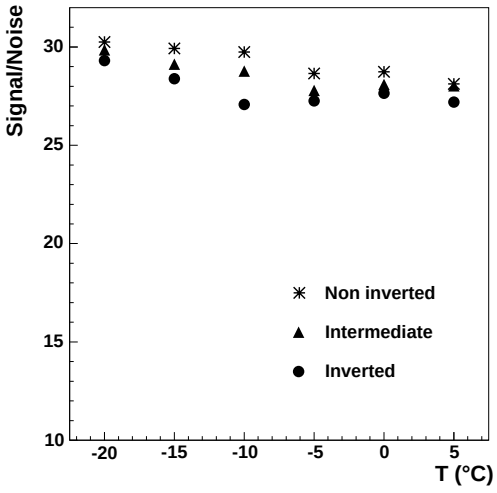

Fig. 3.42: S/N vs. Temperature, $V_{bias} = 200$ V, for the three regions of the wedge detector.

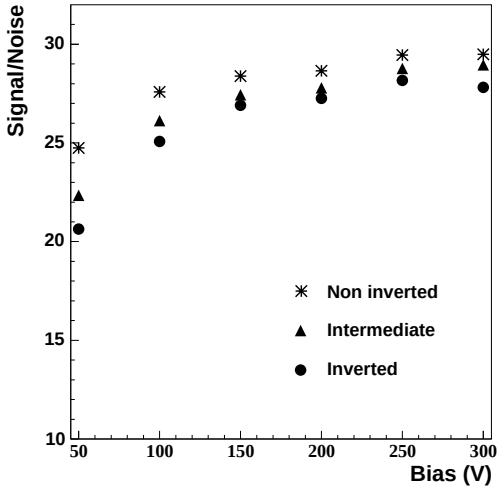

Fig. 3.43: S/N vs. Voltage, T = −5 °C, for the three regions of the wedge detector.

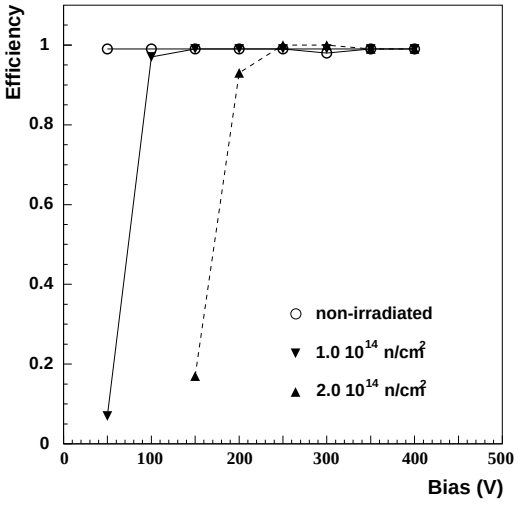

Fig. 3.44: Efficiency as a function of bias voltage. CSEM detectors of 75 μm pitch, 11 cm length, irradiated with neutrons.

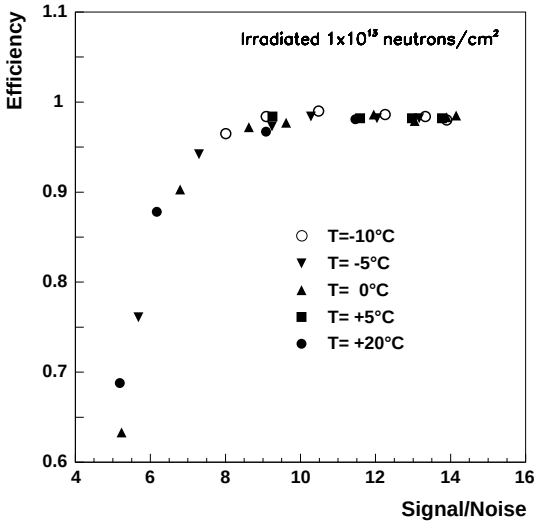

Fig. 3.45: Efficiency vs. S/N for irradiated CSEM detectors of 50μm pitch 6.22 cm length.

We have also measured the charge collection efficiency between strips as a function of the radiation damage. The cluster charge distribution versus the track position between two strips indicates good uniformity of charge collection even in heavily irradiated devices (Fig. 3.46).

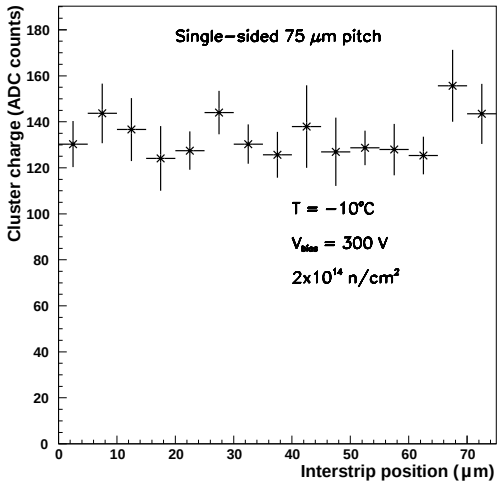

Fig. 3.46: Average cluster charge as a function of the inter-strip co-ordinate in an irradiated device.

3.4.6.3 Response function and spatial resolution

The particle impact point is usually given by the center of gravity of the cluster, the weights being given by the charge collected on each strip. This way of reconstructing positions assumes a linear sharing of the charge released on each strip. To study the deviations from the linear approximation and obtain a correction to the reconstructed position we have studied the response function η [3-23] and its dependence on radiation damage. The response function is defined as $\eta = Q_L/(Q_L+Q_R)$, where Q_L and Q_R are the charges collected on the strips to the left and to the right of the reconstructed hit position, respectively.

Figure 3.47 shows that in the central region, populated by multi-strip clusters, the charge is linearly shared among the strips and hence the linear interpolation is correct, while in proximity of the strips single-hit clusters dominate and a digital response should be assumed [3-23]. Figure 3.48 shows the same plot for a similar device irradiated to 1.8×10^{14} n/cm^2. We see that the shape is very similar.

A typical distribution of the residuals is plotted in Fig. 3.49 for a 50 μm pitch detector. After subtracting the contributions due to multiple scattering and to the extrapolation error, we obtain a resolution of about 11 μm in the co-ordinate orthogonal to the strips. This co-ordinate will be, in the final CMS Tracker, the one measuring $r-\phi$ in the barrel and $z-\phi$ in the end-cap.

The dependence of the resolution on the signal-to-noise ratio, bias voltage and incidence angle is weak both for irradiated and non-irradiated modules. As an example, Fig. 3.50 shows the measured resolution for tracks at 20° incidence angle for irradiated and non-irradiated detectors as a function of the bias voltage.

In order to measure the resolution for the stereo layer of the double-sided layers we have used a double-sided detector [3-23] with the same pitch and stereo angle that is foreseen in the present Tracker configuration. On a detector with a read-out pitch of 100 μm and a stereo angle of 100 mrad, we obtained a resolution of 34 μm orthogonal to the stereo strips and 320 μm in the stereo co-ordinate (Fig. 3.51).

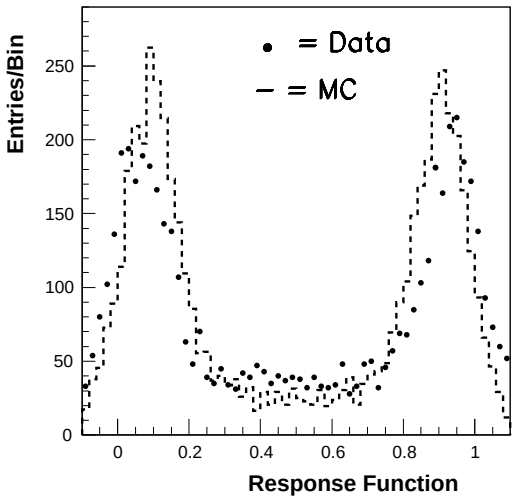

Fig. 3.47: Typical response function distribution. Monte Carlo simulation (dashed line) is superimposed.

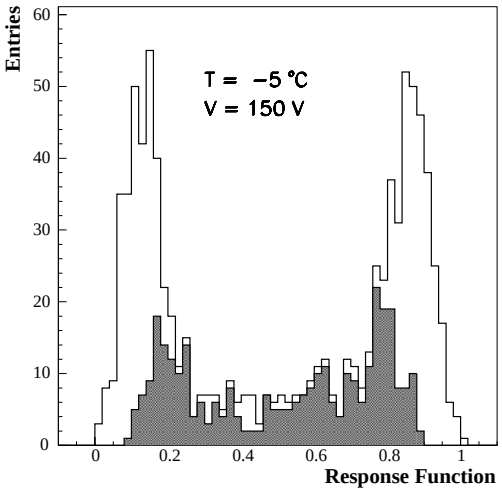

Fig. 3.48: Response function distribution for a CSEM detector irradiated to 1.8×10^{14} n/cm^2.

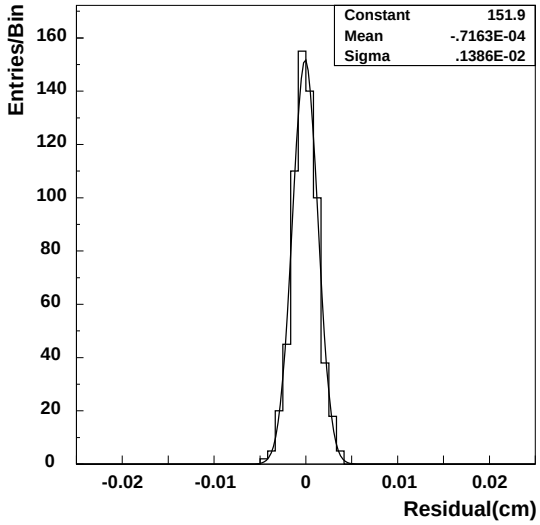

Fig. 3.49: Residual distribution for a 50 μm pitch detector. From the width of this distribution we obtain a value of 11 μm for the intrinsic resolution.

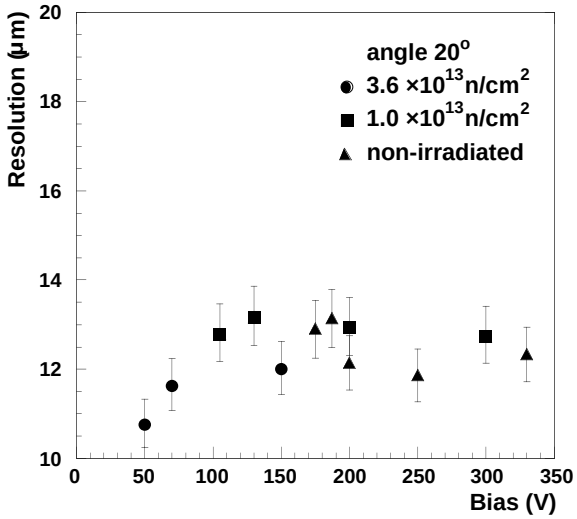

Fig. 3.50: Spatial resolution for tracks with an incident angle of 20°. Same detectors as Fig. 3.35.

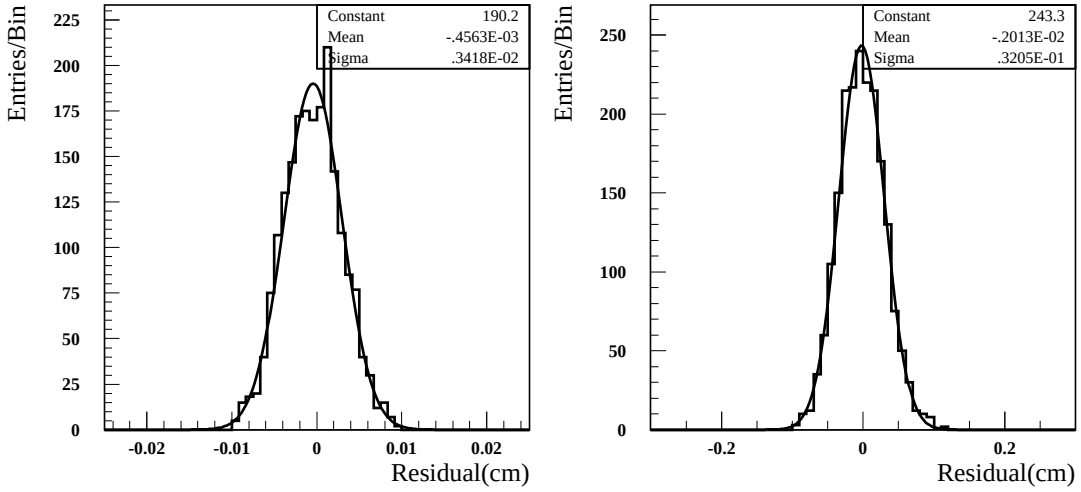

Fig. 3.51: Distribution of the residuals for the stereo strips of a 100 μm pitch SINTEF detector: a) resolution in the co-ordinate orthogonal to the stereo strips, b) resolution in the real stereo co-ordinate.

An example of the dependence of the stereo co-ordinate resolution on the tilt angle is shown in Fig. 3.52 for the same detectors as Fig. 3.51.

The average performance in terms of position resolution for the strips of a wedge detector is shown in Fig. 3.53. The resolution of 7 μm obtained, after subtracting the impact point extrapolation error of 5 μm, is well inside the specifications for CMS.

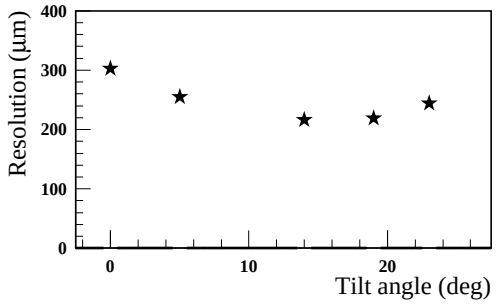

Fig. 3.52: Resolution as a function of the tilt angle. Same detectors as Fig. 3.51.

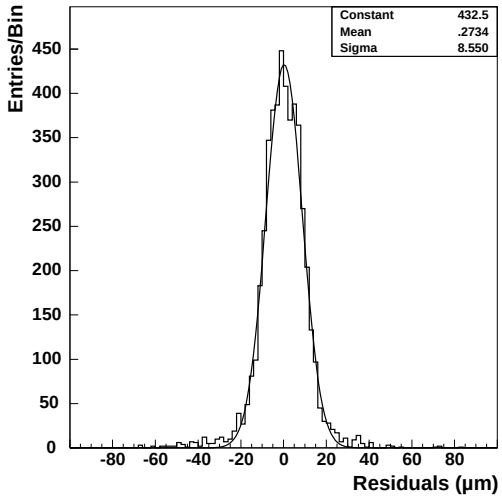

Fig. 3.53: Residual distribution for the wedge detector (6.25 cm long strips, 38–50 μm pitch).

3.4.6.4 Data with low momentum particles

Since a large fraction of particles at the LHC will have momenta well below 1 GeV/c, we studied the detector response to low momentum particles. In a first beam test, data were collected with hadrons between 270 and 408 MeV/c momentum. Figure 3.54 reports the charge collected on the p-side in double-side detectors and shows a clear separation between protons and pions at both energies.

The cluster multiplicity associated to these particles may affect the occupancy. A careful study was performed with 310 MeV/c particles at different angles. Fig. 3.55 shows the cluster multiplicity for protons and pions. The experimental data have been used to simulate the SST response to low momentum hadrons.

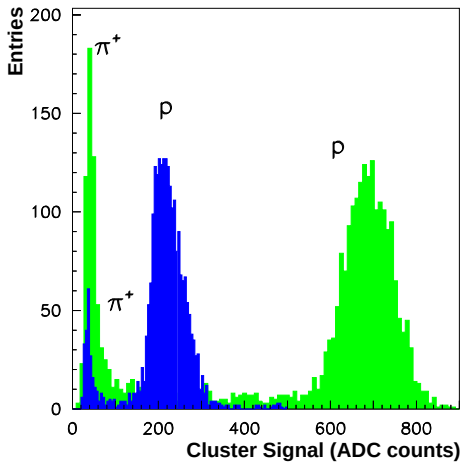

Fig. 3.54: Cluster signal at two different beam momenta of 270 (light area) and 408 (dark area) MeV/c. The contributions due to protons and pions are clearly visible.

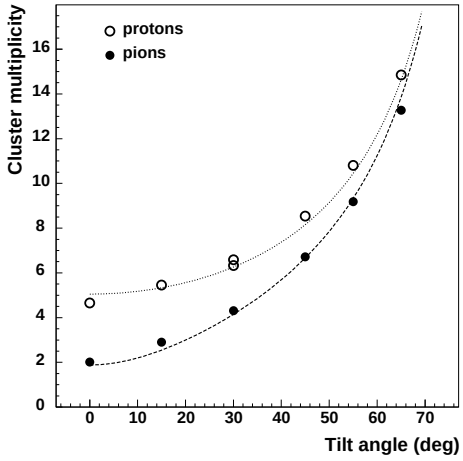

Fig. 3.55: Cluster width as a function of tilt angle for 310 MeV/c protons (empty points) and pions (filled points).

3.4.7 Modeling of silicon micro-strip detectors

Numerical device simulation has been used as a design aid and a validation tool. In particular, device simulation has been exploited for investigating several aspects of micro-strip detector behavior.

The HFIELDS [3-27] program has been adapted to this purpose. The code numerically solves semiconductor transport equations over an almost arbitrary domain; it has been tuned to the particular kind of devices of interests, and enhanced, with respect to the standard, VLSI-oriented version by adding some features related specific to detector devices.

In particular, code customization includes a 'dedicated' transient-analysis mode, which analyzes in detail the motion of a cloud of carriers generated by the particle hit, and an account of radiation-damage effects within the transport equations. Deep-level recombination centers are accounted for and their density is correlated to the radiation fluence; radiation-induced fixed charge, trapped in the insulator layers and at interfaces, is considered as well.

A hierarchy of models has been investigated, including a simple 'effective-doping' approach, a single (donor) deep-level trap and two independent (donor and acceptor) deep-level traps.

The structure sketched in Fig. 3.56 has been simulated. It represents a partial cross-section of an actual micro-strip detector.

A passive characterization of non-damaged detectors has been carried out, mainly focused at investigating noise-related parameters, such as leakage currents or parasitic capacitance.

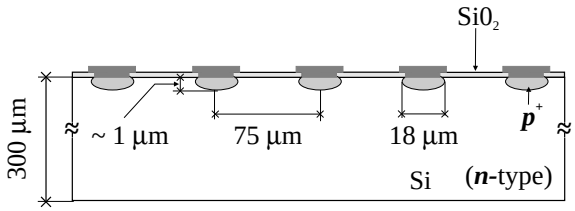

Fig. 3.56: Cross-sectional sketch of the simulated structure.

In Fig. 3.57 the main components of such a capacitance are reported, and compared with actual measurements, performed on a 5.5 cm long detector. We repeat the comparison of the capacitance components for heavily irradiated devices, using a single acceptor level, located slightly above the mid-gap ($E = E_c - 0.55$ eV). In particular, a fluence of 1×10^{14} n/cm^2 has been simulated. Measurements were carried out on some detectors irradiated with neutrons. The comparison is illustrated in Fig. 3.58.

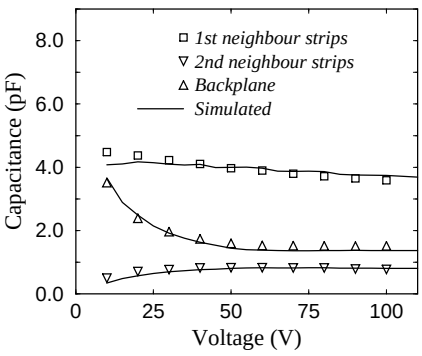

Fig. 3.57: Capacitance of a non-irradiated device versus bias voltage (5.5 cm long detector).

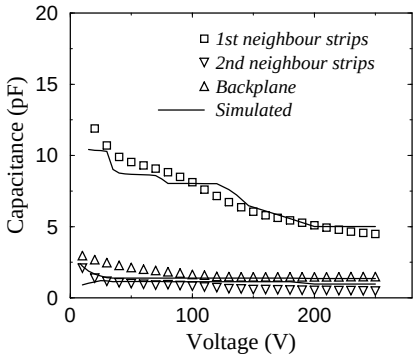

Fig. 3.58: Capacitance of an irradiated device ($\Phi = 1 \times 10^{14}$ n/cm^2) versus bias voltage.

Simulations have been carried out at different fluences. The predicted depletion voltages are collected in Fig. 3.59, and are compared to C-V measurements. The effects of different initial resistivities are reported in Fig. 3.60.

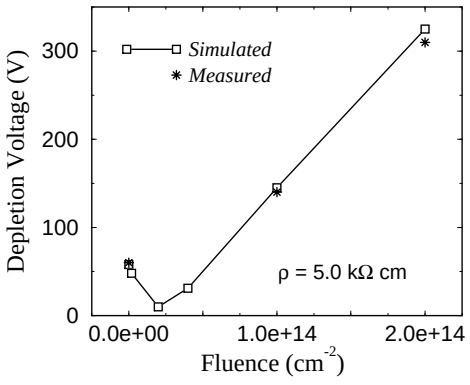

Fig. 3.59: Depletion voltage vs. particle fluence (1-MeV neutrons).

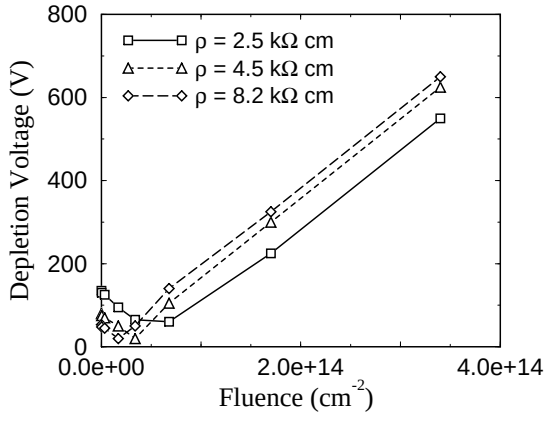

Fig. 3.60: Simulation of depletion voltage vs. particle fluence for different initial resistivities.

In order to study the active behavior of the detector, several transient simulations have been carried out. A single particle crossing the device, hitting the detector in the middle of a strip is considered. Figure 3.61 shows the hole concentration calculated within the device just after the transition of the particle. Currents collected by the strip are plotted in Fig. 3.62, as predicted for

different fluences. The charge collection efficiency, as calculated by integrating the strip current pulses, is reported in Fig. 3.63 for different fluences as a function of the bias voltage, indicating a recovery of collection efficiency for high voltages [3-28]).

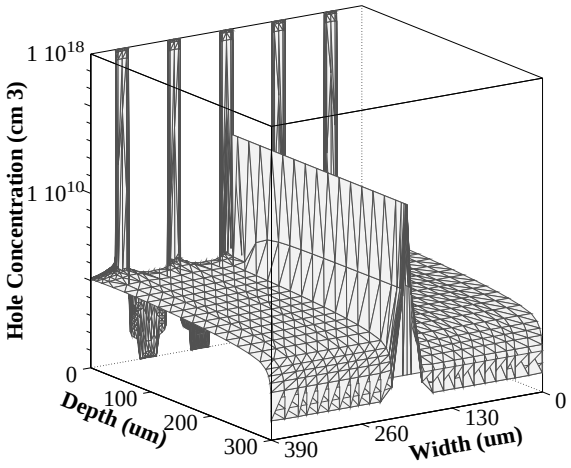

Fig. 3.61: Hole distribution, just after one particle hit.

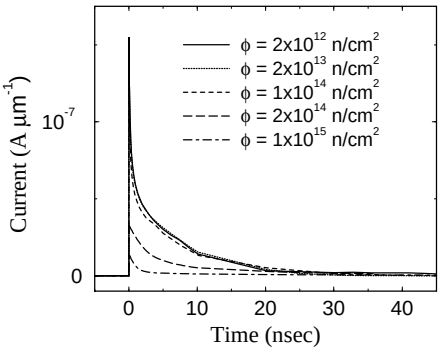

Fig. 3.62: Time-domain responses to a single-particle hit ($V_{bias} = 250$V).

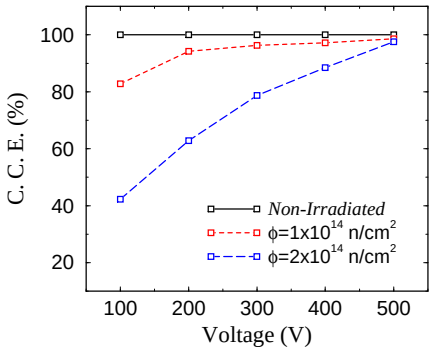

Fig. 3.63: Charge collection efficiency vs. V_{bias}.

3.5 The Read-Out System

The readout system for the SST must fulfill the formidable requirements, in terms of particle fluences, magnetic field, material budget and inaccessibility, imposed by the environment the SST will operate in, in the innermost region of the CMS detector, whilst being capable of functioning at the Level 1 rate of 100 kHz.

The radiation hardness of the front-end components is of special relevance: calculations foresee an integrated dose of 70 kGy over 10 years for the first layer of the SST. On the other hand, in order to achieve the desired tracking performance, the target for the total ENC, all contributions included, over the entire detector lifetime, has been set to less than 2000 electrons, with the additional requirement that the signals from the SST be localized in time to within a single bunch-crossing interval.

3.5.1 General architecture

Each micro-strip in the SST is read out by a charge sensitive amplifier followed by a shaper. The output voltage of the shaper is sampled at the beam crossing rate, and the samples are stored in the cells of an analog pipeline for the maximum Level 1 trigger latency of 3.2 μs. Following a Level-1 trigger, for each strip a deconvolution of the nominal shaper response can be performed in order to recover the single bunch-crossing timing accuracy; in low-luminosity conditions, when single crossing timing might not be critical, this step can be omitted, with the result of a better charge, and therefore position resolution. Analog data are then time-multiplexed, converted to analog optical signals and brought to the FED boards, the VME-based digitizer electronics, through bundles of optical fibers. After conversion and digitization, specialized circuitry (either ASICs or FPGAs) performs a first level of data conditioning and zero suppression, followed by the identification and reconstruction of hit clusters. Cluster data are then transferred to Dual-Ported Memories, where they become part of the CMS general data flow.

The choice to keep analog data as long as possible, instead of using a digital or binary read-out scheme, has been suggested by a number of reasons: apart from the reduction in the front-end chip complexity, and therefore also in the power dissipation within the Tracker volume, and the potentially better position resolution available through charge sharing between detector strips, having the data available as unaltered as possible all the way to the counting room will allow for easier identification, and on-line correction, of possible problems. Also, by performing the data conditioning and the zero-suppression in programmable curcuits on the accessible FEDs, one could easily and inexpensively modify the original algorithms should the need arise, which is not the case should they be hard-coded in the front-end chips.

3.5.2 The front-end chips

The front-end chips for the SST, the so-called APV series, are in the final stage of development in two separate radiation-hard technologies. The differences between the two implementations have been purposely kept minimal. Both implementations are powered from $\pm$ 2V and GND, with a total dissipation of 2.4 mW per channel.

The current design, the APV6, has 128 analog inputs; each channel consists of a pre-amplifier and shaper stage, with a peaking time of 50 ns. The shaper output voltage is sampled at the LHC frequency of 40 MHz, and the samples are stored in an analog pipeline memory which is 160 samples deep, in order to match the maximum Level 1 trigger latency of 3.2 μs.

Upon reception of a trigger, for each channel a series of samples from the pipeline are fed through the APSP, a filter capable of deconvolving the shaper response to the sampled data. Depending on whether the chips are operated in peak or in the deconvolution mode, the output is determined either by the peak amplitude of the shaper output corresponding to the trigger or by the peak amplitude of the data as reshaped by the APSP, thus recovering the single crossing timing at the expense of increased noise: measurements on prototypes of the final design have given an ENC of 510 e + 36 e/pF in peak mode, and 1000 e + 46 e/pF in deconvolution mode. The dependence of the pedestal signal on the location within the pipeline has also been measured and found to be of very little importance when added in quadrature to other noise sources. It has however been taken account of in all noise estimates.

An additional memory buffer, allowing the APSP to process a subsequent set of samples while the current event is still being output, holds the data in preparation for transmission via the output analog multiplexer, operating at 20 MHz. The output of the APV is in current form, in the range of 0 to +600 μA. The data frame generated upon reception of a trigger starts with a pseudo-digital diagnostic header: four samples at +100 μA (interpreted as a logical '1') if no error was detected by the internal logic, or a logical '0' (0 μA output) in the third sample to flag potentially erroneous data packets. A similarly encoded 8-bit number, defining the column

address of the sample within the pipeline for possible on-line pedestal corrections, follow, and finally 128 samples of analog data are output. The baseline offset is fully adjustable in order to maximize the dynamic range available for MIP-equivalent signals, which should be represented by a current of approximately 50 μA.

3.5.3 The front-end hybrids

Apart from the APV chips themselves, the front-end hybrids for the SST house very little: connections and decoupling capacitors for the power and detector bias lines, miniature twisted-pair interfaces for the input and output signals, a Phase-Locked Loop chip used to recover locally the clock signals, and the APVMUX chip. This is a quadruple 2:1 multiplexer, designed to take the outputs from two APV chips, to multiplex them and to drive a (short) twisted-pair transmission line to the external card that houses the lasers and the laser drivers that will transmit the analog data to the digitizers. This arrangement optimizes the number of these relatively expensive components, which come in quad-channel packages, by reducing the potential waste of channels when the number of APV chips per module is not a multiple of eight (which is the case for most of the SST, as can be seen in Table 5.1 for example). Of course, a saving of a factor two is also obtained thanks to the 2:1 multiplexing.

In order to minimize the passive material of the hybrid, investigations are being actively conducted both towards the use of light composites (e.g. Kapton or Upilex) instead of the conventional ceramic substrates and towards the use of aluminum instead of gold-plated copper for the conductive traces.

3.5.4 The FED and the optical link

The optical fibers carrying the analog data from the APV chips emerge from the experimental cavern and connect to the Front End Driver (FED) digitizing boards. A photo-diode-amplifier system receives and converts the data back to electrical levels for conversion by a 10-bit flash ADC. Dedicated circuitry performs strip reordering and pedestal subtraction, with the possibility of introducing more refined zero-suppression and cluster algorithms as luminosity increases. Local memory is available to buffer event data until requested by the global acquisition system. Each 9U VMEbus module contains 64 channels of conversion and digitization electronics together with the pre-processing circuitry.

The feasibility of an optical system for transmission of analog data at 40 Msamples/s has been proven by the RD23 project. The rationales for such a system include immunity from electrical interference, minimization of the material budget for the signal cables, and reduction of the power dissipation inside the Tracker volume. In the general philosophy of relying as much as possible on commercially available components, several edge-emitting semiconductor devices suitable from the point of view of cost, availability and radiation hardness have been identified, and low-mass packages developed in collaboration with industry. Following the current trend in telecommunications, the wavelength of operation is 1310 μm, and the preferred receivers are PIN photo-diodes. The same components are used for the analog readout system and for digital signals from the control system, with the appropriate modifications to the driving circuitry.

Single-mode optical fibers are commonly used in communications technology, and therefore easily available and relatively inexpensive. To allow for testing, installation and maintenance of the system, three breakpoints are foreseen, two within the detector and one on the receiving/driving electronics.

Control and monitoring of the front-end electronics and of detector 'high voltage', trigger distribution to the front-ends and clock synchronization are performed by a separate VMEbus module, the Front End Controller.

3.5.5 Expected performance

The expected performance of front-end electronics coupled to a standard detector in terms of noise and charge collection efficiency can be evaluated analytically.

In our noise estimation we consider: the thermal noise, due to the strip and metal resistance (R_s); the amplifier noise, seen as a noise source applied to the positive input of the amplifier; the shot noise from the reverse bias current of the detector (I_b); and the thermal noise of the bias resistance (R_p). The analytical formulas which express the contribution of each source are reported in Table 3.14. The evaluation of the strip series resistance for noise computations takes into account the fact that the resistance is distributed along the strip. This produces a transmission line effect and it can be shown [3-29] that the appropriate noise is given by the substitution $R_s \rightarrow R_{noise} \approx R_s/3$. The effect of the deconvolution process on the noise has been taken into account using the multiplicative factors shown in the last column of Table 3.14. The values of the specific detector parameters which enter into the calculations have been taken from Section 3.4.5. The noise coming from the circuitry after the amplifying/shaping stages has been assumed to be negligible. The total noise, expressed in terms of an equivalent noise charge (ENC), is the sum in quadrature of all contributions from the four noise sources described above.

Table 3.14: Noise sources, types and relative ENC evaluation formulas. e is the Neper constant, q_e the electron charge, τ the shaping time, C_{tot} the total capacitive load seen from the amplifier input into the detector. The multiplicative factor in the last column takes into account the deconvolution process

Noise source	Type	ENC (r.m.s. e^-)	Useful expression at $T = -10$ °C	Deconvolution
Reverse bias current (I_b)	parallel	$\frac{e}{q_e}\sqrt{\frac{q_e I_b \tau}{4}}$	$\approx 108 \cdot \sqrt{I_b(\mu\mathrm{A})\tau(ns)}$ e^-	×0.45
Polarization resistors (R_p)	parallel	$\frac{e}{q_e}\sqrt{\frac{kT\tau}{2R_p}}$	$\approx 22.5 \cdot \sqrt{\frac{\tau(\mathrm{ns})}{R_p(\mathrm{M}\Omega)}}$ e^-	×0.45
Metal strip resistance (R_s)	series	$\frac{e}{q_e} \cdot C_{tot} \cdot \sqrt{\frac{kTR_s}{6\tau}}$	$\approx 13 \cdot C_{tot}(\mathrm{pF}) \cdot \sqrt{\frac{R_s(\Omega)}{\tau(ns)}}$ e^-	×1.45
Front-end electronics	series	510+36·C_{tot}(pF)	–	1000+46·C_{tot}(pF)

The fraction of collected signal was estimated with network theory, using as input parameters the detector impedance measurements described in Section 3.4.5. A detailed description of the model and the complete set of equations used for the calculations is given in Ref. [3-30].

Figure 3.64 reports the expected performance of non-irradiated detectors as a function of the width/pitch ratio.

An essential feature of Fig. 3.64b is that noise is totally dominated by the front-end electronics. For this reason the capacitive load must be kept as low as possible, which will also ensure the highest charge collection efficiency (Fig. 3.64a). Low values of the w/p ratio are therefore preferred. The signal-to-noise ratio is above 12 for $w/p \leq 0.2$.

The expected performance on irradiated modules has been also investigated. First, we checked the reliability of the analytical method by repeating the calculation for a setup similar to a beam test, which means essentially to take data in peak mode instead of deconvolution mode. Figure 3.65 shows the results of such a calculation superimposed on beam test data, from which we can deduce substantial agreement within errors. The results for irradiated modules, read out in deconvolution mode, are reported in Fig. 3.66. The two curves for each plot in Figs. 3.65, 3.66 correspond to the variation of the input parameters of the calculation within their experimental uncertainties. We can see that acceptable S/N levels are reached for a bias voltage significantly higher than the depletion voltage. This result is confirmed by beam test data analysis, reported in Section 3.4.6.

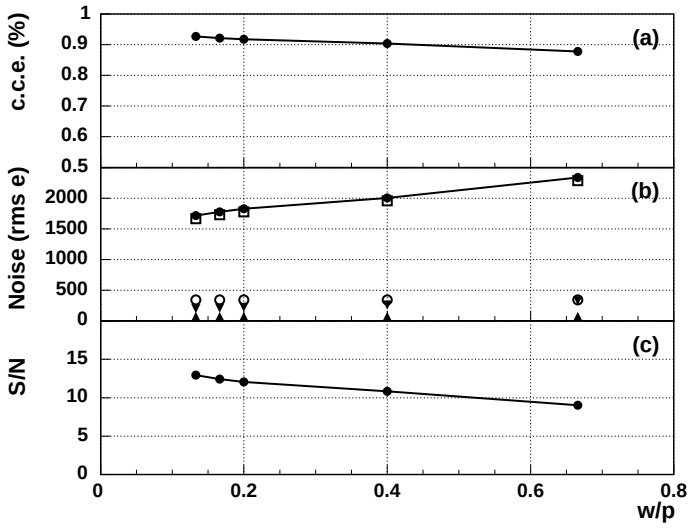

Fig. 3.64: Predicted charge collection efficiency (c.c.e.) (a), noise (ENC) (b) and S/N ratio (c) versus w/p for CSEM detectors. In the noise plot, the solid line represents the sum of all contributions, whereas the unconnected points represent, from top to bottom, noise from: the amplifier, the strip resistance, the bias resistance, and the reverse bias current.

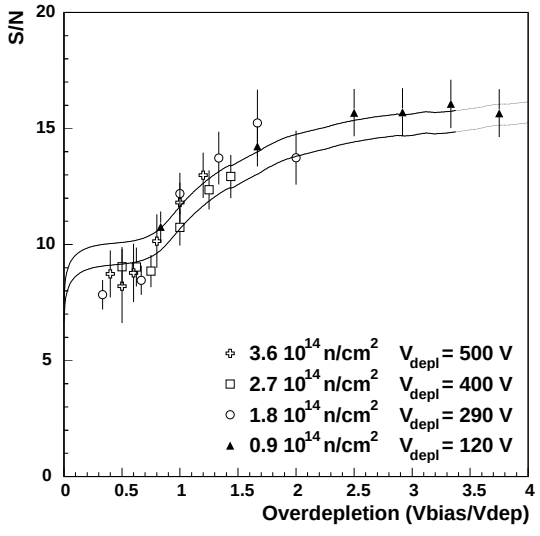

Fig. 3.65: Predicted S/N ratio after irradiation versus bias voltage, in over-depletion units. A configuration similar to a beam test (i.e. no deconvolution) has been assumed. Experimental beam test measurements (see Fig. 3.34) are superimposed on the results of the analytical model.

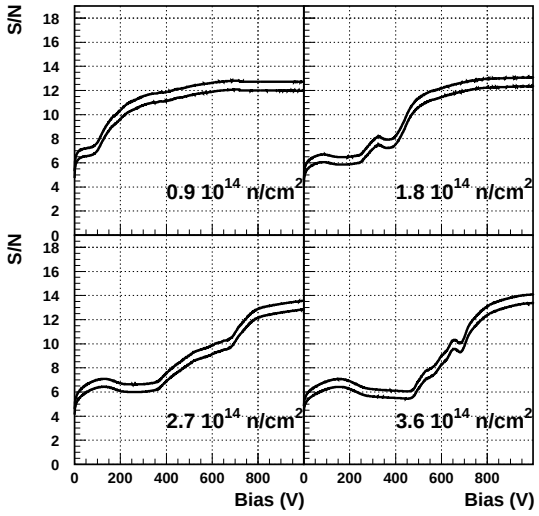

Fig. 3.66: S/N ratio calculation versus bias voltage for detectors of 50 μm pitch, 12.5 cm length, irradiated at four different neutron fluences. The effect of deconvolution has been accounted for in the calculation.

3.6 The Detector Modules

3.6.1 Requirements

A detector module is the basic functional sub-unit of our system, both for the barrel and the end-cap part. It consists essentially of three elements: a set of single-sided detectors, a mechanical support structure and the read-out hybrid. A pitch adapter is located on the hybrid. It matches the detector strip pitches to the 43 μm pitch of the read-out chips.

The basic requirements for the detector modules can be summarized as follows:

- self-supporting structure,
- alignment and mechanical stability,
- cooling,
- low mass,
- radiation hard material,
- easy fabrication, assembly and handling,
- low cost fabrication.

In order to fulfill these requirements, we shall use a single frame, in carbon fiber (CF), as support element onto which the detectors and the read-out hybrids will be glued and aligned.

3.6.2 General layout and choice of materials

Both in the barrel and in the end-caps there are modules providing one or two position co-ordinates, single- and double-sided modules. The single-sided (double-sided) barrel modules carry two (four) rectangular detectors. The single-sided (double-sided) end-cap modules house one (two) or two (four) wedge-shaped detectors.

The detectors and the hybrids are supported by a CF frame. Precision bushings are also placed on the frame to hold the modules in the supporting structure.

The positioning bushings consist of two small aluminum bushes precisely glued to the CF frame. The bushes feature precise holes whose centers define the origin and the main axis of the reference frame for the alignment.

In order to achieve low mass, high stiffness and efficient heat removal, we plan to use a high thermal conductivity (λ), high Young modulus (E), low coefficient of thermal expansion (CTE) carbon fiber composite. Fibers with thermal conductivity as high as 1100 W/(K·m) are commercially available. Starting from prepreg (Amoco K1100X-2K fibers and Fiberite 954-3A cyanate ester resin) we have obtained thin sheets (0.5 mm thick) with λ between 400 and 500 W/(K·m) (similar to copper) and $E \sim 400$ GPa (similar to tungsten and its alloys). The CTE of this material along the fiber direction is less than 10^{-6}/K and the radiation length, X_0, is high enough (25 cm to be compared to 35 cm for the best materials, beryllium and its alloys).

The low CTE prevents significant deformation and thermal stress when the structure is cooled down from assembly (+21 °C) to running (−10 °C) temperature. The difference between the CTE of the CF frame and the CTE of silicon (4.67×10^{-6}/K) is small enough to allow compensation by the thin layer of glue used to hold the silicon detectors on the CF frame.

The very high thermal conductivity allows the use of the supporting element as a heat bridge for the power dissipated by the electronics and the silicon detectors. The CF frame will be in good thermal contact with the cooling tubes incorporated in the main supporting structures.

Requirements for the glue include: good thermal conductivity, high dielectric strength, radiation resistance, long term stability and chemical compatibily with semiconductors.

Among several epoxy glues tested, we have used two: Supreme 11ANHT by Master Bond ($\lambda = 2.8$ WK^{-1}m^{-1} and dielectric strength > 15 kV/mm) and Araldite 2013 by CIBA ($\lambda \cong 1$–2 WK^{-1}m^{-1} and a resistivity $> 1.5 \times 10^{10}$ Ωm). Mechanical, electrical and thermal behavior

under temperature cycling is satisfactory. Studies are under way to establish the behavior under irradiation.

The major request for the micro-bonds is that they should have no deterioration with the stress from the temperature cycling. For this reason we use aluminum-silicon alloy wires.

3.6.3 Single-sided barrel modules

A perspective view of a single-sided barrel module is shown in Fig. 3.67, while the technical drawing is shown in Fig. 3.68.

The high conductivity CF support is 0.375 mm thick and has overall dimensions of 162.8 × 72.8 mm^2, defining the module dimensions.

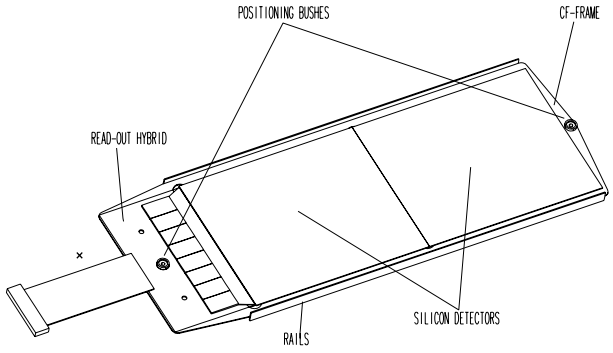

Fig. 3.67: Perspective view of a single-sided barrel module.

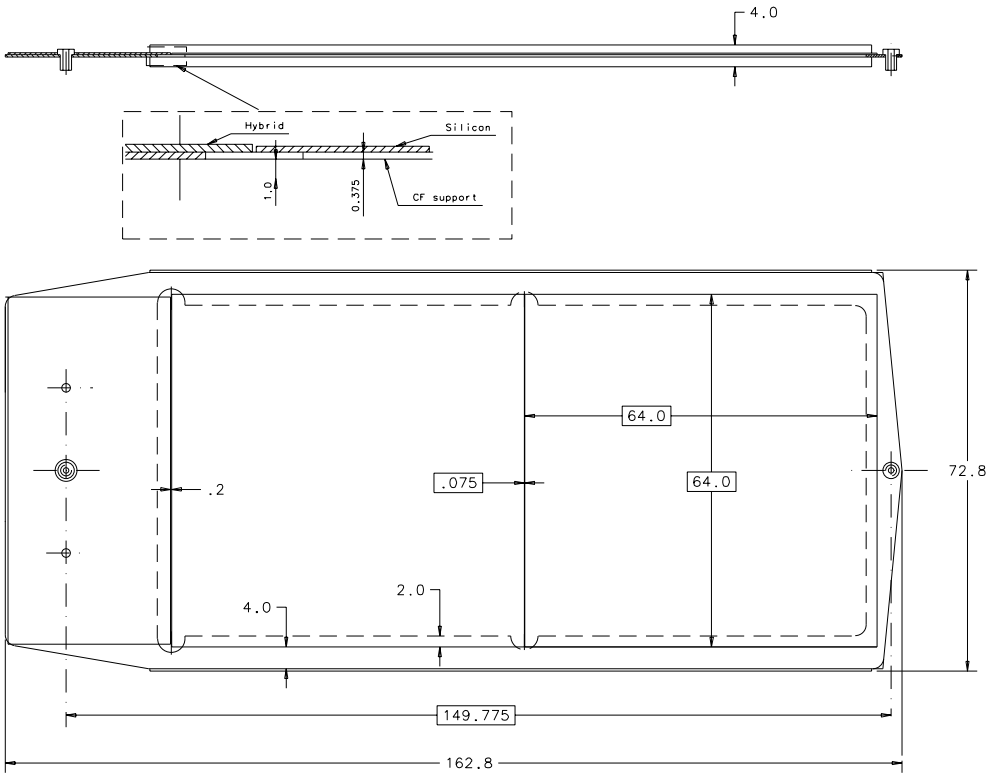

Fig. 3.68: Technical drawing of a single-sided barrel module.

The thickness is imposed by thermal requirements and by manufacturing constraints. In order to increase the mechanical stiffness, the frame has two rails on the long edges ($0.5 \times 4 \times 130$ mm^3), which are orthogonal to the detector plane. These rails, protruding 2 mm on both sides with respect to the detector face, also protect the bonding wires and allow easier handling and transportation of the modules.

Positioning bushings are placed at both ends of the CF frame, defining the main axis of the reference frame for the alignment.

The detectors are aligned and glued head-to-head, leaving about 100 μm between the detector edges to be filled with glue.

Pairs of detectors are glued on top of the CF frame with a 60 μm thick layer of glue. The surface of contact between the detectors and the CF frame is large enough (2×125 mm^2) to guarantee an efficient removal of the heat generated in the silicon after heavy irradiation. The clearance, 4 mm on each side, between the bonding pads and the stiffening rails is large enough to allow an easy micro-bonding path for most commercially available machines. For the same reason, notches are also machined on the frame at the position of the detector joint (see Fig. 3.68).

The read-out hybrid is glued directly to the CF frame. The positioning bushings are used to align the bonding pads of the pitch adapter with respect to the bonding pads of the detectors, making the automatic bonding procedure easier. To improve the thermal contact between the CF frame and the cold ledge of the cooling system two small plastic screws in the hybrid region are foreseen.

3.6.4 Double-sided barrel modules

Double-sided barrel modules are very similar to the single-sided ones (see Fig. 3.69). The outer dimensions of the CF support frame and the precision bushings are identical, while the material thickness is increased to 0.5 mm for better heat load convection.

Detectors are positioned on both sides of the frame: in both cases the ohmic side is located towards the frame.

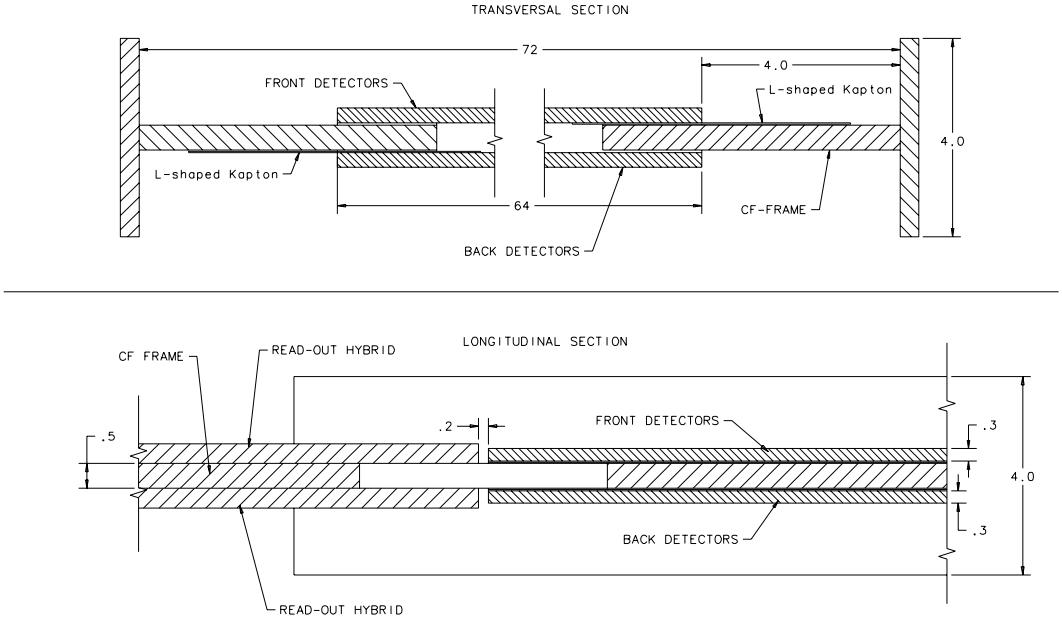

Fig. 3.69: Technical drawing (side-view) of a double-sided barrel module.

The detector pairs are biased and read-out independently through two hybrids one being glued on each side of the CF frame. In order to bring the bias contact to the detector ohmic side, a small L-shaped kapton foil, metallized on the side facing the detectors, is connected with electrically conductive glue to the back side of each pair (Fig. 3.70). The kapton foil is 25 μm thick, including the thin metal layer.

The short side of the L-shaped kapton protrudes 3 mm from the detector edge, leaving enough space for soldering.

Table 3.15 shows the weight breakdown of the modules. The corresponding gravitational sagitta is less than 3 μm.

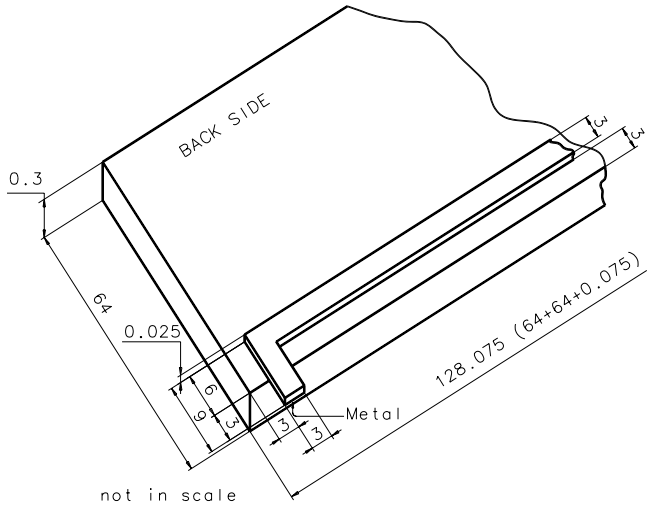

Fig. 3.70: L-shaped Kapton for the double-sided barrel bias.

Table 3.15: Weight of a single-sided and a double-sided barrel module

Elements	Single-sided (gr)	Double sided (gr)
C.F. frame	3.4	4.5
Detectors	5.4	10.8
Bushes	0.1	0.1
L-shaped Kapton	0.0	0.0
Glue	0.37	0.74
Total weight	9.27	16.22

3.6.5 Single-sided end-cap detector modules

On account of the geometrical configuration of the end-cap disks, five different module designs are needed, of which two are single-sided and three double-sided.

The single-sided modules consist of two wedge-shaped detectors of differing dimensions glued together and supported by a CF frame. This frame also holds the front-end electronics hybrid and inserts used as reference points for the assembly phase and to fix precisely the module onto the disk. Because of the mechanical constraints of the disk structure the hybrid is placed on either the narrow or the wider side of the wedge-shaped detector. This position is governed by the need to bring the active silicon to the inner and outer radii and the preference for placing the electronics at the greatest possible radii.

A perspective view of an end-cap single-sided module, with the front-end electronics hybrid at the narrow end of the detector is shown in Fig. 3.71. The other single-sided modules differ only in the detector dimensions and in the location of the hybrid.

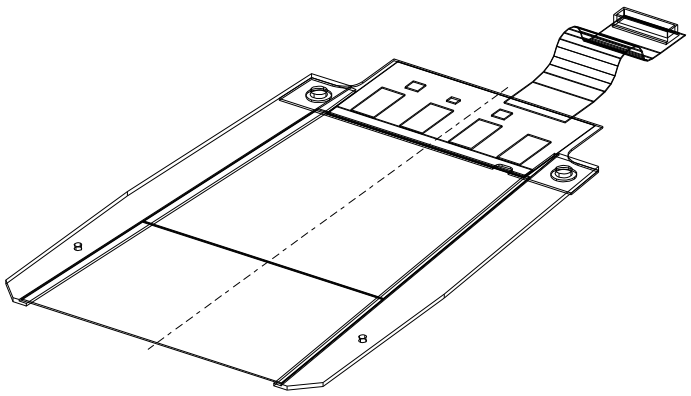

Fig. 3.71: Perspective view of a single-sided end-cap module.

The detector sensors are aligned, glued head-on and then glued to the CF frame. The side-rails of the frame are precisely machined to house the detector leaving just enough space for the alignment operation. They include local notches to allow clearance at the junction between the two sensors where excess glue is present. The bias connections are made by bonding between a pad on the back of the hybrid to the ohmic side of the detector.

The front-end electronics hybrid is thermally coupled to the CF via a high-conductivity glue and physically separated from the detector to reduce the heat propagation from the read-out chips into the silicon.

The detectors make thermal contact to the side-rails of the CF frame through one face, in two bands along their edges. The width of the contact band, enabling detector cooling, is of the order of 1.7 mm. Since the junction must withstand several hundred volts, an additional electrical insulation layer of polyimide film is placed between the two parts. A thermally conductive, electrically insulating adhesive is used. Thermally induced forces due to CTE differences between the frame and silicon are taken up at this layer. The adhesive plane is at the neutral axis of the side-rail to avoid distortion.

The CF frame consists of three parts which are positioned and glued together in a jig. The heat path does not go through the glued joints but directly to the supporting ring at the module fixing points. The side-rail parts are made of of seven layers of high modulus, high thermal conductivity unidirectional fiber prepreg. The side-rails have sufficient rigidity and do not need further stiffening. The hybrid part of the frame is made up of three layers of similar material. The Amoco K1100x carbon fiber/Fiberite 954-2A cyanate ester resin system is used. A cyanate ester resin matrix is used because of its superior stability at different ambient moisture levels. Since they are made in several parts the number of plies as well as fiber direction and thickness in the frames can be more easily arranged for optimum thermal conductivity. This method is also economical in the usage of the expensive fiber prepreg. A thermally conducting compound is used at the fixing point thermal interfaces.

3.6.6 Double-sided end-cap detector modules

The end-cap disks use three different types of double-sided modules. That used on the innermost ring has one sensor depth while all others are made up of two sensors daisy-chained together. The detector sensors of both sides are read out and biased independently through two hybrids.

The preferred technique is to construct two single-sided detector modules, one of which measures the azimuth and a second the radial co-ordinate. This second detector uses double metal detector sensors but on an identical CF frame. These two modules are glued together at the end of the construction process after having been fully tested and characterized as individual units. This allows a much reduced final rejection rate since for most of the process we are dealing with a single-sided sensor module with an accompanying reduction in complexity of jigs and procedure.

Studies are also proceeding using the option of constructing these modules by gluing the detectors to a similar frame modified to accept sensors on both sides at each radial position. The assembly and bonding procedure is similar to that used to produce the barrel double-sided detector modules but with differing geometry. Here the increased risk and complexity would need to be exceeded by the gains in the material budget.

Figure 3.72 shows a perspective view of an end-cap double-sided module.

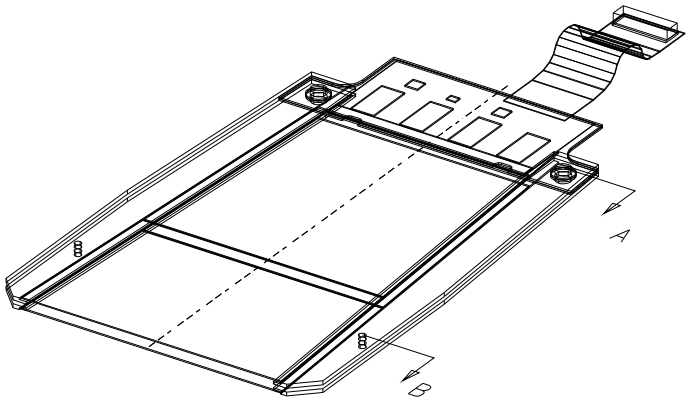

Fig. 3.72: Perspective view of a double-sided end-cap module.

3.6.7 Cooling performance of the detector modules

There are two main reasons why irradiated silicon detectors have to be cooled. First, to avoid reverse annealing in order to limit the increase in depletion voltage with irradiation fluence. This is obtained by keeping the silicon detectors below 0 °C except for short maintenance periods. Second, after irradiation the leakage current in silicon detectors produces a significant amount of heat which increases exponentially with temperature. Given that the power which the cooling system can remove increases only linearly with temperature, there is the potential danger of the power dissipated by the silicon increasing faster than the power which the cooling system can remove. This uncontrolled increase in temperature and leakage current is called 'thermal runaway'. The requirement to avoid it can not be translated into a simple temperature limit, but it is related to the irradiation fluence and the thermal behavior of the detector module, in particular the thermal resistances of the heat paths on the module. It turns out that the risk of thermal runaway imposes the strongest limits on the cooling performance of the detector modules.

The power dissipated by an overdepleted silicon detector of 300 μm thickness and 80 cm^2 surface, irradiated with the LHC dose of $2 \cdot 10^{14}$ cm^{-2}, can be estimated as

$$P_{Si}(T, U_{bias}) \approx U_{bias} \cdot 5000 \, \frac{\mathrm{A}}{\mathrm{K}^2} \cdot T^2 \cdot \exp(-7020.7 \ \mathrm{K}/T). \tag{3.10}$$

On the other hand the temperature of the silicon is a linear function of the power P_{Si} dissipated by the silicon and the power dissipated by the electronics hybrid P_{Hyb}:

$$T_{Si} = k_1 \cdot P_{Si} + k_2 \cdot P_{Hyb} + T_{coolant}. \tag{3.11}$$

In order to study the thermal stability of the detectors, the coefficients k_1 and k_2 have to be measured for the given module design. This has been done in two separate studies for the barrel and the end-cap modules.

In the end-cap case the measurements were performed on the full-size SiF1 milestone prototype disk [3-31]. A detector module was equipped with 16 thermistors (see Fig. 3.73) to measure the temperature distribution over the module for various power dissipations in the silicon and in the front-end hybrid. The heat load in the silicon was simulated by feeding a current through the strip metalizations while the hybrid heat load was simulated by a resistor. The heat load of the neighboring modules was also simulated by resistors.

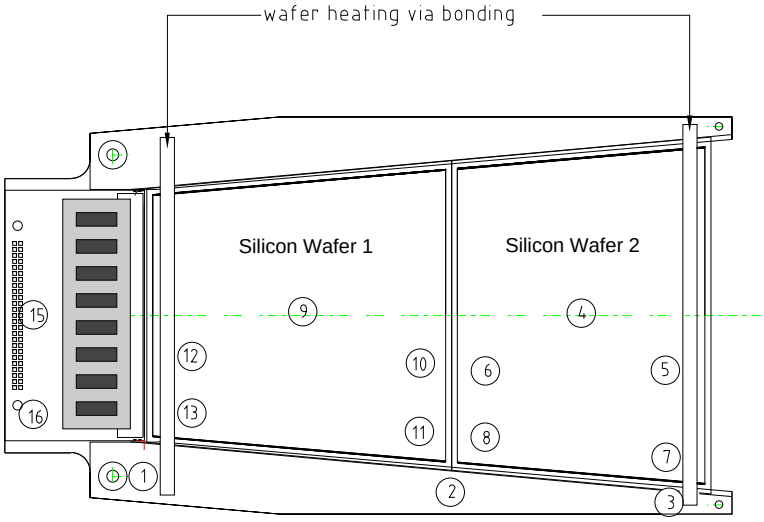

Fig. 3.73: Layout of the end-cap test module used for the temperature measurements. Two dummy detector wafers are glued onto the side-rails of a carbon fiber frame using standard epoxy and a layer of Kapton tape. The electronics hybrid is replaced by a heat load resistor. The module has all the wire bonds of a real module. The power dissipation of the silicon was simulated by feeding a current through the metallization of the strips. The numbers in circles indicate the positions and channel numbers of the thermistors used for the temperature measurements.

Figure 3.74 shows the temperature difference between the average fluid temperature and the temperatures on the module, plotted against the power dissipated in the silicon sensors, where the hybrid power has been kept at 2 W.

From these measurements a worst-case estimate for the silicon temperature in the end-cap has been derived:

$$T_{Si} = 5.5\ \frac{\mathrm{K}}{\mathrm{W}} \cdot P_{Si} + 2.5\ \frac{\mathrm{K}}{\mathrm{W}} \cdot P_{Hyb} + T_{coolant}. \tag{3.12}$$

In the barrel case the measurements were performed on modules of the SiB1 milestone, which are 54 mm wide and have contact to a cooling pipe on the hybrid side of the module (see Section 3.9). The heat loads of the electronics and the silicon detectors have been simulated by heating foils. A model has been worked out in which the module is divided into several regions (see Fig. 3.75). This model takes into consideration both conductive heat exchange ($\dot{Q}_c$) between two regions with a temperature difference ΔT and radiative heat exchange ($\dot{Q}_r$) of a

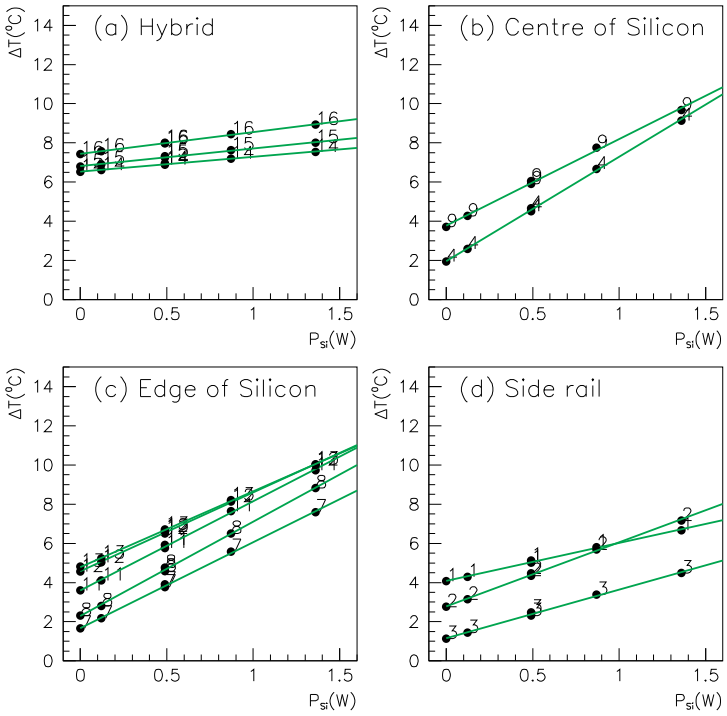

Fig. 3.74: Temperatures measured at various positions on the end-cap module relative to the average cooling fluid temperature as a function of the power dissipation of the silicon for a fixed hybrid power of 2 W. Each line corresponds to a measurement point on the module (see Fig. 3.73).

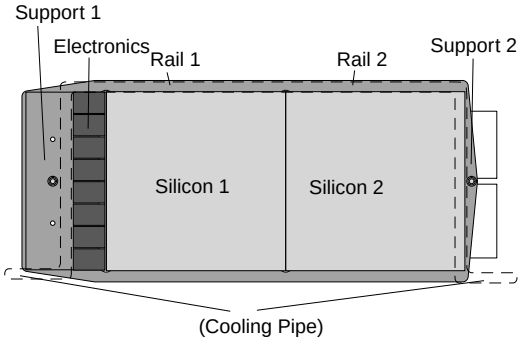

Fig. 3.75: The Si-Barrel module is divided into seven regions to describe the heat fluxes: Silicon 1&2, Side-Rails 1&2, Supports 1&2 and the Electronics.

region at temperature T with the surrounding at temperature T_s. These are described by heat transfer coefficients $k = \Delta T/\dot{Q}_c$ and coefficients $c = \dot{Q}_r/(\sigma(T^4 - T_s^4))$, which are related to the geometry and the thermal properties of the components of the module. Here σ is the Boltzmann constant. In particular this model is used to extrapolate the measurements to the proposed V4 design of the modules in which the far end of the module is also connected to the cooling pipe (Fig. 3.75).

To determine the coefficients k and c the temperature distribution on the module has been measured for various heat loads on the silicon detectors and the read-out hybrid, varying also the ambient and cooling fluid temperatures. An iterative procedure has been used to solve the network of conductive and radiative heat flows and Fig 3.76 shows the resulting 15 coefficients. The contribution of radiative heat exchange is small and does not exceed 10% under reasonable operating conditions. The influence of convection is found to be negligible.

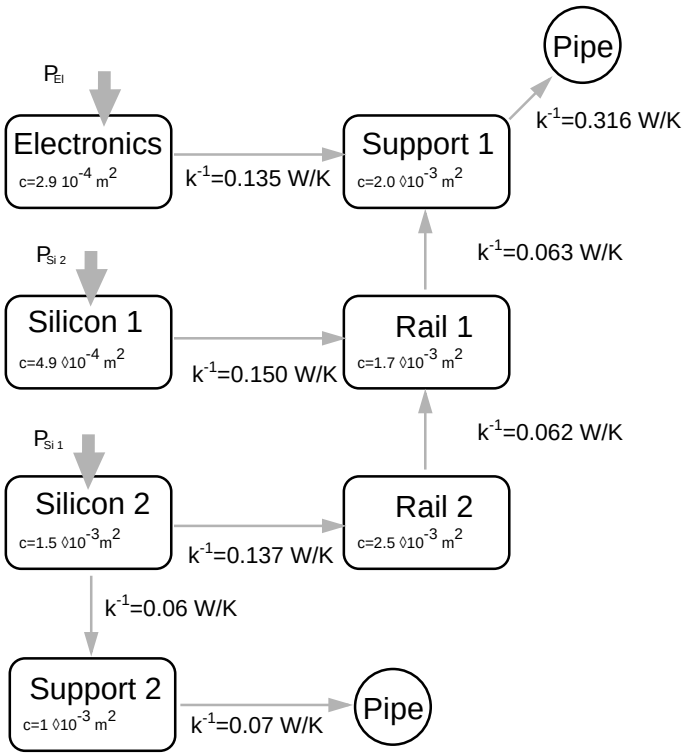

Fig. 3.76: Network describing the heat flow in the Si-barrel module (given the symmetry of the module only one half of the module is considered). For the calculations the worst-case assumption was made, where the surrounding temperature of the module is equal to the warmest part of the module, namely the electronics.

These results can be used in a similar way as in the end-cap case to plot the temperature difference between cooling fluid and each module region against the power dissipated in the silicon sensors (Fig. 3.77).

It can be seen that Silicon 1 shows the highest increase of temperature with silicon power dissipation. Thus, for the barrel we find as the worst case

$$T_{Si} = 5.7\ \frac{\mathrm{K}}{\mathrm{W}} \cdot P_{Si} + 2.2\ \frac{\mathrm{K}}{\mathrm{W}} \cdot P_{Hyb} + T_{coolant}, \tag{3.13}$$

which is quite similar to the result for the end-cap.

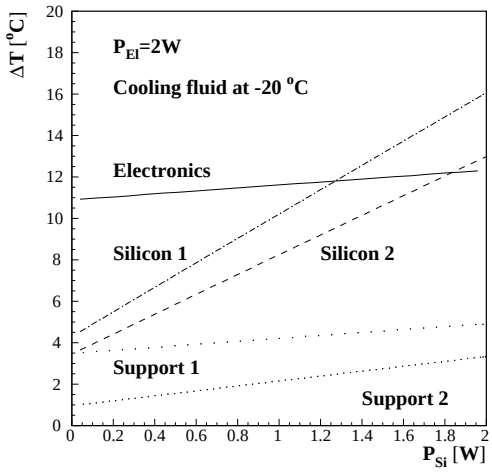

Fig. 3.77: Calculated temperature difference ΔT between the cooling fluid and the module regions as function of the total power disspated in the silicon wafers. The electronics power is kept constant at 2 W.

A stable working regime where thermal runaway cannot occur is found by comparing the power generated in the silicon to the power that can be removed from the sensors at a given temperature. Figures 3.78 and 3.79 show this for the end-cap and the barrel module, respectively. It can be seen that in both cases, taking into account a safety factor of two on the silicon power dissipation, the cooling fluid temperature at the module needs to be -20 °C in order to guarantee safe operation.

3.6.8 The module construction

The assembly procedure which will be used to build both barrel and end-cap modules is based on experience we acquired during the construction of the 1997 milestone. In order to guarantee the required precision while keeping the construction procedure simple, a set of jigs specially designed for this purpose will be used and all the gluing procedures will be done under the constant control of a co-ordinate measuring machine able to determine the position of a three-dimensional point with a precision of at least 3 μm. A CCD camera, coupled to the measuring head of the machine, will allow precise viewing on a TV monitor of the detector's reference marks. To speed up the assembly procedures we plan to use a co-ordinate measuring machine which can contain several assembly jigs on its working surface. In this way we will be able to reduce considerably the deadtime which the curing of the glue will inevitably introduce between the various steps of the process, by pipelining the construction procedures as much as possible.

The assembly procedure consists basically of five steps:

- assembly of the carbon fiber frame;
- alignment and gluing of the detector;
- gluing of the electronics;
- micro-bonding;
- testing.

The single assembly steps are similar for barrel and end-cap modules and are described in the following section.

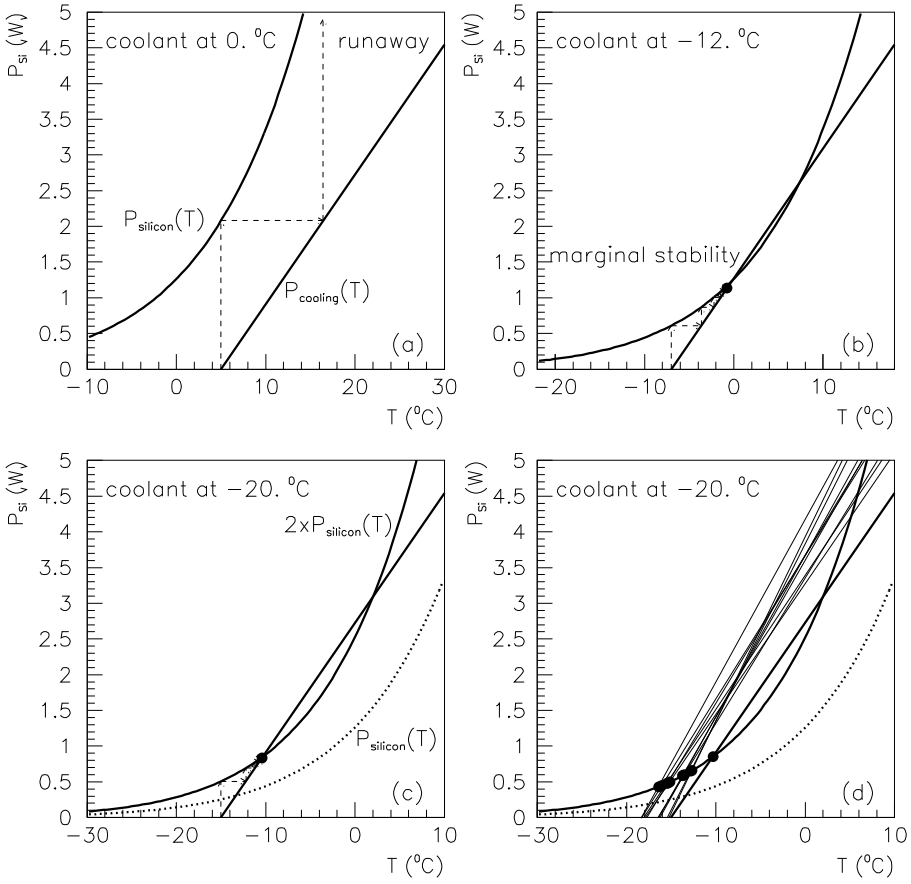

Fig. 3.78: Silicon temperature on the end-cap module for different operating conditions. The thick curve shows the power dissipation of the silicon as a function of temperature, assuming a bias voltage of $U_{bias} = 500$ V. The thick straight line shows the power that the cooling system removes for a given temperature on the silicon. A hybrid power dissipation of 2 W is assumed. (a) coolant temperature 0 °C: the silicon temperature increases steadily (thermal runaway), (b) coolant temperature −12 °C: the equilibrium temperature of the silicon is slightly below 0 °C, the stability is marginal, (c) assuming twice the power dissipation of the silicon and a coolant temperature of −20 °C: the equilibrium temperature of the silicon is around −10 °C (for comparison the nominal power dissipation of the silicon is shown as the dotted line), (d) same as (c), but now the (thin) lines for all the measurement points on the silicon are included.

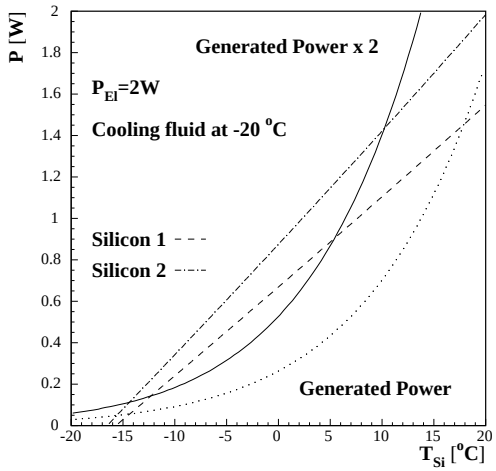

Fig. 3.79: Thermal equilibrium points for the silicon detectors of the barrel module at a coolant temperature of $-20°$C and a constant electronics power of 2 W. The straight lines are the heat that goes from one half of each silicon sensor into the side-rail. The power generation curve (dotted) therefore shows the heat that is dissipated in a quarter of the total silicon area. The solid curve includes a safety factor of two on the power dissipation of the silicon.

3.6.8.1 Assembly procedure and jigs

The assembly steps will now be described in more detail.

Production of the module frames

The mechanical frames of the modules are made out of CF with high thermal conductivity to achieve:

- low mass
- high stiffness
- efficient heat removal

The prepreg was supplied by 'Fiberite Europe', the fibers in the prepreg are unidirectional and of the type K1100X Amoco. They are embedded in the Fiberite 954-2A cyanate ester resin which has high stability at different ambient moisture levels. The fibers have a nominal heat conductivity of 1100 W/mK. The prepreg comes in sheets of 63 and 125 μm thickness.

The CF parts of the modules are either made out of three (forward hybrid carrier), five (barrel modules) or seven (forward side-rails) layers of prepreg. The fiber orientation in the layers is $0°$ and $90°$ and the layers have to be symmetric with respect to the plane running in the middle of the parts.

For curing the prepreg is put in between several layers of release and bleeder films as shown in Fig. 3.80a. Vacuum is applied and the plate is left to cure in an auto-clave. The cure cycle is shown in Fig. 3.80b and consists mainly of a plateau at 180 °C that is held for four hours preceded and followed by ramps to ambient temperature. During the cure cycle a pressure of 6 bar is applied to the plate.

Properties of the milestone modules

Some properties of the plates that were manufactured for the modules of the SiB1 milestone are summarized in Table 3.16.

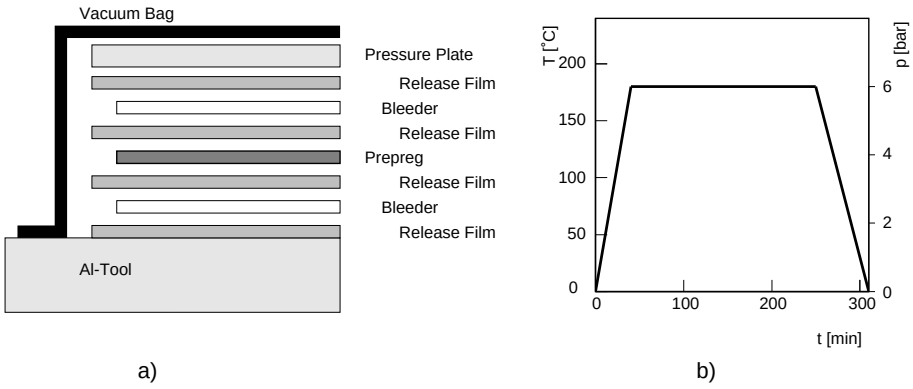

Fig. 3.80: Curing of the prepreg. a) layup; b) cure cycle.

Table 3.16: Properties of the CF plates for the SiB1 milestone

size	780×630 mm^2
thickness	0.50–0.55 mm
density	900 g/m^2
fiber v olume	61%
thermal conductivity (0 °C)	400–500 W/mK

The parts for the frames are cut out of the CF plate by a water-jet. This technique is fast and thus cheap and allows for very thin gaps between the tiles and thus a very effective use is made of the CF.

Alignment and gluing of the detectors

Specific jigs are used to join the pair of detectors together and to the CF frame, which also incorporates the precision bushings and the hybrids. The detectors are glued on top of the CF frame with a thin layer of high thermal conductivity, electrically insulating glue.

For the positioning of the detectors we have used as reference the precision bushings. Precise fiducial marks engraved in the detectors are used to determine the relative position of the detectors between them and with respect to the precision bushings. Two approaches have been used for the positioning of a single-sided module:

1. align and glue head-to-head the two detectors relative to each other and subsequently align and glue this pair onto the CF frame relative to the precision bushings;

2. align and glue the two detectors independently to the CF frame relative to the precision bushings.

The first approach, proposed for both barrel and end-cap, needs two different jigs and is performed in two steps. The gluing of two detectors head-on is an operation that requires an alignment precision which should be much better than the intrinsic resolution of the detector. In our case, the maximum deviation of a strip with respect to the connected one on the other wafer should be of the order of 3–5 μm.

The first step consists of placing a tiny layer of glue on the facing edge of the two detectors by simply dipping them in a $\sim$ 50 μm groove filled with glue. After that, one of the detectors is held in a fixed position on the jig, while the other one can be moved in x, y and ϕ in order to be aligned with respect to the first. The one used for the barrel detectors is very similar with small differences due to the rectangular geometry.

To align the two detectors we first measure the position of four reference marks on the fixed detector. The co-ordinate measuring machine then determines the local co-ordinate system by fitting a straight line to the measured marks. At this point the CCD camera is automatically placed by the measuring machine at the position where the reference marks of the second movable detector should be placed, according to the initial offset parameters which characterize the module dimensions. The detector is then moved, using the micro-metric gauges, till the reference marks are in the correct position. When both are glued together, the silicon marks have a nominal distance of 555 μm, leaving a gap of 60 μm between the detector edges that are filled with glue.

In the second step the detector pair is glued to the CF frame using the jig shown in Fig. 3.81.

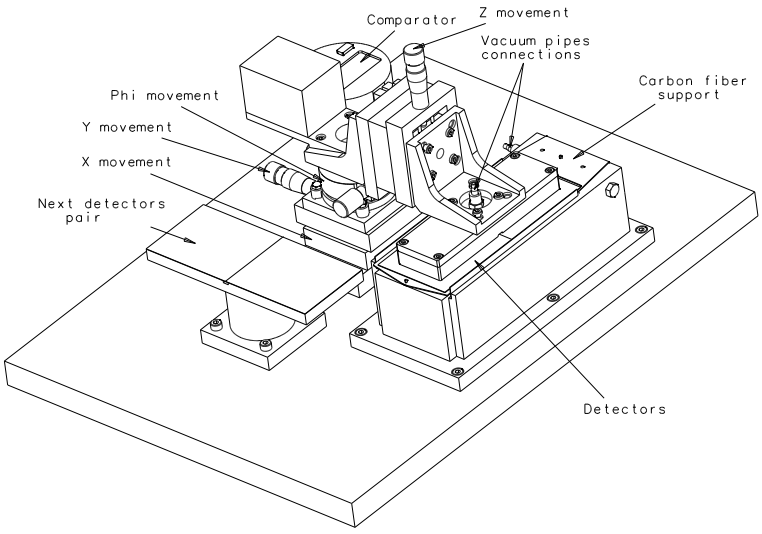

Fig. 3.81: Jig used to glue a detector pair onto the CF frame.

The CF frame is placed precisely on a support using precision bushings and applying vacuum. A movable arm, holding the glued detector pair with vacuum, allows the precise positioning with respect to the precision bushings by micro-metric movements in x,y,z, and ϕ. The movement in z controls the height of the detectors with respect to the carbon fiber frames. As for the head-on gluing the co-ordinate measuring machine find a local co-ordinate system which this time is determined by fitting a line passing through the center of the two precision bushings of the carbon fiber support. The measuring machine then moves the CCD camera to the nominal position where the reference marks on the detector should be placed and the detector is then moved to the correct position.

About 60 μm are left between the detector and the CF frame to be filled with glue. The glue is distributed along a well-defined path on the carbon fiber frame with an automatic dispenser controlled by computer. The planarity of the module is imposed by the parallelism between the plane of the detectors in the holding arm and the plane of the base holding the carbon fiber frame. A planarity of a module better than 10 μm has been reached.

The jig used in the second approach, proposed only for the barrel, is shown in Fig. 3.82.

It consists of a table on which the CF frame is fixed with a screw. Two other tables are used to hold the silicon wafers. These tables also support the side-rails of the CF frame. The silicon is held on the table by a vacuum, while the side-rails can slide freely on the Teflon support. The table is manufactured in a way such that there is a gap of 60 μm between the carbon fiber and the silicon for the glue. The tables for the silicon can be moved in the x- and y-direction and turned around the axis normal to the wafers.

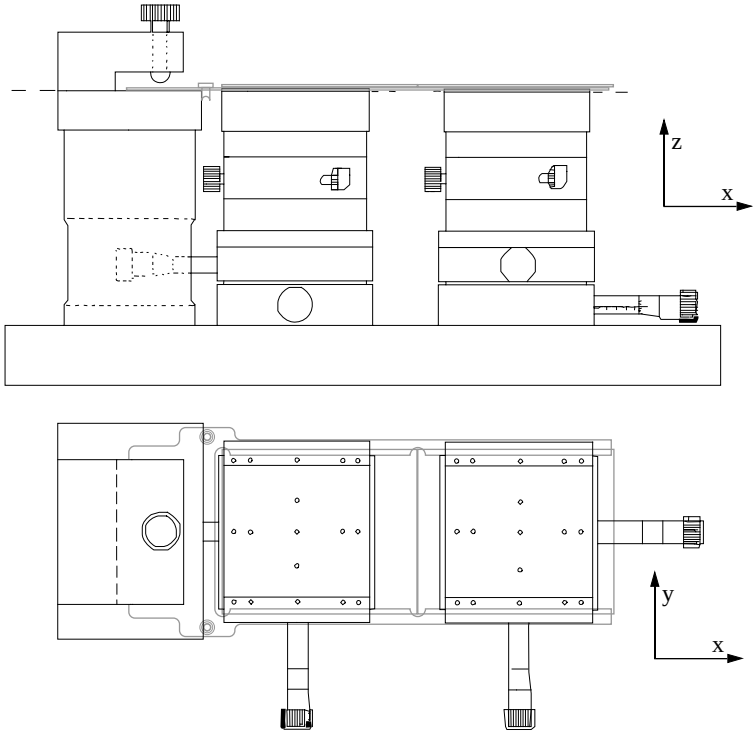

Fig. 3.82: Jig used to glue the silicon on the carbon fiber support.

Only the first approach has been used for assembling the double-sided modules, involving the following steps:

- prepare the two pairs of detectors aligned and glued head-to-head, one made of SS detectors and the other of SSDM detectors;
- glue the L-shaped Kapton strip to the back-plane;
- glue and align the SS detectors pair on the top side of CF frame with respect to the precision bushing, as described before;
- turn the CF frame over, align and glue the SSDM detectors pair on it.

A co-ordinate system is defined by the precision bushings as shown in Fig. 3.83. The silicon detectors are aligned in this co-ordinate system at the positions given in the same figure.

For the end-cap modules, instead, we propose a different approach: first two separate single-sided modules are completely assembled, including the bonding and testing, then they are glued back-to-back. This final step will require an assembly jig very similar to the one used to glue the detector pair to the CF frame. The only differences is in the design of the base that should be shaped in such a way as to be able to hold an assembled single-sided module turned over and in the holding arm that should keep the other module suspended without damaging the bondings.

The gluing procedure consists in placing an overturned module on the base, then placing a small amount of glue on the CF frame surface; at this point the co-ordinate measuring machine will define a co-ordinate system using the precision inserts of the overturned module. Finally the other module will be moved into the correct position and lowered until the CF frame is in contact with the glue.

Gluing of the hybrid

The gluing of the hybrid on the CF frame does not require the high precision needed in the detector alignment. The positioning can therefore either be performed again under the co-ordinate measuring machine, using the bonding pads of the pitch adapter as reference markers

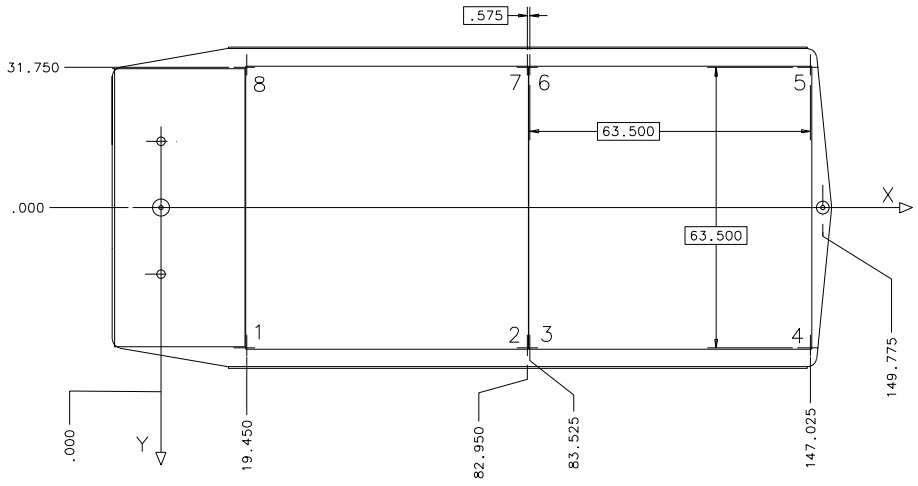

Fig. 3.83: Nominal positions of the fiducial marks with respect to the precision bushings.

for the positioning of the hybrid with respect to the silicon detectors, or using grooves that hold the hybrid and the support in the correct position without further adjustments. A maximum misalignment between the bonding pads of about 20 μm can be tolerated. To guarantee a good thermal contact between the front-end chips and the cooling circuit a high thermal conductivity glue is uniformly distributed under the entire hybrid surface.

Micro-bonding

About 2000 (4000) micro-bonds are needed for the electrical connection of one single- (double)-sided module, a few (about half) of them being on the backside for a single (double) sided module. Special, but simple, vacuum jigs have been built that support the modules during the bonding.

3.6.9 Quality control and tests

Once the module assembly is complete the module undergoes a full quality control test. It consists essentially of:

- survey of detector position. This is done by measuring the reference mark positions on each detector with respect to precision bushings and comparing them with the nominal positions. Deviations from the nominal values should be inside tolerances.
- optical inspection. No evident unglued and/or unbonded zone should exist. Occasional mechanical damage occurred during assembling or handling should be noted and action should be taken.

After that, a module is connected to a test station for a complete electrical and functional check. The test station has a read-out system and a movable x-y table on which the detector is mounted under an infrared laser spot. The read-out system is a standard Si-strip Tracker read-out chain, consisting of the optical link, the FED and FEC modules located in a VME crate connected to computer, and power supplies to bias detectors and front-end hybrids. A computer program synchronizes the movement of the table, the flashing of the laser and the data taking.

The laser wavelength is 1060 nm, which allows the laser light to produce electron-hole pairs uniformly in the full silicon depth, thus simulating, apart from the Landau-like charge fluctuations, a minimum ionizing particle crossing.

The measurements to be done with this system are:

- I–V curves
- Noise measurements
- Laser scans to detect broken/unbonded channels, checking the correspondence with bad channels known from detector tests and bonding maps

This procedure has already been used for the milestone modules.

All the assembling and testing information concerning a module is stored in a database, including information concerning detectors and hybrids used. For each module, the database contains:

- depletion voltage and total leakage current for each detector,
- bad and/or dead strips on detector(s),
- hybrid serial number with an indication of bad and/or dead channels,
- all geometrical parameters together with the complete assembly record,
- bonding map with an indication of bad and/or not-bonded connections,
- operation voltage and total leakage current,
- pedestal maps with an indication of the not working/broken channels.

This information is to be used in the general alignment and track reconstruction programs.

3.7 The Support Structure

3.7.1 General requirements and constraints

To achieve the measuring accuracy envisaged for the Silicon Tracker, the primary requirement on the support structure is to maintain the detector modules in stable, precisely defined positions. However, the amount of material introduced into the Tracker region should be as small as possible. Therefore, low mass combined with structural rigidity are the most important considerations.

It is envisaged that the final inter-alignment of the detector modules, as well as the overall alignment of the SST and MSGC Tracker with respect to each other, will be done by using the measurements of the tracks actually detected by the system. For reasonable statistical samples, the successful convergence of such a procedure requires that the starting value of the position of each strip in space be known to within 100 microns. Therefore, gravitational sagging of the structure due to the weight of detectors, cables etc., distortions resulting from variable mechanical and thermal loads occurring during handling, assembly, transport and operation, as well as long term distortions due to aging, stress-release, moisture pick-up etc. should be kept within these limits. Furthermore, the mechanical structure should allow an alignment and survey procedure during the mounting of the modules, resulting in significantly more precise knowledge of the relative initial strip positions (better than 10 μm) and should provide for accurate survey and monitoring at various stages during the lifetime of the experiment.

The mechanics should also incorporate an efficient cooling system, able to maintain the temperature of the SST at $-10\,^{\circ}$C. Finally, the support structure should permit a safe, simple, and efficient assembly, disassembly, survey, and maintenance of the detector. Its fabrication procedure should be low in cost, respecting the existing budgetary constraints.

3.7.2 General layout and choice of material

The overall layout of the SST has already been shown (Fig. 3.1). In the central part (barrel) ten low mass shells in the form of half-cylinders are used to support the detector modules and their associated services (cables, optical fibers, cooling pipes). The four innermost shells are shorter

to allow for the mini end-caps complementing the barrel cylinders. CF disks form the support structures both for the mini end-cap and for the end-caps.

To achieve the required structural rigidity and conform to the requirement of a light, low mass structure, the shells will be made of flat unidirectional prepreg sheets of high modulus (about 500 GPa) carbon fibers embedded in a resin matrix. Reinforcing elements (ribs and rings) will be made of the same material.

Table 3.17 summarizes the characteristics of the fibers to be used: M55J has a higher modulus but is relatively brittle and will be used for structures which do not exert a lot of strain to the fibers. (e.g. the half-cylinder shells). Structures which require considerable bending of the fibers will be made out of M46J which is less brittle and has a lower modulus.

Table 3.18 shows the mechanical properties of prepreg material with M55J fibers embedded in a cyanate ester resin.

Table 3.17: Properties of the CF to be used in the barrel

Material	Tensile modulus (Gpa)	Tensile strength (Mpa)	Strain %
M46J	434	4216	1.84
M55J	538	3926	0.50

Table 3.18: Mechanical properties of 954-3 cyanate ester prepreg, the curing temperature is 180 °C

Designation	0° Tensile strength R.T. (MPa)	0° tensile modulus R.T. (GPa)	90° tensile strength R.T. (MPa)
M55J	2180	324	35

3.7.3 The cooling system

There are several sources of heat in the SST: the silicon detectors themselves, front-end hybrids, optical fiber links, communication and control units (CCUs). The foreseen cooling system is based on a heat transfer fluid running through a system of small-diameter pipes embedded in the structure and in good thermal contact with the power dissipating elements. The choice of the fluid is important for the overall performance of the system and is presently under investigation.

Table 3.19 shows a comparison of the properties of three heat transfer fluids which might be considered. In the comparison of these fluids the Hydrofluoroether (HFE) has by far the lowest viscosity, which is also quite stable in the range from +20 °C to −40 °C. However, in heat capacity and heat conductivity HFE is inferior to the other fluids. In order to compare the cooling performance of the different fluids, one can compute the resulting flow and temperature gradients along and perpendicular to the pipe for a fixed pressure drop. Assuming a pressure drop of $\Delta p = 1$ bar over a pipe of length $l = 1$ m and inner diameter $d = 2$ mm, one finds the values indicated in Table 3.19. At +20 °C the resulting flow is very similar for all fluids. At −20 °C, however, the flow of the ethanol-water mixture is reduced by a factor 10, while the flow for the other fluids does not change very much. The small flow of the ethanol-water mixture at −20 °C implies large temperature gradients along and perpendicular to the pipe, which rules out this fluid for our application. At −20 °C HFE and SYLTHERM show a similar temperature gradient along the pipe, slightly higher for SYLTHERM. However, in the gradient perpendicular to the pipe the difference is more pronounced, HFE having a temperature gradient which is 30% smaller than that of SYLTHERM.

Our own measurement of the heat capacity of 3M-HFE-7100 gave a value which is $\approx 30\%$ higher than the specifications. Assuming this value, the temperature gradients for HFE are even smaller. As can be seen from the Table, there is no dramatic change in the properties of HFE even down to -40 °C (the freezing point is -153 °C). This means that a cooling system based on HFE is quite flexible in terms of operating temperature.

Table 3.19: Comparison of different cooling fluids. The value of the heat capacity for 3M-HFE-7100, quoted here from the company's specifications, is inconsistent with our measurements which give $c_p = (1555 \pm 70)$ J/(kg·K) at ≈ 23 °C. Assuming this value one finds $(T_{out} - T_{in})/P = 0.044(0.050, 0.054)$ K/W and $\Delta T_{perp} \cdot A/P = 2.0(2.6, 3.1)$ 10^{-4}m^{2}K/W at +20 °C(-20 °C,-40 °C)

Product		3M-HFE-7100 $C_4F_9OCH_3$	SYLTHERM XLT Silicon Oil	Ethanol-water 40:60	Units
density ρ	+20 °C	1506	846	935	kg/m^3
	−20°C	1609	881	962	
	−40 °C	1660	899	974	
viscosity ν	+20 °C	0.405	1.46	2.9	10^{-6} m^2/s
	−20 °C	0.724	3.04	25.3	
	−40 °C	1.067	4.80	172.	
heat capacity c_p	+20 °C	1173	1650	4027	J/(kg · K)
	−20 °C	1093	1547	3727	
	−40 °C	1053	1494	3507	
heat conductivity λ	+20 °C	0.070	0.111	0.361	W/(m · K)
	−20 °C	0.078	0.119	0.344	
	−40 °C	0.082	0.123	0.336	
vapor pressure	+20 °C	0.21	negligible		bar
	−20 °C	0.03	negligible		
	−40 °C	0.009	negligible		
residue		< 2.0	10^6		ppm
cost		≈ 100	≈ 100		CHF/liter
for $\Delta p = 1$ bar, $l = 1$ m and $d = 2$ mm:					
flow	+20 °C	0.58	0.67	0.56	l/ min
	−20 °C	0.52	0.56	0.06	
	−40 °C	0.48	0.35	0.01	
$(T_{out} - T_{in})/P$	+20 °C	0.058	0.064	0.029	K/W
	−20 °C	0.066	0.078	0.270	
	−40°C	0.072	0.128	1.952	
$\Delta T_{perp} \cdot A/P$	+20 °C	2.2	2.7	1.4	10^{-4}m^{2}K/W
	−20 °C	2.9	4.1	20.1	
	−40 °C	3.5	7.1	209.	

Another advantage of HFE is the fact that it evaporates quickly and leaves a very small residue. Actually, HFE is commercially used as a cleaning agent. A small leak in a cooling system filled with HFE would most likely not damage other components and the quantity of fluid lost would evaporate. On the other hand the SYLTHERM silicon oil does not evaporate and it is very difficult to remove. Given the above, 3M-HFE-7100 is presently a promising candidate for the cooling fluid of the SST.

Although direct liquid phase cooling will be by far the main heat removal process, it is envisaged to have the central tracking cavity slowly flushed (one volume exchange - about 5 m^3 per 24 hours) by cold (-10 °C) dry nitrogen gas. This will prevent the accumulation of moisture and assist in establishing a uniform temperature in the SST volume.

As described in Chapter 6, the SST volume will be thermally insulated from the surrounding environment by means of a cylindrical, thermal screen and thin, thermally insulating disks placed at both ends. A preliminary performance test of the cooling system was carried out within the SiF1 milestone (see Section 3.9.2.6).

3.7.4 The barrel structure

3.7.4.1 General layout

The basic structural elements, on which the barrel modules and all their services are mounted, are semi-cylindrical panels. Each panel is formed by two thin carbon fiber (CF) skins (0.375 mm per skin) spaced by longitudinal omega-beams and internal circular rings (see Fig. 3.84 and Fig. 3.85). The spacer beams and the rings are also made of CF. Flanges at the end of each panel reinforce its strength and rigidity. They incorporate service connections, fiducial marks for the alignment and thread holes both for handling (attaching insertion and extraction tools) and for auxiliary cable supports.

Detector modules are arranged on the top and bottom of these structures in a cylindrical geometry with a tilt angle of 9°. In this way it is easy to have the active area of the detectors overlapping in z, while maintaining order in the services (cables, optical fibers, cooling pipes), thus simplifying the cabling (un-cabling) of the detector.

Each of the mini end-caps is contained in a cylinder attached to the end flange of the second barrel layer and made with the same technique as the panels (CF skins spaced by internal CF elements). Disks made from molded CF elements are positioned inside this cylinder and support the mini end-cap detector modules and services. As shown in Fig. 3.3, the modules are arranged in rings on the front and back of each disk and dead zones are avoided by the overlap of their active area both radially and azimuthally. Since the mini end-cap layout is very similar to that of the end-caps, which will be presented in detail later, we focus our attention here on the cylindrical part of the barrel.

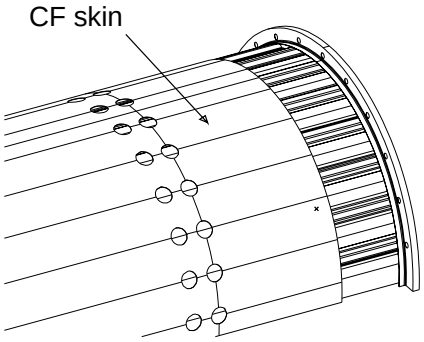

Fig. 3.84: The barrel CF-skin.

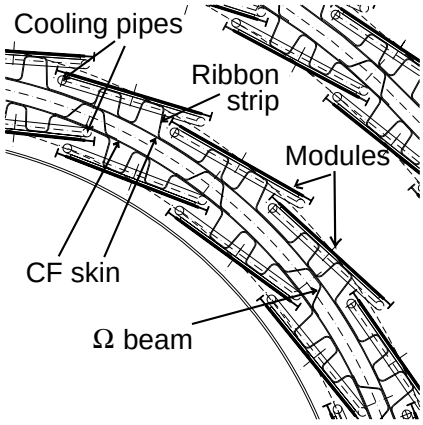

Fig. 3.85: The arrangement of the detectors on the cylindrical skin.

The modules are not mounted directly onto the panels because the latter are not sufficiently precise and do not provide an adequate cooling surface. Therefore, specially prepared mounts consisting of two elements are brought onto the panels: First, molded CF ribbon strips are glued directly onto the panel (see Fig. 3.86). They provide a precise mounting surface and have the rigidity to maintain the required positional accuracy. Flat ledges are then glued on the ribbon strips using a jig providing good control of the glue joint. The ledges are 0.5 mm thick and are made of CF composite material with high thermal conductivity (e.g. values of 400–500 W/K·m

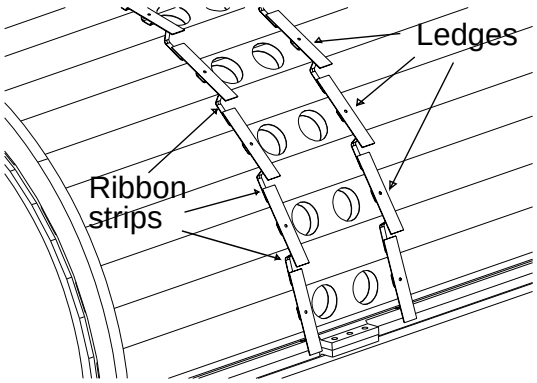

Fig. 3.86: The supports for mounting the modules on the CF skin.

have been reached using prepreg of Amoco K1100X-2K fibers embedded in a cyanate ester resin). They provide the necessary cooling surfaces.

When mounting the modules on the ledges, the front-end hybrids of modules in the same z-row are supported by ledges that are close to each other. In this configuration the two modules can share the optical link card placed on a mounting block between them (see Fig. 3.87). No stringent positional accuracy is required for the optical link.

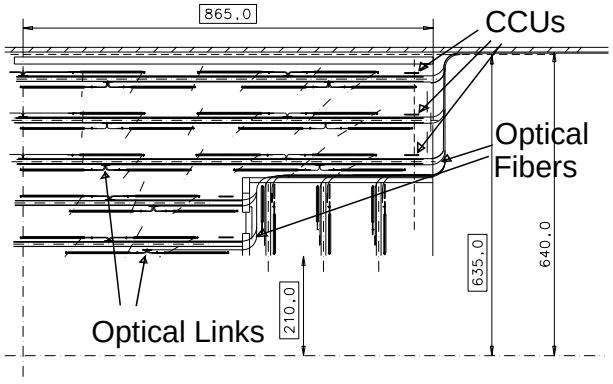

Fig. 3.87: The arrangement of the various services to the inner part of the barrel SST.

Aluminum cooling pipes (4 mm outer diameter, 0.2 mm wall thickness) are glued to the bottom of each ledge with thermally conductive epoxy, cooling the detectors and hybrids. As shown in Fig. 3.88, the pipes run longitudinally along the support panels, bend and run below a ledge, and then make another bend and continue to the next cooling area. In this way, the optical links between detector modules can also be cooled by the same pipes. On each panel end flange there are two cooling manifolds, one on the inside and the other on the outside panel surface, distributing the fluid to all panel circuits. Each manifold has one inlet and outlet and is formed by an aluminum tube (8 mm outer diameter, 0.23 mm wall thickness) bent in a circular loop (see Fig. 3.88).

All services, read-out optical fibers and optical links, power (low voltage), bias (high voltage) and timing cables, as well as the cooling pipes, are organized in longitudinal rows, avoiding crossings among cables and/or optical fibers. In this way defective cables and fibers can be individually accessed and removed at the panel ends. All services including pipes run below the detector modules and are pre-assembled onto the structure so that they do not interfere with the module mounting operations.

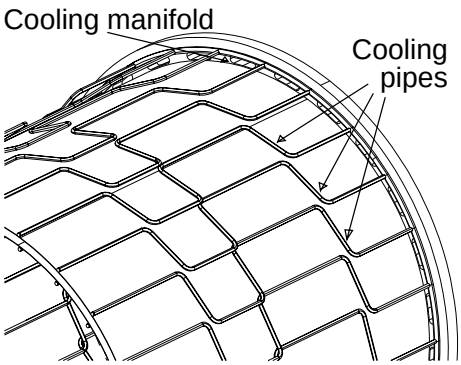

Fig. 3.88: The arrangement of the cooling pipes on the supporting CF cylinder.

Optical link and fibers

As noted above, adjacent modules on a longitudinal row are mounted with their read-out hybrids close to each other and share the optical link situated between them. The optical link is a unit controlling two or four read-out fibers, each fiber being able to read two front-end chips. The link is permanently attached to the fiber ribbon and it is mounted on a card requiring one power line, carried by the mother power cable. It can be easily plugged in or be removed from the card, while the fibers are connected via low mass connectors at the panel end flanges (for the two innermost layers the fiber optic connectors are placed at the end flange of the mini end-cap cylinder, with the fibers passing through slots in the end flange joining the layers to the mini end-cap cylinder and then running on the outside of this cylinder, as shown in Fig. 3.87). Small connectors, surface mounted on the optical link card, are used to connect it to the module hybrids with a zero insertion force. The space available below the modules is sufficient to be able to insert or extract the optical link with all the modules in position.

Timing cables

Timing signals are distributed by the Communication and Control Unit (CCU) along cables of the same length, which should be shielded as well as possible from the power and bias cables. Small individual ribbon cables are envisaged for carrying the timing signals, each of them being able to serve the two hybrids of a double-sided module or be multiplexed and serve the hybrids of two adjacent single-sided modules on the same z-row. To minimize the necessary cable length, the CCUs will be placed at both the $\pm$ z panel ends, each CCU controlling two optical links.

Power cables

Connectors mounted around the ends of the overall silicon support cylinder inside the detector volume are used to transmit the power from outside. The position of the connectors minimizes the effect of their material, while avoiding moisture condensation problems. Starting from the connector, a single Kapton cable supplies the power to the CCU and the associated optical links and hybrids along a $\pm z$ row, as illustrated in Fig. 3.87. For the two innermost layers, the mother cable powers the CCU and then splits into two parts, one going to the top and the other to the bottom of the panel. Each part splits into three tails, one powering the optical link shared by the two detector modules, the other two connecting to the module hybrids. For the outer layers a separate CCU and power cable is needed for the modules on the top and the bottom of the panel. As described above, three tails per pair of detector modules supply power to the optical links and hybrids.

Since the control of the bias voltages is placed outside of the experiment, no voltage regulators are needed inside the Tracker volume. One cable per readout hybrid is needed, i.e. one (two) cables per single- (double-)sided module. Appropriate low mass cables are commercially available.

External shielding

The whole silicon barrel Tracker is placed within an outside CF support cylinder attached to the fifth layer panels. This outside cylinder enhances the overall stiffness of the support structure and provides protection during handling. Being sufficiently conducting, it forms a Faraday cage and can be used as a common ground. Thermally, it is an insulator helping to isolate the SST from the environment. Finally, it incorporates all features needed to handle and slide the system onto the common Tracker support cylinder.

A cylindrical skin made of conducting material on an electrical insulator (Kapton) lines the inner periphery of the silicon barrel. It protects the first layer during the insertion of the beam pipe and of the pixel detector and provides electromagnetic shielding.

The structure is completed by thin sandwich disks placed at either end of the detector volume, which can be removed easily to provide access to the inside. They are thermally insulating and lined with a thin conductive layer on the outside, which can be brought into electrical contact with the inner and outer cylinders to complete the electromagnetic shielding. The disks have holes allowing the cold nitrogen flushing gas to enter and leave the detector volume.

A perspective view of the whole SST barrel detector is shown in Fig. 3.89.

3.7.4.2 Fabrication and assembly

The construction of the barrel structural elements (panels) involves the following steps:

- Molding of the individual CF panel components
- Cutting and machining them to final size
- Gluing together the panels with film adhesive
- Gluing the alignment inserts into the panel end flanges
- Gluing the module mounts (ribbon strip supports and ledges; see Fig. 3.88) onto the panels
- Gluing onto the structure the cooling pipes and mounting all spacers and holders for the services (cables, optical fibers and links etc.)

A mold in the form of a steel cylinder with outer diameter equal to the inner panel diameter (evaluated at 120 °C, the curing temperature of the CF prepreg) will be used to manufacture the CF parts. It will be machined precisely and will have a flat surface, chromium plated and polished to a mirror finish. The mold will be considerably longer than the panel, allowing simultaneous curing of both the inner and outer panel skins (the skins are thin enough that they can be subsequently shaped to conform with the 10 mm radial extent of the panel). The longitudinal omega-beams, circular ribs and the parts defining the panel edges can also be manufactured in the same autoclave cycle by adding to the mold appropriate pieces defining their shape. In this way, we not only save autoclave cycles, but the componets match each other well, since they have been prepared on the same cylindrical surface.

After molding, all parts must be cut, machined to their final shape annd sand-papered to remove resin remnants and to prepare the gluing surfaces. The mold is then used to assemble in a single step the two panels of a cylindrical layer. To this purpose all previously prepared parts are repositioned on the mold and are glued together with film adhesive at a temperature of 60–80 °C. All parts are designed to have mating fittings between them. The only parts that must be held by the mold are the mating longitudinal ribs joining the two panels to form a full cylinder. These are screwed together and clamped to the mold. A vacuum bag placed all around the cylinder assures uniform pressure distribution resulting in structural joints.

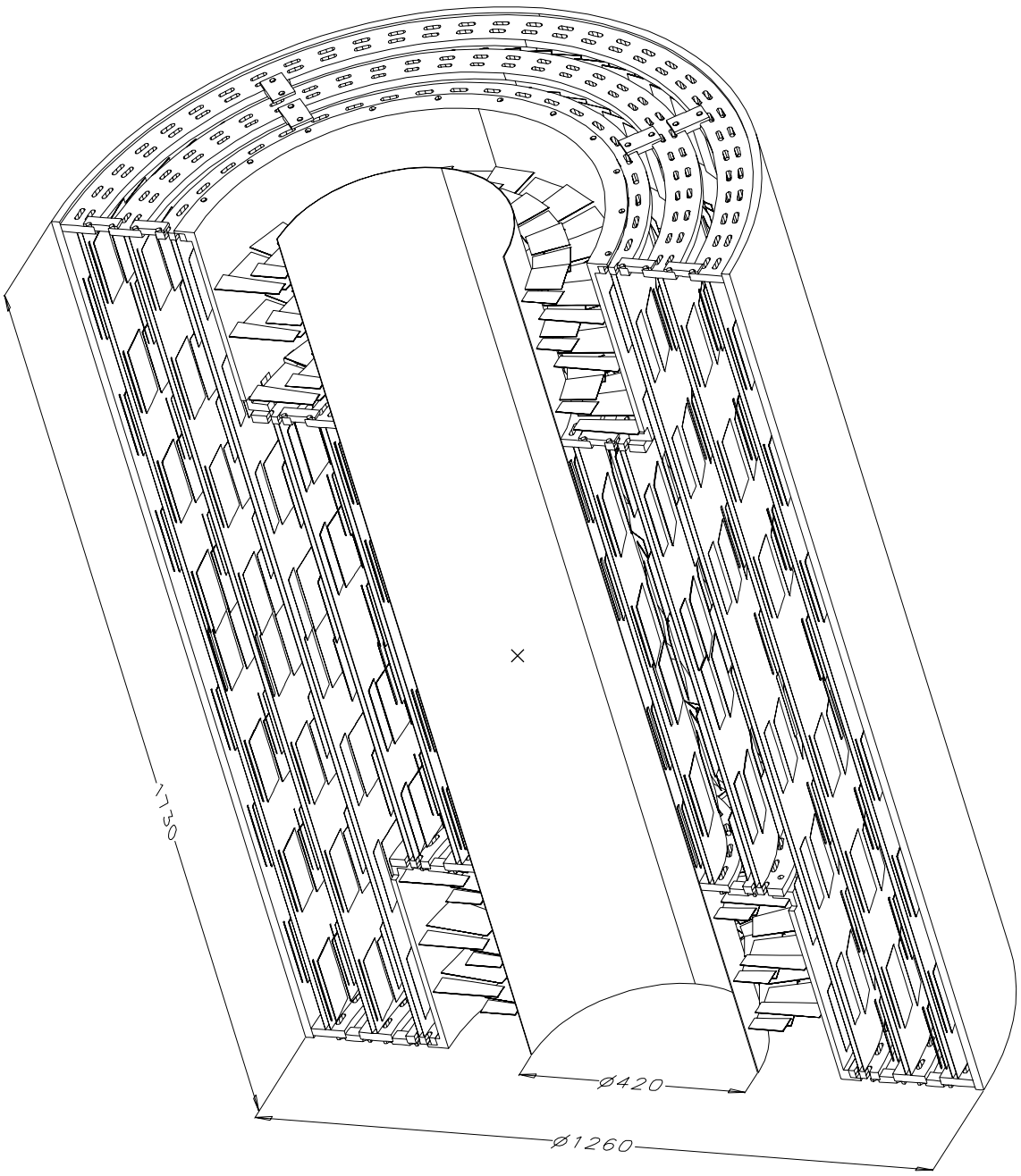

Fig. 3.89: Perspective view of the barrel detector.

To be removed from the mold after gluing, the cylinder is opened in its two halves. For the next step, the panels are joined together again.

Inserts (aluminum bushings with a threaded hole) are glued into the endplate of the cylinder using a precision jig. They are used to adjust the relative position of the two halves so that the cylinder endplate defines a reference plane. The position of the inserts is also used to define the axis of the cylinder and later to locate the cylinders of the various layers with respect to each other and to join them by means of the threaded holes to form the barrel structure.

To mount the ribbon strips supporting the ledges, as well as the ledges themselves, we use a rotary positioning table mounted in a Co-ordinate Measuring Machine (CMM). The cylinder is held on this table so that both its inner and outer surfaces are free. The longitudinal (z) axis of the system is adjusted via the endflage inserts to be parallel to the (horizontal) table of the CMM. The ribbon strips and the ledges, that are to be glued on the cylinder along the same longitudinal row, are mounted on a stiff beam, carefully machined to keep all ledges in the same plane. Strips and ledges are glued to each other on the beam, which is then positioned on the reference table of the CMM parallel to the axis of the cylinder/rotary table system. A tool, aligned with respect to this axis so that it moves only in the z-direction, is then used to transfer the row of ribbon supports and ledges onto the cylinder.

After all rows have been glued on the cylinder, the positions of the ledges must be surveyed. It must also be checked that, separating and then reuniting the two panels forming the cylinder, brings the ledges back to their initial positions.

Finally, the cooling pipes and diverse spacers and holders for the services are glued onto each panel. Thermally conducting glue is used to attach the pipes to the ledges.

The same rotating table is needed to mount the detector modules onto each half-cylindrical supporting panel. The position of each module is measured by the CMM during assembly and a final survey of the panel is performed when all modules have been mounted. The fully assembled panel is then dismounted from the CMM and moved to the test area. Meanwhile, the CMM and the rotating stage are available for the the assembly of the next panel.

After assembly each panel undergoes a set of functionality tests, including powering of the detector modules, pedestal runs and a test of its cooling circuitry.

As mentioned above, mating longitudinal ribs are used to couple the panels to form full cylinders, using the endflange inserts to adjust the relative position of the two halves and to define a reference plane. The same endflange inserts are used in the next operation, which couples all cylinders together to form the barrel structure.

The assembly of the barrel together with the end cap parts to form the SST and the final installation of the latter inside the MSGC system are described in Section 6.7.3.

3.7.5 The end-cap structure

3.7.5.1 General layout

There are 10 disks for each side of the end-cap Tracker (see Figs. 3.90 and 3.91). Each disk is composed of a pair of sub-disks. The radial coverage varies with the z position and the detector sensors extend to $r = 598$ mm. The supporting structure extends from $210 \leq r \leq 605$ mm, the outer dimension being common to all disks. The inner diameter increases progressively along the $|\eta| \leq 2.5$ line (see Fig. 3.91). The detector modules are arranged as successive rings each covering the full azimuth.

3.7.5.2 Supporting disks

The silicon detector devices are fitted to a disk type structure which is a major sub module of the end-cap Tracker. It is proposed that alternate rings of detectors are assembled on adjacent

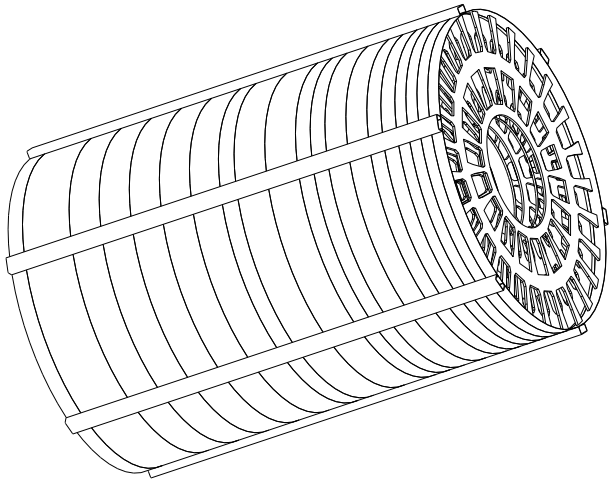

Fig. 3.90: Perspective view of the end-cap system.

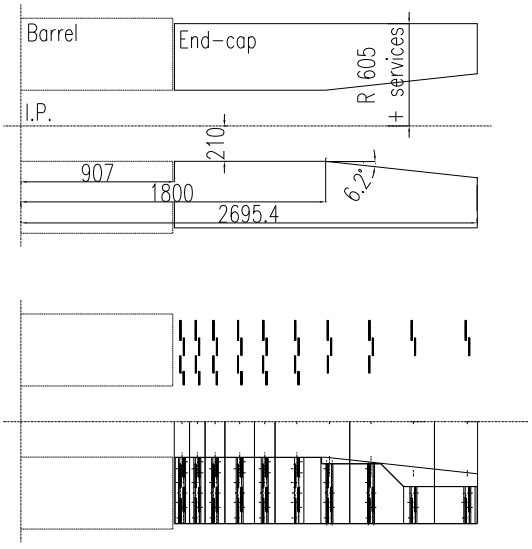

Fig. 3.91: End-cap section.

sub-disks. The sub-disk nearest to the intersection-point (IP) carries rings 2 and 4 while the second sub-disk of the pair carries rings 1 and 3 (see Fig. 3.92).

The sub-disks will be of built-up construction using CF sheets of approximately 0.4 mm skin thickness. A high-modulus fiber having its elastic modulus in the 500 GPa range will be appropriate. A cyanate ester resin system in combination with the very high thermal conductivity CF is proposed. Each sub-disk is stiffened by inner and outer cylindrical rings and by radial ribs. In practice even flat sheets of material do not have an entirely symmetrical behavior due to problems such as resin enrichment of the surfaces etc. Assembly using adhesives allows several parts cut from the same sheet to be positioned and oriented in opposition so as to nullify these effects. The flat sheet pieces will, therefore, be assembled by adhesive bonding to produce the required form. This will be built up on the honeycomb core, although the exact nature of the core material is under study.

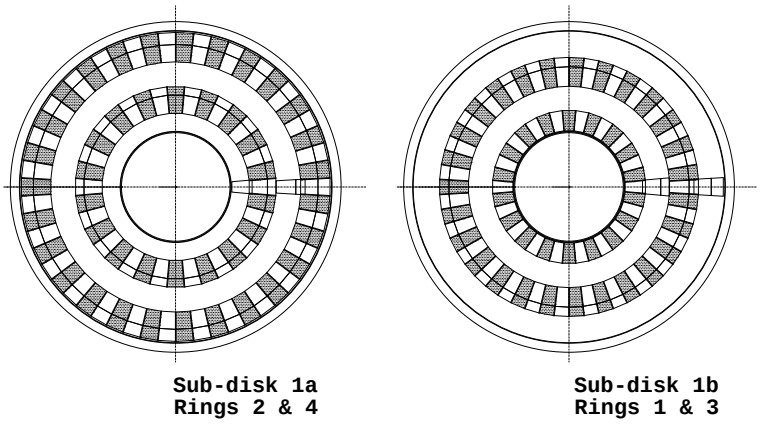

Fig. 3.92: End-cap sub-disks set.

The sub-disk carries, on one face, the supporting rings to which the detector modules are attached (see Fig. 3.93). Following the practice of the milestone prototype (see Section 3.9) openings matching the contour of the appropriate detector modules are cut into the plate allowing access to both faces of the supporting rings. This technique allows the active surface of the detector sensors to overlap. Accessibility can be improved if the sub-disks remain independent. The full complement of service connections will be routed to the outer circumference and then into cable channels at the outer diameter. The low CTE of the proposed materials prevents significant deformation and thermal stresses due to the difference between their fabrication temperatures and the operating temperature of the detector.

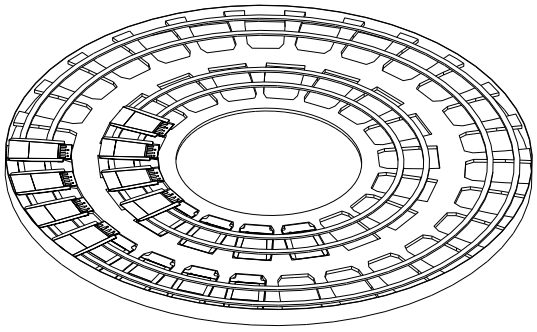

Fig. 3.93: End-cap sub-disk, partially assembled.

The support structure allows assembly of the detector modules to the sub-disks by clamping them to the freely available surface of the supporting rings. The convolutions of the disk section offer a measure of protection against accidental damage during the assembling and testing stage.

3.7.5.3 Cooling system

The proposed cooling method is to circulate fluid in thin-walled metal tubing embedded in a high thermal conductivity carbon fiber ring. The materials used ensure the low CTE and CME values needed for a stable and stress-free structure in the specified temperature range.

The system proposed is constructed by using a core section and thin facing sheets made of CF material and two metal tubes. These parts are encapsulated together to produce a rectangular section ring. Contact to the detectors is made locally through metal inserts glued into this ring. The inserts make the thermal connection to the sensor frames while the tubes and inserts have a large surface contact area to the fiber. Each coolant circuit covers part of the circumference of its corresponding ring. Since there are two coolant circuits they are arranged to present a counter-flow system to reduce apparent temperature rise. The two circuits may also be arranged to give redundancy in case of fluid flow problems etc. In order to equalize the thermal load on each circuit differing diameters of tubing are used. We will use tubes having inside diameters of 1.3, 2.3 and 3.3 mm.

The core section will be moulded using the high thermal conductivity CF, in a multi-layer set-up of the required thickness which is governed by the maximum tube diameter. The successive layers have a $+45°, 90°, -45°, 0°$ symmetry repeated several times to obtain the desired thickness producing a quasi-isotropic laminate. The core is divided into sections 50 mm long so that the fabrication procedure is to make a large number of similar rugged parts. The cooling fluid tubes, core and the outer facings are assembled in a jig using a room-temperature curing adhesive to ensure a minimum of deformation. The thermal conductivity is governed almost entirely by the fiber content of the section and careful assembly is called for. The assembled manifold is then aligned, without constraint, on the machine tool to produce the holes used for fixings. The fixing hardware is designed so that all the threaded parts are replaceable. The fixings also provide dowel locations for the sensor frame. Fixings adjacent to the hybrid are used for this alignment, engaging a cylindrical and a slotted hole in the frame. The holes of the sensor frames have aluminum alloy inserts treated to present a hard wearing surface to the assembly surface.

The manifolds are connected to larger diameter collector tubes on each disk so that two input and two output tubes are routed to each disk. The small diameter connections to the coolant tubes are made by placing a tubular sleeve over the junction to stress relieve it and using a low melting point solder seal. The connection is therefore entirely metallic and of low mass.

All disks of each end-cap will be assembled to enable their insertion into the experiment as a single unit from either end of the supporting tube.

3.7.5.4 Survey and test

Following construction the disks will be assembled with their supporting rings and the connections made to the inlet/outlet tubing. The location points used by the detector modules will then be inspected as a control of the construction process. All data will be logged during construction and will be referenced later during final metrology. Working on both sides, the disk will then be equipped with detector modules. Because of its geometry orthogonal movements alone are adequate to position the modules using a pick/place type of apparatus. In this way the handling is ensured to be consistent over a large number of operations. The apparatus can incorporate an optical recognition system allowing the positions of critical elements to be fixed and measured. Such a machine will simplify several aspects of the assembly.

The assembled disks must then be transferred to an apparatus where the central axis is almost horizontal, inclined as in the experiment. The full survey is then made again using optical, non-contact measuring equipment such that the co-ordinates of each detector can be logged relative to reference targets which remain accessible after the final assembly. This operation should be repeated after temperature cycling.

3.7.6 Access and maintenance procedure

As described in Section 6.8, acces and maintenance of the SST is possible during the long end-of-year shutdowns. Stopping periods of two to three weeks permit opening of the CMS end-caps and allow only access to the Tracker endflanges. During a long shutdown the SST can be extracted and moved into the maintenance area on the surface. In this area we foresee a storage at -10 °C and a repair and dissassembly/assembly area at $+10$ °C. All parts of the detector not requiring intervention will stay permanently at -10 °C. We estimate that the time needed for extraction and re-insertion of the SST - during which the detector will be at $+20$ °C - will not exceed one week per year. The dissassembly, repair and reassembly operations are expected not to exceed a period of 21 days per year. As discussed in Section 3.4.1 such an access and maintenance scenario is consistent with a safe operation of the detector over a 10-year lifetime of the experiment.

3.8 The Alignment System

The internal Tracker alignment system is described in detail in Section 6.5, here, for completeness, we briefly mention the principles involved.

Globally, the position finding of each active detector element can be achieved through the following steps:

1. Positioning and survey of detectors inside modules.

2. Mechanical precision of the module installation inside the smallest sub-units. For the barrel these are half-shelves and for the end-caps sub-disks.

3. Measurement of these sub-unit positions after assembly on their support structures and connection to six external measurable points.

4. Online measurement of movements of these six points to evaluate global displacements of the support structures.

Steps 1, 2 and 3 are carried out during the construction and assembly phase. Step 4 is accomplished by the 'Tracker online position monitoring system'.

This system is based on the displacement measurement of six points sitting on the outermost SST structure radius, with respect to six co-axial lines connecting the two end-flanges of the Tracker. Each object to be monitored is equipped with two sets of six reference points separated by at least 250 mm for out of plane angular measurements. The six channels of each set, the so called alignment channels, are obstacle-free corridors connecting both ends of the Tracker. They allow six parallel axial lines to cross the detector from one end to the other to points which are used as a reference system. Each of these reference points must, of course, be inside the corresponding alignment channel. The evaluation of the object position consists in the measurement of the normal distance and angular position of each of these points with respect to the corresponding reference axis (Fig. 6.27).

For the reference points, we are presently using non-collimated monochromatic light sources. Each independent structure of the SST detector, provides the place to house these reference points.

With such a system we aim at monitoring the movements of individual structures holding the detectors, with an accuracy of ~ 5 μm which is better than the intrinsic SST detector resolution. The proposed system not only monitors these movements, but provides, through the alignment wheels sitting at the end-flange of the Tracker, a geodetic network connecting the Pixel, SST, MSGC and Muon systems and allowing an efficient and precise alignment between them.

3.9 System Tests, Prototypes and Milestones

In 1995 the LHC Committee fixed two important milestones to address the main system problems of the SST. Two large system prototypes of the Barrel (SiB1, see Fig. 3.ii and of the Endcap part of the SST (SiF1, see Fig. 3.iv) have been built for this purpose.

3.9.1 SiB1

3.9.1.1 Overview

The features of the milestone prototype were based on a previous version of the Tracker (V2) where three layers of silicon detectors were foreseen covering the radial region between 20 and 40 cm. The layout of the V2 geometry is shown in Fig. 3.94.

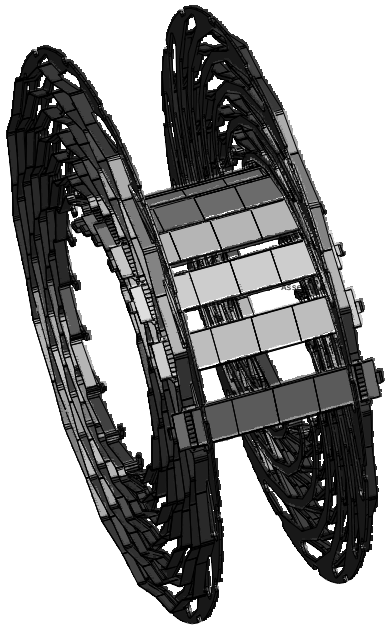

Fig. 3.94: Basic structure of the barrel wheel.

The detector modules are distributed in seven layers on a spiral geometry which leaves enough room for all services (cables, interconnect cards and cooling tubes). The detectors are tilted to partially compensate for the Lorentz angle. The detectors are organized to provide three detection points per track without dead regions in the tracking volume. Detectors overlap in $r-\phi$ over a few millimeters to allow for intermodule alignment. Enough room is left between the seven layers to allow for longitudinal inter-penetrating of detector modules with adjacent wheels overlapping in z.

A total of 112 detector modules are used to equip the entire wheel. To reduce the costs we decided to limit to 14 the number of working modules to be installed in the structure. The other 98 were modules produced with dummy components, mainly to address specific mechanical and thermal studies.

The detector modules used in the structure were based on a preliminary engineered version of the barrel module approved as intermediate milestone in January 1997. The detectors are all single-sided. The hybrids are produced on a ceramic support with standard commercial connectors. The read-out electronics incorporate only the basic elements (pre-amplifiers, shapers and multiplexer) of the final chip and are implemented in radiation soft technology. An interconnect card, separated from the module, houses the components for the control of the read-out. The cables are made out of copper lines etched on thin Kapton ribbons. No optical link was included in the read-out scheme.

3.9.1.2 Support structure

Two machined carbon fiber disks are used as supporting elements coupled by thin inner and outer cylindrical skins. The two end-plates act as supporting elements for the detector modules, defining the exact position of the silicon detectors in space (see Fig. 3.94). The radial position of the detector modules is defined by CF supporting ledges, while the other two co-ordinates are fixed by the coupling between precision pins in the modules and slots precisely manufactured in the ledges. Short Kapton pigtails connect the silicon modules to the interconnect cards located in the inner part of the structure.

3.9.1.3 Fabrication of the CF wheel

The first prototypes of this complicated structure were built in aluminum and carbon fiber. The outcome of this work has been reported as intermediate milestone in July 1996. It was shown that using standard carbon fiber epoxy composite it was possible to machine one disk in a month. The elements were measured, yielding a radial accuracy of the ledges of 70 μm. After an optimization of the fabrication procedure the two final disks were fabricated from a solid block of a new composite material with the carbon fibers held together by a thermoplastic material, PEEK (Poly-Ether-Ether-Keton), cured at high temperature. The disks were manufactured by TAEMA: six thin disks, 5 mm thick, were first produced by using 40 fiber layers interleaved with PEEK cured at 380 °C. The six disks were coupled together by high-temperature curing in order to fabricate the 30 mm solid disks needed for machining. The CF-PEEK composite material has a good homogeneity, a high value of toughness that prevents cracks and a very low moisture absorption. The CF used for the supporting structure has a medium range Young modulus ($E = 227$ GPa), a thermal conductivity of 20 W/(K·m) and a radiation length of about 25 cm that, coupled with PEEK ($X_0 = 30$ cm), gives an overall radiation length for the composite of about 27 cm. The low coefficient of thermal expansion prevents significant deformation and thermal stress when the structure is cooled down from the assembly temperature to the operating temperature. The machining was done in the INFN Pisa laboratory. The total weight of each disk is 2.1 kg. An accuracy better than 70 μm was measured for all of the critical elements.

3.9.1.4 The cooling system

The heat generated by the detector modules in the wheel is removed by a cooling system based on a circulating fluid, with the goal of keeping the temperature of the silicon elements during running below -5 °C. The cooling tubes are arranged in layers in the supporting structure, in good thermal contact with the detector ledges. Each tube layer has two inlets and two outlets to reduce the pressure loss while maintaining a small tube size. The temperature rise of the

cooling fluid has been fixed to 1 °C. Considering a pressure loss in the whole wheel of 0.08 MPa, the fluid will be driven below atmospheric pressure. A film coefficient of 3500 W/(m^2·K) and a thermal resistance of 1.5 K/W is expected when using a mixture of water with 20% of glycol ethylene at −15 °C and a cooling pipe diameter of 3 mm. In these conditions the maximum gradient between the cooling fluid and the silicon detectors is about 10 °C, with an average fluid flow per layer of about 0.6 l/min.

Several measurements have been performed to study the coupling interface between the cooling ledges and the modules. The heat generated inside the modules is simulated by three heating foils, 2 W for the electronics and 0.2 W for each silicon detector. The temperature is monitored by Pt-100 sensors and the cooling fluid temperature is adjustable between −10 °C and 20 °C. The temperature of the environment is regulated by a cooling shield, in the range −20 °C to 20 °C. The whole set-up can be kept in vacuum or dry nitrogen to avoid condensation and to control convection. The use of CF/PEEK composite material for the ledges implies a thermal step greater than 10 °C between the cooling fluid and the electronic support. This value can be reduced by using high thermal conductivity carbon fiber.

3.9.1.5 Interconnect cards and cables

The interconnect cards (ICC) are used to distribute timing and input/output signals between the read-out hybrids and the DAQ system. Each module needs two interconnect cards, therefore 28 ICCs for the real modules and 196 dummy ICCs for the dummy modules have been produced. The cables are made of thin copper strips (35 μm thick) etched on a 75 μm Kapton ribbon, long enough to reach the outer periphery of the wheel.

3.9.1.6 Detector modules

A barrel detector module is fabricated by coupling together two half-modules joined with stiff carbon fiber elements (Fig. 3.95).

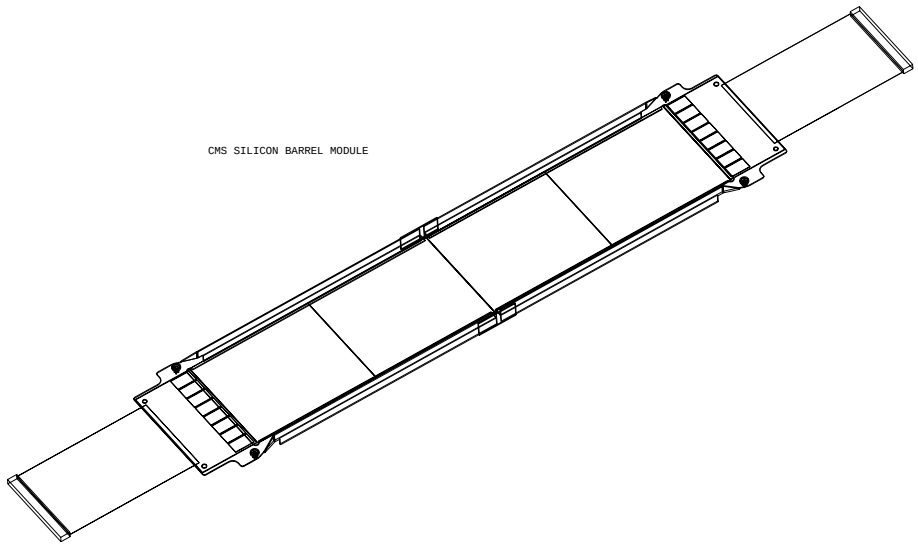

Fig. 3.95: Full detector module for the SiB1 milestone.

Each half-module consists of two silicon detectors glued together head-on. The strips are daisy-chained between the two detectors, giving an effective length of 12 cm. The positioning elements are engaged in precision holes whose centers define the origin and the main axis of the reference frame for the alignment. The hybrid is made of ceramic and contains 8 PREMUX chips to read out 1024 silicon channels. The silicon detectors are single-sided AC-coupled devices, 50 μm pitch, 300 μm thick, with a total area of 5.4×6.4 cm^2. Each dummy half-module consists of two dummy detectors, made out of 400 μm thick silicon wafers with aluminum strips patterned like the working ones. For power dissipation 50 Ω ceramic resistors are used in place of the front-end electronics.

3.9.1.7 Production of the carbon fiber frames

High thermal conductivity CF is used for the mechanical frames of the modules. In the first step carbon fiber plates are produced from prepreg K1100X Amoco embedded in the Fiberite 954-2A cyanate ester resin. Five layers of prepreg are coupled together to form a plate by curing in autoclave. The frames for the modules are cut out from these plates with a water jet cutting machine. The fiber direction runs parallel to the side-rails that support the silicon detectors to optimize the heat removal.

3.9.1.8 Module assembly

The assembly procedure consists of five steps: gluing of the precision positioning elements in the frame, alignment and gluing of the silicon detectors to the CF support, alignment and gluing of the hybrid, micro-bonding, and gluing the two half-modules together. All these steps were repeated in six production centers: Aachen, Bari, Kemi, Padova, Perugia, Pisa. A special jig was used to glue the positioning elements to the CF support giving a position accuracy of 50 μm. A specific jig has been used to glue the two detectors together: one of the detectors is held by vacuum in a fixed position while the other one can be moved in x and y and rotated in ϕ in order to align it with respect to the first. This alignment is done under a 3D measuring machine with a precision of a few microns. The co-ordinate system is shown in Fig. 3.96. A gap of 60 μm is left between the detector edges and filled with glue. Then the pair of detectors is glued to the CF support by using another jig: the support is located on the base using the precision positioning elements. A movable arm, holding the pair of detectors by vacuum, allows the precise positioning with respect to the positioning elements by micrometric movements in x, y, z and ϕ. A vertical clearance of 60 μm is left between the detectors and the support structure, to be filled with glue. The planarity of the half-module is imposed by the parallelism between the plane of the detectors in the holding arm and the plane of the base holding the carbon fiber frame.

Figure 3.97 shows the deviation of one of the fiducial marks on the silicon detectors from its nominal position and the angle between the the x-axis and the strips of each of the two detectors. The strips can be aligned with an accuracy better than 0.1 mrad, whereas the detector position has an accuracy of 8 μm.

The gluing of the hybrid to the CF frame does not require very high precision and can be done using a jig with grooves that hold the hybrid and the support in the correct position. Approximately 2000 micro-bonds are needed for one half-module. Two half-modules are glued together to form the full module by using another dedicated jig. One half-module is held in a fixed position while the other one is on a x-y table that can be rotated around the axis normal to the silicon detectors. Figure 3.i shows the complete SiB1 module.

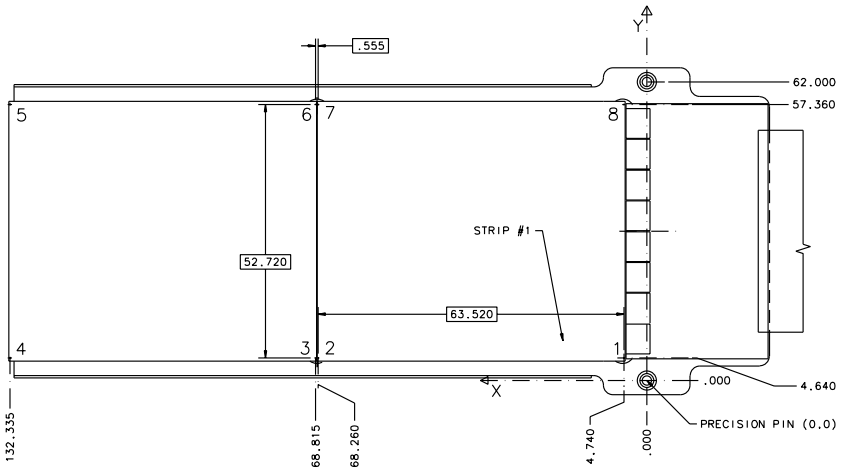

Fig. 3.96: Nominal position of the fiducial marks with respect to the precision pins.

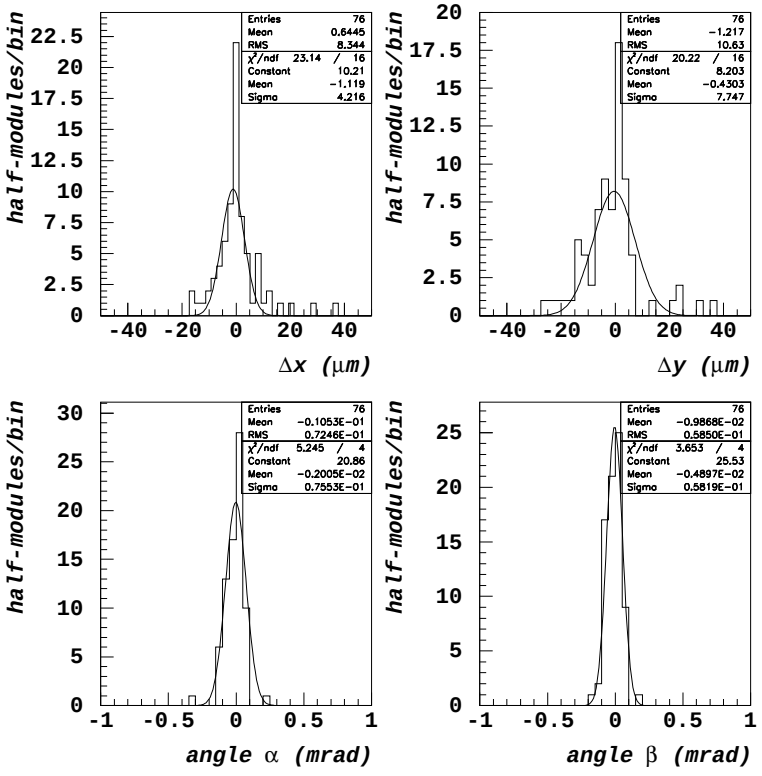

Fig. 3.97: Deviation of the fiducial mark 1 from the nominal value.

3.9.1.9 Tests of the modules

The functionality of the modules was tested by measuring pedestals and noise as well as signals generated by a pulsed LED. One example of the test results is shown in Fig. 3.98 and in Fig. 3.99.

Out of 31 fabricated half-modules, 30 passed the test and were used to build 15 modules for the milestone.

3.9.1.10 Wheel assembly

After machining, the surfaces were cleaned to prepare for gluing.

Thin aluminum tubes (0.2 mm wall thickness, 3.0 mm inner diameter) have been used as cooling pipes. They were preshaped to fit the cooling channel of the wheel. In the outer part of the structure manifolds were placed by gluing properly shaped aluminum tubes (0.5 mm wall thickness, 4 mm inner diameter) to the cooling channels. Checks have been done after gluing to search for leaks.

Two small L-shaped pieces of aluminum have been glued to the CF structure in each detector slot to hold the interconnect cards. These cards are then fixed to the supporting elements and the Kapton cables are positioned in the cable trays.

An assembly tool and a large co-ordinate measuring machine have been used to align the two disks together and to survey the insertion of the detector modules. The alignment tool consists of a solid frame with a precision shaft holding the two disks. This shaft can rotate on two bearings and is connected to a stepper motor. The procedure is based on the assumption that the supporting ledges are orthogonal to the back plane of the CF disks used as primary reference. The two metal disks used to hold the CF disks were initially measured: the flatness of the two disks is better than 50 μm and the parallelism better than 100 μm when measured on the eight points used to hold the wheel in position. This operation allows the use of the plane of one disk as reference The centers of the two disks have been used to define a reference axis, the origin being set at mid-distance. The second CF wheel was aligned with respect to this co-ordinate system. Finally, the position of the reference points on the CF wheel was measured.

After the alignment of the disks, the module insertion was done manually by two operators. A total of 112 modules were installed in one week. At the end, the wheel position was measured again and no significant displacements was found. The assembled wheel is shown in Fig. 3.ii.

A cradle and a Plexiglass cover have been constructed to house the wheel during transport. The transfer to CERN was done with a truck equipped with a shock-protection system. No damage was reported.

3.9.2 SiF1

3.9.2.1 Overview

The SiF1 system has a radial coverage from 215 mm to 411 mm, while the supporting structure extends from 200 mm to 432 mm. The sensors are arranged in two rings of 36 modules each, covering the full azimuth. Thirteen real modules have been fabricated, the remainder being dummies. Modules of the inner ring carry one sensor while those on the outer ring carry two. There is approximately 1% overlap between the sensors of each ring. The different types of modules are assembled into a CF disk structure shown in Fig. 3.100. Three different silicon sensor designs are needed on account of the wedge geometry.

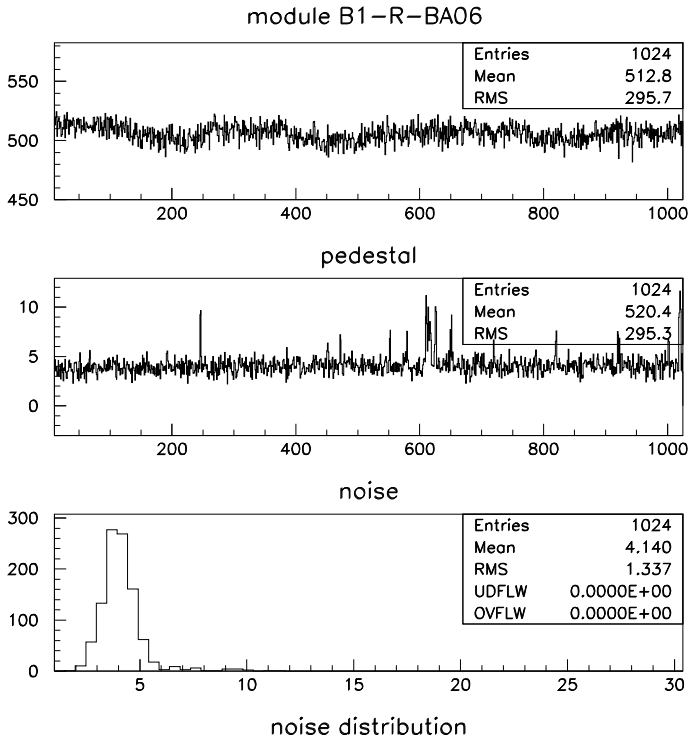

Fig. 3.98: Pedestal and noise of a module.

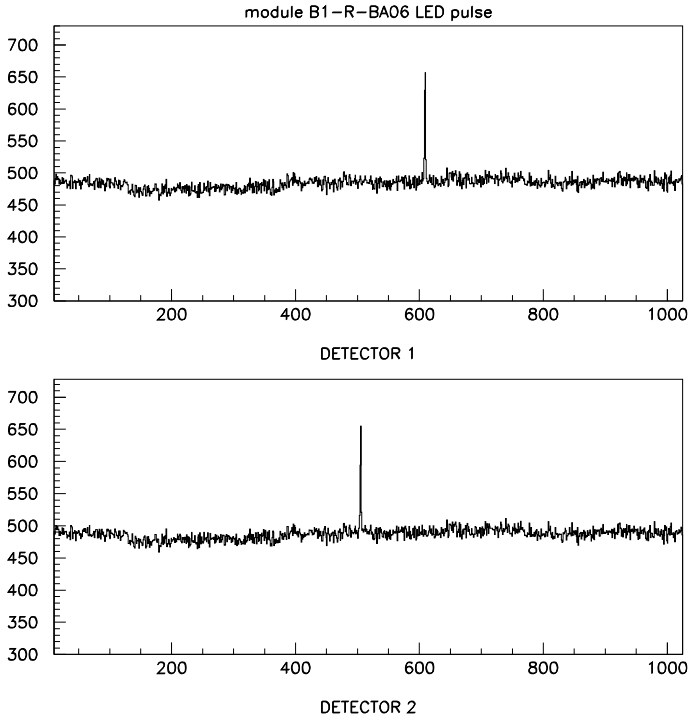

Fig. 3.99: Signals generated by LED pulses.

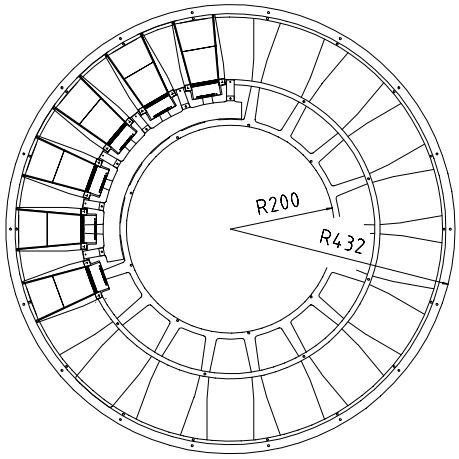

Fig. 3.100: Disposition of modules on a SiF1 supporting structure.

3.9.2.2 Support structure

The CF disk is formed by coupling two similar carbon fiber shell type mouldings. The two shells differ in the details of their machining after the moulding process since they carry either the inner or the outer ring of detectors.

Supporting rings are assembled on the disk to provide precise location of the detector modules. The rings are actively cooled by fluid circulating in tubes embedded in their section during construction.

The sensors themselves are assembled into detector modules by gluing them into a high thermal conductivity CF frame. These frames are clamped to both faces of the supporting rings alternately allowing an overlapping geometry to be used. One ring enables cooling of the hybrid and sensors through the supporting frame while the second is used to cool the sensors and to ensure planarity. The same rings also provide cooling for the electronics on the interconnect ring, near the modules.

The supporting rings as used on the milestone are of built-up construction. All CF used is of the very high thermal conductivity Amoco K1100X type and a cyanate ester resin was selected for optimum CME. An annular moulding is made of 18 layers of fiber, which is then machined to thickness and on its edges to follow the form of the cooling tubes. This part is then used as the core of the ring. The cooling tubes are of 304-type stainless steel (2.00/1.94 mm diameter). The principal rings are near the hybrids and have two coolant circuits while the secondary rings have one. Each of these circuits is further divided into two or three parts according to its length to reduce the pressure drop in the tubes. The facings are moulded as CF rings of 0.45 mm thickness with inner and outer diameters as the finished ring. The parts, including the cooling tubes, are then encapsulated under pressure in a jig using a minimum of cold setting adhesive. Since this final assembly is made at room temperature there is minimal distortion. Holes are then accurately machined and metal inserts glued in place. In the milestone, the aluminum alloy inserts are positioned directly in these holes with no further corrective machining. Stainless steel fixing hardware is arranged such that all the threaded parts are replaceable. The fixings also provide dowel locations for the detector modules. Fixings adjacent to the hybrid are used for alignment, one dowel engaging a cylindrical hole and the second a slot in the frame. The holes in the frame also have aluminum alloy inserts.

The milestone shells are made in a carbon fiber cloth (T300 fiber, 2×2 twill weave, epoxy resin, $t = 0.25$ mm/layer, three layer lay-up).

3.9.2.3 Detector modules

The modules consist of silicon sensors glued into a CF frame. The frames consist of three parts which are positioned and glued together in a jig. Figure 3.101 shows a sketch of such a module.

The preferred heat path goes through the CF frame. The side-rails of the frame are made of seven layers of the high thermal conductivity unidirectional fiber prepreg. The hybrid part of the frame is made of three layers of similar material. Since they are made in several parts the number of plies as well as fiber direction in the frames can be more easily arranged for optimum thermal conductivity which is predominantly in the fiber direction. This method is also economical in the usage of the expensive fiber prepreg. A thermally conducting compound is needed at the thermal interfaces.

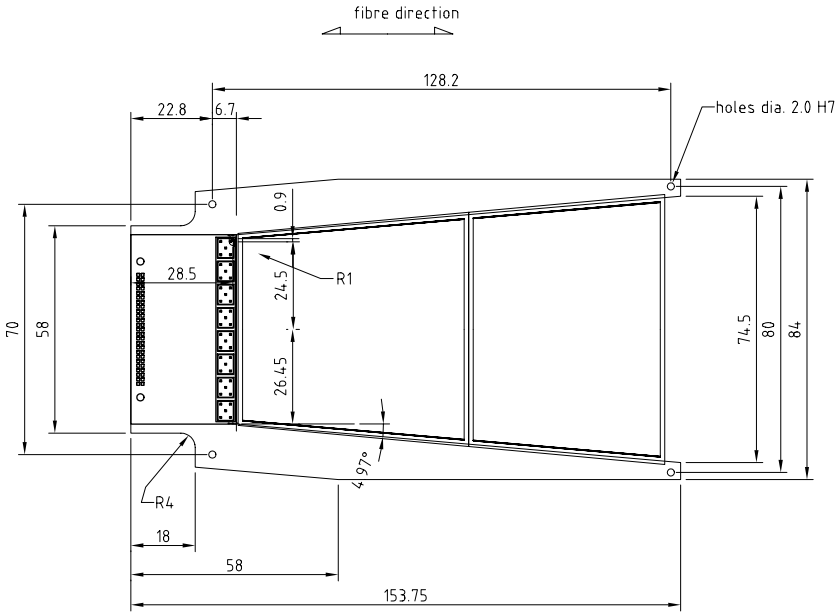

Fig. 3.101: Sketch of the milestone end-cap module.

The module fabrication now proceeds with the head-on gluing of two detectors, then the gluing of the silicon detectors to the CF frame. All these operations are done under the control of a co-ordinate measuring machine with a precision of a few microns, both in Florence and at CERN. The operational surface of the machine is wide enough for the simultaneous use of several jigs, thus allowing parallel steps in the assembly procedure. Detectors are glued with Araldite 2011.

Two different designs (F1, F2) of wedge-shaped silicon detectors have been used. These detectors are first glued together by using an assembly jig able to move one detector with respect to the other in the horizontal plane. The glue is dispensed on one edge of each detector by dipping it in a 50 μm deep groove. The detectors are then placed on the jig and kept in place by vacuum. One detector is kept in a fixed position while the other can be aligned via micrometric movements. The nominal distance between the reference points on the the two detectors is fixed to 580 μm leaving a 100 μm gap between the two detectors. The glue is left cured for half a day, then 12 reference marks are measured on the detectors to check the quality of the procedure. The CF frame is placed on an aluminum base on a special jig that has identical precision inserts as we have on the support rings. A local co-ordinate system is now established by fitting a line passing through the center of the two precision inserts. The detectors are then carried above the frame and aligned by moving with respect to this co-ordinate system. After

this the detectors are lowered to the nominal height for gluing. Some results of final survey of the modules are shown in Fig 3.102, which shows that the alignment between strips on the two detectors is stable throughout the assembly process.

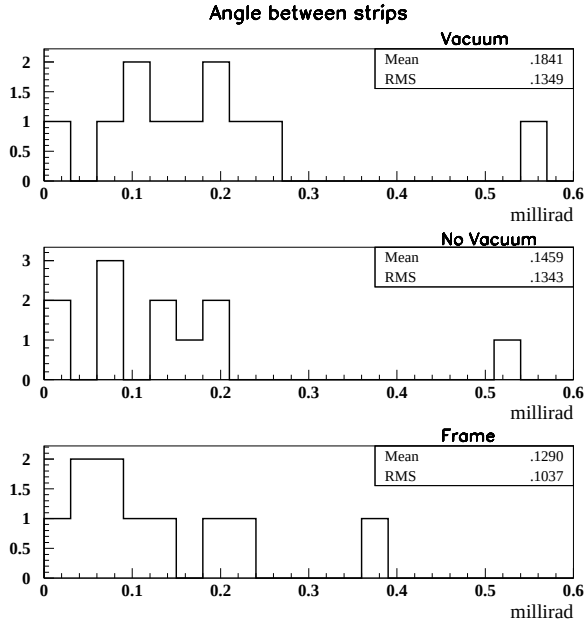

Fig. 3.102: Angle between the strips of the two detectors (top: detector fixed by vacuum; middle: after the vacuum has been released; bottom: detectors glued on the CF frame).

The ceramic hybrid is glued to the frame by using thermally conductive Araldite. The module is then micro-bonded and tested for possible defects. The complete SiF1 module is shown in Fig. 3.iii.

The modules are clamped to the support. The two half-shells are then brought together at the mating faces. The convolutions of the section offer a measure of protection to the detectors. Further access to the inside detectors however necessitates disassembly of the shell pair.

3.9.2.4 DAQ system

The SiF1 milestone is read out by a DAQ system that has been designed for use in beam tests and in the laboratory. This system extensively uses decoupling schemes allowing a fully floating connection to the detector, suitable for double-sided detectors. Furthermore, the evolution of the requirements dictated by the front-end electronics are easily implemented by the use of re-programmable arrays in three logic boards. The system is based on VME and uses standard VME CPU boards for data formatting and for storage on tapes and disks. Analog signals from the front-end electronics are converted and immediately sent to the FIFO buffers located on a VME board via an optical FOXI link. Data transmission to the VME CPU and data storage are parallel to the digitization thus eliminating data transmission overhead.

3.9.2.5 Performance of the modules

The modules have been tested both before mounting and after installation, using calibration pulses to check their performance. One of the modules has been tested in a high-energy pion beam at CERN. The fully assembled end-cap disk is shown in Fig. 3.iv.

3.9.2.6 Performance of the cooling system

Measurements of the temperature gradients in the cooling system have been performed on the SiF1 milestone disk [3-31], which was equipped with heat load resistors simulating the power dissipation of the detector modules. The disk was mounted vertically in a frame (see Fig. 3.103). It was enclosed in a styrofoam box in order to have a defined volume which is decoupled from temperature variations outside of the box. The whole set-up was installed in a cold room which was operated at -10 °C. The input lines to the cooling pipe sections were connected to a large-diameter cooling pipe which itself was instrumented with a pressure-meter and a flow-meter. In the same way the output of the sections was collected in a large-diameter pipe instrumented with a second pressure meter. Thus both the total flow and the total pressure drop could be measured. A combination of these measurements showed that the effective inner radius of the cooling pipes is some 15% smaller than the actual inner radius of the pipe, which is attributed to the inevitable bending and the soldered joints of the pipes. The cooling fluid, 3M-HFE-7100 (see Section 3.7.3), was circulated in a primary circuit which was connected to a chiller unit via a heat exchanger. The temperature of this chiller was set to -11 °C.

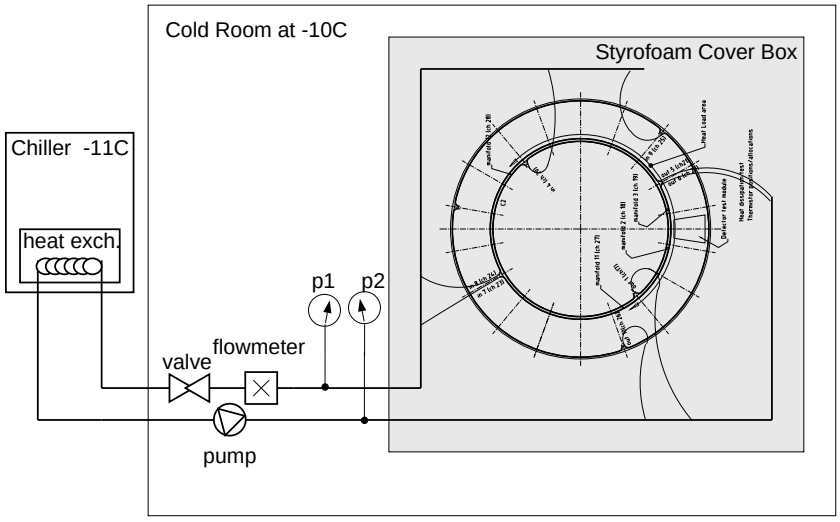

Fig. 3.103: The set-up for the temperature measurements on the SiF1 milestone.

Figure 3.104 (a) shows the temperature increase along the pipe as a function of the flow for one of the two cooling pipes in a counterflow section which is equipped with 18 heat loads dissipating 2 W each. The curve shows the expectation which is in good agreement with the measurement. A fluid temperature increase of 2 °C, which is considered as a reasonable value, is obtained at a flow of around 0.18 l/ min per pipe. Taking into account the counterflow in the two cooling pipes underneath the hybrid side of the modules, the effective temperature of the fluid at the modules is then about 1 °C above its input temperature. Figure 3.104 (b) shows the difference between the temperature on the support ring and the average temperature of the fluid as a function of the flow. Again, the expectation is in good agreement with the measurements. For the flow of 0.18 l/ min per pipe the gradient from the fluid to the surface of the CS support ring is around 3 °C. Summarizing these two contributions, the surface to which the detector modules are attached is around 4 °C warmer than the input cooling fluid temperature for a flow of around 0.18 l/ min per pipe.

Taking into account the additional temperature gradient expected between the CF frame and the detector, this cooling performance is adequate for a stable operation of the system.

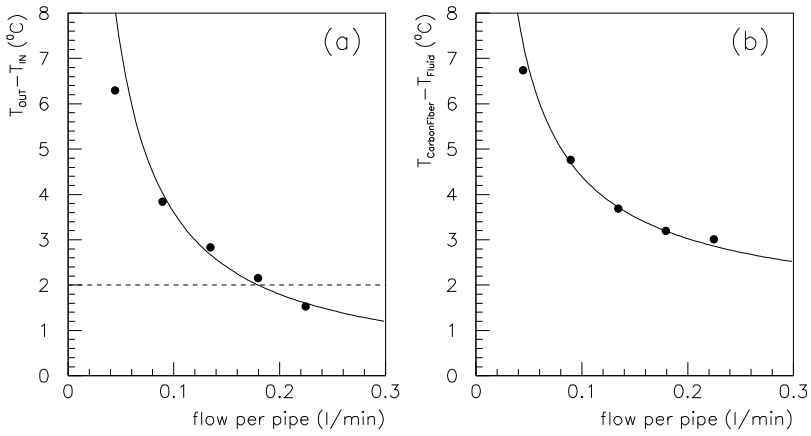

Fig. 3.104: For one of the two cooling pipes in a counterflow section equipped with 18 heat loads (2 W each): (a) Temperature increase along the pipe as a function of the flow. (b) Temperature gradient in the fluid perpendicular to the flow. For details see text. Both measurements were made with the 3M-HFE-7100 cooling fluid at $-10°$C. The solid lines show the expectations.

Chapter 4

The MSGC Tracker

4.1 Overview and Motivations

The main challenge for tracking at LHC is pattern recognition in a highly congested environment. Good pattern recognition means, essentially, low cell occupancy and large hit redundancy. Low occupancy can be obtained by working with high granularity, i.e. small detection cell size, and fast primary charge collection. Redundancy implies as many measured points per track as possible, compatible with an acceptable material budget without impairing too much the electromagnetic calorimeter performance.

To fulfil these requirements the CMS MSGC (a 6 m long, 3 m diameter cylinder in a 4 T magnetic field) tracker has been designed to provide an average number of 6 hits per track with readout pitch of $\sim$200 μm and a strip length between 10 and 25 cm. This immediately implies that the system is built up with millions of individual detection elements (strips). Good momentum resolution with a limited number of points per track requires quite good position resolution (better than 50 μm per measurement) for normal (high momentum) tracks. A system like the one just described cannot be built using the classical, mature, technology of gas proportional wire counters (MWPCs, drift chambers, TPCs etc.) as for the LEP, Tevatron or Hera experiments. Indeed, in these kinds of detectors mechanical tolerances limit the distance between wires to not less than $1 \div 2$ mm, thus severely limiting not only the position resolution but also the charge collection time, the granularity and hence the occupancy.

The introduction of the MSGC/MGC concept, i.e. gas proportional counters made with micro-electronics technology, overcomes this limitation. The MSGC and MGC are gas proportional counters with an electric field structure similar to the one of the MWPC, but, thanks to the use of a technology with sub-micron accuracy, on a much reduced scale. In the MSGC and MGC the distance between the sensing electrodes (the anode strips) is typically 200 μm with an accuracy much better than 1 μm. The spreading of the charge on more than one strip, because of diffusion, allows the use of interpolating algorithms to achieve a position resolution much better than the one dictated by the readout pitch. This is the main advantage of gas micro-strip detectors with respect to solid-state micro-strip detectors. It allows to cover large areas with a reasonable number of electronic channels. The main disadvantage is the speed of primary charge collection that cannot be easily reduced below two LHC bunch-crossings. The inner tracker of CMS has not only to measure the $r - \phi$ coordinate to identify the sign and measure the momentum of the charged particles it has also to unambiguously reconstruct the primary vertex of the 25 minimum bias events produced on average in each bunch-crossing at full luminosity. To do this the tracker has to measure with a millimetre accuracy the position of the event along the beam axis. If one, for material or financial constrains, cannot afford to measure true space points but has to use projective measurements, the most convenient solution is to adopt the technique of small angle stereo pairs measurements. In CMS a stereo angle of

50 mrad will provide an adequate vertex resolution (∼1 mm) while the limited strip overlap controls the appearance of 'ghosts'.

The base-line solution adopted in CMS for the stereo measurement is the *twin chamber* concept, i.e. a back-to-back arrangement of two identical, single-sided MSGCs. As the use of a single module for ϕ and z coordinate measurement has the promise of sizable saving of space, material and money, further R&D is still continuing on the MGC concept, i.e. a true 2-D device, providing two projections with one substrate only (see Section 4.9).

4.2 Experimental Constraints, Layout and Specifications

The MSGC Tracker covers the space between the Silicon tracker and the Electromagnetic Calorimeter which is in between a radius of 675 mm and 1233 mm for a total length of 5520 mm (see Fig. 1.8 and 1.iv).

For optimal precision in transverse momentum measurement and most efficient track reconstruction, the detector elements will be arranged in such a way that the $r - \phi$ coordinates of particle trajectories are determined with the highest precision. In the barrel region, rectangular MSGC counters are arranged in six cylindrical layers, with their sensing electrodes oriented parallel to the beam. To provide the measurement of the z coordinate, some of the modules are equipped with an additional layer with anode strips placed at a small stereo angle with respect to the beam axis. The drift field is perpendicular to the beam and, because in MSGCs the spatial resolution strongly depends on the angle of incidence of particles, it is necessary to compensate the Lorentz angle by a small tilt of the detector. To minimise the amount of material which particles of higher rapidities would traverse by crossing the substrates at a shallow angle, the forward (and backward) part of the MSGC tracker is equipped with disks of detector elements perpendicular to the beam. The forward MSGC counters have a trapezoidal shape with their sensing electrodes pointing radially to the beam. Modules providing a second coordinate measurement have an additional layer with anode strips at a 50 mrad stereo angle to the radial direction. This end-cap configuration offers the additional advantage of having the drifting electric field of the counters parallel to the magnetic field, avoiding all complications brought by the Lorentz angle.

The barrel part of the MSGC tracker will consist of six layers with radius between 700 and 1200 mm, extending up to $|z| = 1205$ mm. The end-cap part of the MSGC tracker will be made of eleven disks, on each side of the barrel, with radius between 700 and 1160 mm and extending up to $|z| = 2760$ mm. The counters on the disks are arranged in four rings.

For pattern recognition purpose and vertex reconstruction needs, it is necessary to measure the second coordinate for at least two impact points within the MSGC layers. To insure this requirement, layers one, four and six of the barrel, the eleventh disk in each end-cap and the innermost and outermost rings of the remaining end-cap disks, will be equipped with double-sided modules.

In the region occupied by the MSGC tracker, the spatial resolution that is required for the first coordinate is of the order of 50 μm for high p_T particles. This can be easily achieved using MSGCs with an anode pitch of the order of 200 μm. For the second coordinate, a precision of $\sim$ 1 mm is sufficient, so that the pitch can be doubled to save on the number of readout channels. The cell occupancy that can be tolerated is of the order of a few per cent. This limits the strip length to about 10–12 cm for the innermost counters but can be significantly larger for the outermost counters.

The charge collection time and signal formation in MSGCs, although very short compared to classic gaseous detectors like drift chambers, cannot be made shorter than about 50 ns. For this reason at least two beam crossing will be superimposed in the MSGC tracker. In order to keep this number at two, special care has to be taken in the choice of the gas mixture and in

the tuning of the readout electronics. The requirement of having a counting gas with high drift velocity is in contradiction with the desire of keeping the Lorentz angle as small as possible in the barrel. This is why a short collection time can only be achieved by working at very high drift field, typically 10 kV/cm.

The severe radiation environment in which the MSGC tracker will be operated at the LHC imposes strong constraints on the choice of the material used for all detector components and for the counting gas, in order to minimise all ageing processes. Special treatment of the substrates is also needed to keep a constant gain at all fluxes and to allow for an efficient detection of minimum ionising particles also in the presence of highly ionising particles.

4.3 Detecting Elements: the Micro Strip Gas Chamber

4.3.1 MSGC: principle of operation

A cross-section of a typical MSGC structure is shown in Fig. 4.1a, while a top view of the electrodes configuration is shown in Fig. 4.1b. Typical voltages applied to the MSGC electrodes are: anode at 0 V (the virtual ground of the readout amplifier), side cathode at -520 V, drift cathode at -3500 V. The shape of the charge collecting electric field at these operating voltage settings is shown in Fig. 4.2. While in the MWPC the anode wires are suspended in a gas volume mid-way between two drift electrodes, in the MSGC the anode strips are located on a semi-insulating glass substrate. Furthermore, in the MSGC there is one drift plane only (drift cathode, the most negative electrode) and the active medium (gas) is present on one side only of the charge collecting strips (the most positive electrodes). The side cathodes set a large fraction of the amplifying field on the anodes. With this electrode configuration the active volume is filled almost everywhere with a *uniform* electric field which acts as the primary charge

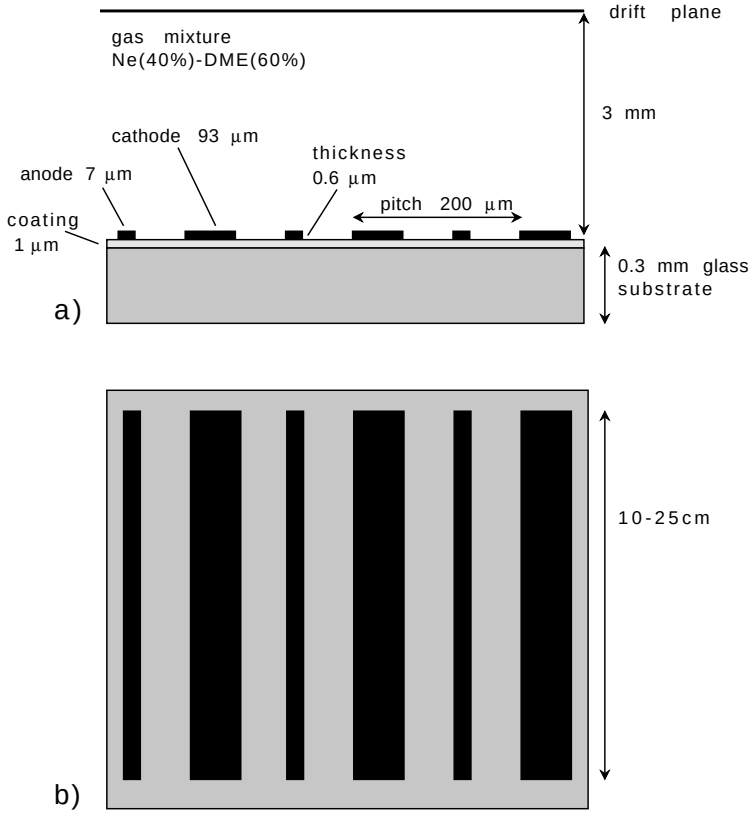

Fig. 4.1: A cross section and a top view of the MSGC detector.

collecting field. At ∼100 μm from the anode strip the electric field starts to increase rapidly above the gas amplification threshold because of the focusing on the anodes of field lines coming from the side and drift cathodes. When a charged particle crosses the active gas volume, the ionisation electrons drift towards the anodes. Close to the anodes the electric field is so strong that gas electron multiplication starts to develop. Electrons produced in the avalanche are quickly collected by the anode strips, while the positive ions migrate towards the side and drift cathodes, inducing negative currents on the anode strips and positive currents on the cathode strips. As in the MWPC, more than 90% of the signal is provided by the motion of positive ions and only 10% by the collection of avalanche electrons. However, a major advantage of the MSGC and MGC concept compared to the MWPC, is the much faster signal development (see Fig. 4.3). After 50 ns, in the MSGC ∼ 70% of the induced charge is already available, while in the MWPC this is only 25%. In the MGC this fraction is 90%.

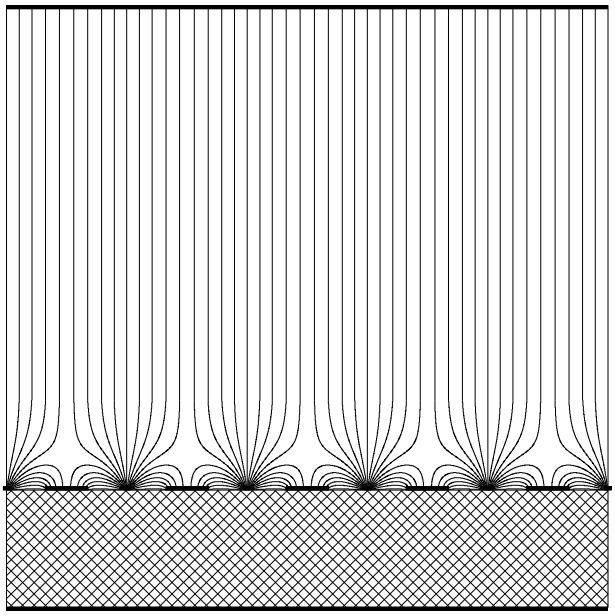

Fig. 4.2: The electric field in a MSGC.

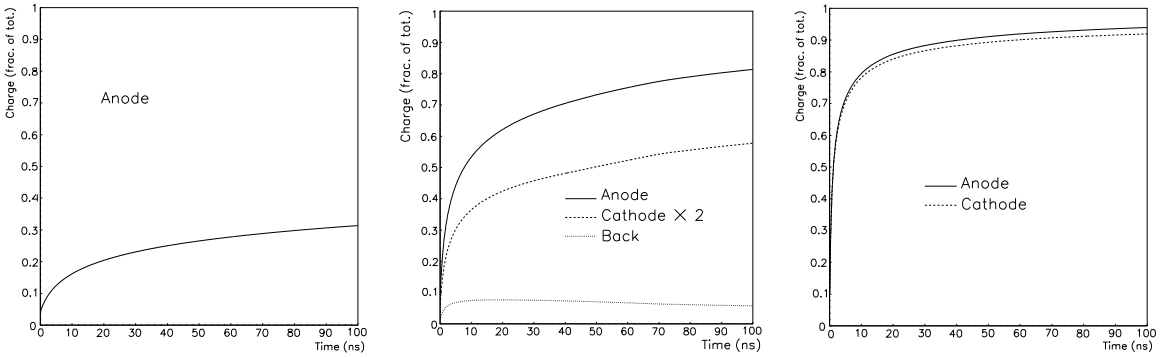

(a) MWPC **(b)** MSGC **(c)** MGC

Fig. 4.3: Time development of the induced charge on the electrodes of a MWPC (a), a MSGC (b) and a MGC (c).

4.3.2 Basic detector properties and substrate characteristic

In the manufacture of a MSGC many parameters significantly affect its performance and lifetime. Substrate, metallisation, processing, gas purity and composition, assembling material and components must be kept under control. Most of these parameters are discussed in the following paragraphs.

4.3.2.1 Coating

The material most commonly used as the supporting substrate for the fabrication of MSGCs is glass. The substrate should not be a perfect insulator. This can be understood by looking at Fig. 4.4, showing the field lines of a MSGC built on a perfectly insulating support. Several field lines leaving the anode strips end on the substrate without reaching the cathode. The avalanche ions which will follow these field lines will charge up the substrate producing a new electric field configuration which modifies the gas gain of the MSGC. The charging of the substrate continues until a new steady-state is reached and no more field lines end on the substrate. In this new electrostatic configuration the E-field at the anode is lower than at the beginning and the gas gain is reduced. This reduction can be as large as a factor 3 or 4. Charging of the substrate is a local, reversible and, at the LHC rates, short-term effect. The new steady-state is typically reached in a few minutes. However, a major drawback of a detector with a large charging effect is the non-uniform response to incoming radiation, whose flux can vary both in space and time. The way to reduce the charging effect to an acceptable level ($\sim 10\%$) is to make the surface onto which the electrode structure is engraved slightly conducting. Figure 4.5 shows the electric field lines of a MSGC in which a thin conducting layer was deposited on the surface of a perfectly insulating substrate before the definition of the strip structure. Now, all the field lines originating in the avalanche region leave the substrate and end on the cathode and ion charging of the substrate is no longer possible. The few charges which eventually end up on the substrate because of stochastic processes (collision, diffusion, etc.) will be drained by the slightly conductive layer and neutralised by the charge collecting electrodes. Coating the substrate acts like a smoothing of the electric field. Indeed, the vertical component of the electric field close to the anode strip is, for the same voltage setting, lower, of opposite direction and extends over a larger volume with respect to an uncoated substrate (Fig. 4.6). Another important implication of the deposition of a thin semiconducting layer on the substrate surface is its *electrostatic shielding* effect. The lower the ratio $\rho_{bulk}^{layer}/\rho_{bulk}^{substrate}$, the more pronounced is this behaviour for both smoothing of the electric field and for the shielding effect. It can be shown [4-1, 4-2, 4-3] that the presence of a semiconducting layer with a bulk resistivity 5 or more orders of magnitude lower than that of the substrate makes the detector fully insensitive to any variation of the substrate bulk electrical characteristics. These variations may be induced by polarisation phenomena or charge trapping under high electric and radiation fields.

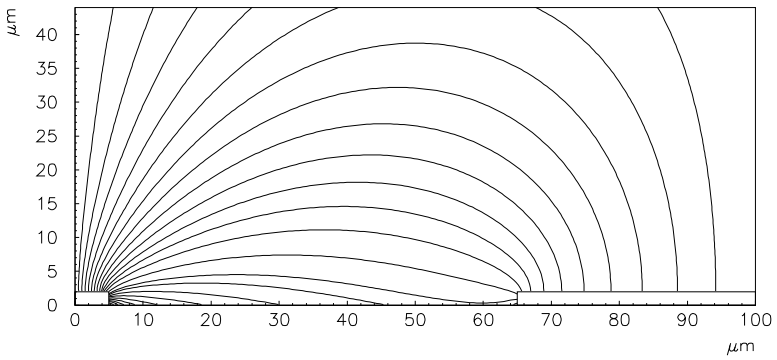

Fig. 4.4: Electric field lines of a MSGC built on a perfect insulator.

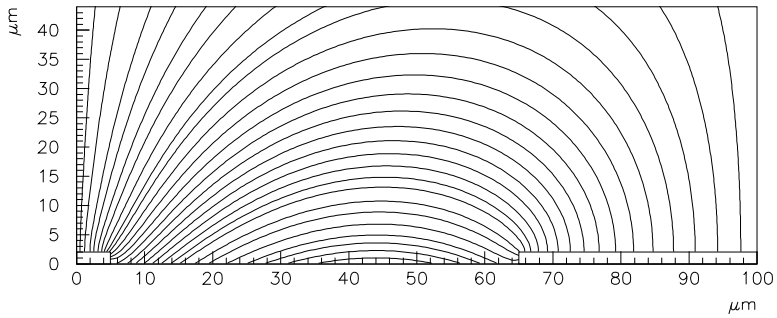

Fig. 4.5: Electric field lines of a MSGC with a thin conductive layer deposited on a perfectly insulating substrate.

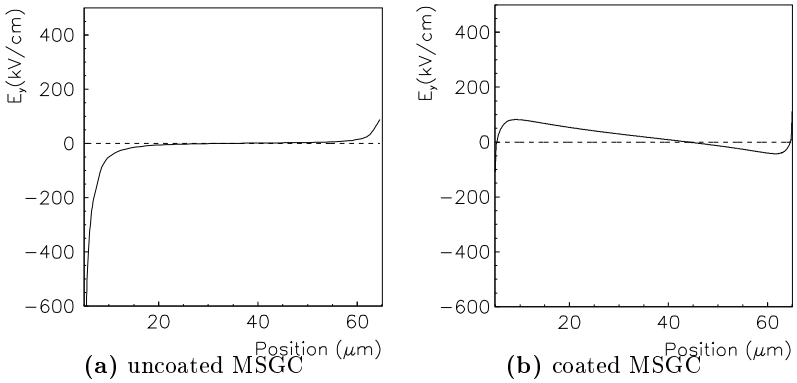

(a) uncoated MSGC **(b)** coated MSGC

Fig. 4.6: The vertical component of the electric field versus the distance to the anode strip in a *uncoated* (a) and *coated* (b) MSGC.

Because of the smoothing effect, in a coated MSGC the gas gain is lower from the beginning but stable and independent of rate. Nevertheless, an unwanted but unavoidable consequence of the surface coating process is the need to operate the MSGC at higher voltages to achieve the same gain as with an uncoated substrate. To minimise this effect we prefer to work at the highest possible resistivity value, compatible with the LHC rates. We found experimentally that a surface resistivity $\sim 10^{16}$ Ω/square is low enough to reduce the charging effect below 10%. Working at 10^{16} Ω/square requires a modest increase of $\sim$ 15V of the operating voltage, while working at $\sim 10^{14}$ Ω/square requires an increase of $\sim$50 V. This fact is important to maintain the longest possible plateau length and large safety margins. In this condition, MSGCs behave experimentally according to our electrostatic model with a ratio $\rho_{bulk}^{layer}/\rho_{bulk}^{substrate} \simeq 10^{-3}$, corresponding to a situation of partial shielding and partial electric field smoothing.

The coating process we have chosen consists of depositing, using a RF magnetron sputtering technique, a thin layer ($0.5 \div 1$ μm) of Pestov glass on the surface which later will be used to photolitographically define the strip structure (undercoating). Pestov glass, as well as its commercial analogue (Schott S8900), is a semiconducting glass with electronic conductivity. Its bulk conductivity which can range from 10^{-9} to 10^{-12} $(\Omega\text{cm})^{-1}$ is provided by a large admixture of iron oxides. Electronic conductivity is preferred to ionic conductivity to avoid the large polarisation phenomena induced by ion migration under high electric field.

We have also studied in depth an alternative technique based on a thin film of a carbon-carbon compound (diamond-like coating, DLC) obtained with a plasma enhanced chemical vapour deposition (PECVD). This technique shows good uniformity and reproducibility of coating comparable to the Pestov one, but we have observed in various beam and laboratory tests

a lower voltage breakdown limit in DLC-coated MSGCs than in Pestov-coated MSGCs. This is probably related to the presence of unstable graphite clusters dispersed in the amorphous diamond matrix typical of these chemically produced films. For this reason, the DLC technique has been ruled out.

4.3.2.2 Metallisation

A fundamental choice for achieving optimal performance of a MSGC is the kind of strip metal used [4-4]. In particular, the use of low specific resistance metals for the anode strips ($< 40\,\Omega/\mathrm{cm}$) is mandatory when working with long strips and fast electronics. It avoids a position dependent attenuation of the signal and an increase of the detector noise. A low resistivity metal, commonly used in micro-electronics, is aluminium or a silicon-aluminium alloy. Unfortunately, aluminium is a very active metal and is known to react vigorously with the species produced in the avalanche plasma. It induces a very fast ageing of the detector [4-5, 4-6]. Conversely, *gold* is chemically inert and has a resistivity even lower than aluminium. It does not interact with the avalanche plasma and, furthermore, it is very difficult for the polymers which are produced in the avalanche by pollutants, to attach to it. Coating by polymers and therefore ageing of MSGCs has been drastically reduced by working with gold strips [4-5, 4-6].

4.3.2.3 Patterning

Many patterning techniques have been tried and could be used to define the electrode structures (plasma etching, reactive ion etching, galvanic growth, lift-off, etc.). The simplest, most economical and least aggressive for the underlying coating layer, is the *lift-off* technique (Fig. 4.7).

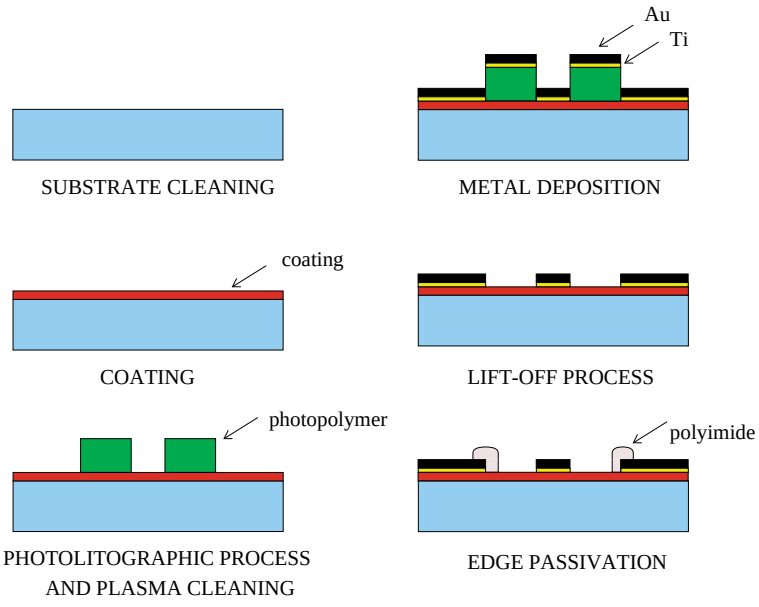

Fig. 4.7: The *lift-off* technique.

With this method a *photo-resist* layer is uniformly deposited on the *coated* substrate and then exposed to a UV light source through a mask which reproduces the strip pattern. A chemical bath then removes the photo-resist layer in the areas not exposed to the light. In the next step, an adhesion Ti layer followed by a gold layer are deposited, by evaporation, over the whole surface to cover both regions of uncovered substrate and photo-resist. At the end of this process the remaining photo-resist is removed with a solvent which also removes the overlaying metal

leaving the desired pattern of gold strips. As the last step in the processing, a thin polyimide layer is deposited on the whole detector surface, photolitographically defined and developed to passivate all the critical edges of the strips. Critical for the production of high quality MSGC plates are the conditions of cleanliness. Indeed, most of the defects found on the plates are due to imperfect cleaning of the substrate itself and/or of the room in which the detectors are manufactured. We have identified some typical defects:

- *dots* - residuals of gold probably due to dust particles that shadow during the photo-resist exposure, or incomplete lift-off. We distinguish different types of dots: cathode dot, anode dot or simply dot, depending if they are on the cathode edge, on the anode edge or in the gap between anode and cathode. Residuals of gold at the edge of the electrodes, in particular along the cathode border, can easily initiate sparks. The strips corresponding to these dots will not be connected to the readout electronics.
- *opens* - interruptions of the anode or cathode strips. They are not dangerous for the operation of the detector but they limit, locally, the spatial resolution.
- *shorts* - due to metallic residuals which connect two or more strips. These strips will not be connected to the readout electronics and left floating.
- *passivation defects* - interruptions or displacements of the passivation line (see Section 4.3.2.5). If the extension of the defect is not too large, the strips will be connected to the readout electronics.

4.3.2.4 Electric field configuration

The electric field in a standard MSGC is the sum of two contributions: the dipole field defined by the potential difference applied between anodes and side cathodes and the drift field defined by the potential difference applied between the drift plane and the strips (see Fig. 4.8). Both fields contribute to the gas gain. There is a great advantage in working at the highest possible drift field and at the lowest possible dipole field. First of all, a high drift field is needed to saturate the electron drift velocity in the gas gap and to counteract the strong Lorentz force on the ionisation electrons induced by the magnetic field in the barrel MSGCs. At 10 kV/cm the Lorentz angle can be limited to $\sim 3.6\,^{\circ}$/Tesla. Secondly, a high drift field allows the gain to be increased in a much safer way than by increasing the strip cathode voltage. It can be seen from Fig. 4.8 that the dipole field and the drift field have opposite direction at the cathode strips, while having the same direction at the anode. Therefore by increasing the drift field we increase also the anode field and the gas gain but, at the same time, we reduce the cathode field which is the critical field in terms of safety of operation. It is at the cathode where electron emission and then self-substained discharges usually take place. If V_d and V_c are respectively the drift voltage and the cathode voltage (both referred to the anode), for each value of the ratio V_d/V_c we can identify within the volume of the MSGC a region where increasing V_d the electric field $\vec{E} = V_c\vec{e_c} + V_d\vec{e_d}$ decreases (see Fig. 4.9). This region always includes the cathode strip for every reasonable value of V_d/V_c. The reverse is true for the electric field at the anode: it is always an increasing function of V_d. Figure 4.10 shows the simulated dependence of the cathode and anode field and of the gas gain on the drift voltage.

Figure 4.11 shows an experimental measurement of the signal charge dependence on the drift voltage at $V_c = -530$ V. To get an idea of the cathode voltage saving a single measurement at the highest drift field and at $V_c = -510$ V is also shown.

An increase of 1200 V of the drift voltage allows a 'saving' of 32 V on the much more critical side cathode voltage, to get the same gain.

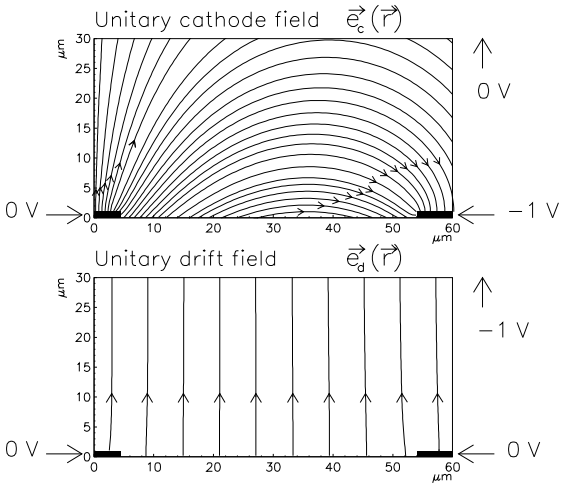

Fig. 4.8: The shape of the dipole field and of the drift field in a typical MSGC (not to scale).

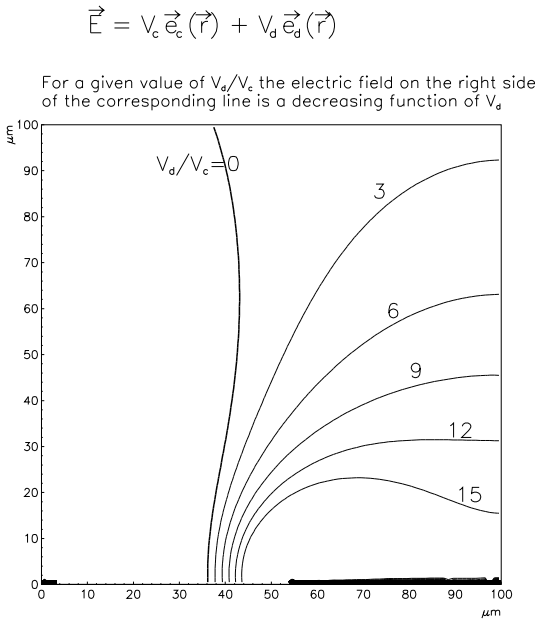

Fig. 4.9: Contour plot of regions of the detector where the electric field is a decreasing function of the drift potential.

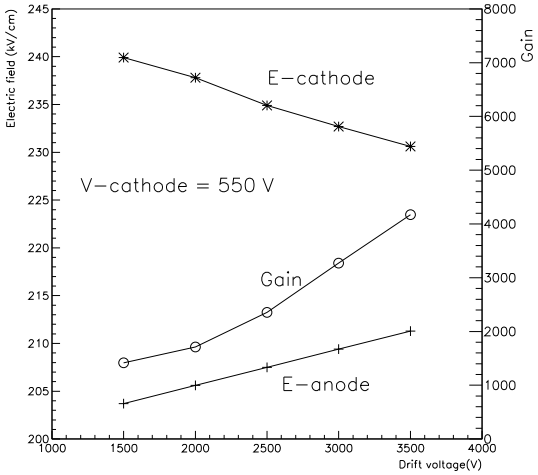

Fig. 4.10: Simulated dependence of the cathode and anode field and of the gas gain on the drift voltage.

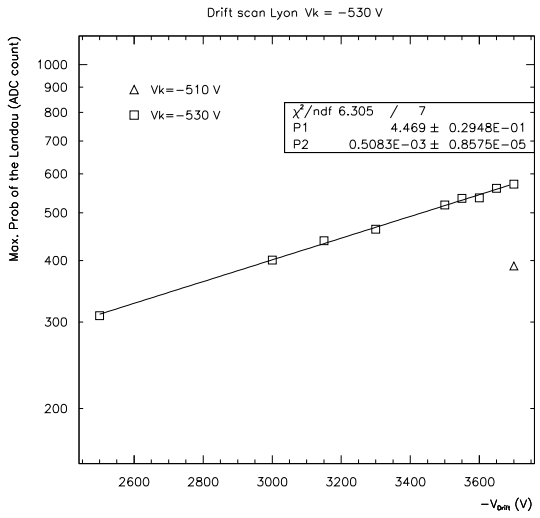

Fig. 4.11: Experimental measurement of the collected charge dependence on the drift voltage taken at $V_c = -530$ V and at -510 V.

4.3.2.5 Advanced passivation

The most critical parts of the MSGCs are the electrode edges. In these very sharp regions the electric field is significantly reinforced. The break-down limit and therefore the length of the efficiency plateau is set, mainly, by the behaviour of these regions of the detector. To prevent extraction of electrons from edges and therefore to extend the range of the operating voltage of the detector we have adopted special precautions. The anode extremity, opposite to the readout pad, has been rounded off and the adjacent cathode strips have been shaped to maintain the correct anode-cathode distance (Fig. 4.12). On the side of the anode readout pad the cathode edges have been also rounded. A further safety factor has been provided by adding on top of the anode-cathode structure, at the detector border, a 200 μm wide passivation layer (*standard passivation*). This layer is made of curable polyimide, a material with a very high dielectric strength (~30 kV/mm). A further improvement has been achieved by covering all the cathode edges, along the strips, with a polyimide layer (*advanced passivation*, Fig. 4.13 [4-7, 4-8]). Since these edge passivating lines are very thin (4 μm) and very narrow (8 μm), they hardly affect the electric field at the anode strips. With these precautions the operating region of the detectors has been significantly extended up to high gain even in the presence of highly ionising particles (see Section 4.3.3.4).

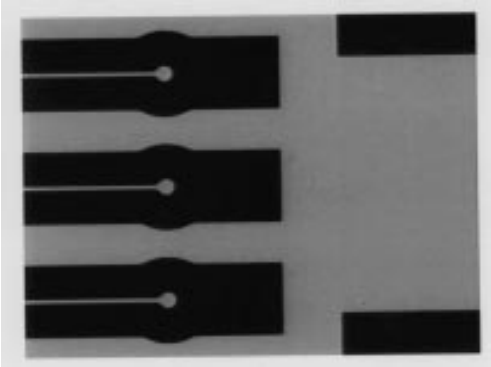

Fig. 4.12: Detail of the optimised layout of the edges of anode strips.

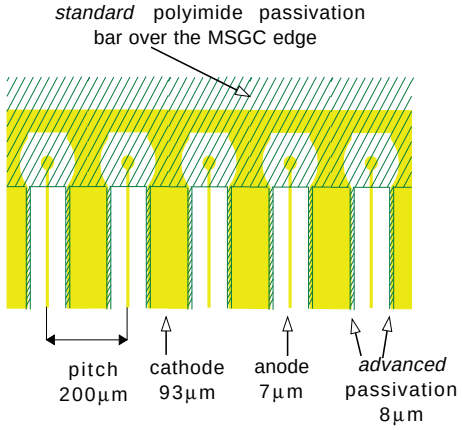

Fig. 4.13: Scheme of the structure of a MSGC where the position of both *standard* and *advanced* passivation is shown.

4.3.2.6 Effect of a missing strip

As discussed earlier, in the patterning section, detectors of such a large area cannot be built 'defect-free' at a reasonable yield.

Defects like shorts or large cathode dots cannot be repaired at low cost. The only practical solution is to disconnect the defective strips from the readout chain leaving them to float and, eventually, reach the cathode voltage of the nearby strips.

At start-up many MSGCs may have a few missing anode strips ($< 2\%$). The removal of an anode strip is equivalent to increase the readout pitch, locally, from 200 μm to 400 μm. Figure 4.14a shows, in real scale, the electric field configuration for an MSGC when a floating strip is present. No major field distortion is visible in almost all of the drift volume. Only a

local distortion of the electric field takes place close to the strips (Fig. 4.14b) because the field lines belonging to the missing anode end now on the two neighbouring anodes. This means that the primary charge will be collected by the neighbouring strips. Therefore a missing strip does not imply any loss of detection efficiency but only a local loss of spatial resolution and a modest increase of the electric field (see Fig. 4.15) and of the gas gain ($\sim 25\%$) on the neighbouring anodes.

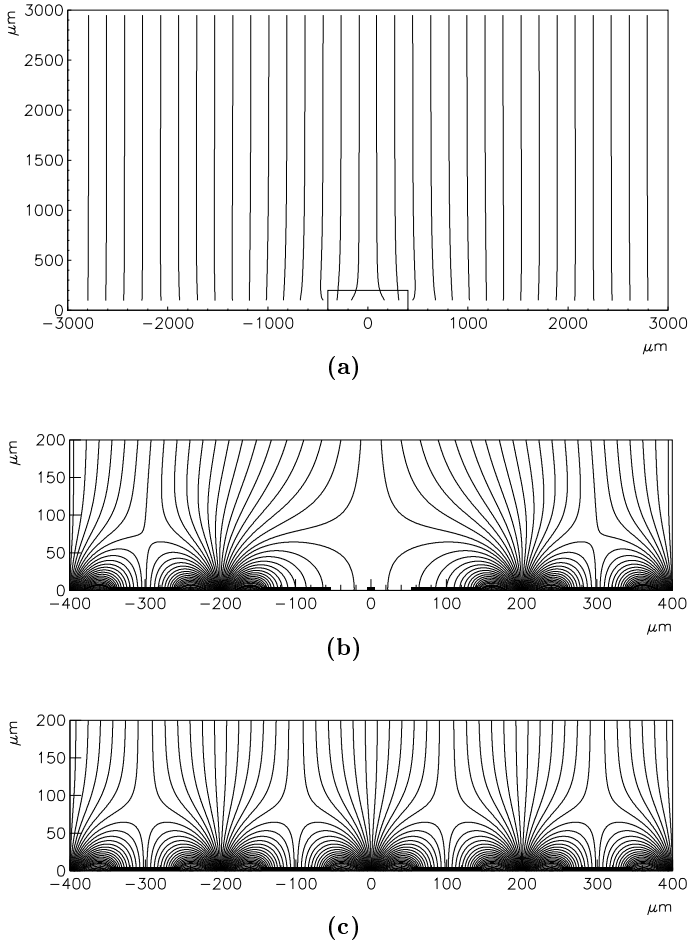

Fig. 4.14: (a) The electric field configuration for a MSGC when a floating strip is present in the middle; (b) an enlarged view of the region in the rectangular box, close to the floating strip, in comparison (c) with the field shape when no floating strips are present.

The preservation of the detection efficiency has been observed experimentally. Figure 4.16 shows a beam profile obtained with a chamber having three disconnected strips. Each hole in the beam profile is accompanied by an increase of counts on the neighbouring strips.

4.3.2.7 Signal cross-talk

The strip specific capacitance is 0.32 pF/cm. If all the cathode strips of a detector with 512 anodes and 12.5 cm strip length are connected together, the overall detector capacitance would be 2 nF. In case of a spark, the considerable amount of energy stored in this large capacitance would be available to sustain the discharge. To limit the possibility of damage to the strips it

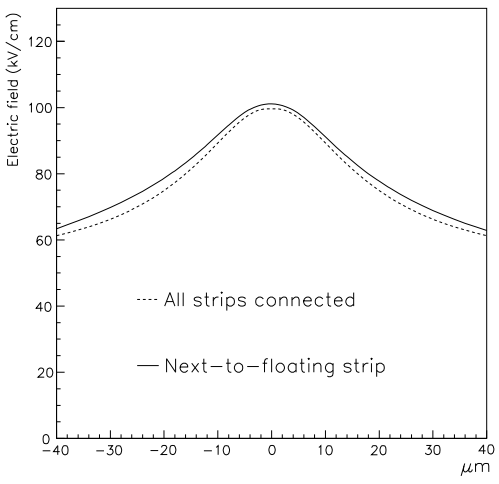

Fig. 4.15: Profile of the electric field at 10 μm above the anode when all the neighbouring strips are connected (dashed line) and when one strip is disconnected (solid line).

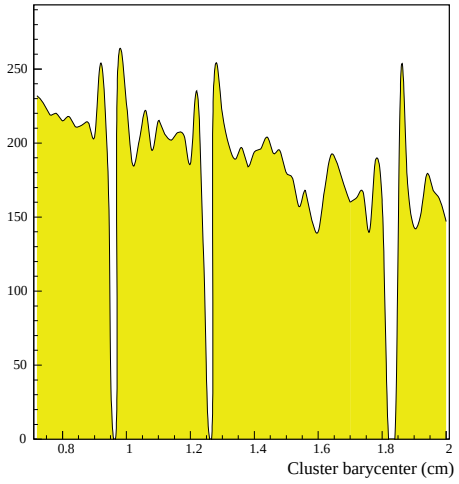

Fig. 4.16: Beam profile obtained with a chamber having three disconnected strips.

is considered safer to subdivide the detectors into groups of 16 strips each connected to high voltage through an individual large limiting resistor (see Fig. 4.17).

A direct implication of this choice is that some, small, cross-talk has to be accepted. Indeed, the positive currents induced on the cathode strips cannot return to ground through the H.V. power supply because of the large impedance provided by these large resistors. They will return to ground via the mutual capacitance between anode and cathode strips. On each anode strips of the group, a positive current equal to the total cathode current divided by 16 (6% cross-talk) will appear. On the anode strips where the avalanche took place, this positive current will reduce the signal current (negative) by 6%. On the other strips of the group a shift in the pedestal is produced. This has been clearly detected experimentally as shown in Fig. 4.18.

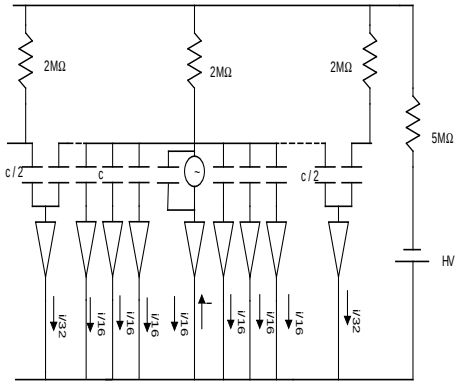

Fig. 4.17: The equivalent circuit of a MSGC.

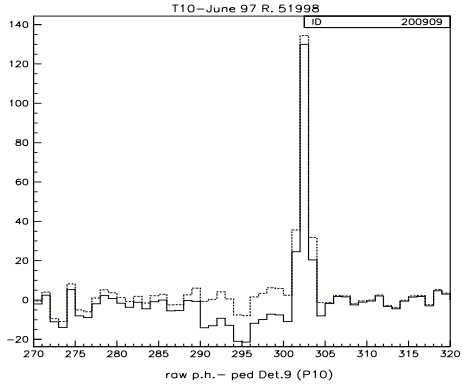

Fig. 4.18: Effect of the cross-talk and its correction (dotted line) with the off-line analysis.

4.3.2.8 Choice of the gas mixture

The major requirements for the MSGC gas mixture are:

- large $\mathrm{d}E/\mathrm{d}x$ to have enough primary clusters from a very thin layer of gas (3 mm)
- large gas gain
- fast primary charge collection for small bunch-crossing pile-up
- working point at lowest possible voltage
- longest possible plateau length
- small Lorentz angle at 4 T
- no, or slow, ageing

Some of these requirements are contradictory (for example small Lorentz angle and fast collection time). The best trade-off we have found is a mixture of 40% neon and 60% Di-Methyl Ether (DME).

DME is a *non ageing* gas with large primary cluster as well as total ionisation density (60 clusters/cm and 180 electrons/cm, respectively, at 2 GeV/c). Its ionisation potential is quite low (10 eV). Neon is a noble gas with low cluster and charge density (13 cluster/cm and 40 electrons/cm, respectively). Its excitation and ionisation potential are, instead, quite high (18 and 22 eV, respectively).

From many points of view, 100% DME would be the best gas filling for CMS. However it would require operating the chambers at too high cathode voltage (well above 600 V) which is not considered safe in case of sparking. The addition of a noble gas is mandatory to lower the cathode voltage operating point. The use of a noble gas with a high excitation potential like neon acts like a dilutant for the DME component [4-9]. The mean free-path between inelastic (exciting) collisions increases, allowing the drifting electrons to acquire a larger kinetic energy from the electrostatic field. This improves the efficiency of the ionisation process for the DME, which has an ionisation potential much lower than the excitation potential of the noble gas. In a mixture based on DME but containing some neon, more collisions will be ionising, instead of exciting, allowing large gains to be reached at reasonably low voltages. This is obtained at the expense of some reduction of the total primary charge. In a gap of 3 mm filled with a mixture of Ne(40)-DME(60) the total number of primary electrons is 40 at 2 GeV/c. Working with this mixture during the T10 beam test we have shown that the operating voltage for full efficiency at the LHC running conditions can be as low as 520 V [4-10]. Neon-DME mixtures have not only a low working point but also a quite long plateau length as determined experimentally in a cosmic ray test (see Fig. 4.19, [4-9]). This is due to the strong suppression of the photon feedback effect. Neon is, contrary to argon and xenon, a quite poor UV scintillator while DME is a very effective UV light absorber. Suppression of UV light and then of electron extraction from the metal electrodes is particularly important in a structure like the MSGC where the electrodes are very close to each other. Suppression of UV light is also considered important for slow ageing of the detector. It is well known that UV light is a strong catalyst and accelerator of the polymerisation processes [4-11]. The production of polymers in the avalanche plasma is mainly responsible for the electrode coating which, ultimately, induces ageing of the detector.

The electron drift velocity of Ne(40)-DME(60) in a drift field of 10 kV/cm is 5.5 cm/μs. The charge collection time in the 3 mm gas gap will then be 54 ns which matches reasonably well with a bunch-crossing pile-up not greater than two. The Lorentz angle at $B = 4$ T, $E = 10$ kV/cm, $v = 5.5$ cm/μs, is 14 °.

A further increase of the drift velocity can be obtained by the addition of a small amount ($10 \div 20\%$) of CO_2. For example, an increase of $\sim 15\%$ of the drift velocity can be obtained by working with a mixture of Ne(45)-DME(45)-CO_2(10). This mixture has the same working point of the Ne-DME mixture and a plateau length 10 V longer [4-9]. These advantages have to be

balanced with the disadvantages of a ternary gas mixture and of the increase of the Lorentz angle in the barrel.

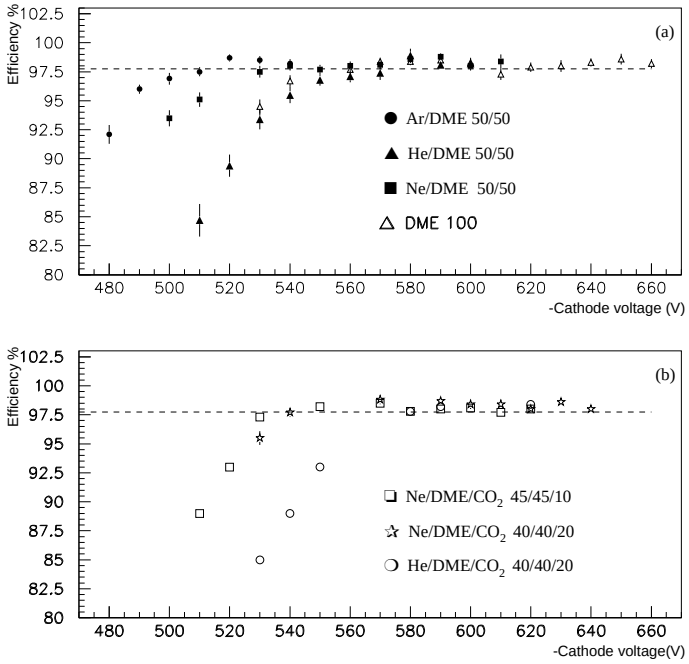

Fig. 4.19: Efficiency as a function of the cathode voltage for different gas mixtures.

4.3.2.9 Performance prototype

For most of the tests described in the next paragraphs we have used a set of MSGCs built according to the CMS specifications regarding substrate properties, assembly materials and components for the module. The following list describes the main features of the so-called *performance prototype*:

- *Substrate*: D263 glass 10×10 cm^2 active area, thickness 300 μm
- *Coating*: 1 μm thick under-coat of Pestov glass with surface resistivity of 10^{16} Ω/square
- *Strips*: gold of at least 0.6 μm thickness; $R = 40$ Ω/cm
- *Pattern*: anode width 7 μm, cathode width 93 μm, pitch 200 μm, 0.32 pF/cm
- *Passivation*: advanced polyimide passivation line 4+4 μm wide, 2 μm thick
- *Readout*: anode readout (with Premux [4-12])
- *Bias*: anode strips at ground potential, cathodes strips at negative bias (-520 V), drift cathode $-3000 \div -3500$ V
- *Resistors*: 1 MΩ per substrate, 200 kΩ per group of 16 cathode strips, no decoupling capacitor
- *Drift plane*: metallised PEEK[1], carbon fibre or glass
- *Gas mixture*: Ne(40)-DME(60), renewal rate less than 5 times/hour
- *Gas gap*: 3 ± 0.1 mm

4.3.3 Tests related to the operating environment

4.3.3.1 Charging-up effects

The process of charging in a MSGC is an interaction between two competing processes, each having a characteristic time constant.

[1] Poly-Ether-Ether-Keton.

The first process is the production and spread of charges on the substrate surface (source), the second is the collection (drain) of these charges through the coating layer (or the substrate in the case of a MSGC with uniform conductivity).

The characteristic time constant for the process of collecting a charge injected in a conductive layer with conductivity $\sigma = 1/\rho$ is given by the relaxation time [4-13]:

$$\tau = \varepsilon/(4\ \pi\ \sigma)\ \text{(Gaussian units)} = \varepsilon_0\ \varepsilon_r\ \rho\ \text{(MKSA)}$$

The constants $\varepsilon_r = \varepsilon$ and σ refer to the material which is responsible for the charge draining, in our case the coating layer (while for MSGCs with uniform conductivity it is the substrate).

The characteristic time constant for the process of charging of a MSGC built on a perfect insulator is given by:

$$t_0 = \eta_0/\mathcal{F}n$$

where η_0 is the number of avalanches per unit area that have to be produced before a fraction of $\sim 2/3$ of the overall gain variation is reached, $\mathcal{F}$ is the particle flux and n is the total number of primary ionisation electrons produced on average in the gas gap by each traversing particle.

Figure 4.20 shows the simulated variation of the gas gain for a MSGC where no drain of the charge ending on the substrate is assumed [4-14]. From this plot we can derive:

$$\eta_0 = 3 \div 4\ 10^7\ \text{avalanches/mm}^2$$

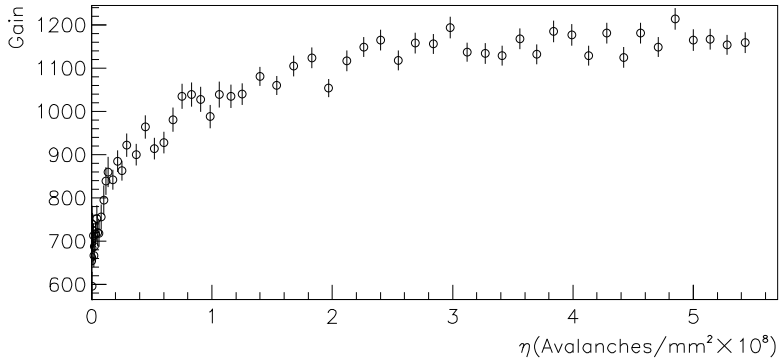

Fig. 4.20: The simulated dependence of the gas gain on the number of collected avalanches per unit area in a MSGC for which no drain of the charge ending on the substrate is assumed.

Thus, different behaviour with respect to charging is possible, depending on the ratio τ/t_0. If $\tau \ll t_0$, charges are drained away as soon as they are deposited on the coating. If, on the contrary $\tau \gg t_0$, the charges accumulate and change the gain of the detector in times of the order of t_0. The gain will decrease in the case of accumulation of positive charges, while it will increase in the case of accumulation of negative charges. From the observation of the shape of the field lines of a coated MSGC (Fig. 4.5) we can realise that the latter will be the case when working with coating layers of too high resistivity. This has been observed experimentally by several groups [4-15, 4-16, 4-17].

In our case, with $\mathcal{F} = 10^4$ mm^{-2} s^{-1}, $n = 40$, $\rho = 10^{12}\ \Omega$ cm, $\varepsilon_r = 4$, we will have $\tau = 0.3$ s and t_0 =100 s. Because $\tau \ll t_0$, very little charging is expected for the Pestov coated MSGC of CMS. This has been studied extensively in a series of laboratory tests reported in [4-15, 4-16]. The main result is shown in Fig. 4.21 showing the signal current as a function of time for a detector never irradiated before, just after the switch-on of the high-intensity X-ray source. The detector response is stable from the very beginning for various gas gains.

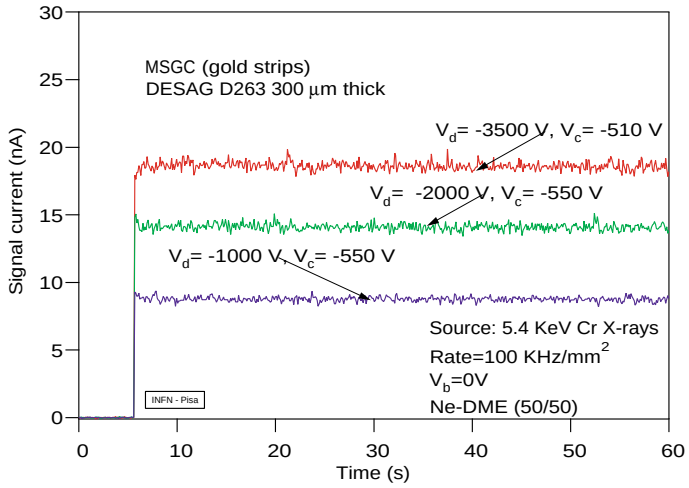

Fig. 4.21: Very short stability of response (charging) at different voltage settings.

4.3.3.2 Rate capability

The MSGCs will be exposed to variable rates depending on their distance from the beam axis. At full luminosity these rates will span the interval between $10^3 \div 10^4$ p/mm^2 s. The rate capability of the MSGCs is the ability to give a uniform response, i.e. equal gas gain, in presence of this dynamic range. The rate capability of the Pestov coated MSGC of CMS is shown in Fig. 4.22, together with the results for a MSGC built on a bare (uncoated) Desag D263 substrate. The improvement of rate capability going from uncoated to coated chambers with progressively lower resistivities is very evident. Chambers coated with films of $\sim 10^{16}$ Ω/square resistivity, such as those of CMS, have a rate capability at least one order of magnitude above the CMS needs. This means that there is room for a further increase of resistivity, if eventually needed.

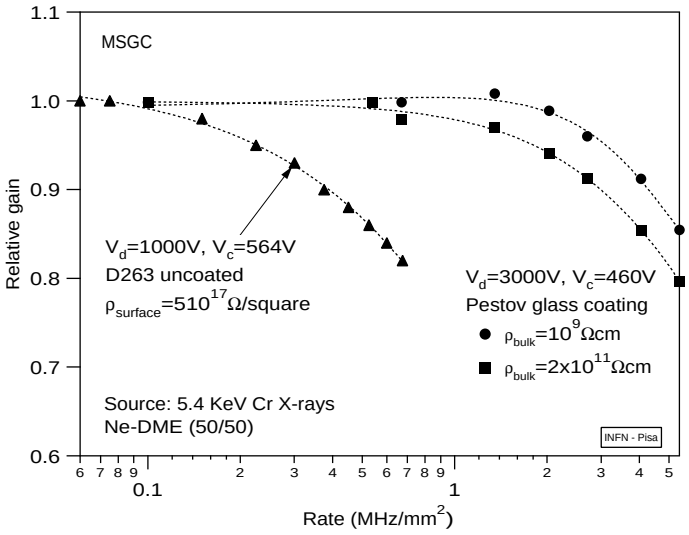

Fig. 4.22: The rate capability of a MSGC coated with a thin film of Pestov glass having two different bulk resistivities. Results of an uncoated detector are also shown.

4.3.3.3 Ageing

Ageing is a local, irreversible, long-term modification of the initial working conditions of the detector. It is due, mainly, to the growth on the electrode structures of deposits of insulating

materials. The main mechanism responsible of this effect is the process of polymerisation of dissociation products caused by ionisation and UV light in the avalanche plasma. Many unwanted effects originate from the *charging-up* of these insulating coatings, like reduction of gain and sparking.

The loss of gain which is measured by the quantity

$$R \;=\; -1/G\; dG/dQ\; (\%perC/cm)$$

depends essentially on the amount of avalanche charge collected per unit strip length.

Five major precautions have to be taken to keep ageing under control:

- *lowest possible gas gain*; to minimise the amount of charge collected by the strips.
- *non active strip metal*; gold, being chemically inert, has very poor attachment properties.
- *non polymerisable gas mixture*; Neon is a noble gas with a very poor UV light yield while DME is a very good UV light absorber well known as a gas difficult to polymerise [4-18]
- *clean gases and clean gas distribution system*; pollutants, like freon, present in the gas bottles or in the gas system can spoil dramatically the ageing resistance of the detector modules. The gas purification and control system is described in Section 6.3.5.
- *clean and low-outgassing module assembly materials and glues*; all the components utilised in the assembly of the individual detector modules have to be carefully tested for their ageing characteristics.

MSGCs built according to the previous specifications have undergone a long series of ageing tests in various CMS labs. The main results are summarised in Fig. 4.23. The modulation observed in the detector response is due to the day–night variation of temperature and pressure.

4.3.3.4 Response to heavily ionising particles and to high rates of charged hadrons

In CMS, the MSGCs have to detect not only the high rate of $10^4/\mathrm{mm}^2$ s of minimum ionising particles (mip's) but also a superimposed low rate of heavily ionising particles (hip's) produced by nuclear interactions of hadrons and neutron with the detector materials (see Appendix A). The typical energy loss of a mip in a 3 mm gas gap is 1 keV, while the energy loss of a hip can range from a few tens of keV to few MeV in the case of production of nuclear fragments. The problem is to see if the efficiency plateau is long enough to cope at the same time with mip's and hip's without sparking and therefore damaging the strips and/or the front-end electronics. The addition of the coating layer has made the problem somewhat more critical. Indeed, after coating, the electric field around the anode strip is smoother and weaker (see Section 4.3.2.1). A higher voltage is needed to get the same gain. After this increase of voltage the field at the substrate is high again but more uniform in a *quasi parallel-plate* configuration. This configuration is known [4-19] to favour the development of unquenched streamers across the anode cathode gap. In the presence of hip's the streamers can evolve into micro-discharges or full discharges that can eventually damage the detector. We have found that the technique of advanced passivation is very helpful to increase the safety margins and to make the plateau long enough to accommodate all possible sources of fluctuations or uncertainties in the signal or in the noise. We have also found that the critical factor is the field configuration more than the gas gain.

Results from laboratory tests

Figure 4.24 shows a laboratory measurement of the spark limit for MSGCs with and without advanced passivation in the case of weakly ionising (X-rays) or heavily ionising particles (*alphas*). A gain curve showing the working point for this specific chamber is also shown. The large increase of the operating voltages range is clearly visible.

In a MSGC a streamer or a micro-discharge generates a signal with a very long decay time detectable on all the channels independent from where it was generated. We have utilised this

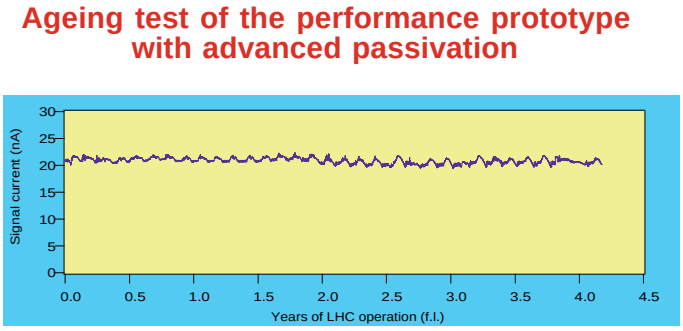

Fig. 4.23: Long-term stability measurement of the performance prototype.

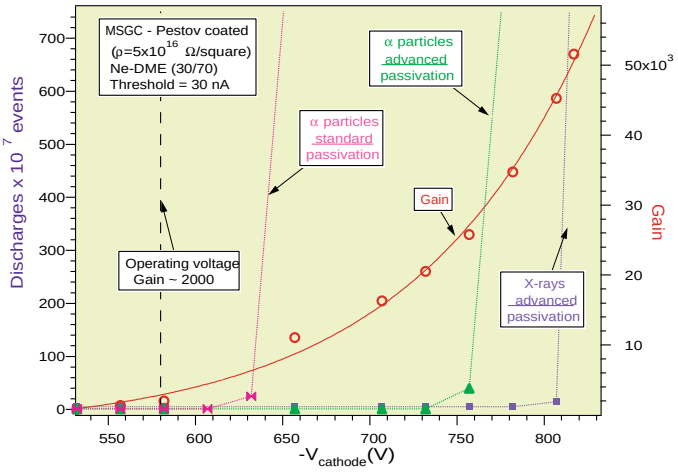

Fig. 4.24: The spark limit for MSGCs with and without advanced passivation in the case of weakly ionising (X-rays) or heavily ionising particles (alpha). The gain curve is also superimposed. This specific chamber has 11 μm anode width.

property to study the point and the shape of the transition into the *streamer regime* in the presence of hip's (alpha particles) [4-20]. Figure 4.25 shows the number of signals with a decay time longer than 4 μs detected per second per strip length as a function of the cathode high voltage. Long signals appear at voltages higher than 700 V, i.e. 100 V above the operating voltage of this specific chamber. As in conventional proportional chambers, one observes in the MSGC a clear separation of the proportional from the streamer regime. The change of regime starts at a well defined voltage.

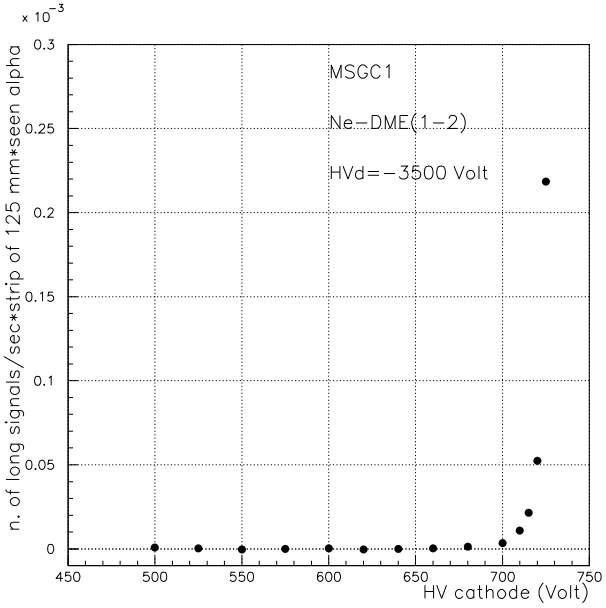

Fig. 4.25: The number of long signals detected per second per strip length as a function of the cathode high voltage ($-V_c$).

Results from exposures to high-intensity hadron beams at CERN and PSI

There are experimental indications [4-21] that the voltage limit for the transition into the streamer regime could be affected (lowered) in a high rate environment. Laboratory studies with α-sources can explore the response of the MSGCs to energy losses up to $300 \div 400$ keV, without the superimposed radiation field of charged hadrons.

To study the full dynamic range of energy deposition in realistic conditions, two tests at high-intensity hadron beams were performed in 1997.

A first set of five MSGCs was assembled according to the CMS baseline specifications (see Section 4.3.2.9) and exposed to 3 GeV/c π beam at the CERN T10 facility. One detector was assembled with the forward CMS tracker layout and read out orthogonally to the other detectors.

A first set of measurements in T10 was dedicated to find the voltage working point at which the MSGCs have to operate in the CMS environment. Figure 4.26 shows the result of a voltage scan on the gas gain, S/N and hit detection efficiency.

The required S/N for the CMS MSGCs is 20. In order to reproduce in T10 the CMS working conditions, we have to introduce a factor 2.2 reduction in S/N (mainly because of increase of noise and ballistic deficit of the final electronics). We can derive from Fig. 4.26 that the required S/N is therefore 44, corresponding to a cathode voltage of -520 V. From the same figure we can also derive that an increase of 50 V of the operating voltage produces an increase of almost a factor 2.7 in the gas gain.

The results obtained in T10 confirm that the MSGC chambers working at a signal to noise ratio of 20 are fully efficient.

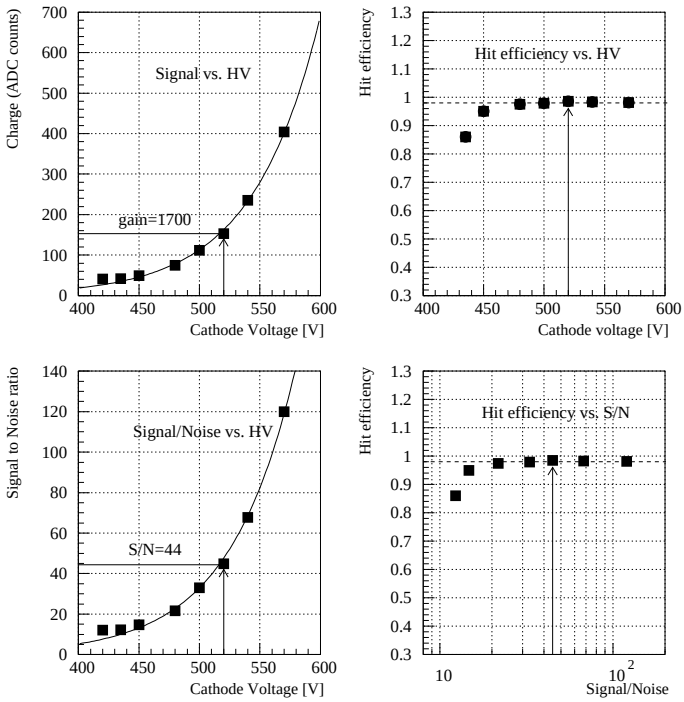

Fig. 4.26: Voltage scan on the gas gain, S/N and hit detection efficiency obtained with a performance prototype at T10.

The T10 beam, which has a duty cycle of 5%, was operated at the highest available intensity. The probability of inelastic interaction of a π with the setup material, producing heavily ionising particles, was estimated to exceed 1% [4-10]. The beam profiles seen by the detectors are well described by a Gaussian curve with $\sigma = 2.5$ cm in both directions. This allowed us to deduce that the central 250 strips of each detector were illuminated at the maximum intensity for 155 hours.

Figure 4.27 shows the rates recorded by a 0.5×0.5 cm^2 counter located a few millimetres off the Gaussian peak, as a function of the integrated running time. The rate measurement should be considered accurate to better than a factor 2 [4-10]. The comparison with expected LHC conditions is shown in the same figure. Considering the T10 duty cycle, the beam test amounts to about 7.7 hours of continuous beam at a rate comparable to or larger than the one expected at the LHC at a radial distance of 100 cm from the beam pipe.

Transient effects of charging up of the substrate have been investigated. We have selected the highest luminosity runs and studied the behaviour of the collected charge as a function of the event number within the spill: the most probable value of the sum of the charge in all detected clusters normalised to the total number of strips fired is reported in Fig. 4.28. Several approaches were adopted to check the stability of the detector operation during the beam exposure. A transition to the streamer regime could be induced by extremely large energy deposition caused by heavily ionising particles produced in nuclear interactions, and in general, by a large instantaneous rate. Sparks between cathodes and anodes would cause local melting of the gold strips, thus shortening the active length of the strip and producing irreversible damage to the chambers. Figure 4.29 shows the beam profile recorded by one of the detectors at the beginning and at the end of the run, with three intermediate stages. The binning of the plots corresponds to the strip pitch; a dead or shortened strip would be revealed by inefficiency of the strip, accompanied by the typical enhancement of counting efficiency on the neighbouring strips (see Section 4.3.2.6).

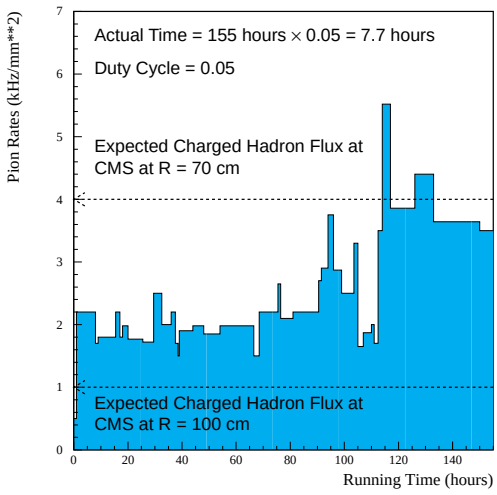

Fig. 4.27: The average particle rates measured by a 0.5 × 0.5 cm^2 counter set close to the region of maximum beam intensity as a function of the integrated running time.

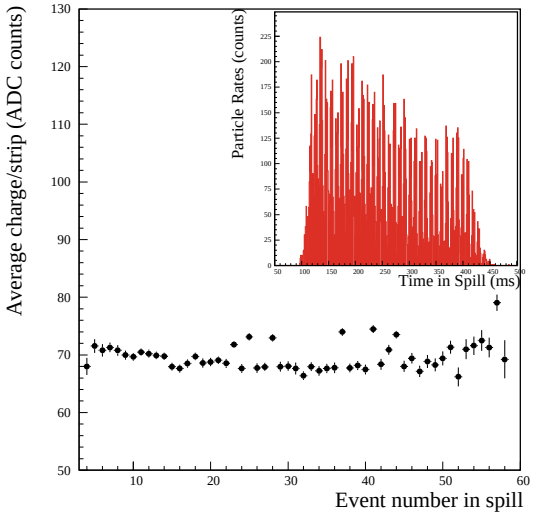

Fig. 4.28: Most probable value of the total collected charge normalised to the total number of fired strips as a function of the event number in the spill. The insert shows the instantaneous rates recorded by the beam finger counters.

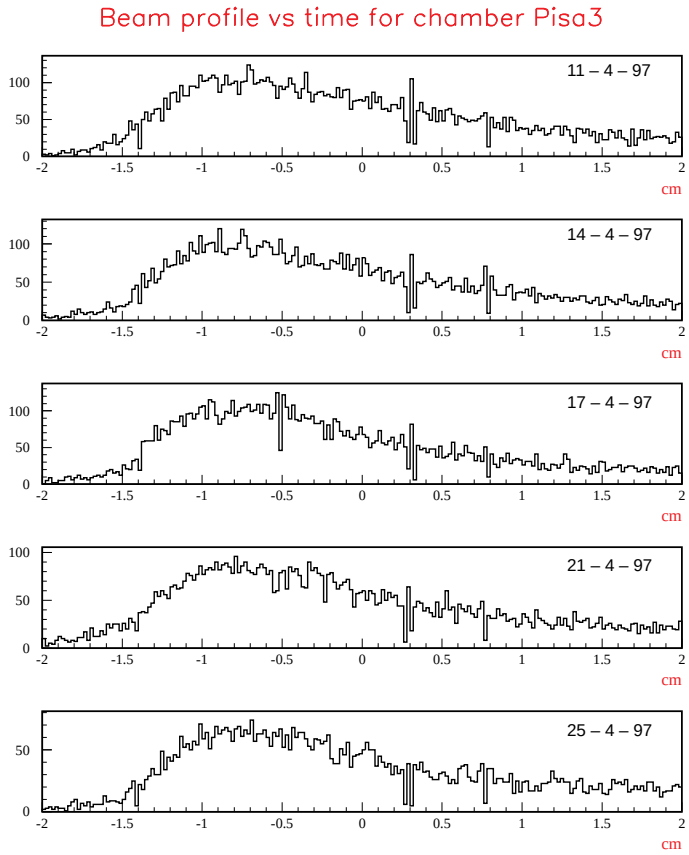

Fig. 4.29: Beam profile seen by a MSGC detector from the beginning (1st plot) to the end (last plot) of the test. No additional inefficient or dead strip is detected.

A visual inspection of the strips through the glass substrate has confirmed the off-line analysis [4-22]: no damage was detected in the MSGCs. The performance of the detectors proved to be extremely stable over the whole period of data taking, in terms of collected charge, noise, S/N ratio, cluster size and hit multiplicity. A summary of the stability study is given in Fig. 4.30 for a specific chamber.

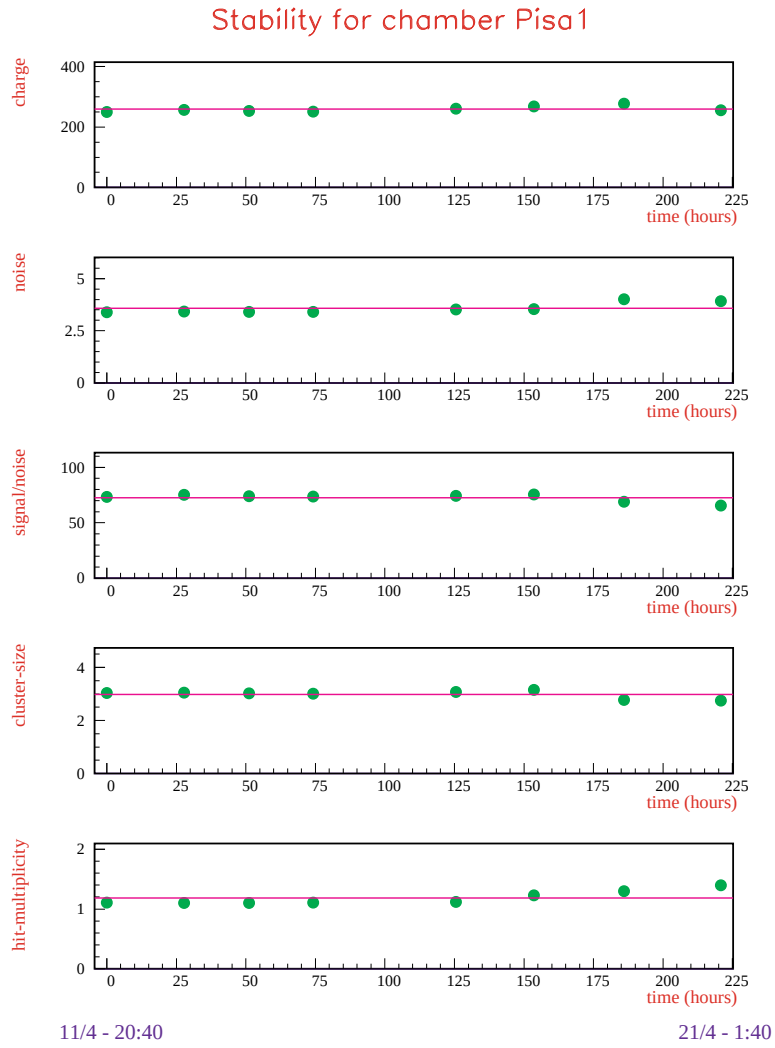

Fig. 4.30: Stability study for a MSGC chamber. All variables are plotted for 225 hours of running time (T10).

In order to increase the total integrated rate on the chambers, a second test was performed at the π $M1$ beam at PSI[2]. The beam was composed of pions and protons of 400 MeV/c ; the proton contamination varied between 40% and 5% during the whole period of exposure. A duty cycle of 100% allowed an increase by a factor 20 in the time of exposure with respect to the T10 test. At the end of 15 days of data taking, the detectors had been kept under high voltage and exposed to high-intensity beam for 161 hours. A set of three chambers from T10 and a fourth Pestov coated MSGC were tested. The detectors were equipped with picoamperometers, used to monitor the beam-induced current and to check for the onset of a possible streamer regime. With respect to T10, the chambers were operated at the same gas gain but at a slightly increased cathode voltage ($V_c = -540$ V) to take into account the difference in atmospheric pressure between CERN and PSI. The observed pulse height was slightly smaller because of the lower pion energy which

[2]Paul Scherrer Institut, Zurich.

yields some 25% less gas ionisation. The PSI test was not aiming at all to study the tracking performances. The experimental conditions were extremely difficult for tracking because of the large multiple scattering and the limited number of chambers available (four in total) with a small solid angle coverage. Nevertheless, an attempt to estimate the tracking efficiency at the working point has been carried out in the off-line analysis for the so called *low-intensity* runs (5 MHz trigger rate). Figure 4.31 shows the tracking efficiency as a function of the cluster threshold in one chamber, using the other three for track reconstruction. The efficiency remains above 92% up to a threshold as large as eight times the strip noise (r.m.s). This indicates that the operating point was well inside the efficiency plateau. Figure 4.32 shows the number of clusters found in one chamber as a function of the threshold. The observation that the number of clusters remains below 1.6 indicates that the overall noise is substantially suppressed even when working at a threshold as low as three sigma, in a quite realistic environment. These results should not be taken as absolute values but, for the reasons said above, only as lower limits. The time stability of the gain was checked by splitting a run (40 min) into 12 different periods (Fig. 4.33). No statistically significant charge fluctuations were observed.

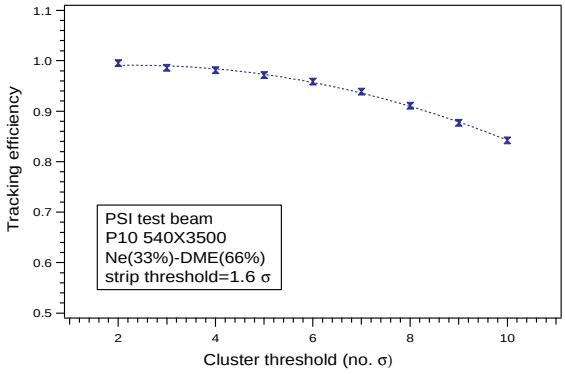

Fig. 4.31: The detection efficiency as a function of the cluster threshold.

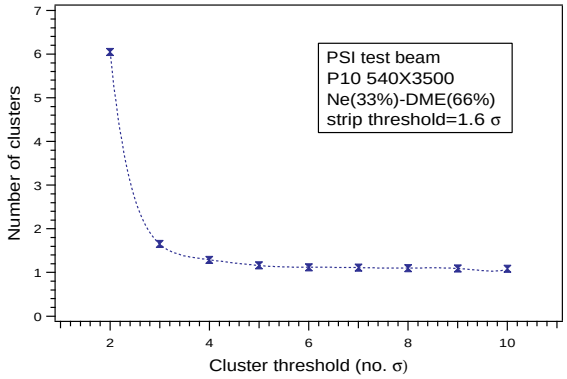

Fig. 4.32: The number of clusters as a function of the cluster threshold.

The rate recorded by the two counters installed in front of the chambers was 10 kHz/mm^2. Complementary information on the actual particle rates was provided by monitoring the beam-induced current in the detectors. We measured a cathodic current of > 80 nA, corresponding to a total anodic current larger than 400 nA.

At a radius of 60 cm in the CMS experiment, a current of 400 nA is expected to be induced by a mip flux of 5 kHz/mm^2 distributed uniformly over the detector surface. Thus, during the 161 hours of operation at this high intensity beam, the chambers were exposed to a rate of charged hadrons higher than the LHC rate at the innermost layer of the MSGC tracker.

To investigate further the operational stability of the detectors, one chamber was ramped to higher voltages. The cathode voltage was increased by 10 V every 3 hours. The transition to the streamer regime was observed only at $V_c = -620$ V and $V_d = -3700$ V, 100 V above the LHC working point. About 100 streamers were observed during two hours of operation. After the study, the detector was brought to the regular working voltage, and continued to operate normally.

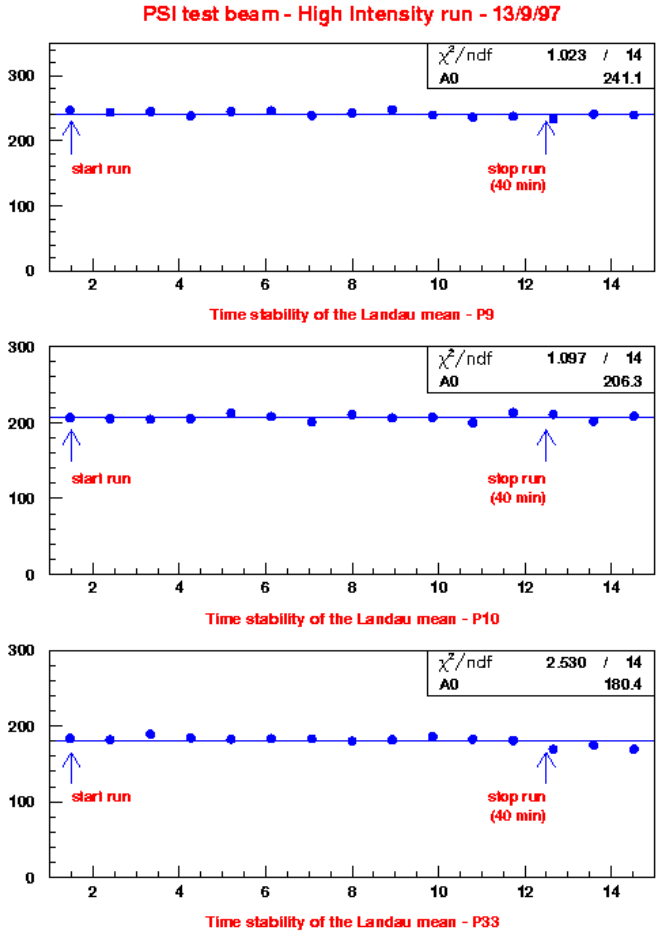

Fig. 4.33: Cluster charge recorded at 12 different periods during a high-intensity run, for three MSGC prototypes (PSI).

The search for strip loss was performed by off-line analysis similar to the one applied in the previous test and by visual inspection. Strip damage was detected in the chamber that had been brought to the unstable regime. Of the 100 streamers observed online, not all of them were destructive: 50 *mouse bites* on the strips have been visually identified. For the remaining detectors a loss of three strips was detected in the first chamber, which was exposed to the huge background produced by the beam impinging the lead shielding. No indication of sparking activity has been detected in the neighbourhood of these strips. The loss is due to further hardening of the detectors. Figure 4.34 shows the beam profile of two chambers taken at the beginning and at the end of the run. No change in the shape of the profile is visible.

4.3.3.5 Response to a fast neutron beam

Subsequent to the exposure to an intense hadron beam at the CERN PS (T10 test April 1997), one of the performance prototype MSGCs was exposed to an intense neutron beam at the cyclotron of Louvain-la-Neuve (Belgium). These neutrons can produce photons and highly ionising charged secondaries (e, p, d, α) in the MSGC detector via nuclear reactions and/or via activation of the materials used for the construction of the detector. The neutron beam is

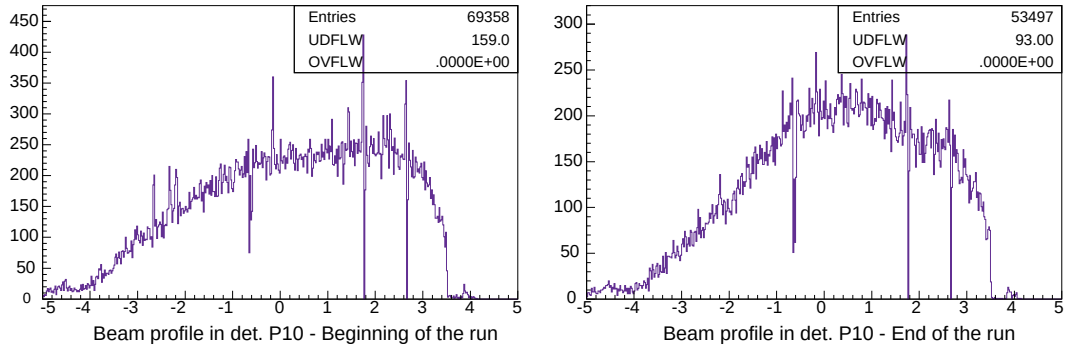

Fig. 4.34: Beam profiles of a chamber at the beginning and at the end of the PSI run period.

generated by the reaction ^{9}Be(d,n)X induced by a 50 MeV primary deuteron beam (intensity up to 10 μA) hitting a 1 cm thick beryllium target. At the location of the detector, 9 cm behind the production target, an absolute neutron flux ($E_n \geq 4$ MeV) of 7.3×10^{7} n mm^{-2} s^{-1} for a 1 μA deuteron current has been measured. The broad energy spectrum of the neutrons extends up to 50 MeV with an average of about 20 MeV i.e. well above threshold for the production of low-energy charged secondaries through nuclear reactions. The beam contamination by gamma rays and charged particles, after a polystyrene, cadmium and lead filter was estimated to be 2.43% and is dominated by gamma rays (2.4%). At the MSGC position 90% of the neutron flux is contained in a disc with a diameter of about 4 cm. The irradiated area of the substrate was chosen to be the same as in the T10 exposure. Details of the neutron beam, the experimental set up and the measurements can be found in Ref. [4-23].

During the exposure that lasted for about eight hours, mainly at 100 nA deuteron current, a total fluence of 3×10^{11} n mm^{-2} was accumulated, corresponding to about three years of LHC operation at full luminosity. Drift and cathode currents were monitored throughout the exposure and the events were readout via Premux electronics and a Sirocco FADC. The following findings are worth highlighting:

- The average ionisation loss of the neutron-induced highly ionising particles was about 65 times larger than for mip's.
- An upper limit for the hip's production yield was determined to be 2×10^{-5} hip's per neutron.
- The anode current drawn at the beginning of the mip efficiency plateau (working point) was about 3 μA for an irradiation area of 12 cm^2, i.e. roughly 30 times the expected one at the LHC at full luminosity.

After irradiation the substrate was optically inspected under a high magnification microscope. In the entire beam spot (T10 followed by the neutron exposure) no change of colour and no damage to any strip or passivation line has been observed.

4.3.3.6 Response to low-energy neutrons

The major component of the background neutron spectrum in the CMS tracker extends from 1–3 MeV. Therefore, a dedicated neutron beam facility has been set up at the 3.5 MeV van de Graaff accelerator at the Forschungszentrum at Karlsruhe. Neutrons in an energy range 0.5 to 2.0 MeV are generated by the reaction ^{7}Li(p,n)^{7}Be. The unavoidable γ background is effectively reduced to less than 1% per neutron by means of a lead filter. The neutron flux of $5\cdot10^{7}$ neutrons/cm^2 s passing the detector has been determined by activation of thin gold foils in front of and behind the detector. Details can be found in Ref. [4-24, 4-25].

Two MSGCs with gold metallisation, one on bare D-263 glass and one on DLC glass, were exposed over 66 hours to a total neutron fluence of 1×10^{13} neutrons/cm^2, corresponding to one year of LHC operation at full luminosity. The chambers were operated with nominal LHC parameters (gain = 2000) and, as in the case of the study with fast neutrons, the drift and side-cathode currents were monitored. The chambers were readout with Preshape electronics and CAMAC ADC.

A pick-up signal from the proton beam in pulsed mode allows to clearly separate neutrons from γ-ray background by time of flight, and to study the energy deposition and the conversion probability of neutrons. Figure 4.35 shows the energy deposition versus time of flight. One finds that neutrons in this energy range induce an ionisation about 30 times that of a mip and have an absolute conversion probability of $(1.0 \pm 0.4) \times 10^{-5}$.

The performance of the chambers was studied before and after irradiation with a ^{55}Fe source and no deterioration was observed. Also optical inspection of the substrate pattern did not show any damage.

In order to test for potential activation of the chamber itself, one detector has been investigated with an high resolution germanium detector. The γ spectrum indicates a negligible activation at the level of 100 Bq, mainly of gold and some short-living β^+ activity.

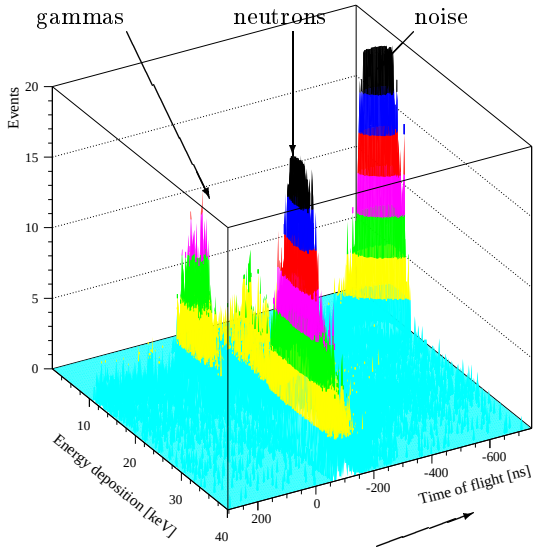

Fig. 4.35: Energy deposition versus time of flight (no lead filter used). The signal of γ's is clearly separated from neutrons. The operational parameters of the MSGC are: $V_d = -2000$ V and $V_c = -500$ V.

4.3.3.7 Induced activation of MSGC material with thermal neutrons

To investigate the effects of slow neutrons on MSGCs, small prototypes fabricated with aluminium or gold strips on coated D263 glass have been exposed to an intense neutron flux in the CEA (Saclay) ISIS reactor facility. Details can be found in Ref. [4-26].

For this test the neutron energy was in the range 0–1 eV, the spectrum was a Maxwell distribution with most probable energy equal to 0.025 eV corresponding to thermal neutrons. MSGCs were exposed during six hours at an instantaneous flux of 10^6 n mm^{-2}, close to the low-energy neutron instantaneous flux expected in the CMS tracker.

Gain measurements made at the laboratory prior to the irradiation and immediately or a few days after irradiation show no significant difference. These measurements show that MSGC performances will not be affected by slow neutrons at the LHC.

A γ spectrum was measured immediately after the ISIS reactor had been shut down (Fig. 4.36). Peaks showing induced activities on gold (411 keV - half life 2.7 days), antimony (564 keV - 2.7 days), sodium (1368 keV - 15 hours) and potassium (1461 keV - 10^9 years) are clearly visible. The other peaks are mainly due to bromine activation (554–1474 keV, 1.47 days).

Antimony, sodium and potassium are constituents of the D263 glass. Gold will be used for MSGC strips manufacture. Bromine is a component which is used for some peripheral elements such as the insulating layers of electric cables.

It should be noticed that for each peak, the recorded activity was below 12 Hz. Both low-energy and thermal neutrons tests show that some constitutive elements of the MSGC may be activated by an intense neutron flux, which may lead to a permanent very low rate background. In any case, no direct effect on the gain has been recorded.

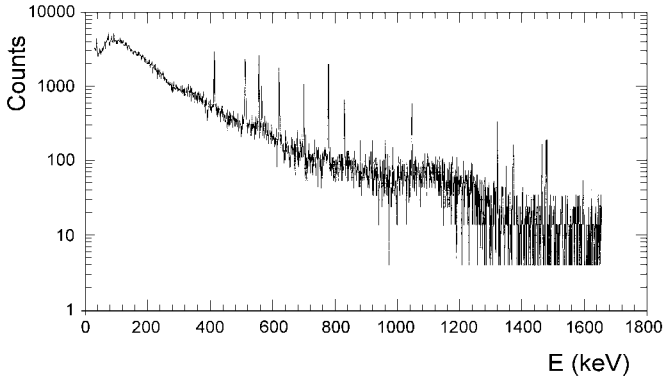

Fig. 4.36: A γ activation spectrum measured after irradiation with thermal neutrons.

4.3.3.8 Summary of operation requirements and design criteria

As a result of an extremely intensive R&D effort and after many beam tests run in very realistic conditions, a full list of operation requirements and design criteria can be set. The CMS MSGCs will have:

- the highest possible surface resistivity, compatible with the LHC rate ($\sim 10^{16}$ Ω/square);
- the lowest possible cathode voltage. This implies narrow anode strips (7μm);
- the lowest possible gas gain ($\sim$ 1700), compatible with full hit efficiency;
- the highest possible drift voltage ($\sim$10 kV/cm). This gives more gain and lower cathode field;
- the lowest possible electronic noise. This is obtained with short strip length and small specific capacitance (no back-plane);
- a UV free gas mixture (no photon feedback);
- the lowest possible group capacitance (no back-plane, 16 strip grouping);
- no blocking capacitor (6% cross-talk accepted);
- passivation of all critical edges (across and along the strips, advanced passivation);
- a sophisticated, on board, HV control. This requires a low trip threshold (selective) and fast response;
- hardening of the device during assembly to remove 'weak' strips.

4.3.4 Detector performances for single track reconstruction

The design goal of the CMS tracker is to reconstruct isolated high p_T tracks with an efficiency better than 95% and high p_T tracks within jets with an efficiency better than 90% over the rapidity range $|\eta| < 2.5$. The momentum resolution required for isolated charged leptons is $\Delta p_T/p_T = 0.15\ p_T \oplus 0.5\%$ (p_T in TeV). Consequently, the MSGCs are designed to provide an intrinsic spatial resolution better than 40 μm and a hit efficiency better than 98%, in the less congested outer region of the tracker. The performance of the detectors has been extensively tested over the last years by using high-momentum mip beams. The results reported below confirm that MSGCs meet the CMS requirements in terms of resolution, efficiency, signal-to-noise ratio, and uniformity of response.

4.3.4.1 Spatial resolution and track efficiency

Recent studies on spatial resolution and efficiency have been performed on five MSGC modules exposed to 30 GeV/c pions at the CERN X7 beam facility [4-27]. Out of the five detectors, three were coated with films of Pestov glass according to the CMS baseline specifications; two other detectors were diamond-like coated. The standard passivation technique was used. Two additional silicon micro-strip detectors were used as a tracking telescope. The typical voltage settings were $V_c = -530$ V, $V_d = -3000$ V, with a gas mixture Ne(25)-DME(75).

The amplitude of the signal produced by the detectors (Fig. 4.37) is well described by a Landau function. The clustering algorithm requires that, for each strip in the cluster the signal-to-noise ratio is larger than 3 and, for at least one strip, larger than 6. The average cluster size is 1.95 $\pm$ 0.01 strips. The corresponding signal-to-noise ratio (S/N is defined as the most probable value of signal-to-noise ratio; N is the noise of one strip averaged on all the strips in the cluster) S/N = 30 allows a hit reconstruction efficiency of 98.5 $\pm$ 0.2% with an occupancy of 1.20 $\pm$ 0.01 hits per detector, where the errors are statistical.

The hit residuals are measured with respect to a track found excluding the chambers under study from the fit. The results show a standard deviation in a range of $35 - 45$ μm for the different chambers tested (Fig. 4.38).

If the contribution of the track error is unfolded from the residual distribution, the intrinsic hit resolutions are measured to be $30 - 40$ μm. The best resolution achieved is 30.5 $\pm$ 0.4 μm.

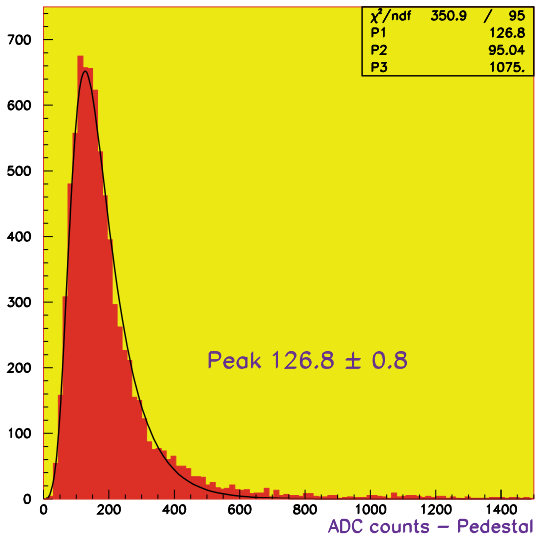

Fig. 4.37: Cluster charge at $V_c = -530$ V, $V_d = -3000$ V, and Ne(25)-DME(75) gas mixture.

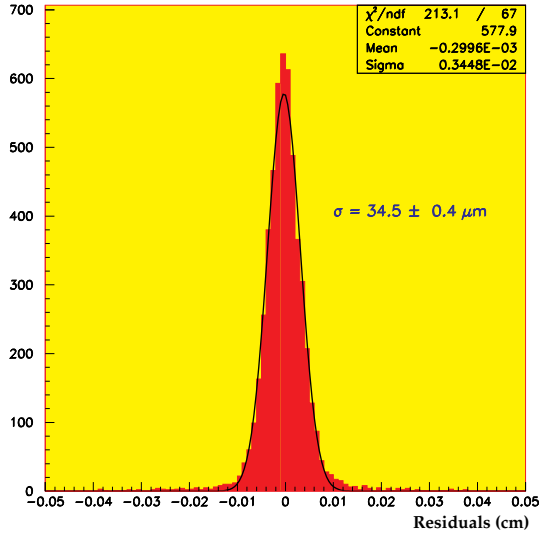

Fig. 4.38: Hit residuals (μm), $V_c = -530$ V, $V_d = -3000$ V, and Ne(25)-DME(75) gas mixture.

The dependence of the detection efficiency upon the choice of the working S/N value is shown in Fig. 4.39 for a given chamber, filled with Ne(25)-DME(75) gas mixture. The clustering algorithm applied here imposes a threshold of 4.1 σ on the strip with the highest signal amplitude and 1.6 σ on the other strips in the cluster, where σ is the average strip noise. The hit multiplicity is lower than 2 hits per detector; the average cluster size is estimated to be 2.2 strips. For a signal to noise ratio larger than 13, a detection efficiency of better than 98% and residuals standard deviation below 43 μm are achieved. At the standard CMS working point, S/N = 20, the hit efficiency is better than 99.5%.

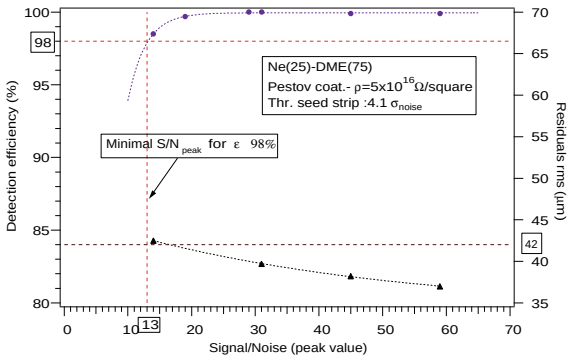

Fig. 4.39: Detection efficiency and standard deviation of residuals as functions of signal-to-noise ratio, Ne(25)-DME(75).

When the azimuthal incidence angle of the particle differs significantly from the normal to the detection plane, the primary charge starts to be collected by several strips. Because of large statistical fluctuations in the charge collected by each individual strip in the cluster, the centroid of the charge distribution also fluctuates. This implies a worsening of the position resolution as a function of the incidence angle as shown experimentally in Fig. 4.40 for a 225 GeV/c muon beam at the CERN SPS [4-28]. The spreading of the charge on many strips could affect also the detection efficiency because the average charge per strip decreases with the angle. The detection efficiency as a function of the incident angle is shown in Fig. 4.41. The dependence of the cluster size and number of clusters upon the incidence angle is reported in Chapter 7; experimental results are compared to simulation and good agreement is demonstrated.

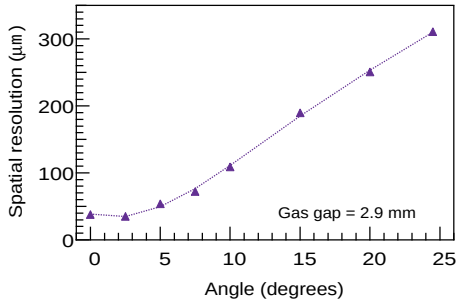

Fig. 4.40: Dependence of the spatial resolution on the incident angle of the tracks.

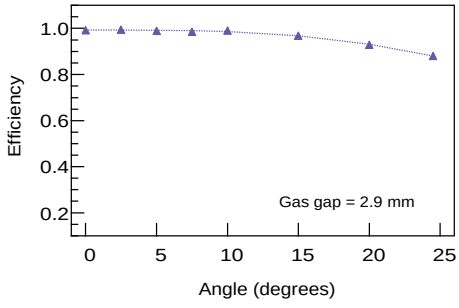

Fig. 4.41: Dependence of the detection efficiency on the incident angle of the tracks.

4.3.4.2 Behaviour in magnetic field

In CMS, the MSGCs will work in a strong, solenoidal, magnetic field of 4 T. In the barrel region, where the strips run parallel to the magnetic field lines, the direction of charge collection is perpendicular to the direction of the magnetic field. Thus the drifting ionisation electrons will experience not only the electric force, proportional to the electric field strength, but also the Lorentz force, proportional to the product $\mathbf{v} \times \mathbf{B}$ (see Fig. 4.42a). The total force is the vector sum of these two forces. It changes the direction of drift by an angle α_L ,given , in a first approximation by the ratio of magnetic to electric force ($\tan\alpha_L = |\mathbf{v_d} \times \mathbf{B}|/E$). As a consequence,the primary charge is spread over a larger number of strips and this results in a displacement of the charge centroid and in a worsening of the spatial resolution and detection efficiency. From a phenomenological point of view, the problem is identical to the detection of a track inclined at an angle α_L with respect to the normal to the detection plane. In principle, the worsening of the spatial resolution and of the detection efficiency could be compensated by a rotation of the MSGC, with respect to the B-field direction, of an angle equal to the Lorentz angle α_L (see Fig. 4.42b). After this rotation infinite momentum tracks no longer enter the detector at 90°, but at $90° - \alpha_L$. The total force on the ionisation electrons is again directed along the track. The electrons will be collected on one or two strips only, as for normal incidence, without magnetic field. Obviously, the gas mixture and the drift field have to be optimised to make this angle of rotation reasonably small to be compatible with the mechanical structure of the tracker. To study quantitatively the effects of the magnetic field on the MSGC operation and the possibility to correct for them, an extensive experimental study has been carried out using the RD5 magnet at the CERN SPS [4-29].

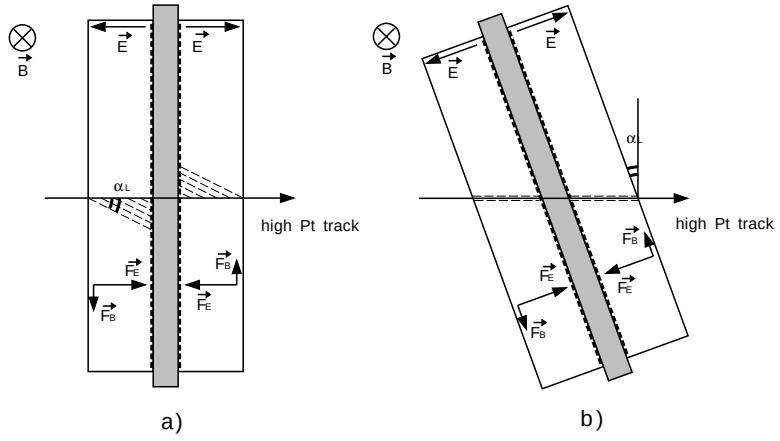

Fig. 4.42: The effect of the magnetic field on the drift of the ionisation electrons (a), the compensation mechanism (b).

Figure 4.43 shows the dependence of the Lorentz angle on the B-field strength for different gas mixtures, while Fig. 4.44 shows the degradation of the position resolution as a function of B at different drift fields and with different gas mixtures, before tilting the chambers.

Figure 4.45 shows the spatial resolution as a function of the drift field at the highest value of B. Figure 4.46 shows the full recovery of the spatial resolution obtained by tilting the chambers at the Lorentz angle.

In the forward region, where the charge collection is in the same direction of the B-field the effect is much less pronounced. The strong magnetic field tends only to limit the transverse diffusion of the ionisation electrons. No effect on the position resolution has been detected in a beam test where the RD5 magnet was oriented in the forward configuration with (Fig. 4.47a) and without (Fig. 4.47b) magnetic field.

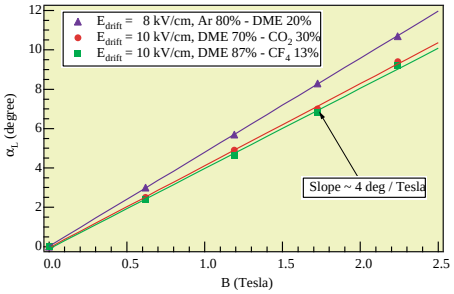

Fig. 4.43: The dependence of the Lorentz angle on the B-field strength for different gas mixtures.

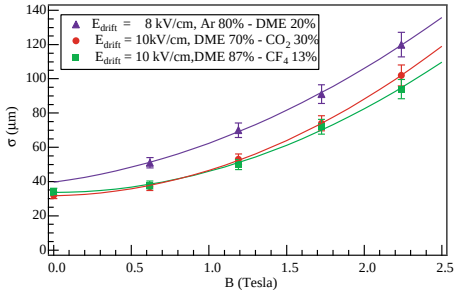

Fig. 4.44: The position resolution as a function of B for different drift fields and gas mixtures.

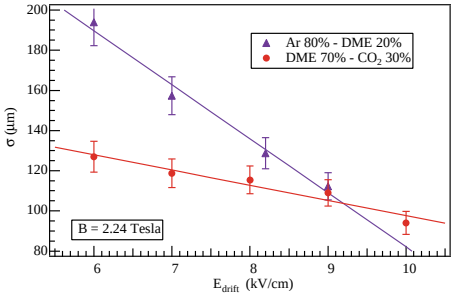

Fig. 4.45: The spatial resolution as a function of the drift field at the highest value of the magnetic field.

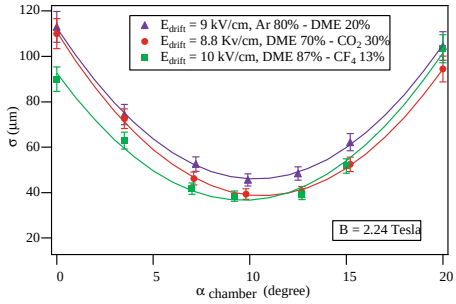

Fig. 4.46: The effect of angular compensation on the position resolution for electrons drifting in high magnetic field.

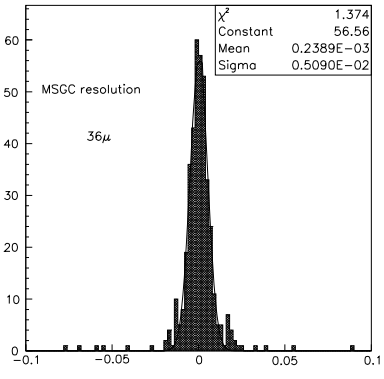

(a) B=2.24 T

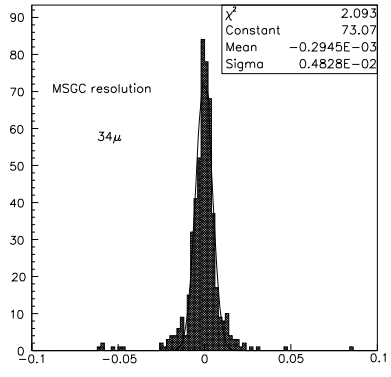

(b) B=0

Fig. 4.47: The spatial resolution of a forward region MSGC.

4.3.4.3 Barrel MSGC: uniformity of response and edge effects

To prove effectiveness of the mechanics and the assembly procedure of the final modules for the CMS detector, the resolution and the gain uniformity near the chamber edges have been studied.

A uniformity scan has been performed across and along the strips of a Pestov coated detector mounted on a movable support, during the X7 beam test. The resolution, expressed as the standard deviation of the hit residuals, was proven to be uniform up to 2 mm from the chamber edge, corresponding to ten readout strips (Figs. 4.48 and 4.49). Good gain uniformity has been measured over the entire chamber surface (Fig. 4.50). Further improvements of the resolution near the chamber edge can be achieved by proper tuning of the guard strip voltage settings. Figures 4.51 and 4.52 show results for two particular field configurations, corresponding to a grounded or floating guard strip.

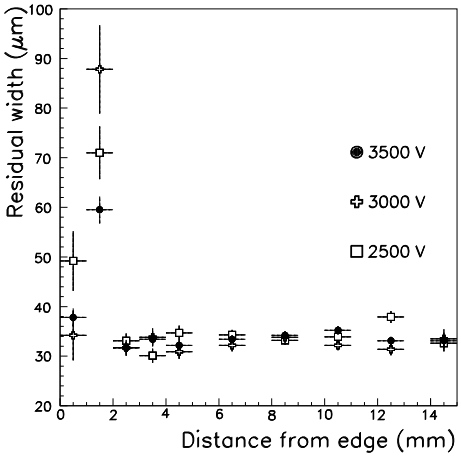

Fig. 4.48: Standard deviation of the residual distribution as a function of the distance from the chamber edge, at $V_c = -540$ V, Ne(25)-DME(75) gas mixture, and for different conditions of the drift voltage ($-V_d$).

The uniformity of the response for coated chambers built with the advanced passivation technique has been studied with data collected during the T10 test [4-27]. The experimental setup allowed investigation of the gain stability over an area of 5 cm across and along the strips (Figs. 4.53 and 4.54). The dispersion of the peak value of the Landau distribution over the area of 5×5 cm^2, for four chambers under study, is measured to be 2.5%.

4.3.4.4 Forward MSGC: uniformity of response and edge effects

In the Forward–Backward MSGC region the design of the detector module differs from that of the barrel region in two respects.

The first difference concerns the geometry of the substrate layout. As it is convenient for pattern recognition to use a radially symmetric detector design, a trapezoidal shaped electrode geometry is chosen. The pattern of the anode and cathode strips points towards the beam pipe. In order to keep a constant gain over the full length of the MSGC substrate the anode width is kept constant at about 7 μm, while the anode–cathode gap and the cathode width follow the so-called NIKHEF formula [4-30]:

$$G = P/8 + 20\ \mu\text{m}, \tag{4.1}$$

where G represents the anode-cathode gap and P the anode pitch. The latter parameter depends on the radial position and varies also inside the module.

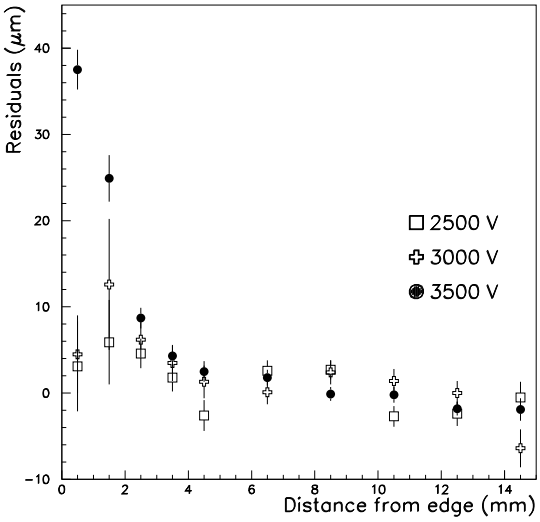

Fig. 4.49: Mean value of the residual distribution as a function of the distance from the chamber edge, with $V_c = -540$ V, Ne(25)-DME(75) gas mixture, for different conditions of the drift voltage ($-V_d$)

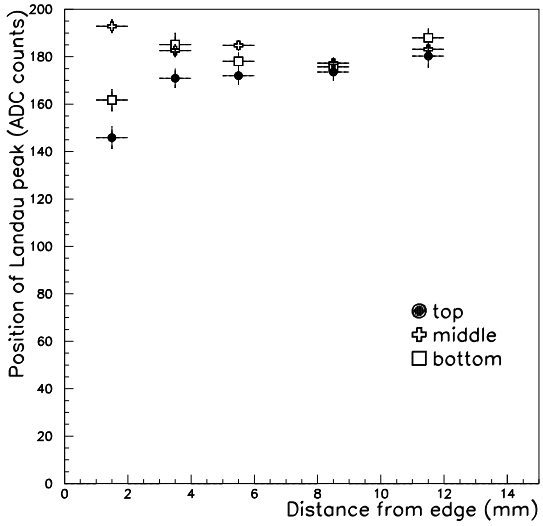

Fig. 4.50: Scan along the strips: peak value of the Landau distribution as a function of the distance from the chamber edge in mm, for $V_c = -540$ V, $V_d = -3000$ V, Ne(25)-DME(75).

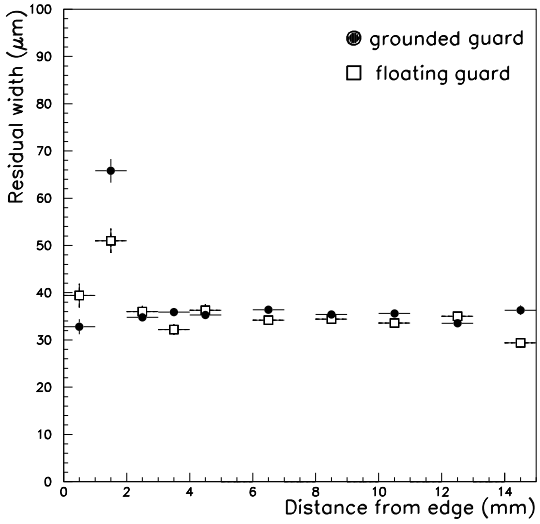

Fig. 4.51: Standard deviation of the residual distribution as a function of the distance from the chamber edge in mm, with $V_c = -570$ V, $V_d = -3000$ V, DME(100), for different settings of the ground strip voltage.

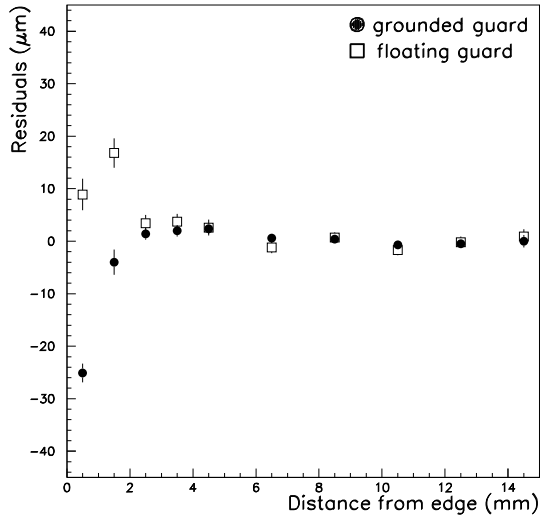

Fig. 4.52: Mean value of the residual distribution as a function of the distance from the chamber edge in mm, with $V_c = -570$ V, $V_d = -3000$ V, DME(100), for different settings of the ground strip voltage.

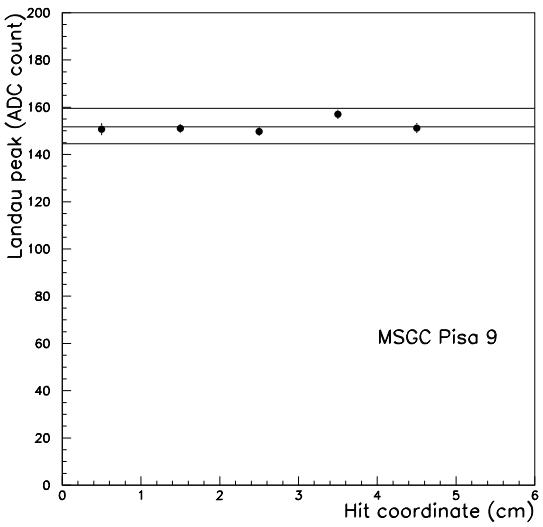

Fig. 4.53: Scan along the strips: mean value of the Landau peak as a function of the local hit coordinate in cm, with $V_c = -520$ V, $V_d = -3500$ V, Ne(40)-DME(60) gas mixture.

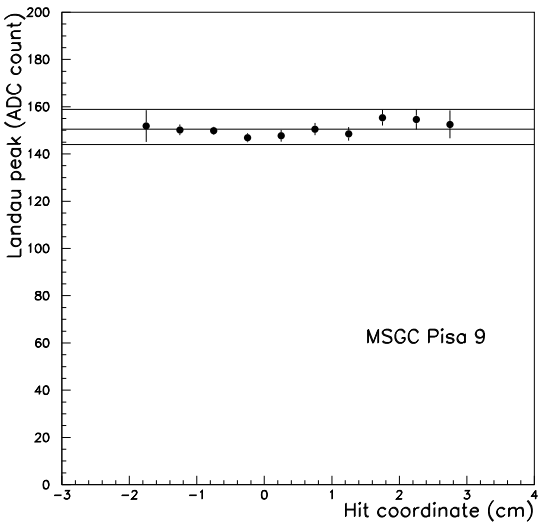

Fig. 4.54: Scan across the strips: mean value of the Landau peak as a function of the local hit coordinate in cm, with $V_c = -520$ V, $V_d = -3500$ V, Ne(40)-DME(60) gas mixture.

The second difference results from the effort to minimise dead space. Therefore, each detector module houses four substrates side by side. The distance of the two outermost anodes of two adjacent substrates is two times the detector pitch.

One of the goal of the MF1 milestone [4-31] was to check the validity of the NIKHEF formula. During the final beam test experiment of this milestone, the 38 MSGC modules realised by various manufacturers (SRON, VOSTOK, OPTIMASK, IMT) have been studied at the CERN X5 area for the uniformity of the gain along the strip and in a cosmic ray test bench for efficiency across two adjacent counters.

In this section we describe the results of these tests which are specific for the Forward–Backward design:

Uniformity of response along the strips

Bare D-263 glass is used for the substrates of the prototype module. Different modules containing four or eight substrates each were tested using the PreMux128 chip for the readout. The effect of the varying pitch of the anode-cathode structure on the signal to noise ratio[3] (SNR) has been analysed for various prototypes and the results are given in Fig. 4.55.

Efficiency between two adjacent counters

A substrate with aluminium strips on bare D263 glass having 512 anodes at 200 μm pitch and 10 cm strip length has been used. A piece of substrate with 2 blocks of 16 strips (6.4 mm wide) was cut away in the centre and the two remaining pieces of substrate, ending by a cathode strip, were mounted side by side at a distance of 70 μm. The distance between the first anode strips adjoining the common edge, called later the *crack*, was twice the nominal pitch as shown in Fig. 4.56.

This prototype, sandwiched between two normal MSGCs, was put in a gas-box filled with a Ne(50)-DME(50) mixture and operated in a cosmic ray telescope. Minimum ionising muons, close to normal incidence, were selected and their tracks reconstructed to predict the impact

[3]SNR here is defined as the ratio of the cluster charge and the cluster noise: $SNR = \sum_{i=1}^{N} d_i / \sqrt{\sum_{i=1}^{N} \sigma_i^2}$. What matters in this measurement are only relative variations.

points in the region of the crack. Figure 4.57 shows the efficiency measured across the ϕ-crack. The efficiency is found constant and at a level of 98.4%, without indication of efficiency loss between the adjacent substrate parts. The absence of a dead zone was expected because the electric field near the missing anode strip deviates the drifting electrons to the neighbouring anode strips as was often observed in MSGCs with an interrupted anode.

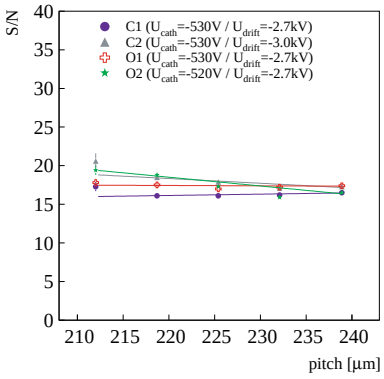

Fig. 4.55: Variation of the signal-to-noise ratio for varying pitch.

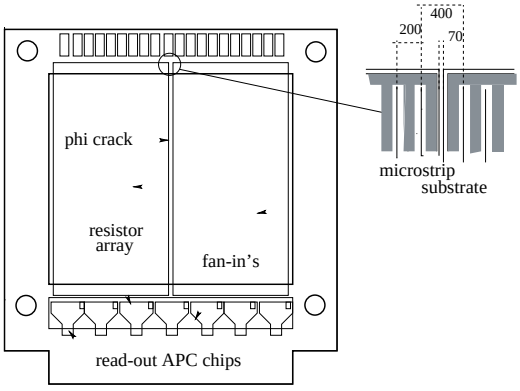

Fig. 4.56: Detail of the common edge of two adjacent counters.

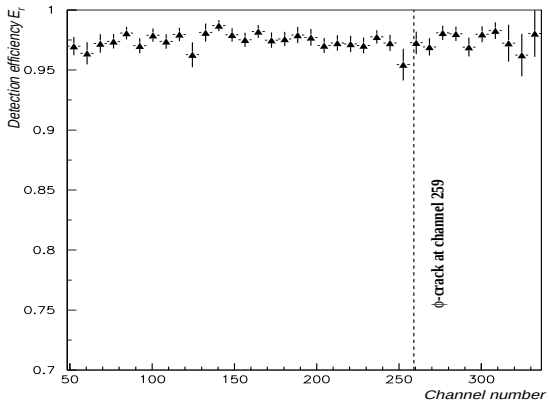

Fig. 4.57: Efficiency measured across the ϕ-crack.

4.4 Barrel Mechanics

The barrel MSGC tracker (Fig. 4.58) consists of six concentric detector layers situated in the radial space from 700 mm to 1200 mm and within ±1205 mm from the interaction point along the beam axis. The layers are equidistant, separated by a gap of 80 mm. In each layer, the MSGC detectors are assembled in modular and stand-alone subsystems called *rods* (Fig. 4.59).

In the barrel there are 736 mechanically identical and interchangeable rods, each housing five detector modules, for a total of 5540 MSGCs (Fig. 4.60 and 4.61). Modules and rods are assembled to guarantee, in every layer, full spatial coverage in both $r-\phi$ and $r-z$ projections. The rods, and detectors, are tilted by an angle of 14° to fully recover the position resolution capability of the MSGC (see Section 4.3.4.2).

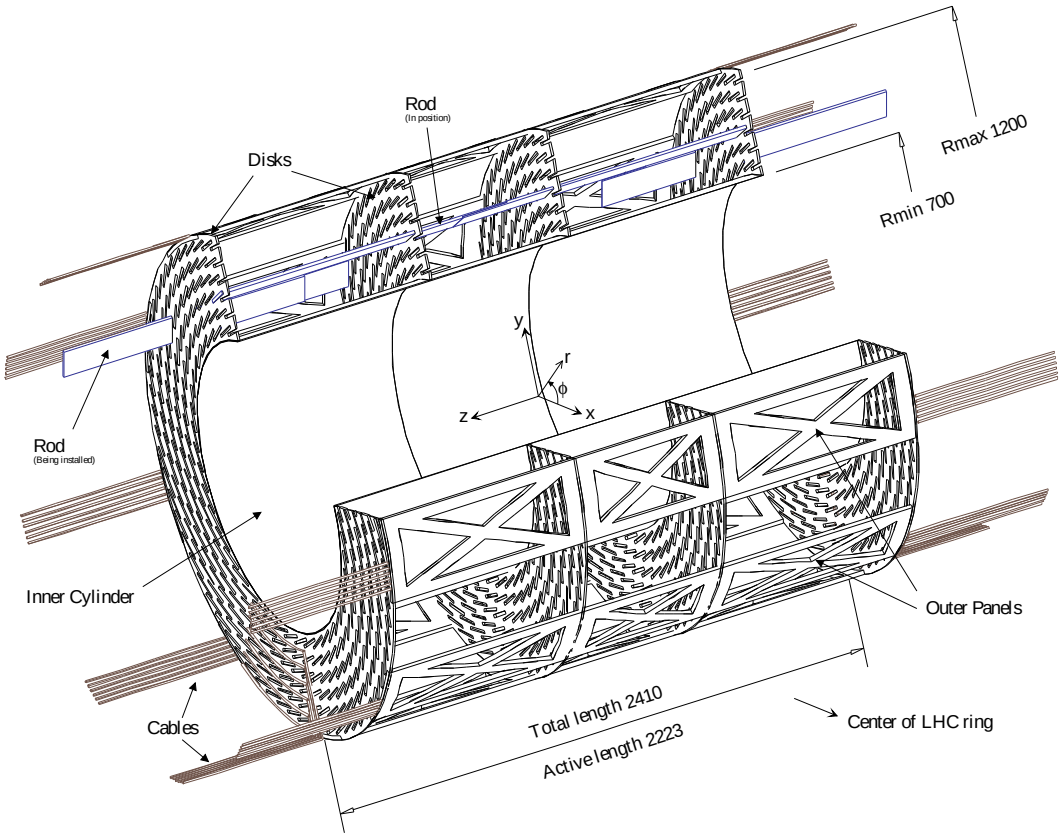

Fig. 4.58: Schematic view of the MSGC barrel.

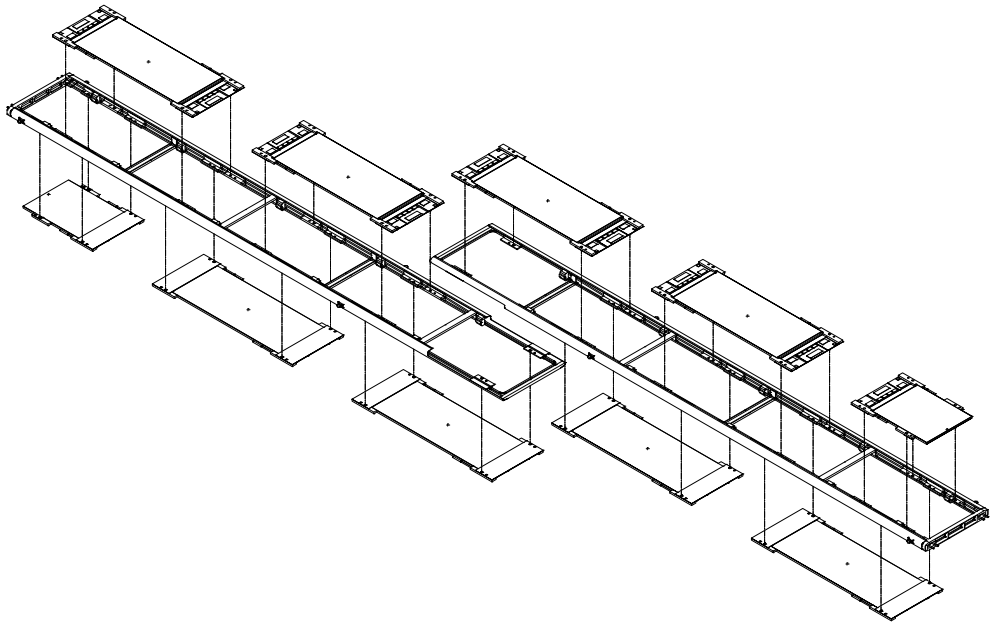

Fig. 4.59: Two rods each of which is to hold five MSGC modules for the $r-\phi$ information or five twin chambers for the stereo measurement.

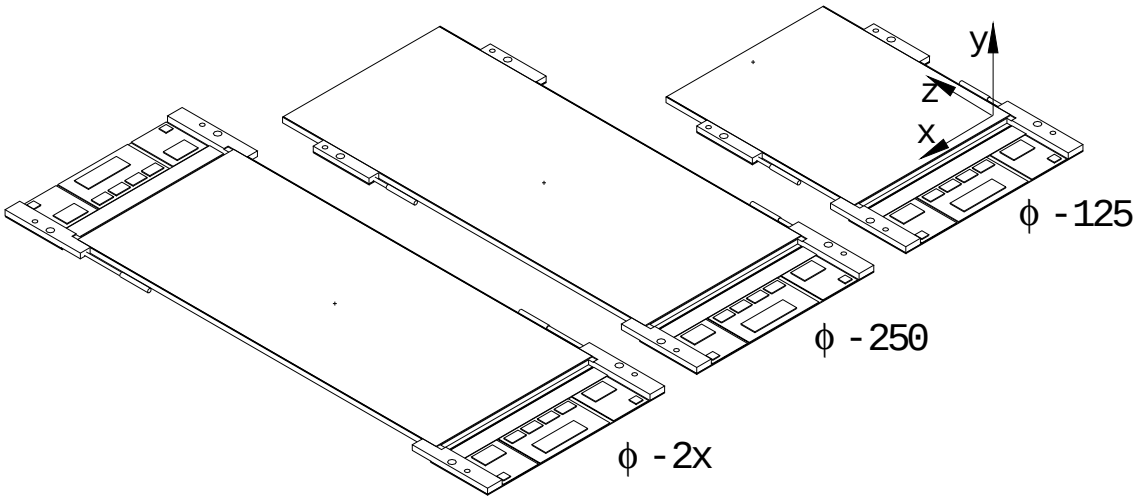

Fig. 4.60: The three types of MSGC module for $r-\phi$ information. The strip length of modules $\phi-2\times$ and $\phi-125$ is 125 mm, while for module $\phi-250$ the strip length is 250 mm.

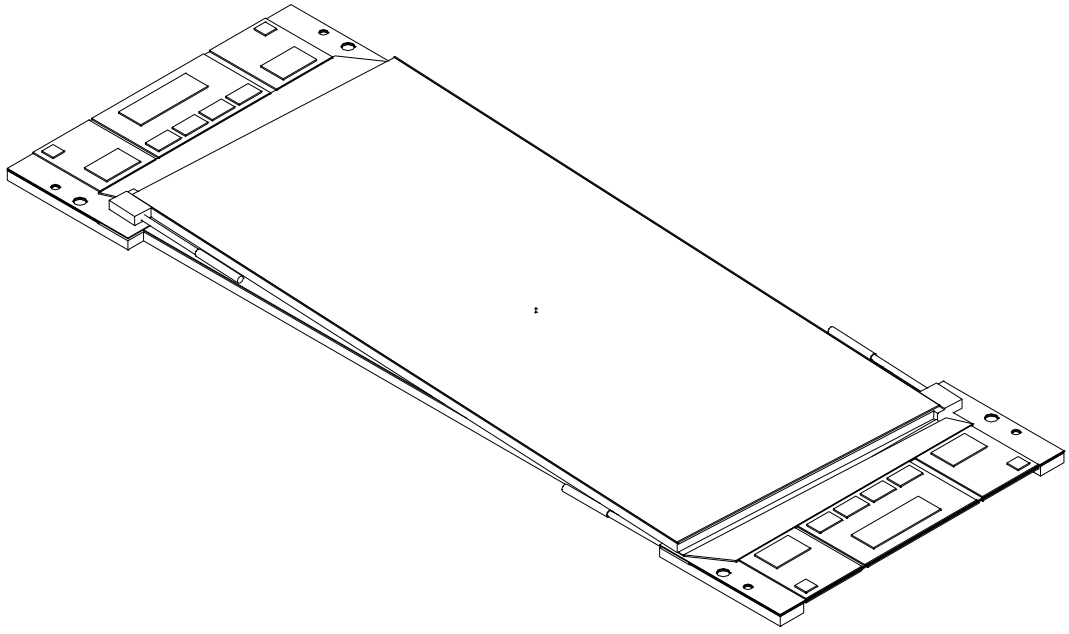

Fig. 4.61: One out of the three types of twin module for $r-\phi-z$ information.

One quarter of the detectors have an active strip length of 250 mm, the remaining of 125 mm length. A small MSGC, with only one electronics hybrid (Fig. 4.59), is mounted at the extremity of each rod at the planar ends of the barrel cylinder to minimise the dead area between barrel and forward region.

Detectors in the first, fourth and outermost layers provide space point informations. The other layers are equipped with detectors that measure only the $r-\phi$ coordinate.

Rods are supported by four identical disks joined to each other by cylindrical elements thus making a monolithic space-frame support structure.

The primary requirements that led the design of the support structure are:

- to maintain the detector modules in stable and precisely defined position
- to minimise the amount of material and distribute it uniformly in space
- to minimise the gap in front of ECAL and the Forward MSGC

Several aspects of the production, assembly and testing procedures have been optimised in the past two years in the framework of the so-called *MSGC B1 milestone*, together with a careful study of the main system problem of the barrel MSGC.

The major parameters of the the barrel MSGCs tracker are summarised in Table 4.1.

Table 4.1: Major parameters of the barrel MSGC tracker

total mass	617 kg
number of layers	6
minimum radius	700 (mm)
maximum radius	1200 (mm)
total length	2410 (mm)
total active length	2223 (mm)
overlap of active area in z	2.4 %
overlap of active area in $r-\phi$	1%–3%
number of rods	736
number of MSGCs for $r-\phi$ information	3680
number of MSGCs for $r-\phi-z$ information	1860
number of readout channels	3511296
number of High Voltage control switches	109728

Layer	Radius (mm)	Measured coordinate	Number of rods	Number of modules	Number of RO or HV hybrid	Number of RO channels	Number of HV switches
1	747	$r-\phi-z$	96	960	1728	663552	20736
2	827	$r-\phi$	108	540	972	497664	15552
3	907	$r-\phi$	118	590	1062	543744	16992
4	987	$r-\phi-z$	128	1280	2304	884736	27648
5	1067	$r-\phi$	138	690	690	353280	11040
6	1147	$r-\phi-z$	148	1480	1480	568320	17760
			736	5540	8236	3511296	109728

4.4.1 Detecting elements

Each barrel module is an independent, self-contained detector, with input output gas pipes, and with readout and individual HV distribution circuits, mounted on a common support.

Six different types of MSGC modules equip the barrel part of the tracker. The modules differ in the strip length, which is 125 mm for the modules installed in the four layers close to the beam pipe, to diminish the hit occupancy. The two outermost layers are equipped with modules that have 250 mm long strips. All modules mounted on a rod extremity are small and have 125 mm long strips.

The major parameters of each module are summarised in Table 4.2 and the mechanical components of the long modules ϕ-type are reported in Table 4.3.

The three modules (ϕ-type, see Fig. 4.60), with 200 μm pitch, are mounted with the strips parallel to the magnetic field to measure the ϕ-coordinate with the highest resolution (~ 40 μm). The *stereo*-type modules have 400 μm pitch. They are used in layers one, four and six where they are mounted back to back with a ϕ-chamber, at an angle of 50 mrad with respect to the magnetic field, to measure the z-coordinate with a spatial resolution of ~ 1 mm (stereo method). The ensemble of a ϕ-type and a *stereo*-type module, mounted at a mean radial distance r, is called *twin* chamber. For each track they measure the two projections x and x_{stereo}. The space point coordinates are:

$$r \; ; \;\; \phi = x/r; \; z = (\tfrac{x_{stereo}}{\cos(50 mrad)} - x)\cot(50 \text{ mrad}).$$

The small stereo angle allows the x and x_{stereo} coordinates to be correlated if they are measured in the same twin chambers with strip length L_{strip}:

$$0 \leq x_{stereo} - x \leq L_{strip} \tan(50 \text{ mrad}).$$

Only if two tracks have a projection inside the above interval at the same time there is a reconstruction problem. Though the spatial coverage of the ϕ-chambers and of the *stereo*-chambers is rather complete, 5% of the two substrates does not overlap. In this region it is not possible to have direct full reconstruction of the 3-dimensional point. More indirect reconstruction strategies have to be implemented.

Table 4.2: Major parameters of the barrel MSGC modules

Module type	Strip length (mm)	Active area (mm^2)	Substrate area (mm^2)	Pitch (μm)	Anode/cath. width (μm)	Number of strips
$\phi - 125$	125	125×102.4	136×112	200	7/93	512
$\phi - 250$	250	250×102.4	264×112	200	7/93	512
$\phi - 2\times$	2×125	125×102.4	264×112	200	7/93	2×512
$stereo - 125$	125	125×102.4	136×112	400	7/293	256
$stereo - 250$	250	250×102.4	264×112	400	7/293	256
$stereo - 2\times$	2×125	125×102.4	264×112	400	7/293	2×256

4.4.1.1 Substrate specification

All the modules substrate are made of 300 μm thick Desag AF45 glass, coated with a thin layer of semi-conductive glass (Pestov or S8900) to obtain a surface resistivity of $\sim 10^{16}$ Ω/square. All strips are realised in gold 0.8 μm thick. A thin polyimide layer, 8 μm wide, is deposited on the cathodes edges to limit the emission of electrons by the field effect (*advanced passivation*, see Fig. 4.13).

Table 4.3: The components of the barrel MSGC module

Component	Material	Radiation length (mm)	Thickness (mm)	Length (mm)	Volume/unit (mm^3)	Quantity
Drift plane	Carbon Fibre	242	0.32	260	9318	1
Substrate	glass	117	0.3	264	8870	1
Drift HV protection	Kapton	284	0.1	260	2912	1
Gas box frame	PEEK	287	3	250	6516	1
Support arms	PEEK	287	3	54	400	4
Gas pipe	PEEK	287	ϕ 2.3/1.8	20	240	2

In all type of modules, adjacent cathode strips are grouped in set of 16 electrodes for security reasons. A further grouping of the cathodes is actuated on the HV hybrid (see Section 4.4.1.2).

Two 2 mm wide strips run parallel to the electrodes close to both substrate edges. They act as guard strips that maintain a uniform field and avoid an increase of gain at the detector edges (see Section 4.3.4.3). In the substrate of type $\phi - 125 \times 2$ the guard strips assure a common grounding of the two sides of the module.

Alignment markers are present on the substrates, and they are visible from both sides of the glass also after the detector is assembled.

The module type $\phi - 2\times$, to be produced in the near future, is a good example of detector design because it implements all relevant features present in all type of modules. Its masks are already designed and the rest of the section is dedicated to its detailed description.

The dimensions of $\phi - 2\times$ substrate are 263.5 mm $\times$ 112 mm $\times$ 0.3 mm. Two independent MSGCs are engraved on it (Fig. 4.62).

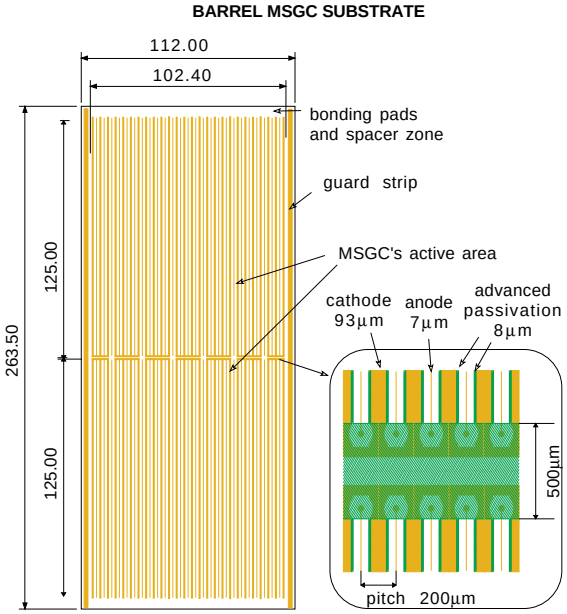

Fig. 4.62: The barrel MSGC substrate for the $\phi - 2\times$ type.

The MSGC strips are 124.75 mm long, the pitch is 200 μm and the anode and cathode widths are 7 μm and 93 μm respectively.

Figure 4.63 shows a detail of the mask design in the dead zone between the two active areas. The anode strips are rounded. The distance between anode and cathode is $\geq$ 50 μm everywhere. The distance between the two sub-detectors is 130 μm. The non-active region, 500 μm wide, is covered with polyimide.

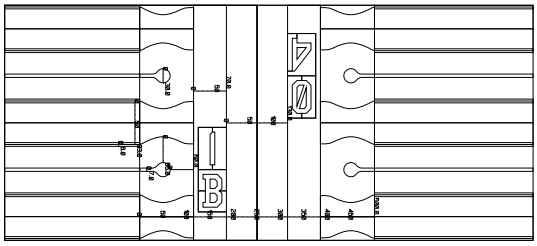

Fig. 4.63: Detail of the 500 μm wide zone between the two active areas.

Figure 4.64 shows the edge of the strips close to bonding pads. The cathode strips are rounded and the anode strips are increased in width up to 30 μm. This part of the substrate is passivated with a polyimide bar of 500 μm width. An additional gap of 500 μm is left before arriving to the region in which the PEEK frame will be glued. The gap and the polyimide prevent any possible contamination of the active region with glue. Figure 4.64 also shows how the anode strips are fanned to leave enough space for the cathode bonding pads.

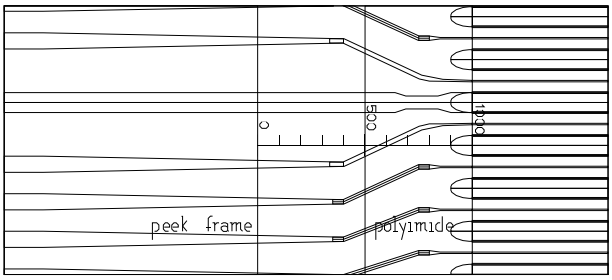

Fig. 4.64: The beginning of the active area. The cathodes are rounded and the area is passivated.

Figure 4.65 shows the bonding pads. The anode bonding pads are 75 μm wide and their pitch is 175 μm. At the centre of each group of 16 anodes there is a cathode bonding pad, 93 μm wide, with an insulation of 203.5 μm. Each bonding pad is identified by a hexadecimal number from 000 on right side of the detector to 1FF on left side. If we put the reference origin in the centre of the chamber, the coordinates of the cathode bonding pads are:

$$X_{cathode} = 49.6 \text{ mm} - i \times 3.2 \text{ mm with } i = 0 \div 31$$

The anode pad coordinates are:

$$X_{anode} = 52.5125 \text{ mm} - mod_{16}(i+8) \times 0.175 \text{ mm} - \frac{i+8}{16} \times 3.2 \text{ mm}$$
$$i = 0 \div 511 \ (i = \text{integer})$$

Two ground strips run on the long sides of the substrate (Fig. 4.66). The strips are shaped corresponding to the edge of the PEEK spacer to avoid surface discharges from drift to the ground line. The inside edges of the ground strip are passivated with 100 μ m wide polyimide strip that protect against discharges and prevent any glue from penetrating into the active area. The bonding pads of the ground strips are at coordinate ± 1. In Fig. 4.66 the reference lines to align the strips to the substrate are also visible. These lines allow the alignment of the strips to the substrate with 0.02 μm tolerance. The glass dimension tolerance is $+0,-200$ μm.

Six markers for alignment are placed at coordinates $x = 0, \pm 51.2$ mm; $y = \pm 130$ mm (Fig. 4.67). They stay outside the spacer and are visible from both sides of the detector.

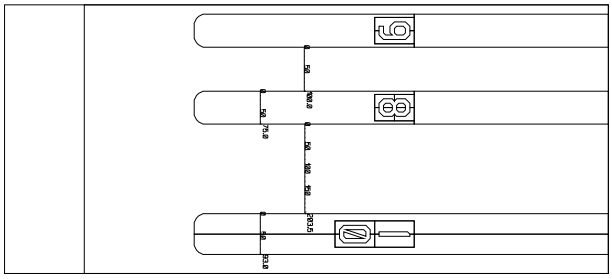

Fig. 4.65: Anode and cathode bonding pads.

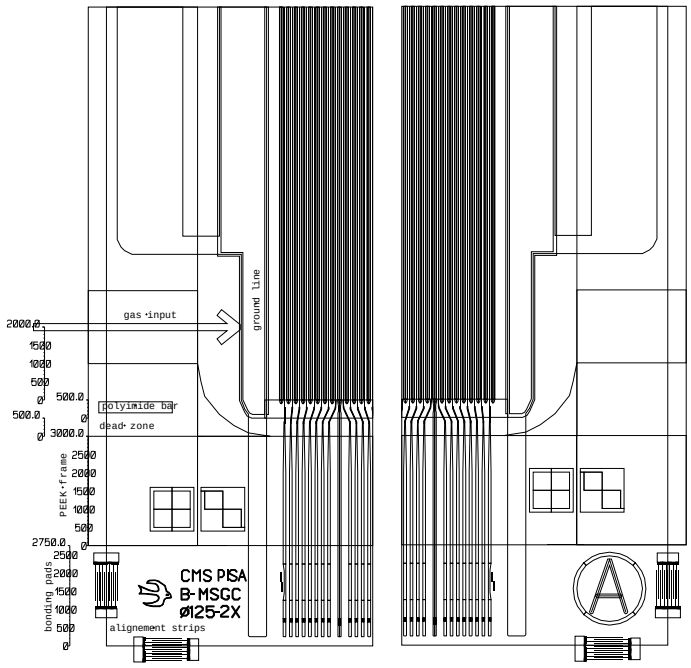

Fig. 4.66: Drawing of the MSGC edge.

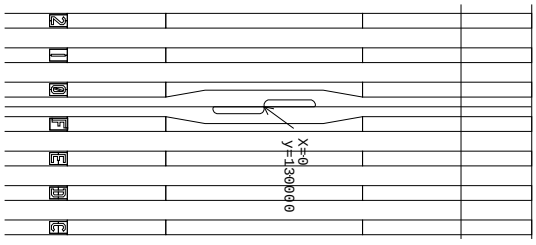

Fig. 4.67: Positioning markers.

4.4.1.2 Module layout

All of the modules [4-32] consist of a glass substrate, a PEEK spacer, whose height defines the drift space, and a carbon fibre drift window. These three elements, glued together, define a gas tight box which is light (the longest modules weigh 57 g without the electronics) but rigid and robust enough to be handled without particular care. The 3 mm thick PEEK spacer has input output gas pipes (Fig. 4.68), positioned on two opposite corners, and arms on both sides to easily support the electronics. The spacer is obtained by a moulding technique. The PEEK is of crystalline type without addition of glass fibres. The section of the walls, 3 mm $\times$ 3 mm, allows the production, by moulding, of this quite thin structure with a good uniformity (< 0.05 mm).

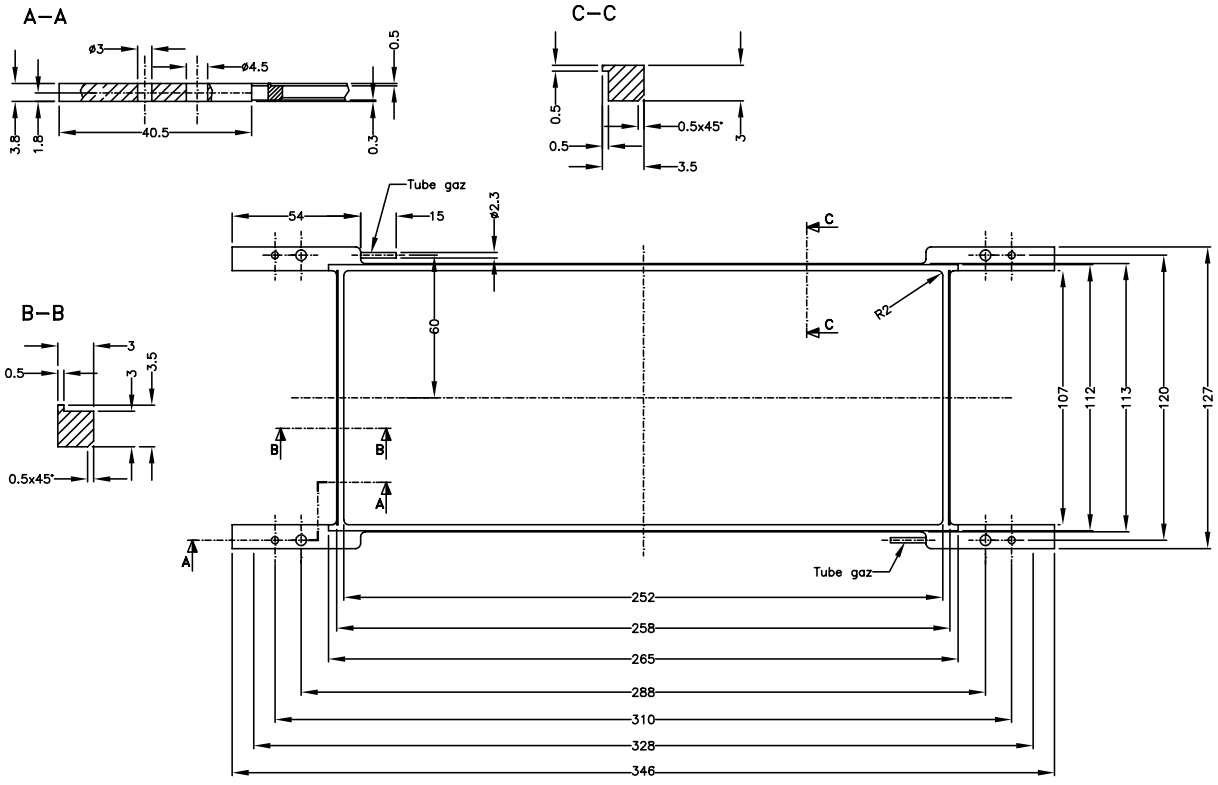

Fig. 4.68: Drawing of the PEEK spacer for the ϕ – *modules*.

The spacer is glued onto the glass over the *non-active* areas of the MSGC leaving 1 mm separation from the amplification region.

Though the PEEK frame has a well-defined thickness, it is quite elastic. The planarity of the module is therefore mainly ensured by the glass substrate and by the drift plane.

These two layers must be flat enough and glued to the spacer with appropriate vacuum chucks to obtain a box with 10% tolerance on the drift space. The drift window is made of a carbon fibre multi-layer 0.33 mm thick, gold-metallised on the side facing the substrate. It is glued directly over the spacer. A metal insert, with a feed-through gas tight connection, allows the drift voltage to be applied to the internal metallised layer. The carbon fibre solution assures a deformation of a few microns under the normal working gas over-pressure of 0.5 mbar. Most of the over-pressure is due not to the chamber impedance but to the regulation of the gas system. At the same over-pressure, the glass substrate deforms by less than 100 μm. (Fig. 4.69). A detailed study of possible room-temperature glues and of gluing techniques has been carried out during the prototyping phase of the project. We have established experimentally that with the appropriate gluing choice, the box can support over-pressure of tens of millibars without breaking.

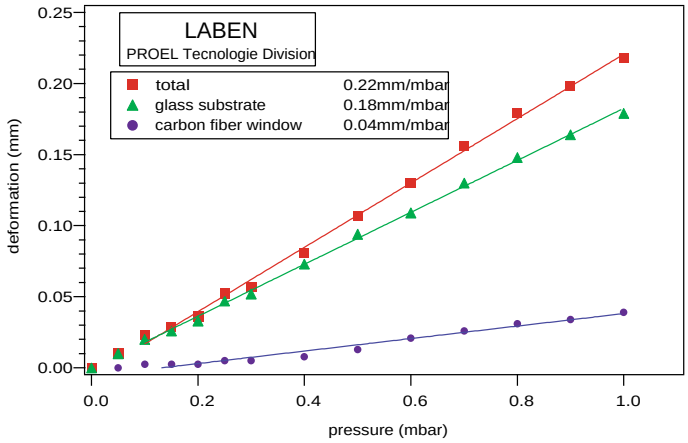

Fig. 4.69: B1 module 250 mm long: measurement of the deformation of the glass substrate and of the carbon fibre window under over-pressure.

A common feature of all the barrel modules is the fact that the HV hybrid and the readout electronics are always on the same side of the substrate, independently of the strip length and number of MSGC engraved on the substrate. An example of this arrangement is described in Fig. 4.70 where the detail of the connections of the anode and cathode strips to their bonding pads and after to the electronics is shown.

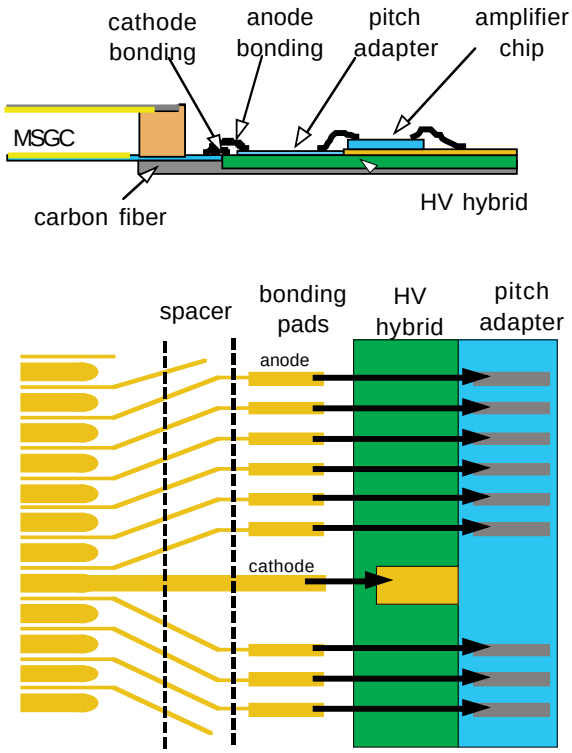

Fig. 4.70: The detail of the connection of a $\phi - 2\times$ module to the anode and cathode circuits.

The hybrid for both readout and HV distribution is made of four pieces (see Fig. 4.70). From bottom to top we find:

– *a carbon fibre plate*, 0.5 mm thick, with high thermal conductivity. The carbon fibre plate is in contact with the cooling pipes (see Section 4.4.2.3).

– *the HV hybrid* on which each cathode group is connected to a 10 MΩ resistors, that limit the amount of charge involved in a discharge or in a streamer event. After the limiting resistors two cathode groups are connected to the same HV switch (see Section 5.8.2). Each switch connects always 32 electrodes to the same bias voltage.

– *the readout hybrid* with the APV chips. It is positioned at the centre of the HV circuit on which appropriate space is left free. The readout hybrid is in direct thermal contact with the carbon fibre plate to guarantee an adequate heat flow from the readout chips to the cooling pipes

– *a glass pitch adapter* 0.3 mm thick that conveys the anode strips (pitch 200 μm) to the corresponding input channel of the APV chip (pitch 40 μm)

4.4.1.3 FEA and the thermomechanical distortions

The MSGC module has been analysed from the thermal and mechanical point of view employing a precise FE model. Several material combinations and load parameters have been tested aiming at an optimum design [4-33].

The key points of the analysis was to study the deformations of the cover and substrate plates, induced by a gas over-pressure, and to check the stress levels at the glued interfaces. Deformations of the electrodes will change the drift length and induce gain variations; changes up to 10% of the drift length can be tolerated. Mechanical or thermal stress in the glue joints must be avoided since this can generate gas leaks.

The validity of our FE model was confirmed by experimental tests on mock-up modules constructed with drift planes of various materials. FE analysis recommends employing a drift window of carbon fibre epoxy ~ 300 μm thick and to extend the readout hybrid support below the glass substrate to add stiffness to the structure. Both solutions were adopted for B1 modules and for the final module production leading to 100 μm maximum drift distance variation under a gas overpressure of 0.5 mbar.

Module deformation induced by thermal loads were investigated. We concluded that, to avoid bi-metallic effects, the drift plane and the electronics support should have coefficients of thermal expansion (CTE) as close as possible to the glass substrate. Carbon-fibre composites with low CTE, close to that of glass, are thus chosen. Another important factor is to manufacture and to keep the modules always at a temperature close to the final operating temperature of 18°C. This decreases the thermal stress, which is of concern especially in the glue joints between the PEEK frame and the substrate or the cover. Figure 4.i shows the module temperature profile when applying the water cooling and the heat of the readout electronics as a thermal load. The FE analysis indicates that temperature differences of ~ 10°C can be applied without compromising the module safety.

4.4.2 Detector supporting elements

The final MSGC modules, the services, the cables and the electronics needed for the functioning of the detectors, are installed into independent and interchangeable supporting elements, the *rods*. The complete barrel consists of 736 identical rods, each one carrying five MSGC modules to provide the $r - \phi$ information or five twin chambers for the stereo measurements.

The use of the rods minimises the handling of the individual detector modules, which will be 5540 in total, during all the assembly and testing phases thus decreasing damage risks.

The rod is a compact unit, easy to handle and mechanically robust, where the detectors and the services can be tested in stand-alone mode for all their functionality. After final checks, rods and modules can be easily and safely stored, waiting for the final mounting into the barrel wheel.

The different components of a rod and the cables, included in the rod structure, and needed for the functioning of the MSGC modules, are summarise in Table 4.4.

Table 4.4: The components of a rod and the cables needed for the functioning of the MSGC modules

Component	Material	Radiation length (mm)	Thickness or inner/outer diameter (mm)	Length (mm)	Volume per unit (mm^3)	Quantity
Front-end piece	CFRP	242	0.5		4000	1
C-profile	CFRP	242	0.7	1225	27325	2
Back end piece	CFRP	242	0.5		2500	1
Connection bars	CFRP	242	0.5	156	2470	4
Module positioning inserts	PEI	290	1		840	20
Heat removal plate	Al	89	0.5		250	20
Cooling pipe	Steel 304	17.6	ϕ 1.86/2	2576	1093	1
Coolant	Water	361	ϕ 1.86	2576	6999	1
Gas pipe	PEEK	287	ϕ 2.5/3	1030	2224	2
Gas joints	PEEK	287	2		1400	10
Screws	Al	89	ϕ 2.5	5	25	20
Water and gas connectors	PEEK	287	2		860	2
Sphere	Al_2O_3	75.5	ϕ 6		113	4
Sphere fixing	PEI	290	1		120	4

Component	Material	X-section (mm^2)	External diameter (mm)	Modularity
HV_c	Al & polyethylene		ϕ 0.75	1/module
HV_d	Al & polyethylene		ϕ 0.75	1/module
Low voltage printed board	Al pists on Kapton	0.672 2.1		1/APV chip 1/module
Printed board from CCU to RO hybrid	Al pists on Kapton	.05 0.5		1/hybrid 1/rod
Twisted pair from CCU to RO hybrid	Cu and polyethylene		0.13	2/rod

4.4.2.1 The rod concept

Figure 4.59 shows two rods and the principle of assembly of the MSGC modules on these support structures.

The five modules are mounted from both sides of the rod with a 1% overlap in the active strip length. Figure 4.71 shows a single complete rod with the five modules in their final position. The rod length is 1225 mm, which is 30% longer than the series of twenty rods constructed and studied during the prototyping phase (see Section 4.4.5).

The main load carrying elements of the rod [4-34] are longitudinal carbon fibre C-profiles interconnected with carbon fibre cross links that guarantee the integrity of the structure. The C-profiles hold injection-molded plastic inserts, suited to support and fix the detector modules. Other inserts are used for distributing the gas to the modules.

Each MSGC module is supported by its four corners against the positioning/cooling inserts of the rod. The planarity of the components in contact guarantees the module positioning and alignment in the radial direction. In the $r - z$ direction the modules are aligned with the

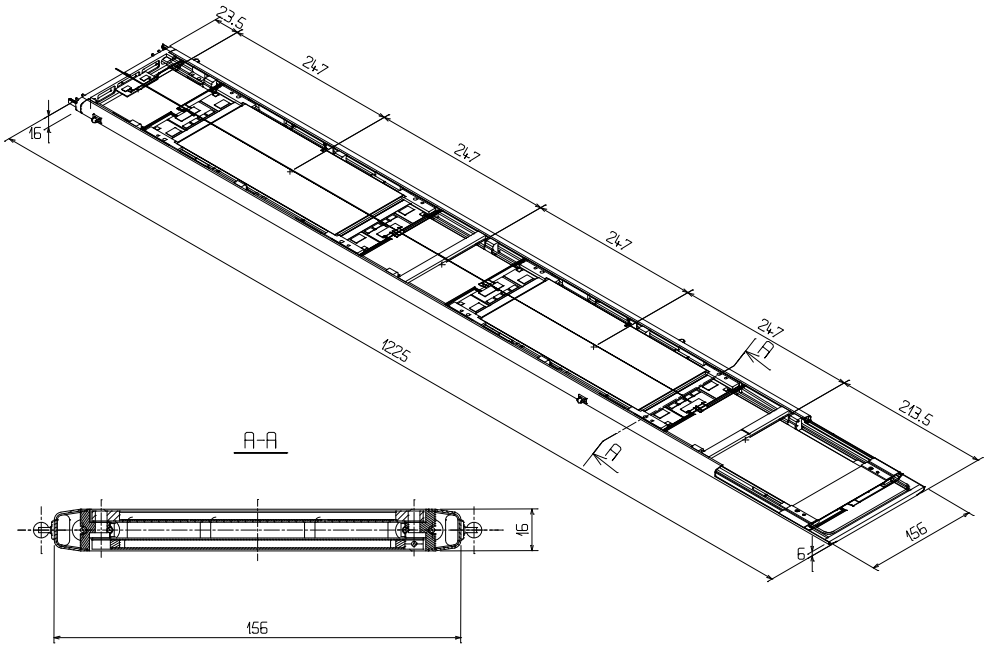

Fig. 4.71: Five MSGC modules installed on the rod.

strips parallel to each other, and parallel with respect to the reference axis of the rod. After the alignment procedure, actuated by means of a micro-metric adjustment tool (see Section 4.6.2.3), the modules are fixed into the final position by means of spring loaded screws.

The reference axis of the rod is defined by two spheres mounted on one C-profile. These spheres, together with the other two mounted on the second C-profile, acts as attachments of the rods to the support disks, and thus link the relative position between the modules and the barrel wheel.

4.4.2.2 Layout of gas pipes and cables

The simplicity of the rod mechanics allows the arrangement of all the services along straight paths inside the rod, or on top of the modules, thus minimising the assembly work, the costs, the failure risk and material budget. The hostile radiation environment, the aggressivity of the gas used, the safety aspect and attention in the minimisation of the radiation length, have influenced our material choices.

Figure 4.72 shows the path of the various services within the rod. Thin aluminium-insulator sandwiches run along one profile and serve for low-voltage powering. To balance the material budget distribution [4-35] and to avoid pick-up noise from the low voltage lines, all the front-end electronics control cables and the high voltage lines run inside the second C-profile. Optical fibres run straight on top of the modules from the readout electronics to the rod extremity. This solution, although not practical during the modules' assembly, is preferred since it minimises the turns and therefore the stress applied to the fibres.

One of the rod extremities serves as a miniature patch panel where all cables or service lines end. The links between the rod services to the lines mounted on the end-plates of the barrel wheels will be done, where possible, by soldering or welding procedures, still in a development phase. The optical fibres will be joined via MT connectors at the end of the rod.

The gas inlet and outlet pipes are realised in PEEK (ϕ 3/2.5 mm). They run along the two C-profiles of the rod (Fig. 4.73) through a series of gas junctions realised with an optimised room temperature gluing technique. A smaller pipe connects the gas junctions to the detectors.

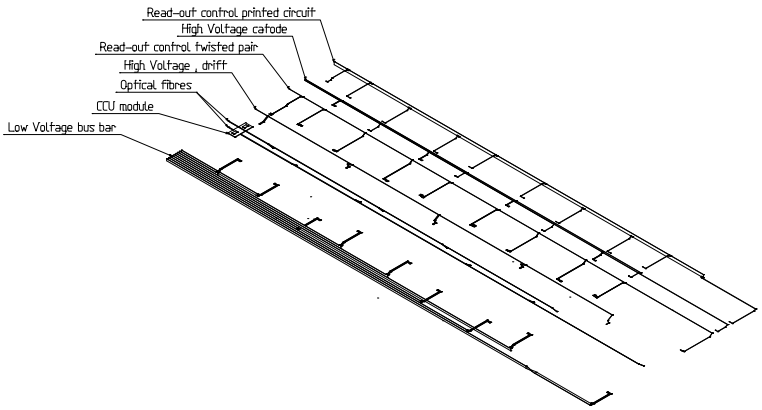

Fig. 4.72: Break-down of all services and their paths in the rod.

The pipe layout and gluing procedure were optimised during the construction of the 20 rods for the B1 milestone prototype.

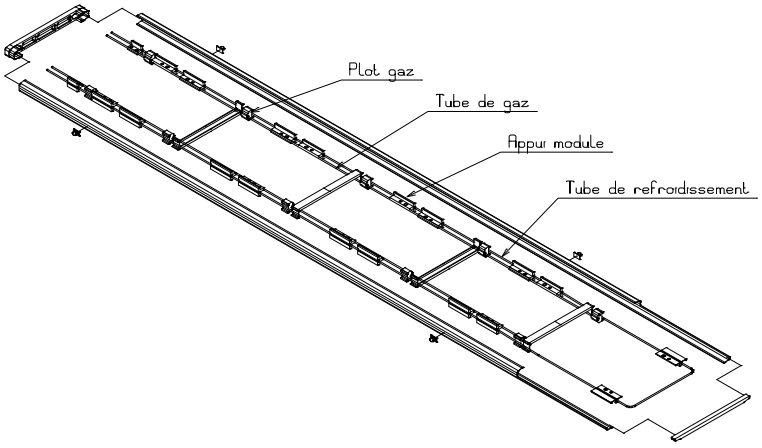

Fig. 4.73: Various services and components inside the rod: gas and cooling pipes, module support–cooling inserts, gas junctions.

4.4.2.3 Cooling system and pipe layout

Most of the heat losses in the MSGC barrel detector system are dissipated in the electronics of the detector modules. The main heat source, some 65 % of the total power, is the front-end amplifiers of the readout chips. The total heat dissipated in a rod equipped with $r-\phi$ modules or twin chambers is 14.3 W or 20.5 W respectively.

The most efficient cooling system removes the heat as close as possible from its source, thus avoiding large temperature differences in the detector. For this reason a water coolant circulation is provided on each rod. The cooling pipes, realised in stainless steel (ϕ 2/1.86 mm), run along the two C-profiles (Fig. 4.73) and they are tied, through an aluminium heat removal plate, to the top surface of each module positioning insert (Fig. 4.74). The shape and material of the positioning insert have dramatically changed from the one tested and produced for the B1 prototype. The reason being a major effort in the minimisation of material budget for those items that contribute more to the total radiation length [4-35].

The rod cooling pipe makes a complete loop along which it has connections to the heat sources. The schematic of the heat removal path from the module electronics to the coolant is shown in Fig. 4.75. The positioning-cooling system guarantees a good thermal contact between

the carbon-fibre cooling plate of the module (see Section 4.4.1.2) and the cooling pipe [4-36]. The efficiency of the heat removal mechanism has been tested and demonstrated in dedicated tests (see Section 4.4.5.1) in the framework of the B1 milestone project.

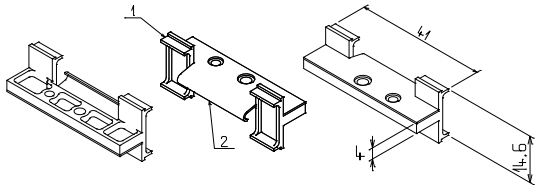

Fig. 4.74: Cooling-positioning inserts -1) fixing points to the rod -2) fixing points to the cooling pipes.

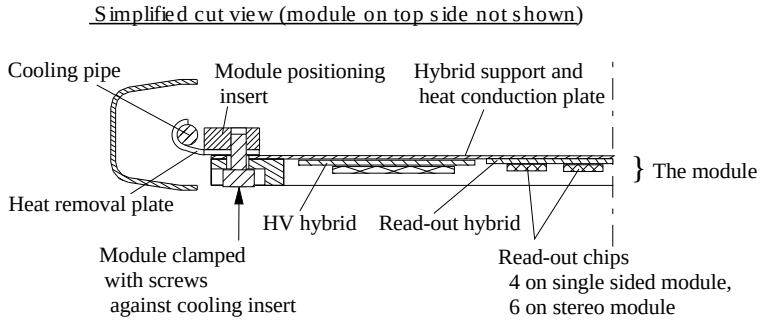

Fig. 4.75: Schematic view of an MSGC module. The electronic hybrid mounted on the carbon fibre support in contact with positioning insert and the cooling pipe.

4.4.2.4 FEA and mechanical behaviour

The rod will have a static distortion due to the gravitational and thermal loads and will be exposed to dynamical loads due to environmental noise like pipe flow, fans, and ground motion. Mechanical distortions should happen within the tolerances that are given for the translation and rotation of the modules.

Our understanding of the the various distortions and the reliability of our modelling was first verified with a careful study of the B1 rod prototype. The behaviour of the B1 rod under static loads was studied both by FE analysis and by experimental measurements. The results differ by less than 20% (see Section 4.4.5.4 for the rod experimental tests).

The behaviour of the final rod was predicted using the results of the prototype B1 as a reference. We applied analytical formulas to calculate the sag of the rod, as a function of its length, for different support points. For each study we optimised the geometry of the C-profiles [4-37] to obtain the minimum deformation employing minimum material. A remarkable reduction in the material budget is achieved when we adopt a rod length of 1.43 m instead of the original 2 m long rod. In the estimates for the final rods, we use a conservative value of 560 g/m as the mass load to be carried by the rod profiles. The mass of the two optimised C-profiles is only 75 g/m, just 12% of the total load.

We predict, for the CMS rod, a maximal distortion of 100 μm under the full load (Fig. 4.ii) of five modules, cables, electronics and services with the first fundamental frequency of $\sim$ 40 Hz.

4.4.3 The barrel wheel

The barrel wheel consists of four identical vertical disks that are joined together by cylinders at the inner radius and by cylindrical panels at the outer radius (Fig. 4.58).

Two of the disks, positioned at $|z| = 1100$ mm, serve to maintain the rods in the correct position and act as supporting elements for services and connections. The other two disks are located at $|z| = 310$ mm and support the rods at optimum locations. The position of the internal support disks was carefully studied, in relation to the shape of the rod C-profile. The present choices minimise the rod deformation and the need for highly rigid and massive structures.

The rods are mounted into the barrel wheel, from both planar ends, with a sliding movement through the openings in the disks. At $\eta = 0$ the rods co-penetrate over several centimetres, providing a 1% overlap of the module active area.

The services are mainly grouped on the ribs of the end-plate disks. The layout is conceived so as to leave as much access as possible to the rod, in order to facilitate their dismounting for maintenance reasons.

The wheel will be supported, from its inner most radius, by the tracker support tube.

For security reasons in case of gas leaks and for making a Faraday cage, the wheel is enclosed by a thin aluminised Kapton foil.

The different components of the wheel are summarised in Table 4.5.

Table 4.5: The components of the barrel MSGC wheel

Component	Material	Radiation length (mm)	Thickness (mm)	Length (mm)	Volume/unit (mm^3)	Quantity
Disk skin	CFRP	242	2		3E6	8
Disk rib	CFRP	242	2	150	4800	1472
Rod support insert	PEI	290	2	20	1257	2944
Inner cylinder skin	CFRP	242	0.5	2140	4.8E6	2
Outer panel skin	CFRP	242	0.5	2140	4.4E5	18
Core of the inner cylinder	Nomex honeycomb	13125	19	2140	1.8E8	1
Core of the outer panel	Nomex honeycomb	13125	19	2140	1.7E7	9
Bolt and nut	Al	89	8	10	640	714

4.4.3.1 The wheel elements

The main elements of the barrel wheel are: four identical support disks (Fig. 4.76) and interconnecting cylinders and panels (Fig. 4.58).

The four support disks have an inner radius of $r = 700$ mm and an outer radius of $r = 1200$ mm. They house six equidistant layers of detectors from $r = 747$ mm to $r = 1147$ mm. The disks have openings for each rod, tilted by the compensation Lorentz angle $\alpha_L = 14°$, and overlapping each other such to guarantee full $r - \phi$ coverage of the module active area (Fig. 4.77 and 4.78).

Different disk constructions were investigated before arriving at the present design, which combines the main advantages of the previous studies [4-38, 4-39, 4-40]. It consists of thin CFRP skins with short semi-radial CFRP strips to stiffen the narrow struts running between the rods. It has the same performance as a disk made of separate rings and connection struts but still offers the cost-effective manufacture of a sandwich plate. The manufacturing method has been verified by constructing a small sector prototype (Fig. 4.78) and a larger prototype comprising two full layers is in preparation.

The four support disks are connected to each other at their inner radius with three cylindrical structures. Three separate cylinders are used instead of a single long one to save radial space. The disks do not need to be slid onto the cylinders and the connections can be made from the side of the disks.

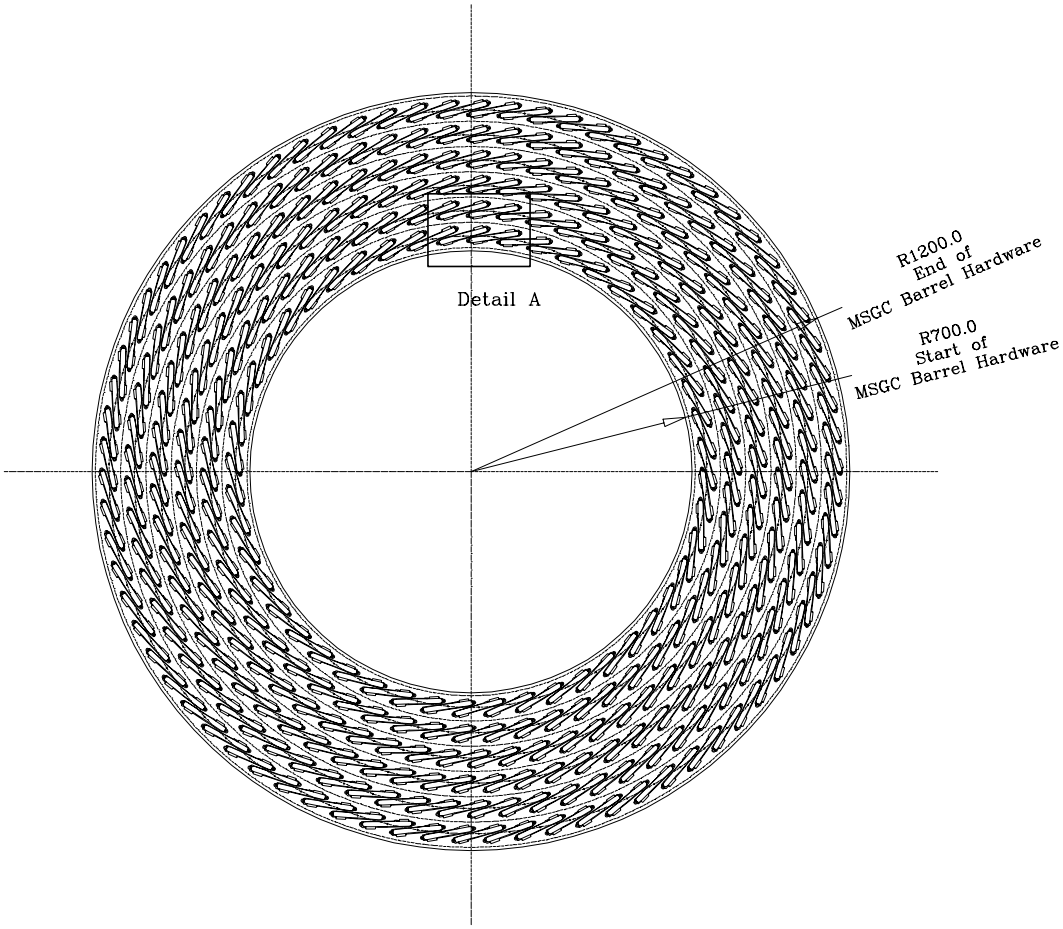

Fig. 4.76: The layout of one of the four support disks.

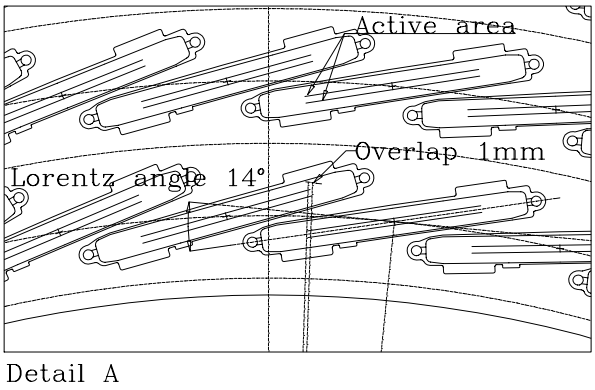

Fig. 4.77: The overlap of the module active areas in $r - \phi$ and the Lorentz angle compensation are realised with the appropriate disk design.

Fig. 4.78: Small carbon-fibre prototype of a disk sector.

The outer cylinder, which connects the support disks at the outermost radius, is made of a number of curved panels to minimise the material budget. The panels are easy to manufacture and assemble and they provide easy access to the barrel if needed. Breaking the outer cylinder into panels decreases the stiffness of the wheel only slightly, such that the effect can be considered negligible.

The inner cylinder and the panels are all 20 mm thick CFRP sandwich structures. The skins are of 0.5 mm thick ultra-high modulus carbon-fibre/epoxy laminate reinforced at the support points, while the cores are in honeycomb. The laminate lay-up of the cylinder will be constructed so that the thermal expansion coefficient will be low ($< 8*10^{-6}/°C$) in the z-direction and in the circumferential direction. The design of the structure is such that small changes due to thermal or other effects in the thickness of the cylinder or panels do not affect the alignment precision of the rods and modules.

4.4.3.2 Rod positioning and fixing method

Two reference spheres are mounted on each C-profile (Fig. 4.79) such as to define a reference plane for the rod. The rod position and orientation in the wheel is therefore defined by the relative position of the sphere-plane with respect to the disk-plane. A support based on three points would be enough, but since the rods are not torsionally very rigid a fourth support point is used to limit the torsional deformations. The reference spheres are glued on the lugs of the C-profiles of the rod in a precise jig.

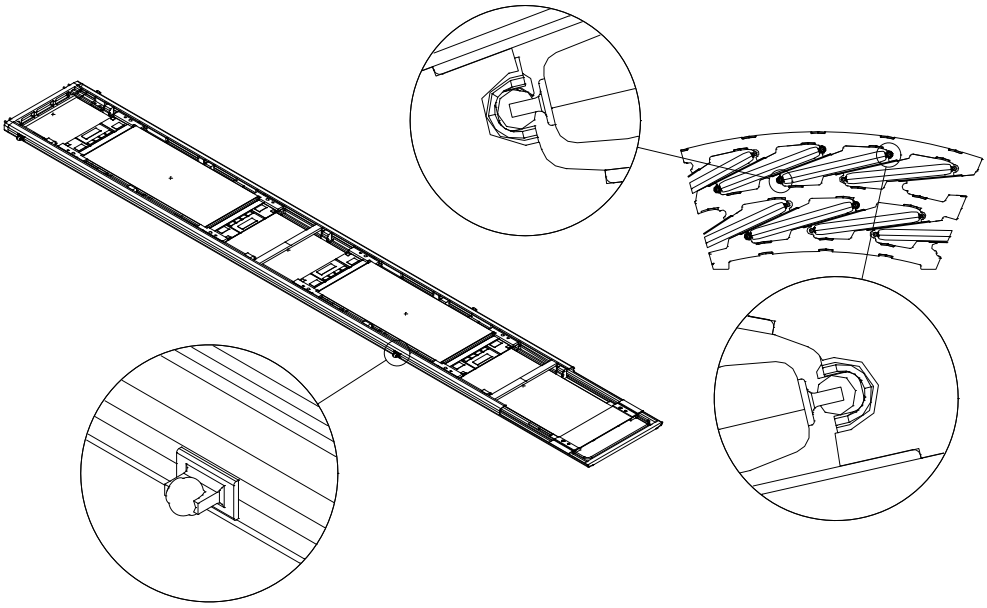

Fig. 4.79: Four spheres and the counter parts define the rod position and alignment.

Similarly, the spheres counter-parts will be precisely glued on the wheel disks using a special jig. In order to guarantee a perfect contact between the spheres and the surfaces of the counter parts, the latter are equipped with springs. The rod is supported semi-kinematically having two over-constraints due the fourth support point. A forced geometric congruence would happen if the fourth point does not lie on the plane defined by the three other points. This is taken into account in the requirements that are set for the precision and inter-alignment of the disks.

The support design is fully symmetric and allows for the rod insertion from both sides of the barrel wheel.

4.4.3.3 Services layout

The services layout on the wheel end-cap is shown in Fig. 4.80. Services are grouped into nine sectors that follow dedicated cabling paths between the ECAL and the forward MSGC. At the level of the outermost ring of the wheel, the services turn and descend along the end-plane as illustrated, for the gas and cooling pipes, in Figs. 4.81 and 4.82.

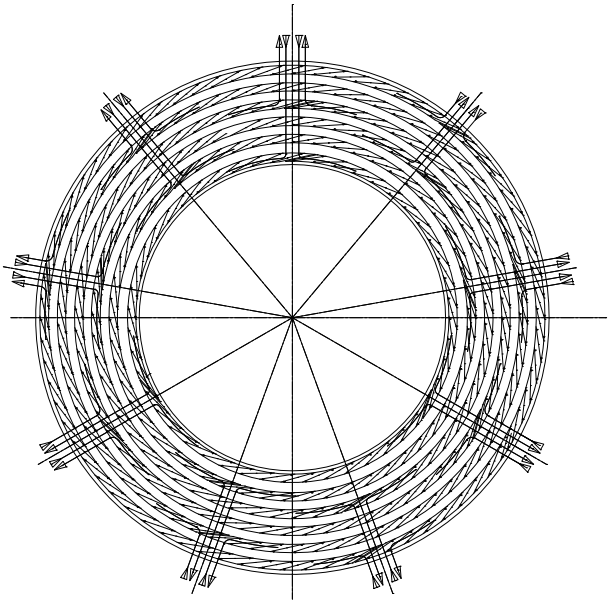

Fig. 4.80: The services on the wheel end-plane are subdivided in nine sectors.

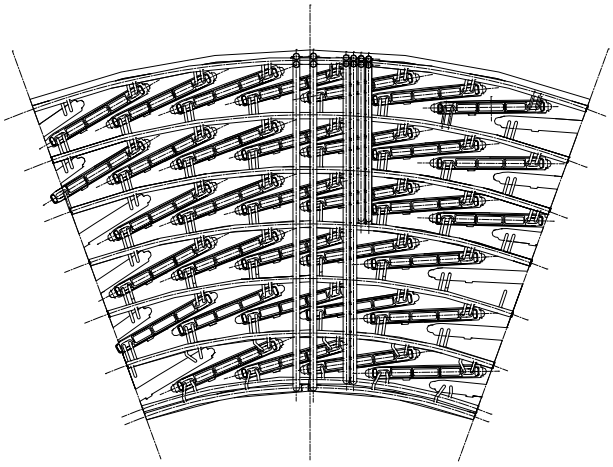

Fig. 4.81: The path of gas and water pipes on the end-plate of the MSGC barrel wheel guarantees access to a maximum number of rods.

Pipes and cables run on the disk in the free space between the detector layers, maintaining the maximum accessibility to the rods. The services are sub-divided into segments. In the cooling system each segment serves between 15 and 25 rods. With this granularity, in case of a failure of a cooling segment, we will be forced to switch off the readout electronic of that specific segment and lose only $\sim 3\%$ of the detectors. For security reasons, the segmentation of the gas system is twice as dense, thus each segment serves from 9 to 12 rods ($\sim 1.5\%$ lost).

A services segment is never shared between several layers. In this way, if a segment needs to be shut down, and the detectors belonging to that layer become inoperative, the MSGC

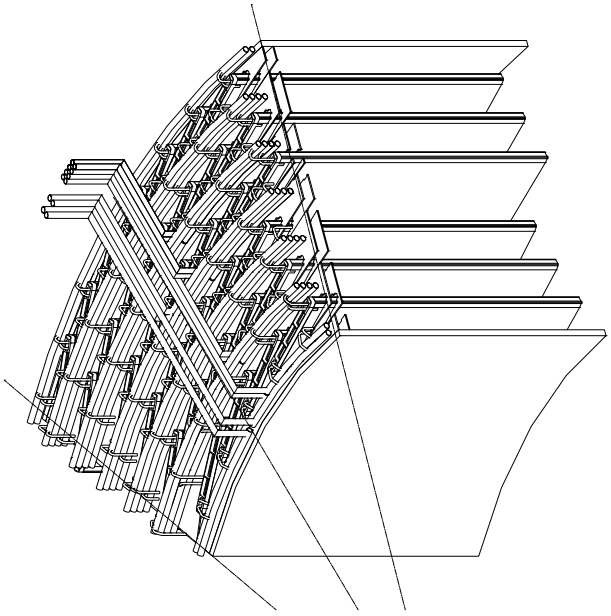

Fig. 4.82: Gas and cooling pipes run between the detector layers.

tracker would lose only one hit in that $r-\phi$ region. Moreover, in the unfortunate case that one complete layer will not be equipped (e.g. due to descoping or staging) the remaining layers will be operational with optimised parameter values.

4.4.3.4 Wheel support system

The barrel wheel is supported by four points located on the horizontal plane at the innermost radius. The supports are embedded in the inner cylinders in between the disks, thus minimising the deformations of the wheel. Each support has an adjustment unit that allows for motion in the vertical or horizontal direction. The adjustment unit is mounted on the tracker central support tube either rigidly or via a rail system (see Section 6.2.7.1). The adjustments of the four support points allow one to correct the orientation of the barrel wheel with respect to the beam axis.

4.4.3.5 FEA and expected distortion

FE modelling has been used extensively to drive the design of the mechanical components of the barrel structure. A simplified beam element model of the complete support disk was made (Fig. 4.iii) to determine the maximum distortions of the disk (16 kg) when it is loaded with the mass of rods and services (450 kg) and supported at the sides of its inner radius. According to the analysis the maximum distortion of an individual disk with 2 mm thick webs is 620 μm in the $r-\phi$ plane [4-41]. The load assumed in the calculation gives a safety factor ~ 3 in the deformation estimate.

A very accurate shell element model of part of a disk was made. Only two out of the six layers foreseen were modelled and the experimental measurements performed on the mechanical prototype (Fig. 4.78) confirmed the validity of our modelling system [4-42].

The whole wheel was then modelled using FEA code to check the maximum distortions of the complete barrel. The disks were modelled with beam elements and the inner cylinder with shell elements. The analysis showed that when the wheel is supported by four fixing points at the horizontal plane of its inner radius, the expected maximum distortion is less than 300 μm.

The maximum distortion of an individual disk was reduced substantially due to the stiffening effect of the cylinder (Fig. 4.iv).

We have investigated in detail the relative displacements between two disks supporting the same rods or, more precisely, the relative displacement of the individual support points connected to the same rod. This kind of displacements directly degrades the alignment accuracy of the rods and therefore must be kept to a minimum. The FE analyses showed that the worst relative displacements are only a few micrometers in the worst regions at the innermost layers.

4.4.4 Propagation of mechanical distortions

In order to define the manufacturing and assembly tolerances of the support structure's elementary parts and sub-assemblies, we have divided the positioning requirements of the strips in *location precision* and in *alignment precision*.

The *location precision* is the maximum allowable distance between the nominal and the actual position of a strip (or its centroid). The location precision does not tell anything about the strip's alignment with respect to the beam line. From the physics point of view less emphasis is given to the a priori knowledge of detector modules' precise locations as long as their positions are stable and the active areas overlap as required. However, in order to do a successful internal alignment with a reasonable statistical sample of the measured tracks, the starting value of the location of each module (or strip) in space should be known with a reasonable precision as discussed in Section 6.5.

The location precision requirements are fairly easy to meet with precise manufacturing and assembly of the support structures, and with the use of alignment and survey procedures during the assembly and installation phases.

The *alignment precision* tells what is the maximum misalignment of the strip line with respect to the beam line (reference line). The requirements for the alignment are much more stringent than for the location. Table 4.6 presents the alignment tolerances given in the local coordinate system of an MSGC module.

Table 4.6: Alignment precision requirements

	Tolerance (mm)
$\mathrm{d}x$	0.02
$\mathrm{d}y$	0.07
$\mathrm{d}z$	1.00

In the MSGC barrel the mechanical errors causing misalignment of the strips arise and propagate in the structural chain consisting of the strip (substrate), the detector module, the rod, the two opposing disk supporting the rod and the MSGC barrel wheel. Table 4.7 presents the estimated maximum values for the main error sources and their effect on the alignment of a single strip. The numbers take into account gravitational sagging of the structure due to weight of the detectors and all the services. It is assumed that the conditions during the handling, assembly, transport, and the beginning of the operation are kept stable, such that the distortions resulting from the mechanical and thermal loads and moisture-pick-up, are minimal. We assume that the propagation of the elemental errors follow a Gaussian distribution and the root mean square method can be used to estimate the propagation of the errors. By using the values of Table 4.7 the estimated total alignment errors are $\mathrm{d}x = 22$ μm and $\mathrm{d}y = 63$ μm, values that fairly meet the alignment precision requirements of Table 4.6.

Table 4.7: Estimated maximum values for the most significant error sources and their effect on the strip alignment

Error source	Maximum error (μm)	Effect on strip (μm)
Curvature of substrate	50	50 in y
Misalignment of the strip with respect to the rod	5	5 in x
Planarity error on module support points on the rod	15	15 in y
Sag of the rod	30 in x	10 in x
	100 in y	30 in y
Location error of the rod support	100	15 in x
points on the support disk	100	15 in y
Rotation error of the support disk	0.1 mrad	15 in x
with respect to the opposite disk		1 in y
Misalignment of pair of disk	100	11 in x
	100	11 in y

4.4.5 Experimental tests and prototype performances

4.4.5.1 Cooling efficiency of the readout electronics system

The efficiency of the cooling system (see Section 4.4.2.3) was investigated with a theoretical calculation and verified experimentally with a dedicated test [4-43].

A detector module was installed on a short rod equipped with a cooling pipe and support inserts. The module electronics was simulated by a set of resistances mounted on a heat exchange plate.

A first calibration test was performed with a heat conductor plate made of copper. All other tests were performed with high-conductivity carbon-fibre plates as in the final detector. The carbon-fibre plates were made of three layers [0,90,0] of Amoco K1100X carbon-fibre cyanate ester unidirectional prepegs. The manufacturer of the prepreg estimated the effective heat conductivity to be about 500 W/mK.

We measured the temperature gradients from the hottest point on the hybrid (central region) to the edge of the hybrid next to the cooling pipe and further down to the cooling pipe itself. We checked temperature gradients inside the module gas volume. Measurements were performed up to 2 W power dissipation on the hybrid, which is estimated to be the maximum power on a twin-chamber hybrid. In Table 4.8 we summarise the test results in comparison with the prediction of the finite element model of the thermal system [4-33].

Table 4.8: Computed and measured temperature gradients

Heating power (W)	Computed ΔT (°C) Cu plate	Measured ΔT (°C) Cu plate 0.05 l/min	Measured ΔT (°C) Cu plate 0.1 l/min	Measured ΔT (°C) K1100X CF plate 0.1 l/min
0.5	0.92	0.85	0.87	0.90
1	1.89	1.72	1.70	1.73
1.5	2.77	2.54	2.56	2.53
2.0	3.43			3.32

For a power dissipation of 2 W, we measured a maximum temperature gradient of ~ 2°C inside the gas volume. This value will not induce any significant gain variation. The temperature difference from the centre of the hybrid to its edge, and from the edge to the coolant was ~ 3°C, thus leading to ~ 6°C as the highest temperature gradient.

Inside CMS we will adopt a cooling system based on parallel distribution to guarantee the most uniform coolant temperature in the detector (see Section 4.4.5.3). Since the barrel MSGC is built up of cells where the heat/cooling load is similar to the one simulated with the setup just described, we can deduce that the maximum temperature differences in the system can be kept within the required $\sim 10°$C. A coolant temperature of $\sim 13°$C, will then allow to run and maintain the detector at the desired operating temperature close to 18° C. The result must, however, be re-confirmed with larger detector arrays, where the effects of height, cable heat loads, and tight spatial packing of modules and rods are included (see Section 4.4.5.3).

4.4.5.2 Mechanical precision under thermal cycling

The MSGC modules need to be appropriately fixed on the rods to maintain their alignment in all operating conditions. Possible loads are expansions and deformations due to temperature differences, mechanical loads due to twisting and bending of the rod and mechanical constraints from the connections to the service lines. The loads due to temperature differences are of the most serious type because of their cyclical nature.

Thermal cycling happens both in situ caused by the heating of the electronics, and during the transport and installation where changes of ± 10 °C are likely to occur. In addition, at start-ups the cooling system can be on while the electronics partially off and this might cause a temperature difference of ~ 5 °C.

The module fixing principle (see Section 4.6.2.3) was tested with a mock-up detector equipped with two copper plates as hybrids and four resistors glued on top of them to provide the correct heat power. One of the copper plates was heated up by supplying the appropriate current to the resistors. As expected, the module expanded for a maximum of 10 μm. After switching off the current the copper plate shrank and the module returned to the nominal position within an error of less than 1 μm.

In the final detector the hybrid support plates will be in carbon-fibre composite with a CTE of about $-1 \times 10^{-6}/°$C which is far less than that of copper, $16.8 \times 10^{-6}/°$C. The thermal deformations will thus be smaller. Since the supporting rod is also constructed from carbon-fibre composites, the thermal cycling will produce minimal effects.

4.4.5.3 Experimental tests on coolant distribution

The dimensions of the segment cooling pipes inside the rods, on the ribs and on the end-plate, have been determined by theoretical calculations but kept to the minimal possible diameter to minimise the large contribution to the material budget introduced by walls and coolant. A coolant distribution test was performed to validate the dimensions of the cooling pipes and the thermal efficiency of the system.

We have built a dedicated rig, equivalent to a single CMS cooling segment. The rig consists of 23 rod-like structures each carrying a loop of cooling pipe (Fig. 4.83). The plates are of full light-weight material in order to simulate the occupancy of the MSGC modules and therefore the limited surrounding gas flow inside the barrel.

A water reservoir/pump/heat exchanger was connected to the set-up. Even if the water inlet and outlet were at the low side of the set-up all air could be removed from the system with a reasonable input pressure of 150 mbar. Measurements of the total pressure loss against flow were performed and showed a good correlation between the calculated and measured values (Fig. 4.84).

With a constant ambient temperature, we varied the coolant temperature by ± 10 °C around its nominal value and we verified that the temperature variation is uniformly reproduced within ± 0.5 °C over the whole cooling segment, meaning ultimately an equal cooling efficiency for all modules.

Fig. 4.83: Mock-up of a cooling sector.

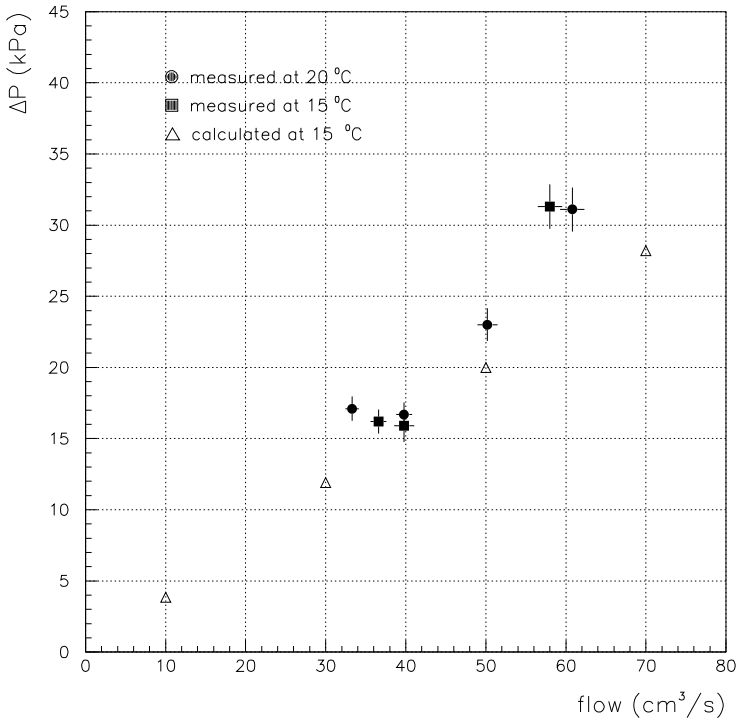

Fig. 4.84: Total pressure drop as a function of total flow in the cooling sector test set-up.

4.4.5.4 Rod mechanical stability

The mechanical stiffness of the rod was verified experimentally on the prototypes produced for the B1 milestone. The final MSGC rod is just 30% longer than the twenty prototypes realised up to now.

Before studying the behaviour of the complete rod the stiffness of the carbon fibre C-profiles, the principal rod elements, was measured. The C-profiles were made by pultrusion with a unidirectional (in profile direction) lay-up of high modulus carbon fibres ($E = 400$ GPa). During the test the profile was supported by two points and loaded with known masses. From the measurements we deduce a bending stiffness of 165 GPa. This number was used as specification for the final C-profiles for CMS.

The rod was supported by four points as it is foreseen for CMS, and mass loads were applied in the centre of the rod. The sag was measured at the same point. The results of the measurements and the finite element calculations agree within 20% and show, as expected, a linear relationship between load and displacement (Fig. 4.85). For the B1 prototype rod under the full load, the FE model predicts a total sag of 100 μm and the first fundamental frequency of 51 Hz.

These results allowed us to rely on the FE model during the phase of optimisation of the rod that followed the B1 milestone. The rod shape was in fact changed from the B1 model, to minimise the contribution to the material budget while still achieving the stiffness specifications.

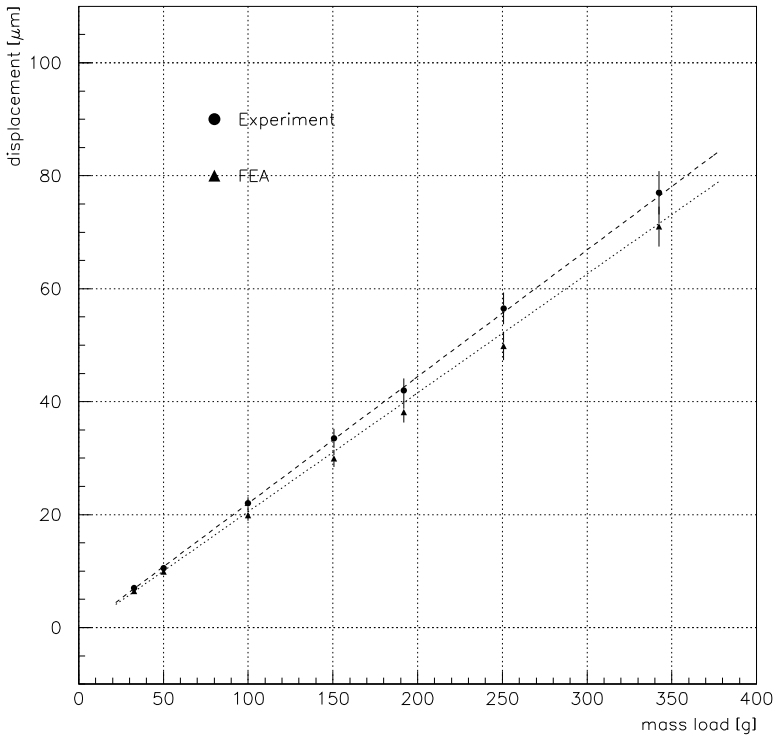

Fig. 4.85: Comparison of the B1 rod static loading test results with the FE model.

4.5 Forward Mechanics

The Forward–Backward regions of the CMS central detector consist of eleven disks on either side of the MSGC barrel, covering the radial region from 700 mm to 1160 mm and extending in z from $\pm$1215 mm to $\pm$2760 mm. In each end-cap all disks are connected to form super-modules as illustrated in Figs. 4.86 and 4.87. The major parameters of the Forward–Backward MSGC Tracker are summarised in Table 4.9.

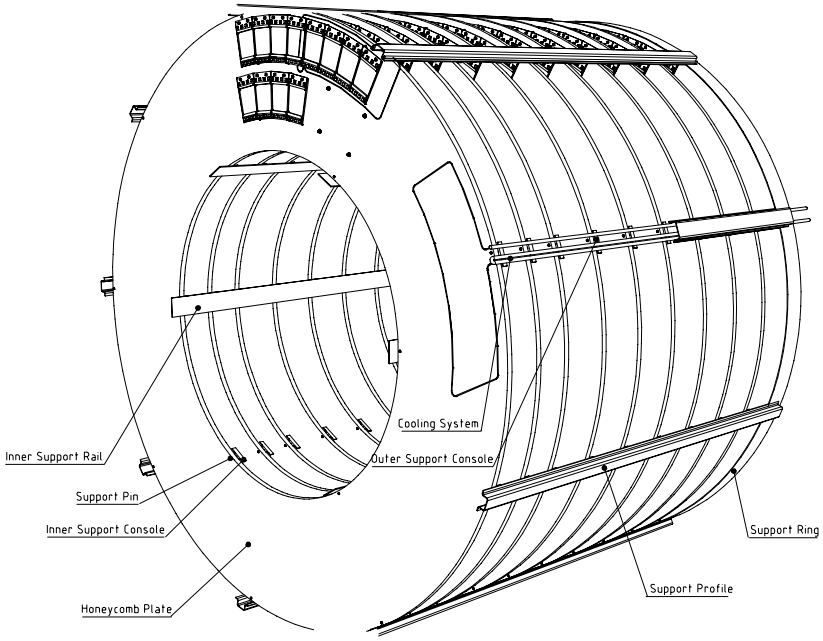

Fig. 4.86: A super-module.

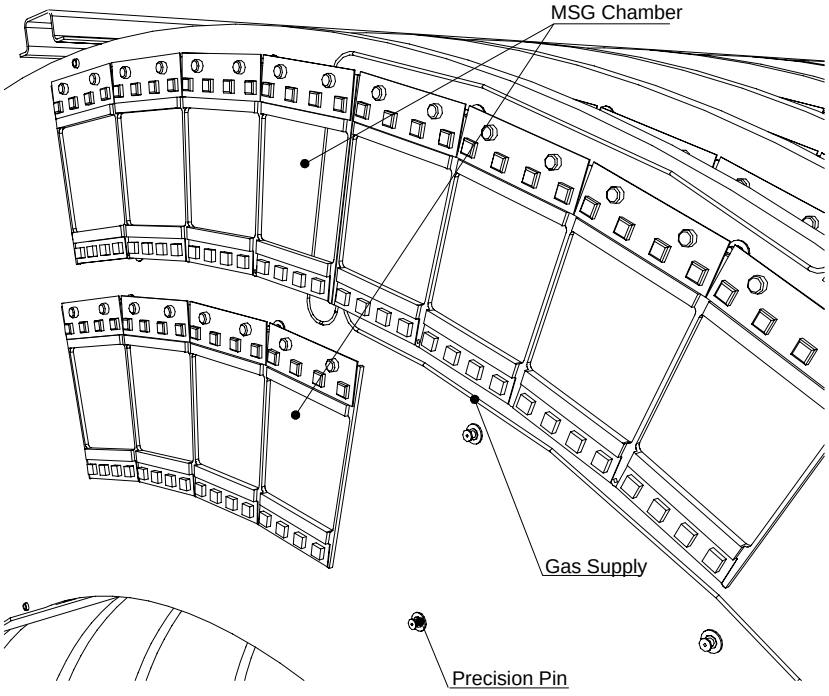

Fig. 4.87: A detailed view of the detector modules mounted on one disk.

Table 4.9: Major parameters of the forward MSGC tracker

minimum radius	700 mm
maximum radius	1165 mm
number of disks	11 each side
number of rings	4 per disk
active length per disk	440 mm
overlap in r	8.6%
dead space in ϕ	1.52% inner ring
	1.24% outer ring
number of MSGCs for $\phi - z$	2240 single chambers
number of MSGCs for $r - \phi - z$	2512 twin chambers
total number of readout channels	3076096

The main design criteria are full radial coverage of the entire Forward–Backward area for each disk, minimisation of dead space between the detector modules, rigidity of the super-modules consistent with material budget constraints, and access for services.

A total of 54 detector modules, each housing four wedge-shaped substrates, are mounted on each disk in four concentric rings as shown in Fig. 4.88 and summarised in Table 4.10. Rings 2 and 4 are located on the front face of the disk (toward the interaction point), rings 1 and 3 on the back. As shown in Fig. 4.88 the front and back rings overlap in radius ensuring full radial coverage for high-p_T particles.

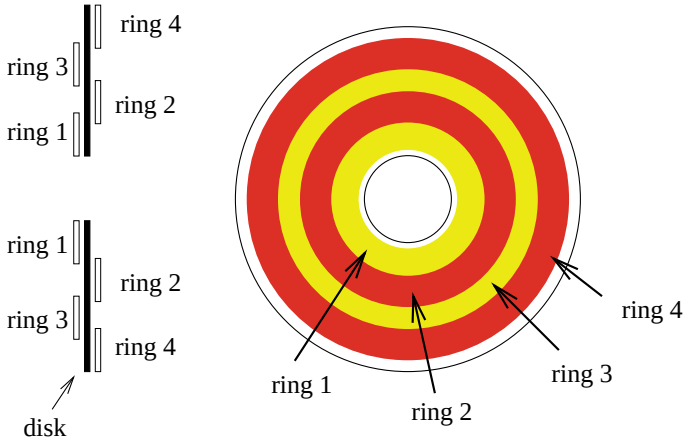

Fig. 4.88: Arrangement of rings on disks.

Table 4.10: Dimensions of rings on the disks. The items in brackets refer to the outermost disks in each end-cap

ring	location	type	r_{in}[mm]	r_{out}[mm]	# substrates	# detector modules
4	front	double	1005.4	1150.0	56×2	14
3	back	single(double)	889.6	1033.1	60(×2)	15
2	front	single(double)	776.1	878.6	52(×2)	13
1	back	double	710.0	797.5	48×2	12

The detector modules of the intermediate rings – 2 and 3 – are single-sided and have radial strips measuring the $r - \phi$ coordinate with a precision of 40 μm. In the outer rings – 1 and 4 – the modules consist of so-called 'twin' chambers, made of two detectors mounted back-to-back. One module has radial strips, while in the other the strips are tilted by a stereo angle of 50 mrad and provide a measurement of the second coordinate with a radial resolution of 1 mm.

The outermost disk in each super-module is entirely equipped with double-sided detectors thus providing at least two space-point measurements for each track in the end-cap MSGC system.

The four wedge shaped substrates in each detector module are mounted side by side forming a quasi-continuous active area in the azimuthal direction (wall-less ϕ crack). Thus the dead space is almost exclusively due to the 3 mm thick frames of the detector modules and amounts to 1.52% (1.24%) for the innermost (outermost) ring.

4.5.1 Detecting elements

4.5.1.1 Substrate specification and dimension

The artwork of the substrates for the Forward–Backward MSGC region will be performed on DESAG glass of 300 μm thickness coated with a layer of semi-conductive glass (Pestov glass or Schott S8900). The artwork itself consists of gold strips deposited over an adhesive layer.

The design and manufacture of the Forward–Backward MSGC will correspond to the specifications defined for the CMS 'performance prototype' successfully tested at CERN, PSI and Louvain-la-Neuve in 1997.

Except for the two outermost rings, all dimensions of the substrates will be optimised in order to allow the use of existing 6-inch industrial production lines. The Forward–Backward MSGCs will be manufactured at various plants in Belgium, France and Russia.

To realise the trapezoidal shape of the MSGC substrates, with a homogeneous detector response across the entire area, the electrode geometry (Fig. 4.89) follows the NIKHEF formula: $G = P/8+20\ \mu m$ [4-30]. Test beam results discussed in Section 4.3.4.4 demonstrate the reliability of the rule. The major parameters of the forward MSGC substrate are summarised in Table 4.11.

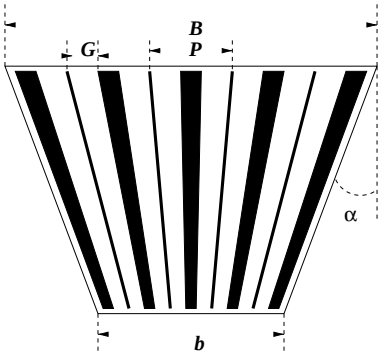

Fig. 4.89: Schematic view of a trapezoidal MSGC substrate.

Table 4.11: Major parameters of forward MSGC substrate

ring	base B (mm)	strip length (mm)	α (deg)	pitch at outer radius (μm)	pitch at inner radius (μm)
4	127.3	144.6	3.2	248	217
3	106.5	143.5	2.9	208	179
2	104.4	102.5	3.4	204	180
1	102.7	87.5	3.7	200	178

4.5.1.2 The detector modules

The detector modules consist of three frames supporting the substrates, the drift cathodes and the electronic hybrids, aligned with respect to each other and providing the required mechanical stiffness. Figure 4.90 gives an overview of the position and the function of the components and Fig. 4.91 gives a representation of the relative dimensions in terms of shape and size of the frames.

This design is based on the experience gained during the prototype phase of our project [4-44, 4-45] and differences in the final modules design can be envisaged after an optimisation process.

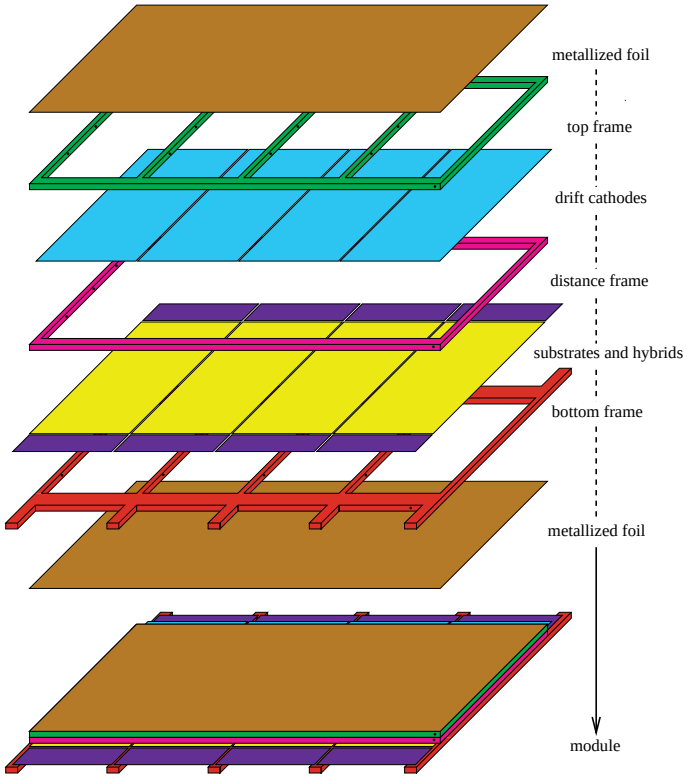

Fig. 4.90: Overview of the module components.

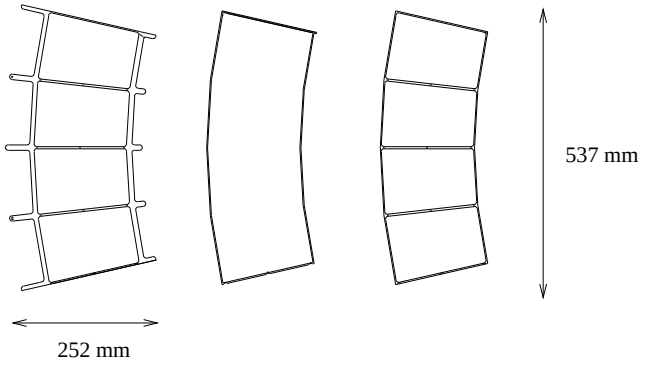

Fig. 4.91: A CAD drawing of the three frames. From left to right: bottom frame, distance frame and top frame.

The substrates are glued to the 2.5 mm thick bottom frame after they are aligned with respect to each other. The straps on the front (back) side of the bottom frame are foreseen to hold the readout and HV hybrid. They are also equipped with precision holes to fix the module to the wheel structure.

Stiffening bars inside the frame are foreseen to avoid deformation of the substrates through sagging. Holes in these bars allow the counting gas to pass through. The distance frame (without any internal bars) separates the substrates and drift cathodes. With 3 mm height it defines the sensitive detection volume. The top frame supports the drift cathodes and is equivalent to the bottom frame holding the substrates. However, it has a height of only 2 mm and no additional straps.

The entire module is closed by a 25 μm Kapton foil that has, on one side, a layer of evaporated aluminium. This foil protects the micro-strips from external pick-up noise and is an essential part of the gas return system in the module as explained in the next section.

The bottom and top frame is made of STESALIT[4] and the distance frame of PEEK (Poly-Ether-Ether-Ketone). PEEK has a smooth surface and is therefore better suited to define the detection volume, since no sharp edges of glass fibres distorting the electric field are present, which could lead to discharges between drift cathodes and substrate surfaces.

For the milestone prototype, the readout hybrid was located at the long base of the trapezoidal shaped substrate, glued to the straps at the bottom frame, and connected via wire bonds to the anode bonding pads on the substrates. The HV hybrids were glued to the straps at the short base and were also connected by wire bonds. For the final layout, in order to extend the radial coverage of the sensitive detector area, the readout and HV hybrids will be mounted on the same support as has been adopted for the barrel MSGCs. In case of the outermost (innermost) ring of detector modules this support will be attached to the straps of the short (long) base of the substrates (see also Section 4.7.2.6). Each detector module has one common drift voltage.

4.5.1.3 The gas return system

The principle of the gas flow in a detector module is described in Fig. 4.92. It is designed to provide equalization of the pressure on both sides of the fragile substrates and drift cathodes.

The gas enters through an opening at the side of the distance frame and passes freely through the sensitive detection volume. It leaves the distance frame via three holes and enters a gas diversion leading to two auxiliary volumes on either side of the chamber. The gas diversion, as well as the auxiliary volumes, are made gas-tight by Kapton foils. The gas finally leaves the module through holes in the bottom and top frames.

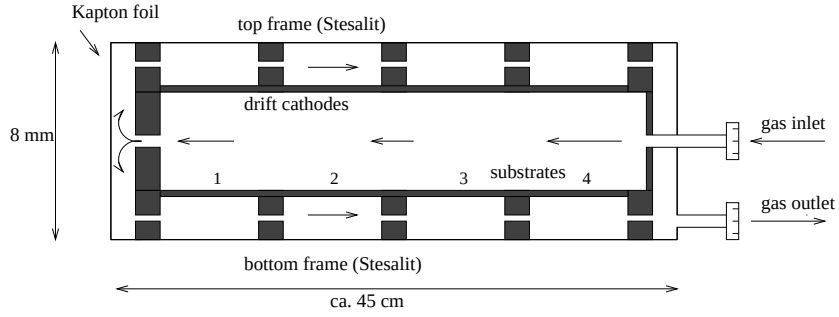

Fig. 4.92: Gas diversion between top and distance frame.

[4]Stesalit AG, Zullwil (Switzerland).

4.5.1.4 The twin chambers

About one-half of the detector modules will be designed to measure a second coordinate to provide space points for charged particle tracking. This coordinate will be measured on wedge-shaped substrates similar to the ones used in the modules described above. However, the anode strips will point slightly off-centre to provide a stereo angle of 50 mrad.

For these detectors a so-called twin chamber design has been chosen. A twin chamber basically consists of two modules of the type described above (see Section 4.5.1.2) mounted back-to-back to each other and using a common support for the two drift cathodes (see Fig. 4.93).

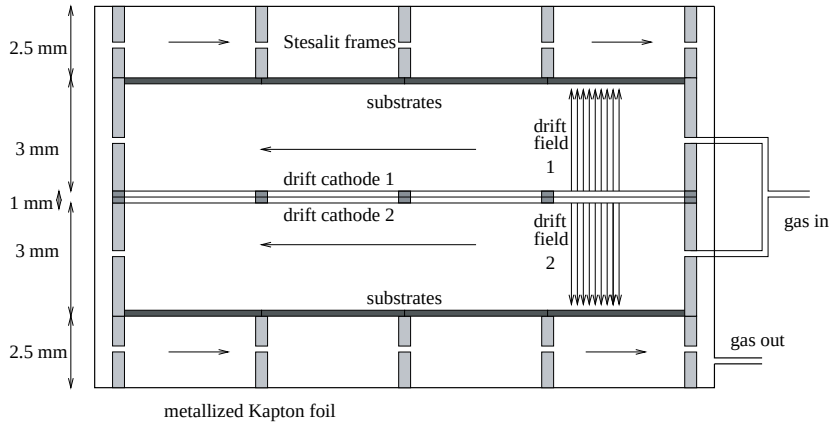

Fig. 4.93: A twin chamber module. The frames are identical to the frames of the original single-sided MSGC detector module.

Two separated drift cathodes provide safe bonding conditions. The half-modules are closed before the bonding procedure and before putting together the two parts to finish the complete twin chamber.

4.5.1.5 FEA and deformation studies

Finite-element calculations were performed by I. S. A. tec[5] with a module shown in Fig. 4.94. The results for the parameters listed in Table 4.12 are given in Fig. 4.v, 4.vi, 4.vii, and 4.viii.

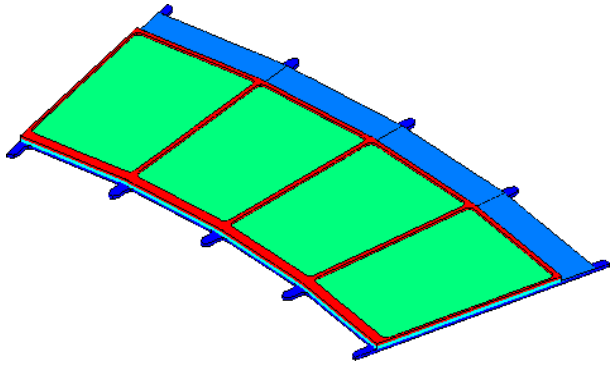

Fig. 4.94: Module layout studied by finite-element methods.

[5] I. S. A. tec, Aachen.

Table 4.12: List of finite element parameters

Structural unit	Thickness (mm)	Material	Mass (g)	Elastic modulus (N/mm^2)	Poisson ratio	Density (g/cm^3)
Bottom frame	3	Victrex	66			
Distance frame	3	450 GL30	33	9700	0.45	1.49
Top frame	2		29			
Glass	0.2/0.3 resp.	DESAG263	112	72900	0.21	2.51
Thermal plates	0.5	PTG/CFC	16	23000	0.29	1.7

Load case	Load	Max. normal displacement (mm)	Global bending stress (MPa)
Centrifugal accel.	1 g	0.005	/
Centripetal accel.	1 g	−0.005	/
Radial force	1 N	−0.005	/
Force normal to plane	1 N	−0.109	$-0.9/+0.5$

4.5.2 The forward disk

4.5.2.1 The mechanical layout

The forward MSGC detector modules are mounted on annular disks. Four concentric rings of modules are mounted on each disk, two on the front and the other two on the back face of the disk. The rings overlap radially to guarantee full detector coverage in the radial direction.

To achieve better planarity and stability, the supporting disks are made out of full plates machined to the appropriate dimensions (inner/outer diameters of 1370 mm/2330 mm, respectively). As shown in Fig. 4.95, the plates consist of honeycomb core material (NOMEX,4.8-32 with density of 0.032 g/cm^3), 20 mm thick, embedded between carbon-fibre (CF) skins. There are two skins on each side, each 0.2 mm thick (total CF thickness 0.4 mm per side) with the fibre direction perpendicular to that of its companion skin ($45°/-45°$ and $-45°/45°$ on the two sides, respectively). We are examining the possibility to reduce the thickness of the honeycomb to 16 mm and that of the skins to a total of 0.3 mm per side, while of course maintaining sufficient stiffness and stability by optimizing fibre quality and orientation.

4.5.2.2 FEA and mechanical distortion

The deformation of the disks under the load of their own weight and of the mounted detectors has been checked through finite element calculations. To this purpose, a disk was considered to hang at an inclination angle of 0.7° with respect to the vertical (caused by the deviation of the plane of the LHC from horizontal at the detector site) and to be fixed at nine points on its outer diameter (see below) and at two additional points on the inner diameter. Table 4.13 lists the parameters input to the analysis together with the main results. Case A corresponds to the mechanical layout adopted and constructed in the prototype phase, while cases B and C correspond to alternative layouts resulting from an optimization process. Figures 4.ix and 4.x describe the disk deformation in the vertical (y) and in the axial (z, along the beam axis) directions for case A. The maximal vertical displacement is 29 μm, while in the axial direction the displacements do not exceed 15 μm. Along the horizontal (x) axis the displacement is negligible. A different orientation of the laminate is chosen for both cases B and C ($0°/60°/-60°$, in a symmetric lay-up). This results in a reduction of the vertical deformation to 12 μm. Reducing, in addition, the overall plate thickness (case C) leads to a gain in material budget with an acceptable deformation of the disk in the axial direction. Although case C is more appealing, our present choice is oriented towards case B for financial reasons.

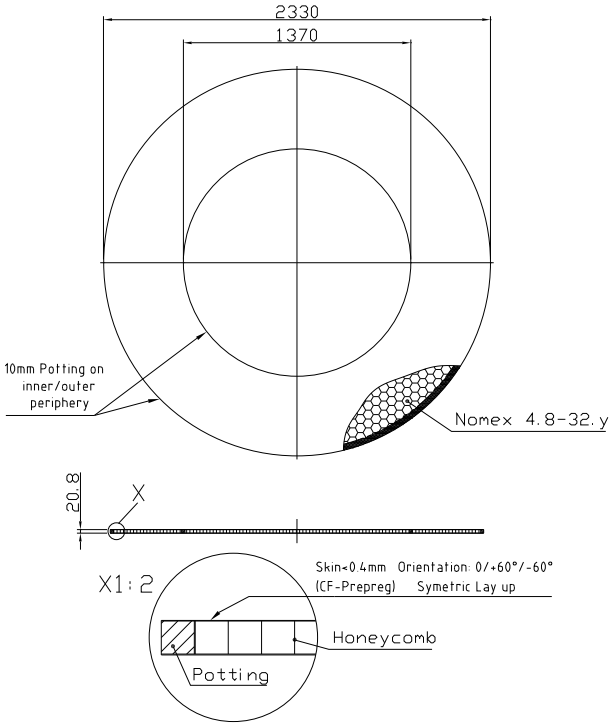

Fig. 4.95: Dimensions of a forward disk.

These results are already within specifications; however, the stiffness of the disks is expected to be further increased by joining all disks of one end-cap together into a single super-module by means of nine U-shaped CF bars on the outer periphery and six rectangular ones on the inside.

Table 4.13: List of finite-element parameters

case	total plate thickness (mm)	skin material type	skin thickness	laminate orientation	core material and orientation
A	22	T300	2·0.4	$45°/-45°$ resp.$-45°/45°$	Nomex, 4.8-32,Y
B	22	T300	2·0.4	$0°/60°/-60°$	Nomex, 4.8-32,Y
C	12	T300	2·0.4	$0°/60°/-60°$	Nomex, 4.8-32,Y

mass support plate (kg)	mass detectors (kg)	y-displacement (vertical) (mm)	z-displacement (axial) (mm)	max. stress (MPa)
6.1	15.6	−0.029	−0.015	$\ll 1$
6.1	15.6	−0.012	−0.011	$\ll 1$
5.1	15.6	−0.012	−0.029	$\ll 1$

4.5.3 The services layout

The U-channels of the nine supporting bars along the outer periphery of the super-module are also used to carry the cooling water and gas supply pipes running to the end-flange. In this way, a bundled supply circuit feeds (approximately) a 40° sector of the super-module. Each U-channel carries six pipes, four for gas and two for cooling water. We anticipate making both the gas and water supply pipes in PEEK with an inner diameter of around 10 mm and 20 mm, respectively.

4.5.3.1 The cooling distribution

The MSGC detector should be operated at a temperature of 18 ± 5°C. The heat generated by the readout electronics should be efficiently removed. The 512 strips of an MSGC substrate are readout by four front-end chips, each channel dissipating 2 mW of power. The total power dissipated by a detector module (four substrates) amounts to 4.1 W for single-sided and 6.1 W for twin modules. Using water as the cooling medium is adequate, however, the water temperature should exceed the dew point in the cavity, which is expected to be 12°C.

The hybrids carrying the front-end electronics reside on 0.5 mm thick plates with high thermal conductivity. To optimise the cooling performance we envisage the use of special materials. In the present scheme, we intend to use commercially available carbon fibres with thermal conductivity as high as 1100 W/Km. Starting from prepreg (AMOCO K1100X-2K fibres and FIBERITE 954-3A cyanate ester resin) we have obtained 0.5 mm thick sheets with a thermal conductivity in the fibre direction between 400–500 W/Km, superior to that of copper, and a Young modulus of about 400 GPa, similar to tungsten and its alloys. The coefficient of thermal expansion along the fibre direction is less than 10^{-6}/K. This material has been used in the silicon barrel and forward milestones for the fabrication of the detector modules (including the plates carrying the front-end electronics). As presented in the reports on these two milestones, it has been found to have excellent performance in providing adequate cooling of the silicon detectors, for which the operational temperature is required to be below −5°C. An alternative, presently under investigation, would be to use plates made of thermal pyrolytic graphite material (TPG) encapsulated in a carbon fibre composite. For such plates the manufacturer (Advanced Ceramics) claims thermal conductivities uniform over the plane of the plate and exceeding 800 W/Km.

The cooling system for the forward MSGC detectors is very similar to that for the barrel ones, which has been studied extensively in the context of the MB1 milestone.

As shown in Fig. 4.96, the cooling pipe for the detector modules is embedded in aluminium heat exchanger elements, making thermal contact with the plates on which the electronics hybrids are mounted. Figure 4.96 shows also details of the heat exchanger.

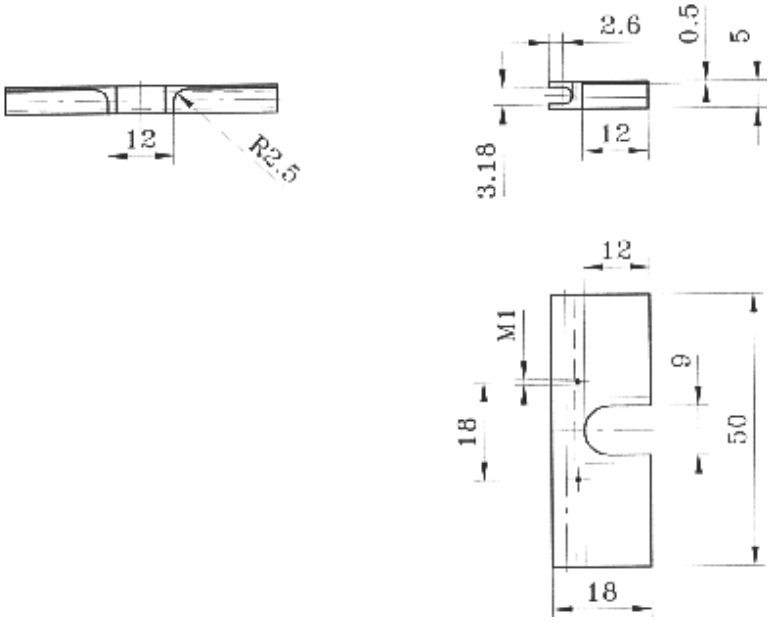

Fig. 4.96: Design of the heat exchanger element enveloping the cooling pipe for the detector modules.

For the connections to the supply manifolds, the same PEEK connectors or soldering procedure are envisaged for the end-cap as for the barrel system. Thirty-six connections are needed for each disk (one input and one output connector for each of the circuits on the front and back of the support disks).

The temperature distribution along the circuit of Fig. 4.97 is plotted in Fig. 4.98, as computed for a stainless-steel pipe with an outer diameter of 3.18 mm and a wall thickness of 0.15 mm. For laminar flow with the Reynolds number fixed to 2000 and the water temperature at the inlet at 16°C, safely above the dew point, it is seen that the temperature of the front-end electronics does not exceed 28°C.

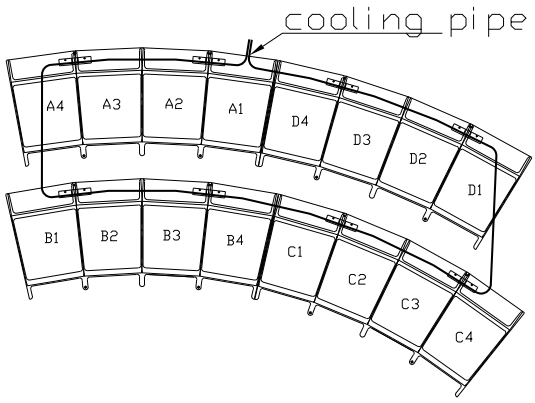

Fig. 4.97: Cooling pipe.

To minimise the amount of material, calculations indicate that the diameter of the stainless-steel piping can be reduced to about 2 mm with a wall thickness of 0.1 mm. The cooling performance can be further increased by introducing a kink in a small section of the pipe before each heat exchanger, thus making the flow locally turbulent.

Calculations show that the pressure drop along the input and output supply pipes is negligible compared to that between them (≈80 kPa).

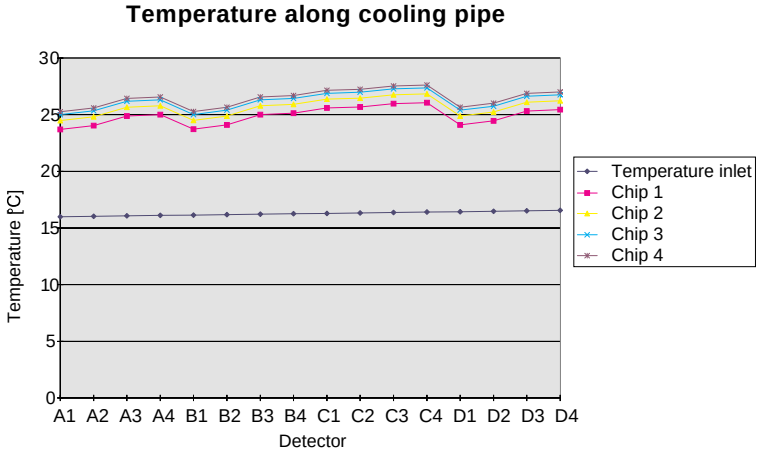

Fig. 4.98: Variation of cooling water temperature along one circuit with four modules.

4.5.3.2 The gas distribution

The basic gas distribution circuit involves three detector modules connected serially all residing on the same disk face. This circuit comes in two variants, one involving two outer ring modules

connected to an inner ring one, the second having a single outer ring module connected to a pair of inner ring ones. Since there is a total of 27 detector modules on each disk face (see Table 4.10), each of the nine service sectors must supply two of the basic circuits per disk, one on the front and one on the back face. There are two supply (and two return) gas pipes in every sector, one supplying the modules on disks 1, 3, 5, 7, 9, 11, while the other feeds those on the disks 2, 4, 6, 8, 10. The effective modularity of the gas distribution is further increased by alternately connecting on successive disks to the circuits (front and back disk face) to the left and to the right of the supply manifold. Distribution from the manifolds to the individual detector modules is done via thin PEEK pipes with an outer (inner) diameter of 2.0 mm (1.2 mm). The same PEEK manifold connectors as for the barrel are to be used (a total of 36 connectors per disk are needed).

4.6 Barrel MSGC Manufacturing and Assembly Sequence

4.6.1 Detecting elements

4.6.1.1 Module production and assembly procedure

The barrel MSGC modules will be produced and delivered by a consortium of Italian companies (Ce.Te.V, PROEL, LABEN) led and represented by LABEN S.p.A. (Milan). All these companies belong to the FINMECCANICA group which is owned mainly by the Italian State. Their standard business is in the field of aerospace engineering, micro-electronics and coatings technology.

All of the steps and procedures described in the next paragraphs have been set up and tested in depth during the realization of the modules for the B1 barrel milestone (Fig. 4.xi).

The production of the substrates will be done by Ce.Te.V, Carsoli, Italy.

Each substrate is fully inspected at the factory with an automatic test station installed in a clean room (class 100). The inspection unit is equipped with a microscope, a camera read by a PC, mounted on two micro metric motorised axes that span the whole module surface. The automatic inspection procedure is capable of identifying defects as small as 5 μm (2 μm per pixel) in a short time: $\sim$1 hour per substrate. The threshold limit, to define a defect which could compromise the good operation of a strip, is programmable. The software is able to discriminate defects on the basis of morphology, size and colour spectrum. A substrate with more than 2% of bad strips is rejected.

The test station is provided with a probe-card with 40 contacts to measure the leakage current of the plate up to 200 V in air.

The next step in the production line is the deposition of the advanced passivation strips on the accepted substrates. Experience gained during the production of the performance prototypes shows that the deposition of the advanced passivation does not create new important defects. Drops of polyimide can only damage the area they cover and not the entire strip. Therefore, after the advanced passivation step, the only required check is a control of the alignment of the passivation strips to the cathode edges (max. alignment error < 3 μm).

Ce.Te.V has a production capability of 5 substrates/day that will reach 10 substrates/day (2000 substrates/year) when the final production line is ready.

The gas box and accepted substrates will be assembled into final modules by LABEN-PROEL Technologies, Florence IT. This factory can match the production rate of the substrates.

The assembly is done in a clean room (class 100) according to the following steps. First the carbon fibre window is glued to the PEEK frame. Then these are glued to the substrate. Vacuum chucks are used to safely handle the different components and to guarantee good flatness of the final module. The assembly procedure is optimised to reduce the time the substrate is left free in air, to avoid contaminations and the risk of breaking the fragile glass. For all the gluing

operations one makes use of automatic glue dispensers that ensure good uniformity of the glue deposition. The last operation in the clean room is the installation of the gas pipes.

When the gas box is closed, the modules can leave the clean room and the gas tightness and distribution is checked. Accepted modules must have a gas leakage rate <0.01 cc/min at 1 mbar N_2 over-pressure, and a differential input-output pressure ΔP <0.04 mbar when the module is flushed at 1 mbar over-pressure with a flow of 8 cc/s.

4.6.1.2 Quality control and acceptance test

The modules assembled by LABEN-PROEL are shipped to the Pisa INFN Laboratories to undergo in-depth operative tests as here described.

Cathode strips are bonded to the HV cathode circuit while the anode strips are bonded to a switch-board that connects each individual anode to ground through a tree structure of switches. The chamber is flushed with a Ne(40)-DME(60) mixture. The leakage current from the drift plane to ground is tested to be <10nA up to 3500 V. The detector is then operated at $V_c \sim -540$ V, $V_d = -3500$ V, voltages that provide a gain 50% higher than the working gain in CMS.

The detector is then exposed to high intensity beta sources. The signal current during irradiation allows a check of the gain and uniformity of the modules, and identification of anomalous strips. Anode strips with large leakage current (>10 nA) or that are not stable are easily found and disconnected by means of the switches.

The Pisa INFN Laboratory will be able to test up to 5 detectors/day. After this test the module is sent back to LABEN for the assembly of the readout electronics. The defective anode strips, identified by the optical and operative tests, are not bonded.

4.6.1.3 Final acceptance test

Following the optical inspection and current acceptance test, each MSGC module, assembled with the final electronics, will undergo a standard series of tests to verify its performance capabilities and the agreements between its operational values with the ones selected by the MSGC community.

These tests will be performed in different laboratories, but with identical equipment. The test set-up consists of a table equipped with a support structure for the module and two motorised arms that move a ^{90}Sr source over the whole detector active area (Fig. 4.99). A stand-alone

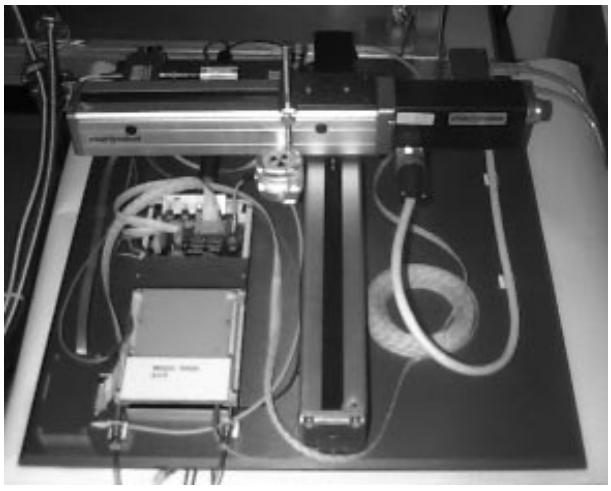

Fig. 4.99: The *xy*-table with a performance prototype under test.

system controls the quality of the gas used in the chamber. A VME crate houses the read-out electronics and the trigger logic. The fully automated data acquisition system includes monitoring and control of the high-voltage power supply (CAEN SY527).

Two independent current monitoring schemes are used in order to record possible fluctuations of the current drawn by the cathode strips. One monitoring scheme is based on the reading of the cathode current using a picoamperometer[6] readout with a properly clocked Sirocco ADC (CAEN V686). The second monitoring scheme makes use of a Keithley 6517A connected through a VME GPIB bus interface. This method provides an absolute charge calibration. The combination of the two methods allows a precision of ~ 1 pA in the monitoring of the cathode currents.

The test stand accomplishes the goal of quantifying the performance capabilities of each MSGC by completing the following measurements and tests automatically:

- A fast (~20 min) uniformity check of the chamber.
- A test for dead/noisy channels and broken or unbonded strips.
- Pulse-height distribution for each strip.
- Gain dependence of the chamber on the drift and cathode voltage (V_c, V_d).
- Determination of the leakage current $I_{cathode}$ as a function of $V_{cathode}$.

All data are logged and the outcome of these tests is compared to a set of reference values, which specify criteria for the acceptance of chambers to be used in CMS.

If a chamber is accepted, all relevant information like pedestals, position of dead strips and operating voltages for each chamber are stored in a database in order to be available for the event reconstruction procedures in the real CMS data taking environment. Next the module is shipped to CERN.

Before installation on a rod the module is again tested on the xy-table and the results are compared with the outcome of the first quality control test. The modules will be accepted and installed only if no difference in the two sets of data is detected.

4.6.2 Detector supporting elements

4.6.2.1 Rod production and assembly procedure

During the prototype phase [4-46] of our project we have manufactured and assembled twenty rods, 30% shorter than the final one (Fig. 4.100 and 4.xii). Following the positive experience acquired during this small production we decided to manufacture in specialised industries all the sub-components of the final rods: carbon profiles, cross-linking bars, support inserts, cooling and gas pipes.

The carbon fibre C-profiles and the cross-bars are produced from carbon-fibre/epoxy prepregs and autoclave cured on molds. This ensures that the essential load carrying components are thoroughly polymerised and stabilised for long-term use. The C-profiles are made out of high rigidity and low mass high-modulus ($E \sim 400$ GPa) carbon-fibres, while for the cross-bars we use cheaper standard modulus fibres ($E \sim 200$ GPa).

The gas inserts and the module support inserts are made by injection molding. This process works particularly well for production of larger quantities of small plastic pieces.

The assembly of the main mechanical structure of the 736 rods is done in industry following the same procedure we have adopted for the production of the B1 rods. A rod is assembled in a custom-made jig that forms it in the correct geometry and allows to glue all the components together. The gluing is done at room-temperature using epoxy resins [4-47]. This technique, contrary to elevated curing temperatures, allows high dimensional precision of the final object to be achieved and avoids the building up of internal stresses due to thermal cycling.

[6] instrument developed and built at Institute de Physique Nucléaire de Lyon.

After assembling at the factory, the rods are transported to CERN in a humidity controlled atmosphere, where they undergo the final acceptance tests (see Section 4.6.2.2).

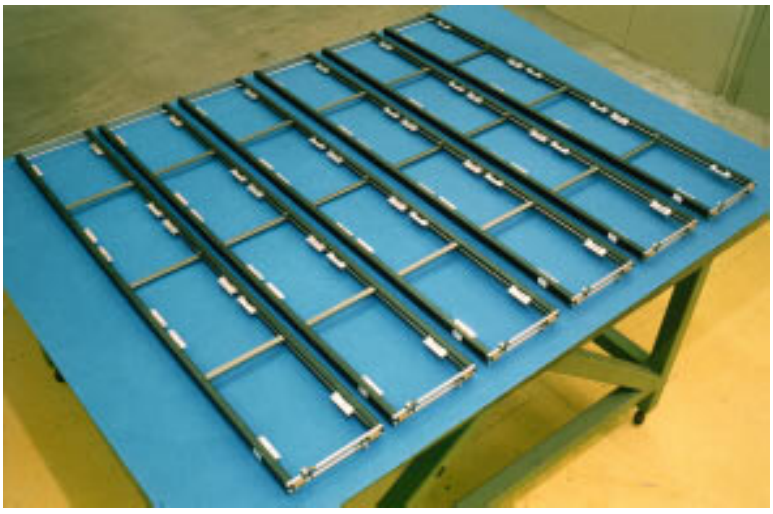

Fig. 4.100: Some of the rods produced for the B1 milestone.

4.6.2.2 Mechanical precision acceptance tests

In the qualification process of a rod, checks are performed on the overall dimensions, planarity, rigidity and leak tightness of cooling and gas pipes.

For the measurements the rod is placed in a jig that holds the rod from the four support spheres, the reference points of the rod. The jig sits on a marble table and it can be rotated by 180° for access to both sides of the rod.

The rod is first measured to verify that its external and internal dimensions are within the specified values. Simple mechanical tools are used for these measurements and a precision of 0.5 mm is sufficient.

The *planarity* is measured by checking the positions of the module support inserts. A measurement precision of 0.005 mm is required, and it is reached by using a electronic height measurement column, used already for the B1 Prototype rod measurements.

To check the *rigidity* the rod is loaded with a reference weight and the resulting displacement is measured using the height measurement column. The rigidity check is performed for two rod orientations corresponding to the two extreme positions in CMS.

The *leak tightness* of the cooling and gas pipes is checked by applying an overpressure of helium in the system, and searching for possible leaks by means of pressure gauges and a helium detector.

4.6.2.3 Assembly of the module on the rod

The assembly procedure of the modules on the rod has been optimised using the modules produced at the factory for the B1 prototype.

For reasons of economy we decided to manufacture the module frame and the rod with a very low internal precision in the detector plane ($\sim 100 - 200$ μm). In the radial direction the mechanical tolerance, 50 μm, is precise enough to match with the uncertainty of the position in which the primary clusters are produced.

The knowledge of the strip position in the $r - \phi$ direction is improved by employing an adjustment system which allows us to recover the initial large mechanical tolerances. The

method relies on the use of a micro-metric adjustment tool to block the module in its final position, and a microscope mounted on a xy-movement for control and verification of the strip position (Fig. 4.101). The most important steps of the assembly sequence are described here in detail:

- the rod, that has already passed the quality acceptance test, is placed on a cabling station where it is equipped with the low-voltage bars, the high-voltage and the control cables. All the cables have been pre-tested.
- the rod is positioned in a reference tool placed on a marble table. The rod longitudinal axis, defined by two of the rod attachment spheres (see Section 4.4.2.1), is made parallel to an absolute reference line thus defining the detector plane. The rod plane is identified with respect to two target pins placed on the rod extremity (Fig. 4.102). Once the rod is in its final position inside the barrel wheel, the target pins are used for monitoring and survey purposes.
- a module is placed in its housing on the rod and kept in place by a single reference pin around which it can pivot. A micro-metric tool (Fig. 4.102) is used to hold the module and to rotate it around the reference pin, without touching the module manually. The module orientation and position is defined by looking, with the microscope, at two targets engraved on the substrate. The targets define a line exactly parallel to the strips. With the micro-metric tool the module is moved such that the line defined by the targets of the module becomes parallel with the rod axis and therefore with the rod support points.
- the module is blocked in its final position by spring loaded screws
- the readout and high-voltage hybrids are cabled and tested
- the position of the module, relative to the rod support points, is verified again and logged in a database
- the same assembly procedure is adopted for the remaining modules
- the modules are connected to the gas distribution pipes
- the modules undergo final tests with radioactive sources

The adjustment system was tested experimentally with dummy MSGC chambers and with the B1 modules. We demonstrated that the modules, constructed with an accuracy in the detector plane of ($\sim 100 - 200$ μm), can be aligned with respect to external reference with an accuracy of better than 10 μm.

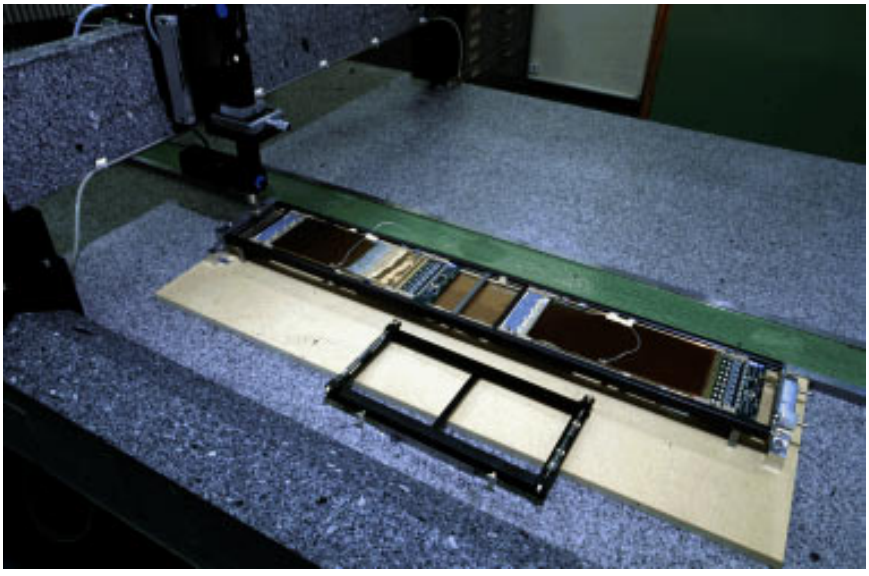

Fig. 4.101: The B1 rod, equipped with three modules, on the alignment table.

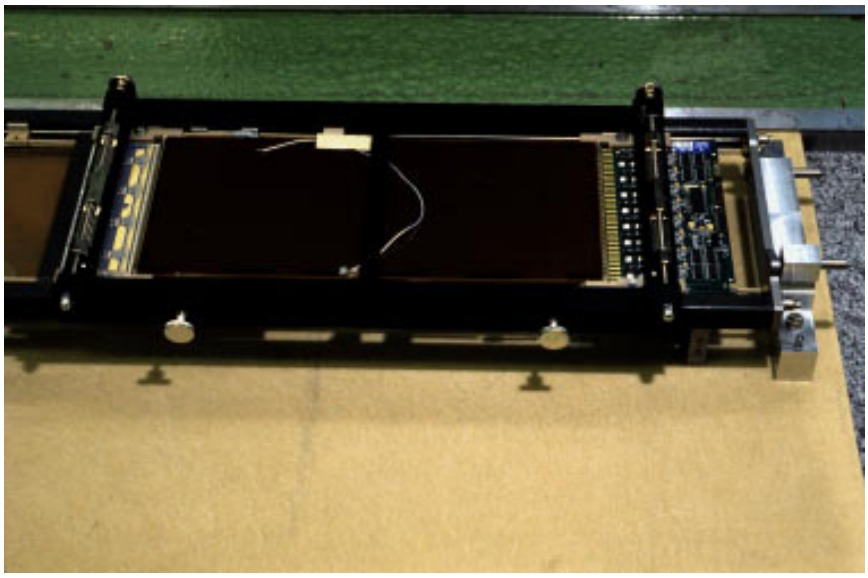

Fig. 4.102: A micro-metric tool is used to align the module parallel to the rod axis.

4.6.3 The barrel wheel

4.6.3.1 Disk manufacture and assembly

A disk consists of the following main elements: two facing plates (skins) and a set of webs between the skins. The webs guarantee the correct distance between the skins, give thickness and stiffness to the structure and reinforce the disk's thin and critical area between the rods. Both the skins and the webs are made from pre-cured quasi-isotropic UHM CFRP sheets by water-jet cutting. The manufacturing procedure was tested by cutting a set of CFRP specimens and inspecting the achieved precision and possible damages [4-41]. The test showed that the accuracy and the economy of water-jet cutting is definitely adequate. Also the resulting surface quality after cutting is good, only a slight smoothening of the sharp edges may be needed to finish the pieces.

The disk assembly and gluing is done on an assembly table, which ensures the flatness of the resulting disk. On the table there are positioning pins that locate the two facing skins with respect to each other. The skins are not complete 2.4 m diameter plates, but cut into sectors to facilitate the handling and to reduce the number of gluings to be effected simultaneously. The location of the webs is given by notches cut into the skins.

The disk assembly (Fig. 4.103) starts from laying and aligning the first skin on the table (a), after the webs are bonded to the skin (b) and to complete the disk the second skin is bonded, sector by sector, to the webs (c,d).

The assembly and bonding of the disk is done at room temperature. It is foreseen to use room-temperature curing to minimise build-up of deformations and internal stresses in the disks. However, since the disks do not need to be highly precise, a thermal treatment can be used to ensure the complete polymerisation of the glue. The adhesives to be used are the same as those planned for the rods, i.e. standard epoxies. As a valid alternative, the disk can be first assembled without any adhesive, then bonded using an adhesive with good capillary properties to penetrate the joints.

After the carbon-fibre structure of the disk is assembled, the ultimate precision is achieved by room-temperature bonding the rod support inserts to the structure. The inserts are precision parts which provide the connection points for the rods. The gluing is done on a flat table, which has precisely drilled holes for positioning pins that give the locations for the inserts. The same

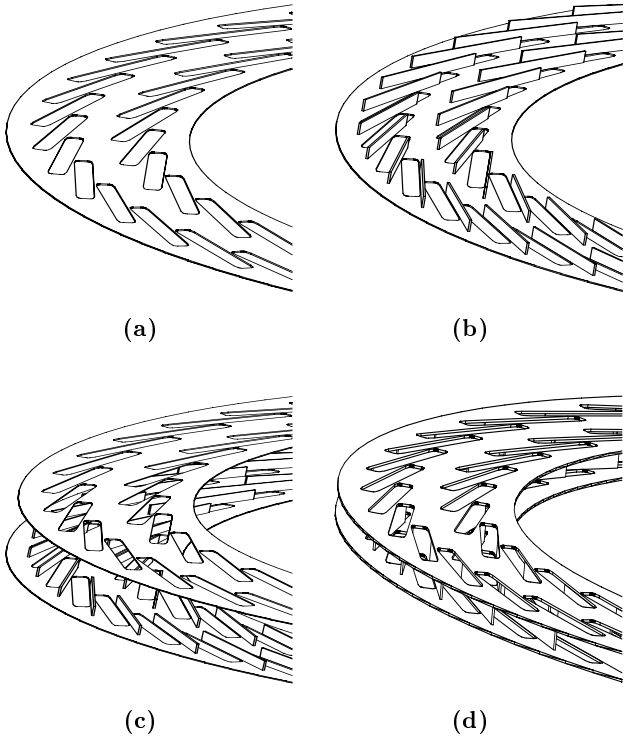

Fig. 4.103: The disk assembly procedure.

table, in the same controlled temperature is used for gluing the inserts in all the four disks, thus providing a set of identical disks.

The main interest in the quality control of the disks is to confirm that they are geometrically identical and behave similarly under loading. The disks will be measured in the horizontal and vertical positions. Contact (measurement columns and 3D co-ordinate measurement machines) and non-contact (optical targets measured with a camera) methods will be used. These measurement principles were applied already in the B1 Prototype [4-48].

4.6.3.2 Cylinder and panel manufacture

The connection cylinders for the innermost radius of the wheel, diameter 1.4 m, are manufactured using filament winding on a mandrel. This is a common industrial manufacturing technique [4-49].

A cylindrical, metallic mandrel is manufactured. After applying the necessary layers of peel-plies on the tool the first skin of wet carbon-fibre/epoxy is wound. A film of adhesive and the honeycomb core are wrapped on the first skin. Re-inforcement and attachment regions at the ends and along the sides of the cylinder are added. A film of adhesive and the second skin are wound on top of the stack.

The assembly is enclosed with the necessary peel-plies and bleeder layers, vacuum-bagged and cured in an autoclave. In the elevated curing temperature the metallic tool will expand more than the carbon-fibre layers, thus providing an extra pressure load from inside. After cooling down, the tooling can be removed as it shrinks more than the carbon-fibre structure on it.

The piece is post-machined to remove the extra carbon/epoxy from the ends, and to define the contact surfaces of the cylinder.

The composite panels that are used at the outermost part of the wheel, diameter 2.4 m, are manufactured using standard prepregging [4-49]. Curved metallic plate is used as a tool on which the carbon-fibre/epoxy skins, the honeycomb core, and the reinforcement and attachment pieces are laid up. After curing in autoclave the piece is post-machined for final dimensions.

4.6.3.3 Wheel assembly

The wheel assembly and pre-cabling will be done in the MSGC barrel assembly station, which consists of four parallel supporting rails and a set of roller units with which the separate pieces, disks and cylinders are guided next to each other and aligned [Fig. 4.104(a) to (d)]. Mobile carrier plates are used around the wheel to allow for ergonomic working positions and to improve access to the ends and to the inside of the wheel. When connecting the cylinders and the disks they are first bolted together only loosely allowing the disks still to move and to be aligned with respect to each other. For measuring the relative positions and orientations of the disks, capacitive sensors and wires running through the disks, laser light and transparent silicon detectors or 'Rasnik' methods will be applied. When the disks are aligned the bolts are tightened to their final tension and secured. Finally, the panels at the outer radius are mounted.

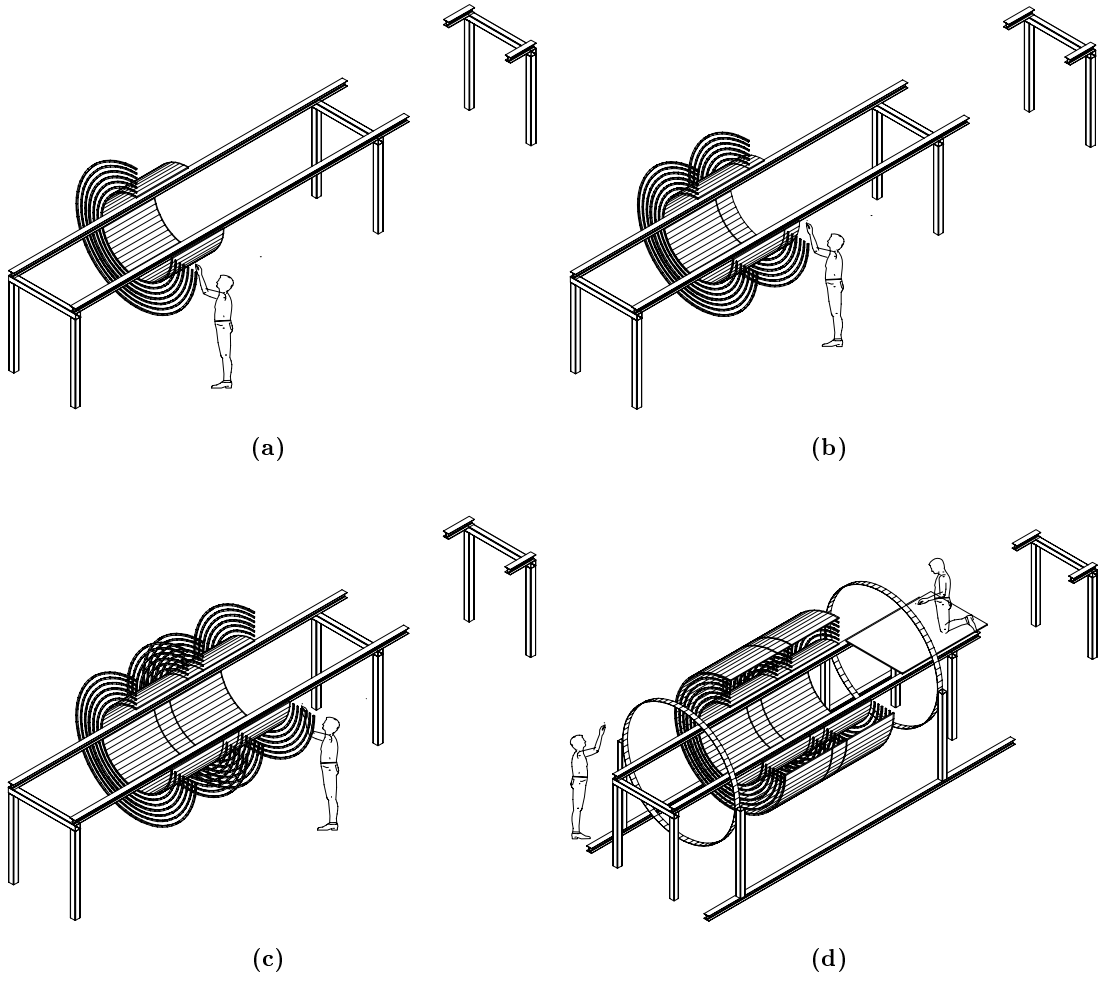

Fig. 4.104: The wheel assembly procedure.

Between the cylinders and panels special connection pieces are used that displace the bolts and their local forces further away from the disks, thus increasing the access and reducing the deformations of the disks. With the adjustment possibilities, the manufacturing tolerances for the cylinders can be held at a reasonable level.

4.6.3.4 Rod installation and alignment

The rod installation is performed from both sides of the wheel (Fig. 4.105), starting from the outermost layer and proceeding towards the centre. Rods are slid through the opening in the end-plate disks till the reference spheres of the rods mate with their counter parts on the disks. The reduced space available for the rod insertion and the critical overlap between consecutive rods at $\eta = 0$, impose the use of dedicated installation tools. The installation is done into two steps. In the first a pilot rod, equipped with mechanical gauges and endoscopes is inserted to check the clearance for the rod to be installed. Afterwards the real rod installation starts with the help of a guiding tool. The guiding tool is comprised of two lightweight rails on which the rod is able to slide. The rails are mounted on the disk within tolerances that allow for the spheres to find the counter parts. The rod is pushed manually until the spheres are mated. The guiding tool is extracted now using the rod as a guide. In case a rod needs to be extracted, the guiding tool is inserted along the rod and the rod is subsequently extracted.

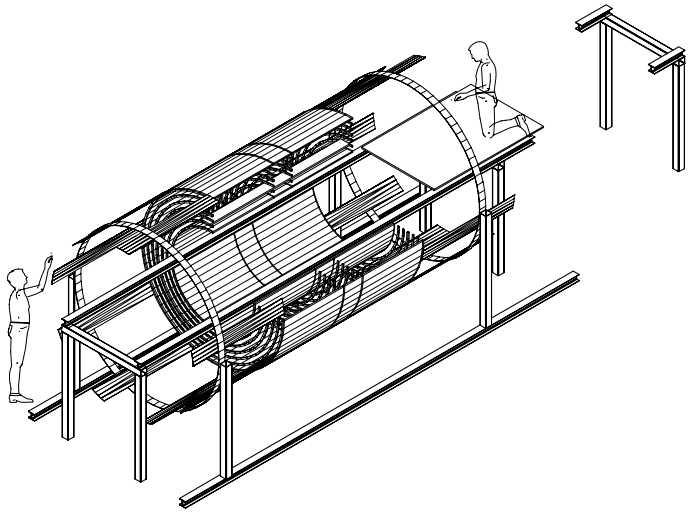

Fig. 4.105: Rod installation.

The precision maintained during manufacture of the rods and the disks guarantees the final position and the alignment. The verification of the rod position can be done using photogrammetry methods, as was successfully done for the survey measurements performed on the B1 prototype ([4-48] and see Section 6.5.3.1). After all the rods of the outermost layer have been inserted and their position surveyed, the cabling procedure starts.

Services lines and cables are pre-assembled and formed into different sector shapes, each one reproducing part of a layer. Pipes and cables are tested and approved for use. The services sectors are brought to the wheel and fixed to the disk ribs and to the external support. All the connections from the rod to the services sectors are performed and the final tests on the complete layer take place. When all the modules are tested and verified to be totally functional, the installation of rods into the internal layers can start.

4.7 Forward MSGC Manufacturing and Assembly Sequence

4.7.1 Detecting elements

4.7.1.1 Substrate production

The detector substrates for the Forward-Backward parts of the MSGC tracker are wedge shaped with 513 cathode and 512 anode strips alternatively engraved upon a Pestov coated Desag glass. The width of the cathode strips as well as the pitch vary according to the NIKHEF formula while the anodes' strip width is constant and about 7 μm. The *advanced passivation* on strip ends and cathode edges is achieved with BCB or polyimide. The electrode metallization consists of gold. Except for shape and sizes, the forward detector substrates should be identical to the barrel ones (see Section 4.3.3.8).

The substrates for the two inner rings of the forward MSGC tracker will be manufactured on 6-inch diameter glass wafers, using the existing automated production lines at IMEC (Belgium) and Vostok (Russia). At IMEC the substrate production line will be run by personnel of the participating Belgian university groups.

The production of the substrates of the two outer rings, exceeding in size a 6 inch wafer, is under discussion with several potential manufacturers in France and Germany. In France, Optimask and Eurisys-Mesures are candidates for substrate production and module assembly, respectively. Thomson-Trixel also is a good candidate in France for the entire production of detector modules. In Germany, negotiations are taking place with IMT-Baumer to install a production line. Each of these regional centres is, or has to be, equipped with clean-room facilities to meet the required cleanness constraints to assembly the detector modules. The anticipated production time is estimated to be about four years.

4.7.1.2 Quality control and acceptance tests

Upon reception, each substrate will be submitted to a quality control protocol.

An electrical acceptance test of all individual anode strips on the substrate is performed on a computer-controlled probe-station. The test procedure consists of sequentially placing probe-needles to an anode bond-pad and a neighbouring cathode strip measuring the conductance and capacitance between these two strips as well as the capacitance between the anode strip and a backplane which is provided by the apparatus. The latter measurement immediately indicates bad contact of the probe-needles to the substrate artwork which could otherwise be interpreted as defects on the strips.

After a fast optical alignment this testing procedure is performed automatically under control of a computer for all anodes on the substrate. For a 512 anode substrate this takes about 90 minutes including the initial substrate alignment by the operator.

The electrical measurement is done by means of an CV analyser (Keithley 590) which applies an AC voltage of 25 mV at 100 kHz to the strips.

High conductance values between anodes and cathodes which can originate from production failures or substrate contamination, are easily identified in the conductance measurement. Interruptions on the anode strips which decrease the active length show up as a reduced capacitance value. The capacitance is a fairly good measure for the remaining connected strip length, which allows easy computation of the missing active substrate area due to broken anode strips.

An example of such a measurement is shown in Fig. 4.106 indicating one broken anode. The upper curve shows the capacitance anode to cathode and the lower curve anode to backplane. The periodic structure in the capacitance values reflects the connection of the cathodes into groups of 16 strips.

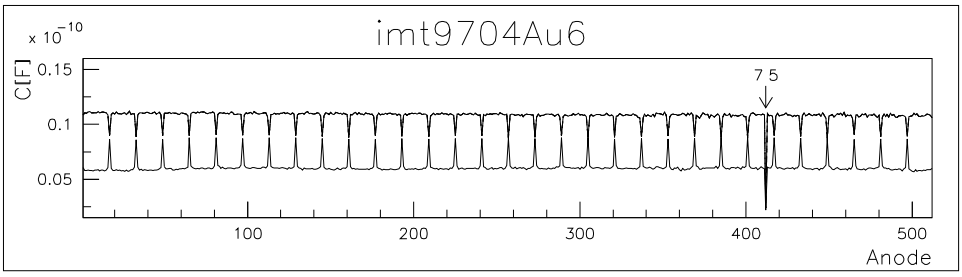

Fig. 4.106: Capacitance values indicating one broken anode.

After the capacity control, the acceptance test continues with an optical inspection to check the quality of the lithography in terms of *mouse bites* and excess of metal spots. If the quality of the substrate fulfils the acceptance criterion, of less than 2% defects, the substrate is cut to the correct size and shape using a diamond scriber and cleaned in an ultrasonic bath with de-ionised water.

The surface resistivity is then measured in dry nitrogen atmosphere by applying high voltage to the cathodes and measuring the current between anodes and cathodes. The aim of this measurement is:

- to check the value of surface resistivity already measured after the coating process;
- to detect substrates with chemical residues invisible during the optical inspection;
- to select substrates with same resistivity for subsequent assembly into the detector modules.

The latter selection procedure ensures the gain uniformity across the module necessary if a single high-voltage supply line is used for the multi-substrate module. After the initial qualification of individual substrates, the detector modules are assembled. Finally the modules are tested at the nominal voltages with radioactive sources and cosmic rays.

4.7.2 The detector module

4.7.2.1 Production of mechanical elements

In the prototype phase, including the milestone MF1, all frames have been machined out of full material. To save money during final production, all three kinds of frames will be manufactured by injection molding to achieve a better yield with PEEK instead of milling the frames out of full plates. The validity of such a method has been demonstrated by the production of the milestone B1 modules. The precision will be 100 μm, compared to that of a CNC machine which was sufficient for prototype modules. Details of the molding procedure are still to be discussed with industry. We have offers for molded frames of the necessary precision, which are assumed for our present cost estimates, but prototypes have still to be looked at. In case the necessary precision can not be provided at the assumed cost, we foresee machining the parts where high precision is required using machines and manpower available in the institutes.

4.7.2.2 Substrate positioning system and tooling

A good tracking performance in the MSGC Forward Tracker requires not only substrates with a good spatial resolution but also good alignment between the substrates. On each of the wedge shaped substrates the strips are all pointing towards the centre. The adjacent anodes on two substrates in a module will continue this scheme if the angular step $\Delta\alpha$ is kept the same as inside the substrates. In a full circle all strips have an angle of:

$$\alpha = n \cdot \Delta\alpha, \qquad n \in \mathbb{Z} \,. \tag{4.2}$$

To achieve this two adjacent substrates have to be aligned in the following manner. The distance between the two outermost anodes has to be an integer multiple of the inter anode distance on a substrate. This leads to non parallel strips and at the edges between two substrates (φ crack), it is necessary to skip one anode strip.

The substrate alignment and the gluing of the substrates to the bottom frame will be done on a special tool which provides the possibility of controlling the substrate positions and fixing the bottom frame to the aligned substrates.

The mechanical set-up is composed of four micro-positioning devices (manipulation in horizontal, vertical and radial direction possible) mounted on a common foundation. On top of the positioning device, vacuum Teflon tables are fixed to hold temporarily the cleaned substrates (Fig. 4.107).

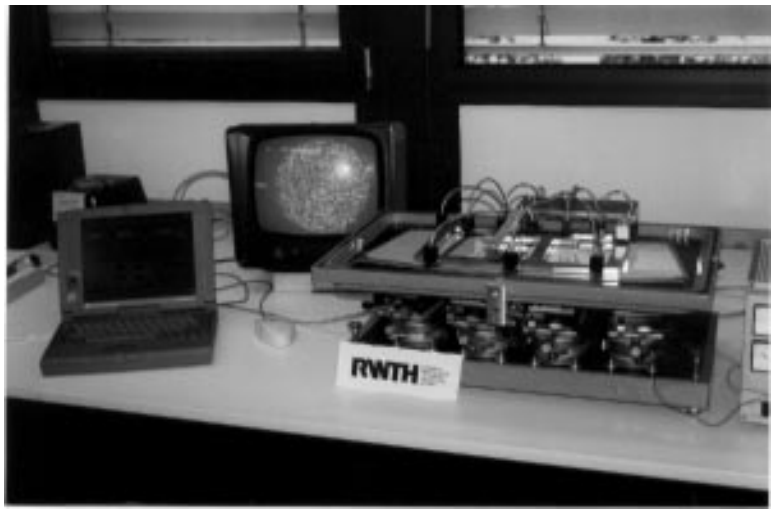

Fig. 4.107: Positioning device and gluing jig. On the screen the picture of a CCD camera.

The bottom frame is inserted in a cardanic fixation that can be manipulated vertically. Once the substrates are aligned the bottom frame is lifted towards the back of the substrates and glued in place.

4.7.2.3 Positioning quality control

The control of the substrate positions is done by an optical fibre system[7] with measuring sensors mounted on a common frame on top of the substrate surfaces (without touching them). LEDs are inserted in the cardanic frame to illuminate the sensors via holes in the bottom frame (Fig. 4.108).

One sensor consists of about 300 parallel fibres with a diameter of 50 μm distributed in a slit of 7.5 mm length. All fibres of the ten sensors enter a CCD camera and the signals are fed into a computer. By combining the information of several fibres the computer delivers 300 light intensity values per sensor (virtual fibre width: 25 μm). Before measurement a white light correction has to be done with a reference glass plate of the same thickness as the substrates.

In the bottom part of Fig. 4.108 the measured gray values of one sensor are shown. The minima are caused by the 100 μm wide cathodes, the anodes with 10 μm are too thin to be detected.

[7] FiberVision GmbH, Hirzenrott 2, D–52076 Aachen.

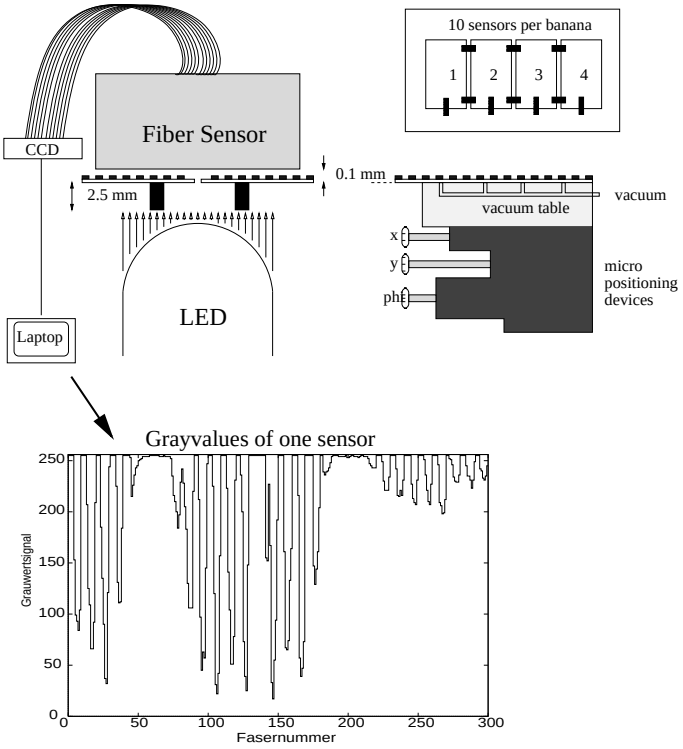

Fig. 4.108: Principal scheme of the fibre scan system. Gray values of one sensor (ϕ-crack at fibre 130). Each fibre has a virtual width of 25 μm.

The computer permanently evaluates the phase difference between the gray values of adjacent substrates. The procedure is the following:

- *Determination of the minima:* Minima are accepted if they exceed a certain threshold given by the user.
- *Eliminating 'wrong' minima:* Wrongly accepted minima caused by irregular illumination or diffraction of light at the glass edges are rejected if the distance of two minima remains below a certain user defined value.
- *Assignment of found minima to cathode numbers:* In case of known cathode distance p a cathode number is assigned to the minima. Minimum n is located at position x and the next minimum at a distance of Δx gets the number $n + \Delta n$ with

$$\Delta n = \left[\frac{\Delta x - p/2}{p} \right] + 1. \tag{4.3}$$

  This extrapolation is continued over the ϕ-crack.
- *Straight line through the manifold of accepted minima on both sides of the ϕ-crack:* On the left and the right side of the ϕ-crack straight lines are fitted to the positions x_i and the extrapolated cathode numbers n_i:

$$x_i = \begin{cases} a_1 n_i + b_1 & \text{for} \quad x_i \text{ left side of the crack} \\ a_2 n_i + b_2 & \text{for} \quad x_i \text{ right side of the crack} \end{cases} \tag{4.4}$$

  The slope of both lines provides the average cathode distance

$$\bar{p} = \frac{a_1 + a_2}{2}, \tag{4.5}$$

  and their distance at the position of the crack (x_s) the absolute distance

$$\Delta s = (a_2 x_s + b_2) - (a_1 x_s + b_1)\ . \tag{4.6}$$

These two values lead to the phase difference

$$\phi = 2\pi \frac{\Delta s \bmod \bar{p}}{\bar{p}}, \tag{4.7}$$

in a region of $[0, 2\pi]$.

Beginning with the outer substrate, all substrates will be aligned with respect to their neighbours with a phase difference as small as possible. The computer program provides the absolute distance between the outermost cathodes which has to be tuned to the inter cathode distance (corresponding to the pitch). The precision of this system is better than ± 5 μm.

4.7.2.4 Final detector module assembly procedure

In some parts of the module the counting gas is in contact with the glue holding the frames and glasses together. Therefore the glue has been chosen among the various products tested for compatibility with DME and for having a limited amount of out-gassing agents. Once the four substrates are aligned some drops of glue are put on the bottom frames. This will be lifted up and contacted with the backside of the substrates. All working steps necessary at the unprotected substrate surface are done in a laminar flow-box (class 100) to avoid dust particles on the artwork. After 12 h of curing time the bottom frame with the substrates will be taken out of the cardanic frames, turned around and the free space built by the bars in the frame and the backside of the substrates will be glued gas-tight with the necessary amount of glue.

A final validation of all procedures described in this chapter has been done in the framework of the MF1 milestone [4-31]. This milestone has been set in order to

- evaluate all system aspects of the Forward-Backward MSGC Tracker,
- check the feasibility of the industrial production,
- set up and check all assembly and test procedures in the institutes involved in the project.

For this milestone, 6 Detector Modules have been realised, with a total of 38 MSGCs. One of the objectives was also to test and optimise the mechanical design for the mass production. Therefore, several design variants of open (electronics inside the counting gas) [4-50] and closed (electronics outside) [4-51] were under test. Figure 4.109 shows one of these Detector Modules, consisting of two prototype modules equipped with four substrates each mounted side by side following the closed design approach.

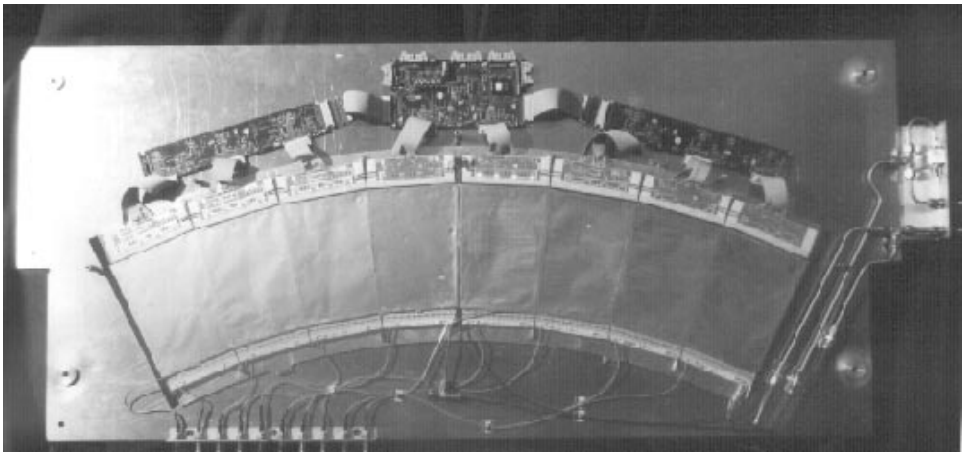

Fig. 4.109: Two prototype modules on a common support plate. At the top of the 8 substrates there are the pre-amplifiers and the the control electronics, able to readout 4096 channels.

In November 1997 a beam test experiment involving all MF1 Detector Modules has been carried out at the CERN X5 area. During this test, all designs have shown to be fully operational, and 19 456 strips grouped in six multi-substrates detector modules have been successfully operated [4-52]. Uniform gain across the entire detector surface was verified and all the wall-less ϕ crack mounting of aligned substrates has been shown to work (Fig. 4.110).

The optimisation of the mechanics results in the closed design described here.

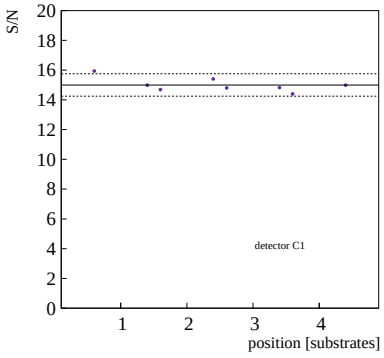

Fig. 4.110: S/N vs. position in the detector module.

4.7.2.5 Final testing procedure of detector module

After the final assembly the detector modules are subject to an extensive test procedure. It consists of:

- a test for gas leaks,
- a test of the bonded front-end electronic,
- the identification of missing bonds and broken strips,
- a high-voltage test,
- spot checks with a source,
- a test of the complete module in a cosmic ray hodoscope.

4.7.2.6 Assembly of detector modules on the disk

To cover the whole Forward-Backward region the detector modules will be mounted on disks as shown in Figs. 4.86 and 4.87.

An extension of the radial coverage of the sensitive detector area is possible if the space necessary for the readout hybrid is reduced. This can be done if the readout hybrid is mounted perpendicular to the substrates. To achieve this a bent pitch adapter has to be used (Fig. 4.111). Pitch adapters made of Kapton capable of flexing by 90° were realised in the AMS project [4-54]. The bending radius for the Kapton pitch adapters is approximately 1 cm. The application of this technique to MSGC forward region will allow the sensitive outer radius of the detectors to be increased by approximately 1.6 cm.

A second possibility, similar to what is adopted for the barrel MSGC, and that we intend to pursue, is to mount both the readout and HV hybrids on the same support. This common support will then be attached to the short (long) base of the substrates in case of the outermost (innermost) ring of detector modules, maximising the radial coverage. For the intermediate rings, the readout/HV hybrid can equally be connected to the strips from the short or long substrate base.

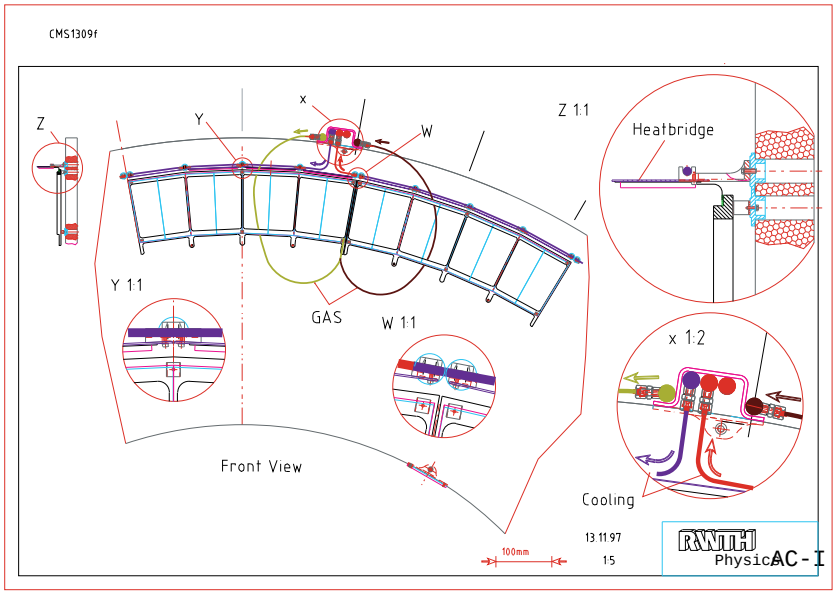

Fig. 4.111: Readout electronics fixed at 90 ° to the MSGCs, in order to reduce the dead space.

4.7.3 The forward disk

4.7.3.1 Manufacturing and assembly

The plates for the forward disks will be produced by commercial firms specialising in CF-composite materials. Two main candidates have been identified, EUROCOMPOSITES, where the plates used in mechanical prototypes were produced, and CONTRAVES. The machining to the final disk dimensions will be carried out in the Aachen workshops (I. Institute).

In an initial step, the disks will be equipped with precisely located fixation points for the detector modules and with the detector cooling and gas distribution piping. This pre-assembly step will also take place in the institutes.

The precision in the relative alignment of the detector modules on the disk is given through the exact positioning of the fixation points. Precision holes are drilled on a CNC machine at the location of the fixation points in a CF plate, which is used as a jig. Corresponding (less precise) holes are made on the honeycomb disk. Figure 4.112 illustrates the method used to precisely position the fixations.

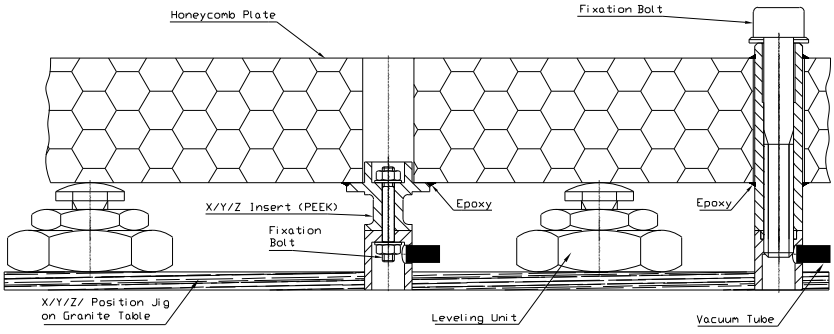

Fig. 4.112: Positioning inserts on honeycomb wheel

The CF jig is laid on a flat granite table and auxiliary feet are placed in the holes and held there by vacuum suction. Precision made PEEK inserts are then mounted on the feet by means of screws. The honeycomb support plate is then placed on this construction and levelling elements are used to adjust it with respect to the PEEK inserts so that it rests freely on them. The inserts that have been precisely placed on the jig now fit into the plate holes (the diameter of the latter is 1 mm larger than that of the insert heads, providing some freedom of adjustment during the placement). A small amount of glue is then used to fix the head of the insert to the honeycomb plate inside the hole. In this way, precision in the direction perpendicular to the face of the plate is guaranteed by the flatness of the granite table (better than 5 μm) and by the milling of the auxiliary feet and insert pieces with a typical precision of 10 μm. In particular, a possible non-planarity of the CF jig is of no consequence. In the plane of the plate the accuracy, again to the level of 10 μm, is given by the precision of the jig.

The honeycomb plate is then removed from the jig by interrupting the vacuum and the auxiliary feet are unscrewed from the PEEK inserts. The latter are now firmly affixed to the plate using glue. Precisely fitting pins are then placed in the inserts and serve for the eventual mounting of the detector modules. The cooling and gas distribution pipes are also pre-assembled on the plate.

4.7.3.2 Final assembly into a super-module

All disks in one end-cap are connected together into a super-module by means of CF bars, as shown in Fig. 4.113.

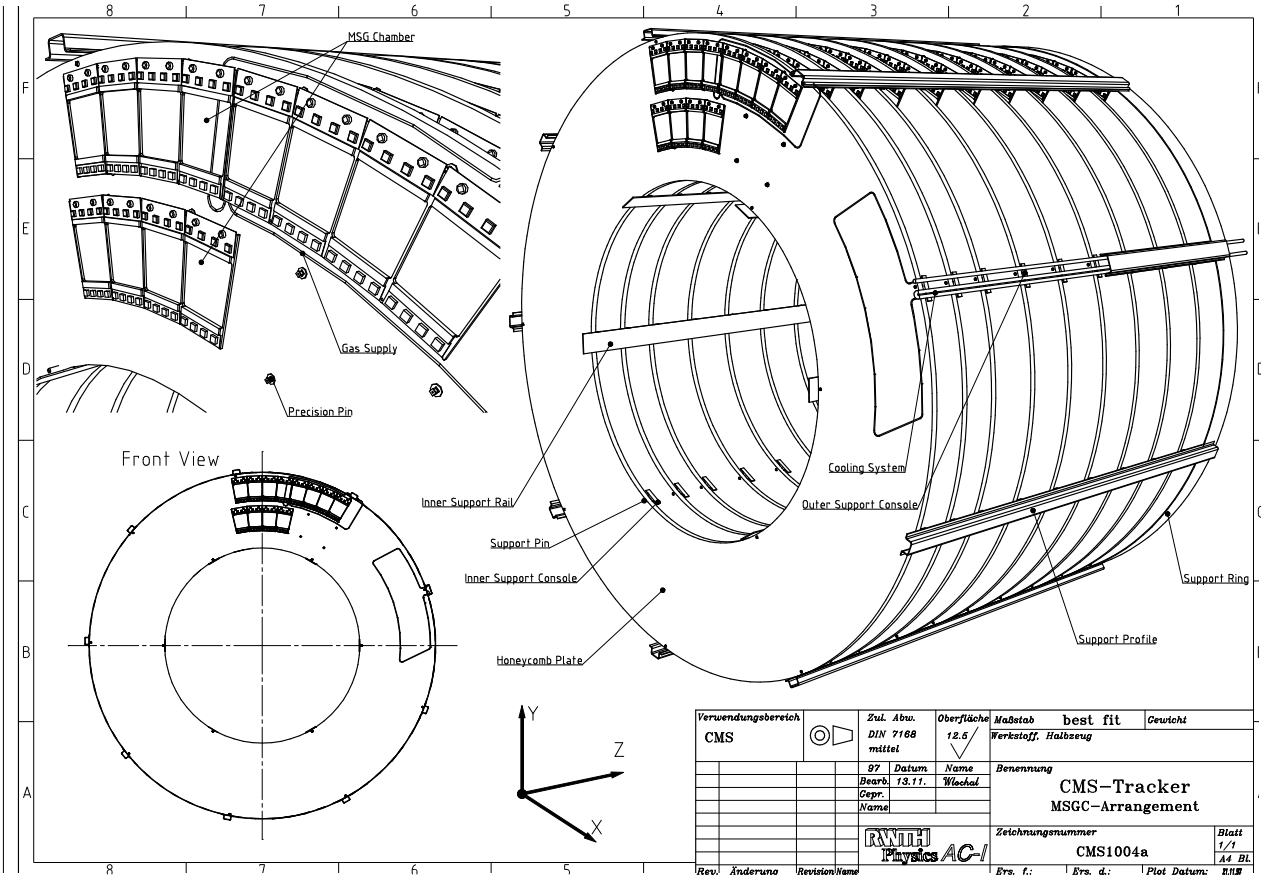

Fig. 4.113: The forward disks assembled into a Super Disk structure

Six rectangular bars (each 80 mm wide and 3 mm thick) run along the inside diameter of the disk, while nine U-shaped ones are attached to the disks around the outer diameter. Both sets of bars are fixed onto the disks by means of aluminium 90° brackets and assembly pins following principles very similar to those employed in equipping the disks with the fixation points for the detectors. As shown in Fig. 4.113, the super-module is terminated by a CF support ring connecting to the end-flange, thus making the whole super-module stiff in the z-direction.

4.8 From the TDR to the Beginning of Construction

The writing of the tracker TDR represents the culmination and, at the same time, the completion of an intensive R&D effort which has lasted for several years. No more significant developments are needed, at least for the baseline choices. Further R&D will continue only for a few back-up solutions like the MGC concept for the stereo measurements (see Section 4.9). The transition phase between the TDR and the beginning of construction will be devoted essentially to the engineering of the mass production techniques and to the preparation of the test lines both in industry and in Institution laboratories. The main goals of this phase will be the fine tuning of the assembly and the test technologies to reach the target costs and throughput. The most important tool to meet these goals will be the construction and test of a pre-series of the final detector modules, both for the barrel and the forward versions. The pre-series modules will be, from the mechanical point of view, identical to the final ones (as described in this TDR). A sizeable fraction of these modules ($\sim 10\%$) will be instrumented with the closest approximation to the final electronics that will be available toward the end of 1998, including the new MSGC version of the APV chip. A new generation of HV and readout hybrids will be developed by the collaboration for this purpose. These kinds of modules will undergo an in-depth beam-test at CERN at the beginning of 1999. The goals of this test will be the re-measurement of the working point, plateau length, signal to noise ratio, hit efficiency and tracking capability with the final mechanics and electronics. A high-rate hadron beam like T10 is the best suited for this kind of measurement. The energy of the particles will be tuned to the lowest CMS reconstruction threshold (2 GeV). Another set of chambers taken from the production pre-series will be tested during 1999 for reliability and resistance at a high duty cycle hadron beam at PSI. For this type of test there is no need for the final electronics and the chambers will be readout with the old generation of hybrids (PREMUX) and/or with picoamperometer, to detect instabilities during operation at very high rate. The completion and exploitation of the pre-series milestone is the last step before construction begins in industry and in the Institutions towards the end of 1999.

4.9 Further Thoughts and Improvements

The R&D activity is substantially completed for all the major baseline technological choices and solutions have been found for all the crucial points. Nevertheless, intensive R&D activity will continue on the small-gap concept (SGC) and on the micro-gap concept (MGC). These are two promising variants of the Micro Strip Gas Chamber technology that could represent valuable alternatives for the 1-D MSGC (the SGC), and for the twin chamber (the MGC). In the Small Gap Chamber the clearance between anodes and cathodes is reduced to ~ 10 μm only, instead of the usual 50 μm (Fig. 4.114). In this way the fraction of exposed insulating surface is reduced to 10% of the total. All the substrate effects (charging, polarisation, etc.) are minimised by construction, and surface coating is no longer needed. This will imply a non-negligible simplification of the detector manufacturing. The use of an advanced passivation technique to protect both the anode and cathode edges is crucial to obtain large gains (see Fig. 4.115). Prototypes of SGCs built on a silicon or on a glass substrate have already been

tested in the laboratory and in low-intensity and high-intensity beams [4-55, 4-8]. Figure 4.116 shows the detected charge, the gas gain and the efficiency plateau measured in a beam test at CERN. Further development of the SGC concept will focus on the production of large area glass

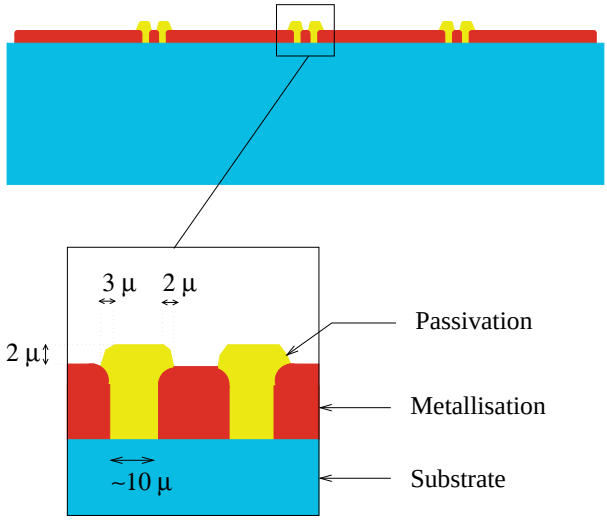

Fig. 4.114: Cross section of the SGC.

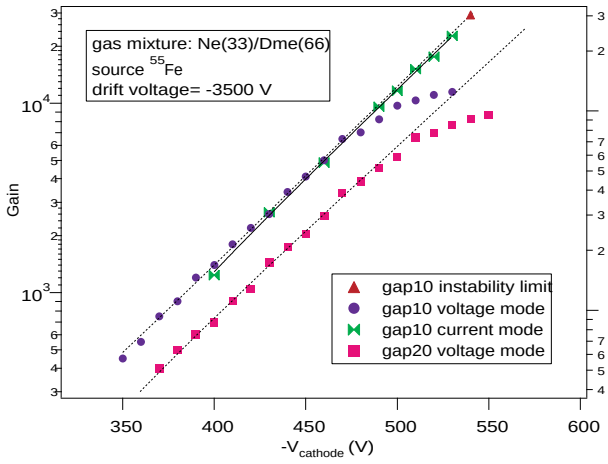

Fig. 4.115: Gain curve of a SGC with two different gas widths.

plates to be tested in a high rate hadron beam at PSI to assess their reliability and safety margins. The MicroGap Chamber (MGC) can be considered as the 3-dimensional evolution [4-56] of the MSGC (see Fig. 4.117). The amplifying electrode structure is no longer in one plane only, but use is also made of the third dimension. The anode and cathodes are now in two different planes with the insulation between them provided by a thin insulating strip. The set of two electrodes can be structured independently, to provide two measurements of the particle position. Viewed from the top, the MGC is a dielectric-free, full metal, device. Charging or other substrate effects are not expected, because there is nothing to charge and the detector is, essentially, *substrate-less*. Several generations of MGC detectors on a silicon or glass substrate have already been built, in small or large areas. The use of glass substrate is mandatory for large plates to avoid large parasitic capacitance toward the substrate. The ratio of cathode signal to anode signal is 0.8 for a glass substrate. The most significant results obtained in the laboratory and in beam-tests are shown in Figs. 4.118, 4.119, 4.120 and 4.121.

Further R&D will focus on the production of large-area glass plates to be tested at PSI for reliability. The main advantage of the MGC concept over the *twin chamber* approach is the non-negligible saving of material, space and money, provided by using one substrate only to get two views of the particle crossing.

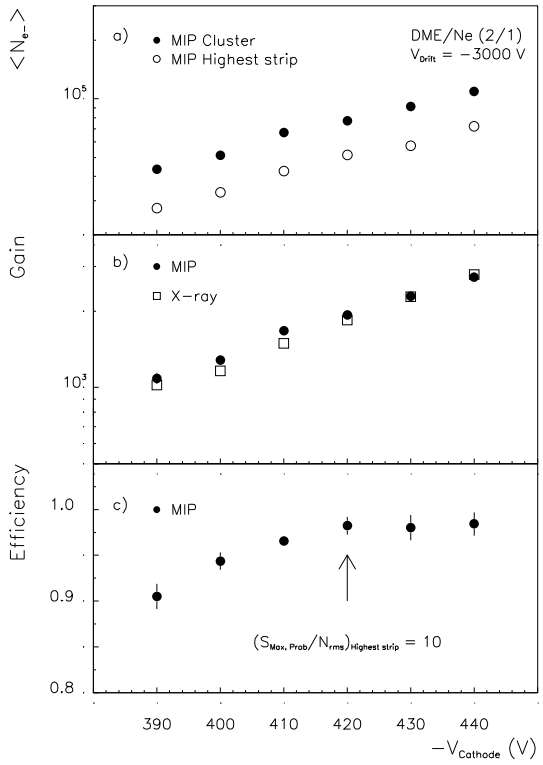

Fig. 4.116: Measured mean number of electrons, gain and efficiency in a SGC as a function of the cathode voltage.

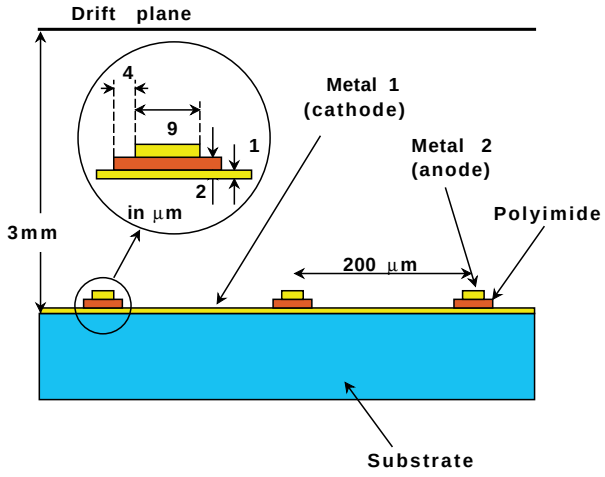

Fig. 4.117: Cross section of the MGC.

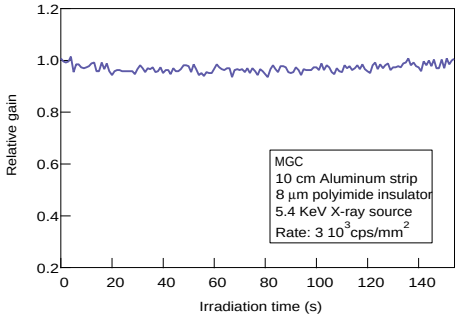

Fig. 4.118: Short-term measurement of gain stability (*charging*) in a MGC.

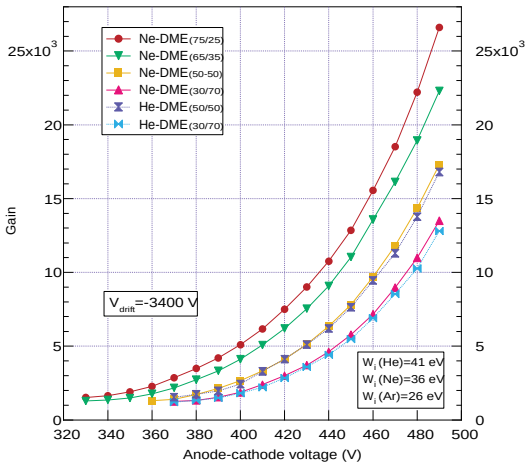

Fig. 4.119: The dependence of the gain with the anode–cathode voltage for different gas mixtures.

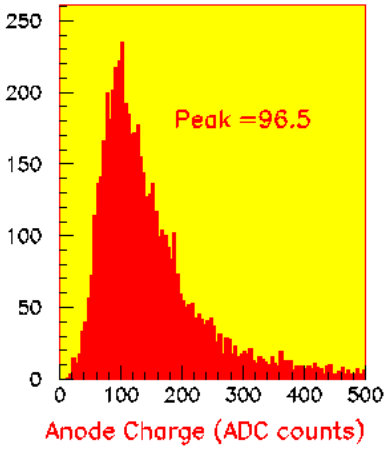

Fig. 4.120: Landau distribution for a MGC.

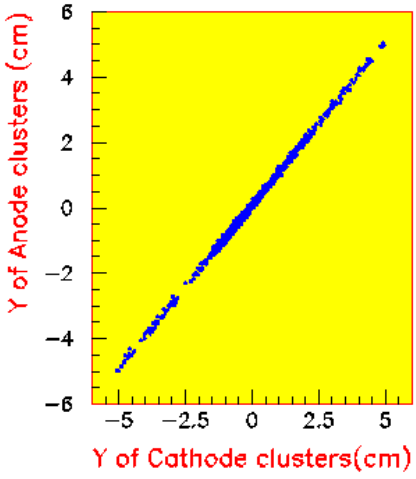

Fig. 4.121: Anode–cathode correlation for a double-sided stereo MGC.

Chapter 5

Microstrip Tracker Electronics

5.1 Overview and Requirements

The microstrip Tracker readout system design has been based on components developed in LHC R&D programmes over the last several years, principally RD20 and RD23. The main goal was to construct a system which would provide analog data from a microstrip Tracker with minimal power, material and sufficiently low noise. These aims are strongly constrained by the requirement to use existing technologies which can be demonstrated to allow production of the system in the relatively short time available until CMS operation is scheduled to start. It is estimated that only three to five years can reasonably be allowed for most of the production of electronics contained within the Tracker volume itself, given the magnitude of the system and the testing and assembly requirements. There are also tight financial constraints which must be observed.

The electronic challenges for the system are principally to ensure a sufficiently low noise level during the full operational lifetime, and adequate bunch-crossing identification, which is ultimately limited by the speed and magnitude of the signal from the detectors as well as by electronics. During irradiation the silicon signal will decrease slightly in magnitude. The MSGC signal is adjustable but low gain operation is preferred to minimise risk as there is little experience of operation of large scale systems.

The target for performance for both silicon and gas microstrips has been to achieve an equivalent noise charge of less than 2000 electrons over the entire detector lifetime, including all contributions, for a power consumption in the front-end chip close to 2 mW/channel. It has been assumed by CMS in simulation studies that the silicon signals would be localised in time to a precision of a single bunch crossing and that MSGC signals would be identified with a precision of two bunch crossings. These requirements have not been translated into a rigid specification, as the detailed performance of several important elements of the system has been unclear and, although considerable progress has been made in defining parameters, some (decreasing) uncertainties are likely to remain even in the future for some considerable time. These include the availability and analog performance of electronic processes suitable for radiation-hard front-end chips, the behaviour of detectors after irradiation, the operating conditions for MSGCs, the noise performance of analog optical links, the linear dynamic range of signals required, etc. While precise performance targets are desirable, the risk factors in constructing such a large system must also be considered and thus, for example, a very high priority has been given to ensuring that the front-end circuits could be constructed in more than one available technology.

5.1.1 Organisation

The high particle fluences, magnetic field and inaccessibility in CMS, along with demanding requirements, raise issues of testing, qualification, operational reliability and long term maintenance, as well as possible impact on performance. The technologies to be employed are in many cases new and even relatively immature, in terms of widespread commercial application, and this is especially true for the Tracker electronics. Additional constraints are due to available manpower and financial resources which must be strictly accounted for. These provide notable challenges to our ability to plan and manage the implementation of the CMS systems as well as to devise working solutions.

While some components have been particularly prominent in the early period of developments, a considerable effort in the last two years has been devoted to developing a complete system, including the control elements which are necessary to operate the complex, remote and distributed system that the Tracker electronics actually comprises. A second high priority has been given to ensuring that the components could allow configuration in a flexible way to match the different topological arrangement of detectors and services in the four major parts of the Tracker, namely Barrel and Forward silicon and MSGC detectors. All the major electronic system elements are now defined, and most prototyped. Necessarily, considerable work remains, particularly on crucial aspects, such as power provision, hybrid design and grounding and shielding, which will be refined during prototyping of modules and intermediate scale systems.

Although the final parameters chosen for the system allow some flexibility, detailed specifications have been developed for components based on present and anticipated future performance of prototypes. A strong emphasis has been placed on defining, reviewing and documenting these specifications for several reasons: interaction with commercial manufacturers, information to system users and maintenance of the system during its operational lifetime. It should also help during the inevitable turnover of personnel which must be anticipated in projects with such long duration as an LHC experiment, and in ensuring that the system is fully self-consistent, as well as compatible with the rest of CMS. The present TDR thus represents a summary of many other documents referred to in the following text.

The activity of the teams contributing to the readout and control system development has been managed through regular system meetings with design reviews of each major component at several stages (initiation of design, midpoint and prior to fabrication). These are foreseen to continue through the lifetime of the project and will now be extended into the next phase of the project when construction starts in earnest.

5.1.2 Motivation for analog data

There are several reasons for preferring an analog to a digital or binary system. One of them is related to achievable position resolution. Charge sharing between detector strips will be frequent as a consequence of non-normal incidence, magnetic field effects and energy loss fluctuations. In the CMS 4 T field the Lorentz effect in silicon detectors will distribute charge over 37 μm on axial p-side strips (and 200 μm on n-side, if they were to be used). Analog readout should improve the MSGC resolution, at least at small angles.

Another argument for analog readout is possible gain in overall performance. The material budget is strongly influenced by front-end electronic functions as the topology of the detector hybrid is determined less by chip design but more by the number of interconnections and cooling requirements. Minimising power consumption has been an important emphasis in the design stages as there is a requirement for cooling all power sources and tolerating power losses in cables. Lower power therefore results in less material in services.

However, the expected robustness of an analog system in the LHC environment is perhaps the major reason for preferring it; past experience has suggested that systems are easier to debug and operate if pulse height information is available. The CMS Tracker system is quite different from those constructed in the past, both in scale and in its distributed nature and very limited access. Excess noise from external sources, such as ground loops or transient pickup, should be expected, as well as common mode effects. It will be difficult to solve such problems, at least in the short term, by direct intervention.

We believe analog data will give greater ability to identify problems and to apply online corrections. Some degradation due to radiation damage both to detector signals and electronics may occur even with hardened technologies, as well as 'minor' damage, such as connector failures. Pulse shapes, amplitudes, occupancies and unexpected effects of radiation damage can be frequently monitored in CMS. Access to external electronics should provide greater reliability than locating it within the Tracker volume and long term maintenance, and possible upgrades, should also be easier. Many of the circuits required, such as 40 MHz FADCs, can be obtained from commercial sources and there is little to be gained by implementing custom, radiation-hard versions, since the cost and performance of commercial components are already evolving favourably without effort on our part.

A digital system may lead to a slightly smaller volume of data to be transferred, but adds potential difficulties such as extra custom radiation-hard front-end electronics and control of thresholds. Data suppression would mean that such a system is entirely asynchronous after the pipeline memory and internal event counters and buffers are required; monitoring its state could become a very complex task. In contrast the CMS system will be entirely synchronous until data arrive at the counting room. The state of the system can be predicted constantly and therefore monitored with relative ease. Naturally this requires reliable clocks and triggers but this is an essential component of all systems; in the CMS Tracker system it should actually be easier to identify behaviour due to this kind of fault.

Finally, the long lifetime of the system and the potential to improve performance over the operational phase should not be completely neglected, even if budgetary considerations are paramount now. The suppression of data on the outside of the Tracker volume, and not internally, leaves open one of the few means by which such a system can be upgraded and take advantage of technology and cost evolution in commercial components.

5.1.3 System summary

Each microstrip is read out by a charge sensitive amplifier with a time constant of 50 ns whose output voltage is sampled at the beam crossing rate of 40 MHz. Samples are stored in an analog pipeline for up to the first level trigger latency of 3.2 μs and, following a trigger, are processed by an analog circuit forming a weighted sum. This confines the silicon signal to a single beam crossing interval and enables measurement of signal amplitude and bunch crossing associated with the hit. For the MSGCs a similar signal processing scheme is being implemented but a final decision on the algorithm awaits evaluation of the filter in tests on chambers. It aims to meet the CMS requirements of high efficiency and timing precision of two bunch crossings.

Pulse-height data are multiplexed from pairs of 128-channel front-end chips by a multiplexer chip on the detector hybrid onto a single differential line which drives signals over a short distance of twisted pair cable to a laser driver mounted in a four-way package. At this point electrical signals are converted to optical and transmitted over a fibre optic cable to the counting room adjacent to the cavern approximately 100 m of cable distant. The optical link employs edge-emitting semiconductor laser transmitters operating at the telecommunications wavelength of 1300 nm mounted in customised low mass packages, which have been developed in collaboration with industry, transmitting through single-mode fibres.

The external data acquisition for the Tracker is based on a VMEbus system housed in the underground counting room adjacent to the experimental cavern after cable paths of approximately 100 m. The pulse height data from each channel of the front-end chips, with no zero suppression, are received by a photodiode-amplifier and converted back to electrical levels matched to the range of a 10 bit ADC. Approximately 2 bits of the range will be utilised to allow for possible level variations within the system which would otherwise need to be compensated for with extra electronics. The remaining 8 bits are easily sufficient for adequate resolution over the range of signals expected. The Front End Driver (FED) is the module which digitises the analog data, performs some signal processing, including re-ordering and pedestal subtraction, and stores the results in a local memory until required by the higher level data acquisition. In high luminosity conditions when the experiment is operating at the maximum trigger rate simple cluster finding will be essential to reduce the data volume to be transmitted. It is envisaged that this will be introduced gradually as experience of the system is gained and will incorporate some programmability, e.g. of cluster thresholds, in an ASIC in the data stream.

A separate VMEbus module, the Front End Controller (FEC), mounted in the counting room is responsible for control and monitoring of the front-end electronics and some other internal features of the system, such as local high voltage. It is also the interface to the global Timing Trigger and Command (TTC) system which distributes the LHC machine master clock and first level triggers to the front-end electronics. Digital optical links, based on laser transmitters identical to those used for the analog data, will send and receive triggers, clocks and control data at 40 MHz speed. Internally, the digital transitions are recovered by photodiodes and amplifiers and distributed electrically by a Communication and Control Unit (CCU) to a series of detector modules. The clock signals are locally recovered by Phase Locked Loop (PLL) chips on each module to ensure high reliability and minimum phase jitter. The relatively small numbers of FECs are located close to the shortest cable route to the cavern, which is one of a series of wide bore, straight tubes, to minimise the contribution to the trigger latency.

A schematic diagram of the proposed system is shown in Fig. 5.1 and a summary of the components and their present status is given in Table 5.1. The numbers of chips refer to the approximate numbers in the final high-luminosity system. Figure 5.2 shows a more practical view of the arrangement of a typical part of the front-end of the system.

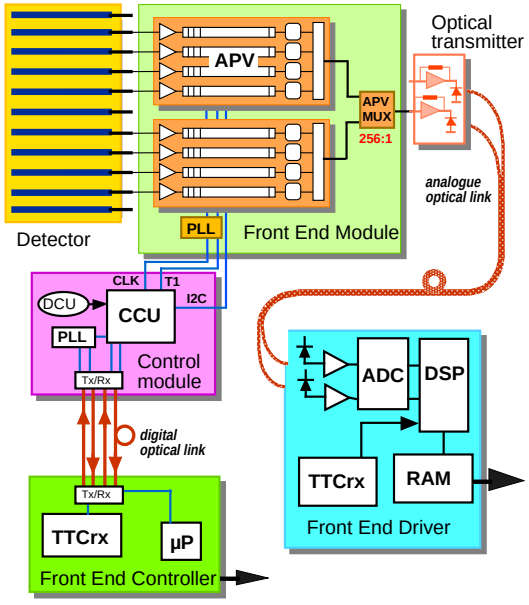

Fig. 5.1: Schematic diagram of Tracker readout and control system.

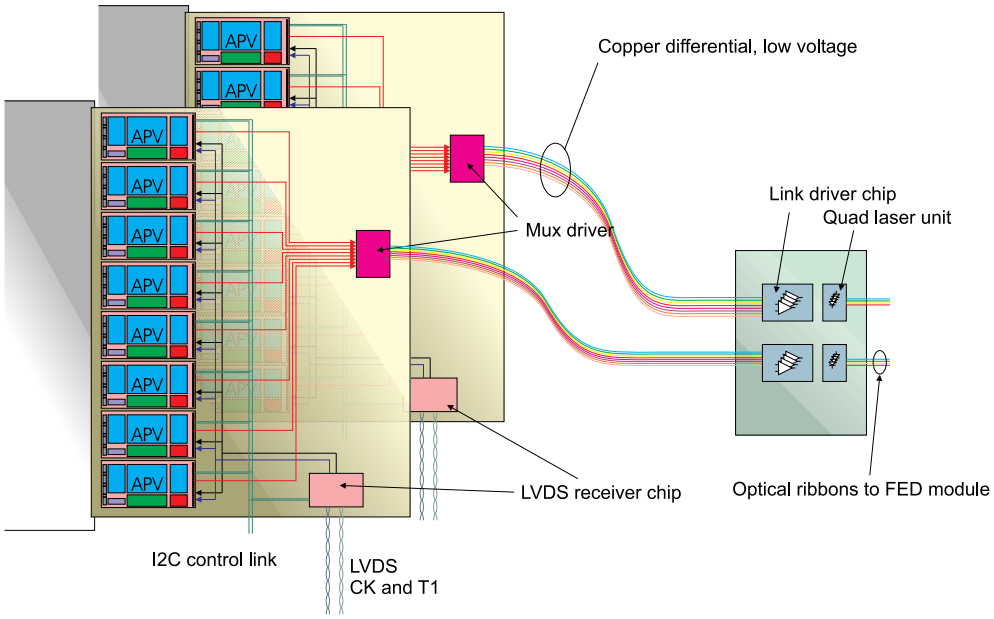

Fig. 5.2: Schematic diagram of a silicon detector module readout.

5.2 Radiation Hardness

The tracking system experiences one of the most severe radiation environments in the whole of CMS with 10-year doses and fluences up to about $\sim$ 100 kGy (10 Mrad) and 2×10^{14} charged hadrons·cm^{-2} at the innermost silicon microstrips and $\sim$ 10 kGy (1 Mrad) and 10^{13} neutrons·cm^{-2} for the outermost MSGCs.

Few of the electronic components required for installation in the Tracker volume can be purchased from formally qualified radiation hardened sources, either for reasons of availability of suppliers or lack of prior knowledge of the radiation tolerance of certain technologies. For this reason a significant burden will fall on the Tracker teams to ensure that the electronics will sustain the radiation levels to be encountered. The Harris AVLSI–RA process has been used for most of the prototyping to date and the two chips developed there are the basis for subsequent translations of designs into a second technology. Although not formally qualified to the Tracker levels, experimental measurements on chips and test structures laid out in each Harris process run have shown excellent results after extremely high levels of irradiation. The only foundry which has indicated a willingness to deliver qualified components at the 10 Mrad, 10^{14} n.cm^{-2} level is Matra–MHS, using the DMILL process developed by CEA (France). While Matra–MHS is expected to be a major supplier of ASICs for the Tracker, their process has only recently become commercially available. We foresee substantial purchases from both manufacturers.

For the complex digital chip which is required for the control system, the CCU, a gate array process has been identified which simplifies considerably the definition and design process. This Honeywell technology has also shown good results after irradiation. The design could be converted to another process with some effort to develop appropriate cell libraries but the gate array approach offers more flexibility during the evolution of the design. Several other small chips required in the system are targeted at DMILL but could be produced, if necessary, in bipolar processes with separate CMOS logic. At present, it does not seem necessary to produce backup designs for all of these. Optoelectronic components, of which the most critical is the laser transmitter, have also shown impressive performance after irradiation. Several sources for the

Table 5.1: Summary of components used with their functions and the technologies to be used

Components	Function	Size (mm^2)	Power per chip (mW)	Number of chips	Technology
APV6/APVD	128 channel silicon front-end amplification and memory	6.4 × 12.0	310	41 k	Harris and DMILL CMOS
APVM/APVMD	128 channel MSGC front-end amplification and memory	6.4 × 12.0	<250	53 k	Harris and DMILL CMOS
APVMUX	2 APV: 1 optical link multiplexer	3.5 × 3.5 (est)	100–200	23 k	Rad-hard BiCMOS
CCU	Distributes clock, trigger, commands and monitoring data	8 × 8 (est)	<400	1400	Rad-hard gate array or ASIC
PLL	Precision clock recovery and delay	2 × 2.5	<50	20 k	Rad-hard BiCMOS
DCU	Optional interface to monitor slowly varying parameters	2.5 × 2.5 (est)	<50	TBD	TBD
Laser Driver 4 channel	Bias and modulate laser Tx current for analog or digital transmission	1.9 × 2.9	200–240 incl. Tx	50–58 k 12–15 k	Rad-hard BiCMOS
Laser Diode Tx	Electrical-optical converter for outgoing analog and digital data	0.3 × 0.2 1.5 × 2 (submount)		50–58 k	III–V semiconductor + silicon submount
Photodiode Rx	Optical-electrical conversion of digital or analog data	0.6 × 0.6 1.5 × 2 (submount)		50–58 k	III–V semiconductor + silicon submount
Analog receiver 1 channel	Transimpedance amplifier for analog signals	NA	Incl in FED	49 k	Commercial bipolar surface mount
Digital receiver 2 channel	Transimpedance amplifier for digital control clock and trigger	2 × 2 (est)	<250	2–5 k	Rad-hard BiCMOS
LVDS Tx/Rx	Conversion of digital electrical levels to standard used in detector (required only if CCU is gate array)	1 × 1 (est)	10	1200–3400	Rad-hard BiCMOS
FEC	Distribution of clock, trigger and control, reception of monitoring data via 16 4-way links	VME9U	< 100 W	20–80	Surface mount board
FED	Reception and processing of 64 optical channels of analog data	VME9U	< 100 W	740	Surface mount board

lasers have been identified with equally good radiation hardness and the results are interpreted as an intrinsic feature of modern semiconductor lasers which employ quantum well technology and small active volumes to achieve low thresholds and high electrical-to-optical efficiency. Several photodiodes, for digital receivers, have also demonstrated adequate hardness for the CMS application, as have fibres and connectors. Thus, assessment of the radiation tolerance of all of the components expected to be used has been a major element of the prototyping to date. Fortunately, with some caveats, the results so far appear to be very promising. Details and references are provided later. A brief summary of the major issues follows.

5.2.1 Technology issues

The major technologies to be utilised by the Tracker are bulk CMOS, silicon on insulator (SOI) CMOS, and bipolar or BiCMOS processes for electronic circuits, and devices based on III–V compound semiconductor materials for optoelectronic components. Each of these has different intrinsic tolerance. In addition, optical fibre, connector and cable materials are subject to degradation under irradiation so samples of these also require testing.

MOS devices rely on conduction in shallow channels very close to the gate oxide interfaces. Thus they are intrinsically very hard against displacement damage and very high neutron levels can be tolerated without degradation; ionising particles are the principal concern. The effects which result are threshold voltage shifts, increased noise and reduced transconductance or gain. Up to now, the measured noise and gain changes have been insignificant in the DMILL and Harris processes and threshold voltage changes are allowed for in the circuit design in the same way as process parameter variations.

Most of the damage to bipolar transistors of interest results from increased recombination in the base region due to bulk and surface (dielectric) damage which can be caused either by neutron or ionising radiation. This reduces the current gain of the transistor which has to be taken into account in the circuit design. Recently, concern has arisen about low dose rate effects in bipolar devices whose magnitude is hard to estimate both because of limited observations and inadequate theoretical understanding. This introduces an additional uncertainty requiring new experimental measurements since long-term irradiation effects are normally simulated by tests carried out at high fluence followed by thermal annealing.

In addition to changes in transistor parameters after irradiation, two other mechanisms for significant damage exist: latch-up and single-event effects. Latch-up is caused by the creation of parasitic bipolar devices via substrate current paths which are enhanced by irradiation. The DMILL process is inherently hard against such damage because of the use of SOI wafers and trench isolation techniques; Harris claim that the epitaxial nature of their AVLSI–RA process also makes it immune to latch-up. Single-event effects result from local ionisation changing the state of circuit nodes. Since this is bound to be strongly dependent on both the circuit design and functions as well as the technology used, only measurement of individual circuits in operation can reveal the likelihood of this phenomenon. The most vulnerable circuits are likely to be dense logic circuits, such as microprocessors, constructed in deep sub-micron processes. However, the circuits and technologies presently envisaged for the CMS Tracker are not expected to exhibit single event upsets at a high rate although this will be hard to verify.

Many III–V semiconductor materials, such as GaAs and other combinations of In, Ga, As, and P, used for optoelectronic devices are expected to be most sensitive to bulk displacement damage which gives rise to defects in the active region of the device. Many compound materials are believed to be rather radiation-hard probably because, relatively speaking, many defects are present in the initial raw material compared to the number created during irradiation. Part of this is due to the fact that the active volumes of optoelectronic devices are deliberately very small, such as in shallow photodiode structures or semiconductor lasers, where the invention of

multi-quantum well structures has permitted the design of low threshold current, high power and efficiency transmitters. This seems to be borne out by radiation studies carried out by the CMS team who have verified that a number of readily available lasers show excellent behaviour after irradiation. Suitable photodiodes for receiving digital signals in the Tracker volume have also been identified.

5.2.2 Testing and qualification

The major task concerns the front-end APV chips as, except for the CCU, other components are less complex and can generally be tested in industry within the cost constraints using well specified procedures defined by the design team. The digital CCU chip should be testable commercially using test vectors defined by the designers. For the mixed signal APV design, where the analog performance is vital, it is not yet clear that commercial testing could be adopted, nor if it is affordable. At present, therefore, we assume that the bulk of this responsibility will fall on a small number of CMS Tracker institutes who are equipped with automatic wafer probing equipment and appropriate expertise, following procedures presently being developed during APV evaluation studies. Production phases for each chip are assumed to extend over approximately three years. There are several reasons for this:

- it is not expected that any foundry will release more than a fraction of its full capacity to produce our wafers, even if it is potentially capable of much more,
- it is not expected that the available cash flow will permit much faster purchasing,
- it is not desirable that chip production should be grossly in advance of testing.

Automatic wafer testing of each chip can begin some months after production has been initiated. This will lead to identified 'known good die' which should be cut from the wafers and assembled onto the hybrids and re-tested prior to module assembly. All of this must be tracked and catalogued. This sets the time at which module assembly can be complete. The testing procedure and its automation, which is essential, has been under development during 1997 using APV6 wafers and although further experience is required, it appears that the time required to test each die on the wafer is around one minute. This defines the number of stations required to carry out the testing; we foresee up to 3–4 centres dedicated to this work. The principal task will be to load wafers, set the system in operation, and scrutinise and catalogue the results; only if problems are identified will the intervention of a senior engineer be required.

Some radiation qualification, even of parts produced in hardened technologies, will be required; the overhead in time and resources is difficult to estimate at present. Until recently all studies had been done using local ^{60}Co sources available within the collaboration. This will not be practical for wafer acceptance where tests should be done under bias. An effort is under way to obtain wafer irradiation facilities using X-ray generators similar to one purchased by CERN to ensure die can be evaluated at regular intervals.

Once known good die have been identified, batches of wafers will be assembled and sent for cutting. Chips will then be distributed to other CMS centres for assembly onto hybrids and then re-tested, automatically. (It is not excluded that hybrid assembly could be carried out in industry but this is still under investigation.) Detector module assembly will be undertaken by other centres within the collaboration.

5.2.3 Purchasing

It is a key element of the CMS strategy to maintain an identical design for both silicon and MSGCs front-end chips in two different processes to ensure that risks due to delays in manufacture,

for any reason, should not have a major impact on the production programme. Since production is bound to extend over several years and the number of manufacturers offering radiation-hard foundry services is very limited, there is considerable risk in relying on only one source, including vulnerability on cost. The time taken to translate the front-end APV design into another well -characterised process and verify it is one to two years so this must be carried out now. In addition, it will be necessary to purchase from both manufacturers, to ensure constant availability and to ensure competitive pricing. The fraction of the purchases from each will depend on price and yield which can only be verified reliably after a significant wafer volume has been acquired. For these reasons, the APV designs have been translated from Harris into DMILL so that two vendors could bid in real competition. For smaller chips, yield is expected to be high, and wafer volumes are much smaller and it is not considered essential to maintain the designs in different technologies as they could be translated into an alternative process within about 4–6 months should problems arise.

5.3 Front-End Electronics

5.3.1 Silicon front-end chip

The front-end chip is based on a design originally developed by the RD20 collaboration [5-1] and denoted as the APV series. It is designed to operate with minimal deadtime up to trigger rates of 100 kHz. Each channel of the APV contains a preamplifier and shaper stage, with a peaking time of 50 ns, followed by a 160 location deep memory into which samples are written at the 40 MHz LHC machine frequency. A data access mechanism allows the marking and queuing of requested locations for output, and embedded logic ensures that the samples awaiting readout are not overwritten with new data. Following a trigger, a series of samples from the memory are processed with a deconvolution filter (APSP), a switched capacitor network, that re-filters the data with a shorter time constant [5-2, 5-3]. The chip can be operated in two modes: *peak* mode, in which the output sample corresponds to the peak amplitude of the amplifier output following a trigger, and *deconvolution* mode, in which the output corresponds to the peak amplitude of the APSP filter. After the APSP the data are held in a further memory buffer prior to switching through an output analog multiplexer which operates at 20 MHz. This additional buffer is required so that as one event is multiplexed out another may be prepared for consecutive transmission.

The APV also contains CMS system features including programmable on-chip analog bias networks, a remotely controllable internal test pulse generation system and a slow control communication interface. Two variants of the silicon APV chip are in late stages of development. A radiation-hardened version, the *APV6* [5-4] Fig. 5.3, has been developed using the Harris 1.2 μm AVLSI–RA bulk CMOS process [5-5]; this has been under test in the laboratory since December 1996. An almost identical chip, *APVD* [5-6], has been fabricated in the Matra–MHS DMILL process [5-7, 5-8] with the same footprint and pad layout, by copying the design with minimal changes; it was delivered in December 1997. CMS plans to purchase chips from both vendors provided the performance and radiation hardness specifications are met. A brief summary of some of the major features of the APV6 and APVD is given below, with a summary of the (minor) differences.

5.3.2 APV6

5.3.2.1 Analog stages

The 128 analog inputs are grouped into four sections of 32. Each section is separated by large power supply pads. These power connections supply the preamplifier stages (where most of the

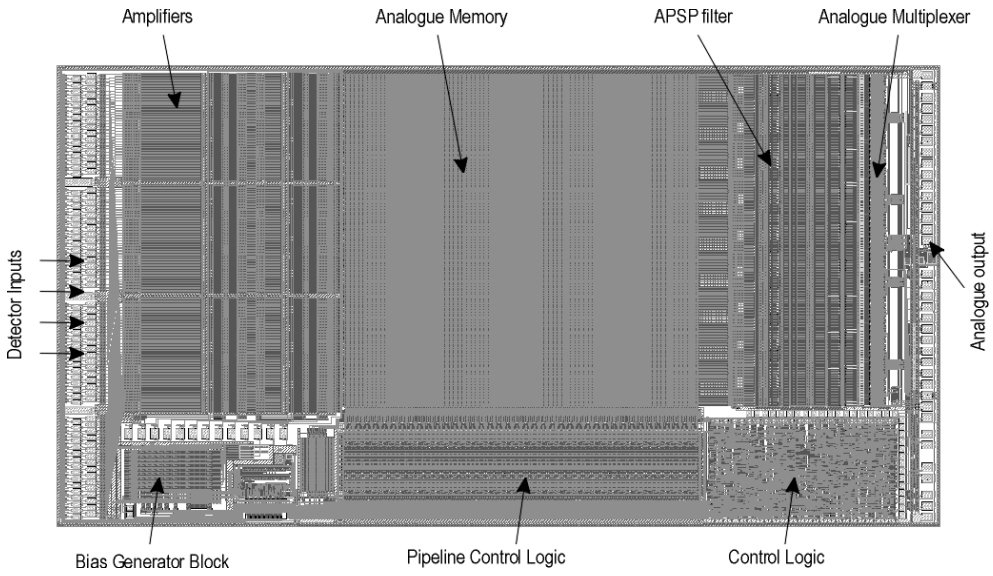

Fig. 5.3: Layout of the APV6 chip whose overall size is 6.4 mm × 12.0 mm.

APV6 power is used) and must be bonded to supply lines close to the chip so that the power losses in the APV6 routing, and thus the area wasted in large power buses, is minimised. Each group of inputs is arranged in two staggered rows, with pads spaced at 86 μm. The analog inputs all have small protection diodes to VSS and VDD which prevent damage during assembly and have proved to be very robust in testing to date. The preamplifier has a PMOS input device of dimensions 3000 μm/1.4 μm and a feedback capacitor of 0.25 pF defining the charge sensitivity. It is a folded cascode design and works with the input device sourced to ground. The power supplies are nominally run at +2 and −2V with the input device running from the negative supply at a design current of 500 μA. This consumes a total of 1 mW and is the dominant contribution to the total APV6 power budget of 2.4 mW/channel. The preamplifier is AC-coupled to the shaper stage which is based on a similar cascode design with an 800/1.4 PMOS input device. The pulse shape at the shaper output closely approximates to an ideal CR–RC form with a peaking time of 50 ns. The gain of the amplifier is approximately 75 mV/MIP.

The pipeline is a 128 by 160 array of capacitor cells. Each cell comprises two transistors, to perform the read or write operation, and a 0.25 pF storage capacitor. The dimensions of each cell are 35 μm × 30 μm so this is the largest single component of the circuit area. The pipeline is read out by the APSP processor which consists of another PMOS input folded cascode amplifier with a switched capacitor network in the feedback loop. The ratios of the capacitors define the weights used by the deconvolution algorithm.

A 128:1 multiplexer drives the analog output from the chip. A nested three-level multiplexer architecture was developed which results in the analog data emerging in a non-consecutive channel order at 20 Ms/s, but allows some power saving since only the final 4:1 stage has to run at full speed. A fifth input to the output stage allows a digital header to be inserted ahead of the analog data stream. Data from two APV chips are interleaved at the APVMUX chip to arrive at the final transmission speed of 40 Ms/s.

5.3.2.2 Control interface

The configuration, bias setting and error states of the APV6 are handled with a two wire serial interface which conforms to the Phillips I^2C standard [5-9] so that it may be controlled by commercial components. The APV address '1111' is reserved for 'global' addressing and when

the '1111' chip address is used in an I^2C transfer all connected APVs will respond; consequently a maximum of 15 APV6 chips may share the same controller and maintain unique addresses. A command register defines which variable or register is to be accessed and specifies the direction of data transfer; up to 13 variables are set or read from the APV6/APVD. These allow the setting of bias currents and voltages in the amplifier and shaper, choice of peak or deconvolution operation, calibration, latency adjustment, and error reporting.

5.3.2.3 Error conditions

The Tracker readout is a fully synchronous system so synchronisation errors must be avoided (which is equally true whether or not internal event counters are provided). It requires genuinely faulty chips to be identified, to avoid corrupting data, and highly reliable trigger and clock transmission, which is discussed elsewhere. There are a small number of ways in which errors could arise and one of the features of the CMS system is that these should be reliably identified. For short periods the APV6 may be triggered at a rate faster than it can output data. When this happens a queue develops whose length is limited by the number of spare locations in the memory and the depth of a FIFO which stores the addresses of columns awaiting readout. As the queue grows, depending on the programmed latency and trigger rate, the FIFO could eventually become full or all the available memory locations become allocated. Either case leads to pipeline failure and must be avoided. This will be done in CMS by a real-time FPGA emulation of the state of the APV chips (which should all be in an identical state) and inhibiting the trigger in case the buffers are full. An estimate of the triggers lost is shown in Fig. 5.4.

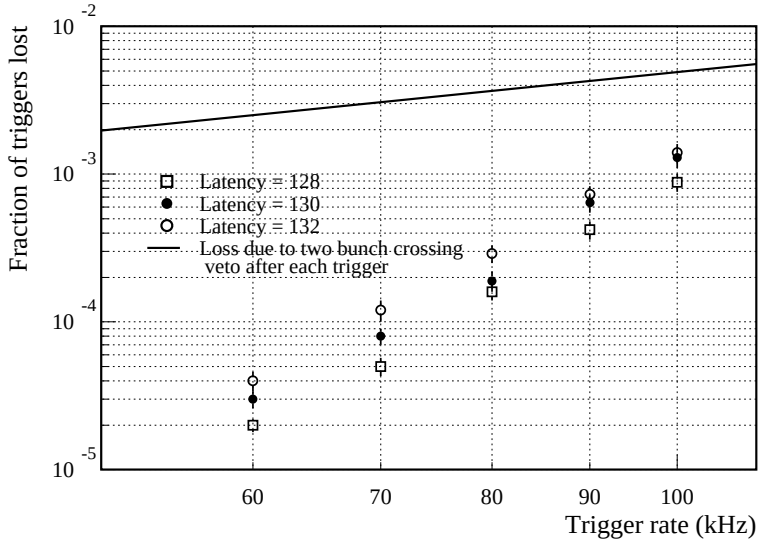

Fig. 5.4: Fractional loss of events caused by vetoing triggers which would cause a buffer overflow in the APV6 pipeline logic.

This adds a small deadtime which is insignificant [5-10] compared to the inhibition of triggers in the two time slots following each trigger (0.5% at 100 kHz), which is imposed to avoid the complex logic to re-use data from the same pipeline location. A second error which could arise, e.g. from radiation-induced soft logic faults, is loss of synchronisation so the latency is continuously monitored by a check on the separation between the write and trigger pointers. It is checked every time the memory is overwritten (at least once every 160 pipeline clock cycles).

5.3.2.4 Operation

Once set up the APV6 requires only one control line, TRG, to run. This control line is normally held at zero. It is possible to send three commands on it, a TRIGGER (a single '1', i.e. a logical high level), a Test Pulse Request (a double '11') and a RESET101 (two '1's separated by a gap). The RESET101 signal is used to clear the pipeline and initialise the pointers. After power-up and appropriate programming of the various control registers described in the previous section a RESET101 is required after which the TRIGGER or test pulse requests can be sent.

The trigger latency is the time (in the number of pipeline clock cycles) between a detector signal being applied to an APV6 input and the cycle in which the TRIGGER signal must be applied to the chip to output that signal at its peak. This number corresponds to the separation of pointers in the memory that specify the read and write locations.

5.3.2.5 Output data stream

The output from the APV6 is in current form in the range of 0 to +600 μA. The output of the chip is at the logic '0' level with single logic '1's (referred to as ticks) every 35 output clock cycles (1.75 μs) when there is nothing to transfer but, when an event has been triggered, data are output in the form shown in Fig. 5.5. A data frame is made up of three parts, a digital header, a digital address and an analog data series.

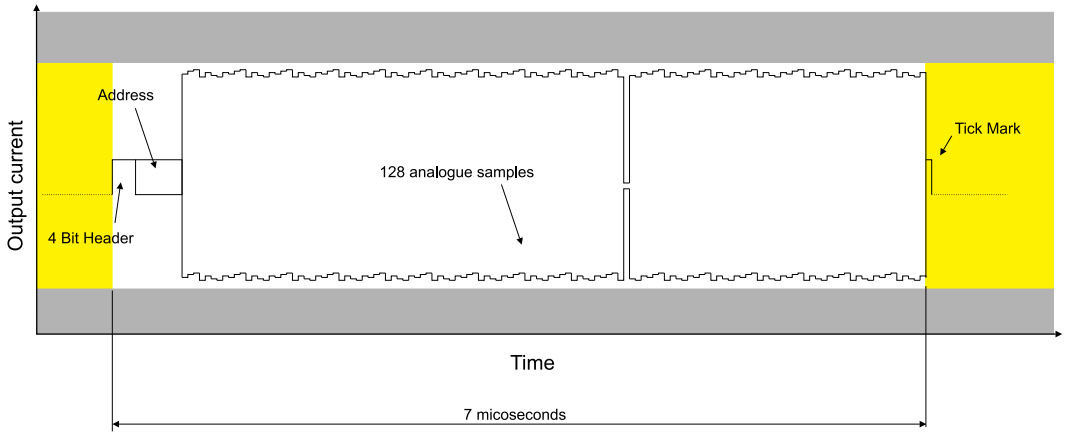

Fig. 5.5: APV6 output data format, showing how the analog baseline is adjusted to handle two signal polarities. In operation of course, only one polarity will be present.

The header comprises four logic samples which should all be high, i.e. 100 μA, compared to the digital baseline. If an error is sensed by the APV6 internal watchdog logic the third sample is switched low so that erroneous data packets in the DAQ can be identified and reported to the control system. Following the header is an 8-bit number which defines the column address used to store the samples in the analog memory, which is used to verify the synchronicity of the system. Finally, 128 samples of analog data follow, where a MIP equivalent signal should be represented by a current of $\sim$ 50 μA. The baseline offset may be adjusted to give optimal dynamic range in the signal polarity in which a chip is working.

5.3.2.6 Calibration

An internal calibration system is provided on the chips, which simplifies acceptance testing and monitoring of operation. The circuit contains two chains of delay elements that are automatically regulated to give a delay of one eighth of a pipeline clock period. When a test pulse request has

been received by the chip a clock pulse is launched down the top delay line. This pulse clocks a toggle flip-flop when it passes the delay chosen with the Delay Set register. The resulting change of state causes analog amplifiers to switch between two states applying a voltage step to the preamplifier inputs in 8 groups of 16. Groups can be masked off by setting bits in the Calibrate Mask Register to allow only one or many to be active at any time.

An important application of this feature is adjusting and monitoring the amplifier pulse shape, which could alter through radiation damage and should be accurately set to ensure optimal performance of the deconvolution processor. Applying a test signal to the APV produces a pulse at the amplifier output of CR–RC form. This cannot be measured directly but an image may be built up by sampling the pulse at a fixed time and progressively shifting the timing of the test pulse and then building the shape from those samples. This is a process which can be easily automated for testing.

5.3.2.7 Analog performance

Figure 5.6 (a) and (b) show the average amplifier pulse shape for a range of externally added capacitance values in peak and deconvolution mode respectively. These pulse shapes are obtained for a single bonded-out channel by fixing the trigger time and varying the charge injection time using an external programmable delay pulse generator. The peak mode pulse shape shows a good approximation to ideal 50 ns CR–RC pulse shaping with little dependence on input capacitance. The deconvolution-mode pulse shape illustrates the effectiveness of this technique in achieving a short pulse shape to allow single LHC bunch crossing time resolution.

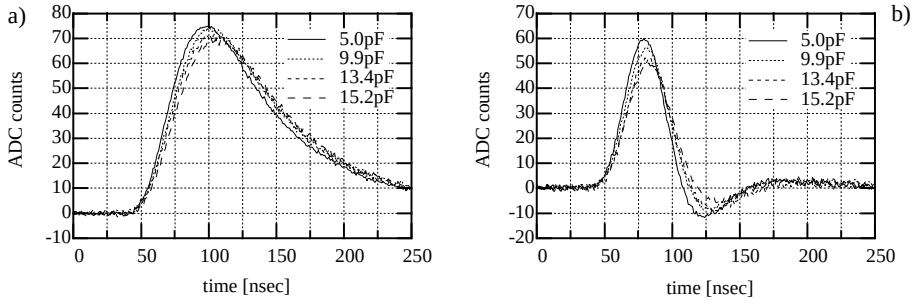

Fig. 5.6: Analog pulse shape in peak and deconvolution mode.

Figure 5.7 (left) shows the linearity of the APV6 in both peak and deconvolution modes for signals in the range ±6 MIPs. There is a difference in polarity between the gains in peak and deconvolution because in peak mode the APSP stores the signal on the capacitor which is flipped to provide the negative weight in deconvolution mode. The gain in peak and deconvolution modes is ≈55 μA/MIP and 45 μA/MIP respectively.

Figure 5.7 (right) shows a histogram of the gain of all channels of an APV6 chip in peak mode. The channel-to-channel spread is adequate but is probably, in any case, dominated by differences in the small on-chip capacitor values used to inject the signal, since this measurement was made using the internal calibration circuitry.

Figure 5.8 (left) shows a typical noise measurement for eight channels of an APV6 in both peak and deconvolution modes. The equivalent noise charge dependence on input capacitance is given by 510e + 36e/pF in peak mode and 1000e + 46e/pF in deconvolution mode.

In peak mode the noise is dominated by noise originating in the input FET. In deconvolution mode there are significant contributions from later stages which give rise to a larger zero capacitance intercept than would otherwise be obtained. APSP noise contributions are enhanced

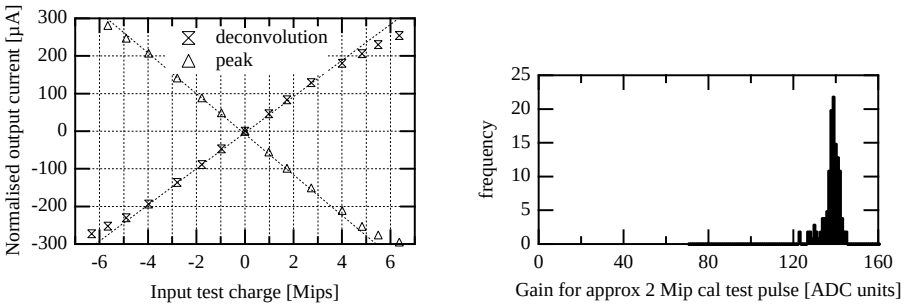

Fig. 5.7: (a) Linearity, (b) Channel-to-channel gain uniformity.

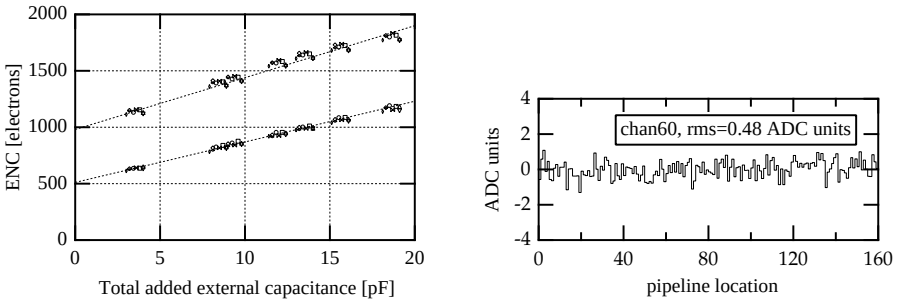

Fig. 5.8: (a) APV6 noise performance, (b) Pipeline pedestals for a typical channel.

in deconvolution mode because the signal is smaller (on the rising edge, not the peak, of the 50 ns pulse shape) and the contribution occurs three times (once for each sample taken from the pipeline). At larger capacitance, corresponding to a realistic detector value, this additional noise becomes less significant. Figure 5.8 (right) shows the pedestal dependence of a single channel on pipeline location (peak mode). The spread of this distribution must be considered as an additional noise source, and this value is histogrammed in Fig. 5.9 (left) for all channels, normalising to the gain to give the noise contribution in r.m.s. electrons. It is clear that this additional noise contribution is small, particularly when added in quadrature to the noise obtained for a realistic detector capacitance. The results and conclusions are similar for deconvolution operation.

Figure 5.9 (right) shows a histogram of the gain of a single channel measured for a signal injected in each of the 160 pipeline locations. The width of the distribution is very small indicating excellent matching between capacitors in the pipeline.

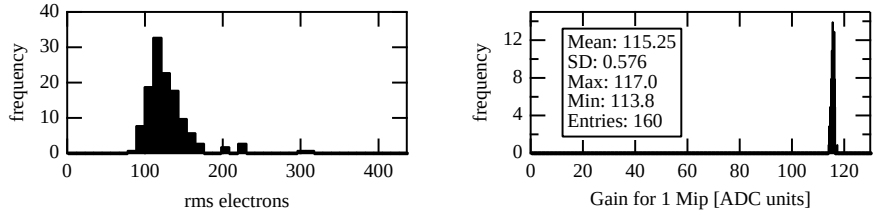

Fig. 5.9: (a) r.m.s. pipeline pedestals for all 128 channels, (b) Pipeline gain uniformity.

5.3.2.8 Radiation tolerance

The Harris process has been extensively studied using transistors and amplifiers inserted in Process Control Monitor (PCM) drop-ins on all of the fabrication runs carried out so far. The results have been published [5-11] and demonstrate that devices from the Harris RTP foundry in North Carolina show hardness to ionising radiation well in excess of the formally qualified level of the process. Irradiations to levels over 100 Mrad were carried out on some runs with minor changes observed in the noise and transconductance properties of the PMOS transistors (Figs. 5.10, 5.11). These are most critical to the APV design since the input transistor of each of the amplifying stages was chosen to be a PMOS device, mainly because of the higher level of $1/f$ noise expected, and observed, in NMOS transistors and the expected greater sensitivity of NMOS transistors to radiation, also borne out in measurements.

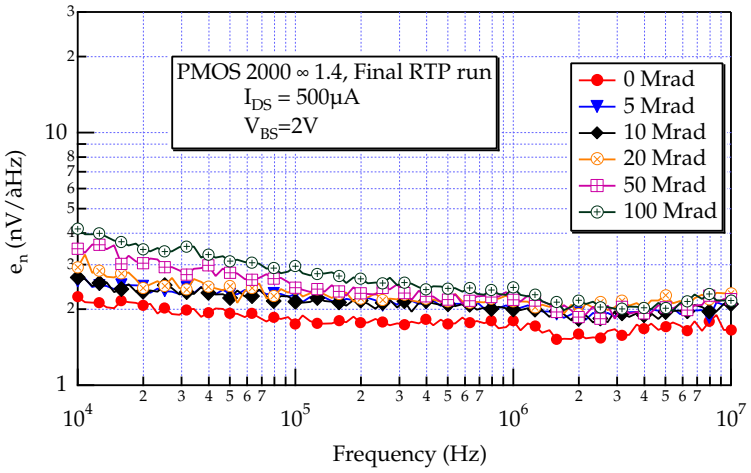

Fig. 5.10: Noise spectral density of PMOS transistors of similar dimensions and bias conditions to the APV6 input device.

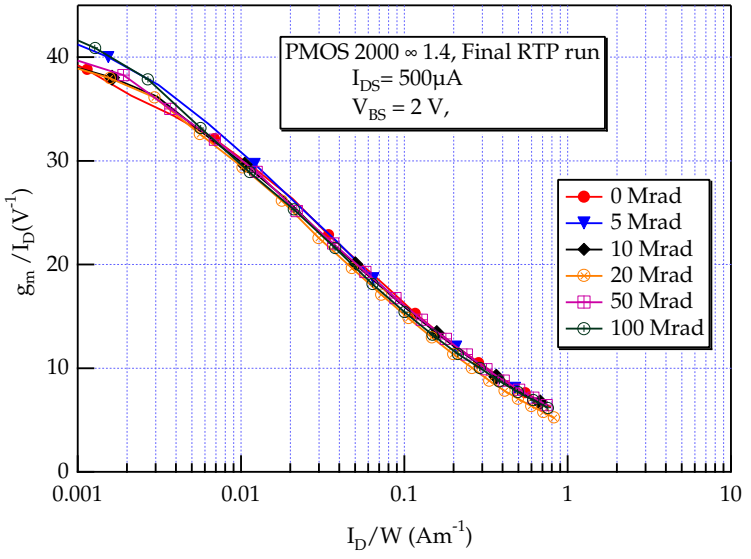

Fig. 5.11: Scaled transconductance of PMOS transistor of similar dimensions to APV6 input device.

In 1995 Harris sold their interest in the RTP foundry to the co-owners, Motorola, for straightforward commercial reasons, having previously announced their intention of transferring the AVLSI processes to their plant in Melbourne, Florida where the major part of their ASIC fabrication is carried out. The transfer of the family of processes, of which the AVLSI–RA represents a radiation-hardened variant with analog features, in particular the precision capacitors, was carried out over about one year and was at an advanced stage, although without formal re-qualification complete, in Spring 1996 when the APV6 was submitted. A series of wafers containing APV6 chips was delivered in December 1996 and shown very quickly to function almost perfectly. However, one minor fault was quickly identified which was due to an error in the metallisation design; it led to full functionality in deconvolution mode but an inability to switch operation to peak mode using the serial control interface. This could be corrected temporarily with a couple of additional bonds onto the chip and permanently with a change in a single mask and modification to the final metallisation of remaining wafers from the run. This was carried out while measurements of PCM test structures were carried out, whose results seemed to be generally in good agreement with those from the final submission to the RTP foundry (Fig. 5.12).

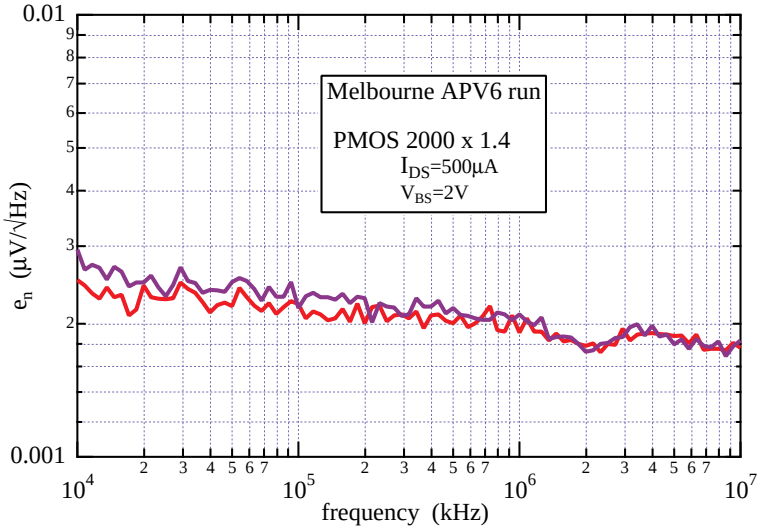

Fig. 5.12: Pre-irradiation noise spectral density of PMOS transistors from the first Melbourne APV6 run.

However, radiation studies of the APV6 began in June 1997 and showed an apparent degradation in performance which was entirely unexpected [5-12]. Individual transistors were then irradiated and showed a degradation in noise and transconductance larger than RTP devices; meanwhile a second APV6 irradiation from another wafer confirmed the results from the first one. Discussions then took place with Harris to identify possible origins of these effects and more detailed irradiations at lower doses began in order to compare the manufacturer's data with our results. While these were under way a number of new facts came to light: some discrepancies between Harris data and our own measurements were explained by a fault in a Harris tester which was identified only when the tester was replaced for service, the PMOS thresholds had been adjusted subsequent to the APV6 processing run and the process had not, at that time, completed its requalification.

The combination of these two circumstances meant the PMOS transistor parameters were actually some way from the specified values and Harris offered to reprocess the wafers in the current process, which they expect to recover much of the previous performance exhibited by

devices from the RTP foundry. APV6 wafers from this manufacturing run were delivered in January 1998 and are currently being prepared for irradiation tests. Full results are not expected for several months as several series of measurements, both before and after irradiation and proceeding in modest dose steps, must be carried out, which is a time-consuming procedure.

5.3.3 Modifications for APVD

A 128-channel CMOS mixed analog–digital circuit (APVD) for the silicon Tracker in CMS has been designed in the radiation-hard technology DMILL and processed in a Multi Project run in TEMIC Matra–MHS [5-6]. It was delivered in December 1997. The circuit is fully compatible with the APV6, whose design was taken as a starting point, and the chip has an identical area and pad layout. The internal features are intended to be as close as possible to the Harris design with modifications motivated either by differences in technology or pre-existing but compatible circuits. The major elements are summarised below.

5.3.3.1 Amplifier

Most of the design of this delicate part was directly taken from a test chip made in a previous DMILL/LETI run to rely not only on simulation but also on experimental results. The preamplifier is exactly the same and the shaper has been slightly modified. The source follower was redesigned and a read bus reset structure was added.

The charge-sensitive preamplifier is made up of a folded cascode amplifier with a 350 fF feedback capacitor and a long channel NMOS feedback transistor. The gain of the charge preamplifier is 11 mV/MIP (1 MIP = 24 000 electrons = 3.8 fC). The input transistor is PMOS with grounded source and size 1544 μm/1.2 μm; it is biased by a 200 μA current, and has an overall power consumption of 740 μW.

The CR–RC shaper is AC-coupled to the preamplifier by a 1 pF capacitor. It is made up of a folded cascode amplifier with a RC feedback which sets the time constant of the filter. The input transistor is a PMOS device whose size is 459 μm/1.2 μm, biased at 115 μA and the feedback capacitor is 96 fF. The difference with the previous DMILL/LETI shaper is in the feedback resistance: a single long channel NMOS transistor was used in the DMILL/LETI test circuit while in the APVD a series combination of a 300 kΩ diffused resistor and a long channel 2.2 μm/60 μm NMOS transistor was preferred. This reduces the non-linearity of the feedback resistor, which could induce distortion in the pulse shape of the filter. The peaking time of the shaper is 50 ns and the gain is 7.7. The overall gain of the preamplifier/shaper stage is 85 mV/MIP, as post-simulated with SpectreS. The total power consumption for the shaper is 415 μW. The buffer is a simple unity–gain source follower, biased at 100 μA between ground and the negative supply, thus giving a power consumption of 200 μW. The equivalent noise charge of the preamplifier/shaper/buffer block was measured in the DMILL/LETI test run. The ENC at 0 pF is 450 e and the slope is 49 e/pF. Simulation of the modified preamplifier/shaper/buffer chain indicates that no change in these numbers are expected in the APVD, provided the technological noise parameters do not change in the DMILL/TEMIC process.

5.3.3.2 Logic and control

All the logical parts were redesigned on the basis of the schematics of the APV6. Whenever possible, the metal routing of the APV6 was kept, while the cells were internally redesigned. The I^2C controller and APSP sequencer was partially compacted in order to save space close to the backend pads, which are somewhat larger than in the APV6 due to the presence of ESD protection. Some more area saving is still possible.

5.3.3.3 Final assembly

Because of the need of full compatibility, it was decided to keep the overall dimensions of the APVD equal to that of the APV6. Since the density of DMILL technology allows some area saving on the circuit, the size requirements did not put any tight constraint on the design, so that some silicon was used to implement the relatively large ESD protections on each pad. Some area is still available for future changes which could be required to improve the performances of the circuit or to implement new functions.

5.3.3.4 Results

The APVD chips were delivered in December 1997 and testing has been under way since then. A small number of problems have been identified but the goal of translating the APV6 into a new technology was successfully achieved since the chip is fully functional and all features can be tested. Figure 5.13 shows the pulse shape measured before and after deconvolution.

The principal features which are not quite as expected are some resistor values which are higher than design values and a fluctuation in the baseline of the readout level. The high resistor values limit the range over which some of the bias parameters can be set and appear to be due to a change at the foundry in the specified parameters for the process. However, the range of settings is sufficient to exercise all the functions over a large part of the range of values required. The origin of the baseline fluctuations has not yet been identified but may represent an oscillation in one of the analog stages near to the input. An MPC re-submission is planned once the faults have been identified and corrected, prior to a full engineering run, so that studies with detectors and large-scale testing can commence.

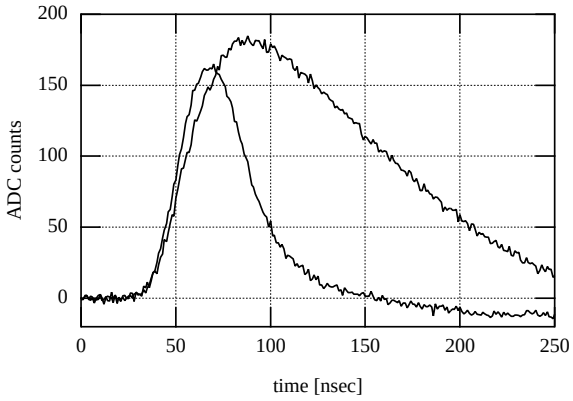

Fig. 5.13: APVD pulse shape before and after deconvolution.

5.3.3.5 Radiation damage studies of DMILL

There have been many measurements verifying the hardness of the DMILL process during its development [5-13] and there is little reason to doubt that the transistors will operate with good performance up to the levels required for the CMS Tracker. However, since noise is an important parameter, it will be necessary to monitor the analog behaviour of DMILL devices, particularly those with dimensions comparable with the input device used in the APVD. Some measurements carried out on test structures designed to be directly comparable with the Harris devices described earlier are shown in Fig. 5.14 and Fig. 5.15 [5-14]; these come from one of the process runs in LETI, before the process was transferred to the commercial foundry. They show

that the differences between the Harris and DMILL processes are small, both before and after irradiation, and it is expected that the APVD and APV6 performance will be very similar.

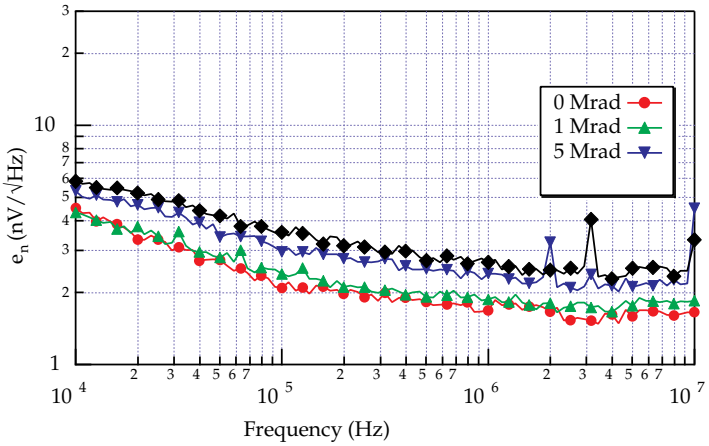

Fig. 5.14: Noise spectral density of DMILL PMOS transistor of similar dimensions to the APV6 input device operated under the same bias conditions.

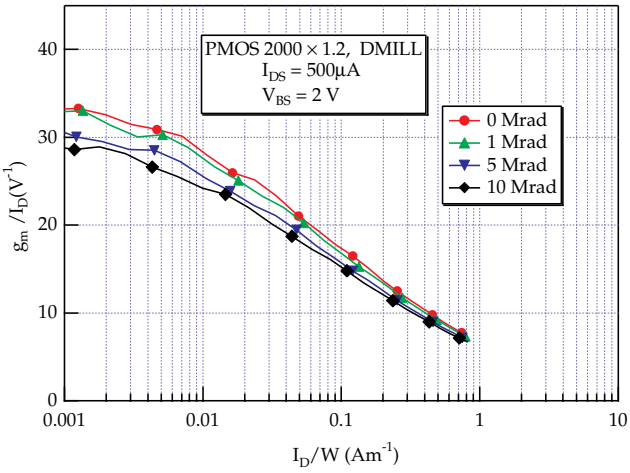

Fig. 5.15: Scaled transconductance of a DMILL PMOS transistor of similar dimensions to APV6 input device.

5.3.4 MSGC front-end chip

Because of similarities in signal sizes and detector capacitance between gas and silicon microstrips, the APV design is also suitable for MSGC readout. However, the time development of signals in the silicon and gaseous microstrips is different. Silicon detector signals approximate to delta impulses, with Landau fluctuations in amplitude, while the charge collection time is around 50 ns in the MSGCs, with large fluctuations in amplitude and in the time structure of the current pulses. Thus the APV6 deconvolution filter will not be optimal for MSGC signals. This has been examined in beam tests using prototypes of the APV (PreMUX and PreShape chips [5-15]) and modelled with MSGC current pulses from minimum-ionising particles processed through simulated electronics [5-16]. Changes to the system have been proposed.

It is inevitable that there must be a compromise between maximising the measured amplitude or efficiency in a given bunch crossing interval unless the detectors are operated with an undesirably high gas gain. The preferred region of MSGC operation is with a gas gain of < 2000. Because of the available bandwidth, only data from a single bunch crossing can be read out, but these data correspond to signals measured in multiple crossings if a weighted summation is formed. The ideal performance goal is to achieve an ambiguity of only two bunch crossings. It appears that a set of three weights can be chosen for the MSGC chip which will meet the CMS efficiency requirements [5-17]. This simplifies the system development considerably since the MSGC chips will always be synchronised with the silicon chips. Any other choice will not provide this desirable feature because of the different sequences of occupied cells in the pipeline and will require careful monitoring of the state of both silicon and MSGC chip logic. However, evaluations of the different algorithms have relied mainly on simulations and should be verified using experimental data before the MSGC version of the APV is finally committed for production. Accordingly the first prototype allows a mode of operation not incorporated in the silicon chip, which permits a sequence of up to 18 consecutive samples to be read out, so that further detailed studies can be carried out in an unbiased way, including variations in shaping in the amplifier.

A number of other features are also incorporated in the MSGC APV: improved input protection, current sensing and, possibly, baseline restoration as explained below.

Input protection diodes in the PreMUX128 chip, which is the non-radiation-hard amplifier–multiplexer chip based on the APV designed for MSGC and silicon prototyping, have proved to be extremely robust. Those in the APV6 are considerably smaller, therefore they have been enlarged in the MSGC APV.

MSGC anodes are DC-coupled to the amplifier inputs, which means that the chip must be capable of sourcing the required leakage current. This is not normally a problem, as tests with the PreMUX chips have shown, as the currents will normally be very small ($\sim$ 1–10 nA). A simple input circuit modification has been implemented which permits larger currents to be absorbed by the amplifier and this also provides a means of monitoring higher leakage currents, which could be an indication of incipient discharge, for example as a result of contamination in the chamber. The leakage current is effectively averaged over ~ 50 μs in groups of 32 channels and an overcurrent state, relative to a threshold stored in an on-chip register, is latched into an error register which can later be interrogated to identify a group which shows a high current. Meanwhile the latches are ORed to provide a single output per hybrid which is connected to an alarm input of the CCU chip. This will instigate a rapid reduction of the cathode voltages of the MSGC controlled by that node of the CCU as well as transmit the alarm condition to the FEC. The FEC will then identify the defective strip group, via interrogation using the I^2C link, and restore the voltage on the groups which are not affected. Another change, which is under study, is the possibility of baseline restoration following the very large MSGC pulses generated by heavily ionising particles (HIPs) which drive the amplifier into saturation for up to a few microseconds. Since it has been observed that this effect couples to all the channels in the chamber, it enhances the system deadtime by a factor ~ 512, so it may be useful to reduce its impact by a sufficiently fast recovery.

The first prototype of the MSGC APV, using the Harris process, has been submitted and is expected back from the foundry in June 1998. The DMILL version will follow as soon as possible.

5.3.5 APVMUX

The matching of laser transmitter units containing up to four channels to different detector module designs, which may contain differing numbers of APVs, is necessary to utilise fully the

optical channels. The laser drivers are mounted a short distance from the front-end APV chips and low-mass 100 Ω impedance twisted-pair cables are used to transfer the APV output signal streams in differential form.

Further savings in link costs are achieved by multiplexing data from two adjacent APVs onto each optical channel, forming a multiplexing ratio of 256 detector channels to each fibre. This is possible with little impact on the deadtime [5-10] since at the maximum 100 kHz trigger rate the data transfer time (7 μs per 256 channels) is significantly less than the average interval between triggers. Multiplexing is done by interleaving data from pairs of APVs transmitting at 20 Ms/s into a 40 Ms/s stream. The multiplexing function together with a driver matched to the 100 Ω twisted pair is the responsibility of the APVMUX chip.

Each APVMUX chip contains 8 APV inputs and 4 differential outputs for driving the twisted-pair lines. The input stage is a low-impedance transconductance buffer that converts the APV output current signals into a form that is then amplified within the chip, mixed by a switching stage, and applied to the output driver.

To control the switching the clock and trigger signals used by the APVs are also received on the APVMUX. Synchronicity is guaranteed by sensing the RESET101 control sequence on the T1 line before subsequently switching between APV inputs on each successive 40 MHz clock period. For optimal performance the data stream from each APV is skewed by 25 ns if its local address is an odd number, with even and odd APVs providing the two inputs, so that maximum settling of the analog levels at the APVMUX inputs is achieved.

This chip has been prototyped in the Harris AVLSI–RA process as a test structure. The test chip has four output channels and two gain settings. It is now under test and is likely to be resubmitted in its final form in 1998. The optimal gain and choice of technology for this component are currently under consideration and a switch to bipolar technology is likely for cost and power optimisation reasons.

5.3.6 Front-end hybrid

The detector module front-end hybrid supports the APV chips, the APVMUX and PLL chips, together with power supply decoupling capacitors. The number of APV chips per hybrid will depend on which detector type it services (silicon or MSGC) and its location (barrel or end-cap regions). Miniature twisted-pair interfaces are required for the control system (40 MHz clock, T1 and I^2C control signals) and the optical transmitter hybrids. The hybrids will have power requirements of −2V, 0V and +2V at currents determined by the number of APV chips mounted. The physical layout of the hybrid must enable efficient transfer of heat to the Tracker cooling system, most of the power being dissipated in the APV chips. Figure 5.16 shows the layout of a prototype hybrid designed to take eight APV6 chips. Two gold-plated copper layers are used on each side of a 500 μm alumina substrate (overall dimensions 6 cm × 3.7 cm) with plated-through holes. Only one of the layers is visible in Fig. 5.16, the other layer being a simple bus structure for power lines and signals common to all chips on the hybrid. The prototype has been used to demonstrate the feasibility of mounting and operating the APV6 on a multichip hybrid and could be used to instrument a 1024 strip detector with 50 μm strip pitch. It is clear that the overall dimensions and simplicity of design are adequate to meet the CMS targets, provided suitable low-mass technologies can be employed. The main question which cannot be answered at this stage is the difficulty of operating a large system with remote power supplies without local voltage regulation.

Further hybrid development is required to incorporate the additional support chips needed, and to evaluate technologies more appropriate to the final system, e.g aluminium instead of copper metallisation and low-mass composites instead of conventional ceramic. The final choice of technology will be strongly driven by material budget requirements. One promising process

developed at CERN [5-18] is based on multilayer aluminium (5 μm) and polyimide (15 μm) on an aluminium substrate. The aluminium substrate is necessary for fabrication. It can be etched away after processing and population of the hybrid with components. Then the resulting flexible hybrid is glued to a carbon fibre or pyrolitic graphite substrate with low mass and high thermal conductivity. Up to five metal layers are possible with a minimum pitch of approximately 50 μm between metal lines and vias between layers with a minimum diameter of about 70 μm. Such features would certainly be adequate to meet the CMS requirements and a commercial route to production appears to be available. We hope to begin evaluating such hybrids during 1998.

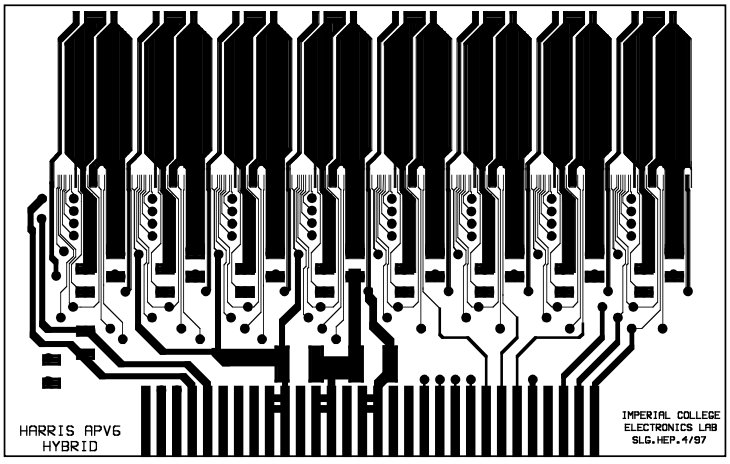

Fig. 5.16: Illustration of prototype front-end hybrid.

5.4 Optical Link

Optical data transmission is essential for the CMS tracking system to transfer data from the Tracker volume with minimal contribution to the material budget. An optical system will also be immune to electrical interference. The bandwidth attainable with fibre optic systems could allow very high speed digital data transmission but would have severe power implications as well as requiring internal analog-to-digital conversion. For this reason, CMS has chosen analog data transmission at 40 Ms/s, which has been shown to be feasible by the RD23 project. The transfer rate is well below the full bandwidth of the fibre link and more than sufficient non-linearity ($< 2\%$) and dynamic range (> 9 bits) for tracking requirements have been demonstrated. The deadtime caused by multiplexing 256 values in 7 μs onto a single fibre is negligible for the APV buffer depths and maximum 100 kHz trigger rate [5-10].

The chosen transmitter is an edge-emitting semiconductor laser on grounds of cost, availability, analog performance and radiation hardness. Several devices have been identified which have the required characteristics with mounted with fibre pigtails in a low mass package developed in collaboration with industry. A minimum threshold current is required before laser action commences since a fraction of photons is lost from the cavity by external emission and internal absorption. However, presently available devices have sufficiently low thresholds and forward voltage drops and high enough electrical-to-optical conversion efficiency that the power consumption is a small fraction of the overall Tracker power budget. Above threshold the light output power is highly linear with current over a wide range.

There is as yet little experience of optical fibre technology in the high-energy physics field and the commercial market is presently evolving rapidly. Single-mode fibre is more commonly used commercially, and is thus less expensive than multimode types, but multimode connectors

require less precision, because of the larger fibre core diameter, and thus are cheaper than monomode connectors. Fibres are not individually as robust as electrical cables and can be damaged, or light transmission altered, by incorrect handling. For many applications they are made up into cables with protective sheaths, often with reinforcements, and suitable cable is currently being specified for CMS. These issues are addressed in more detail below.

The optical link under development for the CMS Tracker is schematically shown in Fig. 5.17. It is a multiway unidirectional system based on edge-emitting laser transmitters (Tx) coupled to single-mode optical fibres, multiway MT connectors and p-i-n-photodiode receivers (Rx). The wavelength of operation is $\lambda \approx 1310$ nm. The driving and receiving electronics is designed according to the system application: analog for the readout, and digital for the control system. Three connector breakpoints (two inside the detector and one on the backplane of the readout or control electronics) allow for easy testing, installation and maintenance of the system. The total length of the link is approximately 100 m, of which about 10 m is within the high-radiation environment.

The philosophy underlying the optical link development effort is to rely, as much as possible, on commercially available products. Laser and p-i-n-photodiode die, fibre and multiway connectors are all off-the-shelf components selected after thorough functionality validation procedures and irradiation tests (see sections 5.4.3, 5.4.4). Custom developments are required for radiation-hard front-end electronics as well as for nonmagnetic, low-mass, multiway optoelectronic packages (see section 5.4.2).

The technological options reviewed and the choices made at the start of the development phase have been described in detail in [5-19, 5-20]. The specifications drafted for the analog and digital links are summarised in Table 5.2 [5-21] and Table 5.3 respectively.

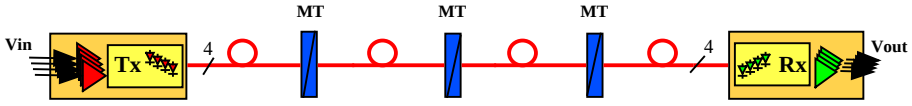

Fig. 5.17: Generic optical link block diagram.

Table 5.2: Principal optical link specifications for analog readout

#	Specification	Min.	Typ.	Max.	Unit	Note
1	Optical wavelength	1290	1310	1330	nm	
2	Length	60	100	120	m	user-specified
3	Gain	1.4	2.85	5.7	V/V	$\Delta V_{\text{out}}/\ \Delta V_{\text{in}}$
4	Signal-to-noise ratio		48		dB	peak signal to rms noise
5	Relative linearity deviation			2.5	%	in any 0.75 V window within output range
6	Bandwidth		70		MHz	
7	Settling time			18	ns	to ±1% of end value
8	Operating input voltage range		±0.4		V	V_{in}, differential
9	Input impedance		100		Ω	
10	Operating output voltage range		±3		V	V_{out}, single ended, terminated with high impedance
11	Output Impedance		50		Ω	
12	Quiescent operating point	user adjustable via I^2C interface				defined at 0 V input
13	Tx hybrid power supply		±2		V	
14	Rx hybrid power supply		±5		V	

Table 5.3: Principal optical link specifications for digital control

#	Specification	Min.	Typ.	Max.	Unit	Note
1	Optical wavelength	1290	1310	1330	nm	
2	Length	60	100	120	m	user-specified
3	Bit error rate		10^{-12}			90% CL
4	Bandwidth		70		MHz	AC-coupled
5	Control data rate		40		Mb/s	
6	Clock rate		40		MHz	
7	Jitter			0.5	ns	peak-to-peak
8	Operating input voltage range		±0.4		V	V_{in}, LVDS standard
9	Input impedance		100		Ω	
10	Operating output voltage range		±0.4		V	V_{out}, LVDS standard
11	Quiescent operating point	user adjustable via I^2C interface				defined at 0 V input
12	Tx hybrid power supply		±2		V	
13	Rx hybrid power supply		±2		V	

5.4.1 System description

The projected layout for the optical readout system is shown in Fig. 5.18 (a). It is a unidirectional link with analog, time-multiplexed information flowing from the front-end (left) to the readout area (right) at a rate of 40 Ms/s. About 50 000 optical links are needed to read out the CMS Tracker, each link serving 256 detector channels. To increase cable and patch panel density, 4-way ribbons are merged to 8 ways at the first patch panel (1) situated at the edge of the Tracker mechanical support structures; 8-way ribbons are then packed into 8-ribbon cables (64-way) at the second patch panel (2) situated in the EM Calorimeter crack. The 64-fibre cable runs out of the detector, across the concrete shielding, towards the counting room. It fans out at the third patch panel (3) situated at the backplane of the Front End Driver (FED) readout board. To accommodate the different Tracker sub-detector modularities and geometries, it is planned to allow for some variants of this baseline architecture.

The projected layout for the optical part of the digital control system (see Section 5.6 for a complete description) is illustrated in Fig. 5.18 (b).

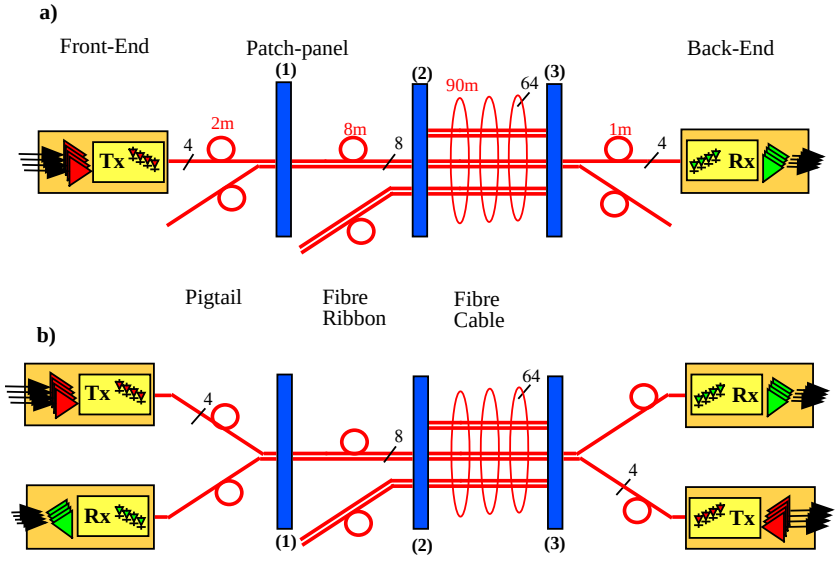

Fig. 5.18: Layout of two optical systems for the CMS Tracker: a) analog readout, b) digital control and timing distribution.

It is a bi-directional link with control data, clock and T1 signals sent from the back- to the front-end on two fibres, as well as status data and clock signals returned from the front- to the back-end, also on two fibres [5-22]. The data transfer rate is 40 Mb/s and the clock frequency is 40 MHz. For reasons of redundancy, the number of lines may be doubled, resulting in a modularity of 4 transmitters or 4 receivers per package, as in the case of the analog readout system.

The similarity between the readout and control system layout is evident from Fig. 5.18. The number of links needed for the control system will be about two orders of magnitude smaller than for the readout, but the technologies and components used will be identical, with the exception of the electronics.

All optics and electronics between the front-end and the second patch-panel (inclusive) are required to be radiation-hard and must therefore be custom designed or at least validated to be resistant to the inner Tracker environmental constraints.

5.4.2 Components

5.4.2.1 Electronics

In order to demonstrate feasibility and to start developing procedures for link characterisation and testing, both analog and digital driving and receiving electronics have been designed, based on commercial off-the-shelf radiation-soft components.

Whereas the analog receiver will always be situated in the counting room and will be based on radiation-soft components, analog laser-drivers, as well as digital drivers and receivers, will have to be integrated into a radiation-hard technology.

As a first step towards realising a set of radiation-hard chips, a 4-channel linear laser-driver has been designed and fabricated in a conventional technology [5-23]. The ASIC is composed of four linear drivers and an I^2C control interface. Each channel in the driver takes as input a differential voltage – originating from one of the Tracker detector hybrids – and converts it into an unipolar current that is used to modulate the laser-diode. Besides signal modulation, each driver in the IC also generates a DC current that serves to bias the laser-diode above threshold in the linear region of its characteristic. To compensate for threshold current variations due to device ageing and radiation-induced performance degradation, each individual laser-diode bias current is programmable through the I^2C interface. Additionally, a 'power-down' function is implemented for each channel allowing reduction in the power consumption of non-used or defective channels.

Each linear driver is designed as a full differential circuit. In this way, the sensitivity to power supply noise is minimised and the amount of power supply noise generated by each driver is reduced, limiting crosstalk. Low distortion analog modulation is achieved by linearisation of the overall driver transconductance using local feedback in each of the amplifying stages.

The laser-driver chip has been fabricated in a standard commercial 0.8 μm BiCMOS process and its dimensions are 1.9 mm $\times$ 2.9 mm. It has been successfully tested both electrically as well as in combination with a laser-diode and an optical receiver. For a power supply of $\pm$2 V, the power consumption per channel lies between 50 mW and 150 mW for minimum and maximum laser-diode bias current respectively. The measured integral non-linearity is less than 0.4% for input voltages within the $\pm$ 400 mV specified operating range. Pulse response tests show that crosstalk between two channels is less than 0.3% for input signals with transition times up to 5 ns. The measured equivalent input noise is 1.8 mV and 4.4 mV for minimum and maximum laser-diode bias current respectively in a bandwidth of about 300 MHz.

A future version of this IC is planned in the DMILL technology to meet the radiation-hardness specifications. The digital laser driver will be a variant of the analog driver ASIC, while the digital receiver is currently being designed.

Optical-to-electrical conversion is required for receiving the clock and trigger into the control ring. A digital receiver chip is required to perform this function (Table 5.4). The optical signal is received by a p-i-n diode connected across the inputs of a preamplifier, see Fig 5.19.

Table 5.4: Specification for digital receiver chip

	Min.	Typ.	Max.	Unit	Comment
DC signal current	0	50	1000	μA	depends on radiation damage level
AC signal current	1	100	500	μA	superimposed on DC current
Analog BW	80			MHz	
Low freq cut off			100	kHz	
Jitter			0.5	ns	peak-to-peak
Supply voltage	+3.6	+4.0	+4.4	V	referenced to −2V

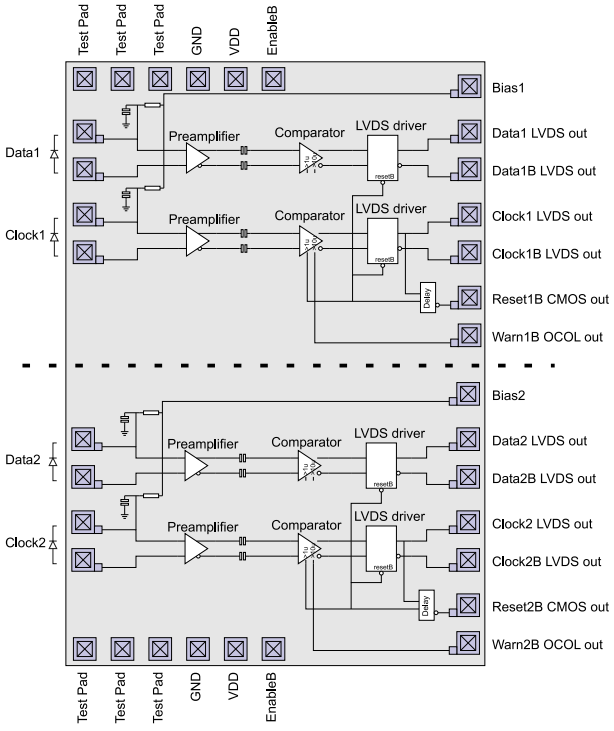

Fig. 5.19: Digital receiver chip functions and schematic layout.

The function of the preamplifier is to accomodate the large dynamic range expected and produce differential signals. The clock and trigger are then AC-coupled to a comparator circuit which recovers logical levels which are then output with an LVDS driver stage.

The control rings are critical to large parts of the system so redundant channels are integrated on the chip as a backup should one channel fail. Each redundant channel is isolated and powered from separate supply connections to the module. Additional features of the circuit include reset outputs automatically enabled in the absence of signal and warning outputs enabled when the signal strength drops below a reasonable threshold. The sensing p-i-n diodes are biased by independent filters on the chip to improve robustness and minimise crosstalk effects. The chip is likely to be manufactured using the AMS bipolar process, which has been demonstrated to be radiation-hard and suited to the small-scale manufacture required.

5.4.2.2 Optoelectronics

Packaged optoelectronic devices have two interfaces: one electrical (pins) and one optical (fibre), the latter being the most difficult to realise technologically. The successful choice of an optoelectronic component thus not only depends on the die alone, but also on the packaging concept and in particular in the scheme used to couple light in or out of the fibre.

The laser-diode chips are commercially available Multi-Quantum-Well (MQW) InGaAsP edge-emitting devices selected for their good linearity, low threshold current ($\sim$ 9 mA), and proven reliability (lifetime well in excess of 10^6 hours). Photodiodes are epitaxially grown, planar InGaAs devices of small active volume. Several laser- and p-i-n-diode types produced by different manufacturers have been evaluated and found to satisfy the CMS constraints. A particular effort has been made to validate chips which could simultaneously be tested in packaged form.

The transmitter and receiver modules are assembled using silicon-submount technology. This technology, now being adopted by all major telecommunications component manufacturers, is well adapted to the fabrication of single-element devices, hybrid assemblies or arrays. Good optical coupling between die and fibre is achieved with micro-machined V-grooves aligned to die-attach metal pads and registration marks. The resulting assembly is a mechanically rugged, low mass, small footprint (typically 2.5 mm $\times$ 1.9 mm) device, which can be easily handled and tested before final packaging. Figure 5.20 schematically shows the one-way laser- and p-i-n-diode assemblies commercially developed by Italtel (Milano) and evaluated by CMS. Chips from different manufacturers can be hybridised on the silicon submounts, thus significantly decreasing the risk in making use of off-the-shelf die for our application.

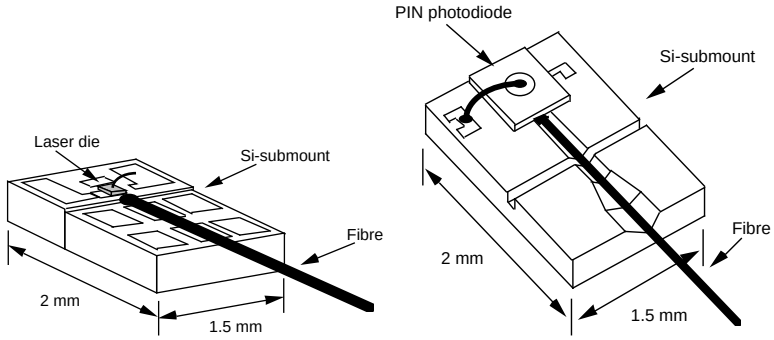

Fig. 5.20: Laser (left) and photodiode (right) assembly showing the Si-submount, semiconductor die, and optical fibre.

The submount assemblies shown in Fig. 5.20 form the basic building blocks of the Tx and Rx modules. Standard one-way mini-DIL packages have been used to validate the technology, but a non-magnetic, low-mass, multi-way package is being custom developed by Italtel for CMS. This 14-p-i-n ceramic DIL package will house up to four (known good) assemblies in a volume of approximately 15 mm $\times$ 10 mm $\times$ 4 mm. Depending on the sub-detector requirements, it will be partly populated, resulting in increased layout flexibility in low granularity regions. On the hybrids, the Tx and Rx modules will be inserted into low-profile sockets, making testing and maintenance activities possible even after installation. A fibre ribbon or bundle, terminated with a multi-way connector will link each package to the first patch panel. Delivery of the first 4-way samples is due in the first quarter of 1998.

5.4.2.3 Optical fibre, cables and connectors

All the passive optical components (fibres and connectors) are commercially available products of the single-mode type.

Fibres with pure silica core, fluorine-doped cladding and UV-cured acrylate coating are intended to be used in the high radiation environment of the detector, while germanium-doped core with pure silica cladding fibre will be used outside. Encouraging irradiation test results, however, indicate that standard germanium-doped telecommunications fibre might be usable throughout the detector, resulting in a homogeneous and cheaper fibre system.

Individual fibres are grouped into multi-fibre ribbons (4- and 8-way) and multi-ribbon cables (typically 8 × 8-way) at patch panels (1) and (2) respectively (Fig. 5.18). The design of a small diameter (8–10 mm), low bending radius (7–10 cm), 64-way cable is currently under way with a leading commercial manufacturer. Each cable will serve one Front-End Driver (FED) board. The choice of the 1310 nm wavelength will permit operation of a Class-1 eye-safe ribbon-based system at power levels compatible with our application.

The three connectorised breakpoints allow for easy testing, installation, and maintenance of the system. Connectors based on single-mode angle-polished MT 4- and 8-way ferrules [5-24] are used throughout, achieving the highest patch panel density currently possible with commercial components. The design of a compact 1536–fibre patch panel to be located in the EM Calorimeter crack (patch panel (2) in Fig. 5.18) is under way under the guidance of two connector manufacturers. It includes a fibre management fixture to allow for easy installation and maintenance of pre-terminated ribbons and cables.

5.4.3 Experimental results

All tests reported in this section have been performed with optoelectronics on Si-submounts housed in one-way mini-DIL packages supplied by Italtel and electronics based on commercial off-the-shelf components. The results are representative of the prototype links which have been evaluated to date, but information on performance spread is still being built up. First evaluations confirm that both analog and digital specifications (Tables 5.2, 5.3) can be met with some safety margin, using the selected components.

5.4.3.1 Analog link

The measured static response of the analog link features a relative deviation from linearity which is in all cases smaller than the specified value of 2% over the operating range. Noise measurements have also confirmed that peak signal to r.m.s. noise ratios of the order of 400:1 (52 dB) can be achieved.

The optical link step-response is shown in Fig. 5.21 (a). The solid line is the normalised link input signal, which is representative of a large pulse delivered by the front-end chip with a rise time of 5 ns and a plateau of 20 ns. The dashed line represents the output signal V_{out}. We measure on the output pulse an overshoot of $\approx 4\%$ of the pulse height and a settling time of $\approx$10 ns to within 1% of the end value. It is worth recalling that signals will be digitised within the 25 ns analog sample period (40 Ms/s transmission rate). The link frequency response characteristic, shown in Fig. 5.21 (b), shows a 3 dB cut-off frequency of 110 MHz, essentially limited by the receiver bandwidth [5-25]. Dots are experimental data and the solid line is a fit with a second-order filter function.

5.4.3.2 Digital link

The digital link performance was assessed by transmitting a pseudo-random NRZ coded bit stream (2^{11}–1) and measuring the Bit Error Rate (BER) as the received optical power was varied with an optical attenuator. Figure 5.22 (a) shows an eye diagram obtained at a bit-rate of 40 Mb/s for a receiver power of $P_{\mathrm{p-i-n}} = -32.2$ dBm.

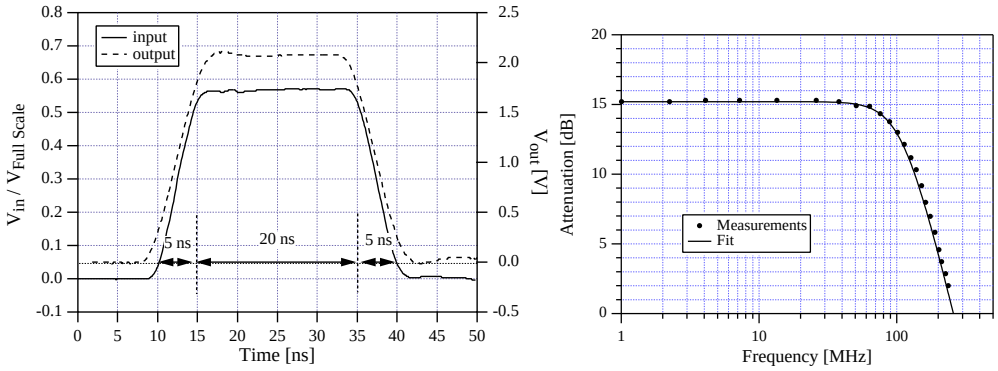

Fig. 5.21: a) Optical link time-response to an input pulse representative of a large front-end chip signal, b) frequency-response.

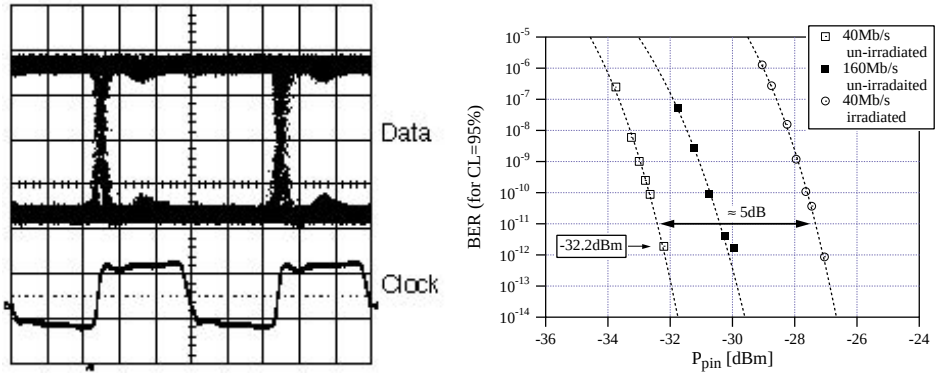

Fig. 5.22: a) Eye diagrams at 40 Mb/s with power at the receiver of -32.2 dBm. The data bits are strobed on the falling edges of the clock (5 ns/div. time-scale), b) BER plot at 40 Mb/s and 160 Mb/s for irradiated and unirradiated p-i-n photodiodes.

The BER corresponding to these conditions is 10^{-12}, as shown in Fig. 5.22 (b). Measurements were performed at 40 Mb/s and 160 Mb/s with a standard p-i-n-diode, and also at 40 Mb/s with an irradiated photodiode having been exposed to a neutron fluence of 6×10^{14} n/cm^2 and a gamma dose of 100 kGy.

A BER of less than 10^{-12} is easily attained with the present digital link configuration. Operating with an irradiated p-i-n diode shifts the received signal level by $\approx$ 5 dB but still preserves an excellent safety margin for operation at the LHC. The 5 dB penalty is well correlated with the $\sim$ 70% loss in the photodiode responsivity observed during the irradiation tests.

5.4.4 Radiation hardness

In view of selecting appropriate components for the CMS Tracker optical links, a great variety of devices, fibres and connectors have been irradiated [5-26, 5-27, 5-28]. In this document, we focus on tests of laser- and p-i-n-diodes assembled on silicon submounts and packaged by Italtel into one-way mini-DIL housings. As explained in Section 5.4.2, the custom developed 4-way modules will be built using the same one-way assemblies as used in the mini-DIL package. This allows us to predict the behaviour of the final components from the results obtained with 1-way packages. Table 5.5 summarises the test conditions for lasers, p-i-n-diodes, fibres and connectors. Neutron tests were conducted at the SARA facility at ISN, Grenoble. Proton irradiation was carried out

using the proton synchrotron (PS) beam at CERN. Pion irradiation took place at PSI, Villigen. The ^{60}Co source at Imperial College London was used for gamma irradiation. All the exposures were carried out at room temperature.

Detailed reports on the irradiation test measurements can be found in Refs. [5-29, 5-30]. A brief summary of the results is given below, confirming that the investigated devices are sufficiently radiation-hard to operate in the CMS Tracker. Obviously, levels of radiation-induced damage are very much dependent on component position inside the detector.

Table 5.5: Irradiation test conditions

Radiation	Devices	Fluence (or dose)	Exposure period (hrs)	Recovery period (hrs)
Neutrons ($\simeq$ 6 MeV)	lasers p-i-n diodes fibres & connectors	up to 10^{15}/cm^2	102	up to 2100
Protons ($\simeq$ 24 GeV)	lasers p-i-n diodes	4×10^{14}/cm^2	10	660
Pions ($\simeq$ 300 MeV)	lasers p-i-n diodes	$3-6 \times 10^{14}$/cm^2	100	600
γ rays from ^{60}Co	lasers p-i-n diodes fibres & connectors	up to 100 kGy	70 to 1200	up to 1000

5.4.4.1 Lasers

Figure 5.23 shows typical behaviour before and after neutron irradiation; a shift in the laser threshold is evident but there is little apparent change in the efficiency (slope). An increase in threshold current corresponds, in operation, to a shift in the DC-bias point and must eventually be compensated for by the driving electronics to avoid falling into the sub-threshold regime of the laser. For a linear device such as the edge-emitters considered here, a varying bias point does not affect the modulated AC signal. In contrast, an efficiency fluctuation will change the link AC-gain, and must therefore be corrected for, in the analog transmission case, by recalibrating the system.

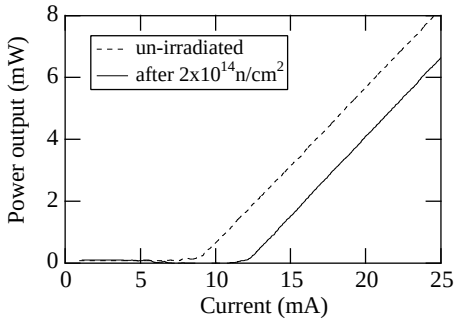

Fig. 5.23: Italtel lasers (TO-can) before and after neutron irradiation.

Neutron damage results are shown in Fig. 5.24 for five devices irradiated at the same time but with different neutron fluxes. Both the threshold increase and the efficiency loss are roughly linear with fluence. Similar effects are seen for proton and pion irradiation, but for a given fluence, protons and pions are 4–6 times more damaging than the $\sim$ 6 MeV neutrons. In contrast, a gamma dose of 100 kGy caused negligible damage. The radiation-induced changes

to threshold current and slope-efficiency annealed with a log(t) dependence, at a rate of about 15% per decade (at 29.5°C). With the combined information of damage and recovery effects, it is possible to predict the threshold current and efficiency change for irradiation over an extended period, such as during the lifetime of the CMS experiment. Preliminary calculations indicate that up to 75% of the damage observed during the accelerated tests might anneal during CMS operation.

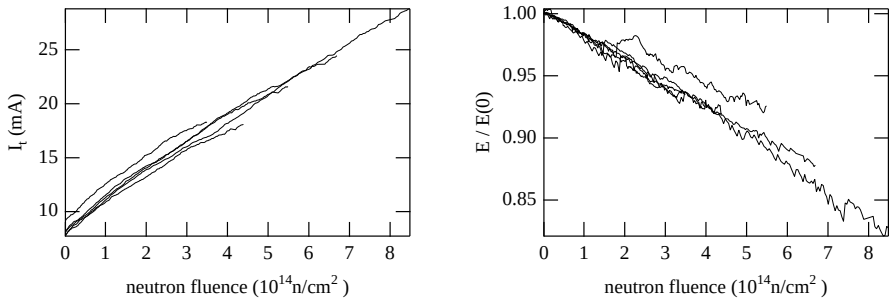

Fig. 5.24: Laser threshold current I_t increases and efficiency E decreases during neutron irradiation.

5.4.4.2 P-i-n photodiodes

P-i-n photodiodes will be used inside the CMS Tracker to detect the digital signals sent by the control and timing distribution system. The effect of neutron and proton irradiation on the p-i-n leakage current and response is illustrated in Fig. 5.25. The leakage currents I_{leak} measured at 2.5, 5, 7.5 and 10 V reverse bias increase non-linearly with fluence by up to 6–7 orders of magnitude above the pre-irradiation values of $\sim$ 10 pA. Approximately 10 times more neutrons are required to cause the same increase in dark current as for protons (and pions). The photocurrent I_{PC}, normalised to the initial pre-irradiation value $I_{\mathrm{PC}}(0)$, is used to estimate the responsivity fluctuations.

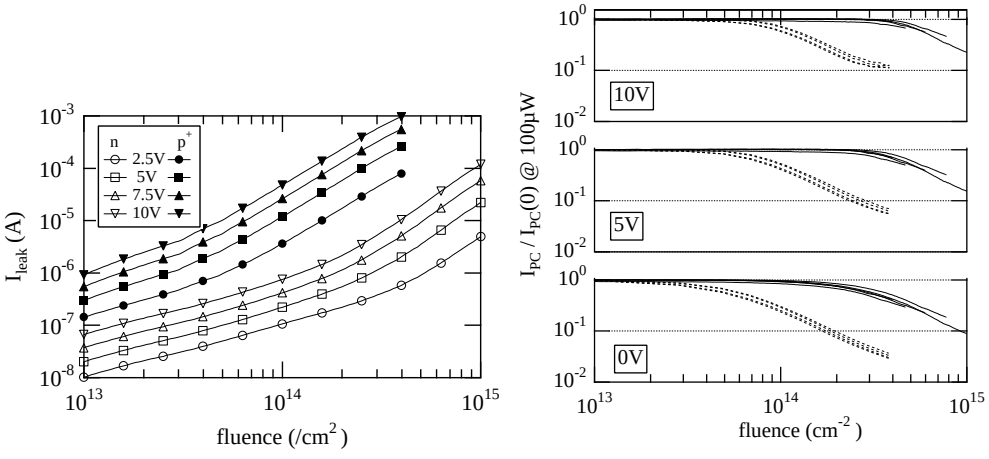

Fig. 5.25: Damage in p-i-n detectors during neutron (n, solid lines) and proton (p, dashed lines) irradiation for bias voltages between 0 V and 10 V. The leakage current increases while the photocurrent I_{PC} for 100 μW optical signal decreases during irradiation.

Up to a certain fluence (around 1–4 $\times$ 10^{14} n/cm^2 or 2–8 $\times$ 10^{13} p/cm^2, depending upon the bias voltage) there is only a small decrease in photocurrent. Above this fluence, there is a rapid decrease of the response. In contrast to the hadron irradiation results, devices that were irradiated with ^{60}Co gammas to 100 kGy showed a much smaller increase in leakage current, of $\sim$ 3 orders of magnitude, and no change in photocurrent.

Annealing of the leakage- and photo-current was also measured after each irradiation test. The neutron-irradiated devices were measured for the longest period (3 months), during which time $\sim$ 20% of the leakage current damage annealed, but no recovery of responsivity was observed. For the gamma-irradiated devices no significant recovery of the leakage current was observed in 80 hours following irradiation. Recovery measurements on the proton and pion-irradiated p-i-n diodes were consistent with the neutron damage results.

In order to assess the impact of the photodiode degradation on the digital system functionality, bit error rate tests were carried out with a heavily damaged photodiode (Section 5.4.3). They confirmed that the digital links could still be operated with considerable safety margin in the Tracker end-of-life conditions. However, in an attempt to understand better the reasons for the sudden responsivity loss of the p-i-n-diodes tested, the behaviour under irradiation of different devices from various sources has been investigated in detail. Preliminary results indicate that some components perform, under similar conditions, significantly better than the photodiodes reviewed here. Discussions with manufacturers are in progress to identify the key technological parameters needed to select the best diode structures.

5.4.4.3 Fibres and connectors

Ionisation is the dominant damage source in optical fibres subject to irradiation [5-28]. The induced loss measured in pure-silica core fibres is $\sim$0.08 dB/m after 80 kGy, compared to $\sim$0.12 dB/m or less in standard telecommunications germanium-doped core fibre. This low level of damage indicates that both fibre types might be suitable for use in the CMS Tracker where only 10 m of fibre will be exposed to high radiation levels.

Extensive connector insertion-loss measurements and repetitive mate-demate tests have been performed on MT8-S ferrules exposed to gamma and neutron radiation levels expected in LHC experiments. No significant degradation of the optical and mechanical performance of connectors could be detected, even after 100 mating cycles [5-30].

5.5 Front-End Driver

The Front End Driver module [5-31] (Fig. 5.26) receives 64 analog signals, each of which is digitised by a fast ADC and digitally processed and packed with event header information before transmission to the next level of the CMS Data Acquisition system, whose description is outside the scope of this document. The FED has been through the first prototyping phase to demonstrate that the density and basic functional requirements could be met [5-32], and gain confidence that the cost target is achievable. The principal functions for the FED are now clear but, providing the prototyping needs of the tracking system can be met, the evolution of the module can continue for longer than most other parts of the system because it is in the external counting room and does not limit the design of internal elements. The major features of the module are summarised in what follows.

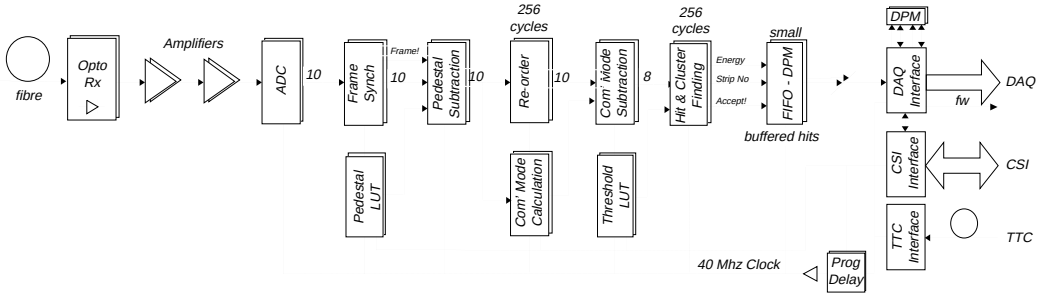

Fig. 5.26: Front-end driver block diagram.

5.5.1 Introduction

5.5.1.1 Optical input stage

Each FED receives analog data from the interior of the Tracker on 64 optical fibres which are grouped as 8-way ribbons, with each fibre carrying data from a pair of APVs. The optical signal is amplitude modulated and requires conversion to electrical levels before it can be digitised and processed by the FED. This is achieved by a p-i-n diode and two stages of amplification located on the main FED motherboard. The opto-receiver packages will be mounted in sockets in the mother board close to the amplifier ADC circuitry with the fibre ribbon pigtails routed through combs on the board to a backplane connector.

An alternative layout which is being investigated is to locate the optical to electrical conversion circuits on a transition module in the rear of the FED crate, which has advantages of modularity but possible drawbacks for interconnections.

5.5.1.2 ADC and Digital Signal Processing

The baseline ADC proposed for use in the FED is a 40 MHz, 10 bit commercial component, already used in prototypes [5-33]. The 64 ADC channels make the largest contribution to the overall cost of the FED. Dual ADC devices are now becoming available, with the potential for further cost savings.

The data from each ADC is processed by its own independent digital parallel-pipelined processing logic running at 40 MHz. Unless there are substantial advances in FPGA or DSP technology in the next few years, the intention is to implement this as an ASIC to meet cost and performance targets: specifically the power budget, processing power, and circuit density.

The description of the processing stages which follows outlines a baseline algorithm which will doubtless evolve over time but should follow the same principles. The design is modular and could be improved easily if better algorithms are identified. Each stage processes a frame as a continuous block, outputting another block after a fixed latency. The processor can handle back-to-back frames (40 Mbytes/s per ADC) with up to two frames in the pipeline simultaneously.

Synchronisation

The first stage recognises the start of an APV data frame, producing a start frame signal in synchronisation with the first analog sample, which triggers the subsequent processing stage. The circuit also extracts the pipeline address from the serial header and performs a nearest neighbour and global synchronisation timing check. It employs an auto-synchronisation method which locks directly to the APV data stream requiring no external trigger. This is necessary because there is no simple method of predicting the arrival of APV data frames relative to the

sending of the trigger (except by state machine emulation) owing to the complex logic of the APV pipeline buffer.

Data from the ADC are clocked continuously into the synchronisation circuit which compares the data stream with a threshold in order to serialise the header, and clocks it through a shift register. The parallel output of the shift register is then compared with a fixed pattern to identify either an APV tick or an analog data frame. Additionally the pattern recognition circuitry is enabled with a time window gate which is opened on tick boundaries or on data frame boundaries as appropriate. This prevents the circuit being active during a data frame or between ticks and misidentifying data or noise.

The synchronisation circuit is initially locked during start-up. After a reset, with no triggers present and the time window gating disabled, the circuit locks to the first tick from the APV after the initial period of no activity. The time window gating is enabled after the first tick after reset and triggers can then safely commence.

The circuit shifts out its serial header to the neighbouring ADC processing channel to check for timing alignment and also to cross-check the APV pipeline number. As well as clocking out nearest neighbour information the channel also receives data from its neighbours which it checks against the serial header from its own ADC. The two headers must align in time and have the same 8-bit pipeline address. If an error is detected then this is signalled through a wired OR line to the computer system interface. A bit is also set in the status word for this frame to inform the DAQ system.

As a further integrity check for APV pipeline synchronisation a global input allows the possibility of a value to be broadcast via the TTC from the APV emulation and checked against the current, next or future frame. This process may not be carried out for every trigger but periodically as required, provided the system configuration allows it.

Re-ordering

The APV outputs detector channels in a non-sequential, but fixed, order so that adjacent strips with charge shared between strips or clusters are not adjacent at the digitisation stage. The cluster-finding logic requires the data to be in channel order and thus the APV frame must be re-ordered before the hit finding processing can be performed.

The re-ordering is triggered by a start pulse from the synchronisation circuitry causing it to clock through the words from the analog data frame. It clocks out a re-ordered data stream 256 cycles later along with a start signal to indicate the first value to the next stage.

The circuit uses a Dual Port Memory (DPM) to re-order the data. The input address is provided by a counter which counts with the APV output sequence. When an APV data frame is stored with this address sequence it is re-ordered in memory by channel order. The APV output sequence is easily emulated in real time by manipulating the output bits of a binary counter. After re-ordering, the data are immediately read from the other port using a binary counter for addressing. Both counters run at 40 MHz and thus, with the output sequence running immediately after the input sequence, the circuit appears externally to behave like a 256 cycle shift register. This 256 cycle delay feature is subsequently exploited by the common mode correction circuit.

The DPM is double buffered (2×256) and re-orders another frame arriving immediately after the first in a second DPM partition whilst the old frame is being read out from the first. Thus the circuit can handle back-to-back data frames at 40 Ms/s.

Pedestal correction

Each APV chip will have a unique static offset level associated with each detector channel due to process manufacturing variations. Although these variations are expected to be small it is still necessary to compensate for them owingto their effect on subsequent processing stages.

This is done by storing the pedestal values in a 256 location SRAM Look Up Table and subtracting them from the data stream as they are clocked through. Values are sequenced from the SRAM LUT by an 8-bit counter which is triggered by the start signal from the previous processing stage. The stream of pedestal values from the LUT are fed into one half of a subtractor with the other input connected to the data stream. The output of the subtractor is a pedestal-corrected data frame which is passed onto the next stage. This circuit has a latency of only a few clock cycles.

Faulty channel correction

In the event that an individual APV channel develops a fault, it is necessary to have the option of ignoring it in all processing stages. For example,if a channel was stuck at full scale then, if uncorrected, that channel would distort the common mode calculation, cause maths range exceptions and would be found as a hit for every trigger.

Channels which are faulty are flagged in a 256×1 SRAM LUT. When the synchronisation circuit generates the start signal it also initiates a counter which sequences the Faulty Channel LUT producing an additional flag bit which is attached to data from each channel. This bit indicates if the channel data should be processed or ignored and accompanies each channel of data through all processing stages.

If every APV channel is marked as faulty in the LUT then the whole APV input can be disabled. This can be used to remove whole APVs or pairs of chips from processing.

Common mode correction

Although more complex scenarios can be envisaged, at present the common mode effect is assumed to be a common DC offset, captured on every APV6 input channel, as observed in prototyping. Although expected to be the same for every channel within an APV, it is different for every APV and different for each trigger. Thus each APV requires a separate calculation for every trigger. In the baseline algorithm we use the average of the data frame as the common mode estimate.

The required level is calculated by summing each incoming APV stream in an independent registered accumulator. This is done before re-ordering, as it is not order sensitive. Since the APV streams are interleaved, each accumulator adds alternate samples which, after 256 cycles, produces two independent sums. These are divided by the number of non-faulty channels to produce the average value and stored.

The values are available as data emerge from the re-ordering, due to the 256 cycle delay mentioned earlier, and a pipelined subtractor removes the common mode averages from the data stream. In the event that there are faulty channels then they will be excluded from the summations. The resulting divisions to calculate the averages may then require full integer division (non power of 2) which will require a greater number of cycles to complete. Additional pipeline delays can be added to the data stream to align it with the availability of the averages.

Cluster finding

The basic principle of the hit finding circuit is to identify which channels are hit and write them into the output buffer ready for readout by the FED DAQ interface.

The hit occupancy per strip is low, around 1–3%, and for each per cent occupancy a data frame will contain on average around 2–3 hits. Only these are written to the output buffer while the remainder of the data frame is discarded. This requires that each hit value must be tagged with a detector channel address (8 bit) as it is no longer uniquely identified by its position in the frame. Thus each hit is coded to two bytes which gives a data compression ratio of around 60:1 for 1% occupancy. Finally the sparsified data, data length and processing history, are clocked into the output buffers (FIFOs) ready for readout by the FED DAQ interface.

The sparsified frame data will also require a header consisting of processing channel identity, status, type and processing history. This header is an overhead which slightly reduces the effective compression ratio and increases the data rate.

The details of the algorithms to be implemented have not yet been defined. In practice the algorithms required for silicon and MSGC are expected to be different due to the different behaviour of each detector type and large-angle tracks creating larger, more complex, clusters for MSGCs. However, promising results have been obtained in studies using simple algorithms based on a seed strip chosen on the basis of a suitable threshold and neighbour strips satisfying a lower threshold [5-34]. Such algorithms are well suited to flexible implementation, using programmed threshold values, in a not too complex ASIC. It is expected that these would gradually be implemented during CMS operation making maximum use of the available bandwidth and the opportunity to tune cuts both online and offline.

5.5.1.3 Output

Assuming a 40 MHz pipeline, approximately 512 cycles after the first analog sample is clocked into the processing chain, the output buffers will contain all the sparsified hits. The model used for this buffer assumes three FIFOs, for data, length, and header data. This is intended only for understanding operation and in practice the buffer may be implemented in a different way for optimal cost.

The FIFOs are capable of buffering multiple events. The number of hits in the data FIFO for each trigger is random so an associated length buffer is required so that the readout interface knows how much data to expect from each triggered event. The header FIFO, which contains information calculated or extracted during the processing phase (e.g. APV pipeline address, maths processing exception flags) has a fixed data size per trigger and does not require a length FIFO.

The Processing Readout Interface then uses the information in these buffers to build an output block for a particular event.

Processing readout interface. This is a synchronous, high-bandwidth, high-efficiency, block transfer bus whose bandwidth sufficiently exceeds the average rate that the processing FIFOs required can be small. The interface signals that data are ready through wired-OR control lines and the DAQ interface transfers the event data (see Table 5.6) to its local buffer, using the Header FIFO and the length FIFO to select the appropriate data in the data FIFO.

Table 5.6: Processing channel data format

Header	ADC ID	6 Bits
	APV6 Pipeline Address	8 Bits
	Status	–
	No Hits	8 Bits
Data Block	Channel Address	8 Bits
	Channel Data	8 Bits
	Channel Address	8 Bits
	Chanel Data	8 Bits
Trailer	Error Detection/correction	TBD

Set-up interface. An additional interface which is linked to the FED Computer System Interface and ultimately to the global computer system is assumed for each ADC processing channel. This allows an external computer to configure all processing and control stages within a channel or group of channels, for example loading and verifying pedestal and threshold LUTs before data taking commences. This interface can also be used for monitoring processing or processing statistics during data taking.

Processing exceptions. Within the FED processing there are a number of error conditions which can occur. Many of them are not fatal and are simply flagged in the header information. They are likely to be caused by random fluctuations in the data rate and the hardware is designed with sufficient capacity that they will occur rarely in normal running conditions.

Table 5.7 shows key parameters within the processing which may be subject to data-induced exceptions. If any of these values exceed pre-programmed thresholds this will be flagged in a status word in the header. Additional action may be taken to prevent out-of-range values from adversely affecting subsequent processing.

Table 5.7: Processing exceptions and actions

Parameter	Condition	Flag	Processing action
Common mode	Out of range	Yes	Ignore
ADC overrange		Yes	Clamp to upper ADC limit
Hit amplitude	Out of range	Yes	Clamp to min or max limit
Number of hits	Out of range	Yes	Discard hits beyond upper limit
Data buffer	Part full	No	Hard-wired signal to DAQ
	Full	Yes	Discard subsequent hits
Length buffer	Part full	No	Hard-wired signal to DAQ
	Full	Yes	Hard-wired signal to DAQ
			Count lost events

Processing latency. Each post-ADC processing stage is designed so that it takes a fixed number of clock cycles. The total processing latency at 40 MHz is expected to be around 600 clock cycles and is dominated by re-ordering and the hit search (256 cycles each).

Calibration and monitoring modes. All calibration and monitoring on the FED is expected to be performed through the FED computer system interface under the direction of the external computing system. The post-ADC processing requires set-up of the processing algorithm, in particular pedestal correction and threshold LUTs which are determined during APV6 calibration.

Implementation. The target is to service eight ADC channels in a single ASIC with eight ASICs on a 64 ADC channel FED. Figure 5.27 shows the generic I/O of such a chip which is expected to have a low I/O count, see Table 5.8, with around 160 pins total.

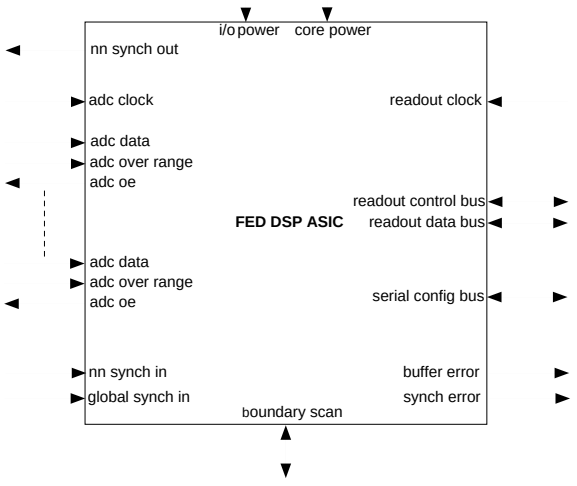

Fig. 5.27: Digital Signal Processing ASIC I/O.

Table 5.8: ASIC I/O description

Signal name	Slots	Pins	Type	Description
ADC data	×8	10	in	ADC digitised analog input
ADC ovr		1		ADC analog input over range
ADC oe		1		ADC tri-state enable
ADC clock	×1	1	in	Phase adjusted 40 MHz system clock
NNsynch in	×1	1	in	Nearest neighbour synch to adj ASIC
NNsynch out	×1	1	out	Nearest neighbour synch from adj ASIC
GlobSynch	×1	1	in	Pipeline address from APV6 emulation
Synch error	×1	1	out	Fast warning – APV6 synch lost
Readout clock	×1	1	in	DAQ interface readout clock
Readout data	×1	∼ 16	out	Readout synch data port
Buffer error	×1	1	out	Fast warning – buffers almost full
Serial config	×1	4	i/o	Serial configuation port
Boundary scan	×1	4	i/o	IEEE standard test port

The serial configuration bus is intended for configuring all internal processing stages, algorithms, LUTs and hit finding circuitry. It will be connected to the FED computer system interface. An IEEE Boundary Scan port is provided to aid with testing during manufacture and could also be utilised for system integrity tests during installation and operation.

There are two power supplies envisaged: one for the 3.3 V I/O buffers and a sub-3 V supply for the core logic depending on the process used. Power consumption is not known in detail at present but it is expected to be well below the 100 W maximum allowed for each board; the principal contributions will come from the optoelectronics conversion and the digitisation stages.

5.5.2 Interfaces

5.5.2.1 DAQ interface

The main function of the DAQ interface is to create on the FED the output data block for each event and transmit this to the DAQ system via the FED-RPDM data link. The data block is created by merging 64 individual data blocks from the post-ADC processing with the TTC and other header information for each triggered event. The circuit is expected to be implemented in an FPGA for flexibility.

The event count and bunch counts are generated and buffered in FIFOs within the DAQ interface under control of the clock, trigger and counter reset signals from the TTC. This avoids fanning signals around the board by generating them within the DAQ interface where they are merged directly with the data stream. They are written into the FIFO with each trigger and are read out in order and merged with each set of processed frames. The Tracker front-end provides no event counters but it is simple for the DAQ interface to provide them on the FED because the readout preserves the data in event order.

After merging, the interface provides dual-ported buffering between the FED and the RDPM to balance the flow of data between the two systems. This buffer will be small owing to the speed of the FED-RDPM link and the RDPM will act as the main buffer into the DAQ.

The DAQ interface may also perform other functions such as integrity checks on the data, generation of error detection trailers for data blocks, creation of monitoring data and exception handling. Exceptions identified by the DAQ in the data stream can be flagged to the CSI so that the global computer system can respond to errors in real time.

5.5.2.2 FED and RDPM interface

The Readout Dual Port Memory (RDPM) [5-35], which is the first stage of the DAQ system [5-36], is designed to receive and merge data from 1 to 8 FEDs, depending on the particular detector sub-system, at up to 400 Mbyte/s via the FED-RDPM data link. In the case of the Tracker the ratio of FEDs to RDPMs will be around 4:1 which allows 100 Mbyte/s per FED and corresponds to an occupancy of 3% at 100 kHz trigger rate.

The choice of the data link involves a number of factors as well as data transfer performance, in particular the ability to vary the ratio of FEDs to RDPMs for each sub-system. This favours some form of network since a backplane connection would require different configurations for each sub-system and would be difficult to reconfigure. There are a number of network topologies which are feasible including bus, ring, or point to point.

Another factor in the choice is the development time-scale for the RDPM and DAQ system, which is expected to be built late in order to take maximum advantage of commercial technology developments. This also appears to favour the use of a network link but in combination with a standard mezzanine slot on each FED which would allow for the late customisation of the network. The use of a plug-in network for the FED-RDPM also allows the RDPM to be located in a different crate from the FEDs.

The most likely commercial standard at present is PCI bus [5-37], implemented as a PMC on the FED. Assuming a 64 bit–66 MHz configuration, this would have a bandwidth for each FED of around 500 Mbyte/s which greatly exceeds all known requirements. The limiting factor would be the FED–RDPM data link, RDPM and subsequent DAQ components.

5.5.2.3 Computer system interface

This provides access to all the FED internal processes to the external computer system for purposes of set-up, control and monitoring. The circuit will probably be implemented in an FPGA for flexibility while the FED CSI-global gomputer system link is likely to be VME-based with a single board computer in the FED crate providing the bridge via the VME backplane.

Internally the CSI provides links to the ADC clock programmable delay lines, the post ADC processing circuits and the DAQ interface to allow set-up and monitoring of these functions by the global computer system. In particular the link to the DAQ interface can be programmed to provide a summary of all exceptions, or other parameters, on an event-by-event basis during data taking. If any exception flags are found in the stream these are tagged, buffered, and made available to the CSI for further analysis by the external system.

5.5.2.4 Trigger, timing and command interface

This is based around the TTCrx ASIC [5-38] using only the minimum set of 9 TTC signals to decode all TTC broadcast information, specifically 40 MHz Clock, trigger, event counter, bunch counter, and the TTC broadcast slow control stream.

The 40 MHz clock is fed into two 4-channel programmable delay lines with each channel de-skewing the clock in 0.5 ns steps over a 25 ns range. These 8 delayed clocks drive groups of 8 ADCs all receiving signals from the same fibre ribbon. This allows for compensation in the lengths of individual ribbons with the assumption that fibres within a ribbon remain closely matched in length.

The 40 MHz clock is also transmitted to the DAQ interface along with the first-level trigger, event and bunch counter reset signals to control the generation and buffering of the event and bunch counts there.

5.5.3 System aspects

The design strategy has been to aim for a high level of integration in order to meet the price-performance target. This is reflected in the reduced number of component types and quantities expected in the design. Figure 5.28 shows the functional implementation of the processing chain consisting of opto-receivers, twostages of op-amps, dual ADCs, processing ASICs and interface FPGAs and dual port memory. Figure 5.29 shows a schematic of the likely physical layout of the module.

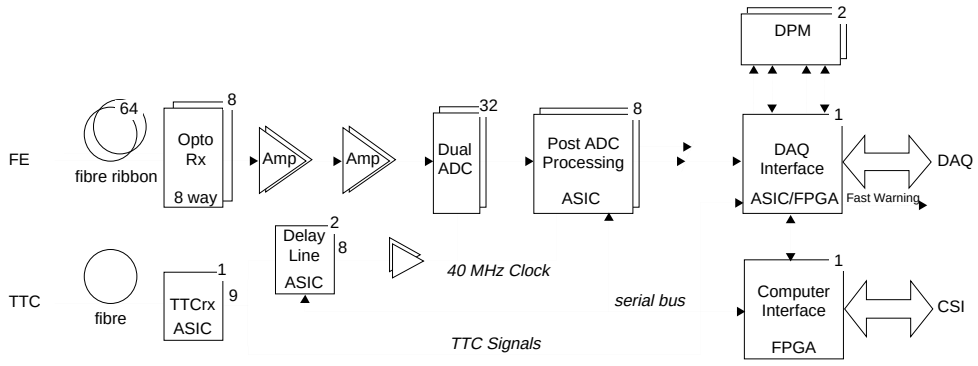

Fig. 5.28: Expected FED functional implementation.

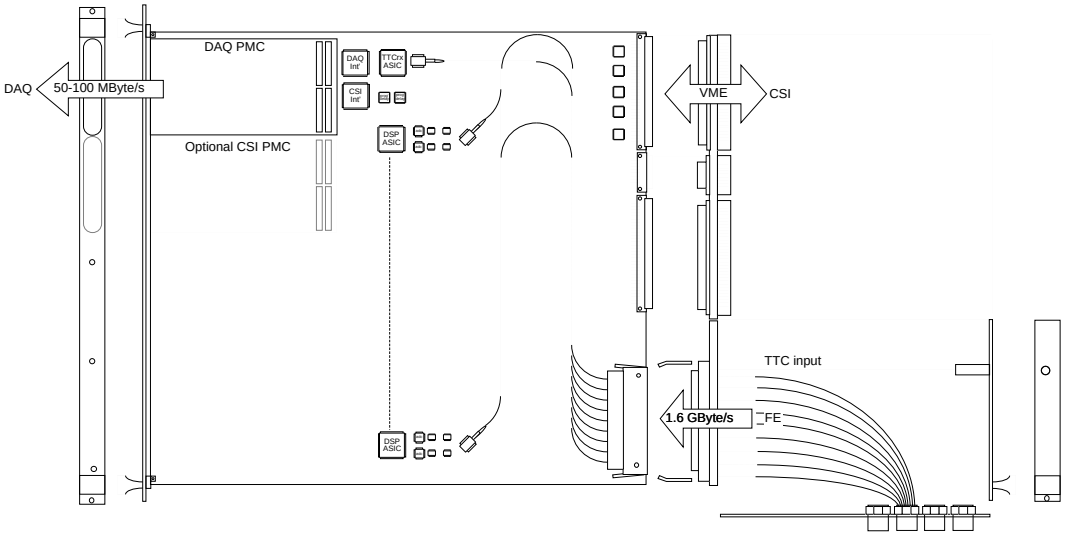

Fig. 5.29: Schematic of possible final FED module.

5.5.4 DAQ

5.5.4.1 Data formats

The FED output data block will consist of a header, a data body, and a trailer. The header consists of unique identifying information such as FED number, event counter, and bunch counter. The body depends on the data format type coded in the header. Different data formats are envisaged for the calibration, monitoring, and data-taking operating modes. The block trailer which

follows the body would include some form of error detection or correction to allow subsequent stages in the DAQ to verify the integrity of the data block.

Table 5.9 shows the data format for normal operation with zero suppression. The hit finding algorithm codes each hit to an address-data pair which requires the start of the data block to include 64 length values to indicate the length of the zero suppressed block from each ADC processing circuit.

The format shown is a minimum format and includes no processing history or status flags which implies that there are no processing exceptions within it. In the event of processing exceptions a different data type can be used which would include additional processing history information for each ADC processing channel indicating the exact nature of exceptions.

Table 5.9: Zero Suppressed Data Format

Sub block	Source	Data field	Word number	Bits
Header	FED	FED Id	0	12
	Fed	Block type = sparse	0	4
	TTC	Event No.	1	32
		Bunch No.	2	12
Data block	ADC 0	Data length	–	8
	ADC 63	Data length	–	8
Data block	ADC 0	Strip address	–	8
	”	Strip data	–	8
	”	Strip address	–	8
	”	Strip data	–	8
Data block	ADC 63	Strip address	–	8
	”	Strip data	–	8
	”	Strip address	–	8
	”	Strip data	–	8
Error detection	–	–	–	–

5.5.4.2 Event sizes and rates

The event size output to the DAQ is a product of the number of detector channels per FED (64), the average occupancy of detector channels served by the FED ($< 3\%$), and the number of bytes used to code the data. For a simple zero suppression scheme each hit would be coded as 2 bytes, namely strip address and signal amplitude. Additionally the event size must include the fixed-length header and trailer data. The data rate is the product of event size and trigger rate.

Table 5.10 summarises these event sizes and rates for an individual FED with the maximum average trigger rate of 100 kHz for occupancies in the range 0 to 3%. The table assumes hit finding and zero suppression with hits coded to 2 bytes and a header–trailer size of 80 bytes. The total event sizes and rates are detailed in Table 5.11.

Table 5.10: FED average event sizes and rates

Chan/FED	Occupancy (%)	Coded hit (Bytes)	Event data (Bytes)	Header (Bytes)	Total (Bytes)	Rate (Mbyte/s)
16 k	0	2	0	80	400	8
	1		320		400	40
	2		640		720	72
	3		960		1040	100

Table 5.11: Tracker average event size and rates

Tracker chan's	Occupancy (%)	Coded hit (Bytes)	Event data (kBytes)	Header (Bytes)	Total (kBytes)	Rate (Gbyte/s)
12 M	0	2	0	80	60	6
	1		240			30
	2		480			54
	3		720			78

In heavy ion running the occupancy of hit detector channels is much higher, up to 18% [5-39] in the MSGC layers (the silicon layers are expected to be switched off), which gives a FED event size of around 6 kbytes. However, the trigger rate is reduced to $\sim$ 8 kHz for Pb–Pb collisions, assuming full acceptance, which gives each FED an output rate of 48 Mbyte/s. This is equivalent to p–p running with a 1% occupancy and a 100 kHz trigger rate. Geometrical restrictions on the trigger lower the rate considerably and it seems more likely that online zero suppression would not be used.

5.5.5 Development time-scale

A 64 ADC channel prototype FED in a 9U by 400 mm VME format has already been developed [5-32] and eight modules are currently in service in several laboratories. The prototype has been demonstrated in a beam test and can be configured with much of the final functionality. It does not yet meet the cost targets.

The next step is to implement a lower cost 8-channel PCI Mezzanine Card (PMC) aimed at enabling the instrumention of larger numbers of APVs required for system prototyping [5-40]. For most of these tests online zero suppression will not be a high priority so the cost of FPGA-based post-ADC processing can be avoided. The PMC module also has the advantage of being compact and can be plugged onto a range of commercial off-the-shelf 6U VME cards. It will be available in mid 1998.

Subsequent steps will make significant moves toward the final system, demonstrating both price and performance Table 5.12. The final module should have maximum integration, with all components located on the main board to minimise the cost of assembly and test. The exception will be the FED–RDPM link which will be implemented as some form of commercial mezzanine card. Although the CSI will be implemented on the main card there will be the option of upgrade through an additional commercial mezzanine slot.

Table 5.12: FED roadmap

Step	Date	Format	Description
0	1996	9U VME	Existing demonstrator prototype
1	1998 Q2	PMC	ADC PMC for detector development
2	1999	6U/9U VME	Opto–ADC–FPGA, DAQ PMC slot
3	2000+	TBD	64 × Opto–ADC–ASIC, DAQ PMC slot
4	2001+	9U VME	Pre-mass-production final optimised version

5.6 Control and Monitoring

The control and monitoring of the Tracker can be divided into two areas:

- the *internal* control of the readout system and monitoring of some Tracker-specific components installed in the Tracker volume itself, which requires custom radiation-hard components. This is described in Sections 5.1, 5.6.6;
- the operation of *external* elements, such as power supplies and gas flow regulators, and the overall computer interface to the users who will operate the CMS experiment. This is a system common to the entire experiment and is summarised in Section 5.6.7.

The *internal* Tracker control and timing distribution system consists of a set of services dedicated to the distribution of the LHC bunch crossing clock and trigger signals and the supervision of the embedded electronics via a dedicated network [5-41].

The mixing of these functions was decided in a fairly early stage of the architectural definition of the system and was determined by the attempt to minimise costs by sharing a common communication infrastructure for the distribution of both the fast and the slow timing signals. This choice ruled out the applicability of most commercial slow control buses (CANbus, Ethernet, Intel USB, MIL1553 etc.); while such buses would be ideally suited for the classical slow control functions, they are not well adapted for the distribution of fast timing signals (the LHC bunch crossing clock and the experiment trigger) with the desired low latency. Furthermore, components are not available in a radiation-hard technology and with the necessary low power and compact size necessary for the Tracker environment.

The integration of the control and timing distribution system [5-38] with the general Tracker readout system is shown in Fig. 5.30. As explained below, the system can be configured in a number of different ways to match the different topologies of regions of the Tracker and to minimise the overall cost. The system is also adaptable to the requirements of the pixel system and is also likely to be exploited by other sub-detectors, such as the Preshower [5-42].

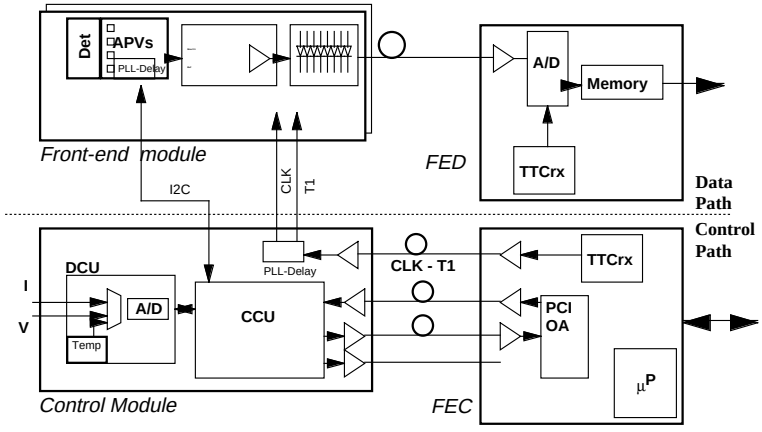

Fig. 5.30: General architecture of Tracker system.

5.6.1 Overview of CMS Tracker control system

The Tracker control system consists basically of three functional blocks:

- an external Front End Controller (FEC) card located in a VME crate houses the intelligence necessary to manage the communication network and interfaces to the CMS slow control system;

– a communication network based on a simple token-ring topology architecture provides the communication between the control room and the embedded electronics. The long sections of this network are implemented over optical fibres, the short ones on low-mass copper cables;
– an embedded Communication and Control Unit (CCU) provides a link between the communication network and the front-end ASICs or any monitoring IC located on the detector. This chip is supported by an external Phase Locked Loop (PLL) ASIC for the recovery and local distribution of the trigger and clock signals.

A key element in the design of this architecture was the requirement to re-use the same optical communication technology developed for the Tracker analog readout. The communication between the embedded electronics on the CMS Tracker and the external electronics is therefore expected to use a ribbon of four optical fibres, i.e. to have the same basic modularity used for the analog data readout. Two fibres are used for sending the timing and data signals to the front-end and two to transmit a return clock and the return data to the external world. Figure 5.31 shows a possible schematic arrangement for the optical part of this digital communication channel.

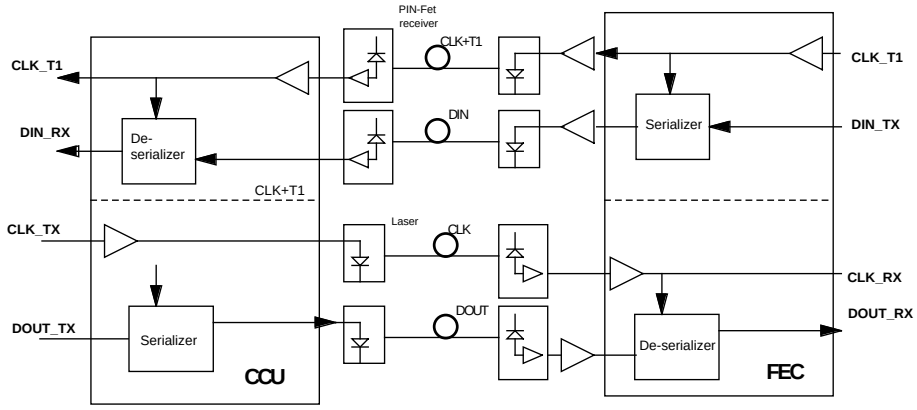

Fig. 5.31: Control system architecture.

Assuming a basic clock speed of 40.08 MHz, each link has a 40 Mb/s capacity. The synchronisation of the FEC and the embedded electronics is provided by a special clock line. For smaller networks or laboratory set-ups a ring not requiring optical fibres can also be built. CCUs are typically mounted on control modules, housing the necessary ancillary electronics, such as line drivers, receivers and level translators.

To minimise the costs of the slow control system, a number of control modules will be connected serially on local parts of the detector resulting in a ring–like arrangement such as the one shown in Fig. 5.32. The Tracker will have a total of about 20 000 front-end modules, and we foresee grouping 10–20 modules on each CCU and, most likely, 1–4 CCUs per ring so, depending on cost and topology constraints, the total number of network rings is expected to be between 300 and 1300.

In Fig. 5.32, DCU refers to a Detector Control Unit; this ASIC is an option in the CMS Tracker and could be used to measure and monitor slowly varying analog signals such as temperature, low and high voltages, detector currents, etc. The DCU is connected to the external FEC via the CCU and is fully supported by the communication protocol.

The arrangement shown in the figure assumes that the connection between the FEC and the first control module is done via optical fibres, the connections between embedded control modules is done electrically using Low Voltage Differential Swing lines (LVDS) [5-43] and the return connection to the FEC is optical. The CCU does not support direct connections to optical

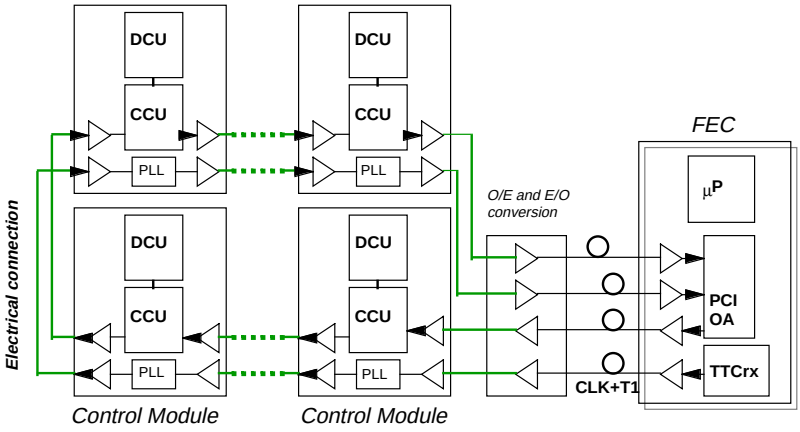

Fig. 5.32: Simplified view of control ring.

elements, and therefore separate optical to electrical interface modules including laser drivers and p-i-n diode receivers are required. The length of a single electrical connections between CCUs is expected not to exceed 50–60 cm for a total length of the electrical ring not exceeding 2–3 metres.

5.6.2 Communication architecture

The communication architecture used in the slow control system is based on two layers:

- The first layer (called the *Ring*) connects the FEC to CCUs and the CCUs between themselves; the protocol on this layer is message based and is implemented in a way similar to standard computer LAN networks. The protocol used on this layer will be called the *Ring Protocol*.
- The second layer connects the Control modules to the front-end chips via so called *Channels*. The protocols used here are called the *Channel Protocols*.

The first layer is unified and common to all CCUs, and is based on a LAN architecture transporting data packets (messages) from the FEC to the channel controllers. The second layer is specific to the channel, and different kind of physical implementations of the channels are foreseen.

The CCU version 1 contains the following channel blocks:

- One node controller (the CCU control itself is seen as a special channel able, for instance, to report the status of the other CCU channels). This is also used for network maintenance.
- Twelve to sixteen I^2C [5-9] master controllers.
- One simple memory-like bus controller to access devices such as memories, A/D converters etc.
- One Event Memory channel to control devices and FIFOs, used for digital detector readout.
- One simple programmable 8-bit I/O-like parallel bus controller.
- One trigger distribution controller.

The dual network layer architecture introduced above is necessary to support applications where long cables/fibres are used between the FEC and the CCUs (therefore generating long delays) and to support the relatively slow buses chosen to interface to the front-end chips, such as the I^2C bus. This architecture assumes that the control is done by sending messages to the respective channels, which interpret the messages as commands, execute them on their physical

ports (for example just a read or write operation to the memory bus), and conditionally return a status reply to the FEC via another message.

This protocol assumes that the remote devices controlled by the CCUs are seen from the FEC as remote independent channels, each one with a particular set of control registers and/or allocated memory locations. The channels operate independently from each other to allow concurrent transactions and can perform transfers to their end-devices concurrently. The high-level ring supervision layer, being a network-like protocol, is controlled by software running on an appropriate microprocessor on the FEC card.

To decouple channel operation from that of the ring, the architecture assumes that all operations on the channels are asynchronous and do not demand an immediate acknowledgement. Basically this means that all commands carried by the ring in the form of network messages are posted to the channel interfaces. To further support some slow channels, input command queues are provided to store multiple outstanding commands before execution.

This is easy to implement for write operations, where one works by posting write operations to the channels. For read operations one instead sends a read request to the channel using a ring packet; the channel performs the operation on its interface and returns a message to the requester using a separate ring packet.

Broadcast operations are supported in a like manner. Only write broadcasts are supported. For example, a broadcast operation to several I^2C ports works as follows:

- a broadcast message is sent to all (or selected) I^2C channels in a CCU,
- the I^2C channels execute the command concurrently but do not necessarily complete at the same time,
- if no error occurs, no acknowledgement is sent back,
- I^2C channels with errors report their status conditions back by sending an error report message back to the FEC.

A FEC can always examine the status of the I^2C channels by interrogating the CCU controller in a CCU at channel #0. A logical view of this architecture is shown in Fig. 5.33.

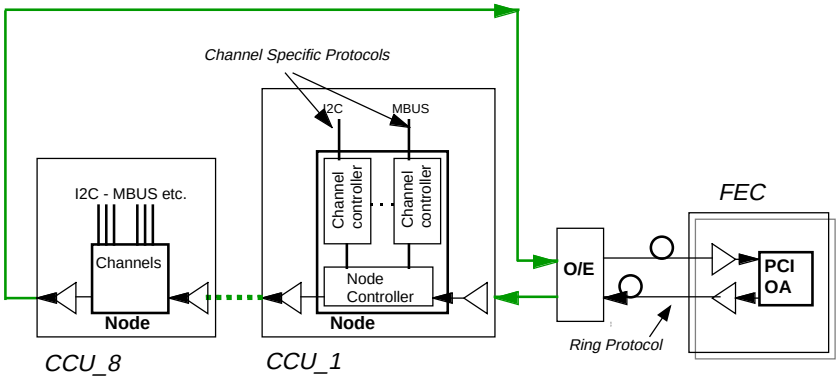

Fig. 5.33: Logical view of control ring.

5.6.3 Token-ring protocol

The architecture of a ring of CCUs is functionally very similar to (and inspired by) the one used by commercial token-ring networks (similar to the IBMs Token Ring or FDDI [5-44]).

The ring consists of a number of node devices (the FEC and the embedded CCUs), which are all capable of accepting and inserting packets in the ring. In the simplest implementation

the ring consists of only two devices, the FEC and one embedded CCU, thus resembling a point-to-point network.

The basic token-ring message transmission protocol for a the ring is based on the following mechanism:

- at start-up the FEC inserts a token in the ring
- all nodes not wanting to transmit will simply forward the token
- all nodes reached by the frame which are not the destination of the current frame forward the frame
- a node which wants to transmit information to another node waits for arrival of the network token, replaces it with a data frame, and transmits it in the ring
- the destination node copies the passing frame, modifies just one 4-bit symbol at the tail of the frame and forwards the entire frame to the network
- the emitting node receives back its original frame with one symbol modified, removes it from the ring and re-emits an empty token.

To guarantee the synchronisation and proper operation of the ring, a token packet is generated automatically and travels around the ring whenever the ring is initialised. The above protocol assumes that the ring has only one circulating token or data packet at any one time. In this network implementation, to simplify the design of the CCUs, the FEC node will contain slightly more complexity, such as the capability of generating empty tokens and of initialising the network.

Handling of communication errors in the ring is a complex issue; the architecture foresees a number of mechanisms directed to the detection and correction of network errors, but given the complexity of the matter these are discussed elsewhere [5-41].

Data packets transmitted on the ring are covered with a 16-bit CRC field. In addition the protocols for the different channel types are well specified and therefore error conditions related to bit-loss in the network can readily be recognised. As no priority mechanism has been included, the network is not meant to support time critical, guaranteed delay messages, but it supports the transport of 'interrupt' messages from the CCUs to the FEC, to inform the outside control program of anomalous situations.

5.6.4 Data encoding

To simplify data encoding and recovery and taking advantage of the fact that the clock signal is available on the network on a separate wire, a simple 4 to 5 bit mapping with NRZI (non-return-to-zero-inverted) coding protocol has been chosen. This choice reduces the effective bandwidth to 32 Mb/s but it is still amply sufficient for our slow control purposes. This coding guarantees good DC balancing on the line and can be implemented on many physical media.

Packets on the network are organised also in a standard manner, as illustrated in Fig. 5.34.

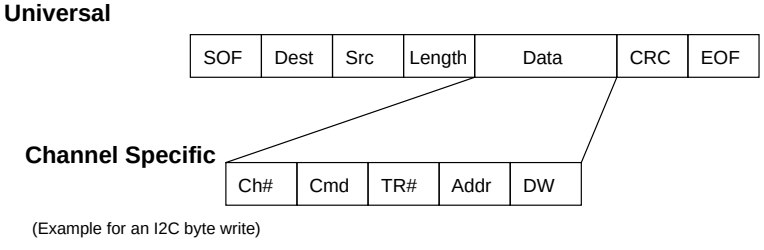

Fig. 5.34: Packet format on ring.

5.6.5 Redundancy specifications

As each ring could control a sizeable number of front-end channels it is important to be able to guarantee a very high reliability for the system. One malfunctioning element in a control ring could mean the loss of control of too many detector elements and would be unacceptable. A redundancy scheme based on doubling interconnection lines and bypassing of CCUs is supported. Figure 5.35 shows the topology used to duplicate the communication paths between CCUs. To avoid losing a complete ring on a broken CCU by a malfunctioning connection, a skip-fault topology is supported.

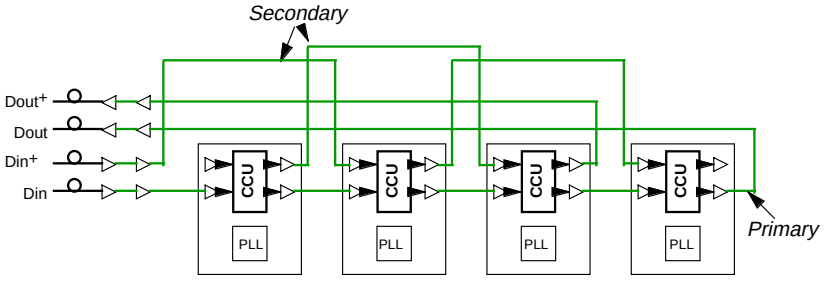

Fig. 5.35: Redundant Skip-fault architecture.

Each CCU is equipped with a set of two network input and output ports. In case of failure of a component in the primary network ring, the preceding CCU can be programmed to send its output messages over the second output port which is wired to bypass the faulty element. All CCUs can receive messages on both input ports. The optical connections are also doubled.

Clearly each duplication of connectivity increases the cost of the system, and the increase of number of system components also increases the number of potential candidates for failure. As in most practical cases malfunctions derive from bad connections, the redundancy scheme chosen only doubles the number of connections and not of ASICs. An unlikely double adjacent failure in this scheme would lead to the loss of less than 1% of the detector control, and this is therefore judged an acceptable risk.

5.6.6 System components

A brief description of the key system components of the control system is given in this section. More detailed specifications for each component are available separately [5-41].

5.6.6.1 Communication and control unit

The CCU ASIC is a special-purpose integrated circuit built in a radiation-hard technology used to implement the dedicated slow control link in the CMS Tracker for control and monitoring of the embedded front-end electronics and distribution of the time critical trigger and of the low jitter clock to the front-end. A block diagram of the CCU is shown in Fig. 5.36.

The CCU interfaces the ring network, for which the CCU is just a node element, to the local embedded front-end chips. Most of these are accessed using the industry standard I^2C bus, which was chosen for its simplicity. This bus is also completely silent (no clock running) outside transfers, thus not generating any potentially dangerous switching noise close to the sensitive front-end chips.

The other interfaces supported by the CCU are a simple 8 bit wide memory-oriented, non-multiplexed bus, programmable in speed from 1 to 8 MHz, a programmable parallel interface which can be used to control or read switches or other semi-static elements, and a decoded

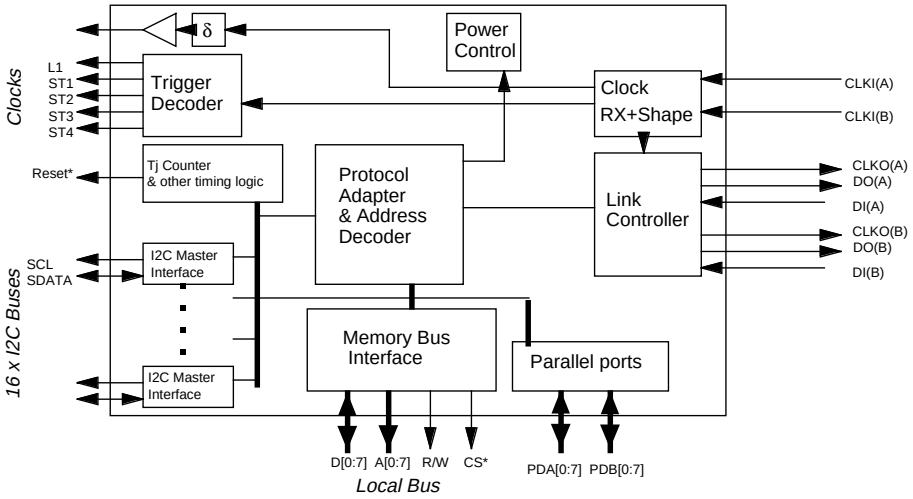

Fig. 5.36: CCU block diagram.

trigger port, where the trigger information which can be encoded in the FEC as up to 3 bits can be made easily available to local electronics (for instance one can encode normal triggers, calibration triggers, reset sequences, etc.).

The CCU is estimated to require up to 50 000 logic gates, depending mainly on the number of I^2C channels which the final version will integrate (currently up to 16 are supported). Based on estimations of switching activity and gate count a power dissipation of less than 400 mW is foreseen. The chip is being designed using a technology-independent, synthesis-driven approach which will allow the implementation of the final production version to be ported on the most suitable and cheapest radiation-hard technology available. A fully functional and synthesisable model is now available. For test beams and pre-production tests a radiation-soft version is being produced in a standard 0.8 μm CMOS standard cell technology.

5.6.6.2 Phase Locked Loop chip

A highly reliable clock (and trigger) will be essential to all sub-detectors at LHC to prevent loss of synchronisation. This is to be ensured by a purpose-designed PLL which is present on the embedded control module and on the front-end modules to provide a very low jitter, phase adjustable clock signal to the local electronics. To simplify recovery of clock and trigger information, the two signals are coded on the FEC with a very simple protocol as shown in Fig. 5.37. Ring data are synchronised with this clock; no data are carried on the network at the position of the missing clock pulse. A clock pulse is removed from the clock train to indicate the presence of a trigger signal. The missing clock pulse and the corresponding trigger signals are regenerated by the PLL. A detailed block diagram of the PLL component is shown in Fig. 5.38.

The PLL has been prototyped successfully using a standard radiation-soft 0.8 μm BiCMOS technology. Its jitter figures are $\sim$ 350 ps p–p when a missing clock pulse is present. The output clock phase can be adjusted from 0 to 25 ns in steps of 1 ns, according to the specifications. The chip measures $\sim 2 \times 2.5$ mm^2 and requires less than 50 mW power. In the final radiation-hard version the I/O levels will be adapted to LVDS.

While the clock distribution only demands to have an adjustable phase as described above, the trigger distribution requires the shortest possible latency, to minimise the length of the level-one buffers in the front-end. Both the TTCrx and the PLL ASICs have been designed with this constraint in mind.

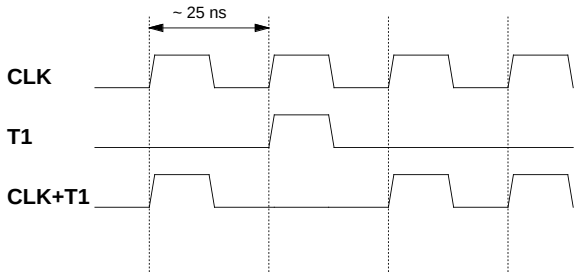

Fig. 5.37: Encoding of the clock and trigger signals.

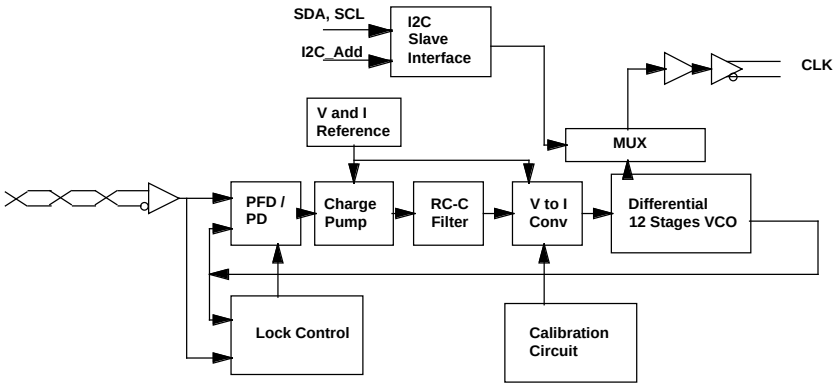

Fig. 5.38: PLL detailed block diagram.

5.6.6.3 CCUM

In the control hierarchy described above, one CCU ASIC is dedicated to the control of a set of Tracker front-end modules. For instance, in the case of the barrel MSGC system, a so-called rod supports several chambers, all of which have 4 to 6 APVs per module. One CCU Module (CCUM) therefore includes one CCU, one PLL, LVDS line drivers and receivers and could also house, if required, one DCU. The CCU includes the I^2C masters necessary to control the individual front-end APVs. The PLL generates only local timing signals, as each front-end module includes its own PLL.

The physical implementation of the CCUM is expected to be on a multi-chip module (MCM). As space is less critical than on the front-end hybrids, an implementation based on a mixed bare die and packaged die solution can be envisaged. This solution offers much greater reliability, as packaged die can be fully tested using standard commercial equipment and are less sensitive to manipulation errors etc.

The scheme described above Fig. 5.39 thus requires for N front-end modules on a rod to have:

- N pairs of I^2C cables (the I^2C protocol only needs a clock and a data line),
- one shielded CLK+T1 line (as clock and level-1 trigger are regenerated locally on each front-end module),
- one wired-OR alarm line shared by all front-end modules to the CCU.

One special optical-to-electrical (and vice-versa) conversion module is also necessary to convert the optical signal used in the long section between the FEC and the detector to the electrical LVDS standard used on the detector. This module includes two pairs (for redundancy) of network receivers and drivers. In addition a simple circuit is included which generates a reset signal

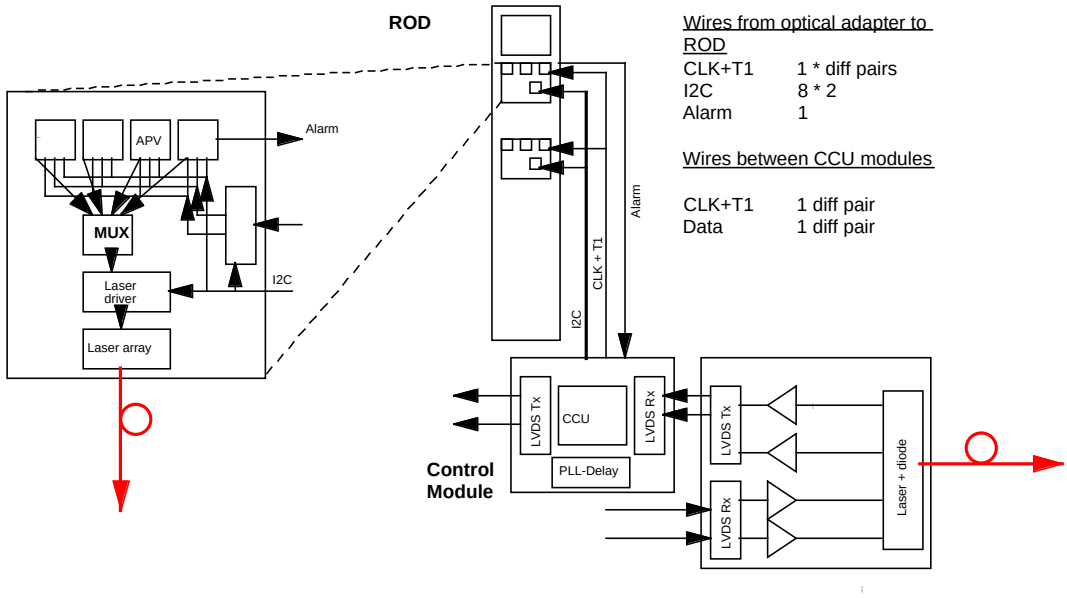

Fig. 5.39: Cabling between CCUM and APVs on an MSGC rod.

along the electrical section of the ring whenever a long sequence of '1's is detected on the optical fibre. This is the only signal that will bring the system into a known state, should anything go completely wrong with the embedded electronics. This module re-uses the same optoelectronics elements used for the Tracker analog readout.

5.6.6.4 Front-End Controller

The FEC houses the intelligence controlling the operation of the slow control ring network. While in principle all nodes on the network are equivalent, some of the vital network monitoring and initialisation functions are generated only on the FEC, and most of these function will be implemented in software.

In its simplest implementation, the FEC could be built around a commercial VME CPU module with a user-definable PCI based optical adapter (on a PMC card) where the actual serialising hardware, specific to the ring protocol, and the optical translation are implemented. Such an approach will allow us to adapt to the most modern commercial cards, by pushing the implementation of most functions onto software, and to restrict the construction of special hardware to the minimum. A FEC card is expected to support from 4 to 8 optical links. The FEC modules will interface via VME to a single board computer in the crate and to the Detector Control System.

The FEC receives the timing and trigger from the TTC system and encodes it a way suitable for the CCUs. This encoding is already implemented in the current version of the TTCrx ASIC and therefore a special PMC housing a TTCrx ASIC will be present on the FEC.

An important function which is expected to be included in the FEC is the emulation of the APV front-end pipeline logic to ensure that buffers do not overflow (Section 5.3.2) by inhibiting the trigger for the small fraction of events which would overfill the pipeline. Since the trigger is distributed to the interior of the Tracker from the FECs, which will therefore be located in the underground counting room near to the trigger crates to avoid an undue increase in the latency, it is natural to locate the emulator at this point in the system.

5.6.7 CMS controls and monitoring

The high-level control and monitoring functions for all CMS detector subsystems are co-ordinated by the Detector Control System (DCS) Group in order to design and implement a single control system to operate the detector. Using guidelines provided by DCS, each of the sub-detector groups are to define and design the monitoring data acquisition and control function needs for their sub-detector. Data from these sub-detectors are available to the global control system which provides console hardware and software, as well as display, archiving and other higher level services.

Parameters to be measured by the control system exist in three locations, the counting room, the side galleries of the cavern, and inside the detector itself. Physically, the electronics in the counting room are expected to be housed in VMEbus crates, all of which include a DCS processor with a network connection to the higher system levels.

5.6.7.1 DCS overview

The DCS hardware architecture consists of three principal layers Fig. 5.40. At the top are operator workstations and general-purpose computers which provide access to all of the DCS services. The front-end or bottom layer consists of large number of distributed front-end processors (VME–based). The middle layer is a dedicated local network interfacing the previous layers. This network is segmented for availability purposes, and is connected to the general CERN network by a filtered access. The general CERN connection provides for world-wide access by authorised persons. The front-end layer connects to detector systems and equipment through direct I/O or through field buses.

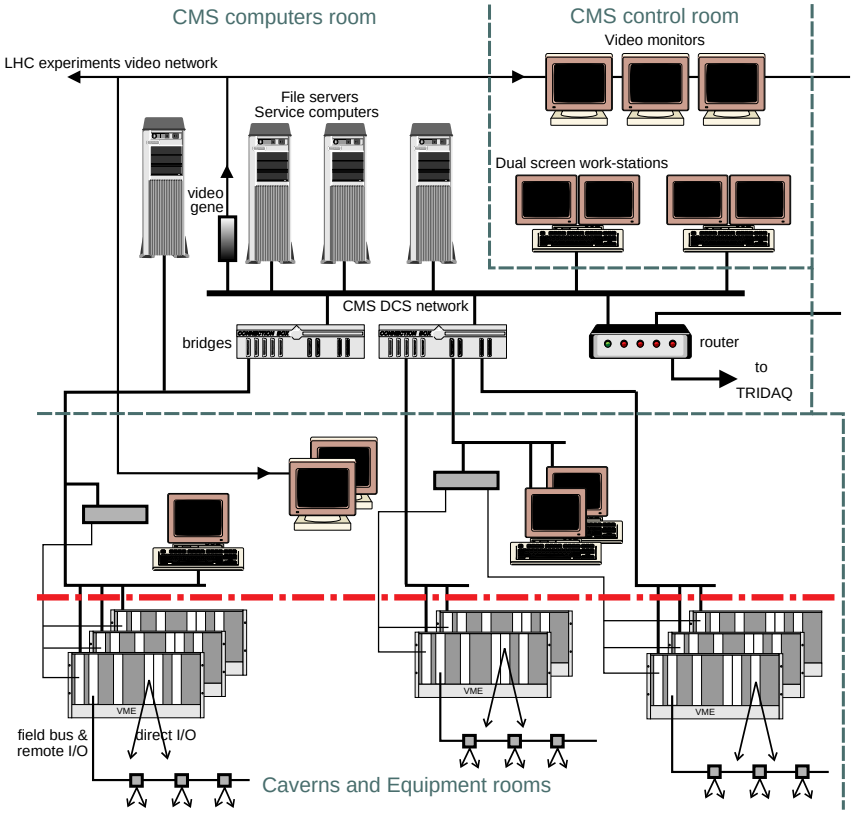

Fig. 5.40: The architecture of the DCS network.

Software Architecture

The software architecture is a co-operating network of dedicated control applications, DCS general services, and gateways to other CMS and CERN systems. The dedicated control applications are the distributed controls for CMS detectors which are composed of real-time process control components and supervision components.

Operations

DCS services are needed for all operational phases of the experiment, from construction and commissioning to physics data-taking runs, calibration tests, and monitoring during shutdown periods. According to the operational phase, one or more operators will concurrently operate the CMS detector. These operations will be done from control rooms, equipment rooms, or remotely via filtering by the DCS access control. DCS provides general services: archiver, logger, alarms, access controls, central repository and a manager for the overall DCS activities. A toolkit is provided to build the dedicated control applications at the individual system level. The kit consists of drivers for the commanded I/O hardware, a control kernel, generic applications and a set of libraries for specific applications.

5.6.7.2 Controls software system

The CMS collaboration has decided to implement a common general services software approach using an existing controls package. Commonality among all four LHC experiments is presently under discussion as well. In CMS and ATLAS, the respective DCS groups are evaluating EPICS as a possible general software system and have demonstration projects underway. EPICS is a highly developed software controls system that is widely used in the high-energy and nuclear physics community and is supported by many laboratories.

To have a specific configuration and software environment, the remainder of this section is based on the use of EPICS in its current VME implementation. In this context, the starting point for the individual detector sub-groups is the EPICS Input-Output-Controller (IOC), a VMEbus-based front-end crate containing a single-board computer running EPICS compatible software. At the present time, IOCs use the VxWorks real-time operating system running on Motorola processor boards. The data request protocol, Channel Access (CA) allows upper level processors to read and set parameters in the IOC. At start-up, each IOC is downloaded with the programs and database entries needed to acquire and process locally the parameters associated with that particular IOC.

Because EPICS is used at many laboratories, software drivers are available for most commercial modules. The DCS group has indicated that they will recommend modules to use for standard analog and digital control system signals. This standardisation goal is to minimise the software effort required to implement sub-detector control and monitoring systems.

An important feature of the total EPICS/IOC software package is an extensive system for alarm monitoring and reporting of analog and digital alarm conditions. Included in the alarm task is the provision for two-tier analog alarms, with independent settings for high and low values, plus high-high and low-low values to distinguish severe conditions. Using this capability, less severe out-of-tolerance conditions can be reported, allowing preventive maintenance to be performed before real hardware failures occur. Alarm system values are part of the data that are downloaded to each IOC at initialisation time.

In EPICS, the database is a key element that allows the system to be adapted to different applications. Database records that are downloaded to the IOCs are processed at a rate dictated by that record. Processing the record may be as simple as reading an analog value, but other operations such as state machines and PID control loops are also implemented by configuring parameters of predefined database entries rather than writing special programs.

Crates and racks

Electronics in the counting room will be implemented in the 9U VME64x format. The design, manufacture, installation, and cooling of the racks and crates is the responsibility of the CMS infrastructure group. Monitoring and control functions are the province of the DCS group.

Archives

The upper levels of DCS will provide archived information for the Tracker. Two types of archives are needed: constants used for calibration and configuration of the detector, and values of monitored parameters. Values include voltage and current readings, temperature measurements, and results of calibration runs.

Testing facilities

Test capability will be needed for the front-end DAQ and trigger electronics located in the counting room. It is expected that boundary scan testing will be incorporated into the design of the digital electronics. All electronics in the counting room will reside in VMEbus crates, so test data and readback will be possible over the DCS network. Test events can be written to and read back from the DAQ buffers using EPICS software in a processor located in each crate. Operational testing and troubleshooting should be accomplished from a remote workstation, located anywhere. Real-time, or pseudo real-time, correlated displays of accelerator data, detector data, and DCS parameter values are essential for diagnostics and troubleshooting. Gateways to the data acquisition processor farm and to the accelerator Controls System should offer this functionality.

5.6.8 Control system integration

The Tracker is subdivided into several subsystems with different groups responsible for each component. It may be wise to assign each subsystem a separate control crate with a Tracker Subsystem Controller (TSC) as interface to DCS and several FEC modules to interface to the front-end. The TSC CPU represents the EPICS Input-Output-Controller respecting all DCS standards. In addition to tasks defined in Section 5.6.7 it will be responsible for the subsystem wide tasks like initialisation and calibration which need a higher level of local co-ordination and synchronicity. The TSC will act as a firewall for conflicting data requests with well-defined safety regulations and priorities to tasks and requests. In this case, remote access will be possible through the DCS, but subject to rules whose supervision must be local, in the control crate. For the MSGCs the HV control will be the most critical task, followed by calibration procedures. Standard data requests interfering with these tasks will be rejected or delayed. If the requests do not interfere, the TSC will pass them via VME to the FEC modules for further relaying.

5.7 Low-Voltage Power Supply

5.7.1 Overview

The very large number of front-end electronics channels requires stable, low-noise power to be supplied to the front-ends with overall currents in the range of 15 kA at the ± 2 V nominal voltage, with a total power dissipation of about 60 kW. The cooling system is required to evacuate the heat generated with negligible rejection into the ambient environment, and to keep the silicon Tracker at a temperature of around -5°C. The task is a very challenging one and several technical issues are still being worked out at the time of writing. This section contains an overview of the main requirements, together with our understanding of the technical aspects and preliminary specifications for the low-voltage power supply system.

5.7.2 General requirements

The granularity of the low-power supply system is determined by various factors, such as detector configuration, material budget, and cost. A major constraint is that the design should not include any voltage or current regulators in the front-ends, where the radiation levels are so high that the feasibility of such power devices is unproven even with radiation hardened processes. The baseline configuration under study is a highly distributed system with individual power supplies feeding groups of detector modules. The natural modularity for the barrel is the MSGC rod, that is an array of approximately 16 detector modules, and its corresponding unit in the silicon barrel. A similar modularity, in terms of sectors, can be defined for the forward disks. The low-luminosity Tracker configuration will thus contain around 1500 detector groups, each connected to an individual power supply.

The current requirements of this power modular unit element vary across the detector layout. They are highest for the barrel MSGC rod, which has power connections at one end only. In this case, the requirements are 15A @ -2 V and 7A @ $+2$ V (approx.). The unbalance is due to the fact that, for design reasons, the APV takes about 90% of its power from the -2 V rail, while the other front-end ASICs use both rails. The general requirements on the power supply modules are summarised Table 5.13.

Table 5.13: Low-voltage power supply module requirements

Parameter	Positive rail	Negative rail
Nominal voltage at load	$+2$ V	-2 V
Tolerance	$\pm 5\%$	$\pm 5\%$
Nominal current	6A (Si), 8A (MSGC)	8A (Si), 18A (MSGC)

5.7.3 Constraints: magnetic field, radiation background, cable cooling

A key issue is whether power supplies should be installed locally (in the cavern) or in the counting room. The current practice is generally to place the power sources close to the load, to simplify regulation and minimise the risk of noise pick-up. However, this approach in the CMS cavern is made difficult by the presence of a relatively strong magnetic field and of a significant radiation level.

The magnetic field is estimated to be around 50 G near the walls, and can reach several hundred gauss on the balconies where electronics racks can be installed. Any inductor or transformer using ferromagnetic material would need adequate shielding if placed close to the detector.

The background radiation level in the cavern may impose even more drastic constraints. Current estimates point to an integrated dose and fluence of about 300 rad and 10^{11} n·cm^{-2} over 10 years in the region where the supplies might be located. The uncertainty on these calculations makes it necessary to adopt a very conservative approach. The total dose effects at these levels can be dramatic on some commercial electronic components, but can be kept within safe limits by choosing off-the-shelf components in appropriate CMOS 'radiation-tolerant' technologies, whenever such components are available. Furthermore, the effects of neutron fluence at the levels indicated can lead to total failure of commercial bipolar devices, such as those used in power circuits, particularly in the conditions of low dose-rate in the cavern.

The preliminary conclusion that can be drawn from these considerations is that if power supplies were to be installed in the cavern, the design and a number of electronic components should be carefully tested and validated for radiation resistance to the required level. The task is made considerably more difficult by the fact that in the case of commercial off-the-shelf components (COTS), the validation is at best limited to a batch which must be traced back to

the vendor. The overall cost and complications of such an approach are quite difficult to assess at this moment [5-45]. Moreover, the failure modes of the power supply should be studied to assess the risk of damaging the expensive load of front-end electronics.

The alternative option is to place the power supply system in the counting room. In this case the LV cables must be water cooled to remove the power losses, since removing heat from the cavern ambient air is difficult and expensive, and the capacity of the air conditioning system is limited. Preliminary calculations have been done for a configuration consisting of a long ($\approx$ 100 m) section from the power supplies to a relay rack on the balconies, and a shorter section ($\approx$ 25 m) from the rack to the patch panel inside the detector. The relay rack is used for adapting cross sections and cooling. The power cables in the long section are copper conductors of the type generally used for magnet windings, with square cross-section (side 4 mm) and a central hole of 3 mm for water flow. The voltage drop for a supply module at the highest nominal load is $\approx$ 1 V. The quantity of copper required is impressive and the cost is significant; however this approach would allow safe use of conventional components in the power supplies. This solution may eventually turn out the most effective, when accessibility and reliability are taken into account. A detailed study is under way and a decision will be taken shortly.

5.7.4 Other constraints: EMC, cable bulk

With power supplied at distance, and without local regulators, electromagnetic compatibility (EMC) is an issue of primary importance. Tests are being carried out on front-end hybrid prototypes using different conductor layouts to find the configuration that leads to the lowest noise performance.

The power cabling from the relay rack to the patch panel should be as compact as possible to reduce the cross-section for services and minimise cracks. For this purpose, the insulator/conductor ratio in the cables should be kept to a minimum. The extruded hollow conductors mentioned above can be insulated by thin layers of polyimide and may offer an effective solution to the problem. A study is being carried out of the conductor layout taking into account the need to minimise the forces due to the very high magnetic field in the detector.

The power distribution on the Tracker frame will be done using multilayer (polyimide-aluminium) laminated bus bars, cooled via thermal coupling to the cooling pipes. Laminated bus bars will allow a low ratio of insulator-to-conductor cross-section for reduced bulk. The equivalent conductor cross-section will correspond to a current density lower than 1.8 $A \cdot mm^{-2}$. With this choice, the steady load voltage drop over the rod ($\approx$ 2 m) will remain below 5% of the nominal supply, which is the accepted tolerance for the front-end electronics. Thus, once the nominal voltage is set at one end of the common rails via sense wires, the voltage on all the electronic modules connected to those rails is within specified limits. The layout and material composition of the LV power cabling have been included in the material budget calculations.

5.8 High-Voltage Power Supply

This section contains an overview of the bias and HV supply systems that are necessary for the operation of the detector. It includes especially the cathode strip HV power supply for the MSGCs.

The HV systems are based on units that can supply a large number of detector modules in parallel, although, for safety reasons, they should share the modularity of the LV system. The actual implementation depends on cost constraints. The techniques required for these systems are essentially those already in use for modern large experiments.

The cathode strip HV supply differs considerably in modularity and has unusual requirements that have motivated a specific development.

The considerations on stray magnetic field and radiation background, as discussed in the LV section, also apply to the HV systems. In fact, constraints may be even more severe because HV semiconductor devices generally show very poor radiation resistance and, in addition, are frequently power devices.

5.8.1 MSGC drift HV and silicon bias voltage power supplies

The requirements for these units are under discussion with possible manufacturers to define specifications so that supplies which match the required modularity of the CMS Tracker can be provided. For the silicon detectors, supplies which will deliver more than 500 V and a few milliamperes per module are required, while for the MSGC drift plane, more than 3 kV with currents in the microampere per module range are necessary. Provided these can be located in the underground counting room adjacent to the cavern, there are no special requirements on magnetic field or radiation tolerance and the units can be based on conventional supplies of which there is much experience.

5.8.2 MSGC cathode strip HV control

To reduce the amount of charge available to sustain the discharge, the cathode strips in an microstrip gas chamber are grouped in clusters and each cluster is connected to a common bias voltage (≈ -520 V) via a series current limiting resistor. The bias voltage is generated by a remote power supply. The total current (signal plus leakage) drawn by a group of strips in normal operation is typically less than 50 nA. When an over-current in a cluster is detected it is necessary to switch off that cluster of strips. This is to prevent any further damage or in case of permanent failure of a strip, while keeping the rest of the chamber fully operational.

For reasons of cost an practicality, it has been agreed to allocate a switch to groups of no less than 32 strips, which still leads to an impressive total of $\approx 200\,000$ HV switches. The two key elements of such a protection system are the detection of the overcurrent in any strip in a group and the HV switch element.

The detection of an overcurrent in a group of 32 adjacent strips is done within the front-end APV chip by a summing amplifier followed by a comparator. The strip current status is latched on a dedicated output and is available for direct action. It can also be read out via the I^2C control bus. The detailed operation is described in Section 5.3.2 and below.

In normal laboratory environments, the switching element that would be commonly used is a high voltage MOSFET. In the Tracker, the task is made very challenging by the high radiation levels, which would increase the switch leakage current to levels well above the operating current (≈ 50 nA) of the group of strips. Moreover, we have established that radiation-hard MOSFETs with the required voltage rating could only be available as expensive semi-custom devices.

Various other alternatives have been investigated. The most realistic one is an optically activated switch [5-46] with several novel features. It consists of a GaAs diode coupled to a vertical cavity surface-emitting laser (VCSEL) diode.

The schematic diagram of the protection circuit is shown in Fig. 5.41 and can be summarised in the following way. The GaAs diode is connected to ground, reverse-biased at the V_c voltage, in parallel with the group of strips. In these conditions the diode leakage current is extremely low, even after irradiation. On detection of an overcurrent, or on command via the Tracker control system, the corresponding VCSEL is turned on. When illuminated by the laser (wavelength $\simeq 860$ nm), the resistance of the GaAs diode drops to a much lower level and the cathode strip voltage is nearly shorted to ground. The operation of the circuit, which requires a limiting series resistor and a bleeding resistor for each group of strips, is described in Ref. [5-46].

Radiation damage tests have been carried out on bulk GaAs diodes with Schottky contacts, and on planar devices. So far, bulk types have shown to offer the best performance in radiation

hardness and HV stand-off. On the other hand, planar types make optical coupling a much easier task, and would be preferred. The development has started recently and will continue through 1998.

VCSEL diodes from various vendors have shown excellent radiation hardness characteristics. Both VCSELs and GaAs diodes are available as linear arrays. The development of a low-cost package for the complete switching multi-element is currently under way, and it is anticipated that prototypes will be available around end 1998.

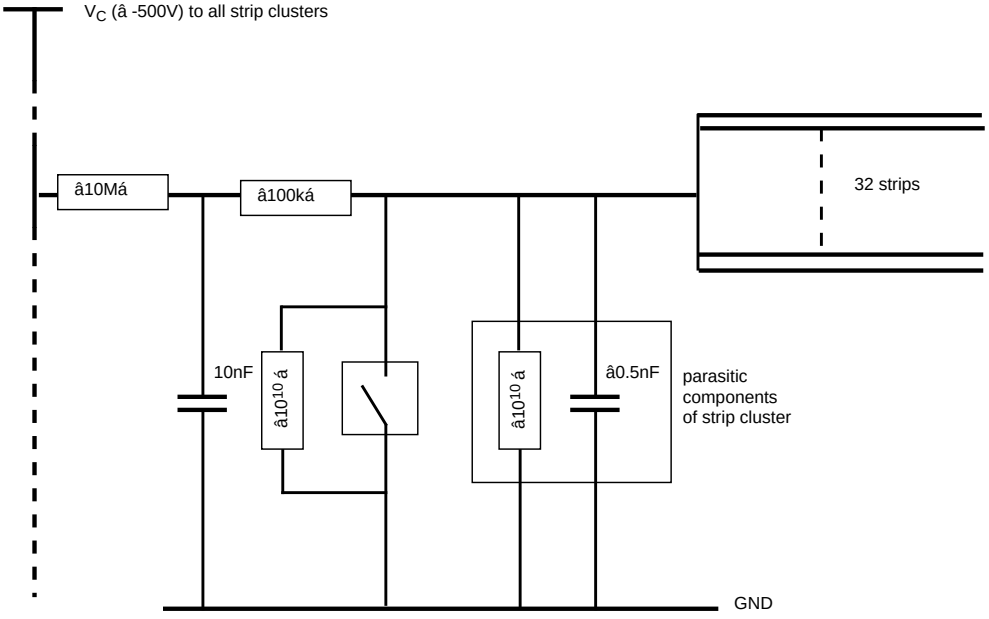

Fig. 5.41: Parallel switch configuration.

5.8.2.1 Links to HV control

The second element of the MSGC cathode voltage control Fig 5.42 is the response of the control system which is implemented via the CCU (Section 5.6.6) following an alarm condition detected on an APV chip. A rapid response is requested, even though most alarms are expected to represent normal fluctuations which will eventually define safe threshold settings for long-term operation. For this reason, action is taken autonomously by the CCU which is then reported to the FEC and overall control system. This sequence of events is:

- an APV senses the average current over an interval of ~ 50 μs and sets a 4-bit alarm latch register after comparison with a programmed value. This register is transmitted as an alarm condition from the detector module,
- an ASIC, which controls the operation of the optically controlled high voltage switches, is triggered by the module alarm and reduces the voltage on all strip cathodes of the module,
- the CCU is informed that an over-current condition has been detected and passes a message to the FEC so that the overall control system is informed,
- the CCU reads the alarm lines from the module signalling the sector of the chamber where the over-current condition has been detected, prepares an alarm message and sends this to the FEC which in turn can perform more checking functions on the chamber and identify the precise location of the fault.

It is important to note that each module has a maximum of four alarm lines which sum over all chips on a detector module. For this reason, when an over-current occurs, it will not be

evident which group of strips has caused it, but reaction is required to be swift. Thus, module high voltage is first reduced, then restored to groups not implicated in the fault.

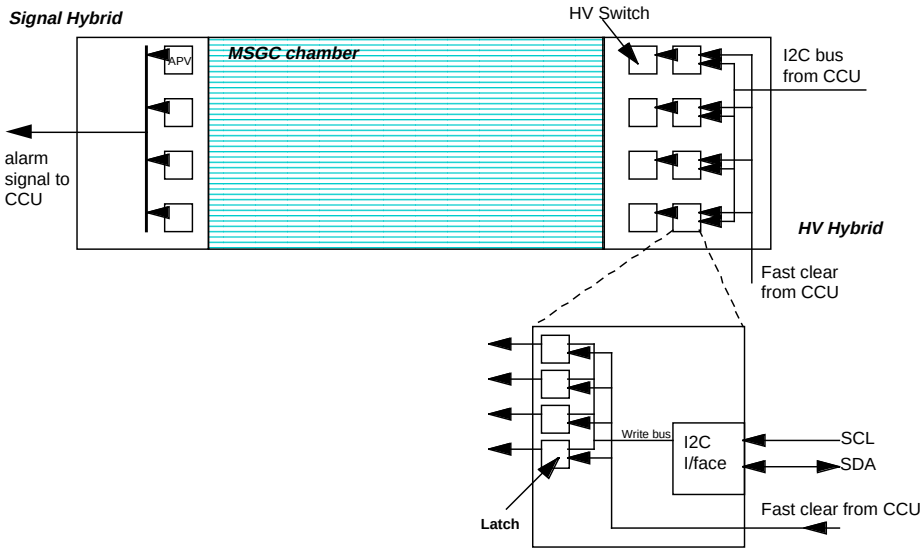

Fig. 5.42: Schematic logical view of the high voltage control for the MSGCs. The physical arrangement of hybrids is not expected to be identical.

5.9 System Operation

5.9.1 Readout milestone

One of the major milestones for the readout system was to demonstrate the important components operating together. This target was set over two years ago, when the technologies to be used for the radiation-hard front-end electronics and the optical link were still very open, with the hope to demonstrate that elements close to their final design would be near to being ready to begin production. This milestone was achieved at the end of 1997 and a readout chain has been operated over a modest but extended period of time with promising results.

In its basic form the prototype consists of the following components (Fig. 5.43): front-end APV6 chip, APVMUX multiplexer, optical data transmission link and VMEbus FED.

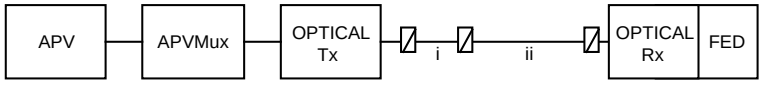

Fig. 5.43: Generalised final CMS Tracker readout chain, showing optical cable with connector breakpoints indicated at (i) $\sim$ 10 m, and (ii) $\sim$ 110 m.

These were assembled into a fully working readout chain which has been operated for a period of over 600 hours.

The readout chain was operated and monitored in two basic forms, as shown in Fig. 5.44. The optical data path was supplemented by a more traditional but short, coaxial cable data path in order that variations in the performance of front-end amplifier could be tracked more easily.

The building blocks of the readout chain assembled for this evaluation follow below, with an indication of how the components compare with the final versions proposed for use in CMS.

Data acquisition was handled by a Macintosh running LabVIEW [5-47], controlling VME modules via an MXI bus. The modules providing timing and I^2C functions were mounted in the same VME crate as the FED. The evaluation set-up is shown in detail in Fig. 5.45.

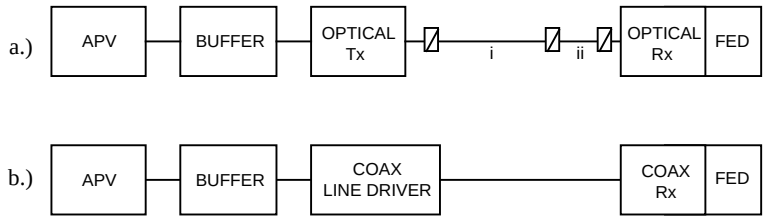

Fig. 5.44: Readout chain implementation showing; (a) optical data transmission with two cable runs (i. $\sim$ 165 m, ii. $\sim$ 10 m), and (b) copper data transmission.

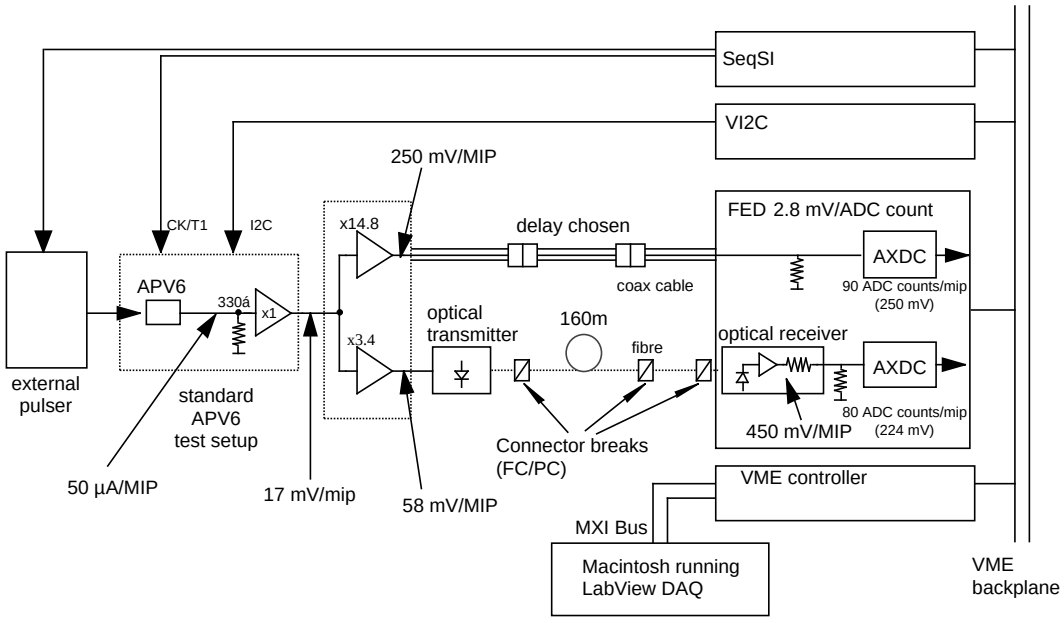

Fig. 5.45: Readout chain evaluation set-up, with approximate gains shown at each stage.

A simple buffering circuit was used in order to match approximately the gains of the optical and copper links. This component replaces the APVMUX which was not available in time. The controlling software enabled regular acquisition of link parameters throughout the monitoring periods at intervals which varied between five and thirty minutes. The chain was monitored for discrete periods, although it has been kept running continuously for several hundred hours (and continues to be operated).

A single channel link consisting of edge-emitting laser and p-i-n diode was used. The optical devices are the same as those envisaged for the final system, but packaged in one-way DIL packages rather than the four-way packages foreseen for the final link. The total length of fibre used in this evaluation was $\sim$ 180 m, a little longer than the $\sim$120 m estimated within CMS. Standard FC/PC type flat polished connectors were used in place of the angle polished MT type connector expected in the final system; the flat polished connectors produce more back reflections, which can increase noise in the type of lasers used, than the angle polished type. The link gain was reduced by a factor of two, due to termination resistors on the receiver and at the input to the FED.

The FED used two 4XADC daughtercards, one each for the coaxial and optical link. The daughter card FPGAs were programmed to perform an oscilloscope function, simply transferring the full 10 bit range of the ADCs to the VME readout.

Functions which will be implemented on the final chip, such as common mode and pedestal subtraction and channel reordering were performed offline. The APV6 was run in peak mode during this evaluation. Measurements of the output pulse shape were made at each acquisition step. Figure 5.46 shows the typical evolution with time. The pulse amplitude after common mode and pedestal subtraction is shown in Fig. 5.47.

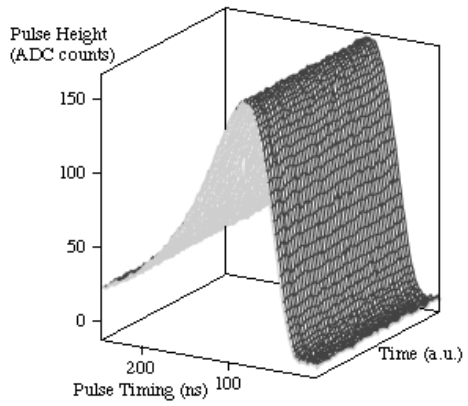

Fig. 5.46: Time development of the APV6 pulse shape, as transmitted via the optical link.

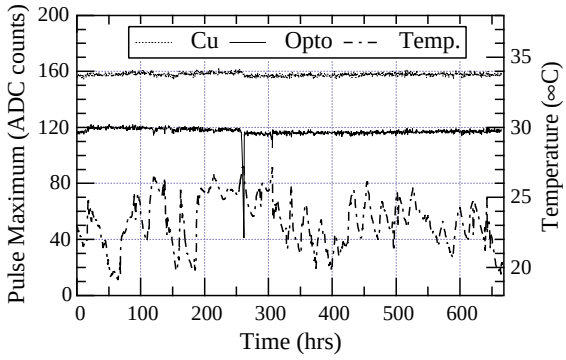

Fig. 5.47: Pulse height due to a ∼2 MIP signal using both electrical and optical transmission. The sharp reduction after about 250 hours is due to temperature changes as explained in the text. The ambient temperature variations are also plotted.

It can be seen that fluctuations are minimal, and not evidently correlated to environmental factors. There is no long-term degradation on this time-scale. As expected, the prototype set-up is sensitive to ambient temperature and the small number of significant amplitude deviations in a short time period in the optical transmission chain are due to variations in optical power of the laser as the external temperature varies [Fig. 5.48 (left)]. These will not be present in the Tracker where such large temperature variations should not occur. However, provided the optical power fluctuations are not unduly large or rapid, they have no effect on the performance of the system since they change the pedestal value but not the gain of the system. However,

from the data of Fig. 5.47, the temperature increase was large enough that the baseline level shifted below the minimum voltage level required by the ADC.

It is also evident that the electrical transmission system has some sensitivity to ambient temperature as well, Fig. 5.48 (right). The origins of these effects require more study but it is clear that careful analysis of the behaviour of all elements of the system is required, and is now possible.

The noise of the readout chain was also recorded during the testing, and is shown in Fig. 5.49. Data are recorded for all channels and represent r.m.s. fluctuations in the baseline at each measurement time. For ease of interpretation data for only a representative channel is shown in Fig. 5.49 but the data show the system noise to be stable with time, except for fluctuations attributable to temperature variations, as observed in the baseline. Clearly, the measurements represent only a simple test of the system but demonstrate the large steps forward which have been made in the last two years.

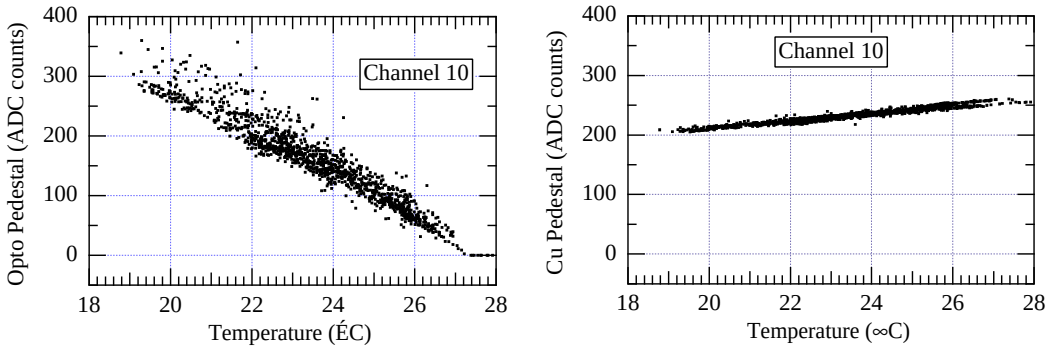

Fig. 5.48: (left) Pedestal variation of optical readout chain with ambient temperature. (right) Pedestal variation of electrical readout chain with ambient temperature.

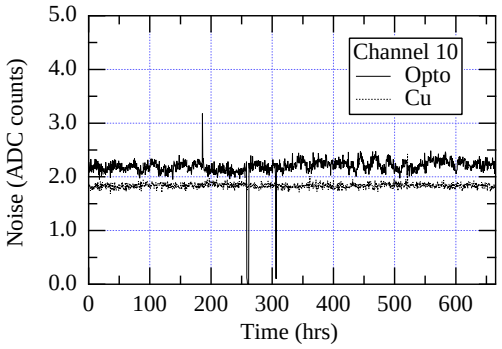

Fig. 5.49: Noise variation of an APV6 channel.

5.9.2 Installation and initial operation

In the early phase of operation of the Tracker system, there will be two major tasks to be carried out: set-up and calibration of the entire electronic system, and synchronisation with the rest of the experiment. In systems the size of LHC experiments, these complex tasks require careful planning and also verification with modest scale prototypes, which is an important reason why an LHC-like test beam is vital during the next few years as automated procedures should be

developed. However, it is possible to foresee broadly how these operations will be carried out and why we believe that the access to analog information will be of considerable value.

5.9.2.1 Initialisation

This is likely to be a data intensive operation and it will be important to have gained experience during prototyping of the system and have developed rapid procedures to ensure that the 100 000 front-end chips and 50 000 optical links can be set to their operating points accurately and quickly.

It is expected that a database will have been created of provisional values of parameter settings which will be used to simplify the process. For example, the transmitters only need to be set to any bias current above the laser threshold but power will be saved by reducing the bias current to a minimal value. The front-end APV chips have more complex settings and a series of bias values for each chip must be downloaded via the serial link followed by a scan of the trigger delay, using calibrate signals generated internally by the APV, to ensure that the pulses are properly set for the trigger latency. At this stage, since peak mode operation is foreseen in the initial low luminosity-LHC conditions, timing precision to about 10–20 ns is likely to be adequate, especially for the MSGCs. Although individual chips are likely to have different settings due to natural variations in production parameters, channels within a chip should be almost identical, thus only a few channels per chip will require to be monitored. It is likely to be most efficient if this task can be carried out under local control of the FEC-FED system avoiding the higher levels of the experiment DAQ.

5.9.2.2 Synchronisation

Once each module has been successfully powered up and has demonstrated a satisfactory response to calibrate pulses, the timing with respect to proton–proton interactions can be verified. While the initial calibration will use synchronous triggers, asynchronous minimum-bias triggers will be the first test of the fine adjustments necessary to accommodate time-of-flight and cable delays which will vary throughout the system. This will certainly be simplified by the slow shaping (50 ns peaking) of the APV amplifier and the absence of pileup. Simple on-line track finding will be the test of this.

Finally it will be necessary to ensure that different sub-detectors assign the same event to identical bunch crossings. One possible solution will be to use a physics trigger, such as a high p_{T} jet, which generates a large number of tracks in a small volume and correlate track segments in the microstrips with energy deposits in the ECAL.

Eventually, when the systems are known to be operating successfully, verification and checking of the system will be possible by utilising the correlation between the LHC beam structure and hits or tracks observed in the microstrip system [5-48].

As LHC luminosity increases, the precision of the timing can be gradually improved, eventually switching to deconvolution mode operation.

5.9.3 Operational performance

5.9.3.1 Noise

The original goal for CMS was to maintain a noise level below 2000 electrons for the lifetime of the detector for both silicon and MSGCs. Given the uncertainties in strip length, pitch and other parameters, this approach was considered the most practical, while keeping the expectations for realistic designs, as they were defined, under review. Detailed calculations have been carried out [5-49]. The actual signal-to-noise value depends on a wide range of additional factors, such

as cluster size, incident angle, Landau fluctuations, gas gain, ballistic deficit, etc., which are fully included in system simulations along with values of electronic noise estimates.

For silicon microstrips the principal contributions to the system noise are from the APV, which is the largest source (as normal for the first element in an amplifying system). It is dominated by the input transistor of the amplifier but with smaller contributions from other elements of the front-end chip. Other contributions come from thermal noise due to the resistance of the microstrip itself (taking into account the distributed resistance and capacitance), leakage current, affected by radiation damage and cooling, thermal noise in the bias resistor, noise due to the optical link, which depends on the gain of preceding elements as well as intrinsic noise from components, and quantisation error in digitisation using a 10 bit ADC, also gain dependent. All values can be calculated from the known performance of the components, except for the optical link. The figures quoted for this element of the system are conservative estimates based on testing so far whose results are likely to be further improved by choice of optimal bandwidth and selection of components, especially connectors and lasers. However, it should be noted that, after combination in quadrature with the rest of the system, the link contributes only about 10% of the total.

Results are tabulated below (Table 5.14) for typical strips in the tracking system. The values are based on measurements of the APV6 performance and include the effect of the weighted sum processing operation (deconvolution) for both silicon and MSGCs. For this purpose a factor 1.47 increase is assumed for the MSGC algorithm.

Table 5.14: Noise estimates for typical CMS detectors

Source	Parameter value	ENC (Si) electrons	Parameter value	ENC (MSGC) electrons
APV		1718		1014
Strip length	12.5 cm		12.5 cm	
Strip pitch	60–120 μm		200 μm	
Strip resistance	200 Ω	608	500 Ω	386
Leakage current	2 μA	486	10 nA	35
Bias resistor resistance	2 MΩ	54	200 kΩ/16 anodes	43
Optical link		600		600
Digitisation		150		150
ENC total		1986		1250

The calculated noise for the silicon microstrip is based on the measured APV6 performance in deconvolution mode. It is known that this is still higher than optimal (see Section 5.3.2.7) and there is scope for further improvement, since the APV6 gain is lower than the design figure. This will be explored once results from the DMILL versions and the next Harris run are available. In addition, lower temperature operation of the amplifier, as will be the case in the silicon Tracker, is expected to reduce the noise; the effect has been observed in non-radiation-hard prototypes. Further measurements are needed to quantify this for radiation-hard circuits.

It is certain that operation of the tracking system will commence with the front-end electronics operating in peak mode, since in low-luminosity conditions pileup will be negligible and noise performance will be significantly better, (typically lower by a factor 1.5). It will also make the system less sensitive to timing errors and precise synchronisation can be established making use of good statistics. Only when leakage currents in the silicon strips and pileup start to become significant will it become necessary to switch to deconvolution mode. We are continuing to investigate the potential for minimising the noise in the system without giving up the fast timing provided by the APV analog filter.

5.9.3.2 Calibration

An important requirement for all LHC systems will be calibration, which should be undertaken regularly especially because of potential for radiation damage. To a good approximation the Tracker is self-calibrating since measurements of pulse height will be available for all strips and the Landau distribution should offer a reliable method of monitoring the system in considerable detail. However, regular electronic calibration should also take place, probably at intervals of a few days, in dedicated runs. The information obtained is not absolute since internal calibrate levels are not known precisely, except by reference to an energy measurement, and (rare) optical fibre disconnection and reconnection is also expected to change the attenuation of the link by a measurable amount. However, amplitudes, pulse shapes, and laser thresholds can be compared and monitored. Calibration during physics data-taking is not anticipated and the control network will be inactive during running, except for any alarms.

Synchronisation errors will also be monitored continuously which can be done at the FEC/ FED level by means of the APV header data which should permit rapid diagnosis, at the chip level, of any aberrant behaviour.

Nevertheless, these and other operational requirements need verification under realistic conditions to gain as much experience as possible before LHC start up. An LHC-like test beam is essential for these studies which should be undertaken with reasonable size prototype systems.

5.9.4 Long-term maintenance

Maintenance will be difficult for much of the Tracker given the inaccessibility of the interior of the Tracker for long periods of time. Even during the early periods, when induced radiation will be at a low level, it will be difficult to exchange internal components without major dismantling of the structure, which should be avoided as far as possible. Prototype system operation will be important to diagnosis potential weaknesses in components, assembly or handling procedures. Once again simulated LHC operation will be essential to learn some of the pitfalls to be avoided.

Over the LHC lifetime, maintenance, and possibly upgrades, of the parts of the system within the counting room can be foreseen by interchanging FEDs and components on them. Replacement of some modules within the Tracker may be possible occasionally and a small reserve of spares will be maintained. As it may be necessary during the operational period to produce more chips, it will be essential to maintain the designs at an appropriate level. The importance of documents specifying all the system components will be essential for this reason.

Reliability will be the key to successful long-term operation. This is an area where techniques and methods employed in particle physics experiments have not generally been conceived with this aspect of performance in mind. Although much attention has been given to radiation damage issues at LHC, component failure may also arise for mechanical reasons or ageing of components for other unexpected reasons. As the system develops further, we hope it will be possible for the team responsible for the readout and control to review it as it is implemented to identify any risks and, where possible, take actions to minimise them either by recommendations of improved techniques or selection of components.

5.10 Schedule and Planning

A global plan for the production of the Tracker electronics has been prepared which provisionally defines the time-scales and allows to identify possible constraints, some of which are budgetary and others practical, e.g. the consequences of delays or significant design changes in components of the system. It presents a 'broad brush' picture of the anticipated schedule and adjustments and fine tuning will be required as progress is made. Nevertheless the picture which emerges is

not likely to change radically for the Tracker to be constructed on the required schedule for CMS operation in 2005. The main constraint on the schedule will certainly arise from the production of front-end chips where the major part of the readout system cost and component numbers lie. These are critical since they influence the production of detector modules, along with some ancillary chips (PLL, APVMUX) which are not expected to present major problems of design or fabrication.

5.10.1 Front-end electronics

The design or development phase of components of the system is based on an assumption of design, fabrication and test cycles which are estimated from past experience. For example, the development phase of the front-end electronic chips assumes that roughly one complete iteration per year can be carried out. This has usually been achieved so far when ASICs are at a fairly advanced stage of design, close to the final one, as is now the case. Less complex chip designs progress faster, even for final implementation in radiation hard form.

Production of the major front-end chips is assumed to extend over three years for reasons explained earlier. Wafer testing will be carried out continuously with deliveries of wafers arriving at regular intervals. This will lead to known good die which should be cut from the wafers, assembled onto hybrids and re-tested prior to module assembly. Testing will be carried out in a small number of institutes with specialised infrastructure. While commercial testing is not excluded, it is likely the costs will be prohibitive for the complex mixed signal front-end electronics. However, this is envisaged for the simpler ancillary chips if insufficient test capability exists or commercial testing is unavailable. In view of the recent commitment by CERN, and plans in other centres, to purchase advanced testing set-ups this is not expected to be the case.

Final definition of silicon modules should be around mid 1999, which is linked to freezing the cables and services and thus the support structure. Hybrid development should have been completed some months earlier. Thus, at this time most of the ancillary chips required on the detector module must have been developed.

5.10.2 Optical link

This part of the plan was developed using input from industrial partners collaborating on the link development. It is foreseen that links are delivered in complete form already tested but further testing will be required once they have been mounted on FEDs, FECs and detector modules which will be the responsibility of the Tracker teams.

For the present the different types of link, analog and digital, are assumed to follow the same production time-scale since they are based mainly on identical components. Although some elements of the link could in principle be purchased late, for budgetary reasons, since they are installed outside the Tracker volume this is not likely to be done since testing will require both ends of a link. Like the analog transmitters, many of the digital receivers and transmitters are located in the radiation zone inside the Tracker so must be available relatively early for testing modules and assembly of the Tracker.

5.10.3 Control system and DAQ

The components of the control system must be produced sufficiently early for assembly into working prototypes and permit assembly of the Tracker where ASICs (eg CCU and DCU) must be mounted on hybrids and installed inside the Tracker. A significant testing phase is foreseen. The component which can be delivered latest is the FEC (Front End Controller) which is foreseen to be a modular VMEbus module located in the underground control room. However, sufficient FECs must be available before and during assembly to evaluate the system. Boards will be

delivered already tested by manufacturers but final acceptance tests will also be needed. Similar comments apply to the FED digitisation modules, which are based on a similar concept. The FED design phase is permitted to run for several more years, including prototype evaluation. The production has been delayed as long as possible implying that the Tracker is fully operational by the end of 2005, which is assumed to be compatible with the debugging of the detector during the first year of operation.

Chapter 6

Engineering

6.1 Overview

The purpose of this chapter is a description of the more global aspects of the Tracker. These are the engineering and design of the overall support structures, the general Tracker services and the assembly and installation scenarios. In addition, questions concerning operation and maintenance will be addressed and related safety issues will be discussed.

Constraints on the general engineering come from conflicting requirements, namely from the need for structures which have to be as light as possible but have to provide a very high stability over long time periods. This stability has to be guaranteed under external stresses such as cable loads and the effect of the magnetic field. Allowed temperature gradients and variations have to be determined.

A large heat load of about 68 kW necessitates robust and flexible cooling systems. Humidity levels need to be very well controlled.

One has to consider the high radiation environment inside the Tracker volume, which necessitates a careful selection of materials.

A precise monitoring of the position of the individual detector elements is needed and the proposed alignment and monitoring technologies are described.

Careful planning will have a crucial role in the coordinated assembly and installation of the complete Tracker. Our present view of the engineering planning will be addressed. An overview of the global Tracker dimensions is given in Fig. 6.1.

6.2 Tracker Support Structures

6.2.1 General requirements

6.2.1.1 Definitions

The term 'Tracker general support structure' includes all the structural parts designed to contain, hold together and support the Tracker detector inside CMS. The 'Tracker assembly procedure' is the complete set of operations performed to position around the General Support Structure the pre-assembled MSGC and Silicon detectors, their services and all the components forming the complete Tracker, with the exception of the Pixel detector. The 'Tracker installation procedure' is the ensemble of operations performed to install the Tracker inside CMS, from the arrival to the surface building at Point 5 to the final positioning inside the experiment. The terms 'Beam pipe installation procedure' and 'Pixel installation procedure' are reserved for the particular operations to be performed *in situ* (i.e. after the installation of the Tracker inside CMS) to install

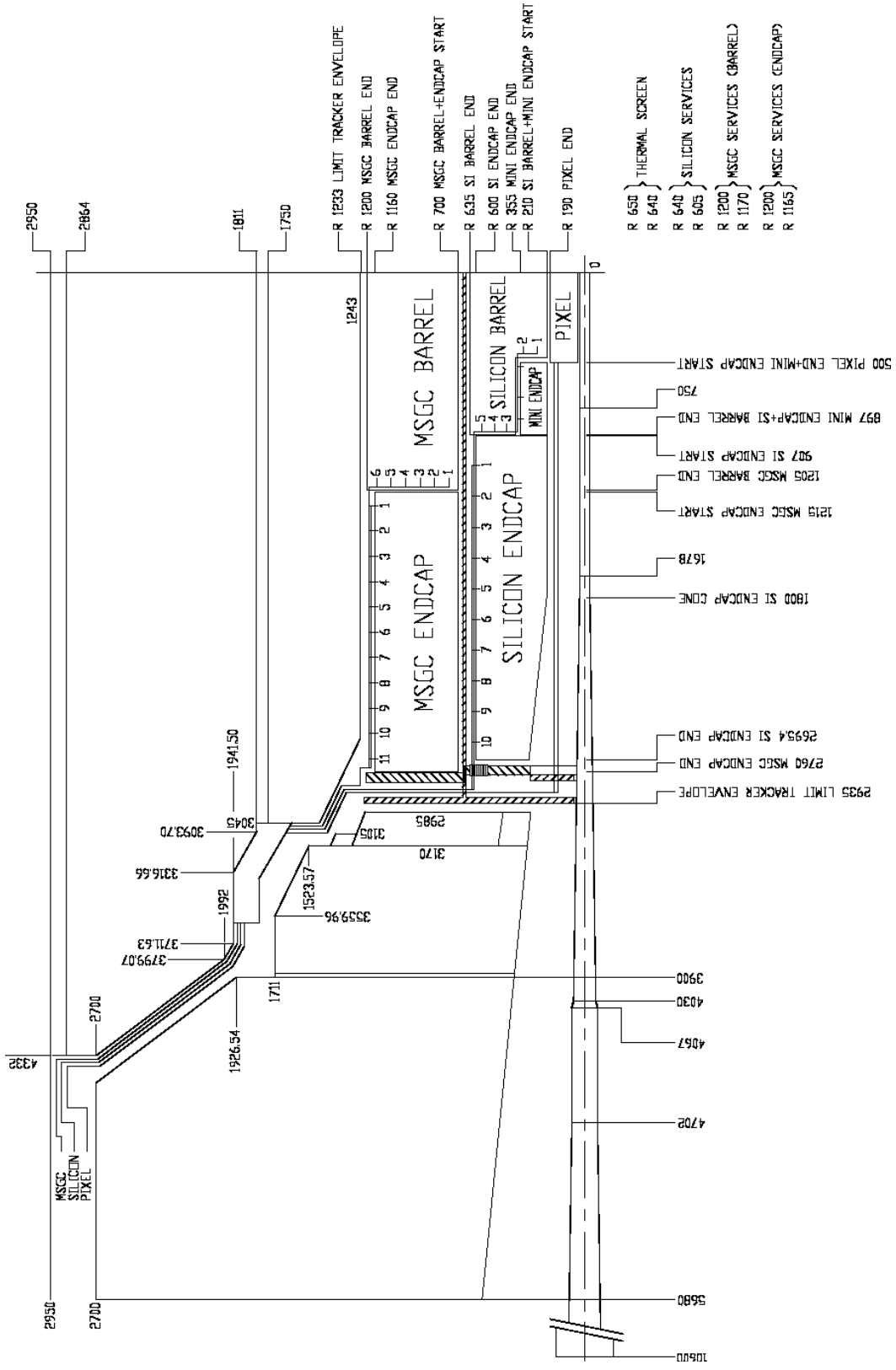

Fig. 6.1: Global Tracker dimensions [mm].

inside the Tracker the central section of the beam pipe and the Pixel system (the subdetector and its services).

6.2.1.2 General task

With a total weight of about 2.5 t the Tracker can be considered as a very light detector when compared to the other CMS sub-systems. The Tracker general support structure must provide the support and the correct positioning in space for all the Tracker sub-detectors (MSGC, Silicon, and Pixel) and for the central segment of the beam pipe. It must ensure the correctness of the relative positioning of any subdetector with respect to the others, and must support their services up to the first connection point outside the Tracker.

6.2.1.3 Overall dimensions

Any part of the Tracker, except the points of attachment to the structure of the experiment and the services coming out of the experiment, should be contained in a cylinder 5870 mm long and 2466 mm in diameter. These dimensions are inclusive of fabrication tolerances and of possible deformations. In particular, the radial figure already includes the installation clearance.

6.2.1.4 Maximal length for installation

During installation inside CMS, the maximal length allowed for the Tracker, including all the tails of services and any installation device, is 9.0 m.

6.2.2 Structural requirements

6.2.2.1 Positioning precision

The general support structure must ensure that each subdetector be positioned in space precisely enough with respect to its nominal position to allow for an efficient software reconstruction of the actual final geometry of the Tracker after assembly. Trade-offs should be considered in order to define the optimum between built-in precision, adjustable supports, stability, cost, material budget and software corrections. Regarding the most critical coordinates (e.g. r-ϕ for the barrel detectors), a positioning precision of each subdetector to within a 0.1 to 0.2 mm with respect to its nominal position is presently considered a reasonable requirement.

6.2.2.2 Stability and vibrations

After assembly inside the Tracker, the stability in time of the position of each subdetector must be below its intrinsic resolution, in order not to notably increase the measuring errors.

Small static deflections and high resonant frequencies of vibration are desirable for such stability. Engineering will strive to minimise static deflections and increase vibration frequencies as much as possible. The limits will be set by the material budget and by production costs.

6.2.3 Tracker-related operational requirements

6.2.3.1 Operating temperatures and thermal separation

The nominal operating temperature of the MSGC detectors will be 18°C , with a temperature stability requirement of a few degrees. The operating temperature of the Silicon and Pixel detector volumes is -10°C to avoid thermal runaway. The Tracker general support structure must provide a thermal separation between these two volumes. This thermal separation must be guaranteed in any possible working or non-working conditions (both volumes powered, both

off, only one volume powered) without any influence on one side deriving from the conditions on the other.

6.2.3.2 Humidity control inside the cold volume

It is mandatory to avoid any condensation inside the cold (Silicon and Pixel) volume. Thus, a full sealing of this region against the external atmosphere must be ensured (in particular through the beam pipe and through the feedthroughs of the services). The atmosphere inside will be kept dry enough to have the dew point below the temperature of the cooling fluid.

6.2.3.3 Gas tightness of the MSGC volume

The gas mixture filling the MSGC counters is flammamble or explosive in the presence of oxygen. In order to reduce the risk of producing such a flammable mixture in the event of gas leak inside the Tracker, the volume of the MSGC detectors should be contained in a sealed envelope, flushed with neutral gas (N_2). Inside this volume the O_2 concentration should be kept below 5%.

6.2.3.4 Pixel detector independent installation and extraction

The possibility of an independent installation and extraction of the Pixel detector at least once per year must be ensured. Although radiation levels must be considered, this operation must be performed inside the experimental cavern, without disconnection of the central section of the beam pipe and with a minimal impact on the other Tracker subdetectors. The extraction operations should be possible during an intermediate machine shut-down, for which a 3 m wide opening of the CMS endcaps is foreseen.

6.2.3.5 Silicon detector maintenance

Given the higher radiation level in the Silicon and the afore-mentioned requirements on temperature and humidity, the possibility of a yearly maintenance independent from the MSGC maintenance cycle is under consideration. The temperature and humidity requirements described in Sections 6.2.3.1 and 6.2.3.2 must be largely maintained during the maintenance phases.

6.2.3.6 Staging scenario

Due to budgetary constraints, both the Silicon and the MSGC systems will be designed foreseeing a staging scenario, according to which they would be only partially equipped at the moment of their first installation inside CMS. An upgrade phase will possibly follow after some years of operation, bringing the subdetectors to their final configuration. The design of the Tracker general support structure must allow for this possibility and facilitate it as much as possible. Also, the general service layout will be from the beginning fully compatible with the final configuration of the detectors. It should be possible to complete such upgrades during one long machine shut-down, when a full opening of both the CMS endcaps is possible.

6.2.3.7 Support and reference for the Tracker internal alignment system

The Tracker general support structure shall provide appropriate support and reference points to the structure of the Tracker internal alignment system.

6.2.3.8 General maintenance schedule

The Tracker general support structure shall be designed so as to allow for a complete cycle of maintenance during a long machine shut-down. Depending on the operational needs, the maintenance cycle could be performed either on the whole Tracker or only on a sub-system and should include the following steps:

Step	Operation
1	experiment opening
2	access
3	removal of the alignment wheels
4	uncabling of Pixel detector
5	extraction of Pixel detector
6	disconnection of the central section of the beam pipe
7	uncabling
8	survey
9	removal from the experiment
10	transfer to the surface laboratory
11	disassembly
12	maintenance

Step	Operation
13	assembly
14	survey
15	transfer to the experimental cavern
16	installation
17	cabling
18	test of cable and pipe connections
19	connection of the central section of the beam pipe
20	*in situ* bake-out
21	installation of Pixel detector
22	cabling of Pixel detector
23	survey and assembly of the alignment wheels
24	testing
25	experiment closure

6.2.4 CMS-related operational requirements

6.2.4.1 Beam pipe support

The central segment of the beam pipe is mechanically decoupled from the remaining part by the introduction of one universal expansion joint per side, and must be supported by the Tracker. The Tracker support structure must provide 3 to 4 attachment points on each side of the interaction point. The connecting elements should be able to minimise transmission of vibrations from the Tracker, while ensuring sufficient mechanical stability for the beam pipe.

6.2.4.2 *In situ* access to the beam pipe

The removal/installation of the central section of the beam pipe must be possible *in situ* (i.e. inside the experimental cavern) requiring only the previous extraction of the Pixel detector and without introducing any disturbance for the Silicon detector. Thus, the attachments to the general support structure should allow for remote connection and disconnection.

6.2.4.3 ECAL barrel interface

No contact between the Tracker and the surface of the ECAL barrel crystals is allowed. The Tracker installation procedure must meet this requirement and guarantee enough clearance between them. On the other hand, the distance between the innermost part of the sensing elements of the ECAL barrel and the outermost of the Tracker must be kept as small as possible. A trade-off must be performed, taking into account the cost and the reliability of the installation procedure. Once the Tracker is in position inside CMS, it should be possible, during one long shut-down, to remove any single ECAL barrel super-module for maintenance work without removing the Tracker. The supports of the Tracker must be designed so as to allow for this possibility.

6.2.4.4 ECAL endcap interface

With the magnetic field on, the central part of the CMS endcap will move towards the interaction point. The maximum axial displacement of an endcap part is presently estimated to be 25 mm.

Taking into account possible underestimation of the displacement, tolerances of fabrication and inaccuracy during the assembly of the facing parts, a safety factor of two is considered necessary. This brings to 50 mm the value of the minimum axial distance in nominal conditions (i.e. magnetic field off) between all the facing points of the Tracker and of the Preshower endcap, attached to the ECAL endcap. This distance must be respected by any object locally protruding from the surface of the Tracker endflange.

To prevent excessive neutron flux from entering the Tracker from the ECAL endcap crystals, a layer of moderating material is attached to the surface of the Preshower facing the Tracker. The design includes the possible addition of another layer of moderator on the Tracker endflanges.

6.2.4.5 HCAL barrel interface

The circumference of the HCAL barrel is divided into 18 flat sectors, each one spanning 20°. In each of these sectors, a region for the Tracker is reserved in front of the ECAL barrel. Two of these sectors (per end) will be used to support and position the Tracker inside CMS. The other 16 sectors will house patch panels and connectors for the Tracker services.

6.2.4.6 Muon detector interface

The Tracker general support structure will provide appropriate support and reference points to the structure of the Muon Link system. The attachment points of the Tracker inside CMS must have adjustable positioning devices. These must be able to correct for possible movements and/or deformations of the interface with CMS, in order to match the positioning requirements of the Muon Link system.

6.2.5 Design guidelines

6.2.5.1 General principles

Given the requirements listed above, some guidelines of a general character should be followed in the design of the Tracker general support structure, to ensure an optimal physics performance:

- Design for low static deflections and high resonance frequencies;
- Minimise the amount of material used;
- Always prefer materials with large values of X_0;
- Avoid lumps of material, try to distribute it evenly over 2π;
- Allow the maximum possible lever arm for the MSGC and Silicon detectors;
- Minimise the radial gap between the MSGC and Silicon detectors;
- Minimise the amount of material in the radial gap between the MSGC and Silicon detectors;
- Minimise the axial gap between the barrel and endcap subdetector systems;
- Distribute material inside the Tracker volume so as to minimise the degradation of the performance of ECAL;
- Minimise the radial gap between the outermost sensitive point of the MSGC and the ECAL barrel crystals.

6.2.5.2 Static loads and deflection

Keeping the detector parts in positions that are stable in time is the primary concern when designing the mechanical structure. The combination of stiff structures with low mass, low thermal expansion and high resonant frequencies improves stability in general. In order to achieve maximal physics performance, it is also important to minimise the amount of material inside

the Tracker. For structural purposes, carbon fibre composites provide optimal solutions, but it remains important to avoid extremely advanced aerospace materials and fabrication processes because of their high cost. Using high performance carbon fibre composites and advanced design methods, it is possible to create structures with static deflections of about 100 μm and resonance frequencies higher than 30 Hz on a component level, and deflections below a few millimetres with resonance frequencies above 10 Hz for entire large detectors. Together with the large amount of damping provided by the large number of cables, these static and dynamic properties will assure the correct functioning of the Tracker.

6.2.5.3 Dynamic properties and constraints

The real criterion for vibrations of all the Tracker structures is one of amplitude, not of frequency. The vibration amplitude should not exceed the allowed limit. Whether structures vibrate at 10 Hz or 40 Hz or 100 Hz is not relevant, except for the effect of the frequency on the amplitude. Through finite element analysis (F.E.A.) the vibration modes of a structure can be calculated to a reasonable degree of accuracy, while the absolute vibration amplitude is considerably more difficult to calculate reliably. It is common in engineering design problems to pick a design frequency that is believed to result, with reasonable confidence based on past experience, in an acceptable vibration amplitude. There are two potential pitfalls with this approach:

1. To obtain the necessary confidence level, the frequency that is chosen is commonly higher than necessary. This often leads to excessively bulky or heavy structures and conflicts with physics requirements for the Tracker.
2. Although the vibration amplitude is proportional to the inverse of the square of the frequency, the amplitude is also a strong function of the coupling of the excitation with the structure's modes. To complicate the issue even more, the coupling of some modes is not critical while the coupling of other modes may be very critical; it depends on the location and direction of the vibration induced by the mode.

Although optimally the design should be purely based on vibration amplitude, a compromise must be accepted and modal analysis used to a large degree as a design criterion. As a general rule, ambient ground motion tends to be predominant in the 3 to 8 Hz range. Thus, it is typical to design accelerator machine structures to be above 10 Hz and preferably above 12 Hz. Since the Tracker has very tight stability requirements, even higher natural frequencies are needed. An important input comes from the environment, including pumps, motors and other sources, which might create noise at arbitrary frequencies. Hence, the spectrum of excitations above ground motion values will not be known, unless they have been measured. Another environmental aspect is that the Tracker sits at the centre of CMS, inside the Magnet/Muon system, the HCAL and the ECAL, which are structures that will selectively filter and possibly amplify specific frequencies.

It has been decided that the preliminary goal is to design the Tracker support structures with a minimum frequency of about 30 Hz, then estimate the vibration amplitude using Random Response Analysis, and finally compare the obtained amplitude with the design criteria to determine whether the safety factor is sufficient. Additional limitations will be set by the material budget and the production cost.

6.2.6 Structural materials

6.2.6.1 Environmental conditions

A good performance of the support structures, in terms of precision and stability, depends largely on the behaviour of the chosen materials in the environmental conditions inside the Tracker.

The parameters that will mainly affect these conditions are:

1. Temperature: the temperature range is around 18°C for the MSGC and −10°C for the Silicon and Pixel. The warm volume has 17 m^3, and the cold one has 7.5 m^3: temperature stabilisation on volumes of such large dimensions cannot be achieved to better than one degree. Variations of this order are able to generate displacements larger than tens of microns in metallic structures due to their generally large values of CTE.
2. Magnetic field: the superconducting solenoid of CMS will produce a magnetic field of 4 Tesla. Therefore, metallic components with magnetic properties should be avoided.
3. Humidity: in spite of having a control which keeps the dew point low enough to avoid condensation, *in situ* measurements performed on previous experiments have shown humidity variations between 20% and 80% depending upon atmospheric conditions [6-1]. Contrary to metals, which are insensitive to these variations, polymeric composites materials absorb moisture when exposed to high humidity environments. The amount of moisture absorbed depends on the fibre finish and on the resin properties.
4. Radiation: The very high luminosity at the LHC will generate a high radiation environment inside the detectors. The integrated radiation doses will be of the order of 10^3 to 10^7 Gy. These large doses can be reasonably withstood by a large majority of metals and by ceramic materials. On the other hand this effect can be very severe on several plastics. Nevertheless, a number of carbon and glass fiber reinforced thermosetting resins are available on the market with a radiation resistance up to 10^8 Gy, perfectly suited for applications in the LHC detectors [6-2].

6.2.6.2 Basic requirements for structural materials

It has been stressed in the previous sections that the support structures for the Tracker must in general satisfy the requirements of low mass and stability in time. More specifically, according to [6-1], an optimal material for a Tracker should fulfil the following criteria:

- Light (long radiation length, X_0) so the particle trajectories are unaffected;
- Stiff (high Young modulus, E) to minimise susceptibility to vibrations;
- Radiation resistant (Radiation Index, $RI > 6$);
- Insensitive to temperature variation (low Coefficient of Thermal Expansion, CTE);
- Insensitive to humidity variation (low Coefficient of Moisture Expansion, CME, and Moisture Absorption);
- Stable with time.

The mechanical design of the support structures puts the emphasis mainly on deflection rather than stress. Many sources of vibration will be present in the experimental cavern and will undoubtedly produce movements in the range of some microns. These movements are due to the ground motion (seismic), in the low frequency range, and to the noise created by ventilation, tubes and pumps, in the high frequency range. Therefore, it is important to optimise the structure's rigidity, which is directly proportional to the Young modulus. This consideration, together with the minimisation of multiple scattering, leads to the maximisation of the product EX_0, an expression depending only on material properties. Figure 6.2 shows a comparison of the values of EX_0 for some of the best representatives of materials available on the market [6-1].

The final selection must also take into account other major general engineering factors such as:

- Availability of the material;
- Technological limitations of the manufacturing procedures;
- Final cost of the manufactured parts;
- Safety problems.

Optimisation generally leads to the choice of materials with high specific modulus.

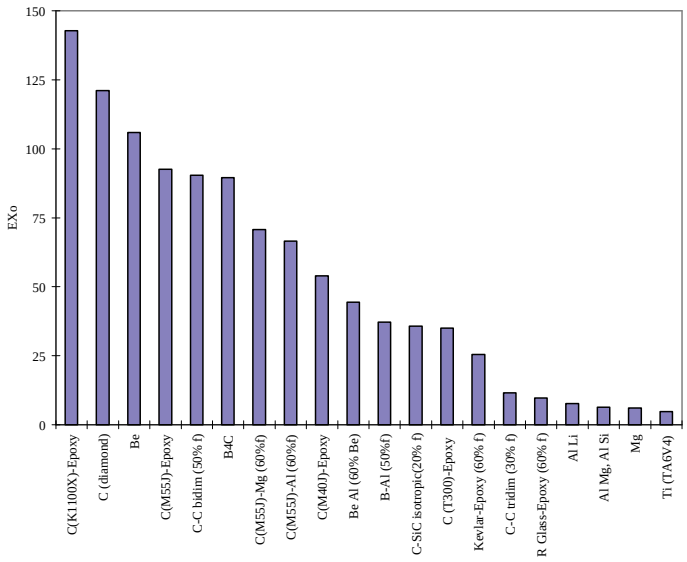

Fig. 6.2: EX_0 product for some materials (unidirectional properties are shown for composite materials) [6-1].

6.2.6.3 Material options

Metals

As is apparent from Fig. 6.2, most metallic materials are strongly penalised by their lower value of the product EX_0. However, due to the high thermal conductivity, good manufacturing properties and low cost, aluminium alloys may find applications in specific regions, where the requirement on X_0 may be relaxed. Also, particular components subjected to very high loads or to wearing of precision surfaces, may require the use of stainless steel.

Beryllium has a unique combination of properties that includes low density, high Young modulus, high strength and good corrosion resistance. The density of beryllium is 1.855 kg/m^3, making it the lightest structural metal except for magnesium. With a Young modulus value at room temperature of 290 GPa (in tension or compression), beryllium presents an exceptionally high stiffness-to-density ratio [6-3]. Unfortunately, major limitations to the use of beryllium include its extremely high cost, low ductility and high degree of anisotropy of structure and properties. Also, its use is not favoured on account of safety hazards during mechanical processing.

Carbon Fibre Reinforced Plastics (CFRP)

These composite materials, based on a polymeric resin filled with carbon fibres, offer high specific stiffness and strength and low thermal expansion.

They possess zero, or slightly negative CTE, in the axial (0°) direction. In the transverse (90°) direction, the CTE is positive and larger. All matrices of whatever type have positive CTE to some degree. Composites will exhibit CTE anisotropy in that the fibres cannot be placed in all orientations. The CTE can therefore be controlled in preferred orientations but not in others. The through-thickness CTE of cross-ply laminates will be positive [6-4]. When using polymeric matrices (resins) the moisture sensitivity of these materials has to be considered thoroughly. The swelling or shrinkage due to moisture results in undesired dimensional changes. The moisture absorption of pure resins ranges from almost zero to roughly 5% weight gain. The CME is increasingly deemed as an important parameter in defining the acceptance of a resin for a composite material. Newer generation of epoxies and the more recent cyanate esters have come

to prominence by offering low CME values. Nowadays, these two families are the most common polymeric matrix materials used for high performance CFRP. Both space-qualified epoxy resins and cyanate ester resins exhibit satisfactory properties of moisture absorption and radiation resistance. The properties of cyanate esters are in general better, but, on the other hand, they have the drawback of higher cost and of a more difficult manufacturing procedure (mainly due to a high sensitivity to moisture during the curing process).

As far as the reinforcing element is concerned, a wide variety of carbon fibres is available on the market. Depending on the particular application inside the Tracker and on the mechanical properties required, suitable materials may range from typical aerospace structural fibres, such as T300, to High Modulus (HM) fibres ($E_{fibre} > 400$ GPa), such as M40J, to Ultra High Modulus (UHM) fibres ($E_{fibre} > 600$ GPa), such as M60J. Also, high thermal conductivity fibres, like P75, P120 or K1100X (k_{fibre} ranging from 400 to 1100 W/mK) may find an application in the design of components particularly subjected to thermal loads. The enhancement of mechanical and thermal properties, from one class to the other, carries a sensitive increase in the cost of the fibre and in the complexity of manufacturing processes.

The combination of different resins and fibres produces a wide range of CFRP, which, in principle, could be designed to match optimally the requirements for the particular application. Furthermore, by optimisation of the laminate lay-up highly desirable properties can be adjusted. In addition to the above-mentioned advantages, the high radiation length of carbon fibres - which nearly matches that of beryllium - makes this material suitable for application inside the Tracker.

Metal Matrix Composites (MMC)

Compared to resin composites, the metal matrix confers to MMC good tensile strength, together with higher thermal and electrical conductivity and no moisture expansion. Compared to non-reinforced metals, carbon fibre reinforcement of metal matrices allows weight saving, higher rigidity, strength and dimensional stability. Magnesium and aluminium matrices seem to be the most promising. The advantages of MMC materials over organic matrix composites are:

- no moisture absorption;
- better transverse/longitudinal thermal conductivity;
- no out-gassing.

And over non-reinforced metals:

- coefficient of thermal expansion near zero;
- better specific modulus;
- lower density.

The factors that limit the usage of MMC include their higher density with respect to CFRP, high processing temperatures (due to a high melting point), reactivity with fibres and susceptibility to corrosion [6-5]. The fact that metal matrix composites are very new materials, combined with the complicated requirements involved in their structural applications and their high production cost, still presents an unacceptable uncertainty level for present engineering design. Thus, it is normally preferred to choose structural/mechanical parts from more traditional materials.

Ceramic/Inorganic Matrix Composites (CMC)

The main advantages of CMC are the relatively low, positive CTE of the matrices, coupled with their complete environmental stability (no moisture pick up, no out-gassing) and their high stiffness. Unfortunately, they are difficult to process because of the high temperature treatment required (above 1000 °C). Some realistic options for commercial developments rely on glass (e.g. borosilicate), Silicon carbide or carbon matrix composites.

Like MMC, CMC have not yet been used in significant quantities in large scale applications, and their technology is characterised by several drawbacks [6-6]:

- they are still rather costly;
- expertise in manufacture is limited;
- they are difficult to machine and fabricate;
- their micro-structures are very complex as are the failure mechanisms;
- mechanical and physical property data is lacking.

6.2.6.4 Conclusions

From the above considerations, one can infer that highly performing CFRP constitute the most suitable class of structural materials for applications in the Tracker. The choice between a typical aerospace structural composite, or a more sophisticated (HM, or even UHM) material, depends on the particular requirements and on the relative importance of the item to be designed.

In general, the number, as well as the orientation of the plies that form a CFRP laminate is chosen in order to meet the design criteria. It is often possible to orient the fibres of the different layers in such a way that the properties of the material become nearly the same in any direction: these laminates are referred to as Quasi-Isotropic Laminates (QIL). For any family of CFRP, QIL represent the minimum performance we can expect from a composite laminate. So these laminates can be used as the starting point of optimisation of ply orientation. On the other hand, when minimum weight is an important criterion, QIL should be the upper bound of the weight. An optimised material, taking full advantage of the directionality of CFRP properties, can only have lower weight than the QIL configuration. Nevertheless, one must carefully consider whether to use an optimised lay-up, or even a unidirectional laminate. For instance, the attractive feature of designing a mechanical component with near-zero CTE in a preferred direction, might be balanced with the risk of internal stresses in the laminate and with the possibility of a transverse swelling, with respect to the fibre orientation, due to anisotropy of CME. Furthermore, off-the-shelf materials are always preferable, whenever possible, to an optimised theoretical solution.

In addition to CFRP, as previously stated, high-performing aluminium alloys may also find place for application in some mechanical components, whenever their position in the detector allows the criterion of minimisation of EX_0 to be relaxed, or they must be designed with a particurlarly complex shape. Stainless steel will only be used for the support brackets, which sit outside the Tracker volume, and for the rails for the MSGC insertion, which are subject to surface wear and local stress concentration through the action of the chariots. These rails are removed after MSGC installation.

6.2.7 The central support tube

6.2.7.1 General concept

The Central Support Tube (CST) is the main support structure for all the Tracker detectors. It has a length of 5740 mm and its inner and outer radii are 655 mm and 675 mm, respectively. The design concept relies on the principle of using one single structural component, which holds in place the Tracker components and to which their relative position in space is referred. The CST is located at the interface between the Silicon and the MSGC detectors, assuming that the former is supported by a slide or rail system on its internal surface, and the latter on its external one. Therefore, installation, positioning and fixation systems are placed on both the inner and outer surfaces of the wall of the CST. The required high positioning precision of the detectors relies just on the fixation points. This allows the manufacturing tolerances on the whole tube to be relaxed, which then has to satisfy only standard geometrical requirements, and at the same time reduces the manufacturing cost. The slides for the Silicon detector insertion are positioned in the bottom part at $\pm$ 30° from the vertical, while the MSGC rails are fixed in the horizontal

plane (0° and 180°). The assembly of the CST, composed of one tube and two endflanges, is shown in Figs. 6.3 and 6.4. The endflanges are disks with an inner radius of 675 mm and an outer radius of 1165 mm, and can be disconnected into two half-disks. They transfer the load of the Tracker to the HCAL barrel by means of two support brackets per side, positioned on the horizontal plane. Considering that the main structural requirement for the CST is to achieve an optimal compromise between high rigidity and a low impact on the material budget, a high modulus CFRP (M55J) has been selected as the base material for manufacturing.

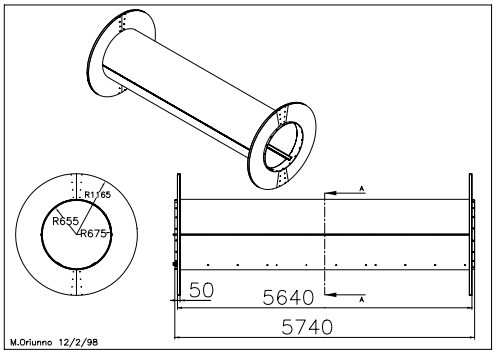

Fig. 6.3: The CMS Tracker Central Support Tube (CST).

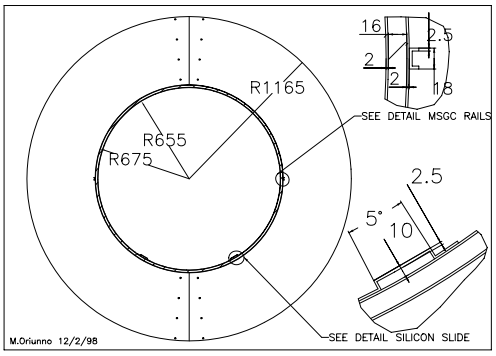

Fig. 6.4: Detail of a CST endflange and of the installation systems for MSGC and Silicon.

Different technologies can be adopted to build the CST: e.g. honeycomb sandwich structure, or skeletal frame sandwich structure. The basic mechanical properties of the structure will not be strongly dependent on the particular manufacturing technology adopted: the final decision will be taken together with the industrial partner chosen for the production and will largely rely on cost considerations.

The choice of a Tracker general support structure positioned between the Silicon and the MSGC volumes has been thoroughly discussed in Refs. [6-7] and [6-8], and has been found to present several advantages:

- It provides a natural positioning reference between the Silicon and the MSGC Tracker in the critical region of the gap between the two volumes, improving the ability of combining the track segments reconstructed separately by the two detectors.
- It allows the radial gap between the outermost layer of MSGC and the crystals of the ECAL barrel to be minimised.
- It minimises the installation clearance of the Silicon volume inside the MSGC detector.
- It optimises the use of space and material in the gap between the cold and the warm volume, where a structural and thermal separation is needed in any case.

6.2.7.2 Loads and constraints

The CST is held in the horizontal plane by two brackets on each side, which link the CST to the HCAL barrel. The loads acting on the CST (Table 6.1) are the weight of the MSGC detectors on the outer part, which are held on the horizontal plane, and the weight of the Silicon volume (Silicon and Pixel detectors) on the inner part, which is held by two guides positioned at ±30° to the vertical.

The load of 230 kg, due to the weight of the CST and its endflanges, has been introduced into the F.E.A. analysis via their mass density.

Table 6.1: Tracker weight breakdown

	Weight [kg]
Beam pipe	7.8
Pixel	34
Silicon barrel	133
Silicon endcaps	170
Silicon routing services	490
Silicon tube	40
Thermal shield	35
MSGC barrel	617
MSGC endcaps	376
MSGC routing service	368
Endflanges	60
Central support tube	170
Total weight	2500

6.2.7.3 Finite Element Analysis (F.E.A.)

A finite element calculation has been performed on the CST using the F.E.A. code ANSYS 5.3. As a manufacturing baseline, the honeycomb sandwich technology has been assumed both for the cylinder and the endflanges. The cylinder has a total thickness of 20 mm and two 2 mm skins with a M55J carbon fibre lay-up that provides isotropic mechanical characteristics (Table 6.2). Each endflange has a total thickness of 50 mm and two 2 mm skins, as for the cylinder, but a standard aerospace CFRP (T300/Epoxy) is used. In the ANSYS code, the four-node SHELL63 element allows the modelling of sandwich shells and provides results of good accuracy. The brackets are simulated by constraining all the degrees of freedom of two nodes of the endflanges in the horizontal plane (Fig. 6.i).

Table 6.2: Equivalent mechanical characteristics of the isotropic lay-up used in the analysis

	Young modulus [GPa]	Poisson modulus	Shear modulus [GPa]
M55J/Epoxy	110	0.31	42.307
T300/Epoxy	60	0.30	23.076

6.2.7.4 Results

The maximum global displacement of the CST, under full load, is 0.395 mm at the middle of the tube (Fig. 6.iii). This value can be regarded as satisfactory.

The global deformation of the CST is the sum of the global bending of the tube as a beam and of the local deformation of the circular section. The latter is more pronounced, since the flexural bending beam rigidity of the CST is quite high. The use of circular frames can drastically decrease the total displacement, but causes radial space consumption (in a critical region) and further complications from the installation point of view. Further calculations have shown that there is no advantage in using high modulus CFRP for the endflanges.

6.2.8 The endflanges

The Tracker endflanges are important elements, to which several tasks are assigned:

– structural support of the CST;

– feedthrough of services coming from the cold volume;
– gas tightness of the cold volume;
– support for fanning out the Silicon and Pixel services;
– connection to Pixel service tubes;
– support for the beam pipe.

In the region of the endcap MSGC the endflanges serve structural purposes: in this region they are made of a sandwich structure, with two CFRP skins, 2 mm thick, and aluminium honeycomb for a total thickness of 50 mm. Each endflange is produced in two halves that are located by means of precision pins and mounted on the cylindrical shell of the CST.

In the region of the Silicon endcap detectors the endflanges do not serve as supporting elements for the Tracker. Here they are made of sandwich disks 50 mm thick, with a thermal insulating foam as a core, in order to complete the thermal enclosure of the Silicon volume. The external ring (R = 550 mm to R $\approx$ 655 mm) carries the encapsulated feedthrough blocks for the Silicon detector services. The internal portion is removable, to allow access to the Silicon services during maintenance, and to permit the *in situ* installation of the Pixel detector. The design of the connection flange between the two portions will ensure a complete seal after their assembly. A sealing element will also be present at the innermost edge, surrounding the beam pipe, to prevent moisture infiltration inside the cold volume. The skins of this innermost part of the Tracker endflanges are designed to hold some structural arms for the beam pipe support.

A side view of the main elements of an endflange is shown in Fig. 6.5.

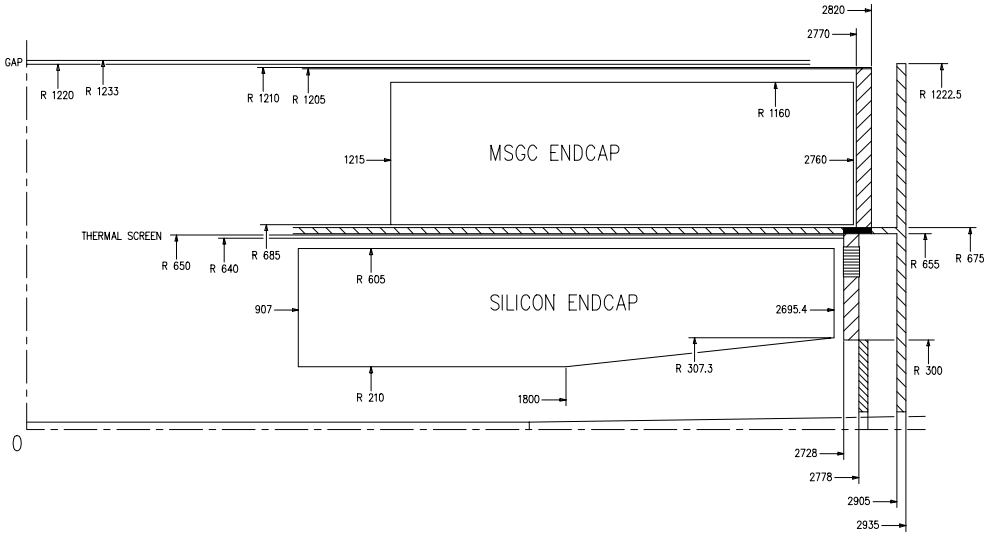

Fig. 6.5: Schematics of the Tracker endflange region.

6.2.9 Tracker support brackets

6.2.9.1 General concept

The weight of the Tracker is initially taken by the Central Support Tube, which then transfers the load, via the endflanges, to the massive iron plates of the HCAL barrel. Two support brackets per side connect the endflanges to the HCAL barrel, occupying 2 of the 18 sectors reserved for the Tracker in this region. Since the HCAL barrel is supported by the Cryostat Vacuum Tank on two rails positioned on the horizontal plane, the Tracker support brackets are also placed in the horizontal plane, in order to improve the load transfer between the detectors. The

brackets must be housed in the crack between the barrel and the endcap part of the experiment, where the Tracker services also have to be routed. Therefore, severe space limitations influence their shape. A drawing of one support bracket, indicating the main dimensions, is shown in Fig. 6.6. Because of its complex shape and critical loading (dominated by shear and torque) this component will be made of stainless steel. However, the crack region is not critical as far as the material budget is concerned. In order to minimise the error in positioning and to correct for possible long term global displacements of the Tracker with respect to the Muon Link System, a fine-tuning positioning system can be interposed between each bracket and its attachment on the HCAL barrel.

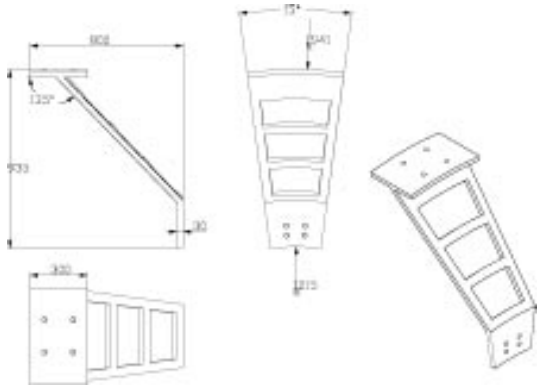

Fig. 6.6: Sketch of one support bracket.

6.2.9.2 Finite element analysis

Taking into account the geometry and the loading conditions, the bracket may be viewed as a highly loaded beam, not subjected to local deformations comparable to the material thickness. Thus, the structural analysis may be fully carried out in the linear elastic field. F.E.A. calculations have been performed with the code Pro/Mechanica, which has the advantage of a full integration inside the 3-Dimensional CAD Pro/Eng, used to model and optimise the shape of this component. The load applied on the surface of the bracket joined to the Tracker endflange is 6250 N (1/4 of total Tracker weight), while all the degrees of freedom have been constrained on the nodes of the surface attached to the HCAL barrel. The results are shown in Fig. 6.iii and indicate a maximum displacement of 0.1 mm.

6.2.10 Beam pipe and Pixel detector support

6.2.10.1 General characteristics

On each side of the Interaction Point, the Tracker general support structure provides 3 to 4 supports to the central section of the beam pipe through specific structures, to which tensioned stainless steel wires are attached. One rigid and stable support per side must also be provided for the Pixel detector: this feature is incorporated in the same structure that provides the innermost attachment point for the beam pipe.

Since the beam pipe has to be made with the minimum amount of material it will be very fragile after the vacuum is established. In order to reduce the stress in the pipe to acceptable levels, several supports are needed inside the Tracker. Tentatively, these are foreseen at the end of the Silicon barrel ($z = \pm 881$ mm), in the Silicon endcap region ($z = \pm 1910 \div \pm 2425$ mm) and at the end of the Tracker ($z \approx \pm 2900$ mm). In addition, in order to mechanically decouple the

central section of the beam pipe from the CMS endcaps, which will move when the magnet is switched on, structures extending out from the Tracker are designed to provide support points at $z = \pm 4000$ mm. A summary view of the location of the beam pipe support structures is sketched in Fig. 6.7. A description of the proposed design of the central section of the beam pipe is given in Section 6.6.

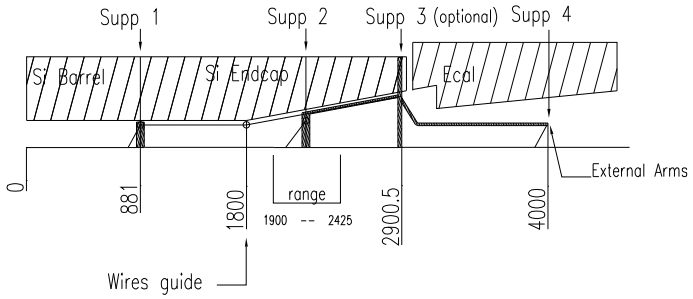

Fig. 6.7: Sketch of the location of the supporting structures.

The position of the inner support point is dictated by the admissible stress in the beam pipe wall and by the length of the Silicon barrel. The position of the external support is fixed by the requirement of providing a beam pipe segment 1 m long, outside the Tracker, free from any supporting device, in order to permit the *in situ* installation of the Pixel detector. The axial position of the intermediate support will be determined during the final design phase of the beam pipe by a compromise between different requirements:

- direct accessibility to the support from outside;
- maximum allowed stress value in the beam pipe wall;
- mechanical stability of the beam pipe under vacuum conditions.

The possible presence of the support positioned at the end of the Tracker depends on the position of bellows placed outside the Tracker, in order to provide structural decoupling between the central section and the rest of the beam pipe. Indeed, it will be only needed if the bellows are positioned between the Tracker endflange and the outer support.

Each wire runs from the beam pipe to a point of suspension (some of them at a small angle with respect to the plane perpendicular to the beam axis), then it is engaged in a pulley, by which it is deflected axially along the shell between the Silicon and Pixel detectors

All supporting structures are designed to allow for the passage of a maximum of four wires equally spaced azimuthally, in order to be adaptable to the stabilisation requirements of the beam pipe. During the *in situ* installation of the Pixel detector only two vertical wires (one up and one down) will be in place. All the wire connections must be demountable to allow for a possible *in situ* removal and reinsertion of the central segment of the beam pipe. The demountable connection may be located either at the pulley level, or at the attachment point on the beam pipe surface.

The supporting structures have been designed so as to have a maximum vertical displacement of the order of 0.1 mm under the worst possible combination of nominal loading conditions. These conditions take into account:

- the weight of the central section of the beam pipe;
- the tension in each wire to provide mechanical stability to the beam pipe;
- the effects induced by a possible lateral displacement in the universal expansion joint (assumed maximum displacement ± 5 mm);
- the effects induced by a possible axial displacement of the beam pipe during the installation and vacuum conditioning phases (assumed maximum displacement of 10 mm).

The critical load assumed is the one resulting from an unforeseen high load accidentally applied to the beam pipe from the outside (typically during a maintenance phase). It is preferable, in this case, to preserve the integrity of the Tracker structure and to accept the breaking of some supporting wires. This leads to the design criterion that the supporting structures must be able to withstand the breaking load of the wires, with a safety factor between 1.5 and 2, without suffering any permanent damage, rupture or plastic deformation.

6.2.10.2 The inner support

The tasks of supporting both the most fragile section of the beam pipe and the whole Pixel detector are merged in the complex inner supporting structure, shown in Fig. 6.8. One CFRP ring structure, supporting the pulleys at R $\geq$ 210 mm, is positioned on each side of the Silicon barrel detector. A CFRP cylindrical shell (R = 210 mm, thickness = 1 mm) connects the two rings together, providing to the ensemble the rigidity of a closed structure, while keeping the Silicon and Pixel volumes separated. On the top and on the bottom of the shell, two CFRP planes (1 mm thick) are attached, on which the rails needed for the insertion of the Pixel detector are fixed: these planes also provide the final support and reference position for the Pixel detector. Two arms connect each ring to the Tracker CST, thus avoiding any direct contact between this supporting structure and the Silicon barrel structure.

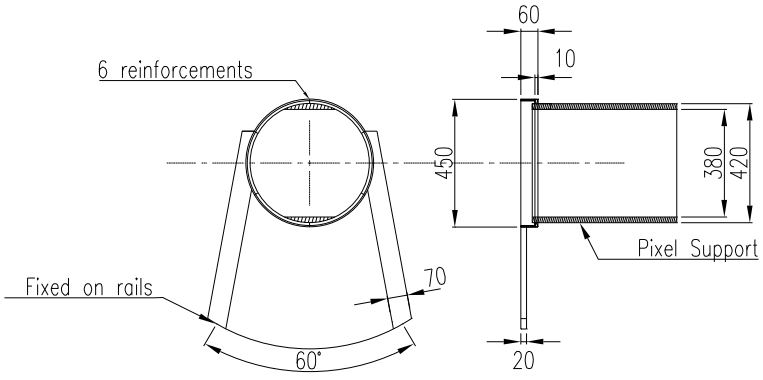

Fig. 6.8: One half of the inner support for Pixel and beam pipe.

To optimise space consumption in the critical transitional zone between the Silicon barrel and the Silicon endcap, the support is designed to stay inside the envelope of the Silicon barrel: the rings are located in the region of the mini endcaps, while the connecting arms use the same space reserved for the radial routing of the barrel services. The support slides over the internal slides of the CST (also used by the Silicon detector elements) and is always inserted and removed together with the Silicon barrel.

F.E.A. calculations show that the maximum expected static deflection of the Pixel supporting region is as low as 0.04 mm. At the beam pipe attachment locations, which are structurally not dependent on the deformation of the Pixel support, the relevant result is that of the vertical displacement (U_y). It is important to guarantee a similar deformation in all the attachment points, in order to prevent unwanted deflections of the beam pipe. Thus the ring structures have been designed to provide a vertical displacement under critical loading conditions $U_y = 0.11$ mm, homogeneous with that of the other supports. The deformations calculated with F.E.A. over the complete model are shown in Fig. 6.iv.

6.2.10.3 The intermediate support

The baseline design of the intermediate support is a ring (CFRP, rectangular cross section 30×30 mm^2, 1 mm wall thickness), connected to the Silicon volume endflange by a conical shell (CFRP, 6.2° aperture, 0.5 mm thickness). The pulleys are attached to the ring. The actual length of the conical shell will depend on the definition of the beam pipe support point position. During *in situ* installation of the Pixel detector, only the vertical wires are kept in place, while the lateral ones are disconnected. Should the lateral pulleys, which protrude slightly from the ring envelope, interfere with the operation, they may be removed and put back in place after the Pixel detector has been installed.

Figure 6.9 shows a drawing of this structure. Calculations have been performed for the (conservative) case of the presence of the additional beam pipe support in the endflange plane. Also, the most critical of the nominal loading conditions has been selected, i.e. the situation in which, during Pixel insertion, the lateral wires are removed and the forces needed to stabilise the beam pipe act only on the vertical attachments. Even under these conditions, the maximum vertical deformation, visualised in Fig. 6.v, remains in the 0.1 mm range. The results of a parametrical analysis show that within the range of interest the vertical deformation is independent of the length of the conical shell.

6.2.10.4 The outer support

In order to provide an external support for the beam pipe, 1 m outside the Tracker, but still held in place by its endflanges, a cantilevered structure is attached to the Silicon endflange. This structure is designed to have no interference with the routing path of the Silicon services and with the alignment ring, and to respect the requirement of a clearance of 50 mm to the surface of the Preshower. The outer support is basically needed to perform the *in situ* installation of the Pixel detector, which requires a 1 m long section of the beam pipe free from any supporting structure in front of the Tracker.

A sketch of the outer support is represented in Fig. 6.10: the four arms, protruding from the Silicon endflange, hold at their ends a ring, to which the beam pipe connecting wires are attached. Several design options are feasible, and the final choice will largely depend on the final design of the central section of the beam pipe. In the example shown, two strong CFRP beams (square cross section 50×50 mm^2, wall thickness 5 mm) provide the main support to the beam pipe during Pixel installation. After completion of the Pixel cabling, two lateral CFRP beams (full rectangular cross section 50×2 mm^2)are added for stabilisation. For the calculations, the Silicon endflange structure has been assumed to be a 50 mm thick sandwich plate, with 2 mm CFRP skins.

Calculations have been performed on different configurations, in order to allow for a possible evolution of the beam pipe design. The results are generally satisfactory, typically providing a maximum vertical displacement $U_y \leq 0.11$ mm. A typical output is shown in Fig. 6.vi. The analysis of the deformation shows that the dominant part of this displacement comes from the local deformation of the endflange surface: thus, an increase of the thickness of the sandwich skins in this (non-critical) region might possibly lower the vertical displacement at the beam pipe attachment point, if needed.

6.3 General Tracker Services

6.3.1 Overview

All Tracker services enter or leave the Tracker volume through the endflanges. The distribution is symmetric with respect to the interaction point, which means that exactly the same quantity

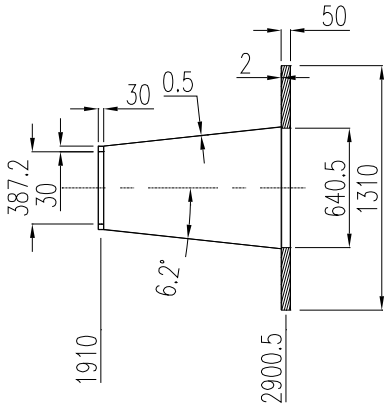

Fig. 6.9: The intermediate beam pipe support.

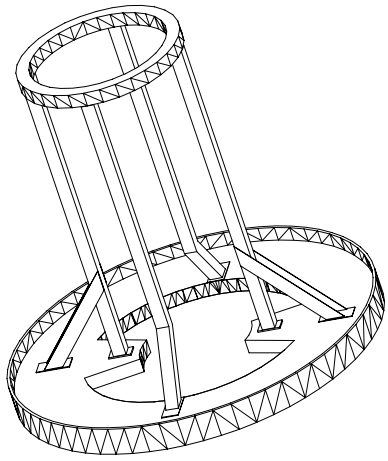

Fig. 6.10: Example of possible design of the outer support for the beam pipe.

of cables and pipes must be accomodated at the $+z$ and $-z$ endflanges. An overview for the services at one end of the Tracker is shown in Fig. 6.11. The total number of connections at each end of the Tracker is given in Table 6.3.

The final configuration of the patch panels still needs to be decided, however, space is reserved in 2×16 locations in front of the HCAL barrel to house most of the connections. These locations will be equipped with the main Tracker patch panels, which have to share the volumes with connections for the ECAL. The patch panels can only be designed once the final quantity of services for ECAL as well as for the Tracker have been determined.

Table 6.3: Total amount of connections at each end of the Tracker

Cooling pipes	250
Gas pipes	160
Low voltage	2500
High voltage and bias	240 (each with 56 individual lines)
Optical readout	450 (each with 64 individual lines)
Internal control	30 (each with 64 individual lines)
DCS control	75 (each with 56 individual lines)

6.3.2 Cabling

In this section we consider all power lines, all bias and high voltage lines and all detector control lines.

We distinguish four main sections for the routing of cables:

- inside the Tracker volume;
- from inside the Tracker volume to the main patch panels;
- from the main patch panels to the underground control rooms (USC55);
- inside the underground control rooms.

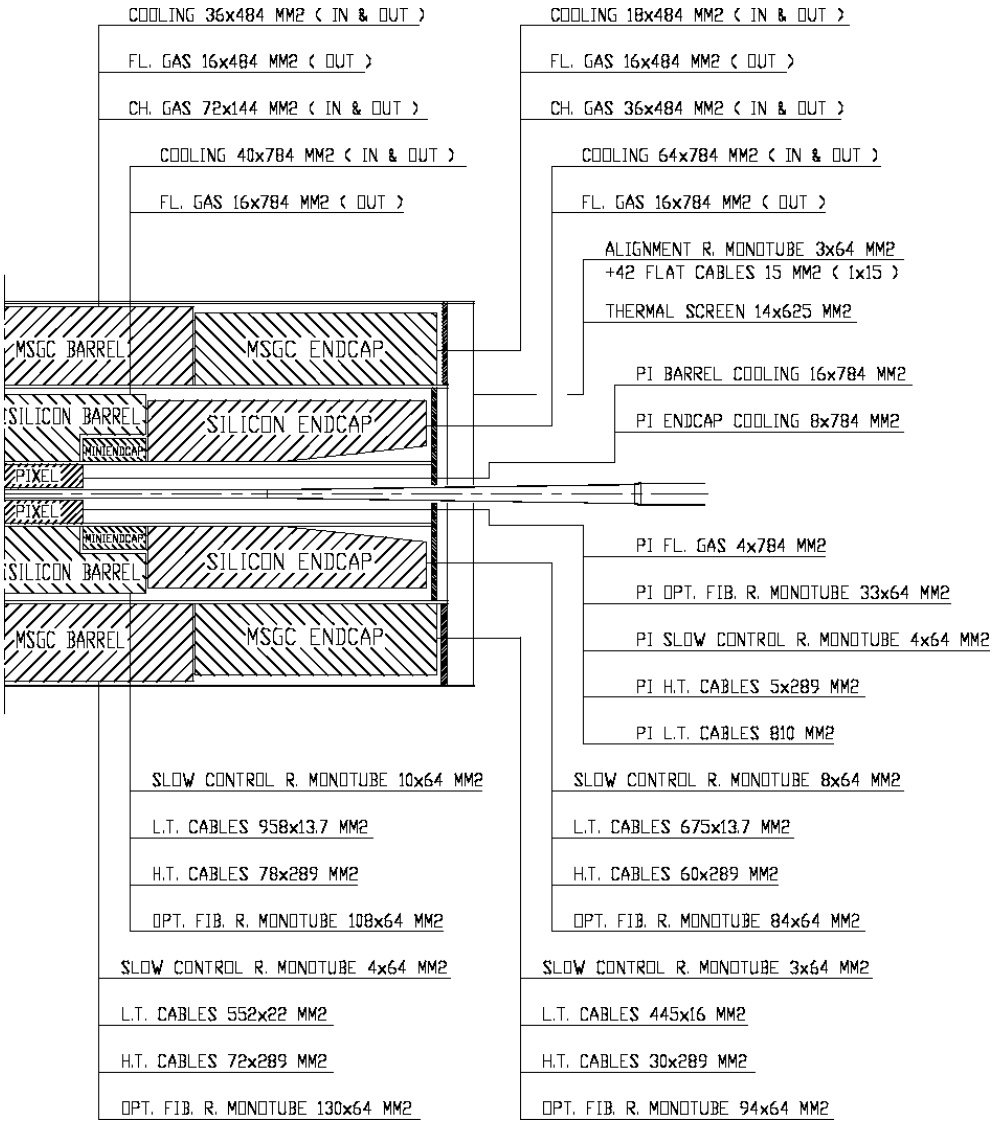

Fig. 6.11: Global summary of Tracker services.

The Tracker internal cable routing for the Pixel detectors makes use of individual service cylinders for the barrel and endcaps. These cylinders are placed inside the nominal Pixel radius of 190 mm and connect the detectors to the Tracker endflange. At the endflange a second connection is foreseen.

The Tracker internal cable routing for the Silicon and MSGC detectors has been designed using the same guidelines. In the barrel detectors all cables are routed along the z axis on individual supporting elements and then radially outwards over the barrel endflanges. At the outer subdetector radius the cables are then routed towards the Tracker endflanges. The services for the endcap detector planes are routed outward on each individual plane and then parallel to the barrel cables towards the endflange (see Fig. 6.12).

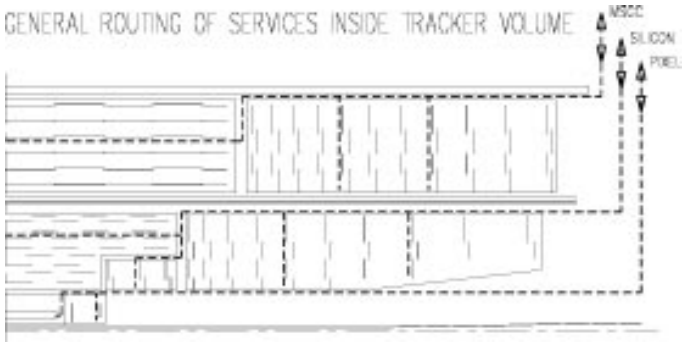

Fig. 6.12: Cable layout inside the Tracker.

The global arrangement is symmetric by grouping the services in 18 sectors where every second sector is reserved for barrel or endcap detectors, respectively, as shown in Fig. 6.13 for the MSGC detector and in Fig. 6.14 for the Silicon detector. Particular care has been taken in order not to obstruct the space in the r–ϕ range reserved for the supporting slides and rails and for the alignment channels.

From the endflange all cables are routed towards the 2×16 main patch panels in front of the HCAL.

Only well protected cables will be used behind the main patch panels. In order to connect the patch panels to the electronics and power supplies inside USC55 we follow the guidelines of the CMS integration teams. The cables are passed through the HCAL 53° crack and then along the inside of the coil in 18 sectors, symmetric on both detector ends. On the outside of the coil they are regrouped into eight super sectors which are routed towards magnet wheel number zero. On wheel zero they are passed radially outward through the Muon chimneys in a staggered way in order to respect the access conditions for the central Muon chambers. Outside of the CMS magnet all cables are then routed through the three service galleries towards the control room.

The detailed layout of the cabling inside the underground control room USC55 has not yet been designed.

6.3.3 Cooling

Four independent cooling systems are foreseen. Three of them are reserved for the individual subdetectors, and the fourth serves the active separation of the different temperature volumes. The principle for all four systems is based on pressurised liquid circuits. The type of liquid has to be chosen according to the subdetector requirements.

No final decision has been taken on the type of fluids. However, excellent candidates are at hand and are being presently tested in the context of the milestone projects. Although the layout of the cooling loops at the detector level is already well understood, the final layout of the

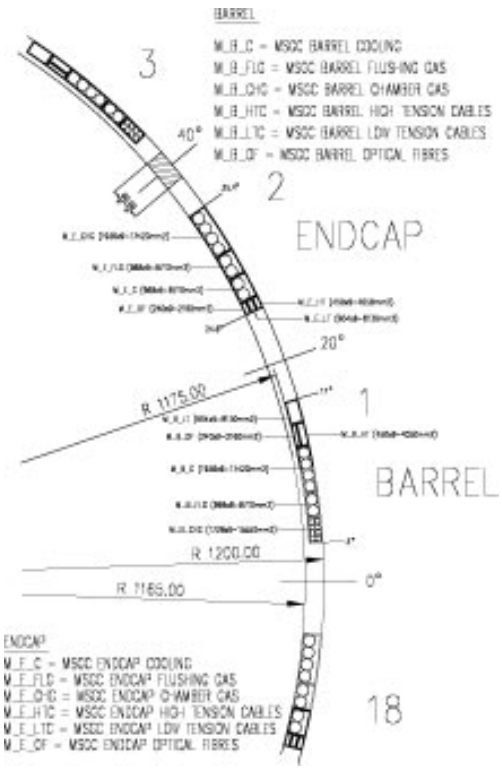

Fig. 6.13: r–ϕ layout of the services at the MSGC level in the endcap region.

secondary cooling loops including reservoirs, filters, pumps and heat exchangers is still under evaluation. The primary cooling loop will be designed in collaboration with the other CMS subdetectors and the integration teams.

The power dissipation breakdown for the full Tracker is given in Table 6.4 and the details for the individual systems at the detector level are given below.

Table 6.4: Breakdown of the power dissipation inside the Tracker

Subdetector	Power dissipation [kW]
Pixel barrel	2.0
Pixel endcap	1.0
Silicon barrel	16.2
Silicon endcap	14.3
MSGC barrel	13.0
MSGC endcap	14.9
Thermal screen	7.0
TOTAL	68.4

6.3.3.1 Pixel cooling system

The total power to be removed by the cooling system is about 3 kW. The temperature of the volume of active detector elements should be $-10°$C. A pressurised liquid system is under design which allows the removal of heat in an efficient way. Turbulent flow is needed with a total pressure drop not exceeding 1 bar. Three independent cooling circuits will be needed, one for the barrel and one for each of the two endcaps. They will be of the same type as the ones proposed for the Silicon detector.

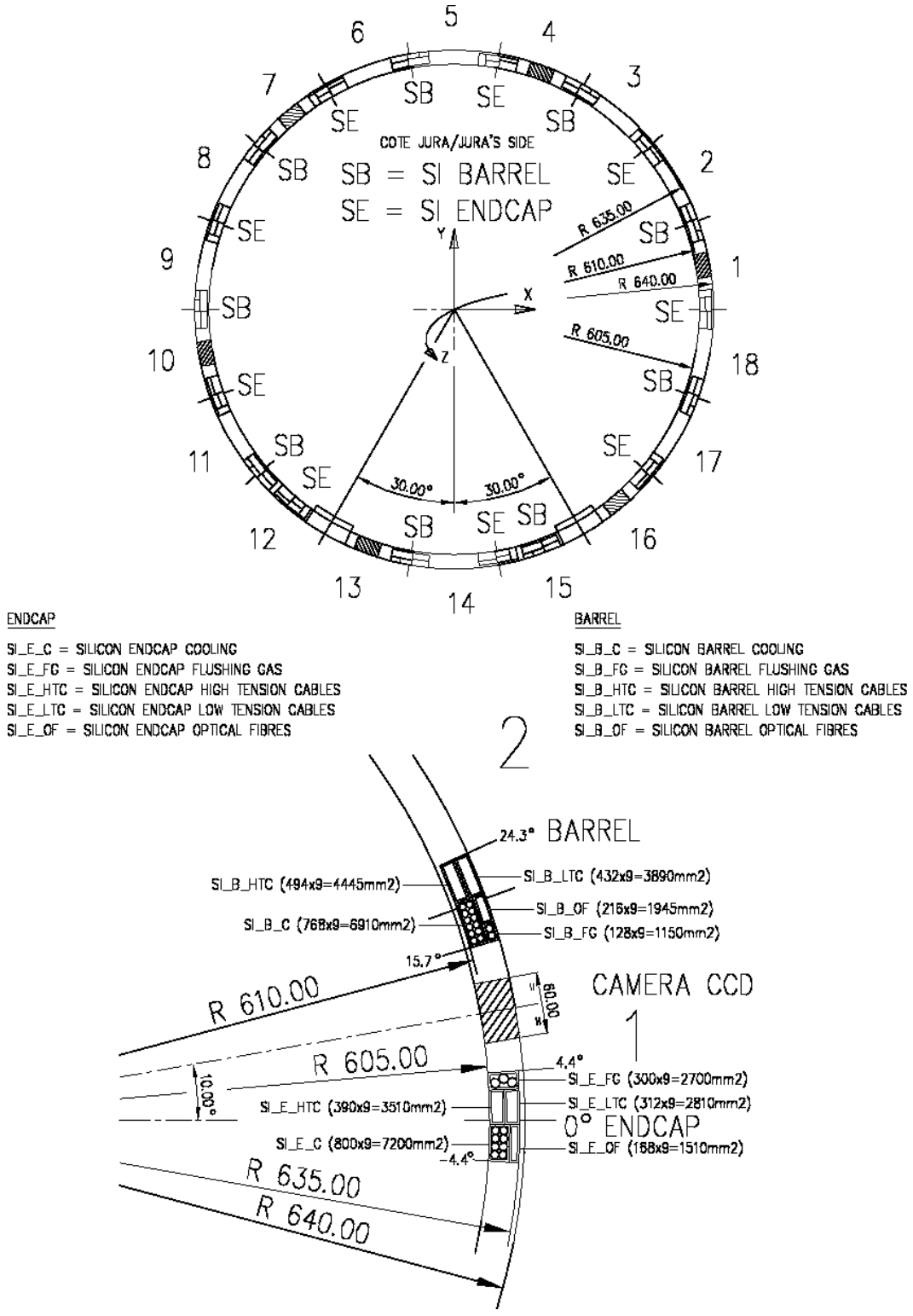

Fig. 6.14: r–ϕ layout of the services at the Silicon level in the endcap region.

The Pixel barrel detector will be supplied by 8 inlet and 8 outlet stainless steel pipes per end, each of them with an inner diameter of 10 mm. Close to the detector there will be a transition to 16 inlet and 16 outlet pipes with an inner diameter of 6 mm. These pipes are made of aluminium and connect to smaller aluminium pipes forming the main part of the barrel support structure. Each of the Pixel endcaps will be supplied by one inlet and one outlet stainless steel pipe, each of them with an inner diameter of 10 mm. Close to the detector there will be a transition into 8 inlet and 8 outlet pipes for each endcap. These pipes are made of aluminium with an inner diameter of 5 mm.

6.3.3.2 Silicon cooling system

The motivation and requirements for the Silicon detector cooling are discussed in Chapter 3. The layout of one cooling circuit is shown in Fig. 6.15, an example taken from the forward Silicon detector.

The supply circuit for the cooling of the barrel detector consists of 20 pipes for the inlet and 20 for the outlet on each end. The proposed pipes are made of PEEK, with an external diameter of 10 mm and a wall thickness of 1 mm. These pipes are connected to manifolds on the endflanges of the barrel, in order to distribute the coolant to the internal aluminium pipes, of smaller diameter, embedded in the supporting structure.

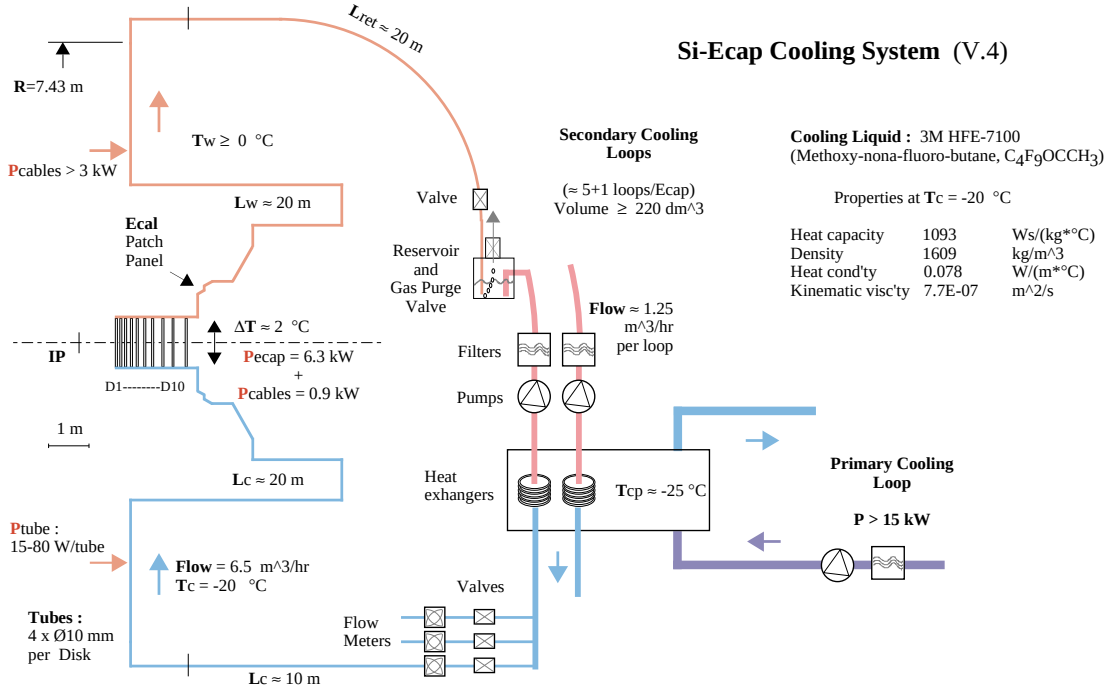

Fig. 6.15: Silicon endcap cooling layout.

The fine distribution of coolant inside the Silicon endcap disks is entrusted to aluminium manifolds positioned along the rings. On each disk, 4 inlet and 4 outlet pipes connect the manifolds to the supply circuit. Thus, the total number of coolant supply lines for the Silicon endcap detector comprises 40 delivery lines and 40 return lines per end. PEEK pipes, 8 mm diameter with a wall thickness of 1 mm, are proposed.

6.3.3.3 MSGC cooling system

Cooling requirements and heat loads

The MSGC Tracker is assembled, transported and operated at room temperature. During operation in CMS, the temperature will be kept constant to minimise gain variation in the chambers and thermal deformation of the structures. The operational temperature is 18±5 °C.

The main heat sources inside the detector are the front-end electronics (some 65% of total power), the control electronics and the optical links. The high-voltage power losses are only some 2–3% of the total. The heat dissipation in the whole MSGC system is 28 kW (13 kW in the barrel, 15 kW in the endcap).

A substantial amount of heat is also dissipated in the low voltage power cabling: 5 kW in the whole MSGC system.

Choice of coolant

Due to the high power dissipation in the detector, any gas-based cooling will not be sufficient since it would require too high flow velocities. Liquid cooling has to be adopted.

The operating temperature of the MSGC Tracker, 18 °C, allows the use of water that has, in the liquid state, a heat capacity about 4 times higher than other common liquid coolants. However, since water presents some safety problems in case of leaks, we consider also the use of alternative inert coolants. Fluorinert liquids, like C_5F_{12}, would be a proper choice regarding safety in case of leaks, but they are very expensive. Therefore, for reasons of cost, the MSGC cooling system makes use of water as coolant but, since the pipe specifications are the same for both water and fluorinert liquids, the possibility of adopting the safer solution later remains open.

Cooling circuitry

The cooling circuitry is subdivided into 54 segments, of which 36 serve the MSGC barrel (18 segments each end), and 18 serve the endcap MSGC (9 segments each end). Each of the 54 segments is an independent unit that can be operated in stand-alone mode.

The distribution system is actuated outside CMS, close to the location where valves and controls are placed. Pumps, heat exchangers, flow-meters, and control valves are situated in the side cavern. Inside UXC55 there are only pipes and temperature and humidity probes for each cooling segment. The schematic of one cooling segment is shown in Fig. 6.16.

Inside the Tracker the coolant is distributed within each cooling segment by a collector pipe that runs from the Tracker services patch panel to the detector (Fig. 6.17).

Each barrel rod and endcap detector module is cooled by a local cooling pipe (see Section 4.4.2.3 and 4.5.3.1). To minimise temperature differences in the system the local cooling pipes within a cooling segment are parallel to each other. For a uniform distribution of the coolant it is necessary for impedance of the local cooling pipe to be much higher than that of the feeding/manifolding pipe. The pipe dimensions were optimised by computation and then verified with dedicated tests.

The local pipes are of a thin-walled stainless steel. This choice allows effective heat removal without excessive amount of material (in terms of X_0, 70 μm wall thickness of SS is equivalent to 350 μm of Al). Stainless steel offers good reliability for long-term operation and easy fabrication. Plastic pipes are used in the feeding system inside the Tracker to reduce the amount of material and to improve pipe flexibility when assembling and mounting the detector. Outside the Tracker standard metallic pipes will be used.

The specifications of the cooling pipes in the barrel and endcap MSGC regions are summarised in Tables 6.5 and 6.6.

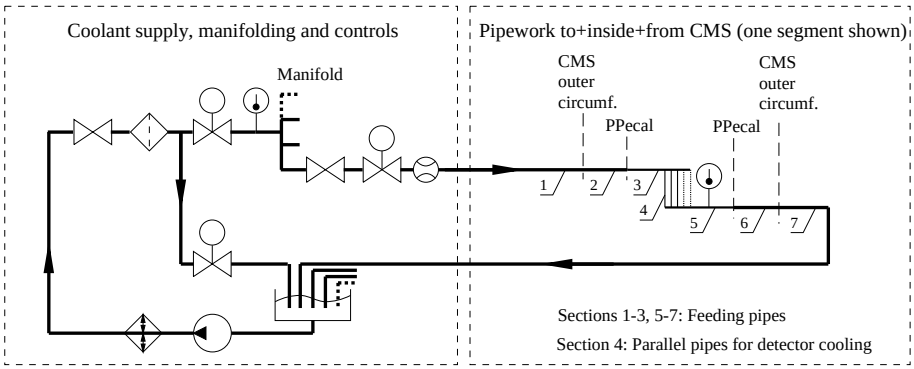

Fig. 6.16: Schematic of the MSGC cooling circuitry.

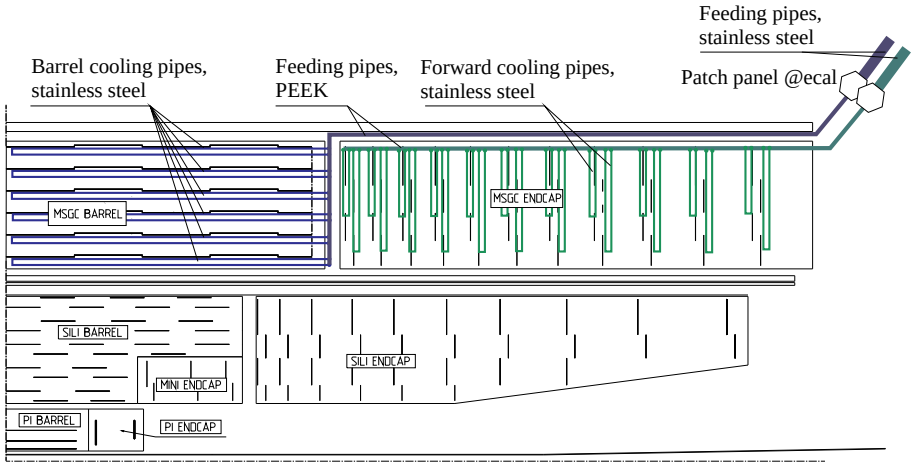

Fig. 6.17: Side view of the Tracker showing the feeding of the local MSGC cooling pipes.

Table 6.5: Dimensions and types of pipes in one segment of the MSGC barrel cooling circuitry

Pipe sec. No.	Descr.	No./ one seg.	Inn. diam. [mm]	Out. diam. [mm]	Wall mat.	L [m]	Re No	Flow speed [m/s]	P. drop [mbar]	Vol. of liq. [dm^3]
1	In. pipe up to CMS	1	12	14	SS	100	6300	0.64	598	11.31
2	In. pipe inside CMS up to PPecal	1	12	14	SS	14	6300	0.64	84	1.58
3	In. pipe, from PPecal to rods	1	8	9	PEEK	5.1	9300	1.4	209	0.25
4	Rod pipe (16 to 25 pipes parallel in one segment)	20.4	1.86	2	SS	2.5	1800	1.2	260	0.14
5	Out. pipe runs from rods to PPecal	1	8	9	PEEK	5.1	9300	1.4	209	0.25
6	Out. pipe inside CMS from PPecal onwards	1	12	14	SS	14	6300	0.64	84	1.58
7	Out. pipe from CMS onwards	1	12	14	SS	100	6300	0.64	598	11.31
Total	Segment								2041	26
Total	Barrel									952
Total	Barrel in Tracker									23

Table 6.6: Dimensions and types of pipes in one segment of the MSGC endcap cooling circuitry

Pipe sec. No.	Descr.	No./ one seg.	Inn. diam. [mm]	Out. diam. [mm]	Wall mat.	L [m]	Re No.	Flow speed [m/s]	P. drop [mbar]	Vol. of liq. [dm^3]
1	In. pipe up to CMS	1	20	22	SS	100				31.42
2	In. pipe inside CMS up to PPecal	1	20	22	SS	14				4.40
3	In. pipe, from PPecal to disks	1	20	21	PEEK	2.8	300 2700	0.018 0.16		0.88
4	Det. module pipe (22 pipes parallel in one segment)	22	2.25	2.45	SS	2.4	2350	1.2	820	0.21
5	Out. pipe runs from disks to PPecal	1	20	21	PEEK	2.8	300 2700	0.018 0.16		0.88
6	Out. pipe inside CMS from PPecal onwards	1	20	22	SS	14				4.40
7	Out. pipe from CMS onwards	1	20	22	SS	100				31.42
Total	Segment								820	74
Total	Endcap									1325
Total	Endcap in Tracker									35

6.3.4 Optical readout

Optical fibres are grouped into multi-ribbon cables (typically 8 × 8-way) at the main patch panels. The design of a well protected and flexible 64-way cable is currently under way. Because of the non-trivial installation of these cables they will be grouped to occupy only 2 of the 18 possible sectors at both ends of the Tracker. Between the CMS magnet and the control rooms a special route has been selected. The Tracker readout and control fibres will be passed through the tunnels originally proposed for the trigger fibres (Fig. 6.vii). As a result, the Tracker makes optimal use of the fastest connection between readout chips and front-end drivers.

6.3.5 MSGC gas system

A gas mixture of 60% DME ($CH_3 - O - CH_3$) and 40% neon has been chosen to operate the MSGC counters in the CMS Tracker.

The basic function of the gas system is to mix the two primary components in appropriate proportions and to distribute the clean gas mixture to the different chamber modules at a pressure of 1–2 mbar above atmospheric pressure. It is, however, important to note a few special conditions in which the MSGC gas system has to operate:

- the lifetime of the chambers is very sensitive to some trace impurities (e.g. halogens) [6-9] which could be present in the gas. Accordingly, all incoming primary gas batches need to undergo a quality examination before connection to the system. Analysis of the return gas from individual sectors of the detector is foreseen.
- DME is a chemically aggressive agent and attacks many plastics and elastomers. Therefore all construction materials to be used in the system have been carefully selected and approved following numerous compatibility and ageing tests [6-10].
- the MSGC gas mixture is flammable and the entire system must fulfil the safety requirements of CERN [6-11].

The MSGC gas system is a single-pass system without direct recirculation in order to avoid an uncontrolled accumulation of impurities which could have an influence on the lifetime of the

chambers. The chambers operate with a gas exchange rate of one volume per hour leading to a nominal gas flow of 1.3 m^3 h^{-1} for the full Tracker. To reduce operating costs it is envisaged that neon will be recovered from the exhaust gas.

The main parameters of the MSGC gas system are listed in Table 6.7. The gas system consists of functional modules, which permits a common gas system to be built for both endcap and barrel chambers; with, nevertheless, independent gas distribution modules (Fig. 6.18).

Table 6.7: Basic parameters for the MSGC gas system

Volume:	
barrel	0.45 m^3
endcaps	0.8 m^3
Number of Gas Channels:	
barrel	72
endcaps	36
Chamber pressure	1–2 mbar above atmospheric
Gas mixture	60% DME + 40% Ne
Gas volume exchanges	1 h^{-1}
Total flowrate	1.3 m^3 h^{-1}

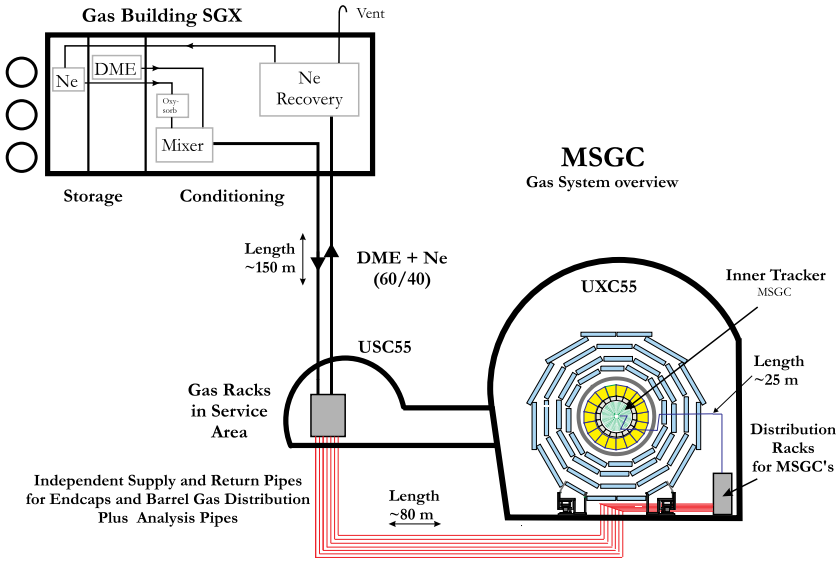

Fig. 6.18: Overview of the MSGC gas system installation.

Gas supplies

The gas ramps to supply DME and neon to the mixing room, are located in the flammable and non-flammable gas storage rooms in the CMS gas building. The neon gas supplies are standard and not described here, while every DME cylinder will pass a special quality control before its connection to the system.

The DME supply consists of three ramps of six cylinders each, with the ability to purge and sample the gas from every individual cylinder. Under operating conditions one ramp is in service; a second ramp is back-up and ready for service; and a third ramp is under preparation as recharge or quality control. On the basis of the current flow expectation, each ramp has running capacity of 4 to 5 days. The third ramp allows for a longer gas analysis procedure, which is carried out by gas chromatography with an automatic sampling and purging sequence

from cylinder to cylinder. Cylinders whose contents are not up to specification can be eliminated before their connection to the distribution system.

Mixer

The flows of component gases are metered by mass flow controllers, which have an absolute precision of ±1% over a year, and have a medium term stability of ±0.3% in constant conditions. Flows are monitored by a process control computer, which continually calculates the mixture percentages supplied to the system. The process control computer compares the running mixture with the required mixture: the required mixture may either be a constant ratio, or alternatively may be derived from comparison of the running mixture with a reference gas mixture in the infrared analyser. In either case the process control computer calculates the correction required to bring the running gas mixture to the required value; this is then fed back to the mass flow controllers as an adjustment of their nominal values. The medium term stability in constant flow conditions is better than 0.1%; absolute stability will depend on the absolute precision of the analysing instrument.

The expected gas flow at operating conditions for the MSGC barrel and endcap system will be about 1.3 $m^3\ h^{-1}$, which corresponds to 30% of full scale on the instruments, thus allowing for variations of the fresh gas flow by nearly a factor three up or down.

Distribution systems

The gas distribution is split into four independent sub-systems (Table 6.8): two for the endcaps and two for each barrel side (Fig. 6.19). Most of the active elements of these distribution systems are situated in the accessible underground service zone (USC55); the manifolds for the distribution to the individual chamber segments are placed in gas racks in the experimental cavern.

Table 6.8: Principal parameters of the MSGC barrel and endcap distribution sub-systems

Subdetector	Nominal flowrate [l h^{-1}]	Gas volume [l]	Chamber modules	No. of segments	Chamber modules per gas segment
1/2 barrel	225	225	2770	36	65–85 single chamb.
1 endcap	400	400	594	18	33

The input pressure is independently regulated for each distribution system using a regulation valve controlled by a pressure transmitter and a PID. This allows individual flow adjustments from the accessible area in the USC55.

The gas racks in the experimental cavern contain manifolds supplying gas to all chamber segments of that sub-system. Every channel has a short flexible metal pipe with a self-sealing quick-connector on the inlet and outlet line. This permits gas channels to be individually disconnected from the circulation system for flushing with inert gas and exhausting to a separate vent line. This facility is also very useful for leak tests of single gas channels.

If a suitable and low-cost channel flowmeter can be found, every supply and return gas line could have a remotely read flowmeter allowing a direct comparison between inlet and outlet flow. Given the strong constraints for the compatibility of materials to be used, it has to be checked if the standard channel flowmeters (currently being developed) can be made compatible with the DME/Ne gas mixture. If these flowmeters cannot be used, a restrictive orifice of suitable size will be installed to equalise the flows in the different segments.

In order to insure proper and long-term chamber operation at moderate flowrates, it is aimed to keep differences in flowrates below the 10% level. Small variations in pipe impedance are unavoidable due to the different pipe lengths on the rod or on the endcap disks. This

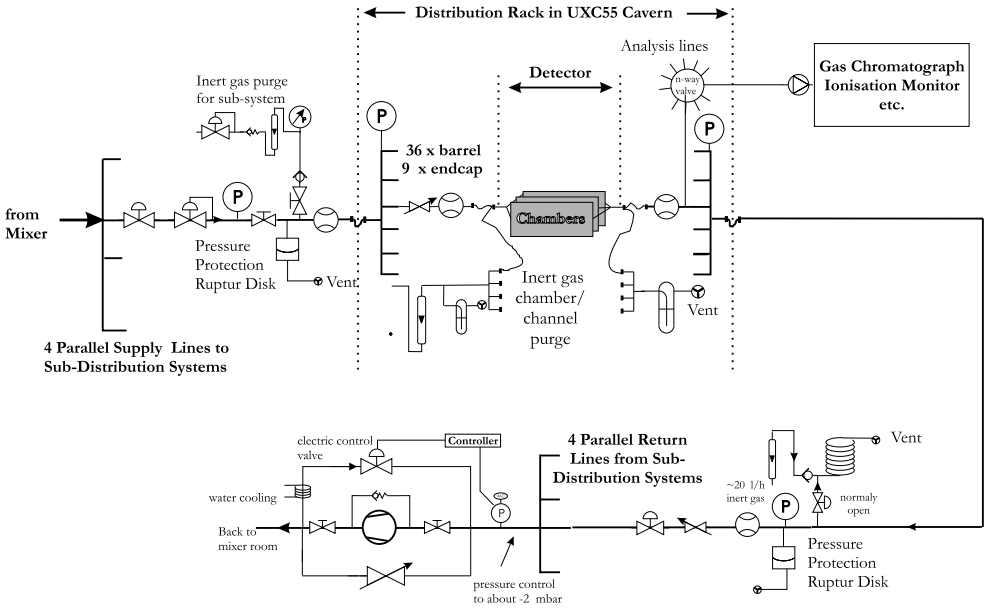

Fig. 6.19: Schematic layout of the gas distribution system.

dissimilarity will be compensated, if necessary, by a suitable orifice at the inlet of the rod or at the inlet of the endcap detector module.

Barrel gas distribution

The barrel MSGC detector comprises a total gas volume of 0.45 m^3, it is split along the z axis into two cylinders, which are supplied independently from the USC area. Thus, each side of the barrel houses 2770 chambers mounted in 6 radial layers. For the gas supply, each detector layer will be split into 4 to 10 r-ϕ segments (Table 6.9 and Fig. 6.19) of nearly equal volume leading to 36 gas channels for each side of the barrel. Within one r-ϕ segment all sub-elements (rods and chambers) are connected in parallel. The 72 (36 supply+36 return) gas pipes enter from both ends of the Tracker and are equally distributed onto the nine 40° pipe-runs which surround the Tracker.

Three out of the six detector layers (Fig. 6.20) are double layers, made of two chambers mounted back to back on the same rod. The r-ϕ segments on these rings are smaller in order to compensate for the increased detector volume.

Table 6.9: Segmentation of the gas distribution for half the MSGC barrel

Layer No.	Chamber type	No. of gas segments	No. of rods	No. of rods/ segment	No. of chambers/ segment	Average volume/ segment [litre]	Volume/ layer [litre]
1	double	6	48	8	80	6.4	38
2	single	4	54	13–14	65–70	5.4	21
3	single	4	59	14–15	70–75	5.9	23
4	double	8	64	8	80	6.4	51
5	single	4	69	17–18	80–85	6.8	27
6	double	10	74	7–8	70–75	5.9	59

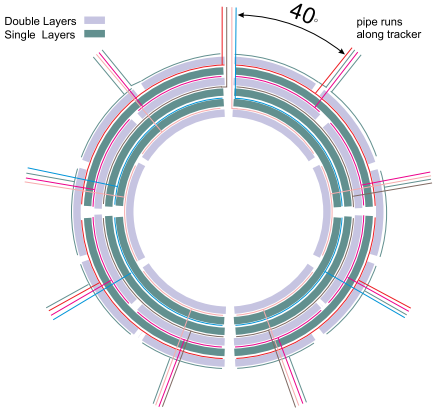

Fig. 6.20: Segmentation of gas channels on one side of the barrel MSGCs. Each layer is subdivided into r-ϕ segments of approximately equal detector volume. Every 40° pipe run houses 2×4 gas pipes of 6 mm inner diameter.

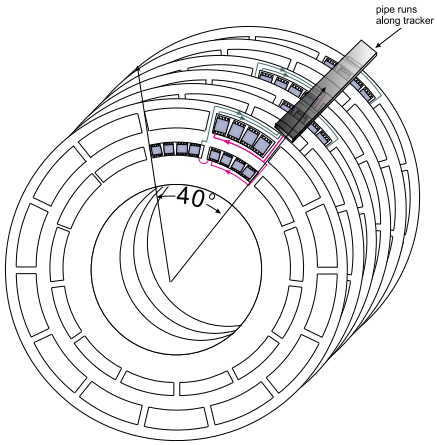

Fig. 6.21: Schematic view of one typical endcap gas channel. Three detector modules within the 40° r-ϕ segment are connected in series.

Endcap gas distribution

Each MSGC endcap comprises a detector volume of 0.4 m^3 and is made of 11 disks, situated along the z-axis. Every disk contains 54 chamber modules mounted in 2 rings on each side of the disk. The chamber boxes, made of carbon fibre sheets, form a gas tight envelope housing four substrates each. Three detector modules (all on the same disk face) are connected serially and form the basic gas distribution circuit (Fig. 6.21). It is foreseen to supply each endcap with 18 independent gas lines, each pair of lines serving a 40° r-ϕ segment. The gas pipes run in U-formed channels along the 11 disks. In each segment, one line supplies the detector modules on disks 1, 3, 5, 7, 9 and 11, the other those on disks 2, 4, 6, 8 and 10. The distribution alternates on successive disks between modules to the left and to the right of the supply manifold, thus increasing the effective modularity of the system.

Return gas analysis

Gas analysis and gas ionisation measurements are powerful monitoring tools for chamber operation. In addition, an oxygen measurement in the return gas flow is a sensitive indication of gas leaks. It is foreseen to sample the chamber output gas on the return manifolds in the distribution systems; the modularity can be at the channel level or at a group of channels. Since the return gas pressure is very small, a pump system must be used to suck the gas back to the USC area. Thus, gas analysis instruments are accessible at any time and can be shared by several sub-systems.

Pressure regulation and protection

Four output pipes return the gas from the detector to the USC area. A membrane pump compresses the gas to approximately 100 mbar for return to the surface and injection into the neon recovery plant. A common back-pressure regulator, in parallel with the pump, controls the pressure to 1 to 2 mbar below atmospheric pressure at the inlet of the pump. The pressure drop in the chamber return pipe is 2 to 3 mbar depending on the flowrate, leading to a chamber

operational pressure near 1 mbar at nominal flow rate. Variations due to hydrostatic pressures differences inside the Tracker (total height less then 2.5 m) can be neglected.

This kind of pressure regulation requires fail-safe operation which is provided in two stages:

1. Two independent pressure transmitters on the supply and return manifolds of each sub-system in the UX-gas rack will compare the effective pressures with the expected values at the gas inlets and outlets. In case of a deviation (typically ± 2 mbar) the gas flow of that sub-system will be stopped and the direct vent line on the outlet will be automatically opened, forcing the chamber pressure to atmospheric level.
2. If (1) fails, and the pressure still deviates further, a purely mechanical bursting disk (rupture disk) is placed at the inlet and outlet of each sub-system. The rupture disks can be adjusted to the desired bursting pressure. A dedicated rupture disk, compatible with the use of DME, has been developed for this purpose.

Pipework

There will be one supply and one return pipe between the SGX building and the underground service area (USC). Each endcap system has one supply and one return pipe connecting the USC area with the experimental zone where the pipes enter from underneath the detector. For the barrel two independent pipes are foreseen serving the two sides of the barrel individually. The pipes from the distribution manifolds in the experimental zone are stainless steel up to the inner connection board near the ECAL, from there on the piping will be in PEEK in order to simplify bending through the Tracker and to reduce their contribution to the material budget (Table 6.10 and Table 6.11).

Table 6.10: Pipes for the gas distribution on one end of the MSGC barrel

Pipe sect. No.	Description	Sup. ret.	No. of pipes	In. diam. [mm]	Pipe mat.	Leng. [m]	Re No.	Gas vel. [m/s]	P. drop at max. Flow [mbar]
	USC55 to UXC55	Sup.	1	20	SS	100	1179	1.17	2.4
1	Rack to det.	Sup.	36	10	SS	50	65	0.13	0.3
2	In. CMS to ECAL	Sup.	36	8	SS	14	82	0.20	0.2
3	ECAL to Tracker	Sup.	36	6	PEEK	5	109	0.36	0.3
4a	On the rod	Sup.	368	4	PEEK	2	18	0.09	0.04
	Rod to chamb.	Sup.	2770	0.8	PEEK	0.1	11	0.26	0.2
	Chamber to rod	Ret.	2770	0.8	PEEK	0.1	11	0.26	0.2
4b	On the rod	Ret.	368	4	PEEK	2	18	0.09	0.04
5	Track. to ECAL	Ret.	36	6	PEEK	5	109	0.36	0.3
6	ECAL out. CMS	Ret.	36	8	SS	14	82	0.20	0.2
7	Det. to gas rack	Ret.	36	12	SS	50	55	0.09	0.2
	UXC55 to USC55	Ret.	1	33	SS	100	714	0.43	0.2

The pipe connections in the underground areas (pit, cavern, galleries, etc.) and on the detector up to the patch panel near the ECAL will all be of welded stainless steel. Only inside the gas racks are compression fittings used. The plastic piping inside the Tracker will use glued connectors or welded pipes.

Neon recovery

To reduce operating costs it is necessary to recover the neon from the return gas. Because of the relatively high difference between the boiling and melting points of Ne and DME respectively, the DME can be removed through liquefaction. The separation plant is shown schematically in Fig. 6.22. The neon–DME mixture is precooled in the heat exchanger before condensation

Table 6.11: Pipes for the gas distribution on one MSGC endcap

Pipe sect. No.	Description	Sup. ret.	No. of pipes	In. diam. [mm]	Pipe mat.	Leng. [m]	Re No.	Gas vel. [m/s]	P. drop at max. Flow [mbar]
	USC55 to UXC55	Sup.	1	33	SS	100	862	0.52	0.7
1	Rack to det.	Sup.	9	16	SS	50	198	0.24	0.2
2	In. CMS to ECAL	Sup.	9	12	SS	14	263	0.43	0.2
3	U-channel	Sup.	9	10	SS	5	316	0.63	0.2
4a	On the disk	Sup.	18	1.2	PEEK	1.5	24	0.40	0.1
4b	On the disk	Ret.	18	1.2	PEEK	1.5	8	0.12	0.0
5	U-Channel	Ret.	9	10	SS	5	316	0.63	0.2
6	ECAL out. CMS	Ret.	9	12	SS	14	263	0.43	0.2
7	Det. gas rack	Ret.	9	16	SS	50	198	0.24	0.2
	UXC55 to USC55	Ret.	1	33	SS	100	862	0.52	0.2

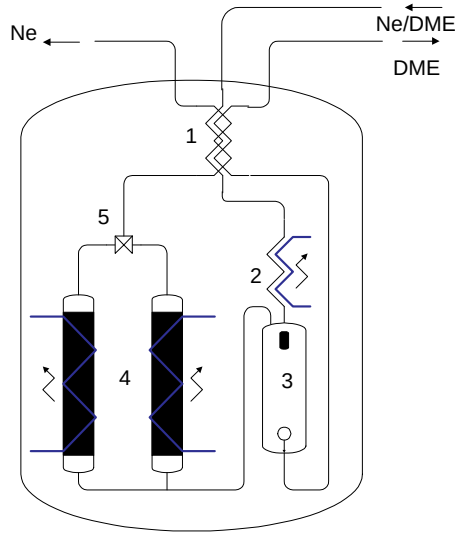

Fig. 6.22: Neon recovery system 1: heat exchanger; 2: condenser; 3: liquid DME storage tank; 4: charcoal cartridges; 5: switching system.

of the DME in the condenser. The liquid DME is collected in the storage tank at $-139°C$ where the temperature is regulated using liquid nitrogen and a heating resistor. The neon is taken off as vapour on top of the liquid DME and is passed through an activated charcoal filter to remove residual DME, nitrogen and other organic impurities. The recovered neon can be directly recycled through the chambers [6-12].

6.3.6 Dry nitrogen gas system

The Pixel, Silicon and MSGC volumes will be flushed with dry nitrogen gas. The main purpose of flushing is the removal of humidity in the cold volume. Cold nitrogen gas provides additional cooling due to convection. For the MSGC volume it solves the safety problem arising from the use of flammable DME gas. Even in case of a chamber gas leak the overall gas mixture must stay below the explosive limit. Dry nitrogen will be provided by three independent systems for the Tracker subdetectors.

The total number of nitrogen tubes for each subdetector is given in Table 6.12.

Table 6.12: Number of nitrogen tubes for each subdetector system

	Number of tubes	Inner diameter [mm]	Precooling temperature [°C]
Pixel	8	8	−10
Silicon	66	10	−10
MSGC	64	10	+12

The minimum exchange rate foreseen for all sub-systems is one volume change per day.

Distribution system inside the Tracker volume: All incoming gas tubes are located at the outer detector radius. The outgoing gas is collected in tubes located at the inner radius of the subdetector. With this layout a homogeneous distribution of the gas within the volumes can be guaranteed. This is particularly important for the endcap zones where the detector layers are vertical and hinder the gas flow.

Within the MSGC volume particular care will be needed to monitor the differential gas pressure inside and outside the chambers. At selected critical locations the oxygen concentration will be monitored which will allow an active feedback to the control system. The dry nitrogen flow will be adjusted according to the needs of DME leakage.

6.3.7 Slow controls

6.3.7.1 General remarks

The Tracker control system will consist of three individual sub-systems, for the Silicon detectors (pixels and strips) and the MSGCs. These sub-systems will be further subdivided into sub-systems with different functionalities. Modularity of the system is essential for simplification and work load distribution. Uniformity is important, provided it does not hinder individual functionalities. Easy and smooth communication between the systems and exchange of information is a crucial point, both for the safety and smooth operation of the detector as well as for logging information important for the general physics output. The main Tracker control sub-systems are:

1. The Pixel (barrel part) control sub-system
2. The Pixel (endcap part) control sub-system
3. The Silicon strip (barrel part) control sub-system
4. The Silicon strip (endcap part) control sub-system

5. The MSGC (barrel part) control sub-system
6. The MSGC (endcap part) control sub-system
7. The engineering parameter monitoring sub-system
8. The internal environment monitoring sub-system
9. The Tracker internal alignment sub-system
10. The cooling sub-system
11. The thermal screen sub-system
12. The central gas supply sub-system
13. The magnetic field monitor sub-system
14. Radiation levels monitoring and control sub-system
15. Experimental hall sub-system
16. Experimental hall temperature and humidity monitoring sub-system
17. Gas leak and fire detector status

Some of these sub-systems are entirely under the responsibility and control of the Tracker community (Pixel, Silicon, MSGC, alignment, engineering parameter and cooling sub-systems). Those individual sub-systems are described in the dedicated subdetector chapters. Some other sub-systems are hybrid; responsibility for the control and monitoring of the quantities in these sub-systems is shared by the Tracker and other sub-systems (central gas supply, thermal screen, radiation levels sub-system, experimental hall power sub-system). For these, a detailed description of the shared responsibilities will be provided by the parties concerned and common actions will be agreed. Finally, there are some sub-systems that are essential to the Tracker performance, but which are not subject to any Tracker control; for those sub-systems, efficient communication is the issue (magnet sub-system, experimental hall, fire detectors).

The high radiation environment, minimisation of material budget, limited space and restricted accessibility make the Tracker environment hostile for the installation of conventional and of the shelf control systems. As a consequence, the control system requires a design in which most sensors will be radiation-hard ICs, optical connections have to be used wherever possible, electrical loops should be eliminated and the number of electric lines should be minimised.

All sub-systems should be designed intrinsically safe and important interlocks should be embedded in the sub-system elements themselves.

On the operators–users site, the sub-systems will be presented in a simplified form and the detector situation will be depicted by a limited number of states. Depending on the detector state, automatic actions will be undertaken by the sub-system itself with parallel communication to the operator–user and (less urgent) actions will demand confirmation before execution. Portability of the software is essential and a lifetime matching that of the detector is demanded.

6.3.7.2 Slow control for the Pixel and Silicon detectors

The control system of the Pixel and Silicon detectors will consist of several individual subsystems. In the current state of the design, the sub-systems are identified as:

1. **The Silicon voltage control system**
   which should include the hardware elements and processes that monitor and control the power supplies for bias voltages and readout electronics.
2. **The Silicon temperature monitoring system**
   which should include the hardware elements and the processes that check on the temperature fluctuations and time evolution as given by the individual thermistors, with a minimum distribution of one per module.
3. **The Silicon electronics cooling system**
   which will consist of the hardware elements and processes that monitor and control the temperature of the front end electronics.

The individual sub-systems will be designed to be independent but communication between them as well as with other sub-systems of the experiment should be efficient and flexible. Commercial products will be used as far as possible, but dedicated radiation hard ASICs will have to be developed for some applications.

6.3.7.3 Slow control for the MSGC detector

The control system of the MSGC detector will consist of several individual sub-systems.

The gas sub-system

The gas sub-system will include the hardware elements and processes that regulate the flow of the gas mixture through the MSGCs and protect the detectors by monitoring critical parameters and setting the appropriate hardware and software interlocks.

The primary alarms and interlocks of the system will be generated by information coming from the central gas supply control system, from the detector distribution system and from the detectors of flammable gas, which will be distributed at appropriate points on the detector and in the experimental cavern. In case of a detected problem in the distributed MSGC gas mixture or of a gas leak, hardwired alarms will disable all high voltage for the detector and the appropriate software alarms will be transmitted to the operator of the experiment and of the gas system. At the same time, the system performing the gas quality evaluation will be set to a safe state.

In Tables 6.13 and 6.14 we have summarised the problems that will result in an interlock or alarm status for the MSGC detectors. The actions that these interlocks or alarms have to provoke will be further investigated and will be modified as experience on detector operation increases.

Table 6.13: MSGC gas sub-system interlocks

Hardware element	In alarm if	Possible action
MSGC gas mixer pressure meter (central gas system)	Off limits (± 0.3%)	HV interlock and set gas analysis system in safe state
MSGC input pressure meter (per line)	Off limits (± 0.1%)	HV interlock and set gas analysis system in safe state
MSGC output pressure meter (per line)	Off limits (± 0.1%)	HV interlock and set gas analysis system in safe state
Input–output pressure difference protection (probably rupture disk)	Off (8 mbar difference)	HV interlock and set gas analysis system in safe state

Alarms which appear after a value set for a controlled unit has been exceeded, will be checked with respect to the time evolution of that unit. This will save the experiment from many false alarms and interruptions of smooth operation.

The MSGC gas system, the Tracker environment and cost limitations impose strong constraints in the choice of the controlling and monitoring instrumentation. In Tables 6.13 and 6.14, the instrumentation has been kept to a minimum. Mass flow controllers giving substantial information on the flow development of the gas distribution are an essential element of such a system and will be included in Tables 6.13 and 6.14 once suitable devices have been identified. Logging the time development of pressure variations is essential, since they will provide valuable information on detector response optimisation.

Table 6.14: MSGC gas sub-system alarms

Hardware element	In alarm if	Alarms reported to
Mixer pressure meter	Off limits (± 0.3%)	Central gas system, HV and gas analysis systems, operator, gas operator
Loss of N_2 pressure	Off limits ± 5% drop	Central gas system, gas analysis system, operator, gas operator
MSGC output pressure meter	Off limits ± 0.1% drop	Central gas system, HV and gas analysis systems, operator, gas operator
MSGC input pressure meter	Off limits ± 0.1% drop	Central gas system, HV and gas analysis systems, operator, gas operator
Input–output pressure difference protection element	Off (8 mbar difference)	Central gas system, HV and gas analysis systems, operator, gas operator

In the current design, the input-output pressure difference of the MSGCs has to be less than 2 mbar to avoid non-uniformity of the gain of the chambers, and less than 8 mbar for security reasons.

The Input-Output pressure difference protection element is currently under optimisation starting from the design of the rupture disk developed for the B1 milestone project.

Gas quality monitoring

The gas quality monitoring sub-system, includes the hardware elements and the processes that check the gas mixture stability, the water and oxygen levels and other possible contaminants in the gas distribution lines. It makes use of instruments like oxygen meters, dew point meters and a gas chromatograph for more detailed scans. The analysis of the gas quality will be validated, when necessary, by the results of independent measurements performed on proportional gas counters which will provide a direct feedback. The proportional chambers will measure the drift velocity and the pulse-height produced in the running gas mixture by the deposition of a known amount of charge from Fe^{55} and Am^{241} sources.

Water and oxygen are monitored at different points in the gas circuit, namely:

- At the input/output of each sector (routinely);
- At the main gas inlet/outlet (routinely, several times per day);
- At the output of the recycling plant (routinely).

The time needed in order to have a satisfactory measurement from the drift velocity and the pulse-height chamber is currently estimated to be 30 minutes. This requirement makes a routine scanning scheme of all the output lines rather lengthy and unsafe for interlocking purposes. Therefore this analysis process will be routed to a particular output channel to provide a confirmation, in case the conventional oxygen/water/other contamination analysis reveals any problem on the specific channel. In normal running mode, the pulse-height response will be recorded and used as a correction factor for potential changes of pressure, or minor variations in the gas mixture. The pulse-height response and the drift velocity measurements will be continuously monitored at the main gas input. Results from these measurements will be used for interlock purposes.

The hardware sampling scheme includes a well controlled piping and pumping system that should be used to drive gas samples from the detector inlet and outlet to the gas chromatography analysis line. For reasons of safety, robustness, and cost this system will be PLC driven.

As in the case of the gas controls, the action of the gas analysis sub-system interlocks (Table 6.15 and 6.16) still needs to be finalised. The current description is the foreseen minimal hardware infrastructure that allows the control system to check reliably the gas quality.

Table 6.15: MSGC gas analysis sub-system interlocks

Hardware element	In alarm if	Possible action
O_2 meter	Off limits (some ppm)	HV and gas analysis sub-systems interlock. Direct the pulse height analyser to appropriate line
H_2O meter	Off limits (some ppm)	HV and gas analysis sub-systems interlock. Direct the pulse height analyser to appropriate line
Gas chromatograph	Not normal peaks	HV and gas analysis sub-systems warning. Direct the pulse height analyser to appropriate line Prepare to repeat the scan

Table 6.16: MSGC gas analysis sub-system alarms

Hardware element	In alarm if	Alarms reported to
O_2 contents	Off limits (some ppm)	Central gas system, HV and gas analysis sub-systems, operator, gas operator
H_2O contents	Off limits (some ppm)	Central gas system, HV and gas analysis sub-systems, operator, gas operator
Pulse height at input	Off limits $\pm 10\%$	Central gas system, analysis sub-systems, operator, gas operator

The high voltage control

The high voltage sub-system is subdivided into two parts. The most complicated, and still under evaluation, is the local control on the strip clusters. The system is activated when an over current in the cluster is detected.

The conventional high voltage sub-system part refers to the controls and monitors of the power supplies that provide the cathode and the drift voltages. The cost-modularity factor is linked to the number of MSGCs that will run with the same voltage. The reproducibility of detector characteristics and the fact that the modules can be preselected on the basis of their gain during assembly, allow us to postpone this choice.

The interlocks to the high voltage sub-system will be produced by:

- The gas control sub-system.
- The gas quality control sub-system.
- The chamber monitoring sub-system.
- The detector environment sub-system.

6.4 Thermal Screen Between Cold and Warm Volumes

6.4.1 Requirements

To improve the resistance of the Silicon modules to the high radiation level produced near the interaction point, they must be operated at a temperature well below 0°C. The presently accepted requirement is maintaining the temperature of the Silicon volume at -10°C. Therefore, a thermal screen must be inserted between this volume and the MSGC volume, which operates at

room temperature, in order to keep them thermally separated: any interaction must be avoided, in all possible conditions (i.e. both detectors *ON*, both *OFF*, only one detector *ON*). On one hand the low temperature requirement of the Silicon must be guaranteed even when the detector is not operated; on the other, the risk of local freezing inside the MSGC volume must be avoided, when this detector is not powered.

The region in which the thermal screen is inserted is critical. The radial gap between the outermost Silicon sensing element and the innermost MSGC one should be kept to a minimum. Furthermore, any additional mass positioned in this region introduces material in the particle paths, thus making more difficult the task of matching the track segments detected by the Silicon and MSGC Tracker.

6.4.2 Global thermal load

The total heat flux from the MSGC detector to the Silicon detector volume through an idealised surface of separation (i.e. no thickness, no thermal resistance) can be calculated through the formula:

$$q = \frac{\Delta T}{\frac{1}{2\pi r_o L h_o} + \frac{1}{2\pi r_i L h_i}} \tag{6.1}$$

where ΔT is the temperature difference between the two volumes, r is the value of the radius, L the axial length of the separation surface, h the convection coefficient due to the dry N_2 flushed over both sides of the surface, the suffix *'o'* refers to the outer side of the separation and the suffix *'i'* to the inner.

Depending on the precise values assigned to ΔT, r and h (an estimate for this coefficient being in the order of 20 W/m^2 K), the formula provides an estimate of the total heat flux in the range of 6 to 7 kW. Thus, the maximum global thermal load acting on the screen may be estimated to be 6.3 kW, assuming that a net residual heat flux into the cold volume of the order of 700 W (~2 % of the total heat dissipated by the detectors in the cold volume) may be accepted as negligible. This heat load may be totally or partially insulated by a layer of insulating material: in the latter case, the remaining part must be removed by an active agent.

6.4.3 Possible solutions

The technically easiest solution, which is also the lightest, relies on the simple interposition of a passive insulating cylinder between the MSGC and the Silicon volumes. Unfortunately, a thickness of insulating material of the order 50 mm would be required to satisfy the above condition on the net residual heat flux (the precise value depending on the thermal conductivity of the selected material). This is not acceptable from the point of view of radial space consumption.

To save space (at the expense of some additional material), one can strongly reduce the thickness of insulating material by adding to the screen a convective layer to remove part of the total thermal load. Forced convection is the most efficient way of removing the excess heat before it reaches the Silicon detector volume. Nonetheless, excessively high flow rates of gas or liquid must be avoided: this implies that some insulating material has to be employed. A trade-off between space needed for the thickness of the insulating layer and flow rate must be made. The convective medium can be a gas or a liquid. The minimal mass addition due to a gas flow (only related to the necessary piping) makes it an interesting candidate. Unfortunately, the poor thermal properties of suitable gases require unacceptably high flow rates, involving the necessity of a large storage tank and increasing the complexity of the whole system. Therefore, a liquid convective medium has been chosen. All these aspects have been developed and examined in Ref. [6-13].

However, neither solution satisfies completely the requirement of avoiding any reciprocal influence between the two volumes. Indeed, when the electronics of the MSGC detector is

not powered, local freezing may occur due to constant heat removal from the thermal screen. Moreover, during operation of the Tracker, the warm and the cold volumes might interact through possible temperature variations. To avoid this problem, an active feedback control on the temperature and the flow rate of the convective medium should be inserted, enormously complicating the whole system.

A complete independence of the MSGC and Silicon volumes can be achieved if the screen between them has the temperature on its outer and inner sides fixed to the nominal temperature of the facing volume. To do this, heat must be continuously produced on the outer surface of the screen and removed from the inner surface. Provided a correct design of the heating and of the cooling layers is performed, the temperatures on both sides of the screen can be permanently maintained at the desired values.

A totally active screen is obtained by wrapping a heating foil around a cooling liner and forcing the desired temperature step between them. In principle, the simple superposition of these two layers might provide the desired thermal separation, with an extremely high temperature gradient in a very limited radial space. On the other hand, this would involve the complete production and removal of the total thermal load, requiring in turn considerable addition of mass (in terms of cables, resistors, piping and liquid) and an extremely large flow rate. The interposition of an insulating layer would clearly lower the net thermal load, at the expense of a larger radial space consumption: again, a trade-off must be performed. It is worth noting that, with this solution, the inlet temperature and the flow rate of the convecting medium can be kept constant, while the feedback control over the behaviour of the screen can be performed through a control of the power dissipated in the heating foil.

6.4.4 Technical solutions

To avoid the practical problems connected with the fabrication of a full cooling liner in cylindrical geometry, the layer of convecting medium can be obtained by joining together an array of pipes by heat conductive plates. In this way, the heat passing between two adjacent pipes is intercepted by the plate and preferentially conducted through it to the pipes, where a cold fluid flows (Fig. 6.23). To cover completely the 5.6 m long, 0.64 m in radius, cylindrical surface enveloping the Silicon detector volume, the cooling jacket can be built in patches, which are then assembled together to form the cylindrical shape.

In order to eliminate difficult and massive thermal joints from the thermal screen, which introduce inefficiency through unwanted thermal resistances, the pipes and the conductive plates should be made of the same material. The safest choice is to use an aluminium alloy (k = 150–210 W/mK), while a more sophisticated solution would rely on CFRP. In this case, a satisfactory value of the conductivity coefficient for the connecting plates is offered by the $P120$ fibre in the unidirectional arrangement ($k \sim 300$ W/mK). Considering the limited structural loads acting on the screen surface, a unidirectional arrangement of the fibres, in the transversal direction with respect to the axis of the detector, can be considered acceptable (Fig. 6.23). The leak-tightness of pipes in CFRP (possibly with an interior metallic coating) is questionable, although pipes of this kind are currently under evaluation for space satellite application.

In both cases, two possible ways of producing the patches of the cooling jacket are shown schematically in Fig. 6.24. In Scheme A, housings for the pipes are moulded in the conductive plates, and the pipes are then bonded onto the plates. A local thermal resistance has to be expected along the contact surface between the two components. This thermal resistance is eliminated in Scheme B, where each cooling jacket patch is produced by gluing together two preshaped half-surfaces. Technical problems may arise in this manufacturing scheme from a possible direct contact between the glue and the cooling fluid. Tests will be performed to select the best manufacturing procedure.

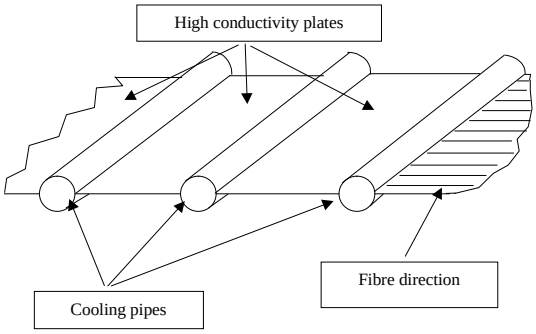

Fig. 6.23: Arrangement of the cooling jacket

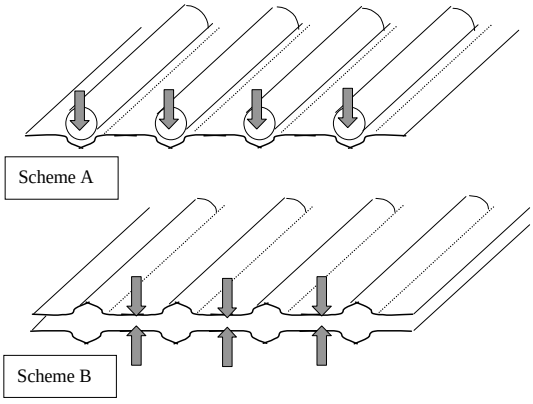

Fig. 6.24: Possible manufacturing schemes for the elements of the cooling jackets.

As anticipated, an insulating layer will be positioned between the cooling liner and the heating foil. This can be done in a very economical way by the deposition of a layer of insulating foam (typically polyimide foam, $k = 0.04$ W/mK) over the cooling jacket. This insulating layer can be then machined and prepared to support the heating foil. More sophisticated materials, such as those belonging to the silica aerogel family ($k \sim 0.02$ W/mK), might be used in order to reduce the thermal load on the active part of the screen for the same thickness, or to achieve the same thermal load with a lower thickness. These materials have found recent interesting applications in space satellites [6-14]. Their applicability to the present case will be investigated, in term of cost and possibility of machining.

The heating foil can be a commercial Kapton foil, 0.25 mm thick, with embedded metallic resistors (e.g. a Minco Inc. Thermofoil heater of the HK series). This will be glued on the external surface of the insulating layer and connected to power cables running outside the Tracker volume together with the cooling pipes. To avoid any unforeseen effect by an off-design condition of one of the two volumes, the value of the temperature on the screen will be continuously monitored at some sample points. The monitored temperatures will then be used as input for a feedback control system of the powering of the heating foil: any deviation from the nominal temperature condition will be corrected by an adjustment of the imposed thermal load.

This thermal screen concept can be adapted to a self-supporting structure, enveloping the Silicon detector volume and designed to slide inside the Tracker Central Support Tube. In this case, all the elements are positioned over a 1 mm thick CFRP shell to reinforce the structural behaviour of the screen, and the services of the Silicon barrel are directly attached to the shell. Another possibility is to keep the structural separation of each single patch of the cooling jacket, protect it by a (thinner) CFRP skin and attach it directly to the inside of the CST before insertion of the Silicon detector. The implications of both solutions in terms of manufacturing, assembly and maintenance will be carefully analysed.

6.4.5 F.E.A. model

Referring to the design concept described, it is evident that, along the radial direction, the heat flow depends only on the thermal conduction mechanism, independent of the azimuthal position. In such a way, it is possible to identify the symmetry of the model and to reduce the geometry from the total cylindrical volume to the volume included between two pipes. Previous

analytical calculations showed that the temperature difference of the liquid along the pipes is, for the typical set of velocities considered, of the order of 0.2°C, hence a 2-D model is a good representation of the problem.

The geometry of the model can be simplified by considering only the space between two pipes. Owing to the small dimensions of the model, this portion can be represented by a small number of finite elements and the calculation time is short. To get symmetric results, the geometry has been modelled with a symmetric mesh. The element used for the ANSYS analysis is the PLANE55, a plane element with a 2-D thermal conduction capability. This element has four nodes with a single degree of freedom (temperature) at each node and is well suited for a 2-D steady-state thermal analysis. The mesh adopted for the calculations is shown in Fig. 6.25.

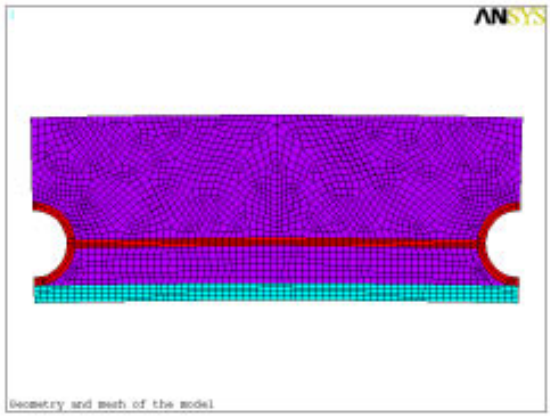

Fig. 6.25: Mesh adopted for the F.E.A.

Regarding the boundary conditions, the symmetry of the problem favours imposing an adiabatic condition on the lateral surfaces of the model. On the other hand, to evaluate the conditions on the external surfaces, it is important to take into account the reference temperature inside the warm and the cold volumes. On the outer surface the heating foil is positioned to keep the temperature of the external side of the screen equal to the reference temperature inside the MSGC volume. Therefore, the boundary condition applied to this surface is a constant temperature of 18°C. For the surface in contact with the Silicon volume, a convective condition seems to be more realistic. Nevertheless, in order to consider the worst operating condition for the screen, the (conservative) condition of a constant temperature of −10°C has been taken: in such a way the heat flow between the MSGC and the Silicon volume is maximum.

The boundary condition applied to the internal pipe surface is a convective one and depends on various parameters. These parameters include the characteristics of the fluid chosen and its velocity along the pipes, these values determining the convective coefficient that characterises the thermal exchange.

6.4.6 Results and discussion

The baseline design is oriented towards safer and less expensive choices, in order to achieve a reliable and conservative solution, still susceptible of further optimisation. Thus, an aluminium alloy with average thermal properties (k = 170 W/mK) has been selected for the pipes and the conductive plates, and a standard polyimide foam has been considered for the insulating layer. For the cooling medium, a fluid of the fluorocarbon family (C_2F_5) has been chosen. The properties of the basic materials are listed in Table 6.17.

Table 6.17: Properties of the materials selected for the baseline design

	Thermal conductivity k [W/mK]	Density ρ [kg/m^3]	Prandtl number Pr	Kinematic viscosity ν [m^2/s]
Aluminium	170	2700		
Polyimide foam	0.04	negligible		
C_2F_5	0.05	1630	8.5	0.6×10^{-6}

The initial analysis performed shows that, in order to obtain a satisfactory performance of the screen, a fairly high convective coefficient is needed for the flow in the pipes, which can only be reached in a fully developed turbulent regime ($Re \geq 10^4$). From the full analysis, in which the effects of a variation of all the relevant parameters were examined, a satisfactory solution was found.

The parameters of this solution are:

- 140 aluminium pipes, 5 mm external diameter, 4 mm internal diameter;
- Aluminium ($k = 170$ W/mK) conductive plates, 0.5 mm thick;
- Polyimide insulating layer, 10 mm thick;
- CFRP support shell, 1 mm thick;
- Resulting total thickness of the screen, 11 mm;
- C_2F_5 flow at 2.5 m/s, -10°C inlet temperature.

Under these conditions, the heat flux entering the pipes and removed by the fluid is $q_{in} = 4037$ W, and the heat flux passing into the cold volume through the screen is $q_{out} = 767$ W. Thus, the total thermal load acting on the screen, to be produced by the heating foil, is $q_{tot} = 4804$ W. For the characteristics of the convective flow in the pipes we determined:

- Reynolds number, $Re_D = 16600$;
- Nusselt number (Colburn formulation), $Nu = 0.023 Re^{0.8} Pr^{0.33} = 111.6$;
- Convective coefficient, $h = Nu \cdot k/D = 1562$;
- Friction factor (Moody formulation), $\frac{1}{\sqrt{f}} = -1.8 \log(\frac{6.9}{Re_D})$, (neglecting the effect of the pipe roughness), $\Rightarrow f = 0.027$;
- Pressure drop, $\frac{|\Delta p|}{L} = \frac{f \cdot \frac{1}{2}\rho u^2}{D} = 0.34$ bar/m.

The main features of the performance of this thermal screen are summarised in Table 6.18:

Table 6.18: Calculated performance the baseline design

Flow rate Q[m^3/h]	Reynolds Re_D	Nusselt Nu_D	removed heat q_{in}[W]	residual heat q_{out}[W]	pressure drop $\Delta p/L$[bar/m]
15.8	16600	111.6	4037	767	0.34

Figure 6.viii shows the result of the calculation for this reference solution, in terms of a vectorial representation of the heat flux.

It is interesting to note that the effect of an enhancement of the thermal conductivity coefficient of the connecting plates on q_{out} is practically negligible. Thus the use of highly conductive CFRP for these components presents the only advantage of a slightly larger X_0 (on a thickness of 0.5 mm).

The variation of other parameters has a stronger effect on the performance of the screen. Considering that higher flow speeds would involve unacceptably high pressure drops, one can take the convective coefficient as a fixed parameter. Table 6.19 lists the effect of varying the

thickness of the insulating layer, keeping the same total amount of material as used for the reference solution.

The effect of the variation of the thermal conductivity of the insulating layer, with the same thickness as in the reference solution, is shown in Table 6.20. The importance of the properties of the insulating agent is apparent.

Finally, Table 6.21 is devoted to the analysis of the variation of the number of pipes (i.e. of the distance between two adjacent pipes). The flattening of the related variation in q_{out} after 140 pipes, suggests that a nearly optimal solution has been found.

Table 6.19: Effect of the insulating layer thickness (k = 0.04 W/mK)

Thickness mm	q_{in} [W]	q_{out} [W]
8	5754	1091
9	4741	899
10	4037	767
11	3518	668
12	3118	593
13	2801	532
14	2543	483

Table 6.20: Effect of the variation of the thermal conductivity

k W/mK	q_{in} [W]	q_{out} [W]
0.04	4037	767
0.03	3035	543
0.02	2028	339

Table 6.21: Effect of the No. of pipes (10 mm ins., $k = 0.04$ W/mK)

Number of pipes	q_{in} [W]	q_{out} [W]
100	3919	809
110	3947	794
120	3978	782
130	4008	773
140	4037	767
150	4065	760
160	4092	754

6.5 Alignment

The Tracker performance, both in stand-alone mode and when integrated in the CMS system, depends upon the intrinsic detector performance and on the stability of the supporting structures. The choice of materials and the engineering of these support structures is such that stability and stiffness with the minimum amount of material is guaranteed at design level and further confirmed at the prototyping phase. However, the experimental environment in which the central Tracker is placed can influence the characteristics and behaviour of these structures. The consequence may be that unforeseen minor displacements or deformations can happen during operation and have an influence on the overall Tracker performance. Among the environmental conditions that can influence the structural behaviour of the detector elements, some are difficult to simulate and to test at laboratory level: for example the full detector powering and cooling under running conditions, temperature and humidity effects; other effects, like the influence of the 4 T magnetic field and radiation effects, are totally unknown.

Thus there is the need for permanent monitoring of the position of the detector support structures, the so-called *alignment system.*

The purpose of this system is to measure with the required precision, relative deviations from their nominal position of all the active elements of the central Tracker, to transfer the coordinates of the Tracker as a rigid body to the Muon detector via the Link system and to have a survey and assembly scheme compatible with the above.

This system is the last of a chain including precise survey at assembly and the knowledge of mechanical properties of the rigid structures supporting the detector modules.

6.5.1 Requirements

To define the requirements on the positioning accuracy of the Tracker detectors, we used a dedicated simulation procedure as described in Chapter 8. The analysis was carried out on single isolated muons with energy between 1 GeV and 200 GeV and on Higgs events (Higgs $\rightarrow$ ZZ $\rightarrow 4\mu$) with a Higgs mass between 150 GeV and 400 GeV. For the reconstruction, the Global Track Finder [7-1] was used and on the Higgs events only tracks associated with muons with $p_t > 5$ GeV/c were considered.

Table 6.22: Ultimate requirements on precision (RMS) in mm

	r [mm]	$r-\phi$ [mm]	z [mm]
MSGC	0.6	0.05	2
Silicon	0.3	0.015	0.5
Pixel	0.1	0.015	0.5

By randomly displacing the detectors and setting upper limits on the degradation of the Tracker performance as compared to the one obtained for the nominal geometry, one is able to derive a set of requirements on the positional accuracy of the detectors that allows efficient use of the reconstruction algorithms. The results on the ultimate precision required are summarised in Table 6.22.

6.5.2 Alignment procedure

In terms of alignment, the Tracker is divided in the following sub-systems (Fig. 6.26); Pixel, Silicon and MSGC, each of them further segmented in barrel and endcap sub-systems. For the Silicon strip and MSGC sub-systems there is a further segmentation into rods and box-frame structures in which the barrel and the endcap detector modules are placed. These are the smallest subunits that we have to deal with in terms of the position monitoring system.

To find the position of each active detector element one has to proceed through the following steps:

1. mechanical precision of the installation of the modules inside the smallest subunits;
2. measurement of the position of these subunits after assembly on their support structure and reference to six measurable external points;
3. online measurement of movements of these six points to evaluate global displacements of the support structures.

Step 1 is carried out by the different subdetector engineering teams and is described in detail in the corresponding chapters. Step 2 is what we call *survey at assembly* and step 3 is the task of the online position monitoring system.

6.5.2.1 Initial survey

Once the subunits containing the detector modules are installed on the respective support structures, they become the only measurable parts of the detector in the initial assembly phase. Therefore we plan to install in these subunits a number of fiducial marks that allow us to define their position in space. These fiducial marks are precisely mounted with respect to the reference points, which were previously used to position the modules inside the subunit structure, and their positions will be measured in the coordinate reference system of the six external points. The task of the survey system at assembly is to define the deviations due to mechanical and assembly tolerances, thus positioning the subunits with respect to the reference system defined

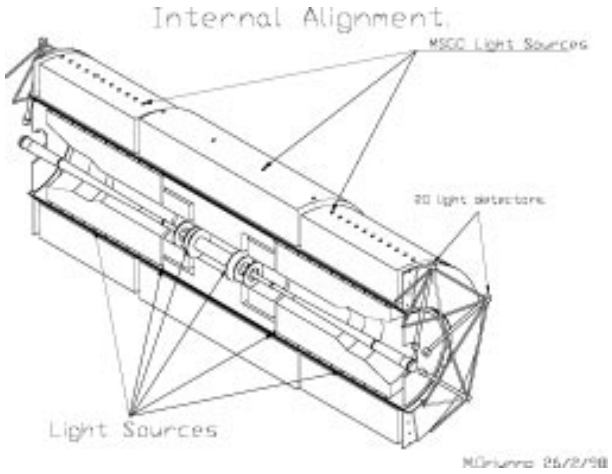

Fig. 6.26: Schematic layout of the Tracker alignment system.

by the six external points. With this method we are able to know the position of each active element from the online position monitoring system measurements.

6.5.2.2 Position monitoring after installation

The position monitoring system should measure possible deviations of the support structures from their initial assembly positions. Owing to space constraints in implementing this system, we employ just three sets of six axial channels located at the outermost radius of each of the Tracker sub-systems. The six channels of each set, the so called *alignment channels*, are obstacle-free corridors connecting both ends of the Tracker. They house six parallel axial lines, used as a reference system, crossing the detector from one end to the other. At the outer radius of the MSGC barrel these channels are exceptionally interrupted and the necessary connection of both ends of the Tracker is provided by a dedicated link mechanism.

Each supporting structure inside the Tracker can be considered as a wheel-like structure, with an internal/external radius and thickness that depends on the particular support under consideration. In order to measure the position of one wheel in the reference system of the six coaxial lines, we place six reference points at the outermost radius of both faces of each wheel. Each of these reference points must, of course, be inside the corresponding alignment channel. The evaluation of the wheel position consists in the measurement of the normal distance and angular position of each of these points with respect to the corresponding reference axes (Fig. 6.27). This system is based on the parallelism of the axes and on the accurate knowledge of the position and stability of their endpoints. To achieve this, we plan to build at both ends of the Tracker cylinder two identical and highly stable structures that define the positions and orientation of these axes. These structures are known as *alignment wheels* and also provide the connection between the reference systems of the Pixel, Silicon and MSGC alignment. They are also used to transport the Tracker coordinates into the Muon alignment via the Link system.

6.5.3 Techniques

The techniques proposed for steps 2 and 3 are digital photogrammetry for survey and a lensless laser straightness measurement system for the position monitoring of the global displacements of the support structures. Their characteristics and performance are described here.

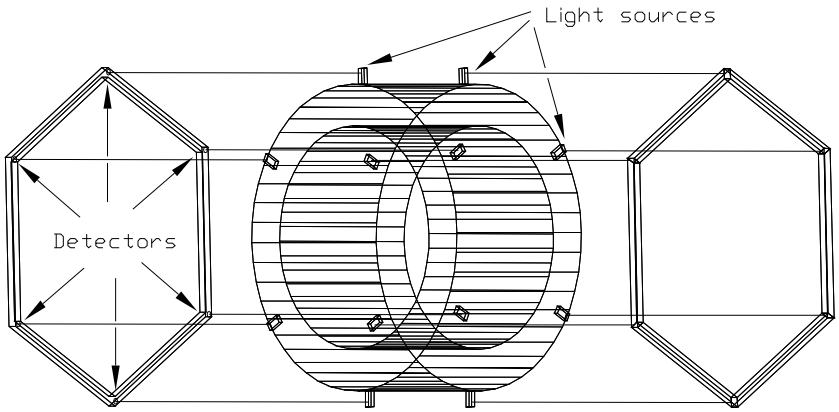

Fig. 6.27: Schematic layout of the Tracker position monitoring system.

6.5.3.1 Digital photogrammetry for survey

Digital photogrammetry is a technique well suited to measure quickly and with high precision a large number of points distributed on relatively large surfaces or volumes. It is used when high accuracy is needed (precisions of 1/200 000th of the dimension of the object under measurement can be obtained).

This technique allows the reconstruction of an object from several images recorded with a non-metric digital camera. Apart from being a fast and extremely precise technique, digital photogrammetry has the possibility to choose the recording stations to get the best possible perspective and ensure a suitable geometry of intersecting rays. It also allows simulation of the survey of an object to obtain a first idea about the accuracy that can be reached. It has the best cost/performance ratio when compared with other precise techniques such as spatial triangulation. The calculation is carried out by the reconstruction of the photogrammetric network from the bundle of rays: the orientation parameters of the network and the object coordinates are estimated simultaneously in a common process called bundle adjustment.

The equipment used to record the image is composed by a lens system (18 mm or 24 mm), camera body and image sensor (CCD camera). Measured points are defined by retro-reflective targets. Specially coded targets allow automated detection and identification to speed up the digital image analysis and improve the performance of the whole process.

To optimise the process, important preliminary work has to be done in order to determine what kind of targets will be used (design, diameter) and also in which position these targets have to be placed on the object to get the best reconstruction. This preliminary work will define the space needed to process digital photogrammetry measurements.

We intend to use this technique for the survey at the assembly phase of the subunits on their support structures, as described before, and also during the final assembly phase of the complete detector. In order to evaluate the possible application of this technique to our problem, a model of the barrel MSGC prototype was built and targets were placed on the two endflanges at the rod end-positions (Fig. 6.28).

The setup represents a half-length of one-eighth of the gaseous barrel part of the Tracker, with a volume of $120 \times 80 \times 60$ cm^3, and we were able to recreate a 3D model of the target positions with the accuracy given in Table 6.23 [6-15], clearly proving that this technique is well suited for our purposes.

Nevertheless, we should not forget that this technique requires optical access to the objects we are measuring. In fact, for a 2 m diameter object, we need to have a clear view from a distance of about 4 m, and each target, of about 10 mm diameter, must be seen inside a cone

Fig. 6.28: First test setup used for evaluation of the digital photogrammetry techniques applied to the Tracker.

Table 6.23: Resolutions obtained by digital photogrammetry on the prototype

	$< \sigma_x >$ [μm]	$< \sigma_y >$ [μm]	$< \sigma_z >$ [μm]
front plate	7	14	9
back plate	9	16	7

with $\pm 60^\circ$ aperture. This requires some care at the assembly procedure [6-16] and some space should be reserved for this purpose.

6.5.3.2 Lensless straightness measurement system for online monitoring

Principle of operation

As we have seen, the basic unit of the position monitoring system is a straightness measurement device to measure the deviations of a known point with respect to a reference axis.

The first tests of this system were done using a lens with a classical linearity measurement system as shown in Fig. 6.29a. Extensive studies were done on the performance of this system and on the development of analysis methods for the image formed on a CCD with this device [6-17]. The tests done with different lenses and different light sources are summarised in [6-18] where r.m.s. residuals of better then one micron are quoted for distances up to four metres. However, the application of this setup is limited because the image size depends on the distance of the light source from the lens. Although the lens collects more light, we intend to use apertures instead (Fig. 6.29b). The reasons behind this choice are:

- the aperture does not suffer from optical distortions;
- the form of the image changes little as the distance between the object and the aperture is changed. This latter point is particularly important because one detector is used to observe objects located at distances varying from a few tens to several hundreds of cm.
- the aperture is a physical object, easy to locate, and thus any calibration becomes simpler when compared to the use of lenses where the focus and the axis are not easy to find;
- if we increase the complexity of the aperture shape, we have the possibility of increasing the amount of information seen by the light detector.

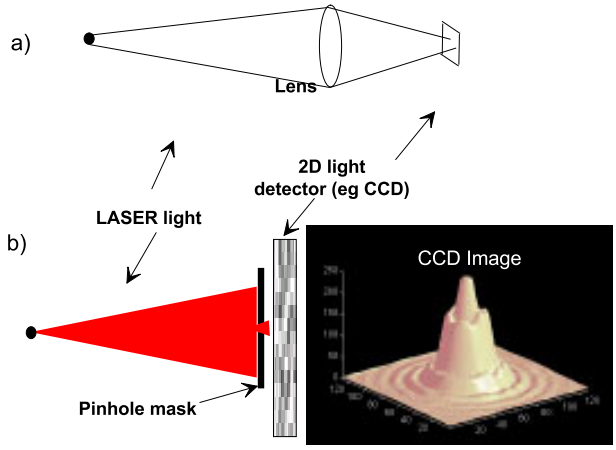

Fig. 6.29: Principle of the straightness measuring system. a) lens system used for the first tests, b) lensless system presently proposed with a real image where the diffraction pattern over a circular aperture is visible.

For the ongoing tests we use a monochromatic light source and circular apertures of small diameter. The diameter is chosen in such a way as to obtain a good amplification ratio between the displacement of the object and the image observed on the detector, and to have the intensity maximum located in the central ring of the circular diffraction pattern. We tested different diameters and distances from the aperture to the detection plane and ended up with a 310 μm circular aperture at a distance of 50 mm, when using HeNe laser light. The apertures were made on 20 μm thick steel foils and we tested different drilling procedures. Holes obtained by mechanical drilling gave the best results (Fig. 6.30). After tests carried out with LEDs and 1.5 mm^2 plastic fibres coupled to white light, we found that the use of optical fibres was advantageous, although the diameter of the fibres was far from ideal and they could not be considered as point sources. In order to have point sources, we should use fibres with core diameter smaller than the intrinsic resolution of the system. Moreover, if we use monochromatic light, in order to avoid interference of the different propagation modes, we must try to use single-mode optical fibres. Since 1995 we have used 4 μm core single-mode quartz fibres, well-suited for the 632.8 nm wave length of our HeNe laser. These fibres were chosen for single-mode propagation at this wavelength, but different types should be considered for other wavelengths. In fact, we are using monochromatic light for these tests in order to profit from the information contained in the diffraction pattern and to allow the use of other methods based on interferometry (Section 6.5.7.1).

Laser diodes are another light source which can be coupled to point-like optical fibres, for use with monochromatic light; light from LEDs or other sources of polychromatic light could also be envisaged. The choice of the light source can have an influence on the global layout of the system and on its cost and performance and is presently under study.

For all the tests carried out so far, we used CCDs with 11 μm pixel size as 2D light detectors. These proved to be accurate and highly precise devices from the mechanic point of view and offer an excellent cost/performance ratio for an off-the-shelf product, which is in constant evolution. The only drawback is the low resistance to radiation; however, the effect of radiation must be evaluated for our specific application. One should mention the existence of commercial devices that can stand doses of several Mrad at room temperature with remote sensing up to 30 m [6-19], without dramatic decrease in the performance. Progress can be expected in this field. Simulations show that the integrated dose over 10 years of LHC operation is ~13, 2.2 and

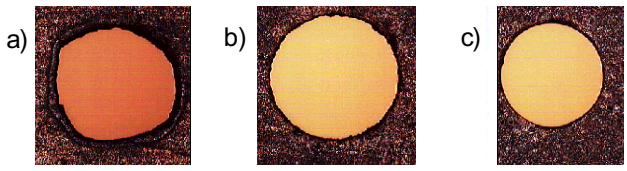

Fig. 6.30: Results of the different techniques tested for making a circular aperture on a 20 μm thick steel plate. a) laser cut (~500 μm diameter) b) Electroerosion (~530 μm diameter) c) drilled (~450 μm diameter).

2 Mrad for CCDs located at the Pixel, Silicon and MSGC level, respectively (see Appendix A on Radiation Environment). Replacement during maintenance periods can be envisaged for the most severely damaged devices.

Experimental results with a CCD readout

In order to test the validity of the proposed method we have an ongoing experimental programme, which started with the single light source measurements over a 4 m long optical bench described above. With this setup we obtained an average accuracy of 6 μm (~2% of the pixel size) in the reconstruction of a straight line when the distance between the light source and the CCD was between 0.8 and 3.1 m [6-20].

Recently, we built a sector of the full setup as shown in Fig. 6.31. This setup represents one-sixth of the inner monitoring system and consists of a plane defined by 2 arms, each containing two CCDs spaced by 400 mm. The distance between the two arms is 5350 mm, the maximum distance available in the laboratory. Each CCD camera (Philips FT800P) was equiped with different sets of apertures placed 50 mm away from the detection plane (currently we are using apertures with a diameter of 450 μm). The cameras are held by invar bars to minimise temperature effects on the system. We use a 5 mW HeNe laser to inject 632 nm red light into 24 single-mode optical fibres with 4 μm core (250 μm external diameter). The light injection is done automatically with a 3 axes step motor system of 0.1254 μm precision controlled by computer. Between the two invar arms we have a calibrated optical marble table where we have placed eight optical fibre light sources on a rigid plane simulating one-sixth of a detector support structure. This rigid plane can be displaced in all degrees of freedom with the help of micrometric screws and the displacements are measured by seven precision sensors (Sylvac) that enable us to reconstruct any relative movement of this plane with a precision better than that of the measuring device under test. The sensors are read by a PC which also reads the CCDs with a frame grabber (DT3152) in a multiplexed way. One of the first tests done with this setup was the evaluation of the single-light-source/single-CCD accuracy for movements in one direction. The results obtained (Fig. 6.32) show the absence of any non-linearity when we displace the light source by $\pm$ 1 mm around the initial position.

A typical image is shown in Fig. 6.33, where we clearly see the diffraction rings of a circular aperture. The results on the linearity were obtained with a modified Centre-of-Gravity (COG) method that takes into consideration the noise characteristics of the readout CCD. We tested other analysis methods that profit from the 2D readout capabilities of our devices and can extract information from this particular diffraction pattern. These methods gave promising results and, although they need further software development, they can be used in case of perturbations in the image intensity.

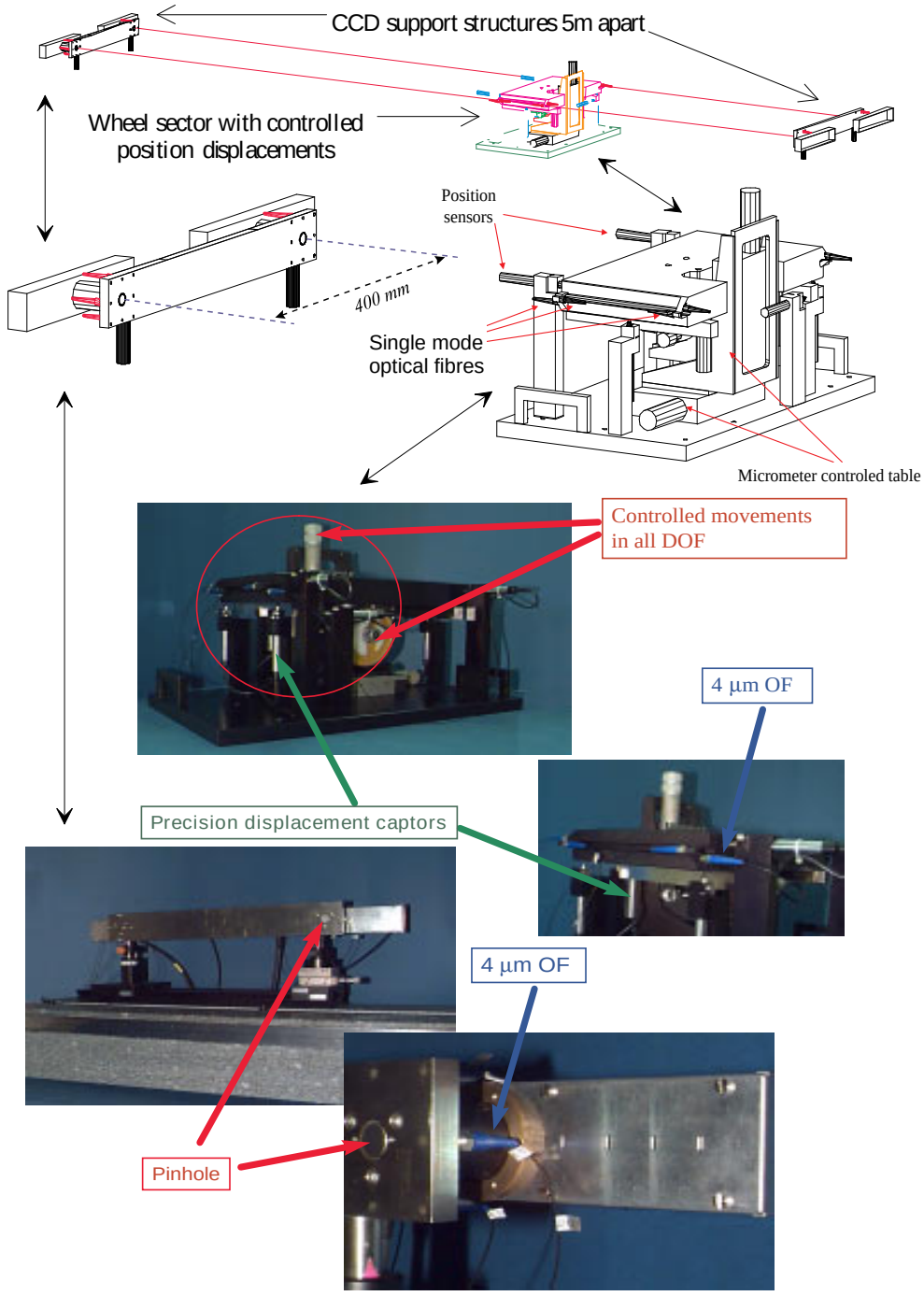

Fig. 6.31: Schematic of the laboratory setup in use to test a sector of the online position monitoring system showing the full setup with 2 invar bars each supporting 2 CCD cameras and apertures, and a movable table in between with 8 light sources representing a sector of a wheel; the blow-up of the bar supporting the 2 sets of cameras and 4 light sources needed for the autocalibration measurements of the facing cameras; a detail of the table with 8 optical fibre light points representing a support structure segment. This table can be displaced in all 6 degrees of freedom with micrometer screws; the displacements are measured with high-precision sensors.

The first results obtained for the displacement in one direction of the simulated wheel structure show an encouraging 9 μm accuracy. This is slightly worse than the 7 μm foreseen by the simulation, but further work is needed to fully understand all the systematic errors inherent in this particular setup and the influence of the variable ambient conditions, under which these measurements were taken. As a first step towards the improvement, we recently installed a fully automatic light injection mechanism into the 4 μm optical fibres. This considerably reduced the data taking time for each position, thus providing insensitivity to possible slow variations of the data taking conditions. We also modified the central table layout to avoid edge diffraction.

Using the COG method without previous calibrations on images obtained from a single source at 2.6 m, we obtained intrinsic detector resolutions of ~2% of the CCD pixel size, allowing to measure the source displacement in one direction with a precision better then 10 μm with the present amplification ratio (Fig. 6.32).

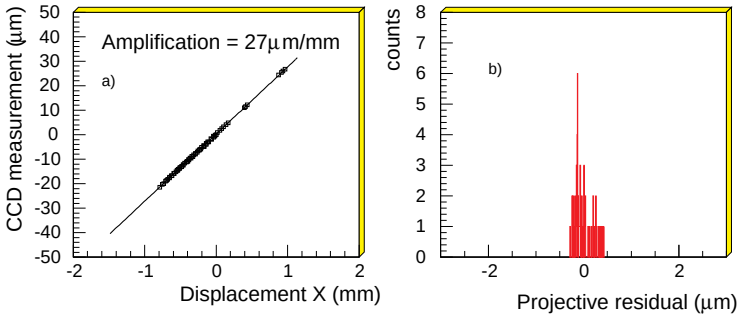

Fig. 6.32: Linearity obtained with one light source in one dimension.

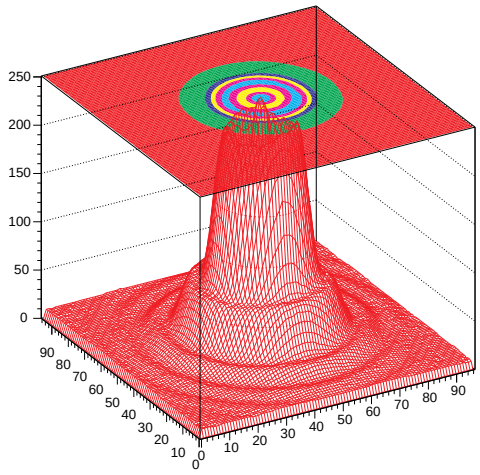

Fig. 6.33: Typical image obtained with one CCD of our experimental setup. Figure shows a 2D image of the light intensity profile, and a contour plot, where the concentric ring profile from the diffraction pattern is clearly seen.

6.5.3.3 Global layout

We propose to use the straightness method described above to measure the deviations from their nominal position of each element of the Tracker. For this purpose we consider the Tracker divided in several longitudinal elements (Fig. 6.26).

The final granularity of the proposed system depends on ongoing laboratory tests. For the moment we suppose that each of the endcaps will be sampled in 3 or 4 disks and that each barrel is considered as a single volume. Each of these structures will have six points to be measured on each face. Since each point must illuminate independently both extremities of the Tracker, this leads to a total of 24 light sources for each element to be measured. For the moment, each of these non-collimated light sources is a single-mode, 4 μm core, optical fibre injected with HeNe laser light from the control room. The 2D position-sensitive light detectors (eg. CCDs) with corresponding apertures, are placed at the endcaps of the Tracker on highly stable and precise support structures. Surrounding each CCD there is a network of four optical fibre light sources, placed at known positions with respect to the aperture, that are seen by the CCD on the opposite alignment wheel. This system ensures the necessary auto-calibration inside the aperture-CCD module and also between the two alignment wheels.

6.5.3.4 The alignment wheel

The alignment wheels, placed at both ends of the Tracker, are fundamental pieces of the position monitoring system Fig. 6.34. They house the detection elements of the Tracker internal alignment, namely the 2D light detectors with the associated pinhole apertures, and provide the mechanical connection between the position monitoring systems of Pixel, Silicon and MSGC detectors. These wheels also support the Tracker part of the Link to the Muon positioning system, namely, the periscopes and their respective light detection systems and three sets of laser levels that measure the ϕ orientation of these wheels with respect to the direction of gravity and provide the relative ϕ orientation between the Tracker and the Muon system with a precision better than 5 μrad [6-21].

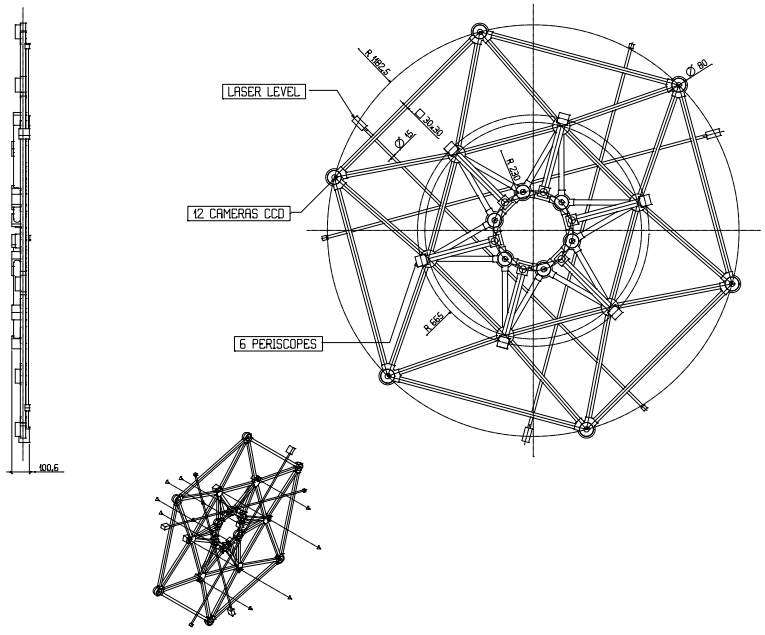

Fig. 6.34: Schematic layout of the alignment wheel showing the triangular structure, and the location of the 2D light detectors for the Pixel, Silicon and MSGC position monitoring system. Also shown are the periscopes and the laser levels (part of the Muon Link system).

The layout of the alignment wheels is mainly dictated by the orientation of the periscope system: one periscope at $\phi = 15°$ and the remaining five equally distributed over 2π. If we want to have the best mechanical connection between the internal alignment and the Link system,

we must have the periscope detection elements mechanically connected to the Tracker internal alignment detectors.

The location of one end of the periscope at the level of the Silicon alignment channels, the need for mechanical stability and for the lightest possible structure of the alignment wheel define approximately the position of all the internal alignment channels.

The parallelism required between the reference axes is guaranteed by the stability and stiffness of each alignment wheel, and by the parallelism between the two wheels. The stiffness is related to the choice of materials and to the mechanical layout of the wheels (see Section 6.5.5.1). Rotations around the three axes have a different impact on the parallelism of the reference lines. Most important is the relative rotation of the wheels in ϕ; these rotations are permanently measured by the laser levels and the parallelism between the axes is measured with roughly one order of magnitude better accuracy than that of these devices. For the other rotations, it is sufficient that the two wheels are parallel to better than 1 mrad. What is left to be measured is the stability of the distance between the light detector elements. The design and engineering studies of the alignment wheel are oriented towards a stable and stiff structure with the minimum amount of material. However, since these structures represent a key point in the performance of the Tracker position monitoring system, we are studying the possibility of installing a simple metrology system that permanently monitors the relative in-plane position of the 2D light detector elements installed on the alignment wheels.

6.5.3.5 Expected performance of the position monitoring system

The expected performance of the position monitoring system is obtained with a simulation program as described in Ref. [6-20]. However, the geometry of the detector is evolving and we are now using a simple geometrical model that describes approximately the behaviour of the system. Assuming that the six reference lines, provided by the aperture–detector connection between the two alignment wheels, are defined without errors, we obtain a precision on the location of a subdetector support structure that is better than 5 μm and a precision on a rotation around the z axis better than 5 μrad (Fig. 6.35). For the other two rotations, the precision relies on the axial distance between corresponding points on the same object, but if we keep this distance larger than 250 mm, we can expect resolutions better than 20 μrad [6-20].

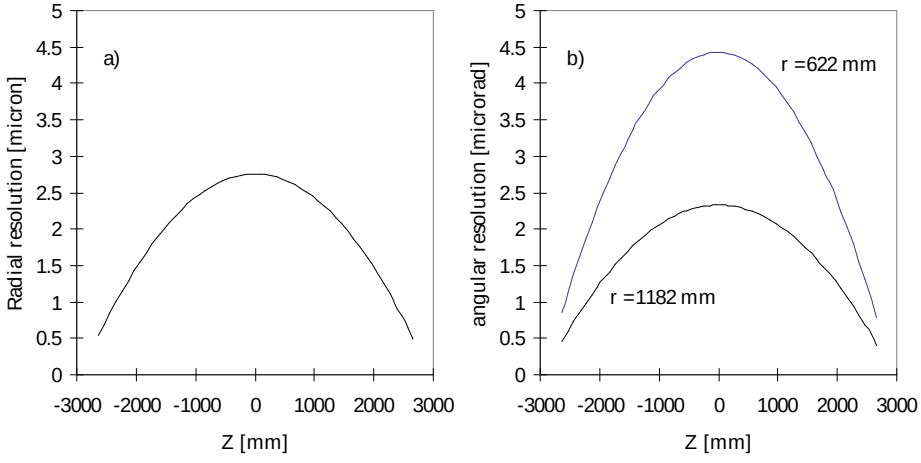

Fig. 6.35: Resolutions obtained with a simple geometric description of the system. a) on the radial position of one wheel depending on its location between the alignment wheels, b) precision on the angular rotations around the beam axis for different radii corresponding to the positions of the MSGC (r=1182 mm) and Silicon alignment channels.

With these results we have a comfortable safety factor before the resolution of our system becomes comparable to the positional uncertainty expected from the assembly of these large structures. More detailed simulations are under study and will be tuned to the experimental results.

6.5.4 Link to the Muon system

The Link to the Muon system is a fundamental part of the CMS Muon alignment, of which the Tracker is an integral part. The complete muon alignment system is segmented in six ϕ planes, to which the three tracking detector systems are connected (Muon barrel, Muon endcap and Inner Tracker). Figure 6.36 schematicaly shows the full alignment setup.

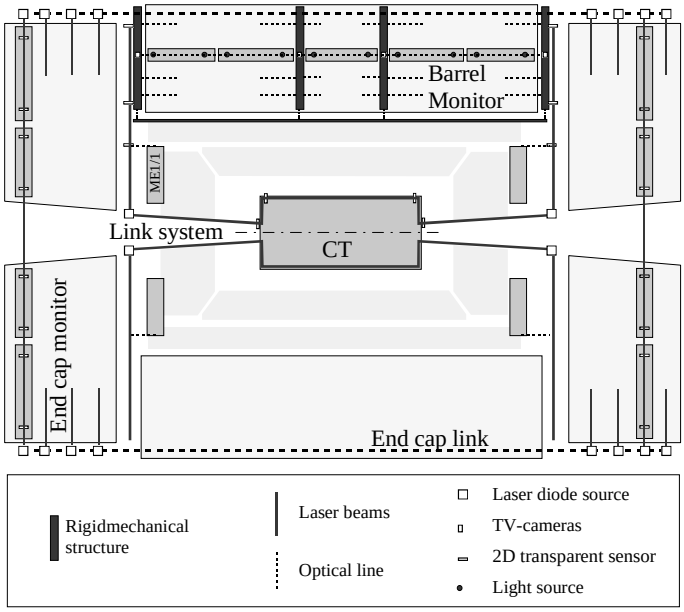

Fig. 6.36: Lateral view of the CMS detector showing the barrel, endcap and Muon Link alignment systems [6-21].

The Link system connects the Tracker alignment system to the MAB structures (Muon Alignment Barrel) to which the Muon endcaps are also referred. It provides a set of six light paths (uniformly spaced at 60° in ϕ) generated from two independent laser light sources (at z±6630 mm) attached to the endcap return yoke. Each light source produces two laser beams at a fixed angle of ∼95.7°, one heading to the MAB and the other heading to the inner part of the Tracker alignment wheel.

The six periscopes placed on the Tracker alignment wheel allow each of the six light beams coming from the Link system to cross the full Tracker detector from one alignment wheel to the other at a radius close to that of the CST. These periscopes are instrumented both at the inner radius ($\eta = 3$) and at the outer radius (CST) with 2D transparent light position detectors, allowing the measurement of movements of the Tracker as a rigid body with respect to the MAB structures. Figure 6.37 shows a schematic drawing of this system.

From the results of simulations, the required precision and stability of the elements of the periscopes are given in Table 6.24. These tight requirements imply a careful design of the alignment wheels and a thorough choice of materials, presently under study both by the Tracker and the Muon alignment teams [6-21], [6-22].

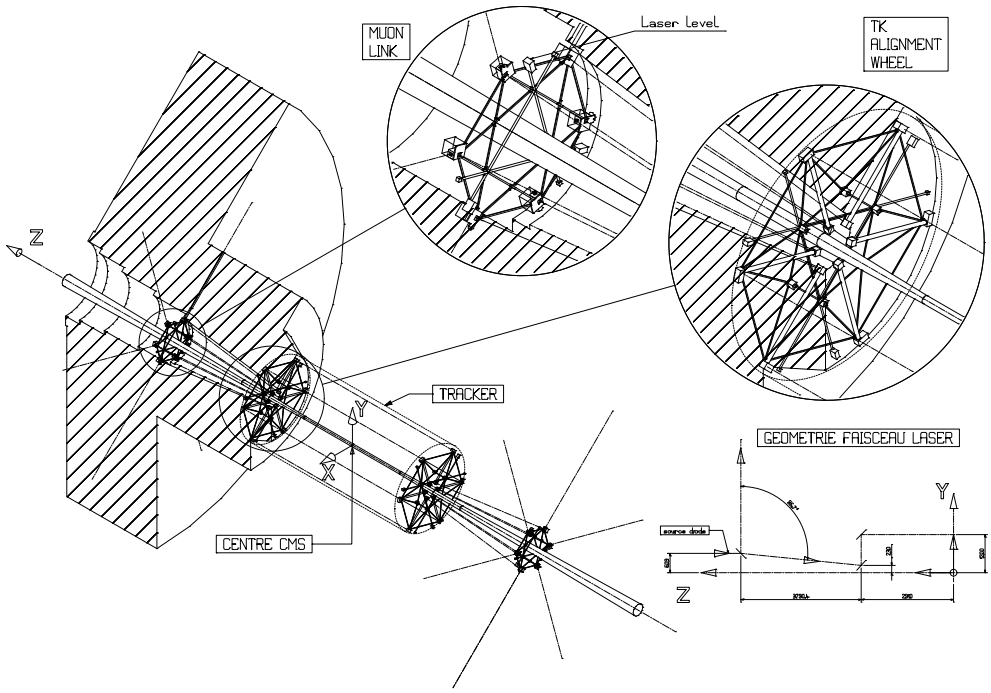

Fig. 6.37: Schematics of the Muon Link system.

Table 6.24: Requirements on the periscope elements [6-21]

		Position tolerance [mrad]	Stability required [mrad]
Periscope positioning	Max. Rot (x)	10	(not critical)
	Max. Rot (y)	10	2
	Max. Rot (z)	6	0.1
Mirror's orientation	Max. Rot (x)	0.7	0.005
	Max. Rot (y)	1.4	0.01
	Max. Rot (z)	1.4	0.01

6.5.5 Engineering and system aspects

6.5.5.1 The alignment wheel

The main design criteria for the alignment wheel support structure are:

- *high dimensional stability* dictating the selection of material and of the assembly process and requiring an adequate test facility to verify it accurately;
- *high stiffness to mass ratio* reflected in the material selection and the dimensioning of the elements;
- *the fixation of the CCD cameras to the alignment wheel support structure, the fixation of the alignment wheel to the Tracker structure, and the internal assembly of the wheel* require a careful study of the choice of material, design and assembly processes.
- *high first natural frequency* of about 30 Hz as suggested in Ref. [6-23].

Material selection

A good performance of the alignment wheel, in terms of precision and stability, is directly dependent on the properties of the chosen materials and on the environmental conditions. As discussed in Section 6.2.6, the main parameters leading to the choice of material are the product of the Young modulus and the radiation length (EX_0), the CTE and the CME. With the stringent design requirements for the alignment wheel, the choice is naturally oriented towards a CFRP, with a highly performing fibre and a resin qualified for aerospace applications (new generation of epoxy, or cyanate ester). The complex shape of the alignment wheel (Figs. 6.38 and 6.39) is mainly dictated by the need to provide a large number of interfaces with the Tracker and with the Link system. The resulting geometry is naturally suited to the exploitation of the anisotropic behaviour typical of composite materials. Thus, a lay-up with orthotropic properties has been selected for the structural elements. In this way the mechanical properties of the material can be optimised in preferential directions, allowing standard high-performance fibres to be selected as candidate materials. We have decided to start the design assuming a standard aerospace-qualified CFRP, in order to achieve a safe and conservative solution. Better performance can then be attained, if needed, by resorting to more sophisticated fibres (e.g high modulus or ultra high modulus fibres).

F.E.A. model

The alignment wheel support structure has been modelled and a finite element analysis (ANSYS 5.3) has been performed to evaluate its mechanical stability. After the optimisation studies [6-24], the two layouts A and B shown in Figs. 6.38 and 6.39 are proposed.

The analysis was performed under the following considerations:

- All the tubes have square cross section: width = height = 30 mm, thickness = 2.0 mm for layout A and thickness = 1.0 mm for layout B;
- The inclination of 1.23% of the LHC tunnel was taken into account;
- The material used is a CFRP, T300/N5208 in an orthotropic layout, with the mechanical properties described in Ref. [6-5];
- The structure was isostatically fixed to the CST at three points.

The structure was modelled with 3D Elastic Beam Elements (BEAM4). The CCD cameras, the mirrors and the periscopes were modelled as simple additional mass using 3D Structural Mass Elements (MASS 21). The periscopes were included in the model considering the worst possible case in terms of performance: they were added as simple mass, therefore not contributing to the rigidity of the structure. For the periscopes[1], we assumed a cross section of 40×40 mm^2,

[1] The material presently under study for the periscopes is fused silica doped with Ti [6-21].

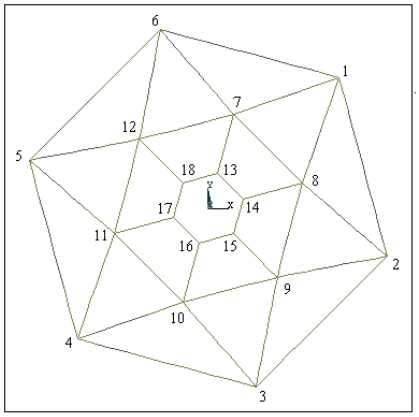

Fig. 6.38: Layout *A* for the alignment wheel support structure.

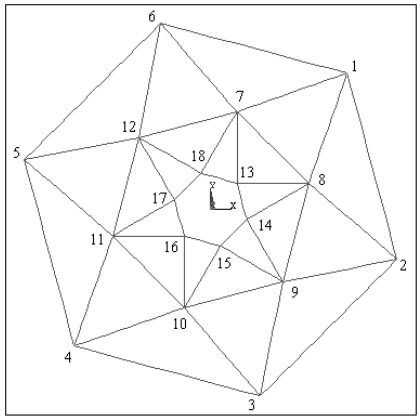

Fig. 6.39: Layout *B* for the alignment wheel support structure.

a length of 0.39 m, silica glass as the manufacturing material and a fixation at the level of the Silicon and Pixel detectors. The additional weight of the six periscopes amounts to 19.8 kg.

Results

The results obtained in ANSYS were compared to the results obtained using another software package and a good agreement was found.

Wheel assembly

The tubes can be assembled in two different ways: adhesive bonded joints and mechanically fastened joints. The decision between bonding and fastening depends upon a number of factors arising from the overall requirements of the structure.

The analyses performed assume two different possibilities. In the first, the tubes are glued at the nodes. The error introduced on the assumption of an ideal gluing can only be calculated once a prototype has been tested. The second possibility consists in assembling the structure with pin joints. Those joints could also have the capability of supporting the CCD cameras inside them and provide an easy way of *in situ* assembly and disassembly of a wheel to allow the Pixel removal/installation. This feature can be modelled in ANSYS by introducing coupling constraint equations at the linking points. This is a simple approach that can give both a qualitative and quantitative measure of this alternative. The results obtained are represented in Table 6.25 and in Fig. 6.40.

The following conclusions can be drawn:

- Assuming the same assembly process, geometry *B* gives better results;
- The assembly scheme only influences the in-plane displacement. This influence is larger for the Pixels when we consider the presence of joints. The displacement out of the plane is equal for both layouts. The rotation in the plane is almost constant for the two assembly possibilities except for the Pixels in the case of geometry *A* with joints;
- The deformations obtained at the level of the CCDs is small when compared to the maximum displacements of the wheel;
- The dynamic behaviour in both layouts is characterised by bending deformations out of the plane;
- Stress level is within allowed values.

Better results can be obtained by optimising the cross section of each tube and the material used. By carefully observing the values of axial direct stress and of bending stress in the structure, the dimensions of the cross section of the tubes can be modified in order to redistribute the load as uniformly as possible. For layout A and considering the structure without joints, the optimisation process of the tube's cross section lead to a decrease of 26% of the maximum displacement, a decrease of 41% in the maximum stress and an increase of 1.4% in the first natural frequency. We verified that the main contribution to the process was an overall decrease of the stress level within the structure.

Table 6.25: Maximum deformations and dynamic behaviour of the proposed layouts

	Lay A glued	Lay A pin joints	Lay B glued	Lay B pin joints
Displacement field [μm]				
max. u_x	4.06	11.12	2.79	9.01
max. u_y	-6.36	-18.38	-5.82	-17.24
max. u_z	1.76	1.76	2.01	2.01
max. u_T	6.57	18.42	5.89	17.53
|Max. stress| [MPa]	0.66	0.38	0.59	0.85
Freq. of the vib. modes [Hz]				
f_1	21.5	0.00	20.5	20.5
f_2	21.5	21.5	20.5	20.5
f_3	36.6	21.5	32.1	32.1

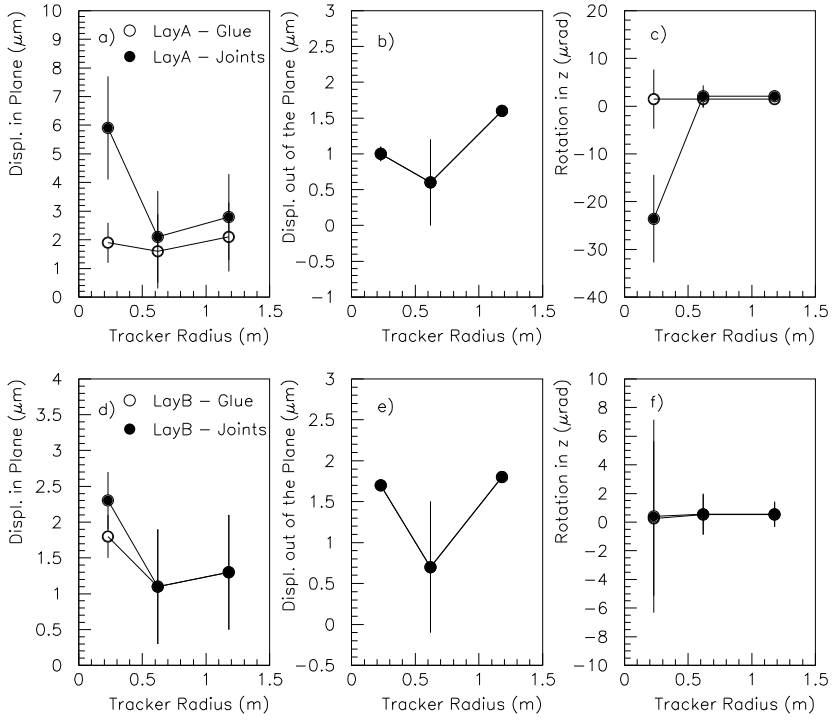

Fig. 6.40: Influence of the assembly process in the behaviour of the two layouts. Average and the standard deviation of the data obtained for the six CCD cameras at the Pixel, Silicon and MSGC radius are presented. a) and d) In-plane displacement. b) and e) Out of plane displacement. c) and f) Rotation in z.

Cross section variation

An alternative and probably cheaper solution to the use of different cross sections is the use of just one cross section. So, picking up layout A without joints (the worst case of the best solution) and layout B with joints (the best case of the worst solution) the influence of varying the cross-sectional parameters on the performance of the structure was studied.

The following conclusions can be drawn:

- For layout A without joints we can observe that an increase of the wall thickness/width/height produces a decrease of maximum displacement and rotation and an increase of the first natural frequency. However, these benefits are more accentuated for thickness values less than 2 mm.
- For layout B an increase of the wall thickness produces an increase of the maximum displacement and rotation. However this tendency cannot be directly extrapolated to all the points within the structure. These results are mainly due to the increase of mass introduced by the increase of thickness and to the fact that the maximum displacement and rotation are obtained in the exterior tubes at the level of the MSGC detectors. An increase of the width/height produces a decrease of the maximum displacement and rotation and an increase of natural frequencies.
- With layout A we can easily obtain maximum displacements in the 10 μm range, maximum rotations less than 20 μrad and natural frequencies around 20 Hz. With layout B we are able to guarantee maximum displacements less than 20 μm, maximum rotations around 40–50 μrad and natural frequencies about 20 Hz. Note that these data refer to maximum displacement values and not to local values at the CCD level.

Another possible analysis is to check the behaviour of the structure at the CCD locations when three different cross sections, with the same area but different inertia moments, are used. Considering the cross sections listed in Table 6.26, the data obtained are shown in Table 6.27 and in Fig. 6.41.

Table 6.26: Studied bar sizes for the two layouts

	Cross sect. No.	1	2	3
Lay. A	width [mm]	25	30	35
	height [mm]	35	30	25
	thick. [mm]	2	2	2
Lay. B	width [mm]	25	30	35
	height [mm]	35	30	25
	thick. [mm]	1	1	1

Table 6.27: Maximum displacement [μm], and first frequency obtained for three different cross sections defined in Table 6.26

	Cross sect. No.	1	2	3
Lay. A	max u_T	5.74	6.57	8.07
	f_1	18.8	21.5	23.9
Lay. B	max u_T	14.31	17.53	23.01
	f_1	17.9	20.5	22.7

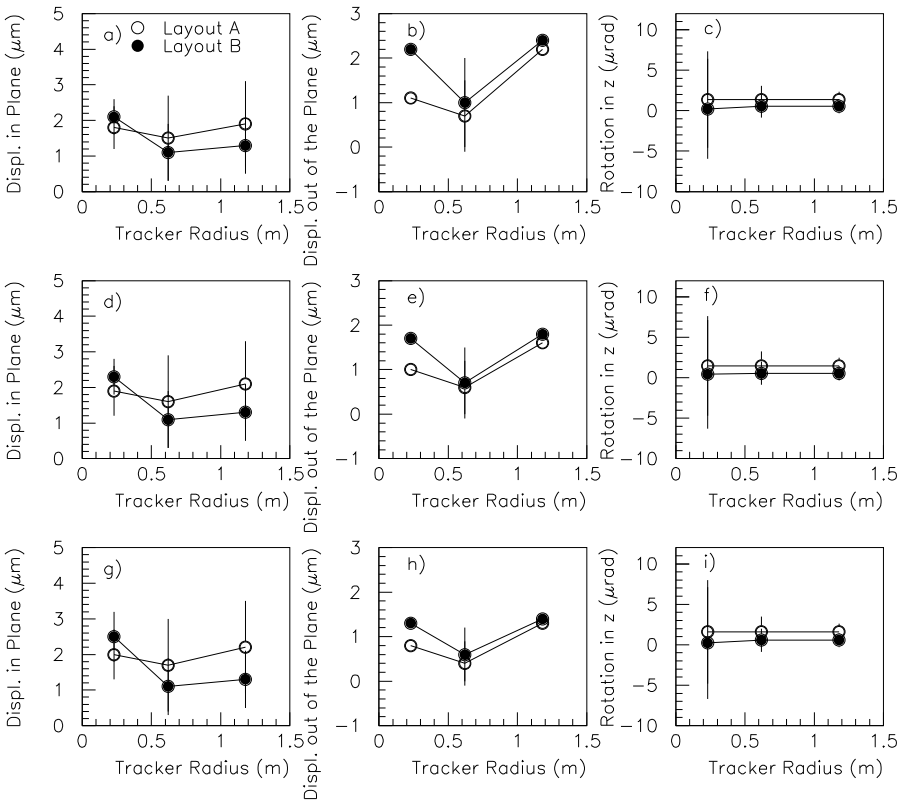

Fig. 6.41: Influence of the cross section on the behaviour of the two layouts. Average values and the standard deviation of the data obtained for the six CCD cameras at the Pixel, Silicon and MSGC levels are presented. a) to c) Cross section 1 (w = 25 mm h = 35 mm). d) to f) Cross section 2 (w = h = 30 mm. g) to i) Cross section 3 (w = 35 mm h = 25 mm).

Comparing the results we can verify that:

- The in-plane (out of plane) displacement increases with an increase in the width (height) of the cross section. The global effect is an increase of the total displacement with the width. This is mainly due to the fact that the forces acting on the wheel are bigger in-plane than out of the plane;
- The rotation in z is almost constant for the three cross sections;
- The out of plane displacement is always bigger for layout B. The in-plane displacement is smaller for layout B, except at the Pixel level;
- The first natural frequency increases with the increase of width.

The choice of the final dimensions for the cross section must take into account all these considerations and the space available in z for installing the wheels inside the Tracker.

Young modulus variation

Another variable which influences the results is the manufacturing material. The influence of varying the longitudinal Young modulus on the performance of the structure was studied. The results are summarised in Fig. 6.42.

We observe that reasonable values can be obtained even with lower performance fibers. A local analysis at the CCD level, indicates that by varying the Young modulus between 180 GPa and 300 GPa (the same range as in Fig. 6.42) the displacement in-plane and out of plane is always less than 3 μm and the rotation in z always less than 6 μrad. The discrepancy between local values and maximum values, mainly for layout B, is due to the deflection of the exterior

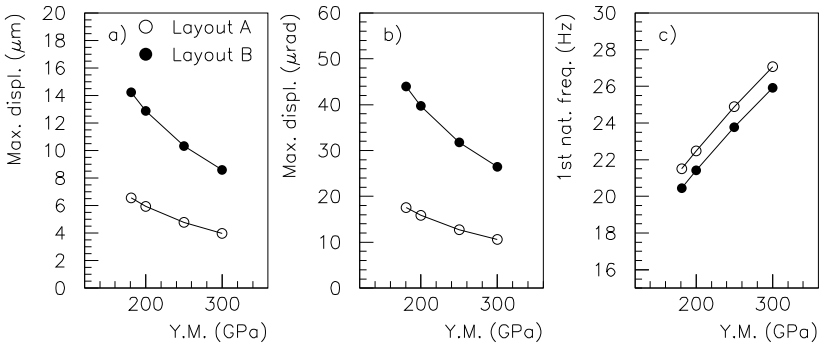

Fig. 6.42: Influence of the composite's Young modulus on the behaviour of layout *A*: glued, w = h = 30 mm, t = 2 mm and layout *B*: pin joints, w = h = 30 mm, t = 1 mm. a) Maximum linear displacement. b) Maximum rotation. c) First natural frequency.

tubes at the MSGC level. In order to decrease these values, another solution would be to glue these exterior tubes and use pin joints for all the rest. By considering layout *B* we observed that the partial pin joint solution gives results lying between the other two cases; the glued one and the one with pin joints everywhere. We also observed that the variation of the transverse Young modulus between 5 GPa and 20 GPa does not influence the results.

The main advantage of the use of a higher Young modulus fibre would be the increase in natural frequencies.

Influence of temperature and moisture

Details of the exact climatic conditions in the alignment wheel area are not yet available, but some estimates predict variations of the order of 10 °C in temperature and 80% in relative humidity (during maintenance periods). Taking these factors into consideration, a stationary analysis was developed. The analysis of the effect of moisture gradients on the behaviour of structures is not directly available in ANSYS. Therefore this kind of simulation must be performed by taking into account the fact that temperature and moisture are related to strain and stress in a similar way. By considering a uniform temperature gradient of 10 °C and a uniform moisture content of 60% relative humidity the following conclusions can be drawn:

- For the case of the considered material (T300/N5208 unidirectional), CTE and CME variations only influence in-plane displacements. Values of transverse CTE and CME do not influence the results due to geometry and to the material used;
- Considering just the CCD locations, we verified that for both layouts that we need a longitudinal CTE lower than $6 \times 10^{-7}/\mathrm{C}^{\circ}$ and a longitudinal CME lower than $10^{-7}/\mathrm{w}\%$, independent of the composite lay-up, in order to have displacements in-plane and out of plane less than 10 μm and rotation in z less than 10 μrad;
- The presence of joints reduces the deleterious effect on structural performance caused by temperature and moisture variations. This effect is more significant for layout *A*.

The study of coupled effects of temperature and moisture has not been developed. On the other hand the exact environmental conditions in the alignment wheel zone are not well known: power cables, cooling pipes and dissipated heat load will certainly play an important role in the definition of the environment. Therefore the objective is to have a CTE and a CME as low as possible.

Comments and conclusions

The F.E.A. calculations performed on several structural layouts of the alignment wheel lead us to the comparison of two promising configurations with different assembly and composite characteristics. Although not completed, this study shows that the proposed layouts can fulfil the requirements on stability and precision imposed by the internal Tracker alignment system and the Muon Link system. To confirm these results, further work, mainly on prototyping, is now starting.

6.5.5.2 Alignment channels layout

The size of each of the six alignment channels at the Silicon and MSGC level is 60×35 mm. However, the alignment channels at the barrel MSGC outer radius must be smaller which prevents an optical free path connection between both ends of the Tracker. A solution under study is the installation of a connecting element at the ends of the barrel MSGC. This element could be two back-to-back CCDs with their respective pinhole apertures. These elements, if properly calibrated, allow the transfer of the endcap MSGC measurements from one side of the barrel to the other, and also allow the internal measurement of the barrel MSGC. The space needed for the alignment channel at the Pixel level has not been optimised. The final technical design of the light source support points has not been finalised. However, prototyping work has been done as shown in Fig. 6.31. As mentioned in the text, the ϕ location of the alignment channels is closely connected to the requirements of the Muon Link system.

6.5.5.3 Electronics and readout

The electronics and readout system for the position monitoring system is obviously dependent on the choice of light detector. At present radiation hard electronics for the transparent Silicon detectors of the CMS Muon alignment system are under development. If rad-hard CCDs are to be used, then a scaled-up system similar to the one presently used in the laboratory tests can be foreseen. This is mainly composed of frame grabbers reading several CCDs in a multiplexed way through a desktop computer. For the other systems, like the periscope detectors and the laser levels belonging to the Link part but within the Tracker volume, a clear definition of the reading sequence and of the electronics to be used must be done in collaboration with the Muon alignment group.

6.5.6 Laboratory tests

6.5.6.1 Full scale test with the Muon alignment system

The aim of this test will be to evaluate the relative position measurement accuracy between the Tracker and the Muon system. The global layout of the test setup is shown in Fig. 6.43. It will be used to measure the performance of the smallest complete set of one of the six planes of the complete CMS Muon positioning system and to develop the integration of the different subsets of this system. Concerning the Tracker part, this could be done in steps of increasing complexity Fig. 6.44, as follows:

A - In a first step, the Tracker will be replaced by transparent light sensors, placed at known positions, in order to evaluate the Muon and Link systems;

B - This test aims to understand the behaviour of the Tracker part of the Link system and the Link system itself. For that, we will place, in each link path, four mirrors and the necessary detectors in order to evaluate the performance and the requirements for the periscope and its supporting structure. Simultaneously, the periscope will be developed

and once a prototype is available, it will replace the previous mirror system. With this new system, we will be able to measure the relative displacements between the Tracker and the Muon system when these are considered as rigid bodies;

C - The next step will be the transport of a point belonging to the Tracker into the global coordinate system. For that we intend to use a scaled-down layout of the Tracker position monitoring scheme.

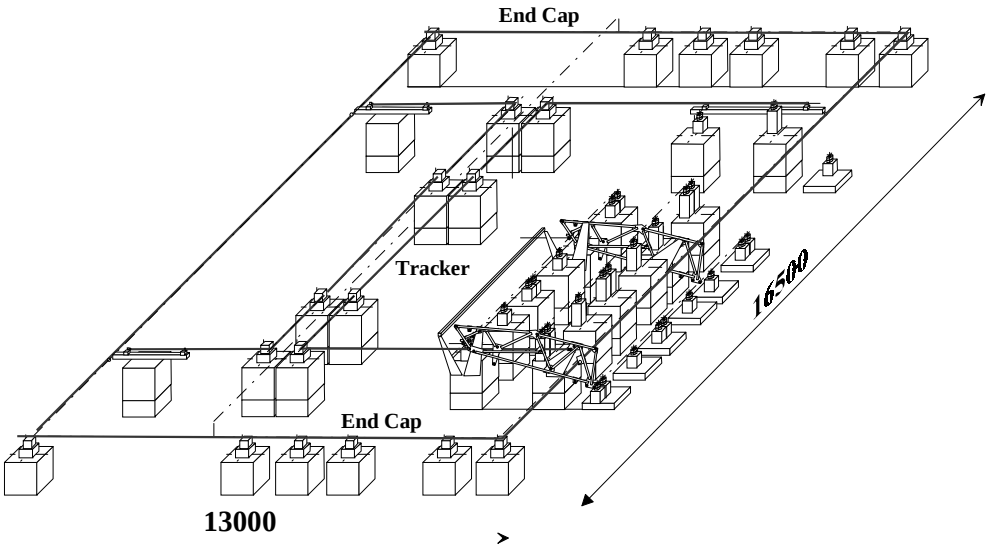

Fig. 6.43: General layout of the proposed test setup for the global alignment system.

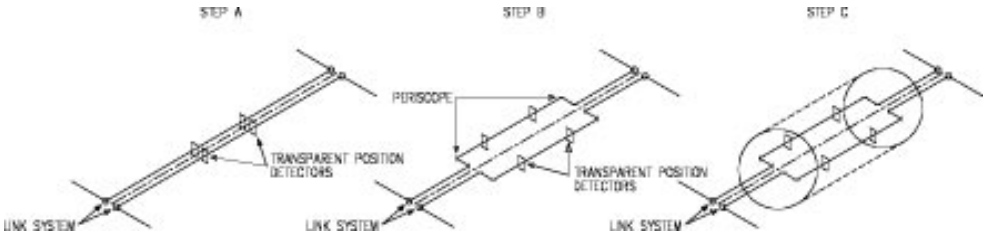

Fig. 6.44: Different steps foreseen on the full scale test with the Muon system. From left to right steps A, B and C as described in the text.

6.5.7 Other techniques under evaluation

6.5.7.1 z-coordinate measurement

High precision is not required for the measurement of the position of the structures supporting the detectors in the axial direction. In fact, the required precision and stability can, in principle, be assured by the mechanical stability and stiffness of the Tracker structures. In this case there is no need for any sophisticated z-measurement system and simple gauges placed on the structures will do the job. However, this will increase the number of active sensors within the Tracker volume, which is something we want to avoid. This is the reason for studying the possible use of alternative optical techniques for distance measurements between the Tracker support

structures, using the existing network of optical fibres in the Tracker with minor changes and without any further modifications inside the Tracker volume.

6.5.7.2 Other 2D light detection mechanisms

Other light detection means are under consideration for possible application in the position monitoring system instead of the CCDs used so far. There are several considerations to take into account regarding the choice of an alternative light detection device. First, it must obviously be sensitive in the wavelength range we are using. The segmentation, in orthogonal directions, must be such as to allow the required precision in localisation with the light spot size in use. For the moment the CCDs we are using have square pixels of 11 μm. With this device we can obtain true 2D readout and a precision in the localisation of the light spot centre of about 2% of the pixel size. If the same distance from aperture to CCD is preserved, then the effect of increasing the pixel size up to 100 μm will be insignificant when compared to the present accuracy obtained in the evaluation of the centre of the image [6-25], for the same signal-to-noise ratio. Up to now, we have not used the 2D capabilities of our CCDs in the evaluation of the spot centre; in fact, we are using a rather simple projective Centre of Gravity (COG) method, modified to account for the noise. However there are some indications that, for special cases, we might have to modify this algorithm and use the full 2D information of the sensor. This might also be needed if we use a different aperture shape. Thus, we aim for a true 2D readout with pixel devices although we keep open the possibility of using 2D projective readout with orthogonal strips. For both cases, tests are foreseen with radiation resistant Silicon pixel detectors and with 2D Silicon strip detectors. Another possibility under evaluation is the use of optical fibres precisely assembled in bundles and placed where the CCDs are sitting. These bundles would carry the 2D picture to a CCD placed in a region where radiation is not so harmful. For this purpose we could use devices similar to commercial ones [6-26].

6.5.7.3 Use of transparent Silicon detectors for the Tracker alignment

Amorphous Silicon strip detectors are currently proposed as transparent straightness monitors for Tracker devices at other experiments [6-27] and are foreseen to be used in the CMS muon alignment system [6-21]. These devices, developed at MPI [6-28] have two sets of orthogonal ITO (indium-tin oxide) strips with 312 micron pitch, with a thin ($\sim$1 μm) layer of hydrogenated amorphous Silicon between them, and are designed to be transparent to visible light, 80% at 690 nm with a sensitivity of 0.1 A/W. The whole detector is sitting on a 500 μm thick glass substrate. With this pitch, available commercially from EG&G Heimann Optoelectronics in Germany, good position accuracy was found on the determination of the COG of a collimated laser beam. These detectors were submitted to high doses of neutrons, $> 10^{14}$n/cm^2, without any noticeable changes of their optical properties, but their detection performance after irradiation has not been evaluated yet. We have the possibility to place the readout electronics several meters away in a location where radiation damage is not so critical, which is certainly an advantage. A straightness monitoring system based on transparent Silicon sensors, can be envisaged for the CMS Tracker instead of the lensless one proposed so far. However, this would increase by a large factor the quantity of information to process and the complexity of the whole system. For example, for the Tracker Silicon and MSGC monitoring system, we would multiply by $\sim$ 6 the number of detectors to read and we will have more than 5000 independent electronic channels. We intend to keep this option as a back-up solution, and we will test the detectors, with a modified pitch, for eventual replacement of the CCDs in our lensless straightness system.

6.5.7.4 Straightness measurement with a stretched wire

Straightness measurement systems based on biaxial Wire Positioning System (WPS) are proposed for the pre-alignment and active control system of the CLIC project [6-29]. These devices are now commercially available [6-30] with precision better than one micron in both directions with respect to a stable and straight stretched wire. The major drawback of the existing systems is the large size of the detector as well as the need to apply a strong tension to the wire to avoid bending and to minimise the amplitude of the vibrations. We tested several detector sizes with home-made electronics. The results obtained with a 200 mm long BeCu wire of 100 μm diameter indicate a resolution better then one micron in both directions with an active detector of $15 \times 10 \times 10$ mm^3 [6-31]. Further tests are foreseen to study the performance of such devices with smaller electrodes and with longer wires, in order to understand if these devices could be used for some small parts of the Tracker alignment.

6.6 CMS Proposal for the Beam Pipe

In the CMS Technical Proposal a beam pipe optimised for high luminosity operation was presented. Soon thereafter it was recognised that the B-physics during the initial low luminosity running would greatly benefit from a pixel layer at smaller radii than foreseen in the Technical Proposal. In order to incorporate such layers another beam pipe was designed to be used only during the low luminosity phase. This low-luminosity version, due to its unfavourable geometry and poor vacuum conductivity, was known to be incompatible with high luminosity operation where radiation background issues become essential design criteria.

In order to avoid a replacement of the beam pipe after the low luminosity phase we propose a design of the beam pipe which can accommodate the low luminosity pixels and at the same time fulfils the special high luminosity requirements Figs. 6.45.

The criteria which have guided the design are:

1. Possibility to insert the pixel detector after bake-out of the beam pipe, when the bake-out jackets have been removed.
2. Acceptable background in the endcap muon chambers – even an optimum beam pipe is responsible for roughly half of the background in ME1/1 [6-32].
3. Sufficient vacuum conductance so that massive ion pumps are not needed inside of the experiment ($|z| < 14.5$ m).
4. Incorporation of a cylindrical section for in-situ cutting and welding and to accommodate bellows. This section has to be outside the Tracker volume, but inside $z = 4.5$ m.

In addition to these, it has been recently argued [6-33] that a minimum radius of about 22 mm is required to ensure sufficient clearance to the beam tails.

While the vacuum quality is not expected to be critical for the experiment [6-34], a limit to the maximum pressure is set to avoid a run-away condition, in which the LHC beam accelerates residual gas ions towards the chamber walls and so leads to more outgassing and to an increase of pressure.

Simple considerations on the relationship between the pressure inside a pipe and its geometry show that a decrease of the beam pipe radius has to be compensated by a reduction of the distance to the pump. In order to avoid lumped vacuum pumps, NEG strips are proposed inside of the experiment. Present NEGs can be deposited only on stainless steel, so the vacuum requirements enter also into the length required for a stainless steel section inside of the detector. If the development work on deposition of NEG strips on aluminium is successful, part of the aluminium sections could also be covered with NEGs thus further improving vacuum quality and possibly reducing stainless steel.

The parameters of the proposed beam pipe are collected in Table 6.28.

Table 6.28: Parameters for the CMS hybrid beam pipe

Material	z-range (mm)	Inner radius (mm)	Wall thickness (mm)	Shape
Beryllium	0–750	25	1.0	cylindrical
Aluminium	750–1678	25	1.5	cylindrical
Aluminium	1678–4030	25–60	2.0	conical
Aluminium	4030–4067	60–70	2.0	conical
Stainless	4067–4702	70	1.5	cylindrical
Aluminium	4702–10600	70–157.8	2.0–4.5	conical
Aluminium	10600–10750	157.8–100	4.5–3.0	conical
Stainless	10750–pump	100	2.0	cylindrical

The central beryllium section is required in order to limit interactions before the first sensitive layer to a minimum. The conical sections are shown to provide the best geometrical solution to reduce the background in the endcap muon system [6-32, 6-34]. The stainless steel section between 4067 mm and 4702 mm accommodates two bellows and the NEG strips and provides the possibility for *in situ* cutting and welding of the pipe. Stainless steel is preferred for the latter operation because *in-situ* welding of aluminium is not yet a fully mature technology.

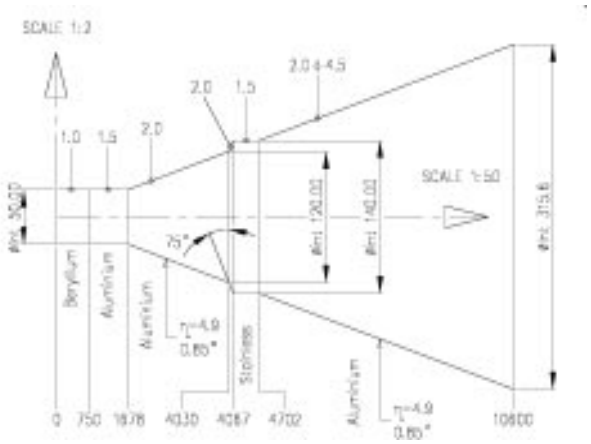

Fig. 6.45: Proposed CMS version for the beam pipe layout.

6.7 Tracker Assembly and Installation

6.7.1 Assembly hall

The different sub-systems of the Tracker will be constructed in regional centers. The size of the sub-systems still needs to be decided: as an example, one can consider the endcap MSGC detectors to arrive at CERN as 2 packed units, or as several packages of 3 to 4 planes, or as 22 individual planes. In any case, the Tracker assembly procedure assumes dealing with 6 pre-assembled sub-systems, 1 MSGC barrel, 2 MSGC endcaps, 1 Silicon barrel and 2 Silicon endcaps, irrespective of whether these blocks are assembled at or outside CERN.

For the general Tracker assembly we propose to use a hall of a typical size of 1000 m^2. The hall needs to be semiclean, equipped with a light crane facility, equipped with water, gas and electricity services and with the necessary cooling machinery for cold operation. An advantage would be to have the hall in close distance to the Silicon and MSGC regional centers at CERN. A candidate for such a hall is building 186 on the Meyrin site. The floor plan of this hall is

shown in Fig. 6.46. The hall is divided into two halves, one used for the Silicon regional centre and storage and the other for the general Tracker assembly. For the general assembly area, the sizes of individual objects such as the MSGC barrel, the Central Support Tube, the assembled Silicon barrel and endcap detector and packages of endcap MSGC detectors are indicated. Also shown are test zones used for MSGC endcap detectors and rods before their installation on the supporting structures. Some of the structures are already equipped with services ('precabled') and with cable and pipe extensions, in order to reach the future patch panel locations. The space required to temporarily support these extensions needs to be reserved.

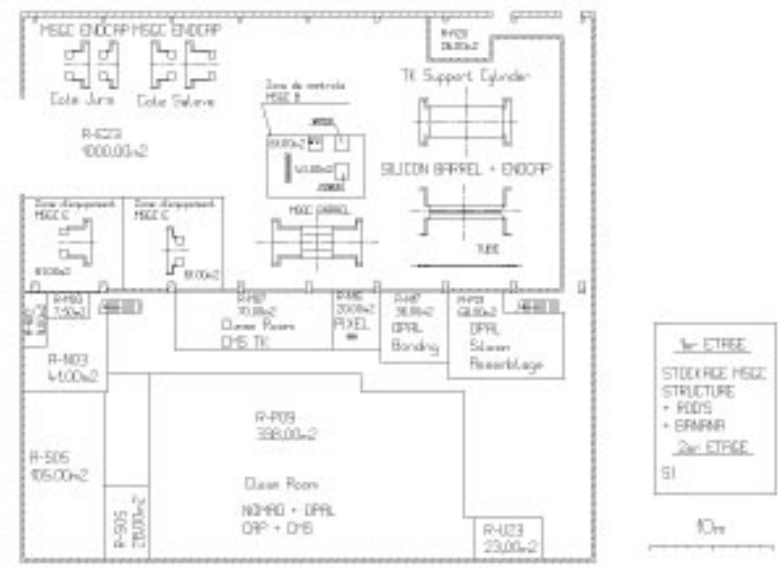

Fig. 6.46: Assembly hall and Silicon regional centre.

6.7.2 General MSGC installation procedure

The MSGC Tracker is assembled on the CST in three preassembled and precabled blocks: the barrel part and two endcaps. Each block travels separately and is supported by a temporary supporting structure, which stands over a movable chariot. The temporary supporting structure might be either cylindrical shells or truss-type beam systems, but must present to the detector the same sliding/rolling interface presented by the CST. An option is to use for this purpose structures, onto which the MSGC blocks are pre-assembled, that would then be designed to allow for a direct connection to the CST.

The connection of the temporary supporting structure to the CST is done through the interposition of a 'connection tube'. This is a short tubular segment, which reproduces exactly a section of the CST and presents a connection interface for the CST at one end, and another for the temporary supporting structure at the other.

Thus, the steps for the general MSGC installation procedure, illustrated in Fig. 6.47, are the following:

1. The Tracker endflanges are mounted on the CST and the full assembly stands on its support feet. The connection tube is attached to the CST and the pre-assembled MSGC

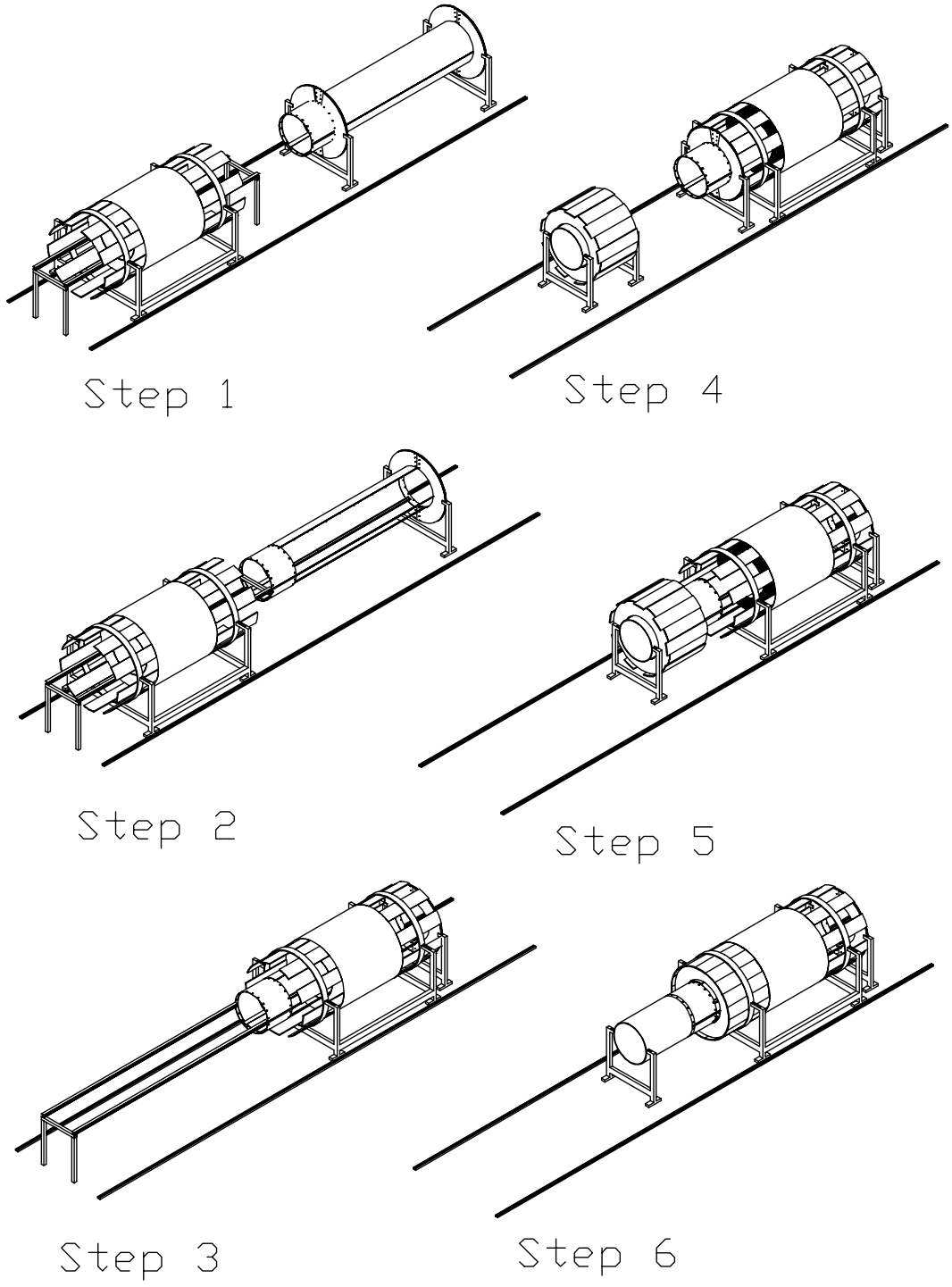

Fig. 6.47: MSGC assembly sequence.

barrel approaches it. In this phase, the service tails are held by a service support frame, that rolls over a rail system and moves together with the barrel (step 1).

2. The MSGC barrel temporary supporting structure is attached to the CST connection tube and the two halves of the facing Tracker endflange are opened and removed. By removal of the corresponding legs of the temporary supporting structure, a continuous sliding guide is obtained (step 2).

3. The barrel detector is tested for final acceptance.
4. The MSGC barrel slides from its temporary supporting structure to the final position on the CST and is fixed there (step 3).
5. The two halves of the removed Tracker endflange are again closed and connected to the CST in their original position. The assembly formed by the CST and the MSGC barrel is now self-supporting, and the temporary supporting structure can be disconnected and removed. The first MSGC endcap block approaches (step 4).
6. Steps 2 to 4 (including the detector test) are repeated for the first MSGC endcap block. The endcap service tails are held by the detector itself (the principal phases are shown in steps 5 and 6).
7. Steps 2 to 4 (including the detector test) are again repeated for the second MSGC endcap block.
8. The MSGC barrel service tails are attached onto the Tracker endflanges, and the service support frame can be removed.
9. A combined test is performed, including powering, cooling and position monitoring.
10. The general MSGC installation is completed.

6.7.3 General Silicon installation procedure

The Silicon Tracker is assembled inside the thermal screen in three preassembled and precabled blocks: the barrel part and two endcap parts. Each block travels separately and slides over an assembly cradle, which is transportable, and presents to the detector the same sliding interface as presented by the thermal screen. The thermal screen is, in turn, positioned over a Silicon installation cradle, which reproduces the slides on the internal face of the CST.

The steps for the general Silicon installation procedure, illustrated in Fig. 6.48, are the following:

1. The thermal screen is positioned onto the Silicon installation cradle, the Silicon barrel is positioned onto the assembly cradle and the two cradles are joined: a continuous sliding guide from the assembly cradle to the internal face of the thermal screen is obtained. The barrel service tails are supported on both ends by temporary supporting frames, sliding on the assembly cradle together with the detector (step 1).
2. The barrel detector is tested for final acceptance.
3. The barrel is slid into its central position inside the thermal screen. All of its services are attached to the allocated spaces on the internal surface of the thermal screen, and the temporary supporting frames are extracted (step 2).
4. The endcap blocks are positioned onto the assembly cradle and are prepared for installation, with the service tails held by the detector structures (step 3).
5. The endcap detectors are tested for final acceptance.
6. The endcap blocks are slid into their final position.
7. All the operations related to the assembly of the two endcap blocks can be performed simultaneously from both ends by two teams, if required.
8. A combined test is performed, including powering, cooling and position monitoring. For this the detector volume must be temporarily closed by the Silicon endflanges (step 4).
9. The Silicon installation cradle is aligned with the CST and the completed Silicon Tracker is moved into its final position inside the tube (step 5).
10. The general Silicon installation procedure is completed.

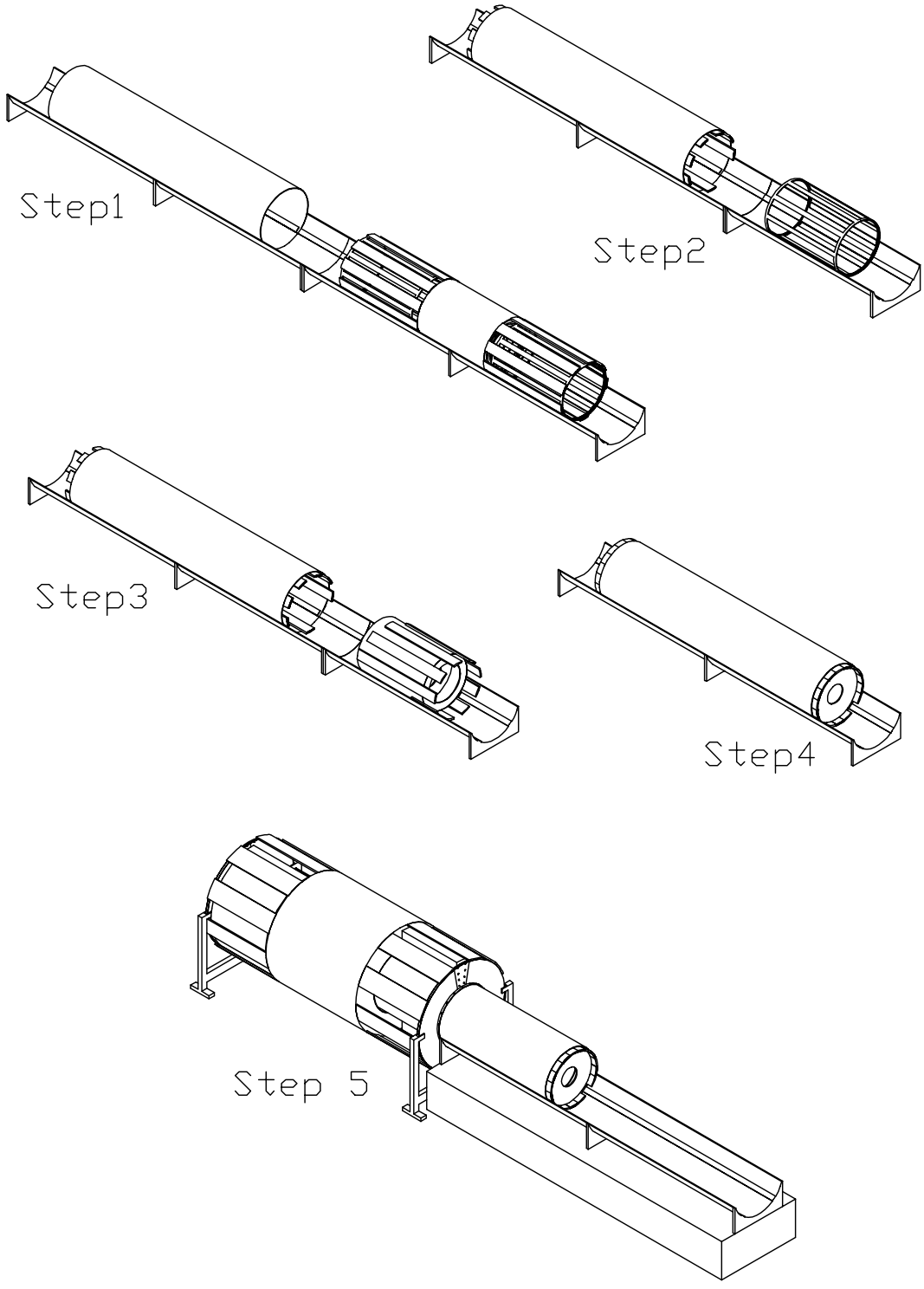

Fig. 6.48: Silicon assembly sequence.

6.7.4 Tracker installation procedure

Before transportation to point 5, the Silicon and MSGC Tracker systems are ready and have been mounted on the CST, which is positioned onto a temporary transport chariot. At both Tracker ends we foresee a storage volume of about 6.5 m^3 (a cylindrical volume of the same

diameter as the Tracker and of 1.5 m length) with temporary service supports to hold the cable and pipes ends, which, after the Tracker installation, must reach the main patch panels. The cable ends are coiled up and fixed to structures held in place on each side by one extension tube element, rigidly connected to the CST. The extension tube consists of individual truss type elements, each one 1.5 m long, that can be connected to CST and to each other, to form a structural prolongation of the CST. During the transport to point 5 and all the installation procedure, one element of the extension tube is fixed on each side of the Tracker, in order to hook, hold and handle it, without interference with the service tails. The MSGC service tails are coiled and supported on the outside of this extension tube element, while the Silicon and the thermal screen service tails are coiled and supported on the inside.

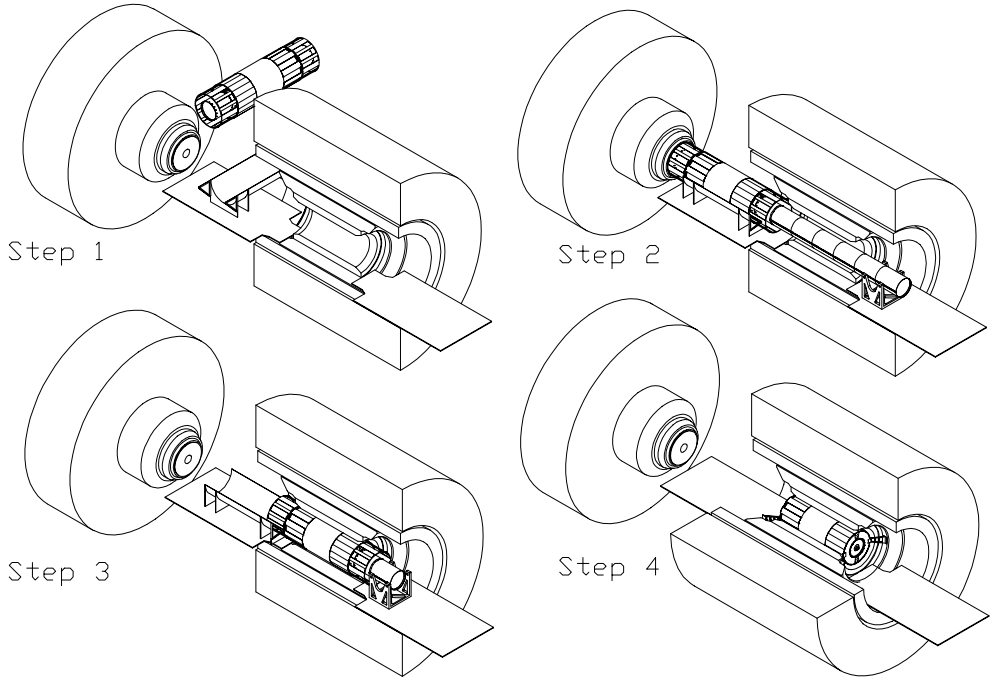

Fig. 6.49: Tracker installation sequence.

The general Tracker installation is performed in a well-defined series of steps, illustrated in Fig. 6.49:

1. The assembled Tracker is moved to point 5 and lowered with the crane down PX 56 to arrive in the underground cavern UXC 55. Both the CMS endcaps are in the fully opened position. The CMS integration team prepares on both ends of the magnet solid installation platforms, providing a reference plane at a level of 1.7 m below the LHC beam height. The Tracker installation cradle stands on the reference plane below PX 56. The manoeuvre for the insertion of the Tracker inside the ECAL barrel starts from a position which is perpendicular to the beam line (step 1).
2. Once the Tracker is lowered onto the reference plane, it can be easily moved by the Tracker installation cradle, which sits on airpads. The consecutive execution of two translations and two rotations aligns the Tracker to the beam line. Meanwhile, on the opposite side installation platform, a supporting portal is positioned: the remaining part of the extension tube slides on it to reach the Tracker on the other side of the experiment. In order to avoid excessive space consumption, each element of the extension tube is connected to the following just before engagement on the supporting portal. The extension tube travels inside the ECAL barrel in a cantilevered configuration, but the large difference in radial

dimensions ensures the absence of any possible impacts. Once the end of the extension tube has reached the element fixed on the Tracker CST, they are connected and the whole structure is again supported on both sides (step 2).

3. The Tracker can now slide into its final position inside the ECAL barrel. During this phase, each element of the extension tube is removed just after its disengagement from the supporting portal (step 3).
4. The support brackets, attaching the Tracker endflanges to the HCAL barrel are installed. The MSGC cables and pipes are installed in their cable trays and connected to the patch panels. The last extension tube elements can now be dismounted on both Tracker sides. After removal of the cable support, the Silicon services are also unrolled and attached to the patch panels (step 4).

6.7.5 Beam pipe installation procedure

We consider several options for the beam pipe installation. Two main scenarios have been worked out:

1. Insertion of the beam pipe into the Silicon detector in the Tracker assembly laboratory, or
2. Insertion of the beam pipe after Tracker installation inside the ECAL in UXC 55.

A permanent system of guides is provided at the inner radius of the Silicon barrel detector. This system is held by the central support tube at $z = \pm 881$ mm through the inner support structure described in Section 6.2.10.2. For the beam pipe installation, a removable rail system, extending the guides from $z = \pm 881$ mm to the outside of the Tracker, is temporarily cantilevered from both sides and connected to the fixed one. In order to insert this temporary guide system, one has to remove from both Tracker ends the alignment wheels: if it is decided to avoid their full disconnection in two halves, they can be held by a simple temporary support sliding on the floor of the installation platform and axially displaced by some metres. Once this operation is completed, a continuous insertion plane runs all along the inner radius of the Silicon detector.

Regardless of the particular installation scenario (installation inside the laboratory or inside the experimental cavern), the central section of the beam pipe must be supported along its full length outside of the Tracker, in a close to continuous way on a special chariot. Once the pipe is slid into position, it can be attached to the upper vertical wires at the different supporting locations by special tools and lifted up from the chariot. The chariot can then be removed, sliding back on the insertion guides, and also the lower beam pipe support wires can be attached and tensioned, to provide mechanical stability to the pipe structure. The tension forces acting on the wires are monitored and adjusted to avoid unwanted deformations and stresses in the pipe walls.

The central segment of the beam pipe is now installed inside the Tracker and is ready to be connected to the machine and to be baked out.

6.7.6 Completion of the installation procedure

After the installation of the combined Silicon and MSGC detector system inside ECAL, the beam pipe is connected to the LHC machine, baked out and pumped to the design vacuum value. Only after removal of the bake-out equipment, can the Pixel detectors be installed. For this, the removable system of guides, already used for the beam pipe installation, must be reconnected to the inner fixed guides. An option is to use this removable guide system also for the insertion and removal of the bake-out equipment: if this is the case, it is simply left in place for the following operation.

In order to allow for the Pixel installation, the beam pipe can only be held in position by vertical wires. If the lateral wires have been attached for the bake-out operation (to provide

lateral stability to the pipe), they must be removed again. Then, the Pixel detector installation is performed, following the steps described in Chapter 2.

Once the Pixel detector is in position and has been surveyed, the removable guide system is finally extracted, the lateral wires are again attached to the beam pipe, the Pixel services are connected to the patch-panels, the detector is tested for final acceptance and the endflanges of the Silicon volume are completely closed.

Finally both Tracker alignment wheels, supporting the light-sensitive detectors and the Muon Link periscopes, are slid back in position onto the Tracker endflanges. Only after this installation, may the fine-position adjustment of the whole Tracker with respect to the Muon system be performed. The position of all the subdetector elements (Pixel, Silicon and MSGC) will be monitored with the use of the Tracker internal alignment system.

After completion of these tests, the CMS endcaps are slid into their final position. During the ramping up of the magnet, the Tracker alignment system continuously monitors any movement of the subdetector systems from their nominal positions.

6.7.7 Tracker installation planning

6.7.7.1 Global schedule

The major target dates for the Tracker installation are shown in Table 6.29.

Table 6.29: Major target dates

Tracker installation	17-9-04 / 3-3-05
Tracker testing	3-3-05 / 4-5-05
Detector ready for circulating beam	8-6-05
Detector ready for physics	18-7-05

6.7.7.2 Initial installation

The installation planning is schematicaly given in Table 6.30.

6.8 Tracker Maintenance

6.8.1 Access time-scales

Access to the Tracker and its electronics must be considered on different time-scales.

- *Short time access*: Short interruptions of the beams ranging from one hour to three days are only of minor importance to the Tracker. It is foreseen to have all electronics, power supplies, etc. in the side tunnel, which is always accessible.

- *Intermediate time access*: Longer access, of the order of two to three weeks, including opening of the endcaps, allows access to the Tracker patch panels located between the electromagnetic calorimeter barrel and forward parts. During these periods the endflanges of the Tracker can also be reached, which allows interventions on the feedthroughs for gas tightness, etc.

- *End of year shut-down access*: As seen from the above statements, repair work to the different Tracker parts can only be done during a long end-of-year shut-down, where removal of parts of the Tracker can be foreseen. Three different scenarios are foreseen:

Table 6.30: Installation planning

	From/to	Time needed
MSGC detector assembled on CST	ready by 8-9-04	
Silicon detector assembled inside the thermal screen	ready by 8-9-04	
Assembly of the Tracker in the surface laboratory	9-9-04 / 13-9-04	5 days
Transport to Point 5	14-9-04 / 16-9-04	3 days
Installation of MSGC and Silicon Tracker (on CST) inside HCAL/ECAL barrel	17-9-04 / 25-9-04	9 days
Initial Alignment/Survey	26-9-04 / 28-9-04	3 days
Start Cabling/Piping MSGC and Silicon	29-9-04 / 3-2-05	4 months
Testing	3-3-05 / 4-5-05	2 months
Installation of the central section of the beam pipe and connection to LHC vacuum tube	ready by 4-5-05	
Bake-out of the beam pipe	5-5-05 / 15-5-05	2 weeks
Installation of Pixel barrel	15-5-05 / 21-5-05	6 days
Installation of Pixel endcap	21-5-05 / 27-5-05	6 days
Cool down of Silicon volume	28-5-05 / 11-6-05	2 weeks
Positioning of internal alignment wheels Check of Tracker internal alignment Check of Link System		several days
Testing	until closing of CMS	

- Removal of the Silicon detector (barrel and endcap)
- Removal of the complete Tracker to be dismounted at the surface
- Extraction of one or both sides of the MSGC forward chambers

In all cases the Pixel detector has to be removed, or at least completely uncabled up to the patch panels, as its cables and service lines cover all the others. Removal of the Silicon detector or of the whole Tracker includes removal of the central part of the beam pipe which is supported from the Silicon detector.

The extraction of the whole or parts of the Tracker is feasible from the mechanical point of view. The real difficulty is the disconnection and handling of the enormous number of cables and service lines (about 3500 per side) during the operations. The layout of the cabling is not yet fixed. Further detailed study is needed in order to overcome this problem.

6.8.2 Maintenance hall

Repair and maintenance of the Tracker is best done at the surface. The Silicon detector must be removed form the Tracker in a semiclean hall of about 14×6 m^2 (twice the length of the Tracker plus some manoeuvring space). The Silicon and Pixel detectors have then to be moved to the foreseen cold area, while the MSGC part can be kept in the semiclean hall.

6.9 Safety

6.9.1 Safety Objectives

The overall objectives for the safety of CMS, which apply to its components and operation have been established as:

- protection of occupational and public health
- protection of major capital investments

The former includes the work-place and adjacent environment during construction, operation, maintenance and dismantling, the latter refers to the success of the experiment and the expectations of the collaboration.

General Principles

The safety requirements for experimental activities at CERN are generally described in SAPOCO/42 which defines the safety policy. As a first step toward implementation of the provisions of the codes and instructions which emerge from this policy, the CMS Collaboration has established a Safety Working Group with membership mainly drawn from the technical design staff of major sub-systems. Coordination with the TIS Commission is ensured by three members from the TIS Division in this working group. The Group Leader in Matters of Safety (GLIMOS) of CMS chairs the group and sees to it that safety hazards are identified in the early phases of the project, in order to eliminate or reduce them and control them.

Safety considerations, as reflected in design or specific measures for safety, in general, have to follow the SAPOCO policy and the CERN Safety Codes and Rules resulting from it. CERN's international status and safety prerogative on its own territory (see SAPOCO/42 for details) empowers it to settle differences between Swiss, French and international standards using its own experience to set its own safety standards to be applied uniformly to a particular site or experiment. A special requirements document for CMS is being established and will maintain a traceable written record of such settlements. Special attention will be given to the correct functioning and reliability of any safety device of the Tracker and supporting systems under the prevailing environmental conditions (magnetic field, electrical fields, radiation, temperatures). Detection and alarm systems, interlocks, safety valves, circuit breakers, rupture disks etc. will be examined for their reliability and redundancy, where needed.

A process of Initial Safety Discussions has been started for CMS and its Tracker Project and has established many of the important safety features outlined below. A detailed worksheet is used for these discussions as a guide to ensure that all aspects of hazards are covered. These are possible scenarios which could cause death, injury or occupational illness, or damage to facilities, systems, equipment or the environment. Special hazards analyses and safety review meetings will focus on further details, some of them with the help of external experts. Such analyses are in progress and/or planned for the near future.

Safety Documentation

As a complement to the existing set of TIS documents which have a CERN wide validity, a number of safety issues specific to CMS and its Tracker system are being summarised or recorded in the following documents:

- A follow-up list of open safety issues, which come up during design, manufacturing or testing, is maintained at the Project Office and pursued until the items are resolved; particular inputs are the results from Initial Safety Discussions and the upcoming Hazard Analyses.
- A CMS Safety Requirements document has been initiated with the purpose of providing clarified requirements to designers, collaborators, subcontractors and experimenters in a

concise, controlled, written form; agreement from TIS has to be obtained for the contents. The Safety Working Group will be used for this.
– Acomprehensive CMS Safety Report is going to be issued in the last quarter of 1998.

Safety Responsibilities

For the safety of the Tracker system the following established functions are important:

– the Group Leader in Matters of Safety as described in TIS documents (GLIMOS);
– the Technical Coordinator as described in the CMS Constitution;
– the Division of Technical Inspections and Safety (TIS) for the setting of standards and rules, independent inspection and safety reviews and, in general, approval of all safety matters;
– the individual designer and manufacturer with documented responsibility for delivery of a safe and reliable component or system commensurate with experiment and safety objectives and requirement;
– important responsibilities have also been defined for gases and site-specific safety surveillance; they are described in the relevant TIS documents and are being coordinated with the GLIMOS functions.

Full-scale Tests

Certain proven rules have to be followed, according to which major components and sometimes their sub-systems are subjected to full-scale tests. The pre-production prototypes (PPP) have a special significance in this regard. The Silicon and MSGC milestone projects are examples.

6.9.2 Mechanical aspects

General Requirements

The structural integrity of the Tracker System and its components are essential to safe and reliable operation during the life cycle of the CMS experiment. Mechanical design requirements comprise functionality over specified (relatively short) lifespans, mitigation of hazards and safety problems to the system, restraint of subsequent, consequential damages to human beings, the environment and vital equipment, under all conceivable conditions during construction, operation and maintenance.

The policy adopted by the Tracker engineering teams calls for adequate safety factors for components, supports and major structures, during normal operation, handling and maintenance (and, if necessary in the framework of hazards-analyses for emergencies). In today's environment of more accurate simulations by F.E.A. methods, safety factors of 1.5 against yield-strength (as stipulated by AISC) are common and acceptable; for less sophisticated analyses, factors of 2 would be more common. In addition, designs and design calculations are the subject of various reviews. Such reviews and the subsequent approvals shall be completed at the latest before commencement of mass production.

Applicable Design Codes and Standards

In general the codes and standards will be taken directly from the relevant TIS documents. While the French CODAP is generally the preferred choice, some ANSI, IEEE, AISC and, in particular ASME standards may be more explicit for the cases at hand; French authorities are

known to have accepted justified usage of such foreign codes and early agreement in that regard will be sought through TIS, where this appears necessary.

Hoists, Cranes, Transport and Handling

Special care has to be taken for any major transport and handling for the Tracker or one of its sub-systems. Lifting equipment is to be designed to CERN Safety Code D1 and to be approved by TIS before operation, preferably before installation or even during the design phase. For the transport of the assembled Tracker from the Meyrin site to point 5 we foresee an air-cushion-equipped truck. During the transport humidity and temperature will be controlled and accelerations will be monitored.

Seismic Design

For the rare event of earthquakes, 0.15 g accelerations generally have to be considered in all three dimensions. This is a quite severe criterion for a European site and is usually taken into consideration by making an addition to the basic static loads. Where such simple consideration imposes undue restrictions in the design of components, which often have to be lean in their support structures, the designer may want to have additional options to fulfil safety objectives and should obtain TIS concurrence.

Mechanical Safety in Specific Components

The design of all the structural components is mainly guided by severe limitations on the allowed deflections, under both static and dynamic loading conditions. As a consequence, low static and fatigue stresses are expected. In particular, for the dynamical behaviour of the structures, the maximum allowed vibration amplitudes are estimated from the intrinsic resolution of the detectors through the application of a fairly large safety factor (about 10) to take into account the unknown coupling between the sources of vibration and the Tracker. In the mechanical design, great care is devoted in redistributing the stress inside the structure, to avoid excessively high local peaks, due to concentrated loads. The extensive use of advanced F.E.A. calculation and integrated CAD software allows reliable solutions to be obtained with safety factors ranging from 1.5 to 2. A careful fatigue analysis will be performed on locally loaded structural parts, such as, for instance, the support brackets and their attachment to the end-flanges. Also, structural laboratory tests of prototypes are foreseen for the most critical items. In principle, all the structural components will be designed with a 'fail safe' concept, to reduce as much as possible the maintenance requirements on structural parts by a 'damage tolerant' design. Local exceptions, on non-critical items, will be carefully taken into consideration.

6.9.3 Electricity and electronics

Overview

The safety of conventional electrical systems for power and lighting, in general, is assured and controlled by adhering to well-developed rules and regulations, in force at CERN, notably Safety Instructions IS23, IS24, IS26, IS28, IS33, and Safety Code C1. For electronics systems, the codes and handbooks for good safety practices are not quite as well developed; they therefore need more specific individual attention as to their safety. While electronic systems are typically characterised by low voltage DC power systems, 5 V and lower, there are still significant hazards in connection with fire, thermal loads and radiation damage. Electricity as a cause for heating, short-circuit and fire cannot be totally excluded, mainly because of the high current capabilities of many of these systems. Low voltage power supplies up to several hundred amperes are not unusual. At present we plan to power the Tracker with about 1500 low voltage supplies each at a maximum current of 15 A on the minus 2 V line. Once detector designs and above all

the cabling and cooling arrangements are finalised, these risks will be analysed and appropriate measures of protection taken.

Conversely there are a number of low-amperage high voltage systems needed for the operation of MSGCs, which need special attention. The standard operating drift voltage of MSGCs is about 3 kV, all equipment will be tested up to 5 kV.

Overcurrent Protection

World HEP experience has shown that lack of adequate overcurrent protection and of temperature monitoring in low-voltage high-current systems are a frequent cause of fires in experimental facilities. This is true to some extent for a whole range of modern high-tech installations. While considering adequate separation, cooling and quality of equipment, a number of additional rules have been established to protect against overcurrents; corresponding review and inspection procedures for design and installation are being established and will also be reflected in the upcoming CMS Safety Requirements document. The draft CERN Design and Implementation Criteria for Low-Voltage High-Current Distribution Systems of April 1997 already cover the following major areas in this connection:

- Power Source Overcurrent Protection
- Connection to Single Load Conductor
- Connection to Multiple Load Conductors
- Material Matching and Connector Mechanics
- Power Rating Engineering

Rack and Crate Protection

CMS planning calls for removal of waste heat from rack-mounted equipment by means of embedded air-to-water heat exchangers and forced ventilation. It is anticipated that some racks in the data aquisition system could produce up to 8 kW from electronics and corresponding low-voltage power supplies. Electrical ignition risks (i.e. from an arching short circuit) can usually be prevented or reduced by proper fuses and circuit breakers. However, these risks may be compounded by thermal loads and water-leaks and must be analysed further (in the risk analyses).

A protective strategy against electrical risks has been developed by using the Detector Control System to monitor off-normal voltages, currents and temperatures. Detection of a minor fault would result in an off-normal condition alarm; a major fault would lead to a rack shut-down.

High Voltage Protection

High voltage direct current is required for the operation of thousands of Silicon and MSGC detectors. Commensurate safety requirements have been developed along recommendations of the International Electrical Commission (IEC publication 479-1), considering damage (namely lethality) to human beings. Safety limits are for currents 10 mA, for exposure duration 20 ms and for absorbed energy 10 J. Secondary effects, such as falls by shock, will be taken into consideration also below these limits. Above these limits such measures as physical barriers and interlocks, as well as permit procedures for hazardous activities and mandatory lockout/tagout will be used.

Magnetic Fields in Relays

The functioning of all magnetic parts of relays or of magnetic valves is checked against the influence of the prevailing strong magnetic fields from the magnet. The external (experimental) fields in general must not exceed 10% of the locally generated field for the functioning of the relay, for example.

6.9.4 Cooling systems

Water cooling systems are the present reference for a number of heat-removal tasks in the Tracker System. The Cooling Working Group is currently looking at one alternate coolant HFE; also the activation levels in coolants are being checked. They depend on the radiation fields coolants pass through and pose some problems during shut-downs. In particular pressurised water systems also present a direct damage risk to nearby electrical equipment, especially energised electronics. Designing the cooling systems with adequate safety margins, quality assurance, reliable and proven connector-systems, leak-detection and proper arrangements (separation) to reduce vulnerability are essential mitigation measures, which have been or will be implemented. A 'leak before break' philosophy will be followed with these measures. Also the pressure, temperature and flow-rates of the cooling systems will be monitored to detect development of abnormal conditions early. Shut-downs of cooling systems will be appropriately interlocked to power shut-downs to avoid overheating of uncooled components. For the cold Silicon and Pixel detectors a pressurised system using Hydrofluoroether HFE 7100 (3M) as mentioned above is under development.

6.9.5 Gases

Flammable Gas Safety for the MSGCs

The MSGCs will use a gas mixture of 60%DME + 40%neon. This mixture is flammable and the normal safety requirements for flammable gas must be observed. The total volume of the MSGCs is $\sim$1.25 m^3 and this gives a total of $\sim$1.8 kg equivalent HC. As this mixture is heavier than air, gas leak detectors should be installed at the bottom of the different gas racks. Gas leak detectors, calibrated with DME, should be installed in the gas bottle rack and the gas mixing rack in SG5 and in the gas distribution rack in the US cavern. A 'sniffer' system using small diameter piping should suck air from around the Tracker volume and from the gas patch-panel in the UX cavern. This air should be sent to a detection system where it will be controlled for flammable gas, using an infrared analyser, and smoke using an opacity detector. Highly sensitive local detectors are an alternative consideration. Ventilation will be needed around the Tracker volume to dilute any leaks that could occur; if the chambers are enclosed in an outer layer containing nitrogen then the risk associated with a gas leak is considerably reduced. Remaining choices of unavoidable flammable gases will be identified, discussed with TIS and its flammability determined; by measuring and controlling O_2 content gas in the chambers can be kept non-flammable. Differential flow-meters are planned to be an important tool for balancing inventories and detecting leaks. Additional appropriate detection and protection measures will be taken inside the gas-racks and the cavern. Around the MSGCs an inert gas envelope is foreseen, reducing the oxygen content to below 5%. In case of gas or fire alarm, interlocks are used to stop as needed, gas flow, HT and LT to the zone at risk. Connections to appropriate general alarm levels, 1, 2 or 3 will be devised.

6.9.6 Fire protection

Prevention

In fire protection at accelerator facilities, emphasis is placed on four principal areas: safety of the operating personnel, program continuity, property protection, and releases to the environment. The size and scope of the CMS detector presents important challenges to fire protection planning and engineering. By its very mission, the detector is not suitable for being partitioned into separate fire zones, as is common for large facilities. The deep underground location compounds some of the problems, in particular with regard to smoke venting and emergency egress.

On the other hand the situation is similar to other high-tech facilities where the cumulative presence of combustible materials is quite high and presents a large hazard, but the probability of ignition is kept low. Strict measure in that regard are taken in the protection of electrical circuitry.

Detection and Suppression

Incipient detection is planned for all interior spaces within the detector and overhead spaces immediately above it. An aspiration, sample-draw smoke detection system is envisaged for the different internal layers with consideration for natural openings, access ways for maintenance and loadings of combustible materials. Maximum advantage will be taken from early warnings, assisted by sophisticated computer systems and a multi-stage adequate response, starting locally. The diversity and redundance of detector systems on the one hand and the screening out of false alarms on the other is still under study. A complicating factor is the replacement of Halon 1211 and 1301, which are ozone depletants. Promising alternatives are being investigated, mainly based on fine mists of water, CO_2 and nitrogen. In the event of a fire incident during accelerator operations, the beam will be aborted and machine interlocks will be broken to allow immediate access for intervention by the safety services. Certain shutdowns will have to be automatic, to switch off electrical supplies which may be a cause or suffer dangerous effects. Ventilation of smoke will precede the preparation of extinguishing and recovery measures as well as easing egress. The simulation of credible fire development scenarios with realistic combustible materials may, however, be necessary to determine quantities of smoke, ventilation rates, environmental aspects for the outside and fresh supplies of oxygen and wind (also as a fire promoter).

6.9.7 Lasers for alignment

The laser-based positioning system is operated with low-energy lasers (35 mW) in the visible light range towards the infrared range. At present HeNe lasers are considered and their placement is such that light tightness is ensured.

6.9.8 Estimate of induced radioactivity

At the LHC we will be confronted with two main mechanisms which induce radioactivity in materials: low energy neutron activation and inelastic hadronic interactions at high energy. Of these the latter will dominate, unless the choice of materials is very unfortunate with respect to neutron activation. Two materials have been identified in the Tracker region, which have high thermal neutron activation cross sections:

- ^{197}Au, contained to 100% in the gold strips of the MSGC detectors, has a thermal neutron capture cross-section of 10^5 mb. The resulting ^{198}Au has a half-life of 2.7 days.
- ^{186}W, contained to 30% in the tungsten of the ECAL crystals. The thermal neutron cross-section is 3.8×10^4 mb and the resulting ^{187}W has a half-life of 24 h. The other tungsten isotopes also have relatively large thermal capture cross sections, but if the isotope abundance, the activation cross sections and gamma intensities of the resulting radionuclides are considered together, ^{186}W is the most significant.

Both of these isotopes have relatively short half-lifes so they will have decayed substantially by the time the CMS endcap has been opened to allow access to the vicinity of the ECAL or the Tracker.

Thus we expect that the dominant component for the activation of the ECAL and the Tracker comes from high energy hadronic interactions. A proper treatment of induced radioactivity requires to establish a full inventory of all created radionuclides and to follow the time dependence

of this set of nuclides. The enormous amount of different radionuclides produced in the $PbWO_4$ crystals makes explicit accounting for all of them difficult but facilitates some simple averaging procedures. The Tracker materials are typically very light so that it is feasible to identify the few nuclides which are radiologically significant. For target materials with $A < 30$ the dominant long lived nuclides are ^{7}Be and ^{22}Na.

Two opening scenarios are foreseen for the CMS detector. During the long shut-down the endcap moves far away from the Tracker but in the intermediate technical stop the opening is only a few metres. Thus the induced activity in the endcap ECAL is likely to give an important contribution to the dose equivalent which a person working at the Tracker end-flange would receive. In order to determine safe access, shielding requirements and access times, we need to consider both, the activation of the endcap ECAL and of the Tracker.

6.9.8.1 Induced activity in the ECAL

For heavy target materials, like the ECAL, the large number of different radionuclides produced allows the use of so called ω-factors [6-35]. These are based on the fact that effects due to individual nuclides are averaged out so that the rate of inelastic hadronic interactions (stars) in the material is directly proportional to the gamma emission rate from that material due to the activity induced in it. In the spirit of this average treatment the decay of the dose rate ($\dot{D}$) can be parameterised with the the Overton–Sullivan formula [6-36]

$$\dot{D} \sim \Phi \ln \frac{t_i + t_c}{t_c} \,, \tag{6.2}$$

where t_i is the duration of the irradiation, t_c is the time since the end of the irradiation and Φ is the activating hadron fluence.

A plot of this time-dependence for the assumed LHC operating schedule is shown in Fig. 6.50. We clearly see the three 60-day operating periods per year, separated by 14 day stops and followed by a longer shut-down. It must be emphasised that the dose for $t_c = 0$ cannot be obtained from Eq. (6.2), which reflects the fact that short-lived nuclides are excluded from the parameterisation. The dose during irradiation, shown in Fig. 6.50, corresponds to $t_c = 1$ h. The most important observation is that after the fast drop during the first day of cooling, a further decrease of induced radioactivity is very slow. Except for the low luminosity start-up phase the dose rate at any instant of time is within a factor of three from the dose rate scaled to $t_i = 60$ days and $t_c = 1$ day. In addition this scaling provides the best value for an access a few days after machine stop when the LHC has been operating long enough so that the activity has reached the saturation level.

Figure 6.51 shows the dose rate expected from the CMS Calorimeters after 60 days of irradiation and one day of cooling. Details of the calculation can be found in the safety chapter of the CMS ECAL TDR [6-37]. The Tracker and the beam pipe, have been excluded from this calculation. We can observe doses of the order of 200–300 μSv/h. A safety margin of at least two should be added, which means that we have to design shielding and plan access in view of dose equivalent rates of the order of 0.5 mSv/h in the high-η region of the endcap calorimeters. Following the general trend of the activating hadron fluence in the detector, the dose equivalent rates at larger radii are substantially lower.

6.9.8.2 Induced activity in the Tracker

The simulation methods used to determine the activity of various Tracker modules are described in Section A.7.8. We consider the contact dose rate with typical Tracker elements like detectors, support structures and cooling pipes. The large variety of objects with different shapes prevents

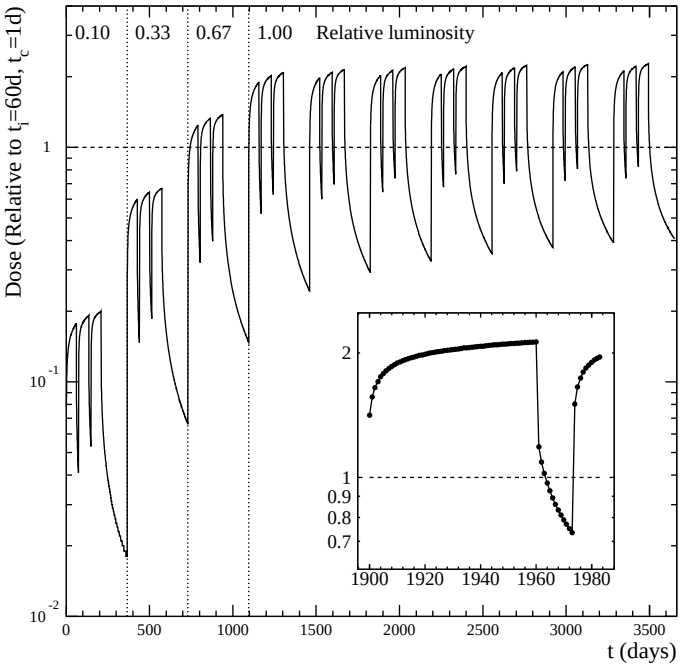

Fig. 6.50: Time variation of induced activity dose rate at the LHC according to the Overton–Sullivan formula. The curve is normalised such that unity (dashed line) coincides with $t_i = 60$ days and $t_c = 1$ day and the maximum average luminosity of LHC (5×10^{33} cm^{-2}s^{-1}). This corresponds to the scaling which is used to present the dose rates in Fig. 6.51. In the small sub-plot the dots indicate individual days.

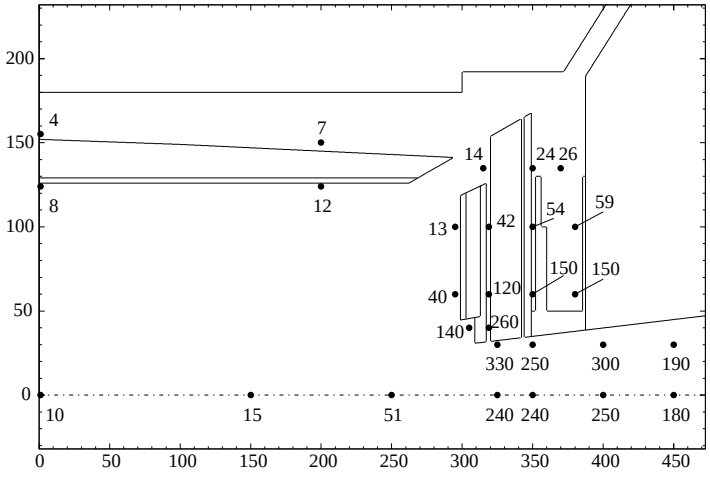

Fig. 6.51: Estimated dose rate in μSv/h around the CMS central calorimeters due to induced radioactivity after $t_i = 60$ days and $t_c = 1$ day (see Fig. 6.50). The average luminosity during the irradiation is assumed to be 5×10^{33} cm^{-2}s^{-1}.

a detailed assessment of the dose for all of them. Thus only some characteristic cases are calculated explicitly.

Of the Tracker materials silicon and aluminium are activated with very similar cross-sections so they can be used as representations of each other [6-38]. Carbon fibre is a good representation for all plastics. Water is introduced to represent the cooling fluids. Iron is used to study the activation of the stainless steel cooling pipes and parts of the beam pipe, but iron activation also gives a good indication for the effects to be expected from copper cables.

The photon dose is calculated by using the emitted energy per unit of volume and scaling it with $0.031\,\mathrm{cm}^2\,\mathrm{g}^{-1}$, which is a good representation of the mass-energy absorption coefficient of tissue over the typical energy range of induced activity photons [6-39]. Figure 6.52 shows the energy emitted in the form of photons for aluminium and iron as a function of cooling time and distance from the beam line. These data form the input for the following estimations of γ-dose rate, the aluminium being treated as representative of silicon and MSGC glass substrates.

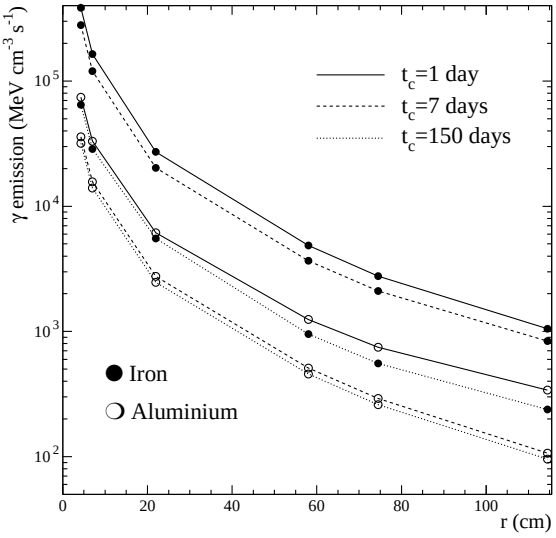

Fig. 6.52: Specific energy emission for aluminium and iron activated at different radii of the Tracker. The values correspond to the end of the tenth year at the LHC and to the indicated cooling time t_c.

The estimation of β dose rate is more complicated due to the large attenuation in materials. A simple estimate can be constructed by assuming the active layer to be infinitely thick so that the dose rate in contact with the surface corresponds to half of the energy emitted per unit of volume in the active material. A detailed simulation of the transport of ^{22}Na β's in a $300\,\mu$m thick silicon plate surrounded by tissue equivalent material shows that the semi-infinite medium assumption decribed above reproduces correctly the dose at the silicon/tissue boundary and overestimates the dose at $70\,\mu$m depth in tissue by a factor of 1.5.

Activation of the detectors

The Pixel detectors are modelled as $600\,\mu$m thick silicon plates in order to include both the sensitive volume and the chips on top of the detectors. A Silicon strip detector is represented by $300\,\mu$m thick plates, i.e. the electronics is not included. For the MSGCs we assume $300\,\mu$m silicon to represent the glass substrate. The drift plane will be carbon-fibre-like material where the activation is negligible compared to the substrate. The activation in the gold strips is significant for the γ dose from the MSGCs, but can be neglected for the β dose rate, since the strips are shielded by the substrate. For the calculation of β contact dose rates all materials are assumed to be semi-infinite. While the γ dose rate is equal on both sides of a complete MSGC module, the β dose rate on the substrate side can be assumed to be negligible.

An inspection of the isotopes produced reveals that, after the first few days of cooling, only ^{22}Na contributes to the dose rate. Thus the dominant uncertainty of the dose estimates given in Table 6.31 comes from the assumed production cross-section of ^{22}Na. A comparison of the prediction of FLUKA [6-40] event generators with experimental data indicates that FLUKA predicts by a factor of 2–3 lower ^{22}Na production. But also the experimental data suffer from significant uncertainties, since only for protons are sufficient data available. Thus the important pion contribution has to be estimated from the proton data, except for a narrow range at few

hundred MeV, where some pion activation data are available. The values given in Table 6.31, which are based on the experimental cross-sections, are about a factor of 2 higher than the FLUKA estimates.

It should be emphasised that the γ dose rates given in Table 6.31 apply only to individual modules when removed from the Tracker. While fixed to the Tracker the contribution from all other modules increases the γ dose.

Table 6.31: Estimated contact dose rates (μSv/h) for individual barrel Tracker modules after 10 years of LHC operation. The β-dose rate estimate corresponds to the skin surface. The γ dose rates correspond to 1 mm distance at the centre of a $10\times10\,\mathrm{cm}^2$ module. At this distance the dependence on the area is small

Radius	Dose type	t_c=1 day	t_c=7 days	t_c=30 days	t_c=150 days
4.3 cm	γ	69	33	33	30
	β	440	170	160	150
7.1 cm	γ	31	15	14	13
	β	200	73	72	66
22 cm	γ	3.1	1.4	1.3	1.2
	β	37	13	13	12
58 cm	γ	0.62	0.25	0.25	0.23
	β	7.7	2.4	2.4	2.2
74.5 cm	γ	1.0	0.25	0.14	0.13
	β	4.6	1.4	1.3	1.2
114.5 cm	γ	0.81	0.16	0.052	0.048
	β	2.2	0.5	0.49	0.45

Activation of the cooling pipes

The cooling pipes are proposed to be either aluminium or stainless steel. Since an individual pipe is a thin object and the geometry of the pipework is complicated, it does not appear feasible to provide estimates of contact dose rates. The contact dose rates given for the detector modules in Table 6.31 give a relatively good indication of the dose to be expected from a group of cooling pipes. The relative differences of steel and aluminium can be deduced from Fig. 6.52, where it can be seen that the difference between these two materials depends on the cooling time. The difference reaches a maximum after about one week of cooling time but thereafter decreases with increasing t_c. A fairly good general approximation is, however, that steel and aluminium give equal dose rate per unit of mass.

Activation of the support structure

The support structures are assumed to be all carbon fibre. There are no radiologically significant long-lived nuclides which could be produced in carbon-fibre composites[2]. After few days of cooling the γ dose rate is dominated by ^{7}Be and the β dose rate by ^{14}C, both of which are radiologically relatively harmless. Thus, compared to the aluminium, silicon and steel elements of the Tracker, the carbon fibre structures give a negligible contribution to the dose.

Activation of the beam pipe

The activation of the beam pipe is an important issue for the Pixel maintenance and any operations on the beam pipe itself.

The installation of the Pixel detector requires work very close to the beam pipe in the region of the stainless-steel/aluminium transition. Therefore we calculate the dose in contact

[2]Tritium is produced with a large cross-section but, due to its very low β-energy, is harmless when contained in a solid material.

with ±1 m long aluminium and stainless steel tubes having radii of 2.5 cm and 7 cm and wall thicknesses of 0.2 mm. The activities are determined using experimental activation cross-sections for aluminium and iron. The results, shown in Table 6.32 indicate that the contact dose rate from the beam pipe is relatively high even after long cooling times. Because of the lower β emission the contact dose rate for a steel pipe drops below that from an aluminium pipe after about one month of cooling.

Table 6.32: Estimated contact dose rates (μSv/h) for the beam pipe after 10 years of LHC operation. The β-dose rate estimate corresponds to the skin surface. Dose rates from aluminium and steel (iron) are compared

Position	Dose type	t_c=1 day	t_c=7 days	t_c=30 days	t_c=150 days
z = 0–167 cm	γ (Al)	610	310	300	270
	γ (Fe)	3000	2200	1200	530
2.5 cm	β (Al)	950	380	370	340
	β (Fe)	1800	860	230	58
z = 400–470 cm	γ (Al)	140	59	58	52
	γ (Fe)	560	420	240	110
7.0 cm	β (Al)	170	59	58	53
	β (Fe)	270	130	33	8

We can observe that the dose rates in contact with the beam pipe are quite high even after long cooling times. People working in the vicinity of the beam pipe will expose their whole body to the radiation; in Fig. 6.53 the estimates of the γ dose rate at various distances from a plain CMS beam pipe are shown.

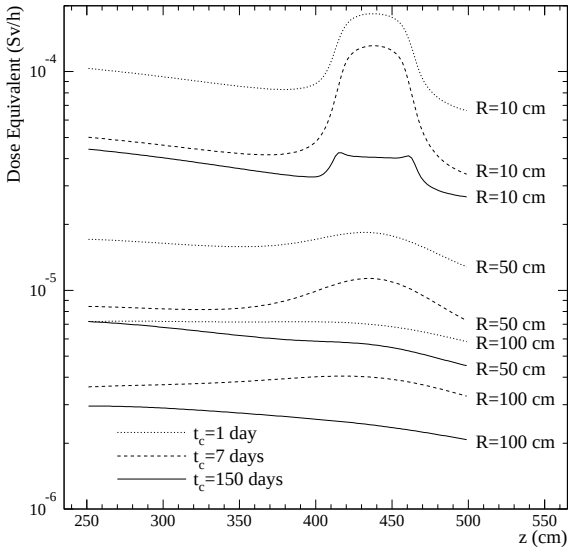

Fig. 6.53: Dose rate at various distances from the bare CMS beam pipe after the indicated cooling time t_c. Values correspond to the end of the tenth year at the LHC.

Dose equivalent rate from the whole Tracker

The preceding sections have discussed the dose rates in contact with individual pieces of the Tracker, which is required input for handling the Tracker elements. The first phase in the Tracker maintenance will be, however, to disconnect the Tracker services. This work has to be performed between the Tracker endflange and the ECAL endcap. The dose rate from the ECAL endcap has been already discussed. In this section we provide an estimate of the γ dose rate from the whole Tracker when viewed from one end flange. Due to their short range the

β's do not need to be considered. The Tracker model used for this calculation consists of two materials, silicon and carbon fibre, distributed uniformly along z. The radial distribution is fitted to reproduce the actual distribution of corresponding materials in the V4 Tracker.

The gamma spectra are calculated for these two materials as described in Section A.7.8. These gamma spectra have then been used to estimate the dose at the Tracker end-flange and around the Silicon Tracker taking attenuation in the Tracker material into account by assuming an average mass-absorption coefficient of $0.025\,\mathrm{cm^2 g^{-1}}$ for all γ-energies and materials. The results are given in Fig. 6.54. The $t_c = 0$ curves are given only to indicate the fast decay of the dose during the first day. In reality access to the Tracker will be possible only a few days after LHC shut-down. It can be seen that the further decay of dose from $t_c = 1$ day to $t_c = 150$ days is relatively small. In all positions at the Tracker endflange the dose during the maintenance period is below 100 μSv/h. The highest dose, observed at small radii, is dominated by the activity in the beam pipe, which in the calculation is included up to $z = 5\,\mathrm{m}$. The middle plot of Fig. 6.54 shows the dose on the side of the Silicon Tracker with beam pipe and Pixel detector removed. During the maintenance period the dose remains below $10\,\mu$Sv/h. The time evolution, based on the assumption of the operation schedule described in Section A.5, shows that during the low-luminosity start-up phase the doses are even lower and reach saturation only towards the tenth year of operation.

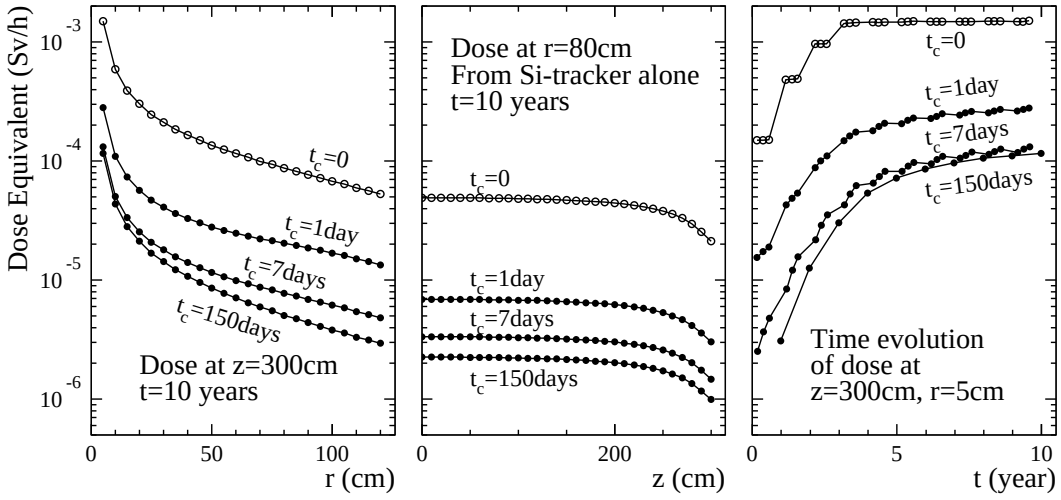

Fig. 6.54: Photon dose rate around the Tracker. The two plots on the left give the dose as a function of position after 10 years of operation for different cooling times t_c (the second curve from below corresponds to $t_c = 7$ days). The plot on the right indicates the time evolution of the dose. The open symbols are based on radionuclide yields from FLUKA directly, the solid ones are based on experimental data.

The slow decay of the activity is due to the fact that, after the first days of cooling, ^{22}Na – with its half-life of 2.6 years – remains as the only significant isotope. A comparison of the values given in Figs. 6.51 and 6.54 shows that the ECAL gives a significant contribution to the dose at the Tracker endflange. The actual dose will depend on the geometry during maintenance, in particular the amount of retraction of the endcap. At the lowest corner of the ECAL, however, the dose rate is so high that some special maintenance time shielding will have to be installed. This shielding will also reduce the dose which people working at the Tracker end flange will receive.

6.9.9 Personal safety, access and egress

Magnetic Fields

Currently valid international standards report that professional and medical short-term exposures of human beings to magnetic fields in the Tesla range have not had any measurable negative health effects. In accessible outside areas (like the control room), fields in the milli-Tesla range are not expected to present health risks for longer stays.

Besides the mechanical design (mentioned earlier), a potential risk for human beings would be secondary effects, like flying tools, accelerated by the strong field. Effective control measures for tools in the area are being studied together with ATLAS, by looking into corresponding organisational and instrumental measures in other accelerators and the nuclear and aircraft industries.

Access

Quite different conditions and requirements rule normal circulation on one hand, and emergency evacuation on the other. Both items are related to safety, but also bear heavily on other items such as site security, efficiency, design and costs. Finding and evacuating people and not leaving tools behind (see above) is important for personnel safety and rules to deal with this are being refined.

Egress

Check-out from experimental facilities and emergency evacuation will also be formalised according to proven procedures. Specific emergency scenarios will be developed and used to design, establish and train emergency egress procedures.

Chapter 7

Simulation

7.1 Overview

The hardware development of a complex detector layout is intertwined with the study of its performance, achieved with beam tests and by simulation and reconstruction tools. The layout of the CMS Tracker has been the object of extensive studies during the last years: the optimisation of its performance has driven several choices concerning soft geometry parameters such as detector pitch, number of measuring stations and their placement within the Tracker volume. Conversely, the increasing knowledge of the hardware involved in the detector has been included in the simulation and relevant parameters such as the Tracker material budget and the pattern recognition and fitting performance have been monitored. A detailed model of the Tracker was developed within the CMS software package; an overview of the computing framework is reported in Section 7.2, while the following sections describe in finer detail the software environment. The magnetic field model is discussed in Section 7.3. The quality of the model of the detector geometry is assessed in Sections 7.4 through 7.6. A careful analysis of the Tracker material budget is reported in Section 7.7. The simulation of the pixel and strip detector response and comparisons with test beam data are discussed in Sections 7.8 through 7.10. In the last section, a study of the digitised detector response to minimum bias events yields an analysis of the Tracker occupancy for high luminosity LHC running conditions.

7.2 Software

The CMS software which was used for detector simulation studies is a part of the CMS simulation, reconstruction and analysis software labelled by the common name of CMSIM [7-1]. The simulation software is written in Fortran and is based on the general purpose detector simulation tool GEANT3 [7-2].

The detector simulation interface with the physics generators Pythia [7-3], Isajet [7-4] and Herwig [7-5] is standardised so that the events are output in a universal HEPEVT [7-6] format in the form of HBOOK n-tuples [7-7]. These n-tuple files serve as kinematics input for CMSIM in generator independent form. In addition, the options of run-time kinematics generation of single particles and simplified minimum bias (MB) events are available [7-8].

Gaussian vertex fluctuation of primary interactions is controlled by a data card. The number of pp interactions in a bunch-bunch collision is determined either by a user defined constant or a Poisson-distributed random number whose mean is calculated from the given luminosity.

The CMS simulation package supports features such as pile-up of minimum bias events, accumulation of a given number of bunch-bunch collisions before and after the triggered event

and simulation of electronics noise; background signals due to the low energy radiation field which is induced by secondaries from pp collisions and beam halo can also be generated.

The energies deposited in the sensitive parts of the detector are transformed into raw data format taking care of the appropriate physics processes in the detectors.

Several GEANT3 routines have been adapted for the CMS simulation in order to manage the special requirements imposed by pile-up and the very high particle multiplicity. Some of the adapted routines are optimised for speed in order to be able to perform the simulation in a reasonable time. Typical execution times for single particle propagation and simulated hits generation are shown in Table 7.1 for different particle types and for two p_T and η values. Transport of secondaries is included in the times. Propagation times were measured from the vertex to the Tracker outer boundary. The machine used was a 167 MHz Sun Ultra workstation corresponding to about 45 CERN units. The simulation of a full MB event through the Tracker alone takes on average about 13 s on the same machine. A MB event simulation in the whole CMS detector takes about 100 s on average.

Table 7.1: Single particle transport times (s) through the Tracker volume

p_T	γ		e		μ		π	
(GeV)	$\eta = 0$	$=1.6$	$\eta = 0$	$=1.6$	$\eta = 0$	$=1.6$	$\eta = 0$	$=1.6$
10	0.04	0.09	0.12	0.19	0.05	0.06	0.12	0.20
100	0.04	0.09	0.13	0.26	0.05	0.06	0.15	0.27

7.3 Magnetic Field

The magnetic field used in simulation has been calculated for the full CMS detector using a 2D model [7-9] which assumes ϕ symmetry of the detector. This implies that the tangential component $r\varphi$ is zero everywhere. In the following we describe the magnetic field properties in the Tracker region.

The large solenoid of CMS provides good uniformity of the field in the Tracker region. This is demonstrated in Fig. 7.1 a) and b), which show the axial and radial components of the field, respectively.

It can be seen that the axial component varies by only a few percent in the whole range of the Tracker and that the radial component is less than one percent of the axial component in

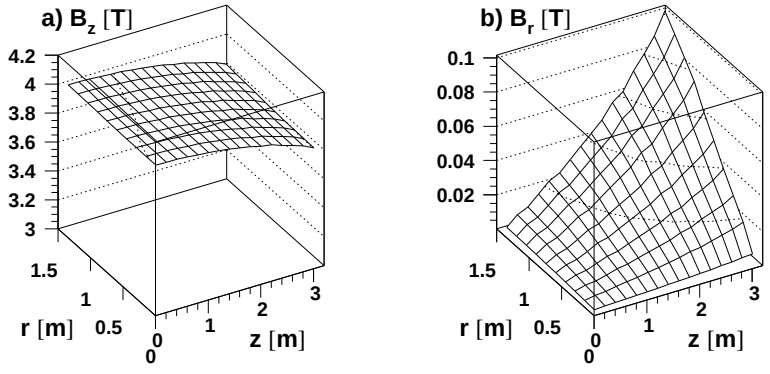

Fig. 7.1: a) Axial component of $\vec{B}$ as a function of rz-position. b) Radial component of $\vec{B}$ as a function of rz-position. Dotted lines on the plotted surfaces indicate constant value of B_z and B_r.

most of the detector and reaches only 2.5% (0.1 T) at the extreme corner of the detector. The high uniformity of the field is beneficial for track finding and reconstruction.

The effect of non-homogeneity of the field is demonstrated in Figs. 7.2 which show the deviation of particle trajectories from an ideal helix. All interactions were removed from the simulation so that charged particles experience only magnetic field effects. Figure 7.2 a) demonstrates the effect of the variation of the axial component B_z and Fig. 7.2 b) the effect of the non-zero radial component. We conclude that the deviation from an ideal helix is small. This is an important feature which facilitates the design of fast level 3 trigger algorithms.

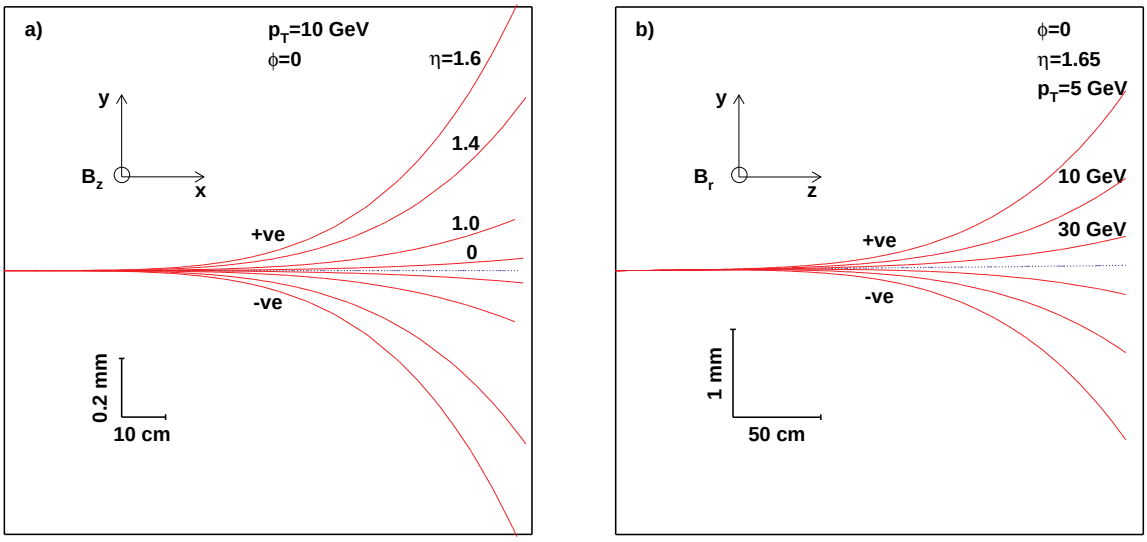

Fig. 7.2: Departure of particle trajectories from an ideal helix due to non-homogeneity of the B-field. Tracks are projected on the transverse plane in a) and on the longitudinal plane in b). The horizontal line represents the projection of an ideal helix.

7.4 Beam Pipe

The beam pipe described in the simulation geometry consists of a central part (within $|z| = 0.75$ m) of 1 mm thick beryllium tube with outer diameter of 60 mm, joined on either side to an aluminium tube of equal inner radius and shell thickness of 1.5 mm. The aluminium tubes extend to $|z| = 1.947$ m. They, in turn, are connected to conical aluminium pipes with inner radius increasing from 29 to 59.1 mm and wall thickness of 1.8 mm at $z = 3.961$ m. The inner radius increases to 70 mm at $|z| = 4.01$ m where the aluminium sections are connected by a 0.571 m long stainless steel tube to the next flared section of aluminium beam pipe, extending to a $|z|$ value of 10.6 m. Beyond that, the rest of the beam pipe is made out of 1.8 mm thick aluminium tube of outer diameter of 120 mm. A perspective view of the beam pipe is shown in Fig. 7.3. The contribution of the beam pipe to the material budget is rather insignificant, amounting to 0.2% of a radiation length at normal incidence and increasing to 1.6% at the end of the Tracker acceptance (at $|\eta| = 2.5$). The current description of the beam pipe corresponds to an earlier optimised design and is less ambitious than the one described in Section 6.6. However, the small difference does not affect the study of material budget and Tracker performance, presented in subsequent sections.

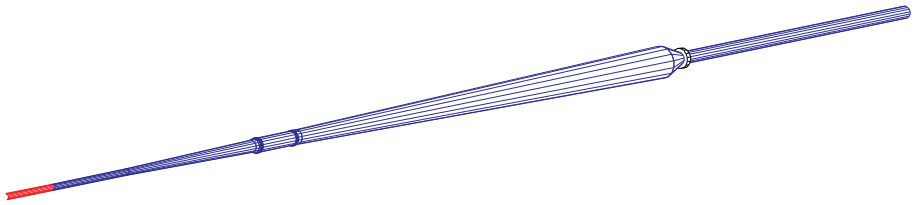

Fig. 7.3: A perspective view of half of the beam pipe as described in the simulation geometry.

7.5 Detector Layout

7.5.1 Phase II CMS Tracker

The CMS Tracker is described inside the simulation program in terms of three detector components, Pixel, Silicon strip and MSGC. Each of these components is further subdivided into its barrel and Forward–Backward parts. Several designs of each of these components are included to study different options of LHC operation. The active layers of the Pixel detector in the high luminosity option are shown in Fig. 7.4. The barrel Pixel detector is described in terms of 608 modules arranged in two cylindrical layers. The wafers are of size 16 mm $\times$ 64 mm and 250 μm thick. Alternate modules in ϕ are positioned radially 6 mm apart at radii 72 mm and 110 mm. Forward–Backward Pixel detectors are positioned at distances of 325 mm and 465 mm from the

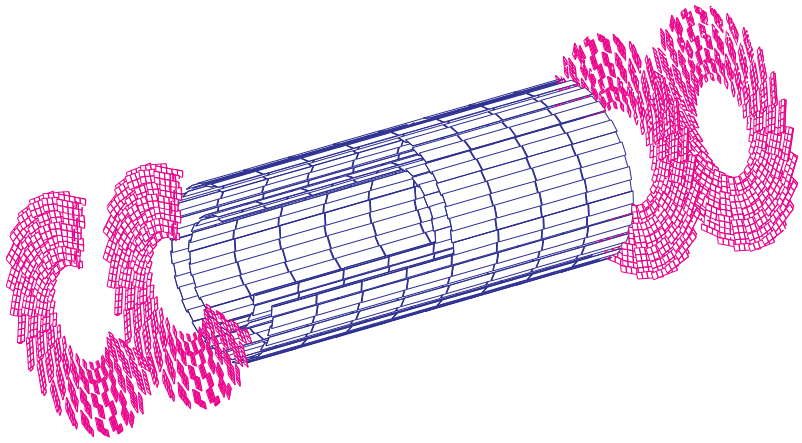

Fig. 7.4: Layout of the Pixel detector modules in the simulation geometry for the high luminosity option.

interaction point on either side. They are made out of 250 μm thick silicon wafers arranged in the form of a turbine with each disk consisting of 26 blades with 7-fold radial segmentation. The active layers of the Silicon detector are shown in Fig. 7.5. The barrel Silicon strip detectors are arranged in five equidistant, cylindrical layers between 210 mm and 629 mm. The first two layers extend in $|z|$ to 445.4 mm while the outer three layers cover $|z|$ to 827.6 mm. Silicon detectors of 64 mm $\times$ 125 mm are positioned around the surface of a cylinder. The detectors along z are alternately inside and outside the cylindrical surface and are radially 35 mm apart. The sensitive planes are tilted by 9° about the z axis. There are 8 detectors along z in the two inner layers and 14 in the three outer layers. The two innermost and the outermost layers are double sided whereas the remaining two are single sided. Double sided layers house detectors mounted back-to-back, for a total silicon thickness of 600 μm . The overlaps in $r\phi$ are typically set at 5.3%; the overlaps in the z direction vary with radius and pseudorapidity to maintain hermeticity for infinite momentum tracks coming from within $|z|$=10 cm ($\pm 2\sigma$) of the mid-point of the nominal

interaction region. The two innermost layers are complemented in z by mini-endcaps consisting of 3 stations of double sided detectors on either side. Each station is made out of two rings of wedge-shaped wafers, staggered in z by 1.25 mm. The $r\phi$ overlap of the sensitive areas is 1.9%, while radial overlaps ensure full coverage. The Forward–Backward Silicon detectors consist of 10 stations on either side of the interaction point. They are arranged in four rings, of which the outermost is double sided. The first six stations in each arm are fully equipped with detectors, with the innermost ring using double sided sensors. The following two stations house three rings while the last two consist of two rings of sensors; the last station houses exclusively double sided detectors.

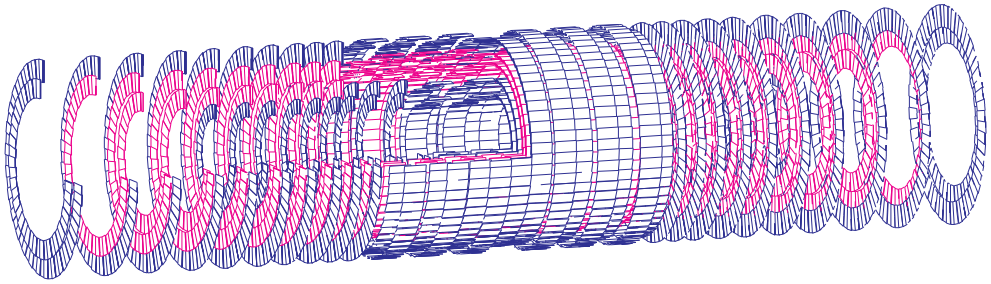

Fig. 7.5: Layout of the Silicon strip detector modules in the simulation geometry.

The active layers of the MSGC detector are shown in Fig. 7.6. The barrel MSGC detector consists of six coaxial cylinders with detectors at radial distances of 747, 827, 907, 987, 1067 and 1147 mm. The detector modules are 250 mm long and can be made out of one or two detectors (single or double ended, see Section 4.4.1.2). A double sided detector is made by mounting two MSGCs back-to-back (twin chambers). The detector modules are tilted at an angle of 14°. The layers at 747 and 987 mm are equipped with double sided double ended modules, the layers at 827 and 907 mm house single sided double ended modules and the layers at 1067 and 1147 mm are instrumented with single and double sided single ended modules, respectively. At each radial position there are 9 detector modules placed along z, having an overlap of 3 mm in the active area covering $|z|$ up to 1111 mm. The current software description differs to some extent from the one reported in Section 4.2. However, the positions of the sensitive detectors and the amount of material in each layer are kept according to the proposed layout. The $r\phi$ overlaps vary between 1% and 3%. The Forward–Backward MSGC's are grouped in eleven stations on either side of the interaction point covering $|z|$ from 1250 to 2731 mm. Each station consists of detectors arranged in four rings with the inner and outermost rings consisting of double sided detectors. Single sided rings house wedge-shaped chambers pointing toward the beam line. Double sided rings are equipped with twin chambers. The stereo side chambers are modelled as slanted wedges, with lateral sides tangent to a circle centred on the beam line. Adjacent substrates in a ring have a typical gap of 1.78 mm; the ring radial overlaps vary with the radius and allow for full coverage.

A total of 93400 volumes has been used to describe the geometry of the Tracker with its detector layers, supports and services. A longitudinal section of the active layers of the entire Tracker, as in the simulation geometry for the high luminosity option, is shown in Fig. 7.7.

7.5.2 Rapidity coverage and hermeticity

The CMS Tracker provides only a modest number of high precision measurements, so a careful optimisation of the layout hermeticity is mandatory. In this section the geometrical coverage is discussed, neglecting detector inefficiency and possible misalignments. A longitudinal view

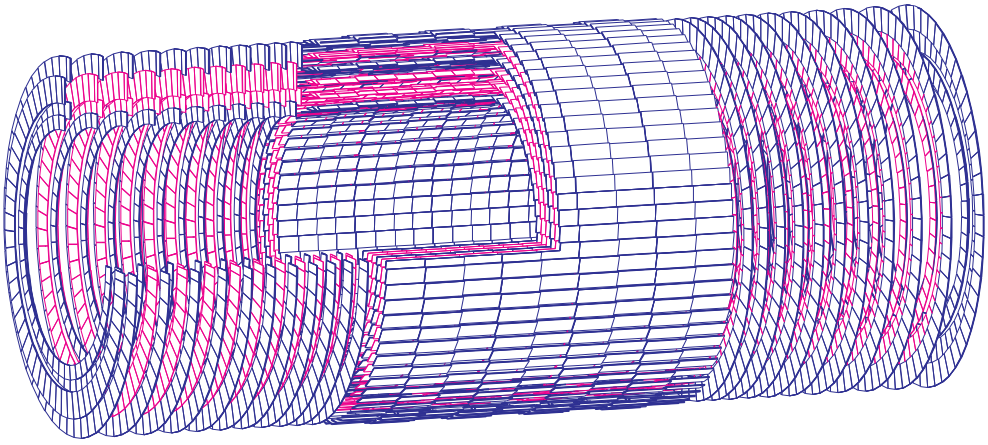

Fig. 7.6: Layout of the micro-strip gas chamber detector modules in the simulation geometry.

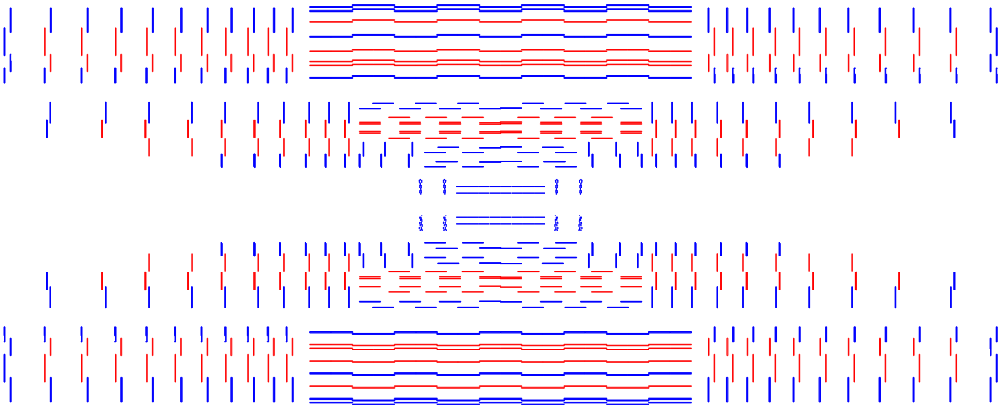

Fig. 7.7: A cut view of the active layers of the Tracker in the simulation geometry.

of a section of the Tracker is shown in Fig. 7.8; constant pseudorapidity lines are drawn for ease of consultation. To probe the Tracker angular coverage, infinite momentum tracks are extrapolated through the detector in the pseudorapidity interval $0 < \eta < 2.5$ and azimuthal range $0 \leq \phi \leq 2\pi$; the number of detectors crossed by each track is shown as a function of η in Fig. 7.9. Hits in double sided detectors as well as geometrical overlaps are counted only once. The origin of tracks along the z-axis fluctuates according to Gaussian statistics, with σ_z=5.3 cm. The upper plot illustrates the hit multiplicity in the overall Tracker and in the subdetector systems; the lower one details the 3D space point multiplicity.

In the central detectors the $r\phi$ coverage is fully hermetic: the average number of hits in the barrel is 13 for $|\eta| \leq 0.8$. In this region, eight space points are nominally recorded for each track. The position resolution of $r\phi$ hits is comparable in all detectors, within a factor two; the z resolution degrades as the radius increases and ranges from $\sim 12 - 15$ μm in the Pixel sensors to $\sim$1.5 mm in the MSGC detectors.

Pixel modules are not overlapped in the z direction and introduce a 2.5% geometrical inefficiency that dominates the RMS of the barrel hit multiplicity. The layout of the Silicon barrel in the z direction has been optimised to ensure hermetic coverage for all tracks originating from a region of $\pm 2\,\sigma_z$ around the nominal detector centre. The size of the overlaps in the z direction increases as η becomes larger, as can be observed in Fig. 7.8; the innermost barrel

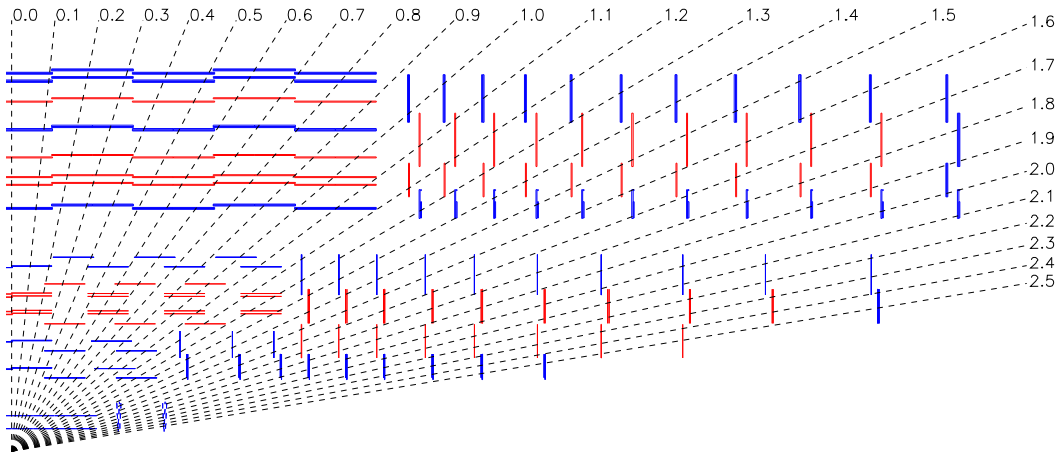

Fig. 7.8: Longitudinal section of the Tracker (1/8). Lines at constant pseudorapidity are drawn originating from the origin of the global frame of reference. In the MSGC barrel, the $r\phi$ overlap of two rods is visible in layers two and six.

layer needs the largest overlaps between adjacent detectors. If all layers are of equal length, this consideration implies that the overall barrel length is set by the requirement of hermeticity in the innermost layer. At larger radii, the simultaneous constraints of barrel length and module length lead to over-instrumentation of the layers. Moreover, an important reduction ($\sim 7\%$) of the silicon surface area needed to maintain full coverage is obtained if part of the large η range is instrumented with disks rather than cylindrical layers. For this reason the two inner barrel layers were shortened and complemented by mini-endcaps. Some price is paid in the trade off, in terms of mechanical layout and radial resolution. However, the z position resolution for tracks at large η is improved and careful layout of the services can result in a reduction of the overall Tracker material budget. In the MSGC barrel, hermeticity is ensured by 3 mm overlaps between adjacent detectors in each rod. The region of overlap is large enough to guarantee good quality hits for alignment purposes since no significant degradation of the hit resolution was measured beyond $\sim$2 mm from the detector edge (Fig. 4.48 through 4.54).

The forward stations have been laid out requiring hermetic coverage up to large η, as well as a stable number of space points along the tracks. The layout is a compromise between this and the need to limit the amount of material encountered by particles at shallow incident angles. The endcap Pixel system is affected by $\sim$2% inefficiency due to imperfect azimuthal overlaps. The endcap stations of the strip detectors are organised in rings which are staggered in z to allow for radial overlaps; the outermost rings are consistently set at smaller z, to maximise the η coverage of each station and reduce the effect of gaps between barrel and forward systems. Radial overlaps are the same in all stations and are defined by the disks set at the most unfavourable pseudorapidity values. The overall hit multiplicity is at least 13 in the range $1.3 \leq \eta \leq 2.0$ and it decreases at larger η, to reach a value of ~ 8 at $\eta = 2.4$; the RMS of the hit multiplicity varies between 5% and 6% in the interval $1.3 \leq \eta \leq 2.0$ and grows to $\sim$10% at larger pseudorapidity. The overall space point multiplicity at $\eta \geq 1.3$ has a regular behaviour; more than 60% of the track hits are space points, as for the barrel region. The detailed dependence of space point multiplicity on η is more complex. For each track crossing the endcaps, the first two measurements in the Silicon detectors, as well as the last, are recorded by double sided sensors. A similar requirement is also fulfilled by the MSGC endcaps, where the innermost and outermost rings are instrumented by twin chambers.

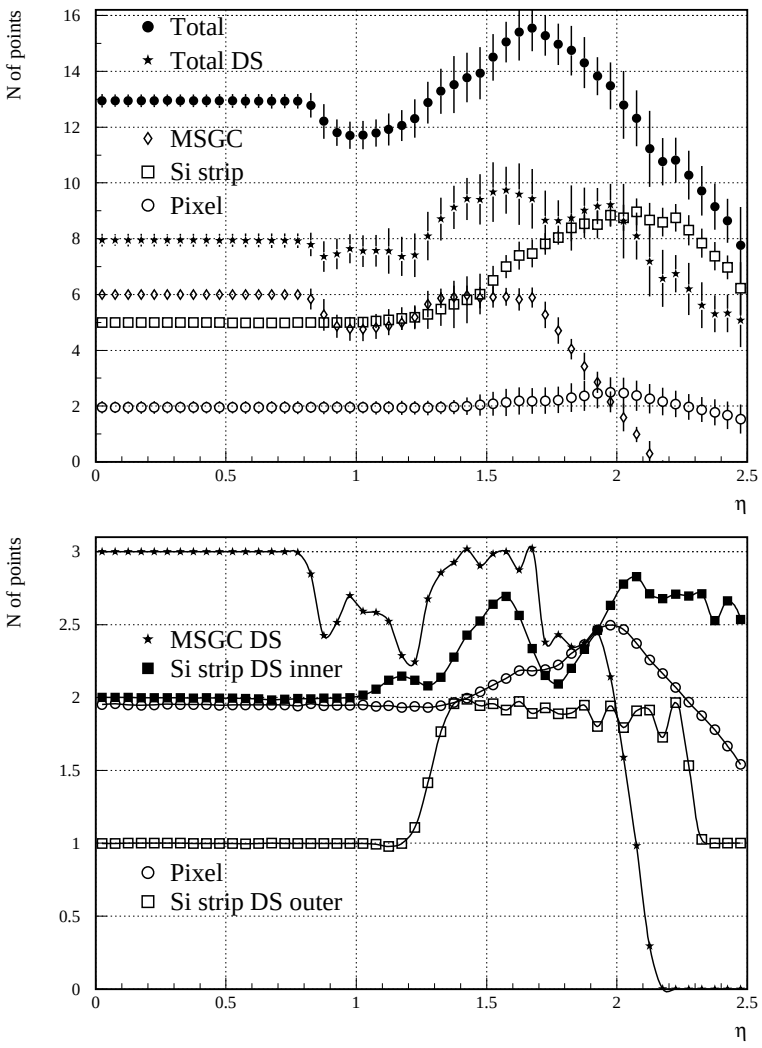

Fig. 7.9: Average number of detectors intersected by infinite momentum tracks as a function of pseudo-rapidity. In the upper plot, the hit multiplicity in the Tracker and in the detector subsystems is shown; the bottom plot details the space point multiplicity. Curves are obtained by simple interpolation; vertical bars represent the RMS of the hit multiplicity.

Critical regions, as far as hermeticity is concerned, are the gaps between barrel and endcaps and the radial separation between Silicon and MSGC detectors. In the transition region between barrel and endcaps, radial services are traversed at shallow angles, active volumes are separated by larger distances and the track hits are often recorded in equal share by barrel and forward detectors. For this reason, care has been taken to avoid alignments of the transition regions. The Silicon endcap layout provides a smooth transition from barrel to endcap regions, while the MSGC barrel-forward gap is probed by smaller η tracks and is visible as a loss of typically one hit in the region $0.85 \leq \eta \leq 1.25$. To minimise the size of the transition region, the MSGC barrel modules at the largest $|z|$ were re-designed so that the hybrids can be mounted on the end facing the interaction region. In the Silicon system, the same measure was easily implemented, since modules carry a single hybrid. In the endcaps, hybrids are mounted on the larger wedge side except for the outer ring, for which it is more convenient to install the electronics on the inner edge. This configuration allows a significant reduction of the distance between Silicon and MSGC detectors, as well as to extension the Tracker to the largest possible radius.

7.5.3 Phase I CMS Tracker

The CMS Tracker layout is significantly modified for the low luminosity start-up period of the LHC. All the detector components, with the exception of the Forward–Backward Pixel detector, are modified in this option. A longitudinal cut-view of the active layers of the entire Tracker, as simulated for the low luminosity option, is shown in Fig. 7.10. The barrel Pixel detectors are now positioned at radii of 43 mm and 71 mm thus requiring 384 detector modules instead of 608 as in the high luminosity option.

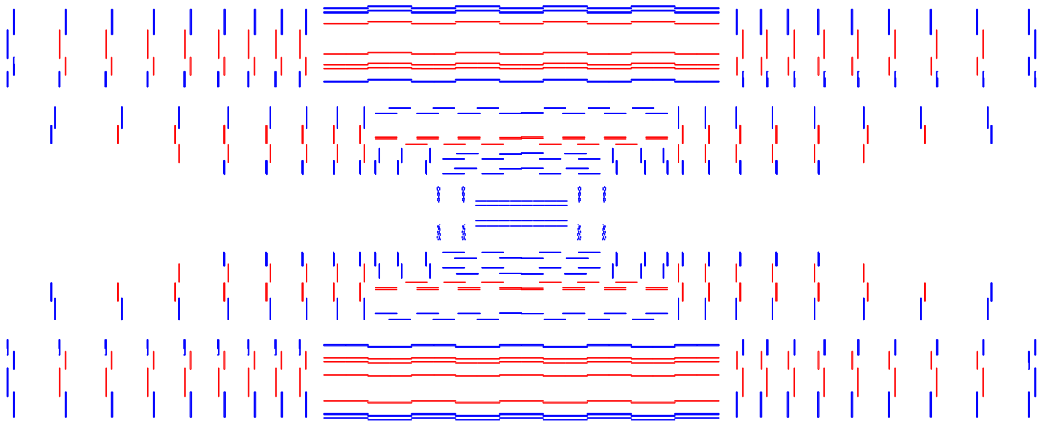

Fig. 7.10: A cut view of the active layers of the low luminosity option of the CMS Tracker as in the simulation geometry.

The fourth radial layer of the barrel Silicon detector is not equipped in this option. This corresponds to 738 fewer single sided detector modules. For the Forward–Backward Silicon system, there are 2 fewer stations on either side and the z positions of the disks are readjusted to optimise the geometrical coverage using 8 stations. The number of detector modules changes from 3168 to 2520.

The fourth radial layer of the barrel MSGC detector of the high luminosity option is not present in the low luminosity option. This layer is equipped with 540 double sided double ended detectors in the high luminosity option. Likewise, the number of stations in the Forward–Backward MSGC system is reduced from 11 to 9 on either side and the z positions are re-adjusted as in the case of Silicon detector. The number of detector modules changes from 4752 to 3888.

Figure 7.11 shows the angular coverage of the Tracker in the low luminosity configuration. From a comparison with the high luminosity version (see Fig. 7.9), the following observations can be made.

- The re-optimisation of the z coordinates of the forward disks in the Silicon strip and MSGC endcaps yields a relatively uniform coverage. The loss of one point in each subsystem in the barrel region is kept basically constant in the forward geometry.
- In the MSGC detector, the space point multiplicity has been degraded, particularly in the barrel/forward transition region.
- The increased distance between adjacent disks in the Silicon endcaps introduces a larger variation in the number of detectors hit by a track at large rapidity, as well as longer extrapolation length between Pixel and Silicon endcaps.
- The low luminosity configuration of the Pixel system provides a better pseudorapidity coverage, and a larger average number of points, as the barrel detectors are now positioned at smaller radii.

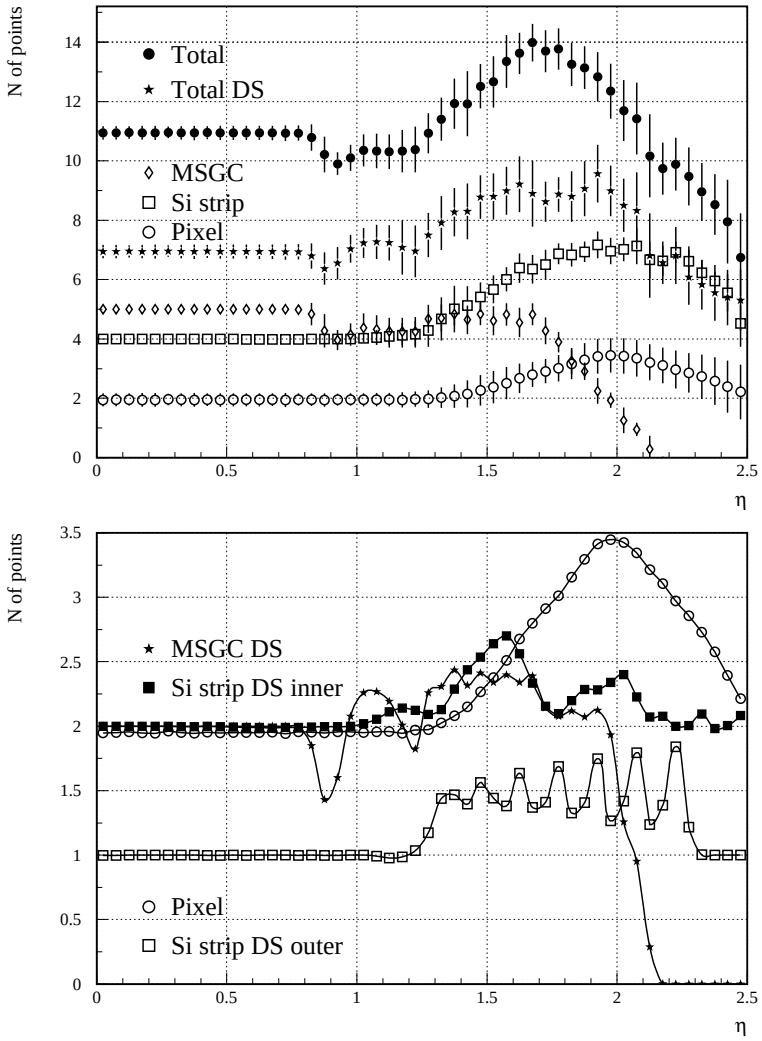

Fig. 7.11: Average number of layers/disks intersected by infinite momentum tracks as a function of rapidity, in the low luminosity configuration. In the upper plot, numbers for the three systems and the total are shown. In the lower plot, the detail for space points is given; lines are drawn to guide the eye.

7.6 Supports and Services

The Monte Carlo description of the CMS Tracker support structures and services is strictly modelled on the hardware design. A review of the passive volumes layout as described by the simulation geometry is reported in the following two sections, where missing items will be explicitly mentioned. Several tables are presented to illustrate the dimensions, material and multiplicity of the analysed items; the quality of the model used for large mechanical structures is more effectively characterised by their weight, while specific geometry information is reported in the text. The density and radiation length of the materials most used in the Tracker are listed in Table 7.2.

7.6.1 Support structures

The Monte Carlo description of a barrel Pixel module reproduces the layout shown in Fig. 2.48; silicon sensors are mounted on a 270 μm thick carbon fibre plate, also used to support cables and readout hybrids. Similarly, the Pixel endcap detector is supported by a 250 μm thick carbon fibre wedge visible in Fig. 2.12. Barrel modules are arranged into ladders supported by aluminium cooling pipes as shown in Fig. 2.4. The barrel endflanges are described by two

Table 7.2: List of main materials used in the Tracker

Material	Density (g/cm^3)	X_0 (cm)	Compound	Density (g/cm^3)	X_0 (cm)
Aluminium	2.70	8.89	Alumina	3.52	7.55
Carbon	2.26	18.85	Polyethylene	0.95	47.9
Copper	8.96	1.43	Water	1.00	36.1
Hydrogen	0.708E-1	865.54	Stainless steel	7.87	1.76
Iron	7.87	1.76	Kapton	1.11	28.4
Neon	8.385E-4	34503.	PEEK	1.32	30.0
Oxygen	0.143E-2	23944.0	Nomex	0.032	1229.0
Silicon	2.33	9.36	Honeycomb	0.05	472.6
Tin	7.31	1.21	Carbon fibre	1.69	25.0
Silver	10.48	0.85	Quartz	2.20	12.3
Gold	18.85	0.33	Hydrofluoroether	1.52	23.1

carbon fibre skins interleaved by honeycomb, shown in Fig. 2.49. In the endcaps, the detector supports are provided by carbon fibre blades arranged into wheels (Fig. 2.5). The blades are supported on the inner faces by aluminium cooling pipes, and at the inner and outer radii by carbon fibre rings. On each side of the barrel, two 0.5 mm thick cylindrical shells are modelled to support the services laid longitudinally to reach the Tracker ends. The inner tubes, utilised by the endcap system, are set at a radius $r = 179$ mm, while the outer ones used by the barrel are set at $r = 189$ mm; these structures are shown in Figs. 2.53 and 2.52. The support structures for the Pixel system are summarised in Table 7.3. Each Silicon barrel and endcap sensor is fixed

Table 7.3: Monte Carlo description of Pixel barrel and endcap supports

Component	Material	Thickness (mm)	Weight (kg)
Barrel module support	Carbon fibre	0.27	4.8×10^{-4} ($\times$ 608)
Barrel endflange disks	Carbon fibre	2×0.26	0.086(×2)
	Honeycomb	5.0	0.024(×2)
Barrel service tube	Carbon fibre	0.5	2.70(×2)
Endcap module support	Carbon fibre	0.25	2.5×10^{-3} ($\times$ 208)
Endcap inner rings	Carbon fibre	1.0	0.01/station
Endcap outer rings	Carbon fibre	1.0	0.065/station
Endcap service tube	Carbon fibre	0.5	2.7 (×2)

by positioning pins on a carbon fibre carrier ('module', described in Section 3.6); one end of the module protrudes to support the readout hybrids. The simulation description of a Silicon barrel module is shown in Fig. 7.12 and detailed in Table 7.4 together with the endcap module.

The weight imbalance between barrel and forward modules is larger than the present hardware estimate. Further optimisation of the forward mechanics has occurred since the formulation of the Monte Carlo model, which has therefore become conservative. In the barrel detector, the modules lay on ten coaxial carbon fibre cylinders (Section 3.3.3.1); each layer consists of two shells, coupled by endflange structures and separated by longitudinal beams. The cylinder model includes several structural elements such as cooling ledges and hybrid support rings. The spacer material for each pair of shells is smeared for some fraction within the cylinder volumes and modelled explicitly as longitudinal rails for the remainder. The shell model is shown in Fig. 7.13. The barrel endflanges are described as annular structures placed at the ends of each layer; the five layers are held together by radial struts. A summary of the barrel supports model is given in Table 7.5.

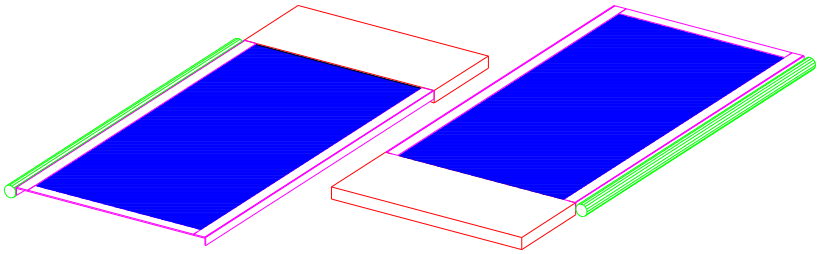

Fig. 7.12: Description of the Silicon barrel module in the simulation geometry. The silicon wafers are mounted on a carbon fibre space-frame, the largest end carrying the readout hybrids. The axial cooling pipe is also visible on one side of the modules.

Table 7.4: Description of Silicon barrel and endcaps space-frames

Component	Height (mm)	Width (mm)	Length (mm)	Material	Weight (g)
Barrel module					
Side rail	2.7	0.375	127.0	Carbon fibre	0.13 (× 2)
	0.375	4.0	127.0	Carbon fibre	0.32 (× 2)
Hybrid support	0.5	64.0	28.0	Carbon fibre	1.51
End rail	4.0	0.375	59.2	Carbon fibre	0.15
Fixation pins				Aluminium	0.064
Total					2.62
Endcap module					
Side rails				Carbon fibre	1.88(× 2)
Hybrid support	0.5	28.0	53.0	Carbon fibre	1.25
Fixation pins				Aluminium	0.5
Total					5.51

The endcap Silicon modules are mounted on support disks equivalent to the shells described in Section 3.7. The annular stiffening structures, also used to support the cooling distribution, are explicitly modelled as two carbon fibre volumes for each ring of sensors. The Silicon mini-endcaps are described exactly like the endcap system. The supports of a fully equipped station are characterised in Table 7.6.

The model of an MSGC double ended module is shown in Fig. 7.14. At the ends of two adjacent chambers, defined by substrates, covers and spacers, the volumes containing the hybrids and their supports are visible; on the sides, two segments of the rod holding the module are drawn (Section 4.4).

Table 7.5: Model of Silicon barrel support structures

Component	Material	Weight (kg)
Cylinders	Carbon fibre	23.40
Cylinder spacers	Carbon fibre	16.0
Hybrid supporting rings	Carbon fibre	1.50
Cooling ledge	Carbon fibre	1.70
Endflanges	Carbon fibre	1.94
	Honeycomb	0.58
Struts	Carbon fibre	0.05
Total		45.17

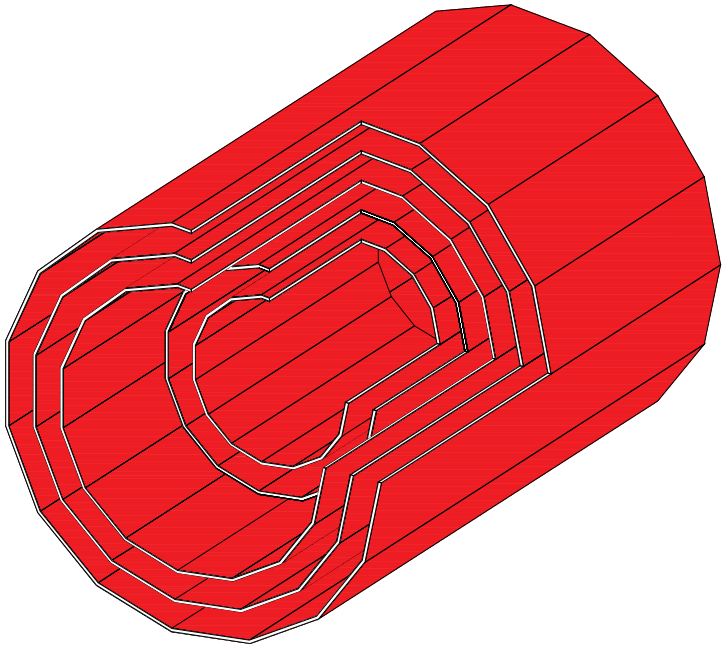

Fig. 7.13: Silicon barrel carbon fibre shells as modelled in the simulation geometry.

Table 7.6: Description of a Silicon endcap station support structure

Component	Material	Weight (kg)
Disk	Carbon fibre	1.01
	Nomex	0.18
Stiffening rings	Carbon fibre	3.55
Total		4.74

Table 7.7: Description of the MSGC barrel support structure

Component	Material	Weight (kg)
Wheels	Carbon fibre	64.0
Rods	Carbon fibre	98.8
Rivets/Pipe supp.	Carbon fibre	22.0
Hybrid supports	Carbon fibre	33.9
Total		218.7

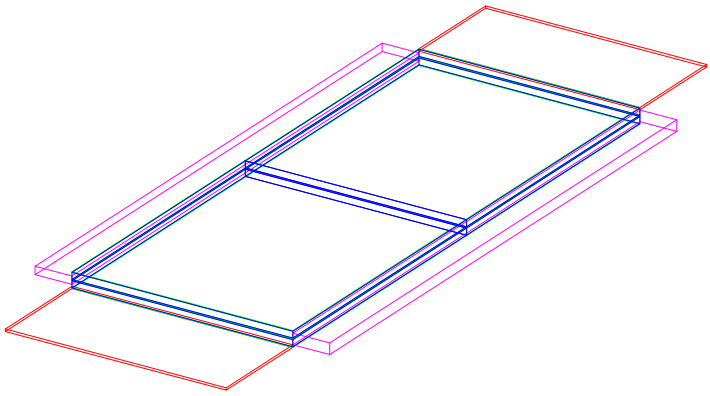

Fig. 7.14: Monte Carlo description of a MSGC barrel double ended module. Two supporting rods and the readout volumes are visible at the sides of adjacent chambers

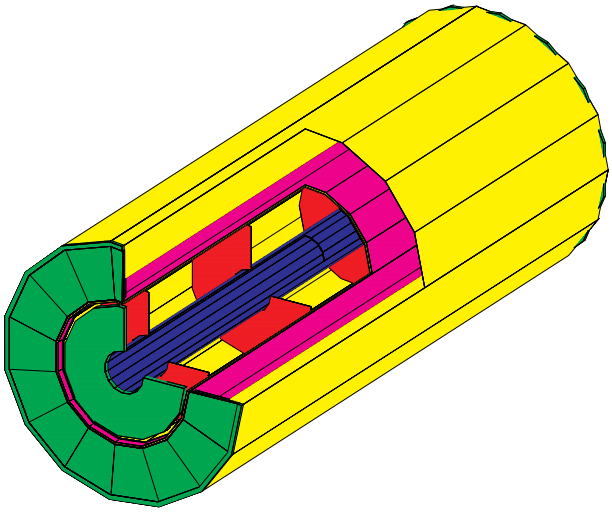

Fig. 7.15: General integration structures in the Monte Carlo model of the CMS Tracker.

The supports and rivets used to hold in place detectors and cooling/gas pipes are taken into account by the description of the rods. Each rod is described by two longitudinal shafts terminated by front panels at each side. Two disks that brace the rods are placed at the barrel ends, with two others acting as middle-flanges; each flange is modelled as seven concentric space frames equivalent to the wheels presented in Section 4.4.3.1. The support structure is detailed in Table 7.7. The MSGC endcap module contains four detecting elements and is described, as in Section 4.5.1, by three space-frames, cover, substrates and hybrid supports. Modules are mounted by fixation pins on either sides of supporting disks, explicitly modelled according to the description in Section 4.5.2.1. Eleven stations on each side of the barrel are grouped in a super-module structure by nine longitudinal beams at the outer MSGC radius and six at the innermost, as described in Section 4.5. Support structures are detailed in Table 7.8. General integration supports are described in the Monte Carlo geometry by several volumes, summarised in Fig. 7.15. Each subdetector system is contained by a carbon fibre shell; an aluminium Faraday cage is modelled for the Silicon system. The cylinder visible in intermediate grey represents the support structure of the Tracker and the thermal screen of the Silicon system, overlaid on the Silicon Tracker shell (Section 6.2.10.3). The central support of the Tracker is modelled according to Section 6.2.7 by two carbon fibre cylinders interleaved by aluminium honeycomb, 2 mm and 16 mm thick, respectively; the thermal screen is described in the next section. At the Tracker ends, the flanges of the support structure and thermal screen are visible; although these are not consistent with the bracket description in Section 6.2.8, as they are placed outside the Tracker volume the model accuracy is unaffected. Additional disks represent the four Pixel and beam pipe supports (Sections 6.2.10.3 and 6.2.10.2). A summary of the integration structures is reported in Table 7.9.

7.6.2 Services

The distribution of gas and cooling together with the routing of power cables and other services are discussed in detail in this section. Each subdetector is fully analysed in turn; for easy of consultation, some synoptic tables are reported at the end of this section to summarise individual service items. The materials used to cool the Tracker and distribute the gas supply, along with relevant dimensions and multiplicity, are shown in Table 7.10. Cables and optical fibres are described in Table 7.11 in terms of their cross section and material. Low voltage cables are

Table 7.8: Description of a MSGC endcap disk support structure

Component	Material	Weight (kg)
Disk	Carbon fibre	3.6
	Nomex	1.7
Frames	PEEK	0.41
Hybrid supports	Carbon fibre	0.88
Module insertion pins	Aluminium	0.065
Total		6.66
Outer shafts (9)	Carbon fibre	8.7
Inner shafts (6)	Carbon fibre	4.2
Shaft fixations	Aluminium	2.1
Total		12.0

Table 7.9: Description of integration structures in the CMS Tracker

Component	Material	Weight (kg)
Pixel cylinder	Carbon fibre	5.8
Silicon cylinder	Carbon fibre+Al	46.2
MSGC cylinder	Carbon fibre	75.0
Tracker support	Carbon fibre	165.8
	Honeycomb	19.7
Tracker endflanges	Carbon fibre+Al	32.8
Pixel&b-pipe supp.	Carbon fibre	7.0
Total		352.3

characterised by the cross section of conductor per chip and the applied scaling law is indicated in the table. The cable thickness is consistent with the discussion reported in Section 5.7. In Table 7.12 dimensions and materials of several connector types are reported. Voltage and optical fibre connectors are modelled on low mass commercial products. Light material cooling pipes are used when outside the heat exchange zones; the connectors used to join metal and PEEK pipes are modelled on custom products. Descriptions of the service hardware layout are found in the engineering and subdetectors chapters.

The Tracker cooling and cables distribution is described in the simulation geometry by a large amount of passive volumes laid axially, i.e. parallel to the beam pipe, and radially, i.e. perpendicular to the beam line; several service bundles also appear as annular shapes, e.g. to distribute power and cooling to the endcap rings.

The Pixel barrel cooling pipes have been mentioned in the previous section as structural elements; the details of the simulated structures are reported in Table 7.10. At the barrel endflanges 16 manifolds are connected to radial inlets/outlets that reach the outer radius of the Pixel system and are routed axially toward the ends of the Tracker. In the endcaps, the disk cooling system is modelled as in Figs. 2.37, 2.38; U-shaped cooling pipes are explicitly modelled and connected to the axial collectors laid on the service tubes. Pixel cables are distributed similarly to the cooling system and details on the material can be found in Table 7.11. At the barrel ends, two service patch boards are explicitly modelled; high and low voltage cables, low mass connectors, optical fibres and optical connectors are smeared over the board and reach the service tube and the Tracker endflanges. In the endcap region, Pixel services are smeared over the entire blade surface. All services are routed axially by the service cylinder from the disks to the Tracker endflanges. The tube is modelled by an average material mixture which includes all the cooling components, power and readout cables of thickness proportional to the number of channels. An electrostatic screen of 100 μm envelopes the Pixel system.

The Silicon barrel cooling in each layer is modelled by axial pipes laid on the side of modules as shown in Fig. 7.12; the bends in the pipe routing, necessary to cool the hybrids and the end-rails, are properly taken into account. At both ends of each layers, four annular cooling manifolds are present. Each manifold has one inlet and one outlet, modelled as part of the radial services exiting the barrel endflanges. The radial pipes of each layer extend up to the outermost radius of the Silicon system and are carried out axially to the Tracker endflanges. Similarly, the cables are laid axially within the barrel and reach the Tracker endflanges following the path described for the cooling pipes. The simulated barrel service layout is shown in Fig. 7.16. At every layer, one bundle is modelled for each row of detectors set at fixed ϕ, and is visible as the

Table 7.10: Description of cooling and gas pipes used in the CMS Tracker simulation geometry

Type	Material	Outer/inner diameter (mm)	Multiplicity
Pixel cooling pipes			
Barrel inner axial pipes	Aluminium	3.8/3.4	76
Barrel endflange manifolds	PEEK	8.0/7.5	16 (× 2)
Barrel radial inlets/outlets	PEEK	8.0/7.5	16(× 2)
Barrel axial pipes	Aluminium	6.6/6.0	16(× 2)
Endcap pipes on disks	Aluminium	4.0/3.6	26/station
Endcap outer axial pipes	Aluminium	6.4/6.0	8 /station
Silicon cooling pipes			
Barrel Inner axial pipes	Aluminium	4.0/3.6	444
Barrel endflange manifolds	Aluminium	8.0/7.4	20 (× 2)
Barrel radial inlets/outlets	PEEK	10.0/8.0	40 (× 2)
Barrel outer axial pipes	PEEK	10.0/8.0	40 (× 2)
Endcap pipes on disks	Aluminium	3.2/2.8	16/station (+loops)
Endcap outer axial pipes	PEEK	8.0/6.0	8/station
Flushing gas pipes	PEEK	12.0/10.0	33 (× 2)
MSGC cooling and gas pipes			
Barrel inner axial cooling pipes	Stainless steel	2.15/2.0	736
Barrel inner axial gas pipes	PEEK	3.0/2.5	736
Barrel endflange cooling manifolds	PEEK	6.0/4.0	14 (× 2)
Barrel endflange gas manifolds	PEEK	6.0/4.0	14 (× 2)
Barrel cooling radial inlets/outlets	PEEK	10.0/8.0	36 (× 2)
Barrel gas radial inlets/outlets	PEEK	10.0/8.0	72 (× 2
Barrel outer axial cooling pipes	PEEK	10.0/8.0	36 (× 2)
Barrel outer axial gas pipes	PEEK	10.0/8.0	72 (× 2)
Endcap cooling pipes on disks	Stainless steel	3.2/2.9	4/station (+loops)
Endcap gas pipes on disk	PEEK	3.0/2.5	4/station (+loops)
Endcap outer axial cooling pipes	PEEK	20.0/16.0	18(× 2)
Endcap outer axial gas pipes	PEEK	20.0/16.0	36(× 2)
Flushing gas pipes	PEEK	12.0/10.0	33 (× 2)

dark axial pattern in the barrel region. Radial outlets are visible as a dark disk at the barrel ends. The axial bundles (24) laid at each side of the barrel represent the service routing to the Tracker endflanges.

In the endcap Silicon disks, two annular cooling pipes are placed on each ring of sensors. Similarly, each readout hybrid is cooled by two pipes. A 4-ring station is equipped with eight pairs of annular cooling pipes and sixteen radial pipes for inlet and outlet distribution. The radial pipes in each disk are connected to eight axial collectors reaching the Tracker ends. The radial distribution is grouped in the simulation into twelve bundles, visible in Fig 7.16 as dark radial segments. To ensure a correct material distribution, each radial bundle consists of four volumes used to supply every ring independently. The axial services at the outermost Silicon radius are modelled as twelve axial bundles for each station. The bundles of each station are rotated with respect to the subsequent stations to avoid large spikes in material density. Power cables are laid alongside the cooling distribution. The mini-endcap service distribution is similarly modelled.

The MSGC service layout is like that of Silicon subsystem in many ways. The MSGC barrel cooling consists of pipes laid along each side of the rods; gas supply is modelled in the same fashion. Low voltage cables lie on the left hand side of the rod structure, whereas high voltage lines, slow control cables and optical fibres lie on the right. Two annular cooling and gas manifolds are modelled on each circular rib of the endflange barrel wheels. At each barrel end, nine 20°-wide circular sectors house the radial services layout. Annular gas and cooling pipes connect to radial collectors that reach the outer MSGC radius and bend toward the Tracker

Table 7.11: Description of cables and fibres used in the CMS Tracker simulation. The symbol A_{core} used in the table indicates the cross section area of a conductor made of a specific material

Cable type	Modularity	X-section (mm^2)	Material
Pixel detectors			
LV ribbons - core	scales with n-modules	4.0×10^{-1}/module	Aluminium
LV ribbons - sheath		5.0×10^{-1}/module	Kapton
HV ribbons - core	scales with n-modules	2.0×10^{-2}/module	Copper
HV ribbons - sheath		5.0×10^{-1}/module	Kapton
LV cables - core	scales with n-chips	5.32×10^{2}/barrel	Aluminium
LV cables - sheath		3.2×10^{1}/barrel	Polyethylene
HV cables - core	scales with n-modules	3.1×10^{-2}	Copper
HV cables - sheath		9.4×10^{-2}	Polyethylene
R/O Optical Fibres	1/(4-8 chips)	1.27×10^{-2}	Quartz
Strip detectors			
LV cables - core	scales with n-chips	1.66×10^{-1}/chip	Aluminium
LV cables - sheath	scales with n-chips	$A_{core} \times 8$	Polyethylene
HV cables - core		2.01×10^{-2}	Aluminium
HV cables - drain		0.79×10^{-2}	Aluminium
HV cables - sheath		0.24×10^{1}	Polyethylene
Temperature Sensors cables	1 twisted pair/det.	$1.33 \times 10^{-2} \times 2$	Aluminium
Temperature Sensors sheath		$A_{core} \times 8$	Polyethylene
I2C cables	n-hybrids×2+1 lines	4.9×10^{-3} (1 line)	Aluminium
	1/cable	1.0×10^{-1}	Kapton
Clock cable - core		$1.33 \times 10^{-2} \times 2$	Copper
Clock cable - sheath		$A_{core} \times 8$	Polyethylene
R/O Optical Fibres	1/(2 APV's)	1.27×10^{-2}	Quartz

Table 7.12: Description of connectors used in the CMS Tracker description

Connector type	Modularity	Volume (mm^3)	Material
Optical fibre conn.	n-APV/8	75.0	Kapton
Water/Gas Pipe conn.		760.3	PEEK
HV Silicon conn.	1/det	46.0	Kapton
		4.0	Copper
HV + I2C MSGC conn.	1/det.	253.6	Kapton
		22.3	Copper
LV Hybrid conn.	1/det	253.6	Kapton
		22.3	Copper

ends. Cables follow the same path. The endcap MSGC cable distribution is the same as used for the endcap Silicon, but with six radial and axial outlets instead of nine. Cooling and gas pipes are laid in annular circuits at each ring and reach out to the axial collectors at the outer MSGC radius. The simulated services layout for the MSGC system is partly shown in Fig. 7.17. Flushing gas is distributed by PEEK pipes which cross the Tracker longitudinally in every subsystem. The thermal screen used to decouple the temperature working point of Silicon and MSGC detectors is described in Table 7.13 and is modelled according to one of the configurations discussed in Section 6.4. Carbon fibre pipes are laid axially at the outer boundary of the Silicon Tracker volume and thermally coupled by a 500 μm thick aluminium foil. At the Tracker ends two large cooling manifolds supply the thermal screen. The outlets at the Tracker endflanges are partially described in the Monte Carlo geometry. With the exception of the Pixel system, all the services described in this section exit the Tracker at $|z| = 287$ cm and are laid radially in front of the electromagnetic calorimeter endcaps.

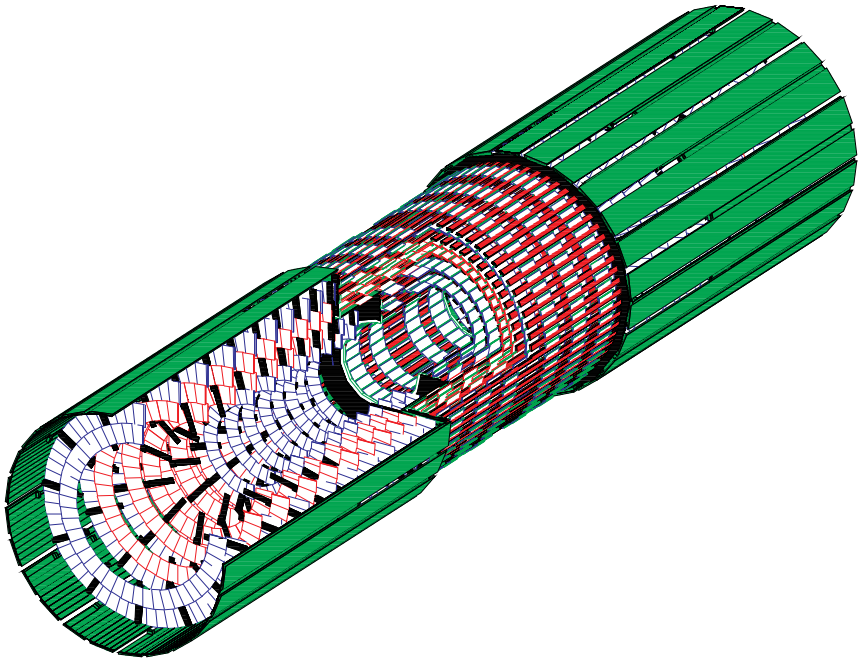

Fig. 7.16: Services layout in the Silicon Tracker.

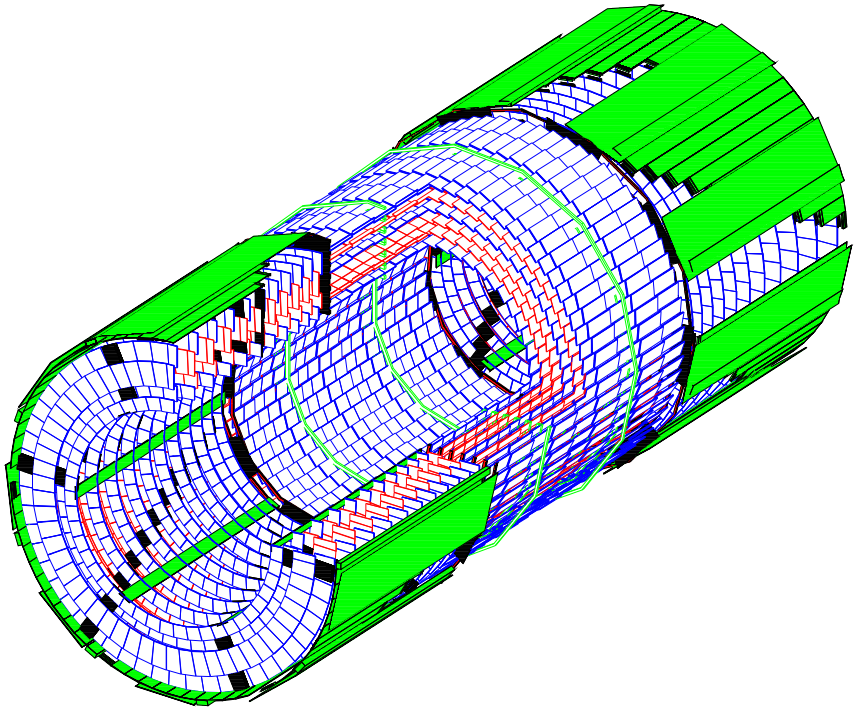

Fig. 7.17: Services layout in the MSGC Tracker.

7.7 Tracker material budget

The amount of material traversed by particles in the Tracker has a high impact on the physics performance of the CMS detector and consequently represents a major optimisation issue in

Table 7.13: Model of thermal screen between Silicon and gas detectors

Component	Quantity	R_{in} (mm)	R_{out} (mm)	Material
Axial Pipes	130	2.0	2.5	Carbon fibre
Foam screen	1 cylinder	641.0	645.0	Foam
Manifold	1 loop at each end	10.0	12.0	PEEK
Endcaps	1 disk at each end	195.0	605.0	Foam (4.0 cm thick)

the definition of the Tracker layout, as well as in several technical choices. The simulation description of the Tracker material is very accurate and yields a careful determination of the Tracker material budget in terms of radiation and interaction length. In order to estimate the importance of different contributions and identify targets for optimisation, the analysis of the material budget is broken down into five items characterised by their function, i.e. sensitive volumes, electronics, support structures, cooling and services. Further information is reported by breaking down the material estimate into barrel and endcap contributions for each subsystem; the Silicon mini-endcaps are considered as part of the barrel. These studies focus on the material distributed within the active volume of the Tracker; cables and structures laid beyond the last measuring point are examined separately and their contribution is quantified in Section 7.7.6. The overall Tracker material budget for electromagnetic processes is discussed in the same section and for hadronic processes in Section 7.7.7.

The Tracker material budget in the simulated detector was determined by propagating 'geantinos' through the Tracker in the range $|\eta| < 2.5$; the primary vertex is fixed at the nominal interaction point $(0, 0, 0)$. Geantinos are fake particles generated in GEANT specifically to gauge the amount of material; they have no interactions, ensuring that all tracks fully traverse the detector, and do not experience deflection by the magnetic field. In the plots shown the material is averaged over $0 \leq \phi \leq 360°$.

7.7.1 Sensitive volumes

This category refers to materials employed in the assembly of detecting elements. The Silicon strip and Pixel detectors contribute 300 μm and 250 μm thick silicon wafers, respectively, whereas the MSGC detectors consist of 300 μm glass substrates, 300 μm charged PEEK covers and PEEK spacers. The material budget analysis is reported in Fig. 7.18. The rather flat behaviour of the sub-system distributions indicates a reasonable optimisation of the relative lengths of the barrels and endcaps. The passage from barrel to endcap region is staggered in the three subsystems, so as to avoid cracks aligned in pseudorapidity.

7.7.2 Electronics

This group of materials includes readout and high voltage hybrids, connectors, communication and control modules (CCUMs) and input/output units (I/O boards) described in Section 5.6.1.

Pixel hybrids are described in the Monte Carlo geometry according to Table 2.9.

The number of chips mounted on the strip detector hybrids is matched to the pitch of the sensors. Silicon hybrids measure 6.4 × 2.8 cm in the barrel, whereas they vary in width in the endcaps to match the wedge shape. Barrel MSGC hybrids measure 10.4 × 4.8 cm while in the endcaps they are 3 cm wide. A description of standard Silicon and MSGC hybrids and their fractional radiation length break-down is shown in Table 7.14 and 7.15, respectively. The fractional radiation length reported in the tables is calculated for normal incidence after smearing all items on the hybrids.

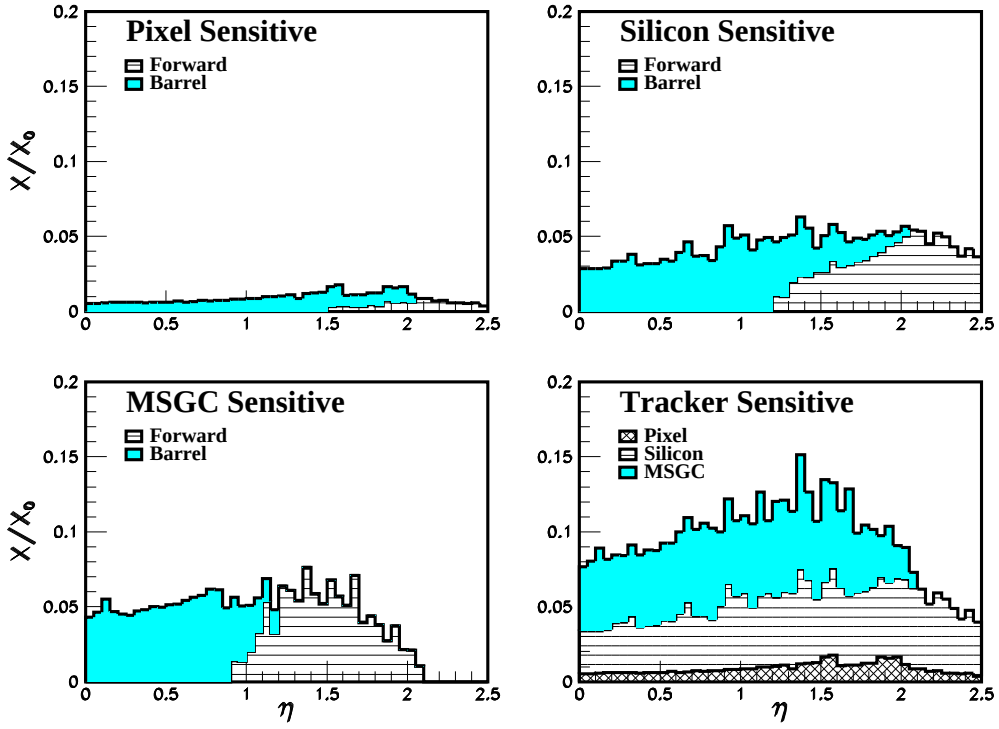

Fig. 7.18: Contribution of the Tracker detecting elements to the material budget.

Table 7.14: Readout hybrid description for an 80 μm pitch silicon detector. Material break-down is shown in the rightmost column in terms of fraction of X_0 at normal incidence

Component	Quantity	x (mm)	y (mm)	z (mm)	Material	X/X_0 (%)
Hybrid	1	64.0	0.15	28.0	Kapton	0.05
	1	64.0	0.15	28.0	Aluminium	0.17
APVs	6 (n)	6.35	0.35	12.0	Silicon	0.09
LV filter	2*n+5	3.2	1.6	1.2	Alumina	
		0.2	1.6	1.2	Ni/Ag/Sn	0.11
Termination	8	3.2	1.6	1.2	Alumina	
Resistors	8	0.2	1.6	1.2	Ni/Ag/Sn	0.03
MUX	1	2.5	0.35	2.5	Silicon	1.3E-3
PLL	1	2.5	0.35	2.5	Silicon	1.3E-3
LVDS	1	2.5	0.35	2.5	Silicon	1.3E-3
Pitch Adaptor	1	60.0	0.5	7.0	Silica	0.10
Connector	1.5	23.0	2.2	5.0	Kapton	
	1.5	22.3	1.0	1.0	Copper	0.19
Laser Driver	1	0.25	0.35	2.5	Silicon	1.3E-3
Laser array	1	10.0	2.0	15.0	Alumina	
	1	10.0	0.5	15.0	Silicon	
	28	0.25	5.0	0.45	Copper	0.32
Temperature sensors	1	5.1	2.0	1.5	Alumina	0.01
Total						1.05

Optical transmitters in the Pixel detector are modelled on a custom device and are mounted on the service tube. CCU boards are placed at each end of the Silicon barrel so that each row of detectors at a fixed ϕ is controlled by two boards. In the endcaps, each station houses the

Table 7.15: Readout and high voltage hybrid description for a barrel MSGC detector

Component	Quantity	x (mm)	y (mm)	z (mm)	Material	X/X_0 (%)
Hybrid	1	64.0	0.15	28.0	Kapton	0.05
	1	64.0	0.15	28.0	Aluminium	0.17
APVs	4 (n)	6.35	0.35	12.0	Silicon	0.02
LV filter	2*n+5	3.2	1.6	1.2	Alumina	
		0.2	1.6	1.2	Ni/Ag/Sn	0.03
Termination	8	3.2	1.6	1.2	Carbon	
Resistors	8	0.2	1.6	1.2	Ni/Ag/Sn	0.01
MUX	1	2.5	0.35	2.5	Silicon	5.0E-4
PLL	1	2.5	0.35	2.5	Silicon	5.0E-4
LVDS	1	2.5	0.35	2.5	Silicon	5.0E-4
Pitch Adaptor	1	60.0	0.5	7.0	Silica	0.07
Connector	2.	23.0	2.2	5.0	Kapton	
	2.	22.3	1.0	1.0	Copper	0.10
Laser Driver	1	0.25	0.35	2.5	Silicon	5.0E-4
Laser array	1	10.0	2.0	15.0	Alumina	
	1	10.0	0.5	15.0	Silicon	
	28	0.25	5.0	0.45	Copper	0.12
HV Switches	1 (16 sw.)	5.0	0.4	2.0	GaAs	
	1	5.0	1.6	2.0	PEEK	2.7E-3
Switch driver	1	2.5	0.35	10.	Silicon	1.9E-3
Resistors	33	3.2	1.6	1.2	Carbon	
	33	0.2	1.6	1.2	Ni/Ag/Sn	0.05
Total						0.64

appropriate multiplicity of CCU boards at the outermost radius of the disks. The same model is used in the mini endcaps. Each rod of the MSGC barrel houses one CCU at a single end whereas the endcaps gas disks implement the same layout as the endcap Silicon system. Every CCUM controls a number of chips varying between 70 and 118. Every group of eight CCUMs is connected to one I/O board. Control units and I/O boards are described in Tables 7.16 and 7.17.

The analysis of the electronics contribution to the material budget is presented in Fig. 7.19. Even though the number of channels in the MSGC Tracker is about 1.6 times larger than in the Silicon strip system, the density of electronics is lower in the MSGCs due to the different strip length and pitch.

Table 7.16: CCU module material break-down

Component	Quantity	x (mm)	y (mm)	z (mm)	Material	X/X_0 (%)
Hybrid	1	52.0	0.15	48.0	Kapton	
	1	52.0	0.15	48.0	Aluminium	
	1	52.0	0.50	48.0	Carbon fibre	0.42
CCU	1	6.35	0.35	12.0	Silicon	0.011
PLL	1	2.5	0.35	2.5	Silicon	1. E-3
LVDS	2	2.5	0.35	2.5	Silicon	1.9E-3
Connector	3.	23.0	2.2	5.0	Kapton	
	3.	22.3	1.0	1.0	Copper	0.30
LV filter	6	3.2	1.6	1.2	Alumina	
	6	0.2	1.6	1.2	Ni/Ag/Sn	0.03
Termination	4	3.2	1.6	1.2	Carbon	
Resistors	4	0.2	1.6	1.2	Ni/Ag/Sn	0.01
Total						0.77

Table 7.17: I/O board material break-down

Component	Quantity	x (mm)	y (mm)	z (mm)	Material	X/X_0 (%)
Hybrid	1	52.0	0.15	48.0	Kapton	
	1	52.0	0.15	48.0	Aluminium	
	1	52.0	0.50	48.0	Carbon fibre	0.42
Laser driver	1	6.35	0.35	2.5	Silicon	1.0E-3
Pin receiver	1	2.5	0.35	2.5	Silicon	1.0E-3
LVDS	2	2.5	0.35	2.5	Silicon	3.8E-3
Laser array	2	10.0	2.0	15.0	Alumina	
	2	10.0	0.5	15.0	Silicon	
	56	0.25	5.0	0.45	Copper	0.47
LV filter	8	3.2	1.6	1.2	Alumina	
	8	0.2	1.6	1.2	Ni/Ag/Sn	0.04
Termination	4	3.2	1.6	1.2	Carbon	
Resistors	4	0.2	1.6	1.2	Ni/Ag/Sn	0.01
Connector	1.	23.0	2.2	5.0	Kapton	
	1.	22.3	1.0	1.0	Copper	0.10
Total						1.04

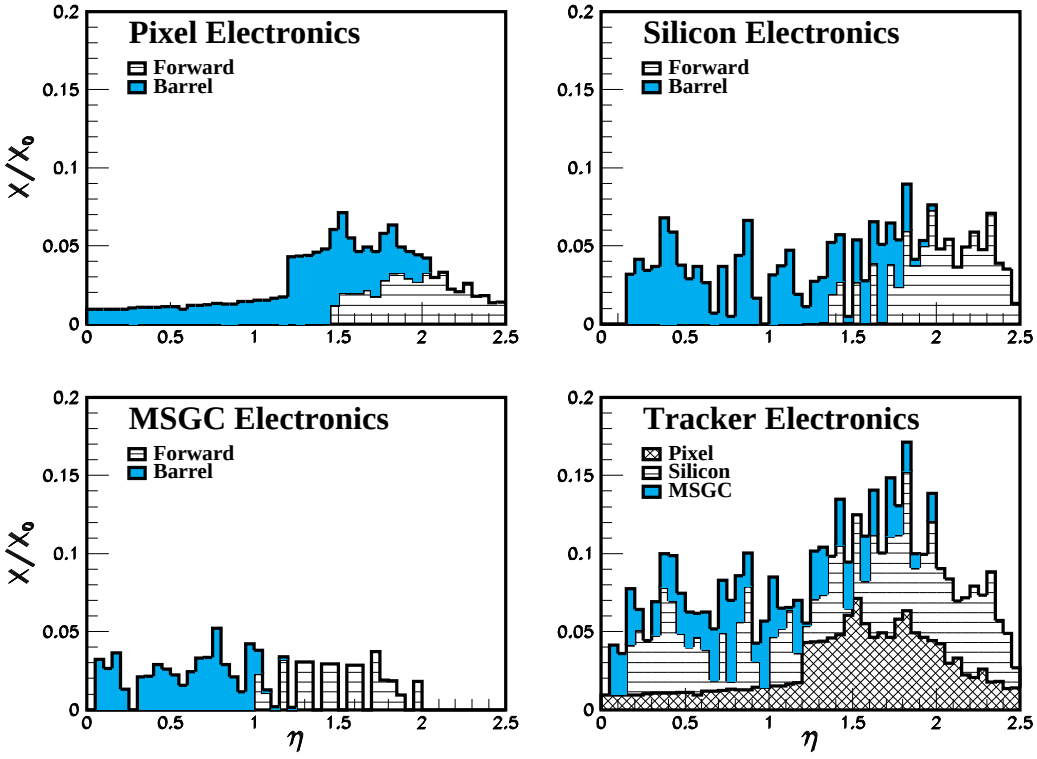

Fig. 7.19: Contribution of electronics to the Tracker material budget.

7.7.3 Support structures

All general integration structures described in Section 7.6 are analysed together with detector module space-frames and electronics supports. Materials that lie beyond the active radius of the Tracker are not considered in this context and will be discussed later in this section. The analysis is reported in Fig. 7.20. The shaded area indicated as 'common' in the Pixel and Silicon plots refers to the cylinders described in Table 7.9. Pseudorapidity plays an unfavourable role in

the material budget of the Pixel system: the material contributed by the whole Pixel detector at $\eta \sim 2$ is about half of the Silicon contribution at the same location in η. Barrel and endcap structures appear to be well balanced in all subsystems. The overall Tracker support system (Table 7.9) is shown only in the bottom right plot, since it is not part of any subsystem; about one third of the total number of radiation lengths at large η is given by this large support. The support structures represent the most sizeable contribution to the Tracker material budget.

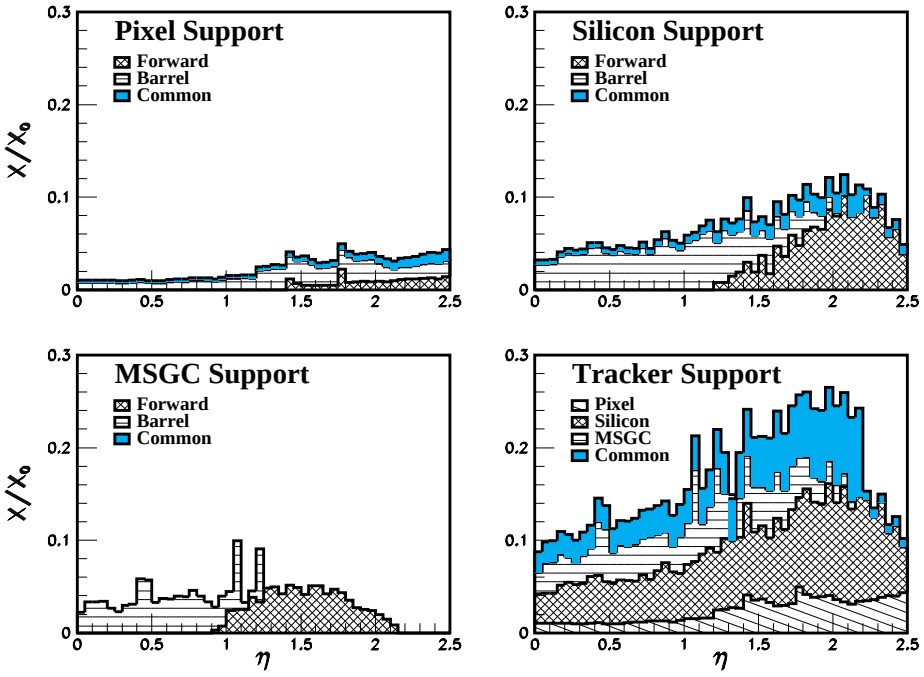

Fig. 7.20: Contribution of Tracker supports to the material budget.

7.7.4 Cables

All cables reported in Table 7.11 have been analysed and the result is shown in Fig. 7.21. Cables are an important contribution to the material budget and care has been taken in the modelling to use routing safety factors; when appropriate, the model takes into account the fanning-out of cable bundles, visualised in Figs. 7.22 and 7.23.

The axial Silicon services are laid at unfavourable pseudorapidity values and tracks cross them at shallow angles; the enhancement between η=1 and η=1.5 corresponds to the barrel end-flange and mini-endcap services, which are being crossed repeatedly by particles in this range. The services material budget is dominated by the low voltage cables, whose total cross section scales with the number of readout chips. As discussed already for the electronics, the Silicon system has a higher channel density than the MSGC system; it should be noted that the MSGC outer axial cables do not contribute to the distributions since they are laid beyond the Tracker active volume.

7.7.5 Cooling

The CMS Tracker cooling system implements two different coolants, water in the gas detectors and hydrofluoroether ($C_4F_9OCH_3$) in the Silicon system (Table 7.2). The contribution of

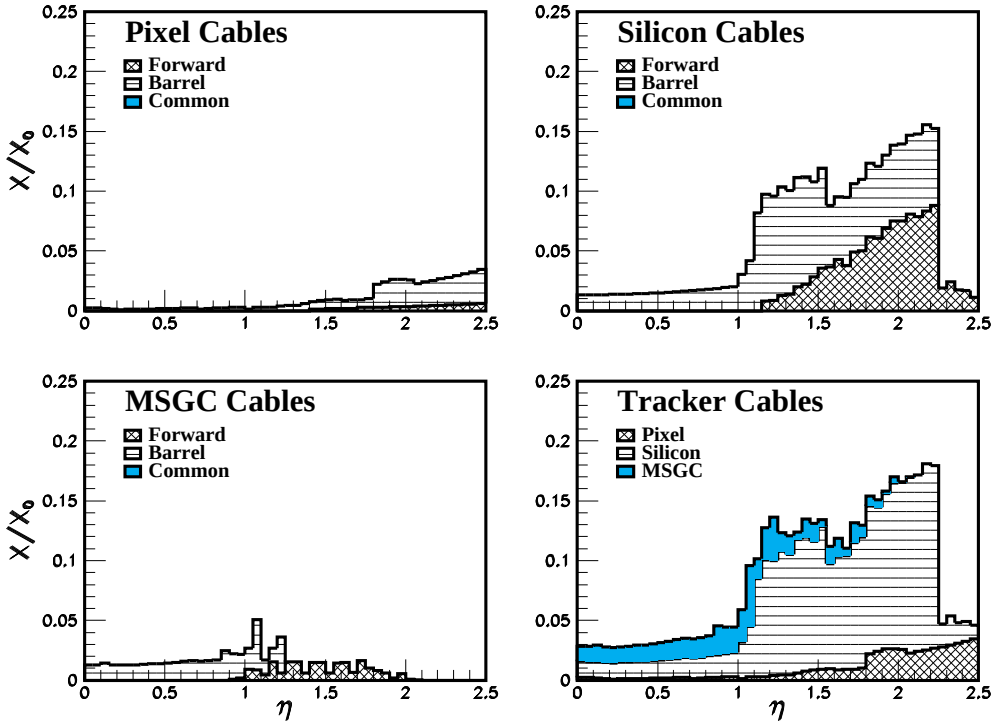

Fig. 7.21: Contribution of the CMS Tracker services to X/X_0. No cooling is included.

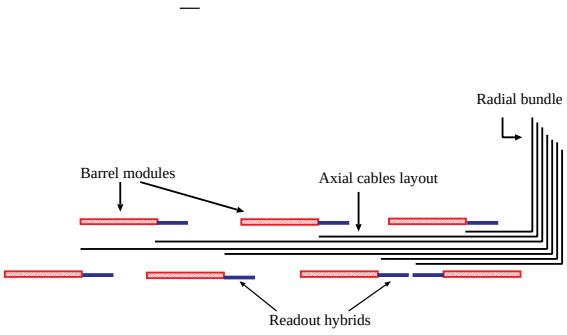

Fig. 7.22: Example of fan-out of cable distribution for barrel inner axial lines.

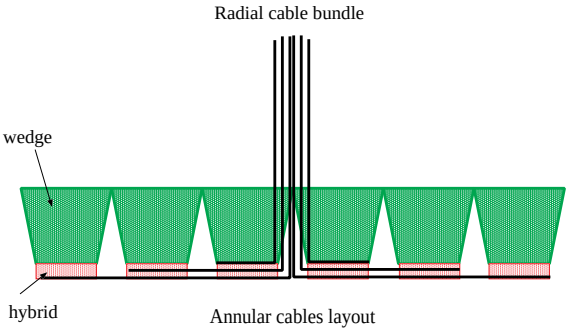

Fig. 7.23: Example of fan-out of cable distribution for endcap annular lines.

cooling to the Tracker material budget is shown in Fig. 7.24. The cooling material budgets are comparable for the Pixel and Silicon systems, whereas that of the MSGC is lower. The material distribution in the region $1.0 \leq \eta \leq 1.5$ of the Silicon system is dominated by the barrel and mini-endcap flanges. The shaded zone in the Silicon distribution represents the Tracker thermal screen detailed in Table 7.13; the screen, which allows the Silicon and Pixel detectors to run at an operating temperature different from that of the MSGCs is assigned here arbitrarily to the Silicon detectors. All outer axial pipes of the MSGC barrel and endcaps are beyond the Tracker sensitive volume and are therefore not included.

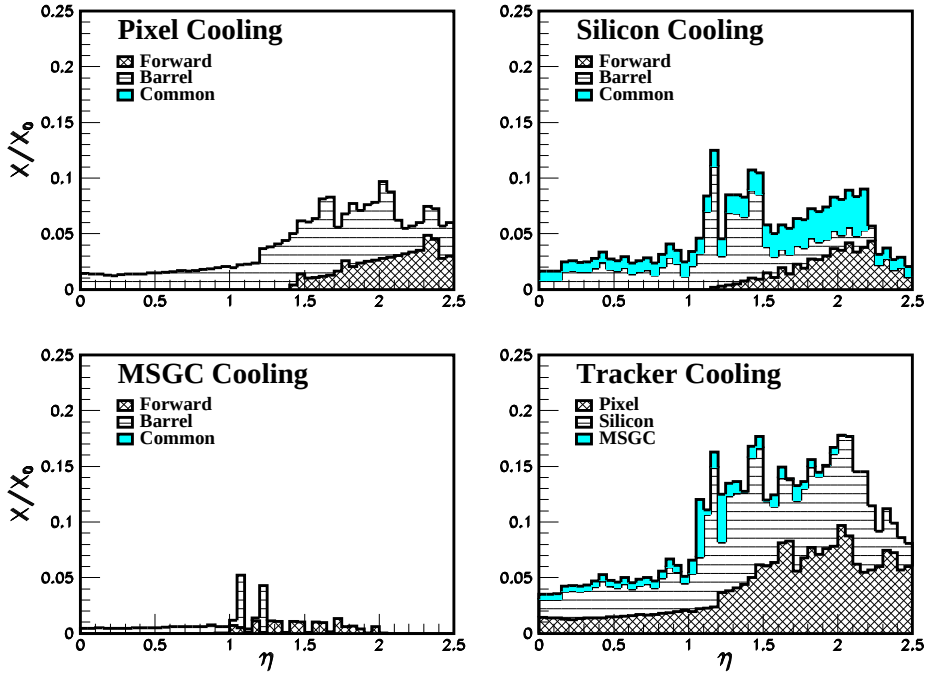

Fig. 7.24: Contribution of the CMS Tracker cooling system to X/X_0.

7.7.6 Total number of radiation lengths

The total amount of Tracker material in units of radiation length, obtained by adding up all contributions discussed in previous sections, is reported in Figs. 7.25 and 7.26. The information is broken down by sub-system or by functionality. A study of the distributions shows that the fractional radiation length in the active volume of the Tracker varies between 30% and 40% for $\mid \eta \mid \leq 1$ and grows up to a rather flat maximum of $\sim 75\%$ in the region $1.5 \leq \mid \eta \mid \leq 2.0$. At larger pseudorapidity, tracks do not cross the outer Tracker axial services any longer and hit the endcap detectors at more and more favourable angles. Figure 7.27 shows how the material is distributed locally within the Tracker as a function of r and z and as experienced by particles. The fractional radiation length in each bin of size $\Delta r \times \Delta z = 2.5 \times 6$ cm is calculated along the particle trajectory between the bin entry and exit points averaging over many trajectories crossing the bin in random position. Multiple scattering effects are rather large and a careful treatment of the covariance matrix is necessary to make good quality track measurements; the effect is illustrated in Fig 7.28 which shows the trajectories of p_T=10 GeV/c pions in the central and forward parts of the Tracker ($\eta = 2$). An initial broadening of the shower where it crosses the beam pipe and several sizeable particle deflections can be observed; the effect is more severe in the endcap region. Photon interactions with the detector are an effective measure of the impact of the material budget on the Tracker performance. A radiography of the Tracker is shown in Fig. 7.29; $H \rightarrow \gamma\gamma$ events were propagated through the detector and the coordinates of the conversion vertices were reported in the scatter plot. The conversion probability as a function of Tracker pseudorapidity is shown by the middle plot in Fig 7.29. The overall percentage of photons converting before leaving the Tracker sensitive volume amounts to 32% while the fraction of Higgs events where neither decay photon interacts with the Tracker material is 46.3%. A cumulative profile of the conversion probability as a function of the radius at which the reaction occurs is reported in the rightmost plot in Fig. 7.29; the rate is integrated over

η. About 60% of the conversions occur within the Pixel and Silicon systems; the effect of the material at the interface between Silicon and MSGC detectors is comparable to the contribution of the whole MSGC subdetector. Early conversions have a higher probability of being recognised and are the subject of Section 9.6.2.1.

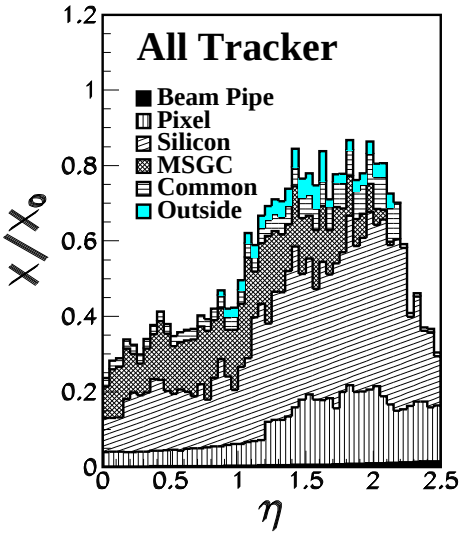

Fig. 7.25: Contribution of the CMS Tracker subsystems to X/X_0. The label 'Outside' refers to all materials installed beyond the active volume of the Tracker.

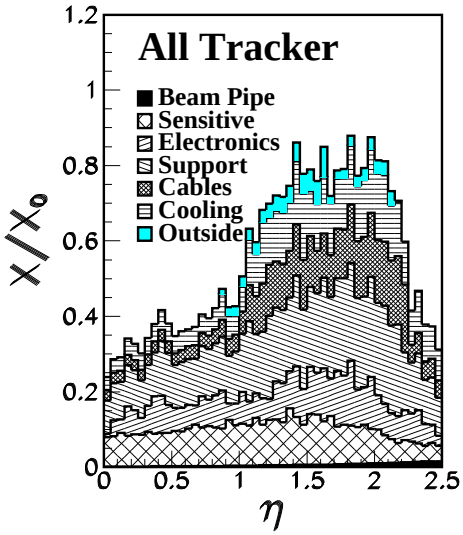

Fig. 7.26: Itemised fractions X/X_0 in the CMS Tracker. The label 'Outside' refers to all materials installed beyond the active volume of the Tracker.

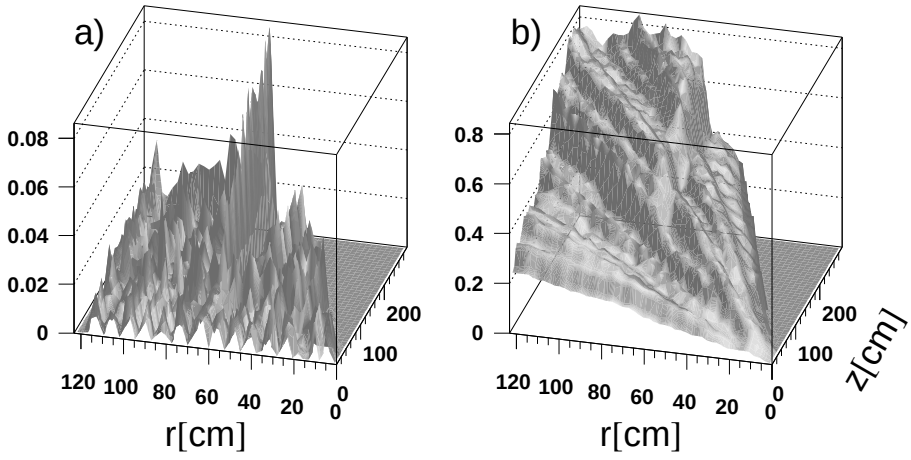

Fig. 7.27: a) Local concentration of material as experienced by particles with $|\eta| < 2.5$ in steps of $\Delta r = 2.5\,\text{cm}$ along the track path. b) Same as a) but cumulative along the track path.

7.7.7 Total number of interaction lengths

The total thickness of the Tracker in units of interaction length (λ_0), from the collision point to the Tracker outer boundary, is shown in Fig. 7.30. It is estimated by using geantinos and the geometry model described in previous sections. The fractional interaction length (λ/λ_0) is smaller than 15% in the region $|\eta| \leq 1$ and reaches at a plateau of approximately 30% for

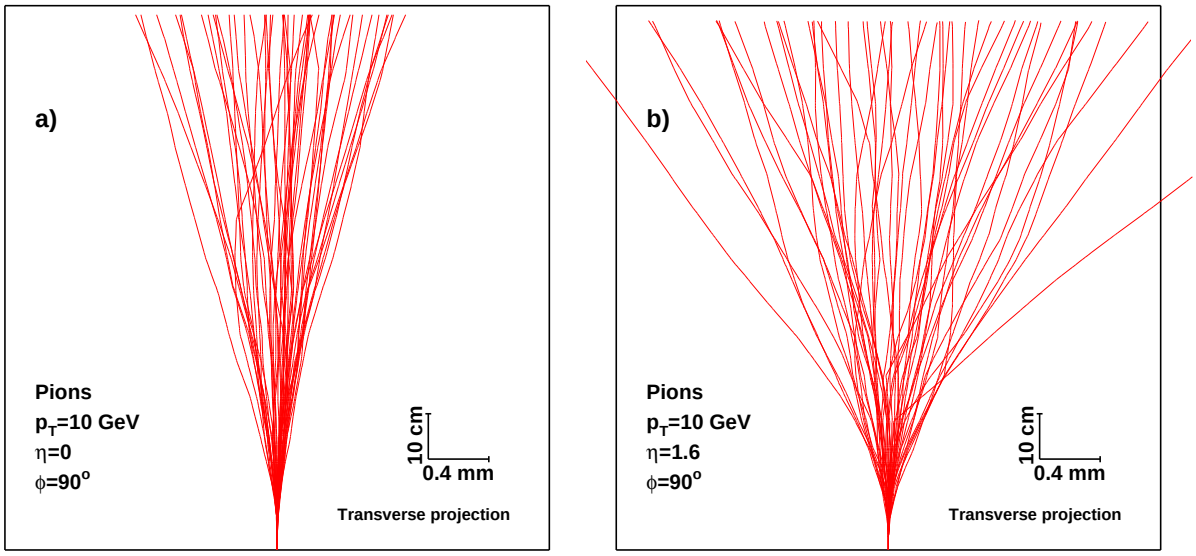

Fig. 7.28: a) Multiple scattering in the Tracker for $p_T = 10$ GeV/c pions in the central region with $\phi = 90°$ b) same as a) but with $\eta = 1.6$.

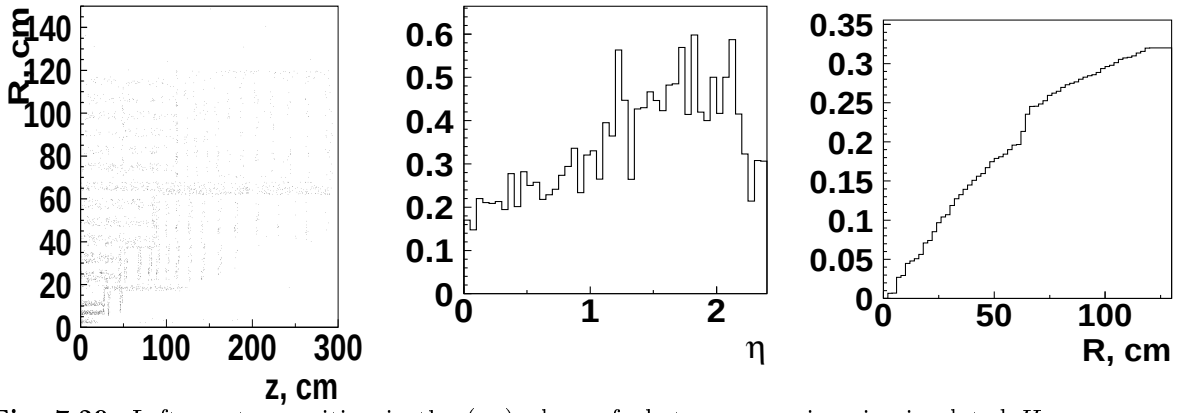

Fig. 7.29: Left: vertex position in the (r,z) plane of photon conversions in simulated $H \to \gamma\gamma$ events in the CMS Tracker. Middle: conversion probability as a function of pseudorapidity. Right: cumulative profile of the conversion probability as a function of Tracker radius.

$1 < |\eta| < 2$. At larger pseudorapidity, where tracks do not traverse the MSGCs, λ/λ_0 drops again below 15%.

A radiography of the Tracker material is obtained by displaying the position where 5 GeV/c transverse momentum pions undergo inelastic interactions, as they traverse the detector (Fig. 7.31 left). The interaction cross section is dominated by materials of sizeable atomic weight such as carbon fibre, silicon and aluminium, which are present in significant quantities in the Tracker. The interaction probability as a function of η is shown in the middle plot of Fig. 7.31; the average probability of tracks undergoing inelastic interactions in the Tracker is 14%. The right hand plot in Fig. 7.31 displays the cumulative contribution of individual subsystems to inelastic interactions, integrated over the whole η range. The material in the Silicon detectors dominates, whereas the MSGC and intermediate services contribute equally at the level of $\sim$ 3%. The reconstruction of short tracks resulting from early interactions is the subject of Section 9.4.2.

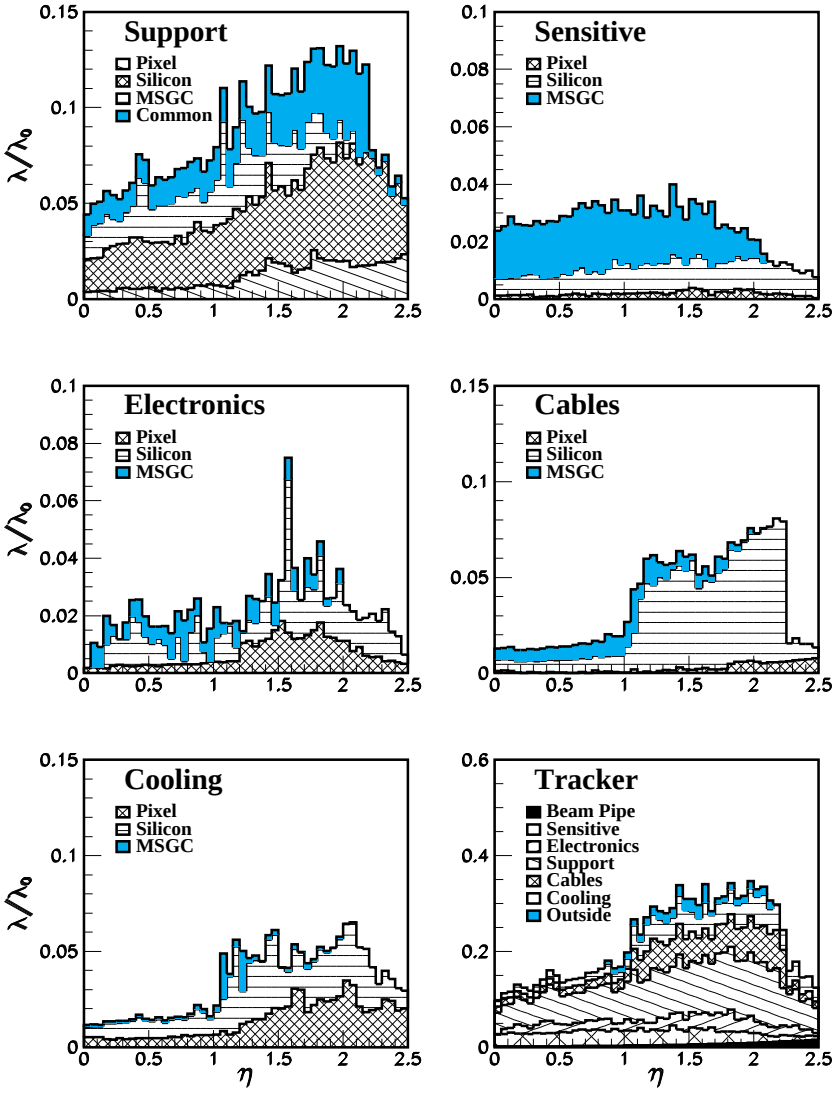

Fig. 7.30: Contributions of the Tracker by sub-system to the number of interaction lengths. The label 'Outside' refers to all materials installed beyond the active volume of the Tracker.

7.8 Pixel detector

7.8.1 Readout configuration

A single Pixel detector wafer is read out by 16 chips in the barrel, and between 2 and 10 chips in the endcaps. One readout chip reads an array of 52 × 53 pixels. The readout is column oriented and therefore the chip is divided into 26 double columns 2 × 53 pixels each. After a trigger, all pixels with collected charge above a preset threshold are read. Although the present design implements 150 μm × 150 μm pixels, several geometries have been simulated and the performance study reported in Chapter 9 is for 125 μm × 125 μm pixels. As shown in Fig. 7.32, the barrel hit resolution is largely insensitive to a change of pixel size from 125 μm to 150 μm and the results presented are not affected by this discrepancy.

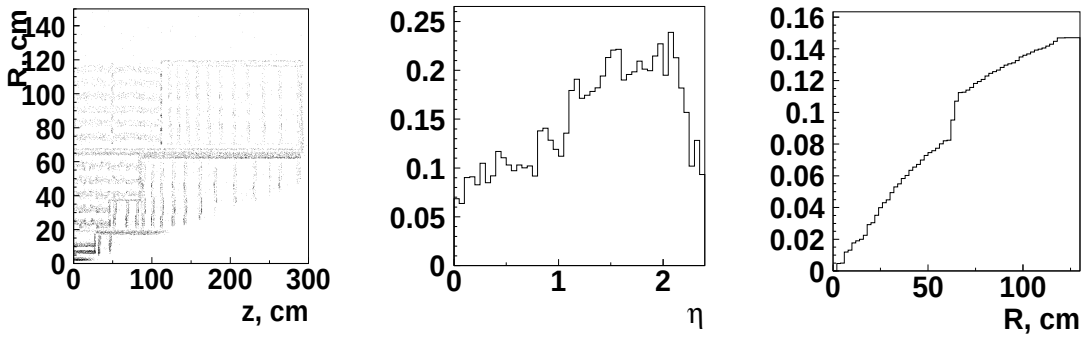

Fig. 7.31: Pion inelastic interactions in the Tracker. Left: interaction vertex position in the rz-plane. Middle: interaction probability as a function of pseudorapidity. Right: Cumulative profile of the interaction probability as a function of Tracker radius.

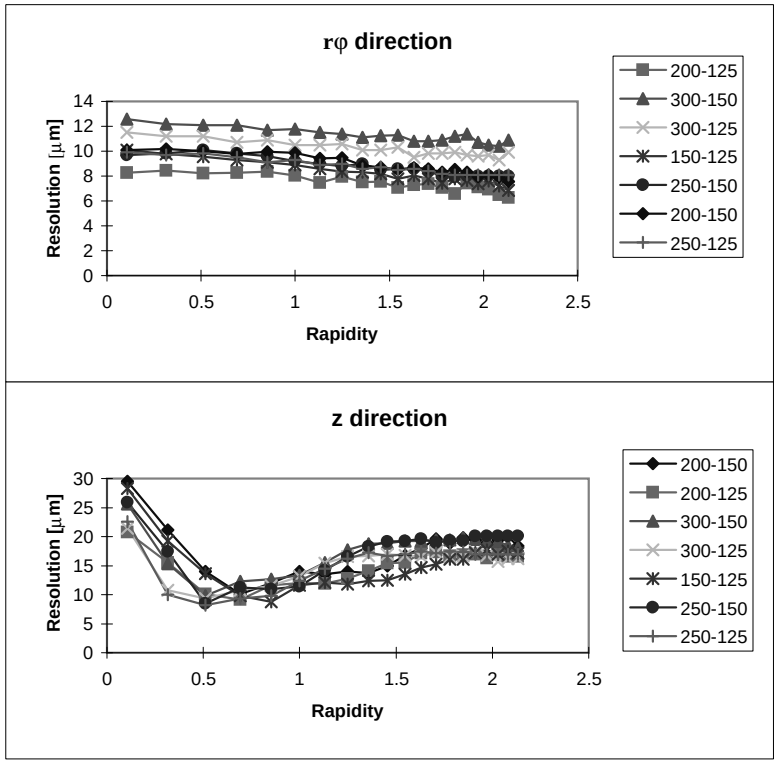

Fig. 7.32: Hit resolution in the ϕ (upper part) and z (lower part) directions. Different curves correspond to different detector geometrical configurations. In the legenda, the first column is the detector thickness in μm and the second the pixel size in μm (square pixels).

7.8.2 Simulation of signal and noise

The entrance and exit points in the pixel sensitive volumes together with the deposited energy are recorded during GEANT track propagation, providing input information for signal simulation. In order to get sufficiently precise hit positions the tolerance on the sensitive volume boundaries is set to 1 μm during propagation. The track path inside the sensor volume is divided into 10 μm long segments. Each segment is assigned a fraction of the energy according to the parametrised distribution discussed in [7-10]. The distribution takes into account Landau fluctuations in thin material layers.

The charge from each track segment is drifted to the detector surface and simultaneously diffused in the plane perpendicular to the electric field. The diffusion is assumed to be Gaussian

with mean value proportional to the square-root of the drift length; the diffusion constant is set at 7 μm for a 300 μm thick detector. The total charge distribution at the detector surface is calculated as the sum of the two-dimensional Gaussian distributions contributed by each segment. The effect of Lorentz shift in the 4 T magnetic field is included.

The resulting two dimensional charge distribution is mapped onto the pixel geometry and the fraction of charge collected by each pixel is determined. A list of hit pixels for all contributing tracks is formed. If a single pixel is hit by more than one track, the charge contributions are added linearly. The pedestal in each pixel is modelled by a Gaussian distribution for the number of electrons with zero mean and $\sigma = 270$.

7.8.3 Digitisation and cluster reconstruction

To digitise the signal collected in each pixel, the charge is multiplied by a gain factor and converted into an integer number simulating ADC digitization. Signals which exceed the ADC range are assigned a saturation value which depends on the ADC range. Both the gain and the number of ADC bits (typically 6) can be adjusted. Pixel zero suppression is simulated by comparing the digitised signal to a threshold in each channel (see Fig. 7.33). The threshold is defined in units of noise and is typically set at 4σ (1080 electrons); this is the lowest value for which the number of noisy pixels remains reasonably small (on average two noisy pixels per single detector module).

Pixels above threshold are analysed by a cluster finding algorithm. A cluster is defined as any set of adjacent pixels above threshold; pixels adjoining just at a corner are considered adjacent. For each cluster, its width in two dimensions and its total charge are estimated. The cluster charge is compared with a threshold which is defined in units of noise and is typically set at 8σ (2160 electrons). The position of selected clusters is estimated independently in both dimensions using an analog average of the charge recorded in each selected pixel.

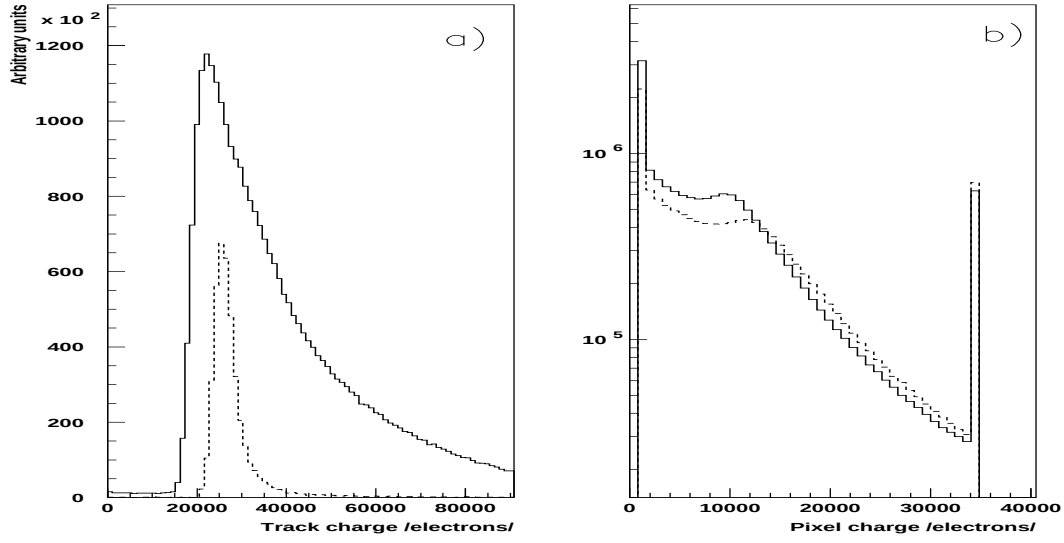

Fig. 7.33: a) Simulated charge distribution deposited by minimum-bias tracks (solid line) in a 250 μm thick Pixel barrel detector at a radius of 7 cm. For comparison, charge from 100 GeV muon tracks at normal incidence is also shown (dashed line). b) Simulated charge distribution seen by a single barrel pixel 125 μm (solid line) and 150 μm (dashed line) large. The peak close to 35000 electrons corresponds to signal saturation and the rise at 1000 electrons is due to noise.

Figure 7.33 shows the simulated charge distribution for minimum-bias events and for single muon tracks (100 GeV). Part a) of the figure shows the total charge deposited in the Pixel barrel by minimum bias (solid line) and muon (dashed) tracks; 18000 electrons correspond to a single

mip signal. Part b) shows the signal seen by a single barrel pixel for 125 μm and for 150 μm pixels. The average signal is about 12000 electrons, which corresponds to the S/N ratio of 40:1 assumed in this simulation.

Figure 2.14 in section 2.4.2 shows the average cluster size in the barrel layer set at 7 cm as a function of rapidity for single muon tracks (100 GeV). The pixel cluster size in $r\phi$ is determined by the Lorentz shift and is about 2 in the whole rapidity range. The cluster size in the z coordinate is determined mostly by the track impact angle and varies with rapidity from 1 to 6.

7.8.4 Spatial resolution and efficiency

The hit resolution depends on several factors: pixel size, detector thickness, magnetic field, track incident angle, noise level, pixel threshold and clustering algorithm.

The pixel charge distribution extends to zero (see Fig. 7.33). This means that any finite threshold clears some pixels, making the analog interpolation slightly less accurate; the dependence on the threshold is weak and by setting thresholds two times larger only a few μm are lost in the position resolution (see Fig. 2.16 in section 2.4.2). In the pixel barrel the amount of charge sharing depends on the pixel size and thickness. The optimum resolution is achieved when roughly 1/3 of the clusters have a size of 1 pixel and the remaining 2/3 have 2 pixels. Figure 7.32 shows the resolution in $r\phi$ and z directions as a function of rapidity, for a number of width/thickness combinations. This simulation includes noise (270 electrons) and the default value of pixel threshold (1080 electrons). A six bit ADC has been implemented in the simulation. The hit resolution in the end-cap pixels, assuming that the pixel size is the same as used in the barrel, is shown as a function of pseudorapidity in Fig. 7.34.

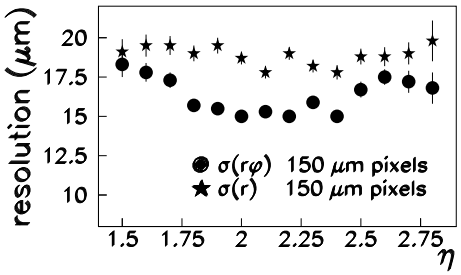

Fig. 7.34: Endcap hit resolution in the $r\phi$ and r directions.

The hit efficiency in the pixel detector is largely independent of the pseudorapidity and is affected mainly by a 2.5% inefficiency of geometrical coverage. However, the efficiency has a stronger dependence on threshold. As shown in Fig. 7.35 the number of pixels per track declines steadily with threshold whereas the cluster finding efficiency is close to one up to a threshold of 10000 electrons. This should be compared with the expected noise of 270 electrons. Therefore, even in the presence of large noise, one can maintain an efficient cluster reconstruction, at a price of some degradation of hit resolution.

7.8.5 Comparison with test beam measurements

The pixel simulation software described above was used to reproduce test beam data (see [7-11]). The measurement consisted of a 8×32 pixel array placed in a magnetic field (0-3 T). The pixels were 125×125 μm^2 wide and 300 μm thick. The pixel hits were generated by the 225 GeV/c SPS negative pion beam. The magnetic field and the detector tilt angle with respect to the beam were varied.

In Fig. 7.36, the simulated cluster sizes (lines) are shown to agree well with the data (points), for three values of the magnetic field and as a function of the tilt angle.

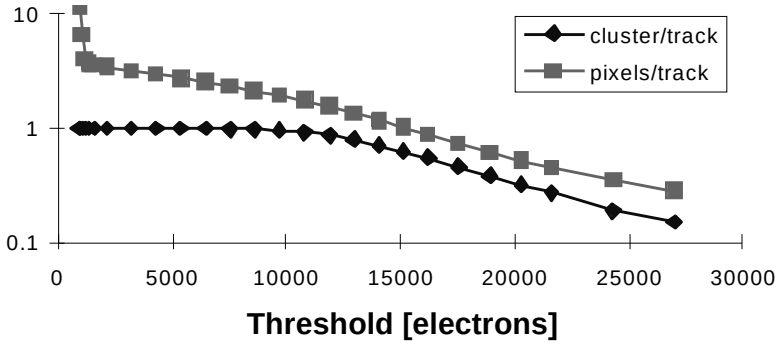

Fig. 7.35: The number of pixels per track (squares) and the number of reconstructed clusters per track plotted versus pixel threshold. The pixel barrel layer at 7 cm is shown and the pixel size is 150 μm. The simulated tracks are from minimum-bias events.

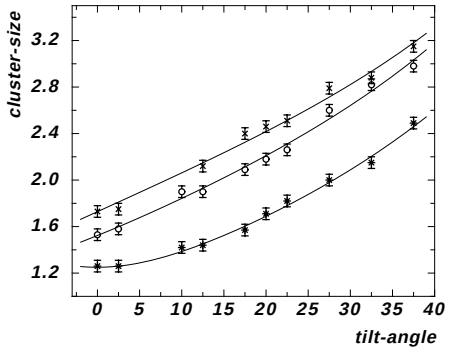

Fig. 7.36: Pixel cluster size vs. tilt angle for B-fields 0 T (*), 2 T ($\circ$) and 3 T (x).

7.9 Si-strip Detector

7.9.1 Readout configuration

The simulated $r\phi$ readout pitch in the barrel sensors is 62.5 μm at the innermost layer, 83.3 μm in the second and third layer and 125 μm in the two outermost layers. In twin detectors, stereo strips are at an angle of 100 mrad with respect to the beam line. In order to avoid dead regions at the corners of the sensor, stereo strips which do not reach the readout hybrid are joined by double-metal connections and read out as a single channel (see Fig. 3.12). The stereo sensors in the first two layers have readout pitch 125 μm whereas the outermost stereo detectors have 250 μm pitch.

In the endcaps, the ϕ strips are laid in the radial direction; the readout pitch is 70 μm, 67.6 μm, 104 μm and 102 μm respectively in the four rings set at increasing radii. The stereo strips are tangent to a circumference centred on the beam-line (see Fig. 3.4); the innermost sensors are read out with a pitch of 101.4 μm, the outermost with a pitch of 203.5 μm. The last station on each end is equipped with 2 rings of which the innermost has a stereo pitch of 208 μm. The mini-endcaps have an identical readout configuration, except for the outermost ring of sensors that has twin detectors with a stereo pitch of 105 μm.

7.9.2 Simulation of signal and noise

The entry and exit points, as well as the energy deposited in the silicon (E_{ion}) by the incident particle, are given by the GEANT package during track propagation in CMSIM (HITS).

Inside the silicon wafer, the track path is subdivided into N_{seg} segments (currently 40) and a fraction of the deposited energy $E_{seg} = E_{ion}/N_{seg}$ is assigned to each. Presently, no Landau fluctuations are applied to E_{seg} : only the total energy E_{ion} fluctuates. However, good agreement between simulation and test beam data is observed suggesting that the effect of Landau fluctuations on the segments is small. The cluster charge distribution recorded with a silicon detector exposed to a 300 GeV/c muon beam is compared to the simulation in Fig 7.37.

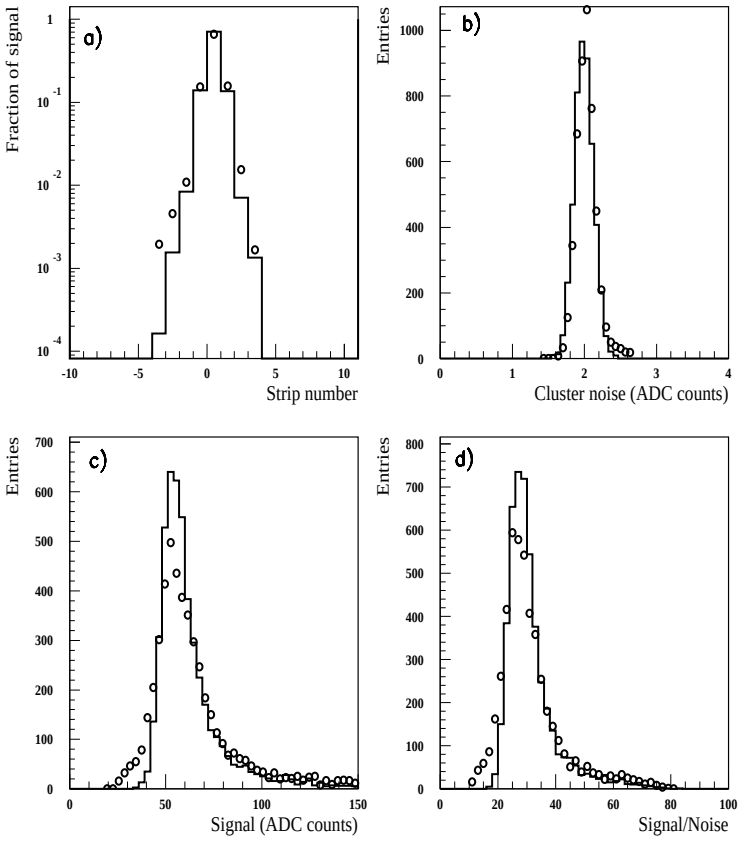

Fig. 7.37: Comparison between Monte Carlo (full line) and data (dots): a) cluster width, b) cluster noise, c) cluster charge, d) signal to noise ratio

For each segment a cluster of hole-electron pairs is created using a calibration factor of $2.77 \cdot 10^2$ pairs/keV: in a 300 μm thick silicon layer about $3 \cdot 10^4$ pairs are produced by a minimum ionizing particle (mip) at normal incidence. For each hole-electron cluster, the drift time and diffusion range are calculated and the deviation of the drift direction due to the magnetic field is taken into account. The fraction of charge Q_i collected by each strip within 3σ of the diffusion cloud is calculated. To take into account the inter-strip capacitive coupling the charge is evaluated by the formula:

$$Q_i^{'} = \sum_{j=0}^{7} C_j \cdot (Q_{i-j} + Q_{i+j})$$

where $Q_i^{'}$ is the charge collected on the read-out strips and C_i are the capacitive coupling coefficients.

The noise on silicon strip detectors consists of two sources: parallel noise introduced by the sensor and serial noise which is generated by the amplifier. For each fired strip and for the four neighbouring strips a serial noise α_i and a parallel noise α_{par} are generated according to Gaussian statistics. The noise is then added to the charge $Q_i^{'}$. Correlation between the serial

noise of fired strip and the serial noise of the closest four neighbouring strips is also taken into account. An example of the agreement obtained is shown in Fig. 7.37 where data from tracks at normal incidence on a p-type 50 μm pitch module are compared to simulation. Cluster size (Fig. 7.37a), noise level (Fig. 7.37b), cluster charge distribution (Fig. 7.37c) and signal to noise ratio (Fig. 7.37d) are well reproduced by the simulation. Two important effects, present in the CMS environment but not in beam tests, are modelled in CMSIM to introduce realistic degradation in the simulated samples.

The final signal in CMS will be processed by a deconvolution chip (see Section 3.5). Deconvolution introduces additional noise which the simulation takes into account by multiplying the serial and parallel noise by a factor ≈1.45 and ≈0.45 respectively. Moreover, as discussed in 3.4.6, the signal to noise ratio is expected to degrade by 20% due to radiation damage, at a chosen value of the bias voltage; the simulated noise level was increased to take this effect into account.

A charge collection efficiency of ≈90% and an average noise of ≈2000 electrons are expected for the CMS silicon sensors; these estimates are derived from test beam measurements and from studies of the front-end electronics (see Section 3.5 and Figs. 3.64, 3.66 and 3.65). By taking into account all estimates reported in this section, a signal to noise ratio of ≈12–14 is obtained for tracks at normal incidence. The signal to noise ratio is defined here as the ratio of the most probable cluster charge to the noise of one strip.

Due to radiation damage deterioration, the signal to noise ratio implemented in CMSIM ranges between 10 and 12, depending on the detector pitch, for tracks at normal incidence. In Fig. 7.38 the signal to noise ratio is shown as a function of the track incidence angle for a sensor housed in the third barrel layer (83.3 μm readout pitch).

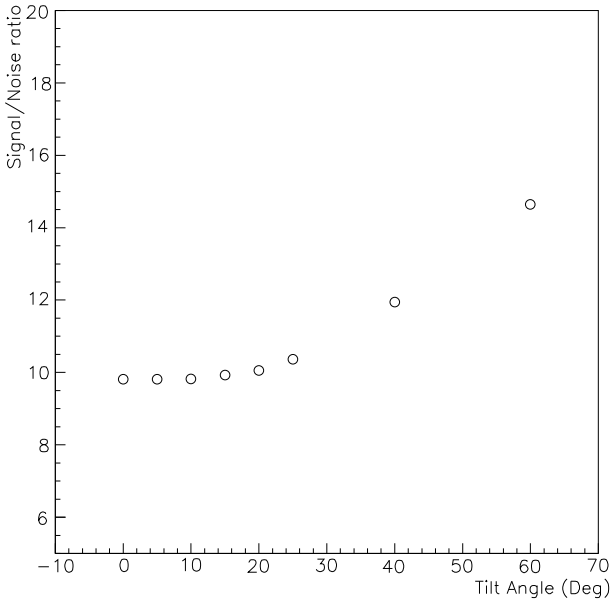

Fig. 7.38: Simulated signal to noise ratio in silicon as a function of the track incident angle

7.9.3 Digitisation and cluster reconstruction

The cluster reconstruction algorithm looks for contiguous strips with charge significance satisfying $S^{(i)}/\bar{N} > 3$, where $\bar{N}$ is the average strip noise (≈ 2000 electrons). Once at least one such strip is found, all adjacent strips with $S^{(j)}/\bar{N} > 2$ are added to the cluster. When no more adjacent strips above threshold are found, the cluster charge $S^{cluster}$ is computed as the sum

of the pulse heights over the accepted strips. If the condition $S^{cluster}/\bar{N} > 5$ is satisfied, the cluster is retained. The same algorithm is applied to barrel and forward detectors.

The cluster finder computes the hit coordinate as the mean of the position of all strips assigned to the cluster, weighted by their pulse heights. For double sided (twin) detectors the stereo coordinates are calculated as well as their covariance term with the precise coordinate [7-12]. This algorithm is a good estimator of the hit position when the charge released on each strip behaves linearly as a function of the hit position within the pitch.

Deviations from the linear approximation have been studied both in test beam data and Monte Carlo by a response function defined as $\eta = Q_1/(Q_1 + Q_2)$, where Q_1 and Q_2 are the charge collected on the two most significant strips, numbered in increasing order; in the case of single strip clusters, the adjacent strip with larger read-out is considered. In Fig. 7.39(a) a typical η distribution for p-type silicon is shown well reproduced by Monte Carlo simulation.

From Figs. 7.39(b), 7.39(c), where clusters are divided into single-strip and multi-strip clusters, it is apparent that in the central region, dominated by the multi-strip clusters, the charge is linearly shared among the strips. However, a majority of clusters populate the non linear η region and more refined cluster finding algorithms can improve the detector resolution performance.

The simulated η distribution is in good agreement with data and gives a strong indication that the basic mechanisms of the silicon response are well reproduced.

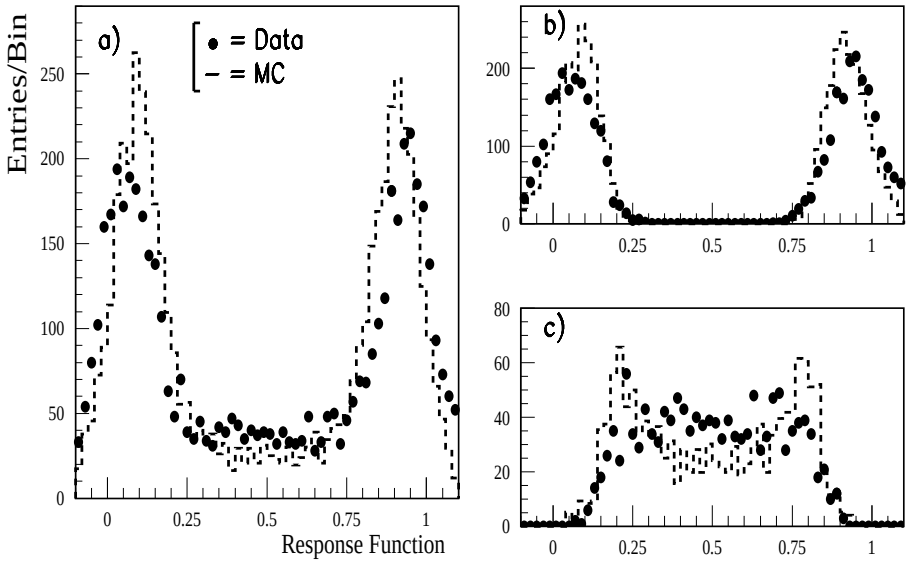

Fig. 7.39: a) Response function with Monte Carlo simulation superimposed; b) and c) same as a) for single and multi-strip clusters, respectively

7.9.4 Spatial resolution and efficiency

Several factors contribute to the spatial resolution: detector pitch, Lorentz angle, signal/noise ratio, direction of the track and the clustering algorithm. The silicon spatial resolution has been measured in several beam tests and for different readout configurations.

The residual distribution measured with a 50 μm pitch p-type detector is shown in Fig. 7.40(e). For each track crossing the detector, the distance between the reconstructed hit and the interpolated track position is reported; tracks were measured by an external telescope.

The intrinsic resolution is then estimated by subtracting in quadrature the tracking error (Fig. 7.40c, 7.40d) from the σ of the residual distribution. Typical resolution values are 12 μm for a 50 μm pitch p-type silicon sensor, 34 μm for a 100 μm pitch p-type stereo detector and $\approx$ 35 μm for a 200 μm n-side silicon detector with a floating intermediate strip.

In general, good agreement between Monte Carlo and data is found, as shown in Fig. 7.40(e) and 7.40(f), where the residual distribution is plotted for a 50 μm pitch sensor and for the stereo side of a double-metal, double-sided sensor (200 μm pitch).

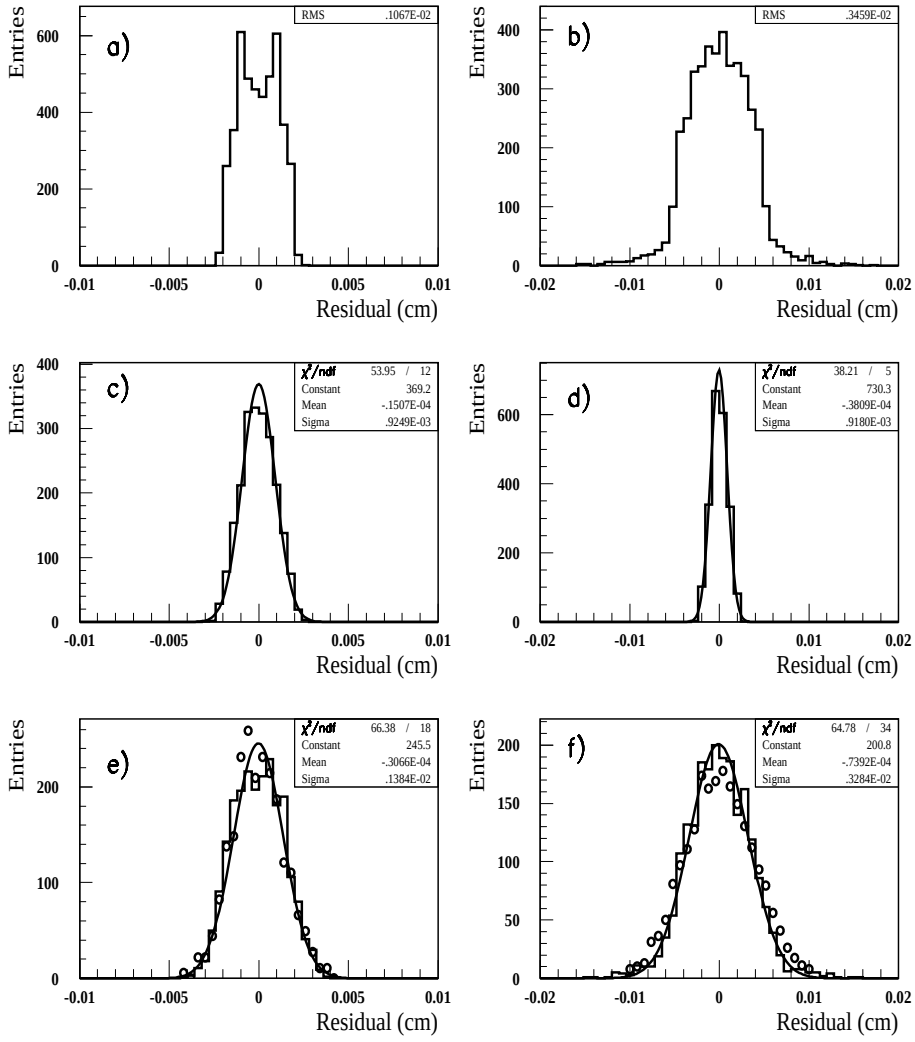

Fig. 7.40: Plots on the first column refer to a 50μm pitch detector while those on the second column refer to a stereo 200 μm pitch sensor: a) and b) Simulated intrinsic resolution; c) and d) Error on track extrapolation point due to multiple-scattering as evaluated by the Monte Carlo; e) and f) Comparison between Monte Carlo (histogram and fit) and data (dots) residual distribution for the two sensors.

The simulated intrinsic spatial resolution for a sensor with a pitch of 81 μm is shown in Fig. 7.41a as a function of the track incidence angle. The best resolution is obtained for an angle of $\approx 15^\circ$ when the two-strip clusters dominate and the charge sharing is linear. The magnetic field introduces a systematic deviation of the charge drift direction inside the silicon sensors (Lorentz-angle).This effect can be seen in Fig. 7.41(b). The tilt angle of 9° implemented in the barrel layout compensates almost completely for the Lorentz shift of the drift direction.

In the simulation, the hit efficiency is defined as the ratio between the number of reconstructed clusters and the number of hits produced by GEANT in the sensor. The silicon sensors efficiency is always ≈99% as confirmed by test beam measurements (see Section 3.4.6). To simulate disconnected or dead strips a random inefficiency of 1% has been introduced.

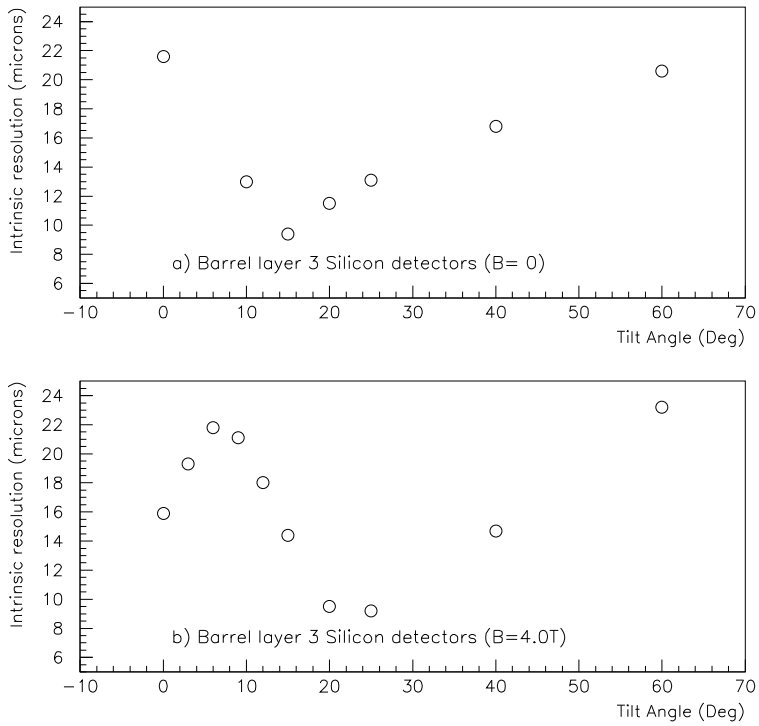

Fig. 7.41: a) Intrinsic hit resolution as a function of the incident angle (no magnetic field); b) same as a) but with a 4 T magnetic field in CMS

7.10 MSGC detector

7.10.1 Readout configuration

The simulated strip layout in the MSGC barrel includes strips parallel to the beam line in detectors measuring the $r\phi$ coordinate with a readout pitch of 200 μm. Twin detectors have strips at a stereo angle of 50 mrad with respect to the $r\phi$ strips and a pitch of 400 μm. In the simulated geometry, twin stereo and $r\phi$ detectors are fully overlapped with each other and the stereo strips are laid at an angle with respect to the twin chamber edge. Due to this configuration, not all strips reach the hybrid and $\sim 5\%$ of the active detector surface is read out as a single channel. This layout differs from the description reported in Section 4.4.1; nevertheless, in terms of performance, it reproduces effectively the hardware description.

In the endcap region, MSGCs implement a radial strip geometry for $r\phi$ strips, with a readout pitch of 200, 204, 208 and 217 μm for the 4 rings set at increasing radii. Twin detectors have a typical pitch of 400 μm; all detector strips are tangent to a circumference centred on the beam line. The central strip of each stereo chamber is set at an angle of 50 mrad with respect to the median of the $r\phi$ back-to-back wedge. Due to the slanted wedge shape of the stereo detectors (Section 7.5) the first and last strips are parallel to the detector sides and all strips reach the readout hybrid.

7.10.2 Simulation of signal and noise

The simulation of the signal in MSGC detectors uses GEANT track propagation to define the entrance and exit points of each particle crossing the sensitive volume. The information is transmitted to a package simulating primary and secondary ionisation, diffusion, drift and avalanche multiplication in a gas mixture Ne (30%)-DME (70%) [7-13, 7-14]. During extrapolation through the gas gap, the generation of δ-rays by GEANT is inhibited to avoid double-counting, whereas

all other physics processes are accounted for by GEANT itself. The correct hand-shaking between GEANT and the specific package is illustrated in Fig. 7.45 by a comparison to data, showing that the Landau statistics of the cluster charge distribution are well reproduced by Monte Carlo.

The MSGC simulation model generates ionisation clusters from primary and secondary electrons along the track path. The distance between the path and clusters is characterised by an 'effective range' R dependent on the energy E of the parent primary electron (δ-ray) as

$$R = \frac{C}{\rho} E^{1.72}$$

where C is a constant dependent on units and ρ is the gas density. The δ-ray energy is approximated by wk, w being the average energy spent by a minimum ionising particle (mip) for the creation of an ion-electron pair and k the size of the cluster.

The cluster size, i.e. the actual number of electrons in a cluster, is generated as [7-21]

$$S(k) = \frac{a}{k^{\delta}} \qquad 1 \leq k \leq 600$$

a being chosen such that $\sum_1^{600} S(k) = 1$. The parameter δ is gas dependent and a choice among 8 of the most used gases is possible, as well as a mixture of any among them.

The distance x between clusters along the track is governed by an exponential law $P(x) = \exp(-x/d)$, d representing the mean path length between ionising collisions. The values of δ and d are derived by imposing the estimates of the average number of clusters n_p and of the total primary and secondary ionisation n_t, available in the literature for pure gases [7-17]. The total number of electrons from primary and secondary ionisation in a gas gap of 3 mm filled by Ne (70%)-DME (30%) is shown in Fig. 7.42.[1]

Each electron then drifts towards the anodes, with a drift velocity set at $v_d \approx 5$ cm/μs and a lateral diffusion coefficient D which is gas dependent [7-18]. No longitudinal diffusion is introduced, as this would scarcely affect the signal shape in the case of MSGC's. All of the gas dependent parameters n_p, n_t, w, D are scaled consistently in the case of gas mixtures.

The effect of a solenoidal magnetic field is accounted for by a deviation of the drift direction with respect to the electric field, described by the Lorentz angle. Measurements of this quantity were carried out for several gas mixtures; combining data and theoretical calculations the deviation for the Ne (30%)-DME (70%) mixture is estimated to be 3.5°/T.

As an electron reaches the end of the drift region, the cell where it arrives is found and a charge signal is added to the corresponding channel, proportional to the size n of the avalanche triggered by the electron. The size is extracted from a Polya distribution

$$P(n) = \frac{4n}{g^2} e^{-\frac{2n}{g}}$$

with RMS $g/\sqrt{2}$ and average gain $g = 2500$, shown in Fig. 7.43, [7-15, 7-16, 7-20].

The simulation procedure just described is tuned to reproduce the chamber response for minimum ionising particles, which have been extensively measured and investigated in beam tests (see for example 4.3.4 and references therein). The dependence of the energy loss on the particle momentum is introduced by an approximate Bethe-Bloch correction function expressed by (Fig. 7.44):

$$\frac{dE/dx_{\text{track}}}{dE/dx_{\text{mip}}} = \left\{ a \left[1 + \left(\frac{m}{p} \right)^2 \right] \left[b - \log \left(\frac{m}{p} \right)^2 \right] - c \right\} \frac{q^2}{d}$$

[1] However δ is presently set at a fixed value of 2.2 to yield the more solid estimate of n_t measured in laboratory tests for the gas mixture of choice, Ne (30%)-DME (70%) [7-19]; only d is a free parameter to be tuned to the correct n_p.

$$a = 0.042 \ ; \ b = 15.0 \ ; \ c = 0.1 \ ; \ d = 0.7 \ ; \ q = \text{charge } (e)$$

A comparison between data and Monte Carlo (Fig. 7.45) shows the correct scaling behaviour for a 3 GeV/c pion at normal incidence, whose energy loss is corrected to be about 10% larger than that of a mip.

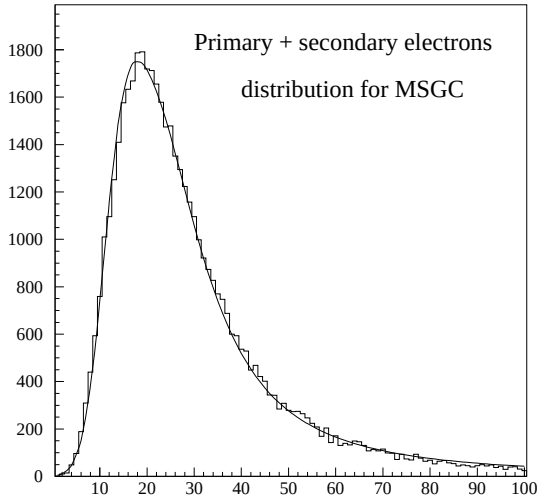

Fig. 7.42: Number of primary and secondary e^- produced by a mip at normal incidence on an MSGC. The gas mixture is 30% Ne-70% DME.

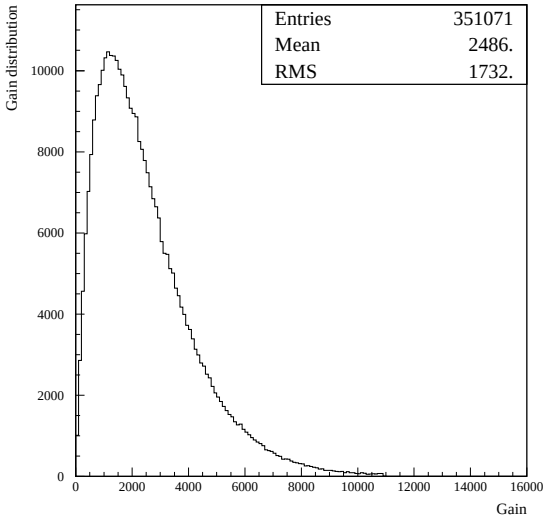

Fig. 7.43: Simulated Polya gain distribution with mean value set at 2500.

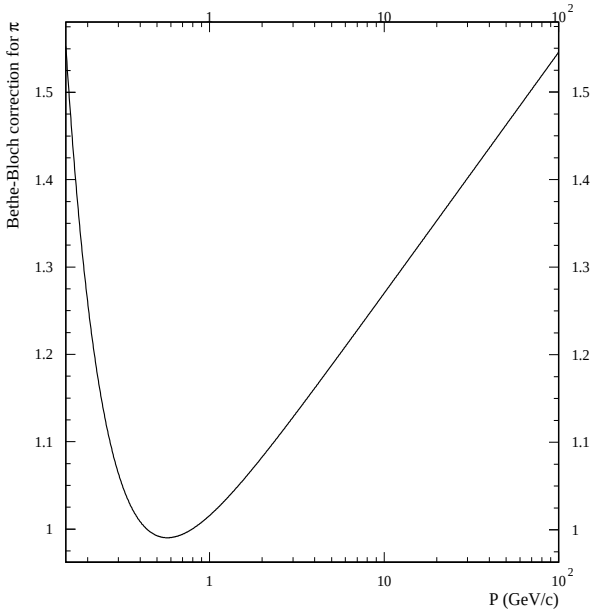

Fig. 7.44: Bethe-Bloch correction function used in MSGC simulation. The energy deposited in the gas gap by a pion, relative to its minimum value, is shown as a function of pion momentum.

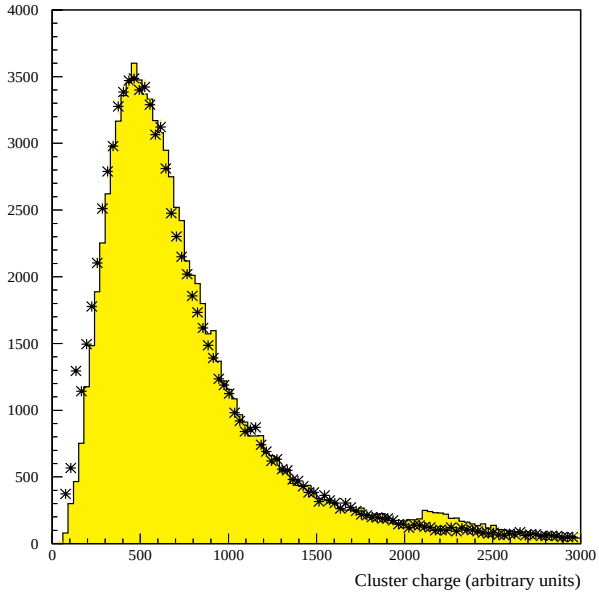

Fig. 7.45: Simulated cluster charge for 3 GeV/c pion at normal incidence, compared to the data collected at the T10 beam test [4-10].

Cross-talk effects due to high voltage filters (Section 4.3.2.7) are simulated, removing 3% of the charge from every strip collecting signal and adding a negative pedestal of equal magnitude to all strips in the same high voltage group.

Strip pedestals are simulated by a Gaussian distribution with a mean of zero and $\sigma = 1400$ electrons for 12.5 cm long strips, as estimated in Table 5.6.

Signal charge, cross-talk effects and pedestal values are summed up during the input to the digitisation phase.

7.10.3 Digitisation and cluster reconstruction

A hardware simulation of the front-end electronics was carried out, assuming a shaping time of 50 ns and using double correlated sampling as the algorithm used to tag the bunch crossing (Section 5.3.4); preliminary results indicate a global charge deficit of $\sim 50\%$.

The front-end electronics is not simulated in detail in CMSIM; the signal on each strip is attributed a reduction factor of 0.54, due to the combined effect of ballistic deficit and deconvolution, and in good agreement with the detailed study.

The charge attributed to each strip is analysed by a cluster finding algorithm that singles out strips exceeding their noise by a factor of 1.8. Adjacent strips with significant charge are grouped in candidate clusters. Candidates are then required to contain at least one strip with a significance of 3.5 σ. Single strip clusters are subjected to the same cuts. The choice not to accept strips below threshold within a cluster is motivated by the requirement to preserve two-track resolution; as an obvious implication, clusters can split into two or more reconstructed hits, depending on the angle of incidence of the tracks. The effect can be observed in Figs. 7.46 and 7.47 showing the size of clusters generated by a stiff track crossing a chamber and their multiplicity as a function of incident angle.

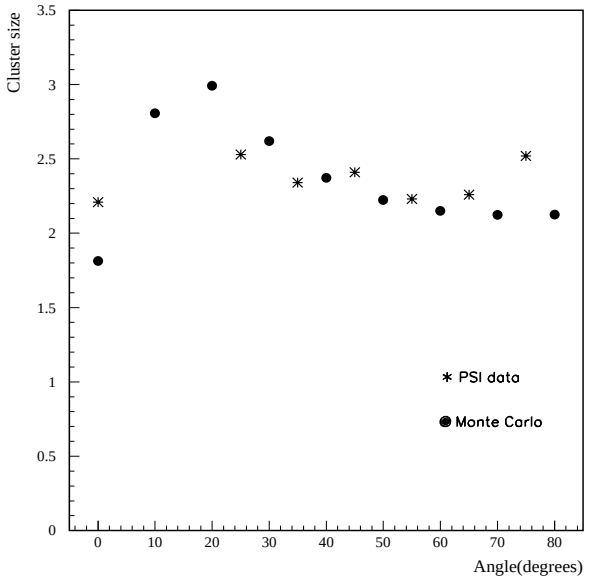

Fig. 7.46: Cluster size in MSGC detectors as a function of incidence angle of a stiff track.

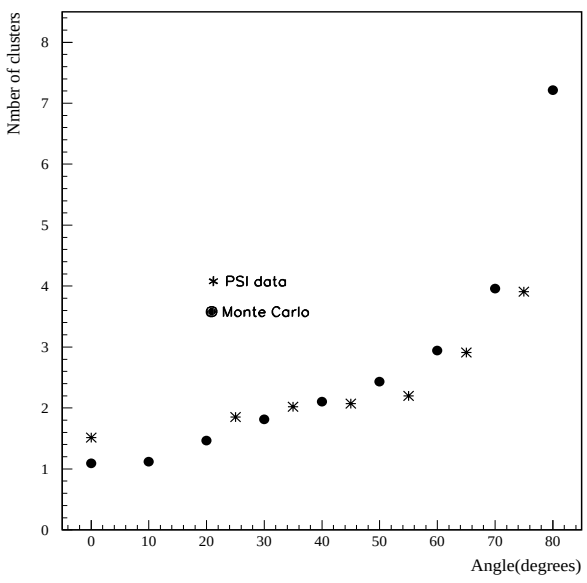

Fig. 7.47: Cluster multiplicity in MSGCs as a function of incident angle of a stiff track.

The cluster size grows up to $\sim 15°$; at larger angles the onset of cluster splitting is visible as an increase of cluster multiplicity as the cluster size gets smaller. A comparison to data recorded at a Paul Scherrer Institute beam facility (Section 4.3.3.4) shows excellent agreement between data and simulation up to very large incident angle.

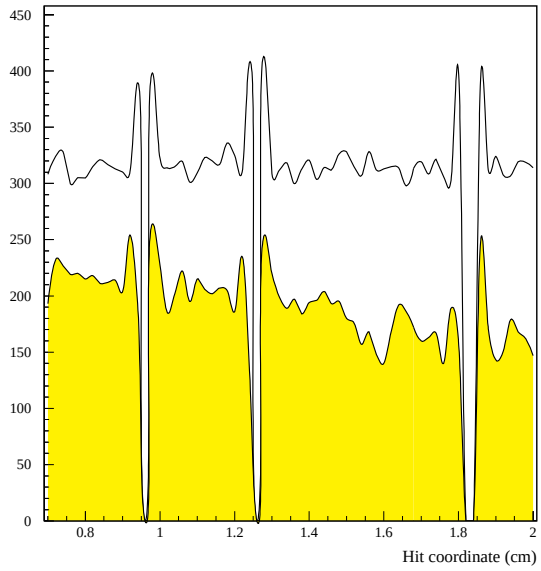

Fig. 7.48: Blow-up of a beam profile recorded by an MSGC at the T10 beam facility. Disconnected strips are visible as empty bins (shaded histogram). Simulated MSGC response is overlaid.

As an estimator of the hit position, the charge barycentre of all strips attributed to the cluster is used.[2] A random inefficiency of 2% per detector is introduced to simulate disconnected or 'dead'strips. Even though the anode-cathode electric field is not modelled, the simulation reproduces rather well the data. An example is illustrated in Fig. 7.48 comparing a simulated beam profile with data collected at the T10 (shaded histogram) facility at CERN [4-10]; the abscissa is the reconstructed hit position as estimated by the cluster finder just discussed. The neighbours of a disconnected strip show an enhancement due to the shift of the charge barycentre off the dead strip. The effect on the hit position resolution is proportional to the undetected fraction of charge. Consistently with other sections, the signal-to-noise ratio (S/N) is defined by the ratio of the most probable value of the cluster charge to the noise of one strip. The choice of basic simulation parameters discussed in this section yields

$$\frac{S}{N} = \frac{N_e \times \text{Gain} \times \text{Deficit}}{\text{Noise}} \simeq 20 \, .$$

The behaviour of S/N as a function of track incident angle is shown in Fig. 7.49; the incident angle as a function of track p_T is shown in Fig. 7.50 for the MSGC barrel geometry, taking into account the 4 T magnetic field; the chamber response at large angle is relevant to the detection of tracks of $\sim$ 1 GeV/c p_T hitting the outermost barrel layers.

The dependence of the Tracker performance on the MSGC signal-to-noise ratio is illustrated in Fig 7.51.[3] The full simulation package was used to generate 300 GeV $b\bar{b}$ jets in the CMS Tracker. The sample was processed by the MSGC digitisation simulation for six different values of S/N, whereas the silicon hits were digitised always at the same working point. The plot reports the track finding efficiency as a function of the MSGC S/N for tracks inside jets, defined by a cone algorithm. Found tracks are required to have $p_T \geq 2$ GeV/c and at least eight points in the detector. Particles undergoing early inelastic interactions are not included in the efficiency definition; generated and reconstructed tracks share at least 50% of their hits. Closed dots and triangles describe different track finding algorithms [Chapter 8], while square symbols

[2] In this section the terms *cluster* and *hit* are used as synonyms.
[3] This study was carried out simulating a previous version of the CMS Tracker.

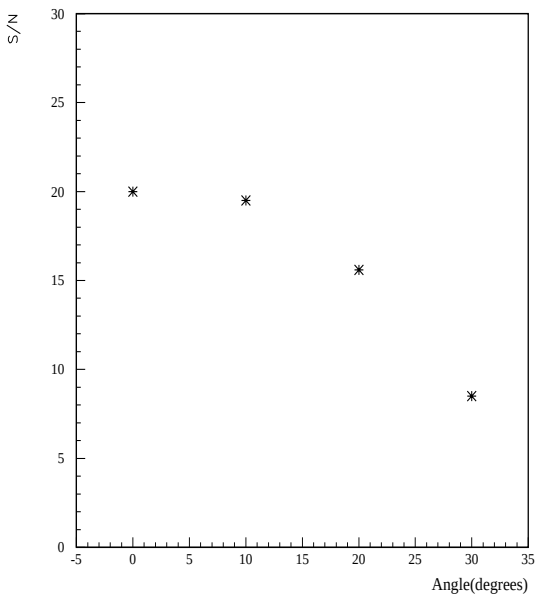

Fig. 7.49: Signal-to-noise ratio in MSGC as a function of the track incident angle. At each point the cluster closest to the track position is considered.

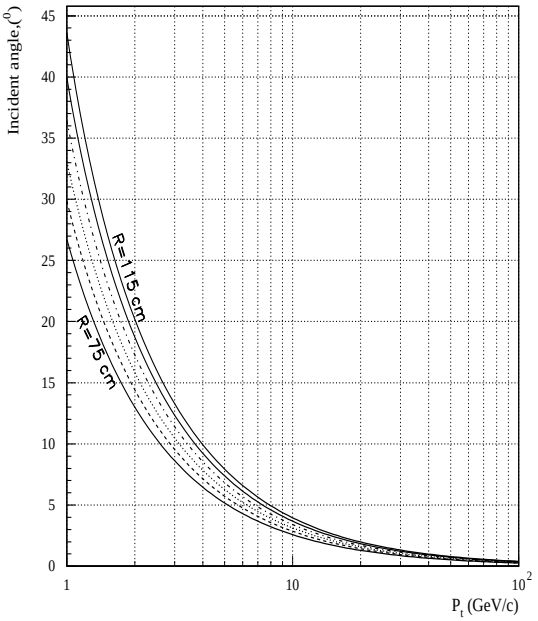

Fig. 7.50: Angle of incidence as a function of track p_T at different radii in the MSGC barrel.

are used to illustrate the performance when high luminosity pile-up [Chapter 9] is added to the simulated event. The study indicates that the track efficiency exceeds 95% when the working point is set at values larger than 12.5. The fraction of mis-reconstructed tracks (ghosts) is fairly independent of signal to noise. (Fig. 7.52). Estimates of the cathode voltage corresponding to the chosen working point are reported in Fig. 7.53. The experimental points (T10 [4-10]) represent the S/N measured with a performance prototype and with different cathode voltages (squares). The information is extrapolated to CMS-like conditions (dots) using a conversion factor accounting for the effect of the deconvolution chip and for the different strip length.[4] The simulation working point correspond to a cathode voltage of $\sim$530 V, most commonly used for extensive periods at beam tests.

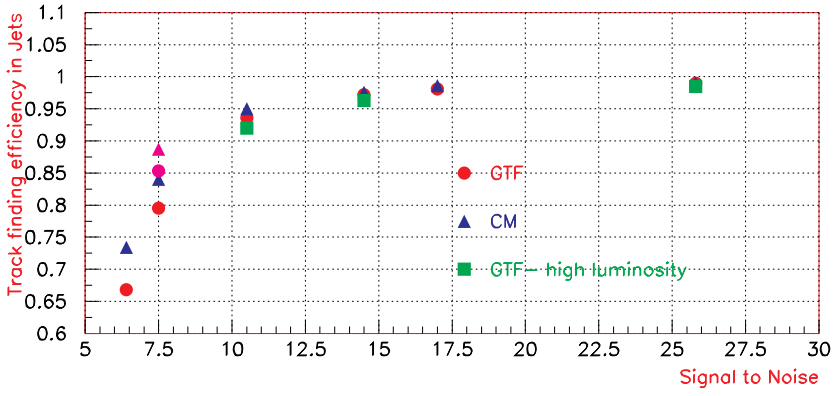

Fig. 7.51: Track finding efficiency in jets as a function of the signal-to-noise ratio simulated for MSGC detectors.

[4]Data refer to 10 cm long strips, the extrapolation refers to 12.5 cm long strips.

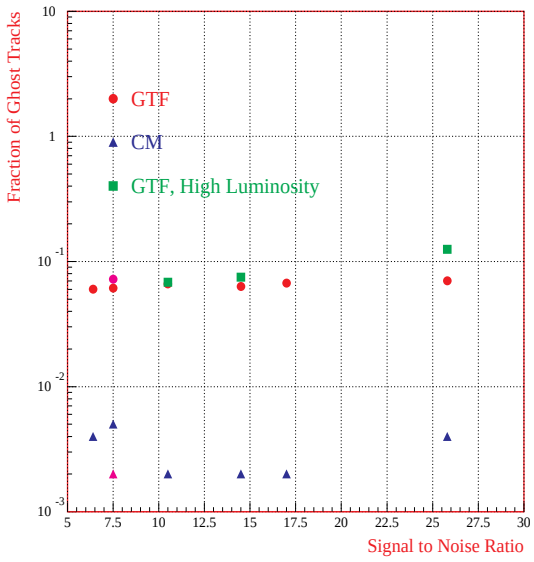

Fig. 7.52: Ghost track reconstruction efficiency in jets as a function of S/N in the MSGC detector.

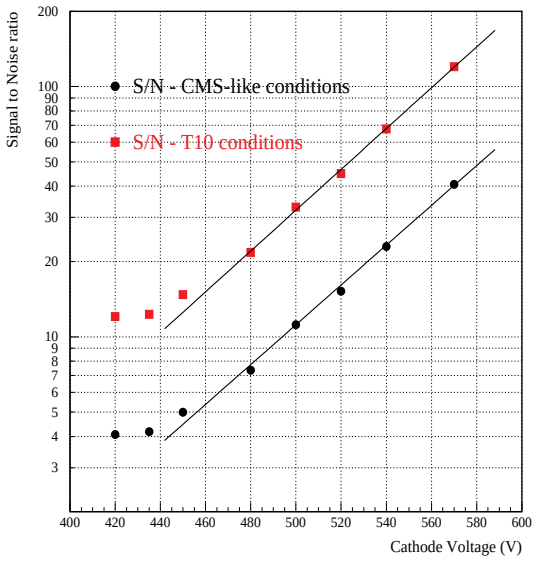

Fig. 7.53: Signal-to-noise ratio measured as a function of cathode voltage at T10 with a prototype (squares). The measurements are extrapolated to CMS conditions (dots).

7.10.4 Spatial resolution and efficiency

The reconstructed hit efficiency of MSGCs as a function of the track incident angle is shown in Fig. 7.55 and compared to the presently available beam test data (X7 facility).[5] The measured efficiency is defined as the ratio of the number of hits reconstructed in a chamber to the number of tracks that crossed it. Hits counted in the numerator are associated to the track by the pattern recognition but not used in the fit; tracks in the denominator are measured by an external tracking telescope. The efficiency drops by $\sim$ 5% at an angle of 40° due to cluster splitting; at larger angles the probability of at least one of the split clusters being reconstructed becomes larger and larger, due to the increase of energy deposited in the gas gap.

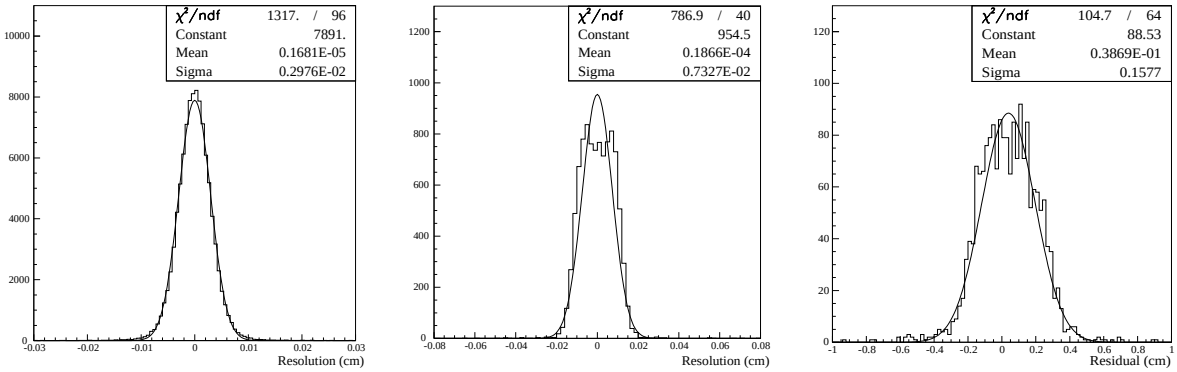

Fig. 7.54: Residual distribution for clusters reconstructed in 200 μm pitch and 400 μm pitch. The rightmost plot shows the z residual distribution for space points, obtained after associating the clusters of back-to-back detectors in the MSGC barrel.

[5] These measurements were made on a non-coated chamber with no advanced passivation and 25 cm long strips.

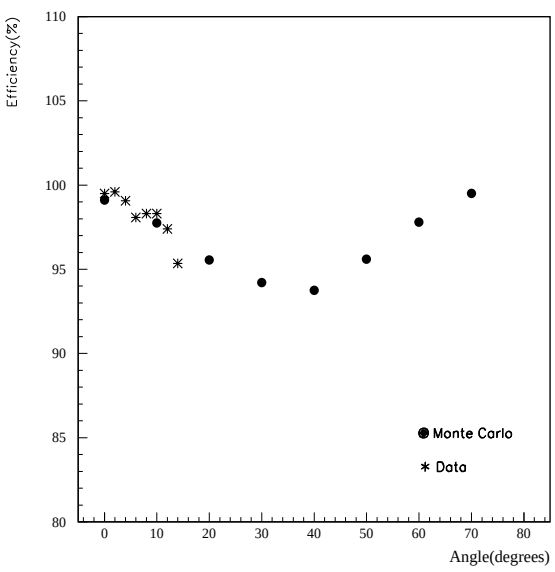

Fig. 7.55: Monte Carlo model of the MSGC hit efficiency as a function of track incident angle. The efficiency measured with 300 GeV/c muons overlaid to the simulated points.

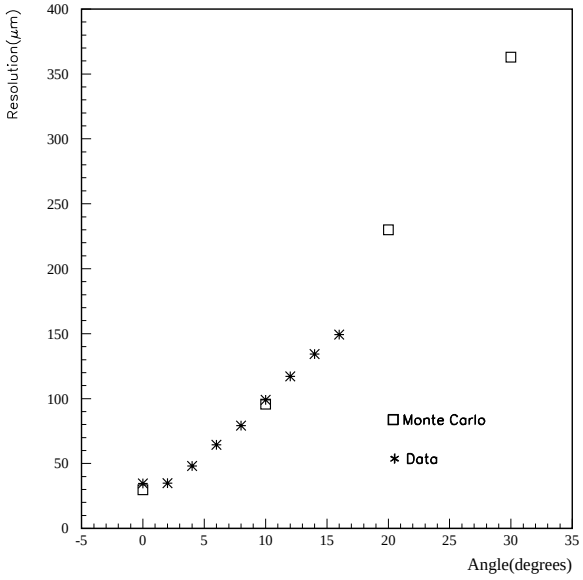

Fig. 7.56: MSGC simulated position resolution as a function of track incident angle. The measured resolution for 300 GeV/c muons is shown to be in excellent agreement.

The hit position resolution (σ_{res}) was extensively investigated at beam tests (Section 4.3.4.1) and is well reproduced by the Monte Carlo model. Resolution is defined here as the σ of the residual distribution, measured as the distance between the reconstructed and the parent hit; Fig 7.54 shows the simulated residual distribution for a stiff track crossing a standard and a stereo MSGC (two leftmost plots). After association of the $r\phi$ and stereo information, a z hit resolution of $\sim$1.6 mm for a space point is estimated as shown in Fig. 7.54. The dependence of the position resolution on the incident angle is shown in Fig. 7.56; data recorded at the X7 CERN beam facility are in excellent agreement with the simulation. The deterioration of the resolution with increasing angle of incidence does not scale simply with the growing cluster size but is in fact strongly affected by cluster splitting effects, already discussed in this section. The $\sigma_{\rm res}$ behaviour makes the MSGC a high resolution detector for tracks of moderate to very high p_T; the placement of the MSGC Tracker subsystem at an inner radius of 70 cm, reached by tracks of $p_T \geq 0.45$ GeV/c, exploits the full performance potential of the detector.

7.11 Occupancy

The study of occupancy in the Tracker characterises the environment to be handled by pattern recognition and data acquisition. The average occupancy induced by minimum bias events is a good estimator of the surroundings of an isolated track; tracks in high energy jets are instead correlated and a study of the local hit topology and of the hit quality is reported in Chapter 9. The occupancy analysis is only reported for the LHC high luminosity conditions, since the large pile-up of events represents the worst case.

A total pp cross section of 100 mb is assumed, corresponding to an inelastic cross section of $\approx$ 70 mb. To take into account empty LHC bunches ($\approx$ 20%) the average number of minimum bias events recorded in triggered events is scaled up by 40%, yielding an average value of 24 events piled up at each bunch crossing; the pile-up is fluctuated according to Poisson statistics. At a bunch crossing frequency of 40 MHz, early and late hits as well as loopers are an important component of the Tracker occupancy. To maintain the simulation memory and time usage at

an affordable level, the occupancy contributed by neighbouring bunch crossings is taken into account by propagating each pile-up event in the Tracker for 500 ns. The MSGC detectors need special handling: the time development of the signal is dominated by the drift time through the gas gap and exceeds the bunch crossing interval; hits from different bunch crossings can be separated with a given resolution. The maximum drift time equals about two bunch crossing time intervals and is accounted for in the simulation by increasing the pile-up by a factor two in MSGC detectors, i.e. by cumulating 48 minimum bias events, 500 ns long, per bunch crossing. The event sample generated to study the occupancy is described in Section 9.2.2 (type A); the GEANT cuts controlling physics effects were set an order of magnitude below their default value. To take into account the occupancy induced by the EM calorimeter, all tracks were propagated outward up to a radius of 140 cm. Background from very low energy neutrons was not simulated.

7.11.1 Pixel occupancy

The average occupancy in silicon pixels is low, due to the high granularity of the detectors.

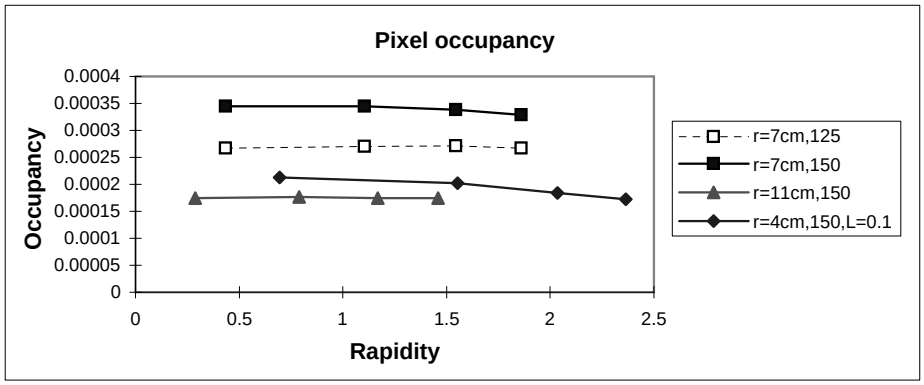

Fig. 7.57: Pixel barrel occupancy calculated for 3 detector radii 4 cm (diamonds), 7 cm (squares) and 11 cm (triangles). The solid lines are for 150 μm pixels and the dashed line is for 125 μm. The simulation is for high luminosity events in the 7 cm and 11 cm layers and for low luminosity events in the 4 cm layer. Noise contribution is also included (see text for details).

The average occupancy in the Pixel barrel as a function of pseudorapidity is shown in Fig. 7.57. The occupancy is defined here as the ratio of the number of pixels, with charge more than 4 σ above the noise level, to the total number of pixels in each layer. In this study a sample of $t\bar{t}$ events embedded in the high luminosity minimum bias pile-up was used. The

Table 7.18: Average pixel occupancy for 125 μm and 150 μm pixels

	Luminosity	Pixel Occupancy	
		150 μm	125 μm
Layer 1	10^{33}	0.00019	0.00015
Layer 2	10^{34}	0.00034	0.00027
Layer 3	10^{34}	0.00017	0.00014
Disk 1	10^{34}	0.00019	0.00015
Disk 2	10^{34}	0.00018	0.00015

occupancy is fairly independent of pseudorapidity since the track density decreases with η while the cluster size increases (Fig. 7.57). As expected, the radial dependence is very strong and is influenced by the magnetic field. The average pixel occupancies presented in Table 7.18 are integrated over rapidity. Values are shown for 150 μm and 125 μm pixels for both barrel and forward disks. As can be seen, the change in occupancy with pixel size is $\approx$ 20%. In the pixel

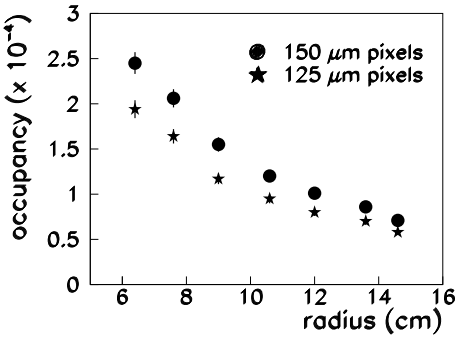

Fig. 7.58: Pixel endcap occupancy as a function of radius, for 150 μm pixels. The simulation is for high luminosity minimum bias events.

endcaps the difference of occupancy between innermost and outermost rings is about a factor of four, as shown for minimum bias events at design luminosity in Fig. 7.58. The results presented here have been obtained by using default energy cuts in GEANT below which the particles are stopped. A smaller statistics sample has been simulated using the lowest thresholds allowed in GEANT. The result indicates an increase of $\sim$20% in the occupancy. Asynchronous neutron background has not been considered in this analysis; separate studies indicate that such background can contribute up to 15% more hits in the pixel detectors.

7.11.2 Strip detector occupancy

7.11.2.1 Kinematics occupancy

High luminosity LHC minimum bias events are characterised on average by the production of $\sim$38500 impacts in the CMS Tracker; by impact we indicate the intersection between a track and a detector, at the GEANT propagation level.[6] The average number of impacts per sensor is shown in Fig. 7.59 and 7.60 for barrel and endcap detectors as a function of radius. The lower curves (open dots) in the plots show the impact occupancy normalised to the total number of sensors in each layer or endcap station (global occupancy); for the upper curves (closed symbols) the impact multiplicity is normalised to the number of detectors crossed by at least one track (local occupancy). In the absence of magnetic field the occupancy integrated over fixed z range is expected to scale as $1/r^2$. The presence of magnetic field introduces a deviation from the $1/r^2$ behaviour, proportional to the slope of the minimum bias p_T spectrum. The p_T distribution is constant between 200 MeV and 400 MeV and the global occupancy in the silicon detectors exhibits the expected inverse quadratic behaviour. Typical p_T values of the particles reaching the MSGC barrel range between 450 MeV and 650 MeV; in this range the production rate varies by about 50% and the global occupancy in the MSGCs decreases at a steeper rate than $1/r^2$. The global occupancy in the MSGCs is higher than the value one could estimate by extrapolation from the silicon detectors; the difference is accounted for by the larger pile-up accumulated in the MSGC detectors. The two outermost layers of the MSGC barrel have larger occupancy than the four innermost ones, since they are twice as long.

The contribution of secondary particles to the detector occupancy is relevant. At each layer, secondaries are produced at a constant rate; the occupancy is strongly affected by the magnetic field that makes very low p_T particles loop in the sensors. Typically 64% of the detectors are hit by at least one track. The fractions of hit detectors in barrel and endcaps are shown in Figs. 7.61 and 7.62. The deviation from a linear behaviour of the innermost silicon layer is due

[6] Each sensor of a twin pair is considered individually.

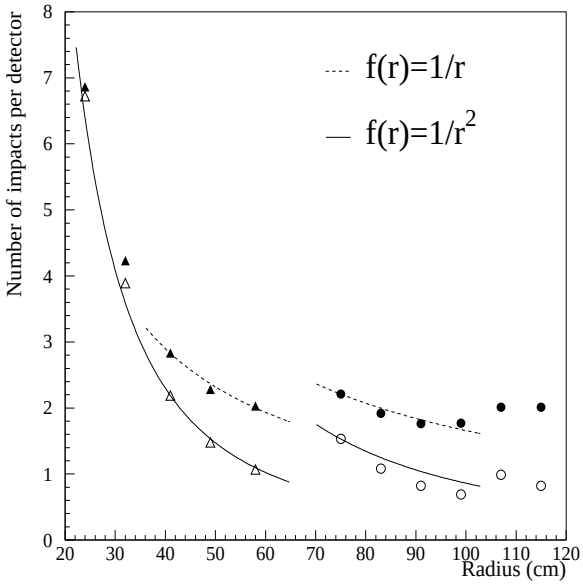

Fig. 7.59: Average number of tracks per barrel module in high luminosity minimum bias events as a function of detector radius. Average values are calculated considering all detectors (open symbols) or exclusively detectors crossed by at least one track (close symbols).

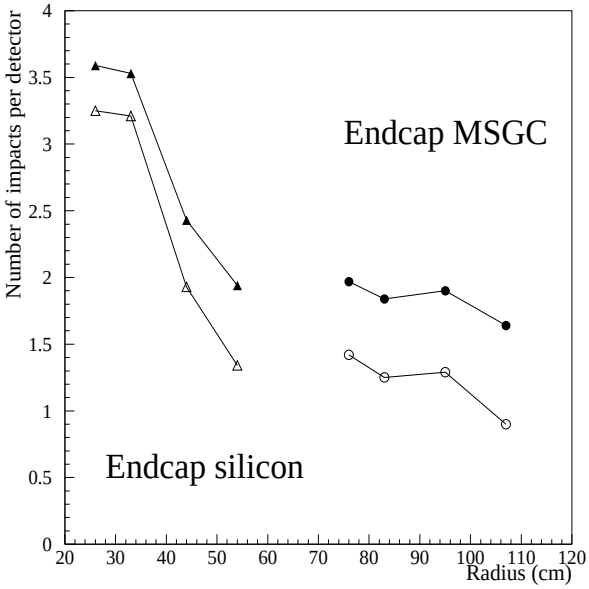

Fig. 7.60: Average number of tracks per endcap detector in high luminosity minimum bias events. Average values are calculated considering all detectors (open symbols) or exclusively detectors crossed by at least one track (close symbols).

to saturation. It is worth noticing that the first barrel layer covers the largest pseudorapidity range in the Tracker with the smallest number of detectors. The local occupancy, defined as the ratio of the global occupancy to the fraction of hit detectors, behaves approximately as $\sim 1/r$, as shown in Fig. 7.59, since as the number of hits decreases like $1/r^2$, the number of detectors grows linearly with the radius.

Similar considerations apply to the endcap occupancy. In this case the global occupancy should scale as $\Delta\eta/N$, where $\Delta\eta$ represents the pseudorapidity interval occupied by a ring and N is the number of detectors in the ring. The estimates shown in Fig. 7.60 reproduce the expected behaviour. The dependence of the impact occupancy on the pseudorapidity is modest and the relevant information is well represented by the occupancy in each ring averaged in the whole η range.

7.11.2.2 Detector occupancy

The channel occupancy is estimated after digitisation and cluster reconstruction. In this study the occupancy is defined as

$$\text{Occupancy} = \frac{\text{Total number of strips in reconstructed clusters}}{\text{Total number of strips}} \tag{7.1}$$

In analogy with the previous section, the denominator can be either the total number of channels in a layer(disk), or the subset including only strips in hit detectors. The first definition is relevant to data acquisition since it gauges the global data volume whereas the second is more relevant to pattern recognition since it characterises local combinatorics. The definition of occupancy relies on cluster zero suppression, since only strips in the reconstructed clusters are considered in the numerator of (7.1); looser requirements in the front-end logic would yield higher occupancy. The Tracker occupancy as a function of detector radius is reported in Figs. 7.63 through Fig. 7.66 for barrel and endcaps, $r\phi$ and stereo detectors.

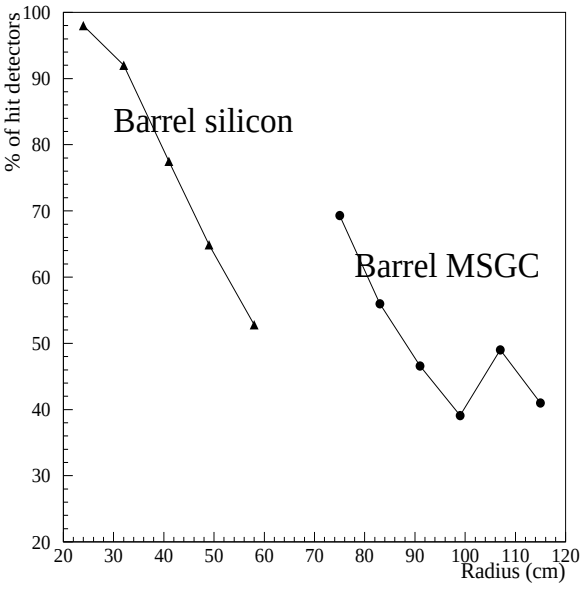

Fig. 7.61: Percentage of barrel detectors crossed by tracks in high luminosity minimum bias events as a function of detector radius.

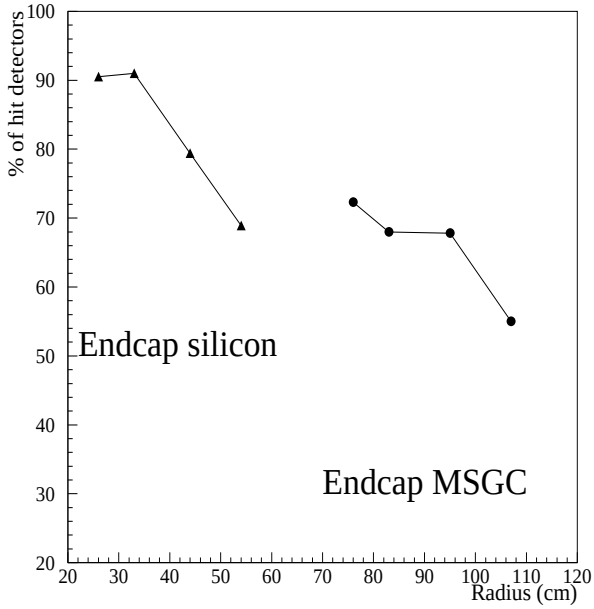

Fig. 7.62: Percentage of endcap detectors crossed by tracks in high luminosity minimum bias events as a function of detector radius.

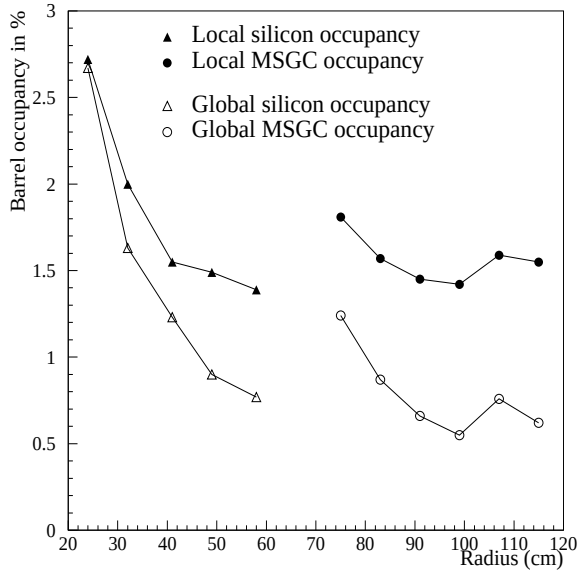

Fig. 7.63: Local and global occupancy in $r\phi$ barrel detectors.

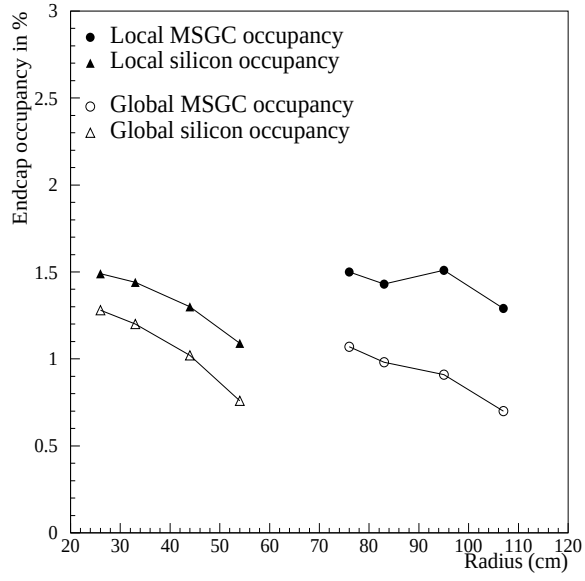

Fig. 7.64: Local and global occupancy in $r\phi$ endcap detectors.

About 35% of the $r\phi$ detectors of the Silicon system are in those layers and disks where the occupancy is less than 1% while 57% of these sensors are in layers and disks with occupancy between 1 and 1.5%. The occupancy in stereo layers is typically 35% larger. For the MSGC, about 30% of the $r\phi$ detectors are in the layers and disks with occupancy larger than 1%. Similarly to silicon detectors, the occupancy in stereo chambers is about 30% higher. The fluctuations of global and local occupancy can be rather large as shown in Figs. 7.67 and 7.68 which illustrate the meaning of the average values just discussed. The local occupancy in each silicon (left) or MSGC (right) detector is plotted in the histograms; the statistics amount to about 100 full luminosity minimum bias events. The width of the distribution is large; the tails

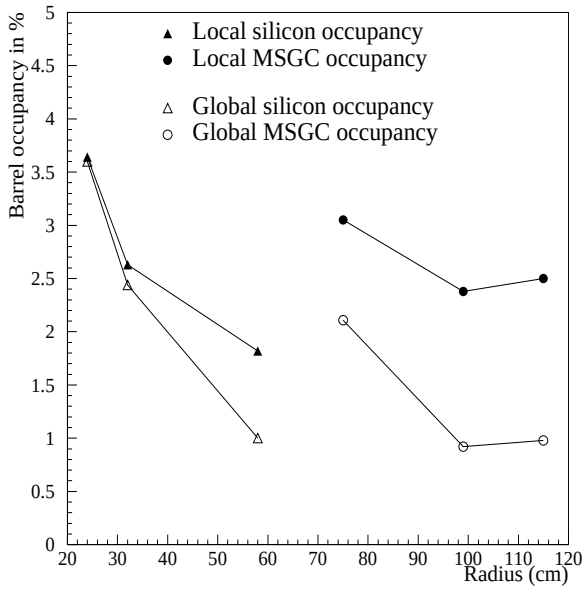

Fig. 7.65: Local and global occupancy in stereo barrel detectors.

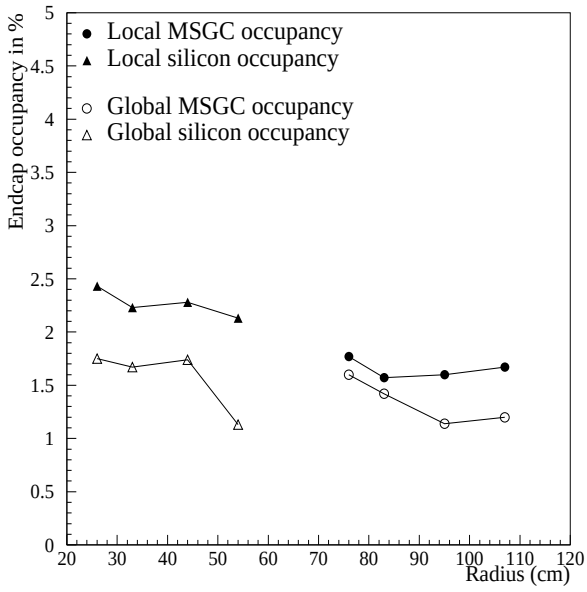

Fig. 7.66: Local and global occupancy in stereo endcap detectors.

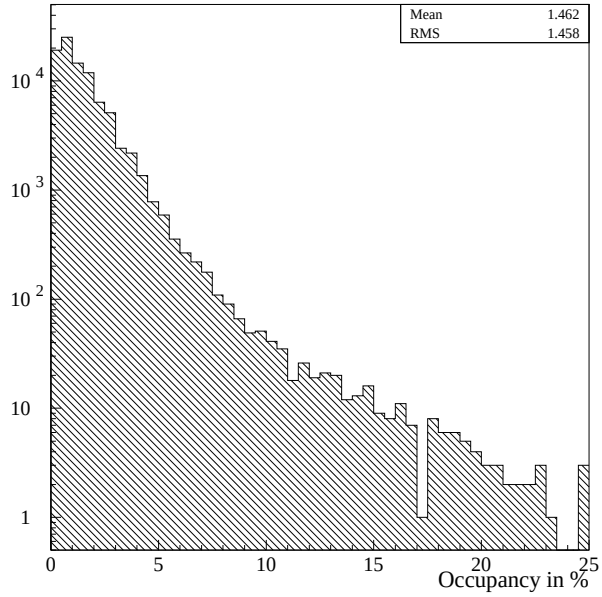

Fig. 7.67: Variation of the local detector occupancy in the silicon system. All endcap and barrel $r\phi$ detectors are considered.

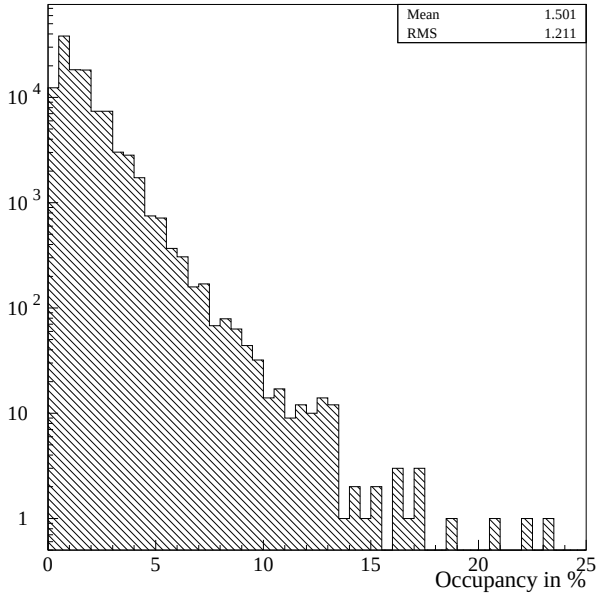

Fig. 7.68: Variation of the local detector occupancy in the MSGC system. All endcap and barrel $r\phi$ detectors are considered.

are dominated by fluctuations in secondary particle production. The average probability that the local occupancy in a silicon detector exceeds 4% (10%) is 5.1% (0.4%). Out of 38500 initial impacts, typically 39500 clusters are reconstructed in 64% of the detectors. The reconstructed hit multiplicity is very close to the impact multiplicity; nevertheless the reconstructed clusters are often associated to more than one impact and conversely several impacts generate more than one reconstructed hit. The two effects are called cluster merging and cluster splitting. They are briefly discussed in the next sections.

7.11.2.3 Cluster merging

Cluster merging is generated by overlapping tracks. Merged clusters can be wider and their position is not accurate for either track, causing occasional deterioration of the track reconstruction performance. The generation of overlapped hits is dominated by the production of secondary particles. The average fraction of merged hits for tracks of $p_T \geq 1$ GeV/c is 9% in the Tracker. If δ-ray emission is inhibited, the fraction reduces to 1%. The cutoff used in the simulation for δ-ray production is one order of magnitude lower than the default set in GEANT. No tuning of this threshold was carried out; the above values represent the limits containing the realistic estimate. The merging rate becomes $\sim 8\%$ in the absence of pile-up.

7.11.2.4 Cluster splitting

Cluster splitting is driven by the track incident angle, which depends in turn on the track p_T and the detector radius. The effect is more important in the MSGCs as discussed in Section 7.10 and it does not increase with pile-up. Cluster splitting is furthermore favoured by the clustering algorithm requiring all strips in a cluster to be above threshold. A recovery procedure can be implemented during reconstruction, after the first estimate of the track p_T has been made. A study of the cluster splitting rate is reported in Figs. 7.69 and 7.70 for barrel and endcap detectors, respectively.

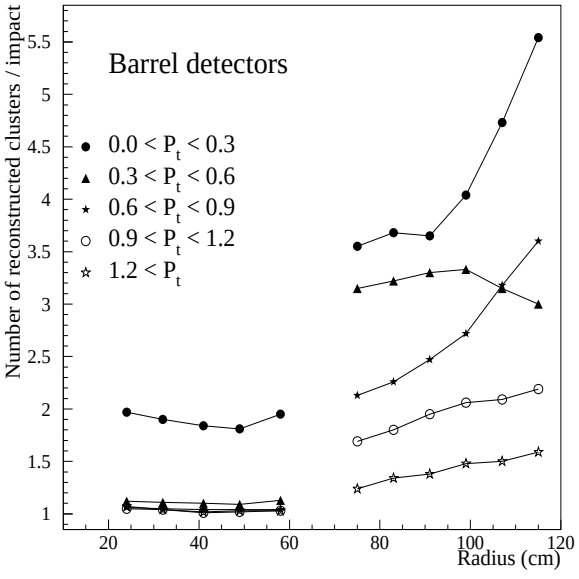

Fig. 7.69: Cluster splitting rate in the barrel Tracker as a function of the detector radius for different ranges of p_T.

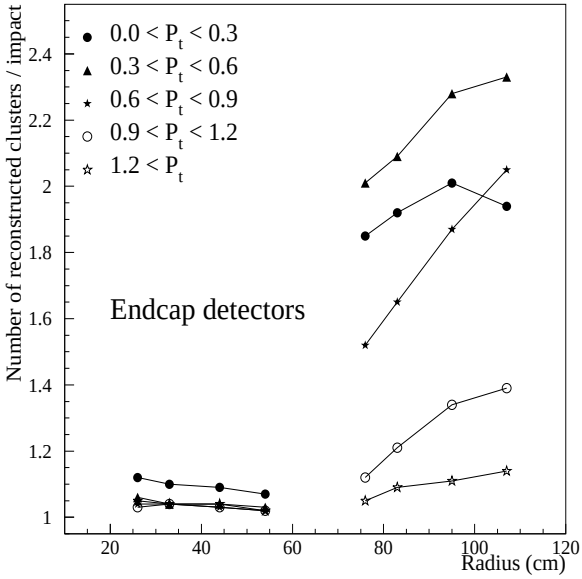

Fig. 7.70: Cluster splitting rate in the barrel Tracker as a function of the detector radius for different ranges of p_T.

Chapter 8

Reconstruction

The first two sections of this chapter are devoted to the description of the pattern recognition and vertex finding algorithms developed for the CMS Tracker. The Tracker alignment strategy problem is discussed in Section 8.3.

8.1 Pattern recognition and track reconstruction

The pattern recognition algorithms adopted for the CMS Tracker have to process a large number of hits per event: typically 5×10^3 hits at low luminosity and ten times more at high luminosity. In order to overcome the severe combinatorial problems the concept of *road* preselection is used in the first stage of the algorithms. In the second stage, the Kalman filter [8-1] is used to carry out final hit selection and track fitting. Three programs have been developed: the Global Track Finder (GTF), the Connection Machine (CM) and the Forward Kalman Filter (FKF). They all require a *learning* phase where the information of the detector geometry is processed once in order to create a database used in the pattern recognition phase. The algorithms work with a simplified geometry:

- detectors are 2D planes organised in layers;
- an average material distribution is used;
- the radial component of the magnetic field is assumed to be zero.

Tracks with $p_T > 0.8$ GeV/c[1] and $|\eta| < 2.4$ originating from the interaction point have ideally between 8 and 15 hits. Typically half of them are 3D points and the rest are 2D points. The hits in the Tracker fall into three categories. Firstly, there are pixel hits which have high accuracy in both local coordinates and they give precise 3D points. Secondly, hits in the individual silicon and gas detectors provide precise position measurements in the direction normal to the strips. Finally, measurements in twin detectors can be combined together to provide 3D points. This procedure, called stereo matching, can cause ambiguities, if the track density is too high. Some measurements may not be matched but can still be used as hits of the second type (2D). Since the two measurement planes are displaced by the detector thickness, the exact stereo coordinates of the matched hits depend on the track direction. At a preliminary stage of the pattern recognition the 3D points in the back-to-back detectors are constructed assuming infinite momentum tracks originating from the nominal centre of the Tracker. During the Kalman filtering the predicted track direction is used.

Of the thirteen or more nominal hits per track available in the detector, some may be missing due to inefficiency or badly measured because of overlapping tracks. The algorithms have to exclude these *bad hits* and skip missing layers during the pattern recognition phase. In the past,

[1] Tracks with $p_T < 0.8$ GeV/c in the 4 T magnetic field do not escape the Tracker volume in the radial direction and spiral towards one of the endcaps.

studies have also been done with the Local Track Finder (LTF) [8-2], a program that creates the roads for the track finder using the trajectories of Monte Carlo generated tracks and uses the detailed material description to account for multiple scattering effects.

8.1.1 Global Track Finder

In this approach, two sets of layers are defined during the learning phase: the Outer Layers (OL) and the Middle Layers (ML). Typically, barrel outer layers are the outmost MSGC layers and middle layers are the silicon layers providing 3D points. All pairs of detectors are considered with one detector belonging to OL and the other to ML. The pair is stored in the List of Starting Detectors (LSD) if the two detectors can be crossed by *interesting* tracks. Typical parameters of the *interesting* tracks are $p_T > 0.9$ GeV/c, $|\eta| < 2.4$ $|z| < 3\sigma_z$, where σ_z is the width in z of the luminous region. LSD consists of several hundred thousand pairs of detectors, ranging from 3×10^5 to 4×10^5 respectively for the low and the high luminosity versions of the Tracker. In addition, for each layer, a list of *nearby* layers is created. A *nearby* layer is defined as the previous or the succeeding layer hit by an *interesting* track when it crosses the layer under consideration.

During the pattern recognition phase the algorithm loops over LSD and searches for pairs where both detectors have hits. For any pair of hits a helix is constructed through the hits and the beam axis. Starting from the hit at OL, the track is then propagated backwards to the next internal layer computing the point of intersection of the trajectory with a specific detector. Hits are searched for in the vicinity of the intersection point. The track is then propagated to the next layer. The propagation ends successfully, when a minimum number of hits is found. If there are too few extra layers to add to the track or if the number of subsequent layers without hits is too large, the track candidate is abandoned.

Track candidates are eventually reprocessed with the Kalman filter using the parameters of the helix computed in the previous step as starting parameters. The track parameters and their covariance matrix are updated when a new hit is assigned to the track. The procedure is iterated with a variable road size taking into account the error introduced by the track extrapolation. When there are several hit candidates in a given detector, they are stored in a stack and tried in turn. Hits are not accepted if the χ^2 increment exceeds a given value. Tracks are eventually accepted if they have a minimum number of hits and an acceptable χ^2 per number of degrees of freedom. A track is rejected if the number of consecutive missing layers is too large.

Accepted tracks are stored in a list. Since the algorithm starts with many detector combinations, it often finds the same track or its segments several times. Duplicates are removed from the list of accepted tracks at the end of the pattern recognition. The longest track is kept, if its χ^2 is smaller than a given value. Otherwise, the track with smallest χ^2 is kept.

In the final step the algorithm performs a forward propagation – from inside to outside the Tracker volume – fitting the track parameters at the last measured point.

Since the algorithm starts from points in OL and ML, it cannot find tracks which do not have hits in those layers[2]. In addition it cannot find very low p_T tracks that do not reach the OL. The efficiency to find tracks with very large impact parameters (as K0 or Λ decay products) is small because the initial track direction is calculated using the beam constraint. On the other hand the algorithm performs well for tracks not too far from the primary vertex, e.g. tracks generated by heavy flavour vertices.

8.1.2 Connection Machine

This algorithm makes use of the concept of *cells* characterising the granularity of the initial track search. A cell may coincide with a detector or a portion of it but may also include several

[2]It still may find interacting tracks provided the produced tracks are collinear with the original track.

detectors placed on the same layer. For each cell a list of backward links with other cells in internal layers is created by propagating a large number of tracks ($\approx 10^9$) through the detector. Any hit cell is linked with the previous hit cell and also, for the sake of redundancy, with the cell hit before that, thus skipping just one layer.

A list of Starting Cells (SC) is also defined typically consisting of all cells in the three outer barrel layers and a large part of the forward layers. Cells that do not have links, the innermost cells, are called Ending Cells (EC).

During the pattern recognition phase the algorithm loops over the SC list searching for non-empty cells. Hits in these cells are connected backward to hits in the linked cells and the procedure is iterated. When the track candidate has at least three hits, the algorithm uses a helix constraint before adding an extra hit. The track parameters computed using the last three hits are compared with those computed using the new hit and the last two hits. The new hit is accepted if the distance between the two helices in the parameter space is not too large.

Once the list of track candidates related to a given SC cell is completed, the candidates above a given track length are reprocessed with the Kalman filter. The three most precise hits in the track are used to compute the starting parameters of the track. The procedure described above is iterated starting again from the SC hits. It uses all the features of the Kalman filter including the so-called *smoothing* or *forward re-propagation* that provides a better description of the extrapolation error.

CM is less sensitive than GTF to kinks, interactions and decays in flight since the track model used to generate the links is very general. However, a large memory is needed to store the links (≈ 30 MB) and the learning step takes several hundred CPU hours for any new geometry configuration.

The present CM version reconstructs tracks with p_T above 0.9 GeV/c. The algorithm can in principle be used for lower p_T tracks but the rapid increase of the number of links with decreasing p_T poses practical problems. Choosing a cell size of $\pi/100$, the typical number of links stored to identify tracks of p_T larger than 0.9 GeV/c is about 10 million and it is halved by increasing the p_T cut to 2 GeV/c.

8.1.3 Forward Kalman Filter

This algorithm starts the reconstruction from the precision pixel layers applying the same strategy as the CM algorithm.

During the learning phase the lists of backward links are created connecting only the detectors of the external pixel layers to those of the internal pixel layers. The SC list contains all detectors in the external pixel layers.

During the pattern recognition phase, the algorithm loops over the SC list searching for non-empty cells. Hits in the external pixel layer are then combined with hits in the linked detectors of the internal pixel layers. For any combination of hits, the helix parameters and their errors are estimated using the constraint that the track comes from the beam axis. If the helix parameters are within the acceptance cuts, the algorithm propagates the track to the outer detectors using the Kalman filter. Tracks are accepted if a minimum number of hits is found. Accepted tracks are eventually reprocessed again with the Kalman filter without the beam constraint in a way similar to the CM algorithm.

The FKF algorithm is particularly suited for b-tagging studies where only well-reconstructed tracks with enough hits in the innermost layers are selected for further analysis.

This method has a much smaller memory requirement than the CM algorithm since only a few tens of thousand links are accumulated in the learning stage. The efficiency is high for tracks that have two pixel hits and the performance is quite comparable to those of the two algorithms described in the previous sections. Since the number of combinations is smaller, it

runs about ten times faster. It reconstructs also low p_T tracks (the present threshold is set at 0.5 GeV/c) and short tracks that have an interaction in the external silicon layers.

A comparison of the execution time for the three algorithms is shown in Table 8.1 that reports the time needed to reconstruct tracks of p_T larger than several thresholds in a high luminosity di-jet event.

Table 8.1: Event Reconstruction Time (ERT) for GTF, CM and KFK; a high p_T di-jet event at high luminosity was reconstructed using three p_T thresholds. The machine used was a Sun Ultra workstation, corresponding to about 45 CERN units

p_T^{cut} (GeV/c)	$\mathrm{ERT_{GTF}}$ (s)	$\mathrm{ERT_{CM}}$ (s)	$\mathrm{ERT_{FKF}}$ (s)
2.0	146	80	17
0.9	670	390	37
0.5			55

8.2 Vertex reconstruction

Primary vertex finding in colliding beam experiments is essentially a one-dimensional problem, since the transverse coordinates, x and y, are determined by the beam line with a high precision. Therefore fairly simple algorithms can do the pattern recognition, and the primary vertex finding efficiency, as well as the two-vertex resolution, depends predominantly on Tracker performance rather than on the algorithm.

The principal task of primary vertex finding is to identify particles produced by the pp collision that caused the trigger and to separate them from tracks produced in superimposed minimum-bias events. Two algorithms to identify vertices are described in the following. The first is dedicated to Primary Vertex search (PVF), whereas the second performs Global Vertex searches (GVF). At the price of a complex formulation, GVF achieves good performance in the reconstruction of secondary vertices.

8.2.1 PVF algorithm

An important feature of this algorithm is to order the reconstructed tracks according to their importance in vertex finding/fitting, i.e. according to the accuracy of their impact parameter determination. High p_T tracks are likely to come from the trigger event and to have precise impact parameter measurements. For these reasons they have a high probability to enter the algorithm first and to create a seed for the primary vertex of the trigger event. The basic steps in the algorithm are qualitatively as follows:

- Track qualities are checked: tracks with too few hits, bad χ^2, very low p_T, large xy-impact parameter or too far from $z = 0$ are rejected.
- The remaining tracks are sorted with increasing z impact parameter error.
- The z-impact point of the first track in the list is taken as a seed of z-coordinate for the first vertex candidate.
- Subsequent tracks in the list are examined in that order. Each track is either associated to the closest vertex candidate, according to tight tolerances, or forms a seed for a new vertex candidate, if it is significantly displaced from all vertex candidates created so far.
- If the track is associated to a vertex candidate, the vertex position is recomputed including the new track.

- After all tracks have been examined, a smoothing procedure is performed: each vertex candidate is refitted in three dimensions with the beam constraint [8-3]; poorly associated tracks are removed from the list for that vertex and the vertex position is recomputed.
- After smoothing, the track-vertex association procedure is repeated until a stable configuration is achieved.

The vertex recognition efficiency and two-vertex resolution are being studied with the algorithm.

8.2.2 GVF algorithm

The global 3D vertex finding algorithm has been developed and used for performance studies [8-4]. The algorithm reconstructs vertices starting from the reconstructed tracks and establishes a unique matching between tracks and vertices. Tracks are eventually refitted using the vertex information.

Three types of vertices are reconstructed in a given event:

- primary vertex, with an arbitrary number of tracks and transverse position constrained to the beam axis;
- secondary vertices, with an arbitrary number of tracks and arbitrary position in the transverse plane;
- V^0 vertices with two opposite-sign tracks and effective mass compatible with a known particle (e.g. K0, Λ).

After preselecting the tracks, the algorithm proceeds in two major steps: the initialisation (seeding) phase and the vertex finding phase.

8.2.2.1 Initialisation

The initialisation step provides a rough estimate of the vertex positions and – for each vertex – the list of assigned tracks and their parameters at the vertex. At this stage a single reconstructed track can be assigned to several vertex seeds.

For 'seeding' the primary vertices an algorithm quite similar to the one described in the previous section is used, exploiting the localisation of the interaction point in the transverse plane. The primary vertex seed is formed using only tracks with small transverse impact parameters and then all tracks whose impact point is not too far away are assigned to the seed.

The initialisation procedure for secondary vertices uses a three-step procedure. In the first step all possible two-track vertices are formed by track pairs with minimal distance in space. In the second step nearby vertices are joined. In the last step other tracks are attached to these identified vertex seeds.

8.2.2.2 Deformable templates algorithm

The optimal match between tracks and vertices is searched for using the deformable templates (elastic arms) approach (DTA) [8-5]. The N vertex seeds found in the initialisation step are used to start the DTA.

Each vertex seed $n \in N$ is characterised by the vertex position $\overrightarrow{x_n}$ and the set M_n of tracks assigned to it (vertex tracks). Each track m belonging to the set M_n is fitted using the vertex constraint and the track parameters at the vertex position are computed ($\overrightarrow{P_n^m}$). Each vertex track m corresponds to a given track k of the set K of reconstructed and preselected tracks. For each track k a fit is performed without vertex constraint giving the parameters $\overrightarrow{\pi_k}$ at the first measured point.

The vertices are obtained by minimising a global fitness function defined as:

$$E[S_{n,k}, \overrightarrow{x_n}, \overrightarrow{P_n^m}, \overrightarrow{\pi_k}] = \sum_{n\in N, k\in K} D_{n,k} S_{n,k} + \lambda \sum_{k\in K} [1 - \sum_{n\in N} S_{n,k}]^2 \ , \tag{8.1}$$

where $S_{n,k}$ is a binary decision unit [8-5] and $D_{n,k}$ is a distance between the k-th reconstructed track and the n-th vertex. The weight $S_{n,k}$ is set to zero when the track k is not related to any vertex track of the set M_n; the 'noise' parameter λ characterises the weight of the second term of Eq. (8.1), which imposes a penalty when some track remains unmatched or is associated to more than one vertex. The term $D_{n,k}$ is defined only for tracks pointed by a vertex track of the set M_n as:

$$D_{n,k} = \sum_{i,j} (R^i_{n,m} - \pi^i_k) A^k_{ij} (R^j_{n,m} - \pi^j_k) \ , \tag{8.2}$$

where $\overrightarrow{R}(\overrightarrow{P_n^m}, \overrightarrow{x_n})$ are the parameters of the m-th vertex track propagated to the first measured point of the corresponding reconstructed track $k = k(n, m)$. Here A^k is the inverse covariance matrix of the reconstructed track parameters at this point.

To further constrain vertex identification, specific vertex properties can be used by modifying the definition of the distance parameter $D_{n,k}$ used in the fit:

$$D_{n,k} \rightarrow C_n (D_{n,k} + D_1) \ , \tag{8.3}$$

where C_n is a constant. The term D_1 brings in the additional constraint. For primary vertices D_1 takes the form:

$$D_1 = A_n (X_n^2 + Y_n^2) \ , \tag{8.4}$$

where A_n represents the inverse of the variance of the collision point in the transverse plane. For V^0's, D_1 is proportional to the squared difference between the reconstructed effective mass and the candidate particle mass.

The constant λ has to be large ($\sim$ 50–100) and it decreases slightly during the minimisation.

Two different approaches have been tested for the minimisation with similar performances: the empirical EM algorithm [8-6] and the simulated annealing algorithm [8-7]. The two approaches perform well in a simple environment, but they fail often when the track density is very high as in the core of a hard jet.

8.3 Calibration with reconstructed tracks

The ultimate position calibration (alignment) will be made using reconstructed tracks. The method uses the best in situ available measurement device, namely the detectors themselves. The smoothness of high p_T tracks introduces a strong position correlation between hit detector elements. It is this correlation which allows the detector elements to be aligned with respect to each other on a statistical basis.

The basic requirements to make track finding and initial reconstruction possible are discussed in Section 8.3.2 below. This simulation study shows [8-8] that a rather loose precision requirement, a few hundred microns, is sufficient for track finding and initial reconstruction of isolated tracks with a 90 % efficiency. Thanks to the precision assembly followed by optical survey of the fiducial marks, the detector positions will be determined to such precision thus providing the necessary starting point for the alignment by reconstructed tracks. In the next sections we describe the strategies and methods of these calibration procedures.

8.3.1 Calibration precision requirements

The precision requirements for the ultimate calibration of the detector positions must be of the order of the intrinsic detector resolution or better. To be more precise let us denote the detector resolution by σ_D and the r.m.s. calibration precision by σ_C and their ratio as $k = \sigma_C/\sigma_D$. Then the effective precision of the detectors is:

$$\sigma_{eff} = \sqrt{\sigma_D^2 + \sigma_C^2} = \sqrt{1+k^2}\ \sigma_D\ , \tag{8.5}$$

where $\sqrt{1+k^2} = \sigma_{eff}/\sigma_D$ is called the 'deterioration factor'. The dependence is shown graphically in Fig. 8.1. For example, allowing a maximum of 30 % deterioration of the effective detector precision, implies that the calibration precision should be better than about 80 % of the detector resolution:

$$\sigma_C \leq 0.8\ \sigma_D\ . \tag{8.6}$$

It can be shown [8-9] that the precision of the fitted track parameters scales with the effective detector resolution at large p_T (in the absence of multiple scattering): scaling of the effective detector resolution by a constant factor, scales the precision of the track parameters by the same factor. Hence in order to achieve less than 30 % (20 %) worsening of the p_T resolution from ideal, the detectors must be aligned to better than about 80 % (65 %) of their intrinsic resolution.

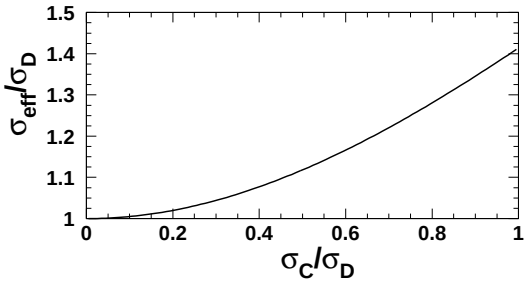

Fig. 8.1: Effective detector precision as a function of calibration precision.

This is a simplified picture of a complicated problem but gives a good idea of the required calibration precision. In reality there are 6 constants which define the position (3 coordinates) and orientation (3 angles) of a detector element. In principle all the 6 constants need calibration. Therefore of the order 10^5 constants are needed to calibrate the full detector which has about 20 thousand detector elements.

A detailed simulation analysis of the precision requirements has been performed [8-8]. The required precisions were deduced for the radial and longitudinal coordinates as well. These results are presented in the following.

8.3.2 Simulation study for requirements

Precision requirements for the Tracker alignment have been studied by a two-stage simulation procedure. In the first stage random offsets from ideal positions were applied to detector modules. Hits in the distorted detector were simulated and the results were stored in a separate file. In the second stage the offset hits were used for track reconstruction with a non-distorted detector description. The reconstruction was performed with the Global Track Finder.

The event samples used in the requirements study were single muons in the energy range 1–200 GeV/c^2 and Higgs events in the decay channel H$\rightarrow$ ZZ $\rightarrow 4\mu$ with 150 GeV/c^2 < M_H < 400 GeV/c^2. Higgs events were used here for practical reasons only. The momentum cut for

muons from Z^0 decays was 5 GeV/c. The following quantities were extracted as a measure of the reconstruction quality: 1) reconstruction efficiency, the fraction of reconstructed tracks associated with initial muons within a corridor in ϕ, θ and momentum; 2) number of hits associated with reconstructed tracks; 3) χ^2/N_D averaged over all tracks; 4) r.m.s. of $(p_T - p_{Tr})/p_T$, where p_T is the true transverse momentum and p_{Tr} is the reconstructed one; 5) r.m.s. of the impact parameter distribution. Two levels of precision requirements for alignment have been considered:

1. precision required in installation and survey,
2. ultimate precision needed in reconstruction.

The first level is set to allow pattern recognition of isolated high p_T tracks with reasonable efficiency. The second level of precision allows the ultimate event reconstruction to be made with the required resolution (see below). At the first level of precision we impose two conditions on the $Z^0 \to \mu\mu$ events: i) the muon reconstruction efficiency has to be more than 0.9; ii) the number of associated hits in each subsystem has to be more than half of the detector layers in this subsystem. These requirements give a starting point for further alignment with reconstructed tracks to obtain precision which provides good performance of the Tracker.

At the second level the following conditions must be satisfied:

1. mean χ^2/N_D less than 1.2 of that with the non-distorted geometry,
2. less than 20 % deterioration of the impact parameter resolution,
3. less than 20 % deterioration of the r.m.s. of $(p_T - p_{Tr})/p_T$.

These requirements were applied to the analysis of Z^0 events and to single muons in the barrel region of the Tracker.

Random displacements of the detector positions were introduced separately for each subsystem in r, ϕ and z with a Gaussian distribution. As an example of the results, the reconstruction efficiency for MSGC *vs* distortion-r.m.s. for the Z^0 events is shown in Fig. 8.2.

Using these and similar results for Silicon and Pixel detectors, and following the criteria described above, the level-1 set of requirements is given in Table 8.2. For both MSGC and Silicon detectors the sensitivity to distortions in r and z appears to be quite low for isolated muon tracks with transverse momentum in the range between 5 GeV and 100 GeV.

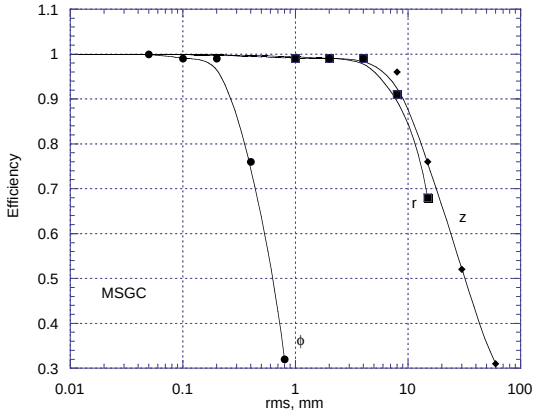

Fig. 8.2: Reconstruction efficiency *vs* distortion r.m.s. for the MSGC barrel.

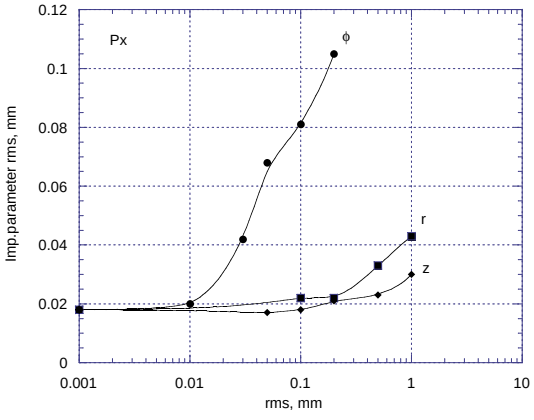

Fig. 8.3: The impact parameter resolution *vs* r.m.s. of the distortion.

Table 8.2: Precision requirements (r.m.s.) at level 1

System	r [mm]	$r\phi$ [mm]	z [mm]
MSGC	8	0.3	10
Silicon	4	0.2	10
Pixel	0.6	0.1	0.8

Table 8.3: Precision requirements (r.m.s.) at level 2

System	r [mm]	$r\phi$ [mm]	z [mm]
MSGC	0.6	0.05	2
Silicon	0.3	0.015	0.5
Pixel	0.1	0.015	0.5

Figure 8.3 shows an example of impact parameter deterioration due to distortion of the Pixel wafers. The full set of required precisions at level 2 is given in Table 8.3.

The sensitivity is again rather low for r and z suggesting that the necessary alignment precision in these coordinates can be obtained by precision installation and survey.

The results presented are considered preliminary particularly for the second-level requirements, because the relationship between general performance parameters, such as χ^2, momentum resolution and impact parameter, and physics performance parameters, such as B-tagging efficiency or reconstruction efficiency of muon in a jet, is not yet precisely established. The deterioration limit of 20 % which was used for all general performance parameters was chosen rather arbitrarily and can be changed when our knowledge about necessary physics performance parameters improves. For the moment we consider the second level of requirements as the minimum precision that should be achieved with the position monitoring system. These requirements are likely to change with the update of the results of the ongoing simulations.

8.3.3 Calibration strategies

Local and global calibration procedures are foreseen. The local calibration aims to align the detectors within a layer using the overlap feature. Tracks down to 1 GeV/c in p_T will be used for this purpose. The global calibration aims to perform longer range alignment of the detectors. High p_T tracks will be used and the most suitable for this purpose are muons from the Z^0 decay.

A number of constraints will be used in the calibration procedure. One of the most important constraints available at the LHC is the beam spot as a precise (about 10 μm in the transverse plane) origin of tracks. Another constraint arises from the precision-assembly: in detector units like rods the individual detectors are assembled very precisely with respect to each other on optical benches. The relative positions of the N detectors in such an assembly unit should remain constant apart from bending and twist effects when taken from the laboratory and assembled in the experimental area. In such a case the $6N$ calibration constants reduce to $6+3$ per unit, where the three special constants would account for possible bending and twist of the unit.

Local calibration

The detector elements in a given layer are arranged in such a way that a small part, typically a few per cent of the detector area, of the neighbouring detectors are overlapped. This means that occasionally a track traverses two nearby detectors in a layer which helps to align the detectors. Multiple scattering reduces the position correlation by introducing an error Δv according to the formula:

$$\Delta v = \frac{13.6\,\mathrm{MeV}}{p}\Delta r\sqrt{h_0}\,, \tag{8.7}$$

where p is the momentum, h_0 is the effective thickness of the detector in radiation lengths and Δr is the distance between the two detectors which are in overlap. For example for the

values $h_0 = 0.025$, $p = 1\,\mathrm{GeV}/c$ and $\Delta r = 3\,\mathrm{cm}$ we get for the multiple scattering fluctuation $\Delta v \approx 70\,\mu\mathrm{m}$. This means that in order to obtain $10\,\mu\mathrm{m}$ calibration precision we need at least $(70/10)^2 \approx 50$ overlapping tracks per detector for the alignment when using $\geq 1\,\mathrm{GeV}/c$ tracks.

The time needed to collect enough events for calibration of the whole Tracker is determined by those parts of the detector which get the smallest particle flux. These are the outermost MSGC detectors in the central region. Assuming $\mathrm{d}N/\mathrm{d}\eta = 8$ charged particles per rapidity unit and that a fraction Q of the particles is used for calibration, the flux of useful particles per one pp event at $\theta = \pi/2$ and $r = 113\,\mathrm{cm}$:

$$\frac{\mathrm{d}N}{\mathrm{d}A} = \frac{Q}{2\pi r^2}\frac{1}{\sin\theta}\frac{\mathrm{d}N}{\mathrm{d}\eta} \approx 1.0 \times 10^{-4} Q\,\mathrm{cm}^{-2}\ . \tag{8.8}$$

Then for the overlap area of $2\,\mathrm{cm}^2$ per detector pair, the flux of particles for calibration is $2 \times 10^{-4} Q$ per pp interaction. Some $Q = 10\%$ of the particles have $p_T \geq 1$ GeV/c. These numbers imply that, in order to obtain 100 particles per detector pair for calibration, the number of pp events needed is of the order 5×10^6. Events from any physics trigger can be used for local calibration, so that detector alignment does not disturb the physics program of the experiment.

The time needed to collect sufficient statistics does not scale inversely with the luminosity, but depends rather on the data acquisition capacity. For the DAQ rate of 5 Hz at high luminosity (≈ 20 pp events per trigger) sufficient statistics will be collected during a day of running. At low luminosity ($10^{33}\,\mathrm{cm}^{-2}\mathrm{s}^{-1}$) the DAQ rate/trigger is higher due to smaller events and sufficient statistics may be obtained in a few days of running the experiment. A once-a-week frequency of the local calibration procedure is perfectly feasible, but only experience will tell how often it will be necessary.

Global calibration

Bending and twist effects will be parametrised and the values of the parameters will be obtained from measurements made in the laboratory (e.g. bending of the MSGC rods). Global sag of the detector will be obtained from the survey measurements and the monitoring system. These pre-determined parameters will be used either as such or as useful constraints in the calibration procedure by reconstructed tracks.

Muons from $\mathrm{Z}^0 \to \mu^+\mu^-$ decays above a p_T limit will be used for global alignment. The number of such events is estimated to be about 10^4, which is sufficient to obtain the related calibration constants with required precision. The cross section is estimated as:

$$\sigma_{\mathrm{Z}\to\mu\mu}(p_T(\mu) > 20\,\mathrm{GeV}) \approx 0.4\,\mathrm{nb}\ . \tag{8.9}$$

Hence the rate of such events is 4 Hz (0.4 Hz) and the necessary event collection time is about 10 min (2 hours) at the luminosity $\mathcal{L} = 10^{34}\ \mathrm{cm}^{-2}\mathrm{s}^{-1}$ ($\mathcal{L} = 10^{33}\ \mathrm{cm}^{-2}\mathrm{s}^{-1}$). In view of these estimates the global calibration can be performed on a daily basis if necessary.

Chapter 9

Performance

9.1 Overview

In order to assess the basic performance of the CMS Phase I and II Trackers we discuss a series of increasingly challenging physics problems using the simulation and reconstruction tools introduced in Chapters 7 and 8.

The algorithms employed to generate single track, minimum bias, di-jet and B-meson-decay events are discussed in Section 9.2. The high luminosity LHC conditions are simulated overlaying the pile-up events described in Section 7.11 on the hard interactions under study.

Single track events are used in Section 9.3 to evaluate the precision of track measurement in the CMS inner detector. Good momentum resolution is essential for the mass determination and background suppression for particles with small natural width. The transverse momentum of the decay products ranges from the very low values typical of B-physics up to a few TeV in the case of new heavy bosons. Accurate momentum measurements are also necessary to calibrate the EM calorimeter. High efficiency of charge determination for tracks up to several TeV is needed to maintain good heavy boson reconstruction efficiency in the kinematic range accessed by the LHC. The probability of charge mis-assignment is studied using single muons of transverse momentum as high as 4 TeV. The track impact parameter resolution, relevant to b-jet identification and lifetime measurements, is studied for muons and pions at several p_T values; the deviation of the momentum and impact parameter resolution from a Gaussian behaviour are discussed for low p_T muons and hadrons, due to their importance in b-jets identification and exclusive B-decays reconstruction.

The efficiency for correctly reconstructing single tracks is analysed separately for muons and hadrons and a possible degradation due to the larger occupancy expected at the high luminosity LHC condition is studied using the Phase II CMS Tracker layout. To limit the impact of the Tracker material budget, dedicated procedures were developed to reconstruct electrons and hadrons, discussed in Section 9.4.

Isolated leptons and photons are a clean signature of bosons and SUSY particles; isolation criteria are effective to suppress jet background and rely on the ability to reconstruct low p_T tracks with high efficiency within jets. Moreover, good track finding efficiency in jets associated to precise measurement of the track impact parameter allows the identification of b-jets. The ability to reconstruct tracks in jets is discussed in Section 9.5 as a function of the jet E_T and at different luminosity conditions whereas b-jet identification with the CMS Tracker is discussed in Section 9.7. Tagging b-jets of high transverse energy is a fundamental tool for Higgs and SUSY particle searches; the expected b-jet transverse energy varies typically between few tens of GeV and 200 GeV for the hardest events; the b-tagging capability of the CMS Tracker is studied as a function of jet E_T and both at low and high luminosity. The identification of heavy flavour secondary vertices is also potentially a powerful tool to tag b-jets and is discussed in

Section 9.6 together with a more general strategy of vertex reconstruction. The primary vertex reconstruction efficiency depends on the vertex topology and good track measurement typically ensures satisfactory performance of relatively simple algorithms. A challenging task is set by the reconstruction of V_0 vertices, needed to identify K_s^0 and access the CP violation sector. This problem is addressed by a study of the $B_d^0 \to J/\psi K_s^0$ reaction. Special attention is given to the reconstruction of photon conversions, which are a large source of background in primary lepton identification. Conversions reconstruction increases the detection efficiency of $H \to \gamma\gamma$ events; moreover a precise reconstruction of the parent photons can be used to localise the reaction vertex in high luminosity events.

In addition to pp operation, the LHC will be able to collide heavy ions, such as lead, calcium and nickel. In a typical running schedule three to four weeks per year will be dedicated to ion collisions. The suppressed production of heavy-quark bound states is a signature to study a Quark-Gluon Plasma state of hadronic matter. The most demanding measurements concern Pb-Pb collisions, that have a centre-of-mass energy of 5.5 TeV per nucleon-nucleon pair and the highest track multiplicity. A study of identification of Υ's produced in Pb-Pb collisions in the CMS detector is reported in Section 9.8. In the following we shall designate the detector consisting of the low luminosity Pixel detector configuration and the staged silicon and MSGC Trackers as the Phase I detector layout. The fully instrumented strip detector combined with the high luminosity version of the Pixels will be referred to as Phase II Tracker.

9.2 Physics Simulation

9.2.1 Single tracks

The single track generator allows the user to choose the identity of particles to be generated as well as kinematic ranges in pseudorapidity η, azimuth angle ϕ and transverse momentum p_T. By default the distributions in η and ϕ are uniform in a user defined range. Two options are available for p_T sampling: 1) realistic p_T distribution whose asymptotic behaviour is ${p_T}^{-\alpha}$ ($\alpha = 3.78$) or 2) flat distribution within a user defined interval.

The single particle generation option is used to study the Tracker single particle performance. An option is also available to generate hits by geantinos (artificial, neutral and non-interacting particles), which were used to estimate the fractional radiation and interaction lengths of the Tracker material.

9.2.2 Minimum bias events

Inelastic minimum bias events are generated using PYTHIA.[1] The pseudorapidity distributions of charged particles is shown in Fig. 9.1a for all p_T and for two different p_T cuts. The plot is normalised to the number of particles per pseudorapidity unit per pp event. In the central region the charged particle density is about seven per unit of pseudorapidity. Charged particles from weak decays, which are not included, would contribute about 10% to the plot. The mean number of non-spiralling particles ($p_T > 0.9$) is about one per pseudorapidity unit. The transverse momentum of charged particles is shown in Fig. 9.1b. The mean p_T is about 0.5 GeV/c and is almost independent of pseudorapidity in the region of the Tracker acceptance. The multiplicity of photons from pp collisions (mainly from π^0 decays) is about 8.3 per unit of rapidity. For high luminosity, $\mathcal{L} = 10^{34}$ cm^{-2}s^{-1}, the mean number of photons from the interaction point in one trigger is about 1000 in the range $|\eta| < 2.5$, assuming about 25 pp events per trigger on average.

[1] The PYTHIA switches were set at msel=1, mstp(2)=2, mstp(33)=3, mstp(81)=1 and mstp(82)=4

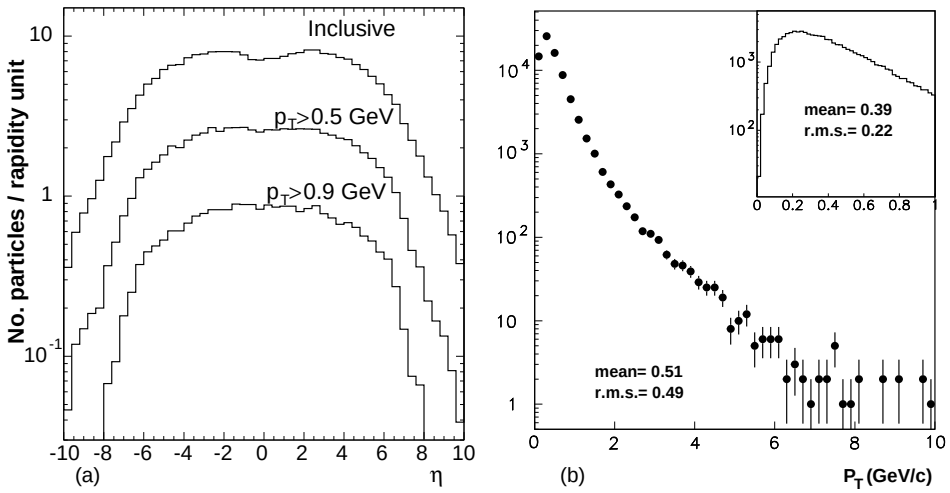

Fig. 9.1: a) Pseudorapidity of charged particles in MB events. b) Transverse momentum of charged particles in MB events.

9.2.3 B-meson decay events

The $B_d^0 \to J/\psi K_S^0 \to \mu\mu\pi\pi$ decay mode, a 'gold plated' channel in the study of CP violation, is chosen to illustrate the Tracker performance in reconstructing the kinematics of B-mesons decays. The accompanying $\bar{B}_d^0$ meson is required to decay semileptonically into a muon. The generation is performed using the $b\bar{b}$ event simulation package [9-1], based on PYTHIA. The sample contains the proper mixture of events generated by gluon fusion and by gluon splitting. All decay products are required to be within the region $|\eta| \leq 2.4$ and only pions with $p_T \geq 0.5$ GeV/c are selected.

The muons produced from the J/ψ decay are required to reach at least two muon stations in order to be identified. To tag the flavour of the accompanying meson, the highest p_T muon not originating from the J/ψ decay is used. To prevent the trigger from introducing artificial charge asymmetry, the tagging muon must reach two muons stations in a region where the detector acceptance and the triggering probability are equal for positive and negative muons. Of the three muons considered, at least two are required to satisfy the trigger requirements. Approximately 3700 events, corresponding to 0.5% of the initial sample, are selected. The total number of $B_d^0 \to J/\psi K_S^0 \to \mu\mu\pi\pi$ events per year satisfying these criteria is expected to be ~32000 at $\mathcal{L}$=10^{33} cm^{-2}s^{-1}. Figure 9.2 illustrates the kinematics of the particles to be reconstructed.

9.2.4 Di-jet events

To evaluate the Tracker performance for charged tracks within high p_T jets, several samples of $u\bar{u}$ events with jet E_T ranging from 20 GeV to 200 GeV were generated in the pseudorapidity interval $|\eta| \leq 2.5$. To study the b-tagging efficiency, $b\bar{b}$ events with jets of diverse E_T and η are used. We required explicitly that the b quark be contained in the jet cone, neglecting in this way the model-dependent inefficiency due to hard gluon emission that may occur during the b quark evolution. The b-tagging fake rate is studied using $u\bar{u}$ events. To estimate the intrinsic capability to reject fake tags, we use the subset of events that do not contain b or c quarks generated by gluon splitting. Jets are clustered in cones of radius $R = \sqrt{\Delta\eta^2 + \Delta\phi^2} = 0.4$ by the PYTHIA routine LUCELL, using exclusively the Monte Carlo generator information. The charged track multiplicity within jets as a function of jet E_T is shown in Fig. 9.3 for tracks of any p_T (closed dots) and for tracks with $p_T \geq 0.9$ GeV/c (dashed line). The transverse momentum

of charged tracks within the jet cones is shown in Fig. 9.4 in which only tracks with p_T larger than 0.9 GeV/c are considered.

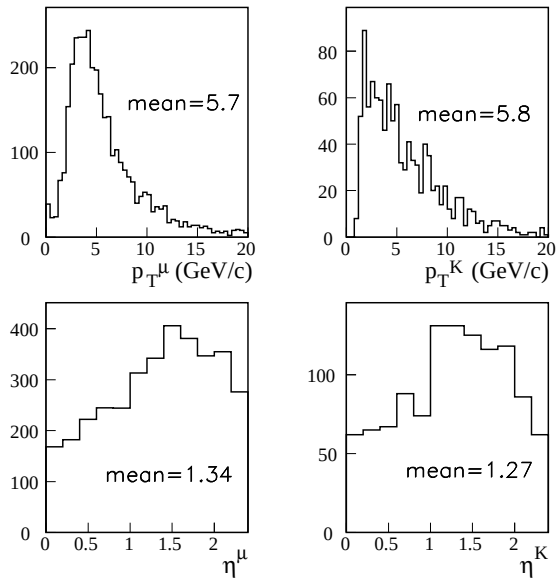

Fig. 9.2: Kinematic properties of the K_S^0 and of the muons produced by the J/ψ and $\bar{B}_d^0$ decays.

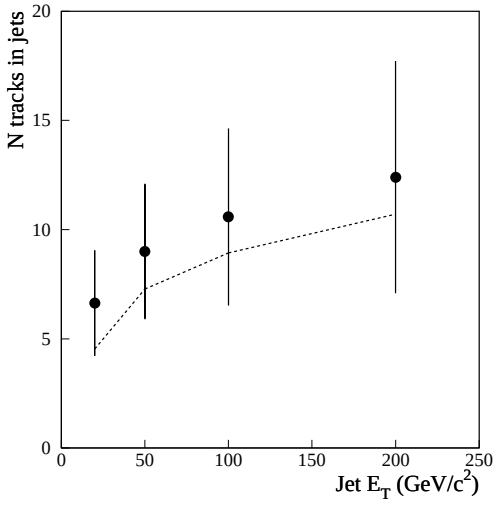

Fig. 9.3: Charged particle multiplicity in jets as a function of jet E_T.

9.3 Single Track Performance

A reconstructed track is described in the CMS convention by six parameters: x_{imp}, y_{imp}, z_{imp}, ϕ_0, c and $\cot\theta$. The quantities x_{imp}, y_{imp}, z_{imp} measure the coordinates of the impact point, i.e. the point on the track trajectory set at the distance of closest approach to the nominal vertex (0,0), measured in the transverse plane. The azimuthal angle of the tangent to the track at the impact point, ϕ_0, and $\cot\theta$ measure the pointing direction of the track, with θ the track polar angle. The signed curvature c is expressed by $B_z q/p_T$, where B_z is the longitudinal component

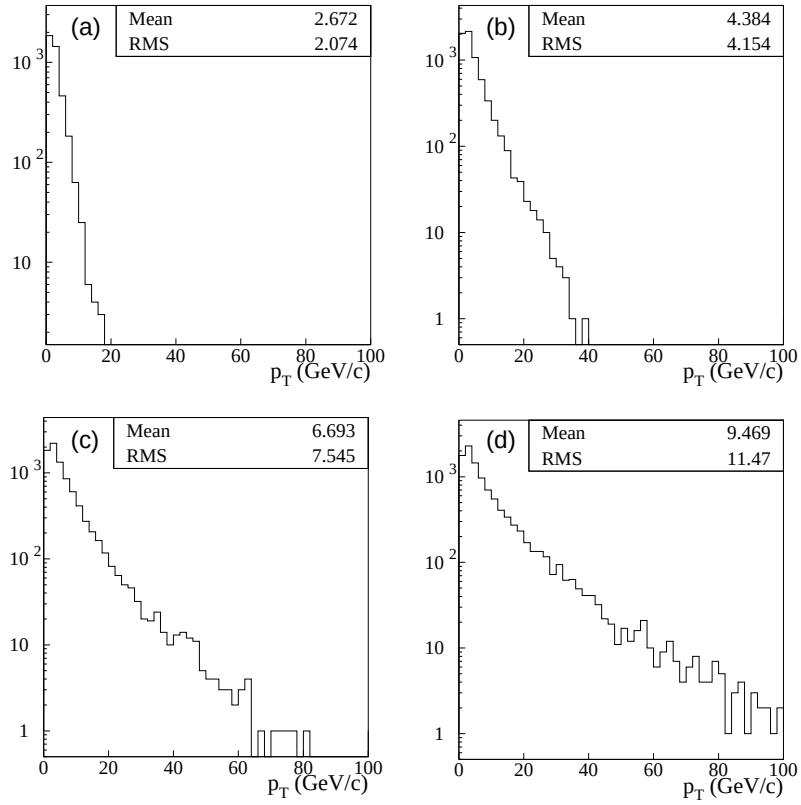

Fig. 9.4: Transverse momentum of tracks in jets of a) 20 GeV E_T b) 50 GeV E_T, c) 100 GeV E_T and d) 200 GeV E_T. All tracks have $p_T \geq$0.9 GeV/c and are within R=0.4 from the jet axis.

of the magnetic field, q and p_T are the particle charge and transverse momentum. The accuracy of the track parameter measurement is estimated using muons of several p_T values. Tracks are reconstructed using the Global Track Finder algorithm (GTF); a comparison between the performance of GTF and the Connection Machine algorithm (CM) is briefly discussed in the next section.

9.3.1 Impact parameter resolution

We define the transverse impact parameter as $d_0 = y_{imp}\cos\phi_0 - x_{imp}\sin\phi_0$. The precision of the impact point measurement is dominated by the Pixel hit position resolution and affected by multiple scattering in the innermost Pixel layer. The d_0 resolution is shown in Fig. 9.5 for the Phase I Tracker layout. We define the d_0 resolution as the difference of the reconstructed and generated parameters and we neglect any deterioration due to misalignment. The track origin is smeared according to the expected Gaussian fluctuations ($\sigma_x = \sigma_y = 15$ μm and $\sigma_z = 5.3$ cm). For high p_T tracks, the accuracy is dominated by the precision of the measurement in the innermost Pixel layer, located at a distance of 4 cm from the beam line; the resolution is independent of η and is about 9 μm. The d_0 resolution is limited by multiple scattering when the track transverse momentum is smaller than 10 GeV/c; the visible degradation at large pseudorapidity reflects the increase of the material traversed by the tracks. In the Phase II layout, the innermost Pixel layer is set at a larger radius (7 cm) and the estimated asymptotic resolution is 12 μm, as shown in Fig. 9.6.

The z_{imp} resolution is shown in Fig. 9.7 for the Phase I Tracker. At low momenta, the presence of multiple scattering degrades the z_{imp} resolution and a strong dependence on $|\eta|$ is

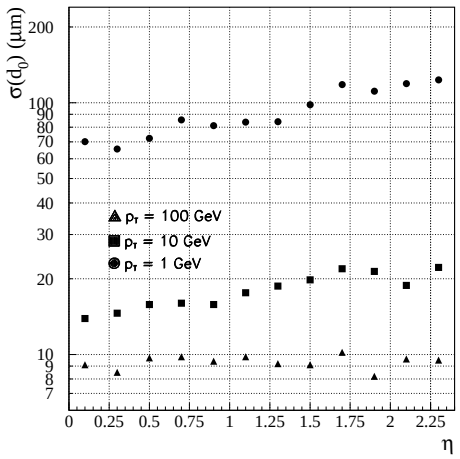

Fig. 9.5: d_0 resolution as a function of η for muons of several p_T values. Phase I CMS Tracker Layout.

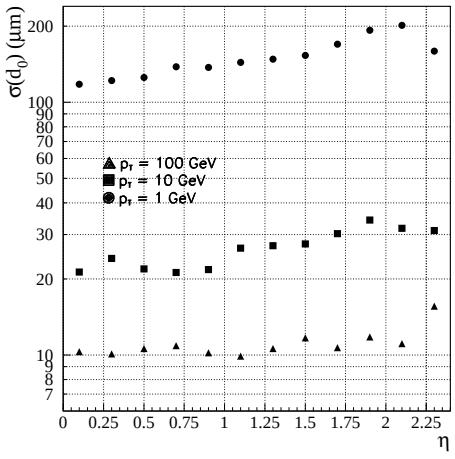

Fig. 9.6: d_0 resolution as a function of η for muons of several p_T values. Phase II CMS Tracker Layout.

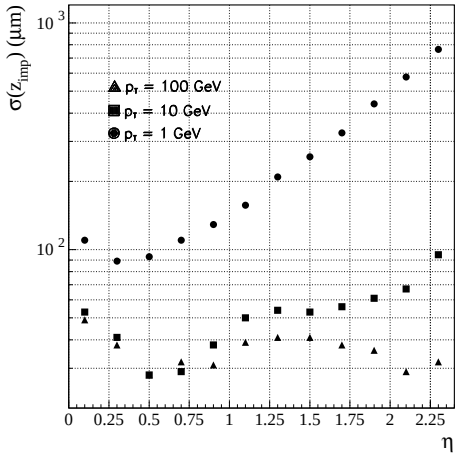

Fig. 9.7: z_{imp} resolution as a function of η, for muons of p_T =1, 10 and 100 GeV/c. Phase I CMS Tracker Layout.

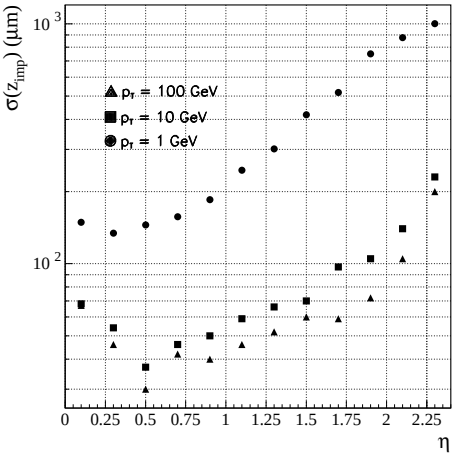

Fig. 9.8: z_{imp} resolution as a function of η, for muons of p_T =1, 10 and 100 GeV/c. Phase II CMS Tracker Layout.

observed. When high p_T muons are measured by the Pixel barrel, the z_{imp} resolution can be approximated by $\sigma_z \sqrt{r_1^2 + r_2^2}/(r_2 - r_1)$, where σ_z is the Pixel hit resolution and r_1, r_2 represent the radii of the Pixel barrel layers. This expression is calculated assuming that the impact parameter is measured using information from only the two Pixel layers. The hit z-resolution varies as a function of η and the cluster size yields the best resolution at $\eta \sim 0.5$. At large η, a degradation of the Phase II detector performance is observed with respect to the Phase I Tracker. In Phase I the innermost Pixel layer extends up to $|\eta| = 2.3$ whereas in the Phase II Tracker the z_{imp} measurement at large pseudorapidity ($|\eta| \geq 2$) is provided exclusively by the

Pixel endcaps. In the forward detectors, which measure the radial position with precision σ_r, the z_{imp} resolution depends on η as $\sigma_r \cot\theta$, as shown in Fig. 9.8 for high p_T tracks.

The comparison between the d_0 resolution estimated by two different pattern recognition algorithms, GTF and CM, is shown in Fig. 9.9. High p_T muons are used in order to disentangle the intrinsic hit precision and fitting performance from multiple scattering effects. Since no significant differences are observed between the two algorithms, only the GTF performance is described in the rest of this section.

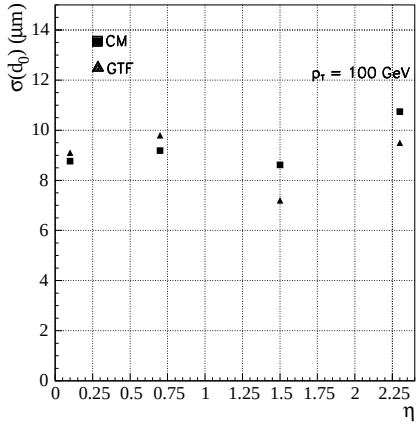

Fig. 9.9: d_0 resolution measured using the two track reconstruction algorithms, GTF and CM. Phase I Tracker layout.

9.3.2 Transverse momentum resolution

The precision of the track curvature measurement is discussed here in terms of $\sigma(p_T)/p_T$. Fig. 9.10 shows the transverse momentum resolution as a function of η for muons traversing the Phase I Tracker. No beam constraint is imposed during the fitting procedure. The momentum resolution for high p_T tracks ($\sim$ 100 GeV/c) has a modest dependence on pseudorapidity in the interval $|\eta| \leq 1.7$, in which we measure $\sigma_{p_T}/p_T \sim$ 1-2%. At larger $|\eta|$ the resolution worsens as the Tracker lever arm decreases. For lower p_T tracks, multiple scattering becomes significant and induces an η-dependence on the momentum resolution, reflecting the amount of material traversed by the tracks. The Phase II and Phase I detectors perform equally well, as can be observed by comparing Figs. 9.10 and 9.11.

9.3.3 Angular resolution

The ϕ_0 resolution measured with the Phase I and Phase II tracking detectors is shown in Figs. 9.12 and 9.13, respectively; it is fairly independent of η due to the constant number of precision hits over the full pseudorapidity range. The $\cot\theta$ resolution is shown in Figs. 9.14 and 9.15 for the two Tracker layouts. The accuracy of the measurement is dominated by the Pixel detector and the behaviour as a function of p_T and η is the same as for z_{imp}, discussed in Section 9.3.1.

9.3.4 Track finding efficiency

The efficiency to reconstruct single muon tracks in the Phase I detector is estimated using GTF. A track is defined to be successfully reconstructed if it shares more than 50% of the hits with the generated helix. Reconstructed tracks are required to have at least six hits. The Tracker is fully efficient for energetic muons in the whole pseudorapidity range, as shown in Fig. 9.16a.

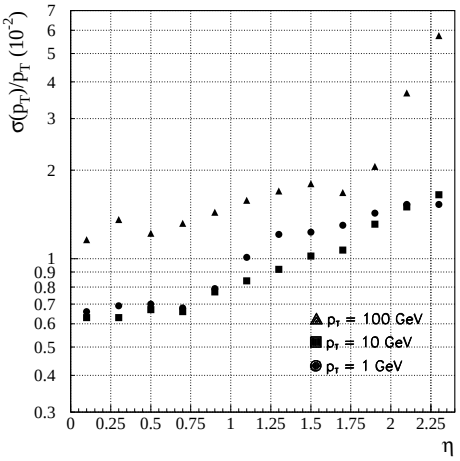

Fig. 9.10: Transverse momentum resolution as a function of η for muons of several p_T values. Phase I Tracker layout.

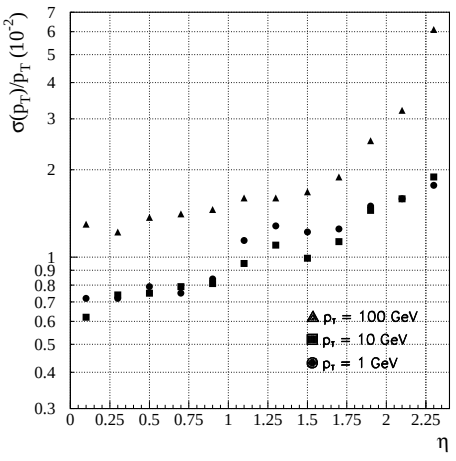

Fig. 9.11: Transverse momentum resolution as a function of η for muons of several p_T values. Phase II Tracker layout.

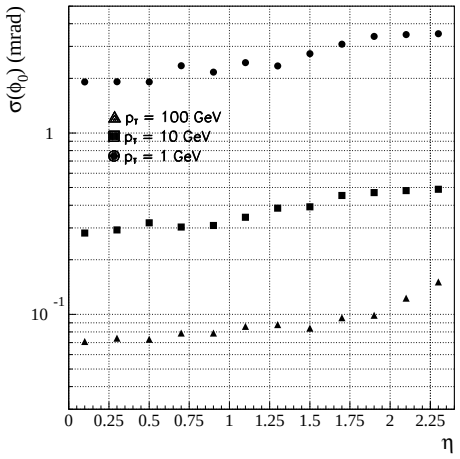

Fig. 9.12: ϕ_0 resolution as a function of η for muons of several p_T values. Phase I CMS Tracker Layout.

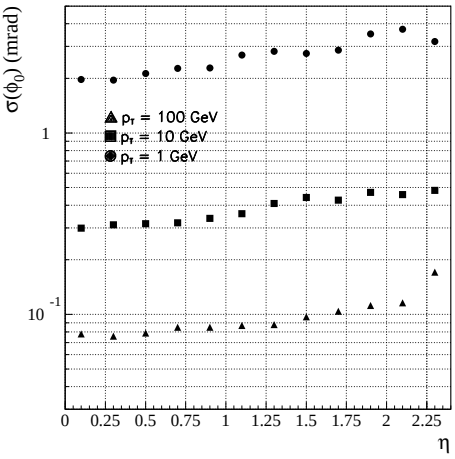

Fig. 9.13: ϕ_0 resolution as a function of η for muons of several p_T values. Phase II CMS Tracker Layout.

A drop in efficiency of about 2% is observed for muons of $p_T = 1$ GeV/c in the region around $\eta = 1$, due to the gap between the barrel and endcap MSGC detectors. In this region the hermeticity of the MSGC Tracker deteriorates slightly and low p_T tracks are affected by the additional reduction of hit reconstruction efficiency due to cluster splitting (Fig. 7.55). GTF makes use of backward propagation and therefore is slightly penalised by the lack of outer hits to seed the track as well as by the occasional loss of two subsequent hits. Moreover, a sizeable amount of material is present in the barrel-endcap transition region, contributed by the barrel services and end-flanges.

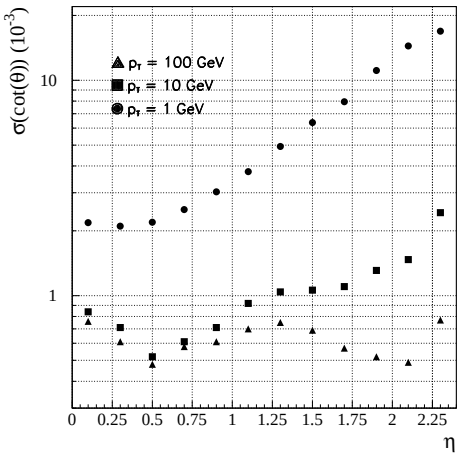

Fig. 9.14: $\cot\theta$ resolution as a function of η, for muons of several p_T values. Phase I CMS Tracker Layout.

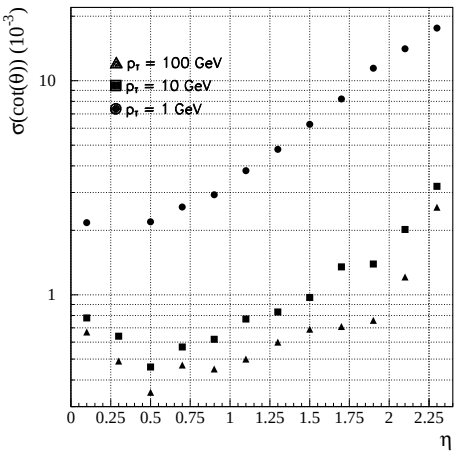

Fig. 9.15: $\cot\theta$ resolution as a function of η, for muons of several p_T values. Phase II CMS Tracker Layout.

In Fig. 9.16b a tighter definition of efficiency is used: a track is considered as properly reconstructed if all of the parameters of the fitted helix differ from the true value by less than five times the fitted error. The efficiency remains very high, which demonstrates the good quality of the fit.

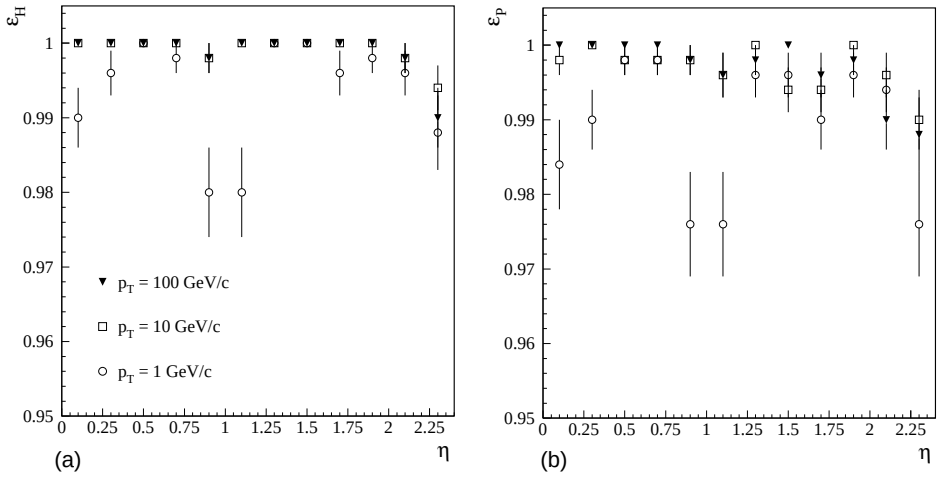

Fig. 9.16: Track finding efficiency for single muons as a function of pseudorapidity, for three different values of the transverse momentum. In (a) the efficiency is defined on the basis of the number of correct hits associated to the fitted track. In (b) a tighter criterion is applied, based on the quality of the fit, as explained in the text.

9.3.5 Charge assignment efficiency

The strong magnetic field in which the Tracker operates provides an excellent charge determination capability. The charge mis-assignment probability is estimated as a function of pseudo-

rapidity for muon tracks of transverse momentum between 1 and 4 TeV/c. Results are shown in Fig. 9.17.

The functional dependence on the pseudorapidity is directly related to the behaviour observed for the momentum resolution. The increase around $\eta = 1$ is due to the gap between the MSGC barrel and endcap. The marked increase at $\eta > 1.7$ is due to the lever arm reduction at the end of the MSGC endcap.

The charge mis-assignment probability for tracks of $p_T = 1$ TeV/c is about 10^{-4} in the barrel region and increases up to 0.5% at the largest pseudorapidity. In the barrel, the charge of tracks with $p_T = 4$ TeV/c is reconstructed with a mis-assignment probability of a few percent.

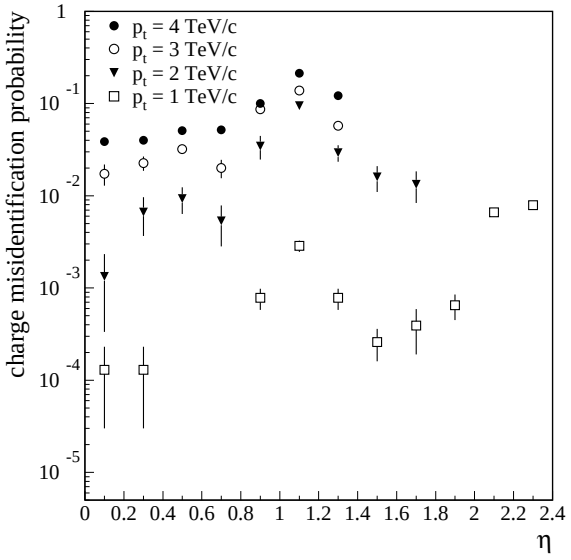

Fig. 9.17: Charge misidentification probability for high p_T tracks as a function of pseudorapidity.

9.3.6 Tails of distributions

The quality of track reconstruction can be studied by analysing the *pull* distributions of the estimated parameters. Pull distributions are defined here as the difference between the reconstructed and generated parameters, normalised to the error on the fitted parameter. A pull distribution of the $1/p_T$ variable, obtained for 10 GeV/c muons at $\eta \leq 0.2$, is shown in Fig. 9.18. The distribution has $\sigma = 1.01$. In order to investigate deviations from a Gaussian behaviour, a study of the pull tails was performed. The 'tail fraction' is defined as the fraction of the pull population satisfying the condition

$$\frac{|P_{reconstructed} - P_{generated}|}{\sigma_P} \geq 3\,\sigma_{pull}$$

where P is a track parameter, σ_P its error and σ_{pull} is obtained from a Gaussian fit of the core of the pull in different η intervals. For this study, the Phase II Tracker layout has been used. The x_{imp} and $1/p_T$ tail fractions are studied for low p_T muons in the pseudorapidity range $0 \leq \eta \leq 2.4$; the robustness of the track reconstruction procedure is evaluated using diverse requirements on the number and type of hits used to fit the track. Tracks with two reconstructed Pixel hits are better measured, as shown in Figs. 9.19 and 9.20. Figures 9.21 and 9.22 show the tail fractions for 1 GeV/c p_T muons, reconstructed requiring a minimum of six hits per track. A comparison is shown with the tail fraction associated to the standard requirement of eight hits per track; the tail fractions are compatible within errors. Two Pixel hits are explicitly required

in both cases. The tail fractions are larger than the value expected for a Gaussian statistics (0.27%). The deviations are partially accounted for by large multiple scattering effects and by the imperfect description of the Tracker material used in the track propagation procedure; in fact, the track reconstruction algorithm uses a simplified geometry model in which the detailed variation of material density in the detector is neglected. As mentioned in the discussion of the track finding efficiency, part of the performance deterioration is also due to badly reconstructed clusters.

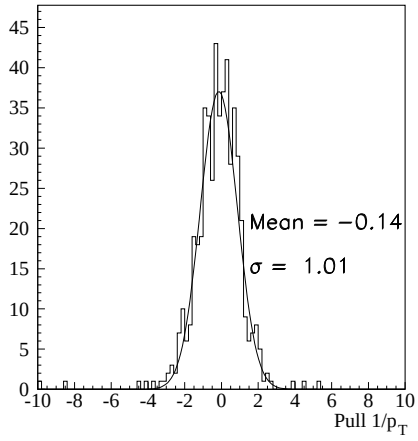

Fig. 9.18: Pull of the $1/p_T$ variable, for 10 GeV/c p_T muons at $\eta \leq 0.2$.

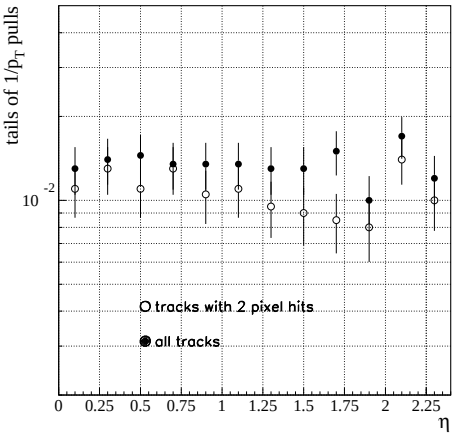

Fig. 9.19: Tail fraction for $1/p_T$ pull as a function of η for 10 GeV/c p_T muons; an explicit requirement of two Pixel hits per track is compared to the standard reconstruction procedure.

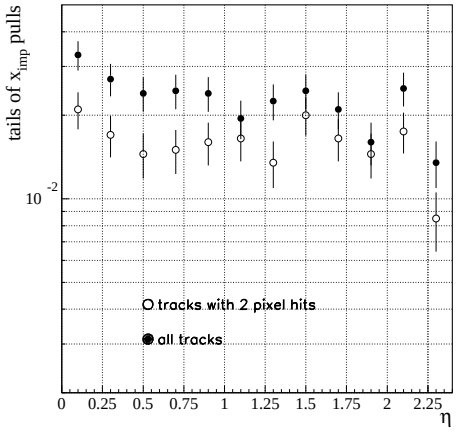

Fig. 9.20: Tail fraction of impact parameter pull as a function of η for 10 GeV/c p_T muons; an explicit requirement of two Pixel hits per track is compared to the standard reconstruction procedure.

9.3.7 Effect of pile-up

The pile-up minimum bias events generate a large number of hits in the CMS Tracker and can affect the track finding efficiency and the fit accuracy. The efficiency to reconstruct p_T =

10 GeV/c muons as a function of pseudorapidity is shown in Fig 9.23. Reconstructed tracks are required to share at least 50% of their hits with the parent helix and to have more than five or 'at least six' reconstructed clusters in the Tracker. The study is performed using GTF. The efficiency is estimated using the Phase II Tracker layout in high luminosity conditions. The track finding efficiency in absence of pile-up is also shown for comparison. No degradation of the performance is observed in the central region of the detector, whereas a loss of 1-2% is noticeable for pseudorapidities $|\eta| > 1$. A study of the tail fractions of the transverse momentum and transverse impact parameter pulls of 10 GeV/c muons is shown in Figs. 9.24. For these tracks we require two Pixel hits. The deviations from Gaussian behaviour of the $1/p_T$ and x_{imp} pulls are unaffected by the presence of pile-up events.

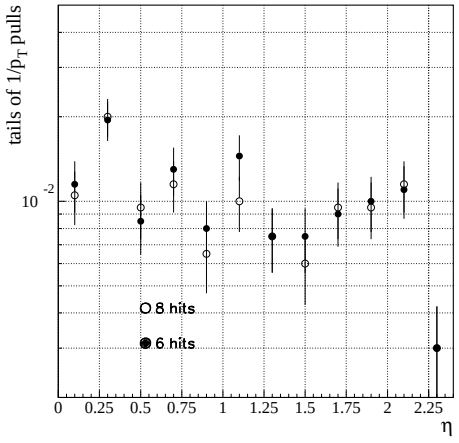

Fig. 9.21: Tail fraction for $1/p_T$ pull as a function of η for 1 GeV/c p_T muons; two different requirements are imposed on the minimum number of reconstructed hits per track. Two Pixel hits are explicitly required in both cases.

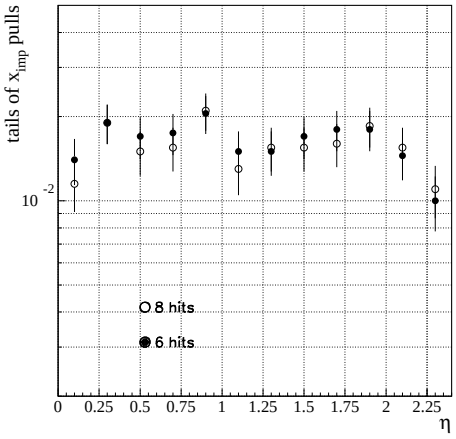

Fig. 9.22: Tail fraction for transverse impact parameter pull as a function of η for 1 GeV/c p_T muons; two different requirements are imposed on the minimum number of reconstructed hits per track. Two Pixel hits are explicitly required in both cases.

9.4 Isolated Tracks

9.4.1 Electron reconstruction

Electrons traversing the Tracker lose energy by bremsstrahlung: on average, the fraction of radiated energy is approximately 20% at $\eta \simeq 0$ and it increases up to 55% in the region where the amount of material is largest ($1.2 \leq |\eta| \leq 2.2$). Standard track reconstruction methods cannot handle sizeable variations of curvature along the track path, which may result either in low quality measurements of the track parameters or in the inability of the reconstruction procedure to identify a track candidate. The track reconstruction efficiency for electrons of 10 GeV/c and 40 GeV/c transverse momentum is shown in Fig. 9.25 as a function of pseudorapidity. Tracks are reconstructed with GTF; they are required to have more than seven hits and to share at least 50% of the hits with the parent track. The track finding efficiency is influenced by the amount of material in the Tracker. The fraction of energy lost by bremsstrahlung is estimated to be largely independent of the electron p_T and therefore low p_T tracks are penalised by larger curvature deviations in the 4 T magnetic field. The electron reconstruction efficiency and momentum

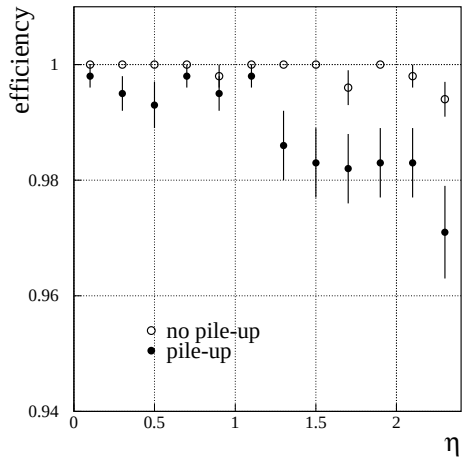

Fig. 9.23: Track finding efficiency for single muons of $p_T = 10$ GeV/c in high luminosity events. Phase II layout.

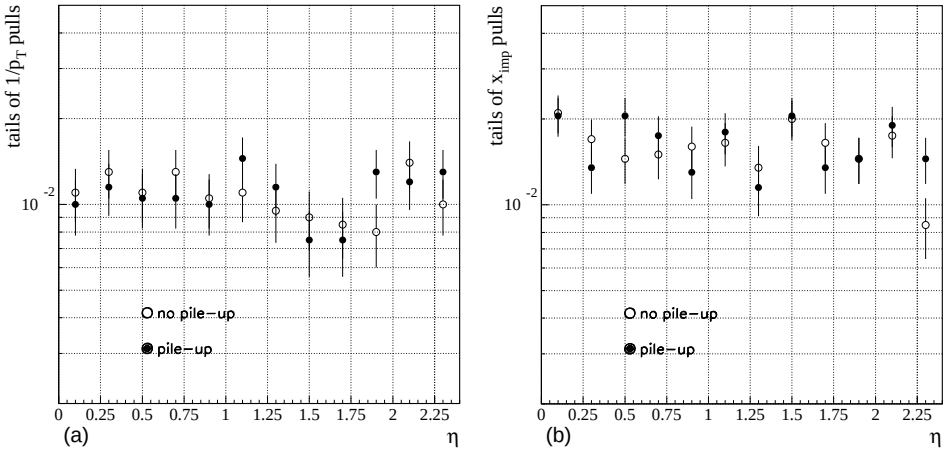

Fig. 9.24: Tail fraction for a) $1/p_T$ and b) x_{imp} pulls as a function of η for p_T =10 GeV/c muons, with and without pile-up. Phase II Tracker layout.

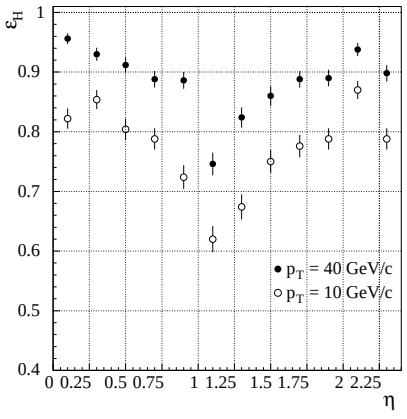

Fig. 9.25: Track finding efficiency for 10 GeV/c and 40 GeV/c p_T electrons as a function of pseudorapidity; tracks are reconstructed using GTF.

measurement can be improved by procedures recovering the effects of bremsstrahlung. In the study reported in the following, we estimate the impact of energy losses on the measurement of electrons in the CMS Tracker, and analyse the effect of a simple recovery procedure. The efficiency to reconstruct electrons of transverse momentum larger than 10 GeV/c becomes larger than 90% even in the η intervals where the Tracker material budget is largest.

9.4.1.1 Bremsstrahlung recovery method

The degradation of the electron momentum measurement due to bremsstrahlung can be partially recovered by using the estimate of the shower position in the EM calorimeter. The energy barycentre of the electron-photon shower is a good estimator of the impact point of the electron in absence of bremsstrahlung; in fact, the $r\phi$ distance between electron and photon is proportional to the fraction of the electron E_T taken by the photon. In this preliminary study, the reconstructed energy of the electromagnetic cluster is approximated by smearing the original electron energy; the position of the cluster barycentre is obtained by smearing the electron point of impact on the EM calorimeter, estimated in absence of bremsstrahlung. The resolutions we use are shown in Table 9.1. These values are obtained by scaling the resolutions estimated for photons in [1-2] by a conservative factor of about 3.5, that accounts for the possible degradation of performance in the complex scenario where the clusters of electron and photons have partial overlap.

Table 9.1: Calorimeter energy and ϕ resolution used in this study together with the expected p_T resolution of the re-fitted tracks; two electron transverse momenta and two pseudorapidity values are considered.

p_T (GeV/c)	η	σ_E (GeV)	σ_E/E (%)	σ_ϕ (mrad)	σ_{p_T}/p_T (%)
10	0.17-0.26	0.68	6.7	4.24	5
10	1.26-1.35	0.78	4.0	3.39	5
40	0.17-0.26	1.04	2.5	3.22	20
40	1.26-1.35	1.59	2.0	2.96	20

The recovery procedure begins by identifying badly reconstructed electrons. Clusters and tracks are associated by their position in the rz plane; the matching quality in the $r\phi$ plane is estimated by a χ^2 relying on the track and EM cluster information and on the E/p estimate[2]. For poorly matched tracks, the transverse momentum is recalculated using the shower barycentre, the beam constraint and the hit measured in the first Pixel layer; this procedure assumes that the bremsstrahlung occurs after the innermost measured point of the track.

The procedure is tested using electrons of 10 GeV/c and 40 GeV/c transverse momentum, generated in the pseudorapidity intervals $0.17 < \eta < 0.26$, close to the barrel centre, and $1.26 < \eta < 1.35$, near the end of the EM barrel, where a larger amount of material is encountered by particles traversing the Tracker. The p_T resolution we expect after the application of the recovery procedure is shown in Table 9.1; in the 4 T field, this measurement has an accuracy of about 5% at 10 GeV/c, limited by the angular resolution of the calorimeter. Better resolution should be achieved by the subsequent use of a Kalman filter that, starting from this momentum estimate, re-fits the whole track taking into account the emission of one bremsstrahlung photon.

[2]In the following, the notation E/p is used for E_T/p_T

9.4.1.2 Performance

Tracks are reconstructed using the GTF algorithm; the requirement that tracks have at least one hit in the Pixel detector will be referred to as a 'fiducial cut' in the following. The E/p distributions for the electrons in the four samples described in Table 9.1 are shown in Figs. 9.26 through 9.29; in each figure, the upper plot shows the raw distribution while the lower plot reports the corrected E/p distribution. The recovery of the non-Gaussian tail caused by bremsstrahlung is visible. The tails of the corrected E/p distributions are different in the $p_T = 10$ GeV/c and $p_T = 40$ GeV/c samples, reflecting the different momentum resolution for the two cases: at 10 GeV/c the recovered momentum and energy resolution are comparable with each other, whereas at 40 GeV/c the poorer resolution on the momentum yields symmetric tails in the E/p distributions.

The track reconstruction efficiencies before and after the fiducial requirement are shown in Table 9.2 and labelled as ϵ_{track} and $\epsilon_{track}^{fiducial}$ respectively. The fraction of fiducial tracks selected by the recovery procedure, $\mathcal{F}_{brems}$, is reported in the fourth column. The last two columns of Table 9.2 report the fraction of good quality tracks, i.e. those satisfying $0.85 < E/p < 1.2$, before and after recovering radiation losses ($\epsilon_{E/p}^{raw}$, $\epsilon_{E/p}^{corrected}$). The two fractions are evaluated with respect to the sample of fiducial tracks. At constant pseudorapidity, the fraction of radiated energy is independent of the electron momentum but, however, the reconstruction efficiency increases with p_T. This is due to the fact that the angle between the photon and electron directions at the emission point is smaller for higher p_T tracks, yielding a better hit collection efficiency. Conversely, the efficiency of the E/p cut is higher for the lower transverse momentum electrons, due to the better match between p_T and E_T resolution. At constant p_T, the fraction of re-fitted tracks is expected to increase with pseudorapidity, as bremsstrahlung effects become more significant. The values of ϵ_{track} reported in the table differ from the efficiency reported in Fig. 9.25 since this study of bremsstrahlung recovery was made using a less accurate description of the Tracker material budget.

Table 9.2: Track reconstruction efficiency before and after fiducial cut together with the fraction of re-fitted tracks and the efficiency of the E/p requirement.

p_T (GeV/c)	η	ϵ_{track} (%)	$\epsilon_{track}^{fiducial}$ (%)	$\mathcal{F}_{brems}$ (%)	$\epsilon_{E/p}^{raw}$ (%)	$\epsilon_{E/p}^{corrected}$ (%)
10	0.17-0.26	87.0	75	6.4	95.4	98.9
10	1.26-1.35	78.2	65	19.0	88.3	99.0
40	0.17-0.26	94.4	84.6	14.2	93.3	97.2
40	1.26-1.35	89.4	74.8	39.8	83.4	90.1

The efficiencies for reconstructing fiducial tracks with GTF are only $\sim 70\%$ in the 10 GeV/c sample and $\sim 80\%$ in the 40 GeV/c sample. The global efficiency of the recovery procedure is penalised by the fact that electrons undergoing large energy losses are often reconstructed only in the outermost part of the Tracker and fail the fiducial selection. To improve the electron reconstruction performance, the electron samples have been re-analysed relaxing the GTF cuts. This results in a non negligible fraction of events with more than one reconstructed track per generated electron (in the previous analysis this fraction vanished) in which case the track with the highest p_T is chosen. The E/p distributions before and after the recovery procedure are shown in Figs. 9.30 through 9.33. The tails of the raw distributions are much larger than in the previous study, as was to be expected.

The efficiencies of track reconstruction, fiducial selection and E/p cut are shown in Table 9.3. The electron reconstruction efficiency is substantially improved and typically more than 90% of

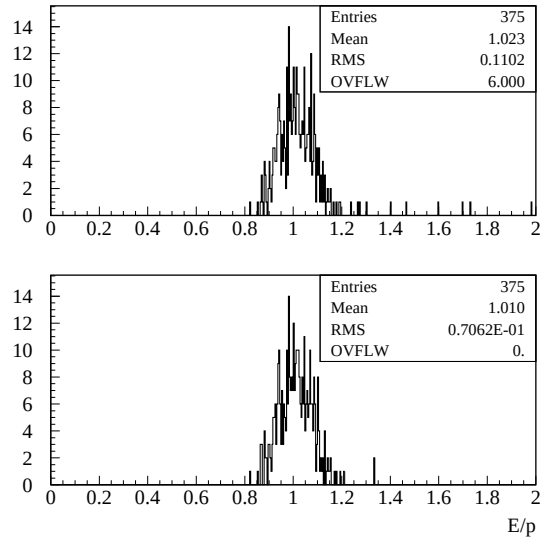

Fig. 9.26: E/p distribution before (top) and after (bottom) radiation recovery, for 10 GeV/c p_T electrons in $0.17 < \eta < 0.26$, reconstructed with GTF cuts.

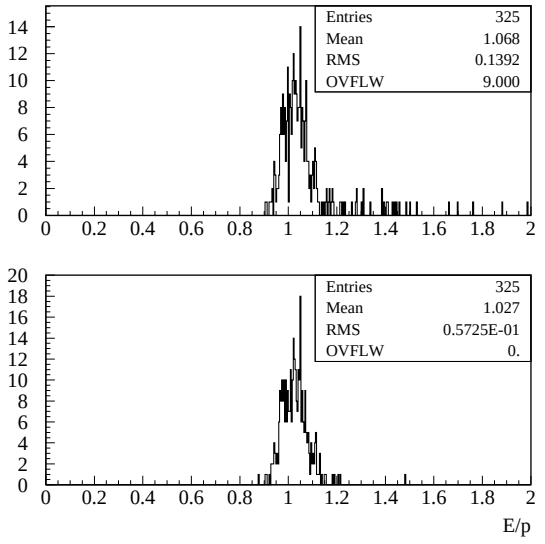

Fig. 9.27: E/p distribution before (top) and after (bottom) radiation recovery, for 10 GeV/c p_T electrons in $1.26 < \eta < 1.35$, reconstructed with GTF cuts.

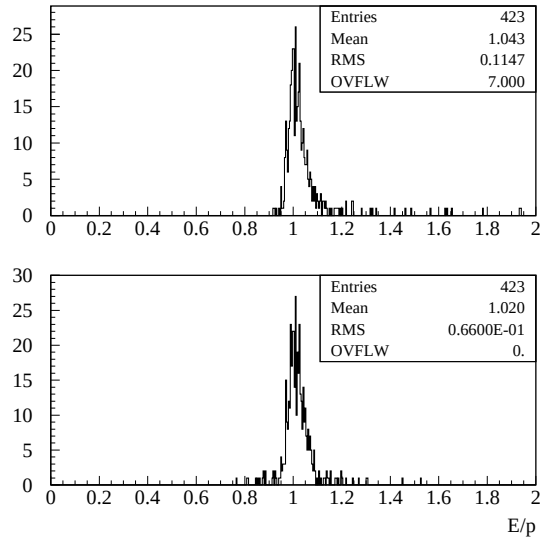

Fig. 9.28: Same as Fig. 9.26, for 40 GeV/c p_T electrons.

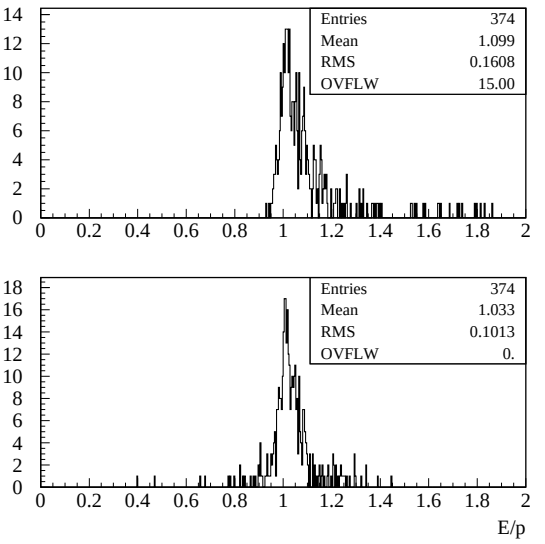

Fig. 9.29: Same as Fig. 9.27, for 40 GeV/c p_T electrons.

the tracks are now fiducial. The efficiency of bremsstrahlung recovery, defined as $\epsilon_{E/p}^{corrected} - \epsilon_{E/p}^{raw}$, has increased by a factor close to three: from 6% to 17% at small η and from 15% to 35% at large η. After correction of the track curvature, more than 95% of the electrons have values of E/p in the selected range. We report in Table 9.4 a study of the sensitivity of the recovery procedure to the assumptions made on the EM calorimeter performance.

This feasibility study shows that the transverse momentum of more than 90% of the generated electrons can be measured without the bias induced by the energy losses in the Tracker material. For more than 95% of the reconstructed electrons the E/p ratio is in the range $0.85 \leq E/p \leq 1.2$. The E/p resolution is dominated by the corrected p_T resolution for electron energies larger

than 10 GeV/c. More sophisticated reconstruction strategies, that improve the accuracy of the transverse momentum estimate, will be the object of future work.

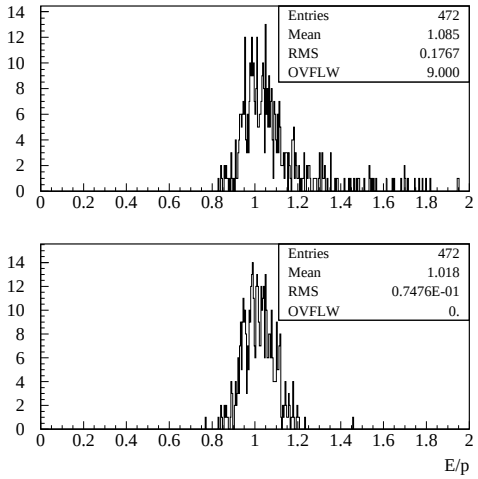

Fig. 9.30: E/p distribution before (top) and after (bottom) recovery, for 10 GeV/c p_T electrons in $0.17 < \eta < 0.26$ and using loose GTF.

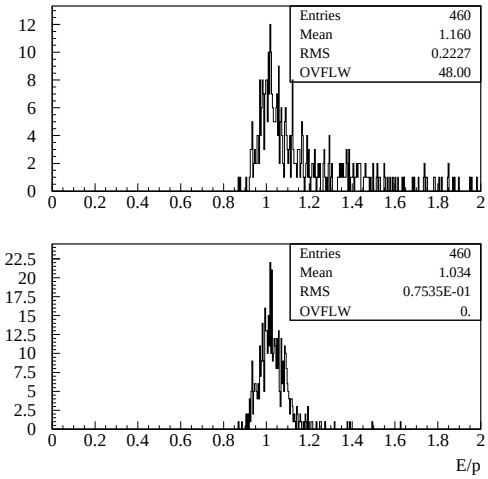

Fig. 9.31: E/p distribution before (top) and after (bottom) radiation recovery, for 10 GeV/c p_T electrons in $1.26 < \eta < 1.35$ and using loose GTF.

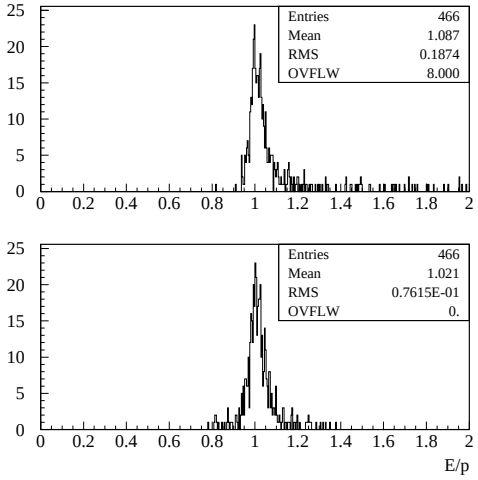

Fig. 9.32: Same as Fig. 9.30, for 40 GeV/c p_T electrons.

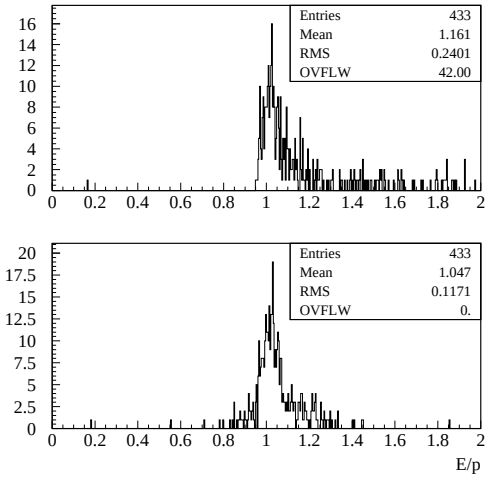

Fig. 9.33: Same as Fig. 9.31, for 40 GeV/c p_T electrons.

Table 9.3: Track reconstruction efficiency before and after fiducial cut, fraction of re-fitted tracks and efficiency of the E/p cut ($0.85 \leq \eta \leq 1.2$). Tracks are reconstructed with GTF, using looser reconstruction cuts than in previous tables, as discussed in the text

p_T (GeV/c)	η	ϵ_{track} (%)	$\epsilon_{track}^{fiducial}$ (%)	$\mathcal{F}_{brems}$ (%)	$\epsilon_{E/p}^{raw}$ (%)	$\epsilon_{E/p}^{corrected}$ (%)
10	0.17-0.26	97.3	94.4	25.6	82.8	98.0
10	1.26-1.35	96.2	92.0	50.0	64.1	97.6
40	0.17-0.26	99.2	93.2	25.1	85.6	94.8
40	1.26-1.35	97.4	86.6	51.0	67.4	88.6

Table 9.4: Efficiency of the E/p cut before and after bremsstrahlung recovery, for 10 GeV/c and 40 GeV/c p_T electrons at $\eta = 1.26$-1.35, for different assumptions on the energy and position resolution.

p_T (GeV/c)	η	σ_E (GeV/c)	σ_ϕ (mrad)	$\epsilon_{E/p}^{raw}$ (%)	$\epsilon_{E/p}^{corrected}$ (%)
10	1.26-1.35	0.26	1.13	62.3	98.4
		0.78	3.39	64.1	97.6
		0.78	6.78	63.2	95.6
40	1.26-1.35	0.53	0.99	67.6	95.3
		1.59	2.96	67.4	88.6
		1.59	5.90	67.8	76.0

9.4.2 Hadron reconstruction

9.4.2.1 Definition of efficiency

As discussed in Chapter 7 (Fig. 7.31), hadron interactions with the Tracker material must be taken into account: the average fraction of pions interacting inelastically in the interval $|\eta| \leq 2.4$ varies between 17.5% at 1 GeV/c p_T and 14% at 5 GeV/c p_T. Early interactions generate very short tracks in the detector, which are reconstructed with low efficiency by GTF and CM. To simplify the discussion, we recall here the definition of tracking efficiency:

$$\epsilon_{H,P} = \frac{N \text{ reconstructed associated tracks}}{N \text{ generated primary tracks}}$$

where tracks may be associated to the parent helix by 1) the requirement that they share at least 50% of the hits (ϵ_H), or by 2) the requirement that all track parameters differ from their true value by less than five times their fitted error (ϵ_P). An implicit requirement that there be at least six hits per reconstructed track is applied. To unfold the contribution of early interactions from the definition of efficiency, a different estimator is used: $\epsilon_{H,P}^{g6}$ is defined by comparing the reconstructed and associated tracks to the subset of the generated helices that have at least six impacts in the Tracker; an impact is defined here as the intersection between a helix and a sensor in the detector. For GTF, the six impacts have to satisfy the topological requirements discussed in Section 8.1.1, e.g. at least one impact should be in the Outer Layers and one in the Middle Layers to seed the track reconstruction procedure. In the following, $\epsilon_{H,P}^{g6}$ will be estimated with respect to those helices with at least six hits that fulfil the GTF pattern requirement.

9.4.2.2 Performance

A study of the track finding efficiency for pions of several transverse momenta was carried out using GTF and the Phase II detector; in Figs. 9.34a and 9.34b the efficiencies for reconstructing single pions, ϵ_H^{g6} and ϵ_H, are shown as a function of pseudorapidity. In Figs. 9.34c and 9.34d ϵ_P^{g6} and ϵ_P are similarly shown. The track finder is fully efficient for hard pions which collect at

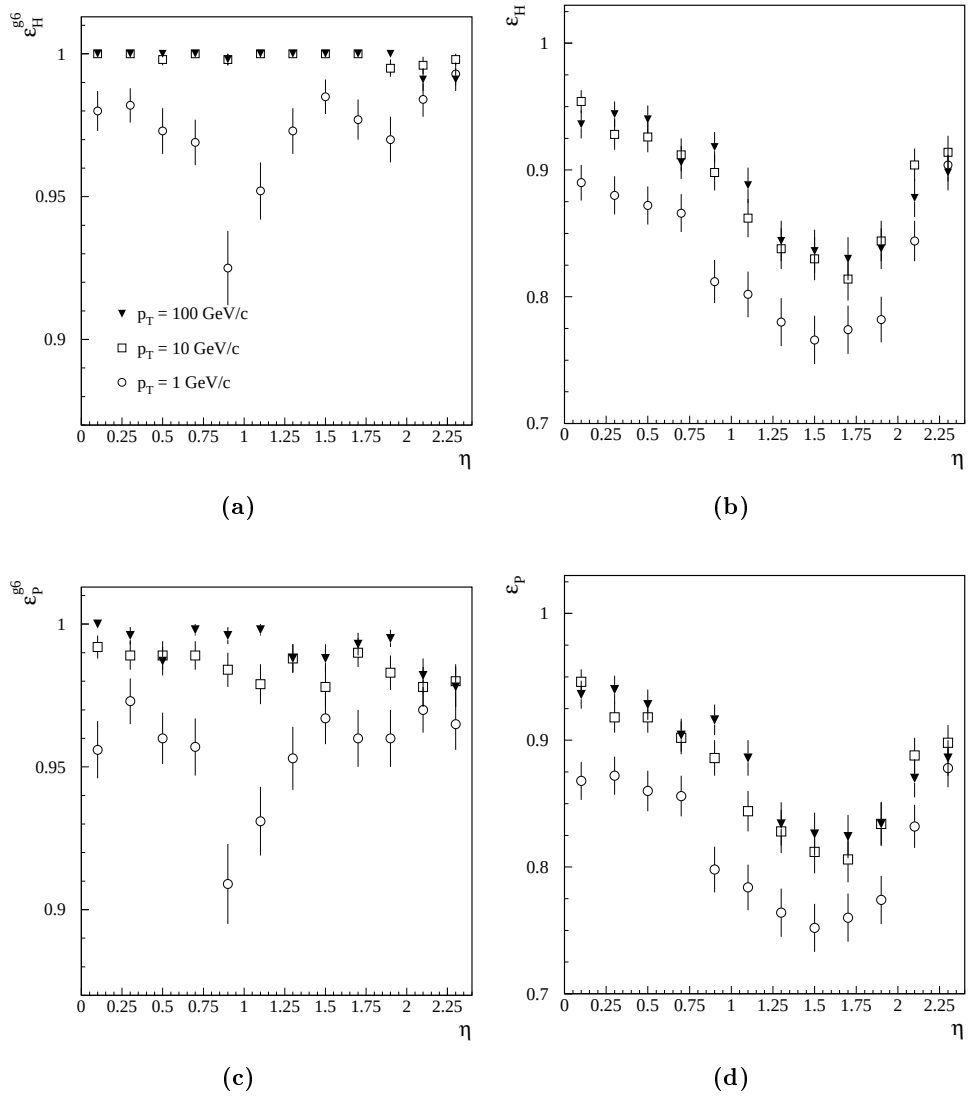

Fig. 9.34: Track finding efficiency for single pions as a function of pseudorapidity, for three different values of the transverse momentum. In (a) and (b) the association between generated and reconstructed track is based on the number of shared hits, in (c) and (d) on the accuracy of the track fit. The intrinsic performance of the track finder is shown in (a) and (c) while (b) and (d) show the global probability of reconstructing a generated track. Phase II detector layout.

least six hits in the Tracker (plot a). An efficiency drop of $2 \div 3\%$ is observed for pions of $p_T = 1$ GeV/c, increasing to $7 \div 8\%$ in the vicinity of the gap between the MSGC barrel and endcaps. The fraction of tracks that interact before depositing the required six hit pattern in the detector amounts to $5 \div 15\%$, depending on η (plots b and d). The η dependence of the inefficiency is obviously correlated to the amount of material that the particles traverse at different angles.

The quality of the hadron fit is worse than for muons, resulting in a loss of efficiency of $1 \div 2\%$ when the association is based on the accuracy of the fitted track parameters (plot c).

The pion study has been repeated for the Phase I Tracker and its results are shown in Fig. 9.35. The overall behaviour is very similar for the two Tracker layouts. The efficiency ϵ_H estimated with GTF in the Phase I detector is compatible within errors with the efficiency estimated using the Phase II layout, because the reduced tracking capability is compensated by a small reduction of the material budget. A preliminary study that relies on the Forward Kalman

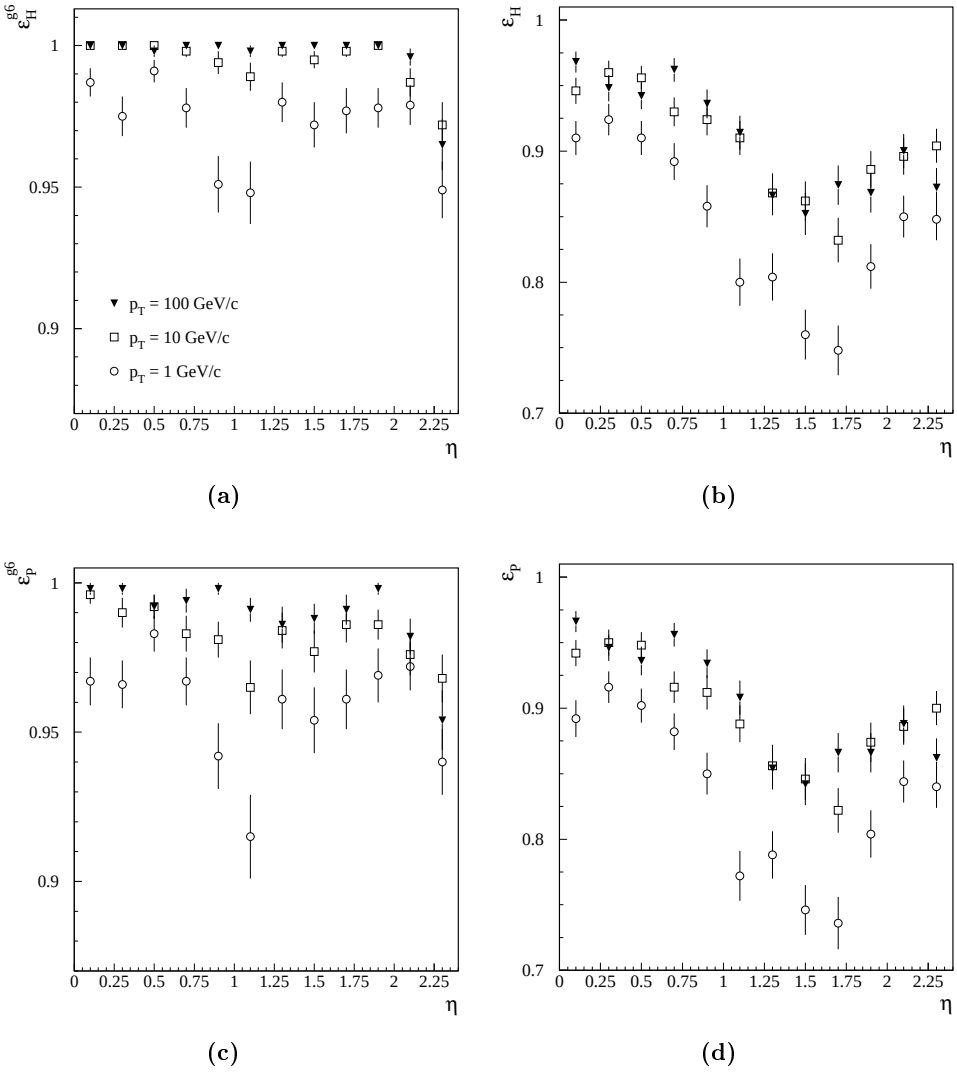

Fig. 9.35: Same study as in Fig. 9.34 for the Phase I detector configuration.

Filter algorithm (FKF) and CM[3] shows that a substantial fraction of the pion reconstruction inefficiency observed using GTF can be recovered. For FKF, the restrictions on the topology of the six impacts required for a track to be 'reconstructible', are largely relaxed. Consequently, the fraction of track candidates examined by FKF is increased with respect to GTF.

We show in Fig. 9.36 ϵ_H for muons and pions, obtained with the FKF algorithm and the Phase I configuration of the Tracker. The efficiency for muons is only slightly better than the

[3]To reconstruct hadron tracks we use FKF in the forward propagation phase and CM for the backward propagation procedure.

one obtained using GTF, while in the case of pions a substantial improvement can be observed (compare with Fig. 9.35b), due to the ability of this algorithm to reconstruct hadrons which interact in the outer silicon layers. The improvement is particularly large in the region $1 < \eta < 2$, where the performance of GTF is limited by the amount of material in the Tracker. In this region the gain in efficiency is of the order of $8 \div 10\%$, which corresponds to a reduction of the inefficiency by more than a factor of two. At the largest $|\eta|$ the track finding performance is affected by the smaller number of detectors, and the gain is more moderate. The recovery of reconstruction efficiency is expected to be even larger in the case of the Phase II Tracker, which provides more measuring stations and has a slightly larger material budget.

The average global efficiency for hadron reconstruction is larger than 90 %. This shows that a sizeable improvement in this efficiency can be achieved by using dedicated techniques.

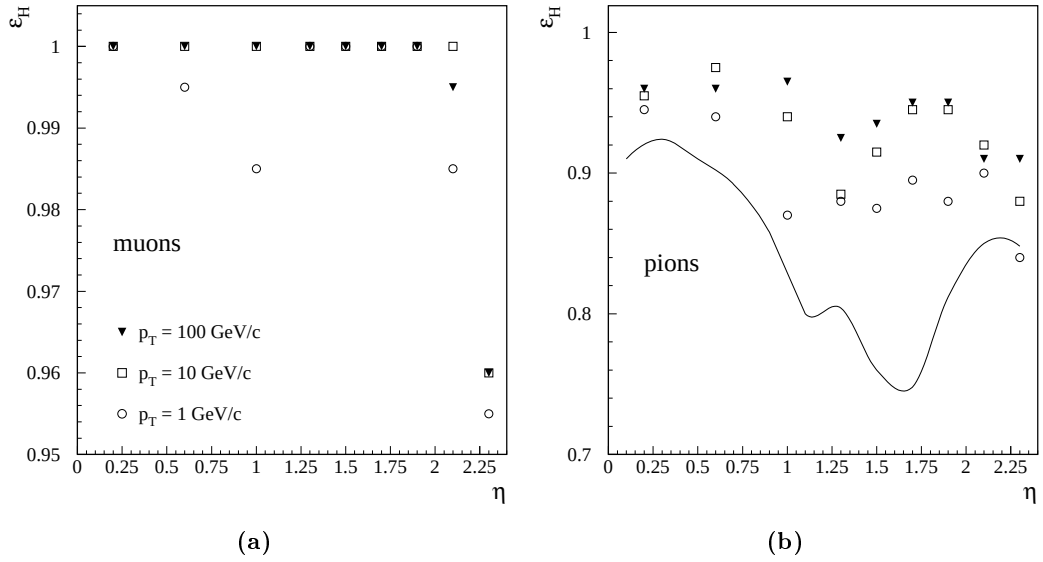

Fig. 9.36: Track finding efficiency for (a) muons (b) pions reconstructed with the Forward Kalman Filter algorithm in the Phase I detector. The solid line in (b) shows the performance of GTF. The efficiency is defined on the basis of the hits shared by the track and the parent helix.

9.4.2.3 Tails of distributions

Good reconstruction of low transverse momentum pions plays an important role in B-physics, e.g. for the reconstruction of B meson decays, and in the identification of b-jets. We test the quality of the track reconstruction by studying the tails of the transverse impact parameter and curvature pull distributions for 1 GeV/c p_T pions, as in Section 9.3.6. The tail fractions are shown in Fig. 9.37 as a function of pseudorapidity; the tail fractions for muons are also shown for ease of comparison. Muons and pions are required to register at least two hits in the Pixel detector. A non-Gaussian tail of less than 1% is observed for the pull of the $1/p_T$ variable, independent of η. The tail fraction of x_{imp} does not exceed 2%. Muon and pion tracks are reconstructed with equal accuracy.

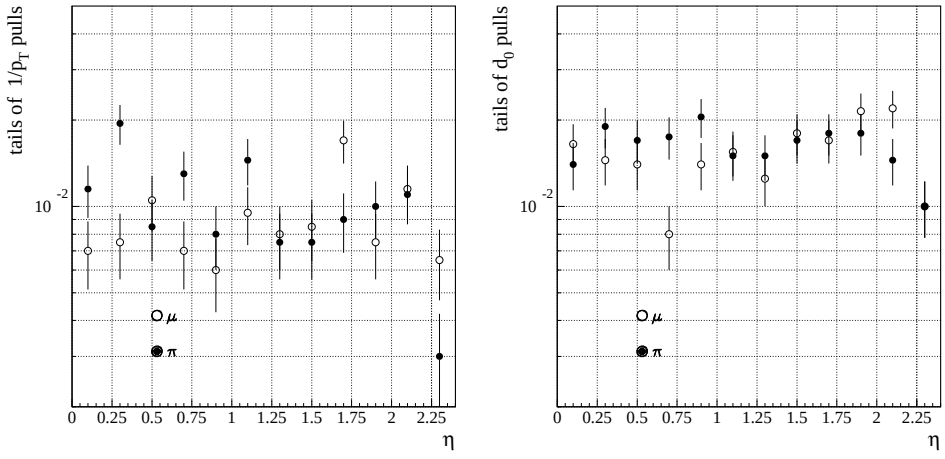

(a) (b)

Fig. 9.37: Tail fraction of the $1/p_T$ and x_{imp} pull distributions for 1 GeV/c p_T pions and muons as a function of pseudorapidity. Tracks are reconstructed using GTF; all tracks are required to have at least two hits in the Pixel detectors.

9.5 Tracks in Jets

9.5.1 Occupancy inside high p_T jets

To probe the environment in which our track finding algorithms must work, it is useful to study the occupancy within high p_T jets, representative of the topology of several physics reactions that will be studied at the LHC. Hard $b\bar{b}$ events were generated embedding 200 GeV transverse energy jets into the minimum bias pile-up events defined in Section 7.11, for high luminosity running conditions. The local occupancy (Section 7.11.2.1) reported in Fig. 9.38 is evaluated by using all clusters in detector centred within the window

$$|\Delta\phi| \leq 0.1, \quad |\Delta\eta| \leq 0.1$$

around the jet axis, defined by the direction of flight of the b quark. The local occupancy contributed by the pile-up alone is shown separately by a solid line. The local occupancies observed inside jets in the Silicon barrel detector are up to $\sim 30\%$ higher than those observed in minimum bias pile-up events. A lesser increase ($\sim 15\%$) is observed in the local MSGC occupancy. The r.m.s. width of each of these distributions is approximately 80% of its mean value.

9.5.1.1 Cluster quality

In a dense environment a wrong cluster may be attached to the track candidate, or it may happen that clusters are produced by overlapping particles. These phenomena will cause either loss of efficiency or mis-measurement of the track helix. There are three relevant factors in this context: the intrinsic hit quality, the 'road size' of the pattern recognition, and the occupancy contributed by spurious hits within the road.

Hit quality is characterised for each cluster by comparing its distance from the parent impact with the intrinsic hit resolution (σ_{res}) of the detector. If the residual distribution has sizeable tails, extending beyond the search road, the hits may be missed, or replaced by wrong ones.

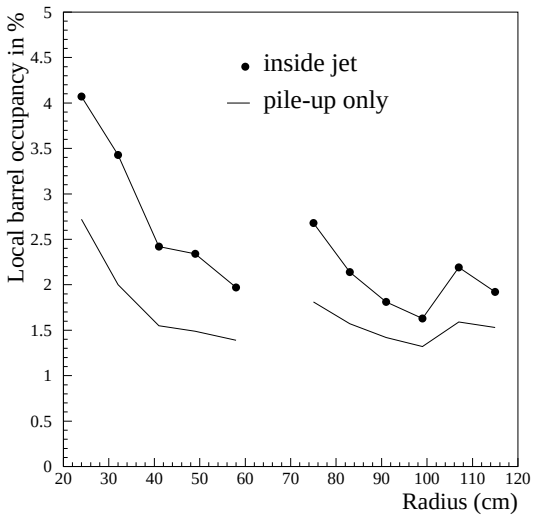

Fig. 9.38: Local barrel occupancy within 200 GeV E_T jets, in high luminosity LHC events recorded by the CMS Tracker. The pile-up contribution is shown separately (solid line).

Once the track is correctly seeded, the comparison between σ_{res}, the tail fractions and the size of the pattern recognition road illustrates the ability of the reconstruction and fitting procedure to choose good hits.

Table 9.5 summarises the σ_{res} and road sizes for the barrel detectors. To measure σ_{res}, reported in the second column, stiff tracks have been embedded inside the high p_T jets in the sample previously described. The intrinsic resolution is extracted by fitting the core of the hit residual distribution with a Gaussian function. The third and fourth columns show the fraction of hits reconstructed at a distance larger than three and five σ_{res} from the parent impact, respectively. In the fourth and fifth columns, the size of the roads used in the preliminary search of the pattern recognition and in the final iteration of the track fit are shown. The size of the road used for the initial search reflects the Kalman filter track finding strategy used by CM and GTF. Kalman filtering becomes selective only after the first few steps. At the earliest stages

Table 9.5: Resolution, tail fraction and track reconstruction roads in the CMS Tracker

Barrel layer	σ_{res} (μm)	Tail fraction $3\sigma_{res}$ (%)	Tail fraction $5\sigma_{res}$ (%)	Initial search road size (μm)	Fit road road size (μm)
Silicon - 1	13.5	8.9	5.5	272	67.0
Silicon - 2	18.8	6.2	3.8	301	83.0
Silicon - 3	18.7	4.6	3.0	509	96.0
Silicon - 4	27.9	3.9	2.4	490	111.0
Silicon - 5	28.5	3.7	2.2	1180	124.0
MSGC - 1	30.4	7.1	3.7	830	116.0
MSGC - 2	29.3	6.1	3.2	1230	119.0
MSGC - 3	29.8	6.9	3.2	2000	125.0
MSGC - 4	29.5	6.3	3.4	2000	150.0
MSGC - 5	29.5	5.7	2.9	2000	205.0
MSGC - 6	29.7	5.5	2.5		286.0

the combinatorial background can be large and fake track seeds can easily be generated in the high hit density environment found within jets. Once a track is correctly initialised, the pattern recognition road is fully efficient. The road used in the final fit (smoothing) is based on realistic error estimates and has rejection power. Clusters within $3\,\sigma_{res}$ and $5\,\sigma_{res}$ of their true position,

typically 3%, can deform the fitted helix and are partially rejected by the fitting procedure whereas most distant hits (3-6%) are mostly dropped. The non-Gaussian tails of the residual distribution are due to cluster splitting, cluster merging and to badly reconstructed hits. The 5-σ_{res} tail fraction is greatest at the innermost radius of the Tracker, where it is most affected by the presence of high luminosity pile-up.

9.5.2 Track finding performance

The efficiency to reconstruct tracks within high p_T jets is investigated using the event samples described in Section 9.2.4. The definition of efficiency used in this study is

$$\epsilon_H = \frac{\text{N reconstructed associated tracks}}{\text{N fiducial generated tracks}}$$

The reconstructed tracks are associated to the parent helix if they share more than 50% of the hits. Generated and reconstructed tracks are selected by several fiducial requirements, reported in Table 9.6. The symbols V_T and V_z represent the position of the generated event vertex in the transverse plane and along the z-axis, respectively. Looser fiducial cuts are imposed on the reconstructed tracks to allow for the finite accuracy of the track parameter measurement. The track fake rate ϵ_{fake} is defined as the fraction of non-associated reconstructed tracks. In this case the fiducial requirements for the generated and reconstructed tracks are reversed.

Table 9.6: Preselection requirements used to define the track finding efficiency.

Generated tracks	Reconstructed tracks
$p_T \geq 0.9$	$p_T \geq 0.7$
$\|\eta\| \leq 2.5$	$\|\eta\| \leq 2.6$
$V_T \leq 3$ cm	no cut on $\|d_0\|$
$\|V_z\| \leq 30$ cm	no cut $\|z_{imp}\|$

The performance of the CMS Tracker is studied using the GTF and CM track finding algorithms. The GTF reconstruction procedure requires tracks to have at least eight hits. The CM and FKF track finders are combined and used for backward and forward propagation, respectively. We shall refer to this combination simply as CM-FKF. The minimum number of hits required by CM-FKF is six and a χ^2 cut is imposed, $\chi^2/\text{ndf} \leq 7$. No smoothing procedure is applied. The reconstruction efficiency for tracks within $R = \sqrt{\Delta\eta^2 + \Delta\phi^2} = 0.4$ from the jet axis is shown in Figs. 9.39 and 9.40 as a function of the jet pseudorapidity. In the barrel part of the Tracker we estimate an efficiency ϵ_H larger than 93%. The efficiency decreases by 8-10% at larger pseudorapidity values. The behaviour of ϵ_H as a function of η is accounted for by the decrease of the hadron reconstruction efficiency at $|\eta| \geq 0.7$. This study must be compared to the one reported in Fig. 9.36b, which also explains the different ability of CM-FKF and GTF to reconstruct tracks within jets. Within the errors, ϵ_H is fairly independent of the jet E_T. The average efficiency estimated using 200 GeV E_T jets tends nevertheless to be 2-3% lower than the ones measured using softer jets. The track fake rate estimated for the Phase I Tracker is shown in Figs. 9.41 and 9.42 for CM-FKF and GTF. We estimate a track fake rate lower than 0.5% in all the event samples, when using GTF. The track fake rate depends only weakly on η. We measure instead a significant dependence of ϵ_{fake} on the jet E_T, obviously correlated to the larger track multiplicity and density within jets of increasing transverse energy. The values of ϵ_{fake} estimated using CM-FKF are larger than for GTF. In fact, the track selection used by GTF biases the track candidate samples to contain higher quality tracks than those preselected by CM-FKF, which pays a small price for a much higher track finding efficiency than GTF. We performed a similar study using GTF and the Phase II Tracker layout. The values of ϵ_H and

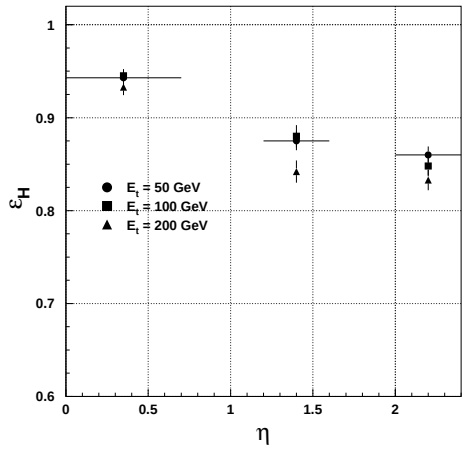

Fig. 9.39: Track reconstruction efficiency within jets as a function of jet pseudorapidity. Tracks are reconstructed with CM-FKF in the Phase I Tracker.

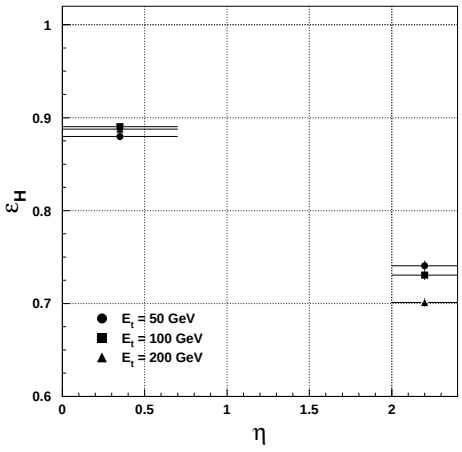

Fig. 9.40: Track reconstruction efficiency within jets as a function of jet pseudorapidity. Tracks are reconstructed with GTF in the Phase I Tracker.

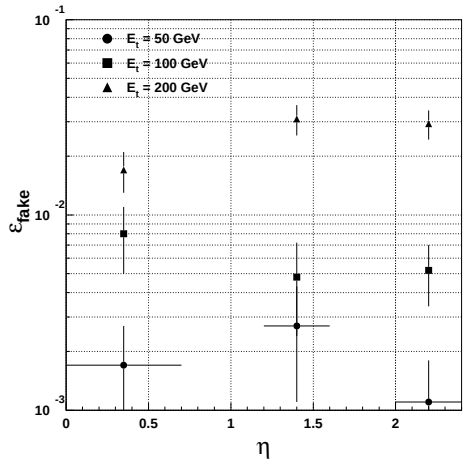

Fig. 9.41: Track fake rate within jets as a function of jet pseudorapidity and transverse energy. Tracks are reconstructed with CM-FKF in the Phase I Tracker.

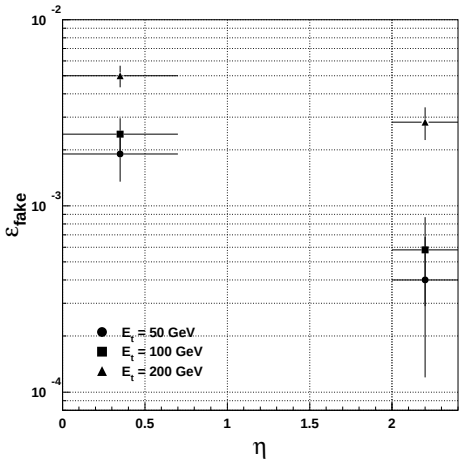

Fig. 9.42: Track fake rate within jets as a function of jet pseudorapidity and transverse energy. Tracks are reconstructed with GTF in the Phase I Tracker.

ϵ_{fake} are shown in Figs. 9.43 and 9.44. The track finding efficiencies are higher than the values measured using the Phase I detector. The ϵ_H estimate at large η is improved by $\sim 10\%$, due to the increased number of measuring stations available in the Phase II Tracker. The values of ϵ_{fake} are reduced by a factor of 1.5-2.0.

The efficiency to reconstruct tracks within jets at high luminosity conditions is shown in Fig. 9.45. The ϵ_H values are the same that we measured in absence of pile-up. The fake rate is in this case about 1% and a detailed study is presently under way.

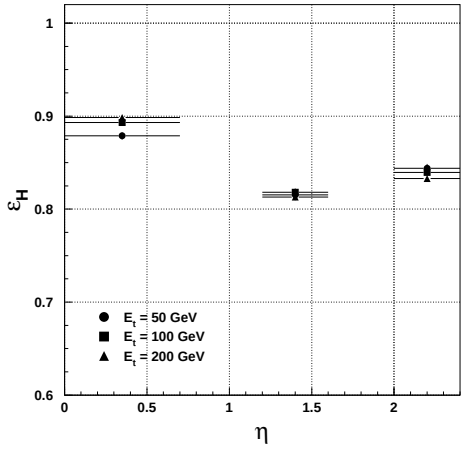

Fig. 9.43: Track finding efficiency within jets as a function of jet pseudorapidity and transverse energy. Tracks are reconstructed with GTF in the Phase II Tracker.

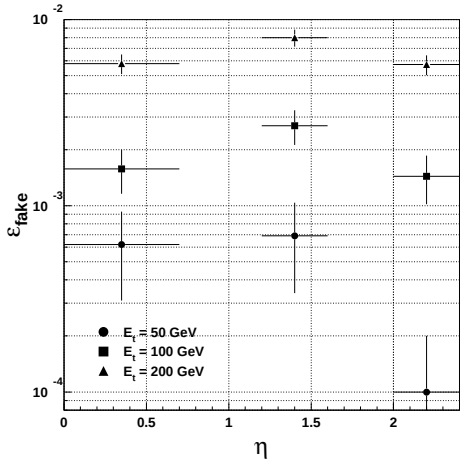

Fig. 9.44: Track fake rate within jets as a function of jet pseudorapidity and transverse energy. Tracks are reconstructed with GTF in the Phase II Tracker.

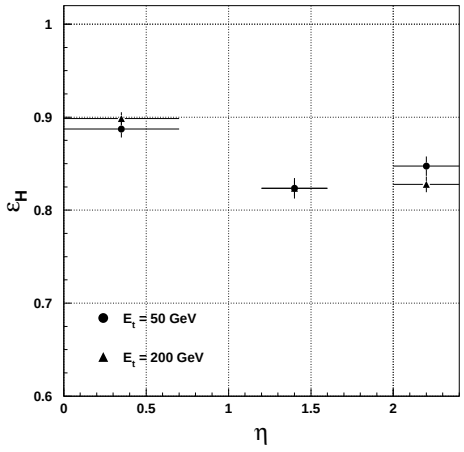

Fig. 9.45: Track finding efficiency within jets in high luminosity events, as a function of jet pseudorapidity and transverse energy. Tracks are reconstructed with GTF in the Phase II Tracker.

9.6 Vertex Reconstruction

9.6.1 Primary vertices

Our studies indicate that primary vertex location is indeed simple provided there are enough high p_T tracks in the event. To illustrate the primary vertex resolution measured with the CMS Tracker, a sample of 50 GeV E_T $u\bar{u}$ jets was generated at $|\eta| \leq 0.7$. Tracks are reconstructed using the FKF algorithm. The GVF algorithm was forced to reconstruct just primary vertices and only the tracks with impact parameter errors less than 100 μm were selected for the vertex search. The collision point is generated using Gaussian distributions of transverse spread of $\sigma_x = \sigma_y = 15$ μm and longitudinal spread of $\sigma_z = 5.3$ cm. The primary vertex resolution is shown in Figs. 9.46 through 9.49 for the Phase I and II Trackers, respectively. For this particular event

sample the z coordinate resolution is about 32 μm (26 μm) for the Phase II (Phase I) Tracker. The resolution in the transverse plane is quite comparable with the transverse beam position smearing.

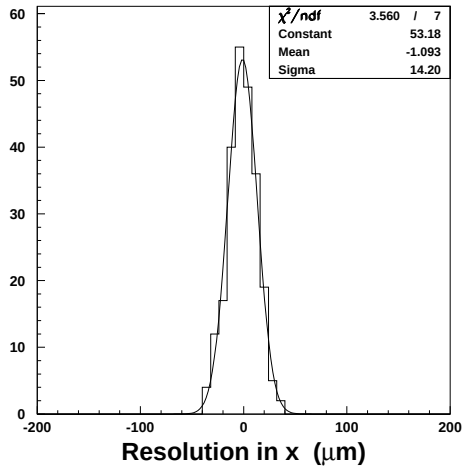

Fig. 9.46: Resolution of the x-coordinate of the primary vertex in di-jet events. Phase I Tracker.

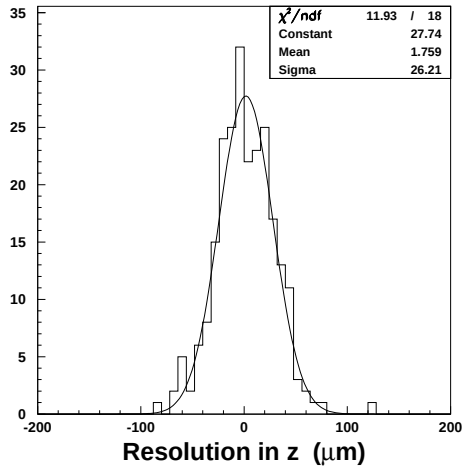

Fig. 9.47: Resolution of the z-coordinate of the primary vertex in di-jet events. Phase I Tracker.

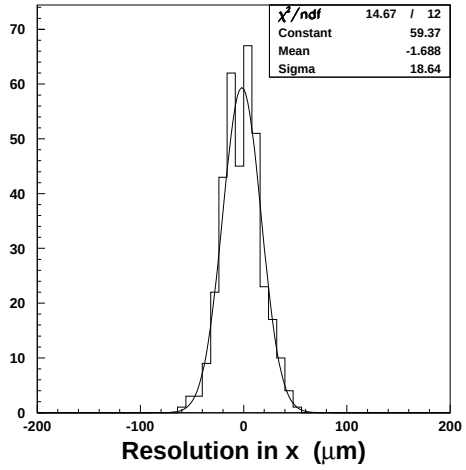

Fig. 9.48: Resolution of the x-coordinate of the primary vertex in di-jet events. Phase II Tracker.

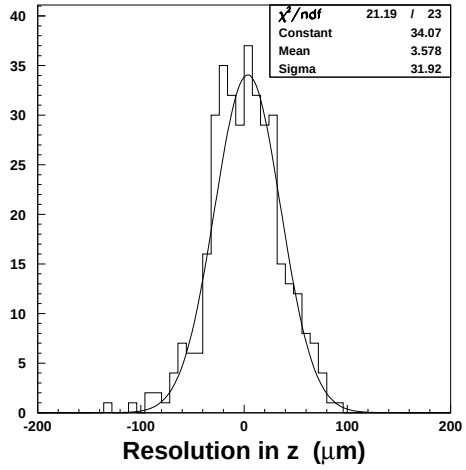

Fig. 9.49: Resolution of the z-coordinate of the primary vertex in di-jet events. Phase II Tracker.

The primary vertex resolution for $H \to \gamma\gamma$ events is studied by the PVF and GVF algorithms. The Higgs events are produced by the $gg \to H$ and the vector boson fusion production mechanisms, using the PYTHIA event generator and $m_H = 100$ GeV/c^2. The result are shown in Figs. 9.50 and 9.51, where the difference between the simulated and fitted vertex position

in z is plotted for the Phase I Tracker. Only charged tracks with $p_T > 0.6$ GeV/c are used for fitting by PVF, whereas GVF reconstructs tracks with FKF and no explicit cut on the track transverse momenta. The central part of the distributions is fitted with a Gaussian function, yielding a resolution of about 50 μm for PVF and about 60 μm for GVF. The non-Gaussian tails in the PVF distribution represent the cases for which the number of large p_T tracks is small. The efficiency of the $H \to \gamma\gamma$ event vertex finding is 100%.

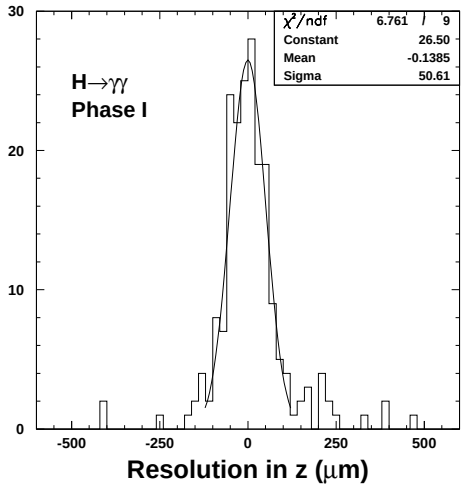

Fig. 9.50: Resolution of the z-coordinate of the primary vertex in $H \to \gamma\gamma$ events reconstructed by PVF in the Phase I Tracker.

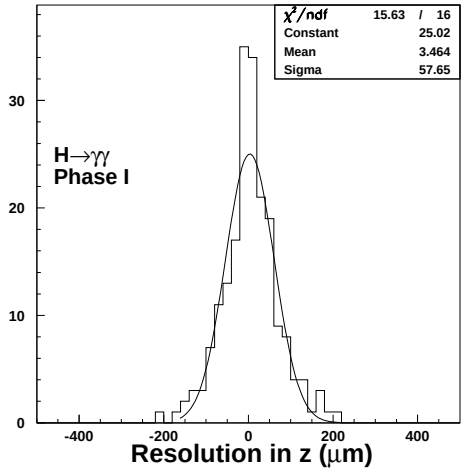

Fig. 9.51: Resolution of the z-coordinate of the primary vertex in $H \to \gamma\gamma$ events reconstructed by GVF in the Phase I Tracker.

9.6.2 V^0 vertices

9.6.2.1 Reconstruction of converted photons

As mentioned in Chapter 7, a large fraction of photons undergo conversion before leaving the sensitive volume of the Tracker. Some of the converted photons can be recovered by reconstructing the e^+e^- pair. A study of the reconstruction efficiency is performed using a sample of 10^5 photons of $p_T = 30$ GeV/c generated at $|\eta| < 0.7$. The fraction of converted photons in the central Tracker volume is found to be 20% and 22%, for the Phase I and Phase II detectors, respectively.

Tracks are reconstructed using GTF for the Phase I layout and both GTF and CM algorithms for the Phase II Tracker. The two track finders require at least six clusters along the reconstructed track. After two tracks of opposite sign have been selected, CM requires a secondary vertex to be reconstructed by GVF. The GTF efficiency to reconstruct converted photons is 29% in the Phase I detector, affected by a reduced number of measuring stations at the outer radii of the barrel. We report the efficiencies of the two methods for the Phase II Tracker in Table 9.7. The first row in the table represents the efficiency of the requirements imposed by GTF and CM for an e^+e^- pair to be 'reconstructible'. About 30% of the conversions occur at large radii and cannot be reconstructed. The second row shows the efficiency of the algorithms, i.e. the efficiency to reconstruct a preselected converted photon. The intrinsic efficiency of the track finders is obviously affected by bremsstrahlung effects, and part of the inefficiency can be suppressed by applying bremsstrahlung recovery corrections. The performance of CM is superior

Table 9.7: Efficiency of track selection criteria, intrinsic track finder efficiency and global efficiency to reconstruct photons undergoing conversion in the Phase II Tracker detector

Reconstruction algorithm	GTF	CM+GVF
Fraction of preselected photons (%)	70	
Algorithm reconstruction efficiency (%)	50	70
Global reconstruction efficiency (%)	35	50

to the one of GTF, which is biased by an initial pattern recognition road defined using the beam constraint. We report in the third row the global reconstruction efficiency, which amounts to 50% for the photons that convert in the barrel.

Once the e^+e^- pair is reconstructed, the coordinates of the photon emission point can be estimated (z^{γ}_{imp}). The obtained z^{γ}_{imp} resolution is shown in Fig. 9.52. Three different populations contribute to the z_{imp} distribution. The central part is due to very early conversions for which the Pixel detector can measure z^{γ}_{imp} with an accuracy of 75 μm in $\sim 15\%$ of the cases. The other components are contributed by conversions occurring in detectors at larger radii or in the passive volumes inside the Tracker. The r.m.s. of the overall distribution is ~ 2.6 mm. Photons whose origin is reconstructed with a precision better than 1 centimetre can be used to determine the position of the primary vertex of the reaction $H \to \gamma\gamma$. The accuracy of the z^{γ}_{imp} measurement is satisfactory for all the reconstructed photons that convert in the barrel of the Phase II Tracker.

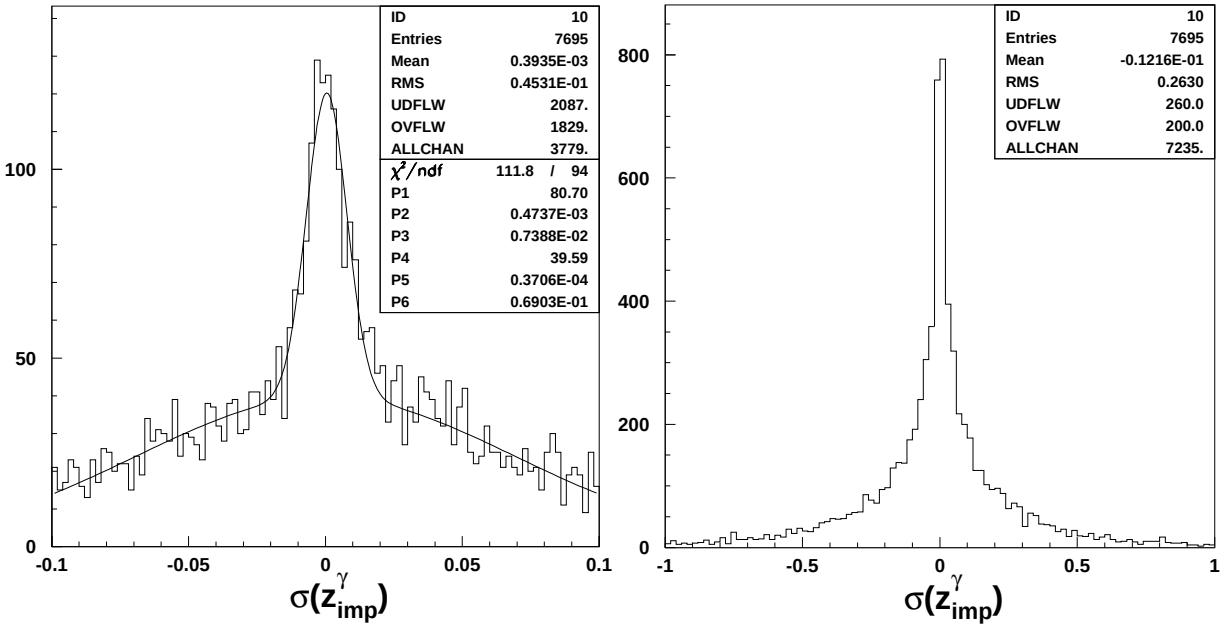

Fig. 9.52: Resolution on the z impact point of the converted photon in the Phase II Tracker layout.

9.6.2.2 K^0_S reconstruction

The V^0 reconstruction performance is tested here using samples of K^0_S generated uniformly in η with p_T values ranging between 2 GeV/c and 15 GeV/c. The Phase I Tracker is used in this study. The CM algorithm is used to reconstruct the pion tracks from K^0_S decay. The tracks are required to have at least six hits and $\chi^2/\mathrm{ndf} < 7$. Once two tracks are reconstructed, the GVF algorithm is used to reconstruct K^0_S vertex. The K^0_S candidates are accepted if the reconstructed

mass is within 25 MeV/c^2 of the K^0_S mass and the reconstructed vertex is at least $3\sigma_D$ away from (0,0) in the transverse plane, σ_D being the error on the transverse decay distance. Alternatively, when $3\sigma_D \leq 1$ cm, an explicit cut of 1 cm is used.

The reconstruction efficiency is defined as the ratio of the number of reconstructed K^0_S to the total number of generated events. No cuts on the pion p_T and K^0_S decay position are applied at the generation level, i.e. global reconstruction efficiency is estimated.

The K^0_S reconstruction efficiency as a function of pseudorapidity is shown in Fig. 9.53 For the K^0_S's generated by primary B-mesons, the efficiency is typically 50% when the decays occur in the barrel Tracker and 33% in the remaining cases. The loss of reconstruction efficiency in the region $|\eta| \geq 0.8$ results mainly from the reduced number of measuring stations in the endcaps of the Phase I detector. Additional inefficiency is due to the low efficiency of the CM track finder for tracks of $p_T \leq 0.9$ GeV/c, which characterise the low p_T kaon decays.

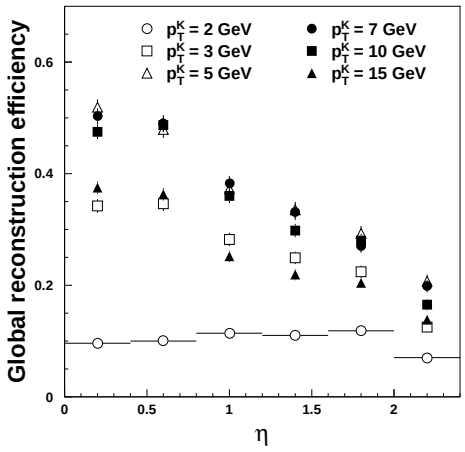

Fig. 9.53: K^0_S reconstruction efficiency as a function of η in the Phase I Tracker detector.

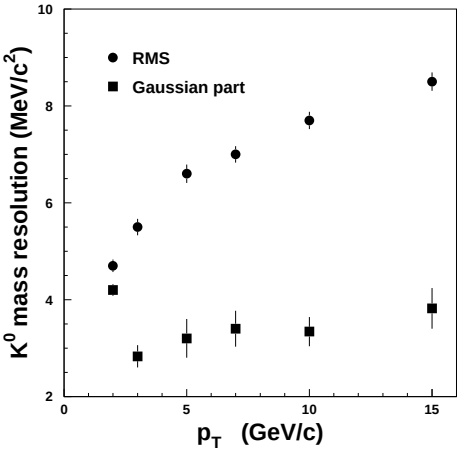

Fig. 9.54: K^0_S reconstructed mass resolution as a function of the K^0_S transverse momentum.

The reconstructed mass resolution, obtained by fitting the Gaussian part of the distribution, is about 3 MeV/c^2 and it is fairly independent of the K^0_S transverse momentum. The r.m.s. of the mass distribution varies by a factor of two as the transverse momentum of the K^0_S increases from 2 GeV/c to 15 GeV/c; the fraction of events in the 3σ-tails of the mass distribution is about 20% for K^0_S's with p_T in the range 3-7 GeV/c, and 25% for larger p_T. The characteristic p_T of K^0_S's from B-meson decay is approximately 5 GeV/c. The accuracy of the decay vertex reconstruction depends on the position at which the decay occurred: as shown in Fig. 9.56, the position resolution is ~ 0.27 mm for the early decays measured by precise detectors and about 2 mm in the remaining cases.

9.6.3 Reconstruction of $B \to J/\psi K_S$

The $B^0_d \to J/\psi K^0_S \to \mu\mu\pi\pi$ decay is a clean channel to measure $\sin 2\beta$ for CP violation studies. The event samples described in Section 9.2.3 are used to illustrate the performance of the Phase I Tracker. The following steps have been followed to reconstruct the sample of $B^0_d \to J/\psi K^0_S$ decays:

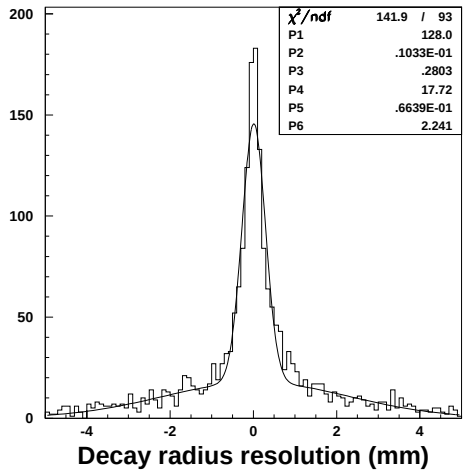

Fig. 9.55: Resolution of K^0_S decay radius.

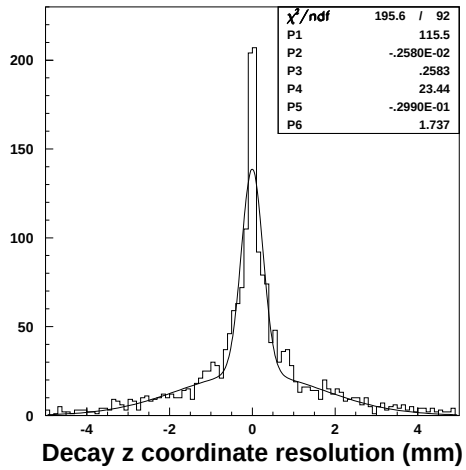

Fig. 9.56: Resolution of the K^0_S decay z position.

1. Global track reconstruction is performed using the CM algorithm with standard cuts. Tracks are required to have at least six hits with $\chi^2/\text{ndf} < 7$. An event is accepted for further analysis if there are at least 3 reconstructed muon tracks.

2. Secondary vertices are reconstructed using the GVF algorithm tuned for two-prong J/ψ and K^0_S vertices. The reconstructed J/ψ mass is required to be within a window of $\min(3\,\sigma, 70\ \text{MeV}/c^2)$ around the nominal J/ψ mass. The J/ψ vertex is required to be at least 2σ away from the beam axis. For K^0_S's, we use a mass window of $\min(3\,\sigma, 25\ \text{MeV}/c^2)$ and a transverse separation between the vertex and the beam axis of $\min(3\,\sigma,\ 1\ \text{cm})$.

3. We select a $J/\psi\ K^0_S$ pair which corresponds to a reconstructed mass inside a window of $70\ \text{MeV}/c^2$ around the nominal B^0_d mass value. We further require the reconstructed K^0_S to point to the measured J/ψ vertex and the reconstructed B^0_d mass to lie within $3\,\sigma$ around the nominal mass.

The global efficiency of this selection is 20%. The inefficiency is dominated by the K^0_S reconstruction. The efficiency to reconstruct 3 muons in an event is about 93%. Figure 9.57 shows the reconstructed mass distributions for the J/ψ and the $J/\psi\ K^0_S$ systems respectively. Gaussian fits to these mass distributions yield a resolution of $24\ \text{MeV}/c^2$ for J/ψ and $16\ \text{MeV}/c^2$ for B^0_d. The J/ψ mass resolution is about $16\ \text{MeV}/c^2$ when both muons are restricted to the barrel part of the Tracker.

Figure 9.58 illustrates the resolution of the reconstructed decay vertex of the B^0_d meson. Gaussian fits yield 40 μm resolution in the transverse plane and 74 μm resolution along the z direction.

Fig. 9.59 shows the resolution in proper time for the B^0_d decay. It corresponds to a resolution of 61 fs, estimated with a Gaussian fit to the distribution.

9.7 Heavy Flavour Identification

We use two different approaches to study the b-jet identification performance. The first method relies exclusively on the good accuracy of the track impact parameter measurement and is used

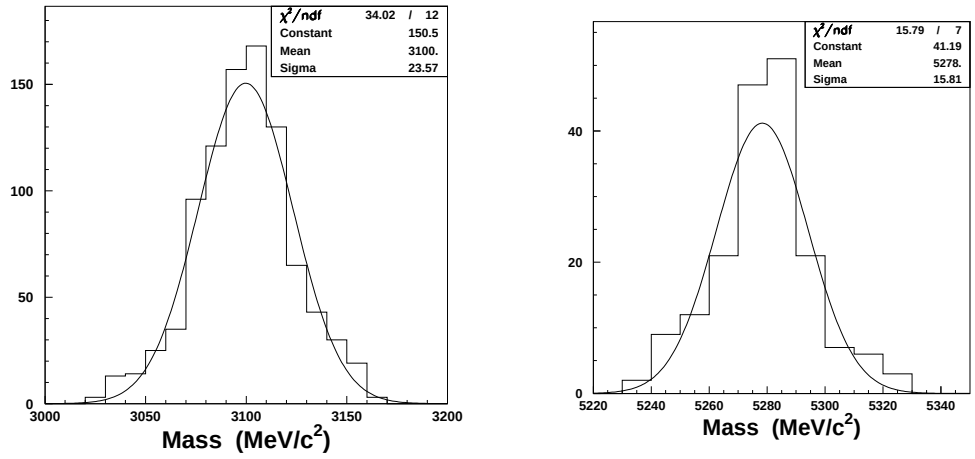

Fig. 9.57: Invariant mass of the reconstructed (a) J/ψ, (b) B_d^0 in $B_d^0 \to J/\psi K_S^0 \to \mu\mu\pi\pi$ decays.

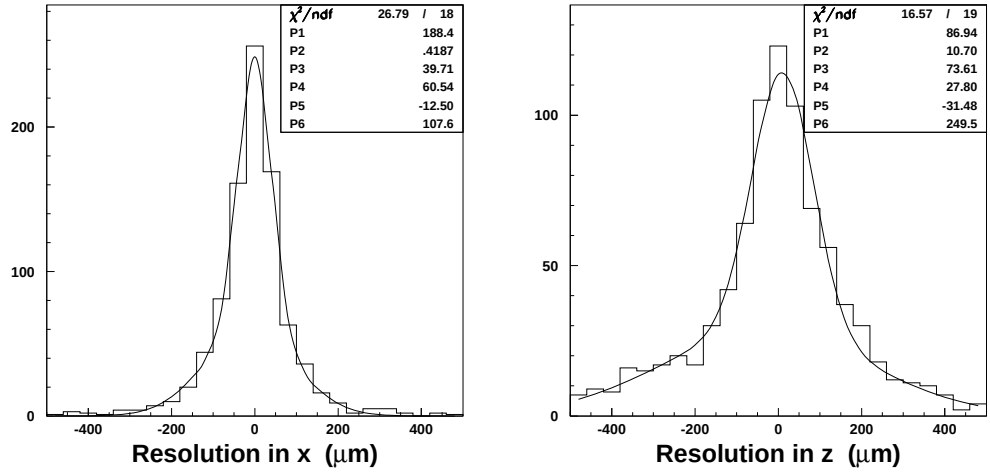

Fig. 9.58: Resolution of the reconstructed B_d^0 vertex along (a) x and (b) z axes. Gaussian fits to the cores yield 40 μm and 74 μm respectively.

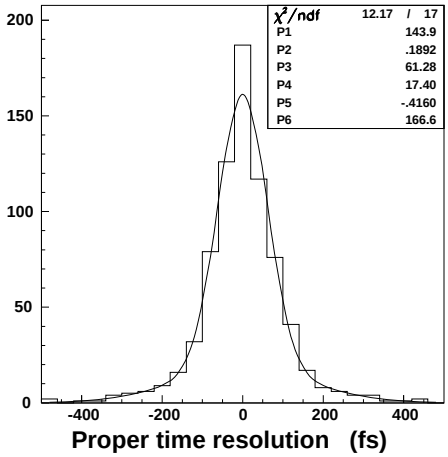

Fig. 9.59: Resolution of proper time for the B_d^0 vertex. A Gaussian fit to peak gives 61 fs.

to investigate the performance of the Phase I and II Tracker layouts. The second method relies instead on the identification of secondary vertices. To study b-jet identification we use the event samples described in Section 9.2.4.

9.7.1 Impact Parameter tagging

The $b\bar{b}$ and $u\bar{u}$ events are reconstructed using GTF, requiring at least 8 hits for track candidates. The tracks are required to lie within R=0.4 from the jet axis and to have $p_T \geq 1$ GeV/c, $d_0 \leq$ 2 mm and at least two hits in the Pixel detector. The sign of the transverse impact parameter is defined here by the sign of the projection of the impact point onto the jet axis, in the transverse plane. This definition of signed impact parameter $\vec{d_0}$ allows to neglect tracks with large impact parameter which are nevertheless 'uncorrelated' with the tracks clustered within the jet cones. A jet is considered tagged if at least N_{tr} of its tracks satisfy the condition that the signed impact parameter significance, $\vec{d_0}/\sigma_{\vec{d_0}}$, be larger than $N\sigma_{\vec{d_0}}$. Appropriate values for N_{tr} and $N\sigma_{\vec{d_0}}$ are 2 or 3, depending on the actual problem under study. Looser requirements improve b-tagging efficiency but also increase the probability to tag a non-b jet (mistagging rate). We show the b-jet tagging efficiency for jets of $E_T = 100$ GeV as a function of the mistagging rate in Figs. 9.60 and 9.61. In these figures, the b-tagging performance of the Phase I and II detectors is shown for three different η regions. At constant η the b-tagging efficiency and the mistag rate are evaluated for four of the possible requirements on N_{tr} and $N\sigma_{\vec{d_0}}$. The highest purity point is obtained by imposing the condition $N_{tr} = 3$ and $N\sigma_{\vec{d_0}}$=3, that we indicate here as $3_T \times 3_\sigma$. In increasing order of efficiency the conditions used are $3_T \times 2_\sigma$, $2_T \times 3_\sigma$, and $2_T \times 2_\sigma$. The b-tagging efficiency is highest for jets in the barrel Tracker. The efficiency drops by $\sim 10\%$ in the endcap region. On average, the mistagging rate varies within a factor two for jets at different pseudorapidities. The mistagging rate varies between 10^{-3} and 10^{-2} for the more stringent requirements $3_T \times 3_\sigma$

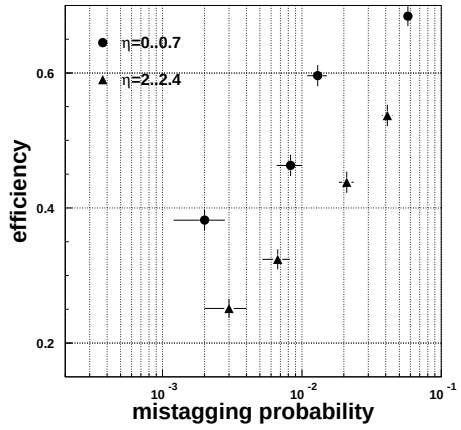

Fig. 9.60: b-tagging efficiency as a function of purity for 100 GeV E_T jets in two pseudorapidity intervals. Different tagging requirement are used and explained in the text. Phase I Tracker.

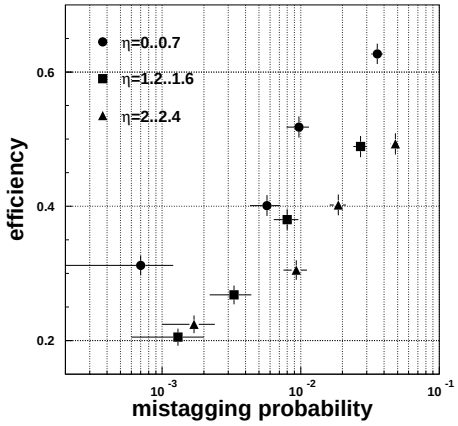

Fig. 9.61: b-tagging efficiency as a function of purity for 100 GeV E_T jets in three pseudorapidity intervals. Different tagging requirement are used and explained in the text. Phase II Tracker.

and $3_T \times 2_\sigma$. A more complete set of results is reported in Tables 9.8, 9.9 and 9.10. We have studied the tagging efficiency and the mistagging rates for jets in three pseudorapidity intervals and for three different values of the jet transverse energy. Each jet sample has been analysed by imposing the four different requirements on N_{tr} and $N\sigma_{\vec{d_0}}$ listed above. When the information is available, the performance of the Phase I Tracker is also shown in the tables. A study of the

tables shows that for equal tagging probability, the mistagging rate is slightly higher in jets of 50 GeV E_T than in the 100 GeV E_T jets. At higher jet E_T the purity decreases rapidly.

Table 9.8: B-tagging efficiency vs mistagging rate at $|\eta| < 0.7$, $p_t > 1$ GeV

	Phase I Tracker			Phase II Tracker		
$N_{tr} \times N\sigma_{\vec{d}_0}$	50 GeV	100 GeV	200 GeV	50 GeV	100 GeV	200 GeV
2×2	55.5 ± 1.6	64.7 ± 1.5	60.8 ± 1.5	48.4 ± 1.6	59.9 ± 1.6	59.1 ± 1.6
	1.40 ± 0.21	2.60 ± 0.29	6.00 ± 0.43	1.33 ± 0.21	2.40 ± 0.28	4.83 ± 0.39
2×3	46.1 ± 1.6	56.3 ± 1.6	52.9 ± 1.6	37.2 ± 1.5	48.9 ± 1.6	49.1 ± 1.6
	0.77 ± 0.16	0.77 ± 0.16	2.40 ± 0.28	0.53 ± 0.13	0.77 ± 0.16	1.73 ± 0.24
3×2	31.5 ± 1.5	44.0 ± 1.6	35.2 ± 1.5	27.0 ± 1.4	38.4 ± 1.5	34.6 ± 1.5
	0.30 ± 0.10	0.23 ± 0.09	1.17 ± 0.20	0.20 ± 0.08	0.33 ± 0.11	0.77 ± 0.16
3×3	23.5 ± 1.3	35.4 ± 1.5	28.0 ± 1.4	18.9 ± 1.2	28.8 ± 1.4	26.8 ± 1.4
	0.10 ± 0.06	0.10 ± 0.06	0.30 ± 0.10	0.07 ± 0.05	0.03 ± 0.03	0.17 ± 0.07

The Phase I Tracker has higher b-jet tagging efficiency since the barrel Pixel detector is closer to the beam pipe. The increase in efficiency for a given b-tagging requirement varies between 2% and 5% and it is in fact more remarkable in the two smaller pseudorapidity intervals considered in this study. The mistagging rates at equal tagging efficiency, are larger for the Phase II Tracker. In this study, standard GTF cuts have been used and no effort to tune the performance for b-tagging has been made. The mistagging rate can in fact be reduced and will be the object of further studies. We show a study of the b-tagging performance as a function of the p_T cut applied on the tracks used to tag the jets in Fig. 9.62a. For jets of $E_T = 100$ GeV in the barrel region of the Phase I Tracker, the tagging efficiency ($2_T \times 3_\sigma$) varies between 60%, for a cut of $p_T \geq 1$ GeV/c, and 37% if a cut $p_T \geq 5$ GeV/c is used ($3_T \times 3_\sigma$). In the same interval, the mistagging rate drops by a factor of 3. The dependence of the tagging efficiency and mistagging rate on the $\vec{d}_0$ significance is shown in Fig. 9.62b, using tracks of $p_T \geq 1$ GeV/c. The role of the Pixel detector in the b-tagging performance is high-lighted in Fig. 9.62c, which shows that at least two measurements in the Pixel detector are necessary to achieve high quality performance.

Table 9.9: B-tagging efficiency vs mistagging rate at $1.2 < |\eta| < 1.6$

	Phase II Tracker		
$N_{tr} \times N\sigma_{\vec{d}_0}$	50 GeV	100 GeV	200 GeV
2×2	39.0 ± 1.6	47.1 ± 1.6	53.6 ± 1.6
	0.90 ± 0.17	1.87 ± 0.25	4.17 ± 0.36
2×3	27.9 ± 1.4	35.8 ± 1.5	43.3 ± 1.6
	0.50 ± 0.13	0.73 ± 0.16	1.63 ± 0.23
3×2	17.9 ± 1.2	25.6 ± 1.4	29.3 ± 1.4
	0.12 ± 0.06	0.23 ± 0.09	0.43 ± 0.12
3×3	10.3 ± 1.0	18.4 ± 1.2	22.2 ± 1.3
	0.07 ± 0.05	0.13 ± 0.07	0.17 ± 0.07

9.7.2 B-tagging with 3D vertex reconstruction

The use of the vertex reconstruction for b-tagging is two-fold. As part of the vertex finding algorithms discussed in Chapter 8, all tracks are re-fitted to test explicitely for compatibility with anyone of the identified vertices. With this set of re-fitted tracks, one can improve the

Table 9.10: B-tagging efficiency vs mistagging rate at $2 < |\eta| < 2.4$

	Phase I Tracker			Phase II Tracker		
$N_{tr} \times N\sigma_{\bar{d}_0}$	50 GeV	100 GeV	200 GeV	50 GeV	100 GeV	200 GeV
2×2	42.4 ± 1.6	51.6 ± 1.6	53.7 ± 1.6	37.5 ± 1.5	46.9 ± 1.6	52.9 ± 1.6
	1.27 ± 0.20	3.17 ± 0.32	8.10 ± 0.50	1.37 ± 0.21	3.40 ± 0.33	7.07 ± 0.47
2×3	31.9 ± 1.5	42.0 ± 1.6	44.3 ± 1.6	27.3 ± 1.4	38.2 ± 1.5	42.9 ± 1.6
	0.67 ± 0.15	1.83 ± 0.24	4.80 ± 0.39	0.30 ± 0.10	1.40 ± 0.21	2.87 ± 0.30
3×2	22.5 ± 1.3	31.3 ± 1.5	30.6 ± 1.5	18.2 ± 1.2	29.6 ± 1.4	33.1 ± 1.5
	0.13 ± 0.07	0.47 ± 0.12	2.20 ± 0.27	0.10 ± 0.06	0.60 ± 0.14	1.47 ± 0.22
3×3	14.2 ± 1.1	23.6 ± 1.3	21.8 ± 1.3	11.3 ± 1.0	21.2 ± 1.3	24.4 ± 1.4
	0.07 ± 0.05	0.27 ± 0.09	$1.23pm0.20$	0	0.17 ± 0.07	0.67 ± 0.15

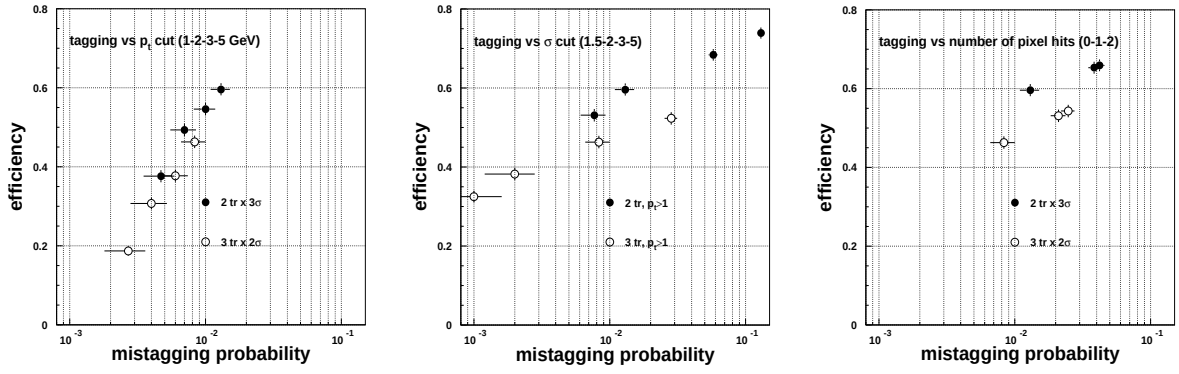

(a) **(b)** **(c)**

Fig. 9.62: Dependence of the b-tagging efficiency and mistagging rate on the a) p_T cut on the tracks within the jets, b) cut on the significance of the impact parameter and c) the number of track hits measured by the Pixel detector. Jets of E_T=100 GeV are used, generated in the barrel of the Phase I Tracker.

results of the conventional impact parameter tagging by removing the tracks associated with the primary vertices or two-prong decay vertices. This approach is referred to as Vertex Impact Parameter tagging (VIP). One can also directly use the reconstructed secondary vertices to tag b-jets (Secondary Vertex tagging, SV). Both approaches are considered for the barrel region of the Phase I Tracker detector, using the same jet event samples as above.

The track reconstruction is performed with the FKF track finder. The tracks with at least six hits, two of which measured in the Pixel detector, and $\chi^2/\mathrm{ndf} < 5$ are selected to identify b-jets. As one can see in Figs. 9.63 and 9.64 these cuts allow to control the reconstructed track quality to a good level even within the core of hard jets. The GVF vertex finder is used to reconstruct primary, secondary, K^0_S and Λ vertices. To suppress the mistagging rate, the GVF parameters were tuned to bias the algorithm to associate tracks with primary and two prong decay vertices.

For the VIP method, the impact parameter cuts are exactly the same as described in the previous section but, in addition, tracks are rejected if they are associated with some primary or V_0 vertex. An analysis of the mistagged jets is shown in Figs. 9.65 and 9.66 for jets of E_T = 100 GeV and E_T = 200 GeV in the barrel of the Tracker. After such cuts the relative mistagging rate due to tracks originating from the primary vertex is at the level of 20% (32%) and the mistagging rate due to K^0_S and Λ decays, is about 5%. The remaining fraction of $\sim$ 75% (64%) originates from the secondary interactions in the Tracker material.

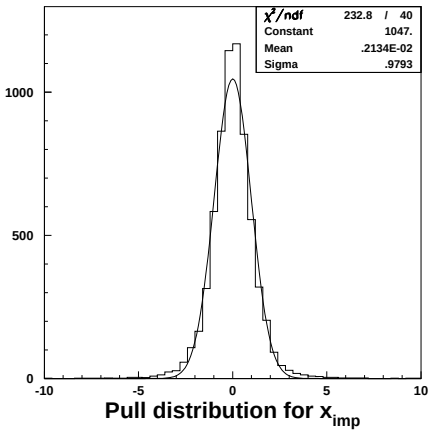

Fig. 9.63: Pull distribution of the x coordinate of the impact point (x_{imp}) for the reconstructed tracks with $p_T \geq 0.9$ GeV/c in the core of $E_t = 100$ GeV jet.

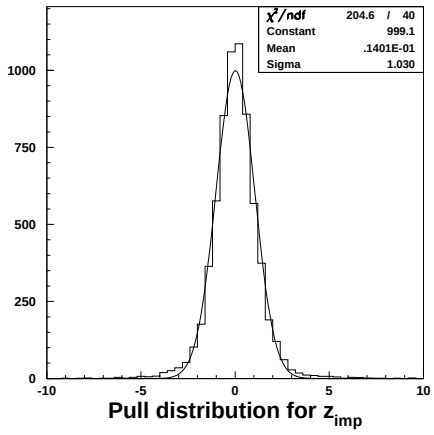

Fig. 9.64: Pull distribution of the z coordinate of the impact point (z_{imp}) for the reconstructed tracks with $p_T \geq 0.9$ GeV/c in the core of $E_t = 100$ GeV jet.

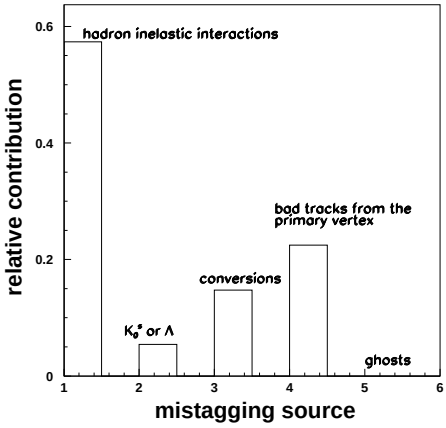

Fig. 9.65: Break-down of the mistagging rate in $u\bar{u}$ jets of $E_t = 100$ GeV. The fractional contribution to the mistagging rate is shown for tracks originated by different processes. All tracks satisfy the requirements $\bar{d}_0 \geq 3\sigma_{\bar{d}_0}$ and $p_T \geq 0.9$ GeV/c. Phase I Tracker layout.

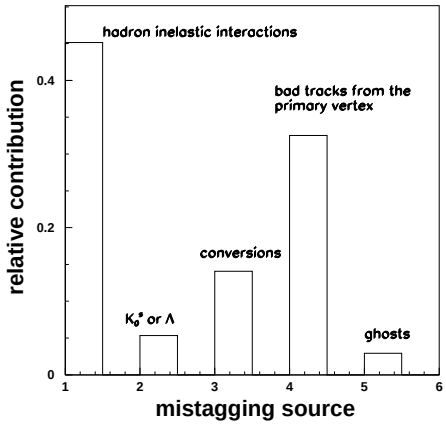

Fig. 9.66: Break-down of the mistagging rate in $u\bar{u}$ jets of $E_t = 200$ GeV. The fractional contribution to the mistagging rate is shown for tracks originated by different processes. All tracks satisfy the requirements $\bar{d}_0 \geq 3\sigma_{\bar{d}_0}$ and $p_T \geq 0.9$ GeV/c. Phase I Tracker layout.

In the SV-tagging method, we consider a jet SV-tagged if a secondary vertex is reconstructed using tracks that lie within R=0.4 from the jet axis. We impose a cut on the significance of the secondary vertex, requiring that the vertex radius be at least three times its error. An upper cut on the vertex radius is set at 3 cm.

To reduce the mistagging rate, two further constraints are tested, namely, 1) an implicit cut on the secondary vertex radial resolution ($\sigma \leq 500$ μm), and 2) the preselection of only tracks with significant impact parameter ($2\sigma_{\vec{d_0}}$) for the secondary vertex seeding (see Chapter 8). We refer to this study as 'SV+extra cuts'-tagging.

Finally, we applied the SV-tagging selection criteria to $u\bar{u}$ and $b\bar{b}$ events at the Monte Carlo level. The Monte Carlo level SV-tagging performance is evaluated in order to estimate the upper bound of its effectiveness and to test how much the present results differ from the best performance. In this case, all secondary vertices generated during the simulation phase are considered. A secondary vertex is selected for b-tagging if: 1) it has at least two 'reconstructible' associated tracks, i.e. tracks with $p_T \geq 0.9$ GeV/c and with at least six reconstructed hits, two of which measured by the Pixel detector; 2) the vertex transverse distance from the beam line is at least 100 μm and less than 3 cm; 3) it is not a K^0_S or Λ decay vertex. The results obtained with this method will be referred to as USV-tagging performance, and correspond to the performance achieved in the case of perfect pattern recognition capability and infinite vertex position resolution.

The b-tagging efficiency and mistagging rate for the four different methods are shown in Figs. 9.67 and 9.68 as a function of jet E_T. The comparison clearly shows the large potential of the SV-tagging method. The present SV algorithm based on the GVF vertex finder yields a sizable increase of b-tagging efficiency at the expense of some loss of purity, which nevertheless remains at the level of a few percent. The improvement is particularly remarkable for soft jets. In this case the purity can easily be maintained at values of $\sim 1\%$. This may be of importance for some physics processes such as the associated production of a light SM Higgs decaying to $b\bar{b}$ or the associated MSSM Higgs production ($gg \to h, H, A + b\bar{b}$ process for $\tan\beta \geq 5 - 7$). The comparison of SV-tagging results and SV + extra cuts-tagging results shows the large flexibility of the SV tagging method. Indeed, the mistagging probability is at the level or even better than for VIP-tagging algorithm. However, as one can see from the USV results, the present SV-tagging results are far from the best performance achievable. A more efficient and more robust vertex reconstruction algorithm, which is expected to improve the SV vertex tagging performance, is currently under study.

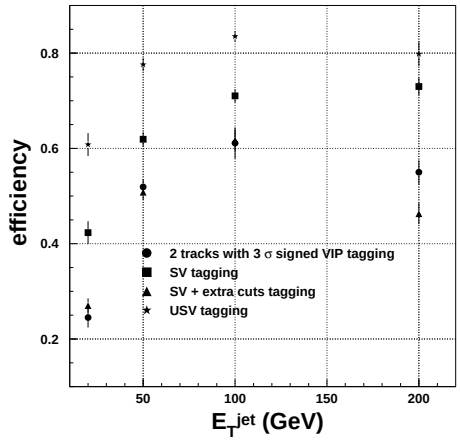

Fig. 9.67: b-tagging efficiency as a function of jet E_T, estimated using the four different approaches explained in the text.

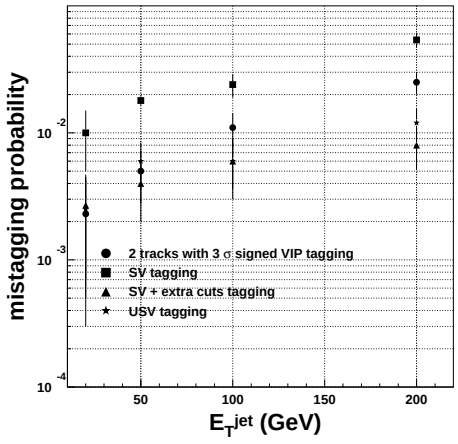

Fig. 9.68: Mistagging rate as a function of jet E_T, estimated using the four different approaches explained in the text.

We observe a sizable degradation of the b-tagging performance for $E_T = 200$ GeV jets. The loss of tagging purity is related with the diminished hit quality in the most precise Pixel and Silicon detectors, which is due to the large track density within the jet cores. The track fake rates or, in general, the fraction of badly reconstructed tracks increases, contributing to the mistagging probability. Moreover, the number of secondary interactions with the Tracker material increases by a factor of two with respect to the $E_T = 100$ GeV jets. However, even for $E_T = 200$ GeV jets b-tagging efficiency close to 50% and mistagging rates of $\sim 1\%$ can be obtained.

9.8 Heavy Ion Physics

9.8.1 Introduction

Heavy ion beams at the LHC will provide collision energy densities well above the threshold for the formation of QGP [9-3]. If such a new state of matter is created, all heavy quark bound states are allegedly suppressed by colour screening. Upsilon states can be detected through their decays to a pair of muons. The expected instantaneous luminosities are $\mathcal{L} = 10^{27}\mathrm{cm}^{-2}\mathrm{s}^{-1}$ and $\mathcal{L} = 2.5 \times 10^{29}\mathrm{cm}^{-2}\mathrm{s}^{-1}$ in the case of Pb and Ca ions, respectively. The design bunch crossing interval is 125 ns, and the expected total cross section in Pb-Pb collisions is 7.5 b, yielding a global event rate of 7.5 kHz. Trigger strategies have been analysed [9-2] that ensure high efficiency and good purity for muons originating from Υ decays. The expected global event rate is suppressed to 60 Hz by the di-muon trigger requirements. The signal events are collected at a rate of 10 Hz. They are predominantly Υ-induced with a smaller contribution from J/ψ or Z^0 di-muon decays. The task of the CMS Tracker is to recognise the muon tracks in an environment of tens of thousands of other tracks coming from the central ion-ion collision. In the most pessimistic scenario, the number of charged (neutral) particles produced in Pb-Pb collisions at $\sqrt{s} = 5.5$ TeV/NN can be as large as 8000 (4000) per unit of pseudorapidity. These particles are mainly low p_T (~ 0.5 GeV/c) pions or kaons. Consequently, the occupancies in the inner strip detectors ($r \leq 700$ mm) are rather large. Only those detectors which have a very high granularity (e.g. Pixel detectors) or which are positioned at large radii will have occupancies low enough to be useful in track finding.

Muons from Υ-decays have on average a transverse momentum of some 4 GeV/c. Though they lose nearly 2 GeV in the calorimeters and in the magnet coil, at least the innermost muon station [9-4] can be used in the pattern recognition process. The study presented here is restricted to the barrel detectors ($|\eta| < 0.8$). The reconstruction strategy employs the two Pixel layers, four outer layers of MSGC and two chamber planes of the innermost muon station.

In this analysis we use an earlier version of the Tracker layout where the strip length of all MSGC layers was 12.5 cm. In the current Tracker design, the two outermost MSGC layers are single ended, leading to a strip length of 25 cm. The increase in occupancy due to increased strip length in these MSGC layers has been estimated. The impact of the increased strip length on the reconstruction efficiency and mass resolution is presently under study.

9.8.2 Reconstruction method

Di-muons from Υ-decays are traced through the CMS detector using CMSIM. The main source of background to the di-muons are π/K decays that we have simulated separately. The signal and background samples are independently mixed with tracks from the underlying event due to the ion-ion collision. The underlying events are generated with varying multiplicity in the pseudo-rapidity interval $|\eta| < 5.0$, with a K/π ratio of 0.2 [9-5]. The shapes of η and p_T distributions are taken from the HIJING model [9-6] and the SHAKER [9-7] event generator, respectively.

The pattern recognition starts with one identified track segment in the innermost muon station. Clusters in the MSGC detectors are selected using a threshold on the signal per strip and a cut on the highest strip signal which depends on the number of strips in the cluster [9-8, 9-9]. Fig. 9.69 shows occupancy rates (ratio of number of fired strips to total number of strips per layer), with a threshold of 3500 e^- per strip, as a function of the radial position of the MSGC layer. The points are obtained from events generated with a rapidity density of 8000 charged particles.

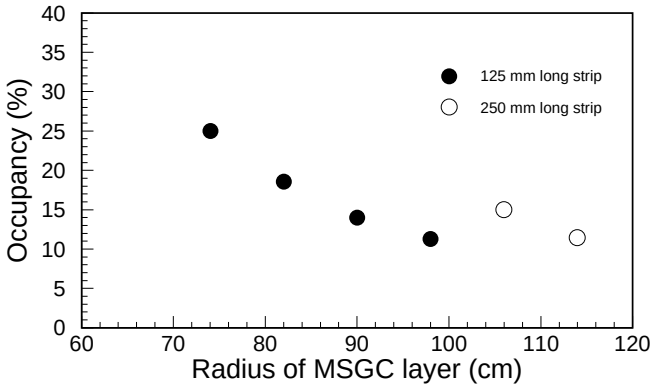

Fig. 9.69: Occupancy in MSGC layers for charged particle density $\frac{dN}{dy} = 8000$.

In the latest design of the Tracker the layers at 1067 and 1147 mm have strip lengths of 250 mm compared to 125 mm for the remaining layers. As can be seen from the figure, the occupancy stays well below 30% for all layers in the final design.

The seed for a track segment uses hits in the second chamber of the innermost muon station. The azimuthal angle, ϕ, is determined assuming the tracks to stem from the origin (0,0,0). The hits are matched with the next inner layer and the difference in ϕ of the two matched hits gives a first p_T estimate for the track candidate. These track candidates are propagated backward to the Tracker by defining a road and looking for a match in azimuthal angle ϕ and p_T. The estimates of ϕ and p_T are improved at each step. The highest level of ambiguity arises at the outermost layer of the Tracker where the predicted road is broadened by multiple scattering in the calorimeter. A road in θ starting from the two outermost MSGC layers is also used. A helix fit is performed through the selected points in the Tracker imposing a beam constraint. A linear fit is carried out in the rz-plane with the two additional muon chamber hits. The χ^2 values from the fits, combined with an estimator defined as:

$$\chi^2 = \sum_i \left(\frac{\phi_i^{predicted} - \phi_i^{measured}}{\sigma_i} \right)^2$$

are used to compute an overall quality parameter [9-8, 9-9] for the track candidate. The three track candidates with the best track quality parameters are preserved.

9.8.3 Identification of $\Upsilon \to \mu\mu$ events in AA interactions

Track pairs, reconstructed as above, are classified as like-sign or opposite-sign di-muons. The opposite-sign pairs are further constrained at the interaction point so that the separations along z and in the transverse plane are small:

$$\left(\frac{dz}{\sigma_z}\right)^2 < 6 \qquad \left(\frac{dr}{\sigma_r}\right)^2 < 14$$

with $\sigma_z = 50$ μm and $\sigma_r = 20$ μm . A quality criterion for each opposite-sign muon pair is defined as the product of the quality of each muon candidate and the vertex quality as:

$$K = \left[\left(\frac{dz}{\sigma_z} \right)^2 + \left(\frac{dr}{\sigma_r} \right)^2 \right]$$

The pair with the highest quality criterion is retained as an Υ candidate.

The mass of the reconstructed di-muon pair is shown in Fig. 9.70(a) for the Υ-decay sample. A narrow peak with a mass resolution of 47 MeV/c^2 can be seen. In contrast, the opposite-sign di-muons from π/K decays give a rather broad di-muon mass spectrum as shown by the solid histogram in Fig. 9.70(b). The dashed histogram in the same figure shows the mass spectrum for like-sign pairs from uncorrelated muons. The two mass spectra in Fig. 9.70(b) are similar except for a peak in the like-sign case at a di-muon mass of about $2m_\mu$ due to the selection of combinations including fake tracks.

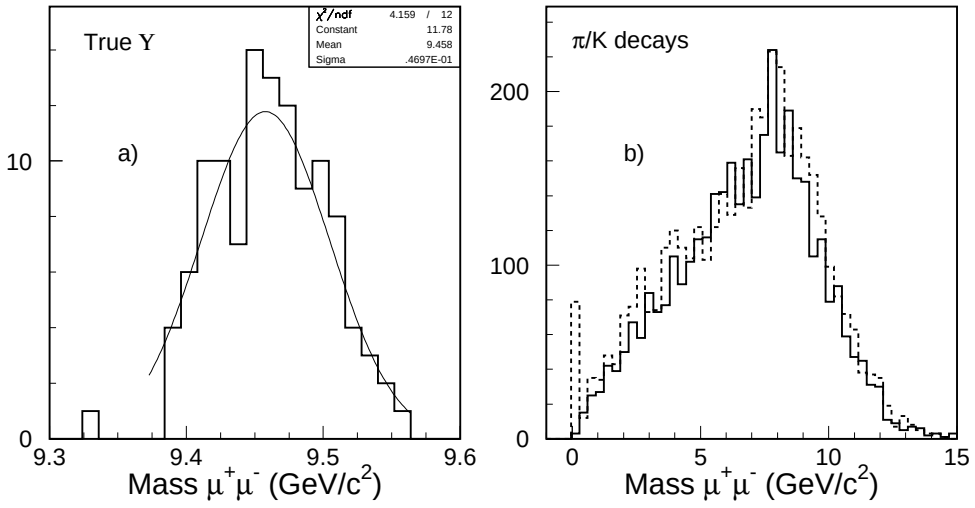

Fig. 9.70: Invariant mass spectrum of opposite-sign di-muon candidates for (a) signal Υ's, (b) uncorrelated background from π/K decays. The dashed histogram is due to like-sign di-muon candidates.

Assuming all MSGC strips to be 125 mm long and the charged particle density to be 8000, the di-muon reconstruction efficiency for Υ decays has been estimated to be 66% with 3% misidentification. A study has been made by dropping the layer at a radius of 1147 mm, keeping the layers at 827, 907, 987 and 1067 mm and choosing the strip length to be 250 mm for the two last layers. This study is more pessimistic than the low luminosity option, which has 125 mm long strips at the radii 827 and 907 mm as well as 250 mm strips at the radii 1067 and 1147 mm. One obtains an efficiency of 54% in this pessimistic scenario. However, the reconstruction efficiency can be improved by using the reconstructed z vertex position rather than the nominal beam position. It has been demonstrated that the z coordinate of the vertex can be determined with a precision of 130 μm using the Pixel detectors (see Fig. 9.71). With this additional information, the efficiency improves from 54% to 60%.

Table 9.11 summarises the reconstruction efficiency for opposite-sign di-muon pairs as a function of particle density. The efficiency decreases from 90% efficiency at low particle density to 66% for a charged particle density of 8000.

These reconstruction efficiencies and detector resolutions have been folded into the event generator information to obtain the di-muon mass spectrum. Fig. 9.72 shows the mass spectrum corresponding to one month's running of the CMS detector with Pb-ion beams. The background

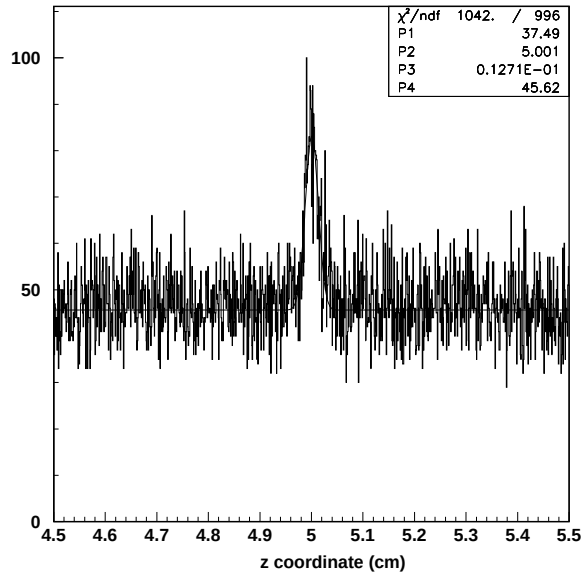

Fig. 9.71: z coordinate of reconstructed vertices using the measurements from the barrel Pixel layers with track density of 8000.

Table 9.11: Reconstruction efficiencies of muon-pair for different event multiplicity in samples where the di-muons come from Υ's, background due to π/K decays, or due to uncorrelated mixture of Υ, b-decays and π/K-decays

Source of μ's	Efficiency (%) for particle density of				
	500	1500	2500	5000	8000
Υ	88	90	88	83	66
π/K, π/K	7.9	7.6	7.8	7.5	5.6
Υ, π/K	19	19	19	18	14
Υ, b	36	35	34	33	25
π/K, b	15	15	14	14	11

subtraction is carried out using the like-sign di-muon mass spectrum. The signal to background ratio for Υ(1S) is 2 in Pb-Pb collisions increasing to 19 for Ca-Ca collision.

9.9 Summary of CMS Tracker Performance

The simulation and analysis of the CMS Tracker performance have been discussed in detail in Chapters 7, 8 and 9. Here we briefly summarise the main conclusions that can be drawn from this study.

As shown in Figs. 9.10 and 9.11, high p_T isolated tracks are reconstructed with a transverse momentum resolution of better than $\delta p_T/p_T \approx (15 \times p_T \oplus 0.5)\,\%$, with p_T in TeV/c, in the central region of $|\eta| \leq 1.6$, gradually degrading to $\delta p_T/p_T \approx (60 \times p_T \oplus 0.5)\,\%$, with p_T in TeV/c, as η approaches 2.5. This resolution is well suited to the reconstruction of narrow states decaying into charged particles, and is sufficient to ensure reliable charge assignment for muons and electrons up to the highest kinematically accessible momenta (Fig. 9.17).

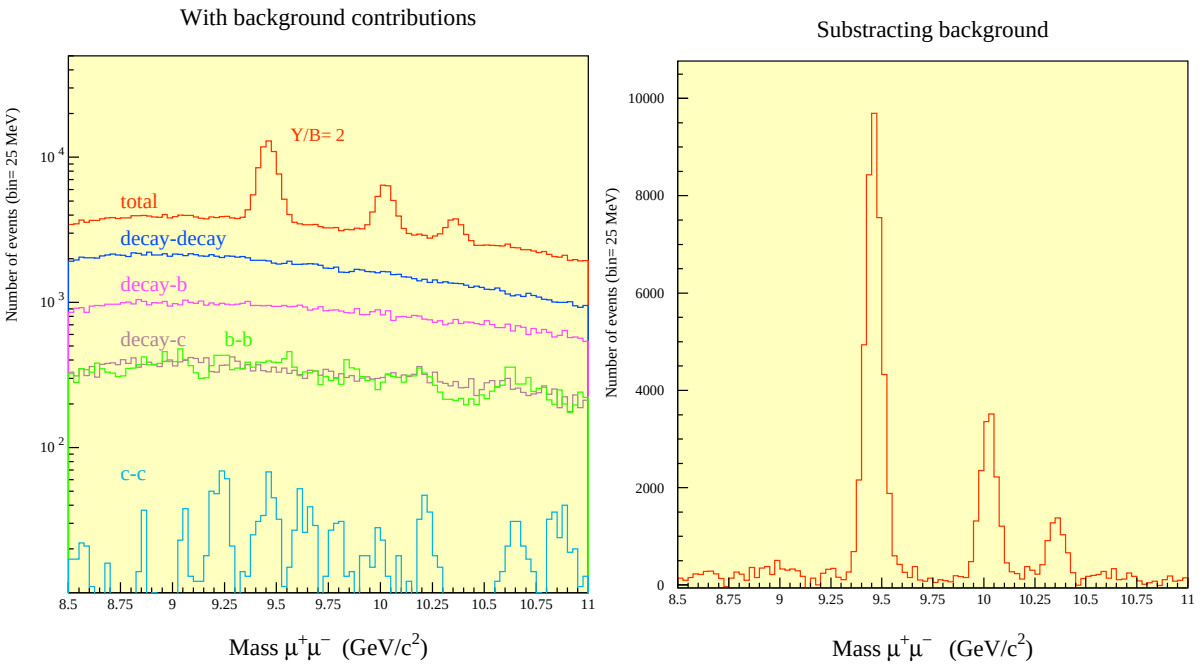

Fig. 9.72: Invariant mass spectrum of opposite-sign di-muon candidates as measured by the CMS detector from one month's running of the LHC with Pb-ion beams (a) without and (b) with background subtraction.

The reconstruction efficiency for muons is better than 98% over the full η range, even for values of p_T as low as 1 GeV/c (Fig 9.16, Fig. 9.23). High energy electrons are reconstructed with an efficiency above 90% (Table 9.3).

In the dense environment of a jet, charged hadrons with p_T above 10 GeV/c are reconstructed with an efficiency approaching 95%, and even hadrons with p_T as low as 1 GeV/c are reconstructed with an efficiency of better than 85% (Figs. 9.36 and 9.39). The highest efficiency is obtained with a pattern recognition algorithm (FKF) which, by taking the innermost layers of the Tracker as starting point and proceeding outwards, is able to efficiently and correctly reconstruct tracks even for a large fraction of those particles which interact inelastically before leaving the Tracker volume.

The impact parameter resolution in the plane perpendicular to the beams, shown in Fig. 9.6, is better than 35 μm over the full $|\eta| \leq 2.5$ range for particles with p_T above 10 GeV/c. The longitudinal impact parameter resolution, shown in Fig. 9.8, is significantly better than 75 μm over most of the rapidity range. At low luminosity it is possible to place the innermost Pixel layer closer to the beam line. This results in an appreciable improvement in impact parameter resolution, as can be seen from Figs. 9.5 and 9.7. Tails due to errors in track reconstruction are at a level well below the rate of displaced vertices due to long-lived particles (Figs. 9.37, 9.63 and 9.64).

In the central pseudorapidity region tagging efficiencies of 50% or better can be obtained for b jets ranging from 50 GeV to 200 GeV E_T, with a mistagging probability of about 1-2%. In the forward pseudorapidity region, for equal mistagging probability, the tagging efficiency remains around 40% (Figs. 9.60 and 9.61 and Tables 9.8 to 9.9).

The Phase I Tracker gives satisfactory performance in the low luminosity conditions, albeit with a noticeable loss of tracking efficiency within jets in the forward direction (Figs. 9.39 and 9.40). For the full Phase II detector, good tracking performance is achieved even within dense jets in the forward direction, and at high luminosity (Fig. 9.45).

Chapter 10

Project Organisation, Responsibilities, Costs and Planning

The CMS Central Tracker Project is based on three independent but largely complementary tracking systems; the Pixel Detector, the Silicon Strip Tracker and the MSGC Tracker. There are 47 Institutions widely distributed over the world and more than 500 physicists and engineers collaborating together in a unique community to construct the central tracking system of CMS.

10.1 Participating Institutes

Institut für Hochenergiephysik der ÖAW, Wien, AUSTRIA
W. Adam, R. Frühwirth, J. Hrubec, M. Krammer, H. Pernegger, M. Pernicka, D. Rakoczy

Université Catholique de Louvain, Louvain-la-Neuve, BELGIUM
K. Bernier, D. Favart, J. Govaerts, G. Grégoire

Université de Mons-Hainaut, Mons, BELGIUM
I. Boulogne, E. Daubie, Ph. Herquet, R. Windmolders

Université Libre de Bruxelles, Brussels, BELGIUM
O. Bouhali, J. Sacton, J. Stefanescu, C. Vander Velde, P. Vanlaer

Universiteit Antwerpen (UIA), Antwerpen, BELGIUM
W. Beaumont, T. Beckers, J. De Troy, Ch. Van Dyck, F. Verbeure

Vrije Universiteit Brussel, Brussels, BELGIUM
O. Devroede, J. Lemonne, S. Tavernier, F. Udo, W. Van Doninck, L. Van Lancker, V. Zhukov

CERN, European Laboratory for Particle Physics, Geneva, [CERN]
D. Abbaneo, V. Arbet-Engels, W. Bell, G. Benefice, M. Bosteels, M. Bozzo, S. Braibant, H. Breuker, A. Caner, A. Cattai, G. Cervelli, S. Da Mota Silva, N. Demaria, G. Dissertori, L. Feld, H. Foeth, A. Furtjes, K. Gill, W. Glessing, R. Goudard, F. Hahn, R. Hammarstrom, M. Huhtinen, S. Ilie, V. Innocente, W. Jank, F. Jensen, Th. Kachelhoffer, A. Khanov, K. Kloukinas, A. Kruse, Ch. Lasseur, Ch. Ljuslin, R. Mackenzie, R. Malina, M. Mannelli, E. Manola-Poggioli, A. Marchioro, Th. Meyer, C. Mommaert, T. Nyman, A. Onnela, M. Oriunno, P. Petagna, M. Pimiä, A. Placci, H. Postema, M.J. Price, R. Ribeiro, P. Rodrigues Simoes Moreira, L. Rolandi, R. Schmidt, B. Schmitt, P. Siegrist, L. Silvestris, N. Sinanis, G. Stefanini, N. Stepanov, T. Toifl, A. Tsirou, F. Vasey

Institute of Chemical Physics and Biophysics, Tallinn, ESTONIA
R. Aguraiuja, A. Hall, E. Lippmaa, J. Subbi

Department of Physics, University of Helsinki, Helsinki, FINLAND
S. Lehti, T. Lindén

Helsinki Institute of Physics, Helsinki, FINLAND
N. Eiden, C. Eklund, A. Heikkinen, A. Honkanen, V. Karimäki, R. Kinnunen, J. Klem, M. Kotamäki, T. Mäenpää, E. Pietarinen, S. Ruotsalainen, H. Saarikoski, K. Skog, J. Tuominiemi

Department of Physics, University of Jyväskylä, Jyväskylä, FINLAND
J. Äystö, R. Julin, V. Ruuskanen

Department of Physics & Microelectronics Instrumentation Laboratory, University of Oulu, Oulu, FINLAND
A. Keränen, L. Palmu, M. Piila, K. Remes, R. Skantsi, E. Suhonen, T. Tuuva

Laboratory of Advanced Energy Systems, Helsinki University of Technology, Helsinki, FINLAND
P.A. Aarnio

Institut de Recherches Subatomiques, IN2P3-CNRS-ULP Strasbourg, LEPSI Strasbourg, UHA Mulhouse, FRANCE
F. Anstotz, Y. Benhammou, G. Berges, J.D. Berst, J.M. Brom, F. Charles, J. Coffin, J. Croix, F. Drouhin, W. Dulinski, H. Eberlé, J.C. Fontaine, W. Geist, U. Goerlach, J.M. Helleboid, Y. Hu, D. Huss, F. Jeanneau, P. Juillot, A. Lounis, J. Michel, Ch. Racca, Y. Riahi, I. Ripp, Ph. Schmitt, J.P. Schunck, B. Schwaller, J.L. Sohler, T. Todorov, R. Turchetta, A. Zghiche

Institut de Physique Nucléaire de Lyon, IN2P3-CNRS, Univ. Lyon I, Villeurbanne, FRANCE
M. Ageron, P. Antilogus, J.E. Augustin, M. Bedjidian, D. Bertini, V. Chorowicz, P. Cluzel, D. Contardo, N. Djaoshvili, O. Drapier, M. Dupanloup, N. Giraud, R. Haroutounian, L. Mirabito, M. Rebouillat, G. Smadja, S. Tissot, J.-P. Walder

Humboldt-Universität zu Berlin, Berlin, GERMANY
Th. Hebbeker, S. Piperov

Institut für Experimentelle Kernphysik, Karlsruhe, GERMANY
P. Blüm, S. Chowdhury, W. de Boer, E. Gregoriev, S. Heising, S. Junghans, K. Kaercher, D. Knoblauch, M. Kraeber, R. Metri, Th. Müller, D. Neuberger, A. Pallares, H.J. Simonis, A. Theel, W.H. Thümmel, S. Weseler

RWTH, I. Physikalisches Institut, Aachen, GERMANY
Ch. Berger, W. Braunschweig, J. Breibach, W. Gu, W. Karpinski, T. Kubicki, Ch. Kukulies, K. Lübelsmeyer, D. Pandoulas, G. Pierschel, F. Raupach, C. Rente, A. Schultz von Dratzig, R. Siedling, O. Syben, F. Tenbusch, M. Toporowsky, W. Wallraff, B. Wittmer, W.J. Xiao

RWTH, III. Physikalisches Institut B, Aachen, GERMANY
S. Bachmann, F. Beissel, K. Boffin, C. Camps, V. Commichau, G. Flügge, K. Hangarter, R. Ischebeck, J. Kremp, D. Macke, A. Novack, G. Otter, M. Petertill, O. Pooth, P. Schmitz, R. Schulte

Panjab University, Chandigarh, INDIA
S. Beri, T.K. Chaterjee, M. Kaur, J.M. Kohli, J.B. Singh

Tata Institute of Fundamental Research - EHEP, Mumbai, INDIA
T. Aziz, Sn. Banerjee, S.N. Ganguli, S.K. Gupta, A. Gurtu, M. Maity, K. Mazumdar, K. Sudhakar, S.C. Tonwar

Tata Institute of Fundamental Research - HECR, Mumbai, INDIA
B.S. Acharya, Sd. Banerjee, S. Dugad, M.R. Krishnaswamy, N.K. Mondal, V.S. Narasimham

Università di Bari e Sezione dell' INFN, Bari, ITALY
M. Angarano, A. Bader, D. Creanza, M. De Palma, D. Diacono, L. Fiore, G. Maggi, S. My, G. Raso, G. Selvaggi, P. Tempesta, G. Zito

Università di Catania e Sezione dell' INFN, Catania, ITALY
S. Albergo, V. Bellini, D. Boemi, Z. Caccia, P. Castorina, S. Costa, L. Lo Monaco, R. Potenza, A. Tricomi, C. Tuve

Università di Firenze e Sezione dell' INFN, Firenze, ITALY
F. Becattini, U. Biggeri, E. Borchi, M. Bruzzi, S. Busoni, M. Capaccioli, G. Castellini, E. Catacchini, C. Civinini, R. D'Alessandro, E. Focardi, G. Landi, M. Lenzi, M. Meschini, G. Parrini, G. Passaleva, M. Pieri, S. Pirollo, S. Sciortino

Università di Padova e Sezione dell' INFN, Padova, ITALY
P. Azzi, N. Bacchetta, D. Bisello, A. Candelori, A. Castro, M. Da Rold, A. Giraldo, M. Loreti, G. Martignon, A. Paccagnella, I. Stavitski

Università di Perugia e Sezione dell' INFN, Perugia, ITALY
G. Anzivino, E. Babucci, G.M. Bilei, P. Cenci, B. Checcucci, P. Ciampolini, P. Lariccia, Y. Li, P. Lubrano, G. Mantovani, A. Nappi, D. Passeri, P. Placidi, A. Santocchia, L. Servoli, M. Valdata, Y. Wang

Università di Pisa e Sezione dell' INFN, Pisa, ITALY
F. Angelini, G. Bagliesi, A. Bardi, A. Basti, F. Bedeschi, S. Belforte, R. Bellazzini, G. Bisogni, L. Borrello, F. Bosi, C. Bozzi, P.L. Braccini, A. Brez, R. Carosi, R. Castaldi, U. Cazzola, G. Chiarelli, M. Chiarelli, V. Ciulli, M. D'Alessandro Caprice, M. Dell'Orso, R. Dell'Orso, S. Donati, S. Dutta, A. Frediani, A. Gaggelli, S. Galeotti, P. Giannetti, A. Giassi, L. Latronico, F. Ligabue, D. Lucchetti, N. Lumb, G. Magazzu, M.M. Massai, E. Meschi, A. Messineo, O. Militaru, F. Morsani, F. Palla, A. Papanestis, G. Punzi, F. Raffaelli, R. Raffo, L. Ristori, F. Rizzo, G. Sanguinetti, G. Sguazzoni, G. Spandre, M. Spezziga, F. Spinella, A. Starodumov, A. Talamelli, R. Tenchini, G. Tonelli, A. Toropin, E. Troiani, C. Vannini, R. Ventola, A. Venturi, P.G. Verdini, Z. Xie

Budker Institute for Nuclear Physics, SB RAS, Novosibirsk, RUSSIA
V. Aulchenko, A. Bondar, A. Buzulutskov, S. Eidelman, V. Nagaslaev, L. Shekhtman, V. Sidorov, A. Tatarinov, V. Titov

Institut für Teilchenphysik, Eidgenössische Technische Hochschule (ETH), Zürich, SWITZERLAND
L. Djambazov, R. Eichler, K. Freudenreich, C. Grab, H. Hofer, F. Pauss, D. Pitzl, D. Ren, U. Roeser, S. Streuli, G. Viertel, H. Von Gunten

Paul Scherrer Institut, Villigen, SWITZERLAND
R. Baur, W. Bertl, P. Dick, M. Fabre, K. Gabathuler, J. Gobrecht, G. Heidenreich, R. Horisberger, D. Kotlinski, R. Schnyder

Universität Basel, Basel, SWITZERLAND
B. Henrich, L. Tauscher, M. Wadhwa

Universität Zürich, Zürich, SWITZERLAND
C. Amsler, R. Kaufmann, F. Ould-Saada, Ch. Regenfus, P. Robmann, S. Spanier, S. Steiner, P. Truöl, T. Walter

Brunel University, Uxbridge, UNITED KINGDOM
J. Matheson, M. Solanky, S.J. Watts

Imperial College, University of London, London, UNITED KINGDOM
G. Barber, J. Batten, R. Beuselinck, D. Britton, W. Cameron, D. Clark, I. Clarke, G. Davies, J. Fulcher, D. Gentry, D. Graham, G. Hall, J. Hays, A. Jamdagni, K.R. Long, B.C. MacEvoy, N. Marinelli, E.B. Martin, D.G. Miller, A. Potts, D.M. Raymond, J. Reilly, F. Sciacca, J. Sedgbeer, C. Seez, L. Toudup, J. Troska

Rutherford Appleton Laboratory, Didcot, UNITED KINGDOM
S.A. Baird, J.A. Coughlan, M.French, R. Halsall, J. Hartley, W.J. Haynes, L. Jones, G. Noyes

University of California at Davis, Davis, California, USA
B. Holbrook, R. Lander, S. Mani, D. Pellett, J. Smith

Fermi National Accelerator Laboratory, Batavia, Illinois, USA
M. Atac, B. Flaugher, U. Heintz, J. Incandela, S. Kwan, R. Lipton, P. Lukens, V. O' Dell, P. Rapidis, L. Spiegel, D. Stuart, S. Tkaczyk

Florida State University - SCRI, Tallahassee, Florida, USA
M.J. Corden, C. Georgiopoulos, S. Youssef

Johns Hopkins University, Baltimore, Maryland, USA
B. Barnett, C.Y. Chien, D. Gerdes, J. Orndorff, A. Pevsner

Los Alamos National Laboratory, Los Alamos, USA
C. Johnson, A. Palounek, B. Smith, H. Ziock

University of Mississippi, Oxford, Mississippi, USA
M. Booke, L. Cremaldi, D. Sanders

Northwestern University, Evanston, Illinois, USA
B. Gobbi, P. Rubinov, R. Tilden

Purdue University - Task G, West Lafayette, Indiana, USA
G. Bolla, D. Bortoletto, A.F. Garfinkel

University of Rochester, Rochester, New York, USA
S. Blusk, M. Kruse

Rutgers, the State University of New Jersey, Piscataway, New Jersey, USA
E. Bartz, J. Conway, T. Devlin, P. Jacques, M. Kalelkar, S. Schnetzer, S. Sherman, S. Somalwar, R. Stone, G. Thomson, T. Watts

Texas Tech University, Lubbock, Texas, USA
D. Benjamin, A. Sill

10.2 Project Organisation

The Tracker project is organised according to the CMS rules described in the CMS constitution and has an organisational structure similar to that of the CMS Collaboration.

The project is governed by the Institution Board and by the Technical Board. The Institution Board is the highest decision-making body in the Tracker Project. It discusses and decides issues of financial, managerial and organisational nature and also endorses technical matters recommended by the Tracker Technical Board and proposed by the Tracker Project Manager. All Institutions participating in the Tracker Project are represented in the Institution Board. The members of the Institution Board elect their Chairperson for a term of two years.

The Tracker Project Manager, appointed by the CMS Spokesperson, heads the project and is assisted by the Tracker Technical Coordinator and the Tracker Resource Manager.

The Tracker Technical Board, chaired by the Tracker Project Manager, discusses technical and organisational matters on a regular basis and formulates proposals and recommendations to the Tracker Institution Board. The composition of the Tracker Technical Board up to the submission of the Tracker Technical Design Report, is shown in Fig. 10.1.

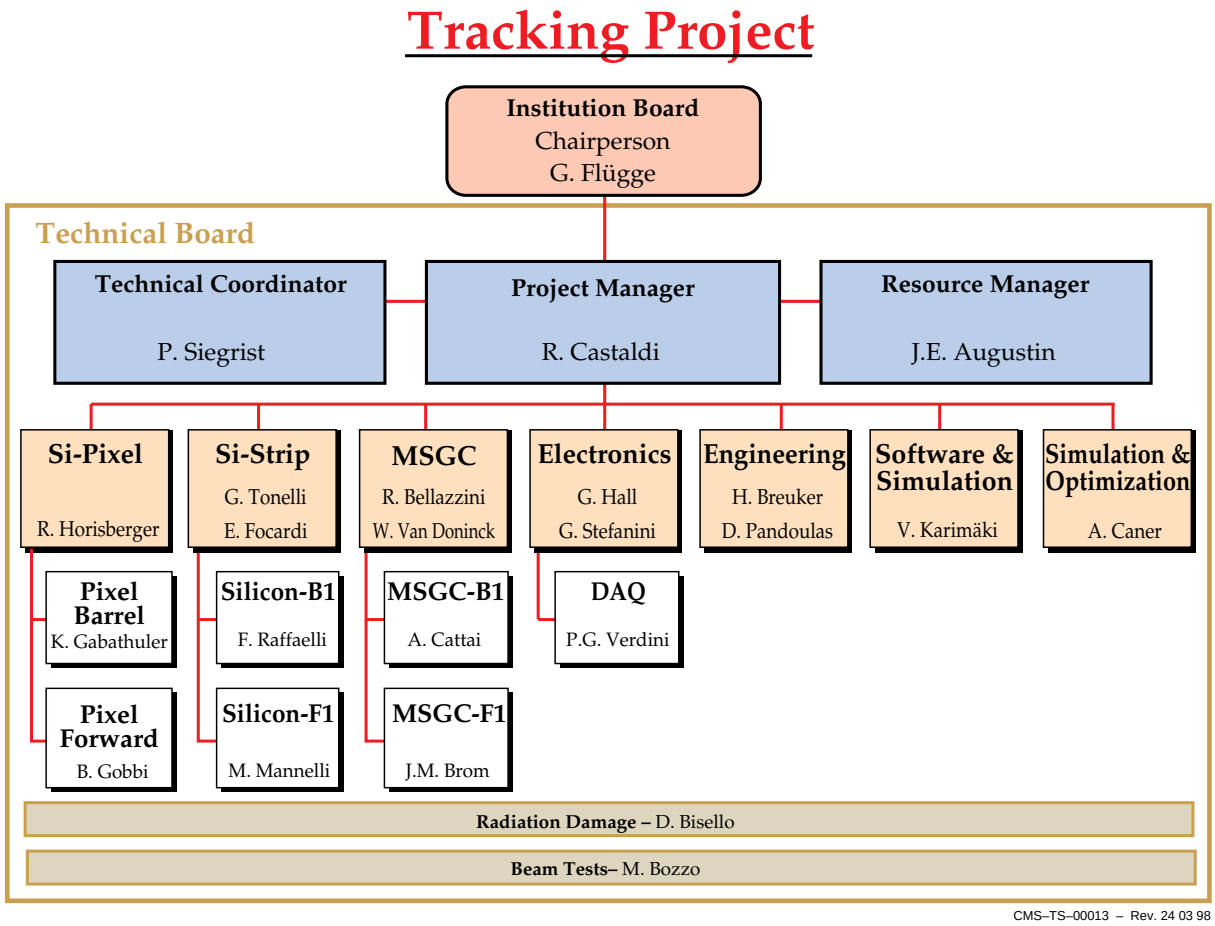

Fig. 10.1: Composition of the Tracker Technical Board in April 1998

The project is divided into a number of subprojects headed by a Coordinator assisted by a Deputy. These Coordinators and Deputies are members of the Tracker Technical Board together with the Project Manager, the Technical Coordinator, the Resource Manager and the Chairperson of the Institution Board. In addition the Coordinators of the major milestones and the Coordinators of special task forces that were needed to arrive at this Tracker Technical Design Report are also members of the Board.

This central structure is complemented by different organisations for the different subprojects. At present seven major subprojects can be identified in the Tracker; three projects for the three subdetectors (Pixel Detector, Si-Strip Tracker and MSGC Tracker) and four common projects (Electronics, General-Engineering/Integration, Software/Simulation and Simulation/Optimisation). Each of the corresponding seven communities organised by its own Coordinator assisted, as appropriate, by his Deputy meets regularly during CMS and Tracker weeks. The meetings are open to all members of the Tracker community and to CMS members in general. They are held regularly to address the most important technical issues, to compare the work of the different groups and to organise activities for the construction effort.

Several special working groups have been set up to address specific problems, to investigate different technical options and to complete prototyping activity. They are composed of groups of specialists from different institutions. Several working groups are permanent (radiation effects, test beam organisation, DAQ, etc.) and meet regularly; others are set up as task forces to study and solve specific problems.

In the case of the Si-strip and MSGC Trackers, where rather large communities are involved, the activity of the physicists and engineers fully committed to build and operate these detectors is organised by the Coordinator and his Deputy with the help of a Steering Committee. Both the Silicon and the MSGC Steering Committees consist, in addition to the Coordinator of the project and his Deputy, of representatives of each participating Institution and technical experts. The two Steering Committees meet regularly every 2/3 weeks. The committees monitor the project, coordinate the activities among the various groups and provide recommendations to the Technical Board and Institution Board of the Tracker.

10.3 Costs and Funding

The cost estimate for the CMS Tracker has been done in great detail, following the procedure and guidelines defined in collaboration with the Cost Review Committee (CORE). The present cost estimate has developed over the last several years and the costs were an important consideration in optimizing the design presented in this Technical Design Report.

The estimates are based on a variety of different approaches. Some of the costs of individual items have been derived from discussions and budgetary quotes with qualified industries, others are based on recent experience in constructing tracking systems and vertex detectors for experiments at CERN (LEP) and Fermilab ($p\overline{p}$ Collider).

The cost of the CMS Tracker will be borne by all institutions participating in the project. At present the participating institutes are expecting to contribute financially to the CMS Tracker as shown in Table 10.1. For most institutes the total funding has already been discussed with the corresponding funding agency. It is expected that the commitments will be made formally by all funding agencies when signing the Memorandum of Understanding (MoU) early this year.

10.4 Institutional Responsibilities

Table 10.2 provides an overview of the division of responsibilities among the institutions participating in the project. For each institution the table also specifies the proposed contribution to the total cost of the project which will be discussed and defined in separate documents corresponding to bi-(multi)lateral agreements (MoU) between CERN and the funding agencies. Codes used for the insitutes in Table 10.2 are explained in Table 10.3. Several common items of the Tracker are the responsibility of the host laboratory CERN. The global Tracker support structure is such a common item. It consists of the central support tube (CST), the endflanges, pixel and beam pipe support structures, the Tracker support brackets and special installation tooling. Further common items are the overall alignment system and part of the monitoring system. The thermal separation screen between the Silicon and MSGC volumes is a common item. CERN's responsibility also includes most of the services between the main patch panels and the underground control rooms.

Table 10.1: Funding of the Tracker project by participating institutes

Cost Estimate Reference	Deliverables	Estimated Cost (Phase II)	Austria	Belgium	CERN	Finland	France-IN2P3	Germany	India *	Italy	RDMS-Russia	Switzerland		United Kingdom	USA		Totals Assigned Funding	Estimated Cost (Phase I)	Balance of Funding vs Cost of Phase I	Balance of Funding vs Cost of Phase II
												ETHZ/Universities	PSI		DOE	NSF				
2.1.1	Detectors (incl. Pre-series)	965										240	410			315	965	965		
2.1.2	Elctronics (incl. Engineering	5'020	170									1'030	2'250		695	675	4'820	5'020	-200	
2.1.3	Module Mechanics	1'010										260	460		290		1'010	1'010		
2.1.4	Support Structures and Asser	480										110	140		230		480	480		
2.1.5	Monitoring	110											60		50		110	110		
2.1.6	Service Systems	655										160	280		215		655	655		
2.1	**Pixel Detector**	**8'240**	**170**									**1'800**	**3'600**		**1'480**	**990**	**8'040**	**8'240**	**-200**	**-200**
2.2.1	Detectors (incl. Pre-series)	10'845	440		1'800	200		650	450	4'400		900					8'840	8'825	15	
2.2.2	Electronics (incl. Engineering	15'605	570		2'700			850	100	5'900		1'100		1'500			12'720	12'790	-70	
2.2.3	Module Mechanics	1'120	170		175			150	50	200		100					845	880	-35	
2.2.4	Support Structures and Asser	2'400			720			150		1'100							1'970	2'320	-350	
2.2.5	Monitoring	400						200									200	400	-200	
2.2.6	Service Systems	120			120												120	120		
2.2	**Silicon Detector**	**30'490**	**1'180**		**5'515**	**200**		**2'000**	**600**	**11'600**		**2'100**		**1'500**			**24'695**	**25'335**	**-640**	**-5'795**
2.3.1	Detectors (incl. Pre-series)	13'465		590	1'335		2'530	1'525		3'590	630	370					10'570	10'755	-185	
2.3.2	Elctronics (incl. Engineering	24'310		2'635	3'375		3'920	2'910		4'300	320	590		1'200			19'250	19'225	25	
2.3.3	Module Mechanics	1'940		35	270	800	50	340			95						1'590	1'630	-40	
2.3.4	Support Structures and Asser	2'640		155	620	1'200	230	395				40					2'640	2'605	35	
2.3.5	Monitoring	100			50			50									100	100		
2.3.6	Service Systems	120		5	50		20	30		10	5						120	120		
2.3	**MSGC Detector**	**42'570**		**3'420**	**5'700**	**2'000**	**6'750**	**5'250**		**7'900**	**1'050**	**1'000**		**1'200**			**34'270**	**34'435**	**-165**	**-8'300**
2.4.1	Overall Support	2'100			2'100												2'100	2'100		
2.4.2	Overall Alignment	800			600	200											800	800		
2.4.3	Service Systems	3'185			2'985												2'985	3'185	-200	
2.4	**General Mechanical Infr.**	**6'085**			**5'685**	**200**											**5'885**	**6'085**	**-200**	**-200**
2.	**Tracker**	**87'385**	**1'350**	**3'420**	**16'900**	**2'400**	**6'750**	**7'250**	**600**	**19'500**	**1'050**	**4'900**	**3'600**	**2'700**	**1'480**	**990**	**72'890**	**74'095**	**-1'205**	**-14'495**

* Pending approval

Table 10.2 DELIVERABLES AND ESTIMATES VALUE (KCHF) BY FUNDING AGENCY

AUSTRIA

Ref.	Institutes	Deliverables	Assigned
2.1.2	AT1	Tracker : Pixel Detector : Electronics (incl. Engineering) Fabrication and testing of pixel electronics	170
2.2.1	AT1	Tracker : Silicon Detector : Detectors (incl. Pre-series) Purchase of silicon detectors	440
2.2.2	AT1	Tracker : Silicon Detector : Electronics (incl. Engineering) Purchase of components of the electronics chain for silicon detectors	570
2.2.3	AT1	Tracker : Silicon Detector : Module Mechanics Engineering and manufacture of silicon detector modules in a Regional Centre	170
		Total Assigned Funding	1'350

BELGIUM

Ref.	Institutes	Deliverables	Assigned
2.3.1	BE1 BE2 BE3 BE4 BE5	Tracker : MSGC Detector : Detectors (incl. Pre-series) Purchase and tests of MSGC Endcap detectors	590
2.3.2	BE1 BE2 BE3 BE4	Tracker : MSGC Detector : Electronics (incl. Engineering) Purchase of components of the electronic chain for MSGC Endcap	2'635
2.3.3	BE1 BE2 BE3 BE4	Tracker : MSGC Detector : Module Mechanics Engineering of MSCG Endcap detector modules	35
2.3.4	BE1 BE2 BE3 BE4	Tracker : MSGC Detector : Support Structures and Assembly Engineering, procurement of MSGC Endcap support structures,	155
2.3.6	BE1 BE2 BE3 BE4 BE5	Tracker : MSGC Detector : Service Systems Cables, gas and cooling from MSGC Endcap detector to patch-panel	5
		Total Assigned Funding	3'420

[CERN]

Ref.	Institutes	Deliverables	Assigned
2.2.1	CERN	Tracker : Silicon Detector : Detectors (incl. Pre-series) Purchase of silicon detectors	1'800
2.2.2	CERN	Tracker : Silicon Detector : Electronics (incl. Engineering) Purchase of components of the electronics chain for silicon detectors	2'700
2.2.3	CERN	Tracker : Silicon Detector : Module Mechanics Engineering and manufacture of Silicon Detector modules at	175
2.2.4	CERN	Tracker : Silicon Detector : Support Structures and Assembly Engineering, procurement of Silicon Endcap support structures,	720
2.2.6	CERN	Tracker : Silicon Detector : Service Systems Cables and cooling from Silicon Barrel and Endcap Detector to	120
2.3.1	CERN	Tracker : MSGC Detector : Detectors (incl. Pre-series) Purchase and tests of MSGC Barrel detectors	1'335
2.3.2	CERN	Tracker : MSGC Detector : Electronics (incl. Engineering) Purchase of components of the electronics chain for MSGC Barrel	3'375
2.3.3	CERN	Tracker : MSGC Detector : Module Mechanics Engineering of MSGC Barrel detector modules	270
2.3.4	CERN	Tracker : MSGC Detector : Support Structures and Assembly Engineering, procurement of MSCG Barrel support structures,	620
2.3.5	CERN	Tracker : MSGC Detector : Monitoring Participation in Slow Controls and purchase of sensors	50
2.3.6	CERN	Tracker : MSGC Detector : Service Systems Cables, gas and cooling from MSGC Barrel detector to patch-panel	50
2.4.1	CERN	Tracker : General Mechanical Infrastr. : Overall Support Procurement of complete support system (CST, endflanges,	2'100
2.4.2	CERN	Tracker : General Mechanical Infrastr. : Overall Alignment Procurement of part of the Overall Alignment system	600
2.4.3	CERN	Tracker : General Mechanical Infrastr. : Service Systems High-voltage and low-voltage cables, gas and cooling distribution	2'985
		Total Assigned Funding	16'900

ESTONIA

Ref.	Institutes	Deliverables	Assigned
2.3.6	EE1	Tracker : MSGC Detector : Service Systems Contribution to be defined	
		Total Assigned Funding	

FINLAND

Ref.	Institutes	Deliverables	Assigned
2.2.1	FI1 FI2 FI3 FI5	Tracker : Silicon Detector : Detectors (incl. Pre-series) Purchase of silicon detectors	200
2.3.3	FI2	Tracker : MSGC Detector : Module Mechanics Manufacture and assembly of the carbon fibre structure of the "Rods"	800
2.3.4	FI2	Tracker : MSGC Detector : Support Structures and Assembly Manufacture, assembly and transportation of the MSGC Barrel wheel (4 disks and the cylinders)	1'200
2.4.2	FI2	Tracker : General Mechanical Infrastr. : Overall Alignment Procurement of part of the Overall Alignment system	200
		Total Assigned Funding	2'400

FRANCE-IN2P3

Ref.	Institutes	Deliverables	Assigned
2.3.1	FR4 FR5	Tracker : MSGC Detector : Detectors (incl. Pre-series) Purchase and tests of MSGC Endcap detectors	2'530
2.3.2	FR4 FR5	Tracker : MSGC Detector : Electronics (incl. Engineering) Purchase of components of the electronics chain for MSGC detectors, including engineering runs for MSGC ASICs	3'920
2.3.3	FR4 FR5	Tracker : MSGC Detector : Module Mechanics Assembly and tests of MSGC Endcap detector modules including mechanical elements	50
2.3.4	FR4 FR5	Tracker : MSGC Detector : Support Structures and Assembly Participation in the assembly and installation of MSGC Endcap detector modules	230
2.3.6	FR4 FR5	Tracker : MSGC Detector : Service Systems Small parts of services	20
		Total Assigned Funding	6'750

GERMANY

Ref.	Institutes	Deliverables	Assigned
2.2.1	DE1 DE3	Tracker : Silicon Detector : Detectors (incl. Pre-series) Purchase of silicon detectors	650
2.2.2	DE1 DE3	Tracker : Silicon Detector : Electronics (incl. Engineering) Purchase of read-out electronics for Silicon Detector modules	850
2.2.3	DE1 DE3	Tracker : Silicon Detector : Module Mechanics Frames and engineering of Silicon Detector modules, assembly and tests of these modules in a Regional Centre	150
2.2.4	DE1 DE3	Tracker : Silicon Detector : Support Structures and Assembly Mounting of silicon modules on the support structures	150
2.2.5	DE1 DE3	Tracker : Silicon Detector : Monitoring Participation in Slow Control and purchase of sensors	200
2.3.1	DE2 DE3 DE5	Tracker : MSGC Detector : Detectors (incl. Pre-series) Purchase of MSGC Endcap detector substrates	1'525
2.3.2	DE2 DE3 DE5	Tracker : MSGC Detector : Electronics (incl. Engineering) Purchase of read-out electronics for MSGC Endcap detector modules	2'910
2.3.3	DE2 DE3 DE5	Tracker : MSGC Detector : Module Mechanics Purchase of frames and assembly of MSGC Endcap detector modules	340
2.3.4	DE2 DE3 DE5	Tracker : MSGC Detector : Support Structures and Assembly Engineering, procurement of MSGC Endcap support structures, mounting of MSGC Endcap modules on the support structures	395
2.3.5	DE2 DE3 DE5	Tracker : MSGC Detector : Monitoring Participation in Slow Controls and purchase of sensors	50
2.3.6	DE2 DE3 DE5	Tracker : MSGC Detector : Service Systems Cables, gas and cooling for MSGC Endcap detector	30
		Total Assigned Funding	7'250

INDIA

Ref.	Institutes	Deliverables	Assigned
2.2.1	IN3 IN4 IN5	Tracker : Silicon Detector : Detectors (incl. Pre-series) Purchase of silicon detectors	450
2.2.2	IN3 IN4 IN5	Tracker : Silicon Detector : Electronics (incl. Engineering) Purchase of components of the electronics chain for silicon detectors	100
2.2.3	IN3 IN4 IN5	Tracker : Silicon Detector : Module Mechanics	50
		Total Assigned Funding	600

ITALY

Ref.	Institutes	Deliverables	Assigned
2.2.1	IT01 IT03 IT04 IT06 IT08 IT09	Tracker : Silicon Detector : Detectors (incl. Pre-series) Purchase of silicon detectors	4'400
2.2.2	IT01 IT03 IT04 IT06 IT08 IT09	Tracker : Silicon Detector : Electronics (incl. Engineering) Purchase of components of the electronics chain for silicon detectors	5'900
2.2.3	IT01 IT03 IT04 IT06 IT08 IT09	Tracker : Silicon Detector : Module Mechanics Engineering and manufacture of Silicon Detector modules at the Regional Centres in Bari-Catania, Firenze-Padova, Perugia and Pisa	200
2.2.4	IT09	Tracker : Silicon Detector : Support Structures and Assembly Engineering, procurement of Silicon Barrel support structures, mounting of silicon modules on the support structures	1'100
2.3.1	IT09	Tracker : MSGC Detector : Detectors (incl. Pre-series) Purchase and tests of MSGC Barrel detectors	3'590
2.3.2	IT09	Tracker : MSGC Detector : Electronics (incl. Engineering) Purchase of components of the electronics chain for MSGC Barrel detectors	4'300
2.3.6	IT09	Tracker : MSGC Detector : Service Systems Cables, gas and cooling from MSGC Barrel detectors to patch-panel	10
		Total Assigned Funding	19'500

RDMS-RUSSIA

Ref.	Institutes	Deliverables	Assigned
2.3.1	RU1	Tracker : MSGC Detector : Detectors (incl. Pre-series) Purchase and tests of of MSGC Endcap detectors	630
2.3.2	RU1	Tracker : MSGC Detector : Electronics (incl. Engineering) Purchase of components of the electronics chain for MSCG Endcap detectors	320
2.3.3	RU1	Tracker : MSGC Detector : Module Mechanics Engineering of MSGC Endcap detector modules	95
2.3.6	RU1	Tracker : MSGC Detector : Service Systems Cables, gas and cooling from MSCG Endcap detectors to patch-panels	5
		Total Assigned Funding	1'050

SWITZERLAND-ETHZ/Universities

Ref.	Institutes	Deliverables	Assigned
2.1.1	SW1 SW3 SW4	Tracker : Pixel Detector : Detectors (incl. Pre-series) Purchase and testing of Pixel Barrel sensors	240
2.1.2	SW1 SW3 SW4	Tracker : Pixel Detector : Electronics (incl. Engineering) Purchase and testing of Pixel electronics	1'030
2.1.3	SW1 SW3 SW4	Tracker : Pixel Detector : Module Mechanics Bump bonding and assembly of Barrel modules	260
2.1.4	SW1 SW3 SW4	Tracker : Pixel Detector : Support Structures and Assembly Construction of half-shells and assembly of Barrel modules	110
2.1.6	SW1 SW3 SW4	Tracker : Pixel Detector : Service Systems Cables and cooling system for Pixel detector	160
2.2.1	SW1 SW3	Tracker : Silicon Detector : Detectors (incl. Pre-series) Purchase of silicon detectors	900
2.2.2	SW1 SW3	Tracker : Silicon Detector : Electronics (incl. Engineering) Purchase of components of the electronics chain for silicon detectors	1'100
2.2.3	SW1 SW3	Tracker : Silicon Detector : Module Mechanics Engineering of Silicon Detector modules	100
2.3.1	SW4	Tracker : MSGC Detector : Detectors (incl. Pre-series) Purchase and tests of MSGC Forward detectors	370
2.3.2	SW4	Tracker : MSGC Detector : Electronics (incl. Engineering) Purchase of components of the electronics chain for MSGC Forward detectors	590
2.3.4	SW4	Tracker : MSGC Detector : Support Structures and Assembly Engineering, procurement of MSGC Forward support structure, mounting of MSGC Forward modules on the support structures	40
		Total Assigned Funding	4'900

SWITZERLAND-PSI

Ref.	Institutes	Deliverables	Assigned
2.1.1	SW2	Tracker : Pixel Detector : Detectors (incl. Pre-series) Purchase and testing of Pixel Barrel sensors	410
2.1.2	SW2	Tracker : Pixel Detector : Electronics (incl. Engineering) Purchase and testing of Pixel electronics	2'250
2.1.3	SW2	Tracker : Pixel Detector : Module Mechanics Bump bonding and assembly of Barrel modules	460
2.1.4	SW2	Tracker : Pixel Detector : Support Structures and Assembly Construction of half-shells and assembly of Barrel modules	140
2.1.5	SW2	Tracker : Pixel Detector : Monitoring Temperature and radiation monitoring	60
2.1.6	SW2	Tracker : Pixel Detector : Service Systems Cables and cooling system for Pixel detector, insertion tooling	280
		Total Assigned Funding	3'600

UNITED KINGDOM

Ref.	Institutes	Deliverables	Assigned
2.2.2	UK1 UK2 UK3	Tracker : Silicon Detector : Electronics (incl. Engineering) Design, develop and procure part of the front-end driver units and part of APV6 front-end chips	1'500
2.3.2	UK1 UK2 UK3	Tracker : MSGC Detector : Electronics (incl. Engineering) Design, develop and procure part of the front-end driver units and part of APV6 front-end chips	1'200
		Total Assigned Funding	2'700

UNITED STATES-DOE

Ref.	Institutes	Deliverables	Assigned
2.1.2	US03	Tracker : Pixel Detector : Electronics (incl. Engineering) Purchase and testing of Pixel electronics	695
2.1.3	US10 US13 US26 US35	Tracker : Pixel Detector : Module Mechanics Bump bonding and assembly of Endcap modules	290
2.1.4	US03 US10 US26 US3	Tracker : Pixel Detector : Support Structures and Assembly Construction of half-disks and assembly of Endcap modules	230
2.1.5	US03 US23	Tracker : Pixel Detector : Monitoring Temperature and radiation monitoring	50
2.1.6	US23	Tracker : Pixel Detector : Service Systems Cables and cooling system for Pixel detector	215
		Total Assigned Funding	1'480

UNITED STATES-NSF

Ref.	Institutes	Deliverables	Assigned
2.1.1	US17	Tracker : Pixel Detector : Detectors (incl. Pre-series) Puchase and testing of Pixel Endcap sensors	315
2.1.2	US17 US33	Tracker : Pixel Detector : Electronics (incl. Engineering) Purchase and testing of Pixel electronics	675
		Total Assigned Funding	990

Table 10.3 Institute Codes in the Collaboration

Country	Code	Institute
Austria	AT1	Institut für Hochenergiephysik der OeAW, Wien
Belgium	BE1	Université Catholique de Louvain, Louvain-la-Neuve
	BE2	Université de Mons-Hainaut, Mons
	BE3	Université Libre de Bruxelles, Brussels
	BE4	Universitaire Instelling Antwerpen, Wilrijk
	BE5	Vrije Universiteit Brussel, Brussels
[CERN]	CERN	CERN, European Laboratory for Particle Physics, Geneva, Switzerland
Estonia	EE1	Institute of Chemical Physics and Biophysics, Tallinn
Finland	FI1	Department of Physics, University of Helsinki, Helsinki
	FI2	Helsinki Institute of Physics, Helsinki
	FI3	Department of Physics, University of Jyväskylä, Jyväskylä
	FI5	Dept. of Physics & Microelectronics Instrumentation Lab., Univ. of Oulu, Oulu
	FI6	Laboratory of Advanced Energy Systems, Helsinki Univ. of Techn., Helsinki
France	FR4	IReS Strasbourg, IN2P3-CNRS-ULP, LEPSI Strasbourg, UHA Mulhouse
	FR5	Institut de Physique Nucléaire de Lyon, IN2P3-CNRS, Univ. Lyon I, Villeurbanne
Germany	DE1	Humboldt-Universität zu Berlin, Berlin
	DE2	Institut für Experimentelle Kernphysik, Karlsruhe
	DE3	RWTH, I. Physikalisches Institut, Aachen
	DE5	RWTH, III. Physikalisches Institut B, Aachen
India	IN3	Panjab University, Chandigarh
	IN4	Tata Institute of Fundamental Research - EHEP, Mumbai
	IN5	Tata Institute of Fundamental Research - HECR, Mumbai
Italy	IT01	Università di Bari e Sezione dell' INFN, Bari
	IT03	Università di Catania e Sezione dell' INFN, Catania
	IT04	Università di Firenze e Sezione dell' INFN, Firenze
	IT06	Università di Padova e Sezione dell' INFN, Padova
	IT08	Università di Perugia e Sezione dell' INFN, Perugia
	IT09	Università di Pisa e Sezione dell' INFN, Pisa
Russia	RU1	Budker Institute for Nuclear Physics, SB RAS, Novosibirsk
Switzerland	SW1	Institut für Teilchenphysik, Eidgenössische Technische Hochschule (ETH), Zürich
	SW2	Paul Scherrer Institut, Villigen
	SW3	Universität Basel, Basel
	SW4	Universität Zürich, Zürich
United Kingdom	UK1	Brunel University, Uxbridge
	UK2	Imperial College, University of London, London
	UK3	Rutherford Appleton Laboratory, Didcot
USA	US03	University of California at Davis, Davis, California
	US10	Fermi National Accelerator Laboratory, Batavia, Illinois
	US13	Florida State University-SCRI, Tallahassee, Florida
	US17	Johns Hopkins University, Baltimore, Maryland
	US19	Los Alamos National Laboratory, Los Alamos, New Mexico
	US23	University of Mississippi, Oxford, Mississippi
	US26	Northwestern University, Evanston, Illinois
	US30	Purdue University, West Lafayette, Indiana
	US32	University of Rochester, Rochester, New York
	US33	Rutgers, the State University of New Jersey, Piscataway, New Jersey
	US35	Texas Tech University, Lubbock, Texas

10.5 Organisation of Construction

10.5.1 Pixel Detector Construction

Several years of development and prototyping work are still required before any mass production of the CMS pixel modules can start. The insertion of the pixel detector into CMS will occur at a very late stage after the installation of the beam pipe (spring 2005). The detector must be assembled and tested within the preceeding six months. The number of modules to be produced for the low luminosity pixel system is relatively modest; a construction time of two years, including extensive testing at various stages, should be sufficient. With the mass production of the modules starting in the fall 2002, the first lots of the final sensors and readout chips must be ordered at the beginning of 2002. During the year 2001 first pixel modules with readout chips incorporating the full column drain architecture must be fabricated and tested. Several intermediate steps will be required before reaching this goal:

1998:	Design of various blocks suitable for the proposed column drain architecture. e.g. (150 μm)^2 pixel unit cell, 300 μm wide column periphery. Design of 40 MHz analogue signal driver chip.
1999:	Design of complete double column of 2 $\times$53 pixels with periphery. Definition and design of Control&Interface block for the readout chip. Layout of final analogue block.
2000:	Design of full readout chip.

In the years 1998 and 1999, an optimisation program for sensors with (150 μm)^2 pixels will be carried through, with special emphasis on the robustness to high voltage operation. First prototype sensors will be fabricated in the year 2000.

A procedure for large volume bump bonding must be developed, preferably in collaboration with industrial firms, to be ready in the year 2001.

First prototypes of mechanical structures for barrel and end-cap disks will be built in 1998, followed by cooling tests in 1999. The final design of the mechanical/cooling structures starts in the year 2000.

The CMS pixel system consists of three independent parts: The barrel and two end-cap disk systems. These parts will only be combined into the full pixel detector at the insertion into the centre of the CMS detector.

The complete Pixel barrel will be built in Europe by a collaboration from Switzerland (Institut für Teilchenphysik ETH Zürich, Paul Scherrer Institut, Universität Basel, Universität Zürich), Austria (Institut für Hochenergiephysik der ÖAW, Wien) and Germany (RWTH, I. Physikalisches Institut, Aachen). The pixel barrel will be assembled and tested at PSI.

The complete end-cap disk systems, including the services, are in the hands of a US collaboration centred around Fermilab, where the final assembly and test before shipment to Europe will be done. The contributing institutes are University of California at Davis, Fermi National Accelerator Laboratory, Florida State University–SCRI, Johns Hopkins University, Los Alamos National Laboratory, University of Mississippi, NorthWestern University, Purdue University, Rutgers University and Texas Tech University.

10.5.2 Si-Strip Tracker Construction

The following twentythree institutions from eight countries have signed this TDR and are committed to the construction of the Si-Strip Tracker:

RWTH I Aachen, Università di Bari e Sezione dell'INFN, Brunel University, Università di Catania e Sezione dell'INFN, CERN, ETH Zürich, Fermilab, Università di Firenze e Sezione

dell'INFN, Helsinki Institute of Physics, Humboldt University Berlin, Imperial College London, Northwestern University Evanston, University of Oulu, Università di Padova e Sezione dell'INFN, Panjab University, Università di Perugia e Sezione dell'INFN, Università di Pisa e Sezione dell'INFN, Rochester University, Rutherford Appleton Laboratory, Tata Institute EHEP, Tata Institute HECR, Texas Tech University Lubbock and Institut für Hochenergiephysik der ÖAW Wien.

It is therefore imperative to coordinate centrally the design, specification, ordering and purchase of all critical components (sensors, front-end electronics, optical links, hybrids, power supplies). Specifications for less critical items and ancillary equipment (supporting structures, cables and connectors, off-detector electronics, cooling, alignment, control and monitoring systems) will also be centrally defined, but such items may be purchased separately by the collaborating institutes.

Given the large number of detector modules needed to equip the SST (a total of 6336 modules, 2920 single sided and 3416 double-sided, plus spares are required), it is anticipated that their assembly and test will be divided among eleven production centres (Aachen, Bari-Catania, CERN, ETH-Zürich, Fermilab, Florence, Oulu, Padova, Perugia, Pisa, Wien). The necessary components will be produced at companies and delivered to these centres, where functionality and quality checks will be done. A commonly agreed set of acceptance criteria for the components, as well as assembly, testing and quality control procedures for the modules, will be used in order to guarantee product uniformity.

Under the responsibility of a coordinator for quality assurance, each centre should be able to undertake a significant part of the production. In addition to a specialised workshop with dedicated technicians, a centre will have available a "clean area" (class 10000 will be sufficient) equipped with a 3-D measuring machine, an automatic microbonding machine and inspection facilities (microscopes, CCD cameras). Furthermore, semi-automatic probe stations, DAQ and power supply systems should be available for testing the detectors. Almost all of the production centres mentioned above are already operational.

Following their production and test, the individual modules will be mounted on the supporting structures (cylindrical panels or disks) in three sub-assembly centres (CERN, Fermilab, Pisa). These should have the metrology equipment necessary for module inter-alignment. Final assembly and survey of the barrel and end-cap detectors will take place at Pisa and CERN, respectively.

Overall assembly and survey of the entire detector will take place at CERN, where the three subunits of the SST (the barrel and the two endcaps) will be mounted together and aligned with respect to each other.

In preparation of the construction effort we foresee the following intermediate steps:

Spring	1999:	Production of final prototype and full test of barrel and end-cap detector modules equipped with the final read-out system.
Summer	1999:	Full specification of the critical elements (detectors, supporting structures, power supply, read-out electronics).
Fall	1999:	Tendering and ordering.
End	1999:	Start of the production.

The construction effort will start at the beginning of the year 2000 after the final tuning of the production chains.

10.5.3 MSGC Tracker Construction

The MSGC Tracker consists of three mechanically independent parts: the barrel and the two Forward–Backward detectors. Each of these parts is, in turn, subdivided in many subunits. In

the barrel we can identify four logical and physical subunits: the MSGC module, the rod, the disk and the wheel. In the Forward–Backward regions, a smaller number of subunits has to be considered: MSGC detector modules housing four substrates and the disks. Two Super-Modules, corresponding to the two Forward–Backward regions, have to be assembled.

This high degree of modularity enables a high degree of parallelism and a much easier geographical distribution of the construction and testing work. The specification and the design of all critical components, such as MSGC substrates and electronics will be coordinated centrally. The assembly, testing and quality assurance procedures will follow a common approach but will be tailored to the specific requirements of the barrel and Forward–Backward subunits.

Before entering the full mass production phase, the MSGC community will go through the definition and exploitation of a series of pre-construction milestones:

Spring	1999:	Completion of the engineering of industrial production of the barrel and forward MSGC substrates and modules including construction of a pre-series to achieve the target price and throughput.
Summer	1999:	Production and test of final prototype, i.e. barrel and forward MSGC detector modules identical to the production ones equipped with the final read-out system.
Fall	1999:	Full specification of the final barrel and forward MSGC modules. Tendering and ordering.
End	1999:	Start of industrial production of final MSGC substrates and modules.

10.5.3.1 Barrel MSGC Construction

The complete barrel subunit will be built by the common effort of three institutes: CERN, Helsinki Institute of Physics and INFN.

A specific feature of the barrel MSGC is the industrial production of the detector modules. The participating institutions will receive from the industrial companies MSGC barrel modules already equipped with their H.V. and read-out electronics, ready for final acceptance tests before being mounted on the barrel rods.

INFN has the responsibility of monitoring the industrial production to guarantee quality levels and the observation of specifications. INFN will also be in charge of the preliminary tests on the substrate before its acceptance for mechanical assembly. We also expect to automatize and transfer to industry the substrate quality test as soon as the industrial process has reached a high degree of stability and a large statistical sample has been collected.

The final acceptance tests on the modules will be performed in all the participating institutions, roughly in proportion to the number of modules they purchase.

Massive construction of MSGC modules is planned to start at the beginning of 2000 after the final tuning of the mass production tools. Construction and test of MSGC modules will last up to the end of 2003 or the beginning of 2004. We aim at a global throughput of 5 MSGC barrel modules per day.

The manufacture of the rod and wheel components and the partial assembly of the rod, will take place in industry with Helsinki as the main responsible institute. The manufacture of the rod components will take place during 2000. The disks, cylinders and panels for the wheel will be manufactured during 2001 and early 2002.

The quality check and cabling of the rods and the wheel will take place at CERN. The CERN group also has responsibility for assembling the MSGC modules on the rods, performing the final acceptance tests, assembling the rods into the wheel and survey of the Barrel MSGC Tracker.

10.5.3.2 Forward–Backward MSGC Construction

The two super modules will be built by the common effort of eleven institutions in Belgium, France, Germany, Russia and Switzerland: ULB/VUB Brussels, Louvain-La-Neuve, Antwerpen, Mons, IPN-Lyon, IReS-Strasbourg, Aachen I and III, Karlsruhe, Novosibirsk and University of Zürich.

Germany has responsibility for the production of all mechanical elements (frames, forward disks), while the responsibility for the production and testing of the MSGC substrates will be divided between France, Belgium, Germany Russia and Switzerland. The assembly and final mounting will be done in several regional centres.

With the completion of the TDR we enter the preparation phase for a pre-series of detectors in 1999 and final production in 2000. The tooling corresponding to the design presented in this document is being set up in the regional centres for module production: Aachen, Brussels, Strasbourg, Lyon, Karlsruhe and Novosibirsk. At the same time bidding and tendering for substrates, frames and other parts needed for the module production will proceed.

Pre-series of detector modules will be built and undergo final tests in 1999, and at the same time the production of the detector elements will start in all countries involved in the Forward MSGC Tracker. At the beginning of 2000 the final production of detector modules and assembly with the final electronics will start in the regional centres.

Starting in 2001 fully assembled modules with electronics will be assembled on forward disks in the regional centres and / or at CERN.

The final assembly of Super-Modules and system tests at CERN will be due at the end of 2003 or at the beginning of 2004 so that the installation of the two completed super-modules into the Tracker can proceed in September 2004.

10.5.4 Readout and Control Electronics

The electronics required for the silicon and MSGC Trackers will, to a large extent, be common to both. The major items which are not common to both are the front-end circuits, hybrids and certain specialised items, such as the HV control components for the MSGCs. Purchasing and testing will be coordinated centrally. We foresee common purchases of the wafers containing front-end circuits followed by testing in a small number of specialised institutes or in industry, where appropriate. At present we must plan for evaluation by CMS institutes of the mixed signal front end circuits because of the specialised evaluation requirements and difficulty, and probable expense, of defining testing procedures which could be carried out in industry. However, this will be kept under review in case it should become possible once the designs are complete.

Production phases for front-end chips should extend over approximately three years with wafers delivered to CMS centres followed automatic wafer testing to identify known good die. Chips will then be distributed to CMS module production centres, some of which will be the same chip testing centres, for assembly onto hybrids and re-testing. It is not excluded that hybrid assembly could be carried out in industry but this is still under investigation. Detector module assembly will be undertaken by other centres within the collaboration, as described. All of this must be tracked and catalogued. The same institutes will evaluate both silicon and MSGC chips.

Some radiation qualification will be required which should be carried out on sample die evaluated at regular intervals using suitable laboratory irradiation facilities, plus module tests.

Optical links and Front End Drivers and Controllers will be fabricated and tested mainly in industry, followed by acceptance tests by CMS and assembly of complete units, e.g. optical receivers mounted on FEDs and FECs.

The main goal to be met before production starts is verification of the two (silicon and MSGC) front end chip designs in two radiation hard technologies and evaluation of the optical

links assembled in the final form for mounting in CMS. These are expected to be completed in 1999.

The institutes contributing to the electronic design and production are Brunel University, CERN, Imperial College London, Karlsruhe, Lyon, Pisa, Rutherford Appleton Laboratory, Strasbourg, with support from CEA Saclay for DMILL developments.

10.6 Construction schedule and Planning

The planning of the construction of the CMS Tracker is integrated in the overall CMS planning. The general CMS construction planning is given in the Technical Design Report of the CMS Magnet Project. This schedule integrates the schedule for the experimental halls, the magnet, and all the CMS subdetectors including the Tracker.

Details of the construction and installation schedules of the various components of the Tracker (Pixel Detector, Si-strip Tracker, MSGC Tracker Barel and Forward–Backward, Electronics and General Mechanics and Installation) are given in Figs. 10.2 to 10.7.

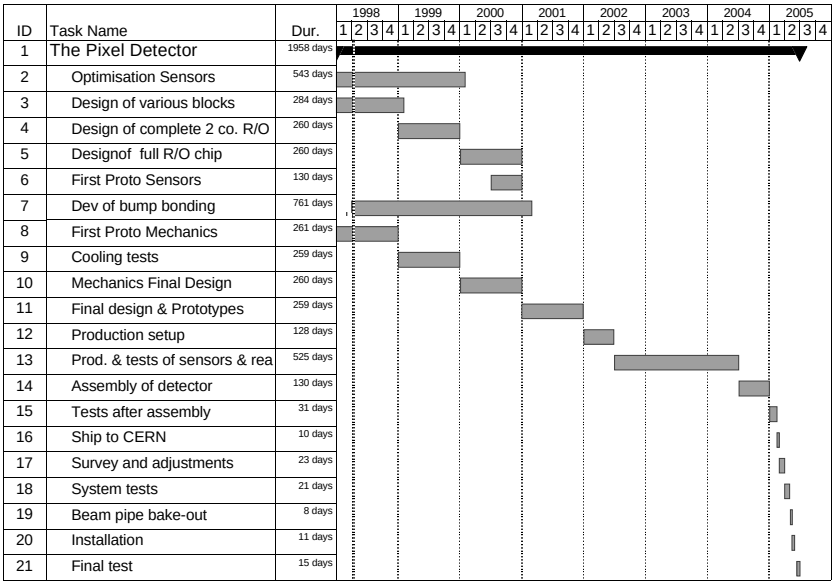

ID	Task Name	Dur.
1	The Pixel Detector	1958 days
2	Optimisation Sensors	543 days
3	Design of various blocks	284 days
4	Design of complete 2 co. R/O	260 days
5	Designof full R/O chip	260 days
6	First Proto Sensors	130 days
7	Dev of bump bonding	761 days
8	First Proto Mechanics	261 days
9	Cooling tests	259 days
10	Mechanics Final Design	260 days
11	Final design & Prototypes	259 days
12	Production setup	128 days
13	Prod. & tests of sensors & rea	525 days
14	Assembly of detector	130 days
15	Tests after assembly	31 days
16	Ship to CERN	10 days
17	Survey and adjustments	23 days
18	System tests	21 days
19	Beam pipe bake-out	8 days
20	Installation	11 days
21	Final test	15 days

Fig. 10.2: Pixel Detector Schedule

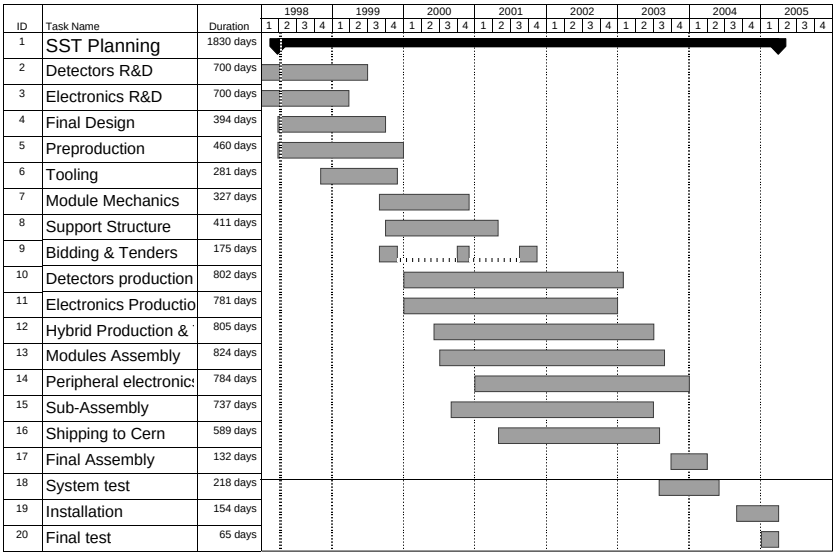

ID	Task Name	Duration
1	SST Planning	1830 days
2	Detectors R&D	700 days
3	Electronics R&D	700 days
4	Final Design	394 days
5	Preproduction	460 days
6	Tooling	281 days
7	Module Mechanics	327 days
8	Support Structure	411 days
9	Bidding & Tenders	175 days
10	Detectors production	802 days
11	Electronics Productio	781 days
12	Hybrid Production &	805 days
13	Modules Assembly	824 days
14	Peripheral electronics	784 days
15	Sub-Assembly	737 days
16	Shipping to Cern	589 days
17	Final Assembly	132 days
18	System test	218 days
19	Installation	154 days
20	Final test	65 days

Fig. 10.3: Si-strip Tracker Schedule

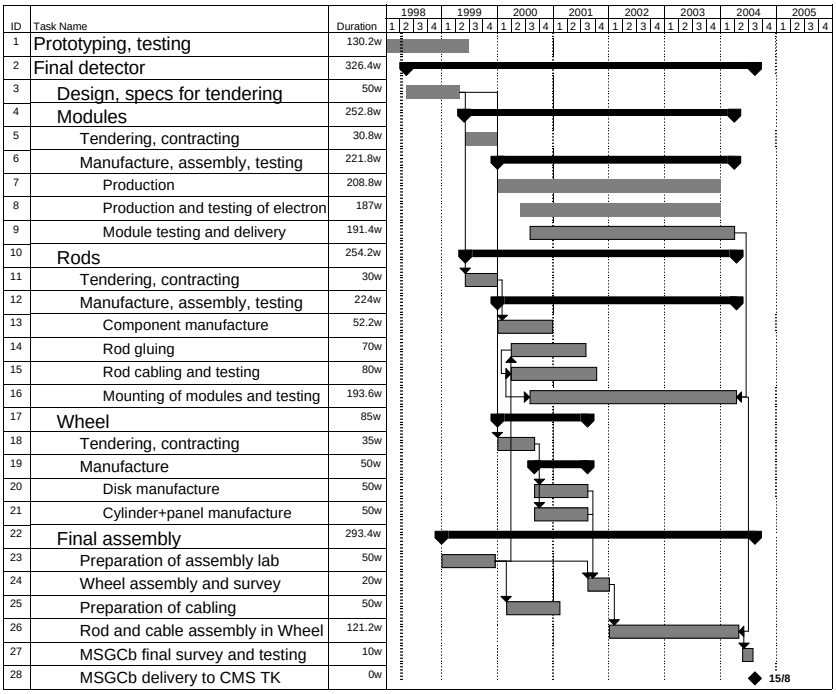

ID	Task Name	Duration
1	Prototyping, testing	130.2w
2	Final detector	326.4w
3	Design, specs for tendering	50w
4	Modules	252.8w
5	Tendering, contracting	30.8w
6	Manufacture, assembly, testing	221.8w
7	Production	208.8w
8	Production and testing of electron	187w
9	Module testing and delivery	191.4w
10	Rods	254.2w
11	Tendering, contracting	30w
12	Manufacture, assembly, testing	224w
13	Component manufacture	52.2w
14	Rod gluing	70w
15	Rod cabling and testing	80w
16	Mounting of modules and testing	193.6w
17	Wheel	85w
18	Tendering, contracting	35w
19	Manufacture	50w
20	Disk manufacture	50w
21	Cylinder+panel manufacture	50w
22	Final assembly	293.4w
23	Preparation of assembly lab	50w
24	Wheel assembly and survey	20w
25	Preparation of cabling	50w
26	Rod and cable assembly in Wheel	121.2w
27	MSGCb final survey and testing	10w
28	MSGCb delivery to CMS TK	0w

Fig. 10.4: MSGC Barrel Tracker Schedule

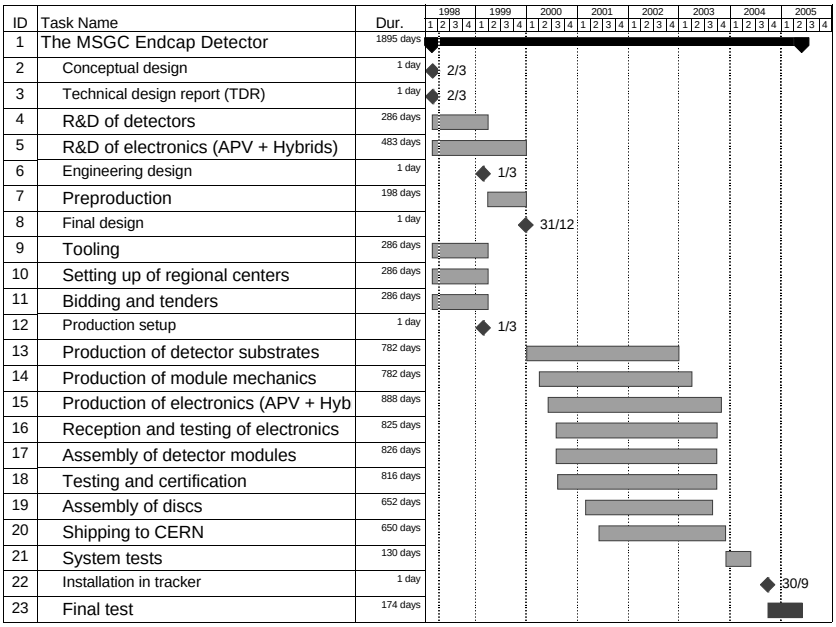

ID	Task Name	Dur.
1	The MSGC Endcap Detector	1895 days
2	Conceptual design	1 day
3	Technical design report (TDR)	1 day
4	R&D of detectors	286 days
5	R&D of electronics (APV + Hybrids)	483 days
6	Engineering design	1 day
7	Preproduction	198 days
8	Final design	1 day
9	Tooling	286 days
10	Setting up of regional centers	286 days
11	Bidding and tenders	286 days
12	Production setup	1 day
13	Production of detector substrates	782 days
14	Production of module mechanics	782 days
15	Production of electronics (APV + Hyb	888 days
16	Reception and testing of electronics	825 days
17	Assembly of detector modules	826 days
18	Testing and certification	816 days
19	Assembly of discs	652 days
20	Shipping to CERN	650 days
21	System tests	130 days
22	Installation in tracker	1 day
23	Final test	174 days

Fig. 10.5: MSGC Forward–Backward Tracker Schedule

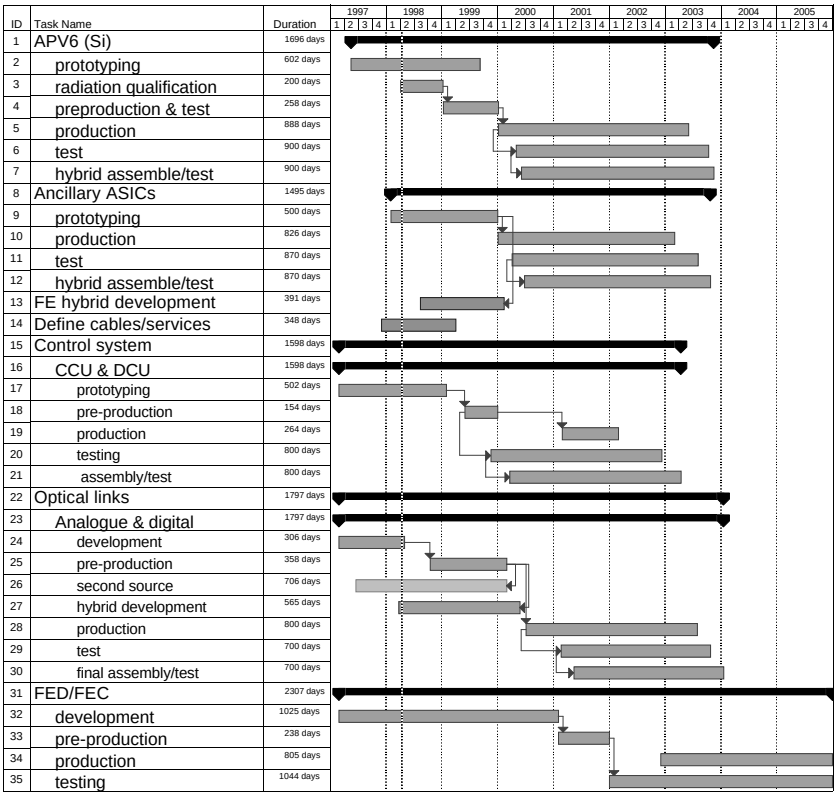

ID	Task Name	Duration
1	APV6 (Si)	1696 days
2	prototyping	602 days
3	radiation qualification	200 days
4	preproduction & test	258 days
5	production	888 days
6	test	900 days
7	hybrid assemble/test	900 days
8	Ancillary ASICs	1495 days
9	prototyping	500 days
10	production	826 days
11	test	870 days
12	hybrid assemble/test	870 days
13	FE hybrid development	391 days
14	Define cables/services	348 days
15	Control system	1598 days
16	CCU & DCU	1598 days
17	prototyping	502 days
18	pre-production	154 days
19	production	264 days
20	testing	800 days
21	assembly/test	800 days
22	Optical links	1797 days
23	Analogue & digital	1797 days
24	development	306 days
25	pre-production	358 days
26	second source	706 days
27	hybrid development	565 days
28	production	800 days
29	test	700 days
30	final assembly/test	700 days
31	FED/FEC	2307 days
32	development	1025 days
33	pre-production	238 days
34	production	805 days
35	testing	1044 days

Fig. 10.6: Electronics Schedule

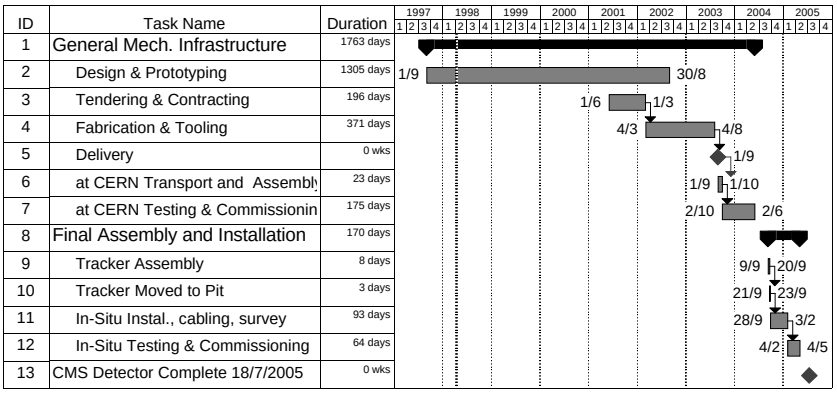

ID	Task Name	Duration
1	General Mech. Infrastructure	1763 days
2	Design & Prototyping	1305 days
3	Tendering & Contracting	196 days
4	Fabrication & Tooling	371 days
5	Delivery	0 wks
6	at CERN Transport and Assembly	23 days
7	at CERN Testing & Commissionin	175 days
8	Final Assembly and Installation	170 days
9	Tracker Assembly	8 days
10	Tracker Moved to Pit	3 days
11	In-Situ Instal., cabling, survey	93 days
12	In-Situ Testing & Commissioning	64 days
13	CMS Detector Complete 18/7/2005	0 wks

Fig. 10.7: General Mechanics and Installation Schedule

Appendix A

Radiation Environment

A.1 General Features of the Radiation Environment

The nominal luminosity of LHC, 10^{34} cm^{-2}s^{-1}, together with the 7 TeV beam energy, will create a very hostile radiation environment. It has been known since the first LHC feasibility studies, that the inner Tracker of an LHC experiment will have to deal with unprecedented radiation levels. Estimates for the radiation environment expected at the CMS Tracker have been given in several publications over the last years for different assumptions of the Tracker layout and electromagnetic calorimeter material [A-1, A-2, A-3, A-4].

Although radiation damage and high background rates in detectors have become a principal design parameter for the LHC detectors, most of these radiation issues are connected with low energy phenomena, which are the same at almost all existing hadron accelerators. However, at LHC the high beam energy combined with the very high luminosity results in numerous intense cascades, which all end up in an immense number of low energy particles. In fact particle energies exceeding 10 GeV are expected to be very rare in the minimum bias background at $|\eta| < 3$. Therefore the radiation studies, with the exception of a few special cases, have to focus on the energy range around 1 GeV and below. In general, physics simulations evaluating the detector performance do not fully account for all low energy background effects so these have to be addressed in specialized radiation environment simulations.

In the inner parts of the Tracker region the radiation environment is dominated by the secondaries from the pp collisions, but neutron albedo from the surrounding electromagnetic calorimeter starts to dominate at radii larger than about 50 cm.

Starting from a constant particle multiplicity per unit of pseudorapidity (η) in the central region, it can be shown that the flux in the absence of magnetic fields and material is independent of the z-coordinate and varies as $1/r^2$, where r is the distance from the beam-line. The presence of the 4 T magnetic field and the Tracker material cause this $1/r^2$ law not to be exactly obeyed in CMS. However, Fig. A.i demonstrates that the z-independence of the flux originating from the vertex is preserved relatively well.

The neutron albedo from the calorimeters leads to an almost uniform neutron flux in the central parts of the tracking volume. Figure A.ii illustrates how this flux increases towards the ECAL endcaps, which are the most intense neutron source in the central CMS detector.

A.2 Definitions of Radiation Units

Flux is defined as the tracklength of particles per unit of volume per unit of time. For particles arriving at an angle to a flat surface the flux is the number of particles crossing a unit surface per

unit of time, weighted by $1/\cos(\theta)$, where θ is the angle to the normal of the surface. Fluence is the time integral of flux and is usually expressed in units of cm^{-2}.

Absorbed dose (abbreviated to dose) is the amount of energy deposited per unit of mass and is expressed in Gy (= J/kg).

The component of the radiation field which causes most of the damage depends on the detector type. In particular particle fluence and absorbed dose, although correlated for a given particle type and energy in a given medium, should never be treated as synonyms.

A.3 Radiation Damage in Silicon

A significant part of LHC related R&D work has concentrated on radiation hardness studies of detectors and electronics. This is especially true for the the silicon detectors to be used in the CMS inner Tracker. Details on different types of damage are given in the relevent detector specific sections. Below, only the aspects important for relating the radiation environment to the damage are described.

A.3.1 Surface damage

Surface damage is usually the most important damage mechanism for electronics components. It is caused when the charge, generated by the passage of an ionizing particle, gets trapped in the oxide layer. Ionization is by far the dominant energy loss mechanism of charged particles traversing matter. Thus surface damage is a function of the absorbed dose. The latter is a well-defined quantity and arises as a simple number from the radiation simulations. Except for low energy photons, or for hydrogen-containing materials in a radiation environment dominated by neutrons, the material dependence of dose is relatively weak.

A.3.2 Bulk damage

At the LHC the lifetime of silicon detectors will be limited by bulk damage, which causes an increase of leakage current and changes in the effective doping concentration. The latter effect ultimately leads to very high depletion voltages. Contrary to surface damage, bulk damage depends in a complicated way on the incident particle spectrum. Therefore the use of experimental silicon bulk damage data in order to deduce detector life-expectancies from simulation results, is far more complicated than in the case of surface damage.

All experimental data available at the moment are consistent with the NIEL hypothesis, which states that the bulk damage in silicon has a linear dependence with the non-ionizing energy loss (NIEL) in the silicon. Considerations of cross sections and kinematics show that the NIEL is very small for incident electrons or photons and moderate for muons. It starts to be significant for heavier projectiles, i.e. all hadrons. Since the NIEL is a very small fraction of the total $\mathrm{d}E/\mathrm{d}x$ of a charged particle – and since this fraction is almost zero for electrons – bulk damage has essentially no relationship to radiation dose. Semi-theoretical calculations of the energy and particle type dependence of NIEL [A-5] agree quite well with available experimental data [A-6]. Both the data and the calculations indicate that for the hadron types and energy spectra expected at the LHC the damage in silicon varies by a relatively small factor. The only exception are neutrons for which the damage below 100 keV of energy is practically negligible. Often damage constants are expressed with respect to 1 MeV neutron equivalent fluence. This is a defined quantity, corresponding to a NIEL of 95 MeV mb [A-7]. The LHC spectrum can be averaged with the presently available information of the energy-dependent damage functions to arrive at the average damage constant (= NIEL). The results of such a procedure can be found in Table A.1 for various regions of the CMS Tracker assuming the spectra to be presented

in forthcoming sections. There is a clear tendency for the average NIEL to decrease when the average energy increases, i.e. towards small radii and high pseudorapidities. It should be remembered, however, that due to the lack of consistent experimental data the damage constants are not firmly known over the whole range of LHC energies and particle types. In particular for pions, which dominate the fluence at the inner Tracker layers, experimental data are limited to a narrow energy range around 300 MeV and the calculated values [A-5] are likely to underestimate the NIEL below the Δ-resonance. Thus the values in Table A.1 include significant uncertainties and their relatively small spread around $\sim$95 MeV mb should be taken as an indication that to a good approximation it is sufficient to integrate the flux at LHC over all hadron types and energies (>100 keV for neutrons) and to use the result together with damage constants expressed for 1 MeV neutron equivalent fluence.

Finally, it should be emphasized that Table A.1 and all the associated discussion is valid only for silicon. Even the 100 keV threshold energy for neutrons is a property of silicon. Thus none of these damage arguments should be extended to other materials in a quantitative way.

Table A.1: Average NIEL (MeV mb) for the hadron spectra in different parts of the Tracker. The calculations are based on the damage functions given in Ref. [A-5]. The NIEL of 1 MeV neutrons is defined to be 95 MeV mb [A-7]

	$\|\eta\|$ = 0–0.9	$\|\eta\|$ =0.9–1.8	$\|\eta\|$ =1.8–2.7
r = 0–20 cm	75	69	62
r = 20–40 cm	88	85	82
r = 40–65 cm	100	95	92
r = 65–120 cm	109	106	104

A.4 Shielding Requirements and Materials

Inside CMS the shielding is constrained by the very limited space available. Therefore materials have been selected to provide the most efficient shielding in the smallest space. In addition, the shielding strategy must not jeopardize the performance of the detectors through inert material placed in front of them. Both aspects are of utmost importance for the shielding design inside of the ECAL. Most of the neutron flux, which is harmful to the inner Tracker, is generated by hadronic interactions in the ECAL crystals. The choice of the ECAL material significantly affects the neutron albedo; the heavier the elements in the absorber the more albedo [A-1]. In this respect the $PbWO_4$ crystals chosen by CMS are not very favourable. Without any protection, the neutron fluence in the Tracker region would be in the range 5–30 $\times$ 10^{13} cm^{-2} for an integrated luminosity of 5×10^5 pb^{-1} [A-4]. The highest values would occur close to the ECAL endcap and the lowest at a radius of about 50 cm in the centre of the Tracker.

The most efficient method of neutron moderation is based on elastic scattering from hydrogen nuclei. Therefore the main parameter, when trying to minimize thickness, is the hydrogen density per unit of volume. In this respect polyethylene, paraffin and water are almost equivalent. Of these, polyethylene is the easiest to handle and to machine into the desired shape. It also has the advantage of a relatively large radiation length and so does not introduce an unacceptable amount of material in front of the ECAL.

An important consideration is that effective shielding of silicon devices only requires that the neutron energy is lowered below 100 keV. There is no need to absorb the neutrons. Therefore special neutron capture elements like boron or lithium would actually be a disadvantage since they would lower the hydrogen content of pure polyethylene. Similarly, any impregnation or lowering of the average density would reduce the effectiveness of polyethylene.

Most neutrons are produced by evaporation and have an energy around 1 MeV. Owing to the relatively large (n,p) elastic cross section, a few centimetres of polyethylene are sufficient to slow most neutrons below the 100 keV limit. The attenuation of the neutron spectrum produced in the crystals is shown in Fig. A.1 for several neutron energy cut-offs. For the important 100 keV cut-off energy there is no single attenuation length – after a rapid drop during the first centimetres the spectrum becomes increasingly hard and the polyethylene loses its effect. This is due to the fact that the high energy part of the spectrum, which is very weakly attenuated by the polyethylene, starts to form a dominant contribution beyond a thickness of about 10 cm. This suggests that a reasonable thickness for a moderator layer is between a few centimetres and 10 centimetres. Figure A.1 also illustrates the fact that boron-doped polyethylene is a worse moderator than pure polyethylene.

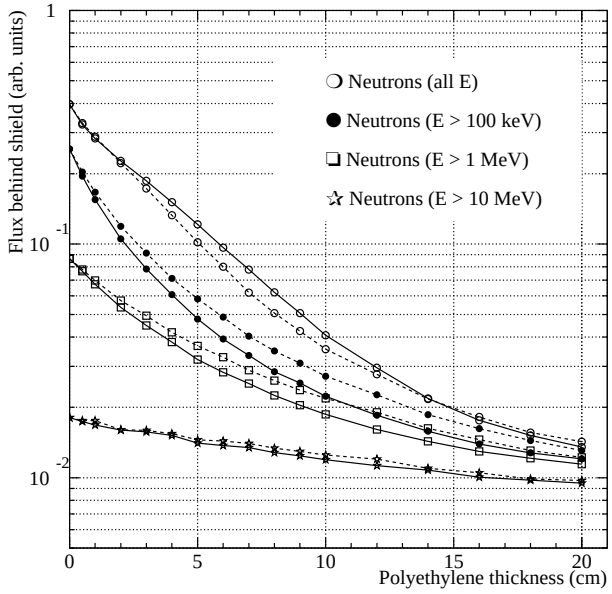

Fig. A.1: Simulated neutron flux behind a polyethylene wall, irradiated with the neutron spectrum produced in the ECAL crystals. Each curve shows the integrated flux above the indicated threshold. For silicon, the 100 keV threshold is the significant one. The solid lines correspond to pure polyethylene of density 0.95 g/cm^3. The dashed lines are for borated polyethylene of density 0.93 g/cm^3.

A.5 LHC Parameters

A.5.1 Luminosity

The usually quoted LHC luminosity of 10^{34} cm^{-2}s^{-1} is in fact the value at the beginning of the fill when the machine is operating at its nominal parameters. During the fill the beam intensity goes down due to various loss processes and the luminosity decreases correspondingly. No final decision on the number of fills per day has been taken, but it has been shown that about the same day-averaged luminosity can be reached with either one or two fills. In both cases this average is roughly half of the nominal value [A-8].

The LHC will not commence with its nominal luminosity but a low-luminosity start-up phase of several years will precede the high luminosity operation. Following the suggestions in Ref. [A-9] we assume that the luminosity during the first year is 10% of the nominal value and rises to 33% in the second year and 67% in the third year. From the fourth year onwards the LHC is assumed to operate at its nominal parameters.

A.5.2 Assumed operation schedule

Depending on the detector type and the expected radiation effects, either integrated or instantaneous values of fluxes or dose rate are most relevant. Detector occupancies, for instance, depend only on the instantaneous particle rate, whereas radiation damage is often a cumulative effect. For the estimation of induced activity, even differences in the irradiation histories have to be considered. This is because residual nuclides are produced proportionally to the integrated luminosity, but the decay of radioactive isotopes takes place simultaneously and, for a given nuclide, is only a function of time. The time profile of irradiation can also become important for silicon damage, since annealing and reverse annealing are not simple functions of the integrated luminosity, but depend also on the actual time. Therefore an assumption of the machine schedule has to be included in some calculations.

Following the suggestion of [A-9], three periods of 60 days, pp operation per year have been assumed. These periods would be separated by 14-day shutdowns in between. Under these conditions and including a low-luminosity start-up phase, an integrated luminosity of 5×10^5 pb^{-1} is expected over ten years of LHC operation. This corresponds to 5×10^7 seconds of operation at LHC peak luminosity.

Heavy-ion operation is foreseen for a relatively short period per year. Tentatively six weeks have been suggested [A-9]. The peak luminosity in the Pb–Pb mode will be 1.95×10^{27} cm^{-2}s^{-1}. Although the inelastic cross section and the average multiplicity in Pb–Pb interactions are expected to be significantly larger than in proton–proton collisions, the average background from Pb–Pb-operation remains about three orders of magnitude below that of the high-luminosity proton–proton collision mode. Thus the heavy-ion operation is not expected to add any significant contribution to the accumulated dose and fluence in detectors and has not been taken into account in the simulations. It should be kept in mind, however, that the instantaneous particle rate and thus the instantaneous energy deposition during a central Pb–Pb collision are expected to be about 50 times higher than during a high-luminosity proton–proton bunch crossing.

A.6 Induced Radioactivity

While induced radioactivity is negligible at electron–positron colliders, it will be a major concern at the LHC, especially for personnel safety issues. At a hadron accelerator we are confronted with two distinct mechanisms which create remanent radioactivity in materials. These are low-energy neutron interactions [(n,γ), (n,p), (n,α)...] and high-energy hadronic interactions. The former lead from a given target isotope to a well-defined daughter nuclide. The cross sections are, in general, well known up to 20 MeV. Most activation reactions are characterized by thresholds at few MeV and relatively low cross sections. Some materials, however, have very large thermal cross sections for (n,γ) reactions, which can result in radioactive isotopes. In the Tracker the gold strips of the MSGCs represent a material which is susceptible to neutron activation by (n,γ) reactions and in the surrounding ECAL the tungsten isotopes will be activated by thermal neutrons.

At energies above 20 MeV we deal with the high-energy regime. Here the final daughter nucleus cannot be deduced from the knowledge of the colliding particles. A high-energy hadronic interaction can, in principle, lead to any residual nuclide with A and Z below those of the target [1]. Nevertheless, peripheral reactions with the removal of only a few nucleons usually dominate, so that most residual nuclei are relatively close to the original target. Roughly 30% of high-energy inelastic hadronic interactions create long-lived radionuclides [A-10, A-11] which contribute to the induced activity dose rate in the experimental area during access periods. This activity

[1] Capture and charge exchange reactions can also lead to A and Z just above those of the target.

decreases relatively slowly after the end of irradiation, so that even long cooling times do not significantly decrease the dose rate.

If the production cross section of a given radionuclide is σ_j and the constant irradiation flux is ϕ, then the activity per unit of volume in a sample after an irradiation time t_i and a cooling time t_c is given by

$$A(t_i, t_c) = \rho \frac{N_A}{M} \sum_j \sigma_j \phi \left[1 - e^{-\lambda_j t_i}\right] e^{-\lambda_j t_c}. \quad \text{(A.1)}$$

Here ρ is the density of the sample, M its molecular mass and N_A is the Avogadro number. The decay constant, λ_j is related to the half-life τ_j by $\lambda = \ln 2/\tau$.

Equation (A.1) does not include the effect of possible cumulative decays, i.e. nuclides decaying into other radionuclides. Equation (A.1) shows that if $t_i \to \infty$, the activity does not increase indefinitely, but approaches a saturation value which is equal to the production rate of radionuclides.

Induced activity is usually regarded as a safety issue only. However, radioactive decays are not taken into account by the simulation codes so the γ's and β's, which might give an additional contribution to detector background, are not accounted for. In this context it has to be remembered that – contrary to safety issues – even nuclides with very short half-lifes have to be considered.

A.7 Simulation Methods

A.7.1 Generation of minimum bias events

The radiation environment simulations are based on minimum-bias events obtained from the DPMJET-II event generator [A-12]. DPMJET-II is the most recent of the Dual Parton Model generators, which are specially suited for simulation of minimum-bias hadronic collisions. As one of the updates with respect to the older DTUJET93 [A-13] program, DPMJET-II includes a complete description of charm production. The high-p_{T} physics has been further complemented by adding a proper fraction of pure b-events from PYTHIA [A-14] to the DPMJET-II events. Differences between DPMJET-II and DTUJET93 event sets are mainly in high-p_{T} and diffractive events. As far as the Tracker is concerned both generators give very similar results.

Figure A.2 shows the charged multiplicity and transverse momentum distribution for the DPMJET-II events and, for comparison, minimum-bias events obtained from PYTHIA 5.7. When comparing the distributions from the two event generators it should be noted that the multiplicity is not independent of the assumed cross section. In particular the PYTHIA multiplicity decreases if the cross section is forced to increase [A-2]. The DMPJET-II events, which include single diffraction, correspond to 80 mb inelastic cross section, whereas the inelastic cross section corresponding to the PYTHIA events is only 65 mb. Thus, even though the multiplicity per event is higher with PYTHIA, the average multiplicity per unit of time is lower than with DPMJET-II.

The global scaling parameter for the radiation levels at LHC is the inelastic interaction rate, which is the product of the luminosity and the inelastic cross section. For the latter a value of 80 mb will be assumed. This includes a sizeable fraction of diffractive events. Some 15% of the collisions are expected to be single diffractive. In these events one participating proton continues with only a small transverse deflection, as in elastic scattering and only the dissociated proton contributes to the radiation background in the experimental area. Double diffraction is a relatively rare process and as far as the radiation environment is concerned it will be essentially equivalent to normal inelastic collisions.

To understand broadly how energy is distributed in the experimental area, the angular distributions of the particles emerging from the generated minimum-bias events are analysed.

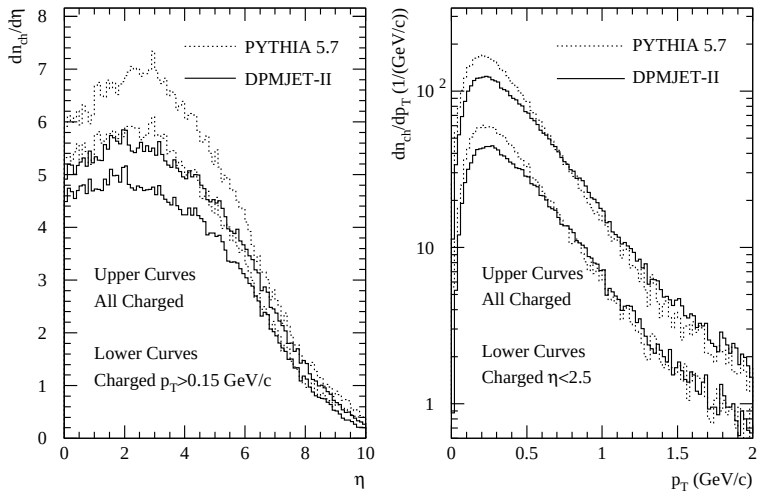

Fig. A.2: Charged particle multiplicities as a function of pseudorapidity and transverse momentum according to DPMJET-II and PYTHIA 5.7 event generators. The differences are compensated by the corresponding cross sections which are 80 mb and 65 mb, respectively.

Table A.2 shows the average total energy distribution into different η regions, obtained with DPMJET-II.

The DPMJET-II minimum-bias event file used for the simulations includes 2000 events. For the radiation studies the 25 ns bunch structure of the LHC is not significant and even the correlations within a single event can be neglected. This allows for both files to be randomized, i.e. the secondaries were randomly reordered resulting in a smoother source at the cost of destroying the event structure. The average total multiplicity per event is used to scale the simulation results to the proper luminosity.

Table A.2: Average energy distribution of one inelastic minimum-bias event into different pseudorapidity regions according to predictions from the DPMJET-II event generator. The values represent a sum of both sides of the detector. The magnetic field and particle decays are neglected

η = 0.0–3.0 Central detector	η =3.0–5.3 Forward calorimeters	η =5.3–7.8 Collimators	η >7.8 Leaving area
100 GeV	760 GeV	4200 GeV	8900 GeV

A.7.2 Radiation transport codes

The radiation simulations are independent of the general detector simulations and are performed with the FLUKA [A-15] simulation code, which is specially designed for radiation physics.

FLUKA has a full treatment of high-energy physics, but special emphasis has been put on effects occurring around energies of a few GeV and below. The main FLUKA features, which are important for the radiation environment simulations at the CMS Tracker are:

- generation of hadronic interactions from thermal neutrons up to 20 TeV,
- pre-equilibrium cascade model for inelastic interactions below 1.3 GeV and for capture reactions at rest,
- nuclear evaporation and gamma de-excitation after inelastic interactions,
- extended version of the EGS4 electromagnetic shower code [A-16, A-17],
- multigroup transport of neutrons below 20 MeV with detailed kinematics for (n,p) scattering and accounting for self shielding effects in some materials,
- neutron capture reactions with explicit photon emission,

- accurate multiple scattering and magnetic field transport even in thin layers,
- full accounting for ionization loss, including explicit δ-electron production and latest parametrizations for the density effect at high energies and shell corrections at low energies.

A.7.3 General geometry description

A substantial effort has been devoted to finding the best parameters and approximations to describe the CMS system so that it remains feasible to implement with the relatively unsophisticated geometry routines of FLUKA. Roughly 2000 volumes are needed to achieve this for the full CMS detector including shielding, the surrounding hall and the V4 Tracker version. Each detector has been described with the minimum accuracy which was considered sufficient. For the Tracker this means that a quite rough description for the outer detector parts is sufficient whereas the Tracker itself has to be described in sufficient detail to reproduce mass distributions properly.

A major approximation is that everything is assumed to have cylindrical symmetry. This is enforced by the fact that azimuthal averaging has to be applied in order to obtain results with sufficient statistics.

Since outer parts of the CMS detector and the experimental cavern have negligible impact of the radiation field within the central detector the cascade development in them has been disfavoured with the powerful biasing techniques available in FLUKA. By reducing the amount of CPU time per particle this allows better statistics to be collected in the Tracker region, while preserving possible effects due to external elements, in particular the forward calorimeter.

A.7.4 Energy cuts and transport parameters

The lower threshold for neutron transport was set to thermal energy at 293 K. Although the thermal neutron group of FLUKA ranges from 10^{-5} eV to 0.414 eV, the cross sections in the 293 K group correspond to a mean thermal neutron energy of 0.025 eV. The transport cut for charged hadrons was set to 10 keV. Antineutron transport was stopped at 50 MeV, which is dictated by available cross section data. Energy cuts for electromagnetic particles are more problematic because of the intolerable increase of computing time if cuts are set too low. Therefore the energy thresholds for photon, electron, and positron transport were adjusted according to the region. The absolute lower cut was 100 keV for electrons and 30 keV for photons, which was used in all detectors directly visible from the Tracker. In outer regions these cuts were raised considerably in order to save CPU time. At the cuts the action of the simulation code depends on the type of particle. For electromagnetic particles the energy is deposited on the spot but the photons emitted in positron annihilation are further transported. Other charged particles are ranged out to rest and, if applicable, capture on a nucleus is enforced. Neutral particles are transported until they decay or get captured. Antineutrons falling below the threshold are forced to interact after having travelled a distance corresponding to the cross section at threshold.

The full 2-dimensional (azimuthally symmetric) magnetic field map of CMS was used in the region of the central detector.

Multiple scattering was performed down to the Molière limit. Delta electrons were produced above 100 keV. Pair production and bremsstrahlung were explicitly simulated for high-energy muons and charged hadrons.

A.7.5 Scoring

The particle fluxes have been obtained by using a tracklength estimator in the the detector layers. For silicon the scoring was done in 600 μm thick silicon plates, representing the sensitive volume and part of the averaged services and electronics, and for the MSGCs in 3 mm wide gas gaps. All charged hadrons and neutral kaons have been grouped together. The antineutron fluence, significant only at the pixel detectors, has been combined with the neutron fluence.

The dose has been obtained as total energy deposition in the silicon plates or the glass substrates of the MSGCs.

For a detailed estimation of radiation damage and activation issues the energy spectra of the particles are indispensable. These have been obtained in 9 regions limited by radii of 20 cm, 65 cm and 120 cm and η-lines of 0.9, 1.8 and 2.7. In these regions the spectra were scored as tracklength in the detector elements.

A.7.6 Estimation of error margins

All simulations have been divided into several independent batches of equal size. These have been used to estimate the statistical errors arising from fluctuations in the event sampling and during cascade simulation. In the figures only these statistical error estimates are indicated, as 1 σ error bars. Systematic errors are usually more important.

Uncertainties arise from the extrapolation of existing data to the inelastic proton–proton cross section at 14 TeV as well as from the estimates of event multiplicities and momentum distributions of the minimum-bias events. These lead to an underlying uncertainty of about 30% from the pp events alone [A-2] which probably cannot be reduced before LHC minimum-bias data is available. This error is the dominant one as far as charged hadron fluxes in the CMS Tracker are concerned. Table A.3 shows the longitudinally averaged hadron and neutron fluences at some layers of the barrel Tracker for three different event generators. The cross section suggested by PYTHIA, single diffraction excluded, is 65 mb. For DTUJET93 and DPMJET-II a cross section of 80 mb was used. Both of the latter include single diffractive events. We can observe very good agreement between the results obtained from these three event generators. Although DPMJET-II and DTUJET93 are to a large part the same code, PYTHIA differs from these substantially. Thus the good agreement gives some confidence in the extrapolation of minimum-bias event generation to $\sqrt{s}$ = 14 TeV. Although the difference between the three event generators compared is small, some other models – like the one used for the Technical Proposal – give higher fluences, which justifies the use of an error bound, as large as 30%, for the charged particle fluences.

For particles other than the pp secondaries, uncertainties in the cascade development dominate. The accuracy of the cascade simulation is affected by approximations in the geometry description and incompleteness of physics models and cross section data sets.

Table A.3: Longitudinally averaged particle fluxes ($10^6 \mathrm{cm}^{-2}\mathrm{s}^{-1}$ at LHC peak luminosity) at some layers of the barrel Tracker for three different event generators

Radius	Particle type	DPMJET-II	DTUJET93	PYTHIA5.7
7.1 cm	Ch. hadron & K^0	17.5±0.01	17.9±0.02	15.4±0.02
	Neutron (E >100 keV)	2.16±0.02	2.08±0.07	1.55±0.08
22 cm	Ch. hadron & K^0	2.41±0.03	2.58±0.04	2.23±0.08
	Neutron (E >100 keV)	0.69±0.02	0.70±0.02	0.64±0.05
98.5 cm	Ch. hadron & K^0	0.08±0.00	0.08±0.00	0.07±0.01
	Neutron (E >100 keV)	0.23±0.00	0.24±0.01	0.18±0.00

FLUKA has been benchmarked in several small scale experiments using neutron counters and activation foils. The agreement with measurements is of the order of few tens of per cent even after several attenuation lengths of shielding [A-18]. Nevertheless these relatively simple experiments cannot be guaranteed to give a reliable error bound for the case of the neutron albedo from the CMS ECAL, which is dominated mainly by the accuracy with which the neutron production in hadronic collisions is described. This is hadron physics around a few GeV which is a difficult domain for Monte Carlo modelling, because of a mixing of nuclear structure and high-energy effects. Intercomparisons between different Monte Carlo models for the CMS ECAL suggest that an uncertainty of a factor of 2 should be expected in the neutron albedo.

Since the charged hadron flux dominates in the most exposed part of the silicon Tracker, a total safety factor of about 1.5 should be applied to the fluences presented in the following sections. For the pixel detector this factor could be reduced slightly but correspondingly it should be increased in regions dominated by the neutron albedo.

The induced activity calculations are a special case. The uncertainties in the cascade simulation are negligible compared to those of the radionuclide production cross sections or residual nuclei yields as given by the simulation codes. In addition the geometries and material distributions used for the calculations involve quite significant approximations. The reader should not be misled by the number of digits with which data are given in plots and tables. Usually the accuracy is introduced only to indicate local variations of the values, i.e. relative differences. The absolute values given by the induced activity calculations should not be assumed to be accurate to better than a factor of about 5, although in some special cases a better accuracy can be achieved. Thus the induced activity dose rates and particle fluxes should be interpreted merely as indicators of the order of magnitude.

A.7.7 Simulation of LHC beam losses

It can be expected that for the Tracker the worst beam loss condition would be if beam particles, heading towards the experiment, would be lost in the low-β section or on the copper collimator. With its $r = 17$ mm aperture the collimator serves as an efficient protection against losses in the experiment itself.

Loss patterns or probabilities of such events have not yet been provided by the LHC machine experts. A study of realistic loss patterns and accidental loss conditions has been initiated within CMS and a preliminary indication is that some accidental conditions could lead to a loss of a significant fraction of the full beam in the low-β section. No indication has been found so far that losses could happen directly on the collimator.

Since these studies are in a preliminary stage and also require cross-checking by the LHC machine experts, we prefer to do a simplified case study by simulating beam losses on the collimator. Although this will be pessimistic with respect to losses further upstream, it serves the purpose of giving an indication of how a beam loss close to the experiment is reflected at the Tracker. Before more detailed studies are ready, we do not make any statement about the possible loss rates but normalize all results to one proton incident on the collimator.

A proton could hit the collimator either at the end or at grazing angle at the inner aperture. The latter can be expected to be more dangerous, since grazing protons would not see the full attenuation length of the collimator. Beam losses were simulated by shooting 7 TeV protons at the back end of the collimator, uniformly distributed between radii of 16 mm and 18 mm and having an angle of 60 μrad to the beam axis. Secondaries were transported through the collimator, the shielding, and the forward calorimeter and fluences and radiation dose were scored in the inner Tracker.

A.7.8 Estimation of induced radioactivity

The residual nuclide yield in high-energy interactions is difficult to estimate, since experimental cross sections are only rarely available for the particle, target, energy combinations of interest [A-19]. Some extrapolations of available data are possible, but the associated uncertainties are significant. The hadronic event generators of some simulation codes, like FLUKA, can be used directly to estimate the residual nuclide yields. But although the interaction models have improved over the last years, there are still significant uncertainties, especially concerning the residual nuclei.

If we consider safety aspects, we can neglect all nuclei with very short half-lifes, since these will have disappeared after a reasonably short cooling time. Thus it is often relatively easy to explicitly identify the nuclides which need to be considered in a safety analysis. This is true, especially, for light target materials (A <30), where the most important radioisotopes are ^{7}Be, ^{22}Na and ^{24}Na. The experimental cross sections can be used together with the fluxes from the simulations to arrive at production rates of individual radionuclides. For the Tracker this procedure has been followed with cross sections for aluminium and iron and results are reported in Section 6.9.8.

The situation becomes much more complicated if we consider increased rates in detectors during operation. In this case none of the short-lived nuclides can be excluded. Experimental data on production rates of such more exotic nuclei is too incomplete to be useful. So the only way to estimate this effect is to use the hadronic event generators to obtain the production cross sections. In addition chain decays are very common for such short-lived nuclides. Thus Eq. (A.1) is not valid and the decay chains have to be followed explicitly. We use the DeTra code [A-20] for this task. This code allows one to calculate analytically the decay chains of some 4400 nuclides in its database and to extract the explicit photon and β-spectra at any instant of time during an arbitrary irradiation/cooling cycle.

The estimation of detector background requires an accounting for induced activity in the Tracker itself, but also in the beam pipe and the surrounding ECAL. These activaties have been determined from results of FLUKA simulations. The time dependence is followed with the DeTra code and the induced activity photons are transported in the Tracker geometry using FLUKA. More details on the simulations can be found in Ref. [A-21].

A.8 Pixel Detector

The pixel detector is located closest to the interaction point where the radiation environment is dominated by the pp secondaries directly. The particle fluences and radiation dose at the three barrel layers and the two forward disks can be found in Fig. A.3. We can observe a very strong radial dependence of the charged particle fluence and a less pronounced variation of the neutron fluence. In both cases the variation along the z-axis is small. The dose follows roughly the behaviour of the charged hadron fluence.

The independence on the z-coordinate allows fluences over z to be averaged in order to arrive at characteristic values for each radial layer. The averaged results are given in Table A.4, which also shows the proportion of different hadron types. For the relatively compact pixel detector these averaged data are directly applicable to the endcap disks at the corresponding radius.

Figure A.4 demonstrates how all spectra become harder towards higher pseudorapidity and that the charged hadron fluence is dominated by pions with protons and charged kaons each accounting for about 10%. The maximum of the spectrum occurs between 400 MeV and 2 GeV depending on the η-range considered.

The photon spectrum shows a high-energy component due to π^0 decays and a significant flux of low energy photons which is mainly produced by neutron capture and nuclear de-excitation.

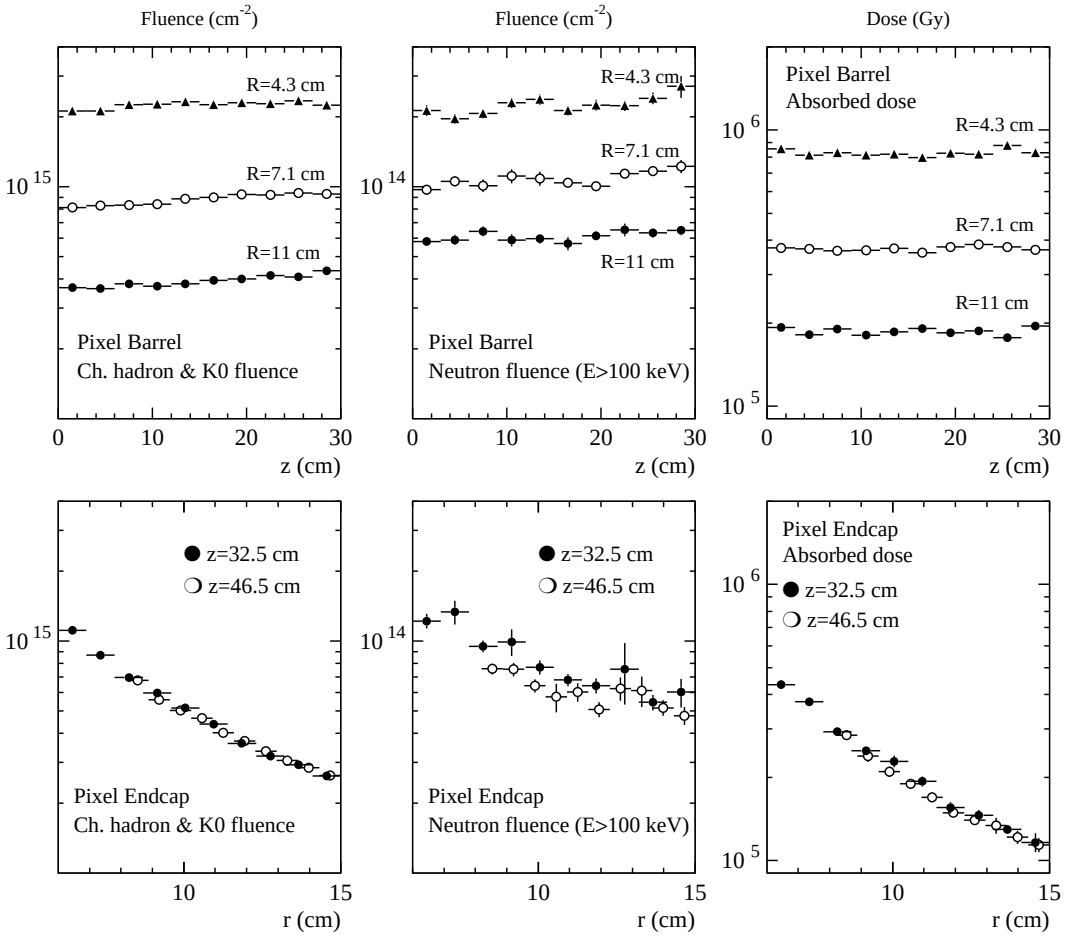

Fig. A.3: Energy-integrated charged hadron and neutron fluences and absorbed dose in the pixel detector. All values are for an integrated luminosity of 5×10^5 pb^{-1}.

Table A.4: Longitudinally averaged hadron fluences in the three layers of the barrel pixel detector. All fluence values are given as 10^{13} cm^{-2} for an integrated luminosity of 5×10^5 pb^{-1}. The fast hadron fluence is the sum over the first five rows of each column and serves as a good approximation to the 1 MeV equivalent fluence. The indicated errors refer to the simulation statistics only

	4.3 cm	7.1 cm	11 cm
Charged pions	180±1	71.8±0.3	32.6±0.2
Protons	15.5±0.2	6.1±0.1	2.66±0.07
Charged kaons	17.3±0.2	6.2±0.1	2.48±0.04
Neutral kaons	11.0±0.2	3.60±0.08	1.33±0.03
Neutrons (E >100 keV)	22.6±0.4	10.8±0.2	6.11±0.1
Thermal neutrons	5.6 ±0.5	5.0±0.2	5.2±0.2
Neutrons total	29.2±0.6	16.8±0.3	12.3±0.2
Fast hadrons	246±1	98.5±0.4	45.2±0.2
Absorbed dose (kGy)	828±7	371±4	187±2

The neutron spectrum at the pixel detector is remarkably hard in all three η-regions, but especially at the higher η-values. This indicates that the majority of the neutrons are secondaries emerging from the pp collision.

The pixel optical link transmitters will also be situated close to the interaction point. In order to estimate the radiation levels at their location the dose and particle fluences have been simulated for a cylinder of radius 18.7 cm extending from $z = 32.6$ cm to $z = 46.6$ cm. The

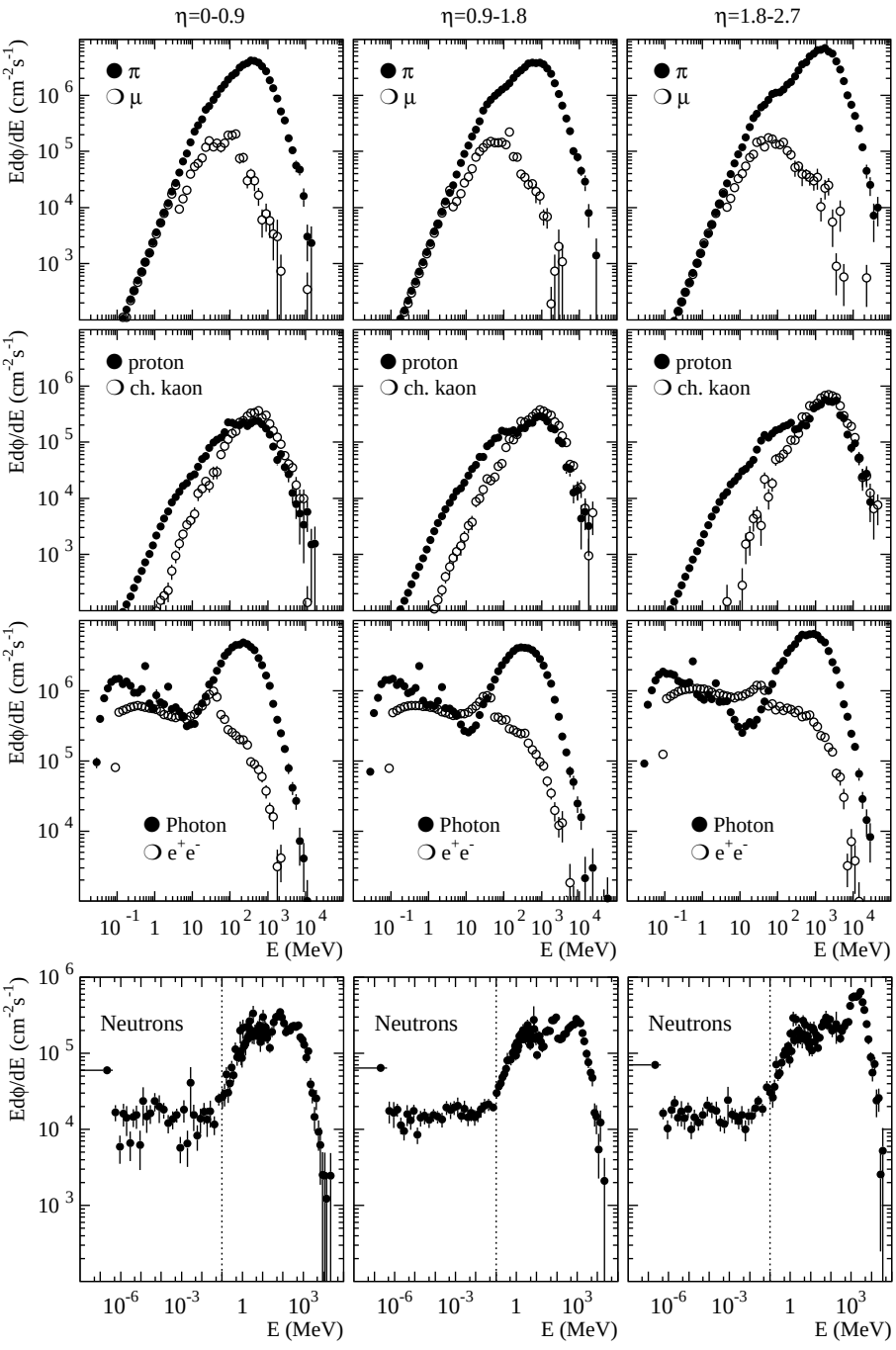

Fig. A.4: Energy spectra of the most important particles types in the pixel detector. The vertical line indicates the critical 100 keV limit for neutrons. All values are for a luminosity of 10^{34} cm^{-2}s^{-1}.

radiation dose is 80±2 kGy, the charged hadron fluence is (1.69±0.03)×10^{14} cm^{-2} and the neutron fluence above 100 keV is (4.0±0.2)×10^{13} cm^{-2}. The optical links will not be silicon devices hence the 100 keV cut applied on neutrons may not be approppriate and the corresponding fluence should only be taken as an indicative value [A-22]. Since, however, the fluence between 100 keV and the thermal regime is only 1×10^{13} cm^{-2}, the neutron fluence shown with the 100 keV cutoff should not be too optimistic by more than 25%.

A.9 Silicon Tracker

The silicon Tracker extends from an inner radius of just over 20 cm to about 60 cm. Along the z-axis it spans the whole length of the Tracker. The barrel detector consists of five concentric layers. Each endcap has 10 disks distributed along the available space in z. Figure A.5 shows the charged hadron and neutron fluences and the radiation dose at the barrel layers and some endcap disks. Like for the pixel detector there is a relatively strong radial variation but only weak z-dependence of the charged hadron fluences. The neutron fluence shows a clear increase at the endcap disks closest to the ECAL. The radial variation of the neutron fluence is relatively small, the excess at small radii being due to the neutron and antineutron fluence from the vertex.

The longitudinally averaged values for the barrel Tracker are given in Table A.5. As can be concluded from Fig. A.5 the neutron fluence, especially, increases towards the endcap ECAL. Even the charged fluence increases slightly with the z-coordinate in the most exposed $r = 22$ cm layer. Thus the average fluence of $(1.57 \pm 0.01) \times 10^{14}$ cm^{-2} given in Table A.5 is pessimistic for $z = 0$ (actual fluence $(1.50 \pm 0.03) \times 10^{14}$ cm^{-2}) and optimistic for $z = 48$ cm (actual fluence $(1.66 \pm 0.03) \times 10^{14}$ cm^{-2}).

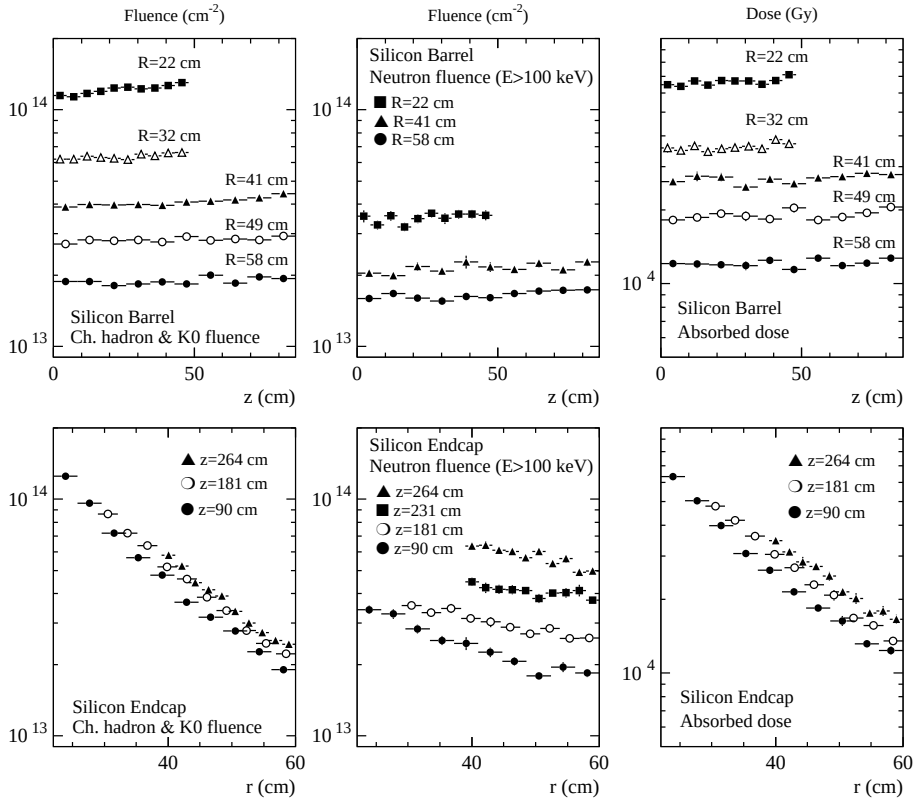

Fig. A.5: Energy-integrated charged hadron and neutron fluences and absorbed dose in the silicon Tracker. All values are for an integrated luminosity of 5×10^5 pb^{-1}. For the endcap disks it should be noted that values are averages over the indicated radial range.

Correspondingly, an extrapolation of the barrel averages to the endcap disks is not exactly justified for the silicon Tracker. Since the radial variation is significant over the 4 cm wide bins used for the scoring in the endcap disks, the data shown in Fig. A.5 do not reproduce the fluence maxima accurately. A finer binning together with a suitable interpolation has been used to deduce these values for the low edges of the endcap disks. The values obtained are listed in Table A.6. The most exposed point in the silicon Tracker is at the low edge of the sixth endcap disk, where the fast hadron fluence reaches $(1.91 \pm 0.02) \times 10^{14}$ cm^{-2}.

A comparison with the CMS Technical Proposal shows that the fluence and dose values presented now are systematically lower. The main part of the reduction arises from the use of latest event generators which include most recent parton structure functions and thus give lower particle multiplicities than the DTUJET92 generator used for the Technical Proposal [A-2]. Also the assumption of 80 mb inelastic non-diffractive cross section in the Technical Proposal has been corrected to about 67 mb[2] to bring it in agreement with generally agreed extrapolations.

Table A.5: Longitudinally averaged hadron fluences and absorbed dose in the five layers of the barrel silicon Tracker. All values are given as 10^{13} cm^{-2} for an integrated luminosity of 5×10^5 pb^{-1}. The fast hadron fluence is the sum over the first five rows of each column and serves as a good approximation to the 1 MeV neutron equivalent fluence. The indicated errors refer only to the simulation statistics

	22 cm	32 cm	41 cm	49 cm	58 cm
Charged pions	10.3±0.1	5.39±0.07	3.40±0.04	2.33±0.03	1.53±0.03
Protons	0.96±0.02	0.54±0.01	0.41±0.01	0.31±0.01	0.235±0.004
Charged kaons	0.61±0.01	0.28±0.01	0.177±0.005	0.125±0.003	0.087±0.003
Neutral kaons	0.30±0.01	0.128±0.004	0.08±0.00	0.053±0.001	0.038±0.001
Neutrons (E >100 keV)	3.50±0.07	2.54±0.05	2.15±0.03	1.85±0.03	1.65±0.02
Thermal neutrons	5.0±0.1	5.1±0.1	5.15±0.09	5.08±0.08	5.09±0.09
Neutrons total	9.5±0.1	8.5±0.1	8.3±0.1	7.9±0.1	7.7±0.1
Fast hadrons	15.7±0.1	8.88±0.09	6.22±0.05	4.67±0.04	3.54±0.04
Absorbed dose (kGy)	66.6±0.6	36.1±0.5	26.9±0.4	19.1±0.3	12.1±0.2

Table A.6: Hadron fluences at the lowest edges of some silicon endcap disks. All values are given as 10^{13} cm^{-2} for an integrated luminosity of 5×10^5 pb^{-1}. The fast hadron fluence is the sum over the first five rows of each column and serves as a good approximation to the 1 MeV neutron equivalent fluence. The indicated errors refer to the simulation statistics only

z-coordinate (cm)	90	128	162	206	264
Radius (cm)	22 cm	22	22	29	39 cm
Charged pions	11.7±0.1	11.9±0.2	12.6±0.2	7.8±0.2	4.6±0.1
Protons	1.09±0.05	1.20±0.05	1.29±0.06	0.97±0.04	0.75±0.04
Charged kaons	0.69±0.04	0.76±0.03	0.80±0.03	0.48±0.03	0.24±0.02
Neutral kaons	0.42±0.03	0.35±0.02	0.34±0.02	0.17±0.02	0.11±0.01
Neutrons (E >100 keV)	3.6±0.1	3.4±0.1	4.1±0.1	3.9±0.1	6.4±0.2
Fast hadrons	17.5±0.2	17.6±0.2	19.1±0.2	13.3±0.2	12.1±0.2

It can be seen from Fig. A.5 that charged hadrons dominate the fluence at all radii in the barrel. In the forward region the situation is different; because of the intense albedo from the endcap ECAL the neutron fluence at the last disks clearly exceeds the charged hadron fluence. Thus the fluence at these disks is dominated by albedo neutrons and the importance of moderators around the ECAL should not be underestimated. The present layout foresees a total of 8 cm high-density ($\rho = 0.95$ g/cm^3) polyethylene at the endcap. Previous simulations [A-4] have shown that the neutron fluence at the last Tracker endcap disks would increase by a factor of about 2 if the moderator thickness would be halved and by a factor of 5 if the moderator would be completely removed.

The energy spectra of most important particles are shown in Fig. A.6. The strong dominance of charged pions is clearly illustrated. The neutron spectrum is not as hard as at the pixel detector and the typical evaporation peak at about 1 MeV and the quasi-elastic peak at 70 MeV are distinguishable. The photon spectrum is dominated by photons below 10 MeV.

[2]We assume 80 mb but include diffractive events, leaving a non-diffractive cross section of about 67 mb.

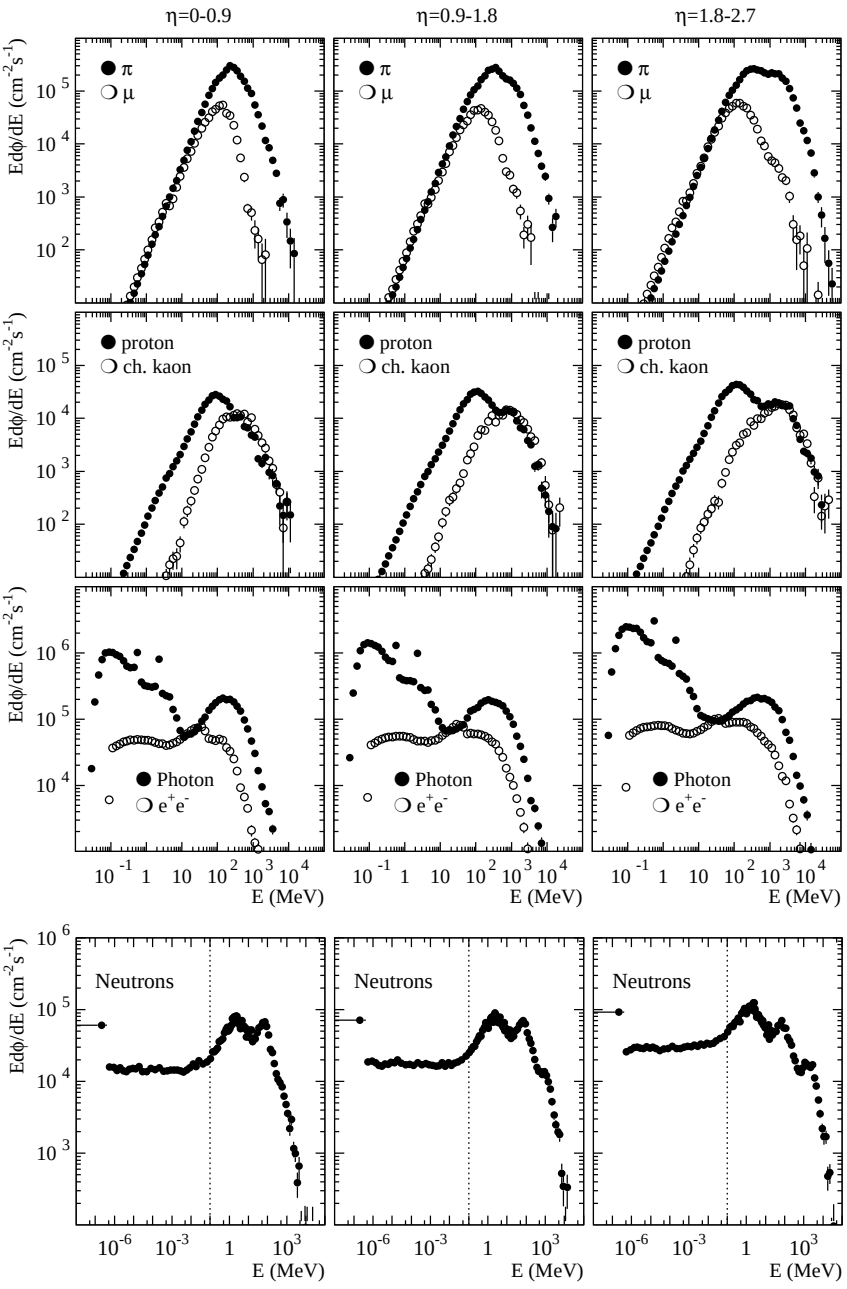

Fig. A.6: Energy spectra of the most important particles types in the silicon Tracker. The vertical line indicates the critical 100 keV limit for neutrons. All values are for a luminosity of 10^{34} cm^{-2}s^{-1}.

A.10 MSGC Tracker

The outermost layer of the CMS tracking system is formed by the MSGC Tracker. The MSGCs are gas detectors with a 3 mm gas gap enclosed between a glass substrate and a drift plane. Thus the MSGC detectors themselves do not suffer from bulk damage like the silicon detectors. But the readout electronics is similar to the silicon Tracker and will be susceptible to radiation damage. For the electronics the absorbed dose should be most significant, but for completeness also the charged particle and neutron fluences in the MSGC gas gaps are shown in Fig. A.7. The absorbed dose, shown in Fig. A.7, corresponds to energy deposition in the glass substrate which is a good representation of the electronics chips.

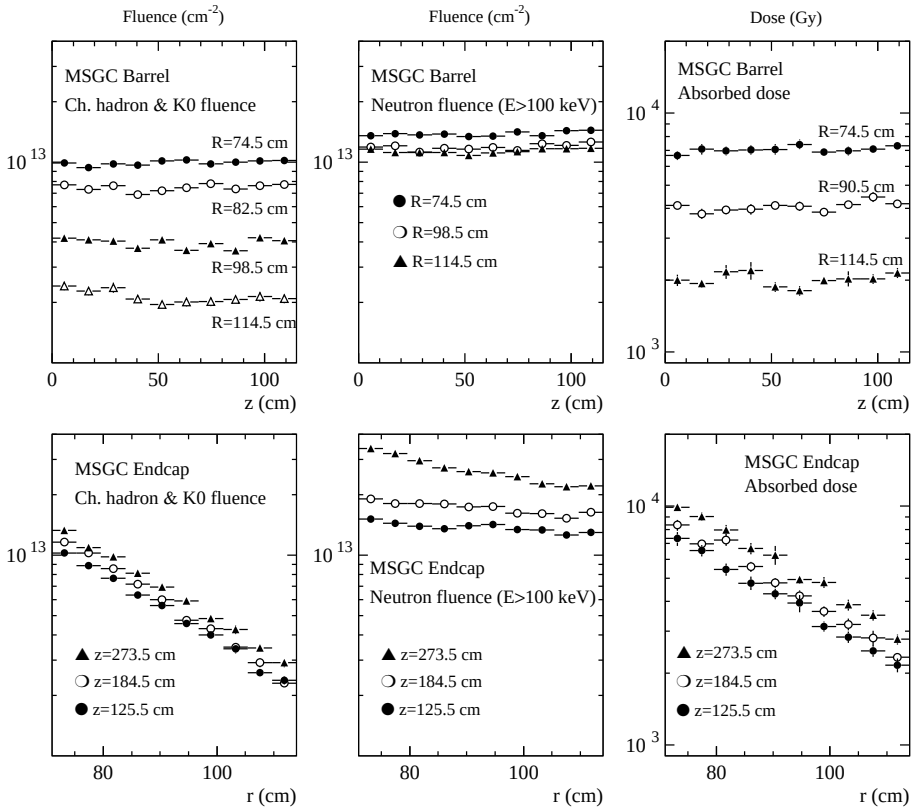

Fig. A.7: Energy-integrated charged hadron and neutrons fluences and absorbed dose in the MSGC Tracker. All values are for an integrated luminosity of 5×10^5 pb^{-1}.

The longitudinally averaged values for the barrel detector can be found in Table A.7. We can conclude from Fig. A.7 that the neutron fluence increases slightly at the last endcap disks whereas the charged hadron fluence and the dose are essentially independent of the z-coordinate. Thus an extension of the barrel averages into the endcap is valid, except for the neutron fluences at the last disks.

The particle spectra are especially important for the MSGCs, since secondary effects, like highly ionizing particle rates can be estimated only from detailed information of energy and particle type. These data are given in Fig. A.8. Also the thermal neutron fluence, given in Table A.7 has a special role for the MSGCs, because the gold strips have a thermal neutron activation cross section of 10^5 mb.

Table A.7: Longitudinally averaged hadrons fluences in five layers of the barrel MSGC Tracker. All values are given as 10^{13} cm^{-2} for an integrated luminosity of 5×10^5 pb^{-1}. The indicated errors refer to the simulation statistics only

	74.5 cm	82.5 cm	90.5 cm	98.5 cm	114.5 cm
Charged pions	0.78±0.01	0.576±0.009	0.420±0.007	0.290±0.005	0.151±0.004
Protons	0.142±0.004	0.117±0.003	0.086±0.002	0.070±0.002	0.042±0.002
Charged kaons	0.050±0.002	0.037±0.002	0.030±0.001	0.024±0.001	0.013±0.001
Neutral kaons	0.022±0.001	0.018±0.001	0.015±0.000	0.012±0.000	0.008±0.000
Neutrons ($E > 100$ keV)	1.38±0.02	1.30±0.01	1.24±0.01	1.19±0.01	1.13±0.01
Thermal neutrons	5.00±0.06	4.89±0.07	4.85±0.07	4.77±0.06	4.57±0.06
Neutrons total	7.31±0.08	7.13±0.09	7.04±0.09	6.91±0.09	6.68±0.08
Absorbed dose (kGy)	7.0±0.1	5.3 ±0.1	4.06±0.07	3.32±0.06	2.03±0.05

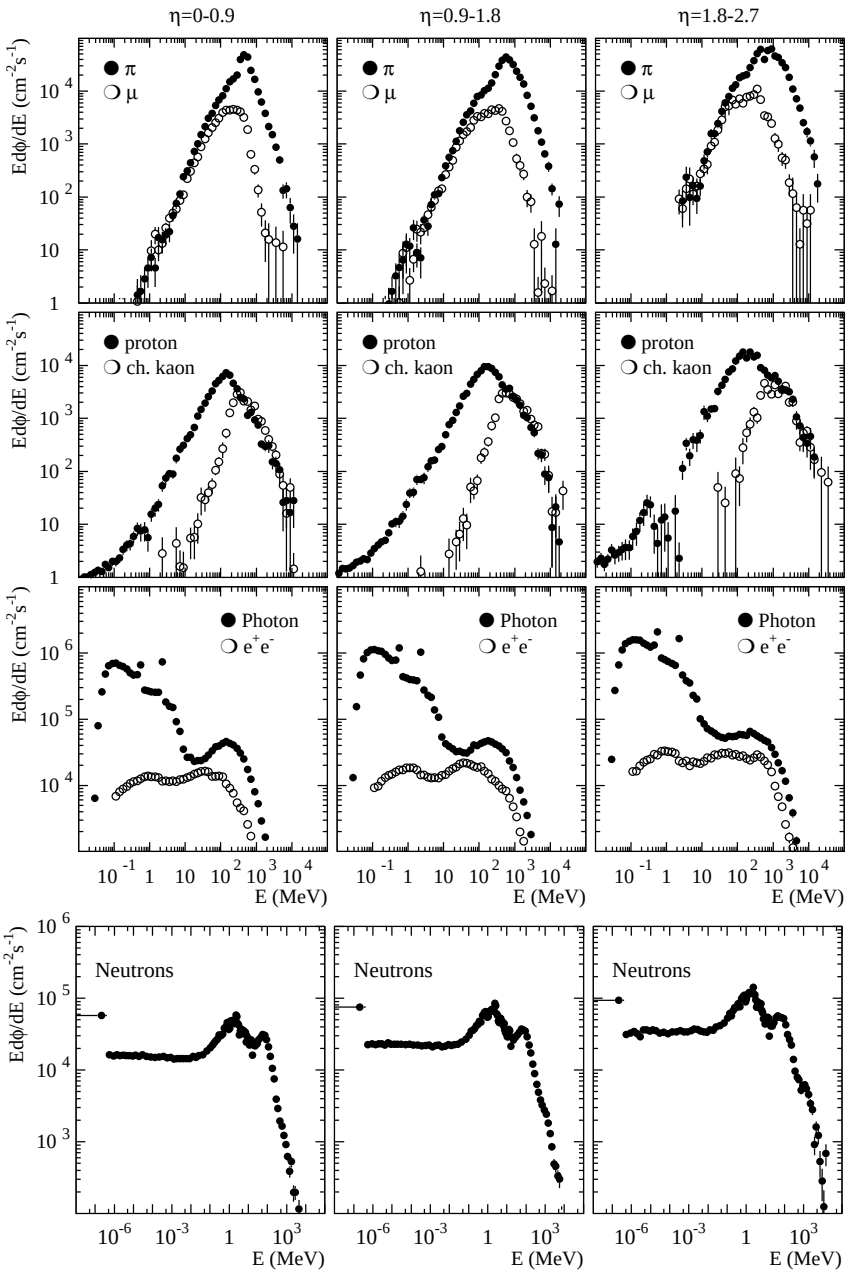

Fig. A.8: Energy spectra of the most important particles types in the MSGC Tracker. All values are for a luminosity of 10^{34} cm^{-2}s^{-1}.

A.10.1 Highly ionizing particle rates

MSGC detectors can be susceptible to destructive sparks if the safe operational window is exceeded. In a given environment this window is bounded from below by the requirement to have sufficient efficiency for detection of minimum-ionizing particles (mip) and from above by the onset of the streamer regime.

If the cathode voltage is at the higher limit the chamber may survive perfectly well minimum ionizing tracks, but the passage of a slow heavy particle could trigger a spark.

In Ne/DME the energy loss of a minimum-ionizing particle is of the order of 400 eV/mm. Each slow heavy fragment is characterized by a maximum energy deposition occurring at a characteristic energy. At energies lower than this, the stopping power decreases. For a proton

this maximum deposition is about 300 times higher than the average deposition of a mip, but a silicon ion can reach up to 10^4 times the mip ionization density.

Heavy recoil ions are produced at the LHC in hadronic interactions, which take place in the substrate, the drift plane, the gas or the gold strips. Detailed simulations [A-23] have shown that the gold strips play a particularly important role, since they are the origin of the most densely ionizing particles. Although most of the heavy fragments are stopped before entering the sensitive gas volume, it has been estimated that about once per minute a fragment with more than 10^4 times the mip ionization power is observed per cm^2 in a MSGC at $r = 75$ cm if the LHC is operating at its peak luminosity. Figure A.9 shows the simulated spectrum of maximum energy depositions expected from inelastic hadronic interactions at the LHC. This is the dominant contribution at the highest ionization densities. Elastic interactions and neutron reactions, which are important for ionization densities below 100 keV/500 μm, reach only to a maximum deposition of about 1 MeV/500 μm [A-23]. In Fig. A.9 the fragments originating from the different parts of the MSGC are shown separately, clearly illustrating the special role of the gold strips.

It has been shown in Ref. [A-23] that the behaviour of the chambers at the LHC can be reliably tested in a low-energy (300 MeV–3 GeV) hadron beam, which produces a fragment spectrum very similar to that expected at the LHC.

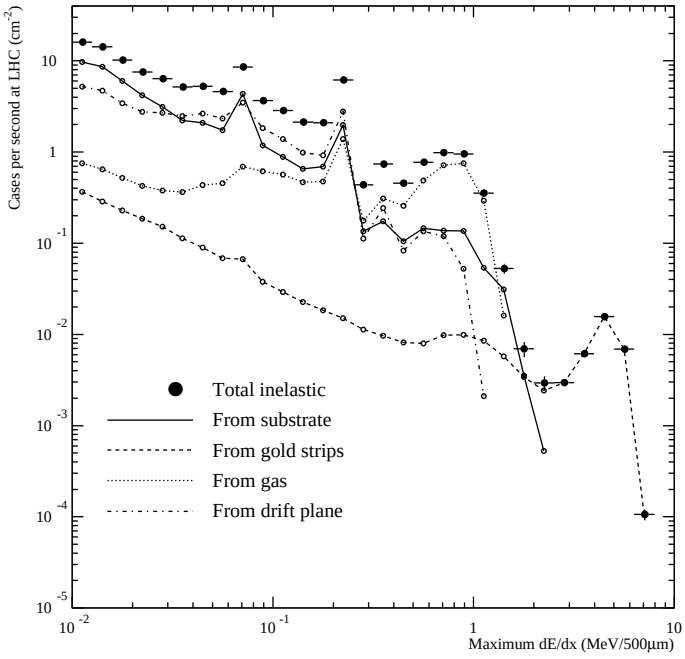

Fig. A.9: Probability distribution of maximum ionization densities in the MSGC gas [A-23]. The chamber is exposed to a fluence expected at a radius of 50 cm when the LHC operates at peak luminosity. The average deposition of a mip would be about 200 eV/500 μm and so would lie far left, out of the plot.

A.11 Alignment System

The alignment system will utilize sensors for detection of laser light. These will be positioned at three different radii at the end of the Tracker. Although the small number of sensors makes a replacement feasible, it should be ensured that the radiation hardness is sufficient at least for the period between two annual shutdowns.

Table A.8 gives the dose rates and fast hadron fluences at the presently foreseen sensor positions. The dose values correspond to dose in air, but the dose in silicon is only slightly

higher. Local material concentrations close to the sensors are likely to be more significant, since they could affect the dose. The hadron fluences are not sensitive to the presence of small amounts of material.

The values of Table A.8 are given for an integrated luminosity of 5×10^5 pb^{-1}. According to the assumed operation schedule, the first years will remain far below the nominal luminosity but when the LHC has reached its design performance, about 0.75×10^5 pb^{-1} could be accumulated per calendar year. Thus, for sensors to last from one shutdown to the next at a later phase of the LHC, they should survive at least one-sixth of the radiation doses and fluences reported in Table A.8.

Table A.8: Radiation dose and fast hadron fluences at the position where sensors of the alignment system are foreseen. The values correspond to an integrated luminosity of 5×10^5 pb^{-1}

Radius (cm)	Dose (kGy)	$E > 100$ keV neutrons (10^{13} cm^{-2}s^{-1})	Charged hadrons (10^{13} cm^{-2}s^{-1})
19	138 ± 5	12.3 ± 0.5	20.5 ± 0.4
63	22.3 ± 0.9	4.5 ± 0.1	1.91 ± 0.05
117	2.3 ± 0.2	2.09 ± 0.07	0.23 ± 0.01

A.12 Beam Loss Related Contribution

Figure A.10 shows the dose, the neutron flux ($E > 100$ keV) and the charged hadron flux per proton lost on the collimator. A comparison with the fluences during pp operation shows that even a loss of 2×10^{14} protons would expose the Tracker to only about one per cent of the total fluence expected for 5×10^5 pb^{-1} of normal pp operation.

Although this shows that beam losses cannot be expected to give significant contributions to the bulk damage of the silicon detectors, this result should not be interpreted to imply that beam losses could not damage the Tracker.

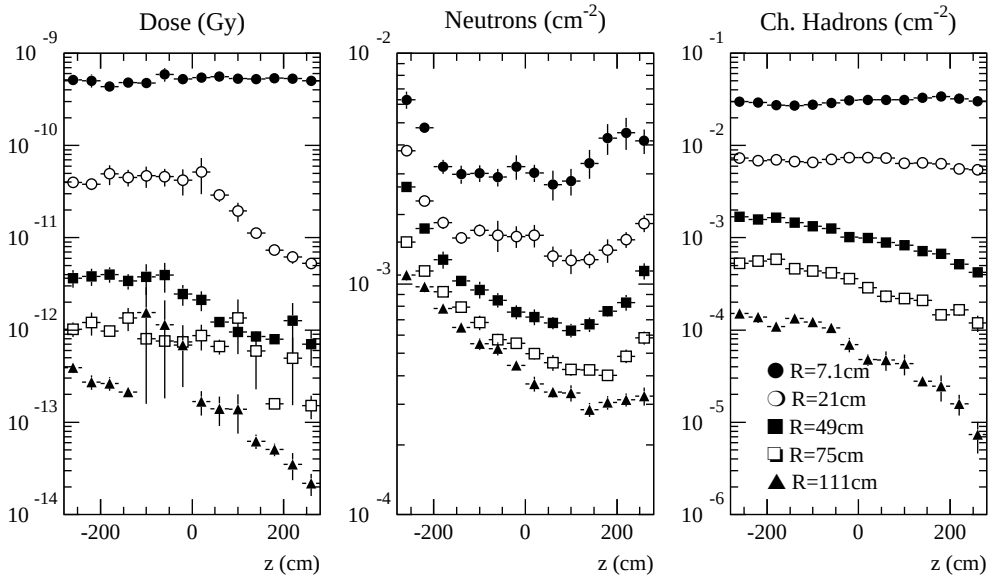

Fig. A.10: Absorbed dose and hadron fluxes for one 7 TeV proton lost on the collimator at positive z (proton heading towards negative z). The explanation of symbols given in the rightmost figure applies also to the other plots.

In particular an instantaneous loss of a fraction of the beam could lead to a very high occupancy at the Tracker. This could generate pulses which permanently damage the electronics of the detectors. Assuming a beam loss duration of 1 μs, a comparison of Fig A.10 and the dose values in Table A.5 show that a loss of about 100 protons on the collimator would give an instantaneous dose comparable to normal pp operation.

As discussed in Section A.7.7 this assumption of losses on the collimator is made only to illustrate the effect of beam losses close to the experiment. A study of realistic loss patterns in accidental conditions is under way and preliminary results predict no losses on the collimator, but there is indication that significant beam losses could take place in the low-β string. With more attenuating material between the loss point and the Tracker the effect of such losses on the Tracker would be less than the estimates in Fig. A.10 suggest. However, detailed loss information is needed before quantitative statements are possible. The present study only serves to indicate that accidental beam losses, due to the potentially high instantaneous particle rates, have to be considered in detail for the Tracker design.

A.13 Detector Background Due to Induced Radioactivity

The motivation to consider background due to induced activity explicitly for the Tracker is that radioactive decays are not included in the standard simulation codes. Often these effects are negligible, but for the Tracker this cannot be assumed without a detailed simulation.

The reason is that photons can travel relatively large distances in the Tracker and thus give non-local effects. So a highly activated region could in principle affect the background in a lower occupancy area. For the Tracker such potential sources are the highly activated beam pipe, inner parts of the Tracker with respect to outer ones, but also the massive ECAL, surrounding the whole Tracker. The simulation of the induced-activity photon flux is described in Section A.7.8 and Ref. [A-21]. The photon flux estimates obtained in these simulations are given in Table A.9 for the barrel detector layers. For comparison the flux of photons, as given by the normal FLUKA simulations, is given for the corresponding positions.

Table A.9: Left: comparison of the photon flux caused by induced activity and the prompt photon flux due to the hadronic and electromagnetic cascades. The latter includes neutron capture and de-excitation photons. Right: comparison of local flux due to induced activity β-particles and the charged flux expected at the barrel layers. The values of prompt γ-fluxes and charged fluxes correspond to LHC peak luminosity, the induced activity fluxes to the end of the tenth year of operation. The values are averages over the indicated barrel layers and are given in $\mathrm{cm}^{-2}\mathrm{s}^{-1}$

	γ-flux (ind. act.)	γ-flux (prompt)	β-flux	Charged flux
$r = 7.1$ cm	9.7×10^4	4.9×10^7	4×10^3	2.4×10^7
$r = 22$ cm	5.8×10^4	5.9×10^6	5×10^2	3.8×10^6
$r = 58$ cm	3.8×10^4	3.3×10^6	8×10^1	6.9×10^5
$r = 74.5$ cm	3.2×10^4	2.9×10^6	1.6×10^2	3.9×10^5
$r = 114.5$ cm	2.3×10^4	2.2×10^6	1.4×10^2	1.2×10^5

At the pixel detector 88% of the induced-activity photon flux originates from the Tracker and beam pipe structures and 10% is due to the ^{187}W produced in the ECAL crystals. At the outermost barrel MSGC layer 52% of the photon flux is from the Tracker structures and 40% from the ^{187}W.

The spectrum of the induced-activity photons is very different from the prompt photon spectrum. The most important difference which can be seen in Fig. A.11 is that the high-energy component, originating mostly from π^0 decays is not present in the induced-activity spectrum.

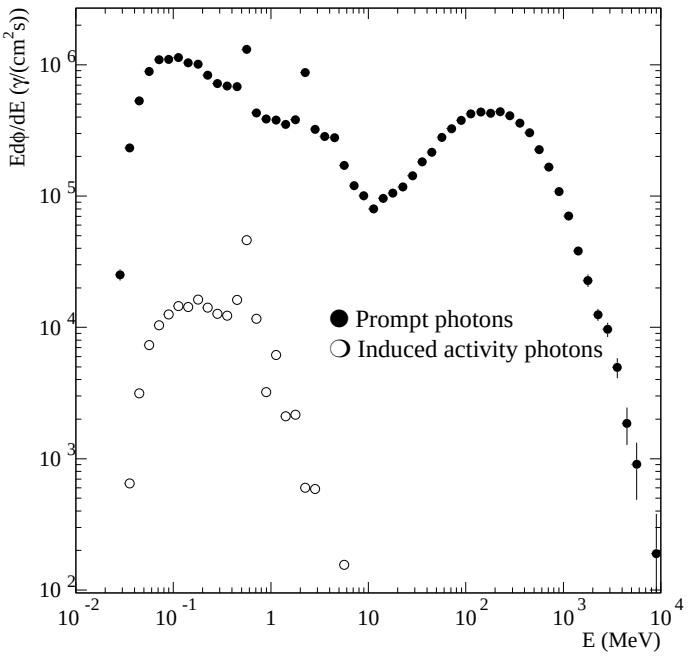

Fig. A.11: Energy spectra of prompt photons and induced-activity photons in the silicon Tracker in the region $|\eta|$ <0.9 between radii of 20 cm and 40 cm.

It is obvious from the values given in Table A.9 and from the spectra shown in Fig. A.11 that the photon flux from induced activity cannot significantly increase the occupancy in the Tracker.

Compared to the photons the effects of β-activity are much more local and affect the detector only at the position where the activation occurred. Since the detector elements are much thinner than a hadronic mean free path the saturation activity will locally always be a small fraction of the activating flux. Since this activating flux consists mostly of charged hadrons, this implies that local β-activity cannot form a significant fraction of the background. Services and support structures close to the detector and neutron activation can increase the ratio between β-rate and charged activating flux. Thus we provide in Table A.9 an estimate of the β-flux in barrel detectors at different radii. The values, obtained with quite pessimistic assumptions concerning services [A-21], prove that radioactive β decays do not contribute significantly to the Tracker occupancy.

Appendix B

Acronyms and Abbreviations

The following acronyms and abbreviations are used in the Technical Design Report:

ADC	Analogue to Digital Converter
AISC	American Institute of Structural and Civil Engineering
AMS	Alpha Magnetic Spectrometer
ANSI	American National Standards Institute
APV	Front-end Readout Chip: Analogue Pipeline (Voltage mode)
APV6	Silicon APV in Harris CMOS
APVD	Silicon APV in DMILL CMOS
APVMUX	APV Multiplexer
ASIC	Application Specific Integrated Circuit
ASME	American Association of Mechanical Engineering
BER	Bit Error Rate
CCD	Charge Coupled Device
CCU	Communication and Control Unit
CCUM	CCU Module
CF	Carbon Fiber
CFRP	Carbon Fiber Re-enforced Plastic
CME	Coefficient of Moisture Expansion
CNC	Computer Numerically Controlled milling machine
COG	Centre of Gravity
CST	Central Support Tube
CTE	Coefficient of Thermal Expansion
DAQ	Data Acquisition System
DCS	Detector Control System
DCU	Detector Control Unit
DIL	Dual In-Line (package)
DLC	Diamond-Like Coating
DME	Dimethyl Ether
DPM	Dual Port Memory
EB	Electromagnetic Calorimeter Barrel
ECAL	Electromagnetic Calorimeter
EDMS	Engineering Data Management System

ESD	Electro-Static Discharge
FEA	Finite Element Analysis
FEC	Front-End Controller
FED	Front-End Driver
FIFO	First In First Out Buffer
FPGA	Field Programmable Gate Array (=PLD)
GLIMOS	Group Leader in Matters of Safety
HB	Hadron Calorimeter Barrel
HCAL	Hadron Calorimeter
HE	Hadron Calorimeter Endcap
HIP	Highly Ionizing Particle
HM	High Modulus
HV	High Voltage
I2C	Philips two wire serial command protocol
IC	Integrated Circuit
IEEE	Institute of Electrical and Electronics Engineering
IOC	Input-Output Controller
LAN	Local Area Network
LED	Light Emitting Diode
LUT	Look Up Table
LV	Low Voltage
LVDS	Low Voltage Differential Swing
MAB	Muon Alignment Barrel station
MB	Minimum Bias
MCM	Multi-Chip Module
MIP	Minimum Ionizing Particle
MPC	Multi-Project Chip
MSGC	Micro-strip Gas-Counter
PBS	Product Breakdown Structure
PCI	Peripheral Component Interface
PCM	Process Control Monitor
PEEK	Poly Ether Ether Keton
PID	Process Internal Detection
PLC	Programmable Logical Controller
PLD	Programmable Logic Device
PLL	Phase Locked Loop (chip)
PMC	PCI Mezzanine
PPP	Pre Production Prototype
QIL	Quasi Isotropic Laminate
RDPM	Readout Dual Port Memory

SE	Pre-shower Endcap
SST	Silicon Strip Tracker
TDR	Technical Design Report
TIS	Technical Inspections and Safety
TPG	Thermal Pyrolytic Graphite
TSC	Tracker Sub-system Controller
TSS	Temprorary Supporting Structure
TTC	Timing Trigger and Command
TTCrx	TTC receiver
UHM	Ultra High Modulus
WBS	Work Breakdown Structure

References

[1-1] CMS Collaboration, The Magnet Project, Technical Design Report CERN/LHCC 97–10.

[1-2] CMS Collaboration, The Electromagnetic Calorimeter Project, Technical Design Report CERN/LHCC 97–33.

[1-3] CMS Collaboration, The Hadron Calorimeter Project, Technical Design Report CERN/LHCC 97–31.

[1-4] CMS Collaboration, The Muon Project, Technical Design Report CERN/LHCC 97–32.

[1-5] CMS Collaboration, Technical Proposal, CERN/LHCC 94–38.

[2-1] R. Horisberger, Pixel detectors at LHC, Proceedings of the 4^{th} Int. Workshop on B–Physics at Hadron Machines, Rome, (1996), Nucl. Instr. & Meth. A 384 (1996) 185.

[2-2] W.J. Xiao et al., High Fluence Proton Irradiation of GaAs Detectors at Room Temperature and at -8 °C, Nucl. Phys. B (Proc. Suppl.) 61B (1998) 427.
W.J. Xiao, Investigation of radiation hardness of SI GaAs detectors for their application in the tracking system at the LHC experiments, PhD Thesis, RWTH Aachen, (1998).
K. Lübelsmeyer et al., Investigation of the radiation damage of GaAs detectors by protons, pions and neutrons, Nucl. Instr. & Meth. A 390 (1997) 33.
W. Braunschweig et al., Investigation of the radiation damage of GaAs detectors by neutrons and photons, Nucl. Instr. & Meth. A 372 (1996) 111.

[2-3] C. Bauer et al., Recent results from the RD42 Diamond Detector Collaboration, Nucl. Instr. & Meth. A 383 (1996) 64.
W. Adam et al. (RD42-Collaboration), Development of Diamond Tracking Detectors for High Luminosity Experiments at the LHC, Status Report RD42, CERN, LHCC 97-3 (Jan. 1997).
W. Adam et al., Diamond Particle Detectors, Preprint Inst. f. Hochenergiephysik, Vienna, HEPHY-PUB 674-97 (to be published in Nucl. Instr. & Meth.).

[2-4] B. Henrich, W. Bertl, K. Gabathuler and R. Horisberger, Depth Profile of Signal Charge Collected in Heavily Irradiated Silicon Pixels, CMS Note 1997/021.

[2-5] D. Pitzl et al., Evaluation of double sided, AC-coupled, double metal silicon strip detectors for H1 at HERA, Nucl. Instr. & Meth. A 348 (1994) 454.

[2-6] We are indebted to G. Lutz for drawing our attention to this problem.

[2-7] Fabricated at CSEM, Neuchatel, Switzerland.

[2-8] John Hopkins University in collaboration with the instrumentation group at BNL (led by Zheng Li).

[2-9] ROSE collaboration, CERN RD48.

[2-10] H. Bichsel, Straggling in Thin Silicon Detectors, Rev. Mod. Phys. 60 (1988) 663.

[2-11] *DMILL* process (Durci Mixte sur Isolant Logico-Lineaire):
M. Dentan et al., A Mixed Analog-Digital Radiation Hard Technology for High Energy Physics Electronics, R&D Proposal (RD29), CERN, DRDC 92-32, May 1992, p42.
M. Dentan et al., DMILL, A Mixed Analog-Digital Radiation-Hard BiCMOS Technology for High Energy Physics Electronics, IEEE Trans. Nucl. Sci. 43 (June 1996) 1763.
RICMOS IV (Honeywell) process:
S. T. Liu et al., Total dose hard 0.8 μm SOI CMOS Devices, Proceedings of the First Workshop on Electronics for LHC Experiments, (1995) 33.
S. T. Liu et al., Radiation hard SOI and CHFET Technologies for LHC Applications, Proceedings of the Second Workshop on Electronics for LHC Experiments, (1996) 407.
S. T. Liu et al., Further Radiation Hardened SOI CMOS Technology, Proceedings of the Third Workshop on Electronics for LHC Experiments, (1997) 130.

[2-12] S. Kavadias, K. Misiakos and D. Loukas, Calculation of Pixel Detector Capacitances through Three Dimensional Numerical Solution of the Laplace Equation, IEEE Trans. Nucl. Sci. 41 (1994) 397.
L. Bosisio, F. Forti and E. Tomacruz, Measurement and Tridimensional Simulation of Silicon Pixel Detector Capacitance, Proceedings of the 1993 IEEE Nuclear Science Symposium, San Francisco, (1993) 338.

[2-13] M. Lechner, PhD. Thesis, ETH Zürich (1998) in preparation.

[2-14] Measurements done by W. Karpinski from RWTH Aachen (1997).

[2-15] Circuit designs implemented by RWTH Aachen, U.C. Davis and PSI.

[2-16] R. Horisberger, K. Gabathuler and D. Kotlinski, Readout Architecture for CMS Pixel Vertex Detector, CMS TN/96-046.

[2-17] Design and simulation done by R.Schnyder, R. Kramert and R. Horisberger, PSI, Feb. 1997.

[2-18] B.Meier, Diploma-Thesis, Institut für Teilchenphysik, ETH Zürich, April 1998.

[2-19] S. Cittolin, J.F. Gillot, A. Racz, R. Halsall and B. Haynes, Front End Driver in CMS DAQ, CMS TN/95–020.

[2-20] LN Industries SA in Grandson, Switzerland.

[3-1] B. Mours et al., The design, construction and performance of the ALEPH silicon vertex detector., Nuclear Instruments and Methods in Phys. Res. A379 (1996) 101.
G. Anzivino et al., The DELPHI silicon strip microvertex detector., Nuclear Instruments and Methods in Phys. Res. A263 (1988) 215.
M. Acciarri et al., The L3 silicon microvertex detector., Nuclear Instruments and Methods in Phys. Res. A351 (1994) 300.
S. Anderson et al., The extended OPAL silicon strip microvertex detector., submitted to Nuclear Instruments and Methods in Phys. Res. A.

[3-2] J. Sharka et al., Construction of the CDF silicon vertex detector., IEEE Transactions on Nuclear Science 39 (1992).

[3-3] The CMS Collaboration The Compact Muon Solenoid Technical Proposal., CERN/LHCC 94-38, LHCC/P1 (1994).

[3-4] G. Batignani et al., Operational experience with a large detector system using silicon strip detectors with double sided readout., Nuclear Instruments and Methods in Phys. Res. A326 (1993) 183.
P. Collins et al., Experience with silicon detectors at the DELPHI experiment at LEP., Nuclear Instruments and Methods in Phys. Res. A383 (1996) 1.
M. Acciarri et al., 1994 running experience with the L3 Silicon Microvertex Detector., Nuclear Physics B, Proc. Suppl. 44 (1995) 296.

[3-5] G. Tonelli et al., Double-sided radiation resistant microstrip detectors: technology and results., Nuclear Instruments and Methods in Phys. Res. A377 (1996) 422.

[3-6] R. Dell'Orso et al., Tests of the CMS milestone silicon detectors., submitted to Il Nuovo Cimento.
RD20 Collaboration RD20 Status Report 1995, CERN/LHCC/96-2 (1996).

[3-7] S. Sotthibandhu Radiation Damage Studies of Silicon Detectors., PhD thesis, Imperial College, Rutherford Appleton Laboratory RALT-025 (1994) and references therein.

[3-8] K. Gill et al., Radiation damage by neutrons and photons to silicon detectors., Nuclear Instruments and Methods in Phys. Res. A322 (1992) 177.

[3-9] E. Barberis et al., Temperature effects on radiation damage to silicon detectors., Nuclear Instruments and Methods in Phys. Res. A326 (1993) 373.

[3-10] T. Ohsugi et al., Radiation damage in silicon microstrip detectors., Nuclear Instruments and Methods in Phys. Res. A265 (1988) 105.

[3-11] A. Chilingarov et al., Radiation studies and operational projections for silicon in the ATLAS inner detector., Nuclear Instruments and Methods in Phys. Res. A360 (1995) 432.

[3-12] The RD2 Collaboration RD2 Status Report, CERN/DRDC 94-34 (1994).

[3-13] The RD48 Collaboration RD48 Status Report, CERN/LHCC 97-39 (1997).

[3-14] F. Lemeilleur et al., Study of characteristics of silicon detectors irradiated with 24 GeV/c protons between -20 °C and +20 °C., Nuclear Instruments and Methods in Phys. Res. A360 (1995) 438-444.

[3-15] S. J. Bates et al., Proton irradiation of silicon detectors with different resistivities., CERN/ECP 95-18 (1995).

[3-16] S. J. Bates et al., Proton irradiation of silicon detectors with different resistivities., IEEE Transactions on Nuclear Science 43 (1996) 199.

[3-17] E. Fretwurst et al., Reverse annealing of the effective impurity concentration and long term operational scenario for silicon detectors in future collider experiments., Nuclear Instruments and Methods in Phys. Res. A342 (1994) 119-125.

[3-18] H. Feick et al., Refinement of the Hamburg Group Damage Models., Presented at the 3rd ROSE Workshop on Radiation Hardening of Silicon Detectors, DESY, Hamburg, 12-14 February 1998. To be published.

[3-19] M. Da Rold et al., Radiation effects on breakdown characteristics of multiguarded devices, IEEE Transactions on Nuclear Science 44 (1997) 721-130.

[3-20] A. Bischoff et al., Breakdown protection and long-term stabilisation for Si-detectors, Nuclear Instrument and Methods in Phys. Res. A326 (1993) 27-34.

[3-21] A. Messineo et al., Study of breakdown effects in silicon multi-guard structures, submitted to IEEE Transactions on Nuclear Science.

[3-22] N. Bacchetta et al., High Voltage operation of silicon devices for LHC experiments, presented at the 7th Pisa Meeting, to be published on Nuclear Instruments and Methods in Phys. Res. A.

[3-23] O. Adriani et al., Beam Test results for single and double-sided silicon detector prototypes of the CMS Central Detector., Nuclear Instruments and Methods in Phys. Res. A396 (1997) 76.

[3-24] E. Babucci et al., Temperature dependence of the behaviour of a single-sided irradiated silicon detector., CMS Note 98-011 (1998).

[3-25] C. Bozzi et al., Characterization and simulation of LHC-type silicon microstrip detectors., submitted to Il Nuovo Cimento.

[3-26] S. Baccaro, A. Festinesi, B. Borgia Gamma and neutron irradiation facilities at ENEA - Casaccia Center (Roma), CMS TN/95 - 192 (1995).

[3-27] G. Baccarani, P. Ciampolini and A. Pierantoni Three-dimensional simulation of semiconductor devices: state of the art and prospects., Nuclear Instruments and Methods in Phys. Res. A326 (1993).

[3-28] D. Passeri et al., TCAD-Based Analysis of Radiation-Hardness in Silicon Detectors., IEEE Transactions on Nuclear Science 45 (1998).

[3-29] G. Hall, talk given at the CMS MSGC Meeting, CERN, October 1996.

[3-30] C. Bozzi, Signal-to-Noise Evaluations for the CMS Silicon Microstrip Detectors., CMS Note 97-026 (1997).

[3-31] L. Feld et al., Thermal Properties of the Silicon Microstrip Endcap Detector., CMS Note 98-018 (1998).

[4-1] R.Bouclier et al., IEEE Trans. Nucl. Sci., NS-41 (1994) 821

[4-2] F.Angelini et al., NIM, A336, (1993) 106

[4-3] S.Schmidt et al., NIM, A344, (1994) 558

[4-4] F.Angelini et al., NIM, A360, (1995) 22

[4-5] J.E.Bateman et al., RAL-TR-95-032 (1995)

[4-6] F. Van Der Berg, Proc. of the Int. Workshop on MSGC, Lyon, France (1995)

[4-7] T.Nagae et al., NIM, A323, (1992), 236

[4-8] R.Bellazzini et al., Substrate-less, spark-free micro-strip gas counters, Proceedings of the VII Pisa Meeting on Advance Detectors 'Frontier Detectors for Frontier Physics', Isola d'Elba, Italy 1997

[4-9] O. Bouhali et al., Operation of Micro Strip Gas Counters with DME based gas mixtures, submitted to NIMA

[4-10] D.Abbaneo et al. Test of a CMS MSGC Tracker Prototype in a High Intensity Hadron Beam, Proceedings of the VII Pisa Meeting on Advance Detectors 'Frontier Detectors for Frontier Physics', Isola d'Elba, Italy 1997 and CMS internal note CMS 98 002

[4-11] M. Millard, Techniques and Applications of Plasma Chemistry, eds. J.R. Hollahan and A.T. Bell (Wiley, New York) 1974

[4-12] L.L.Jones, PreMux128 Specification, RAL note December 1994

[4-13] P.Lorrain, D.P.Corson, F.Lorrain, Electromagnetic fields and waves, W.H.Freeman & Co., Third Edition

[4-14] R.Bellazzini and M.A.Spezziga, La Rivista del Nuovo Cimento, vol.17, n.12 (1994)

[4-15] W.G.Gong et al., NIM, A374, 1996 144

[4-16] F.Angelini et al, NIM, A382 (1996) 461

[4-17] R.Bouclier et al., NIM, A336 (1994) 106

[4-18] J.A.Kadyk, NIM, A300, 1991 436

[4-19] V. Peskov et al., Feedback and Breakdowns in Microstrip Gas Counters , Preprint NASA/MSFC 1996, submitted to NIMA

[4-20] M.Bozzo, A. Cattai and A. Tsirou, Tests on MSGCs with advanced passivation, B1 internal note 97.4, http://cmsdoc.cern.ch/user/c/cattai/alpha/alpha.html

[4-21] B. Boimska et al., Investigation of discharge limits in diamond coated microstrip gas chambers, CMS note 96-016

[4-22] The analysis results can be found in http://edms.cern.ch/cms-tk

[4-23] K. Bernier et al., MSGC test with fast neutrons, CMS note 98-014.

[4-24] R. Metri, Diplomarbeit 1998, University Karlsruhe.

[4-25] R. Metri et al., CMS note 97-071.

[4-26] V. Mack et al., Effects of slow neutrons on MSGCs, submitted to NIM.

[4-27] E.Albert et al. Performance of a prototype of the Microstrip Gas Chambers for the CMS experiment at LHC , Proceedings of the VII Pisa Meeting on Advance Detectors 'Frontier Detectors for Frontier Physics', Isola d'Elba, Italy 1997

[4-28] F. Angelini et al., Development of a very large are Microstrip Gas Chamber for the CMS central tracking system, Nucl. Instr. and Meth. A 360 (1995) 22.

[4-29] F. Angelini et al., NIM A343 (1994) 441

[4-30] CMS The Compact Muon Solenoid, Technical Proposal, CERN/LHCC 94-38 (1994)

[4-31] The Forward-Backward MSGC Milestone Status Report, CMS note (pending)

[4-32] B1 team, Definition of B1 modules, B1 internal note 96.1

[4-33] A. Mugnai, Finite Element Analysis and experimental tests of a Barrel MSGC Detector Module, B1 internal note 96.7,CMS note 96-004

[4-34] B1 team, Conceptual design of MSGC Rod, B1 internal note 96.20 - in preparation -

[4-35] A. Caner and A. Cattai, Detailed simulation of the MSGC barrel, B1 internal note 96.23

[4-36] R. MacKenzie, Heat exchanger calculation for MSGCs, B1 internal note 96.8, TA1/96-12

[4-37] A. Onnela and T. Nyman Points of support and the C-profile design of the final MSGC barrel Rods., B1 internal note june.97.7

[4-38] N. Eiden, A study investigating a mechanical disk support, B1 internal note 97.3

[4-39] N. Eiden, Narrow members of a quasiisotropic laminate, B1 internal note 97.5

[4-40] N. Eiden, Sensitivity study on the height of the rings in the MSGC barrel support disks, 28 Oct 97, B1 internal note 97.15

[4-41] N. Eiden, Preliminary Design of a Radiation Penetrating Support Structure, master thesis at the Helsinki University of Technology, 1997

[4-42] T. Nyman, FEA for the CMS barrel two ring prototype, B1 internal note 98.3

[4-43] E. Löytynoja and M. Kotamäki, Experimental studies on cooling of a MSGC chamber assembly, B1 internal note 96.9

[4-44] S. Bachmann et al., Beam Test Performance of a Closed Microstrip Gas Chamber Module for the CMS Forward Tracker, CMS note 97-063

[4-45] S. Bachmann et al., Spatial Resolution of a Wedge Shaped MSGC Module, CMS note 97-077

[4-46] B1 team, Status report of MSGC B1 mechanics and module engineering, B1 internal note 97.10

[4-47] F.S. Guarino, C. Hauviller and J. Kenny, Development and Characterisation of Radiation Resistant Structural Adhesives Cured at Room Temperature, technical note CERN-PPE-TA1/97-12

[4-48] J.C.Gayde, C. Lasseur, CMS - Central tracker - Prototype B1 - test cible. Mesure par photogrammtrie numerique, Internal note EST/SU/EXP - B1 internal note 97.11–draft–

[4-49] P.K. Mallick, Fiber-reinforced composites Materials, manufacturing and design 2nd ed., Marcel Dekker, Inc., New York 1993

[4-50] O. Bouhali et al., A possible approach for the construction of the CMS Forward-Backward MSGC Tracker, CMS-Note/1997-081 (1997)

[4-51] S. Bachmann et al., The Closed MSGC design : Detectors and mechanical structures, MF1 report (1997)

[4-52] O. Pooth, Report on the CMS Forward-Backward MSGC milestone (presented at the Vienna Wire Chamber Conference 1998), CMS-CR/1998-006

[4-53] B1 team, Status report of MSGC B1 prototype, B1 internal note 97.14

[4-54] AMS Technical Proposal; S.C.C. Ting in: Spacestation Utilisation Symposium, ESA SP-385

[4-55] V. Chorowicz et al., NIM A401 (1997) 238

[4-56] F.Angelini et al., NIM, A, A335 (1993) 69

[5-1] CMS Technical Proposal CERN/LHCC 94-38 (1994);
RD20 status report. CERN DRDC/94-39 (1994)

[5-2] S. Gadomski et al., The deconvolution method of fast pulse shaping at hadron colliders, Nucl. Instr. Methods A320 (1992) 217

[5-3] N. Bingefors et al. A novel technique for fast pulse shaping using a slow amplifier at LHC, Nucl. Instr. Methods A326 (1993) 112

[5-4] M. French, APV6-RH Requirements. Rev 3.0, Rutherford Appleton Laboratory Project Specification, February 1995;
M. French, APV6 User Manual, Rutherford Appleton Laboratory internal document, April 1997;
M. French et al., APV6RH: a 128 channel radiation hard pipeline chip for the silicon tracker in CMS, Procs 2nd Workshop on Electronics for LHC Experiments. CERN/LHCC/96-39 (1996) 463.

[5-5] Harris Semiconductor Inc., Melbourne, Florida USA 32902-0883.

[5-6] S. Gardien et al., APVD: a CMOS mixed analogue-digital circuit for the Silicon Tracker in CMS Procs 3rd Workshop on Electronics for LHC Experiments. CERN/LHCC/97-60 (1997) 163.

[5-7] TEMIC Semiconductors, Matra MHS, CP3008, F-44087 Nantes Cedex France.

[5-8] M. Dentan, Results of industrial transfer of DMILL, Procs 3rd Workshop on Electronics for LHC Experiments. CERN/LHCC/97-60 (1997) 134.

[5-9] I2C Bus Specification, Application Note, Philips-Signetics, January 1992

[5-10] M. Millmore, APV6 pipeline emulation, CMS note 1997/045

[5-11] M.Raymond et al., Measurements of transistors and silicon microstrip detector readout circuits in the Harris AVLSIRA rad-hard CMOS process , Nucl. Instr. Methods A351(1994) 449;
M. Raymond et al., Radiation hard electronics for LHC , Nucl. Instr. Methods A360(1995) 162;
M. Millmore et al., Measurements of radiation hardened transistors from Harris and DMILL technologies, Procs 2nd Workshop on Electronics for LHC Experiments. CERN/LHCC/96-39 (1996) 415;
M. Millmore et al., Radiation hardened transistor characteristics for applications at LHC and beyond, Nucl. Instr. Methods A399 (1997) 129.

[5-12] J. Matheson et al., Radiation damage studies of the APV6 chip , Procs. 3rd Workshop on Electronics for LHC Experiments. CERN/LHCC/97-60 (1997) 168.

[5-13] M. Dentan et al., DMILL - A Mixed Analog-Digital Radiation Hard technology for High Energy Physics Electronics, RD29 Status report. CERN/LERB/97-15 (1997).

[5-14] M. Millmore et al., Measurements of radiation hardened transistors from Harris and DMILL technologies, Procs 2nd Workshop on Electronics for LHC Experiments. CERN/LHCC/96-39 (1996) 415.

[5-15] L. Jones, PreMUX128 Specification Vsn 2.3 Rutherford Appleton Laboratory internal document (1995).

[5-16] R. Sachdeva, Signal Processing Algorithms and Radiation Hard Electronics for the CMS Tracking Detector, Ph. D thesis, Imperial College (1995);
F.Angelini et al., Study of the bunch crossing identification at LHC using Microstrip Gas Chambers , Nucl. Instr. Methods A368 (1996) 345–352;
J.F. Clergeau et al., Proposal for the Read-out Electronics of Gas Micro-Strip Detectors in the CMS Tracker, CMS Note/1997-013 (1997);
F.G. Sciacca, Impact of Fast Shaping at the Front-end on Signals from Micro Strip Gas Chambers, CMS Note/1997-105(1997).

[5-17] F.G. Sciacca, Definition of the Front-end Signal Processing Algorithm for MSGCs in CMS, CMS IN/1997 - 021 (1997).

[5-18] A. Gandi, CERN. Private communication.

[5-19] G. Hall et al., Fibre optic link technology for the CMS tracker, Technical note CMS Note 1996/012, Dec. 1996.

[5-20] F. Vasey et al., Laser based optical links for the CMS tracker: options and choices, Technical note CMS Note 1997/053, Jul. 1997.

[5-21] F. Vasey, CMS tracker optical readout link specification, preliminary version 1.1, 1997.

[5-22] K. Kloukinas et al., A system for timing distribution and control of front-end electronics for the CMS tracker, Procs. 3rd Workshop on Electronics for LHC experiments, CERN/LHCC/97-60 (1997) 208-12.

[5-23] A. Marchioro at al., An integrated Laser Driver Array for Analogue Data Transmission in the LHC Experiments, Procs. 3rd Workshop on Electronics for LHC experiments, CERN/LHCC/97-60 (1997) 282-286.

[5-24] S. Nagasawa et al., A high–performance single–mode multifibre connector using oblique and direct endface contact between multiple fibres arranged in a plastic ferrule, IEEE Photonics Technology Letters, Vol. 3, No. 10, pp. 937-9, 1991.

[5-25] V. Arbet-Engels at al.,Characterization of optical links for the CMS experiment, Procs. 3rd Workshop on Electronics for LHC experiments, CERN/LHCC/97-60 (1997) 287-92.

[5-26] K. Gill et al., Neutron damage studies of semiconductor lasers for the CMS tracker optical data links, Procs. 2nd Workshop on Electronics for LHC experiments, Balatonfuered, September 23-27, 1996, pp 387-91.

[5-27] J. Troska et al., Neutron, proton and gamma radiation effects in candidate InGaAs pin photodiodes for the CMS tracker optical links, Technical note CMS Note 1997/102.

[5-28] K. Gill et al., Gamma and neutron radiation damage studies of optical fibres, Journal of Non-Crystalline Solids 216, 1997, pp 129-34.

[5-29] K. Gill et al., Radiation damage studies of Optoelectronic components for the CMS tracker optical links, Procs. 4th European Conference on radiations and their effects on devices and systems, RADECS, Cannes, 1997.

[5-30] J. Batten et al., Resistance of MT multi-way single mode connectors to gamma and neutron irradiation, Procs. 4th European Conference on radiations and their effects on devices and systems, RADECS, Cannes, 1997.

[5-31] CMS FED Prototype User manual, V2.0, System Design Group, Rutherford Appleton Laboratory (1996),
< ftp://ftp.te.rl.ac.uk/cms/fed/FED_UM_18_12_96.pdf >,
< ftp://ftp.te.rl.ac.uk/cms/fed/FED_UM_18_12_96.pdf.hqx >.

[5-32] R. Halsall, W. Haynes, The Front End Driver of the CMS Tracker , Procs. 1st Workshop on Electronics for LHC Experiments, CERN/LHCC/95-96 (1995) 119;
M. de Fez-Laso et al., Status report on the Front End Driver for the CMS tracker, Procs. 2nd Workshop on Electronics for LHC Experiments, CERN/LHCC/96-39 (1996) 499;
R. Halsall et al., Front End Readout Developments in the CMS Data Acquisition System , Procs. 3rd Workshop on Electronics for LHC Experiments, CERN/LHCC/97-60 (1997) 427.

[5-33] Signal Processing Technologies SPT7861 data sheet, http://www.spt.com/.

[5-34] See Chapter 7.

[5-35] S. Cittolin et al., Dual Port Memories in LHC Experiments , CMS Technical Note CMS-TN 95/004 (1995).

[5-36] A. Racz, CMS Front End Model and VME64 Sequencer, Procs. 3rd Workshop on Electronics for LHC Experiments, CERN/LHCC/97-60 (1997) 441,
http://cmsdoc.cern.ch/~cittolin/tridas.html.

[5-37] PCI Local Bus Specification, Revision 2.1, PCI Special Interest Group Draft Standard for Common Mezzanine Card Family CMC, IEEE P1386, Draft Standard for Physical/Environmental Layers for PCI Mezzanine Cards, IEEE P1386.1.

[5-38] B. G. Taylor, Timing Trigger and Control distribution for LHC detectors, Procs 1st Workshop on Electronics for LHC Experiments, CERN/LHCC/95-56 (1995) 180, http://www.cern.ch/TTC/intro.html;
P. Moreira et al., TTCrx User's Reference Manual,
http://pcvlsi5.cern.ch/MicDig/ttc/MANUAL22.PDF

[5-39] M. Bedjidian, Talk given at CMS Electronics Meeting, Jan 1997.

[5-40] CMS FED PMC specification Rev 1.2, System Design Group, Rutherford Appleton Laboratory (1997), <ftp://ftp.te.rl.ac.uk/cms/pmc/adc_spec_v1.2.ps>.

[5-41] A. Marchioro, A System for Timing Distribution and Control of Front End Electronics for the CMS Tracker, Procs 3rd Workshop on Electronics for LHC Experiments. CERN/LHCC/97-60 (1997) 208.

[5-42] CMS Electromagnetic Calorimeter Technical Design Report CERN/LHCC/97-33 (1997).

[5-43] P. Moreira, CMS Tracker LVDS specification (1998),
http://trackercontrol.cern.ch/CMSTControl/manuals.htm

[5-44] IBM Corporation Token Ring Network-Introduction and Planning Guide, Reference manual GA27-3677-05, December 1992.

[5-45] RD49 status report, CERN/LHCC/97-63 (1997).

[5-46] G. Stefanini, HV switches for MSGCs, CMS Technical Note, in preparation.

[5-47] LabView: Graphical Programming for Instrumentation. National Instruments (1995).

[5-48] J. Varela et al., Trigger Synchronisation circuits in CMS, CMS CR/1997-017 (1997).

[5-49] C. Bozzi, Signal-to-Noise Evaluations for the CMS Silicon Microstrip Detectors, CMS Note/1997 - 026 (1997).

[6-1] C. Hauviller, Advanced Materials for High precision Detectors, Proceedings of the International Workshop on Advanced Materials for High Precision Detectors, Ed. B Nisquevert, C. Hauviller,CERN, Geneva,3-7, 1994

[6-2] H. Schonbacher, M.Tavlet, Radiation Effects on Structural Materials for High Energy Particle Accelerators, in [6-1]

[6-3] N.Levoy, K.Raftery, R.White, High Specific Stiffness Beryllium and Beryllium Alloys, in [6-1]

[6-4] P.K.Mallick, Fibre-Reinforced Composits: Materials, Manufacturing and Design, Marcel Dekker Inc, second edition 1993

[6-5] Bhagwan D. Argarwal, Lawrence J. Broutman, Analyses and Performance of Fibre Composits, John Wiley & Sons Inc., second edition, 1990

[6-6] D.Eaton, A.Pradier, The Use of High Stiffness Material and Dimensionally Stable Materials in Spacecraft Applications, in [6-1]

[6-7] H. Breuker et al., Trade-off between different CMS Tracker SUpport and Installation Schemes, CMS IN 1998/001, January 5th, 1998

[6-8] A. Frediani et al., A Conceptual Design of the CMS Tracker, CMS IN 1998/002, January 5th, 1998

[6-9] R.Bouclier et al., Results on Wire Chamber Ageing, Nucl. Instr. and Meth., A346 (1994) 114-119,

J.Wise, Chemistry of Radiation Damage to Wire Chambers, PhD Thesis, Lawrence Berkley Laboratory, USA, LBL-32500 (1992)

[6-10] S. Ilie, MSGC's polymeric materials: tests in liquid DME, CERN-CMS TK-B1, Status Report, Jan. 1997

M. Capens, Study of the Ageing of Gaseous Detectors and Solutions for the use of MSGCs in High Rate Experiments, PhD Thesis, University of Santiago de Compostela, Spain

[6-11] CERN Flamable Gas Safety Manual 1996, Ed. Technical Inspection and Safety Commision (1996)

[6-12] M.Bosteels, S.Ilie, Neon recovery from Microstrip Gas Chambers (MSGC) Neon-DME gaseous mixture with a view to its re-use. CMS IN 1996/010

[6-13] A.Carraro, Studio dei problemi termici relativi alla realizzazione del rivelatori CMS al CERN, Diploma Thesis, Universita Degli Studi di Genova, 1995-1996

[6-14] G.S.Hickey, Thermal insulation for Mars surface exploration, SAE 27^{th} Int. Conf. on Environmental Systems, Lake Tahoe, Ca, July 1997

[6-15] C.Lasseur, C.Humbertclaude, J-C.Gayde, CERN/EST/SU Report.

[6-16] C.Lasseur, CERN/EST/SU, private communication

[6-17] See for example Bertsen, B., Price, M.J, Accurate remote distance measurement using a CCD camera, Nucl. Inst. and Meth., A364, pp. 103-107, (1995), [6-18], [6-20] and references therein.

[6-18] B.Berntsen, Investigation of a principle for the alignment system of the inner tracker of CMS, Diploma Thesis, University of Trondheim, Norway, May 1994

[6-19] CIDTEC MegaRAD1 devices, product catalog 1997

[6-20] F.Klumb, Nouvelles techniques de videometry: Application au controle micrometrique tridimensionnel de objects volumineux, PhD Thesis, University Louis Pasteur, Strasbourg, 1997

[6-21] CMS Muon TDR, CERN-LHCC/97-12

[6-22] S.Mota da Silva, R.Ribeiro, Eng. Studies on the Tracker alignment wheel, CMS-IN, in preparation

[6-23] M. Libkind, Summary of Work on CMS Central Tracker Global Support Structures, LLNL-CMS-96-007, CMS Document 1996-202

[6-24] S.Mota da Silva, Tracker alignment progress reports on Optimization of the alignment wheel, Report 1 to 13, CERN 1997/98

[6-25] M.J.Price, Technical Note, CERN-TA1/95-14

[6-26] SIT Inc. - SITe Fibre Optic CCD Imagers, product catalog 1997

[6-27] Atlas Inner Tracker TDR, CERN-LHCC/97-16

[6-28] W.Blum et al., Nucl. Instr. and Meth., A367 (1995) 413,
W.Blum et al., Nucl. Instr. and Meth.,A377 (1996) 404,
Max Plank Institute for Physics report MPI-PhE/95-13

[6-29] Coosemans,W., Mainaud,H., CLIC Note 316, CERN, 1996

[6-30] Fogale Nanotech, product catalog, 1997

[6-31] Ruotsalainen,S. Development of straightness measurement system based on streched wire and capacitive pick-up Master's Thesis, Helsinki University of Technology, Espoo, Finland. 1997

[6-32] P.A.Aarnio and M.Huhtinen, CERN-CMS IN/97-025 (1997)

[6-33] R.Veness, presentation at the LHC Experimental Beampipes Meeting, CERN, 25 Sept., (1997)

[6-34] M.Huhtinen and P.A.Aarnio,HU-SEFT R 1994-07 (1994)

[6-35] J. Ranft and K. Goebel, Estimation of induced radioactivity around high energy accelerators from hadronic cascade star densities obtained from Monte Carlo calculations, CERN HP-70-92 (1970).

[6-36] A. Sullivan and T. Overton, Health Physics 11 (1965) 1101.

[6-37] CMS Collaboration, The ECAL Project Technical Design Report, CERN/LHCC 97-33 (1997).

[6-38] A. S. Iljinov et al., Production of Radionuclides at Intermediate Energies, Landolt-Börnstein, New Series Vols 13a-e, ed. H. Schopper, Springer (1991-1993).

[6-39] A. B. Chilton, J. K. Shultis and R. E. Faw, Principles of Radiation Protection, Prentice-Hall, 1984.

[6-40] P. A. Aarnio et al., FLUKA86 user's guide, CERN TIS-RP/168 (1986)
P. A. Aarnio et al., Enhancements to the FLUKA86 program (FLUKA87) CERN TIS-RP/190 (1987)
A. Fassò et al, FLUKA: present status and future developments, Proc IV Int. Conf. on Calorimetry in High Energy Physics, La Biodola, Sept 20-25, 1993, Ed. A. Menzione and A. Scribano, World Scientific, p. 493 (1993).
A. Fassò et al., FLUKA: performances and applications in the intermediate energy range, Specialists' Meeting on Shielding Aspects of Accelerators, Targets and Irradiation Facilities, Arlington, Texas, April 28-29, 1994

[7-1] CMSIM User's Manual and Reference Guide.

[7-2] GEANT3 – Detector Description and Simulation Tool, CERN Program Library entry W5013, CERN Geneva, Ed. March 1995.
R. Brun et al., GEANT3, CERN DD//EE/84–1, revised 1987.

[7-3] T. Sjöstrand, Computer Physics Commun. 82 (1994) 74.

[7-4] F.E. Page and S.D. Protopopescu, Isajet - A Monte Carlo event generator for pp and $\bar{p}p$ reaction.

[7-5] G. Marchesini et al., Computer Physics Communications 67 (1992) 465.

[7-6] Lynn Garren, Monte Carlo Standardization at FNAL, StdHep 3.01, PM0091.

[7-7] HBOOK - Statistical Analysis and Histogramming, CERN program library, Y250.

[7-8] T. Pitkänen and V. Karimäki, Hadron p_T generation for single particle simulation, CMS TN/96–131.

[7-9] R. Loveless and F. Feyzi, Magnetic and structural analysis of the CMS endcaps, CMS TN 94–277, 1994.

[7-10] H.Bichsel, Rev. of Mod. Phys., 60(1988)663.

[7-11] R.Kaufmann, Ph.D. thesis, Zuerich University (1997).

[7-12] V. Karimäki, Hit covariance formalism for stereo detectors, Nucl. Instr. and Meth. A374 (1996) 367 and CMS TN/95-170.

[7-13] F. Sauli, Principle of operation of multiwire proportional chambers, CERN 77-09, 1977.

[7-14] V. Palladino and B. Sadoulet, Application of classical theory of electrons in gases to drift proportional chambers, Nucl. Instr. and Meth. 128 (1975) 323.

[7-15] G.D. Alkhazov, Statistics of electron avalanches and ultimate resolution of proportional counters, Nucl. Instr. and Meth. 89 (1970) 155.

[7-16] G.D. Alkhazov, Mean value and variance of gas amplification in proportional counters, Nucl. Instr. and Meth. 75 (1969) 161.

[7-17] F. Lapique and F. Piuz, Simulation of the measurements by primary cluster counting of the energy lost by a relativistic ionising particle in Argon, Nucl. Instr. and Meth. 175 (1989) 297.

[7-18] F. Fulda-Quenzer et al., Measurement of longitudinal and transverse diffusion of single electrons drifting in gases, Nucl. Instr. and Meth. A235 (1985) 517.

[7-19] M. Geijsbert et al., Test of the performance of different gas mixtures in MSGC, Nucl. Instr. and Meth. A313 (1992) 377.

[7-20] J. Schmitz, Results on Monte Carlo simulation of MSGC, Nucl. Instr. and Meth. A323 (1992) 638.

[7-21] H. Fischle et al., Experimental determination of ionisation cluster size distribution in counting gases, Nucl. Instr. and Meth. A301 (1991) 202.

[8-1] R. Frühwirth, NIM A262 (1987) 444

[8-2] N. Stepanov and A. Khanov, Local Track Finder, CMS NOTE/1995-200.

[8-3] V. Karimäki, Effective vertex fitting, CMS NOTE/1997–051.

[8-4] N. Stepanov and A. Khanov, NIM A389 (1997) 177

[8-5] M. Ohlsson et al., Comput. Phys. Commun. 71 (1992) 77

[8-6] Dempster A.P., Laird N.M. and Rubin D.B, J. Royal Stat. Soc. B39 (1977) 1

[8-7] S. Kirkpatrick, C.D. Gelatt and M.P. Vecchi, Science 220 (1983) 671.

[8-8] A. Bondar et. al, Influence of misalignment on CMS Tracker performance, CMS IN/1997–016.

[8-9] V. Karimäki, Explicit covariance matrix for particle measurement precision, CMS NOTE/1997–064, to be published in NIM A.

[9-1] M. Konecki and A. Starodoumov, $b\bar{b}$ Events Simulation Package, Users Manual, available at http://cmsdoc.cern.ch/user/b/bphys/BPHYS/TNCMS/manual.ps

[9-2] G. Wrochna, Muon trigger for heavy ion physics, CMS note 1997/89.

[9-3] See for example, E.V. Shurayak, Quark Matter 90, Nucl. Phys. A525 (1991) 3.

[9-4] CMS - The Muon Project, Technical Design Repor, CERN/LHCC 97–32.

[9-5] M. Bedjidian, Heavy ion beams in CMS and dimuons detection, CMS TN/95–188.

[9-6] K. Eggert and A. Morsch, AT Group Report 95–01 (DI).

[9-7] F. Antinori, Internal Note, ALICE/MC 93–09.

[9-8] O. Kodolova and M. Bedjidian, Pattern recognition and track reconstruction in heavy ion collisions, CMS TN/95–124.

[9-9] O. Kodolova and M. Bedjidian, Dimuon reconstruction in heavy ion collisions, CMS NOTE 1997/095.

[A-1] P. A. Aarnio and M. Huhtinen, Hadron fluxes in inner parts of LHC detectors, Nucl. Instr. and Meth. A336 (1993) 98.

[A-2] M. Huhtinen and C. Seez, Uncertainties in fluences and doses at the CMS inner tracker, CERN CMS TN/95-133 (1995).

[A-3] M. Huhtinen, Radiation Environment simulations for the CMS detector, Proc. of SARE2 workshop, CERN/TIS-RP/97-05 (1997) also CERN CMS TN/95-198 (1995).

[A-4] M. Huhtinen, Studies of neutron moderator configurations around the CMS inner tracker and ECAL, CERN CMS TN/96-057 (1996).

[A-5] M. Huhtinen and P. Aarnio, Pion induced displacement damage in silicon devices, Nucl. Instr. and Meth. A335 (1993) 580.

[A-6] P. Aarnio et al., Damage observed in silicon diodes after low energy pion irradiation, Nucl. Instr. and Meth. A360 (1995) 521.
S. Bates et al., Pion induced damage in silicon detectors, Nucl. Instr. and Meth. A379 (1996) 116.

[A-7] ASTM Annual book of standards, vol 10.02 (1985) 323.

[A-8] K. Potter and G. R. Stevenson, Average interaction rates for shielding specification in high-luminosity LHC experiments, CERN LHC Note 310 (1995).

[A-9] M. Hoefert, K. Potter and G. R. Stevenson, Summary of design values, dose limits, interaction rates etc for use in estimating radiological quantities associated with LHC operation, CERN TIS-RP/IR/95-19.1 (1995).

[A-10] M. Huhtinen, Method for Estimating Dose rates from Induced Radioactivity in Complicated Hadron Accelerator Geometries, to be published.

[A-11] R. Thomas and G. Stevenson, Radiological Safety Aspects of the Operation of Proton Accelerators, IAEA Technical Report Series 283 (1988).

[A-12] J. Ranft, DPMJET-II, a Dual Parton Model event generator for hadron-hadron, hadron-nucleus and nucleus-nucleus collisions, Presented at SARE2 workshop, CERN, 9-11 October, 1995, Proceedings: CERN/TIS-RP/97-05 (1997)

[A-13] P. Aurenche et al., DTUJET-93: sampling inelastic proton-proton and antiproton-proton collisions according to the two-component Dual Parton Model, Computer Physics Commun. 83 (1994) 107.

[A-14] T. Sjöstrand, High energy physics event generation with PYTHIA 5.7 and JETSET 7.4, Computer Physics Commun. 82 (1994) 74.

[A-15] P. A. Aarnio et al., FLUKA86 user's guide, CERN TIS-RP/168 (1986)
P. A. Aarnio et al., Enhancements to the FLUKA86 program (FLUKA87) CERN TIS-RP/190 (1987)
A. Fassò et al, FLUKA: present status and future developments, Proc IV Int. Conf. on Calorimetry in High Energy Physics, La Biodola, Sept 20-25, 1993, Ed. A. Menzione and A. Scribano, World Scientific, p. 493 (1993).
A. Fassò et al., FLUKA: performances and applications in the intermediate energy range, Specialists' Meeting on Shielding Aspects of Accelerators, Targets and Irradiation Facilities, Arlington, Texas, April 28-29, 1994

[A-16] W. Nelson, H. Hirayama, D. Rogers, The EGS4 code system, Report SLAC-265 (1985).

[A-17] P. Aarnio et al., Electron-Photon transport: always so good as we think? Experience with FLUKA, CERN TIS-RP/93-10 (1993).

[A-18] A. Fassò et al, A comparison of FLUKA simulations with Measurements of fluence and dose in calorimeter structures, Nucl. Instr. and Meth. A332 (1993) 459.
C. Birattari et al, Measurement and characterization of high energy neutron fields, Nucl. Instr. and Meth. A338 (1994) 534.

[A-19] A. S. Iljinov et al., Production of Radionuclides at Intermediate Energies, Landolt-Börnstein, New Series Vols 13a-e, ed. H. Schopper, Springer (1991-1993).

[A-20] P. A. Aarnio, CERN CMS NOTE in preparation.

[A-21] P. A. Aarnio and M. Huhtinen, CERN CMS NOTE in preparation.

[A-22] T. F. Luera, et al, Neutron damage equivalence for silicon, silicon dioxide and gallium arsenide, IEEE Tarns. Nucl. Sci., Vol. NS-34, No. 6 (1987) 1557.

[A-23] M. Huhtinen, Factors to scale highly ionizing particle rates in MSGC irradiation tests to the LHC radiation environment, CERN CMS NOTE 1997/073 (1997).

Appendix C

Colour Pictures

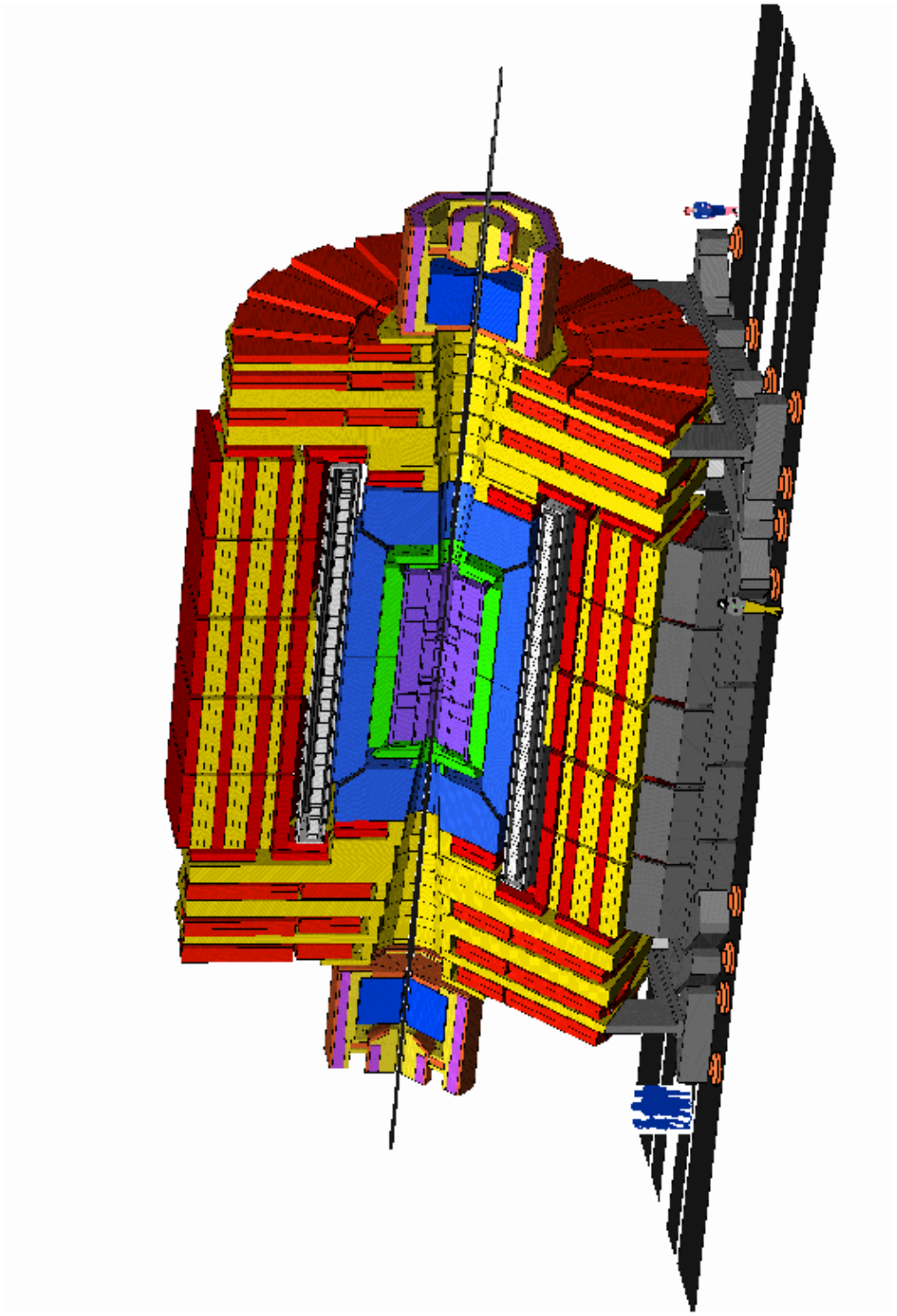

Fig. 1.i: Overall view of the CMS detector.

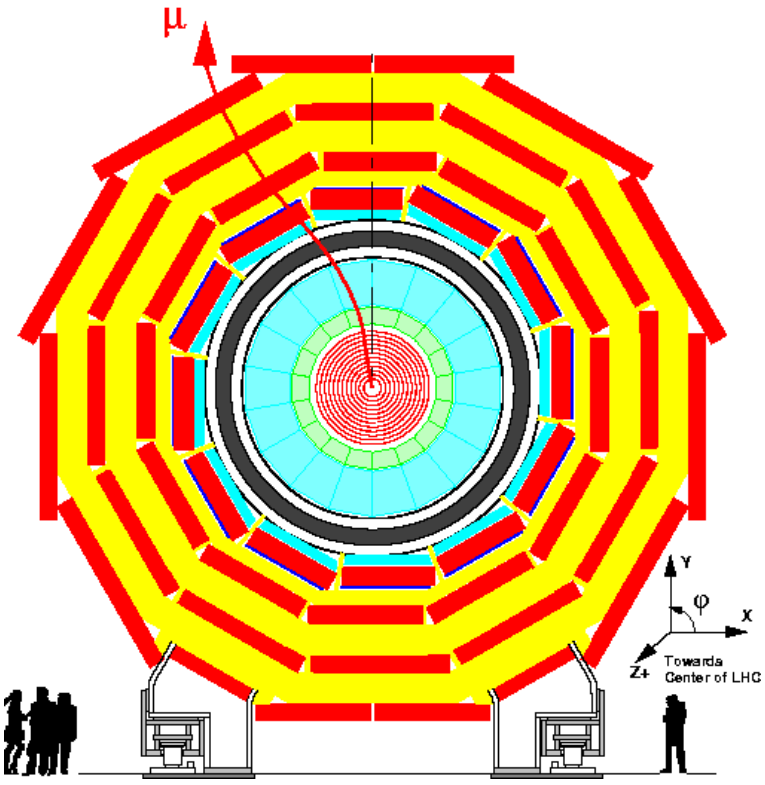

Fig. 1.ii: Transverse view of the CMS detector.

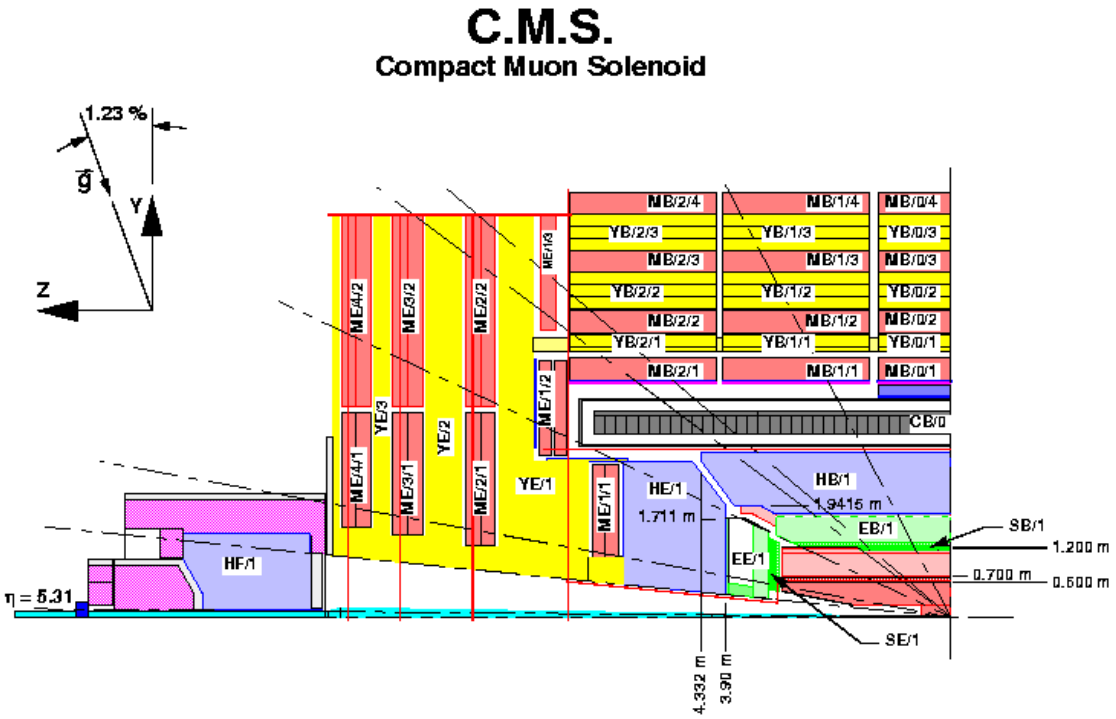

Fig. 1.iii: Longitudinal view of the CMS detector.

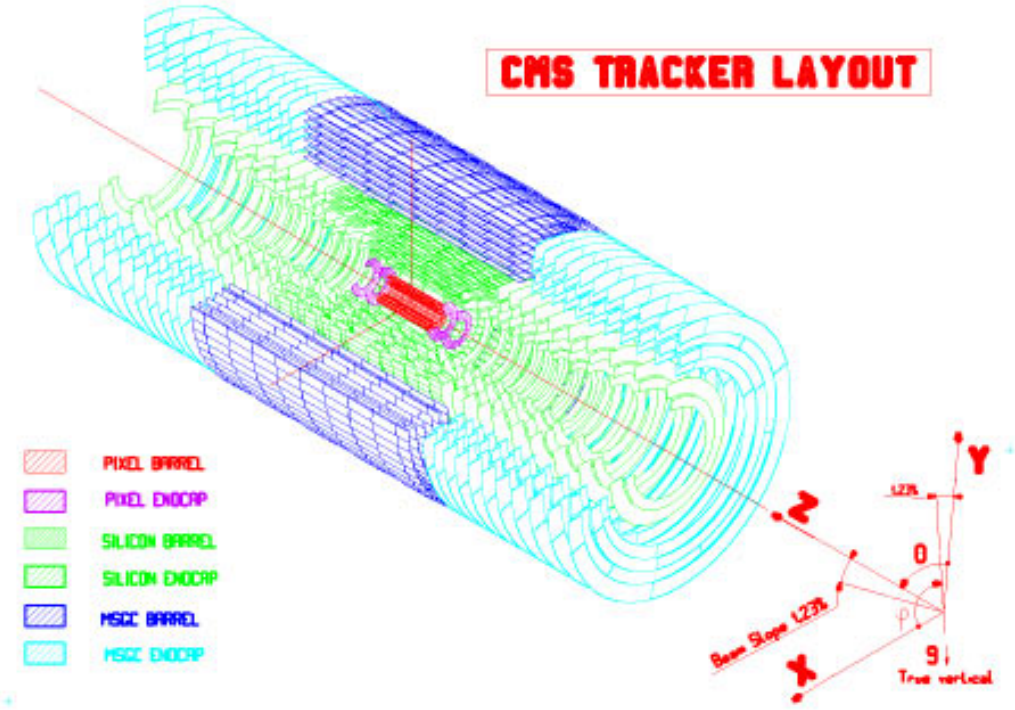

Fig. 1.iv: Geometry of active detector elements.

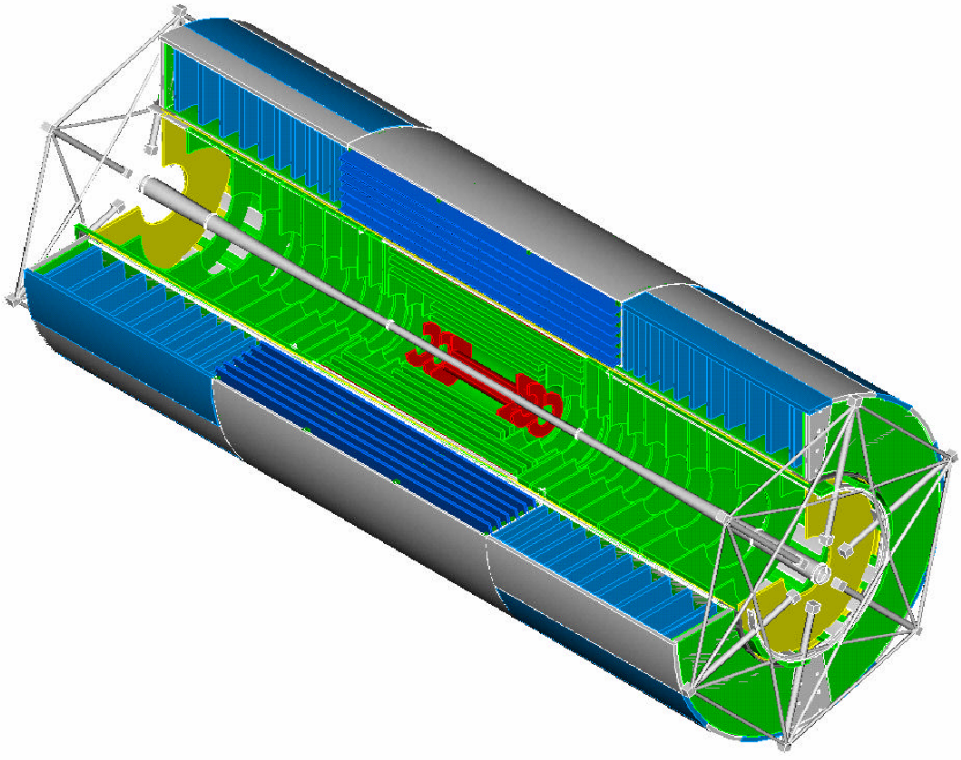

Fig. 1.v: Support structures.

Fig. 3.i: SiB1 barrel module.

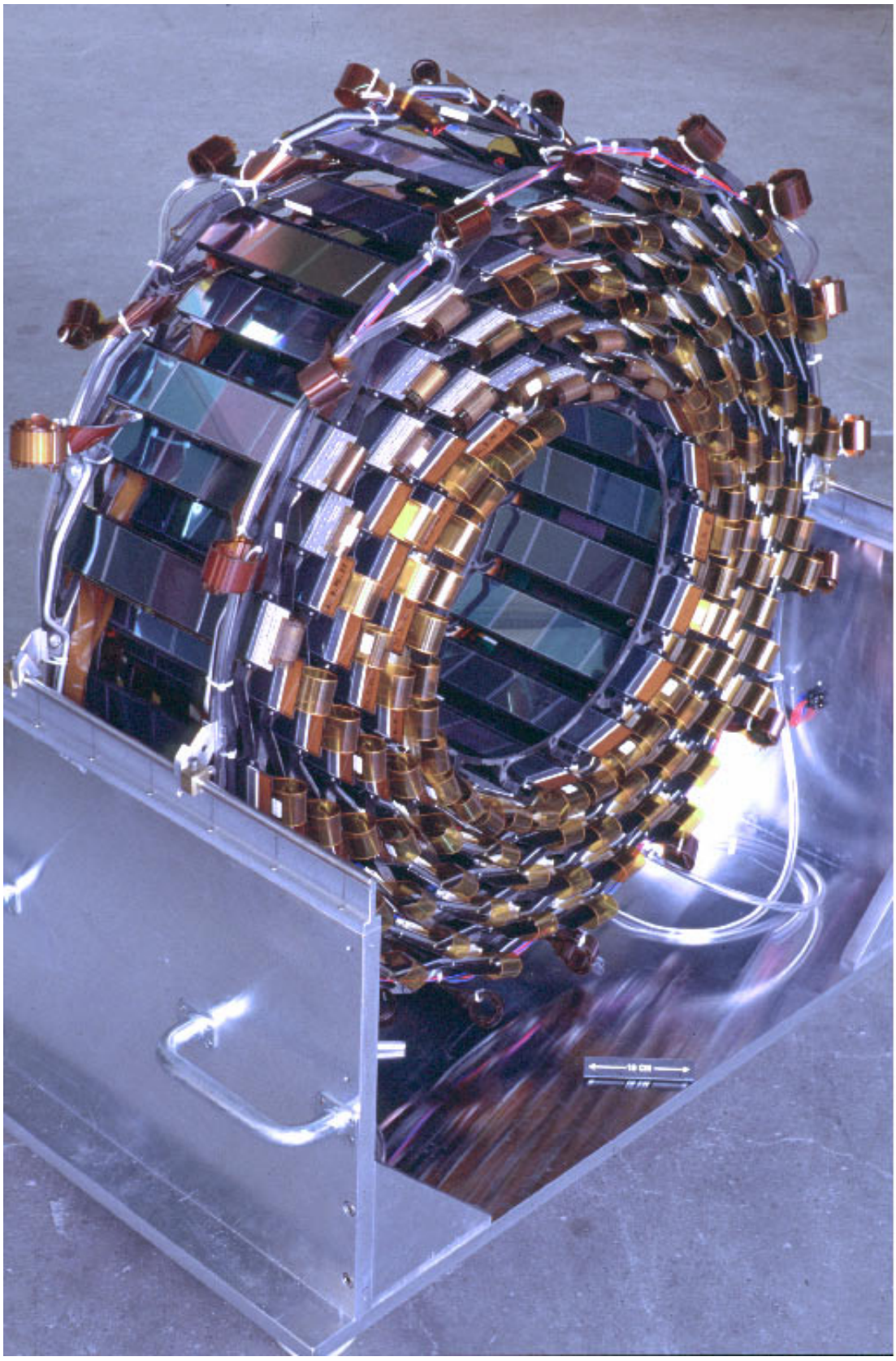

Fig. 3.ii: The fully equipped SiB1 wheel.

Fig. 3.iii: SiF1 endcap module.

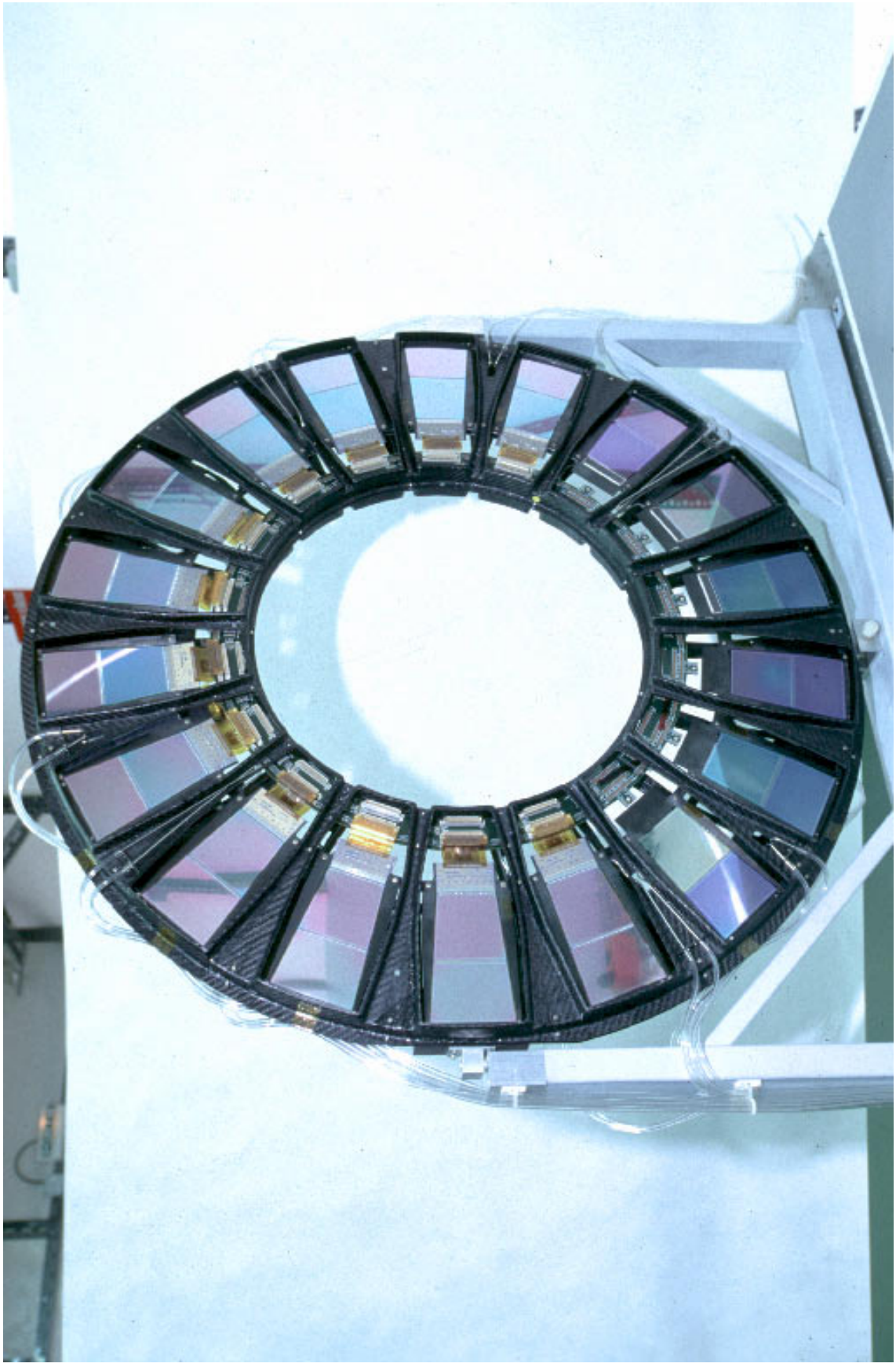

Fig. 3.iv: SiF1 fully equipped disk.

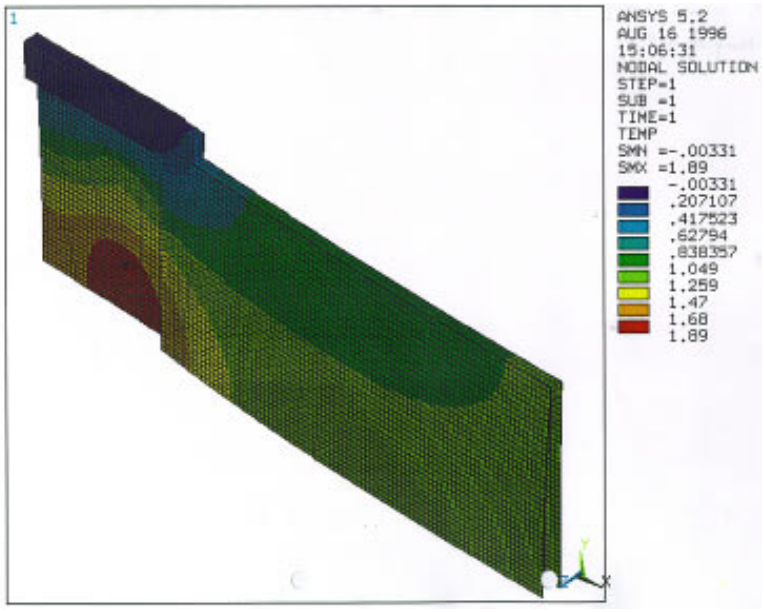

Fig. 4.i: Relative temperature distribution over a MSGC barrel module equipped with a 1 W power hybrid.

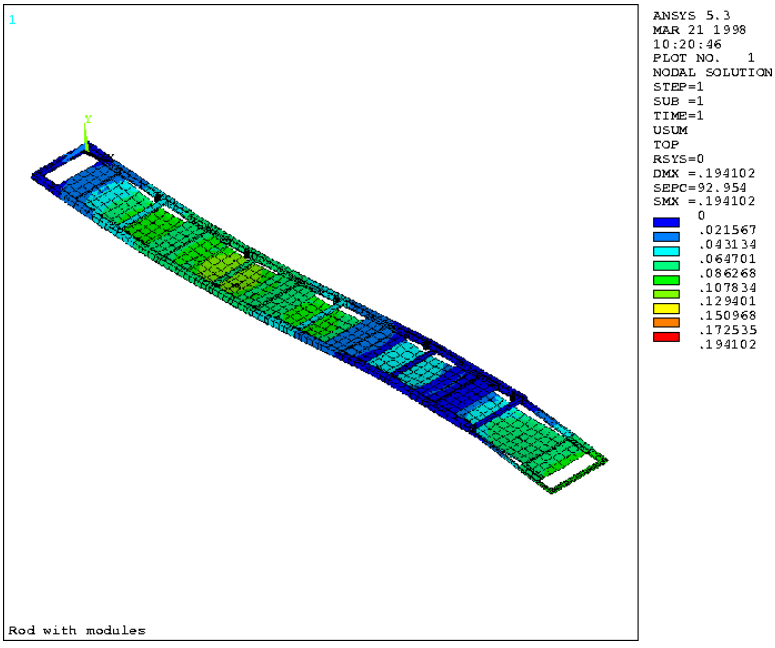

Fig. 4.ii: The MSGC barrel rod under gravitational loads: maximum effective displacements are about 100 μm.

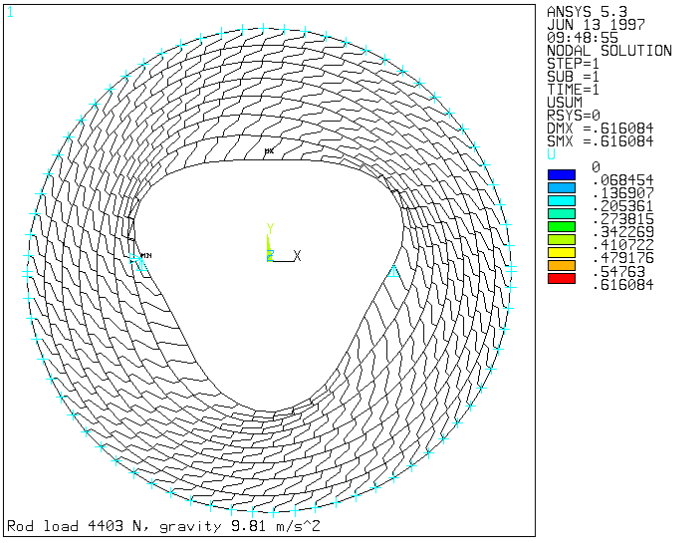

Fig. 4.iii: FEA model of the MSGC barrel disk with beam elements. The disk is supported at the side of the inner radius.

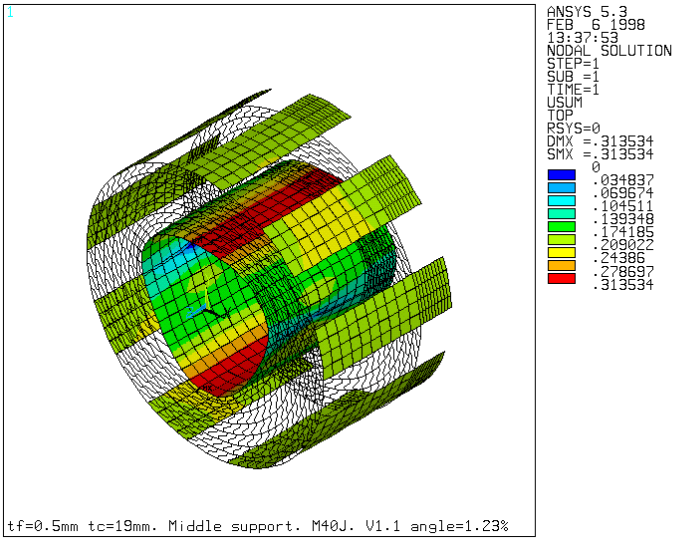

Fig. 4.iv: Maximum distortions (mm) of the inclined MSGC barrel wheel under full load. Only a half wheel is analysed due to the symmetry of the structure.

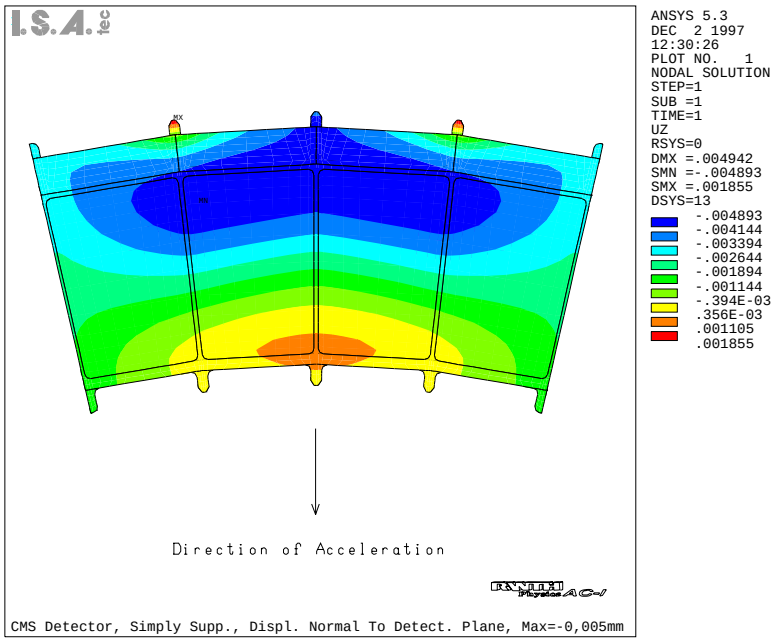

Fig. 4.v: FEA result: Gravitational sag on a forward MSGC detector module located on the top part of the disk as indicated by the arrow. Results are given in μm.

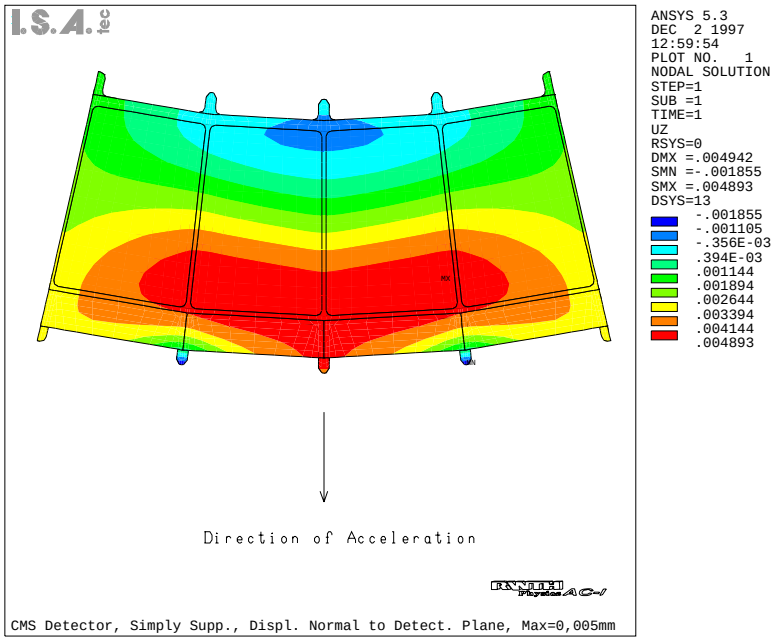

Fig. 4.vi: FEA result: Gravitational sag on a forward MSGC detector module located on the bottom part of the disk as indicated by the arrow. Results are given in μm.

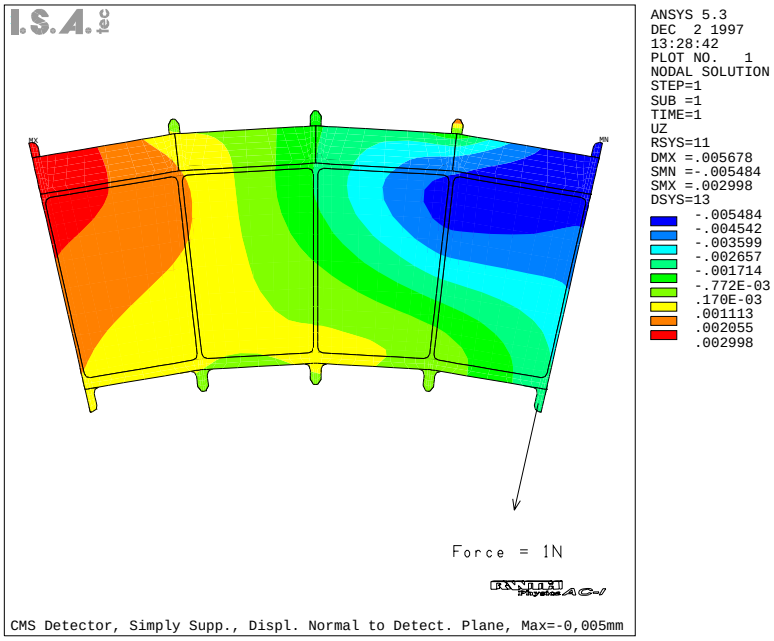

Fig. 4.vii: FEA result: Deformation (μm) of a forward MSGC detector module due to a force resulting from the gas connection. The force is acting radially.

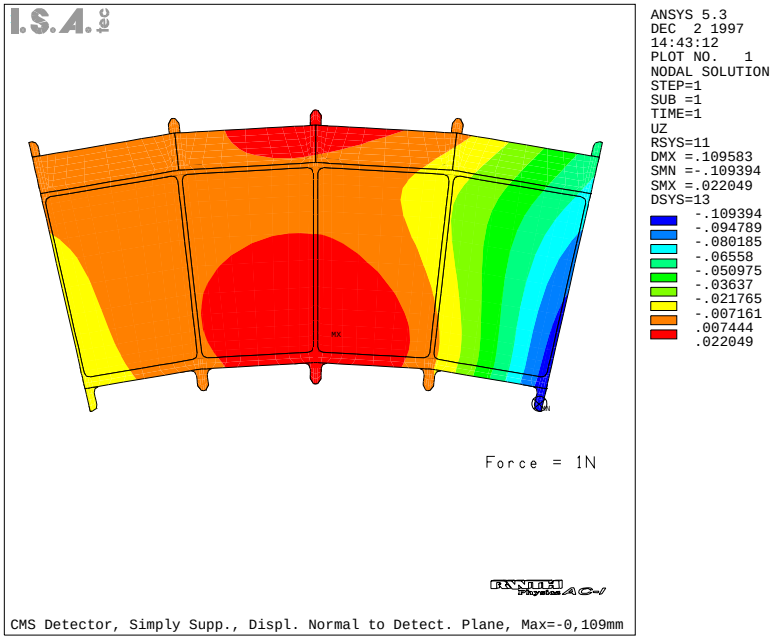

Fig. 4.viii: FEA result: Deformation (μm) of a forward MSGC detector module due to a force resulting from the gas connection. The force is acting perpendicular to the detector plane.

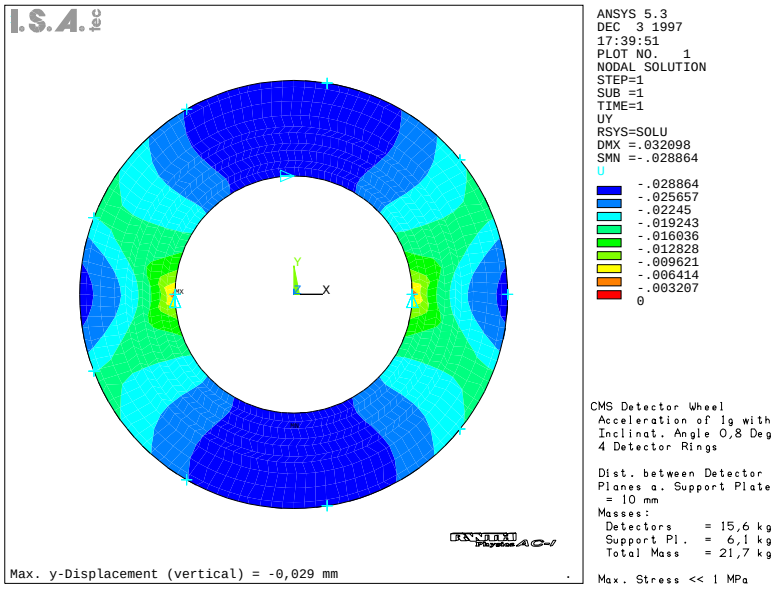

Fig. 4.ix: In-plane deformation of a forward MSGC support disk.

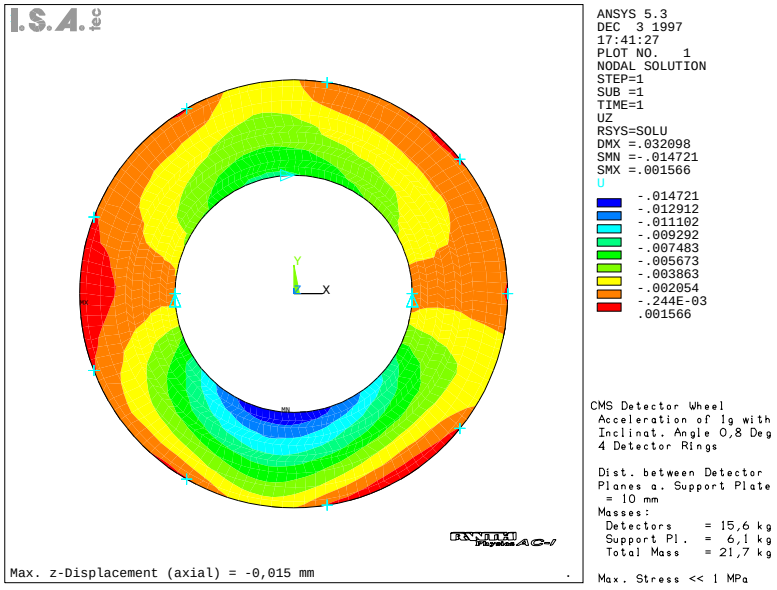

Fig. 4.x: Out-of-plane deformation of a forward MSGC support disk.

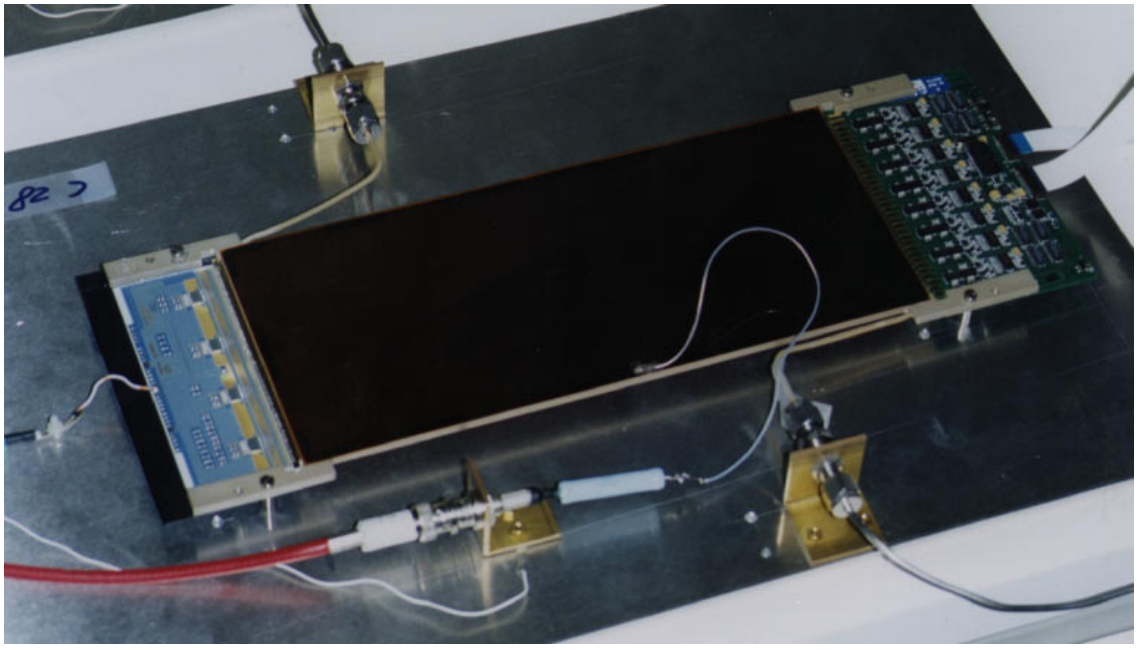

Fig. 4.xi: The MSGC B1 module under test.

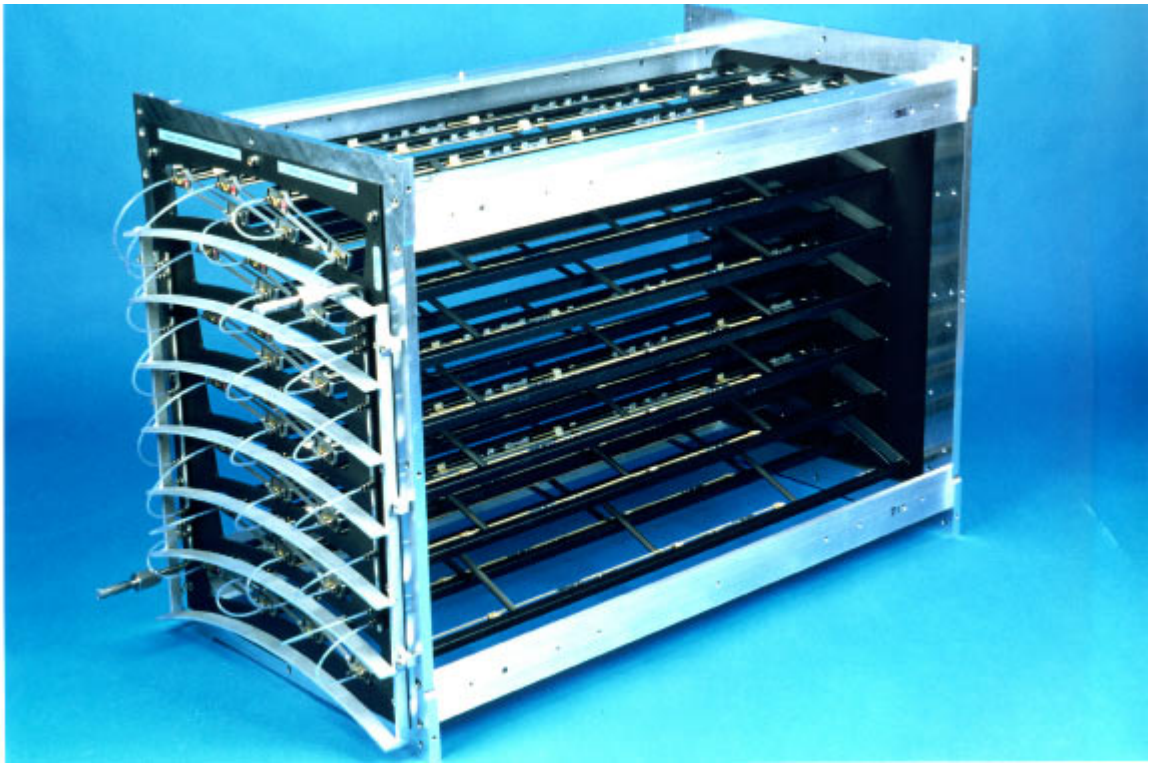

Fig. 4.xii: The MSGC B1 milestone. Sixteen rods are installed in the mechanical structure. Water and gas pipes, that act as cable supports, are visible on the front plane.

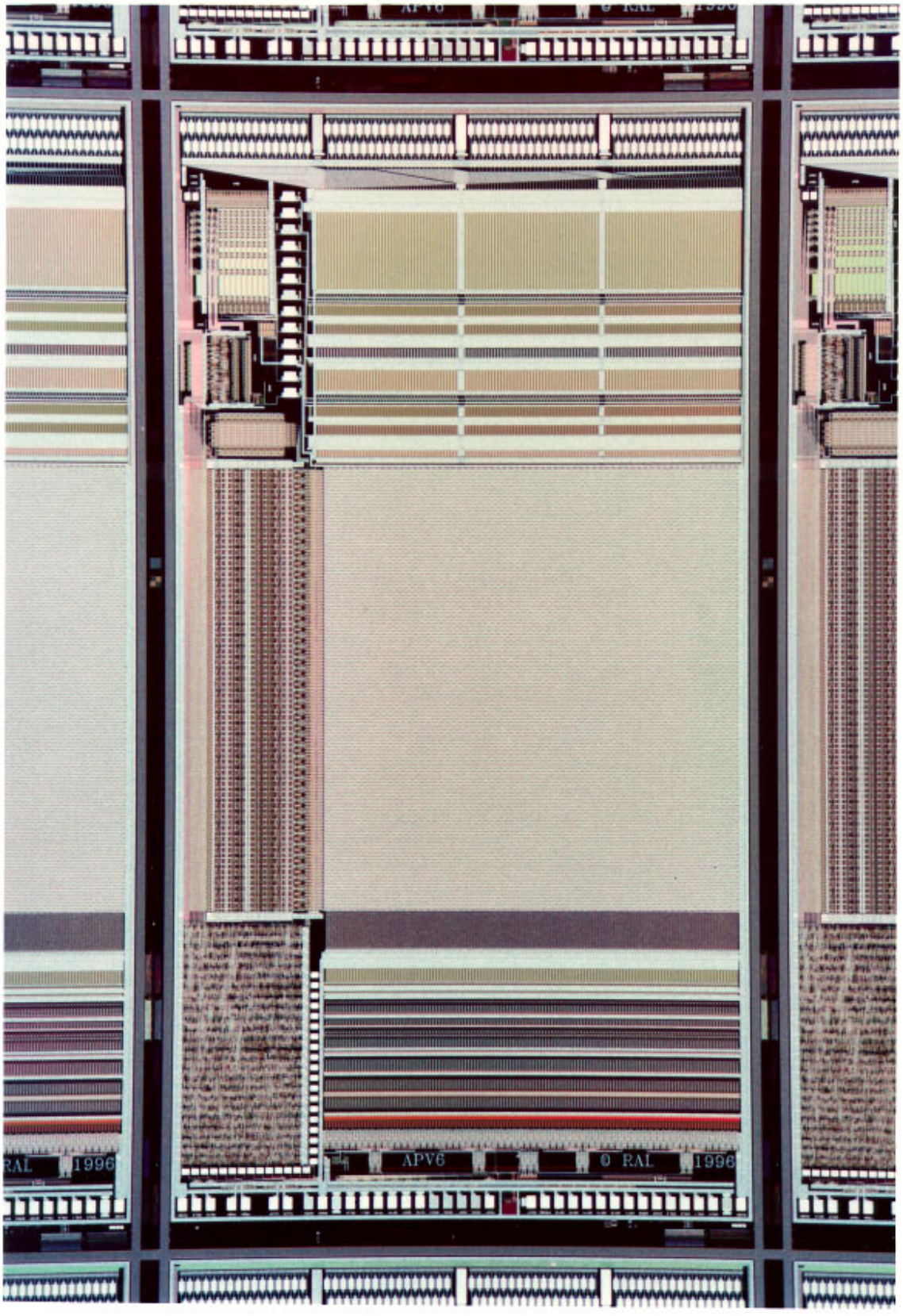

Fig. 5.i: The APV6 front-end readout circuit, prototyped in a radiation hard CMOS technology. The chip dimensions are $6.4 \times 12.0\,\mathrm{mm}^2$. The largest area is occupied by the pipeline, in the centre of the chip. Preceding the pipeline are the amplifier stages and following it are the signal processing and multiplexing.

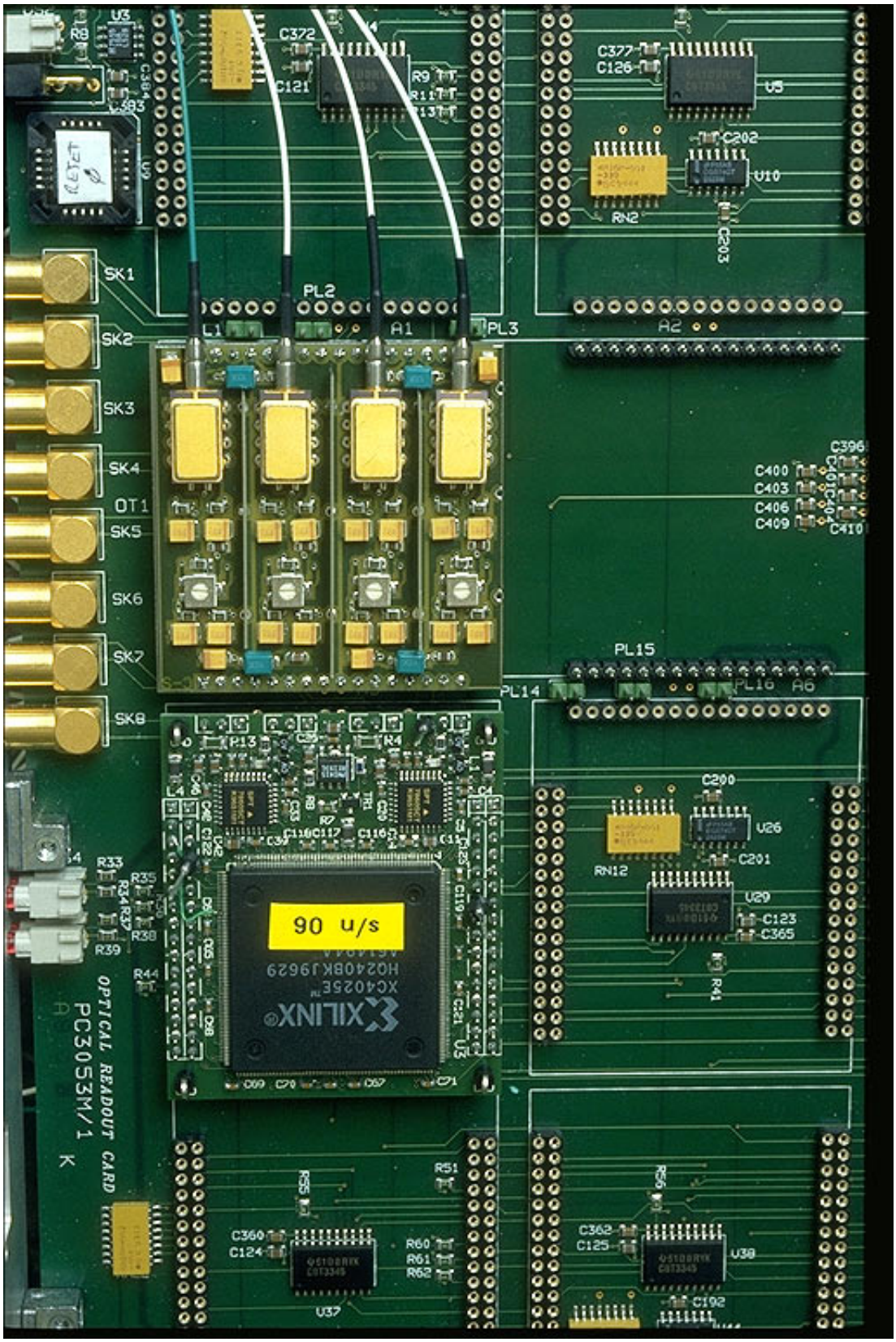

Fig. 5.ii: A series of prototype laser emitters coupled to optical fibres which are used for studies of the analogue optical link. They differ from the final version only in the external packaging and that up to four transmitters will be assembled into a single unit. They are seen mounted on a prototype Front End Driver module.

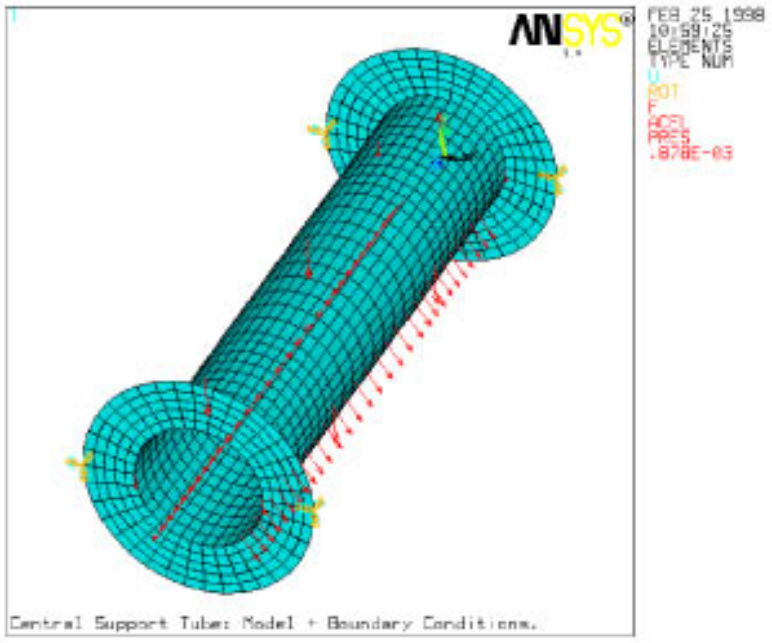

Fig. 6.i: Mesh, constraints and load distribution used in the FEA calculations of the Tracker central support tube.

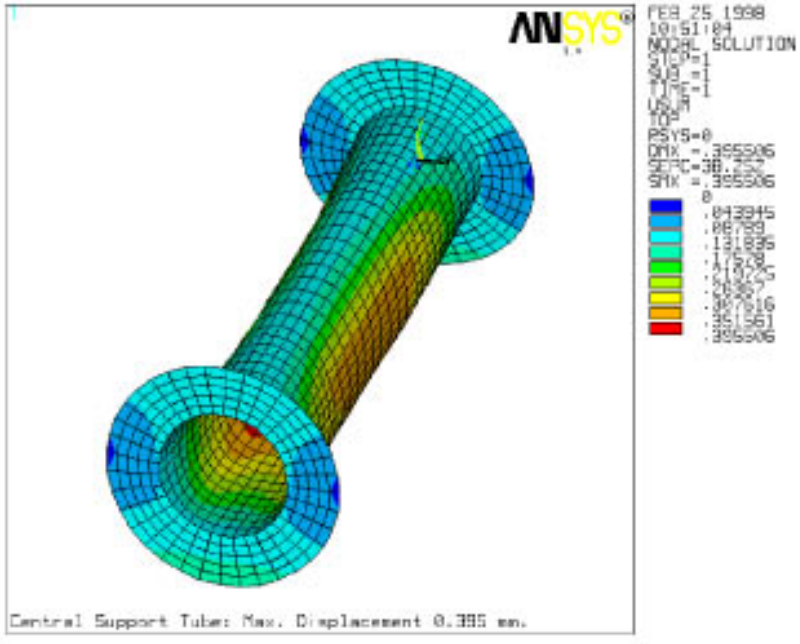

Fig. 6.ii: Deformed shape calculated for the central support tube, indicating a maximal deformation of about 400 μm.

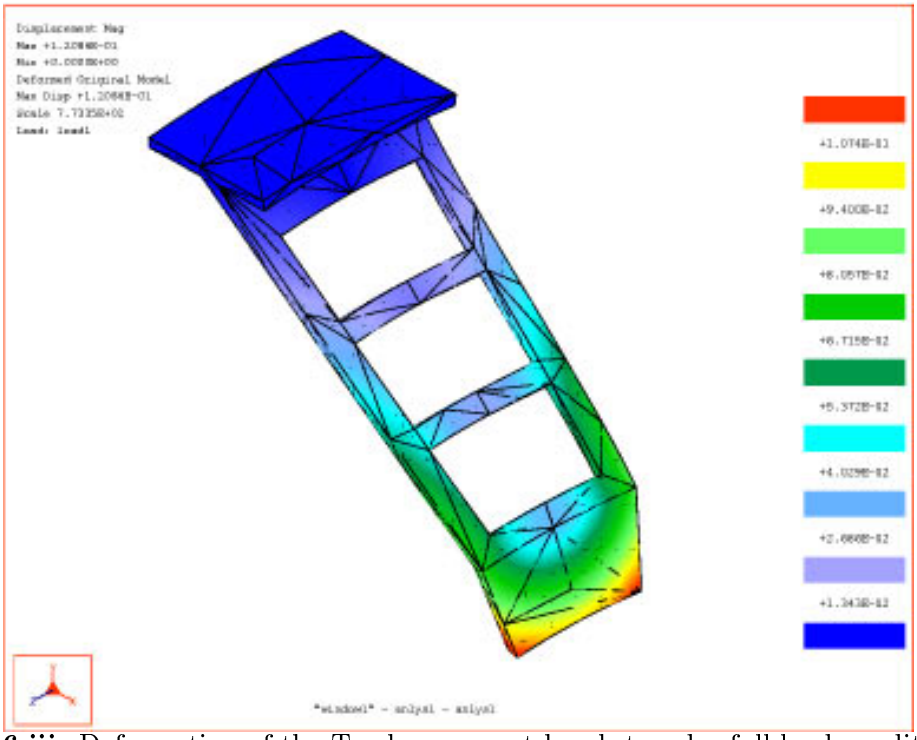

Fig. 6.iii: Deformation of the Tracker support bracket under full load conditions.

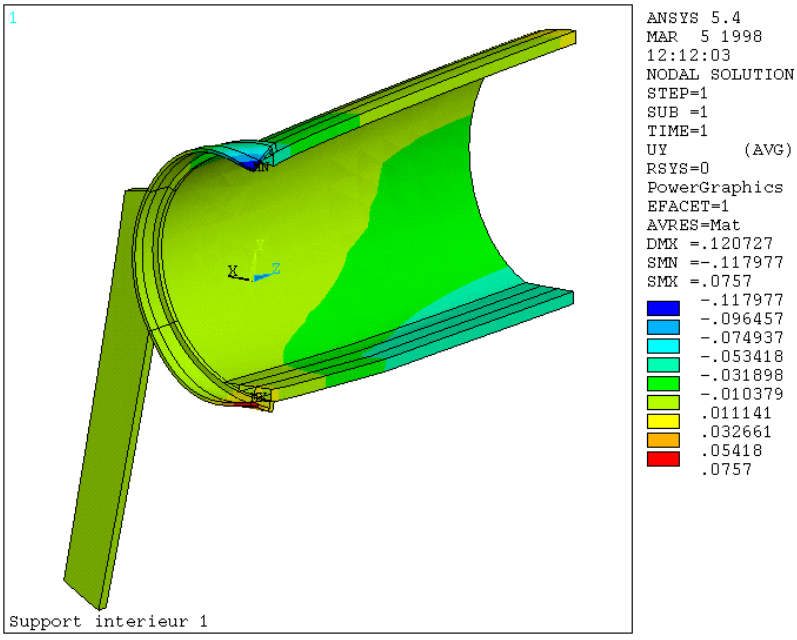

Fig. 6.iv: Output of FEA for the inner Pixel and beam pipe support.

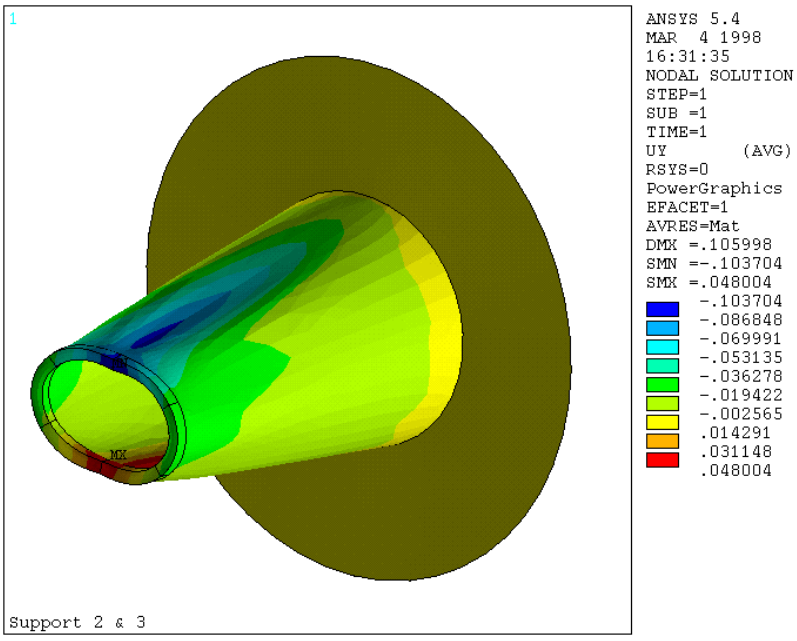

Fig. 6.v: Deformations calculated for the intermediate beam pipe support.

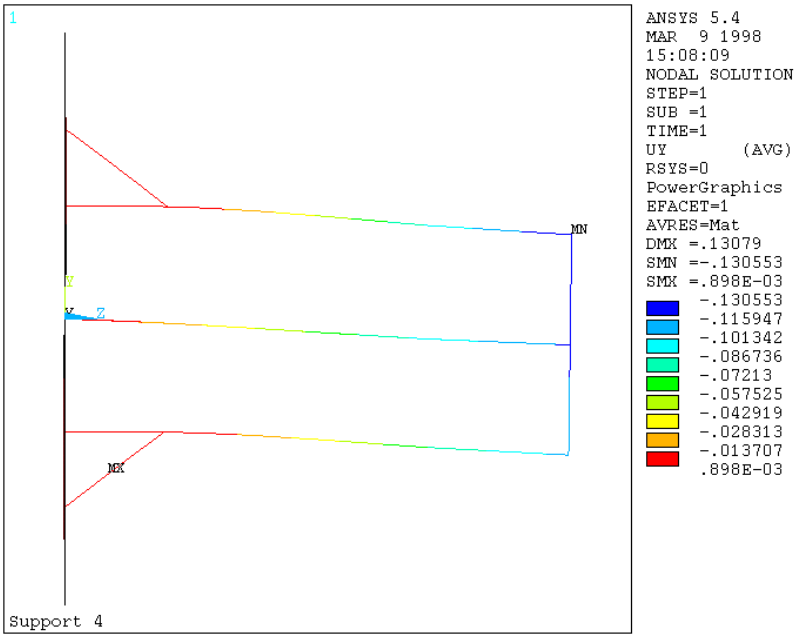

Fig. 6.vi: Deformations calculated for the outer beam pipe support.

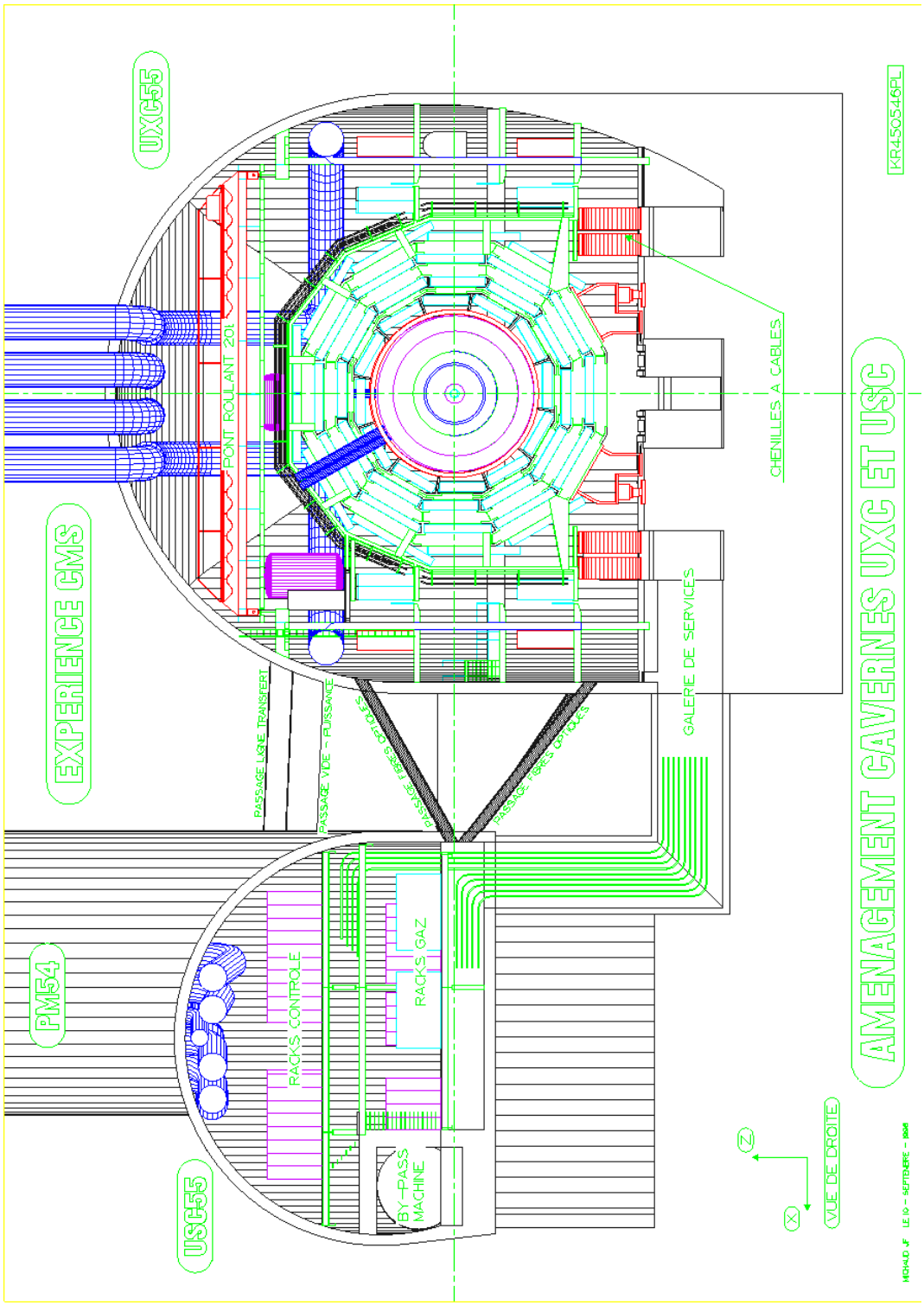

Fig. 6.vii: Optical fibre cable path.

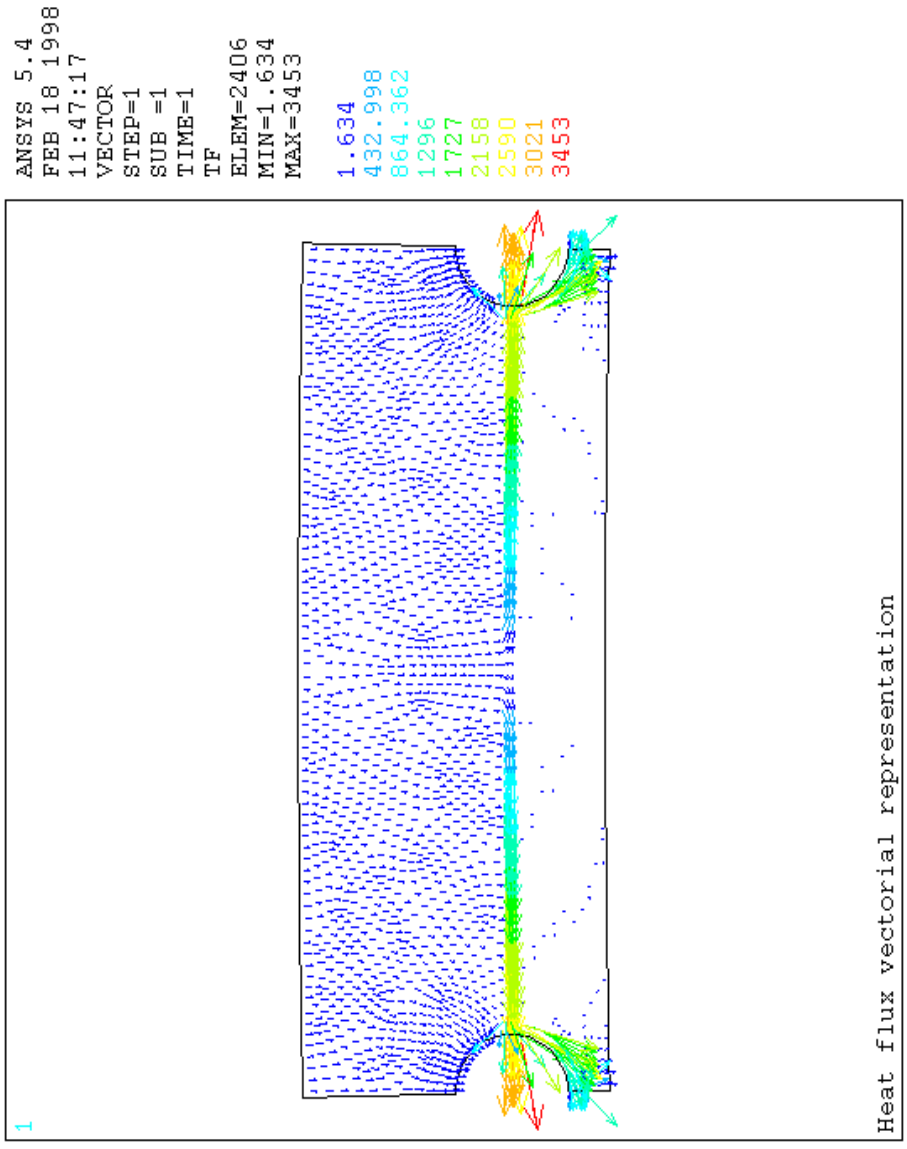

Fig. 6.viii: Vectorial representation of the heat flux in the thermal screen separating the SST and MSGC volumes.

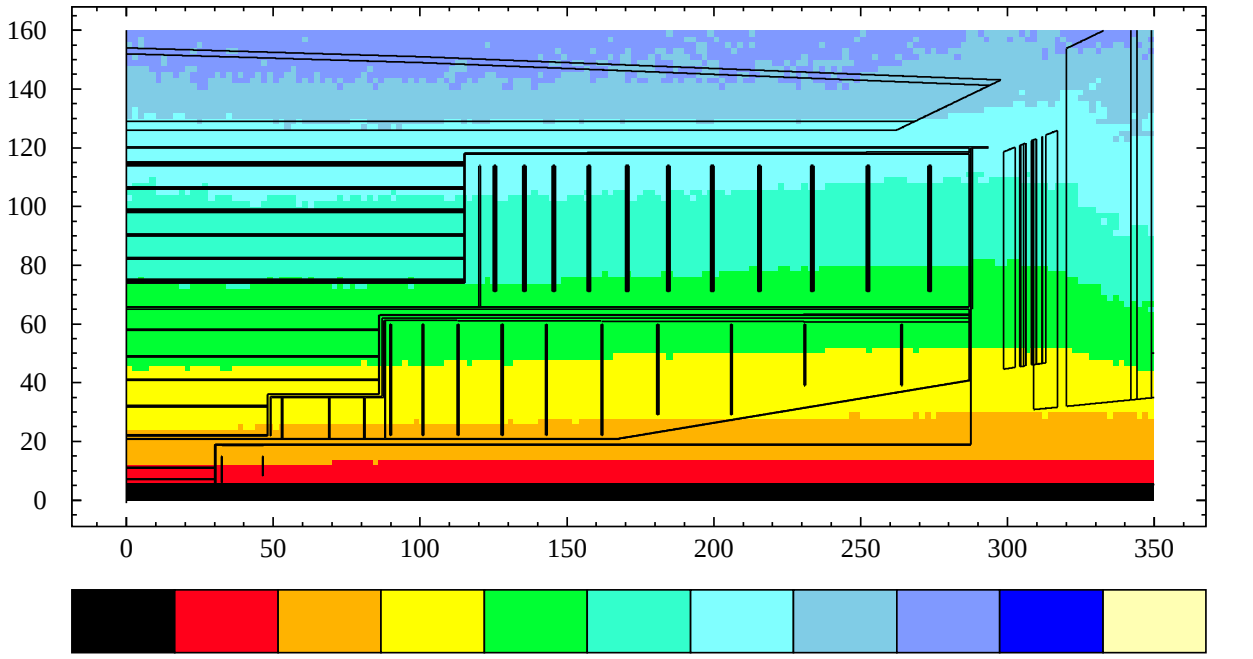

Fig. A.i: Charged hadron fluences (cm^{-2}) in the CMS Tracker. Values correspond to an integrated luminosity of 5×10^5 pb^{-1}.

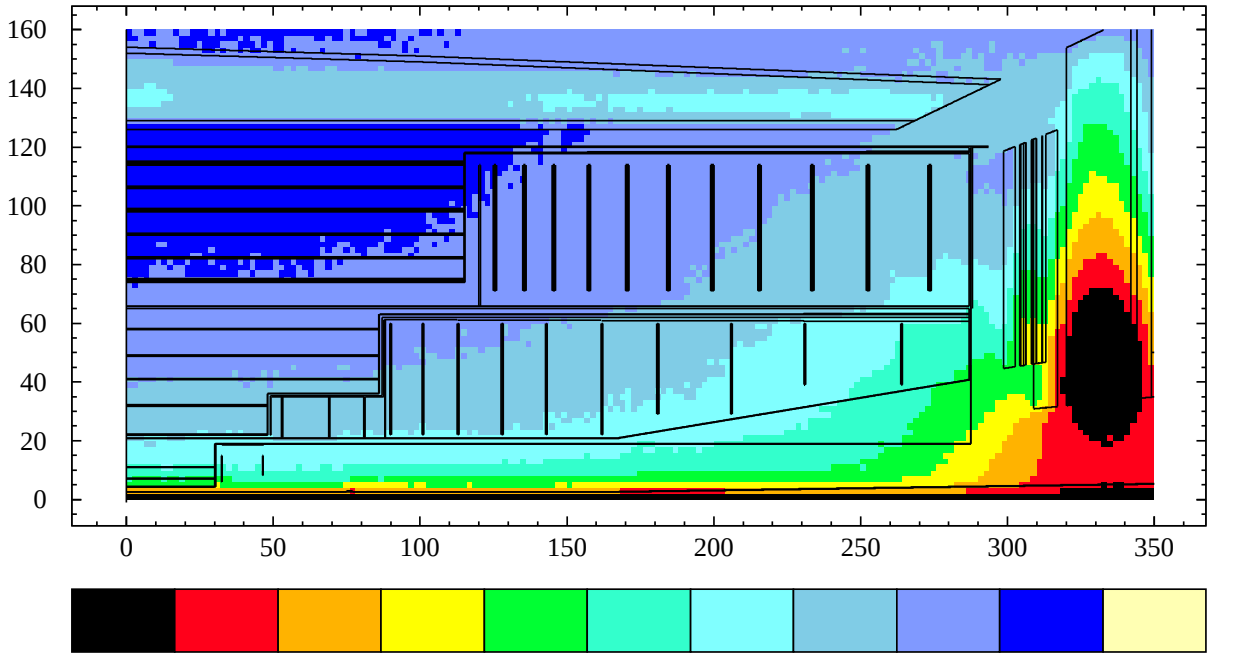

Fig. A.ii: E>100 keV neutron fluences (cm^{-2}) in the CMS Tracker. Values correspond to an integrated luminosity of 5×10^5 pb^{-1}.